SINTEF
PROCEEDINGS 11

ICEC 2026 – the 33rd International Conference on Electrical Contacts
Trondheim, Norway, 21 – 25 June, 2026

Proceedings of the 33rd International Conference on Electrical Contacts



ICEC 2026

SINTEF

SINTEF Proceedings

Editors:
Magne Runde, Kaveh Niayesh, Åsa Kassman Rudolphi

Proceedings of the 33rd International Conference on Electrical Contacts

Trondheim, Norway
21–25 June, 2026

SINTEF Academic Press

SINTEF Proceedings 11
Editors: Magne Runde[1], Kaveh Niayesh[2], Åsa Kassman Rudolphi[3]

[1] SINTEF Energy Research, https://www.sintef.no/en/sintef-energy/
[2] Norwegian University of Science and Technology (NTNU), https://www.ntnu.edu/
[3] Uppsala University, https://www.uu.se/en

Proceedings of the 33rd International Conference on Electrical Contacts
Trondheim, Norway, 21–25 June, 2026

Cover illustration: ICEC-logo
150 copies printed by Merkur Grafisk

ISSN 2387-4295 (online)
ISBN 978-82-536-1888-3



© The Authors. Published by SINTEF Academic Press 2026.
SINTEF has the right to publish the conference contributions in this publication.
This is an open access publication under the CC BY-NC-ND license, https://creativecommons.org/licenses/by-nc-nd/4.0/

SINTEF Academic Press
Address: Børrestuveien 3
PO Box 124 Blindern
N-0314 OSLO
Tel: +47 40 00 51 00

www.sintef.no/community
www.sintefstore.no

SINTEF Proceedings
SINTEF Proceedings is a serial publication for peer-reviewed conference proceedings on a variety of scientific topics.
The processes of peer-reviewing of papers published in SINTEF Proceedings are administered by the conference organizers and proceedings editors. Detailed procedures will vary according to custom and practice in each scientific community.

Conference Chair's Message

It is my great pleasure to welcome you to the **33rd International Conference on Electrical Contacts**. This marks the first time ICEC is held in Norway and only the second time in Scandinavia, following the 2000 conference in Stockholm, Sweden.

The technical program over the coming days features 56 paper presentations organized into 14 sessions. These contributions have authors from 15 countries. The papers show the broad scope of our field, covering applications ranging from milliamp to kiloamp circuits, arcing and non-arcing contacts, stationary and sliding contacts, as well as both AC and DC applications. The program also addresses a wide array of related topics, including materials science, environmental effects, diagnostics, reliability, and more.

In addition to the paper presentations, we are pleased to offer two invited talks. René Smeets will present on the challenges associated with replacing SF_6—the most potent greenhouse gas known—in high-voltage switchgear. John Marsh will focus on sustainable design approaches for contacts and connectors. Both topics reflect pressing regulatory developments that are already shaping our industry and will continue to have a significant impact in the years ahead.

I would also like to acknowledge our sponsors, whose generous support has been essential in making this conference possible. I encourage you to visit their stands and learn more about their latest products and innovations.

Beyond the technical program, ICEC provides a valuable opportunity to connect with colleagues, friends, and collaborators from around the world. We also hope you enjoy your stay in Trondheim and take some time to explore this historic city, with its rich heritage spanning more than a thousand years.

On behalf of the conference organizers, I warmly welcome you to Trondheim and to ICEC 2026.

Magne Runde
Conference Chair

History of the Conference

The first International Conference on Electrical Contacts was organised by Dr. Ragnar Holm and Professor R. E. Armington in 1961 and took place at the University of Maine, in Orono, USA. Since then, the Conference has been held every two years at venues around the world.

The ICEC has become recognized as the principal worldwide meeting place for electrical contact scientists and engineers. It is a forum for the presentation and discussion of research on contact phenomena, developments in technologies and advancement in manufacture of a whole range of connective devices.

Recent Venues

- 2024 Annapolis, Maryland, USA
- 2022 Sapporo, Japan
- 2020 Online in 2021 from Switzerland
- 2018 Albuquerque, New Mexico, USA
- 2016 Edinburgh, United Kingdom
- 2014 Dresden, Germany
- 2012 Beijing, China
- 2010 Charleston, South Carolina, USA
- 2008 Saint Malo, France

Conference sponsors

We proudly acknowledge the ICEC 2026 sponsors:

GOLD SPONSORS

FUDAR

Heraeus Precious Metals | Choksi Heraeus

Hindustan Platinum

SAXONIA® TECHNICAL MATERIALS

SILVER SPONSORS

ABB

ECL Electrical Contacts Limited

ELECTRACON PARADISE

Littelfuse®

Organizing Committee

The ICEC 2026 is a Norwegian – Swedish collaboration.

- Magne Runde (Conference Chair), SINTEF Energy Research
- Kaveh Niayesh (Conference co-Chair), Norwegian University of Science and Technology (NTNU)
- Åsa Kassman Rudolphi (Conference co-Chair), Uppsala University
- Professional Congress Organizer (PCO): NTNU Conferences

The International Advisory Group

- M. Runde (Chairman), Norway
- J.W. McBride (Vice Chairman), United Kingdom
- Th. Schoepf (Secretary), Honorary Member
- F. Berger, Germany
- Ch. Kroepfl, Austria
- R.S. Timsit, Canada
- X. Li, China
- S. Noël, France
- M. Hasegawa, Japan
- P. Jaeger, The Netherlands
- Å. Kassman, Sweden
- W. Johler, Switzerland
- P.G. Slade, U.S.A.
- P. Borkowski, Poland

Reviewers

Vincent Andarud
Margarita Baeva
Frank Berger
Piotr Borkowski
Isabell Buresch
Zhuanke Chen
Pierre Corfir
Yann Cressault
Naghme Dorraki
George Flowers
Diego Gonzalez
Sergey Gotschakow
Lukas Graber
Tag Hammam
Makoto Hasegawa
Johannes Herrmann
Engelbert Hetzmannseder
Christian Hildmann
Toni Israel
Peter Jaeger
Werner Johler
Åsa Kassman Rudolphi
Chistian Kröpfl
Tom Kufner
Michael Kurrat
Pat Lees
Xingwen Li
John McBride
Ralf-Peter Methling
Hans Kristian Hygen Meyer
Bogdan Miedzinski
Kento Mitani
Timo Mützel
Kaveh Niayesh
Sophie Noel
Henrik Nordborg
Magne Runde
Stephan Schlegel
Clemens Schrank
John Shea
Paul G Slade
Armin Strahl
Roland Timsit
Dirk Uhrlandt
Wolfgang Widl

Contents

CONFERENCE CHAIR'S MESSAGE **3**

HISTORY OF THE CONFERENCE **4**

RECENT VENUES **4**

CONFERENCE SPONSORS **5**

ORGANISING COMMITTEE **6**

THE INTERNATIONAL ADVISORY GROUP **6**

REVIEWERS **7**

HIGH-VOLTAGE SWICHGEAR

1.2 Additively Manufactured Contact Geometries as Opportunity for Future Contact Designs **13**
David Cziumplik, Andreas Laufer, Marius Hinz, Karen Flügel, Dirk Bösche, Michael Kurrat

1.3 Data-Driven Identification of Equivalent Physical Parameters for Arc Quenching Performance of Gassing Materials **19**
Weidong Cao, Guanyu Wang, Qian Wang, Boya Zhang, Xingwen Li

NON-ARCING CONTACTS

2.1 Investigation of electric and magnetic field in bolted copper busbar joints **27**
Toni Ivas, Philipp Scheidegger, Rolf Brönnimann, Jonas Diaz, Jacim Jacimovic, Lorenz Herrmann

2.2 Investigation of Wear in High-Voltage Circuit Breaker Electrical Contacts **33**
Vincent Niggel, Lorenz Herrmann, Andrew Fairbrother, Rowena Crockett

2.3 Understanding of the High-Frequency Impedance Characteristics of Micro-scale Gold-plated Contact Interfaces **38**
Yinnan Zhang, Chao Zhang, Yuchen Liao, Wanbin Ren

2.4 The performance of offshore charging contacts with and without maintenance with contact grease **44**
Kristian Solheim Thinn, Niklas Magnusson, Erik Bjerrehorn, Olve Moen

VACUUM INTERRUPTERS

3.1 Current Chopping of Vacuum Interrupters with Stainless Steel Contacts **49**
Christoph Kenel, Siobhan McKeown, Roman Mukin, Dietmar Gentsch, Julien Rault

3.2 Comparative Study on Arc Dynamics and Thermal Recovery of different CuCr Contacts for Vacuum Interrupters **55**
Naghme Dorraki, Sergey Gortschacow, Andreas Lawall, Thomas Brauner, Frank Graskowski

3.3 Evaluation of Surface Temperature of Switching Contacts in Vacuum by Optical Methods **60**
Sergey Gortschakow, Gregor Gött, Ralf Methling, Dirk Uhrlandt

3.4 Effect of Laser Surface Remelting on the Electrical Performance of CuCr Electrical Contacts 66
Ming Yu, Peng Li, Yong Wang, Xiaojun Wang, Ning Han, Xiaofei Yao

3.5 Multi-Parameter Investigation of Magnetron Currents in Vacuum Interrupters 72
Patrick Rumpelt, Philipp Hauch, Marco Thönnessen, Michael Weuffel

ENVIRONMENTAL EFFECTS

4.1 A framework for holistic durability assessment of wire-connector systems under vibrational load – The influence of connector arrangement and wire routings..... 77
Roman Probst, Dirk Hilmert, Frederik Kiel, Jian Song

4.2 Effect of water content on ablative mechanism of gassing materials under arc action..... 83
Qian Wang, Yi Shang, Weidong Cao, Wanmeng Zhao, Yuxuan Liu, Xu Zhong

4.3 Intrusion of particles in open vent hole type relays and related failure modes 90
Thomas Herrle, Dieter Volm

4.4 Effects of Aging on the Mechanical Drop-Shock Performance of SAC305 Solder Interconnects 96
Saddam Daradkeh, Abdallah Alakayleh, Sufyan Tahat, Waad Tarman, Elizabeth Gainey, George Flowers, Sa'd Hamasha, Jeffrey Suhling

DIAGNOSTICS AND RELIABILITY

5.1 Part 1: Analysis of Electrode Ageing Based on Signatures of Electrical Arcs..... 102
Raul Carreira Rufato, Malyk Benmouffok, Cyril Van de Steen, Patrick Schweitzer

5.2 Part 2: Reflection and Methodology for Arc Database Signal Generation in Aircraft Systems 107
Malyk Benmouffok, Raul Carreira Rufato, Cyril Van de Steen, Patrick Schweitzer

5.3 Contact characteristics monitored by AI-Methods 111
Daniel Kupka, Armin Strahl, Thomas Zimmermann, Arthur Zimmermann

5.4 Diagnostic of DC Arc Plasmas in Aeronautic Conditions: Application to Arc Fault Detection 117
Arthur Hellé, Robert Hugon, Frédéric Brochard, Grégory Marcos

5.5 Frequency Band Importance Estimation for Arc Faults via Multi-Branch Neural Networks..... 123
Abdelhak Maoukouf, Patrick Schweitzer

ARCING CONTACTS

6.1 Image Processing–Based Quantification of Contact Microstructure for Erosion Assessment in High Voltage Gas Circuit Breakers 129
Milad Mohammadhosein, Kaveh Niayesh

6.2 Electrical Performance Study of AgSnO2In2O3 Materials with Different Preparation Processes under High Current Surge Conditions 135
Yibo You, Yangfang Chen, Dai Wan, Xiaofang Yan, Qinghong Wei, Zhenyang Song

6.3 Contact material testing - modern model switch methods 140
Armin Strahl, Daniel Kupka, Andreas Kammerl, Marina Logvinova

6.4 The current transfer to a copper cathode in low-voltage, low-current arcs of short length 146
Margarita Baeva, Jonas K. C. Ballentin, Dirk Uhrlandt

SUSTAINABILITY

7.2 Pathway to Sustainability in Connector Development: Influence of material and design changes 152
Isabell Buresch

7.3 Sustainable Contact Materials: Comparison between Different Contact Materials for MV Switchgears regarding their Resistance and CO2 Equivalent 158
Nils Wilm Rosebrock, Michael Kurrat

FUNDAMENTALS

8.1 Geometric Influence on Repulsion Forces in Butt Contacts 164
Sergey Perekopskiy

8.2 An integrated BEM-FEM simulation framework for the calculation of constriction resistances be-tween rough surfaces 170
Robert Scherr, Thomas Wielsch

8.3 Setup for electrical and mechanical characterization of copper junctions at the microscale 176
Jonas Diaz, Toni Ivas, Rafael Philipona, Philipp Scheidegger, Rolf Brönnimann, Jacim Jacimovic, Johann Michler, Lorenz Herrmann

8.4 Mass transfer from a molten bridge to separating electrodes 181
Paul G Slade, Roland S Timsit

8.5 Influence of contact geometry and interfacial force on contact behaviour: Combined theoretical and simulation validation 187
Akshata Sangle, Stefan Goetz, Florian Bruhn

COATED CONTACTS

9.1 Contacting of Copper Clad Aluminum Hairpins for Electric Drives using Laser Welding .. 197
Felix Wirthmann, Marcel Baader, Tobias Zürrlein, Fabian Giesbert, Thorsten Ihne, Florian Risch

9.2 Effect of Ag/TiO_2 Nanoparticles on the Electrical Performance and Durability of Silver Coatings for Electrical Contacts 203
Alsayed Abdel Aal, Michael Blauth, Jian Song

9.3 Advanced Silver Coatings for Connector Applications in E-Mobility 209
Sönke Sachs, Isabell Buresch

9.4 Tribological and electrical properties of electrodeposited tin zinc coatings 215
Aurore Brézard Oudot, Sophie Noël, Julien Acquadro, Thierry Leblanc, Philippe Testé, Frédéric Houzé

9.5 Silver reduction through high-performance composite technologies and non-precious metal sub-layers 221
Timo Mützel, Havva Cinaroglu

ELECTRIC ARCS

10.1 Simulation of the Electrical Arc Motion between Busbar Electrodes 226
Camille Gouze, Yann Cressault, Flavien Valensi, Malyk Benmouffok, Michael Darques, Cyril Van de Steen

10.2 Big-Data-Driven Screening and Optimization Design of Gassing Materials (PAs) for DC Circuit Breakers 232
Qian Wang, Yuxuan Liu, Weidong Cao, Xinzgan Chen, Yi Shang, Xu Zhong

10.3 Investigation of dynamic microarcs in air complementing a unified nonequilibrium model 238
Jonas Karl Christian Ballentin, Margarita Baeva, Dirk Uhrlandt

10.4 Comparison of numerical solving for electric arc modelling 244
Cyril Van de Steen, Camille Gouze, Malyk Benmouffok, Yann Cressault

SPECIAL APPLICATIONS

11.1 Advanced Contact Materials for Hot-Switching MEMS Relay Applications 249
Martin Köhne

11.2 Characterisation of Pt/PEDOT/Si Layered Structures for MEMS Contacts 255
Nasser Aldhahri, Yoshishige Tsuchiya, Tomoyuki Kurioka, Punvinai Vinaisuratern, Joji Higuchi, Tso-Fu Mark Chang, Masato Sone, Liam Boodhoo, Thomas Bull, Yan Yang, John W. McBride

11.3 Mating Cycle Component-Level Testing for E-Mobility: Mating Force, Micro-Ohm Contact Resistance, and Wear 262
Felix Greiner, Soenke Sachs, Frank Ostendorf

11.4 Innovative Stamped Terminals plated with Reel-to-Reel Silver Graphite for Auto-motive Connectors 268
Maxime Porte, Rene Lehmann

DYNAMIC PHENOMENA

12.1 Investigation of contact dynamic welding mechanisms of silver tin-oxide based on the evolution of eroded surface morphology 274
Chao Zhang, Guoliang Chen, Yubin He, Wanbin Ren

12.2 Experimental verification on forming carbon films onto the friction surface of contact wires when using metalized carbon contact strips 281
Kento Mitani, Yoshitaka Kubota, Fumiko Morimoto

12.3 Influence of current waveform on km/s range electric sliding contact in the context of electro-magnetic launchers 287
Vincent Andraud, Paul Gapenne, Quentin Hassler, Philippe Baumann, David Bluntzer, Markus Schneider

DC SWITCHING

13.1 Enhancing the Interrupting Capability of Low-voltage DC Hybrid Circuit Breakers 293
Caizhi Gao, Zhaozi Zhang, Silei Chen, Xingwen Li, Yinfang Huang

13.2 Post-arc erosion of metal surfaces 299
Pierre Corfdir, Luca Sulmoni, Christoph Kenel, Patrick Sütterlin

13.3 Experimental Characterization of DC Fault Arcs and Comparative Analysis with AC Fault Arcs 305
Frederik Mingers, Verena West, Willem Leterme

13.4 Break arc behaviors of Ag, AgSnO2, AgNi and AgZnO in inductive DC loads up to 20V/20A under magnetic field application 310
Makoto Hasegawa, Reo Oikawa, Haruto Oiwa, Yuna Onishi

13.5 Determination of post-arc conductance by hybrid switching of low voltage DC currents 316
Diego Gonzalez, Luz Gonzalez

NON-ARCING CONTACTS

14.1 LPBF-based, additively manufactured contact ring segments for closed-form coil stators 322
Alexander Vogel, Felix Wirthmann, Muhammed Kilic, Thorsten Ihne, Jörg Franke, Florian Risch

14.2 Separable connection of prismatic batteries 328
Tag Hammam, Peter Andersson, Lars Gunnarsson, Therese Källgren

14.3 Evaluation of current-carrying capacity of silver-based oxide contact pairs 334
Chang Sun, Chao Zhang, Yinnan Zhang, Wanbin Ren, Yinghua Fu

14.4 The Role of Mechanical Stress in Electrical Contact Elements during Short-Circuits 341
Toni Israel, Tom Kufner, Philipp Strehler, Julian Angel Czajor, Michelle Pomsel, Christian Hildmann, Stephan Schlegel

AUTHOR INDEX 347

Additively Manufactured Contact Geometries as Opportunity for Future Contact Designs

David Cziumplik
elenia Institute for High Voltage Technology and Power Systems
TU Braunschweig
Braunschweig, Germany
david.cziumplik@tu-braunschweig.de

Andreas Laufer
elenia Institute for High Voltage Technology and Power Systems
TU Braunschweig
Braunschweig, Germany
andreas.laufer@tu-braunschweig.de

Marius Hinz
elenia Institute for High Voltage Technology and Power Systems
TU Braunschweig
Braunschweig, Germany
marius.hinz1@tu-braunschweig.de

Karen Flügel
elenia Institute for High Voltage Technology and Power Systems
TU Braunschweig
Braunschweig, Germany
k.fluegel@tu-braunschweig.de

Dirk Bösche
elenia Institute for High Voltage Technology and Power Systems
TU Braunschweig
Braunschweig, Germany
d.boesche@tu-braunschweig.de

Michael Kurrat
elenia Institute for High Voltage Technology and Power Systems
TU Braunschweig
Braunschweig, Germany
0000-0001-6289-0975

Abstract— Vacuum interrupters (VIs) are widely used in medium- and high-voltage switching devices due to their high dielectric strength, long service life, and low maintenance requirements. Axial magnetic field (AMF) contacts are commonly used in vacuum switching devices to generate diffuse vacuum arc. Conventional AMF contacts are typically manufactured using cutting based manufacturing, which limit geometric complexity and achievable magnetic field strength. This paper investigates metal additive manufacturing (AM) as an alternative approach for realizing AMF contact geometries. The increased design freedom enables coil-based structures that cannot be produced using conventional manufacturing techniques. Fully AM AMF contact concepts have not yet been reported in the literature. The proposed contact designs are evaluated using finite element method (FEM) simulations. The resulting axial magnetic flux densities are compared with characteristic values known for conventionally manufactured AMF contacts. The results indicate that AM designs are capable of generating higher AMF strengths. These findings suggest that AM represents a viable approach for further development of AMF contacts, with potential benefits in terms of electromagnetic performance and material efficiency. The concept provides a basis for future investigations, particularly for applications involving larger contact gaps.

Keywords—Axial magnetic field (AMF) contacts, FEM, additive manufacturing (AM), selective laser melting (SLM), vacuum interrupter (VI), vacuum circuit breaker (VCB)

I. INTRODUCTION

Circuit breakers are an important component of the power distribution grid and are designed to interrupt fault currents. Circuit breakers must meet the following requirements: they must reliably conduct the current until interruption, breaking high short-circuit currents to protect other components in the grid, withstand the transient recovery voltage after current zero, and withstand the voltage stresses of the grid in the open position [1]. In the past, oil was used as switching and insulating fluid for these purposes. Then came gas circuit breakers, which used enclosed high-pressure gas, and vacuum circuit breakers (VCB), whose internal pressure is less than 10^{-7} hPa. Today, VCB are common in medium-voltage grids with rated voltages of up to 52 kV, while gas circuit breakers containing sulphur hexafluoride (SF_6) are mainly used in high and extra high voltage grids [2].

Climate change is the reason why binding emission reduction targets were set for the first time in the United Nations Kyoto Protocol of 1997. The agreement on measures to reduce greenhouse gases was ratified by 192 countries. Between 2008 and 2012, emissions were to be reduced by 5 % compared to 1990 levels [3]. Following this, a series of further targets for reducing emissions of carbon dioxide (CO_2) and other climate harmful gases. The 2014 United Nations Sustainable Development Goals highlighted the need for climate neutrality. For instance, protecting the planet, combating climate change, and protecting the environment [4]. SF_6 has the highest global warming potential (GWP) of all climate harmful gases. The Intergovernmental Panel on Climate Change has set the 100-year GWP for SF_6 at 23,500 [5]. To be able to reach the climate goals, the European Union regulates the use of fluorinated gases like SF_6. The 2024 Regulation on fluorinated greenhouse gases regulates that climate-neutral solutions take priority [6]. By 2030, the use of SF_6 in medium-voltage systems will be prohibited, and technologies with a GWP < 1 are to be preferred in high-voltage systems.

SF_6 is ideal for use as arc extinguishing and insulating gas due to its high electric strength and electronegativity [7]. It has therefore been used in high-voltage components and switchgear for many years. The European Union ban and growing climate awareness have led to research and development efforts to find alternatives. High-voltage VCB are an option for replacing SF_6 switchgear [8]. Vacuum and gas mixtures from air components are used to meet the most important requirements of climate neutrality and non-toxicity.

Already over 90 % of global production of medium-voltage switchgear is based on VCB technology [9]. For high and extra-high voltage applications, new switchgear based on vacuum switching technology is launched on the market at regular intervals. The advantages of VCB technology are being utilised: the maintenance-freedom, a large number of operating cycles, and the compact design [10]. Further benefit for a switch is the rapid dielectric recovery of the vacuum after switching and the ability to interrupt the current

after a delayed restrike [2]. In light of this background, the present study investigates scalable contact geometries enabled by selective laser melting SLM that preserve the advantages of AM while targeting improved performance. By leveraging the design flexibility offered by SLM, complex current paths and coil configurations, unattainable through traditional manufacturing methods, are actualized to augment the attainable AMF. This approach has not yet been addressed in the extant literature; consequently, the presented work addresses an identified research gap.

II. VACUUM INTERRUPTER

The central components of the VI are the contact electrodes, which allow current to flow when closed but interrupt the current flow when opened. The design of a VI can be seen in Fig. 1.

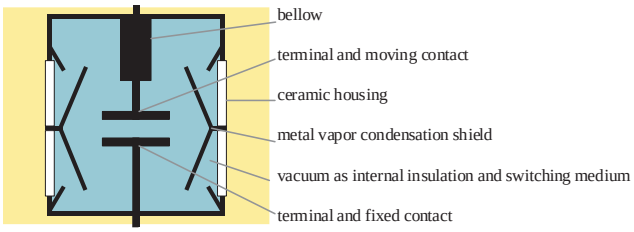


Fig. 1. Illustration of a cross section of a VI [11]

The electrodes are surrounded by a vacuum, which in industrial switching chambers is below 10^{-7} hPa [10]. The function of the bellow is to allow axial movement of one contact while maintaining the vacuum integrity of the interrupter. During the switching process, the flow of current is maintained by a plasma, whereby a vacuum arc forms between the contacts. The surrounding metal vapor condensation shield protects the ceramic housing from deposits by the metal. The charge carriers of the vacuum arc are provided by the evaporation of the contact material, which erodes with each switching operation. Progressive contact erosion can negatively affect the switching behaviour and reduce the service life of the VI. The amount of contact erosion depends on the charge input per area. The charge input cannot be changed by the design of the VI, but the charge input can be distributed specifically over as large a contact surface as possible in order to reduce high local erosion.

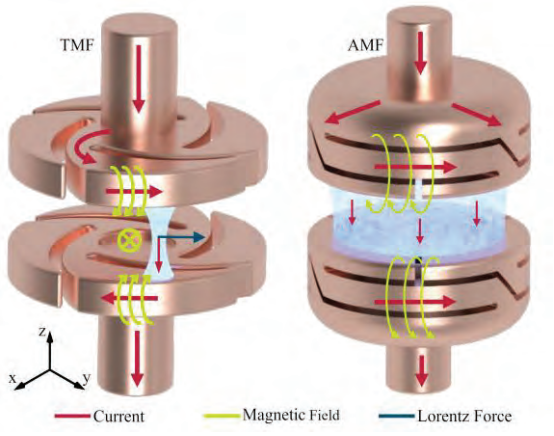


Fig. 2. Comparison of TMF and AMF contacts [12]

For this purpose, various contact geometries are used, which can be categorised into the groups of Transversal Magnetic Field (TMF) and AMF contacts, as shown in Fig. 2. The TMF contact generates a transversal magnetic field, which exerts a Lorentz force on the current-carrying vacuum arc and forces the vacuum arc into a circular motion. An AMF contact induces an axial magnetic field in B_z-direction, which counteracts the contraction of the vacuum arc and causes a diffuse vacuum arc on the contact surface. These geometries can significantly increase the lifespan, switching capability and number of switching operations of VIs compared to contact geometries, which are not designed to influence the vacuum arc with their magnetic field [13].

How this magnetic field can be achieved with different AMF contact geometries will be discussed in the next section.

III. AMF CONTACTS

For VIs employing AMF contacts, a wide range of contact geometries has been proposed and investigated in the literature. These geometries differ significantly in their electromagnetic behaviour, manufacturing complexity, and suitability for high-current interruption. The primary purpose of this section is to introduce the most relevant AMF contact types reported in the literature and to summarize their performance with respect to the achievable AMF strength. While phase shift effects between the source current and the generated AMF are known to influence the interruption process, particularly around current zero, a detailed discussion of this phenomenon is omitted here for the sake of conciseness. Phase shift effects however, represent an important secondary design criterion in AMF contact development, but are not discussed in detail in this work.

The analysis presented in this paper builds upon three key studies by Wang et al. [14], Wang et al. [15], and Li et al. [16], each of which investigates different AMF contact geometries under distinct experimental or numerical conditions. Fig. 3 shows the researched contact geometries.

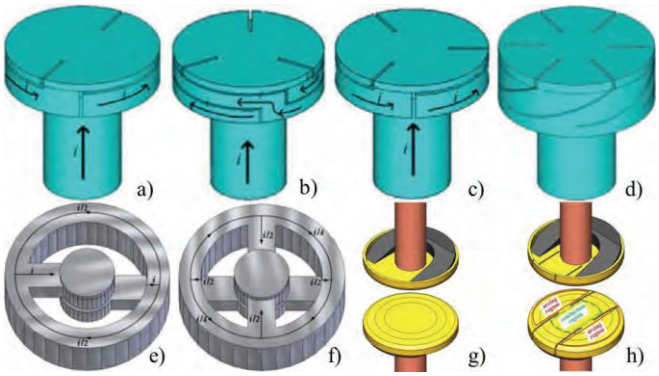


Fig. 3. Overview of AMF contact geometries reported in the literature: a) 1/2 coil-type, b) 2/3 coil-type, c) 1/3 coil-type, d) cup-type (a–d adapted from [15]); e) bipolar-type (internal structure), f) quadrapolar-type (internal structure) (e–f adapted from [14]); g) horseshoe-type, h) slotted horseshoe-type (g–h adapted from [16]).

Due to variations in contact diameter, gap distance, current magnitude, and test methodology, a direct quantitative comparison of absolute magnetic field values is not meaningful. Nevertheless, a qualitative and relative comparison of contact performance can be established by evaluating the reported residual AMF strengths across all investigated geometries.

To this end, the results of the mentioned studies are collected in Table I, which provides a comparative ranking of all considered AMF contact types. The table summarizes the relative performance of quadrapolar-, cup-, bipolar-, coil-, horseshoe-, and slotted horseshoe-type contacts with respect to the generated axial magnetic field.

At the lower end of the performance spectrum, 1/3 coil-, quadrapolar- and cup-type contacts exhibit the weakest AMF generation. All three geometries are characterized by comparatively simple current paths and limited effective circumferential current flow, which restricts their ability to generate strong axial fields. While the cup-type contact benefits from a simple and cost-effective manufacturing process, its electromagnetic performance is consistently inferior to more advanced designs.

TABLE I. Comparison of AMF strengths of different AMF contact geometries

Contact Geometry	AMF strength in mT/kA	Paper
1/3 coil-type	7.06	[15]
quadrapolar-type	7.1	[14]
cup-type	7.6	[14]
3/4 coil-type	11	[16]
1/2 coil-type	12.13	[15]
2/3 coil-type	13.27	[15]
horseshoe-type	15.25	[16]
slotted horseshoe-type	17.25	[16]
bipolar-type	17.8	[14]

Coil-type contacts form a relevant group among AMF contact geometries. Their defining characteristic is the division of the current into multiple branches that partially wrap around the contact circumference. As summarized in Table I, coil-type contacts generally exhibit an increase in axial magnetic field strength with increasing percentage of circumferential coil coverage. However, the relationship is not strictly monotonic, as the 3/4 coil-type contact does not outperform all configurations with smaller coverage. This indicates that, in addition to the circumferential fraction, further design parameters such as contact diameter, coil height, and coil width significantly influence the resulting AMF strength [10]. As a result, coil-type contacts represent a well-established compromise between electromagnetic performance and manufacturing feasibility and are widely regarded as a reference design for AMF contacts.

Beyond classical coil-type geometries, horseshoe- and slotted horseshoe-type contacts demonstrate higher AMF strengths among the investigated configurations. In particular, the slotted horseshoe-type contact achieves the second strongest axial magnetic field, exceeding even the 2/3 coil-type contact. This superior performance is attributed to the tailored current paths and the presence of slots, which effectively enhance the axial field component in the contact gap. These geometries, however, are associated with increased manufacturing complexity and may impose tighter tolerances during fabrication.

In summary, the comparison presented in Table I does not reveal a clear or monotonic relationship between geometric complexity and axial magnetic field strength. The wide spread of normalized AMF values indicates that the electromagnetic performance of AMF contacts is governed by multiple interacting design parameters, including current distribution, branch configuration, contact dimensions, and material layout. Consequently, no definitive ranking of contact geometries can be derived from this comparison alone.

Nevertheless, the results consistently demonstrate that coil-type contacts provide a reliable combination of comparatively high AMF strength and moderate geometric complexity. In addition to their favorable electromagnetic performance, coil-type geometries are comparatively straightforward to manufacture, making them an attractive and well-established reference for both experimental investigations and the development of novel AMF contact concepts. This observation motivates the subsequent numerical analysis of a newly developed, coil-like contact structure. For improved comparability, all magnetic field values are normalized with respect to the current and expressed in mT/kA.

IV. Additive Manufacturing

AM of metals is a manufacturing approach in which components are fabricated layer by layer based on digital, three-dimensional data. Unlike conventional manufacturing processes, AM allows for the production of near-net shapes with minimal material waste and a high degree of geometric freedom [17]. This enable the fabrication of complex structures that are difficult to achieve using traditional methods [17]. Metal AM technologies are generally categorized into powder bed fusion (PBF) and directed energy deposition (DED) processes, depending on the method of material delivery and energy input [18], [19].

In PBF processes, thin layers of metallic powder are selectively consolidated using a concentrated energy source. Prominent PBF techniques include SLM, direct metal laser sintering, and electron beam melting [18]. Fig. 4 schematically illustrates the fundamental operating principles and main components of a PBF. In laser-based implementations of this technology, an inert gas atmosphere is employed to prevent oxidation [20]. Electron beam melting uses an electron beam as the energy source and is conducted in a vacuum environment (< 10^{-4} hPa) [20]. These processes can produce components that are 99.99 % dense, have fine microstructural features, and are dimensionally accurate [19]. However, residual stresses and surface roughness may necessitate post-processing steps such as heat treatment or surface finishing [18], [19], [21].

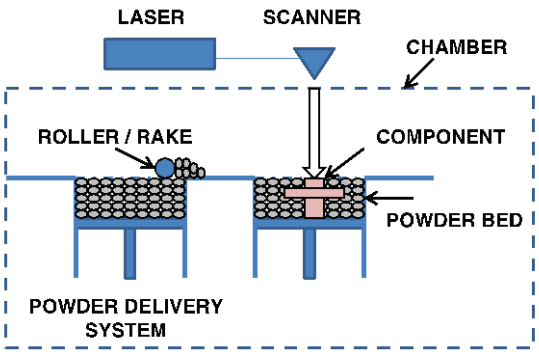


Fig. 4. Schematic illustration of metal AM PBF system [21]

DED technologies are characterized by the simultaneous delivery of feedstock material and localized melting using a high-energy source [19]. As illustrated in Fig. 5(a) and (b), the material can be supplied either in powder form or as a solid wire and is melted by a laser, an electron beam, or an electric arc. Representative processes include laser engineered net shaping and direct metal deposition [19]. DED is well suited for repairing and modifying existing components, depositing functionally graded materials, and fabricating large-scale structures [21]. However, it has lower geometric resolution than PBF processes [21].

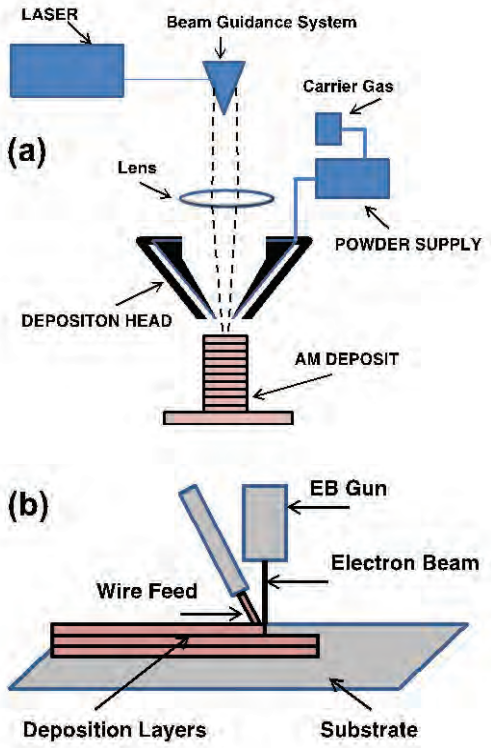


Fig. 5. Schematic illustration of metal AM systems: (a) powder-fed DED, and (b) wire-fed DED. [21]

From an application perspective, metal AM offers significant advantages, including design-driven property optimization, functional integration, and rapid prototype iteration [19]. These capabilities are particularly interesting for high-voltage engineering applications, including additively manufactured electrical contacts. Conventional, mechanically manufactured electrical contacts are often associated with limitations such as high component mass, susceptibility to thermal softening or local melting under high current loads, and contact welding caused by arc-induced overheating. The geometric freedom of metal AM extends the design space for electrical contacts beyond the constraints of conventional manufacturing methods.

The ability to customize contact geometries, surface topographies, and internal material distributions allows for the targeted optimization of current density, electric field distribution, and thermal dissipation. Furthermore, AM facilitates the integration of internal support or lattice structures within the contact body. These structures can be designed using alternative materials or reduced infill densities to decrease weight while maintaining mechanical stability and electrical functionality. This design flexibility offers the potential for significant improvements in terms of thermal management, operational reliability, and switching capability.

V. ADDITIVELY MANUFACTURED CONTACT GEOMETRIES

A sufficiently strong AMF is essential for maintaining a diffuse arc during switching operations, as it suppresses arc constriction and reduces localized thermal stress on the contact surface.

To enable a meaningful comparison of magnetic field performance across different studies and experimental conditions, the axial magnetic flux density is commonly normalized to the applied current and expressed in mT/kA. This normalization approach is well established in the literature. Fenski et al. report a threshold value of approximately 4 mT/kA as favorable for promoting diffuse arc behavior and thereby mitigating contact erosion [22]. Similar values on the order of 4.1 mT/kA can be extracted from the results reported by Morimiya et al. [23]. In contrast, Stoving et al. identify a higher threshold of approximately 5.8 mT/kA [24].

The relevance of these threshold values lies in the fact that stronger axial magnetic fields enhance the radial expansion of the metal-vapor arc column, which reduces current constriction, mitigates localized heating, and limits contact erosion. It should be noted that the reported threshold values are influenced by the measurement methodology. Comparable to the present work, Fenski et al. and Morimiya et al. evaluated the magnetic field in the central plane of the contact gap, whereas Stoving et al. performed measurements directly at the contact surface.

In this study, two additively manufactured contact concepts are investigated to assess the influence of coil interconnection on the resulting axial magnetic field. The first design consists of three coils connected in parallel, resulting in a distributed current flow and reduced current stress per coil. The second design also employs three coils but connects them in series, such that the full current contributing to the axial magnetic field flows through each coil. While this configuration is expected to increase the achievable AMF strength, it also leads to higher current loading of the individual coils compared to the parallel arrangement.

A comparison of the contact designs shown in Fig. 6 and Fig. 7, design A with parallel-connected coils and design B with series-connected coils, reveals that design B not only achieves higher normalized axial magnetic field levels overall, but also exhibits a significantly larger area in which the normalized magnetic flux density exceeds the threshold of 4 mT/kA.

At the center plane of the contact gap, design A reaches a normalized axial magnetic field strength of 10.3 mT/kA, whereas design B achieves 29.8 mT/kA at the same location. For reference, the corresponding values evaluated at the contact surface are 22.2 mT/kA for design A and 50.2 mT/kA for design B. These results demonstrate that, in relative terms, design B generates axial magnetic fields that are more than twice as strong as those produced by design A. The presented simulations primarily serve to demonstrate the feasibility of generating high axial magnetic fields using

additively manufactured coil structures, rather than to propose a mechanically optimized contact design.

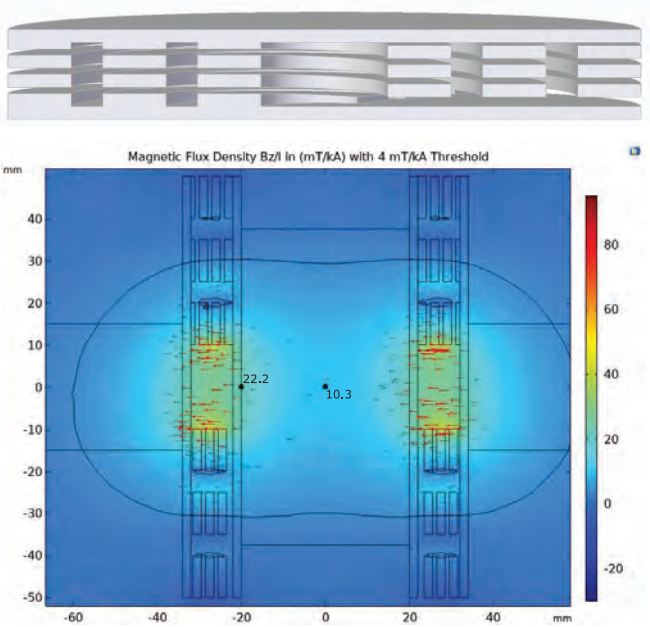


Fig. 6. Additively manufactured AMF contact geometry with three coils connected in parallel and the corresponding axial magnetic field distribution normalized to the current (mT/kA).

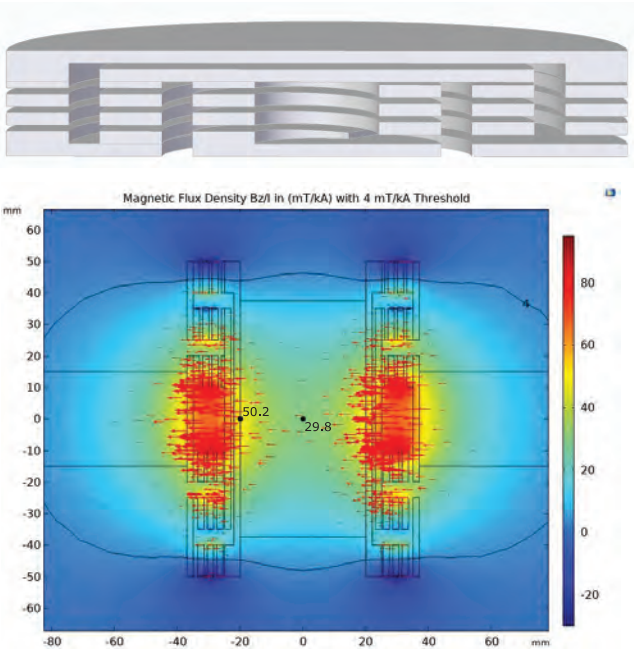


Fig. 7. Additively manufactured AMF contact geometry with three coils connected in series and the corresponding axial magnetic field distribution normalized to the current (mT/kA).

VI. Discussion

Although the investigated additively manufactured AMF contact designs demonstrate the potential to generate very high AMF strengths, they are not yet suitable for practical switching operations. In their current form, the contacts exhibit significant mechanical weaknesses, as they lack a dedicated support structure capable of withstanding the mechanical and thermal loads occurring during interruption processes.

Furthermore, the present coil geometries are expected to be subject to pronounced eddy current effects, which may lead to increased electrical losses and additional thermal stress. These aspects have not yet been optimized and require further investigation.

Nevertheless, the presented results clearly demonstrate the direction in which this design approach can be further developed when combined with the capabilities of additive manufacturing. In particular, the study shows that complex coil structures, unfeasible with conventional subtractive manufacturing, can be realized and can generate axial magnetic field strengths exceeding those typically reported for established AMF contact geometries.

Significant potential for further optimization remains. Future designs may incorporate mechanically reinforced or electrically active support structures that simultaneously contribute to magnetic field generation. In addition, the reduction or elimination of passive support material, as well as targeted optimization of current paths, magnetic field distribution, electrical losses, and mechanical stability, represent promising directions for continued development.

Overall, the presented concepts should be regarded as a proof of feasibility rather than finalized contact designs. The ability to achieve magnetic field levels unattainable with conventional manufacturing methods strongly motivates further investigation of additively manufactured AMF contacts.

The applicability of the referenced manufacturing process to currently used vacuum contact materials still requires further investigation and testing. However, Tang et al. [25] demonstrated that CuCr alloys can be produced by additive manufacturing and may exhibit high mechanical properties.

VII. Conclusion

This study addresses the question of whether the manufacturing of AMF contacts using SLM represents a viable design approach. By combining a qualitative assessment of manufacturing advantages and limitations with FEM-based electromagnetic simulations, it is shown that AM enables contact geometries capable of generating exceptionally high AMF. While further optimization is required before practical application, the results demonstrate the strong potential of this approach and justify continued research into additively manufactured AMF contact concepts.

VIII. Outlook

The presented results demonstrate the general feasibility of additively manufactured AMF contact concepts and motivate further investigation. Future work should focus on the systematic design and optimization of contact geometries tailored to AM, followed by fabrication and experimental validation. In this context, relevant electrical parameters such as contact resistance, current distribution, and phase shift under AC excitation should be characterized.

In addition, the performance of additively manufactured contacts under vacuum conditions and during repetitive switching operations must be assessed, particularly with respect to long-term stability, plasma interaction, and erosion behavior. The reduced material usage and increased geometric freedom offered by AM provide opportunities for

lightweight designs, optimized field shaping, and the realization of multi-material contact concepts.

These advantages are expected to be especially relevant for applications involving larger contact gaps, where enhanced AMF and pinch effects play a more significant role in arc control. Overall, AM opens a promising design space for future AMF contact development.

REFERENCES

[1] M. Kapetanovic, “High voltage circuit breakers”, Univerzitet U Sarajevu, 2011.

[2] H. Ito “Switching equipment”, Springer, 2019.

[3] United Nations Framework Convention on Climate Change (UNFCCC), “Kyoto Protocol to the United Nations Framework Convention on Climate Change”, Kyoto Climate Change Conference, Kyoto, Japan, 1997.

[4] UN. General Assembly. Open Working Group on Sustainable Development Goals, “Report of the Open Working Group of the General Assembly on Sustainable Development Goals”, UN General Assembly, New York, USA, 2014.

[5] IPCC: Climate Change 2013, “The Physical Science Basis. Contribution of Working Group I to the Fifth Assessment Report of the Intergovernmental Panel on Climate Change”, Cambridge University Press, 2013.

[6] REGULATION (EU) 2024/573 OF THE EUROPEAN PARLIAMENT AND OF THE COUNCIL of 7 February 2024 on fluorinated greenhouse gases, amending Directive (EU) 2019/1937 and repealing Regulation (EU) No 517/2014, Official Journal of the European Union 2024/573, 2024.

[7] K. Niayesh, “Green HV switching technologies for modern power net-works”, The Institution of Engineering and Technology (IET energy engineering series, 236), 2023.

[8] T. Heinz, S. Giere, J. Teichmann et al., “Why vacuum technology is not a simple scaling from medium to high voltage?”, International Symposium on Dielectrics and Electrical Insulation in Vacuum (ISDEIV), Okinawa, Japan, 2023.

[9] L. T. Falkingham, “The Strengths and Weaknesses of Vacuum Circuit Breaker Technology”, 1st International Conference on Electric Power Equipment - Switching Technology, Xi’an, China, 2011.

[10] P.G. Slade, “The Vacuum Interrupter, Theory, Design and Application”, CRC Press, 2008.

[11] K. Flügel, D. Gentsch, M. Kurrat, “External Field Control for Vacuum Interrupter”, VDE Hochspannungstechnik, 5. ETG-Fachtagung, Berlin, Germany, 2024.

[12] B. Weber, “Automated Multivariate Analysis of Vacuum Arcs between TMF-Contacts”, PHD-Thesis, Technische Universität Braunschweig, 2024.

[13] P. G. Slade, R. K. Smith, “Electrical Switching Life of Vacuum Circuit Breaker Interrupters”, IEEE Holm Conference on Electrical Contacts, Montreal, QC, Canada, 2006.

[14] Z. Wang, Z. Liu, X. Zhang, Y. Zeng, J. Wang, “Comparison of Axial Magnetic Field Characteristics of Four Axial Magnetic Field Vacuum Interrupter Contacts”, International Symposium on Dielectrics and Electrical Insulation in Vacuum (ISDEIV), Matsue, Japan, 2006.

[15] L. Wang, K. Wang, C. Yan, W. Shi, S. Jia, “Experimental investigation of vacuum arc characteristics of four kinds of AMF Contacts”, International Symposium on Dielectrics and Electrical Insulation in Vacuum (ISDEIV), Padova, Italy, 2020.

[16] H. Li, Y. Geng, Z. Liu, J. Wang et al., “Development of 126 kV Single-break Vacuum Circuit Breaker”, 46th IEEE Holm Conference on Electrical Contacts, Albuquerque, USA, 2018.

[17] S. Patel, Y. Liu, Z.Siddique et al., 2024 “Metal additive manufacturing: Principles and applications”. Journal of Manufacturing Processes, 1179-1201.

[18] T. DebRoy, H. L. Wei, J. S. Zuback, et al. “Additive manufacturing of metallic components – Process, structure and properties.” Progress in Materials Science, 92, 112–224, 2018.

[19] T. Nancharaiah, “A Review Paper on Metal 3D Printing Technology”, Advances in Materials Processing and Manufacturing Applications, 251-259, 2021.

[20] D. Herzog, V. Seyda, E. Wycisk, C. Emmelmann, “Additive manufacturing of metals.” Acta Materialia, 117, 371–392, 2016.

[21] W. E. Frazier, “Metal additive manufacturing: A review.” Journal of Materials Engineering and Performance, 23, 1917–1928, 2014.

[22] B. Fenski, "Characteristics of a vacuum switching contact based on bipolar axial magnetic field," IEEE Trans. Plasma Sci., 1997. ISSN: 0093-3813, eISSN: 1939-9375

[23] O. Morimiya, "High current vacuum arcs stabilized by axial magnetic fields," IEEE PES Winter Meeting, 1999, pp. 1723-1732

[24] P. Støving, "Finite element analyses of AMF vacuum contacts," in Proc. 18th Int. Symp. Discharges Electr. Insul. Vac., 1998, pp. 522-529

[25] X. Tang, X. Chen, F. Sun, P. Liu, H. Zhou, and S. Fu, “The current state of CuCrZr and CuCrNb alloys manufactured by additive manufacturing: A review,” Materials & Design, vol. 224, p. 111419, 2022.

ACKNOWLEDGMENTS

The authors acknowledge the use of the AI language model ChatGPT (OpenAI) for language editing support. The AI system was used only to improve clarity and readability of the authors’ original text and did not generate scientific content or results. We thank Maik Kahn for encouraging and inspiring us to write this paper.

Data-Driven Identification of Equivalent Physical Parameters for Arc Quenching Performance of Gassing Materials

Weidong Cao
State Key Laboratory of Electrical Insulation and Power Equipment
Xi'an Jiaotong University
Xi'an, P.R.China
wdcao@stu.xjtu.edu.cn

Guanyu Wang
State Key Laboratory of Electrical Insulation and Power Equipment
Xi'an Jiaotong University
Xi'an, P.R.China
wangguanyu@stu.xjtu.edu.cn

Qian Wang
School of Optoelectronic Science and Intelligent Instrumentation
Xi'an University of Technology
Xi'an, P.R.China
qianwang@xaut.edu.cn

Boya Zhang
State Key Laboratory of Electrical Insulation and Power Equipment
Xi'an Jiaotong University
Xi'an, P.R.China
zhangby@xjtu.edu.cn

Xingwen Li
State Key Laboratory of Electrical Insulation and Power Equipment
Xi'an Jiaotong University
Xi'an, P.R.China
xwli@xjtu.edu.cn

***Abstract*—The rapid transition towards 1500/2500V direct current systems and equipment miniaturization imposes stringent requirements on the arc-quenching capability of gassing materials in low-voltage circuit breakers. To overcome the limitations of traditional trial-and-error approaches and univariate analysis, this study proposes a physics-informed data-driven framework to identify the "equivalent physical parameters" quantitatively governing arc extinction. A comprehensive database was constructed for 30 distinct gassing materials, integrating standardized breaking experiments with theoretical equilibrium plasma calculations over a temperature range of 300–30,000 K. By employing a multi-scale temperature segmentation strategy and mathematical feature recombination, a high-dimensional feature space was generated to capture the synergistic couplings of thermodynamic and transport properties. Statistical screening revealed 29 composite physical features exhibiting very strong linear correlations ($|r| \geqslant 0.7$) with the average arc voltage. The analysis suggests that the fluctuation intensity of these composite parameters across the arc temperature spectrum is a critical determinant of quenching performance, highlighting the importance of property stability over static magnitudes. Furthermore, an uncertainty-aware weighted Ridge Regression model was established based on the optimal 29-feature subset. The model achieved a weighted R2 of 0.7936, with 86.7% of the predicted values successfully falling within the experimental measurement range. This framework provides a robust quantitative tool for the rational design of next-generation gassing materials.**

Keywords—component, formatting, style, styling, insert (*key words****)***

I. INTRODUCTION

Low-voltage circuit breakers (LVCBs) are critical equipment in electrical safety and control systems [1]. Currently, the rapid development of renewable energy, particularly photovoltaic power generation, is driving a fundamental shift in power infrastructure towards a direct current (DC) system. This shift places increasingly stringent demands on switchgear: on the one hand, to accommodate high-capacity DC transmission, rated operating voltages are increasing from the traditional 750V to 1500V, and even as high as 2500V; on the other hand, the high-density integration requirements of photovoltaic combiner boxes necessitate a significant reduction in equipment size [2].

This trend of "higher voltage ratings" and "smaller sizes" presents an unprecedented challenge to arc-quenching technology. The combination of elevated arc energy and confined extinguishing spaces means that traditional magnetic blowout and splitter plate technologies are approaching their physical limits. In this context, gassing materials have emerged as the critical component determining the breaking capacity of next-generation LVCBs [3]. Under the intense thermal radiation of the arc, these materials undergo pyrolysis to generate high-velocity gas flows. This process not only pressurizes the confined chamber to increase the dielectric strength but also induces strong convective cooling to dissipate the arc energy. Consequently, the performance of the gassing material directly dictates whether an LVCB can successfully interrupt high-voltage DC faults within a miniaturized structure.

However, despite their critical industrial role, the design and optimization of high-performance gassing materials remain largely reliant on empirical trial-and-error approaches. The interaction between the ablation plasma and the electric arc is a highly complex magnetohydrodynamic process involving the coupling of electromagnetic, thermal, and fluid fields [4]. Historically, researchers have attempted to correlate arc-quenching performance with individual physical properties, such as thermal conductivity, specific heat, or ionization potential. While these univariate analyses provide partial insights, they often fail to explain the dynamic quenching capability comprehensively [5]. For instance, a material with high thermal conductivity might fail to interrupt the current if its resulting plasma lacks sufficient dielectric strength, or if the ablation pressure is inadequate. This limitation suggests that the arc-extinction process is not governed by any single scalar property but by the synergistic coupling of multiple physical parameters. Consequently, the lack of a quantitative structure-property relationship (QSPR) describing these complex interactions has become a bottleneck, hindering the rational design of novel materials capable of meeting the 2000 V and miniaturization targets.

To address this challenge, this study proposes a "physics-informed data-driven framework" to identify the "equivalent physical parameters" that quantitatively govern arc-quenching performance. In this framework, "physics-informed" denotes that the input features are rooted in equilibrium plasma theory and Magnetohydrodynamic coupling, while "data-driven" signifies the use of statistical screening and regression algorithms to map these physical features to experimental outcomes. We constructed a comprehensive database integrating standardized breaking experiments with theoretical equilibrium plasma calculations for 30 distinct materials. Through high-dimensional feature engineering and rigorous stability analysis, the dominant composite parameters driving the extinction process were successfully identified. The findings of this study provide a quantitative theoretical foundation and a high-fidelity QSPR model, offering a rational roadmap for designing high-performance gassing materials tailored for the next generation of high-voltage DC circuit breakers.

II. Research Methodology

A. Overall Technical Framework

The primary objective of this study is to identify the equivalent physical parameters that quantitatively govern the arc-quenching performance of gassing materials. To achieve this, a systematic framework integrating experiments, plasma calculations, and data-driven analysis was established. As illustrated in Fig. 1, the roadmap comprises two distinct steps:

Step 1: Construction of Integrated Database. This phase compiles a comprehensive dataset for 30 gassing materials by merging experimental metrics with theoretical properties:

- Target Variable Acquisition: Average arc voltage, serving as the quantitative benchmark for quenching capability, was acquired through standardized breaking experiments (Section II.B).
- Initial Feature Seven fundamental thermodynamic and transport properties were derived using equilibrium plasma calculations (Section II.C) to serve as the foundational input.

Step 2: Physics-Based Feature Engineering and Parameter Identification. To capture complex multiphysics interactions, fundamental properties were transformed into equivalent physical descriptors through a four-step process:

- Mathematical Recombination: Base parameters were mathematically combined to generate composite physical curves, representing potential high-order interactions governing arc behavior.
- Time-Series Feature Extraction: The tsfresh toolkit was utilized to transform these temperature-dependent curves into a high-dimensional scalar feature space via statistical and time-domain analysis.
- Statistical Screening: The feature space underwent rigorous filtering to remove non-informative (zero variance) and redundant (high multicollinearity) data.
- Parameter Identification and Modeling: Finally, Pearson correlation analysis was employed to identify the most influential features, which were then used to construct a QSPR model linking physical parameters to arc-quenching performance.

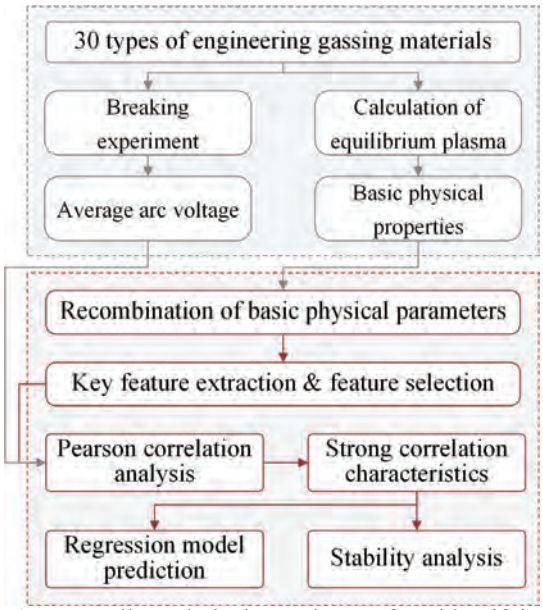


Fig. 1. Overall technical roadmap for identifying of equivalent physical parameters for arc quenching characteristics of gassing materials

B. Breaking experiment based on standard model

The experimental evaluation employed the standardized arc chamber model proposed in previous work [2]. Specimens representing the 30 distinct engineering gassing materials were machined into identical geometries and positioned consistently relative to the arc initiation point. It should be noted that the specific chemical compositions of these 30 materials are withheld due to non-disclosure agreements with industrial collaborators. Readers interested in the detailed empirical performance comparison of specific commercial formulations are referred to our previous work [2]. The current study utilizes this diverse dataset strictly to validate the proposed data-driven parameter identification framework rather than evaluating individual material performance. To simulate the long-duration short-circuit interruption process, a synthetic circuit was utilized under strictly controlled conditions. These conditions included a circuit frequency of 11 Hz, a charging voltage of 800 V, and a prospective short-circuit current of 5 kA, ensuring that all variables other than the material composition remained constant.

During the interruption process, transient arc voltage was acquired utilizing a high-voltage differential probe coupled with a high-frequency oscilloscope. Fig. 2 presents a representative voltage waveform recorded during the initial single experiment. To quantify the steady-state quenching capability, the average arc voltage extracted from the quasi-steady arcing phase was selected as the primary performance metric. Specifically, the initial arc ignition peak and the final arc extinction peak were excluded, and the arithmetic mean of the remaining voltage values was calculated to better reflect the continuous arc-quenching capability. To guarantee data reliability and experimental repeatability, each gassing material underwent three consecutive interruption tests under identical conditions. The final performance indicator for each specimen, as summarized in Fig. 3, was derived from the

arithmetic mean of the quasi-steady arc voltages obtained from these three valid operations.

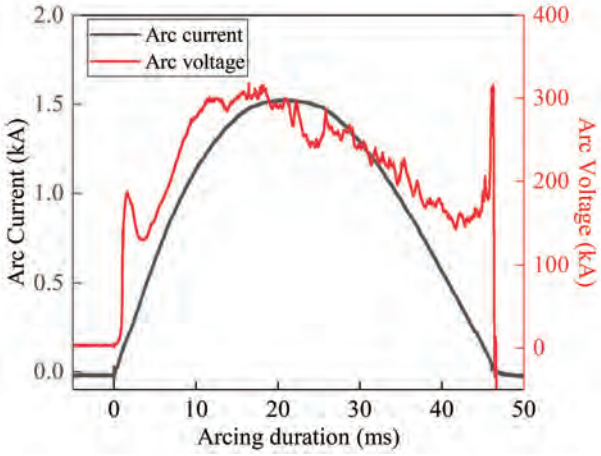


Fig. 2. The representative arc voltage

Fig. 3 summarizes the comparative average arc voltage results for all 30 gassing materials. The data reveal a significant dispersion in arc-quenching performance across the sample set. Given the identical circuit parameters and geometric configurations used throughout the testing, the observed wide variation in average arc voltage confirms that the chemical composition of the gassing material plays a decisive role in modulating arc characteristics. This distinct performance gap provides a robust and discriminative dataset necessary for the subsequent identification of equivalent physical parameters.

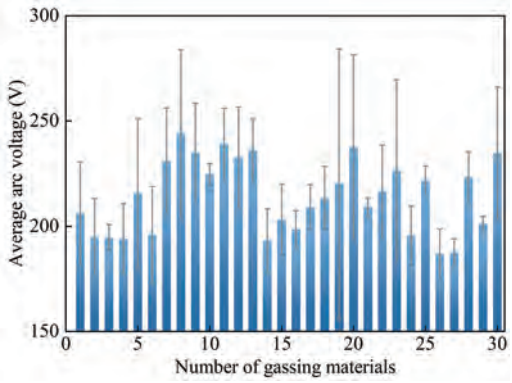


Fig. 3. Average arc voltage of 30 gassing materials

C. Calculation of Equilibrium Plasma Properties

To quantify the material response under high-temperature arc conditions, the study employed the equilibrium plasma calculation method. Relying on the local thermodynamic equilibrium assumption [6], [7], [8], the computation follows a streamlined two-step procedure. First, the equilibrium composition, encompassing the concentrations of molecules, atoms, and ions, is determined by the minimization of Gibbs free energy. Subsequently, the macroscopic thermodynamic and transport properties are derived utilizing statistical thermodynamics and the Chapman-Enskog theory.

Fig. 4 illustrates the calculated temperature-dependent profiles for seven fundamental properties: density ρ, enthalpy h, specific heat c_p, electrical conductivity σ, thermal conductivity λ, viscosity μ, and speed of sound v. These profiles cover a wide temperature range from 300 K to 30,000 K at a pressure of 1 atm, revealing the complex physicochemical evolution of the ablation medium.

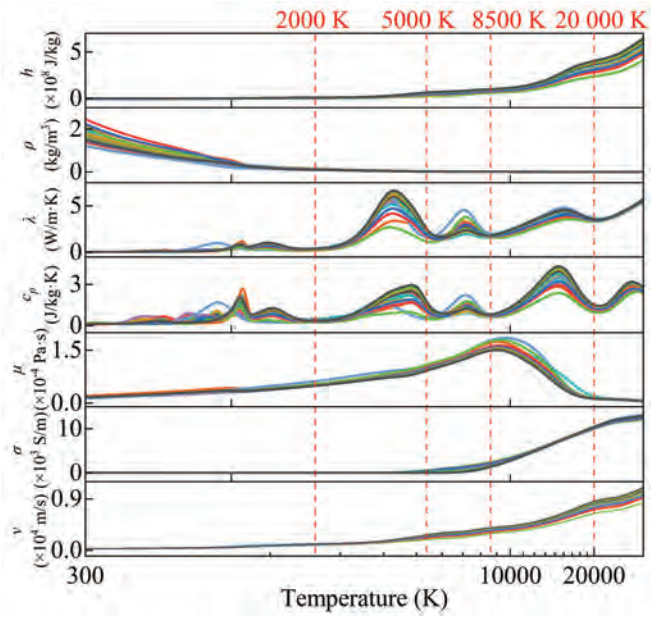


Fig. 4. 7 basic physical property parameters of 30 materials

D. Physics-Based Feature Engineering

The interaction between the gassing material and the arc plasma is a complex multiphysics phenomenon not governed by any single physical property in isolation. Instead, it is determined by the synergistic coupling of electromagnetic, fluid, and thermal fields described by the Magnetohydrodynamic equations. Within these governing equations, material properties invariably appear in combined forms rather than as independent scalars.

To capture the multiphysics interactions described above, the seven base properties were expanded into a high-dimensional feature space through mathematical recombination. As detailed in Table I, 1,778 composite physical curves were generated by combining up to seven base parameters using multiplication and division operators. The physical logic behind this expansion is to generate terms that represent specific physical capabilities.

TABLE I
MATHEMATICAL FORMULATION OF COMPOSITE PHYSICAL FEATURES

Complexity Order	Mathematical form	Number of parameters
Binary (2nd Order)	A*B A/B	63
Ternary (3rd Order)	A*B/C A/(B*C)	210
Quaternary (4th Order)	(A*B*C)/D (A*B)/(C*D) A/(B*C*D)	385
Quinary (5th Order)	High-order combinations	630
Senary (6th Order)	High-order combinations	364
Septenary (7th Order)	High-order combinations	126

Note: A, B, C, D… represent non-repeating parameters from the set of seven base properties.

A prime example is the Volumetric Heat Capacity (ρc_p) [9]. This combination quantifies the energy required to raise the temperature of a unit volume of plasma. In the context of radial energy transport, this composite term is physically more decisive for determining the arc radius constriction and

temperature decay speed than either density or specific heat alone.

Since the derived composite features manifest as functional curves that vary drastically with temperature, quantifying the contribution of material properties requires evaluating specific stages of arc evolution. To achieve this, the tsfresh library [10] was employed to extract scalar features from the curves based on a multi-Scale temperature segmentation strategy. Instead of relying solely on discrete physical stages, we expanded the domain into 15 distinct temperature intervals to capture both local physicochemical events and broad cumulative effects. These intervals are categorized as follows:

- Discrete Elementary Zones: To isolate specific microscopic physical events, the domain was divided into five sequential, non-overlapping intervals: 300–2000 K (initial pyrolysis), 2000–5000 K (main decomposition), 5000–8500 K (mild dissociation), 8500–20,000 K (complete dissociation to atomic transition), 20,000–30,000 K (fully ionized plasma), and 300–30,000 K (the Global Range).
- Cross-Regional Combination Zones: To explore potential coupling effects between adjacent physical stages, nine intermediate sliding windows were established: 300–5000 K, 300–8500 K, 300–20,000 K, 2000–8500 K, 2000–20,000 K, 2000–30,000 K, 5000–20,000 K, 5000–30,000 K, and 8500–30,000 K.

This comprehensive segmentation strategy generated a high-dimensional feature matrix containing tens of thousands of potential predictors for each gassing material. Given the extensive overlap between these temperature intervals, the feature space inherently contains significant structural redundancy. To address this, a two-stage screening strategy was implemented to identify the key physical parameters.

Step 1: Multicollinearity Reduction. Given that many derived physical quantities are mathematically interdependent (e.g., polynomial combinations), the feature space inherently contains significant redundancy. To address this, collinearity analysis was performed to eliminate features exhibiting zero variance or correlation coefficients exceeding 0.95.

Step 2: Physics-Based Relevance Identification. To identify the physical parameters that truly govern arc-quenching performance, Pearson correlation analysis was employed as a quantitative screening tool. The correlation coefficient (r) was calculated between each physical feature and the average arc voltage. In the context of this study, the sign of r carries specific physical implications: a positive coefficient signifies that an increase in the physical parameter promotes the rise of arc voltage (enhancing quenching performance), whereas a negative coefficient implies a suppressive effect. To filter for the most valid parameters, a strict selection threshold was applied. Features exhibiting an absolute correlation coefficient $|r|\geq 0.8$ were categorized as having a very strong linear correlation, while those falling within the range $0.6\leq|r|< 0.8$ were considered to have a strong linear correlation [11].

III. Results and Discussion

A. Distribution of Correlation with Arc Voltage

To quantitatively evaluate the impact of physical properties on arc quenching, Pearson correlation coefficients were calculated between the generated high-dimensional features and the average arc voltage. Fig. 5 illustrates the frequency distribution histogram of these coefficients, exhibiting three distinct characteristics regarding the relationship between material properties and arc performance.

Unlike a normal distribution, the histogram exhibits a multimodal structure with a significant extension into the negative tail. This negative skew reflects the underlying physics: conductivity-related parameters, which inherently lower arc resistance and voltage, dominate the high-correlation negative region.

High-quality predictors are extremely sparse. As indicated in the figure, out of the massive feature set, only 246 features meet the threshold for strong correlation ($|r|\geq 0.6$), and merely 29 features achieve very strong correlation ($|r|\geq 0.7$). This sparsity validates the necessity of the high-dimensional expansion strategy to uncover the few dominant descriptors hidden in the parameter space.

The red dashed lines ($|r|=0.6$) delineate the critical tails of the distribution. Consequently, the 29 top-tier features located in the extreme tails were identified as the primary candidates for the subsequent physical mechanism analysis.

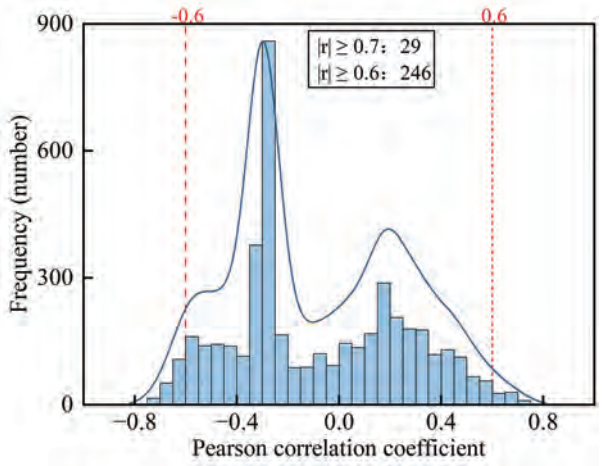


Fig. 5. Correlation distribution between mean arc voltage and underlying physical parameters

B. Stability analysis of key features

To intuitively visualize the strong linear relationship identified by the screening process, Fig. 6 presents the scatter plot of the feature exhibiting the highest correlation coefficient, with an r value of 0.7678, against the average arc voltage. The data points for the 30 materials cluster tightly around the regression line, indicating that this specific feature exerts a dominant influence on arc-quenching performance.

The identified top feature is derived from the composite interaction of c_p, σ, and λ over the broad temperature range of 300–20,000 K. Mathematically, this feature calculates the Benford Correlation of the composite curve.

Physically, this metric serves as a descriptor of the dynamic range and evolutionary complexity of the material's properties. Benford's Law typically governs datasets that

span multiple orders of magnitude resulting from natural power-law processes. A high Benford correlation implies that the energy balance term (the coupling of c_p, σ, and λ) evolves continuously and drastically across orders of magnitude throughout the pyrolysis, dissociation, and ionization stages. This suggests that materials capable of maintaining a robust, wide-spanning physical response, without stagnating in narrow value bands, are more effective at suppressing the arc.

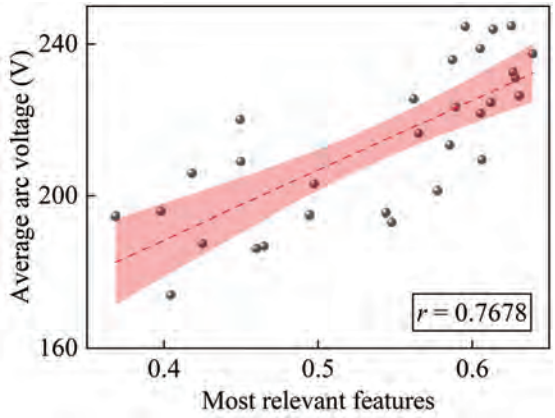


Fig. 6. The distribution of most relevant features and mean arc pressure

However, a critical question arises regarding whether this high correlation reflects a universal physical law or is merely a statistical artifact driven by the specific distribution of the current dataset. In data-driven modeling, particularly with small-to-medium datasets where N=30, a static high correlation coefficient can be deceptive. It might be inflated by influential outliers or specific sample biases. If the identified feature relies heavily on such statistical coincidences, the resulting model will lack generalization capability and fail when applied to new material systems.

To resolve this concern and distinguish truly robust physical descriptors from spurious correlations, the study moved beyond static evaluation to implement a Dynamic Stability Evaluation Framework. This framework assesses whether a feature maintains its strong correlation across varying data subsets through a three-step procedure:

Step 1: Establishment of Candidate Pool. We first screened all physical features with a strong correlation ($|r| \geqslant 0.6$) to the average arc voltage, forming a Candidate Feature Pool. These features serve as the subjects for the stability test.

Step 2: Multiscale Iterative Subsampling. We implemented an iterative subsampling strategy to simulate data perturbations. From the total sample set (N=30), we generated subsets of varying sizes, decreasing from 30 down to 20 with a step size of 2 (e.g., subset sizes of N = {28, 26, 24, 22, 20}). This approach tests the feature's sensitivity to sample size reduction.

Step 3: Monte Carlo Resampling Analysis. For each subset size, we recalculated the Pearson correlation coefficients for all features in the candidate pool. To address the computational challenge posed by the combinatorial explosion (e.g., selecting 20 samples from 30 results), we adopted a Monte Carlo resampling approach [12]. When the theoretical number of combinations for a specific subset size exceeded a preset threshold (set to 10^4 in this study), we performed 10,000 independent random samplings. This ensures that the statistical distribution of the feature's stability is accurately captured without the need for exhaustive enumeration.

Fig. 7 visualizes the results of the Monte Carlo stability analysis, displaying the average Pearson correlation coefficients and their corresponding standard deviations (represented by error bars) for the top 5 identified physical features across varying sample subset sizes. The detailed statistical behavior reveals three critical findings:

As observed in the bar charts, the average absolute correlation coefficients (represented by bar heights) for the top 5 composite features exhibit remarkable stability. Even when the sample subset size is reduced from 28 to 20, the mean absolute correlation values remain relatively constant. Specifically, the top-ranking feature maintains a mean value of approximately 0.77 across all sampling scales. This flat trend indicates that the strong relationship between these physical features and arc voltage is invariant to sample selection. It is not driven by a specific subset of lucky data points but reflects a universal physical mechanism shared by the majority of the gassing materials.

The error bars in Fig. 7, representing the standard deviation of coefficients from 10,000 Monte Carlo simulations, increase monotonically as the subset size decreases. This reflects the natural rise in uncertainty when data becomes scarcer. Crucially, even at the smallest subset size (N=20), the lower bound of the error bars for the top feature remains above 0.72 (well above the 0.6 threshold for strong correlation). This confirms that even under the most unfavorable sampling conditions, these features maintain a statistically significant relationship with arc voltage, ruling out spurious correlations caused by outliers.

Among the top candidates, the feature $c_p \cdot \sigma/\lambda$ (represented by the dark blue bar) consistently demonstrates the highest correlation magnitude and relatively low variance across all scales. Its mean absolute correlation consistently outperforms other combinations. This stability analysis firmly establishes $c_p \cdot \sigma/\lambda$ as the most robust equivalent parameter for predicting arc-quenching performance, suggesting that the synergistic coupling of specific heat, electrical conductivity, and thermal conductivity plays the decisive role in the energy balance of the arc plasma.

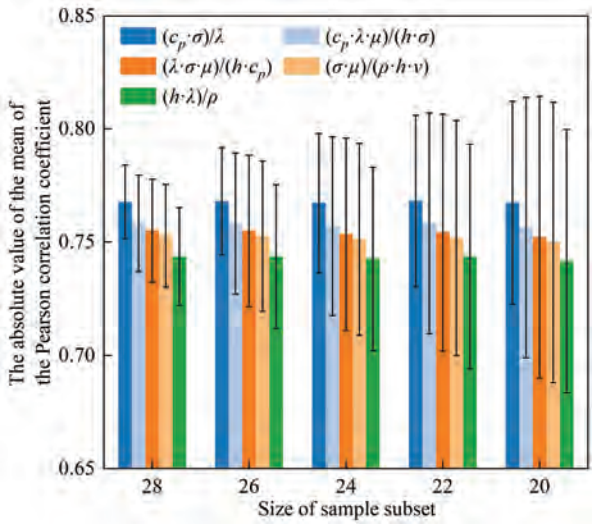


Fig. 7. The distribution of most relevant features and mean arc pressure

To contextualize these findings with established industrial experience, the top-identified composite parameter, $c_p\sigma/\lambda$, can be utilized to physically explain the performance of "classic" baseline materials. For instance, conventional gassing materials like PA6 are known to exhibit strong arc-quenching capabilities. Under our theoretical framework, this aligns with PA6's robust multi-scale pyrolysis behavior, which maintains a high c_p and optimized λ over a wide temperature range, thereby maximizing the $c_p\sigma/\lambda$ indicator. Conversely, materials like PTFE, while offering high dielectric strength, often exhibit different decomposition kinetics that may result in a lower synergy of this specific energy balance term during the quasi-steady phase, corroborating empirical observations. Therefore, while the explicit chemical formulations of the 30 investigated samples remain proprietary, the identified high-order physical parameters serve as universal quantitative criteria that successfully bridge empirical intuition with theoretical plasma dynamics.

C. *Establishment of QSPR Model*

Although the Pearson correlation analysis successfully identified thousands of physical features statistically related to the arc voltage, reliance on univariate analysis possesses inherent limitations. Linear correlation coefficients evaluate features in isolation, effectively neglecting the multicollinearity among physical parameters and the potential synergistic effects of complex feature combinations. Furthermore, the direct input of high-dimensional features into a regression model inevitably leads to overfitting and poor generalization. To address these challenges, a two-stage modeling strategy integrating coarse screening and fine selection was proposed, as illustrated in Fig. 8.

Stage 1: Dimension Reduction (coarse screening). To ensure computational feasibility, the feature space was first filtered for strong correlations ($|r|\geq 0.6$), retaining only the top 100 candidates. This step significantly reduces dimensionality while preserving the vast majority of critical physical information for the subsequent precision screening.

Stage 2: Forward Feature Selection (fine selection). Within the reduced pool, the Forward Feature Selection (FFS) algorithm was employed to identify the optimal subset. Through an iterative greedy search, features maximizing the 5-fold cross-validation weighted R^2 were sequentially added to the model until performance saturation was observed.

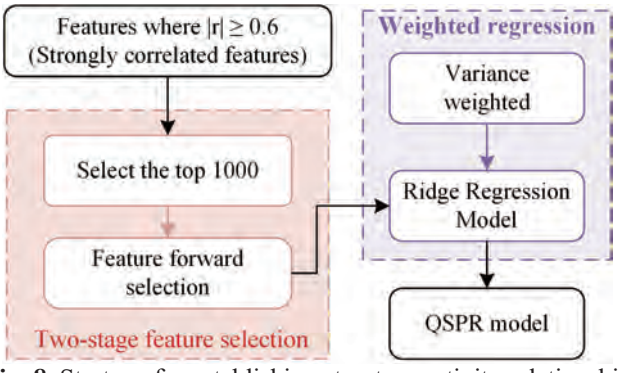


Fig. 8. Strategy for establishing structure activity relationship model

The underlying model employs Ridge Regression with L2 regularization to effectively mitigate feature collinearity. Crucially, to strictly account for experimental uncertainty, an uncertainty-aware weighting strategy was implemented. Since the standard deviation of the three repeated breaking tests reflects data stability, the training weight for each sample was set to the inverse of its standard deviation. This strategy ensures that samples with stable voltage signals dominate the parameter optimization process, thereby enhancing the model's robustness against experimental noise..

Fig. 9 illustrates the optimization trajectory of the model performance throughout the forward feature selection process. The weighted 5-fold cross-validation R^2 exhibits a rapid ascent as the feature subset expands, culminating in a global maximum of 0.7936 when the feature count reaches 29. Beyond this critical point, the introduction of additional features yields no performance gain and induces a slight decline, indicating that the information gain has been saturated by noise or redundancy. Consequently, the 29-feature configuration was identified as the optimal model. Furthermore, the inset scatter plot compares the predicted arc voltages against the actual experimental measurements for the validation set. The tight convergence of the data points along the $y=x$ ideal diagonal confirms the high fidelity of the QSPR model, demonstrating its capability to accurately capture the macroscopic arc-quenching performance based on the identified physical descriptors.

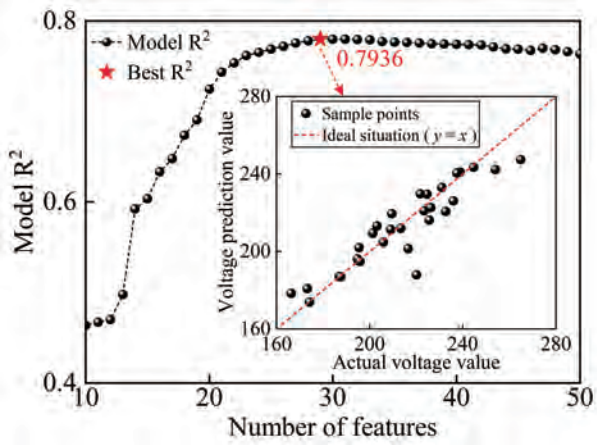


Fig. 9. Model R^2 as a function of the number of features and the optimal R^2

To provide full transparency regarding the optimal QSPR model, Table II details the mathematical formulations of all 29 selected composite physical features. These features represent the most critical high-order synergistic couplings governing the arc-quenching process within the identified temperature windows.

TABLE II
THE 29 EQUIVALENT PHYSICAL PARAMETERS USED IN THE QSPR MODEL

Composite Feature	Temperature Window (K)	Feature Name
$(v\cdot\lambda\cdot\sigma)/(\rho\cdot h\cdot c_p\cdot\mu)$	300_5000	binned_entropy__max_bins_10
$(\rho\cdot h\cdot v)/(c_p\cdot\lambda\cdot\sigma)$	300_30000	binned_entropy__max_bins_10
$(\lambda\cdot\sigma)/(\rho\cdot h\cdot v)$	300_5000	binned_entropy__max_bins_10
$(h\cdot\lambda)/\rho$	300_8500	ratio_beyond_r_sigma__r_1.5
$\sigma/(\rho\cdot h\cdot c_p\cdot\mu)$	300_5000	binned_entropy__max_bins_10
$(c_p\cdot\sigma)/(\rho\cdot h\cdot v)$	300_5000	binned_entropy__max_bins_10

$(v \cdot c_p)/(\rho \cdot h \cdot \sigma \cdot \mu)$	300_5000	linear_trend__attr_"rvalue"
$(c_p \cdot \mu)/(\rho \cdot v \cdot \sigma)$	5000_8500	ratio_beyond_r_sigma__r_0.5
$(c_p \cdot \sigma)/\lambda$	300_20000	_benford_correlation
$(h \cdot c_p)/\rho$	300_5000	benford_correlation
$(\lambda \cdot \mu)/(\rho \cdot h \cdot v \cdot \sigma)$	300_5000	agg_linear_trend__attr_"rvalue"__chunk_len_5__f_agg_"mean"
$(h \cdot v)/(\rho \cdot c_p \cdot \lambda \cdot \sigma)$	300_8500	quantile__q_0.3
$c_p/(\rho \cdot h \cdot v \cdot \sigma)$	300_20000	index_mass_quantile__q_0.6
$(c_p \cdot \lambda)/(\rho \cdot h \cdot v \cdot \sigma)$	300_5000	agg_linear_trend__attr_"rvalue"__chunk_len_5__f_agg_"mean"
$\sigma/(\rho \cdot h \cdot \lambda \cdot \mu)$	300_2000	quantile__q_0.4
$(c_p \cdot \lambda \cdot \mu)/(h \cdot \sigma)$	300_20000	linear_trend__attr_"rvalue"
$(c_p \cdot \sigma)/(\rho \cdot h \cdot v \cdot \lambda \cdot \mu)$	300_2000	quantile__q_0.3
v/λ	5000_8500	ratio_beyond_r_sigma__r_0.5
$\sigma/(\rho \cdot h \cdot \lambda \cdot \mu)$	300_2000	quantile__q_0.2
$(v \cdot c_p)/(\rho \cdot h \cdot \sigma)$	300_5000	linear_trend__attr_"rvalue"
$(c_p \cdot \sigma)/(\rho \cdot h \cdot v \cdot \lambda)$	300_2000	quantile__q_0.3
$(c_p \cdot \sigma)/(\rho \cdot h \cdot \mu)$	300_5000	binned_entropy__max_bins_10
$(c_p \cdot \lambda)/(\rho \cdot h \cdot v \cdot \sigma \cdot \mu)$	300_30000	linear_trend__attr_"rvalue"
$(c_p \cdot \lambda \cdot \mu)/(h \cdot \sigma)$	300_5000	agg_linear_trend__attr_"rvalue"__chunk_len_5__f_agg_"mean"
$\rho/(v \cdot c_p \cdot \lambda)$	5000_30000	ratio_beyond_r_sigma__r_0.5
$(v \cdot c_p \cdot \lambda)/(h \cdot \sigma)$	300_5000	agg_linear_trend__attr_"rvalue"__chunk_len_5__f_agg_"mean"
$(v \cdot c_p \cdot \sigma)/(h \cdot \lambda)$	300_2000	quantile__q_0.3
c_p	5000_30000	ratio_value_number_to_time_series_length
$h/(\rho \cdot c_p \cdot \lambda \cdot \sigma)$	300_20000	quantile__q_0.7

Fig. 10 presents the target plot distribution for the optimal 29-feature model. This visualization compares the predicted arc voltages against the experimental measurements, specifically assessing whether the predictions fall within the measurement range (defined as the experimental mean ± standard deviation). As indicated in the legend, the predicted values fall within the experimental error bars for 26 out of 30 tested gassing materials, while 4 samples exhibit deviations outside this range. This corresponds to a hit rate of 86.7%, indicating that the model captures the performance bounds of the majority of materials relative to the experimental variance.

In summary, a QSPR model driven by 29 equivalent physical parameters was constructed using the proposed feature engineering and statistical selection framework. The validation results suggest that the model possesses sufficient generalization capability to serve as a quantitative tool for predicting the arc-quenching potential of material formulations.

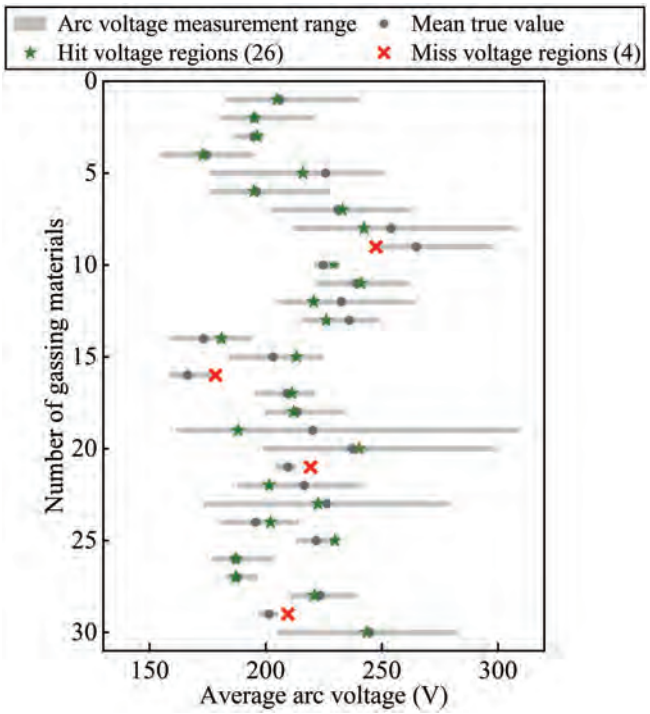


Fig. 10. Distribution of predicted values for 30 gassing materials falling within the voltage range

IV. Conclusion

This study proposed a physics-informed data-driven framework to quantify the arc-quenching performance of gassing materials. The key conclusions are as follows:

1) A systematic methodology was developed to identify governing physical parameters via mathematical recombination and feature engineering. This approach overcomes the limitations of traditional univariate analysis, providing an unbiased pathway to discover complex structure-property relationships often overlooked by empirical observation.

2) Rigorous screening identified 29 composite physical features exhibiting very strong correlations ($|r| \geq 0.7$) with arc voltage, validated by dynamic stability analysis. While the deep physical mechanisms of these specific features warrant further investigation, the proposed screening methodology is generic and readily extendable to other circuit topologies and voltage levels.

3) A QSPR model was successfully constructed using an uncertainty-aware weighted ridge regression strategy. The model demonstrates high predictive fidelity (R^2=0.7936), serving as a reliable tool for the rapid pre-screening and reverse engineering of candidate formulations for next-generation gassing materials.

References

[1] [1] X. Li, 'Gaseous Switching Arc and Extension to Pulsed Plasma', in 2022 *IEEE 67th* Holm *Conference on Electrical Contacts (HLM)*, Oct. 2022, pp. 1–12. doi: 10.1109/HLM54538.2022.9969803.

[2] W. Cao, C. Luo, Q. Wang, T. Zhuang, Y. Zhang, and X. Li, 'Evaluation and analysis of gassing material performance used in low-voltage circuit breakers', *IEEE Trans. Power Del.*, vol. 40, no. 2, pp. 728–738, Apr. 2025, doi: 10.1109/TPWRD.2024.3516725.

[3] W. Cao *et al.*, 'Atomic-scale insight into arc plasma radiation-induced gassing materials ablation: photothermal decomposition behavior', *J. Phys. D: Appl. Phys.*, vol. 57, no. 19, p. 195204, Feb. 2024, doi: 10.1088/1361-6463/ad2562.

[4] Zijie Liao, Qian Wang, and Xingwen Li, 'Effect of Gassing Material on Partial Discharge Characteristics in MCCB', in *2022 IEEE 67th Holm Conference on Electrical Contacts (HLM)*, 2022, pp. 1–7. doi: 10.1109/HLM54538.2022.9969789.

[5] W. Cao *et al.*, 'A theoretical model considering the photochemical and photothermal behavior of arc radiation-induced gassing materials ablation', *J Phys D Appl Phys*, vol. 57, no. 37, p. 375201, June 2024, doi: 10.1088/1361-6463/ad5601.

[6] X. Guo, X. Li, A. B. Murphy, and H. Zhao, 'Calculation of thermodynamic properties and transport coefficients of CO_2–O_2–Cu mixtures', *J Phys D Appl Phys*, vol. 50, no. 34, p. 345203, Aug. 2017, doi: 10.1088/1361-6463/aa7bce.

[7] X. Li, X. Guo, A. B. Murphy, H. Zhao, J. Wu, and Z. Guo, 'Calculation of thermodynamic properties and transport coefficients of C5F10O-CO2 thermal plasmas', *J Appl Phys*, vol. 122, no. 14, p. 143302, Oct. 2017, doi: 10.1063/1.5006635.

[8] X. Guo, A. B. Murphy, and X. Li, 'Thermodynamic properties and transport coefficients of two-temperature helium thermal plasmas', *J. Phys. D: Appl. Phys.*, vol. 50, no. 12, p. 125202, Feb. 2017, doi: 10.1088/1361-6463/aa5d25.

[9] J. Liu, Q. Zhang, J. D. Yan, J. Zhong, and M. T. C. Fang, 'Analysis of the characteristics of DC nozzle arcs in air and guidance for the search of SF6 replacement gas', *J. Phys. D: Appl. Phys.*, vol. 49, no. 43, p. 435201, Sept. 2016, doi: 10.1088/0022-3727/49/43/435201.

[10] M. Christ, N. Braun, J. Neuffer, and A. W. Kempa-Liehr, 'Time series FeatuRe extraction on basis of scalable hypothesis tests (tsfresh – a python package)', *Neurocomputing*, vol. 307, pp. 72–77, Sept. 2018, doi: 10.1016/j.neucom.2018.03.067.

[11] 'Statistical methods for transport demand modeling'. Accessed: Jan. 04, 2026. [Online]. Available: https://www.sciencedirect.com/science/chapter/monograph/abs/pii/B9780128115138000054

[12] S. Karakaya, 'Enhanced resampling scheme for monte carlo localization', *Intell. Serv. Rob.*, vol. 17, no. 3, pp. 703–714, May 2024, doi: 10.1007/s11370-024-00530-9.

Investigation of electric and magnetic field in bolted copper busbar joints

Toni Ivas
Advanced Materials & Surfaces
Empa
Dübendorf, Switzerland

Philipp Scheidegger
Transport at Nanoscale Interfaces
Empa
Dübendorf, Switzerland

Rolf Brönimann
Transport at Nanoscale Interfaces
Empa
Dübendorf, Switzerland

Jonas Diaz
Advanced Materials & Surfaces
Empa
Dübendorf, Switzerland

Jacim Jacimovic
ABB Ltd.
Turgi, Switzerland

Lorenz Herrmann
Advanced Materials & Surfaces
Empa
Dübendorf, Switzerland

***Abstract*— Bolted busbar joints in electrical machines are critical for electrical transport applications, While the electrical behaviour of such joints has been studied experimentally and numerically [6, 7, 24, 25], a spatially resolved, combined experimental and simulation approach that captures both current distribution and local resistance along the joint remains lacking. Small changes in contact resistance can lead to considerable losses in high-current applications. This work investigates contact resistance evolution in real-size four-bolt copper joints under realistic high-current conditions up to 1.6 kA DC current. At the same time, we vary contact resistance by accelerated grown intermediate oxide layers of different thicknesses. A custom measurement setup with voltage probes and magnetic field probes enables spatially resolved investigation of current distribution during operation. The measurements are complemented with electromechanical finite element simulations. By measuring both local current distribution and local voltage drop, we present a spatially resolved resistance measurement along the joint, supported by finite element simulations building on Holm theory and CMY (Cooper-Mikic-Yovanovich) contact models. With all bolts tightened to the same torque, the contact resistance depends on proximity to the bolted areas and on oxide thickness. It decreases near the bolts because the higher contact force improves electrical contact.**

Keywords – contact resistance, Cu-busbars, FEM electro-mechanical

I. INTRODUCTION

Busbars connecting power converters and electrical machines are critical components for electrical power transmission. This study investigates how current distribution and contact resistance in Cu–Cu joints depend on oxidation and joint geometry. Due to relatively large current density (0.5-0.8 A/mm^2) the dissipated power is significant even in pristine joints and can readily produce power losses and temperatures as high as 50-65 ^{o}C. Depending on how efficiently heat is removed locally within the electrical device, even small increases in contact resistance can create hot spots exceeding 100 ^{o}C.

In this work, we study both experimentally and theoretically a simplified model consisting of a three busbar bolted connection that forms two symmetric busbars joints, as visualized in Figure 1. It consists of standard copper plates with dimensions 252x100x10 mm with M12 screws (DIN). While the busbar geometry appears straightforward at first glance, accounting for all mechanical and electrical factors, as well as the physical processes at the interface, introduces substantial complexity, notably in the vicinity of the bolts.

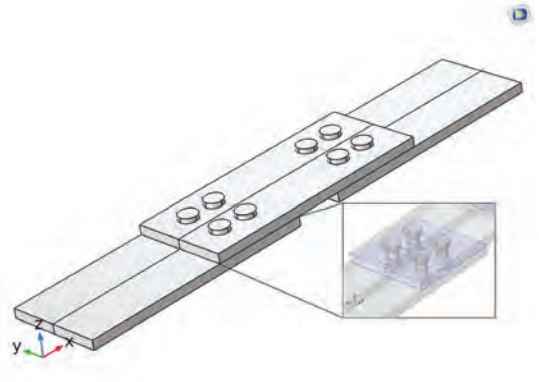


Fig. 1 Object under test: Geometry used for our investigations, depicted here as a model geometry: the inset shows the Contact Pair used in our FEM model.

Several factors influence how current is distributed across the contact area: oxidation of the contact surface [1], distribution of contact pressure as well as microstructure properties of the surface like roughness and hardness [2]. To enable continuous operation under high current loads, busbars joints must maintain low resistance and be resilient against thermal runaway. The latter can have its root cause in multiple characteristic failure modes, including oxidation or corrosion of the contact area [3], an increase of the contact resistance caused by wear or fretting, and a reduction of the contact force due to recrystallization or stress relaxation of the Cu-ETP (CW004A, EN 13601) material, or simply a failed bolt. In previous work, electrical contacts have been investigated using a range of experimental setups [4], [5]. Braunovic investigated the contact resistance and temperature of bolted connectors [6] as well as effect of connection design on bolted joints [7].

Fuhrmann et al. studied the contact behavior and permissible temperature limits of stationary bolted joints with coated conductors [25]. On much smaller scale, Dutta et. al. [8] performed in-situ electrical contact resistance measurements using a table-top indenter setup , directly measuring the adhesion force and current at contact interfaces for different surface conditions. Several studies have also examined the electro-thermal performance of automotive connectors [9]. In addition to experimental work, theoretical studies employ a range of numerical methods to model electric contacts, notably boundary element [8],[9],[10] and FEM methods [13], [14].

Multiphysics approaches coupling different physics processes have also been reported in the literature [15], [16], [17]. Using COMSOL, for instance, several authors have developed coupled fluid-solid heat transfer models [18] and derived design guidelines to improve both the performance and reliability of electrical contacts [19]. With regard to our experimental setup, which is described in the next section, the numerical studies on the performance of pin and socket electrical contacts by Kim et. al [20] were particularly useful. Furthermore, the work by Duan et. al. [21], which developed a fully coupled mechanical-thermo-electrical model of electrical contact shrink range, as well as the ABAQUS and FE-SAFE implementations by Luo et al. [22] are methodologically highly relevant to our work, especially in the context of fatigue and reliability assessments of electrical connectors.

II. TEST PROCEDURE

A. Test Object

The aging of the busbar contact surfaces was conducted in a dedicated oven at 100°C for exposure durations of 48, 96, and 144 hours. To accelerate surface oxidation, the busbars were aged in an unfastened condition. Following oxidation, the test samples were assembled with torque of 50Nm. The electrical measurement setup is shown in Figure 2(a). To achieve a current density of 0.5-0.8 A/mm^2, a relatively large current of 1600 A is applied. For electrical safety reasons and due to the available power supply, the experiments are conducted at low voltage, which we consider an acceptable simplification that still yields representative results. The measurements of voltage drop along the joint were done by an in-house developed test setup shown in Figure 2(b). The measurement is based on recording the voltage difference between a reference point on the lower busbar and one of twelve spring contacts arranged in sequence on the upper copper busbar. The measured voltage drop includes contributions from the specific resistance of the material and the contact resistance. A schematic view is shown in Figure 2(c).

This setup enables reproducible measurements of the very small voltage drops. The spring contacts are spaced 10 mm apart and arranged in three rows, forming a grid for spatially resolved voltage sensing.

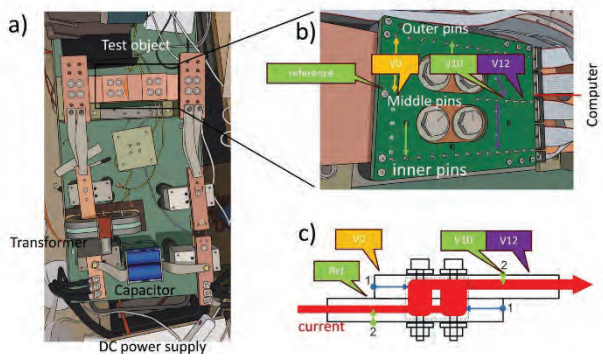


Fig. 2 Test rig and local measurement of the voltage drop across the joint (test specimen): (a) electrical test circuit with main components (b) PCB with local voltage probes on the joint surface (c) cross-section of test specimen.

To obtain a direct measure of the current distribution footprint, spatially resolved magnetic field measurements were carried out. Therefore, an in-house sensor has been developed, consisting of 12 Hall-effect sensors mounted on a Printed Circuit Board (PCB) as shown in Figure 3(a).

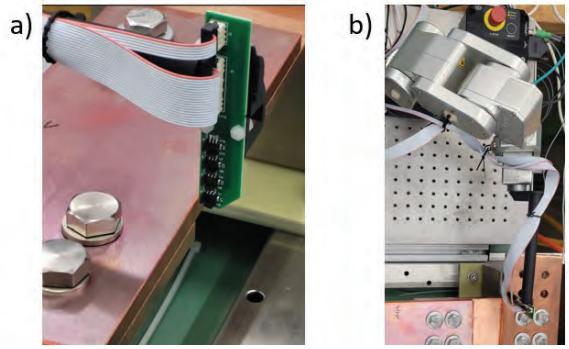


Fig. 3 (a) The PCB with 12 Hall-effect sensors used to measure the magnetic field, the sensors are arranged in four groups in order to measure the field at four positions. (b) Industrial robot arm with a mounted 3d-printed arm measuring the magnetic flux at the test rig.

III. THEORETICAL MODEL

The busbar model is implemented in COMSOL ver. 6.3. In the following, we define the governing equations of the physical system under investigation.

A. Formulation of heat equation and electromagnetic field

During the operation of the busbar, a substantial current flows inside the cross-section of the copper bar, which causes self-heating and limits current carry capacity. The thermal behavior is modeled using the heat equation, given by:

$$\rho c_p \partial T/\partial t + \nabla q = Q \qquad (1)$$

where the ρ is density, c_p is specific heat, T is temperature field. The heat flux is given by $q = -k\nabla T$, where k is the thermal conductivity, and Q denotes the volumetric heat source term. All thermophysical properties required to model the busbar system during operation are listed in Table 1.

TABLE I. MATERIAL CHARACTERISTICS OF THE MODEL

Property	Variable Name	Cu	Stainless Steel	Unit
Elec. conductivity	sigma_iso	5.988×10^{7}	4.032×10^{6}	S/m
Ther. conductivity	k_iso	400	44.5	W/mK
Density	rho	8960	7850	kg/m^3
Young's modulus	E	110	205	GPa
Poisson ratio	nu	0.35	0.28	1
Heat capacity	Cp	385	475	J/(kgK)
Coeff. Thermal expansion	alpha_iso	17×10^{-6}	12.3×10^{-6}	1/K
Resistivity	rho0	1.72×10^{-7}	59×10^{-8}	Ωm
Res. Temperature coeff.	alpha	0.0039	0.002	1/K

For stationary solution of Maxwell's equations, we use The Magnetic and Electric Fields Interface in COMSOL with:

$$\nabla \mathbf{J}=0 \quad (2)$$

$$\nabla\times\mathbf{H}=\mathbf{J} \quad (3)$$

$$\mathbf{B}=\nabla\times\mathbf{A} \quad (4)$$

$$\mathbf{E}=-\nabla V \quad (5)$$

$$\mathbf{J}=\sigma\mathbf{E} \quad (6)$$

where **J** is current density, σ is electrical conductivity, **E** is electrical field, and V is electrical potential. The magnetic flux density **B** is obtained from the magnetic vector potential **A**.

B. Bolt pretension and contact model

To fasten the copper plates (see Fig.1) the top plate is bolted with screws and nuts to the bottom plates. The final preload force in each bolt is set to P=35 kN.

$$\nabla\mathbf{S}+\mathbf{f_v}=0 \quad (7)$$

The Solid Mechanics Interface is used to model the stress distribution in the bolted assembly. The Equation (7) describes the linear-elastic material behaviour, where ***S*** is the stress tensor and $\mathbf{f_v}$ represents the sum of external body forces acting on the system. The contact model used in this study is based on the Copper-Mikic-Yovanovic (CMY) formulation and is described by the following equations:

$$\mathbf{n}_1\mathbf{J}_1=h_c(V_u-V_d) \quad (8)$$

$$\mathbf{n}_2\mathbf{J}_2=h_c(V_d-V_u) \quad (9)$$

$$h_c=1.25\sigma_{contact}\,m_{asp}/G_{asp}(p/H_c)^{0.95} \quad (10)$$

where $\sigma_{contact}$ is:

$$\sigma_{contact}=2\,\sigma_u\,\sigma_d/(\sigma_u+\sigma_d) \quad (11)$$

The first set of equations, Eqs. (8)-(9) describes current flow between upper and lower contact surfaces, where V_u and V_d are the potentials at upper and lower surfaces, respectively. Likewise, $\mathbf{J}_1$ and $\mathbf{J}_2$ denote the electrical currents in upper and lower contact surfaces.

The contact conductance coefficient h_c is given by Eq.(10). It depends on the electrical contact conductivity $\sigma_{contact}$ and on geometrical characteristics of the contact surface: m_{asp} is the mean asperity slope, and G_{asp} is the mean asperity height. The coefficient depends on the local pressure distribution p across the contact interface. The H_c is microhardness of the contact surface. The formulation follows the Cooper–Mikic–Yovanovich (CMY) model [23]. The values of the CMY model are given in Table 2.

TABLE II. CMY MODEL PARAMETERS

Parameter name	Value	Unit
m_{asp}	0.4	1
G_{asp}	10	μm
H_c	3	GPa

IV. FINITE ELEMENT METHOD (FEM) SIMULATION RESULTS

A fully three-dimensional model is developed with commercial software COMSOL ver. 6.3, which is used to analyze the mechanical, thermal and electromagnetic aspects of the contact problem. The model geometry is shown in Figure 1. The complete model consists of three copper plates and eight M12 screws, which are made of stainless steel (AISI 4340). All material properties are listed in Table 1.

A free tetrahedral mesh with ~360k elements is used, with an average quality of 0.65. The mesh is refined in the contact region between Cu-plates to obtain a more accurate contact pressure distribution. The model consists of three steps: the first is solving the bolt pretension model as described in the last section followed by the solution of the stationary solid mechanics problem. During simulation of mechanical contact between two Cu-plates as shown in Figure 4(a) we observe a pressure concentration near the screws that decreases markedly with distance from the center of the holes, forming a bell-shape.

To validate the mechanical simulation results, the pressure cone geometry is compared against the analytical prediction of VDI Guideline 2230, using the Rötscher substitution body method. For an M12 bolt with preload $P = 35$ kN and plate thickness $t = 10$ mm, the guideline predicts a pressure cone half-angle of $\varphi = 25°$ and a cone diameter of $DA = 27.0$ mm at the contact interface, corresponding to an effective contact area of 441 mm². The resulting mean contact pressure is $\sigma m = 79.4$ MPa, which is 39.7% of the copper yield strength (200 MPa), confirming that the joint operates in the elastic regime. The extent of the pressure cone (radius 13.5 mm from bolt center) is in good agreement with the bell-shaped pressure distribution observed in the FEM results (Figure 4(a)), validating the simulation.

Second, stationary solutions for magnetic field and current density are computed, as shown in Figure 4(c). Finally, the

Electromagnetic Heating Multiphysics coupling is used to model resistive heating by coupling the heat transfer with electromagnetic fields. Here, the coupling of thermal and electrical resistances by means of mechanical contact pressure produced by the elastic deformation of the region around the bolted screws is considered. The variation in the electric field amplitude along the current path is illustrated in Figure 4(b) using a Streamline Multislice mode visualization.

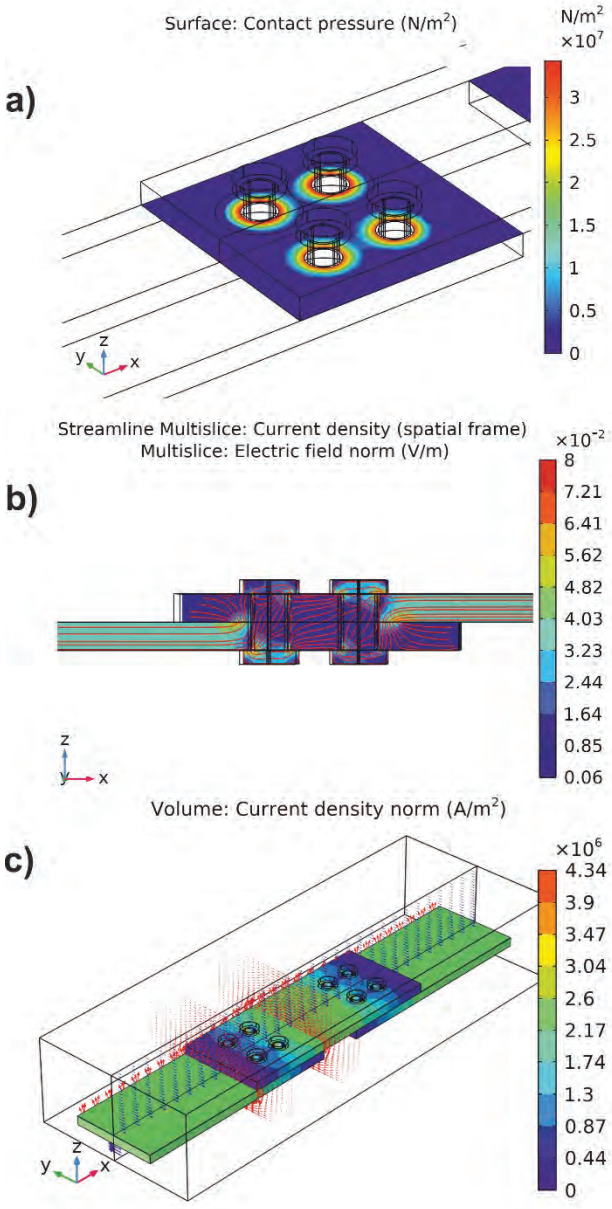


Fig. 4 FEM simulation results: (a) Contact pressure for given screw torque of 50 Nm (b) electric field distribution due to interface voltage drop and resulting current lines through the test object (c) magnetic flux and current density calculated for DC current of 1.6 kA.

V. Experimental Results

A. Magnetic measurements

Using our experimental setup, together with pristine and aged samples and the developed simulation framework, we obtained first results on both the spatially resolved current distribution in bolted joints and DC resistance profile along the joint axis. Magnetic measurements were performed as described in Figure 2. It is important to note that the Hall-sensor array measures the magnetic field generated by the current at a distance above the busbar surface, which reflects the current distribution integrated through the busbar cross-section. The current distribution within the contact plane itself cannot be directly resolved by this method, but the FEM simulations validated against these measurements provide insight into the current distribution at the contact interface. An exemplary measurement for the z-component of the magnetic field of a pristine busbar joint is shown in Figure 5(a). For comparison, the simulated z-component of the magnetic field *Bz* is presented in Figure 5(b) showing good overall agreement with the measurements. It is clear from the presented results that we reproduce correctly the distribution of the magnetic field in the z-direction. A notable observation is the remanent magnetization of the stainless steel M12 bolts, which is clearly visible in the measured magnetic field map.

B. Measuring voltage and resistance profiles

In order to obtain the local contact resistance values along the joint axis, as defined in Figure 2 (c), we measure the voltage drop between successive probe locations and divide it by the total current *I* flowing in the busbar. This yields:

$$R_p=(V_{ref}-V_p)/I \qquad (11)$$

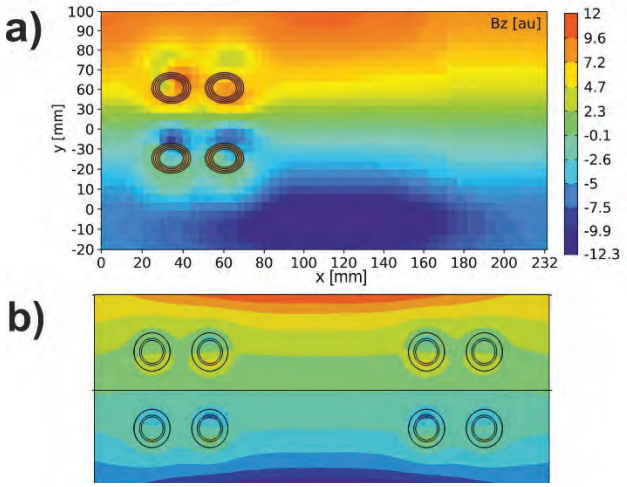


Fig. 5 Magnetic field measurement revealing current distribution across joint. (a) measurement in good agreement with (b) simulation. The results are shown exemplary for the z-component of the field as explained in Figure 5. Data is in arbitrary units.

for p=1…12, where R_p is resistance of probe *p*, V_p is the voltage measured at probe *p* on the upper plate, and V_{ref} is reference voltage at the lower plate. These measurements are performed for joints with different interfacial oxide thicknesses, obtained by applying different oxidation times at 100°C, in disassembled (un-bolted) condition. One way to quantify the oxidation level of the copper bars is to compute the performance factor [24] , defined as the ratio of the resistance across the connection to the resistance of the bare conductor measured over the same length. The values measured for four aging conditions are reported in Table 3.

TABLE III. VALUES OF PERFORMANCE FACTOR FOR DIFFERENT LEVELS OF OXIDATION

Oxidation level	Performance factor
Pristine	0.93
Oxidized 48h	1.26
Oxidized 96h	1.5
Oxidized 144h	1.04

The results for the different quality factors are presented in Figure 6(b). Again, we use the results from our FEM modeling to verify our experimental results (dotted line for pristine case). The average slope of the resistance curves in Figure 6(a) is approximately 19 μΩ/mm. For the three aging conditions in Figure 6(b), the voltage drop increased by 1.131, 1.318 and 0.924 mV respectively, compared with the pristine state. We attribute this increase to higher contact resistance caused by growth of an oxide layer. Interestingly, for 144h aging time, the busbar shows lower contact resistance than for 48h and 96h. One possible explanation is spallation of the Cu-oxide layer due to bolt clamping force as the oxide passes from cuprous to the more brittle cupric state, but further investigation is required. In terms of the total resistance of the busbar joint, this corresponds to 1.38, 1.44, 1.41 and 1.47 μΩ for the different aging times.

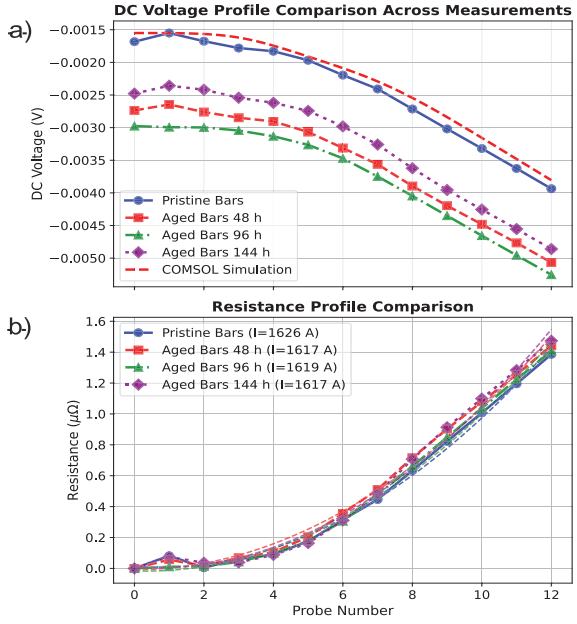


Fig. 6 (a) Corresponding voltage measurements for different aging cases and computed FEM solution for clean Cu-sample.
(b) Measured resistance profiles at middle line for different aging cases: clean sample, 48 h at 100 °C, 96 at 100 °C and 144 h at 100 °C.

VI. CONCLUSIONS

This study presents a spatially resolved experimental and numerical investigation of current transport in full-scale, bolted Cu–Cu busbar joints under realistic high-current conditions. A dedicated test setup, combining closely spaced voltage probes with integrated Hall-sensor measurements enabled the simultaneous mapping of local voltage drop, resistance, and current distribution across the joint.

The DC measurements show that contact resistance is consistently lower in the vicinity of the bolts due to locally increased contact pressure. Accelerated thermal aging in disassembled state at 100 °C produces homogeneous surface oxidation and, consequently, a measurable increase in contact resistance and larger spatial gradients. These results highlight the strong sensitivity of joint performance to surface oxidation.

The dominant aging mechanisms in current-carrying bolted Cu joints include thermal oxidation of the contact surfaces, fretting corrosion due to differential thermal expansion under cyclic loading, and stress relaxation or creep of the copper, which reduces bolt clamping force over time. Importantly, these mechanisms are mutually reinforcing, as reduced clamping force raises contact resistance, which accelerates local heating and further oxidation. In future work, both inhomogeneous contact force as well as inhomogeneous oxidation of the contact joint surfaces will be investigated. This will provide insight into the consequences of realistic aging phenomena in bolted busbar joints, such as loose or defective bolts and partial surface oxidation.

ACKNOWLEDGMENT

This work has been supported by Innosuisse Innovation Contract 114.696 IP-ENG.

REFERENCES

[1] L. P. He *et al.*, “Effects of oxidation layer and roughness on the fretting wear behavior of copper under electrical contact,” *Mater. Res. Express 2020, 6, 1265e3*, 2020.

[2] D. Qiu, L. Peng, P. Yi, and X. Lai, “A micro contact model for electrical contact resistance prediction between roughness surface and carbon fiber paper,” *Int. J. Mech. Sci. 2017, 124, 37-47*, 2017.

[3] M. H. Muser and A. Wang, “Contact-patch-size distribution and limits of self-affinity in contacts between randomly rough surfaces,” *Lubricants 2018, 6, 85*, 2018.

[4] P. G. Slade, “Electrical Contacts: Principles and Applications, 2nd ed.; CRC Press: London, UK, 2017”.

[5] S. V. Angadi, R. L. Jackson, V. Pujar, and M. R. Tushar, “A Comprehensive Review of the Finite Element Modeling of Electrical Connectors Including Their Contacts,” *IEEE Transactions on Components, Packaging and Manufacturing Technology*, vol. 10, no. 5, pp. 836–844, May 2020, doi: 10.1109/TCPMT.2020.2982207.

[6] M. Braunovic, “Effect of Current Cycling on Contact Resistance, Force, and Temperature of Bolted Aluminium-to-Aluminium Connectors of High Ampacity,” *IEEE Transactions on Components, Hybrids, and Manufacturing Technology*, vol. 4, no. 1, pp. 57–69, Mar. 1981, doi: 10.1109/TCHMT.1981.1135772.

[7] M. Braunovic, “Effect of connection design on the contact resistance of high power overlapping bolted

joints," *IEEE Trans. Comp. Packag. Technol.*, vol. 25, no. 4, pp. 642–650, Dec. 2002, doi: 10.1109/TCAPT.2003.809108.

[8] S. Dutta, G. N. V. R. Vikram, M. S. Bobji, and S. Mohan, "Table top experimental setup for electrical contact resistance measurement during indentation," *Measurement 2020, 152, 107286*, 2020.

[9] A. Beloufa, "Numerical and experimental optimization of mechanical stress, contact temperature and electrical contact resistance of power automotive connector," *Int. J. Mech. 2010, 4, 94-104*, 2010.

[10] L. Frerot, M. Bonnet, J.-F. Molinari, and G. Anciaux, "A Fourier-accelerated volume integral method for elastoplastic contact," *Comput. Methods Appl. Mech. Eng. 2019, 351, 951-976*, 2019.

[11] Y. Xu and R. L. Jackson, "Boundary element method (BEM) applied to the rough surface contact vs," *BEM in computational mechanics. Friction 2018, 7, 359-371*, 2018.

[12] J. Gwinner and E. P. Stephan, "BEM for Contact Problems," *In Advanced Boundary Element Methods. Springer Series in Computational Mathematics; Springer: Cham, Switzerland, 2018; Volume 52, pp. 389-449*, 2018.

[13] M. Szulborski, S. Lapczynski, L. Kolimas, and D. Zalewski, "Transient Thermal Analysis of the Circuit Breaker Current Path with the Use of FEA Simulation," *Energies 2021, 14, 2359*, 2021.

[14] C. Zhang, W. Ren, and G. A. Wang, "Finite Element Method to Investigate Electrical Contact Behaviors Considering Asperity Interactions," presented at the In Proceedings of the 2020 IEEE 66th Holm Conference on Electrical Contacts and Intensive Course (HLM), San Antonio, TX, USA, 30 September-7 October 2020; pp. 98-104, 2020.

[15] S. R. Gonzalo, "Coupling of Mechanical and Electrical Contact Behavior of Current Carrying Connections in Finite element Models," Universidad de Valladolid, Escuela de Ingenierias Industriales, Valladolid,Spain, 2021.

[16] Y.-H. Li, F. Shen, and L.-L. Ke, "Multi-physics electrical contact analysis considering the electrical resistance and Joule heating," *International Journal of Solids and Structures*, vol. 256, p. 111975, Dec. 2022, doi: 10.1016/j.ijsolstr.2022.111975.

[17] F. Shen and L.-L. Ke, "Numerical Study of Coupled Electrical-Thermal-Mechanical-Wear Behavior in Electrical Contacts," *Metals*, vol. 11, p. 955, Jun. 2021, doi: 10.3390/met11060955.

[18] J. Zhang, L. Huang, T. Chen, and G. Su, "Simulation based analysis of electrical fire risks caused by poor electric contact between plug and receptacle," *Fire Safety Journal*, vol. 126, p. 103434, Dec. 2021, doi: 10.1016/j.firesaf.2021.103434.

[19] F. Guo, X. Gu, L. Li, Z. Wang, T. Wang, and S. Jia, "Effect of surface microparameters on contact temperature of sliding electrical contact," *IEEE Trans. Ind. Inform. 2021, 18, 5972-5981*, 2021.

[20] S.-H. Kim and K.-W. Lee, "Numerical approach to joule heating analysis for electrical parts using MSC Marc," *J Mech Sci Technol*, vol. 29, no. 5, pp. 2081–2087, May 2015, doi: 10.1007/s12206-015-0429-y.

[21] K. Duan, F. Zhu, Y. Li, K. Tang, S. Liu, and Y. Chen, "Contact resistance investigation of electrical connector with different shrink range," presented at the In Proceedings of the 2014 15th International Conference on Electronic Packaging Technology, Chengdu, China, 12-15 August 2014; pp. 1146-1149, 2014.

[22] S. Luo, B. Wang, J. Jiang, J. Li, G. Zou, and L. Zeng, "Numerical analysis on mechanical and fatigue behaviors of aviation electrical connector considering structural effect," *Int. J. Numer. Model. Electron. Netw. Devices Fields 2024, 37, e3183*, 2024.

[23] M. G. Cooper, B. B. Mikic, and M. M. Yovanovich, "Thermal contact conductance," *International Journal of Heat and Mass Transfer*, vol. 12, no. 3, pp. 279–300, Mar. 1969, doi: 10.1016/0017-9310(69)90011-8.

[24] S. Schlegel, M. Gatzsche, C. Hildmann, and T. Israel, *Contact and Long-Term Behavior of Current-Carrying Connections in Electrical Power Engineering: Theory and Practice on Behavior, Calculation Approaches, as well as Design and Dimensioning Criteria*. Berlin, Heidelberg: Springer Berlin Heidelberg, 2024. doi: 10.1007/978-3-662-69644-6.

[25] T. Fuhrmann, S. Schlegel, S. Großmann, and M. Hoidis, "Investigations on Stationary Electrical Joints with a Bare and a Silver or Nickel Coated Contact Partner Regarding the Permissible Temperature Limit According to ANSI IEEE and IEC," in Proc. 60th IEEE Holm Conference on Electrical Contacts (Holm 2014), New Orleans, LA, USA, Oct. 2014, pp. 241–248.

Investigation of wear in high-voltage circuit breaker electrical contacts

Vincent Niggel
Advanced Materials & Surfaces
Empa
Dübendorf, Switzerland

Lorenz Herrmann
Advanced Materials & Surfaces
Empa
Dübendorf, Switzerland

Andrew Fairbrother
Hitachi Energy Ltd.
Zürich, Switzerland

Rowena Crockett
Advanced Materials & Surfaces
Empa
Dübendorf, Switzerland
rowena.crockett@empa.ch

***Abstract*— The performance and lifetime of high-voltage circuit breakers strongly depend on the tribological behaviour of their electrical contacts. In particular, the sliding interface between the spiral contact ring and the puffer cylinder is subjected to repeated mechanical loading, which can lead to wear, increased friction, and degradation of contact stability. In this work, the wear mechanisms of a silver-coated spiral contact ring sliding against a silver-coated aluminium puffer cylinder are investigated using reciprocating tribological tests. Friction behaviour and surface degradation are analysed as a function of sliding cycles under dry and greased conditions. The coefficient of friction is monitored during testing, while surface and subsurface damage are characterised using optical microscopy, profilometry, scanning electron microscopy, and focused ion beam cross-sectioning. The results reveal a transition from mild abrasive wear to severe wear involving material tearing, transfer, and redeposition under unlubricated conditions, leading to a sharp increase in friction. In contrast, lubrication stabilises the friction coefficient at low values and significantly limits wear. These findings provide insight into the degradation mechanisms of silver-coated contacts and underline the importance of lubrication for improving the reliability of high-voltage circuit breakers.**

I. Introduction

High-voltage circuit breakers (HVCBs) are essential components in electrical power systems, ensuring safe interruption of fault currents and reliable switching during normal operation. Their functionality relies on the combined electrical and mechanical performance of internal contacts, which experience repeated sliding under load throughout the service life of the device. Degradation of these contacts can result in increased friction, unstable motion, and ultimately reduced operational reliability [1-2].

Moreover, controlling the wear in this system is very important as wear particles can be redispersed and influence the arc quenching properties as it reduces for instance the breakdown voltage of SF_6 gas [3-6]. The different contacts in the HVCB can be a source of wear particles as they are subject to repeated mechanical stresses from the opening and closing operations with speeds up to several meters per second [7]. Some of these contacts are coated with silver for improved conductivity and oxidation protection. However, the friction and wear behavior of the contacts is dependent on the contact pairs material [8]. While silver provides excellent electrical conductivity, its relatively low hardness makes it susceptible to wear, plastic deformation, and material transfer under sliding conditions. The exact wear mechanism of silver as coating seems to be dependent on several parameters such as presence of corrosion on the surface, thickness of the coating or its hardness but involves adhesive and abrasive wear [9-12].

In this study, a simplified reciprocating sliding configuration is used to experimentally investigate the friction and wear behaviour of a silver-coated spiral contact ring segment in contact with a silver-coated puffer cylinder segment. The samples are typical parts for transmission voltage level breakers (>145 kV). Tests are performed for increasing numbers of cycles under dry and lubricated conditions. By combining friction measurements with detailed surface and subsurface characterisation, the dominant wear mechanisms are identified and their evolution with sliding cycles is discussed. The objective is to provide experimental insight relevant to the durability and reliability of silver-coated contacts in high-voltage circuit breakers.

II. Materials and Methods

A. Materials

The spiral contact ring segments are fabricated from copper wire with a diameter of approximately 1.5 mm and are coated with a ~20 µm thick silver layer. The puffer cylinder segments are made of aluminium and coated with a ~20 µm silver layer with adhesion improvement through a thin underlayer. Both ring and cylinder segment where sonicated for 10 minutes in both water and ethanol before the tribological tests. The lubricant used in the tribological tests is a grease composed of a commercial non-polar synthetic base with polyurea thickener.

B. Methods

Reciprocating friction tests were performed using a Bruker UMT TriboLab tribometer in air at room temperature (~22°C and 50% humidity). No electrical load was applied. The spiral contact ring segment served as the upper specimen and was slid against a cylinder segment, as illustrated in Fig. 1.

The reciprocating tests consisted of 10, 100, or 1000 cycles, conducted either with or without grease applied to the puffer cylinder surface. Each cycle included a 1 s dwell period, followed by a 35 mm sliding stroke in one direction along the Y-axis, another 1 s dwell period, and a subsequent 35 mm stroke in the opposite direction. Thus, one full cycle is 70 mm of travel. The sliding velocity v_y was set to 10 mm/s, and a constant normal force F_z of 1 N was applied throughout all tests. The coefficient of friction (COF) was recorded at a sampling rate of 20 Hz. Due to transient effects at the beginning and end of each stroke, only data acquired between 5 and 30 mm of the sliding path were analyzed. Two values were defined: COF1 and COF2, corresponding to forward and backward sliding, respectively (see Fig. 2).

Optical images shown in Fig. 4 were acquired using a Leica M205 A coded stereo microscope equipped with a 0.63× objective. Surface profiles presented in Fig. 5 and Fig. 6 were obtained using a Bruker Dektak profilometer with a 2 µm stylus under a normal force of 20 µN. Profiles were measured along the X-axis with a lateral sampling interval of 1 µm and a line spacing of 25 µm. Scanning electron microscopy (SEM) images shown in Fig. 7 were acquired using a Hitachi S-3700N scanning electron microscope operated at an accelerating voltage of 5 kV in secondary electron (SE) mode. Cross-sectional samples (Fig. 8) were prepared using a TFS Helios 5 Laser Hydra UX system with a xenon plasma focused ion beam (FIB) operated at 30 kV. Initial bulk milling was performed at 2.5 µA, followed by finer milling steps at 1 µA and 0.5 µA. Imaging was carried out at 2 kV using both SE and backscattered electron (BSE) modes.

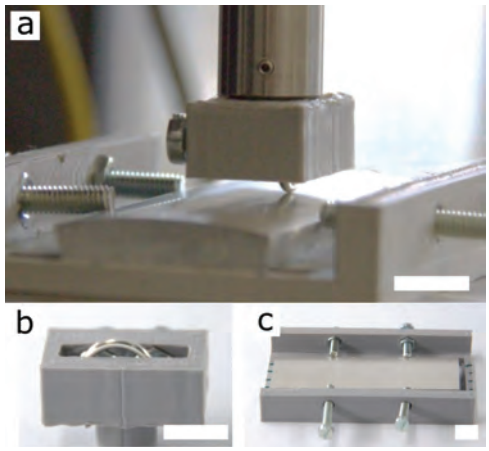


Fig. 1. a- Setup used for the tribology tests. b- Spiral contact ring segment and its holder. c- Puffer cylinder segment and its holder. The white scale bars are 1 cm.

III. Results

A. Reciprocating tribology tests

For the ungreased tests, the mean COF1 values initially remained around 0.4 before increasing to values exceeding 1 after a limited number of cycles. The onset of this transition was not consistent across tests, occurring after approximately 10 cycles in one case and after about 100 cycles in another. Following the transition, a clear difference between forward and backward sliding friction values (COF1 and COF2, respectively) was observed.

In contrast, the COF1 values measured in greased tests remained stable with increasing number of cycles, with an average value of approximately 0.08. This value is significantly lower than that observed for ungreased tests, and no difference between forward and backward sliding friction was detected (see Fig. 3).

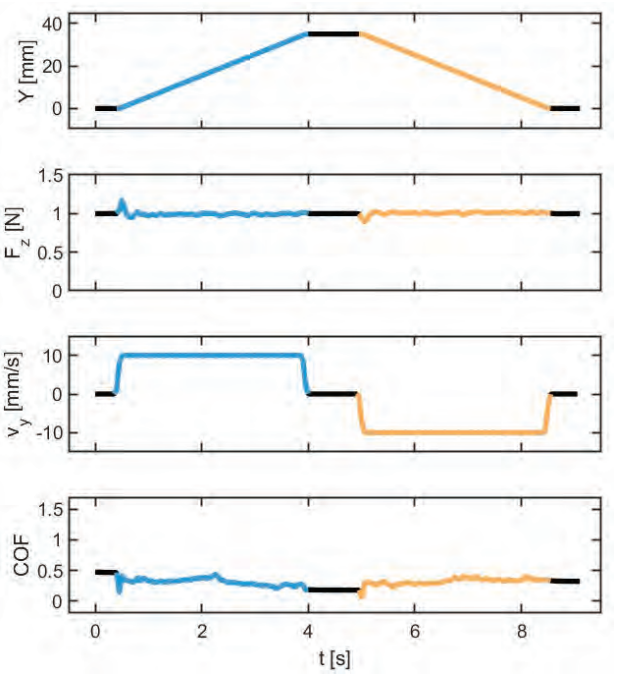


Fig. 2. Evolution of Y, F_z, v_y and COF over time for one cycle of the reciprocating tests. The blue and red colours highlight respectively the forward and backward sliding. Dashed lines in the COF plot indicate the cutoff to exclude transient effects at the beginning and end of each stroke.

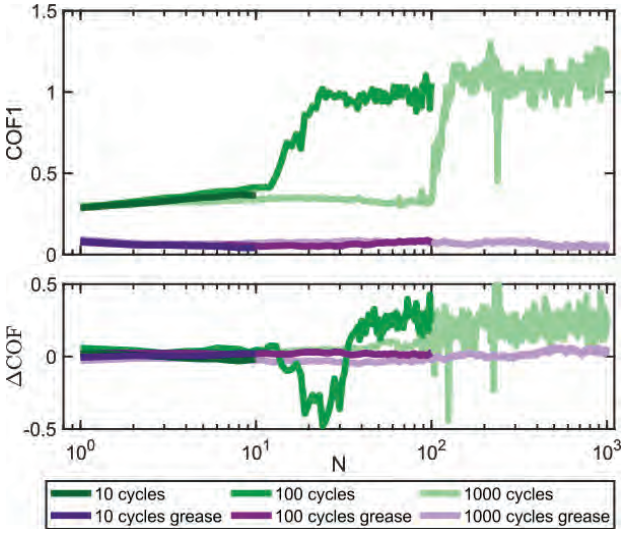


Fig. 3. Evolution of COF1 and ΔCOF = COF2 – COF1 as the number of cycles N for different reciprocating tribology tests with ungreased and greased samples.

B. *Optical microscopy images*

Optical microscopy revealed the formation of wear tracks on both the spiral contact rings and the puffer cylinders. With increasing number of cycles, the wear track width increased on the puffer cylinder, while the wear-affected area expanded on the spiral contact ring. Notably, the wear observed on the greased puffer cylinder after 1000 cycles was significantly less pronounced than that observed on the ungreased puffer cylinder after only 10 cycles (see Fig. 4).

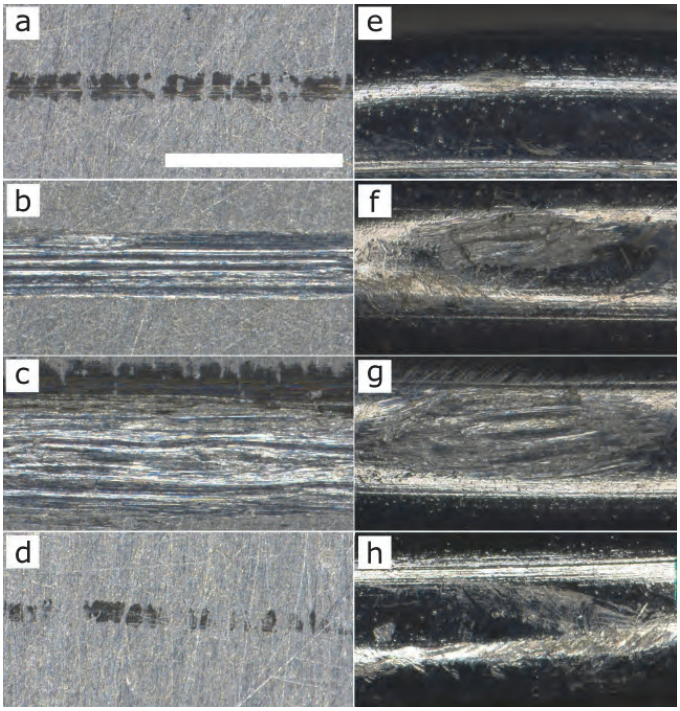


Fig. 4. Images of the surface of the ungreased puffer cylinder (left column images) after 10 cycles (a), 100 cycles (b), 1000 cycles (c) compared to 1000 cycles with greased surface (d) and of the surface of the ungreased spiral (right column images) after 10 cycles (e), 100 cycles (f), 1000 cycles (g) compared to 1000 cycles with greased surface (h). All the images are at the same scale, and the white scale bar is 1 mm.

C. *Wear profiles*

The surface profiles of the ungreased samples corroborate the observations from optical microscopy. In addition to the widening of the wear tracks, grooves aligned with the sliding direction were observed, with increasing depth as the number of cycles increased. The 100-cycle sample exhibited grooves up to 6 µm deep, whereas the 1000-cycle sample showed grooves reaching depths of up to 20 µm. Concurrently, raised features ("protrusions") were detected, with heights up to 10 µm for the 100-cycle sample and up to 30 µm for the 1000-cycle sample (see Fig. 5).

The measured arithmetic mean surface roughness (Sa) was 0.55 µm for the unworn puffer cylinder surface adjacent to the wear track, 0.50 µm on the wear track after 10 cycles, 2.2 µm after 100 cycles, and 5.92 µm after 1000 cycles. Ungreased spiral contact rings exhibited comparable trends, with grooves approximately 5 µm deep and protrusions up to 40 µm high after 100 cycles and grooves up to 30 µm deep with protrusions reaching 20 µm after 1000 cycles (see Fig. 6).

No measurable wear was observed in the surface profiles of the greased experiments.

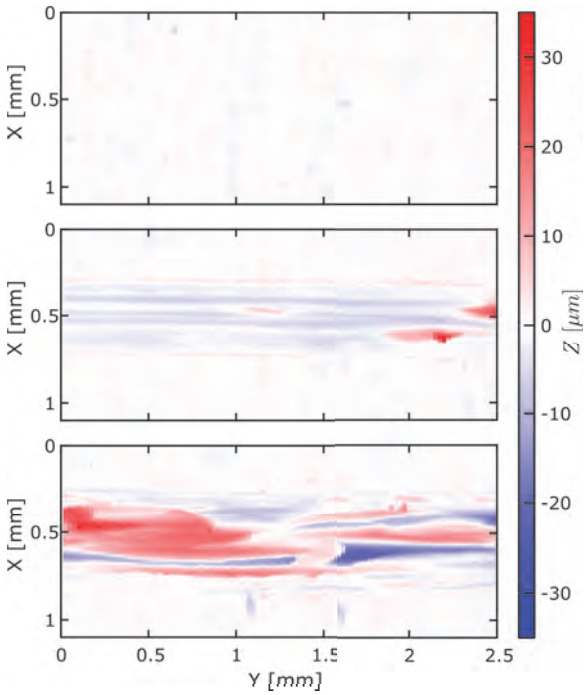


Fig. 5. Profile of the ungreased puffer cylinder after 10 cycles (top), 100 cycles (middle) and 1000 cycles (bottom).

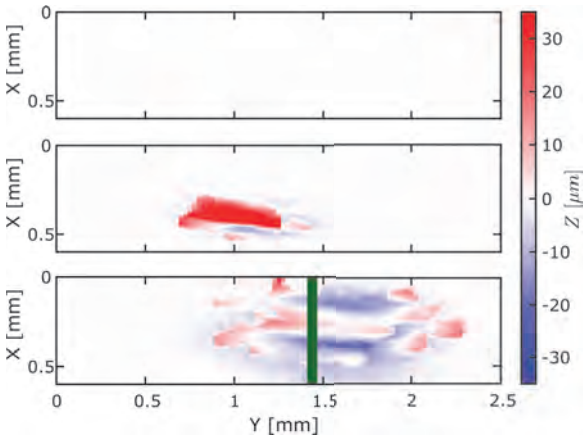


Fig. 6. Profile of the ungreased spiral contact ring after 10 cycles (top), 100 cycles (middle) and cycles (bottom). The vertical green line on at 1000 cycles profile indicated the region where the FIB section was made.

D. *SEM observations*

SEM analysis of the ungreased samples after 10 cycles revealed predominantly abrasive wear on both contacting surfaces, accompanied by limited plastic deformation that led to smoothing of the highest asperities. Shallow grooves aligned with the sliding direction were also observed. After 100 cycles, deeper and wider grooves formed on the puffer cylinder surface, while the spiral contact ring surface exhibited evidence of material detachment and subsequent redeposition at other locations.

The 1000-cycle samples displayed the most severe surface damage. Both surfaces showed extensive material redeposition, with transferred fragments exceeding 100 µm in size, resulting in a highly rough and irregular surface morphology (see Fig. 7). Cross-sectional analysis of the 1000-cycle samples confirmed these observations, revealing regions with overhanging material and significant local variations in silver coating thickness, with some areas exceeding and others falling below the nominal thickness (Fig. 8).

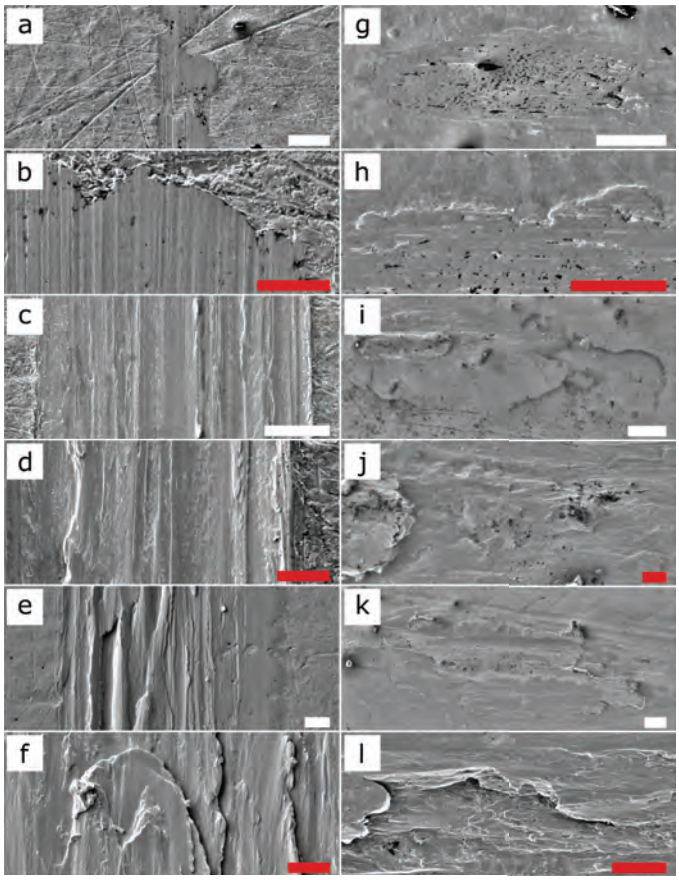


Fig. 7. SEM images of the wear path on the ungreased puffer cylinder (left column images) after 10 cycles (a and b), 100 cycles (c and d) and 1000 cycles (e and f) and of the wear path on the spiral contact ring (right column images) after 10 cycles (a and b), 100 cycles (c and d) and 1000 cycles (e and f). The white scale bars are 100 µm and the red scale bars are 25 µm.

IV. Discussion

Based on the combined tribological, profilometric, and microscopic analyses, a friction and wear mechanism for the silver-coated spiral contact rings and puffer cylinders can be proposed. Under unlubricated conditions, the initial coefficient of friction of approximately 0.4 is characteristic of a wear regime dominated by mild abrasion and progressive surface flattening. This friction level and wear behaviour are comparable to those reported by Å. K. Rudolphi *et al.* [12] for corroded silver coatings.

After a critical number of sliding cycles, the contact undergoes a transition to severe wear, marked by the occurrence of adhesive tearing and material transfer. Fragments detached from the contact interface are either redeposited locally or transferred to the counter surface, with characteristic sizes reaching several hundred micrometers. As sliding continues, the combined effects of abrasive wear, adhesive wear, and plastic deformation lead to the formation of pronounced surface asperities and deep valleys. This multi-scale roughening of the surface topography results in increasingly unstable contact conditions and is accompanied by a sharp rise in the measured friction coefficient to values exceeding 1. Similar friction levels and wear mechanisms were also observed by Å. K. Rudolphi *et al.* [12] for uncorroded silver coatings. This suggests that, in the present system, the initial sliding cycles remove the corroded silver layer, exposing uncorroded silver and thereby promoting strong adhesive interactions that drive the transition to severe wear. The forward–backward asymmetry in friction coefficient likely arises from the development of directional surface textures due to ongoing material detachment and transfer [13].

In contrast, the application of grease significantly alters the tribological response of the system. Lubrication reduces the friction coefficient to approximately 0.08 and remains stable with increasing number of cycles. The presence of a lubricant film limits direct asperity-to-asperity contact, thereby suppressing adhesive tearing and material transfer. Under these conditions, wear is restricted to mild abrasion and small-scale plastic deformation, resulting in substantially reduced surface damage. These observations demonstrate the critical role of lubrication in controlling friction and wear mechanisms in silver-coated sliding contacts and in preventing the transition to severe wear regimes.

V. Conclusion

The friction and wear behaviour of a silver-coated spiral contact ring sliding against a silver-coated aluminium puffer cylinder has been investigated using reciprocating tribological tests representative of contact conditions in high-voltage circuit breakers.

Under unlubricated conditions, the contact initially exhibited moderate friction associated with mild abrasive wear and surface smoothing. With increasing number of cycles, a transition to severe wear occurred, characterized by material tearing, transfer, and redeposition on both contacting surfaces contributing to the adhesive wear. At this stage, surface interactions are involving abrasive and adhesive wear as well as plastic deformation. This transition led to a pronounced increase in friction and to the development of very rough surface topographies, which are detrimental to contact stability and long-term performance. This transition in friction and wear might be due to the transition from corroded to uncorroded silver surface.

In contrast, lubrication resulted in a consistently low friction coefficient and a substantial reduction in wear, even after extended sliding. Grease effectively limits surface damage, suppressing material transfer and severe plastic deformation. These results demonstrate that lubrication plays a critical role in controlling wear mechanisms and

preserving the integrity of silver-coated puffer-cylinder contacts.

Overall, the study highlights the transition from mild to severe wear as a key degradation mechanism in dry sliding contacts and confirms the effectiveness of lubrication in extending component lifetime. The findings provide valuable guidance for material selection, surface treatment, and lubrication strategies aimed at improving the reliability and durability of high-voltage circuit breakers. However, to make the results more readily transferrable to actual applications, the operating conditions, such as speed, ambient, and electrical load, should be explored in future work.

Acknowledgement: This work has been supported by Innosuisse Innovation Contract 115.297 IP-EE.

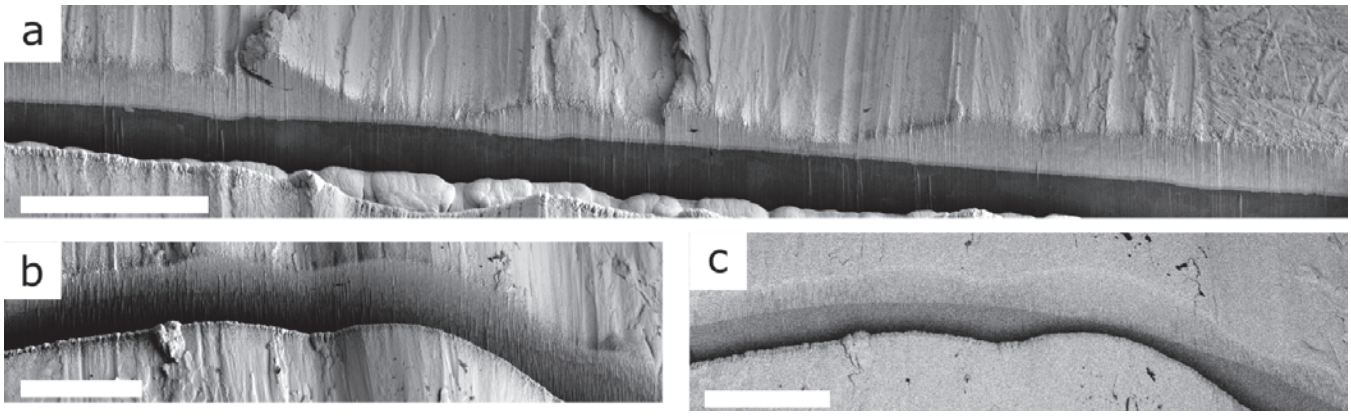


Fig. 8. a-Cross section of wear track on puffer cylinder in SE mode. Cross section of wear track on spiral in SE (b) and BSE (c) mode. The white scale bars are 100 µm.

VI. REFERENCES

[1] G. Balzer and D. Drescher, Evaluation of failure data of HV Circuit-Breakers, CIGRE, 2004.

[2] A. A. Razi-Kazemi, Review On High Voltage Circuit Breaker Failure Modes, Advances in Reliability, Safety and Security, Part 9, ESREL Monograph Book Series, 2024, pp.145-152.

[3] S. Xiao, X. Zhang, R. Zhuo, D. Wang, J. Tang, S. Tian and Y. Li, The influence of Cu, Al and Fe free metal particles on the insulating performance of SF6 in C-GIS, IEEE Transactions on Dielectrics and Electrical Insulation, vol. 24, no. 4, 2017, pp. 2299-2305, DOI: 10.1109/TDEI.2017.006343.

[4] C.M. Cooke, R.E Wootton and A.H Cookson, Influence of Particles on AC and DC Electrical Performance of Gas Insulated Systems at Extra-High-Voltage, IEEE Trans. Power App. Syst., Vol. 96, No. 3, 1977, pp. 768–777.

[5] Jian Wang, Qi Hu, Yanan Chang, Jingrui Wang, Ruixue Liang, Youping Tu, Chuanyang Li, Qingmin Li, "Metal particle contamination in gas-insulated switchgears/gas-insulated transmission lines", CSEE Journal of Power and Energy Systems, vol.7, no.5, 2021 pp.1011-1025.

[6] A. H. Cookson, Review of high voltage gas breakdown and flashover of insulators in compressed sulfur hexafluoride, Proceedings of the 3rd International Conference on Properties and Applications of Dielectric Materials, Tokyo, Japan, 1991, pp. 369-376 vol.1, DOI: 10.1109/ICPADM.1991.172075

[7] R. D. Garzon, High Voltage Circuit Breakers-Design and Applications, Second Edition, CRC Press, 2002, pp185-204, DOI: 10.1201/9780203910634

[8] S. Noël, A. B. Oudot, T. Leblanc, A. F. Karam, D. Comte and J. Toran, Analysis of Friction and Wear Mechanisms Occuring During Durability Tests of Connector Contact Pairs, 2024 IEEE 69th Holm Conference on Electrical Contacts (HOLM), Annapolis, MD, USA, 2024, pp. 1-8, DOI:10.1109/HOLM56222.2024.10768396.

[9] S. -Z. Kure-Chu *et al*., Sliding friction, wear and tribofilm formation of silver films electro-plated on copper alloy sheets, 2016 IEEE 62nd Holm Conference on Electrical Contacts (Holm), Clearwater Beach, FL, USA, 2016, pp.135-140, DOI:10.1109/HOLM.2016.7780021.

[10] P.G. Slade (Ed.), Electrical Contacts: Principles and Applications, Second Edition, (2nd ed.), CRC Press, 2014, pp.413-441 DOI:10.1201/b15640

[11] M. Antler, Sliding Wear of Metallic Contacts, IEEE Transactions on Components, Hybrids, and Manufacturing Technology, vol. 4, no. 1, pp. 15-29, 1981, DOI: 10.1109/TCHMT.1981.1135784

[12] Å. K. Rudolphi, S. Jacobson, Stationary loading, fretting and sliding of silver coated copper contacts - influence of corrosion films and corrosive atmosphere, Tribology International, Volume 30, Issue 3, 1997, pp.165-175, DOI:10.1016/S0301-679X(96)00031-X

[13] B. Mohanty, T. Alexander Ivanoff, A. S. Alagoz, T. Karabacak, M. Zou, Study of the anisotropic frictional and deformation behavior of surfaces textured with silver nanorods, Tribology International, Volume 92, 2015, pp.439-445, DOI:10.1016/j.triboint.2015.07.027

Understanding of the High-Frequency Impedance Characteristics of Micro-scale Gold-plated Contact Interfaces

Yinnan Zhang
School of Electrical Engineering and Automation
Harbin Institute of Technology
Harbin, China
23B906032@stu.hit.edu.cn

Chao Zhang
School of Electrical Engineering and Automation & School of Instrumentation Science and Engineering
Harbin Institute of Technology
Harbin, China
zhangchao100@hit.edu.cn

Yuchen Liao
School of Electrical Engineering and Automation
Harbin Institute of Technology
Harbin, China
1541729065@qq.com

Wanbin Ren
School of Electrical Engineering and Automation
Harbin Institute of Technology
Harbin, China
renwanbin@hit.edu.cn

***Abstract*—The contact impedance spectrum of the connector is closely correlated with the contact area and the interfacial gap between contact pairs at the microscopic scale. In this paper, the contact impedance spectrum in the frequency range of 100 kHz to 300 MHz, together with the DC resistance characteristics, between the gold-plated testing probe and the flexible pin of the high-speed connector are experimentally investigated under normal loads ranging from 0.01 to 0.1 N. The measured spectra results exhibit a pronounced resonance and systematic load dependence: increasing load reduces the low-frequency resistive level and results in a higher resonant peak with a narrower bandwidth, accompanied by a minor shift in resonant frequency. To elucidate these observations, an equivalent loop model is established, comprising bulk parasitics in series with an interfacial branch representing resistive loss, effective contact inductance, and gap capacitance. Furthermore, a physics-informed inverse identification strategy is proposed to explicitly extract the interfacial reactive parameters primarily from the imaginary impedance, which is validated by the consistency with the real part. The identified DC resistance−force regimes reveal the transition from film-affected conduction to constriction-dominated behavior, providing a physical basis for interpreting the load dependence of the extracted parameters. These results offer a quantitative link between interfacial evolution and the high-frequency impedance behavior of gold-coated contacts.**

Keywords—Contact resistance, high-frequency impedance, low contact force, gold-plated surface

I. INTRODUCTION

With the rapid advancement of 5G communications and high-performance data centers, the demand for high-frequency signal transmission has increased significantly [1-2]. In these systems, electrical connectors are critical components. Unlike low-frequency applications where direct current (DC) continuity is the primary concern, high-frequency applications require strict impedance matching to minimize signal reflection and insertion loss [3-4]. Consequently, ensuring signal integrity across the contact interface remains a vital challenge in the design and reliability assessment of modern electronic systems.

It is well known that the impedance characteristics are influenced not only by the geometric structure and dielectric materials but also by the contact interface status [5]. Based on Holm's contact theory, due to surface roughness, the real contact area consists only of discrete contact spots (a-spots). As signal frequency increases, current constriction at these spots generates contact resistance and localized inductance. Meanwhile, the non-contacted regions between rough surfaces act as micro-capacitors, introducing parasitic capacitance [6-7]. The schematic of these parasitic elements is illustrated in Fig. 1. These parameters create impedance discontinuities and degrade high-frequency performance. Therefore, a clear understanding of the electrical signal characteristics of the contact interface is critical to the optimization of connector performance.

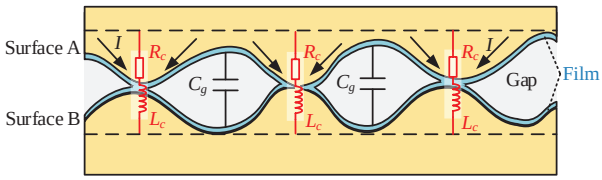


Fig. 1. Schematic diagram of the contact interface impedance.

Despite extensive studies on high-speed interconnects, the specific role of the contact interface in governing the measured impedance spectrum remains not fully clarified. Prior works often treat the interface as an empirical lumped element or focus on macroscopic signal-integrity metrics. However, a quantitative correlation linking spectral features (e.g., phase evolution and resonance behavior) to the interface-derived resistance, localized inductance, and gap capacitance is still limited for rough plated surfaces. In particular, a robust procedure to explicitly extract the effective interfacial parameters (L_c, C_g) from impedance spectra, and to elucidate their load dependence in the context of interfacial conduction-regime evolution, is currently lacking.

In this work, the high-frequency impedance of micro-scale Au-plated contact interfaces is experimentally investigated and interpreted explicitly. A single-contact-spot theoretical model representing the entire circuit loop incorporating the probe and terminal has been established. Furthermore, a method to extract effective inductance, resistance, and capacitance from impedance spectra (up to

300 MHz) is proposed by establishing equivalent circuit topologies. Finally, the DC *R-F* response is utilized to characterize the evolution of interfacial conduction mechanisms. These identified regimes provide a physical basis to elucidate the observed variations of the extracted high-frequency equivalent parameters with normal load.

II. Experimental Details

An automated test equipment has been designed to enable the in-situ measurement of DC contact resistance and high-frequency contact impedance of gold-plated contacts under controlled normal loads. The test rig was engineered to achieve the following specific goals:

1) To establish a stable single-spot contact between an ultra-fine gold-plated probe and a gold-plated terminal specimen.

2) To allow for the flexible, variable, and continuous application of normal load in the vertical direction achieving controlled elastic–plastic or plastic contact deformation.

3) To perform in-situ electrical characterization, measuring contact resistance via a DC method or contact impedance using an impedance analyzer.

4) To provide in-situ visualization of the contact region contour with microscale pixel resolution.

The schematic diagram of the test apparatus is illustrated in Fig. 2. The system is composed of a precision mechanical unit coupled with electrical measuring instruments and an optical observation module. The actuation module utilizes a piezoelectric actuator (LTC2013-013, PiezoMotor AB, Sweden) to drive the test probe in the vertical direction with a displacement step of 5 nm. The normal contact load is monitored by a strain-gauge force transducer (QDT, Avery Weigh-Tronix, UK) with a resolution of 0.015 μN. To realize precise alignment, the contact angle and position between the probe and terminal are adjusted via a set of manual multi-axis translation and rotational stages.

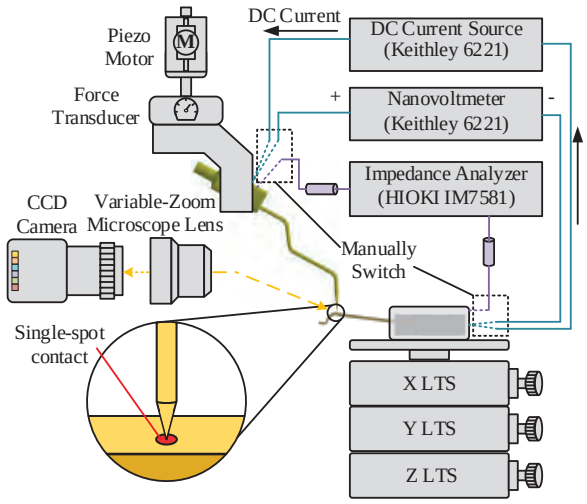


Fig. 2. Schematic diagram of the test apparatus.

Real-time observation of the contact interface is achieved by an optical module featuring a color CCD camera (MV-SUA1600M, MINDVISION, China) equipped with a variable-zoom microscopic lens. The system provides a high spatial resolution of up to 335 nm, effectively identifying the contact spot and contour.

For electrical characterization, the DC contact resistance is measured using a four-wire Kelvin setup with a current source (6221, Keithley) and a nanovoltmeter (2182A, Keithley). The high-frequency impedance (100 kHz–300 MHz) is acquired by an impedance analyzer (IM7581, HIOKI). To ensure measurement accuracy, these two procedures are not performed concurrently. The test leads are manually switched between the DC and high-frequency configurations. Meanwhile, the high-frequency probe is coaxially shielded with only an approximately 3 mm exposed tip. This design localizes the RF return path and minimizes the effective loop area. Data acquisition and processing are controlled through a personal computer.

Detailed experimental conditions are summarized in Table I.

TABLE I. Details of Experimental Conditions

Parameters	Value
Range of load force	0.01 N~ 0.1 N
DC current load	100 μA
Frequency range	100kHz~300MHz
Temperature	26 ℃
Humidity	52±1% RH

III. Results and Discussion

A. Typical Impedance Spectrum

Fig. 3 presents a representative impedance spectrum measured at F=0.01N, including the impedance magnitude $|Z|$ and phase angle $\angle Z$ as functions of frequency. In the low-frequency range(100kHz-1MHz), $|Z|$ remains close to a constant level and the phase stays near zero, indicating that the response is predominantly resistive. With increasing frequency, $|Z|$ gradually increases and the phase becomes positive, implying an increasingly inductive behavior of the measurement loop. A pronounced impedance peak appears at f_0=81.675MHz, accompanied by a phase zero-crossing. Beyond this frequency, the phase rapidly turns negative and a second zero-crossing occurs near 236MHz, after which the net reactance becomes inductive again and $|Z|$ shows a slight rise toward the upper end of the measured band.

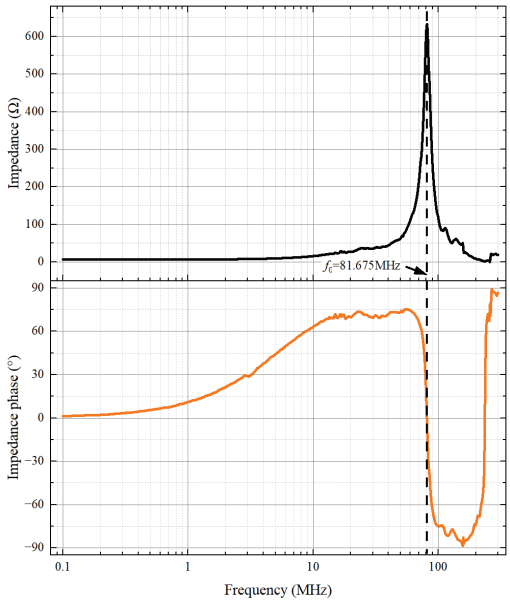


Fig. 3. Measured impedance magnitude and phase angle versus frequency at F=0.01N

For clarity, the measured |Z| and ∠Z are converted into real and imaginary parts using Re(Z) = |Z| cos(∠Z) and Im(Z) = |Z| sin(∠Z), as plotted in Fig. 4. The real part exhibits a sharp peak around f_0, while the imaginary part changes sign across the resonance and shows a characteristic dispersive shape. The observed spectral characteristics suggest that the contact behavior deviates from a purely resistive model. Consequently, reactive effects originating from the interface and the series current path become prominent within the 60–300 MHz band.

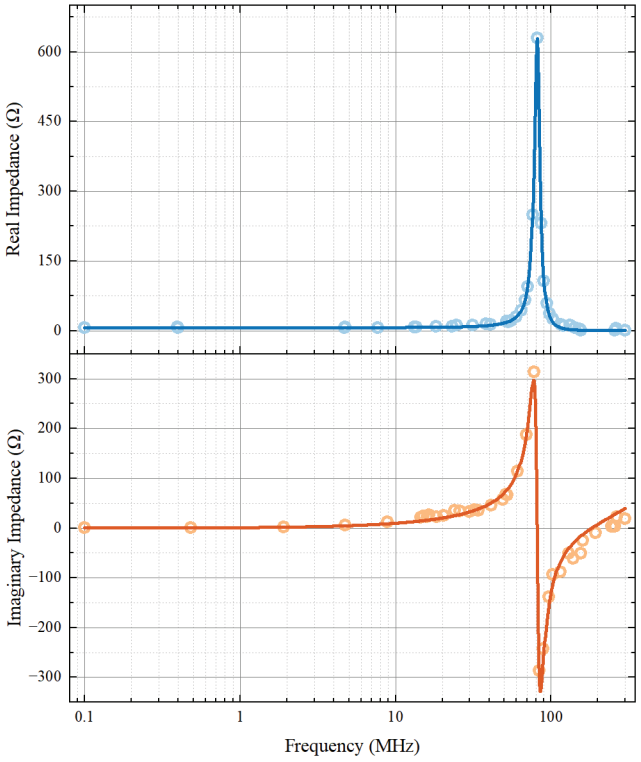


Fig. 4. Real and imaginary parts of impedance at F=0.01N obtained from |Z| and ∠Z

B. *Load-Dependent Impedance Spectra*

Fig. 5 illustrates the measured impedance spectra in terms of magnitude |Z| and phase ∠Z under load forces ranging from 0.01 N to 0.1 N. With increasing load force, impedance magnitude in the low-MHz range exhibits a systematic decrease, while the phase curve shifts upward. In the vicinity of the dominant resonance identified in Section III.A, the resonant peak becomes noticeably higher and exhibits a narrower bandwidth. Meanwhile, the resonant frequency shifts only slightly (e.g., f_0 decreases from 81.675 to 80.056MHz, whereas the peak |Z| increases from 633.3Ω to 916.4Ω).

The corresponding Re(Z) and Im(Z) responses are depicted in Fig. 6. In the low-frequency region, Re(Z) approaches a quasi-constant plateau and decreases monotonically with load force, indicating a reduction of the effective resistive contribution of the loop. This trend correlates well with the physical expectation that compressing the interface improves electrical conduction and lowers resistive loss. Simultaneously, Im(Z) remains negligible at low frequencies but increases with frequency, implying that the net response becomes progressively more reactive. Since tan(∠Z) = Im(Z)/Re(Z), the reduction in the resistive denominator (Re(Z)) amplifies the influence of the reactive component, which accounts for the observed upward shift of ∠Z (e.g., from 1.2° to 8.7° at 100kHz).

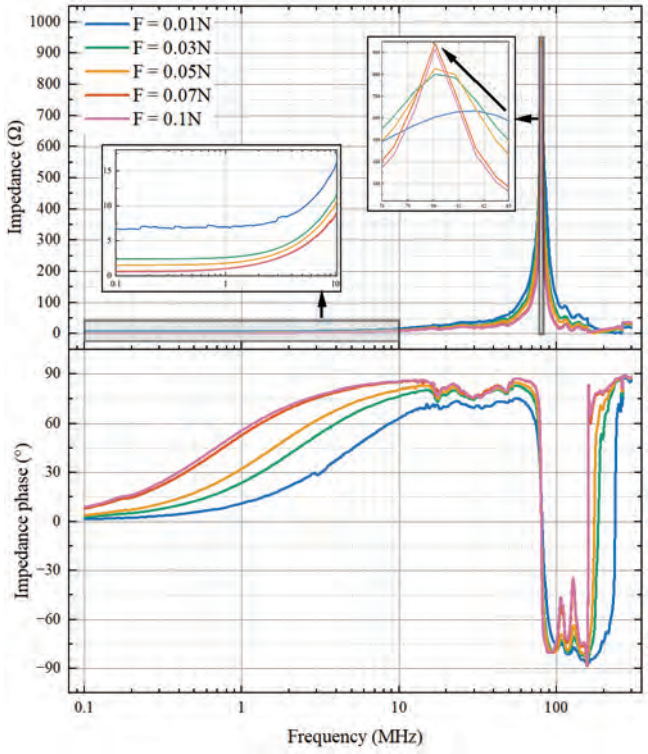


Fig. 5. Impedance magnitude |Z| and phase angle∠Z spectra under different load forces(F=0.01-0.1N). Insets highlight the low-frequency region and the vicinity of the dominant resonance.

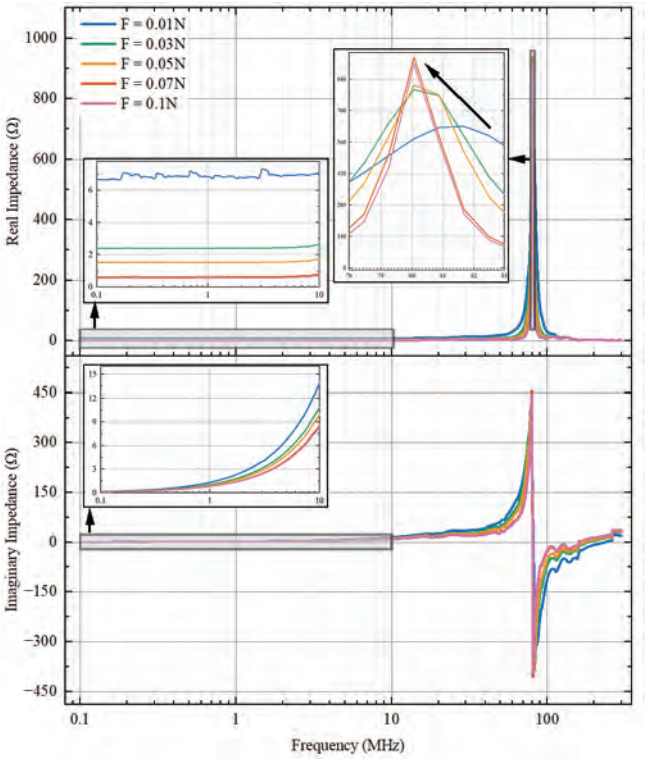


Fig. 6. Real and imaginary parts of impedance versus frequency under different load forces(F=0.01-0.1N).

Near the resonance, the sign reversal of Im(Z) and the pronounced peak in Re(Z) collectively indicate a resonance governed by the balance between energy storage and

dissipation. The load-induced increase in peak magnitude and the narrowing of the bandwidth can be attributed to a reduction in effective damping: as the interface becomes more conductive under higher loads, resistive losses diminish, rendering the resonance less damped. Additionally, the slight downward shift of f_0 suggests that the effective reactive contribution of the contact system undergoes minor variations with load force, which will be further elucidated in the subsequent equivalent circuit analysis.

It is noted that the primary load sensitivity is manifested in the effective resistive component at low frequencies, whereas reactive effects dominate the spectral evolution around the resonance.

C. DC Contact Resistance–Force Characteristics

Fig. 7 shows the measured DC contact resistance R as a function of the applied load force F over 0.01-0.1 N. During loading, R decreases monotonically from 6.5 Ω at 0.01 N to 0.42 Ω at 0.1 N. Two characteristic force levels, F_1=0.05 N and F_2=0.065 N, partition the loading branch into three regimes (Stage I–III). In contrast, the unloading branch does not retrace the loading path and exhibits a much weaker dependence on F, indicating pronounced hysteresis.

When plotted on log–log axes, the curve can be approximated by piecewise quasi-linear segments, suggesting a piecewise power-law dependence within continuous force intervals. To concisely capture this observation, the experimental data are fitted using the empirical relation

$$R \propto F^{-m} \tag{1}$$

which yields m=1.02, 3.85, 0.53 for Stages I–III, respectively.

According to Holm's theory[8], under the fully plastic contact assumption, the film-controlled contact resistance scales approximately as $R_f \propto F^{-1}$, whereas the constriction resistance follows $R_c \propto F^{-0.5}$. Notably, the measured exponents in Stage I (m=1.02) and Stage III (m=0.53) are consistent with these limiting trends, implying that Stage I is predominantly governed by the surface-film pathway, while Stage III is mainly governed by metallic constriction. Similar multi-regime R-F behavior has been reported for plated contact surfaces, where distinct force-dependent regimes were attributed to the competition and transition between film-affected conduction and metallic constriction conduction [9].

The corresponding interfacial pictures are schematically illustrated in Fig. 8(a) and Fig. 8(b), where Stage I is characterized by an intact film layer within the nominal contact region, and Stage III by a dominant metallic conduction core surrounded by residual films and gaps. Stage II exhibits a significantly steeper power-law exponent (m=3.85), suggesting a transitional regime rather than a simple contact-mechanics scaling law. In this regime, localized rupture of the surface film establishes metallic conduction paths within the nominal contact area; thus, the total conductance is modeled as the residual film conductance in parallel with the metallic constriction conductance. For $F>F_2$, the metallic constriction resistance becomes much smaller than the residual film resistance, such that R is primarily dominated by constriction. The small exponent on unloading (m=0.22) further supports the presence of irreversible plastic deformation and film damage during loading, which preserves conductive channels and reduces the sensitivity of R to the load force during unloading.

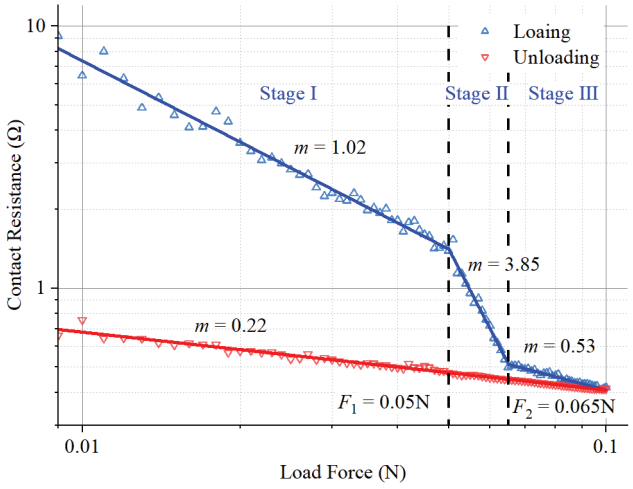


Fig. 7. DC contact resistance versus load force during loading and unloading.

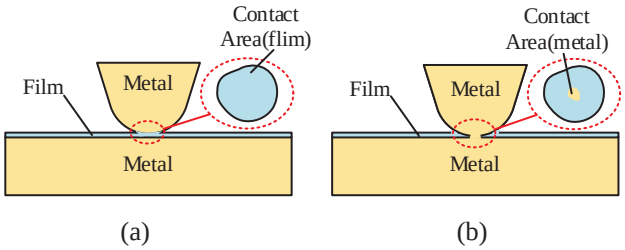


Fig. 8. Schematic illustrations of interfacial conduction regimes. (a) film-affected conduction in Stage I. (b) metallic constriction-dominated conduction in Stage III.

D. High-frequency Equivalent Circuit Model and Parameter Extraction

For the electrical contact between the probe and the terminal, the configuration and the equivalent circuit model of the electrical contact between the probe and the terminal are illustrated in Fig. 9.

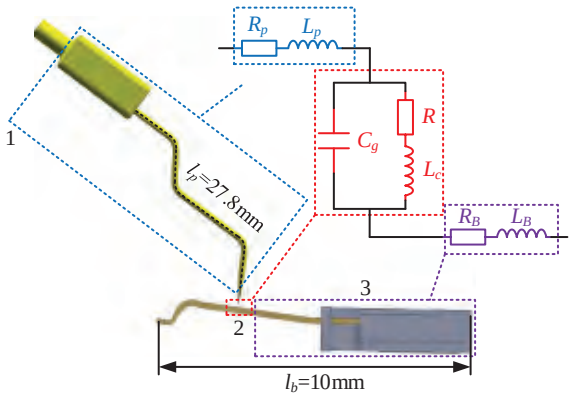


Fig. 9. High-frequency equivalent circuit model for the contact system.

As illustrated in Fig. 9, the probe and terminal sections located between the de-embedded reference planes exhibit physical lengths of l_p and l_b, respectively. Given that these dimensions are less than one-tenth of the shortest wavelength at 300 MHz, the electrical contributions of the probe and

terminal can be characterized by lumped impedances. Consequently, the total loop impedance is modeled as a series combination of the effective probe impedance $Z_P(\omega)$, the contact-interface impedance $Z_c(\omega)$, and the effective terminal impedance $Z_B(\omega)$ (corresponding to regions 1, 2, and 3, respectively). Thus, the total impedance $Z(\omega)$ is formulated as

$$Z(\omega) = Z_P(\omega) + Z_c(\omega) + Z_B(\omega) \tag{2}$$

The probe impedance $Z_P(\omega)$ consists of its bulk resistance R_P and bulk inductance L_P in series, and can be written as

$$Z_P(\omega) = R_P + j\omega L_P \tag{3}$$

Similarly, the terminal impedance $Z_B(\omega)$ is composed of its bulk resistance R_B and bulk inductance L_B in series, and can be expressed as

$$Z_B(\omega) = R_B + j\omega L_B \tag{4}$$

The contact interface between the probe and terminal consists of metallic contact spots surrounded by surface films and air gaps. Current flowing through the constriction zone generates contact resistance R. The associated current crowding and near-field magnetic energy storage in the contact region and its immediate surroundings give rise to an effective interfacial inductance L_c. Meanwhile, the residual non-contact gaps together with interfacial films provide an effective interfacial capacitance C_g. Therefore, the interface impedance $Z_c(\omega)$ is modeled as a series branch of resistance R and inductance L_c in parallel with the capacitance C_g.

$$Z_c(\omega) = \left[R + j\omega L_c\right] \| \frac{1}{\left[j\omega C_g\right]} \tag{5}$$

By substituting Eqs. (3)–(5) into Eq. (2), the overall loop impedance can be written in a compact form as

$$\begin{aligned} Z(\omega) = R_P + R_B + \frac{R}{(\omega R C_g)^2 + (\omega^2 L_c C_g - 1)^2} \\ + j\omega\left[L_P + L_B - \frac{R^2 C_g + L_c(\omega^2 L_c C_g - 1)}{(\omega R C_g)^2 + (\omega^2 L_c C_g - 1)^2}\right] \end{aligned} \tag{6}$$

Based on Eq. (6), the measured loop impedance can be interpreted as the superposition of a frequency-independent resistive baseline (R_P+R_B), a frequency-dependent interfacial contribution governed by (R, L_c, C_g), and a series inductive term associated with the current return path (L_P+L_B). This formulation explicitly elucidates the typical $|Z|$–$\angle Z$ characteristics observed in Section III.A. In the low-frequency regime, the denominator in Eq. (6) is dominated by the constant term, and the reactive contribution is negligible; consequently, $Z(\omega)$ approaches a quasi-resistive value determined by (R_P+R_B) and the low-frequency limit of the interfacial term, yielding $\angle Z \approx 0$. As frequency increases, the imaginary component becomes progressively influenced by the series inductance and interface reactance, leading to a positive phase shift and a gradual rise of |Z|. This behavior is consistent with the inductive trend observed in the low-to-mid MHz range.

Significantly, Eq. (6) predicts a resonance when the interfacial susceptance approaches zero (i.e., $\omega^2 L_c C_g \approx 1$). Under this condition, the interfacial branch exhibits a high equivalent impedance, resulting in a sharp peak in $|Z|$. Simultaneously, the sign reversal of Im(Z) across the resonance accounts for the phase zero-crossing in the measured $\angle Z$. Beyond the resonance, the capacitive reactance becomes dominant within the interfacial network, driving Im(Z) negative over a frequency interval. However, as the series inductive term $j\omega(L_P+L_B)$ continues to increase, the net reactance transitions back to an inductive state at higher frequencies. This mechanism correlates well with the second phase reversal and the slight upturn of |Z| observed near the upper limit of the measurement band.

In practice, the stochastic surface topography and interstitial voids at micro-scale gold-coated interfaces render it challenging to determine the interfacial reactive components solely from theoretical contact models. Consequently, an inverse identification strategy is adopted based on the loop impedance model in Eq. (6) and the equivalent circuit in Fig. 9, with the detailed workflow summarized in Fig. 10.

Specifically, the bulk parasitics of the probe and terminal (R_P, L_P, R_B, L_B) are considered known quantities (obtained from separate simulations or measurements), whereas the interfacial resistance R at each load is determined by the measured DC contact resistance. The remaining unknown reactive parameters $\boldsymbol{\theta} = [L_c, C_g]$ are identified by solving a nonlinear least-squares problem that minimizes the discrepancy between the measured and modeled imaginary impedance over N frequency samples, i.e.,

$$\min_{\theta} S(\theta) = \sum_{i=1}^{N} [\mathrm{Im}(Z_{meas}(f_i)) - \mathrm{Im}(Z_{model}(f_i, \theta))]^2 \tag{7}$$

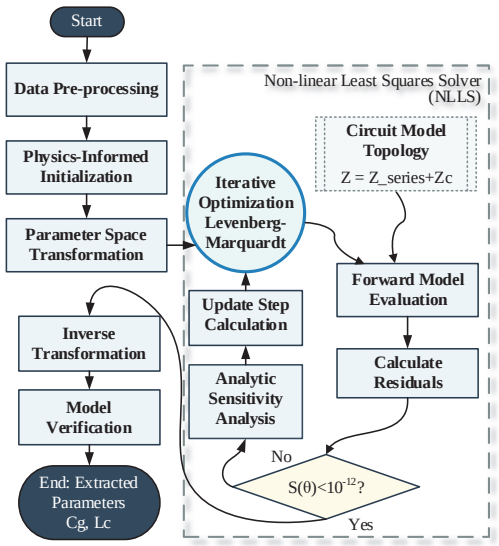


Fig. 10. Flowchart of the proposed physics-informed parameter extraction algorithm.

To enforce positivity and improve numerical conditioning, the optimization is performed in the logarithmic space, employing a Levenberg–Marquardt solver

with sensitivity-based updates. Physics-informed initial guesses are derived from the dominant resonance condition $\omega_0 \approx 1/\sqrt{L_c C_g}$, thereby improving robustness and mitigating convergence to local minima. Upon convergence, the identified parameters are substituted back into Eq. (6) to predict both Re(Z) and Im(Z); the resulting curves correspond to the solid lines in Fig. 4. Finally, the model validity is assessed by comparing the predicted Re(Z) against the measured data, yielding a goodness-of-fit of $R^2 \approx 0.97$. This agreement confirms that the proposed loop topology and the imaginary-part-driven identification strategy effectively capture the dominant spectral features, providing a reliable basis for extracting the effective interfacial inductance L_c and gap capacitance C_g.

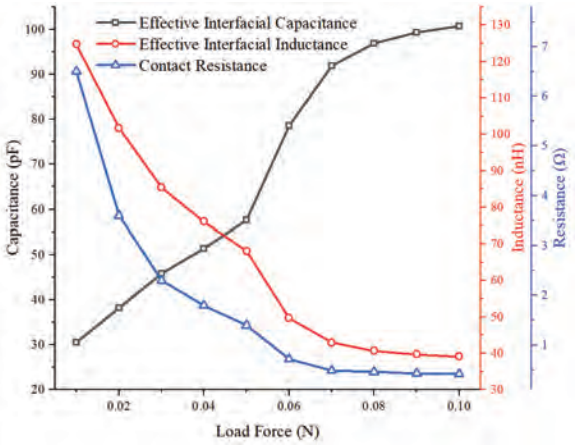


Fig. 11. Extracted effective interfacial parameters versus load force

Fig. 11 summarizes the load dependence of the effective interfacial parameters extracted from the impedance spectra. Specifically, the interfacial resistance R is given by the measured DC contact resistance, whereas the effective interfacial inductance L_c and effective interfacial capacitance C_g are derived using the proposed iterative identification procedure.

As the normal load increases from 0.01 N to 0.1 N, both R and L_c exhibit a monotonic decrease, while C_g shows an increasing trend. These behaviors correlate well with the conduction-regime evolution inferred from the DC R–F characteristics discussed in Section III.C. The increasing load promotes more efficient current constriction through the interface, thereby reducing resistive loss. Simultaneously, this process is accompanied by a shortening and "widening" of the effective current paths, which naturally results in the reduction of the extracted L_c.

In contrast, the evolution of C_g is governed primarily by the geometry of the surrounding non-contact gaps and interfacial films. Most notably, a pronounced surge in C_g is observed within the transition range of 0.05–0.065 N, which coincides with the onset of partial film disruption and the rapid expansion of metallic contact spots. In this regime, film rupture and asperity flattening substantially reshape the local gap distribution, leading to a significant increase in the effective capacitance. For F>0.065 N, C_g approaches a plateau, indicating that subsequent loading mainly enlarges the metallic conduction area (reflected by the continued decrease in R and L_c), while inducing comparatively minor changes in the geometry of the residual non-contact gaps.

IV. Conclusion

A micro-scale single-spot contact between a gold-plated probe and a gold-plated connector terminal was experimentally characterized under normal loads of 0.01–0.1 N by combining DC contact resistance measurements with impedance spectroscopy from 100 kHz to 300 MHz. The impedance response exhibits a pronounced resonance and systematic load dependence: increasing load reduces the low-frequency resistive plateau and yields a higher, sharper resonant peak with only a minor shift in resonant frequency. The DC R-F curves reveal three loading regimes, transitioning from film-affected conduction to a rapid transition with emerging metallic paths, and finally to constriction-dominated behavior, together with clear unloading hysteresis. Based on an equivalent loop model that separates bulk parasitics and interfacial impedance, a physics-informed inverse strategy is developed to quantitatively identify the effective interfacial inductance L_c and effective interfacial capacitance C_g as explicit functions of load force, and is validated by the agreement between predicted and measured Re(Z). The extracted trends show monotonic decreases in R and L_c with load, whereas C_g increases rapidly in the transition regime and then approaches saturation, consistent with conductive-spot growth and concurrent reconfiguration of residual non-contact gaps. Future work will link the evolution of true contact area to the extracted L_c and C_g to further understand the physical origin of their load dependence.

Acknowledgment

The authors express their gratitude for the kind support provided by National Natural Science Foundation of China (Contract Number 52407166).

References

[1] C. Wang, J. Gao, and K. Song, “Effect of vibration-induced degradation in high-speed backplane connectors on digital signal transmission,” in Proc. 2023 IEEE Holm Conf. Electrical Contacts, Seattle, USA, October 2023, pp. 1–8.

[2] Y. Yang, Q. Wang, and J. Anderson, “Experimental Investigation of 400 Gb/s Data Center Interconnects,” Applied Sciences, vol. 9, no. 12, 2455, June 2019.

[3] Q. Li, J. Gao, G. T. Flowers, G. Xie, and R. L. Jackson, “Effect of electrical contact degradation on analog signal transmission,” IEEE Transactions on Components, Packaging and Manufacturing Technology, vol. 9, no. 12, pp. 2374–2382, December 2019.

[4] J. Fan, X. Ye, J. Kim, B. Archambeault, and A. Orlandi, “Signal integrity design for high-speed digital circuits: Progress and directions,” IEEE Trans. Electromagn. Compat., vol. 52, no. 2, pp. 392–400, May 2010.

[5] R. Ji, J. Gao, G. T. Flowers, G. Xie, Z. Cheng, and Q. Jin, “The effect of electrical connector degradation on high-frequency signal transmission,” IEEE Trans. Compon., Packag. Manuf. Technol., vol. 7, no. 7, pp. 1163–1172, July 2017.

[6] E. Dervos and D. Michaelides, “The effect of contact capacitance on current-voltage characteristics of stationary metal contacts,” IEEE Trans. Compon., Packag., Manuf. Technol., vol. 21, no. 4, pp. 530–540, December 1998.

[7] L. Boyer, J. Goldstein, and P. Wolf, “The influence of surface roughness on the capacitance between a sphere and a plane,” J. Phys. D: Appl. Phys., vol. 27, no. 7, pp. 1504–1508, July 1994.

[8] R. Holm, Electric contacts: theory and application, 4th ed. Berlin, Germany: Springer-Verlag, 1967.

[9] T. Tamai, Y. Saitoh, S. Sawada, and Y. Hattori, “Peculiarities in characteristics between contact trace and contact resistance of tin plated contacts,” in Proc. 54th IEEE Holm Conf. Elect. Contacts, 2008, pp. 337–343.

The performance of offshore charging contacts with and without maintenance with contact grease

Kristian Solheim Thinn
Electric Power Technology
SINTEF Energi AS
Trondheim, Norway
kristian.solheim@sintef.no

Niklas Magnusson
Electric Power Technology
SINTEF Energi AS
Trondheim, Norway
niklas.magnusson@sintef.no

Erik Bjerrehorn
Electric Power Technology
SINTEF Energi AS
Trondheim, Norway
erik.bjerrehorn@sintef.no

Olve Moen
Electric Power Technology
SINTEF Energi AS
Trondheim, Norway
olve.moen@sintef.no

***Abstract*—To accommodate electrification of marine transportation, robust connector solutions are required to allow safe and reliable power transfer. Accelerated aging tests have been performed to determine the influence of coastal climate (salt mist) on connectors for use to transfer power from a hub in the ocean to vessel batteries. The test objects were four 400-A ac connectors for such applications. Contact grease was applied to the contact surfaces on two of the connectors as a maintenance measure. The tests simulate about four years of operation in Norwegian coastal environments (marine corrosion index 8). The recorded resistance increases were low for the population that were regularly maintained with contact grease. An excessive contact increase was recorded for the population that was not maintained but the increase was still not large enough to cause the connectors to fail due to overheating during the simulated four years of operation.**

Keywords—Contacts, connectors, maritime, aging, corrosion, maintenance

I. Introduction

Under the framework of the project Ocean Charger [1], offshore charging solutions were studied, typically to enable charging hubs at offshore wind power plants for support vessels for installation, commissioning and maintenance of the wind farms, and for other ships in need of battery charging at sea to e.g. extend their operating range.

To accommodate electrification of maritime vessels, safe and reliable contacts between the vessel and the charging station are crucial [2]. The absence of a common standard for plugs and electric charging systems for maritime applications is a possible barrier to the electrical transition. However, in many aspects maritime contacts face the same issues as contacts for charging electric vehicles, an application with extensive field experience. Hence, charging contacts can rely on similar principles for design of the contacts and for testing as onshore applications, with some additions for the special conditions in coastal areas or at sea. Among the aging mechanisms for vehicle contacts (inside the car), fretting wear and fretting corrosion were identified as the most common failure mechanisms [3]. For electric vehicle charging connectors, failures were identified in certain connectors when increasing the charging current due to higher power requirements. Improvements in the design of the contacts resolved the issue leading to stable connectors in the heat cycle tests performed [4].

A question becoming more important for maritime applications than for charging of electric cars, is the connectors' long-term properties in salty environments. Studies have been performed on aluminium busbar contacts for on-board battery systems in corrosive environments [5], and closer to the present study on Type 2 connectors originally designed for electric vehicle charging but studied for charging of small fishing boats [6].

Heat cycling (by applying an ac or dc electric current) is the preferred testing method for contacts to be used in clean environments, such as in the IEC 61238 standard [7]. This standard is considered reliable, as very few correctly assembled connections that pass it fail in service. Connectors passing the test program have completed 1000 cycles where the temperatures of the connectors have been varied between 35°C and approximately 100°C.

Connectors for maritime vessels operate in challenging conditions, both considering the maritime environments (salt and humidity) and the charging cycles (0 to 100% load, sometimes several times a day). Consequently, knowledge about connector performance under these operating conditions is of high interest. Evaluations of the maritime factors are not commonly found in the literature nor in the most relevant standards for the application, such as IEC 60309-1 [8], IEC 62613-1 [9], and IEC 62196-1 [10], even though they play an important role for contact quality in other aspects.

Currently, a maintenance method for maritime contacts is to regularly add contact grease to the contact surfaces of the plug pins. In the present study, four connectors of a type currently used for ship charging in the harbour were alternately exposed to heat cycles and a corrosive environment. The purpose of the laboratory test was to determine the influence of corrosive environments on the long-term contact quality of connectors with and without maintenance with contact grease.

This work was a part of The Green Platform Initiative by the Research Council of Norway under Grant number 340936, "Ocean Charger - maritime value chain for offshore energy transfer within offshore wind" (2023-2025). The project was led by Vard Design AS.

II. Test Objects

The tested ac connectors were produced according to IEC 80005-3 (Low Voltage Shore Connection) [11], four sockets and two plugs from vendor A and two plugs from vendor B, with current ratings of 350 A (socket) to 420 A (plug) and voltage rating of 690 V (vendor A) to 1100 V (vendor B), see Fig. 1 and the key data in Table I. To support higher power requirements which in many instances may be needed at sea, connectors should be produced according to IEC 80005-1 (High voltage shore connection) [12]. However, the key difference between the standards is the dielectric properties of the connectors, and not the electrical connection (pins and socket), and hence, contact tests on low-voltage connectors are indeed relevant for the contact properties of high-voltage connectors. The cross section of the stranded copper conductor was about 185 mm^2.

III. Test Programme

The connectors were alternately heat cycled and exposed to maritime environment. During heat cycling, a load current (350 or 400 A) was switched on and off, allowing the connectors to almost reach the steady state temperature at the current, and cool down to approximately 35°C (for the 350 A current). Exposure to maritime environment was (except for the last exposures) done in a salt mist chamber where the connectors were either in closed position (mated) or in open position (exposing the pins directly to salt mist). In the last salt exposures, the plug was submerged in seawater for one minute.

Contact grease was applied to the contact surfaces on two of the four connectors (Connectors 3 and 4) at the start of the test and after maritime environment exposure as a maintenance measure. At the start of the test, after each period of heat cycles (125 or 250) and maritime environment exposure, the contact resistance was measured. See the test timeline in Fig. 3.

A. Heat Cycles

The heat cycle test is based on the IEC 61238 standard for electrical contacts. Compared to standards developed for e.g., car charging connectors, the test comprises a higher number of heat cycles and higher loads, providing a better understanding of the long-term effects of the connector quality.

Each heat cycle lasted for three and a half hours: two and a half hours heating and one hour cool-down. This was the time needed to reach near stationary heating conditions and close to ambient cooling conditions. The applied current was 350 A for the first 1000 heat cycles, and 400 A for the remaining 500. The current was increased in the last part to accelerate aging. The tests were performed in a room with stagnant air and ambient temperature of about 20°C. See the test set-up in Fig. 2.

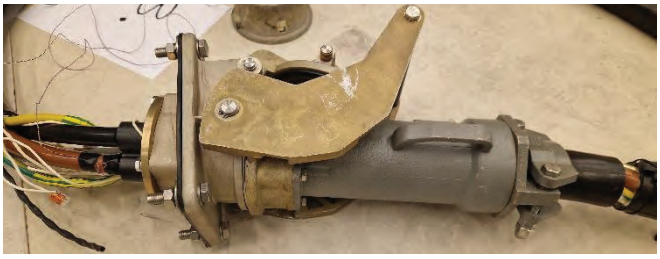


Fig. 1. Object No. 3 during installation.

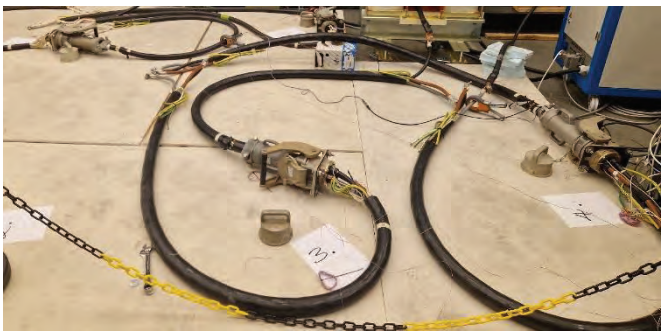


Fig. 2. Test loop during heat cycling.

TABLE I. Key Data For the Test Objects

Object No.	Model	Specifications	Vendor
1 socket	3PX5 (X5DF318-LV95) 19/22	350 A / IP 67 / 690 V	A
1 plug	PC5-TX04-18504R (PC-20170929)	420 A / 1100 V	B
2 socket	3PX5 (X5DF318-LV95) 19/22	350 A / IP 67 / 690 V	A
2 plug	3PX5 (X5PF315S-LV50) 51/20	420 A / IP 67 / 690 V	A
3 socket	3PX5 (X5DF318-LV95) 19/22	350 A / IP 67 / 690 V	A
3 plug	3PX5 (X5PF315S-LV50) 51/20	420 A / IP 67 / 690 V	A
4 socket	3PX5 X5DF318-LV95 19/22	350 A / IP 67 / 690 V	A
4 plug	PC5-TX-04-18504R (PC-20170931)	420 A / 1100V	B

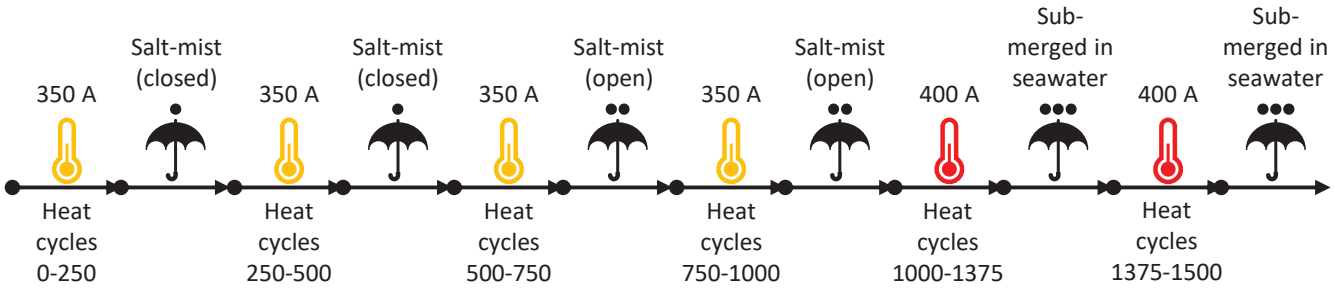


Fig. 3. Test timeline.

The heat cycle test current is usually higher than the rated current to simulate accelerated aging. The current used is based on engineering judgement for each of the connectors and is adjusted during the test period as needed. A proper test current should be high enough to stress the contacts, but low enough to avoid degrading the reference connectors. The purpose of these tests is to determine the influence of the coastal climate, that cannot be concluded if the reference connectors are excessively degraded. For comparison, connectors tested according to IEC 61238 are usually loaded about 20% above nominal current and good contacts should hence withstand such a load.

Thermocouples were placed in the conductor, and in the plug (inside the air volume of the enclosure, ~30-cm from the plug pins) and socket (in the cable, where it enters the enclosure). Figs. 4 and 5 show typical temperature responses at 350 and 400 A, respectively.

B. Maritime Environment

All connectors were environmentally exposed in a salt-mist chamber multiple times and submerged in saltwater for one minute once (plugs 1 and 2 were submerged twice). During exposure in the salt-mist chamber, the cables were protected by thick plastic hoses to prevent salt ingress from the ends and through punctures in the cables that were used for contact resistance measurements. Inserting these hoses and moving them to the salt mist chamber required some handling, but well within what should be expected during regular use.

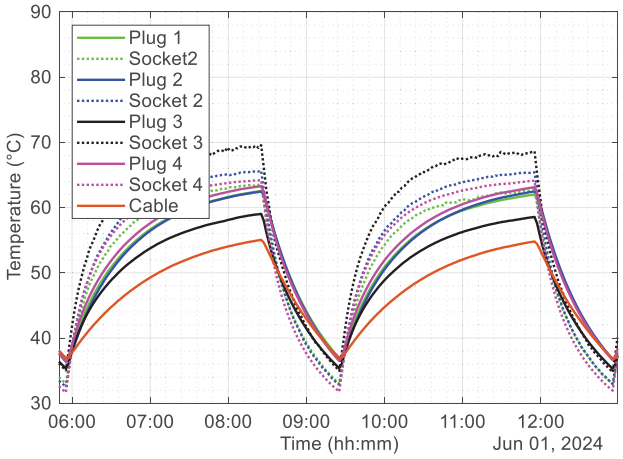


Fig. 4. Cable and socket temperatures during cycling with 350 A.

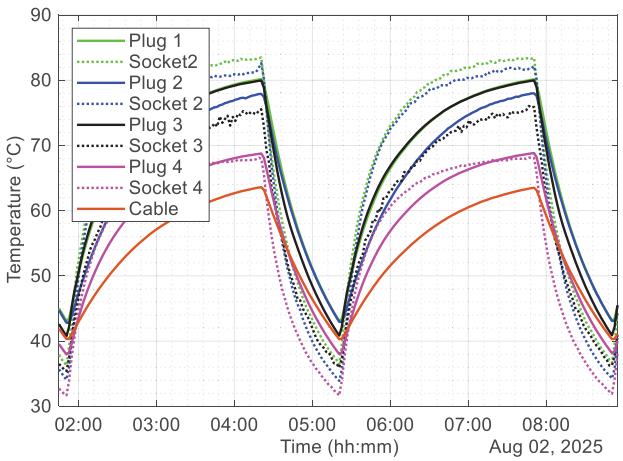


Fig. 5. Cable and socket temperatures during cycling with 400 A.

The maritime environment exposure was:

- After 250 and 500 heat cycles: 16 days in salt-mist chamber (8 salt-mist cycles), simulating one year in Norwegian coastal climate. The connectors were in closed position (mated), see Fig. 6.
- After 750 and 1000 heat cycles: As at 250 and 500 cycles, but the connectors were in open position (not mated), see Fig. 7.
- After 1375 and 1500 heat cycles: The plugs (only 1 and 2 after 1500 cycles) were submerged in saltwater, with salinity of 3.5%.

For the exposures in the salt-mist chamber, a marine corrosion index (MCI) 0 of 8 was applied, corresponding to Norwegian coastal climate. The sequence and parameters for accelerated aging in the salt-mist chamber were:

1. Salt exposure: t = 24 h, $T_{chamber}$ = 35°C, $T_{moisture}$ = 35°C (DIN 50021 SS). DIN: Deutsches Institut für Normung (German Institute for Standardization).
2. Conditioning: t = 8 h, $T_{chamber}$ = 40°C (DIN 50017 KFW).
3. Drying: t = 8 h, $T_{chamber}$ = ambient (DIN 50017 KFW).

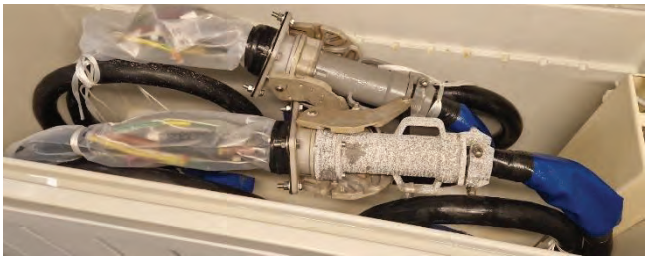


Fig. 6. Two connectors in salt-mist chamber (mated).



Fig. 7. Two connectors in salt-mist chamber (open).

C. *Maintenance*

After every exposure to maritime environment, contact grease (Würth electro grease, elektrofett, 0890 104 038) was applied to all three phase pins of plugs 3 and 4. The purpose of the grease is to limit oxidation. As a side effect, some of the salt coating was removed during the application of the grease.

D. *Resistance measurements*

At regular intervals (every 250th cycles up to 750 cycles and every 125th cycle thereafter) the resistance was measured over the entire connector for each phase; from the cable on one side to the cable on the other side, see Fig. 8. The measurement was done at ambient temperature (~20°C) using the 4-wire method: injecting a dc measurement current of 30 A through the cables, and measuring the voltage drop across the contacts.

Furthermore, after the test, the connectors were cut open and the resistance was measured over each contact individually, see Fig. 9.

IV. Results and Discussion

A. *Resistance measurements during test*

In Fig. 10, the measured resistances over the 1500 heat cycles are presented. Note that the resistances are the total resistances from the cable at one end to the cable at the other end, including five contacts and the bulk resistance of the respective parts inside the connector. For comparison, the bulk resistance over an equally long part of the 185 mm^2 copper cable is approximately 60 μΩ. The baseline for the resistance is in the 100-150 μΩ range. Hence, the observed differences in resistance represent a significant resistance increase of a single contact.

The resistances for connectors 3 (green line) and 4 (blue line), that are maintained by contact grease, are in general stable and only to a limited degree affected by the exposures of the test. On the other hand, two of the phases for connectors 1 and 2 (red and black lines), not maintained with contact grease, show significant resistance increases.

B. *Postmortem investigation*

After the test, firstly holes were drilled through the insulation to allow for resistance measurements over the individual contacts, and secondly the insulation was removed to visually inspect the contacts. Fig. 9 shows the different components inside the connectors together with the voltage probe positions for the resistance measurements. Between each component there is an electric contact, making it in total five contacts: socket cable-to-socket crimp, socket crimp-to-socket pin, socket pin-to-plug pin, plug pin-to-plug crimp, and plug crimp-to-plug cable.

The resistances over the individual contacts after the test are shown in Fig. 11. The most important contact for this study is the socket pin-to-plug pin contact, since it is the one that is either maintained with contact grease or not. For this contact, the resistance of connector 1, phase A is 220 μΩ and connector 2, phase C is 380 μΩ, whereas for all other socket pin-to-plug pin contacts, the resistances are 100 μΩ or lower. Hence, the enhanced resistances occur on contacts not maintained with contact grease.



Fig. 8. Resistance measurement points over the connector. There are three measurements for each connector (one per phase), making it in total twelve resistance measurements, six with and six without maintenance with contact grease.

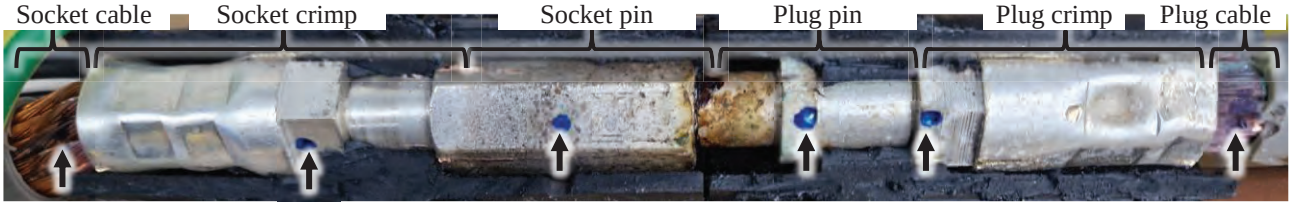


Fig. 9. The parts of the connector with the probe positions for resistance measurements indicated.

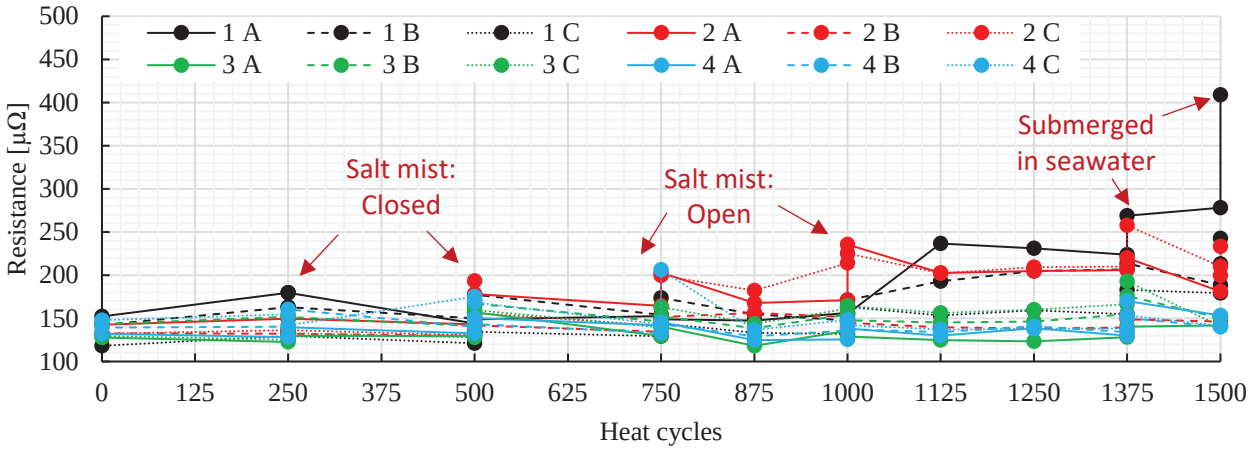


Fig. 10. Resistances over the connectors measured during the test.

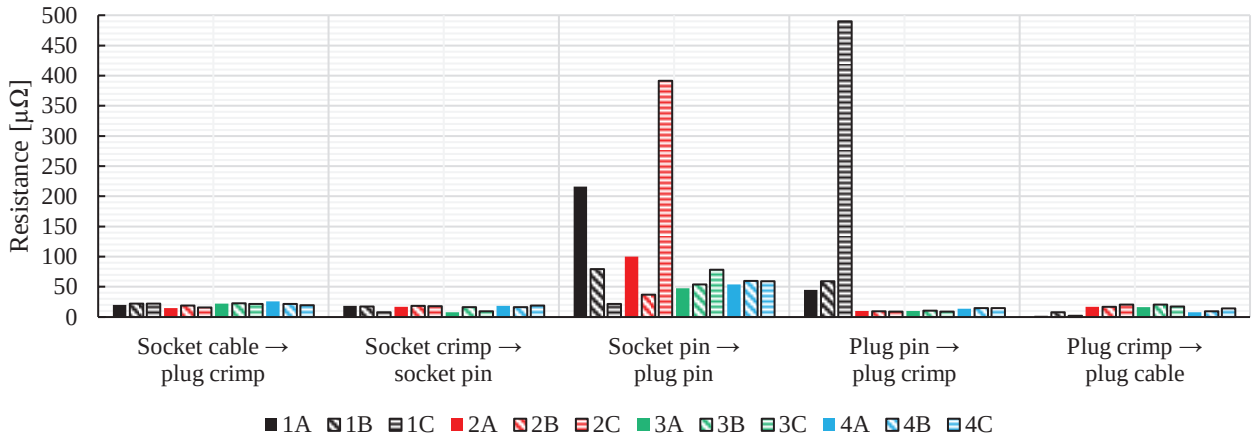


Fig. 11. Resistances over the individual contacts.

Notably, the plug pin-to-plug crimp contact was high for connector 1, phase C. However, during the examination, it was revealed that this contact was faulty installed (and that to a lesser degree also applied to the other phases of connector 1), making the contact loose, at least after being dismantled, and that being the cause of the high resistance.

Apart for the contacts mentioned above, none of the contacts showed enhanced resistance values. Hence, the four contacts inside the connector (that is all but the socket pin-to-plug pin contact) showed no degradation during the test. These contacts were not maintained with contact grease but protected by the enclosure. For the centre contact, socket pin-to-plug pin, none of the six contacts maintained with contact grease showed any degradation, whereas two of the six not maintained did.

V. Conclusion

Although the sample size is small, the test shows that exposure to a coastal or ocean environment is a factor to consider for connectors for battery charging. The test also indicates that maintenance with contact grease of the socket pin-to-plug pin contact (the one easily accessible) has a positive effect on the long-term properties of the connector. The other contacts within the connector were not influenced by the exposures.

References

[1] https://www.vard.com/articles/the-ocean-charger-project-has-officially-started, February 2023.

[2] E. B. Mehammer, H. Strand, N. Magnusson, K. S. Thinn and E. Eberg, “How to Plug in the Fishing Fleet: Connectors in charging infrastructure for small fishing boats,” IEEE Electr. Mag., Vol. 11, pp. 73-82, 2023.

[3] J. Song, D. Hilmert, and F. Kiel, “Mechanisms of failure and state analysis of electrical connectors in automobiles,” Eng. Fail. Anal., vol. 173, 109427, 2025.

[4] P. Reid, C Mittelstadt and T Faber, “Electric vehicle conductive charge couplers,” 2014 IEEE 60th Holm Conference on Electrical Contacts (Holm), New Orleans, LA, USA, 2014, pp. 1-7, doi: 10.1109/HOLM.2014.7031062

[5] A. Elkjaer, G. Ringen, R. Bjørge, C. H. Musinoi Hagen, S. Lædre and N. Magnusson, “Reliability of Bolted Aluminum Busbars for Battery Systems: Effect of Nickel Coating and Corrosive Environments,” IEEE Trans. Transport. Electrific., vol. 9, pp. 1060-1071, 2023.

[6] K.S. Thinn, N. Magnusson, N.M. Thomsen, O. Moen, and E. Bjerrehorn, “Long-Term Properties of Shore-to-Vessel Connectors in Maritime Environments,” 2025 IEEE Electric Ship Technologies Symposium (ESTS), Alexandria, VA, USA, 2025, pp. 185-191, 2025, DOI: 10.1109/ESTS62818.2025.11152411

[7] “IEC 61238-1-3 Compression and mechanical connectors for power cables - Part 1-3: Test methods and requirements for compression and mechanical connectors for power cables for rated voltages above 1 kV (Um = 1,2 kV) up to 30 kV (Um = 36 kV) tested on non-insulated conductors”, International Electrotechnical Commission, May 2018.

[8] “IEC 60309-1 Plugs, fixed or portable socket-outlets and appliance inlets for industrial purposes - Part 1: General requirements”, International Electrotechnical Commission, Jun. 2021.

[9] “IEC 62613-1 Plugs, socket-outlets and ship couplers for high-voltage shore connection (HVSC) systems - Part 1: General requirements”, International Electrotechnical Commission, May 2019.

[10] “IEC 62196-1 Plugs, socket-outlets, vehicle connectors and vehicle inlets - Conductive charging of electric vehicles - Part 1: General requirements”, International Electrotechnical Commission, May 2022.

[11] “IEC 80005-3 Utility connections in port — Part 3: Low-voltage shore connection (LVSC) systems — General requirements”, International Electrotechnical Commission, September 2014.

[12] “IEC 80005-1 Utility connections in port Part 1: High voltage shore connection (HVSC) systems – General requirements”, March 2019.

D. P. Doyle, T. E. Wright. Rapid Methods for Determining Atmospheric Corrosivity and Corrosion Resistance. Atmospheric Corrosion, edit. by W.H. Ailor, John Wiley and Sons 1982:227-24

Current Chopping of Vacuum Interrupters with Stainless Steel Contacts

Christoph Kenel
ABB Switzerland Ltd
Baden-Dättwil, Switzerland
christoph.kenel@ch.abb.com
ORCID: 0000-0003-0800-2986

Siobhan McKeown
ABB Switzerland Ltd
Baden-Dättwil, Switzerland
siobhan.mckeown@ch.abb.com
ORCID: 0009-0009-1854-9687

Roman Mukin
ABB Switzerland Ltd
Baden-Dättwil, Switzerland
roman.mukin@ch.abb.com
ORCID: 0009-0003-9847-393X

Dietmar Gentsch
ABB Germany Ltd
Ratingen, Germany
dietmar.gentsch@de.abb.com
ORCID: 0000-0003-1874-5206

Julien Rault
ABB Switzerland Ltd
Baden-Dättwil, Switzerland
julien.rault@ch.abb.com
ORCID: 0000-0002-2450-5535

***Abstract*— The sudden and random extinction of the metal vapor arc in a vacuum interrupter before the current zero crossing is known as chopping. This can produce large over voltages in a circuit. Chopping is a complex phenomenon depending on the current level, specific circuit configuration, and the contact material used. This paper presents current chopping characteristics of stainless steel contacts as candidate materials for VI applications. Three commercial steels are compared: AISI 304, 316L and 316Ti (1.4301, 1.4404 and 1.4571). Testing is performed and repeated for 500 operations per VI to generate a data set representative of the chopping current distribution. Analysis shows that the steel grade has a significant effect on the median chop current as well as the occurrence of rare high chopping current events. The log-logistic distribution best approximates the data. This validated model enables extraction of statistical parameters (median, mode, percentiles) from smaller datasets in future screening tests. The steel microstructures are characterized by SEM EBSD/EDX, and their surfaces are measured after testing. With this we can demonstrate that while stainless steel equipped VIs show a similar median chopping current compared to conventional CuCr, it is perhaps not suitable for sensitive applications due to a tendency to produce very high current chopping events.**

Keywords—chopping, stainless steel, vacuum interrupter

I. INTRODUCTION

At low currents, arcs in vacuum interrupters experience a complex phenomenon where the vacuum arc is extinguished before current zero with very fast changes in current level (high dI/dt). This sudden current drop is called a “chopping” event. Typical current values at which chopping occurs range from 0.5 – 20 A depending on the contact material and, crucially, the (test) circuit, current and other variables. The high dI/dt at interruption leads to very high overvoltage spikes, especially with highly inductive loads such as motors and transformers. As the voltage spikes become multiple times larger than the nominal voltage, the insulation in the connected devices can be damaged and the equipment can subsequently be destroyed. Chopping is controlled on a microscopic level by the physics of the contact material interaction with the plasma. Thus, low chopping in commercial vacuum interrupters is achieved through a judicious choice of contact material. In circuit breakers generally (modified) CuCr is used. However, since the magnitude of current chopping, and thus the overvoltage level, increases as the RMS current level decreases [1], whenever VIs are used to switch low currents, a material with an even lower intrinsic chopping level is required. In contactors, designed to switch low nominal currents, this is typically achieved by using AgWC [2]. A limited number of materials are compatible with the high vacuum environment and production routes for vacuum interrupters, which are typically constructed from Cu and Cu-based alloys, Cu and Ag-based contact materials, austenitic stainless steel, all sealed by brazing with suitable alloys to an insulating glass or ceramic body [3]. Here, the use of austenitic stainless steels, typically only used as shields or structural elements, as contact material is explored and the chopping current characteristics are studied. The microstructures and surfaces are analyzed by SEM-EBSD and EDX. The electrical and thermal conductivity of stainless steels is very low compared to typical electrical contact materials (<5% of Cu), but this detriment could be overlooked in cost-sensitive applications without substantial nominal loads, where use of a low-cost contact material could be desirable.

II. CURRENT CHOP TESTING AND ANALYSIS

A. Synthetic test setup for chopping

Fig. 1 shows the synthetic test setup for measuring current chopping. The chopping test circuit consists of charging a capacitor bank (C1) of 16 mF that feeds two circuit loops. Once C1 is charged to 400 V, a thyristor is triggered, and current flow is generated in the two circuit loops. The secondary circuit loop contains the test object (TO), in this case a vacuum interrupter with stainless steel contacts. The primary/secondary circuit setup is acting as a current divider to ensure a controlled and reliable low current in the vacuum interrupter under test. The setup generates a peak current in

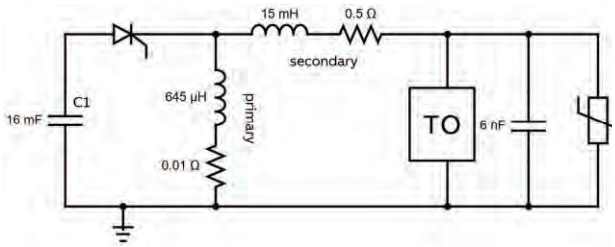


Figure 1 – Synthetic test circuit for current chopping.

the vacuum interrupter of approximately 75 A (57 A rms) at a frequency of 50 Hz. A metal oxide varistor (MOV) surge arrester and 6 nF capacitor are placed in parallel to the test object in order to limit the overvoltage after the current has chopped in the vacuum interrupter. The overvoltage on the vacuum interrupter is capped at 1.5 kV. This parallel branch will impact the magnitude of the chopping current and is therefore kept identical for all tests. For the low current measurement, a Pearson A110A probe was employed, whereas the voltage was determined by means of a differential probe with a ratio of 1:200 and a maximum frequency of 25 MHz (Teledyne LeCroy). All tests are performed with a single polarity, with the fixed contact as anode and the moving contact as cathode (ground). The chopping current is then extracted from the measured current curve.

B. Stainless steel contacts

The contacts were manufactured from three commercially available austenitic stainless steels compatible with the high vacuum environment and production processes of a vacuum interrupter: AISI 304, 316L and 316Ti (1.4301, 1.4404 and 1.4571). Table I shows their nominal composition ranges. The main differences are an increasing Ni content and the addition of Mo in 316L/316Ti and Ti in 316Ti. All contacts were mounted and tested in prototype vacuum interrupters.

TABLE I. Nominal compositional range of the tested steel grades in wt.%. Limits of impurities are shared: Mn <2, Si <1, P <0.045, and S <0.015.

Steel grade	C	Cr	Ni	Mo	Ti
1.4301 / 304	<0.07	17.5-19.5	8-10.5	-	-
1.4404 / 316L	<0.03	16.5-18.5	10-13	2-2.5	-
1.4571 / 316Ti	<0.08	16.5-18.5	10.5-13.5	2-2.5	5*C

C. Material analysis

The microstructure of the steels is analyzed by cross-section and embedding followed by standard metallographic preparation with grinding and polishing. Final surface preparation is performed using Ar ion beam flat milling. Contact surfaces are analyzed after chopping tests, directly after opening the vacuum interrupters. Scanning electron microscopy is performed using a Tescan Mira4 equipped with energy-dispersive X-ray spectroscopy (EDX) and electron backscatter diffraction (EBSD) detectors (Oxford Instruments). Compositions are measured using X-ray fluorescence using a FischerScope X-ray XDV. Roughness is measured with a Mahr MarSurf SD 26.

III. Current Chopping of Stainless Steel

Fig. 2 shows the observed chopping currents for 304, 316L and 316Ti stainless steel contacts for 500 operations. The stability across all operations allows reliable statistical analysis of the measurement datasets of each material.

A. Statistical analysis of chopping currents

The stochastic nature of arc extinction in a chopping event means that a given VI, subjected to many identical tests, will exhibit a distribution of chopping current levels rather than a single deterministic value. This inherent variability arises from the complex physical processes governing arc plasma behavior, contact surface conditions, and the statistical nature of charge carrier generation and recombination during current interruption.

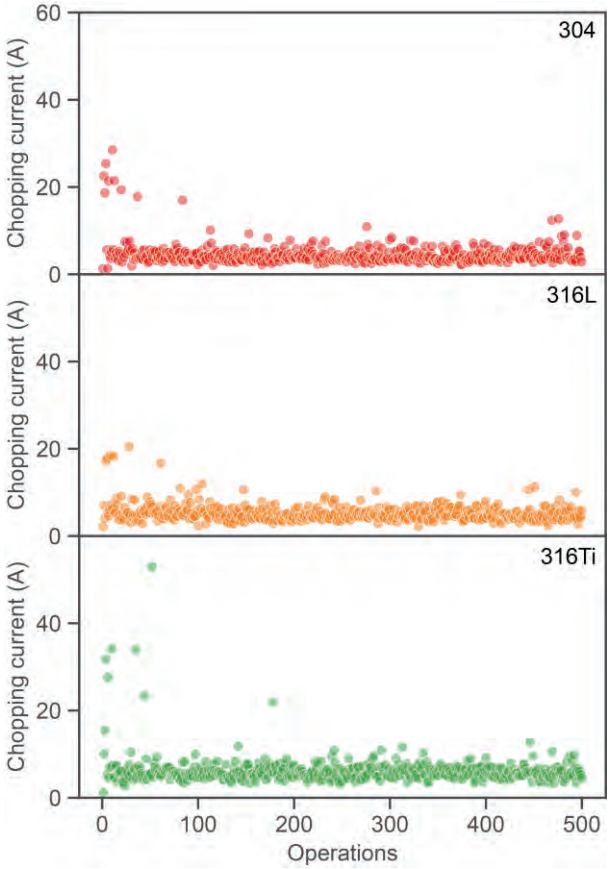


Figure 2 – Chop currents for contacts from 304, 316L, and 316Ti austenitic stainless steel.

Fig. 3 presents box plots of the chopping current distributions for all three materials on a logarithmic scale. The visualization reveals several key characteristics:

- Strong right-skewness: All distributions exhibit substantial positive skewness, with long tails extending toward higher current values.
- Presence of outliers: Multiple data points extend well beyond the whiskers, indicating extreme values.

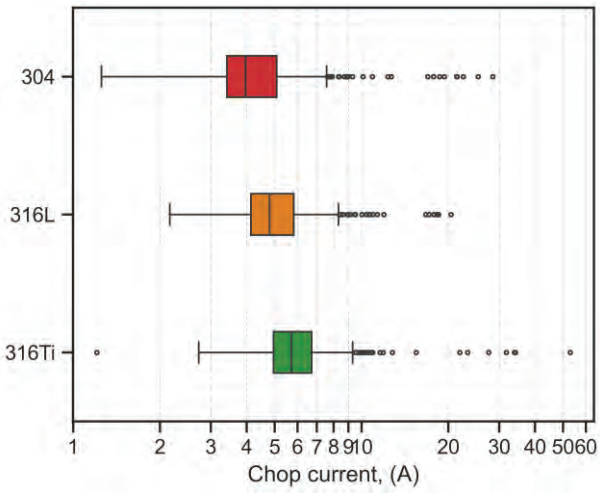


Figure 3 – Box plots of chopping current distributions for three contact materials (logarithmic scale). The boxes represent the interquartile range (IQR), with the median shown as the central line. Whiskers extend to 1.5*IQR, and outliers are shown as individual points.

- Apparent differences between materials: The median values and overall distributions appear to differ among the three materials.

Table II summarizes the fundamental descriptive statistics to quantify the distributional characteristics of each dataset. These measures provide insight into the central tendency, variability, and shape of the distributions [4], which are essential for selecting appropriate statistical tests and understanding the physical behavior of the vacuum interrupters under test conditions. The substantial positive skewness values (ranging from 3.45 to 7.52) confirm the non-normal nature of the distributions. The mean exceeds the median in all cases, which is characteristic of right-skewed distributions.

TABLE II. Descriptive statistics for chopping current measurements by material

Statistics	304	316L	316Ti
Sample size	500	499	500
Mean, (A)	4.62	5.27	6.27
Median, (A)	3.96	4.80	5.71
Std. deviation, (A)	2.71	2.05	3.64
Minimum, (A)	1.25	2.16	1.21
Maximum, (A)	28.49	20.43	52.98
25th percentile Q1 (A)	3.42	4.14	4.96
75th percentile Q3, (A)	5.08	5.82	6.71
IQR (Q3-Q1), (A)	1.66	1.68	1.75
Skewness	4.98	3.45	7.52

Given that the data are not normally distributed, the Kruskal-Wallis H-test is employed. This non-parametric method makes no assumptions about the underlying distribution and is based on rank transformations, making it robust to outliers. We want to test if the contact material has a statistically significant effect on the characteristics of chopping current. This is confirmed with the H-test yielding a p-value << 1E-6. To verify that the sample sizes are sufficient to detect meaningful differences between materials, we assess the statistical power of our test. For the H-test the observed effect size is large (ε^2=0.199), thus with 500 measurements per material, our study has excellent statistical power (approaching 100%) to detect differences of the observed magnitude, allowing us to draw reliable conclusions based on the statistics presented in TABLE II.

B. Sequential Distribution of Outliers

To investigate whether outliers occur uniformly throughout the test sequence or concentrate during specific operational phases, a sequential outlier analysis was conducted. This analysis is particularly relevant for identifying potential conditioning or ageing effects, where contact behavior may stabilize after initial operations.

Outliers were identified based on the interquartile range (IQR) criterion, consistent with standard box plot conventions with the limits given by: Q1−1.5*IQR or Q3 + 1.5*IQR. The latter corresponds to roughly the 95th percentile. The sequential distribution of these outliers for all three steels reveals a conditioning effect. If outliers were uniformly distributed throughout the test, we would expect approximately 25% to occur per 125 chopping experiments. However, we observe that 42-65% of outliers occur during the first 125 operations (25% of the test). This indicates a conditioning effect, with extreme chopping events occurring more often early on in the life of a VI with stainless steel contacts. This sequential analysis suggests that contact behavior during early operational cycles varies significantly by material composition, with 316L requiring the longest conditioning.

C. Distribution of chop currents

We have demonstrated that here, the size of the datasets is large enough that the fundamental descriptive statistics calculated directly from the data can be used to detect meaningful differences between the steels. However, this requires a large number of experiments. When only limited data is available, a fitted probability density function enables characterization of the chopping current distribution. Below, the presented chopping current data sets are used to find a suitable distribution for this purpose. Four different distributions are compared here: normal (Gaussian), log-normal, inverse Weibull, and log-logistic. The normal distribution function is symmetric, while log-normal, inverse Weibull and log-logistic are right-skewed with extended tails towards higher values. The normal distribution is nonetheless included here, as it is regularly used in published work. Table III shows the results from the Goodness-of-fit (GOF) evaluation. This demonstrates that for the three steels tested here, the log-logistic distribution function is a good approximation to describe the chopping current data.

TABLE III. Goodness-of-fit results including Anderson-Darling (AD), Akaike Information Criterion (AIC) and Bayesian information criterion (BIC) for the different distributions showing that log-logistic is a good approximation for the chopping current data.

Steel grade	Value	Normal	Log-normal	Inverse Weibull	Log-logistic
304	AD	-	10.5	7.8	3.6
	AIC	2419	1869	1824	1779
	BIC	2428	1876	1832	1788
316L	AD	25.8	4.6	4.3	1.5
	AIC	2134	1836	1819	1789
	BIC	2143	1844	1828	1798
316Ti	AD	-	10.8	22.9	1.7
	AIC	2714	2059	2127	1929
	BIC	2722	2068	2136	1938

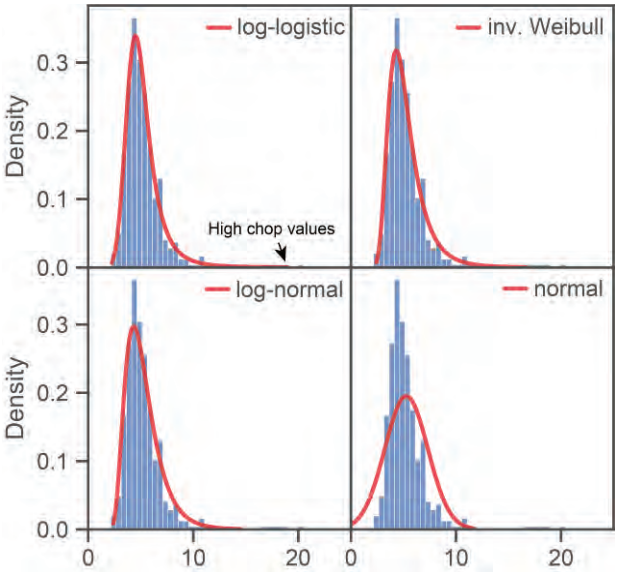


Figure 4 – Comparison of normal, log-normal, inverse Weibull and log-logistic distribution functions with the measured chop current distribution of 316L. The log-logistic distribution provides the best representation.

Fig. 4 shows the comparison of the four different tested distributions for 316L, demonstrating also visually that the log-logistic distribution accurately describes the observed chop current distribution <15 A. Inverse Weibull and log-normal would be valid choices as well, albeit with a poorer GOF score in this case and not suited for the other steels. The symmetric normal distribution clearly deviates from the measured values, especially for the low current tail. Note that the rare high current chop values >15 A are not captured by the log-logistic distribution, which is important when assessing the probability of very high chop values. The fact that the distribution of chopping currents is non-normal demonstrates that using the mean (average) chopping value alone to describe chopping current distributions can be misleading. For example, it does not correspond to the most likely chopping current, i.e., the peak of the distribution.

Fig. 5 shows the chopping current distributions for 304, 316L and 316Ti and the fitted log-logistic distribution functions that well approximate the measured data. The median (mode) chop current derived from the fitted log-logistic distributions are 4.1 (3.8) A, 4.9 (4.7) and 5.7 (5.5) A for 304, 316L and 316Ti, respectively. Note that the values obtained from the fitted distribution are close to the values extracted directly from the measured data (see Table II). Since the log-logistic distribution well approximates the data of all three steels, it can be used to characterize the median, mode and 95th percentile of the chopping current distribution of other VIs based on a reduced number of experiments. This allows a reduction of the experimental effort, for example, for screening contact materials.

IV. Microstructure and Chop Surface Analysis

A. Bulk microstructure and composition

Fig. 6 shows the microstructures of the three tested stainless steels after all thermal treatments during manufacturing, measured by SEM-EBSD to reveal the grain structure and phases present. The orientation is perpendicular (i.e. a side view) with respect to the machined contacts. The 304 stainless steel consists of predominantly equiaxed grains with twinning and isotropic texture. The measured mean grain size is 59 ± 21 µm. The major phase is fcc austenite. A small amount of bcc ferrite is detected (~0.9%), present in vertical bands. 316L consists of large, equiaxed grains with isotropic texture and a mean size of 88 ± 30 µm. Major phase is again fcc austenite. The content of bcc ferrite is minimal (~0.03%). MnS inclusions typical for steels are also observed in both 304 and 316L as dark vertical stringers (not indexed in EBSD). 316Ti shows equiaxed grains with a mean size of 6 ± 3 µm, significantly smaller than 304 and 316L. This is a consequence of the stabilization of the steel microstructure by the addition of Ti, typically present as carbides and nitrides. Larger TiN inclusions are observed here by EBSD as well as the formation of sigma phase. The major phase is fcc austenite with minor amounts of bcc ferrite (~0.1%), TiN particles (~0.1%) and a finely distributed Sigma phase (~2.2%). Sigma phase is a Fe-Cr-Mo-based intermetallic phase with a wide compositional range and its formation kinetics are accelerated by the presence of Ti [5], conditions all met in 316Ti. The phase forms typically in a range of 600-900 °C and slow cooling conditions. This temperature range overlaps with typical brazing temperatures when using Ag-based alloys. It is thus likely that the observed Sigma phase is precipitated during the VI production steps.

Table IV shows the measured composition of the tested stainless steels. Note that the Ni content in all of them is at the low end of the specified range. Also, the 304 steel contains a small amount of Mo, despite not being a required addition.

TABLE IV. Bulk composition of the tested steel measured by XRF. All values reported in wt%.

Steel grade	Cr	Ni	Mo	Mn	Ti
1.4301 / 304	18.1	7.91	0.29	1.67	-
1.4404 / 316L	16.6	9.80	2.04	1.51	-
1.4571 / 316Ti	16.9	10.5	1.96	1.81	0.25

B. Surface structure

Fig. 7 shows the surfaces of 304, 316L and 316Ti stainless steel after 500 chop operations. Imaging is performed at an oblique angle (20° relative to the surface). This reveals topography better than top-down imaging. For all steels, the entire surface is covered in shallow craters with smooth center areas and rounded protrusions along the edge. Some protrusions are also formed by droplets landing on already solid areas. The overlapping surface marks also indicate multiple melting and solidification events as the cathode spots travel over the already restructured surface. Smooth crater centers are up to ~100 µm in size. XRF and EDX measurements on the surface yielded no significant differences in composition from the bulk (<0.2% for the main

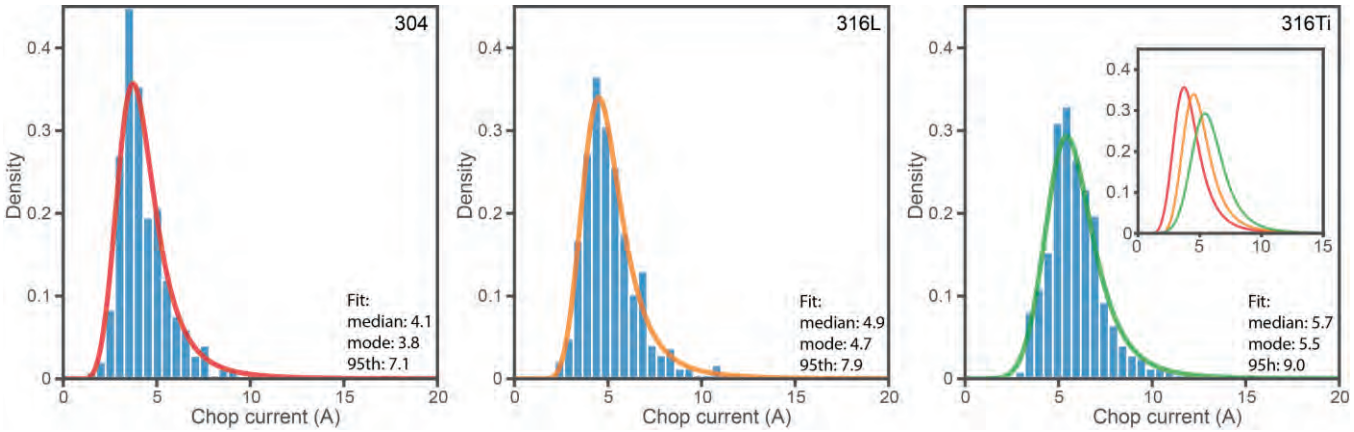


Figure 5 – Chop current distributions of 304, 316L and 316Ti stainless steel contacts. The fitted log-logistic distribution function is shown overlaid. The ordinate is clipped at 20 A, maximum values exceed this limit. Inset: Overlay of the fitted log-logistic distributions.

elements Cr, Ni, Mo, Mn). This indicates that evaporation is approximately equal for all elements and compositional shift is not occurring during the short melting when chopping at low current. Table V shows the surface roughness after 500 chopping operations. Ra provides an average over the surface, while Rz and Rmax give an indication of the depth difference of the craters, protrusions, and rims formed by the cathode spots. After chopping, 304 shows the lowest roughness values, 316L intermediate, and 316Ti the highest values. In general, all three steels become rougher than the original machined surface. Maximum crater depths range from ~35 to 45 µm, showing significant surface restructuring by the low current chopping experiment.

TABLE V. Surface roughness of the contact surface after 500 chopping operations.

Steel grade	Ra (µm)	Rz (µm)	Rmax (µm)
1.4301 / 304	5.4	33.2	38.2
1.4404 / 316L	6.9	41.6	46.1
1.4571 / 316Ti	7.3	40.8	44.0

V. Discussion

The observed chopping current distributions demonstrate that the steel type used has a significant influence on the chopping current, its distribution and extremes. For all tested steels, it is notable that they are prone to outlier chopping currents far exceeding the median value. Outlier chopping current events observed here reach up to 5-9x the median and 3-6x the 95th percentile. This should be kept in mind for any potential application of such steel contacts where the load insulation would need to resist not only the overvoltage generated by the most often occurring chopping current, but also be able to handle the rare events with much higher voltage spikes.

The median chopping current of 304 and 316L stainless steel is slightly lower than that of CuCr contact materials (5.5-6 A), while 316Ti is similar [6]. Chopping currents are thus substantially higher than those observed for AgWC (~1 A) [7]. This work on AgWC also demonstrated that log-logistic fitting can be successfully used in AgWC to extract metrics from smaller datasets. As such, the tested stainless steels are not low-chop materials but offer some cost savings compared to CuCr-based materials. It would be interesting to compare the other metrics of the chopping distributions of CuCr and stainless steel contacts in the future. For example, to establish if the shape and outlier behavior of the distributions are also similar. Because between two contact materials with the same median, materials with a lower 95th percentile and lower maximum are preferred, as even a single such rare event can lead to destructive overvoltage levels.

Several factors are expected to potentially play a role in the differences in chopping current for 304, 316L and 316Ti, including composition, microstructure and phases, surface, and physical properties:

- Composition: The obvious difference between the three steels is the increasing amount of Mo from 304 to 316L and the addition of Ti in 316Ti. Measurements also reveal an increasing amount of Ni, concurrent with the increasing chopping current. Changes in Cr appear not to be directly correlated.
- Microstructure: All three steels show different bulk microstructures and grain sizes. The coarsest grain size is observed for 316L (88 ± 30 µm), the finest for 316Ti, with grains ~10x smaller compared to the other two (6 ± 3 µm).
- Phases: EBSD analysis confirms that the major phase in all three steels is fcc austenite. Ferrite is detected in all three steels at low levels of <1%. MnS inclusions are observed in 304 and 316L. 316Ti contains TiN and ~2.2% Sigma phase (Fe-Cr-Mo-based intermetallic).
- Surface: The surface structure of all three steels is similar with wide craters, a completely molten and resolidified surface and rounded protrusions. Roughness increases from Ra 5.4 µm for 304 to 7.3 µm for 316Ti.

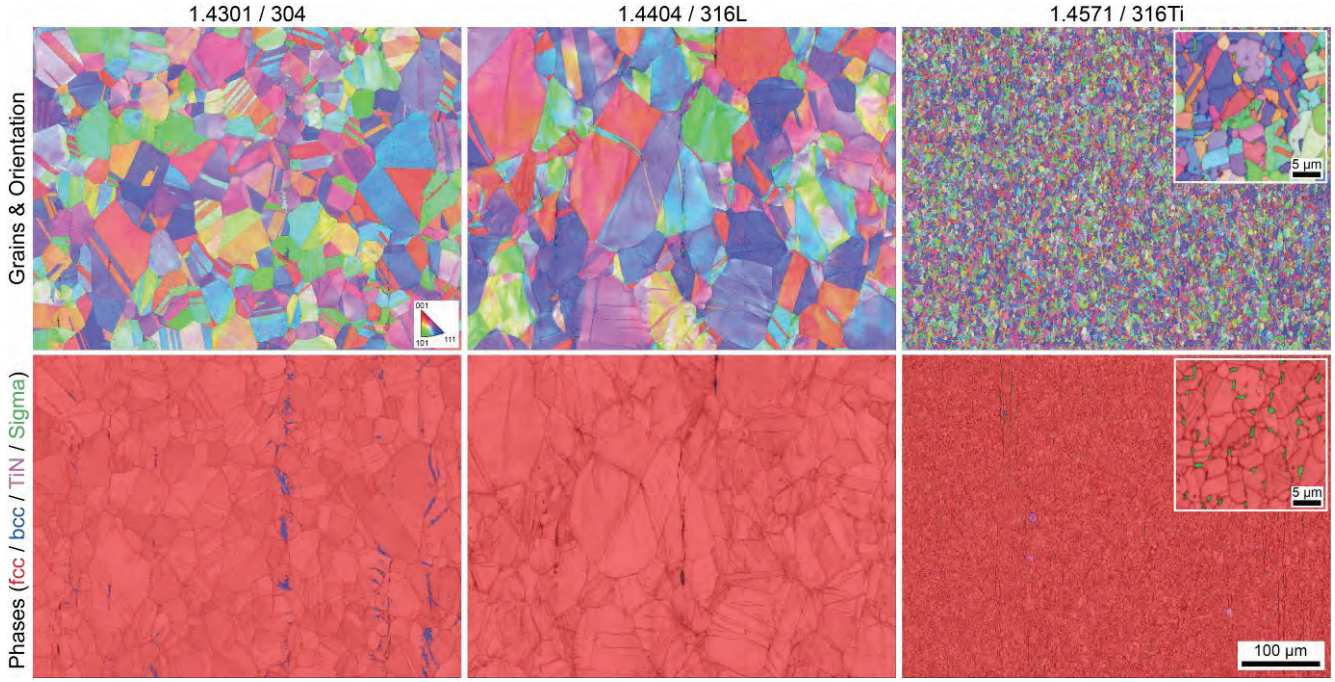


Figure 6 – Microstructure of 304, 316L and 316Ti steel by SEM-EBSD. Top: grains and orientation, bottom: phase mapping. Insets: magnified section of the microstructure for 316Ti, showing the small grain size and presence of sigma phase.

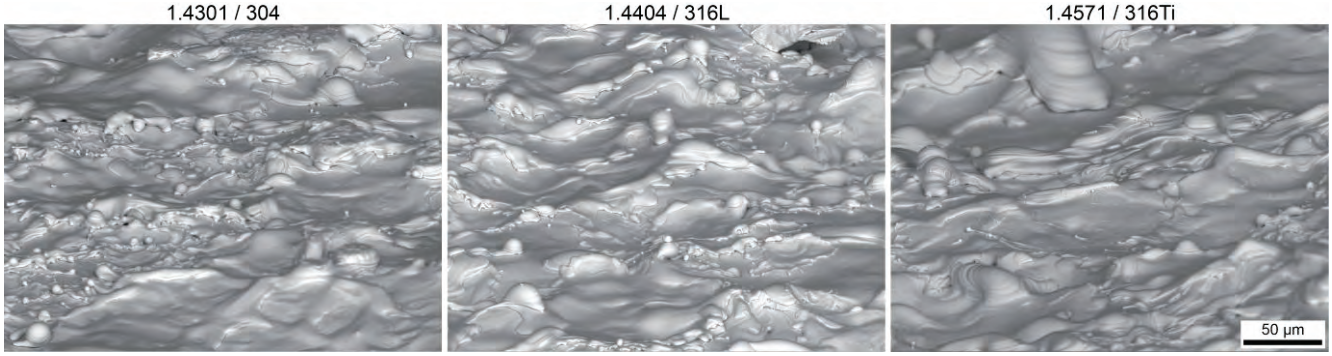


Figure 7 – Surface structure of 304, 316L and 316Ti stainless steel contacts (cathode) after 500 chopping current operations. Imaging is performed at an oblique angle.

- Physical properties: Due to the similarity in composition, the reported thermal and electrical properties of the tested steels are very similar. No dedicated measurement campaign was performed in this work for the specific grades tested.

Naturally, the impacts of all these factors are convolved in the three tested commercial steels. However, it is hypothesized that composition, liquid properties and surface structure (during arcing) play the major role while bulk microstructure and phases have smaller effects. During the lifetime of a cathode spot, the arc interacts with a hot, liquid surface. To what extent the additional phases present in the bulk survive these conditions for the duration of the lifetime of a cathode spot remains unclear for now. The median chop levels remain stable for the 500 operations tested, suggesting that the restructured surface behaves similar to the original machined surface of the contact.

VI. SUMMARY

Austenitic stainless steel grades 304, 316L and 316Ti are studied as contact material in vacuum interrupters and their chopping current behavior is characterized.

- Chopping tests are performed for 500 operations, which is sufficient to draw reliable conclusions based on fundamental descriptive statistics alone.
- Sequential outlier analysis shows that, despite a stable median chopping current through testing, the highest chop values are observed within the first 100-200 operations indicating surface conditioning.
- The chopping current distribution is non-normal and right-skewed for all three steels.
- Comparing different statistical distributions, the resulting chopping current distribution is best represented by a log-logistic distribution function. The often-used normal distribution is not suited for the asymmetric distributions observed experimentally. Moreover, the shape of the distribution is material specific, and a complete description requires multiple metrics.
- Fitting a log logistic distribution is established as a consistent way to characterize the chopping current distribution, even for smaller data sets.
- The fitted median chopping currents are 4.1 A, 4.9 A and 5.7 A for grade 304, 316L and 316Ti, respectively. Mode chopping currents are 3.8, 4.7 and 5.5 A, respectively . 95^{th} percentile are 7.1, 7.9 and 9.0 A, respectively. Maximum observed chopping currents are 28.5, 20.4, and 53.0 A, respectively.
- Microstructure characterization shows varying grain size of 59 µm, 88 µm and 6 µm for 304, 316L and 316Ti steel. All steels are mainly fcc austenite with small amounts of bcc ferrite present. 316Ti contains ~2.2% of intermetallic Sigma phase and TiN inclusions.
- The surface structure after 500 chopping operations consists of wide, smooth craters and rounded protrusions. Surface roughness is highest in 316Ti (Ra 7.3 µm) and lowest in 304 (Ra 5.4 µm).

REFERENCES

[1] R. P. P. Smeets, "The Origin of Current Chopping in Vacuum Arcs", Transactions on Plasma Science, vol. 17, no. 2, pp. 303-310, 1989.

[2] P. G. Slade, Electrical Contacts: Principles and Applications. CRC Press, 1999.

[3] P. G. Slade, The Vacuum Interrupter – Theory, Design, and Application. Taylor & Francis, 2007

[4] J. Cohen, Statistical Power Analysis for the Behavioral Sciences. Taylor&Francis, 1988.

[5] N. Kherrouba, B. Mehdi, R. Kouba, R. Badji, C. A. Dekik, Y.T. Tounsi, "Experimental study and simulation of the σ phase precipitation in the stabilized 316Ti austenitic stainless steel", Materials Chemistry and Physics 266 (2021).

[6] M. Fischer, D. Christl, M. Beltle, S. Tenbohlen, D. Gentsch, W. Ebbinghaus, "Influence of axial magnetic fields and different contact materials in vaccum interrupters on the chopping behavior of swithcing arcs", 26th International Conference and Exhibition on Electricity Distribution - CIRED, Geneva/online, 2021.

[7] L. Scherf, R-P. Sütterlin, M. Böhm, T. Delachaux, T. Schmölzer, "The effect of WC/Ag contact material composition on chopping currents in MV contactors", ICEC2020, St. Gallen, Switzerland.

Comparative Study on Arc Dynamics and Thermal Recovery of different CuCr Contacts for Vacuum Interrupters

Naghme Dorraki
Siemens AG

Berlin, Germany
naghme.dorraki@siemens.com

Sergey Gortschakow
INP
Leibniz Institute for Plasma Science and Technology
Greifswald, Germany
sergey.gortschakow@inp-greifswald.de

Andreas Lawall
Siemens AG

Berlin, Germany
andreas.lawall@siemens.com

Thomas Brauner
Siemens AG

Berlin, Germany
thomas.brauner@siemens.com

Frank Graskowski
Siemens AG

Berlin, Germany
frank.graskowski@siemens.com

***Abstract*—Vacuum interrupters are widely used in medium-voltage switching devices due to their reliability and environmental advantages. This study evaluates CuCr40 disk-shaped contacts produced through sintering and arc-melting process. To investigate their behavior during arc interruption, experiments were conducted at four different current levels and different polarities. We used near-infrared (NIR) spectroscopy, combined with high-speed photography, to measure electrode surface temperature. Additionally, a second high-speed camera captured arc dynamics, accompanied by arc electrical characterization during the 50 Hz half-cycle current. Arc mode transition curves indicate that, as current zero approaches, the arc-melted material shows a higher tendency to diffused mode compared to sintered material. This observation is supported by mass loss and surface temperature results, where the sintered material shows slightly higher mass loss and slower cooling rate. This comparative analysis highlighted the effect of electrical contact material process technologies on the thermal interruption phase of vacuum interrupters.**

Keywords—vacuum interrupter, contact material, surface temperature, arc dynamics

I. Introduction

Vacuum interrupters (VIs) are critical components in medium and high-voltage switchgears, known for reliable interruption with strong dielectric performance, compact design, and minimal maintenance requirements without harmful green-house gases. Because current interruption in a VI occurs within the contact gap and does not rely on quenching gases, the switching performance of vacuum circuit breakers (VCBs) is highly dependent on the contact material and design. During interruption, evaporization of the contact surface and the generation of particles due to arc-induced erosion are the primary mechanisms that can lead to arc re-ignition within the VI at the instant of current zero [1,2].

Copper–chromium (CuCr) compositions are now recognized as the standard contact material for vacuum interrupters due to their combined electrical, thermal, and mechanical performance. Copper provides high conductivity and heat dissipation, while chromium enhances arc resistance, and weld bearing, reduces contact erosion. The resulting composition thus forms a balanced material system capable of supporting sustained operation under thermal and electrodynamic stresses. The manufacturing process of CuCr material has a direct influence on microstructure and subsequent performance. Two key production routes—sintering and arc melting—are widely employed in industrial practice. Sintered CuCr is produced by pressing copper and chromium powders and then heating them to bond the particles together. A variation of this method uses a porous chromium skeleton into which molten copper is infiltrated. These routes are widely used because they are economical and allow good control of composition and final shape. However, the chromium typically remains as separate hard particles within the copper, which can lead to uneven properties and sometimes lower toughness when the contacts are exposed to arcing and mechanical stresses. Melting and very fast freezing is another process to produce CuCr composition. Induction melting of a chromium copper powder mixture or arc melting chromium copper rods is the first stage. The molten mixture is then very rapidly cooled. The molten composition forms a cleaner and more uniform structure when it solidifies, which usually improves erosion performance and contact reliability [3].

This work compares CuCr40 contacts manufactured by arc melting and sintering for high-current vacuum interrupter applications. Near-infrared (NIR) spectroscopy and high-speed imaging are applied to measure anode surface temperature and characterize arc dynamics.

II. Methodology

This section describes the experimental test setup and diagnostic methods applied to evaluate the arc behaviour and the contact surface changes.

A. Experimental setup

The experiments were conducted in a model vacuum interrupter chamber, which is evacuated using a two stage pumping system enabling a pressure below 10^{-6} mbar (Fig 1). The chamber is equipped with four glass windows to facilitate optical diagnostic during current interruption

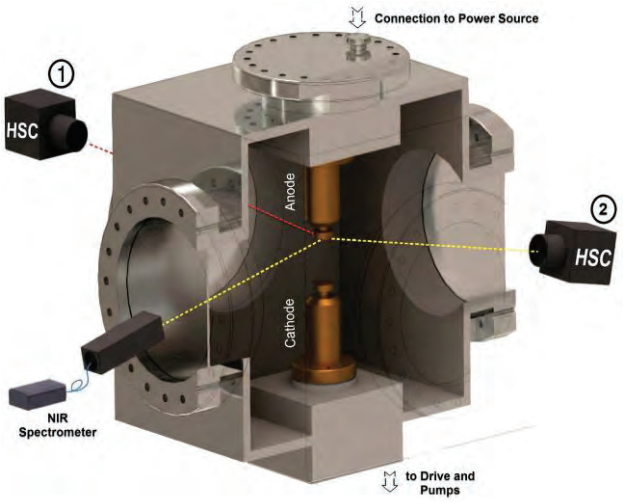


Fig 1. Schematic view of the model vacuum switch with the position of NIR spectrometer and the high-speed cameras (HSC)

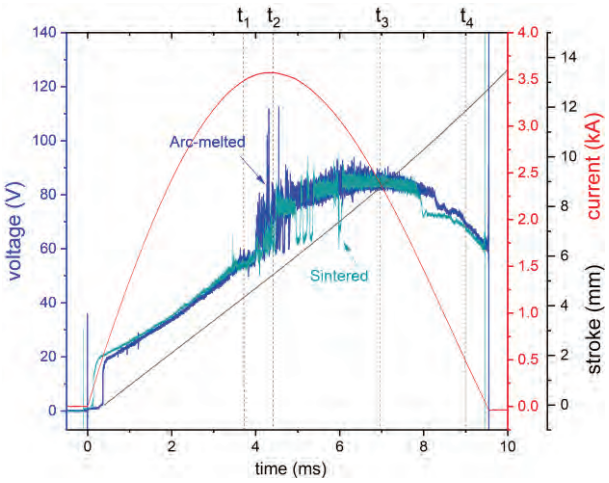


Fig 2. Current (red) and voltage (blue) waveforms, and the contact displacement curve as stroke (black)

experiments. Disk-shaped CuCr (60/40) contacts with a diameter of 22 mm are mounted inside the chamber. The upper contact is fixed and connected to the power source, and the moving contact is mounted to a pneumatic actuator for contacts separation with an average opening speed of 1.2 m/s. A 50 Hz AC current source powered by a capacitor bank supplies current to the test object.

B. Diagnostic methods

The tests are performed at a current range of 1 to 3.5 kA (rms) at both positive and negative polarities. Same test sequence was applied to both type of contacts, arc-melted and sintered CuCr (60/40). The arc voltage and arc current are measured by a Rogowski coil (PEM CWT 1500) and a high voltage probe (Tektronix P6015A, bandwidth 75 MHz). An example of arc voltage and current for arc melted and sintered material at 2.5 kA (rms) is shown in fig 2. The contact displacement curve shows the contacts are at 12 mm at the instant of current zero. The transferred charge and arc energy are calculated to evaluate the vacuum arc transition between diffused and constricted arc for sintered and arc melted CuCr.

The anode surface temperature was determined using a combined optical measurement approach employing near-infrared (NIR) spectroscopy and high-speed filtered imaging. The diagnostic configuration consisted of a compact NIR spectrometer (Hamamatsu C114GA), and a high-speed camera (Photron Nova S6, HSC 2 in Fig 1) positioned on opposite sides of the vacuum chamber with side viewing toward the anode surface. A focusing optic system imaged a small area of the center of the anode contact surface onto the spectrometer entrance fibre. The camera was equipped with a narrow band metal interference filter (MIF) with a centre wavelength of 891 nm (FWHM ~10 nm) to suppress plasma radiation during the arcing phase. The NIR spectrometer operated with exposure times on the order of 50–200 µs and a temporal resolution of approximately 1.25 ms, and the high-speed camera HSC2 records with speed of 100’000 fps and exposure time of 10 µs.

The anode surface emission recorded by high-speed camera started with the instant of contacts separation and stops shortly after the current zero. The spectra recorded by NIR spectrometer started slightly before current zero and continued for few milliseconds after current zero instant. The measured spectra were corrected using calibration data obtained from a tungsten reference lamp. The temperature was evaluated by fitting the calibrated radiances to Planck’s radiation law. To obtain temperature information during the arc, the emission intensity recorded by the filtered high-speed camera was correlated with the absolute temperature measured by NIR spectrometer at the same surface location. This correlation enabled retrieval of the anode temperature in time intervals where direct NIR evaluation was interrupted by arc radiation. For this method, temperature measurements below 1000 K are not considered in the analysis because of high uncertainty in this range. Detailed descriptions of the calibration routine, correlation strategy, and treatment of high-luminosity arc phases are available in [4, 5].

In addition to the optical and electrical diagnostics characterizations, the burn-off rate of contacts was estimated by measuring the contact mass after the test routine using a scale with an accuracy of ±0.0001 grams.

III. Results and Discussion

The anode surface temperature was measured during the tests with a maximum peak current of 3.5 kA at positive

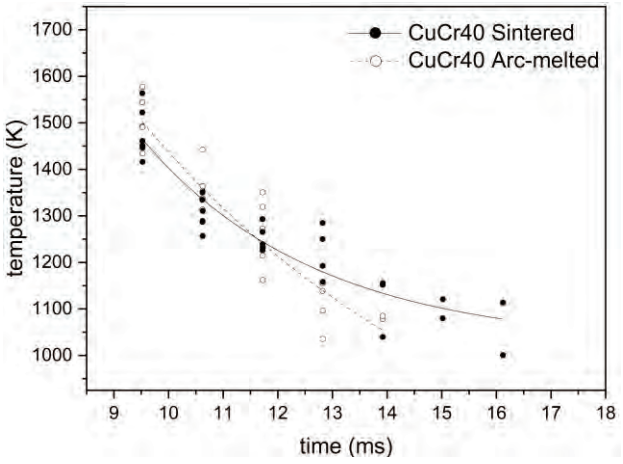


Fig 3. Temporal evolution of anode center temperature after current zero for sintered and arc-melted CuCr40.

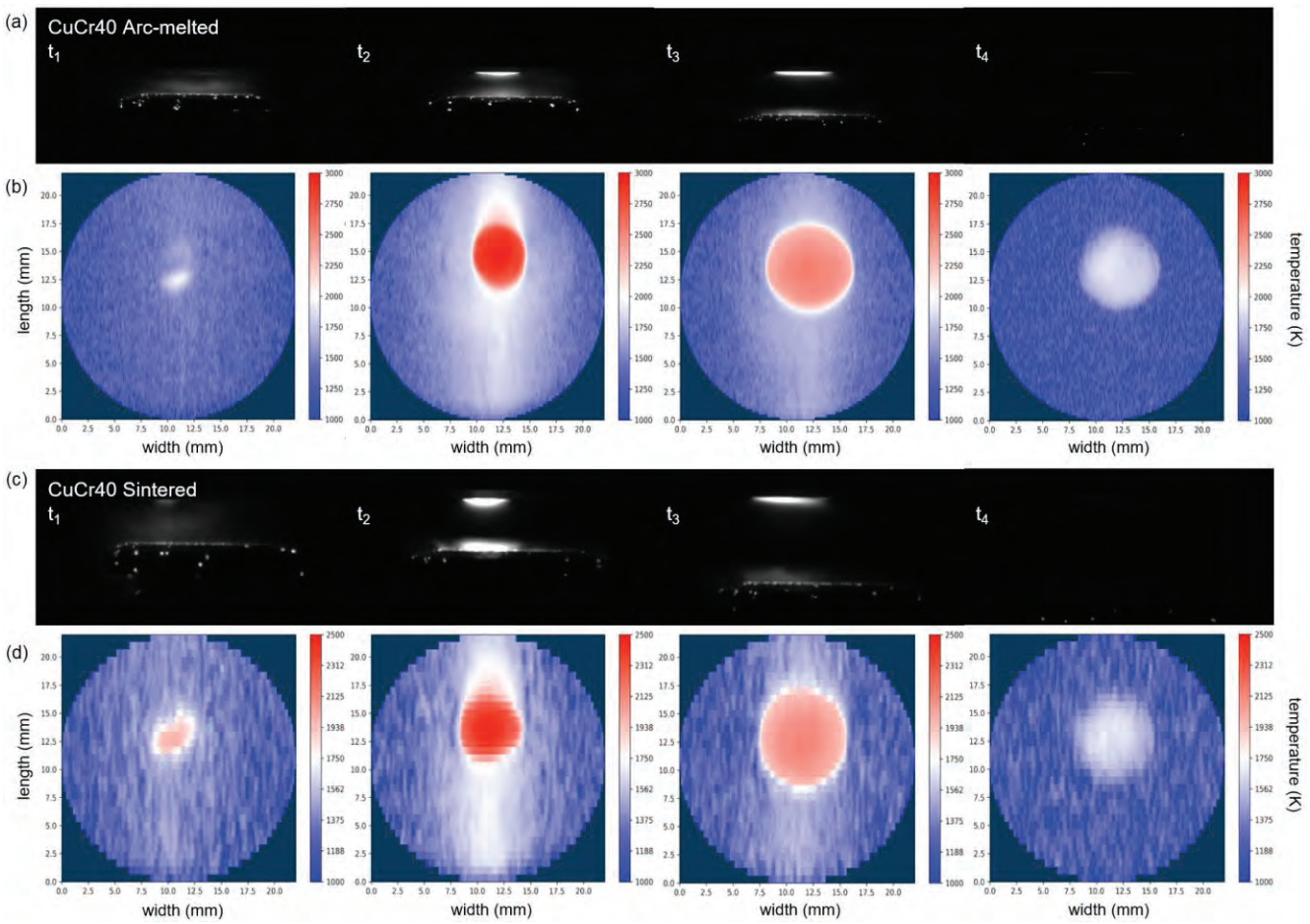


Fig 4. Anode surface temperature with the view of arc at the instants of t_1-t_4 for CuCr (60/40) arc-melted [(a) and (b)] and sintered [(c) and (d)]in Fig 2. Peak current 3.5 kA.

polarity, where the fixed contact was anode and the moving contact was cathode. Fig 3 presents the average temperature of the center area of the contact surface for times after 9 ms from the current initiation. Each datapoint represents an individual surface temperature measurement. The temporal temperature variations show the cooling rate for arc melted material is faster than sintered material.

Shortly after current zero moment, the arc-melted material shows a slightly higher temperature at the center of the contact surface compared to sintered material, as shown in Fig 3. Temperature profiles of the contact surfaces during arcing (Fig 2) were measured for the arc melted and sintered contacts. Four time points during the arcing period, marked as t_1 – t_4, are shown in Fig 2. The corresponding anode surface temperatures and parallel arc views at instants t_1 – t_4 are presented in Fig 4 for both the materials.

The spatial resolution difference in temperature profiles is due to varying recording speeds, however the exposure time was maintained at 10 µs for both material types, enabling direct comparison. The temperature distribution across the contact surface during arcing demonstrates similar behaviour for both materials. The anode spot appears approximately 4 ms after current initiation. At this moment, the maximum surface temperatures reach 3000 K for arc-melted material and 2500 K for sintered material. The temperature subsequently decreases as the current approaches zero value. By comparing the contact surface area where anode spot appears, both contact materials display a similar heat dissipation characteristic.

To compare material performance at different current levels, the instantaneous arc energy and transferred charge versus contacts stroke are calculated for each test with currents ranging from 1 to 3.5 kA (rms). The moment at which the arc transforms from diffused to constricted mode (vice versa) is considered to determine the threshold curve. This moment is defined as appearance or disappearance of the anode spot during the arcing period. The area below each transition curve represents the region where the arc keeps diffuse mode and the area above the curve corresponds to the constricted arc region. These transition curves are defined separately for positive and negative polarities. Fig 5 represents the arc transition curves for both sintered and arc-melted contact materials at positive polarity, with the fixed contact as the anode and moving contact as the cathode. Fig 6 illustrates the curves for negative polarity, where the moving contact is the anode and the fixed contact is the cathode.

At the initial stage of contact separation, the arc is predominantly constricted. This condition is independent of the contact material. Therefore, the evaluation of the arc transition mode is started from a contact gap of 3 mm. For positive polarity (fig 5 (a)), it's unlikely that the arc transition from constricted to diffuse mode occurs by increasing the contact stroke up to 8 mm. According to the curves, the transition primarily happens when the arc energy

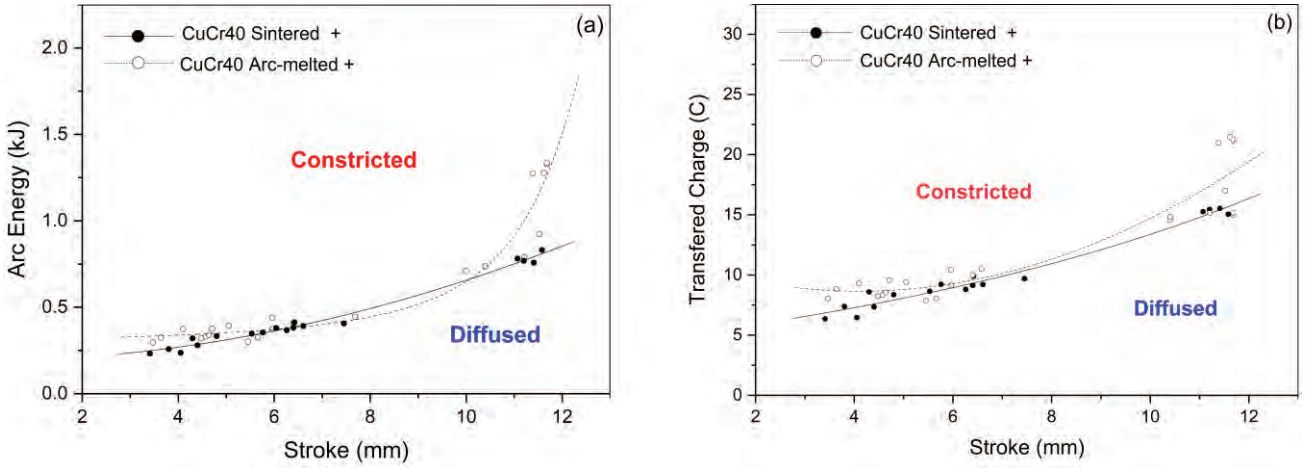


Fig 5. Transition curves to define constricted and diffused regions based on arc energy (a) and transferred charge (b) versus contacts stroke at positive polarity (anode as fixed and cathode as moving contacts) of current range 1-3.5 kA (rms) for CuCr40 sintered and arc-melted material.

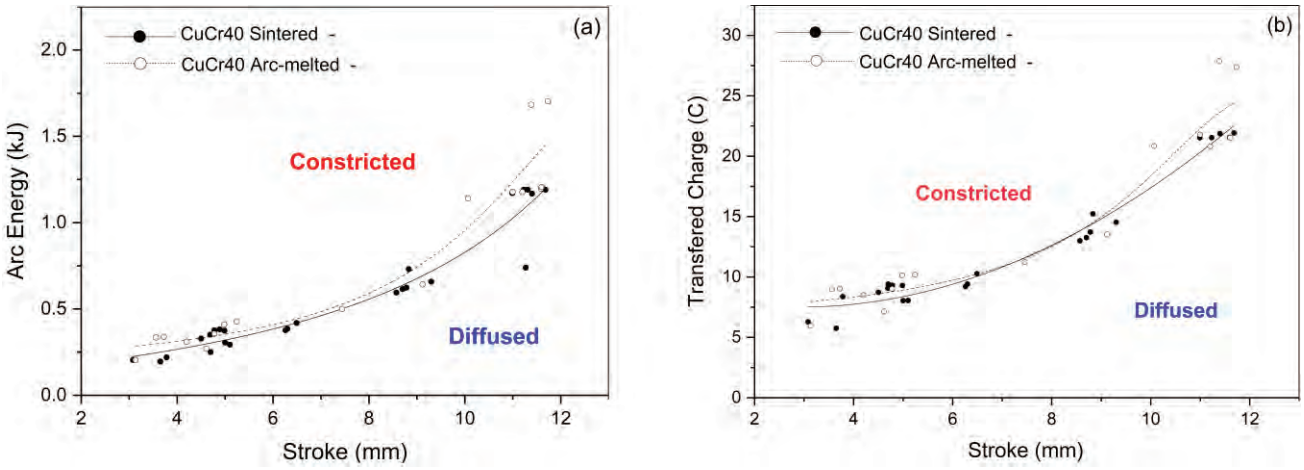


Fig 6. Transition curves to define constricted and diffused regions based on arc energy (a) and transferred charge (b) versus contacts stroke at negative polarity (cathode as fixed and anode as moving contacts) of current range 1-3.5 kA (rms) for CuCr40 sintered and arc-melted material.

is lower than approximately 0.35 kJ, which by increase in arc current, the probability is low. Between 8 mm to 12 mm stroke, the range of arc energy associated with the diffuse mode is broader for arc-melted material than for sintered material. Considering an opening speed of 1.2 m/s, this range correspond to the period approaching current zero. Therefore, for arc-melted material at positive polarity, the probability of transition from constricted to diffuse arc is higher as current zero approaches. This transition is advantageous, as stationary constricted arc is more destructive than the diffuse arc and may lead to current interruption failure at current zero moment.

In fig 5 (b), the transition curves for transferred charge under positive polarity indicate the arc-melted and sintered materials show similar behaviour across contact stroke. By comparing the arc energy transition curves to the transferred charge curves in Fig 5, the results indicate that arc voltage plays a important role in determining the arc mode transition. Studies have shown that arc voltage is influenced by contact erosion, as well as parameters such as electrode fall voltage close to the contact surfaces, which depends on the material properties [3, 6]. However, for both sintered and arc-melted materials, the electrode fall voltage was measured in the range of 18 – 20 V.

For negative polarity (fig 6), both arc energy and transferred charge show comparable behaviour to those observed at positive polarity (fig 5). However, the region associated with the diffused arc is broader for negative polarity (cathode fixed and anode moving contacts) than for positive polarity (anode fixed and cathode moving contacts). This difference could be attributed to the moving contact as the anode under negative polarity conditions.

To investigate the contacts erosion, the mass loss of the contacts was measured following the test routine. As mentioned before, identical test sequences were performed for both arc-melted and sintered materials for a current range of 1 to 3.5 kA (rms) at both positive and negative polarities. Consequently, approximately similar amount of charge was transferred between the contacts in each case. For arc-melted material, a mass loss of 11.9 mg for fixed contact and 5.7 mg for moving contact were recorded. The burn-off rate according to the total transferred charge was measured 16.06 µg/C and 7.69 µg/C for fixed contact and moving contact, respectively. For sintered material, a mass loss of 13.4 mg for fixed contact and 7.2 mg for moving contact were

recorded. The burn-off rate according to the total transferred charge was measured 16.68 µg/C and 8.96 µg/C for fixed contact and moving contact, respectively. The sintered material shows slightly higher mass loss for both fixed and moving contacts compared to the arc-melted material. This observation agrees with the results of surface temperature after current zero and the arc transition modes inferred from the dissipated arc energy.

IV. Conclusion

The arc-melted and sintered CuCr40 contacts are investigated for vacuum arc interruption. Experimental results show similar contact surface temperature distribution over arcing time. The arc-melted material shows a faster cooling rate after current zero instant than the sintered material. Arc transition curves indicate that as current zero approaches, the likelihood of transition from constricted to diffuse arc mode is greater for arc-melted material under positive polarity. Analysis of mass loss and burn off rates shows the sintered material experiences slightly higher erosion than the arc-melted material, which agrees with the contact surface temperature findings after current zero and arc transition modes observations. These findings underline the importance of both material properties in optimizing contact performance and minimizing erosion in switching applications.

References

[1] P. G. Slade. “The Vacuum Interrupter: Theory, Design, and Application.” CRC Press, 2018.

[2] K. Niayesh. “Green HV Switching Technologies for Modern Power Networks.” Vol. 236. (IET, 2023).

[3] P. G. Slade. “Electrical contacts: principles and applications.” CRC press, 2017.

[4] R. Methling, S. Franke, S. Gortschakow, et al. “Anode surface temperature determination in high-current vacuum arcs by different methods.” IEEE Transactions on Plasma Science, vol. 45(8), pp. 2099–2107, 2017.

[5] S. Gortschakow, S. Franke, R. Methling, et al. “Advanced optical diagnostics for characterization of arc plasmas.” IEEE Transactions on Plasma Science, vol. 49(9), pp. 2505–2515, 2021.

[6] Y. Yokomizu, T. Matsumura, R. Henmi, and Y. Kito, “Total voltage drops in electrode fall regions of, argon and air arcs in current range from 10 to 20 000 A,” *J. Phys. D: Appl. Phys.*, vol. 29(5), pp. 1260, 1996.

Evaluation of Surface Temperature of Switching Contacts in Vacuum by Optical Methods

Sergey Gortschakow
Leibniz institute for plasma science and technology
Greifswald, Germany
sergey.gortschakow@inp-greifswald.de

Gregor Gött
Leibniz institute for plasma science and technology
Greifswald, Germany
gregor.goett@inp-greifswald.de

Ralf Methling
Leibniz institute for plasma science and technology
Greifswald, Germany
ralf.methling@inp-greifswald.de

Dirk Uhrlandt
Leibniz institute for plasma science and technology
Greifswald, Germany
dirk.uhrlandt@inp-greifswald.de

***Abstract*—The lifetime of the electrode system in switching applications is mainly limited by accumulated thermal load of the electrode surface. The contact surface changes its morphology when it is loaded with a high current due to melting, evaporation and solidification processes. This can affect the arc properties, like e.g. arc voltage and arc current behaviour, arc dynamics, surface temperature dynamics and erosion rate. The right choice of the electrode material is very important for long lifetime and stable operation. The diagnostics of the electrode surface plays, therefore, an important role for understanding of basic phenomena and parameter optimization. Recently, two optical methods have been developed for quantitative characterisation of surface temperature: near infrared radiation (NIR) spectroscopy and high-speed camera imaging enhanced by narrow-band filters. NIR spectroscopy determines the electrode surface temperature mainly after current zero crossing. During the arcing phase, a high-speed camera equipped by a narrow band filter can be applied for acquisition of time dependent two-dimensional distribution of the electrode surface temperature. Basics of each method are presented. Their use is illustrated on an example of CuCr contacts conventionally used for switching applications.**

Keywords—switching arc, vacuum arc, surface temperature, optical emission spectroscopy, high-speed imaging

I. Introduction

Vacuum switching devices have a number of advanced features comparing to gas-filled devices like e.g. large number of operations under standard load conditions and emission-free operation [1, 2]. For improvement and optimization of switching devices deeper understanding of physical processes taking place during their operation is required. The fundamental knowledge about the vacuum arc plasma, and in particular about its interaction with the electrodes is necessary. The lifetime of the electrode system in switching applications is mainly limited by accumulated thermal load of the electrode surface. The right choice of the electrode material is very important for achievement of desired lifetime and stable operation. The diagnostics of the electrode surface is, therefore, a useful instrument for understanding of basic phenomena in arc-electrode interaction as well as qualification of electrode material. During the high-current operation, multiple sequencies of melting, evaporation and solidification processes cause significant changes in surface morphology and might lead to significant electrode erosion. The peculiarity of switching vacuum arc is that it can't exist without electrode erosion, as the evaporated electrode material is the source of the arc plasma. A certain erosion is, therefore, desirable for stable operation. A switching arc in vacuum is initiated by bridge explosion when the electrode separation under current load begins [1]. The arc column can be either diffuse or constricted, depending on operation conditions. In order to control the arc behaviour and to prevent the localized thermal load on the electrode external magnetic field is applied. Dependent on the dominant component of this field, the arc column remains diffuse (in case of axial magnetic field – AMF - contacts) or a constricted arc column rotates over the electrode surface (radial or transverse magnetic field - RMF or TMF contacts) [1]. The fundamental issues of arc-electrode interaction, however, can be studied using model contacts made of conventional material (butt contacts), as the arc appearance (diffuse or constricted) is driven by current. Therefore, such contacts are often used for research purposes [3,5,13,14].

Optical diagnostics is widely used for acquisition of various parameters and analysis of arc plasma [3-5]. Speaking about the surface temperature diagnostics, several optical methods are available: near-infrared (NIR) spectroscopy [4,6], high-speed pyrometry [7] and high-speed thermography [3-6, 8-10]. Each of those methods has certain advantages, limitations in applicability as well as technical limits. Two of them, NIR spectroscopy and method based on high-speed camera technique, have been successfully used for all types of contacts [3-14]. Those methods are presented below more in detail.

II. Experimental Setup

Conventional vacuum switching devices use a non-transparent housing, which makes the arc inaccessible for optical diagnostics. Therefore, special experimental setups are often used for studies of the arc properties. Those setups reproduce the basic features of commercial devices like e. g. vacuum level, current and voltage level, contact movement, electrode type and materials. Some of standard components are, nevertheless, not used. Since the vapor shield hinders the access to the arc plasma, it is not present in the test arrangements. This might have some impact, when the breakdown behaviour is studied or dielectric withstand tests are performed. An example of experimental setup with optical access is presented in Fig. 1. It consists of a model circuit breaker, equipped with pumping system and pneumatic drive for electrode movement, a power source and diagnostic equipment.

A. *Model Circuit Breaker*

The main part of the model circuit breaker is a vacuum chamber which is equipped with four optical viewports and mechanical adapters for mounting of various electrodes. The chamber is connected to pumping system, which consists of roughing pump and turbomolecular pump and provides a vacuum level of few 10^{-7} mbar. A pneumatic drive, is used for opening operation. Typical averaged contact opening velocity was about 1-1.25 m/s. The upper electrode, mainly powered as anode, is fixed, while the lower electrode is grounded and is moveable. As in real operation, the arc ignition occurs by contact separation during the current flow. The typical electrode separation is about 10 mm. Figure 2 shows an example of model electrodes used in the study. Flat cylindric contact plates made of CuCr alloy. The Chromium content of 25 - 50% (mass fraction) is commonly used.

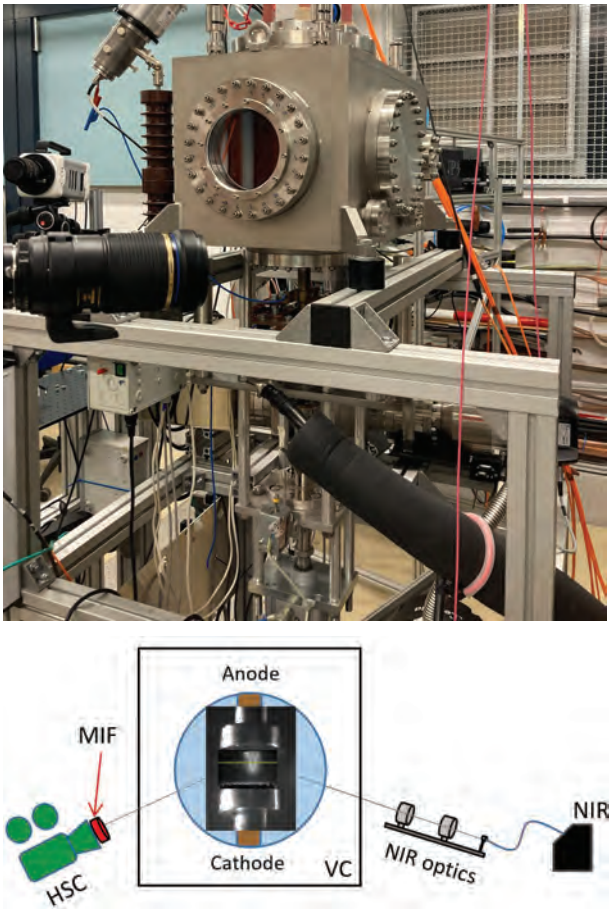


Fig. 1. (top) Photograph of vacuum chamber with optical access. (bottom) Sketch of diagnostic alignment: VC – vacuum chamber, HSC – high-speed camera, MIF – metal interference filter, NIR – near-infrared spectrometer, NIR optics – focusing optics. The high-speed camera and the focussing optics are placed at the same viewing angle to the suface of uppr electrode



Fig. 2. Example of model electrodes: material CrCr, diameter 20 mm

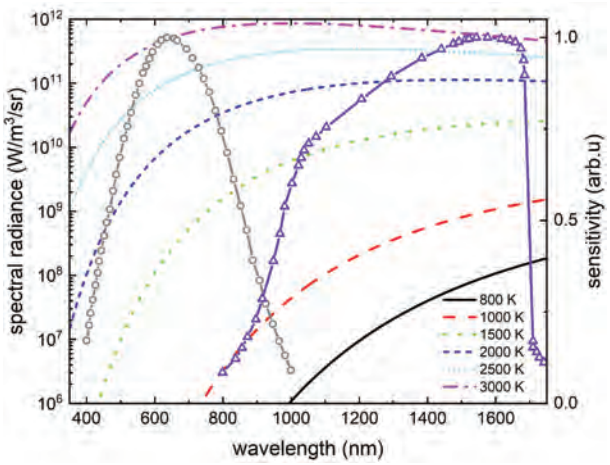


Fig. 3. Temperature dependent spectral radiance of ideal Planck radiator (curves without symbols) along with normalized sensitivity curves for HSC (grey circles) and NIR compact spectrometer C11482GA(violet triangles)

B. *Power Source*

Synthetic test circuits with various design are widely used as power sources. For presented results a pulsed current generator [11] was used. It consists of a series of LC elements with adjustable charging voltage and variable output current. The values of capacitances and inductances provide a damped AC operation with power frequency about 50 Hz. Typical arc duration is in the range 1 - 9.5 ms.

C. *Diagnostic Equipment*

Each measurements campaign comprises electrical and optical measurements. The current was measured by a Rogowski coil PEM CWT 1500 and voltage signals were measured by a high voltage probe Tektronix P6015A. The signals have been registered by the transient recorder HBM GEN7t.

Various optical diagnostics is usually applied for arc characterisation. The general arc dynamics was monitored by a high-speed camera Photron FASTCAM NOVA S12. For the determination of the surface temperature two complementary diagnostic methods have been used. Analysis of the electrode surface radiation in specified spatial position was performed with a spectroscopic system, which consisted of NIR compact spectrometer Hamamatsu C11482GA and focussing NIR optics. A high-speed camera Photron FASTCAM NOVA S16 equipped with narrow band optical filter 891±5 nm was used for determination of two-dimensional distribution of surface temperature. Details of both methods are presented in the next section.

III. Optical Diagnostics for Characterisation of Electrode Surface Temperature

The boundary condition for the determination of electrode surface is that the temperature is high enough for production of measurable thermal radiation. The intensity of this type of radiation follows the Planck law:

$$B_\lambda(\lambda,T)= \varepsilon(\lambda,T)\, 2hc^2/\lambda^5/(e^{hc/\lambda kT}-1), \quad (1)$$

where B_λ is the spectral radiance, ε – surface emissivity, h is the Planck constant, k – Boltzmann constant, c – speed of light, λ – the wavelength and T is the surface temperature. The curve of spectral radiance shifts toward shorter wavelength with increasing surface temperature (Fig. 3). The change of intensity approaches seven orders of magnitude when the temperature rises from 800 K to 3000 K in visible range. In NIR range this difference is less, about four orders of magnitude. Taking into account higher dynamic range of spectrometers (typically 16 bit), broader temperature range can be covered by this type of devices.

Normalized sensitivity curves of a monochrome high-speed camera and a NIR compact spectrometer shown in Fig. 3 clarifies, that there is a small wavelength region where both instruments are applicable and have similar sensitivity. This region is around 900 nm. This region is used, in particular, for calibration of two-dimensional temperature distributions determined from high-speed camera measurements.

A common challenge for both methods is the presence of plasma radiation in front of the electrode. The solution approaches differ for HSC and for NIR method.

A. NIR Spectroscopy

Spectroscopic measurements of surface radiation are usually performed for selected region of the electrode surface. Using a focussing system and optical fibre the surface emission is led to the entrance slit of an NIR spectrometer. The measurements are restricted in space, but can provide a temporal resolution typically of 1-1.5 ms. Figure 4 shows an example of NIR spectra registered at the instant of current maximum (5 ms) and 1.5 ms after current termination (11 ms). During the arcing phase significant plasma radiation is present. Most intense arc plasma radiation is mainly related to the line emission, but in the case of constricted arcs the continuum radiation of the arc column might have a significant contribution. Therefore, the measurements usually follow close to and after the instant of current zero crossing. Depending on the current level, the total number of acquired spectra per one shot varies between 1 and 10.

Determination of surface temperature from NIR spectrum is based on comparison of acquired spectral radiance with theoretical values given by Eq. (1). The method requires several steps: (i) acquisition of a spectrum by corresponding device (result – wavelength-dependent surface emission intensity in counts) (ii) correction of the spectrum by subtraction of background, (iii) correction of the signal by transmission of optical system, (iv) calibration of corrected intensity by comparison with the data of calibration source (result – spectral radiance), (v) determination of surface temperature from two-parameter fit (emissivity and temperature) according to Eq. (1).

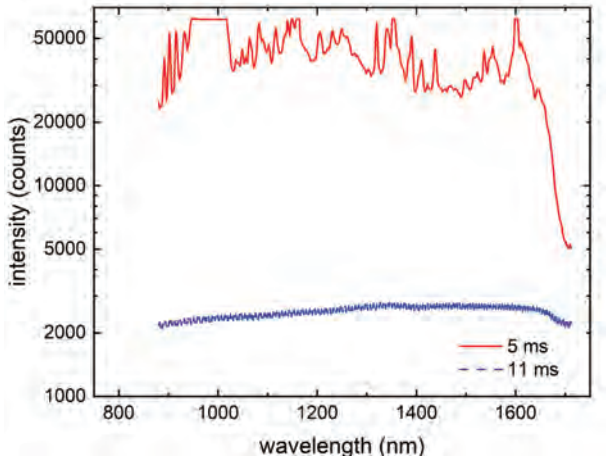


Fig. 4. Example of NIR spectra acquired at different time intants, current maximum (red solid line, 5 ms) and 1.5 ms after current interruption (dashed blue line, 11 ms)

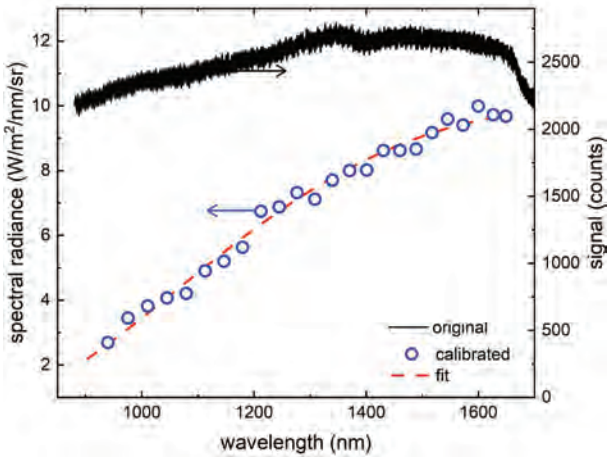


Fig. 5. Example of NIR spectra before (black solid line) and after data processing and calibration (blue circles) along with corresponding Planck fit (red dashed line). Evaluation instant 11 ms.

An example of successful temperature evaluation is shown in Fig. 5. The corresponding Planck fit gives the parameters ε=0.22 and T=1610 K.

B. Enhanced High-Speed Camera Techniques

Modern high-speed cameras (HSC) provide the frame rate up to 16k fps in full frame modus (resolution 1024 x 1024 pixel) or up to 2M fps for image with restricted size, sensitivity up to ISO 64000 in the spectral range 400 – 1000 nm, dynamic range of 12 bits, high sensitivity as well as exposure times from 500 ns to several seconds. Those features make HSC suitable for detailed studies of temporal and spatial arc behaviour. In combination with special equipment, the high-speed cameras provide powerful tool for analysis of surface radiation. For this purpose, however, the radiation from the surface has to be separated from that from the arc. In the case when the arc current is not too high and the arc is almost diffuse, the radiation spectrum is dominated by lines (Fig. 6), while the contribution of continuum plasma radiation is negligible. Thus, when the line radiation is blocked, for example by a narrow-band filter, the registration of surface radiation becomes possible (Fig. 7). The multilayer metal interference filters (MIF) are characterised by a bandwidth of 1 - 10 nm (FWHM) and, thus, allow for selective light registration. As it is illustrated by Fig. 6, such a window exists around 890 nm. The intensity of acquired electrode images is then proportional to the surface temperature. In order to determine the absolute temperature a calibration routine is necessary. One of the methods is based on simultaneous acquisition of surface radiation by a high-speed camera and NIR spectrometer [3-6, 13, 14]. The mean intensity of radiation in selected region

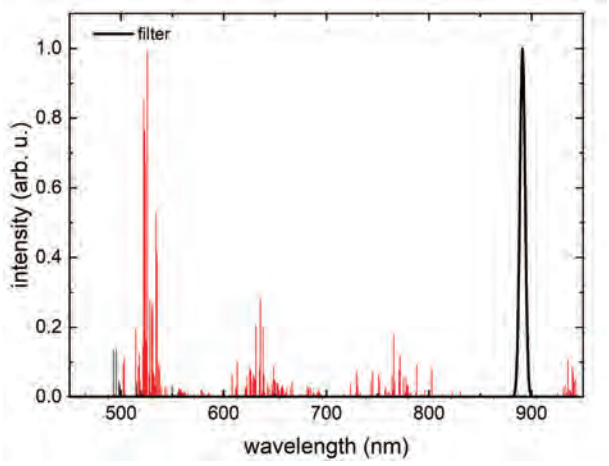


Fig. 6. Example of normalized emission spectrum of diffuse arc (thin red lines) and transmission curve of used narrow-band filter (thick black line)



Fig. 7. Example of temperature evaluation with HSC technique. (top) arc image, (bottom) spectrally filtered image of the anode. Anode is fixed and located at the top of the image, the cathode is moveable and located at the bottom of the image. Arc plasma radiation is completely blocked by filter (upper figure)

measured by HSC is related to the temperature determined from NIR spectra for the same region and at the same time instant. This relation is unique, i.e. one point of the curve is enough to find out the reference position and to restore the two-dimensional temperature distribution from relative radiation intensity values. The method was successfully applied for different types of electrodes in [4, 6].

In some specific cases, the continuum part of arc radiation cannot be completely blocked by the filter. The method proposed in [6] allow for exclusion of arc radiation by mathematical routine for diffuse arcs.

The temperature of the electrode diminishes rapidly when the current zero instant is approaching. Emission registered



Fig. 8. Arc images demonstrating two anode modes with significant electrode erosion – anode spot (left) and anode plume (right). Anode is on the top, cathode on the bottom

by HSC also vanishes. The method is, therefore, applicable mainly during the arcing phase, before the current zero crossing. Typical frame rate varies between 2k and 100k fps, which provide between 20 and 2000 evaluation points per single shot.

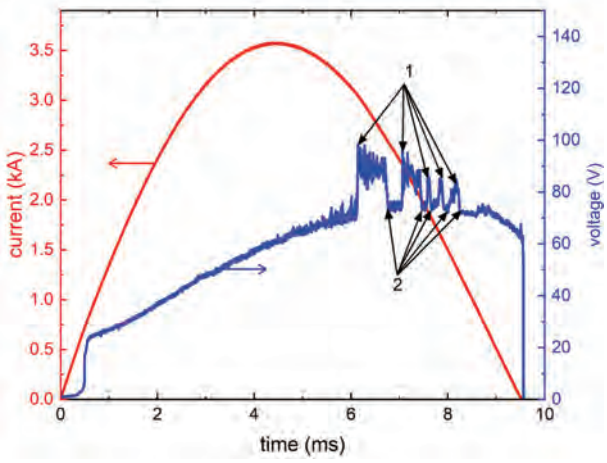


Fig. 9. Example of arc current and voltage evolution in case of anode mode formation. The numbers denote the instant of mode transitions: 1 – anode spot, 2 – anode plume

IV. Examples of Method Applications

The electrode activity has different impacts on a vacuum arc. On the one hand, the electrodes are the source of switching medium – metal vapour, i.e. evaporation and sputtering are essential for the arc existence. On the other hand, this activity must be immediately terminated after current interruption in order to prevent the arc re-ignition. The electrodes, the cathode and the anode, contribute to erosion in different manner. In case of the cathode, small-size rapidly moving spots are the source of metal vapour. This vapour consists mainly of ions and it is, therefore, possible to control its behaviour via electromagnetic field. Material eroded from the anode appears mainly in form of neutral atomic gas, which is much hardly to control. The anode erosion starts above a certain current level when the heat flux toward the anode is high enough to reach the melting point of electrode material. The anode melting is usually related to partial or full constriction. Considering the anode-driven constriction, several high-current modes are distinguished: footpoint mode, anode spot (type 1 and type 2) and anode plume [12]. In particular, the anode spot and anode plume modes (Fig. 8) cause intense material evaporation and surface degradation. Characterization of those modes is, therefore, in focus of intense research in the last decade [3,6–8,10,12-14].

Figure 9 presents an example of electrical characteristics in the case of anode mode formation. Transitions between the modes are accompanied by abrupt changes in the arc voltage. Voltage jumps correlate with anode spot formation and voltage fall with anode plume appearance. Depending on electrode composition, anode mode transitions may occur ones or multiple time times per shot [13,14].

An example of surface temperature evaluated at the position of anode spot centre is presented in Fig.10. As it can be expected, higher current causes lower anode spot temperature close to the instant of current zero crossing. The difference is about 250 K. The temperature decay in case of higher current takes longer time. The reason might be bigger volume of the spot/melted pool, which acts as additional heat source after termination of external heat flux from the arc.

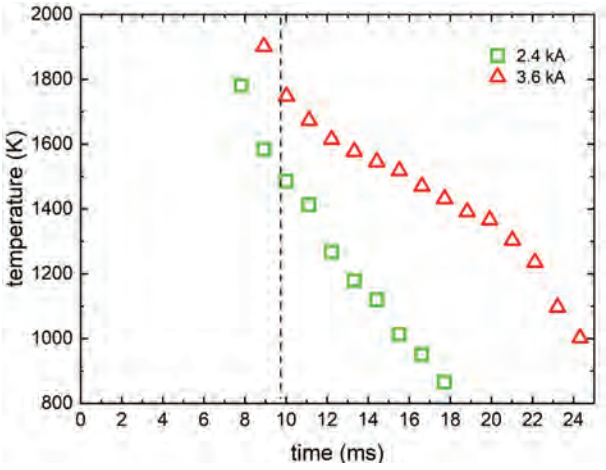


Fig. 10. Surface temperature evaluated at the position of anode spot centre for two different currents. Dashes line shows the position of current interruption (current zero crossing)

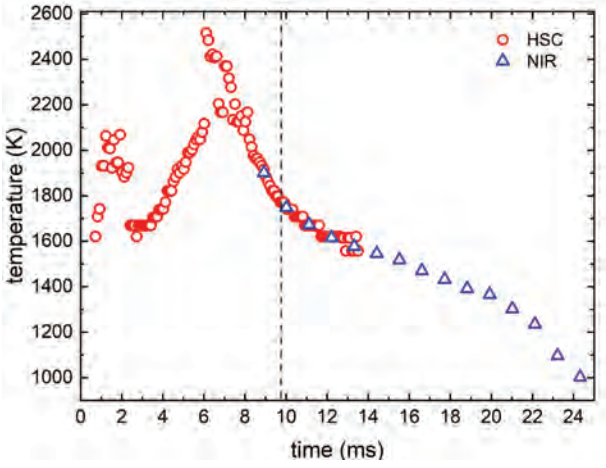


Fig. 11. Surface temperature evaluated at the position of anode spot centre by two methods – high-speed camera (HSC, red circles) and NIR spectrometer (NIR, blue triangles). Arc current 3.6 kA Dashes line shows the position of current interruption (current zero crossing)

Temperature evolution at the centre of the anode spot determined by both methos is shown in Fig. 11. Temperature values for the instants around current zero crossing determined from HSC and NIR measurements show an excellent correlation. The variations before 3 ms are related to the ignition process, i. e. the temperature correspond to the rests of the metal bridge. The surface temperature increases linearly between 3 and 6 ms from about 1600 K to about

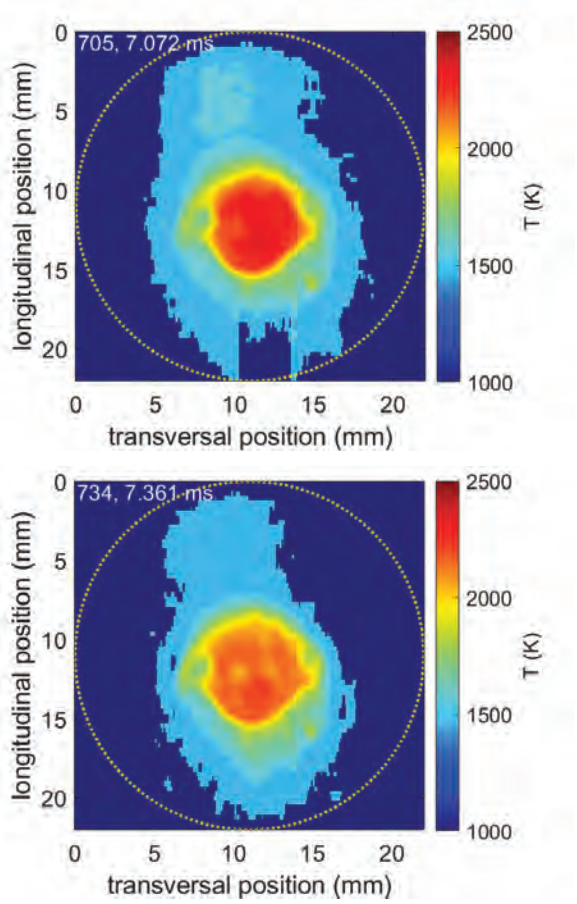


Fig. 12. Distribution of anode surface temperature at the instants of anode spot (7.07 ms) and anode plume (7.36 ms) appearance. Corresponding arc images are shown in Fig. 8

2100 K. Formation of the anode spot at 6.1 ms is accompanied by fast temperature rise to about 2250 K. After this instant both the lowering of the heat flux coming from the arc and evaporation contribute to decrease of temperature. The HSC method delivers reliable values up to about 2 ms after current termination. The NIR spectroscopy provides first reliable value at about 8 ms, i. e. 2 ms before the current zero crossing. The overlap of applicability regions is, thus, about 4 ms. After current interruption, the temperature decay from ca 1650 K to ca 1000 K lasts about 14 ms.

More information about the surface degradation can be achieved from the analysis of two-dimensional temperature distributions shown in Fig. 12. Localized surface erosion occurs in the region of about 5 mm in diameter. Formation of the anode plume is accompanied by abrupt expansion of melted anode material in form of a neutral gas cloud (Fig. 8, left). This transition leads to immediate surface cooling (Fig. 12 bottom). In presented case the difference amounts to about 200 K.

V. Methods Applicability and Limitations

Applicability of presented methods requires the fulfilment of certain conditions. The most important is optical accessibility of object under diagnostics (electrode surface). As the conventional switching devices have non-transparent housing, a general optical access, therefore, is possible in model arrangements only. Hence, presented

methods are suitable for research and development purposes, but up to now not for monitoring in real applications. Furthermore, an optical access to the electrode surface can be hindered by arc plasma, by massive flow of droplets, by smoke as well as by switching dust. The last two issues are not related to vacuum switching devices, as those devices do not contain any gas or plastics. The issue related to the presence of the arc plasma in front of electrode was already discussed in Section III. Either the diagnostics should be limited to the instants when the contribution of plasma radiation is negligible, or additional efforts for subtraction of corresponding contribution from measured signal. Notice, that such subtraction works well in the case of homogeneous symmetric objects. Therefore, the HSC method is currently not suitable for analysis of constricted moving arcs, like e.g. in case of TMF electrodes (spiral contacts which produce dominantly transversal magnetic field). In the case when the whole electrode surface becomes melted, significant electrode erosion in form of micro particles and droplets might occur. Those particles/droplets are additional source of radiation. Therefore, the corresponding contribution has to be carefully analysed.

Another important issue is sufficient temperature of the surface, as the surface radiation decreasing drastically with temperature lowering (cf. Fig. 3). In addition, the temperature maximum shifts toward longer wavelength, i. e. the sensitivity curve of detector (spectral response range of spectrometer or CCD matrix) should cover the corresponding wavelength range. Lower limit for precise temperature determination is therefore around 1400 K for HSC and about 1000 K for NIR spectroscopy. Above those limits the methods accuracy is estimated as good as 50 K [6]. Below those limits increasing errors up to 30% may arise. Better results for low temperature range might be expected by use of detectors in MIR range (2 - 11µm wavelength), similar to those of pyrometers or thermographic cameras. However, from recent experience, measurements in MIR spectral range had no success due to rather long exposure times necessary for reliable signal detection.

Sufficient temporal resolution is further) important issue. Electrode surface heating and cooling is not solely dependent on thermal conductivity, but rather on form of surface erosion (dynamic evaporation, sublimation). Here at least the micro second resolution is required. Actual temporal resolution of HSC based measurements is about 20 µs, of NIR spectroscopy 1 ms.

VI. Conclusions

Presented results demonstrate, that optical diagnostics provides powerful tools for characterisation of electrode surface temperature in the arcing phase as well as after current interruption. The high-speed cameras in combination with optical filters can be used for both qualitative and quantitative surface temperature measurements restricted to arcing phase. NIR spectroscopy is an appropriate method for surface temperature determination close to current interruption instant and in the early post-arc phase. Corresponding results give a rise in understanding of physical processes and in the improvement of electrode materials for switching devices. Nevertheless, the research on complex physics of switching vacuum arcs can profit from further development of methods and techniques. Thus, the intensity of radiation varies by few orders of magnitude during the arc evolution. Correspondingly, a high temporal resolution and a high dynamic range for a deeper physical analysis are necessary. So far, the diagnostic devices which unify those properties are missing. Further development is, therefore, highly desired.

References

[1] P. G. Slade, The Vacuum Interrupter: Theory, Design, and Application, CRC Press, Boca Raton, 2008.

[2] St. Giere, D. Hellig, M. Koletzko, S. Kosse, Th. Rettenmaier, Ch. Stiehler, and N. Wenzel, “Vacuum interrupter unit for CO_2-neutral 170kV/50kA switchgear,” in ETG-Fb. 157: VDE-Hochspannungstechnik 2018, Berlin, VDE Verlag GmbH, ISBN 978-3-8007-4807-5, 2018, pp. 28-31.

[3] S. Gortschakow, St. Franke, R. Methling, D. Gonzalez, D. Uhrlandt, S. Popov, A. Batrakov,“ Advanced optical diagnostics for characterization of arc plasmas,“, IEEE Trans. Plasma Sci., vol. 49, pp. 2505-2515, Sept. 2021, doi: 10.1109/TPS.2021.3096289

[4] S. Gortschakow, D. Gonzalez, R. Methling, St. Franke, D. Uhrlandt, A. Lawall, E.D. Taylor, F. Graskowski, “Determination of surface temperature of switching RMF and AMF contacts by optical methods,” in Proc. 6th Int. Conf. Electr. Power Equip.-Switching Technol. (ICEPE-ST), Mar. 2022, pp. 58–62, doi: 10.1109/ICEPE-ST51904.2022.9757081.

[5] S. Gortschakow, “Diagnostic methods for switching vacuum arcs based on high-speed camera technique,”, IEEE Trans. Plasma Sci., vol. 52, pp. 4382-4389, September 2024

[6] R. Methling, St. Franke, S. Gortschakow, M. Abplanalb, R.-P. Sütterlin, Th. Delachaux, and K. O. Menzel, “Anode surface temperature determination in high current vacuum arcs by different methods”, IEEE Trans. Plasma Sci., vol. 45, pp. 2099 – 2107, August 2017.

[7] T. Pieniak, M. Kurrat, and D. Gentsch, "Surface temperature measurement of transversal magnetic field contacts using a thermography camera," *2016 27th International Symposium on Discharges and Electrical Insulation in Vacuum (ISDEIV)*, Suzhou, China, 2016, pp. 1-4, doi: 10.1109/DEIV.2016.7748694.

[8] A. M. Chaly, I. N. Poluyanova, V. V. Yakovlev, K. K. Zabello, A. A. Logatchev, and S. M. Shkol'nik, "Experimental study of anode surface temperature after current zero for a range of current levels," *27th International Symposium on Discharges and Electrical Insulation in Vacuum (ISDEIV)*, Suzhou, China, 2016, pp. 1-4, doi: 10.1109/DEIV.2016.7748737.I. S. Jacobs and C. P. Bean, “Fine particles, thin films and exchange anisotropy,” in Magnetism, vol. III, G. T. Rado and H. Suhl, Eds. New York: Academic, 1963, pp. 271–350.

[9] A. A. Logachev, I. N. Poluyanova, K. K. Zabello, D. I. Begal, and S. M. Shkol'nik, "Analysis of Cathode Surface State and Cathode Temperature Distribution After Current Zero of AMF-Contacts," *28th International Symposium on Discharges and Electrical Insulation in Vacuum (ISDEIV)*, Greifswald, germany, 2018, pp. 329-332, doi: 10.1109/DEIV.2018.8537127.

[10] A. Daibo, Y. Niwa, N. Asari, W. Sakaguchi, Y. Sasaki, and T. Y. Toshiba, "Measurement of transient temperature distribution at anode surface after current zero in vacuum interrupter," *29th International Symposium on Discharges and Electrical Insulation in Vacuum (ISDEIV)*, Padova, Italy, 2021, pp. 143-146, doi: 10.1109/ISDEIV46977.2021.9587325.

[11] R. Methling S. Gorchakov, M. V. Lisnyak, St. Franke, A. Khakpour, S. Popov, A. Batrakov, D. Uhrlandt, and K.-D. Weltmann,”Spectroscopic investigations of high-current vacuum arcs”, *IEEE trans. Plasma Sci*., vol. 43, pp. 2303–2309, August 2015.

[12] H. C. Milner, “Vacuum arcs”, *IEEE Trans. Plasma Sci*., vol. 51, pp. 1585–1594, 2023. doi:10.1109/TPS.2023.3261779.

[13] N.Dorraki, R. Methling, S. Gortschakow, „Advanced temporal analysis of anode activity during mode transitions in high current vacuum arcs”, *J. Phys. D: Appl. Phys*., vol. 58, 075204 (11pp), 2025, doi: 10.1088/1361-6463/ad96c5

[14] S. Gortschakow, N. Dorraki, “Study of correlation between voltage variation and surface temperature during anode mode transitions in a model vacuum switch”, *Plasma Phys. Technol*., vol. 12, pp. 107-111, 2025. doi: 10.14311/ppt.2025.2.107

Effect of Laser Surface Remelting on the Electrical Performance of CuCr Electrical Contacts

Ming Yu
ShaanXi Sirui Advanced Materials. Co., LTD
Xi'an, China
yuming@sirui.net.cn

Peng Li
ShaanXi Sirui Advanced Materials. Co., LTD
Xi'an, China
lipeng@sirui.net.cn

Yong Wang
ShaanXi Sirui Advanced Materials. Co., LTD
Xi'an, China
wangyong@sirui.net.cn

Xiaojun Wang
ShaanXi Sirui Advanced Materials. Co., LTD
Xi'an, China
wangxiaojun@sirui.net.cn

Ning Han
ShaanXi Sirui Advanced Materials. Co., LTD
Xi'an, China
hanning@sirui.net.cn

Xiaofei Yao
State Key Laboratory of Electrical Insulation and Power Equipment, Xi'an Jiaotong University,
Xi'an , China
yaoxf85@mail.xjtu.edu.cn

***Abstract*—This study systematically investigates the effect of Laser Surface Remelting (LSR) technology on the electrical performance of three typical CuCr contact materials (vacuum cast CuCr30, arc-melted CuCr30, and arc-melted CuCr50) under high-current breaking conditions and elucidates the underlying mechanisms. By comparing the electrical wear rate, surface ablation morphology, and cathode spot dynamics of the contacts before and after LSR treatment during 20 breaking operations at 20 kA, and combining these observations with changes in microstructure, electrical conductivity, and hardness, the micro-mechanisms by which LSR improves the arc erosion resistance of CuCr contacts are revealed. The results show that LSR treatment significantly reduced the electrical wear rate of vacuum cast CuCr30, arc-melted CuCr30, and arc-melted CuCr50 by 46.9%, 26.4%, and 37.0%, respectively. The core mechanism lies in the fact that LSR achieves surface microstructure ultra-refinement and high compositional homogenization through rapid solidification, which in turn regulates cathode spot behavior, transforming intense local ablation into mild and uniform material consumption. This research demonstrates that LSR is an effective surface modification method for selectively enhancing the electrical performance of CuCr contacts via microstructure refinement, and it holds significant engineering application value.**

Keywords—Copper-chromium contact; Laser surface remelting; Microstructure refinement; Arc erosion; Electrical performance

I. INTRODUCTION

Copper-chromium (CuCr) alloys are widely used as contact materials in vacuum interrupters (VIs) across various voltage levels due to their high hardness, excellent electrical conductivity, and outstanding arc erosion resistance [1]. As the core component of electrical switching devices, contacts function by carrying current in the closed state and extinguishing the arc during breaking to control circuit connection and disconnection [2]. During repeated contact opening and closing operations, high-energy arcs act on the electrode surfaces [3], leading to material erosion, increased contact resistance [4], surface ablation, welding, and even failure [5], directly impacting the breaking performance and service life of the circuit breaker. With the increasing demands of power systems for higher breaking capacity and reliability of vacuum circuit breakers, further optimization of CuCr contact material performance has become an urgent necessity.

Research indicates that the breaking performance and service life of vacuum circuit breakers are closely related to the microstructure of the contact material [6], with the size and distribution of the chromium (Cr) phase being particularly critical [7]. A refined grain structure helps reduce chopping current and improve dielectric strength. Concerning the influence of microstructure on vacuum arc characteristics[8], studies have found that nano-crystalline CuCr contacts can stabilize cathode spot movement [9] and make vacuum arc behavior more controllable [10]. Therefore, starting from the regulation of material microstructure, refining the grains of CuCr contacts through surface modification technology is an important research direction for enhancing their performance.

Among various surface modification techniques, Laser Surface Remelting (LSR) exhibits unique advantages in engineering material surface treatment due to its high energy density, rapid heating and cooling (cooling rates up to 10^3–10^8 K/s), and precise area control capability [11]. LSR involves melting a thin surface layer of the material with a laser beam and allowing it to solidify rapidly, thereby forming a strengthened layer with homogeneous composition, refined structure (Cr phase can reach nanometer scale), and metallurgical bonding with the substrate. In light of this, this paper employs a high-power laser to perform surface remelting treatment on three typical CuCr contact materials produced by different processes (vacuum cast CuCr30, arc-melted CuCr30, and arc-melted CuCr50). It systematically investigates the electrical wear behavior, surface ablation morphology, and cathode spot dynamics of the contacts under 20 kA high current before and after LSR treatment. By combining these findings with the evolution of microstructure, electrical conductivity, and hardness, the physical mechanisms behind the improvement of arc erosion resistance in CuCr contacts by LSR are deeply revealed. This study provides a new surface engineering approach for the development of high-performance CuCr electrical contacts, with broad industrial application prospects.

II. Experimental Setup

A. Materials and Laser Surface Remelting

Three types of CuCr alloys were selected for the experiments: vacuum cast CuCr30 (denoted as CuCr30/C), arc-melted CuCr30 (denoted as CuCr30/A), and arc-melted CuCr50 (denoted as CuCr50/A). The materials were machined into slotted disc-shaped contacts with a diameter of 45 mm and a thickness of 6 mm. Their basic physical properties are listed in Table I. Fig. 1 shows the as-received metallographic microstructures of the three materials, where dark circular or elliptical particles are the Cr phase embedded in the bright Cu matrix. It can be observed that the Cr phase size is approximately 50–80 μm for CuCr30/C, and 30–50 μm for CuCr30/A. For CuCr50/A, the Cr phase size is also in the range of 30–50 μm, while its volume fraction is significantly higher than that of the former two materials.

TABLE I. Physical properties of the CuCr contact materials.

Material	Physical properties		
	Electrical conductivity (Ms/m)	*Hardness (HB)*	*Density (g/cm^3)*
Vacuum casting CuCr30	29.2-30.5	80.5-83.7	8.2-8.3
Arc-melting CuCr30	30.2-30.3	80.9-82.7	8.2-8.3
Arc-melting CuCr50	21.6-22.2	94.0-96.0	7.9-8.0

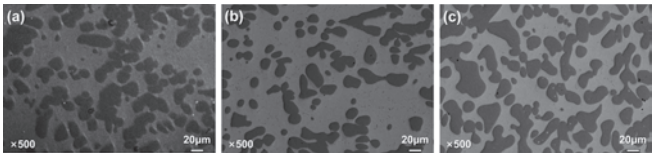


Fig. 1. Cr phase size and distribution (a) CuCr30/C, (b) CuCr30/A, (c) CuCr50/A.

LSR treatment was performed using a fiber laser. The process parameters were set as follows: laser power 390 W, scanning speed 3000 mm/s (3 m/s), and hatch spacing 0.08 mm. The process was conducted in a chamber filled with high-purity argon gas (O_2 < 30 ppm, H_2O < 100 ppm) to suppress oxidation. An air-cooling system was used to assist in cooling the samples to control thermal stress. A schematic diagram of the LSR experimental setup is shown in Fig. 2. Untreated contacts served as the control group (CuCr30/C, CuCr30/A, CuCr50/A), and LSR-treated contacts constituted the experimental group (correspondingly denoted as CuCr30/C-LSR, CuCr30/A-LSR, CuCr50/A-LSR). Fig. 3 shows a comparison of the macroscopic surface morphology of CuCr30/C contacts before and after treatment.

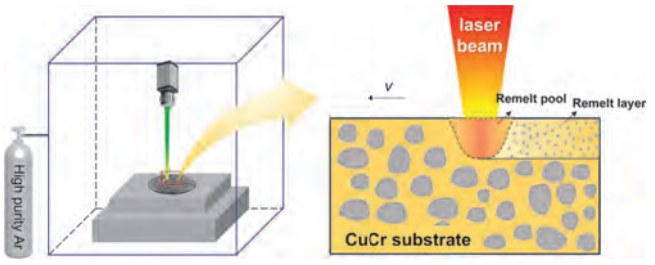


Fig. 2. (a) Schematic diagram of the LSR experimental setup, (b) schematic illustration of the LSR process.

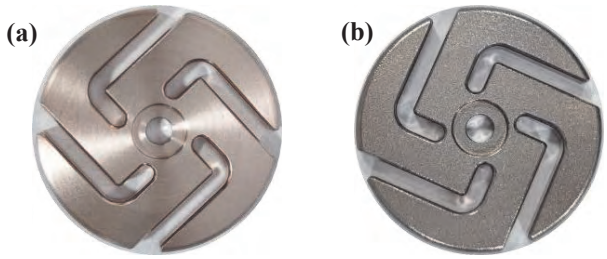


Fig. 3. Top view of the CuCr30/C contact (a) untreated, (b) LSR-treated.

B. Electrical Performance Testing and Characterization

High-current breaking tests were conducted in an LC oscillatory circuit, with a schematic of the experimental setup shown in Fig. 4. Contact samples were assembled in a demountable vacuum interrupter chamber maintained at a pressure of 5.0×10^{-5} Pa. The rated short-circuit breaking current was set to 20 kA with an arcing time of 8 ms. Voltage and current waveforms were recorded using an oscilloscope. Mass loss measurement was performed exclusively on the moving contact (cathode) of each contact pair. Before pre-test and post-test weighing, the moving contact samples were ultrasonically cleaned in anhydrous ethanol for 15 min and dried to constant weight. The mass was measured 3 times with a 0.1 mg-precision electronic analytical balance, and the average value was used for total mass loss calculation. The electrical wear rate was defined as the ratio of the total mass loss of the moving contact after 20 breaking operations at 20 kA to the total total charge transferred during the test of the test, in the unit of μg/C. Simultaneously, a high-speed camera was used to record the dynamic behavior of cathode spots within the last 0.5 ms before arc extinction through observation windows.

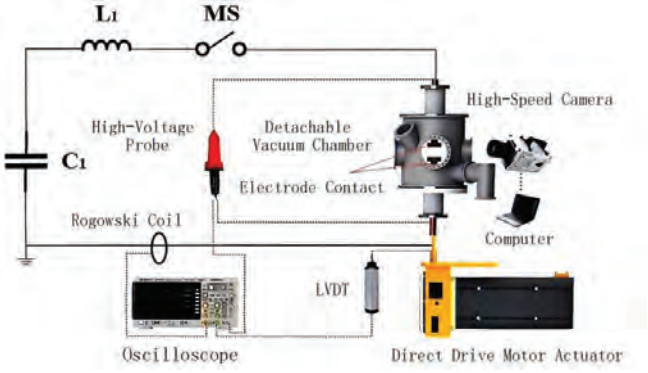


Fig. 4. Schematic diagram of the test circuit.

C. Microstructure and Property Analysis

The surface/cross-sectional micro-morphology was observed and analyzed using a Scanning Electron Microscope (SEM). Surface hardness was measured using a Brinell hardness tester (load 2450 N, dwell time 15 s). The electrical conductivity of the materials was measured using an eddy current conductivity meter.

III. Results and Discussion

A. Microstructural Characteristics

Fig. 5 shows the cross-sectional microstructure of the three CuCr materials after LSR treatment. Under identical laser processing parameters, a continuous, metallurgically bonded remelted layer free of cracks and visible porosity was successfully fabricated on the surface of all samples. The

measured thickness of the remelted layer exhibited a distinct material-dependent characteristic: for the vacuum-cast CuCr30/C, the remelted layer thickness was determined to be in the range of 59.9 μm to 65.6 μm; for the arc-melted CuCr30/A, the thickness ranged from 45.2 μm to 46.6 μm, featuring the narrowest thickness fluctuation and the lowest average thickness among the three materials; for the arc-melted CuCr50/A, the thickness varied between 60.1 μm and 73.3 μm, with the highest average thickness.

This discrepancy in remelted layer thickness is mainly attributed to the differences in thermophysical properties and initial microstructure of the three materials. Chromium has a significantly higher melting point (1857 °C) and laser absorptivity at the processing wavelength than the copper matrix (melting point 1085 °C). The elevated Cr content in CuCr50/A increases the overall laser energy absorption of the alloy, which promotes the formation of a deeper melt pool under the same laser energy input. In contrast, the arc-melted CuCr30/A possesses a denser, more homogeneous initial microstructure with inherently finer Cr phases, which enhances the in-plane thermal conductivity of the material and accelerates heat dissipation into the bulk substrate, ultimately resulting in a shallower remelted layer.

Fig. 6 presents high-magnification micrographs of the Cr phase morphology within the remelted layer. The Cr phase in the remelted zone exhibits two typical morphologies: fine spherical Cr grains and curved, elongated Cr bands, with the latter extending toward the top surface of the melt pool (i.e., the sample surface). This morphological feature confirms the presence of intense Marangoni convection and stirring within the laser melt pool during rapid solidification. Comparing Fig. 6(b) (CuCr30/A) and Fig. 6(c) (CuCr50/A), the Cr phase refinement is more complete in CuCr30/A under identical laser parameters, while a higher fraction of banded Cr phases is observed within the remelted layer of CuCr50/A. This phenomenon is mainly ascribed to the fact that high-Cr-content alloys require higher specific energy input to achieve full melting and compositional homogenization of the primary Cr phase. Accordingly, the optimization of laser process parameters tailored to alloys with different Cr contents is critical for achieving an ideal remelted layer structure with uniformly refined Cr phases.

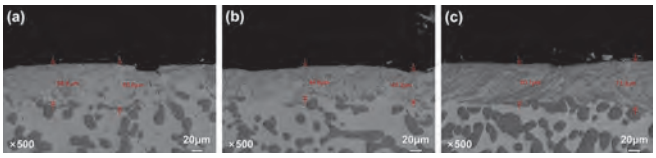


Fig. 5. Cross-sectional microstructure of the laser-surface-melted CuCr alloy (a) CuCr30/C, (b) CuCr30/A, (c) CuCr50/A.

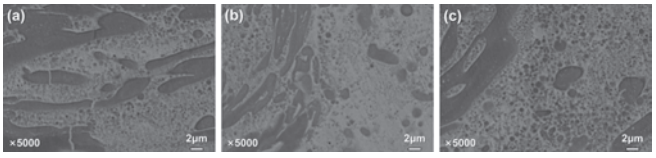


Fig. 6. Magnified images of Cr grain morphology (a) CuCr30/C, (b) CuCr30/A, (c) CuCr50/A.

B. Analysis of Basic Physical Properties

The effect of LSR treatment on the basic physical properties of the contacts is shown in Table II. Regarding electrical conductivity, all materials showed a slight decrease of approximately 5-10% after LSR treatment. This is mainly attributed to the enhanced electron scattering caused by the high density of crystal defects (such as point defects, dislocations) and refined grain boundaries introduced by rapid solidification. In terms of hardness, the surface hardness of all three materials increased. The increase in hardness for CuCr30/C and CuCr30/A was relatively small (about 2-3 HB), while the increase for CuCr50/A was very significant, with its maximum value rising from 96 HB to 115 HB, an increase of about 20%. This is primarily due to the grain refinement strengthening [12], dislocation strengthening, and, particularly important for high-Cr alloys, second phase (Cr phase) strengthening induced by LSR. The refinement and uniform distribution of the Cr phase after remelting formed a more effective strengthening network. Overall, despite the reduction in electrical conductivity of CuCr contacts after laser surface remelting (LSR), the conductivity still fully meets the engineering application requirements for vacuum contact materials [13]. The slight decrease in conductivity only leads to an increase in steady-state Joule heating, while during the 20 kA high-current breaking process, the energy released by the vacuum arc is 3 to 4 orders of magnitude higher than steady-state Joule heating, making this adverse effect negligible [14]. Meanwhile, despite the minor reduction in electrical conductivity, LSR treatment optimizes the microstructure and improves the hardness of the contacts, which reduces the electrical wear rate by 26.4% to 46.9%. This significant improvement in arc erosion resistance completely offsets the negligible negative impact caused by the slight decrease in conductivity, resulting in a remarkable enhancement of the overall performance of the CuCr contacts.

TABLE II. COMPARISON OF ELECTRICAL CONDUCTIVITY AND HARDNESS OF THE CUCR CONTACT MATERIALS.

Material	***Group***	**Physical properties**	
		Electrical conductivity (Ms/m)	***Hardness (HB)***
Vacuum cast CuCr30	Control	29.2-30.5	80.5-83.7
	LSR-treated	27.0-29.0	82.5-85.1
Arc-melted CuCr30	Control	30.2-30.3	80.9-82.7
	LSR-treated	27.0-28.5	82.3-85.3
Arc-melted CuCr50	Control	21.6-22.2	94.0-96.0
	LSR-treated	19.0-21.0	95.0-115.0

C. Arc Erosion Resistance Performance

Fig. 7 illustrates the effect of LSR on the cumulative electrical wear rate (characterized by mass loss) for three different CuCr contacts after undergoing 20 breaking tests at 20 kA. In the figure, the blue bars represent the control group, and the red bars represent the remelted group. Quantitative data indicate that laser remelting significantly improved the electrical wear performance of all three materials. For CuCr30/C, laser remelting drastically reduced its electrical wear rate from 92.44 μg/C to 49.12 μg/C, a reduction of 46.9%. For CuCr30/A after laser remelting, its electrical wear rate decreased from 119.53 μg/C to 87.95 μg/C, a reduction of 26.4%. For CuCr50/A, laser remelting reduced its electrical wear rate from 98.79 μg/C to 62.21 μg/C, a reduction of 37.0%. Analysis of the results shows that LSR significantly enhanced the arc erosion resistance of all three CuCr contact materials, but the degree of improvement exhibits clear material dependency. CuCr30/C showed the

greatest improvement at 46.9%. This suggests that its original as-cast structure may have contained relatively large dendrite arm spacing, compositional segregation, or casting defects. The rapid solidification process of laser remelting greatly refined the microstructure, homogenized the composition, and eliminated defects, thereby constructing a highly homogeneous and dense surface layer that maximized its resistance to arc erosion. The wear rate of CuCr50/A was reduced by 37.0%, indicating a similarly significant improvement. The high Cr content (50 wt%) itself tends to form more hard Cr phases. Laser remelting likely optimized the size, morphology, and distribution of the Cr phase, reducing its tendency to act as stress concentration points or easily detachable particles under arc action, while simultaneously enhancing the bonding between the copper matrix and the Cr phase, resulting in a synergistic improvement in overall erosion resistance. CuCr30/A showed the relatively smallest improvement (26.4%). Considering its original manufacturing process (arc melting inherently yields a relatively fine and dense structure), the alloy's initial state may already possess a relatively good foundation for erosion resistance. The additional benefit from further microstructural refinement brought by laser remelting is relatively limited.

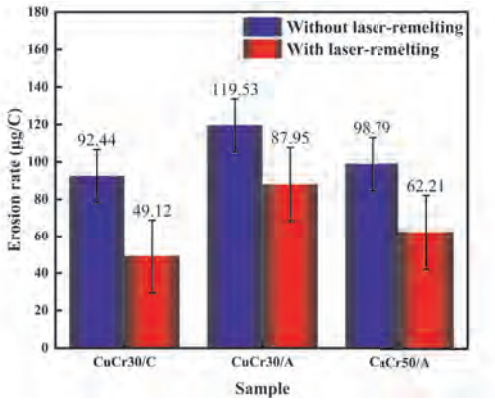


Fig. 7. Electrical wear rate data of CuCr contacts in different states afterbreaking tests (20 kA, 20 operations).

TABLE III. SURFACE ROUGHNESS PARAMETERS OF CUCR CONTACT SPECIMENS AFTER 20 KA/20 BREAKING OPERATIONS.

Material	Group	3D Arithmetic Mean Height Sa (μm)	2D Profile Roughness Ra (μm)	Maximum Surface Height Sz (μm)	Sa Reduction Rate
Vacuum cast CuCr30	Control	3.44 ± 0.65	2.83 ± 0.78	46.78 ± 3.25	-
	LSR-treated	2.71 ± 0.98	1.77 ± 0.58	42.69 ± 13.47	21.2%
Arc-melted CuCr30	Control	4.41 ± 0.52	4.08 ± 0.92	53.26 ± 6.12	-
	LSR-treated	4.18 ± 1.18	3.46 ± 1.17	44.25 ± 8.79	5.2%
Arc-melted CuCr50	Control	3.88 ± 0.95	3.20 ± 2.01	49.18 ± 10.21	-
	LSR-treated	2.93 ± 0.97	2.30 ± 0.96	46.94 ± 6.79	24.5%

To quantitatively evaluate the surface ablation degree of the CuCr contacts after high-current breaking tests, the 3D surface topography of the ablated working surface was characterized by a white light interferometer, and the core roughness parameters were measured in strict accordance. For each contact specimen, 5 independent test points were uniformly selected on the arc-affected working area, and the average value of 5 parallel samples was adopted for each material group. The detailed test results are summarized in Table III.

The results show that all LSR-treated contacts exhibited lower surface roughness than the corresponding control group after 20 breaking operations. The reduction rate of the core 3D roughness Sa is 21.2% for CuCr30/C-LSR, 5.2% for CuCr30/A-LSR, and 24.5% for CuCr50/A-LSR, which is highly consistent with the variation trend of electrical wear rate. The lower surface roughness of the LSR-treated group directly confirms that the laser remelted layer effectively suppresses the formation of local severe melting pits and material splatter during arcing, and achieves a uniform and mild ablation mode, which is in good agreement with the surface morphology observation in Fig. 8. This quantitative result further verifies the positive effect of LSR treatment on improving the arc erosion resistance of CuCr contact materials. Comparing the ablation morphology of the contacts before and after remelting, as shown in Fig. 8, the surfaces of contacts with the remelted layer after ablation exhibit significantly better flatness and uniformity compared to the control group. This uniform ablation mode directly confirms that the remelted layer effectively suppressed local intense melting and splashing, resulting in more uniform and gradual material loss.

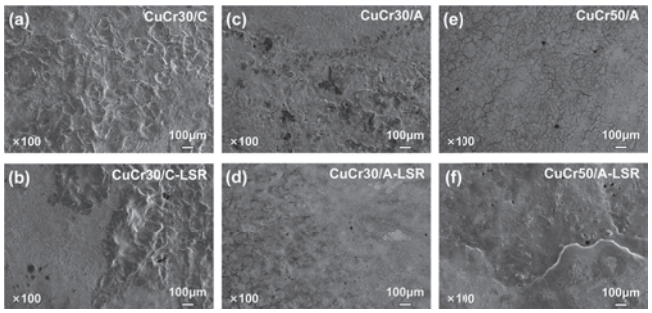


Fig. 8. SEM micrographs of contact surface ablation morphology for control and LSR-treated groups after 20 breaking operations at 20 kA

D. Cathode Spot Behavior Analysis

High-current Figure 9(a) shows the cathode spot images of CuCr30/C recorded by a high-speed camera 0.1–0.5 ms before arc extinction. The left side shows the control group without laser remelting treatment. The results indicate that within the 0.5 ms before arc extinction, the number of cathode spots is relatively small, but their distribution across the entire contact surface was highly scattered. In contrast, the remelted group on the right panel showed a significant increase in the number of cathode spots during the same time period, and their spatial distribution is highly concentrated in localized areas of the contact. Simultaneously, comparing the data on the current carried by a single cathode spot before and after remelting, as shown in Figure 9(b), the data for the remelted group is significantly lower than that of the control group. This result forms a logical closure with the previous finding of a 46.9% reduction in electrical wear rate. Laser remelting homogenizes the surface microstructure, leading to an increase in the number of spots, a more concentrated distribution, and a reduction in the current density of each spot, thereby decreasing thermal impact and erosion damage to the surface. Additionally, the uniform surface can better disperse arc energy.

Figure 10(a) shows the cathode spot images of CuCr30-A recorded by a high-speed camera 0.1–0.5 ms before arc extinction. The control group on the left shows a moderate

number of cathode spots during the time sequence from 0.5 ms to 0.1 ms before arc extinction, with a dispersed distribution across the contact surface and relatively large distances between individual spots. During the same time sequence, the number of cathode spots in the remelted group is not significantly different from or slightly higher than that of the control group. However, their spatial distribution exhibits a more pronounced tendency for local aggregation, with some spots closely adjacent to each other. The bar chart data for the current carried by a single cathode spot, shown in Figure 10(b), indicates that the average current per cathode spot in the laser remelted group is slightly lower than that of the control group. This differs from the analysis of CuCr30/C, where the remelted group showed a clear increase in the number of spots, while here the change is minimal. This may be due to differences in the original state of the materials. CuCr30/A is prepared by arc melting, which inherently results in a relatively uniform microstructure. Therefore, the homogenization effect brought by laser remelting is less drastic, leading to a less noticeable change in the number of spots.

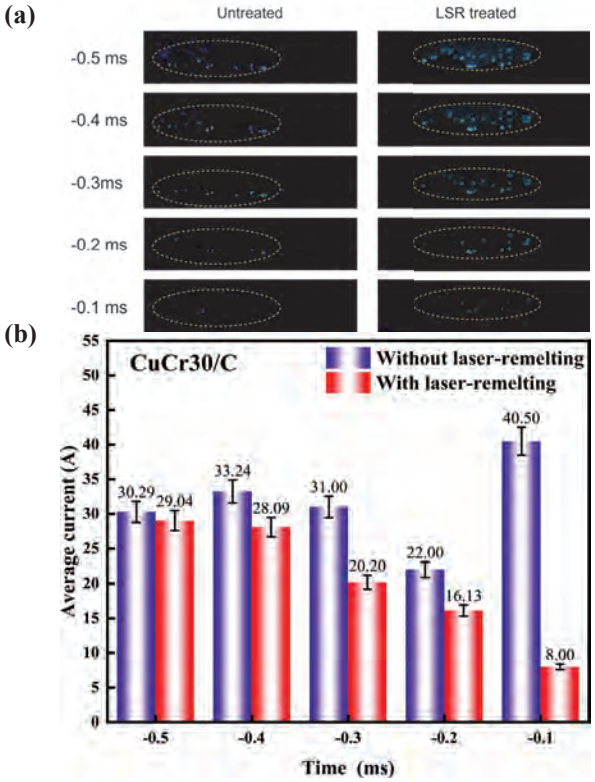


Fig. 9. (a) Cathode spot on CuCr30/C at 0.1-0.5 ms before arc extinction. (b) Current carried by a single cathode spot.

Figure 11(a) shows the cathode spot images of CuCr50-A recorded by a high-speed camera 0.1–0.5 ms before arc extinction. The control group on the left shows a relatively small number of cathode spots during the time sequence from 0.5 ms to 0.1 ms before arc extinction, with a sparse and dispersed distribution across the contact surface. The remelted group on the right side shows a significantly higher number of cathode spots during the same time sequence, with a more uniform and dense distribution covering a broader surface area, without obvious large-scale aggregation phenomena. The bar chart for the current carried by a single cathode spot, shown in Figure 11(b), reveals that the average current per cathode spot in the laser remelted group (27.35 A) is significantly lower than that of the control group (36.74 A), a reduction of 25.6%. The high Cr content may affect the material's electrical conductivity and thermal conductivity, thereby influencing spot behavior. After laser remelting, the more uniform microstructure may make it easier for spots to form, but the intensity of individual spots decreases

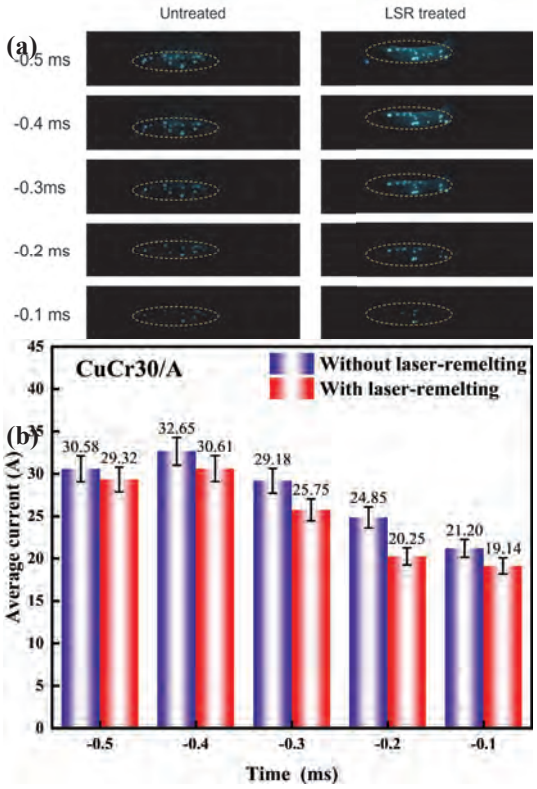


Fig. 10. (a) Cathode spot on CuCr30/A at 0.1-0.5 ms before arc extinction. (b) Current carried by a single cathode spot.

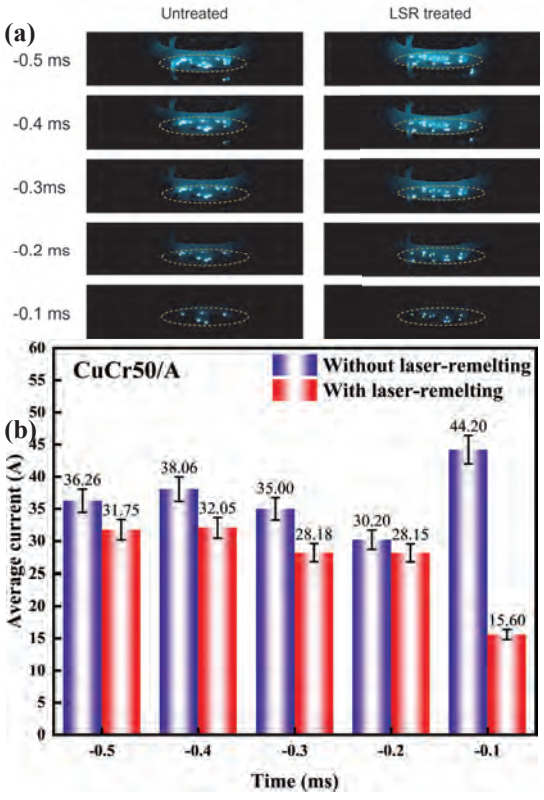


Fig. 11. (a) Cathode spot on CuCr50/A at 0.1-0.5 ms before arc extinction. (b) Current carried by a single cathode spot.

The voltage and current waveforms during the breaking process were recorded in real time by a high-bandwidth oscilloscope, and a typical waveform of the 20 kA breaking test is shown in Fig. 12. The current zero crossing (CZ, the moment of arc extinction) was defined as the time reference origin (t=0 ms), and the dynamic behavior of cathode spots was recorded by a high-speed camera within the time window of 0.5 ms before CZ (i.e., t=-0.5 ms to t=0 ms), to ensure the consistency and comparability of the observation results under the same arcing stage. Each contact pair underwent 20 consecutive breaking operations under the same test conditions. All cathode spot images in this section were recorded in the time window of 0.5 ms before current zero crossing, with the time reference strictly calibrated according to the breaking current waveform shown in Fig. 12.

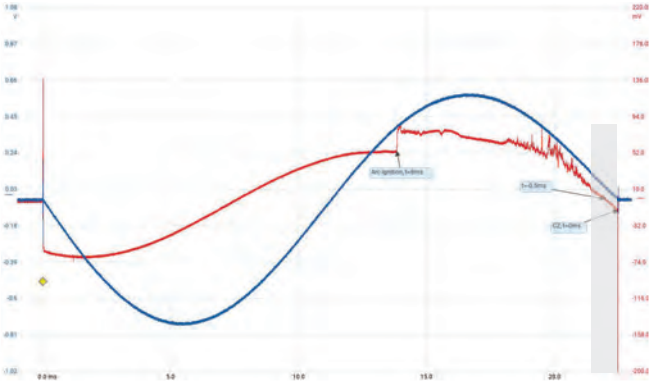


Fig. 12. The typical waveform of the 20 kA breaking test.

IV. Conclusion

This study employed LSR technology to modify the surface of three types of CuCr contacts produced by different processes. It systematically evaluated the effect on resistance to high-current arc erosion and revealed the related mechanisms. The main conclusions are as follows:

1) LSR can significantly enhance the resistance of CuCr contacts to high-current arc erosion, but the extent of improvement exhibits strong material dependency. For the CuCr30/C contact material with a relatively coarse and non-uniform microstructure, LSR provides the greatest benefit, reducing the electrical wear rate by 46.9%; for the CuCr30/A contact material, which already has a relatively uniform original microstructure, the improvement is limited (26.4%); while for the high-chromium CuCr50/A, LSR also significantly reduces the wear rate (37.0%).

2) The microscopic mechanism behind the performance improvement stems from the surface homogenization induced by LSR and its regulation of arc physical behavior. LSR treatment refines the microstructure, eliminates compositional segregation, and creates a highly homogeneous and dense surface layer. This leads to a fundamental transformation in cathode spot behavior, thereby dispersing the arc energy and achieving a shift in the ablation mode from intense local destruction to uniform global consumption.

3) After LSR treatment, the surface hardness of all materials increases (with CuCr50/A showing particularly significant enhancement), which directly strengthens the material's ability to resist mechanical and thermal erosion caused by the arc.

4) Comprehensive evaluation indicates that LSR technology holds broad application value. Future process optimization should focus on ensuring the consistency of Cr particle size in the remelted layer and reducing or even avoiding the formation of banded Cr particles, in order to fully unlock its performance potential.

References

[1] X.Y. Wan, W.B. Xie, H.M. Chen, F.Y. Tian, H. Wang, B. Yang, First-principles study of phase transformations in Cu–Cr alloys, J. Alloys Compd. 862 (2021), 158531.

[2] Zhai G F, Bo K, Zhou X, et al. Transactions of China Electrotechnical Society, 2017, 32(22) , 251 (in Chinese).

[3] Wang Q P. Electric and arc theory, China Machine Press, China, 1991 (in Chinese).

[4] Chen Z K, Mizukoshi H, Sawa K. IEEE Transactions on Components Packaging and Manufacturing Technology: Part A, 1994, 17(1), 113.

[5] Zhang X, Ren W, Zheng Z, et al. IEEE Access, 2019, 7, 133079.

[6] C.Y. Zhang, Z.M. Yang, B.J. Ding, Low electrode erosion rate of nanocrystalline CuCr-50 alloy in vacuum, Mod. Phys. Lett. B 20 (2006) 1329–1334.

[7] X. Yang, D.P. Shen, H. Zhang, W.P. Tong, Investigation on the structure and property of a gradient nanostructure CuCr25 with high hardness and high electrical conductivity, Vacuum 146 (2017) 225–232.

[8] Z.M. Yang, Q.L. Zhang, Q.F. Wang, C.Y. Zhang, B.J. Ding, Vacuum arc characteristics on nanocrystalline CuCr alloys, Vacuum 81 (2006) 545–549.

[9] M.S. Benilov, M.D. Cunha, W. Hartmann, S. Kosse, A. Lawall, N. Wenzel, Modeling spots on composite copper-chromium contacts of vacuum arcs and their stability, IEEE Trans. Plasma Sci. 43 (8) (2015) 2253–2260.

[10] K.V. Kuskov, A.S. Rogachev, S.G. Vadchenko, N.F. Shkodich, S. Rouvimov, A. S. Shchukin, E.V. Illarionova, V.A. Kudryashov, A.S. Mukasyan, Resistance of microcrystalline and nanocrystalline Cu/Cr pseudo alloys to vacuum discharge, J. Alloys Compd. 750 (2018) 811–818.

[11] ZHANG Litian, YU Gang, LI Shaoxiao, et al. The effect of laser surface melting on grain refinement of phaseseparated Cu-Cr alloy[J]. Optics & Laser Technology, 2019(119): 105577.

[12] Quanfeng Han, Xin Yi, A unified mechanistic model for Hall–Petch and inverse Hall–Petch relations of nanocrystalline metals based on intragranular dislocation storage, Journal of the Mechanics and Physics of Solids, Volume 154, 2021, 104530.

[13] Jin-ru Han, Zhi-he Dou, Ting-an Zhang, Wang An, Review of the recent Chinese research on the electrical properties of CuCr contacts for vacuum interrupters, Journal of Materials Research and Technology[J], Volume 25, 2023, 1585-1598.

[14] D. Gentsch, Contact Material for Vacuum Interrupters based on CuCr with a Specific High Short Circuit Interruption Ability, 2006 International Symposium on Discharges and Electrical Insulation in Vacuum, Matsue, Japan, 2006, pp. 437-442

Multi-Parameter Investigation of Magnetron Currents in Vacuum Interrupters

Patrick Rumpelt
ABB AG
Electrification - Distribution Solutions
Ratingen, Germany
patrick.rumpelt@de.abb.com

Philipp Hauch
ABB AG
Electrification - Distribution Solutions
Ratingen, Germany
philipp.hauch@de.abb.com

Marco Thönnessen
ABB AG
Electrification - Distribution Solutions
Ratingen, Germany
marco.thoennessen1@de.abb.com

Michael Weuffel
ABB AG
Electrification - Distribution Solutions
Ratingen, Germany
michael.weuffel@de.abb.com

***Abstract* — Vacuum interrupters represent the state-of-the-art technology for load and fault current interruption in medium-voltage distribution networks. A critical aspect of their manufacturing and lifetime assurance is the determination of the residual gas pressure, which must remain below 10^{-4} hPa over the device lifetime. The magnetron method, in which a discharge current sustained in the interrupter volume serves as a pressure-dependent diagnostic, provides a non-invasive means of internal pressure quantification through an empirically derived proportionality factor. In this study, the ignition characteristics of magnetron discharges are systematically examined and indicate the influence of multi geometric parameters on the expected internal pressure characteristic. By means of an experimental test setup that consists of a vacuum test system to vary the internal pressure in punctured, non-vented VIs with active getter elements, experimental test series under variation of internal pressure and different geometric dimensions were carried out. The findings support an accurate characterization of internal pressure and the determination of the geometric influence to precise the verification of the ultra-high vacuum during production or in quality cases as well as in an on-site condition assessment. The paper discuss the impact of the observed effect on internal dimensions depending on the contact geometry, the metal vapor shield design and the resulting enclosed volume.**

Keywords* —Arc discharge, lifetime prediction, magnetron method, vacuum, vacuum circuit breaker (VCB), vacuum integrity, vacuum interrupter (VI), vacuum switching, internal pressure

I. Introduction

Vacuum switching technology has been established in the medium voltage level since the 1980s and today represents the state-of-the-art technology for load and fault current interruption in medium-voltage distribution networks. With their high reliability, large number of possible switching operations and current interruptions, low maintenance requirements and long lifetime, vacuum interrupters (VIs) have considerable advantages over other switching principles. In particular, the operating life of VIs is specified as up to over 30 years, and in many cases continued operation beyond the specified service life is possible. [1] A critical aspect is the internal pressure of a VI. The internal pressure must not exceed a critical value in the range of $p_{critical} = 10^{-4} \ldots 10^{-3}$ hPa. [2] The magnetron method is well established for the internal pressure measurement of VIs. Its application during the manufacturing process and after a considerable period of service, e.g. towards the end of the expected service life for its extension, is crucial for determining the vacuum quality. [3] Evaluating the magnetron measurement at any stage during its entire lifespan requires precise knowledge of a wide range of parameters: Appropriate choice of applied direct high voltage and magnetic flux density, residual gas composition, the influence of the high purity metallic surfaces in the VI due to gas binding effects, [3] development of internal pressure in VIs immediately after a current interruption operation are just a few important aspects to consider. [4, 5]

Measuring the internal pressure of vacuum interrupters via the magnetron method is complex and involves a number of parameters which you ought to be conscious of. When determining pressure-discharge current calibration curves, creating the ultra-high vacuum, applying the voltage to the specimen, simultaneously applying a homogeneous magnetic field, piercing under ultra-high vacuum and finding a set of parameters for igniting a magnetron discharge at different pressures makes the measurement complex.

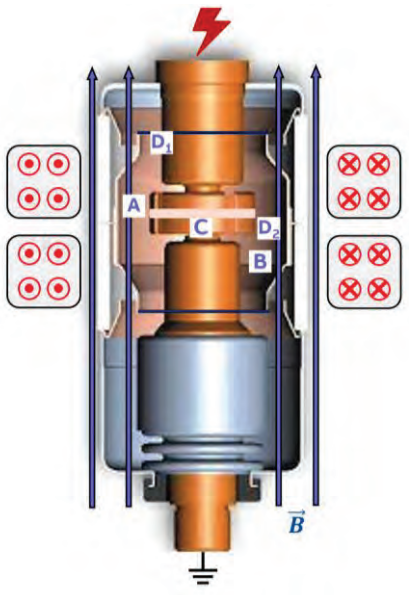


Fig. 1. Magnetron principle: VI inside a coil arrangement and high voltage applied across the open contacts inlc. the observed and analyzed sections: A - D

Fig. 1 shows the basic concept of pressure measurement using the magnetron principle. Applying a high voltage to electrodes leads to an electric field in which charge carriers,

e.g. from field emission, get accelerated, especially at locations within the area of the middle shield containing the volumes A and D as well as the surfaces B and C. Because of the long mean free path length inside vacuum, no significant discharge occurs, with only high voltage applied.

However, if the VI is additionally located in an axial magnetic field, due to the Lorentz force, the distance traveled by the electrons from the cathode to the anode is increased by a hypocycloid trajectory movement allowing collisions with other gas molecules. The current flow of this magnetron discharge is proportional to the number of gas molecules. [6]

The magnetron principle is therefore based on trapping electrons that trigger a discharge. In VIs with a symmetrical design and a middle shield at floating potential, this results in two discharges in series between each contact and the middle shield [7, 8]. The accumulation areas of the electrons form, on one side, between the outer radius of a contact and the central middle screen and, on the contrary side, between the edge of the middle shield and the copper rod opposite it. [8]

In order to compare the measured magnetron discharge current with reference internal pressure characteristics, precise knowledge of each individual vacuum interrupter is required. This is where the present research topic comes in and allows an approach to predict magnetron discharge currents of unknown vacuum interrupters via geometric dependencies. The magnetron discharge is a type of low-pressure gas discharge [5], as a result of which the forced extension of the electron paths within the cylindrical electrode arrangement is dependent on geometric influences.

Geometrical parameter	TO 1	TO 2 (reference)	TO 3	TO 4
A: Volume enclosed by the middle shield	40 %	100 %	125 %	170 %
B: Area given by the middle shield	50 %	100 %	125 %	140 %
C: Contact perimeter surface area	80 %	100 %	140 %	190 %
D: Estimated accumulation volume area of the magnetron discharges	60 %	100 %	190%	230 %

Tab. 1. Size comparison of the geometrical parameters of the test objects normalized to test object 2

The approach of the investigations includes a sum of four different test objects, see Table 1. These four VIs differ fundamentally in size and physical dimensions. Nevertheless, all four specimens use a middle shield at floating potential and thus, a comparable field grading principle. Subsequently, they provide the basis for investigating the dependencies of the magnetron discharge on the total VI volume, the volume enclosed by the middle shield (A), the surface area given by the middle shield (B), the outer radial electrode surface of the contacts (C) and the estimated accumulation volume area of the two occurring magnetron discharges (D).

II. Ignition parameters of the magnetron discharge

According to [9], the critical voltage of a magnetron discharge depends on the geometric dimensions of the cathode and anode, and the applied magnetic flux density B. Smaller VIs require a lower critical voltage than larger VIs at constant magnetic flux density.

To ensure comparable results, it is essential that the ignition parameters are selected appropriately and are applicable to all cases in the test campaign. The major ignition parameters include the applied DC voltage U_{DC}, the magnetic flux density B and the contact stroke s. According to [10], the velocity of the electrons increases with increasing electric field strength and constant magnetic field, which leads to higher kinetic energy and fundamentally increases the probability of ionization. At the same time, however, the electrons reach the anode more quickly and experience fewer ionization collisions on the way there. As a result, the investigations also show that, with coordinated test voltage U_{DC} and magnetic flux density B, the test voltage has no significant influence on the measurable pressure range of the magnetron discharge.

Based on the geometric dimensions of the anode and cathode, a higher minimum flux density B_{min} is usually needed to ignite the magnetron discharge at VIs with smaller dimensions than VIs with greater sizes. Also, the required minimum flux density depends on the internal pressure of the VI. At lower internal pressures, a higher B_{min} is necessary to initiate a discharge at a constant test voltage. In order for the magnetron discharge current to become largely independent of the magnetic flux density, it is, moreover, necessary to have a higher magnetic flux density $B > B_{min}$ [7]. The variation in the contact stroke has no significant influence on the ignition or amplitude of the magnetron discharge, as this occurs exclusively radially between the contact surfaces or the stem surfaces and the middle shield. There is no magnetron discharge in the axial direction between the contact themselves, as there is insufficient extension of the electron trajectories in this area, which would be necessary for effective impact ionization.

For the test campaign, a constant set of parameters was found for the ignition of the magnetron discharge, which is reliable for the influencing parameters considered: total volume, volume enclosed by the middle shield, impact of contact surface area and dependencies by the area given by the middle shield.

III. Internal pressure characteristics

Keeping the described set of parameters, the high voltage feeding direction and the filling gas nitrogen (N2) consistent, the measurement results were recorded to be correctly mapped with a coefficient of determination in a range of 98% to 99%.

The evaluation of the internal pressure characteristic curves shown in Figure 3 reveals that magnetron discharges of varying strengths are developed towards lower pressures. As stated, test object 1 is the structural smallest VI and test object 4 the largest VI of the examination objects. A direct correlation can be observed between the magnetron discharge current and the interrupter size, with the effect being more pronounced at low pressure of 1×10^{-7} hPa than at increasing pressure up to 4×10^{-3} hPa.

At a pressure of 1×10^{-7} hPa, the discharge current in test object 4 is approximately 3×10^{-6} A, while a current of about 3.5×10^{-7} A is measured in test object 1. At a pressure of 4×10^{-4} hPa, the discharge current in test object 4 rises to approximately 7×10^{-3} A, while test object 1 has a discharge current of approximately 5×10^{-3} A. Across the entire investigated pressure range, the magnetron discharge current measured in test object 4 is always higher than that in test object 1.

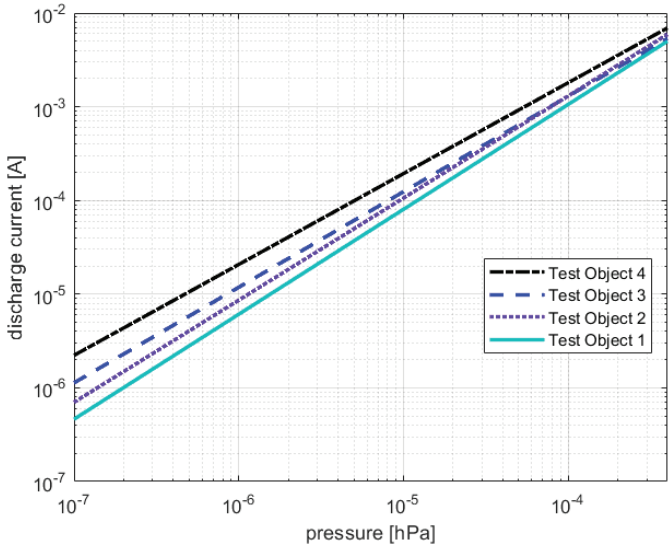


Fig. 3. Internal pressure curve depending on total volume

A. *Dependencies of the magnetron discharge of the volume enclosed by the middle shield*

The relationship between the magnetron discharge and the volume enclosed by the middle shield is depicted in Figure 4.

The magnetron discharge current exhibits a direct proportionality to the pressure within the vacuum interrupter and the volume enclosed by the middle shield. It is imperative to note that test objects 1, 3, and 4 have been normalized in relation to test object 2, which is designated as the reference point and has been set to 100%. Test objects 1, 3, and 4 have volumes of about 40%, 125%, and 170% of test object 2, respectively.

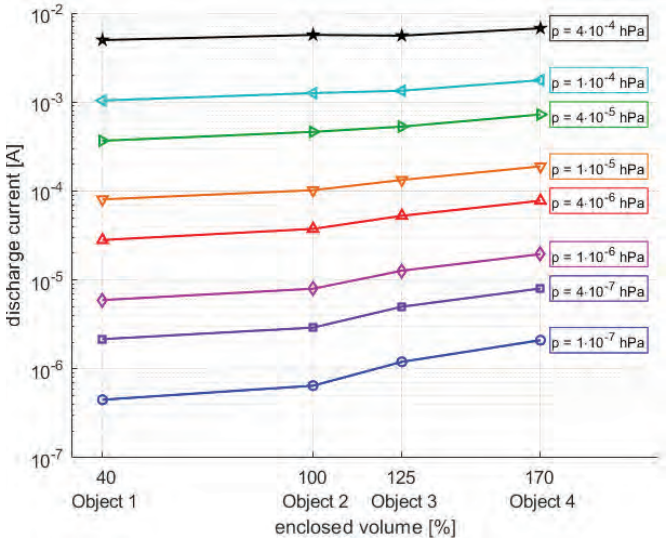


Fig. 4. Discharge current in relation to the volume enclosed by the middle shield

An increase in magnetron discharge current is observed with increasing VI pressure and volume. This effect is particularly pronounced at a pressure of 1×10^{-7} hPa and decreases with increasing pressure up to 4×10^{-4} hPa. At a pressure of 1×10^{-7} hPa, test object 1 reaches 70% of the current value of test object 2, while test objects 3 and 4 reach 185% and 325%, respectively. Conversely, at 4×10^{-4} hPa, test object 1 exhibits a nearly constant current value of approximately 90% of the reference value, which remains relatively stable throughout the pressure decrease. At the highest pressure level, test object 3 approaches 95% of the reference magnetron discharge current, while test object 4 attains approximately 120% of this value.

This phenomenon is attributable to underlying ionization processes. As the volume increases, the number of electrons and ions generated by impact ionization along the discharge path concomitantly increases. The magnitude of the aforementioned quantity is directly proportional to the density of the free electrons that are already present. The resulting discharge current is contingent upon the emission and ion currents, exhibiting a direct proportionality to the number of electrons and ions generated by collision ionization. Therefore, an increase in the number of available electrons results in an increase in the discharge current, a phenomenon that is more pronounced at larger volumes.

B. *Dependencies of the magnetron discharge of the area given by the middle shield*

The investigation of the influences on the magnetron discharge of the area given by the middle shielding are illustrated in the subsequent Figure 5 and indicate a correlation with its effective internal surface area. Based on this relationship, it is possible to apply the results illustrated in Figure 4 and the phenomenon described to the relative influence of the middle shield area.

In Figure 5, normalization to test object 2 as a reference corresponds to an area of approximately 50% for test object 1, while the test objects 3 and 4 have values of approximately 125% and 140%, respectively.

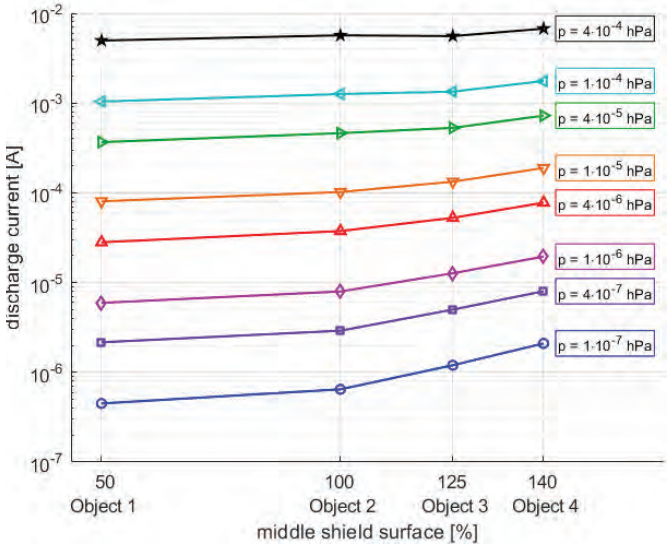


Fig. 5. Discharge current in relation to the area given by the middle shield

The magnetron discharge currents shown and their reference values to test object 2 correspond to the same values as in Figure 4. However, these scale differently across the different geometric sizes, so a new perspective must be applied. The chosen perspective results from the geometric relationships defined by the ratio of discharge current to the geometry under consideration in reference to test object 2. As a result, the influence of the geometric parameter under consideration can be described and compared in correlation with the pressure. For clarification, the ratio for the pressures 1×10^{-7} hPa and 4×10^{-4} hPa is evaluated. This shows a trend

whereby at low pressures of 1×10^{-7} hPa, the ratio of discharge current to the area given by the middle shield of test object 1 to test object 4 doubles. In contrast, at higher pressures of 4×10^{-4} hPa, the ratio between test objects 1 and 4 is reduced by approximately 40%.

These observations indicate a direct proportionality between the discharge current and both the effective shield area and the VI pressure. The influence of the shield area is more pronounced at low pressures than at elevated pressures.

C. *Dependencies of the magnetron discharge of contact perimeter surface area*

In addition to the previous shown parameters: enclosed volume and middle shield area, another geometric parameter has a measurable influence on the magnetron discharge. The contact circumference area has a direct correlation with the previous parameters A and B and thus has an equivalent influence on the discharge.

As displayed in Figure 6, the magnetron discharge current is depicted as a function of the contact area, with the data on test object 2 being adjusted to a benchmark. The contact area of test object 1 is approximately 80% of that of test object 2, while test object 3 has approximately 140%, and test object 4 has about 190% of the reference area.

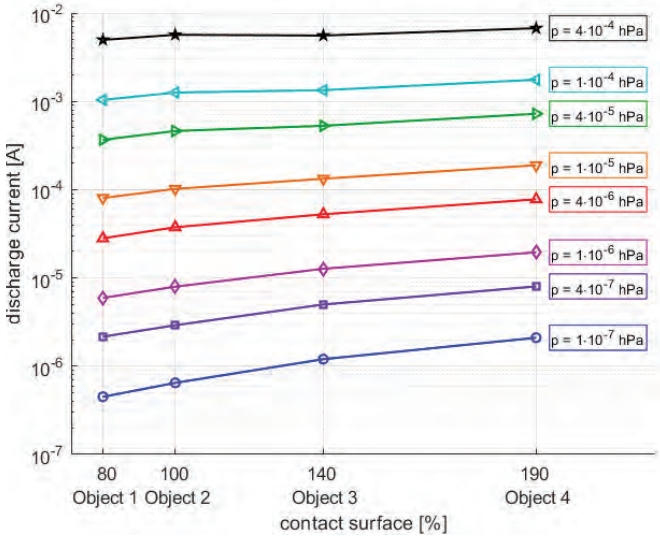


Fig. 6. Discharge current in relation to the contact perimeter surface area

This analysis also examines and compares the ratio of discharge current to the geometry under consideration or contact perimeter surface area. The equivalent trend can also be seen here, with an increase of 70% at 1×10^{-7} hPa between test objects 1 and 4. At lower pressures of 4×10^{-4} hPa, the current to geometric factor ratio also decreases by approximately 100%.

The analysis of the contact perimeter surface area shows that the discharge current increases with growing contact perimeter surface area. This relationship can be explained by surface ionization processes, which describe the release of electrons through field emissions or secondary processes from the cathode surface. Surface ionization processes contribute to the initiation of magnetron discharge in addition to volume ionization processes (e.g. collision ionization). Field emission contributes to the initial supply of electrons through microscopic irregularities on the surface of the cathode due to strong local electric fields. A larger contact perimeter surface area increases the probability that there will be enough of these field amplification points on the surface, thereby increasing the total number of electrons emitted. An additional mechanism for electron release is secondary field emission: ions strike the cathode and release electrons from the surface. As the contact area increases, the probability that more ions will strike the cathode also increases.

D. *Dependencies of the magnetron discharge of the estimated accumulation area*

The parameters studied above illustrate the fundamental influence on magnetron discharge without defining the actual area of the magnetron discharge in more detail. For a specific view of this region, the accumulation area is used. This area approximately describes the sum of two ring volumes located at the height between the contact and the shield, and between the shield and the stamp on the opposite electrode, where the distance is smallest (see D_1 and D_2 in Fig.1). In this two regions the highest probability of the most dense charge carrier accumulation exists.

In Figure 7 the generated discharge current is plotted in relation to the volume of the estimated accumulation areas. The volumes of test objects 1, 3, and 4 correspond to 60%, 190%, and 230% of the volume of test object 2, normalized. The diagram displays an approximately linear increase in current values comparing the volumes of the test objects on the logarithmic scale, which is less significant for pressure values above 1×10^{-5} hPa.

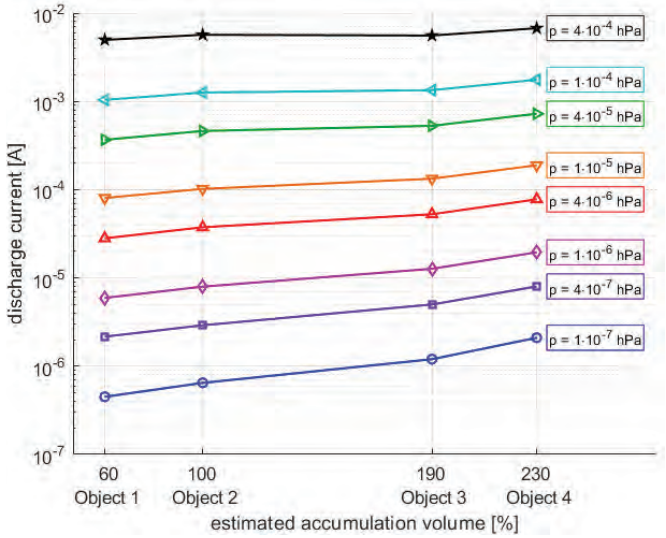


Fig. 7. Discharge current in relation to the estimated accumulation volume area

At the lowest measured pressure of 1×10^{-7} hPa, the ratio of the discharge current to the estimated accumulation volume is 110% for test object 1 and 140% for test object 4, resulting in a trend of +25% for larger geometries and this pressure range. At a pressure of 4×10^{-4} hPa, there is again a decreasing trend of –65% between test objects 1 and 4.

The phenomenon observed in Figure 7 and the consideration of the ratio of discharge current to the specified geometry repeatedly confirm the dependencies of the geometric parameters in both small and larger pressure ranges. This shows the direct correlation between the current that occurs and the available accumulation volume of the charge

carriers contributing to the two magnetron discharges in series in this test arrangement.

IV. CONCLUSION

The magnetron method is a well-established test procedure for the internal pressure measurement of VIs. Its application during manufacturing process and after a considerable period of service and towards the end of the expected service life for its extension, is crucial for determining the vacuum quality. The magnetron measurement requires a precise knowledge of a wide range of parameters: direct high voltage, magnetic flux density, feeding direction, design criteria and many more.

In this study, the ignition characteristics of magnetron discharges are systematically examined and indicate the influence of multi geometric parameters on the expected internal pressure characteristic. The basic principles of the Magnetron discharge is the result of the extension of electron trajectories within a cylindrical electrode arrangement, that is primarily dependent on the presence of a residual gas volume. In order to analyze this dependence, geometric influencing factors are identified, and the magnetron discharge current is examined and visualized as a function of variations in the total volume, the enclosed volume by the middle shield, the area given by the middle shield, the contact perimeter surface area and the estimated accumulation area. The proportionality of the magnetron discharge to the gas volume in areas where the electric and magnetic fields are orthogonal to each other is specified on the basis of real application cases. The extension of the charge carrier paths and the resulting measurable current amplitude for the geometries investigated are described in a pressure range from 1×10^{-7} hPa to 4×10^{-4} hPa.

The results demonstrate that the discharge current is contingent on geometry and pressure, with an augmentation in the magnetron discharge current concomitant with an increase in the geometric parameters under consideration. The correlation is more pronounced at low pressures and decreases with increasing pressure. The consolidation of the results suggests that magnetron discharge is predictable within a specific range of discharge currents. It demonstrates that there is a direct relationship between the volume enclosed by the middle shield, the area given by the middle shield, the contact perimeter surface area and the estimated accumulation area of the dominant charge carriers which trigger the magnetron discharge.

Further investigations are necessary to describe the interactions between contact size and middle shield at constant shield design. This approach can highlight the dependence on geometric factors and enables predictions to be made about the internal pressure and its characteristics. At the same time, the significance of the measurement results must be taken into account and substantiated by a large number of samples. The use of statistics in future investigations, such as confidence intervals and distribution functions, allows the significance of the influences to be evaluated in more depth.

REFERENCES

[1] D. Gentsch, T.Fugel, “Measurements by residual gas analysis (RGA) inside vacuum interrupters / devices”, XXIII-rd Int. Symp. on Discharges and Electrical Insulation in Vacuum, Bucharest, Romania – 2008.

[2] R. Renz et al., “Vacuum Interrupters – Sealed for Life”, 19th International Conference on Electricity Distribution, CIRED, Vienna, 2007.

[3] M.Weuffel et al., “Influence of the Residual Gas Composition and the Getter-Ion Effect on the Measurement of the Internal Pressure in Vacuum Interrupters”, XXVI Int. Symp. on Discharges and Electrical Insulation in Vacuum - Mumbai, India – 2014.

[4] M.Weuffel et al., “The Influence of Current Interruption Operations on Internal Pressure in Vacuum Interrupters”, IEEE Transactions on Plasma Science, Vol. 45, No. 8, 2017.

[5] Frontzek, F., König, D., Heinemeyer, R., “Electrical methods for verifying internal pressure of vacuum interrupters after long-time service”, IEEE Transactions on Electrical Insulation, Vol. 28, pp. 635–641, August 1993.

[6] M.Weuffel et al., “The Influence of Temperature on Internal Pressure in Vacuum Interrupters in a Liquid Nitrogen Environment”, XXVIIth Int. Symp. on Discharges and Electrical Insulation in Vacuum, Suzhou, 2016.

[7] M. Weuffel, „Schaltkammerspezifische Einflussgrößen auf die Vor-Ort Messung des Innendrucks von Vakuum-Schaltkammern mit dem Magnetron-Verfahren“, Aachen, Deutschland: Dissertation, RWTH Aachen, 2018.

[8] K. Hencken et al., “Modeling and Simulation of Magnetron Discharges inside a Vacuum Interrupter as a Method to Analyze the Vacuum Status”, XXVIIth Int. Symp. on Discharges and Electrical Insulation in Vacuum, Suzhou, China, 2016

[9] A. W. Hull, „The Effect of A Uniform Magnetic Field on the Motion of Electrons Between Coaxial Cylinders.,“ Physics Review, Bd. 18, pp. 31- 62, 1921.

[10] M. M. Alenka Vesel, „Discharge characteristics of a magnetron cell in ultrahigh vacuum,“ Vacuum, Bd. 67, Nr. 5, p. 629–633, 2002.

A framework for holistic durability assessment of wire-connector systems under vibrational load – The influence of connector arrangement and wire routings

Roman Probst*, Dirk Hilmert, Frederik Kiel, Jian Song
Precision Engineering Laboratory
OWL University of Applied Sciences and Arts (TH OWL)
Lemgo, Germany
*Corresponding author: roman.probst@th-owl.de

***Abstract*—This research investigates the influence of electrical connector orientation and wire routing on wear behavior and vibration response under dynamic loading. Different connector configurations were evaluated, including flat and standing options combined with straight and angled wire routings. The results demonstrate that the flat connector option represents the critical case, exhibiting the highest wear depth and longest wear scars. In contrast, the standing options show an improved performance, largely independent of whether the wire routing is straight or angled. For identical wire lengths between the connector housing and wire fixation, bending of the wire does not markedly affect wear characteristics.**

Beyond geometric effects, the experiments reveal a strong dependence of connector vibration behavior on wire fastening conditions. Mounting elements such as spacer sleeves can amplify structural resonances, leading to increased dynamic loading at certain frequencies, whereas stiffened wire attachments effectively suppress these resonances and produce a vibration response closer to the target excitation. These findings highlight that connector durability is affected not only by connector geometry and wire routing, but also by the dynamic properties of the mounting structure. Therefore, connector service life evaluation should be conducted at the system level, considering the coupled interaction between connector, wire and attachment base.

Keywords—electrical connectors; dynamic loading; wear behavior; connector orientation; wire routing; vibration dynamics

I. Introduction

Electrical connectors in automotive, aerospace, and industrial applications are frequently exposed to complex vibrational loads throughout their operational lifetime. These loads can induce micro-motion which causes fretting wear and fretting corrosion at the contact interface, ultimately contributing to an increased electrical resistance, degraded signal integrity and connecting failures. While the influence of vibration on connector wear has been addressed in previous studies, the combined effects of conductor orientation, wire routing and geometry remain insufficiently quantified for wire-connector systems [1, 2, 3, 4].

Connectors are usually tested in a standardized configuration with a flat arrangement and the wire in line with the connector. In practical installations, connectors are used in various configurations of the connector arrangement and wire routings due to spatial constraints and packaging limitations. The wire harness dynamics can result in diverse motion directions of contact elements. These motions can alter the mechanical coupling between the wire and the connector housing, modifying the local mechanical loads within the contact region. Furthermore, the mechanical impedance of the wire, governed in part by its diameter, may influence the amplitude and frequency spectrum of transmitted vibration [5, 6, 7].

In order to obtain a robust understanding of these interacting factors, this study investigates the wear behavior of electrical connectors subjected to controlled vibrational loads across multiple conductor orientations and wire routings. The primary objective is to identify the worst-case combination of parameters that leads to the most severe wear within the wire-connector system. This worst-case scenario will serve as the foundation for subsequent, more detailed investigations and will ultimately influence the development of a predictive simulation model capable of estimating connector degradation under operational vibrational profiles and in various combinations of connector arrangements and wire routings.

II. Test Setup

A. Overview

The test setup is designed to create a controlled and repeatable vibrational environment for evaluating connector wear across multiple parameter combinations. All tests use the same base connector type, with variations only in the parameters under study: conductor orientation and wire routing.

B. Connector-wire Options

Each connector is mounted on a rigid fixture directly coupled to an electrodynamic shaker system. The fixture is designed to shift the resonance frequencies to a frequency range outside the test or application cases and to ensure that the dominant vibrational energy is transmitted through the connector and attached wire. Connectors with a blade width of 6.3 mm and attached wires with a diameter of 6 mm² are used for this study.

Two different wire routings are evaluated:

- Straight orientation: The wire is aligned with the connector's longitudinal axis (Fig. 1).

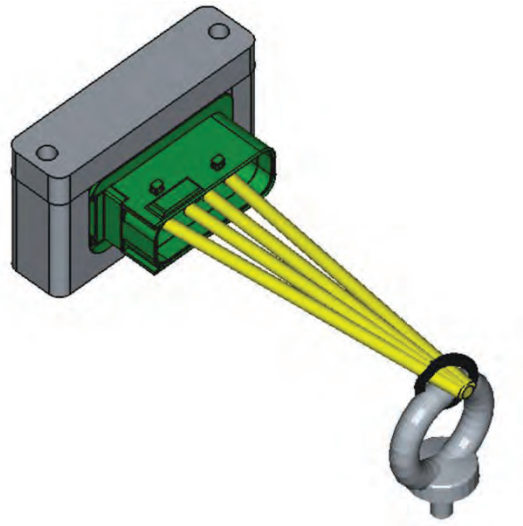


Fig. 1. Exemplary illustration of the straight wire orientation

- 90° angled orientation: The wire exiting the connector is bend by 90°. A consistent bend radius is used to standardize cross-test comparability (Fig. 2).

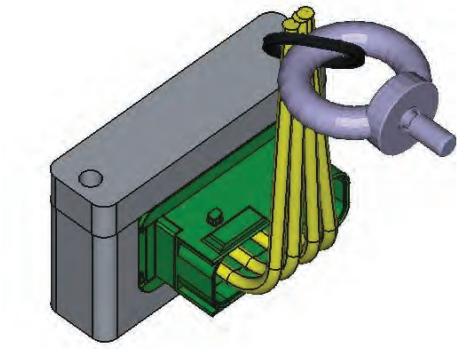


Fig. 2. Exemplary illustration of the 90° angled orientation of the wire

III. Methods

A. Experimental Matrix

A factorial test design is implemented to evaluate the independent and interactive influences of the studied parameters. Each combination of:

- conductor orientation (flat, upright, standing), and
- wire routing (straight, 90° angled with a radius of approx. 15 mm)

is tested under identical environmental and vibrational conditions. Selected test cases are replicated to verify repeatability.

The various orientations and wire routings are presented in Fig. 3. For the testing of both parameters with two and three factors respectively, a total number of six different mountings is necessary. These combinations are summarized in Table I.

TABLE I. Summary of the different mounting orientations and wire routings used

Connector options on the test plate	Sample name
Option 1	Upright angled
Option 2	Flat straight
Option 3	Upright straight
Option 4	Standing angled
Option 5	Standing straight
Option 6	Flat angled

B. Vibration Excitation

Vibration tests are conducted according to the vibration profile defined in TLF0214 – PG 17 – Vibration Class V4 [4], representing a severe mechanical environment characteristic of demanding automotive applications. The profile specifies acceleration levels, frequency content, and load duration necessary to achieve realistic vibrational loads on the connector interface.

The main excitation test includes:

- Swept sinusoidal vibration from 100 to 440 Hz
- Acceleration level: 111 m/s² (11.3 g)
- Sweep rate: 1 octave per minute
- Continuous excitation for 22 h without pauses

Acceleration control is based on direct feedback from the fixture-mounted accelerometers to ensure full compliance with the Vibration Class V4 profile.

Resonance characterization is performed using a swept sine excitation with the following parameters in order to specifically scan the frequency band both upward and downward:

- Frequency range: 10 Hz to 2,000 Hz
- Acceleration level: 19.62 m/s² (2 g)
- Sweep rate: 1 octave per minute

This excitation profile is selected to enable clear identification of the resonance frequencies. The frequency band selected is identical to that used in the random vibration test. At the same time, a controlled and repeatable load condition (19.62 m/s² or 2 g) is maintained across the entire relevant frequency spectrum.

C. Test Procedure

Before testing, all connector assemblies are electrically verified to ensure correct baseline conditions. Accelerometer data ensure real-time validation of the applied vibration spectrum. For this, the weighted average of data from two vibration sensors (one sensor is placed directly at the shaker, another sensor is placed close to the connectors / contact points on the test plate) is used to control the shaker. Analogical to TLF0214 – PG 17 [4] strain-relief elements are applied at a defined distance of 100 mm to the connector housing.

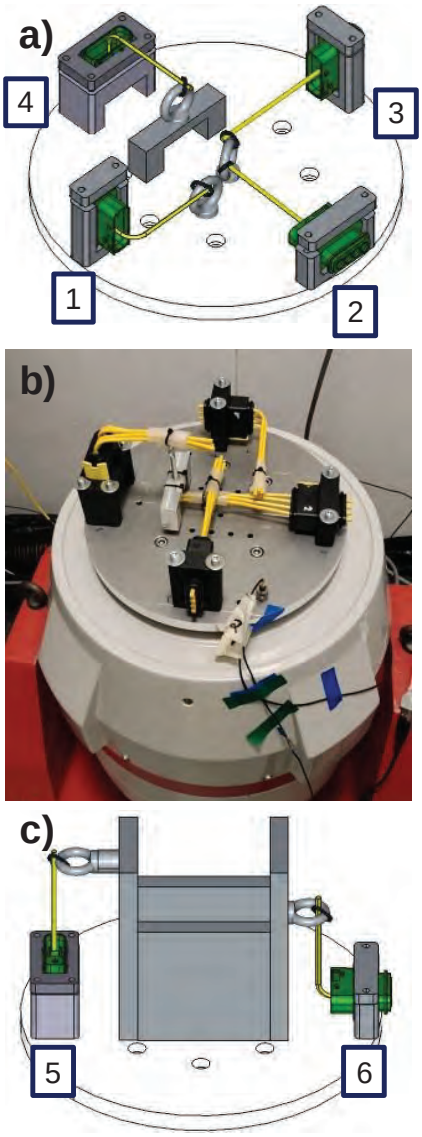


Fig. 3. Overview of the various mounting options of the connectors; a) shows a schematic illustration of test rig 1; b) shows the test rig 1 mounted on the shaker and c) illustrates test rig 2

D. *Wear Analysis*

After each test, connectors are removed from the fixture, disassembled, and subjected to a systematical analysis of wear. This includes:

- Optical microscopy to document the overall wear pattern and to determine the extent of the wear scars.
- X-Ray fluorescence analysis to quantify wear scar depth and material loss.

As a first step, the contact blades are examined using digital light microscopy. The length of the wear scars is measured as illustrated in Fig. 4.

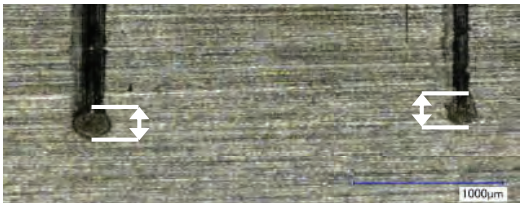


Fig. 4. Exemplary measurement of the wear scar length

In addition to this, the wear depth is measured by means of x-ray fluorescence analysis. The remaining coating thickness is measured and subtracted from the reference value. For the blades, 3 reference values are measured on each side of each blade. For the receptacles however, the reference coating thickness cannot be measured reliably on the tested connectors due to the rounding of the contact points. For this reason, the coating thickness of the receptacles is measured on unused connectors. 5 connectors with 4 lamellas each and 3 measuring points per lamella result in a total number of 60 values. Here the average value of 2.85 µm silver is also taken as reference.

Wear metrics from all options are compared to identify the degree of wear of every combination of parameters and especially the parameter combinations that resulted in the most severe and the lightest degradation. The identified worst-case scenario will provide the foundation for future extended testing and the calibration of a predictive simulation model. The best cases serve as the preferred options of connector arrangements and wire routings.

IV. Test Results

A. *Swept Sine for Critical Orientation*

Wear tests are conducted in order to ascertain the critical orientation of electrical connectors during vibrational loads. Once the 22 h vibration test has been completed, the electrical connectors are removed from their housings and prepared for wear analysis.

Exemplary wear scars of both blade and receptacle of the worst-case option (connector 2; flat straight) are shown in Fig. 5.

The following Fig. 6 summarizes the results of the wear scar analysis. The numbers in each column represent the respective rank of the option where 1 means the worst-case with the largest wear scars and 6 the best case with the lowest wear. The options “flat straight” and “flat angled” result in the largest wear scars both in wear depth of the lamellas (approx. 0.8 µm and 0.7 µm respectively) and length of the wear scars of the blades with approx. 140 µm and 155 µm respectively.

Options “standing straight” and “standing angled” result in the smallest wear scars (approx. 0.5 µm wear depth each; approx. 126 µm and 121 µm wear scar length) and are therefore the preferred installation directions. The two upright options lie in between these options. However, there are only minor differences between all options with overlapping spreads (±1 standard deviation) of the results. In addition, no significant differences between the straight and angled options can be observed.

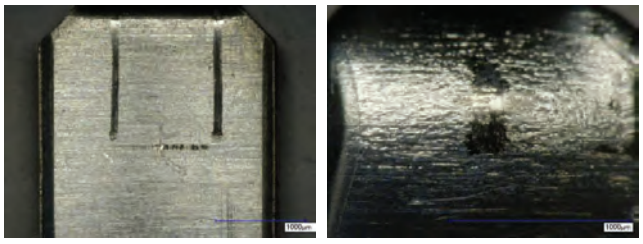


Fig. 5. Exemplary wear pattern of a blade with flat straight orientation (option 2) (left side) and the respective receptacle (right side)



Fig. 6. Results of the wear scar analysis of the swept sine test; the left column of each block represents the wear depth of the lamellas on the left Y-axis; the right column represents the wear scar length of the blades on the right Y-axis

B. *Random Vibration Load and Resonance Analysis*

1) *Objective*

In addition to the test conducted with the swept sinusoidal vibrational load (100 to 440 Hz), a further test with a random vibration profile is performed. This test is also carried out in accordance with Vibration Class 4 of the TLF0214 – PG 17 [4] (10 to 2,000 Hz). Here, severe wear on the surfaces of connectors in combination 5 (standing connector with straight wire) is observed which is contradictory to the sine-test results and a previous research project [8]. For this reason, resonance tests are carried out on the test rig in order to evaluate how the structural characteristics of the test setup—particularly test height, mounting position, and connection elements—influence the fidelity of the applied vibration profile relative to the shaker input. Special attention is paid to deviations caused by local resonances, as these can significantly alter the effective loading at the connector interface.

2) *Test Rig*

As shown in Fig. 3 four vertically installed aluminium plates are fixed to the base plate, forming a rigid tower structure at its center. This modular design enables different effective test heights corresponding to the straight and 90° conductor options used in the main wear tests. For the resonance test, two measurement positions are evaluated as indicated in the setup schematic (Fig. 7).

- (a) represents the standard case used for the initial test
- (b) uses the largest possible spacer block for this test setup, without colliding with the test specimen

In each of these cases, an additional third accelerometer is mounted as a monitoring sensor to record the local vibration response. Shaker control is achieved using the two accelerometers mounted on the base plate and on the shaker head itself, as described in section III-C. The control signal is derived from the weighted average of these two sensors to ensure stable excitation and minimize local bias effects.

3) *Results and Observations*

The measurements reveal a clear dependence of vibration fidelity on both sensor position and mechanical interface configuration. The acceleration responses of different mounting positions and fixtures are shown in Fig. 8.

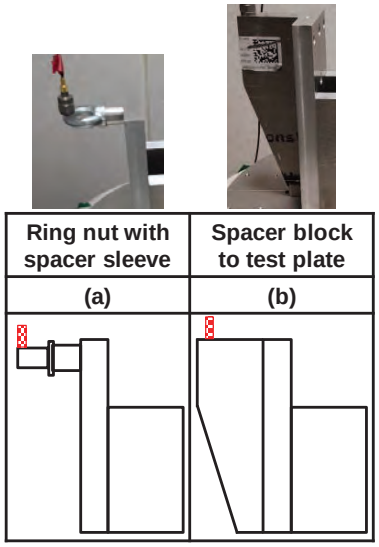


Fig. 7. Different test setups used for the resonance analysis

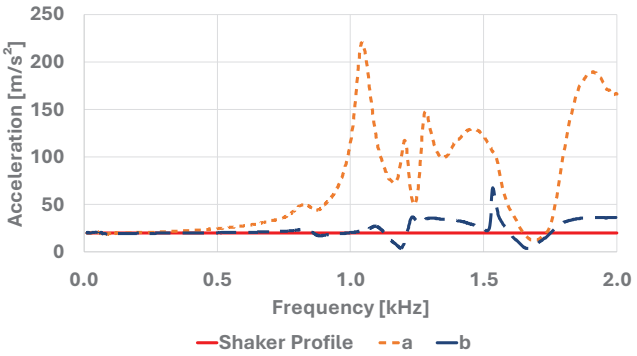


Fig. 8. Overview of the acceleration responses of the initial mounting position (a) and improved fixture (b) in comparison to the shaker profile

Measurements with configuration (a) when the spacer sleeve is used (orange dashed line) show pronounced deviations near resonance frequencies. The inclusion of spacer sleeves introduces additional compliance into the load path, amplifying local resonance effects. Three dominant resonance peaks are consistently identified at approximately 1,050 Hz, 1,210 Hz, and 1,290 Hz leading to acceleration peaks of approx. 215 m/s², 115 m/s² and 146 m/s², respectively.

In contrast, configuration (b) with the largest possible spacer block (dark blue dashed line) exhibits a significantly smaller deviation from the intended shaker-driven vibration profile. This position displays a more uniform acceleration response across the frequency range with the only peak at approximately 1,530 Hz.

Without the spacer sleeve, the deviation from the target vibration profile at these peak frequencies is reduced by approximately 50–70 % compared to the configuration with spacer. This indicates that minimizing compliant interfaces significantly improves vibration transmission fidelity. The stiffening of the frame shifts the resonance frequency upwards from 1,050 Hz to 1,530 Hz.

The same behavior can be detected when observing the deflection response of the different configurations (Fig. 9). At about 1,050 Hz configuration (a) shows a large deviation from the shaker profile. The maximum oscillation of the shaker at

this frequency according to the vibration profile is only 1 µm, whereas in configuration (a) with the spacer sleeve a maximum oscillation of approx. 10 µm is observed. Configuration (b) with the spacer block reaching all the way to the base of the test setup shows a large improvement with the only significant peak at 1,530 Hz with a deflection of only 1.5 µm. At this frequency, the maximum oscillation of the shaker is approximately 0.5 µm, which represents an improvement from a factor of 10 to approximately a factor of 3. Thus, the resonance vibration is significantly reduced with the stiffening of the frame.

The reduced resonance effects are also reflected in the wear pattern of the contacts. As previously mentioned, the results of the test with random excitation differ from those with the swept sine excitation. On the one hand, the wear values are significantly higher for the random excitation tests. In the worst case of this test, the wear depth is now approx. 2 µm compared to about 0.8 µm in the worst case of the swept sine test. On the other hand, however, option 5 (standing arrangement with straight line routing), also shows the most severe wear pattern, whereas this arrangement is still one of the options with the lowest wear pattern in the swept sine test. The results of the test with random vibrational load are shown in Fig. 10. The wear results for the stiffened attachment point are also illustrated in this figure. It is clear that reinforcing this attachment leads to a significant decrease in the wear depth. Specifically, the maximum wear depth decreases from approximately 2 µm to approximately 1.6 µm. Under random vibrational loading, the excitation encompasses a broad frequency range and therefore interacts with multiple natural frequencies of the system. Consequently, the resulting wear ranking differs from that observed in the swept-sine excitation case. While increasing the stiffness of the attachment point mitigates the influence of resonant responses, it does not fully eliminate resonance-induced wear effects.

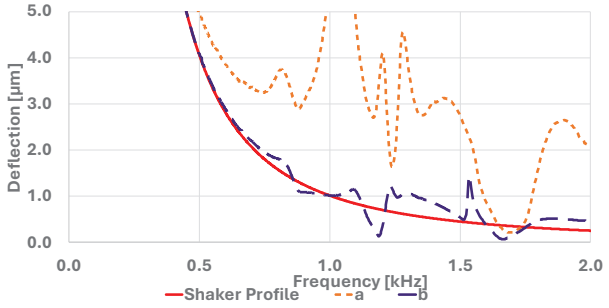


Fig. 9. Overview of the deflection responses of the initial mounting position (a) and improved fixture (b) in comparison to the shaker profile

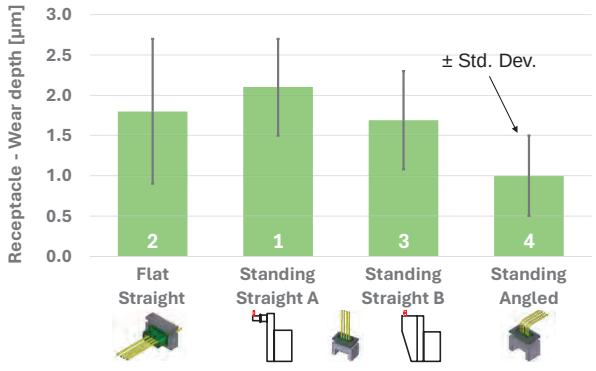


Fig. 10. Results of the wear depth analysis of the random test

4) Implications for Connector Systems and Wear Testing

The resonance investigation demonstrates that connector durability under vibrational loading depends not only on wire routing and conductor orientation, but also strongly on the mechanical properties of the structure on which the connector is mounted. While optimized wire routing can mitigate bending loads, the results demonstrate that local mounting compliance can significantly alter the effective vibration experienced at the connector interface.

Mounting elements such as spacer sleeves were shown to amplify structural resonances, leading to increased dynamic loading at specific frequencies. In contrast, a stiff and mechanically continuous mounting interface substantially reduced resonance effects and improved alignment with the intended vibration profile.

This finding is especially relevant for automotive applications, where connectors are often attached to flexible brackets or thin sheet-metal structures with variable boundary conditions. As a result, connector service life must be evaluated at the system level, considering the combined dynamics of the connector, wire, and mounting base rather than wire-connectors alone.

V. Conclusion

This study illustrates the influence of the arrangement of electrical connectors and their wire routings. It can be seen that the flat option of the connector represents the worst-case behavior for both wear depth and wear scar length. In contrast to this, the standing options both with straight and angled wire routings appear to be the favorable arrangement.

As the results show, a bending of the wire does not appear to have a significant impact on the wear pattern of the connectors. Both in terms of wear depth and wear scar length, the variants with straight wire routing and angled wire routing are very similar. It should however be noted, that the wire length between the housing and the wire fixing was identical in both cases at 100 mm.

The tests revealed a clear dependence of connector vibration behavior not only on the vibration type but also on the fastening of the wires: mounting elements such as spacer sleeves can amplify structural resonances and increase dynamic loading at specific frequencies, whereas stiffening the wire attachments substantially attenuates these resonance effects and yields a vibration response closer to the intended profile. For the investigated attachment stiffening configuration, the dominant resonance was shifted toward higher frequencies; however, complete compensation was not achieved. This finding demonstrates that connector performance depends not only on the connector geometry and wire routing but also on the dynamic characteristics of the mounting structure. Accordingly, ongoing work focuses on further mitigating resonance effects through targeted design modifications.

Consequently, connector service life should be assessed at the system level, accounting for the coupled behavior of the connector, wire, and attachment base, rather than merely considering the wire-connector system in isolation.

ACKNOWLEDGMENT

This study is financed by the German Federal Ministry for Economic Affairs and Energy (BMWE, IGF, 23011 N).



The authors would also like to thank TE Connectivity for providing the test specimens.

REFERENCES

[1] H. Yuan, D. Hilmert, A. Shukla and J. Song, "Effect of Direction of Motion on Fretting Corrosion Behaviour," *2021 IEEE 66th Holm Conference on Electrical Contacts*, pp. 38-45, 2021.

[2] J. Swingler, J. W. McBride and C. Maul, "Degradation of road tested automotive connectors," *IEEE Transactions on Components and Packaging Technologies*, pp. 157-164, 2002.

[3] S. Fouvry, J. Laporte, O. Perrinet, P. Jedrzejczyk, O. Graton, O. Alquier and J. Sautel, "Fretting wear of low current electrical contacts: Quantification of electrical endurance," *2017 63th IEEE Holm Conference on Electrical Contacts*, pp. 1-11, 2017.

[4] N.N., "Validation of Low Voltage Automotive Connectors," *Technical Guideline - TLF 0214*, ZVEI, 2024.

[5] R. Probst and J. Song, "Vibration of Wire-Connector Systems and its Influence on Micro Motion of Electrical Contacts," *2024 IEEE 69th Holm Conference on Electrical Contacts*, pp. 135-140, 2024.

[6] F. Zhang, G. T. Flowers, R. N. Dean, J. Suhling and J. Gao, "A Study on Axial Vibration-induced Fretting Corrosion in Electrical Connector Pair," *2016 IEEE 62nd Holm Conference on Electrical Contacts*, pp. 146-151, 2016.

[7] B. Amel, C. Erwann, B. Noureddine, T. Laurent and Z. El Mostafa, "Influence of Cable Vibrations on Connectors Used in Automotive Applications," *Journal of Electrical and Electronics Engineering*, vol. 5, no. 2, pp. 11-16, 2012.

[8] D. Hilmert, K. Krüger and J. Song, "Vergleichende Untersuchung der Verschleißbilder von Steckverbindern aus Reibverschleiß- und Vibrationsprüfungen mit unterschiedlichen Prüfrichtungen," *Tribologie und Schmierungstechnik*, pp. 41-49, 2021.

Effect of water content on ablative mechanism of gassing materials under arc action

Qian Wang
Xi'an University of Technology
Xi'an, China
qianwang@xaut.edu.cn

Yi Shang
Xi'an University of Technology
Xi'an, China
1730190487@qq.com

Weidong Cao
Xi'an Jiaotong University
line 4: Xi'an, China
wdcao@stu.xjtu.edu.cn

Wanmeng Zhao
Xi'an University of Technology
Xi'an, China
zhaowanmengg@qq.com

Yuxuan Liu
Xi'an University of Technology
Xi'an, China
1132045156@qq.com

Xu Zhong
Xi'an University of Technology
Xi'an, China
3433615644@qq.com

Abstract—The rapid development of renewable energy poses a serious challenge to the disconnecting ability of direct current (DC) circuit breaker in power system. The gassing material can significantly enhance the breaking performance of DC circuit breakers. However, the exposure of circuit breaker gassing materials to high-humidity environments, commonly in humid southern regions, can adversely affect the breaking performance of the circuit breaker due to moisture absorption. Therefore, it is important to study the influence of water content on the decomposition products of gassing materials. The decomposition process of PA66 at various water contents was simulated through reactive force field molecular dynamics. Based on the simulation results, the underlying reaction mechanisms were further explored and explained. The addition of an appropriate amount of water promotes the decomposition of PA66 and the formation of small-molecule products, tar, and coke. Conversely, excessive water content may inhibit decomposition. The research provides a theoretical basis for the decomposition principle of gassing materials under humid conditions, and supports the rational selection of these materials for DC circuit breakers in humid regions.

Keywords: Breaker, Decomposition, PA66, ReaxFF, Water Content

I. INTRODUCTION

In response to China's national carbon peak and carbon neutral goals, photovoltaic, hydrogen, and other green energies have been developing rapidly[1] [2]. In the power transmission and distribution system, DC circuit breakers play a vital role. In cases of system disturbances, such as short circuits or overloads, circuit breakers automatically trip to prevent further losses. However, the DC circuit breaker does not have the natural zero point of the AC circuit breaker the DC circuit breaker lacks the natural zero of an AC breaker, which makes arc extinction more difficult and increases the risk of contact ablation, equipment damage, or even fire. To maintain the stable and secure operation of the electrical power system, it is necessary to apply special arc extinguishing technology. During circuit breaker interruption, the gassing material is specially designed to decomposes under the action of the arc, rapidly generating a large number of gases with high thermal conductivity (such as hydrogen).This process can quickly cool the arc, reduce the diameter of the arc column, and increase the strength of the medium, thereby improving the breaking capacity and overall performance of the circuit breaker[3]. Specifically, this work focuses on low-voltage direct current (LVDC) circuit breakers, where polymeric gassing materials are commonly used to generate arc-quenching gases. Although the arc temperature in low-voltage DC circuit breakers is relatively high, the gassing material (PA66) studied in this work undergoes pyrolysis already at 300 K. In simulation calculations, higher temperatures are typically chosen to accelerate the reaction. Therefore, we selected 1700 K for the simulation.

To improve the breaking performance of circuit breakers, The most direct way to enhance the breaking performance of circuit breakers is to design and conduct targeted experiments. In reference [4], a disassembly-type experimental prototype was developed to compare and analyze the effects of different materials on arc characteristics at various current levels. Indices for evaluating polymer properties were further proposed, providing a theoretical basis for the selection of gassing materials. In reference [5], polyisobutylene was analyzed by gas chromatography, and its high-temperature pyrolysis products were investigated in combination with ReaxFF. However, with the advancement of large-scale computing, simulation capabilities have significantly improved, allowing increasingly complex systems. To reduce costs and resource consumption, accurate and reliable simulation calculations can be employed to screen potential material candidates before conducting specific experiments. Reference [6] and [7] used density functional theory (DFT) to optimize the structure of different materials. Reference [8] studied the durability of fiber-reinforced polymer composites through multi-scale mechanical and molecular dynamics simulations.

Traditional molecular dynamics simulations rely on Newtonian mechanics to calculate interatomic forces, which limits their ability to describe chemical bond breaking and formation; nevertheless, they are still widely applied in engineering fields such as materials science, energy materials, and organic synthesis. Although density functional theory (DFT) calculations based on quantum mechanics are capable of accurately describing these chemical changes, their high computational cost generally renders them impractical for molecular systems containing more than 1,000 atoms[9]. To address this issue, Van Duin developed an approach called the Reactive Force Field (ReaxFF) [10]. Unlike conventional molecular dynamics, ReaxFF can track real-time changes in chemical

This work was supported by the National Natural Science Foundation of China (52277163) and Shaanxi Provincial Department of Education key laboratory project (22JS025).

bonds, including bond formation and breaking, and model systems comprising millions of atoms. As a result, ReaxFF is an ideal tool for analyzing large-scale simulations of chemical bond changes and is widely used in engineering fields such as materials science, energy materials, and organic synthesis. As reported in Ref. [11] and [12], the ReaxFF-MD method was used to study the steam gasification of polypropylene (PP) and the pyrolysis of polyethylene (PE), respectively. In literature [13], the ReaxFF method was used to simulate the effect of water content on the activation energy of PA66, revealing that increasing water content reduces the activation energy of PA66, although the products of PA66 were not analyzed in detail. Based on ReaxFF, Reference [14] calculated the micro-pyrolysis mechanism and macro-pyrolysis kinetics of a typical gassing material, PA66, and the results were compared experimental data. The study investigated the decomposition of PA66 and the generation of its products under hot-field conditions, providing a methodological basis for evaluating the performance of gassing materials used in DC circuit breakers. However, limited research has focused on the behavior of gassing materials under humid conditions.

From the perspective of molecular dynamics, the effect of water on the pyrolysis of gas-producing materials and the properties of their products was studied using the ReaxFF simulation under electric field heating. Taking the most widely used polyamide 66 (PA66) as the research object, ReaxFF was used to simulate it at the atomic scale to study the effects of different water contents and temperatures on the decomposition of PA66 and the formation of main products. It was concluded that an appropriate water content (10%) has the most significant promoting effect on the decomposition of PA66. The promoting effect decreases when the water content is either higher or lower than this value. The promoting effect weakens when the water content deviates from the optimal value, whether higher or lower. The addition of water can significantly promote the formation of tar and coke. High-temperature conditions significantly increase the pyrolysis rate of PA66, promoting more complete decomposition. However, some intermediates may polymerize to form new clusters (C40+), indicating an increased likelihood of coke formation.

II. METHODS

ReaxFF enhances the force field of classical molecular dynamics by incorporating the concepts of bond order and bond energy. It determines the formation or breaking of bonds between atoms based on their interatomic distances. Additionally, ReaxFF introduces the effects of van der Waals forces and Coulomb forces, building upon the principles of Newtonian mechanics. Equation (1.1) defines the commonly used total energy expression in the ReaxFF system, which was proposed by K. Chenoweth. For details on the meaning of each parameter, please refer to reference [15].

$$E_{system} = E_{bond} + E_{lp} + E_{over} + E_{under} + E_{val} + E_{pen} + E_{coa} + E_{C2} + E_{triple} + E_{tors} + E_{conj} + E_{H-bond} + E_{vdWaals} + E_{Coulomb} \quad (0.1)$$

Using Materials Studio modeling software, we constructed models of PA66 monomers and water molecules. In the simulations, considering both computational efficiency and accuracy, a PA66 chain with a degree of polymerization of 8 was selected, and water molecules were placed in a $5\times5\times5$ nm³ simulation box. PA66 molecules and their polymer chains are depicted in Figure 1, where different colors indicate different types of PA66 atoms.

To enhance the realism of our simulation, we replicated a single PA66 molecule to create an array consisting of 18 molecules, thereby increasing the total number of PA66 molecules in the system. We employed the Nose-Hoover thermostat method to equilibrate the system, which contains 6048 atoms. The initial density of the model was set to 0.027 g/cm³.The built-in QEq scheme was employed, with a maximum of 10.0 iterations per step and a convergence tolerance of 1×10^{-6}e. The charge equilibration was performed at every simulation step with a time step of 0.1 fs, and the neighbor list cutoff was set to 2.0 Å. The reactive potential function proposed in Reference [10] was employed.

At a temperature of 1000 K and a pressure of 1000 atm, we conducted isothermal and isobaric relaxation for 20 picoseconds (ps), during which the density increased to 0.909 g/cm³. Subsequently, the pressure in the x-direction was reduced to 1 atm, and the density was gradually decreased to 0.788 g/cm³ over an additional 20 ps of heating. Then, the pressure in the y-direction was also adjusted to 1 atm, and the density was gradually increased to 1.125 g/cm³ through another 20 ps of heating. Finally, after a 20 ps annealing process, the temperature of the entire system was reduced to 300 K, and the final density stabilized at 1.155 g/cm³. Following annealing, the dimensions of the simulation box were adjusted to 8.0×2.9×2.7 nm³. Formal simulation calculations commenced once the relaxation process was complete.In this work, the built-in QEq scheme was employed with a maximum of 10.0 iterations per step, a convergence tolerance of 1×10^{-6} e, and an execution frequency of every single step. The integration time-step was set to 0.1 fs, and the neighbor-list cutoff was 2.0 Å. Bond cleavage was determined by the instantaneous bond order provided by the potential function; a bond-order cutoff of 0.3 Å was adopted. The potential function is identical to that utilized in refs. [15].

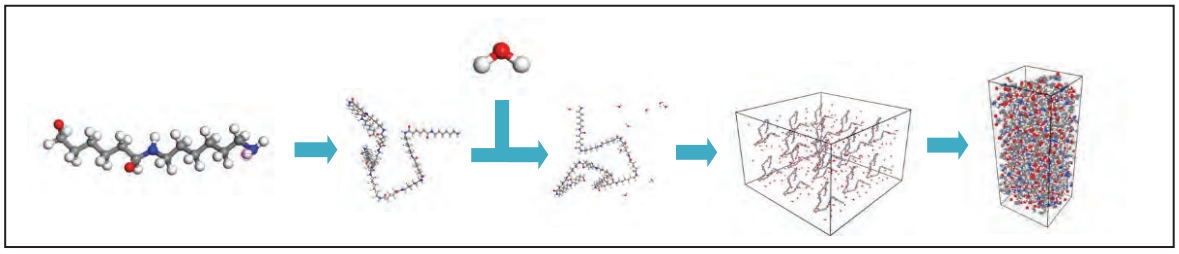


Fig. 1 Model establishment flow chart

In Reference [16], a simulation method was proposed in which a periodic electric field is applied to the system to simulate the heating effect of arc radiation.Among the key factors, the electrical frequency and intensity are two critical parameters that must be determined. Following the approach outlined in this paper, the frequency of the electric field was set at 3653 cm^{-1}. If the electric field strength is too low, the resulting temperature rise will be minimal, thus extending the simulation time. Conversely, if the electric field strength is too high, the temperature may rise too rapidly, potentially resulting in unrealistic molecular configurations. Therefore, we initially set the electric field intensity E_0 to 0.3V/Å, and then reduced it to 10^{-5}V/Å once the system temperature reached the desired level, in order to simulate the shielding effect of the ablator.

In the subsequent sections of this paper, we first examine the effects of varying water contents (0 wt%, 5 wt%, 10 wt%, 15 wt%, 20 wt%) on the decomposition rate and primary decomposition products of PA66. To accelerate the heating rate during the initial stage, the electric field intensity E_0 is set to 0.3 V/Å, and when the temperature reaches 1700 K, E_0 is adjusted to 10^{-5}V/Å. Subsequently, we investigate the impact of temperature on the decomposition products of PA66 in a system containing 10 wt% water. Initially, E_0 is set to 0.3 V/Å, and when the temperature reaches 1700 K respectively, E_0 is reduced to 10^{-5}V/Å. Periodic boundary conditions are applied in the x and y directions of the simulation box, while fixed boundary conditions are used in the z direction to facilitate the application of voltage.

III. Effect of water content on decomposition of PA66

To ensure timely replacement of circuit breaker devices and maintain stable operation under wet conditions, this chapter employs molecular dynamics simulations to calculate and compare the impacts of various water content levels (0%, 5%, 10%, 15%, 20%) on the decomposition rate and primary decomposition products of PA66. The study investigates how different water contents affect the decomposition rate of PA66 at 1700 K and analyzes the reasons behind these effects. Additionally, the production rates and quantities of major small molecule products, tar, and coke are also examined

.

A. Effect on decomposition rate of PA66

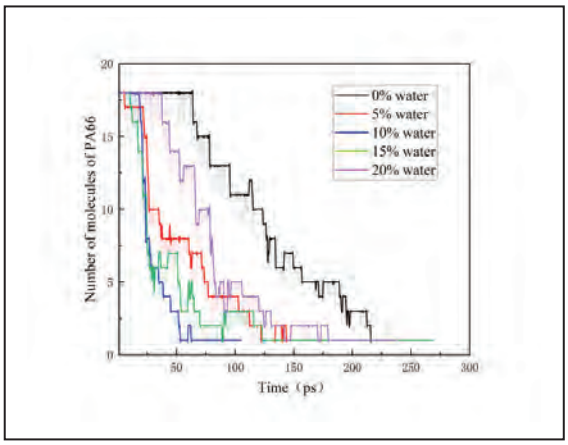


Fig. 2 Decomposition process of PA66 at different initial water content at 1700K

In the figure above, the 0% water content system exhibits the latest initial decomposition, with stable decomposition commencing at approximately 75 ps, indicating the slowest decomposition rate. In the 5%, 10%, and 15% water systems, the initial decomposition times are roughly the same, with stable decomposition beginning around 20 ps. The 5% water system lags slightly, and its decomposition rate starts to decline noticeably at 25 ps, while the 15% water system shows a decline at 40 ps. Only 10% water system has the fastest decomposition rate and the shortest consumption time. As the initial H2O content increases, its promoting effect on PA66 decomposition rises, reaching a maximum at 10%, and declines with further increases.

Upon analysis, it is concluded that: in the early stage, water molecules form hydrogen bonds and van der Waals interactions with the polar amide groups (-CONH-) and other polar groups in PA66. These interactions lead to adsorption of water on the polymer surface, thereby promoting the pyrolysis of PA66. However, when the water content is increased to 10%, the physical adsorption reaches saturation and the promoting effect reaches the maximum, and further increasing the water content will not bring more promoting effect [17]. At high water content, the interaction between polymer chains is enhanced, resulting in a gelation reaction which becomes more likely to occur, thus inhibiting the pyrolysis process. Water molecules participate in the pyrolysis reaction of polymers, such as hydrolysis, which promotes the fracture of polymer chains. However, the hydrolyzable bonds in polymer materials are limited, and when these bonds are exhausted, the further increase of water will not produce more catalytic effects on pyrolysis. In addition, at high water content, water molecules will compete with PA66 molecules for pyrolysis sites, and the activation energy is small, so high water content will affect the decomposition of PA66 molecules.

B. Effect on small molecule products

Figure 3 shows the quantity changes of major small molecule products under different water content systems of 1700K. Through the comparison of the total number of small molecule products, it can be found that among the five products, the initial appearance time of small molecule products in the system of 0% water is the latest, and the final number of small molecule products is also the least. Overall, as the initial water content increases, the number of small-molecule products rises, reaching a maximum at 10%. Beyond this point, further increases in water content lead to a decline in the promoting effect. The specific reason is the same as the above effect of water content on the decomposition rate of PA66, because water can promote the decomposition of PA66, so the addition of H_2O can promote the generation of major small molecule products. However, it can be seen from Figure 3(c) that except for the anhydrous system, the variation trend of water molecules in other systems is first decreased and then increased, which indicates that water molecules participate in the decomposition process of PA66 molecules. The change in the number of water molecules is relatively low, which is due to the low temperature of the system.

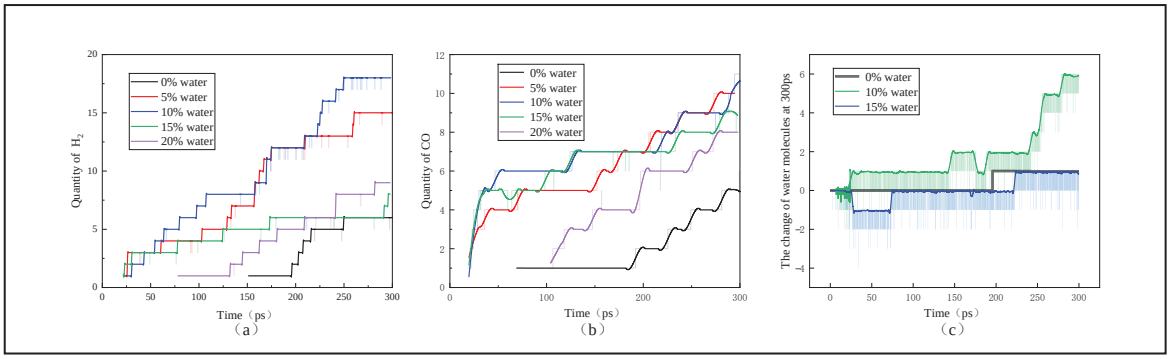


Fig. 3 Changes in the quantity of small molecule products: (a) the quantity of H_2. (b) the quantity of CO. (c) the quantity of H_2O

C. *Influence on tar and coke*

In circuit breakers, continuous ablation of flame-retardant materials by the arc leads to the formation of tar and coke. Hence, understanding the formation mechanisms of these products is crucial for improving the performance and reliability of circuit breakers. In industry, C-containing molecules are usually divided into the following categories according to the number of C atoms in the molecule: C1-C4 (gaseous hydrocarbons), C5-C11 (light tar), C12-C40 (heavy tar), and C40+ (coke). Compared with the system without water, the amount of light tar and heavy tar in the 10% water system increased significantly, from 20, 26 to 35, 41; Although the increase of heavy tar in the 20% water system is not obvious, the amount of light tar has a significant change, from 20, 26 to 28, 29. In addition, comparing the overall situation of the three figures, it can be found that whether it is C5-C11 or C12-C40, the initial decomposition time in the 10% water system is faster than that in the 20% water system, and the final quantity is also higher than that in the 20% water system.

Figure 7 shows that as the water content increases, the proportion of C1-C4 products initially rises and then declines, while the fraction of C5+products follows an opposite trend. The 10 wt% water system yields the largest amount of C1-C4and the smallest amount of C5+ products. Because C5+ species are the main contributors to tar and coke, this indicates that although water promotes the overall formation of tar and coke, it also facilitates the generation of small molecules, thereby lowering their relative proportion. The promoting effect reaches its maximum at 10 wt% water, beyond which it gradually weakens. Given that the maximum water absorption rate of PA66 is about 9 wt% [13], circuit breakers should be protected from humid environments whenever possible. In situations where moisture exposure is unavoidable, designing new materials with higher water absorption capacity may help mitigate coke formation.

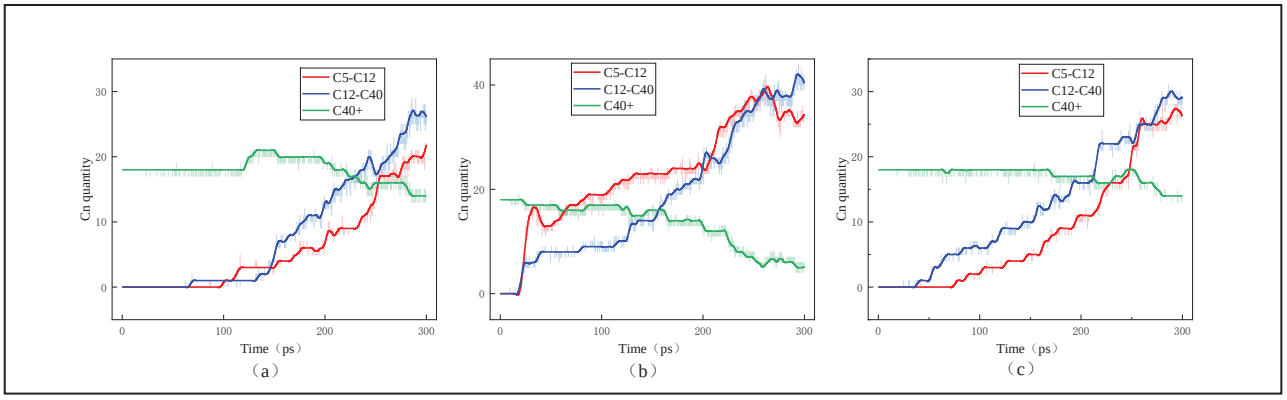


Fig. 4 Changes in light tar, heavy tar and coke quantities over time. (a) 0% water system. (b) 10% water system. (c) 20% water system.

IV. Mechanism analysis

In order to understand the effect of water content on the decomposition of PA66, the mechanism of molecular bond breaking was analyzed from the microscopic point of view. By using RMD_Digging[18] software to analyze the simulation results, the decomposition path of PA66 and the generation path of the main product are obtained, and the results are analyzed.

A. *Mechanism of influence of water content on decomposition rate of PA66*

The following figure shows the specific decomposition path of a PA66 chain. It can be seen from the decomposition path that the amide bond will break under the action of water, and the PA66 chain will first break between the α position N and C of the amide bond. This is because the NH-CH_2 bond has the lowest dissociation energy and is the easiest to meet the fracture conditions during the heating process, so the N-C bond breaks the earliest, which is consistent with the conclusions in other literature [19]. Then the NH-CO bond of C-C bond, C-H bond, C-O bond and amide bond of PA66 began to break, and the break of C-H bond generated free •H. With the increase of •H, •H had a greater chance to collide with other components. Part •H combines with each other to form H_2; Some recombine with the free •OH to form H_2O. In addition, under the influence of •OH decomposed by water molecules, with the increase of decomposition degree, the breaking of

amide bonds will also form CO, NH_3, CO_2 and other small molecular products.

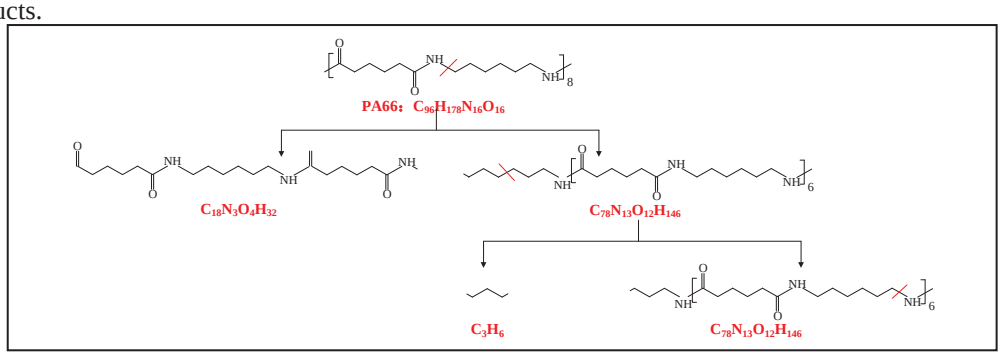


Fig. 5 Specific decomposition path of PA66 chain.

B. Influence mechanism of water content on main product

In order to study how the addition of H_2O affects these small molecule products, the formation paths of H_2O, CO and H_2 are analyzed respectively. The following figure shows the main chemical reactions and main formation paths of H_2O, CO, and H_2 in a 10% water system, where the blue number on the arrow indicates the number of reactions that occur, and the right side shows one of the formation paths of the corresponding molecules. In the figure, the brown, purple, blue and green atoms represent the four types of atoms C, O, N and H respectively, and only the atoms contained in the final molecule are represented by a ball.

Figure 6(a) reveals that the formation pathways of water primarily consist of two types: In the initial stage, due to the addition of water, water molecules decompose into •H and •OH as the temperature rises. Concurrently, during the early stages of PA66 decomposition, a significant number of •H and •OH radicals are released from PA66 molecules. Given the abundance of •H and •OH radicals, free •H and free •OH will then combine to form water molecules. The second type involves dehydration reactions occurring between PA66 and its intermediate products during the decomposition process. These reactions remove water molecules, form dehydration products, and simultaneously release water.

Figure 6(b) depicts the formation process of a water molecule. One oxygen atom and one hydrogen atom originate from the amide bond within PA66, while the other hydrogen atom comes from a free •H radical. During the decomposition, the oxygen and hydrogen atoms on the amide bond successively detach and combine with another free •H radical to form a water molecule.

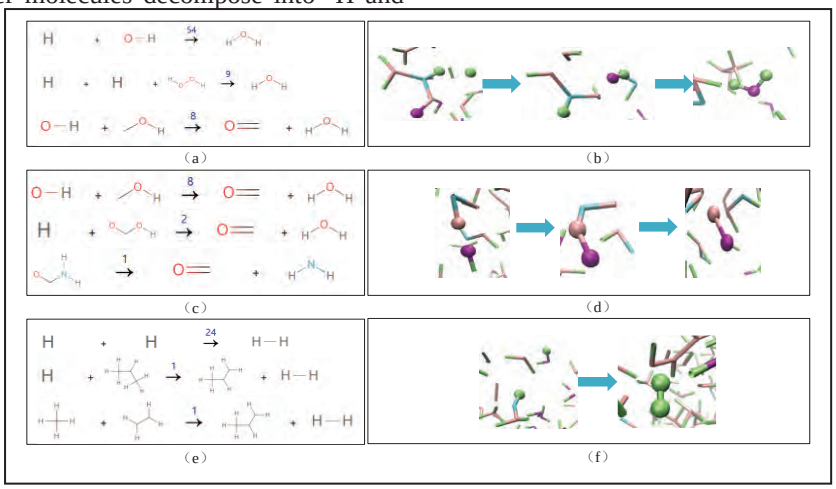


Fig. 6 Main formation paths and specific molecular formation processes of major small molecule products in 10% water system.

Figure 6(c) shows the main path of CO formation. It can be seen that CO is formed mainly by free •OH or •H attacking C-H bond, and then H_2 and CO are formed, followed by chain breaks between amine and carboxyl groups in PA66 molecule or the intermediate products, which is the same as described in literature [20]. Therefore, it can be considered that in the water addition system, there is a situation that H_2O and PA66 compete for the pyrolysis point. When the water content is relatively low, this phenomenon is not obvious, and the direct disconnection of PA66 molecules is still the main factor. However, in the system with 20% water, this effect begins to appear. In the initial stage, H_2O will compete with PA66 for the pyrolysis site, and PA66 fails to absorb the energy required for decomposition, so the decomposition of PA66 is delayed. However, in the subsequent process, H_2O and PA66 will decompose a large number of free •OH and •H, so the CO generation reaction is greatly promoted, and the amount of CO generation increases. Fig. 6(d) shows the generation path of CO. It can be seen that O in carbon monoxide comes from •OH which is free and C atom comes from C adjacent to N. During the generation of CO, it can be seen that O and H in •OH are separated and then linked with C. Finally, the C-N bond also breaks under the action of electric field, forming CO.

Figure 6(e) shows the main generation paths of H_2, and it can be seen that the main generation paths of H_2 include the following types of paths: The main one is that free •H combines with each other to form H_2; the second one is that •H attacks PA66 molecule or its intermediate product, causing it to shed the next •H free radical, and the latter two combine to form H_2. In the third category, the conjugations and H_2 are formed by removing one •H from each of the two molecules containing •H at the same time, which is consistent with the results in reference [21]. Fig. 6(f) shows an H_2 generation path, from which it can be seen that the two •H of hydrogen come from •H in water and •H in one of the amide bonds, respectively. During the decomposition process, H is separated from H_2O and amide bonds respectively, and then the two •H radicals combine to form H_2.

In both cases, it can be found that they result from the combination of small molecular groups produced by the decomposition of PA66. so the initial generation time of small molecules has a great relationship with the decomposition of PA66.

The formation of ring structures in tar and coke is common in the pyrolysis process, and these ring structures have an important impact on the properties and applications of products, so the change of the number of carbon rings in the decomposition process is explored. In this paper, a special carbon chain structure is defined, that is, annular carbon chain, which is a closed-ring structure consisting of carbon atoms linked by chemical bonds. According to the number of carbon atoms in the ring, cyclic carbon chains can be classified as three-membered rings, four-membered rings, five-membered rings, etc. When the number of carbon atoms in a ring exceeds six, the structure is often referred to as a heterocyclic ring. This classification method provides a more rigorous framework for characterizing and analyzing the structural characteristics and reactive behaviors of various cyclic carbon structures across different chemical processes. By observing the figure 7, it can be found that in the C rings of pyrolysis products, ternary rings are the main, followed by five-membered rings and six-membered rings, while four-membered and heterocyclic rings are the least common.This is because the stability of the ring is affected by factors such as the size of the ring, the molecular configuration and the tension of the ring, the smaller ring leads to an increase in the coulomb repulsion between the closer carbon atoms due to the larger degree of bending, making it relatively unstable. The four-membered ring has a small internal angle, which causes the bond Angle between the carbon atoms in the ring to distort, resulting in a large angular tension. This angular tension makes the four-membered ring structure relatively unstable, so the four-membered ring is more likely to open than the five-membered ring and the six-membered ring, resulting in its lower abundance in the simulation results. Figure 8 are snapshots of different rings.

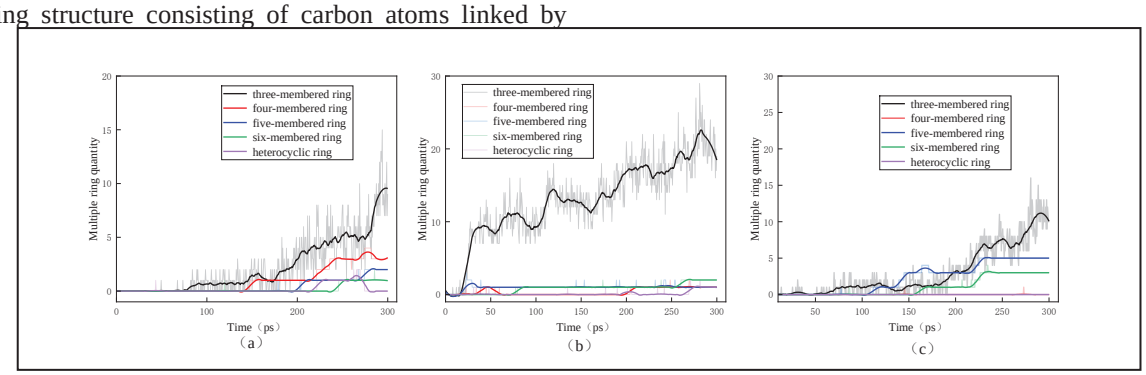


Fig. 7 Changes in the number of multicomponent rings under different water content. (a) 0% water system. (b) 10% water system. (c) 20% water system.

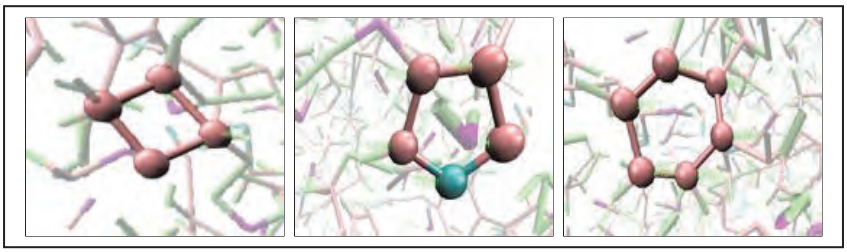


Fig. 8 Snapshots of four-membered, five-membered and six-membered rings

V. Conclusion

Through the above simulation analysis of the water-containing PA66 system under the Reaxff force field, the following conclusions can be drawn:

1) The addition of water is predicted to promote the decomposition of PA66 and the generation of small molecule products. Water is expected to decompose into •H and •OH free radicals in the system, which then attack PA66 molecules, thus accelerating the decomposition of PA66. The decomposition rate increases with water content, and the decomposition rate is predicted to be fastest when the water content reaches 10%; beyond that, too many water molecules compete with PA66 for pyrolysis sites, resulting in a decline in the decomposition rate.

2) In the high-temperature system at 1700 K, the addition of water is predicted to significantly promote the formation of tar and coke, especially when the water content is 10%, where this promotion effect is most significant. The increase in water content is predicted to enhance the formation of relatively stable rings such as five-membered and six-membered rings,

which has important practical implications for optimizing process conditions and reducing the amount of tar and coke produced.

VI. References

[1] Wang. C. Y, Duan. Q. Q, Zhou. K, Yao. J, Su. M., Fu. Y. C, Ji. J. Y, Hong. X, Liu. X. Q, Wang. Z. Y (2020) Optimization of Convolutional Long and short memory hybrid neural network model for photovoltaic power generation prediction based on Genetic algorithm. Acta Physica Sinica 69(10): 149–155.

[2] Liu HF, Ampah JD, Afrane S, Jin C, Yao MF (2024) Potential benefits and trade-offs of hydrogen energy use in the transportation sector under diversified CO2 removal methods. Science Bulletin 69(1):34-39.

[3] Wu JL, Wang MD (2017) Optimal design and experimental study of arc extinguishing chamber in plastic-case circuit breaker. Journal of Engineering Design 24(4):480-486.

[4] Yin J, Wang Q, Li X, Tian T, Liu H (2020) Experimental Evaluation of Outgassing Characteristics of Polymers on Air Arc Behavior. In: Proceedings of the 2020 IEEE 66th Holm Conference on Electrical Contacts and Intensive Course (HLM), San Antonio, TX, USA, pp. 15-19, September 2020.

[5] Liu ZJ, Wang W, Fu K, Kong LM, Yu YJ, Li CY (2024) Study on Pyrolysis Mechanism and Influence Factor of Polyisobutylene Based on ReaxFF. High Voltage Electrical Apparatus 60(3):170-179.

[6] Tang Y, Wu J, Xu JJ, Guo TX, Hu JB, Zhang H, Liu YG, Yang YF (2024) Spectral analysis of amino acids in near-infrared disharmonic vibrations by density functional theory. Spectroscopy and Spectral Analysis 44(11):3149-3156.

[7] Wang PZQ, Diao YF, Li ZH (2024) Density functional Theory study on the effect of molecular chain length on NO2 oxidation of PPS oligomers. Journal of Molecular Science 40(3):267-274.

[8] Lin K, Wang Z (2023) Multiscale mechanics and molecular dynamics simulations of the durability of fiber-reinforced polymer composites. Commun Mater 4:66.

[9] He XC, Chen DZ, Mei ZF, Adili B, An Q (2021) ReaxFF MD Study and Mechanism analysis of CaO Catalytic PE pyrolysis and H2O Effect on Catalytic process. Journal of Chemical Engineering 72(9):4665-4674.

[10] Van Duin ACT, Dasgupta S, Lorant F, Goddard WA (2001) ReaxFF: a reactive force field for hydrocarbons. The Journal of Physical Chemistry A 105(41):9396-9409.

[11] Liu Y, Hu J, Hou H, Wang BS (2020) ReaxFF reactive force field development and application for molecular dynamics simulations of heptafluoroisobutyronitrile thermal decomposition. Chemical Physics Letters 751:137554.

[12] Xuan WW, Dong YW, Wang HL (2022) Study on Steam gasification mechanism of waste PP plastics based on ReaxFF-MD and DFT. Journal of Chemical Engineering 73(11):5251-5262.

[13] Arash B, Thijsse BJ, Pecenko A, Simone A (2017) Effect of water content on the thermal degradation of amorphous polyamide 6,6: A collective variable-driven hyperdynamics study. Polymer Degradation and Stability 146:260-266.

[14] Wang Q, Zhao WM, Cao WD, et al. (2025) Analysis of pyrolysis and kinetics of gassing materials based on ReaxFF. Journal Transactions of China Electrotechnical Society40(10):3082-3096. https://doi.org/10.19595/j.cnki.1000-6753.tces.240616

[15] Kowalik M, Ashraf C, Damirchi B, Akbarian D, Rajabpour S, VanDuin ACT (2019) Atomistic scale analysis of the carbonization process for C/H/O/N-based polymers with the ReaxFF reactive force field. The Journal of Physical Chemistry B 123(25):5357-5367.

[16] Cao WD, Li XW, Zhang YF, Wang Q, Yu RJ, Chen ZY, Zhuang T (2024) Atomic-scale insight into arc plasma radiation-induced gassing materials ablation: photothermal decomposition behavior. Journal of Physics D: Applied Physics 57:195204.

[17] Miao YZ, Wang XT, Xie MS, Qi KZ, Chu ZG, Sun QJ (2020) Thermal decomposition kinetics of nylon 66 and its composites. Journal of Materials Research 34(8):599-604.

[18] Liu Q, Liu S, Lv Y, Hu P, Huang YJ, Kong MQ, Li GX (2021) Atomic-scale insight into the pyrolysis of polycarbonate by ReaxFF-based reactive molecular dynamics simulation. Fuel 287:119484.

[19] Wang JM, Shi YJ, Bai Y, Zou WQ, Wang MH, Gao X, Hao XM (2024) Thermal decomposition mechanism of polyamides with different molecular structures. Journal of Analytical Testing and Testing 43(9):1338-1347.

[20] Cao WD, Li XW, Luo CJ, Wang Q, Yin JN, Zhang YF, Zhuang T (2024) A theoretical model considering the photochemical and photothermal behavior of arc radiation-induced gassing materials ablation. Journal of Physics D: Applied Physics 57:375201.

[21] Zeng X, Wang LM, Wang F, Hu DD, Wu P, Lai XY (2023) Comparison of reaction characteristics and kinetics between tar thermal cracking and steam reforming in a micro fluidized bed reaction analyzer. Journal of Analytical and Applied Pyrolysis 169:105846.

Intrusion of particles in open vent hole type relays and related failure modes

Thomas Herrle
PCL
Panasonic Industrial Devices Europe GmbH
Pfaffenhofen a.d. Ilm, Germany
thomas.herrle@eu.panasonic.com

Dieter Volm
New Business Development
Panasonic Industry Europe GmbH
Ottobrunn, Germany
dieter.volm@eu.panasonic.com

***Abstract*—Particle ingress into open-vent-hole relays is examined, revealing that not only gaseous contaminants—such as silicone vapors, phosphorus compounds, or moisture—but also solid particulates can penetrate relays through vent openings approximately 300–400 µm in diameter, with significant implications for relay reliability.**

Although the prospect of solid particles entering via such relatively small openings may appear remote, field data—especially from high-volume sectors like the automotive industry—demonstrate that a substantial proportion of relay failures can indeed be attributed to externally introduced particles.

The study analyzes different sources of these intruding particles and correlates them with distinct failure modes observed in relays. Examples include elevated contact resistance caused by particle deposition on contact surfaces, as well as mechanical interference within the relay mechanism, such as particles lodged between the core and armature, preventing proper operation.

Several mitigation strategies to address these vulnerabilities are proposed and evaluated. The findings underscore the importance of considering particle ingress in the design and quality control of open-vent-hole relays to ensure long-term functional reliability.

Keywords—failure analysis, relay, particle, contact resistance, vent hole, sealed, flux tight, wash tight

I. Introduction

Open-vent-hole and flux-tight relay designs are widely employed in electronic assemblies for several practical and economic reasons. Their use eliminates the need for hermetic sealing, thereby reducing manufacturing costs, and the continuous air exchange within these relays has been shown to prolong electrical lifetime by reducing arc duration in a less ionized atmosphere [1-3]. Moreover, for larger relay types subjected to reflow soldering, open vent holes are essential to prevent internal pressure build-up, which can otherwise lead to deformation or malfunction.

Despite these advantages, open-vent-hole and flux-tight relays are inherently susceptible to environmental ingress. Various gaseous contaminants are known to diffuse into relay housings and negatively impact performance. The most prominent issue arises from volatile organic silicone compounds present in the relay's surroundings. These species decompose into short-chained molecules that migrate into the relay and oxidize at the contact surfaces to form insulating layers of silicon dioxide, ultimately resulting in elevated contact resistance [4-7]. Similarly, plastics containing red-phosphorus flame retardants can release phosphorus-bearing vapours, which transform into phosphine and phosphorous acids under humid conditions. These reaction products settle on relay contacts and likewise induce contact resistance failures [8-10]. Additional degradation can occur in sulphurous atmospheres, where sulphur species react with silver contacts, or under humid conditions, where moisture ingress may lead to the formation of nitric acid. Nitric acid can corrode copper and soft-iron relay components, generating salts that migrate to the contacts and impair their functionality. In severe cases, corrosion of the copper coil wire may even cause coil interruption [8, 11-13].

While such gas-induced failure mechanisms are well documented in relay failure analysis, the potential impact of solid particulate contamination has received considerably less attention. Particles originating from printed circuit board assembly (PCBA) processes or from the operating environment may enter the relay through the vent hole, although this scenario is often regarded as unlikely. Nevertheless, when such ingress occurs, particles can reach critical internal components, including the contact system, and trigger functional degradation. Distinguishing these externally introduced particulates from those generated by relay materials or during relay manufacturing poses an additional analytical challenge.

This work presents several case studies in the automotive industry illustrating failure mechanisms caused by particulate ingress of various origins in open-vent-hole relays, highlighting both the underlying contamination pathways and the diagnostic considerations required for accurate failure attribution. In the automotive industry the relay failure rate normally lies below 1 ppm. All values lying considerably above need further investigation.

II. Relay Failures in electronic closure supports

In a first example, an electronic closure support for the trunk of a passenger vehicle failed during end-of-line testing at the electronics manufacturer showing failure rates considerably higher than 100 ppm. The failure was traced to an increased normally-closed contact resistance of an open-vent-hole-type relay (Fig. 1.1).

To determine the underlying cause, the relay was opened and examined using optical microscopy. Distinct glass-fibre imprints were observed on the corresponding contact pairs (Figs. 1.3-4). Scanning electron microscopy (SEM) provided further detail, revealing not only the imprinted glass fibres but also additional particulate contamination on the contact surfaces (Figs. 1.5-6). There are several mechanisms which support the transfer of these particles to the contact surfaces where they cause the failure. In this case the amount of contamination was quite high which alone increases the failure probability by entropy. Furthermore, in the end-of-line testing, the relays are switched with a certain load. Both the scattering of the contacts and the electric field between the contacts promote the migration of the particles to the relay contacts. Besides that, there are self-centring processes which lead to the migration of residues to the touching point of the relay contacts [7].

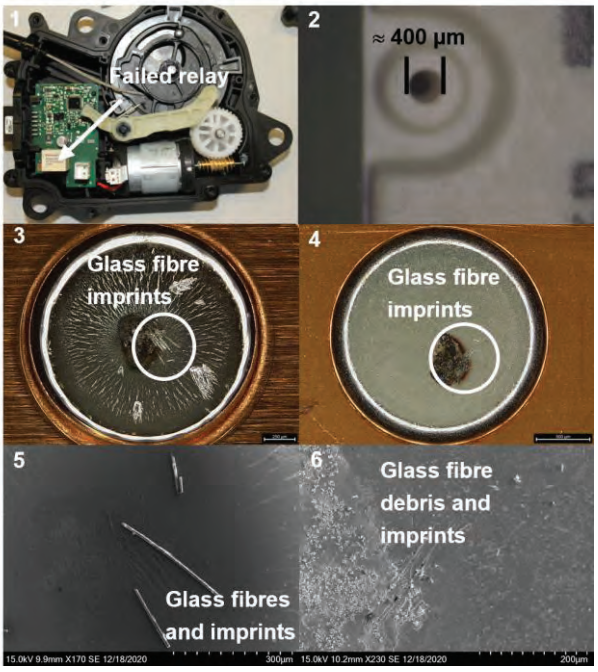


Fig. 1. 1: Electronic trunk closure with failed relay. 2: Open vent hole of relay with a diameter of 400 µm. 3-4: Optical microscope images of the moveable and stationary contacts of the failed relay showing particles, glass fibres and imprints on the contact surfaces. 5-6: Corresponding SEM-images of the moveable and stationary contacts.

A combined scanning electron microscopy-energy dispersive spectroscopy (SEM-EDS) analysis showed that the glass fibres consisted primarily of oxygen (O), aluminium (Al), silicon (Si), and calcium (Ca) (Fig. 2). The fibres exhibited an average diameter of approximately 10 µm.

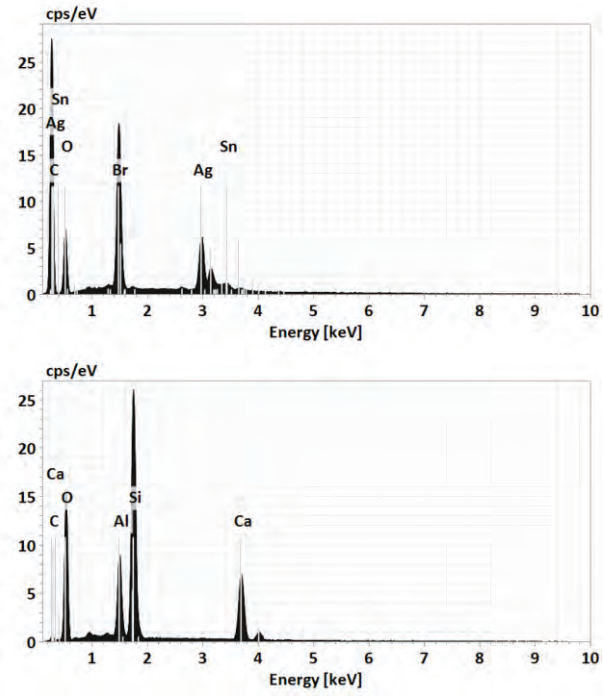


Fig. 2. Top: EDS-spectrum of the contaminations on the relay silver (Ag) contacts showing especially bromine (Br). Bottom: EDS-spectrum of a glass fibre on the relay contacts showing especially oxygen (O) and silicon (Si).

TABLE I.

Material	Found elements					
Contamination	C	O	Al	Si	Ca	**Br**
PC-board	C	O	Al	Si	Ca	**Br**
Glass fibre		O	Al	Si	Ca	
Relay plastic	C	O	Al	Si	Ca	
Relay glue	C	O			Ca	

In addition to the fibres, several particles found on the contacts were analysed and were found to contain carbon (C), oxygen (O), aluminium (Al), bromine (Br), silicon (Si), and calcium (Ca) (Fig. 2). Fourier-transform infrared (FTIR) spectroscopy identified these particles as epoxy resin (Fig. 3).

The relay components themselves consist of two different glass-fibre-reinforced polymer materials and could therefore initially be considered as potential sources of the glass fibres observed on the contacts. However, neither of these polymer materials contains bromine. Epoxy is also used to bond internal relay parts, but this adhesive does not include glass fibres or brominated constituents.

A summary of the elemental constituents of the various materials discussed is provided in Table I. As shown in Table I, among all potential sources of contamination, only the printed circuit board (PCB) material contains bromine (Br), matching the composition of the particles found on the relay contacts. Based on these findings, it was concluded that dust generated during the PCB cutting process entered the relay through the open vent hole and caused the malfunction.

This hypothesis was further supported by the discovery of particles, including glass-fibre debris, near the open vent hole of the failed relay (Figs. 4.1-2). A side view of the PCB is shown in (Fig. 4.3). Corresponding SEM images of the PCB cross-section (Figs. 4.4-5) clearly reveal the layered structure of glass-fibre fabrics constituting the laminate.

As an immediate countermeasure, the PCB manufacturer applied a sticker over the relay vent hole after soldering and before PCB separation. Nevertheless, failures continued to occur.

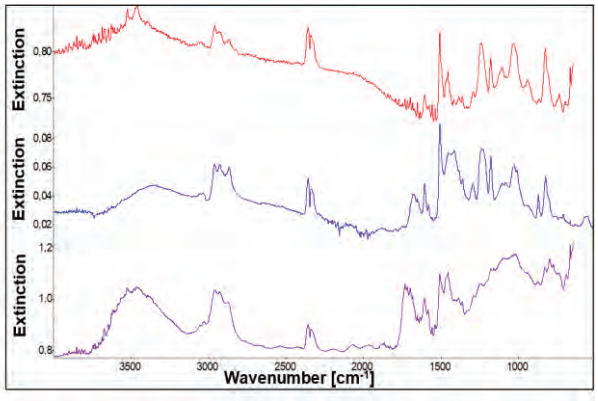


Fig. 3. FTIR-spectrum of the contaminations (top red curve) on the relay contacts which shows good agreement with epoxy resin (middle blue curve) and PC-board material (bottom purple curve).

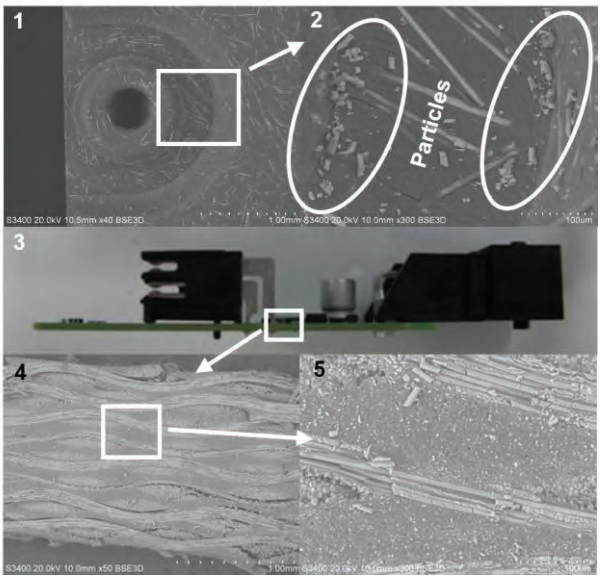


Fig. 4. 1: SEM-image of open vent hole. 2: SEM-image of region around vent hole in detail showing PCB-dust particles. 3: PCB in side view. 4: SEM-image of PCB material in side view, especially showing the glass fibre layers. 5: Enlarged SEM-image of the PCB material.

A subsequent investigation revealed the cause: during or prior to the cutting process, the sticker partially detached, reopening the vent hole. The detachment was most likely induced by vibrations from the cutting operation. Owing to its adhesive surface, the partially detached sticker collected PCB dust generated during the cutting process (Fig. 5).

The contaminants on the sticker included glass fibres and bromine, and FTIR spectroscopy again confirmed the material to be epoxy resin. Taken together, these results provide conclusive evidence that the relay failure was caused by particulate debris originating from the PCB cutting process.

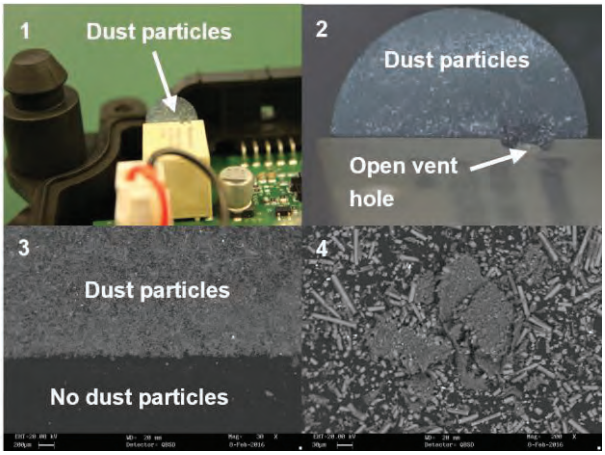


Fig. 5. 1: Partly detached sticker, reopening the vent hole. 2: The glued surface of the sticker, close to the open vent hole, collected the PC-board dust caused during the PCB cutting process. 3: SEM-image of the sticker showing the upper half which came undone and gathered the PCB-dust. The lower half of the sticker was still attached to the relay and therefore is PCB dust-free. 4: SEM-image of the PCB-dust on the sticker in more detail showing especially the glass fibres.

As a final and effective countermeasure, the PCB manufacturer decided to seal the open vent hole using a hot-stamp process after soldering and before PCB cutting—analogous to the production process applied to sealed-type relays.

III. Relay Failures in Power Distribution Modules

In another example, bi-stable relays failed to maintain their set position and repeatedly returned to the reset position. These relays were installed on power distribution modules located in the motor compartment of a vehicle. The failure rate in the field was several tenth of ppm. X-ray analysis revealed that metallic particles situated between the armature and the core prevented proper closing of the magnetic circuit (Fig. 6).

To further investigate the failure mechanism, the relay was opened, and both the armature and the core were examined using optical microscopy. Multiple particles were detected on these components (Figs. 7.1-4). Subsequent SEM-EDS analysis showed that the particles consisted predominantly of iron (Fe) with minor amounts of oxygen (O) as shown in Figs. 8 and 9.

Relays do not normally contain loose iron particles. The only internal components composed of soft iron are the magnetic circuit elements, but these parts are nickel (Ni) coated. Therefore, if internal wear or abrasion were the source, SEM-EDS should have detected significant nickel content. Since this was not the case, it was concluded that the iron particles entered the relay from the external environment, most likely through the open vent hole—similar to the contamination pathway described in Section II.

To validate this hypothesis, the area surrounding the relay was examined. Near the open vent hole, a particle consisting solely of iron (Fe) was discovered as shown in Figs. 8 and 9. Furthermore, two types of particles were found distributed across the PCB.

The first group consisted of spherical particles composed mainly of oxygen (O) and iron (Fe), with an average diameter of approximately 95 µm.

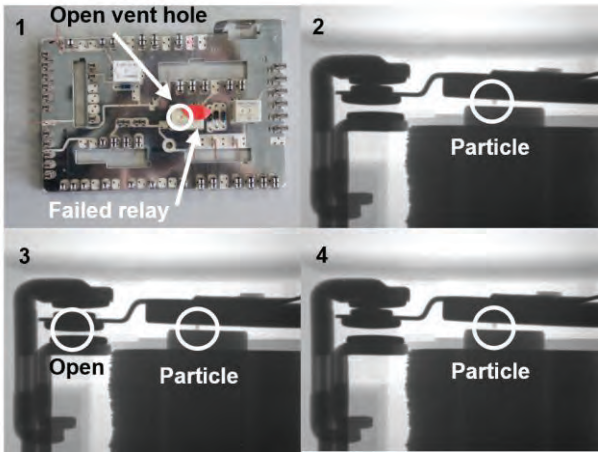


Fig. 6. 1: PCBA with failed relay. 2: X-ray image of the un-powered relay in the reset state. 3: X-ray image of the relay, powered with 12V to be set. The relay does not close properly. 4: X-ray image of the un-powered relay after setting but fallen back to the reset position.

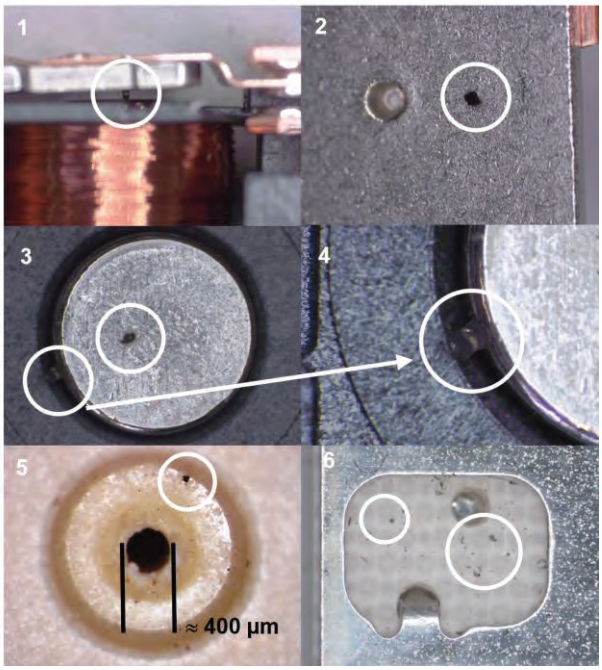


Fig. 7. 1: Particles between armature and core of failed relay. 2: Particle residue on armature. 3: Particle residue on core. 4: Particle on edge of core which caused the failure of the relay. 5: Particle close to the open vent hole of the relay. 6: Particles on the PC-board.

The second group consisted of irregularly shaped particles composed almost entirely of iron (Fe) as shown in Figs. 8 and 9. All of these particles were smaller than the 400 µm diameter of the open vent hole, making ingress into the relay feasible.

The source of these particles was traced to the motor compartment, where the power distribution module was installed. The PCB assembly (PCBA) was housed in an enclosure that was permeable to particulate matter originating from the engine bay.

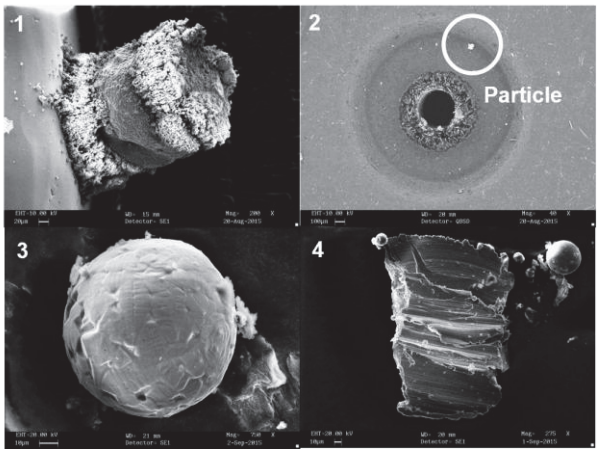


Fig. 8. 1: SEM-image of particle on core of relay which caused the failure. 2: SEM-image of particle found next to the open vent hole on the outside of the relay. 3: SEM-image of spherical particle found on the PC-board. 4: SEM-image of irregularly shaped particle also found on the PC-board. All above particles are small enough to be able to enter the open vent hole of the relay.

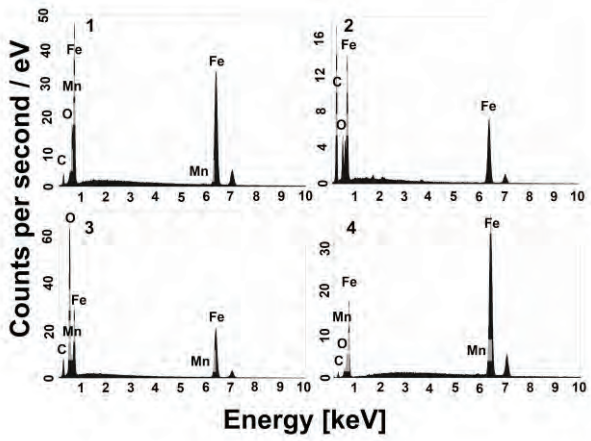


Fig. 9. 1: EDS of particle on core of relay which caused the failure. 2: EDS of particle found next to the open vent hole on the outside of the relay. 3: EDS of spherical particle found on the PC-board. 4: EDS of irregularly shaped particle also found on the PC-board. All above particles consist of iron (Fe). The spherical particles contain more oxygen (O) than the others.

As a final countermeasure, the PCBA manufacturer replaced the open-vent-hole relay with a sealed-type relay to prevent particle ingress. Once again, the relay failures could be conclusively attributed to external particles entering the relay through an unsealed vent hole.

IV. Relay Failures in Electronic Parking Brake Control Units

The final example, involving an electronic parking brake (EPB) control unit, demonstrates how the construction process of the printed circuit board assembly (PCBA) can strongly influence relay failure mechanisms. Two different EPB manufacturers reported relay malfunctions, typically manifesting as infinite contact resistance. In both cases the failure rates in the field were around 100 ppm.

For one manufacturer, X-ray analysis frequently showed that the armature of the relay did not close properly. As a consequence, the corresponding contact remained open, resulting in infinite contact resistance (Fig. 10).

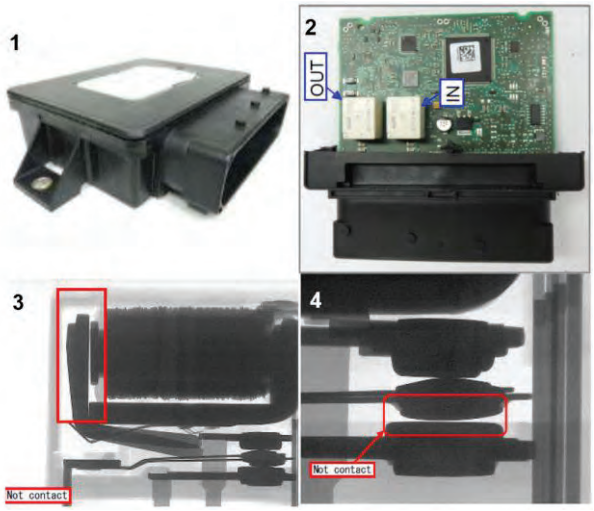


Fig. 10. 1: EPB box. 2: Opened EPB box showing two relays. 3: X-ray image of failed relay showing that the armature of the relay does not close properly. 4: X-ray image of the failed relay showing that due to the not closing armature also the normally open contact does not close.

Optical microscopy and SEM examination revealed a black plastic particle lodged between the armature and the core of the relay, thereby preventing proper closing (Figs. 11.1-4). FTIR spectroscopy identified this particle as polybutylene terephthalate (PBT) (Fig. 11.5). Since the EPB housing is also made of PBT, whereas the relay housing is composed solely of liquid crystal polymer (LCP), the origin of the particle appeared to be external to the relay.

To ensure that the PBT particle had not originated from the relay production line—where both PBT- and LCP-type relays are manufactured—an EDS analysis was conducted. This analysis confirmed that the PBT particle found between the armature and core contained no antimony (Sb) or bromine (Br), in contrast to the PBT used in the relay production process. Thus, the particle could be attributed to the EPB box rather than the relay itself.

The EPB box consists of a body and a cover. The body is reinforced with glass fibres similar in composition to those found in the relay materials, containing oxygen (O), magnesium (Mg), aluminium (Al), silicon (Si), and calcium (Ca). The cover, however, contains glass beads as fillers, which additionally include sodium (Na). The elemental compositions determined by EDS are summarized in Table II.

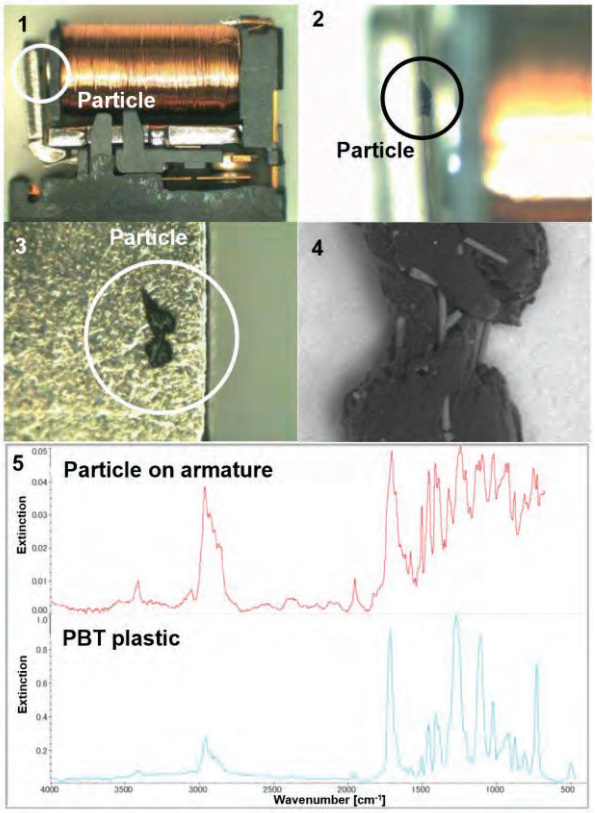


Fig. 11. 1: Relay inside view with particle between armature and core. 2: Detail showing the particle on the armature. 3: Black particle on armature. 4: SEM image of the particle on the armature. 5: FTIR-spectrum of the particle on the armature showing good agreement with PBT plastic.

TABLE II.

Material	Found elements								
Contamination	C	O		Mg	Al	Si	Ca		
Relay PBT type	C	O		Mg	Al	Si	Ca	**Sb**	**Br**
EPB box body	C	O		Mg	Al	Si	Ca		
EPB box cover	C	O	**Na**	Mg	Al	Si	Ca		
Glass fibre		O		Mg	Al	Si	Ca		
Glass ball		O	**Na**	Mg	Al	Si	Ca		

For the second EPB manufacturer—who also experienced failures characterized by increased or infinite contact resistance—glass beads from the EPB cover and their imprints were detected on the surfaces of the affected relay contacts (Fig. 12). EDS analysis showed that these glass beads consisted mainly of oxygen (O,) sodium (Na), magnesium (Mg), aluminium (Al), silicon (Si), and calcium (Ca) Table II, (Fig. 13).

Glass beads are not used in relay manufacturing. Therefore, both the PBT particles and the glass beads identified inside the relays must have originated from the materials used in the EPB box. Further inspection revealed that these contaminants were already present on the PCB around the relay (Fig. 14).

A more detailed investigation showed that both the PBT plastic particles and the glass beads were generated at the interface between the EPB box body and cover, where the two components are joined by a friction welding process (Fig. 14). This process produces wear debris in the form of loose glass beads and PBT particles. The glass beads typically have a diameter of approximately 50 µm, while the plastic particles range from 100 µm to 280 µm in size. All of these particle types are sufficiently small to pass through the 300 µm wide vent hole of the relay.

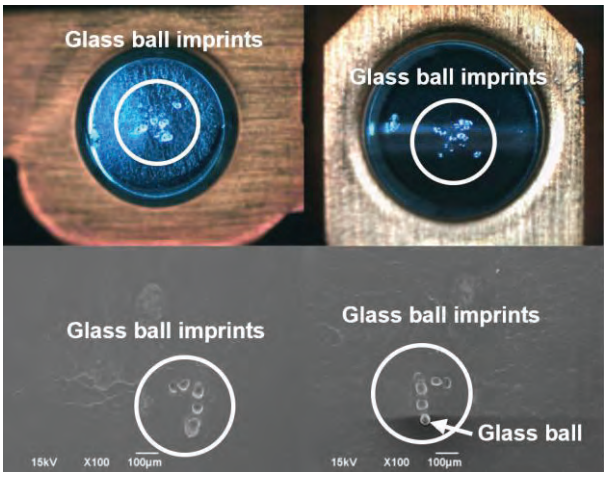


Fig. 12. Top: Optical microscope images of stationary (left) and moveable (right) normally closed contacts with glass ball imprints. Bottom: SEM images of stationary (left) and moveable (right) normally open contacts with glass ball imprints and a glass ball on the moveable contact.

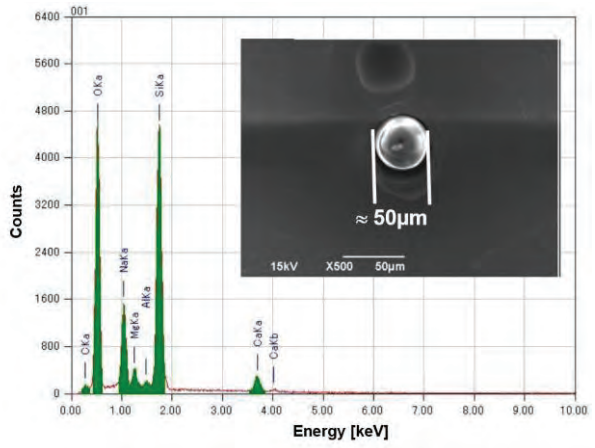


Fig. 13. EDS of a glass ball (inset) showing mainly oxygen (O), sodium (Na), magnesium (Mg), aluminium (Al) and calcium (Ca).

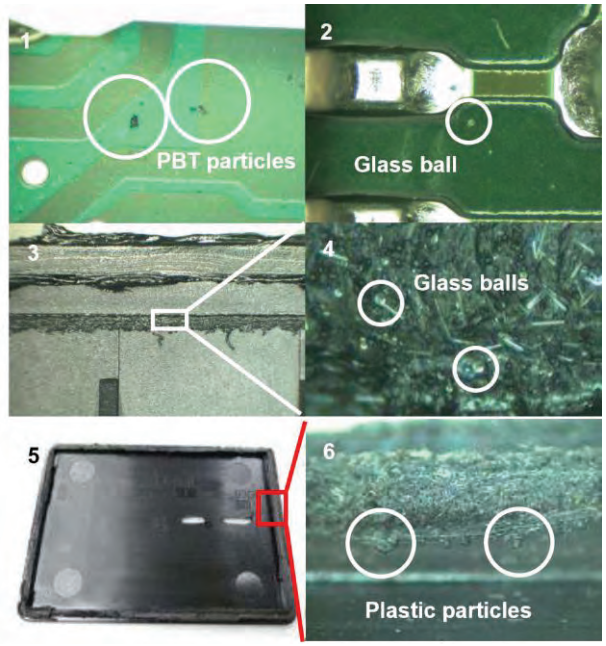


Fig. 14. 1: Plastic particles of the EPB box on the PC-board near the relay. 2: Glass ball of the EPB box on the PC-board. 3: EPB box body with the friction welding seam. 4: Glass balls on the welding seam. 5: EPB box cover. 6: Plastic particles on EPB cover at the welding seam.

In an initial attempt to mitigate particle ingress, a different relay type was tested in which the top vent hole was closed, leaving only a 70–90 µm opening at the bottom. However, this modification proved insufficient, as loose glass beads were still able to enter the relay through the remaining bottom gap.

As a final countermeasure, both customers adopted a solution analogous to that described in Section II: sealing the relay's vent hole with a hot-stamp process after soldering, similar to the manufacturing approach used for fully sealed relays. This measure effectively prevented the intrusion of friction-welding-generated particles and resolved the observed failures.

V. SUMMARY

The presented case studies demonstrate that particle ingress into open vent-hole relays is a significant and often underestimated reliability risk, particularly in high-volume automotive applications. This is one reason why sealed relays were not used in the above applications right from the beginning. Another is the need for a reflow soldering process which is not possible for sealed relays because the elevated temperatures leading to internal pressure and relay bulging.

A key analytical challenge was to determine whether contaminants found inside failed relays originated externally or may have been produced by relay materials or manufacturing processes themselves. In all examples, corrective actions were implemented—primarily by tightening the relay structure or switching to fully sealed relay types—addressing the entry path rather than the actual generation of contaminants. By sealing the relays, the expected electrical life will drop down to about ¼ to ⅕ of that of unsealed relays depending on switching frequency. These are typical values out of internal laboratory tests.

From a relay manufacturing perspective, several concepts are under consideration to mitigate particle ingress without fully sealing the relay. Potential solutions include covering the vent hole with a semi-permeable membrane that allows gas exchange while preventing particulate intrusion, or integrating a filter structure within the vent hole. However, to date, the cost-benefit ratio has not justified implementing these approaches in mass production.

REFERENCES

[1] J. J. Shea, Dielectric recovery characteristics of a high current arcing gap, Proceedings of the Forth-Seventh IEEE Holm Conference on Electrical Contacts (IEEE Cat. No.01CH37192), Montreal, Quebec, Canada, 2001, pp. 154-160, doi: 10.1109/HOLM.2001.953204.

[2] D. Shin, I. O. Golosnoy, T. G. Bull and J. W. McBride, Experimental study on the influence of vent aperture size and distribution on arc motion and interruption in low-voltage switching devices, International Conference on Electric Power Equipment - Switching Technology, pp. 213-217, Oct. 22-25, 2017.

[3] J. W. McBride, K. Pechrach and P. M. Weaver, Arc root commutation from moving contacts in low voltage devices, Electrical Contacts - 2000. Proceedings of the Forty-Sixth IEEE Holm Conference on Electrical Contacts (Cat. No.00CB37081), Chicago, IL, USA, 2000, pp. 130-138, doi: 10.1109/HOLM.2000.889922.

[4] Tamai, T: Characteristic morphology of contact-trace caused by electrical make-brake operation under silicon vapour. Proc. Int Conf. Electr. Contacts, Nagoya 1999, 49-56

[5] Tamai, T, Aramata, M.: Effect of silicone vapour concentration and its polymerisation degree on electrical contact failure. IEICE Trans. Electron., vol. E79-C, no. 8, Aug 1996; 1137-1143

[6] Volm D.: Silicon contamination caused by diffusion of silicone into plastic sealed relays, ICEC 2002

[7] Vogel, Gert, Failure mechanisms of electromechanical relays on PCBAs - PART I, EDFAAO (2018) 1: 4-8

[8] Vogel G., Failure mechanisms of electromechanical relays on PCBAs - PART II, EDFAAO (2018) 2: 4-8

[9] Uske K., Roth M., Minges Ch.: Prevention of Contact Corrosion (Stabilizing Flame Retarded Plastics against Plate-Out), Kunststoffe international 9/2015 pp. 68-70

[10] Volm D., Herrle Th., Fauth B., Influence of red phosphorous flame retarded plastic materials on relay contacts and electronic components, Conference: ICEC 2020 - 30th International Conference on Electrical Contacts - At: St Gallen, June 2021

[11] Aaron John Ihde, The development of modern chemistry, Courier Dover Publications (1984) p. 678

[12] Karl Fisher; William E. Newton, G. J. Leigh, ed. Nitrogen fixation at the millennium, Elsevier, (2002) pp. 2–3

[13] Volm D., Herrle Th., Kraus M., Relay corrosion effects due to the generation of nitric acid and their impacts under high inductive load condition, Conference: 31st International Conference on Electrical Contacts June 13-16 - At: Sapporo, Hokkaido, Japan, June 2022

Effects of Aging on the Mechanical Drop-Shock Performance of SAC305 Solder Interconnects

Saddam Daradkeh
Industrial and Systems Engineering
Auburn University
Auburn, AL USA
sdf0020@auburn.edu

Abdallah Alakayleh
Industrial and Systems Engineering
Auburn University
Auburn, AL USA
aha0019@auburn.ed

Sufyan Tahat
Industrial and Systems Engineering
Auburn University
Auburn, AL USA
sat0063@auburn.edu

Waad Tarman
Mechanical Engineering
Auburn University
Auburn, AL USA
wqt0001@auburn.edu

Elizabeth Gainey
Mechanical Engineering
Auburn University
Auburn, AL USA
epg0016@auburn.edu

George Flowers
Industrial and Systems Engineering
Auburn University
Auburn, AL USA
flowegt@auburn.edu

Sa'd Hamasha
Systems Science and Industrial Eng.
Binghamton University
Binghamton, NY USA
shamash1@binghamton.edu

Jeffrey Suhling
Mechanical Engineering
Auburn University
Auburn, AL USA
Jsuhling@auburn.edu

***Abstract*— The reliability of solder joints as interconnects between Printed Circuit Board (PCB) and electronic components is critical to the performance of electronic devices, particularly with the widespread adoption of lead-free alloys such as Sn–3.0Ag–0.5Cu (SAC305). Solder joints are among the most failure-prone elements in electronic assemblies because they are subjected to complex mechanical and thermal stresses. During soldering, intermetallic compounds (IMCs), including Ag_3Sn and Cu_6Sn_5, form and play a key role in determining the mechanical behavior and long-term reliability of the joints. Thermal aging promotes the growth and coarsening of these IMCs, leading to microstructural evolution that can degrade mechanical integrity. This study investigates the effect of isothermal aging on the drop-shock reliability of SAC305 solder joints. A chip array ball grid array (CABGA208) package assembled on a printed circuit board with an immersion tin (ImSn) surface finish was used as the test vehicle. Isothermal aging was conducted at 125 °C for 0, 2, 10, and 60 days. Drop-shock testing was performed at a peak acceleration of 1500 G with a maximum pulse duration of 0.5 ms. Microstructural characterization was carried out to correlate IMC layer evolution with drop performance. The results demonstrate that thermal aging significantly degrades drop-shock reliability, primarily due to the thickening of brittle IMC layers, which facilitates crack initiation and propagation.**

Keywords—solder joint, intermetallic compounds, drop/shock, failure analysis, aging.

I. INTRODUCTION

Electronic devices frequently operate under harsh environmental and mechanical conditions that can compromise their reliability. Among electronic components, solder joints are particularly vulnerable and often represent the primary failure site under thermal cycling and mechanical shock, such as accidental drops during handling, use, or transport. Repeated drop impacts can induce interfacial or bulk cracking, leading to cumulative damage and eventual structural failure. Consequently, the reliability of microelectronic interconnections remains a critical design consideration [1].

Solder joint aging refers to the gradual degradation resulting during service over time. Aging significantly alters the microstructure and mechanical properties of solder joints, directly affecting their reliability [2]. A major aging-related concern is the growth of the intermetallic compound (IMC) layer at the solder/substrate interface. As aging time and temperature increase, enhanced atomic diffusion accelerates IMC thickening, leading to reduced joint strength and increased brittleness [3], [4]. The mechanical mismatch between the brittle IMC and the surrounding ductile solder generates stress concentrations and promotes crack initiation, especially under mechanical or thermal loading [5]. Previous studies have reported substantial reductions in the shear strength and drop shock life of both SnPb-based and SAC solder joints after prolonged aging, primarily attributed to IMC thickening and precipitate coarsening [6], [7].

The mechanical performance of solder joints under drop shock loading is also strongly influenced by the surface finish. ENIG finishes provide excellent solderability and corrosion resistance and form Ni3Sn4- and Cu6Sn5-based IMCs with SAC305 [8], [9]. However, these IMCs, along with the presence of a phosphorus-rich layer, tend to be brittle and are prone to early failure under high strain-rate loading, making ENIG less favorable for drop shock reliability despite its good thermal cycling performance [10]. In contrast, the Immersion Tin (ImSn) finish primarily forms Cu_6Sn_5 IMCs, which are more ductile and uniformly distributed. This microstructure enhances shock absorption, reduces interfacial failure, and improves mechanical performance under impact loading [11], [12].

Isothermal aging also affects solder joint hardness through IMC formation and coarsening, which in turn influences drop shock reliability. Elevated temperatures generally reduce joint strength while promoting the formation of thicker, more brittle IMCs [13]. Hardness plays a critical role in drop shock performance, as increased hardness enhances resistance to deformation during impact; however, an optimal balance between hardness and ductility is required to maximize reliability [14].

The objective of this study is to systematically compare the drop shock reliability of SAC305 solder joints under various isothermal aging conditions. Drop shock life, failure modes, and IMC evolution were evaluated after four aging

durations. Correlations between aging time, IMC thickness, and failure life were established. This work addresses a gap in the existing literature by providing an assessment of how surface finish and aging collectively influence solder joint reliability, offering valuable insights for material selection and design of robust interconnections for electronic assemblies.

II. EXPERIMENTAL EQUIPMENT, SETUP, AND PROCEDURE

A. Test Vehicle Configuration

This study focuses on the SAC305 solder, an alloy composed of Sn with 3% Ag and 0.5% Cu. Immersion tin (ImSn) was selected as the surface finish because, as discussed above, it has favourable characteristics for drop shock applications. Four aging conditions were examined: no aging, 2 days, 10 days, and 60 days. In accordance with JEDEC standards, all tests were conducted using a peak acceleration of 1500 G with a maximum pulse duration of 0.5 ms, as illustrated in Fig. 1. For each test condition, 17 boards were evaluated. The sample size was selected based on reliability studies and JEDEC recommendations, which suggest that 15–20 samples are adequate for reliable estimation of characteristic life using a two-parameter Weibull distribution [15] . The test matrix is presented in Table 1. All testing was performed in compliance with JEDEC standard JESD22-B111A.

Table 1: Test Matrix Summarizing Experimental Conditions

Alloy	**Surface finish**	**Aging time (days)**	**Sample size**
SAC305	ImSn	0	17
		2	17
		10	17
		60	17

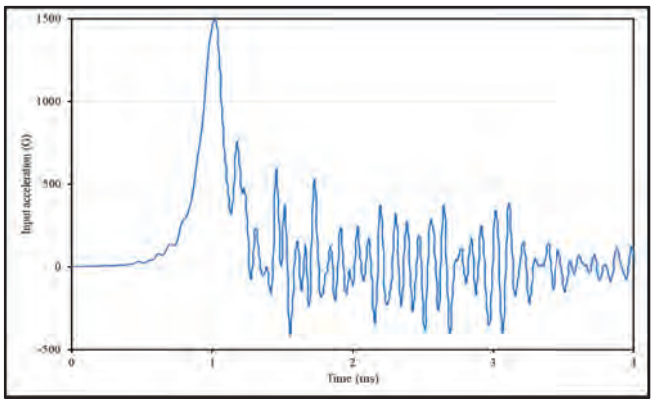


Fig. 1: Mechanical drop shock acceleration profile applied during this study, showing the acceleration in G versus time in ms.

The test board incorporated a single CABGA208 component with daisy-chain packaging and 208 I/O connections. The solder spheres had a diameter of 0.457 mm. The component body measured 15 mm × 15 mm and was arranged in a 17 × 17 array with a pitch of 0.8 mm. The package thickness was 1.5 mm, and the test vehicle dimensions were 76 mm × 76 mm × 1 mm, as shown in Fig. 2. A schematic of the package structure and its components is provided in Fig. 3.a. A cross-sectional view of the component and solder joint geometry is provided in Fig. 3.b.

The test boards were fabricated using a high-temperature glass epoxy laminate (FR-406) substrate with a glass transition temperature of 170 °C. Each board consisted of eight layers and employed solder mask–defined (SMD) pads. To mitigate laminate-related failures, such as pad cratering, copper pads were defined by the solder mask [14], [16]. Aging was performed in a dedicated oven at 125 °C for four durations: no aging, 2, 10, and 60 days.

For testing, the solder joints were electrically connected in a daisy-chain configuration. The test vehicle included five monitoring pads: channels C1, C2, C3, and C4 were used to monitor the resistance of corner joints, which experience higher stress during drop events, while channel S1 monitored the remaining joints.

The component was mounted onto the PCB using standard surface-mount assembly techniques. Solder paste was deposited onto the PCB pads using a DEK Europa stencil printer with a 6 kg squeegee load and a printing speed of 30 mm/s. Component placement was performed using a GSM XE006 pick-and-place machine. Reflow soldering was carried out in a nitrogen-controlled reflow oven (BTU Pyramax 125N) following the temperature profile shown in Fig. 4. Thermocouples were attached to each PCB to accurately monitor board temperature during reflow. After assembly, electrical continuity was verified on all completed boards.

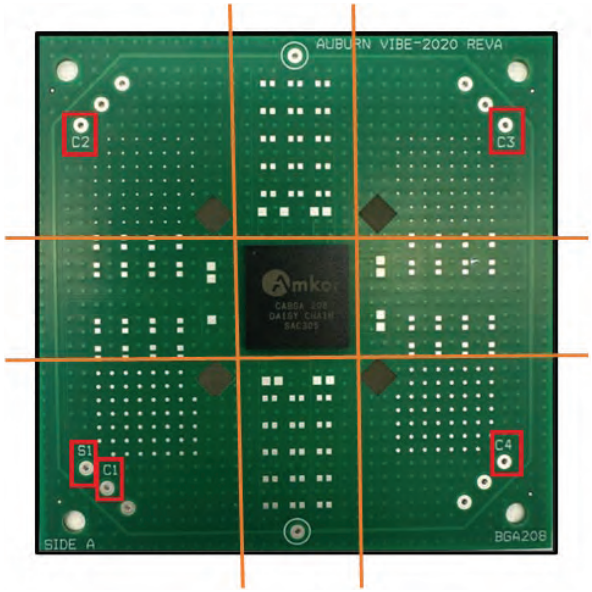


Fig. 2: The test vehicle shows the board substrate, component, and the cutting plane for cross-sectioning.

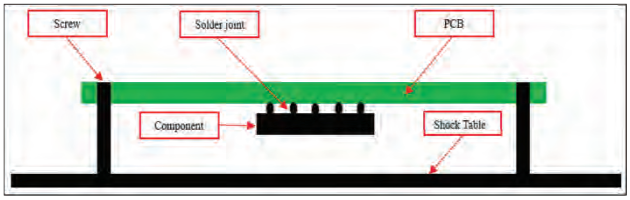


Fig. 3.a: Schematic diagram of test sample.

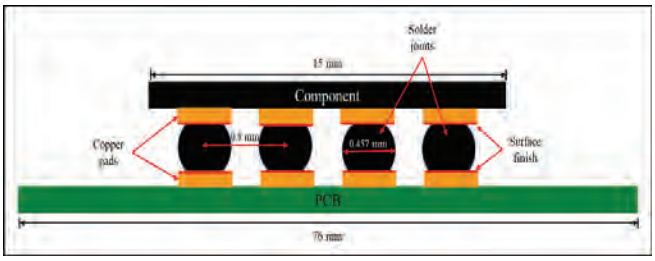


Fig. 3.b: Cross-sectional schematic of the component-on-PCB assembly. It illustrates the mounting of a chip on a PCB using solder joints.

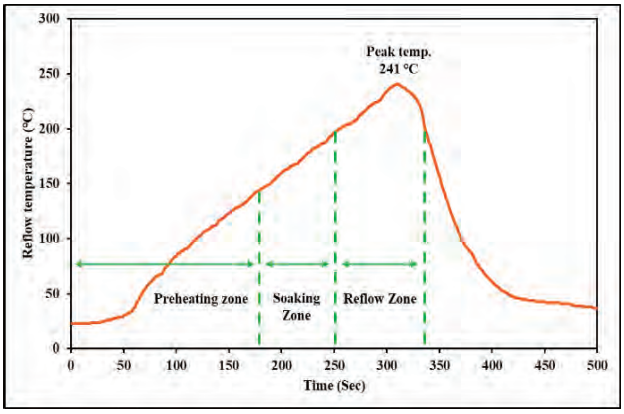


Fig. 4: Reflow temperature profile for SAC305 solder joints assembly.

B. Drop tower

A Lansmont Model 23 mechanical drop shock system was used to conduct the drop tests in this study. The system is equipped with a release mechanism that allows drops to be initiated either manually or automatically. During testing, the shock table holding the test board undergoes free fall and impacts a rigid or semi-rigid surface. The test boards were secured to 12 mm hex standoffs using the four corner tooling holes and mounted on the drop table with the component side facing downward, as illustrated in Fig. 5. The standoffs were tightened to a torque of 0.565 N·m.

Each test board was connected to a Keysight DAQ970A data acquisition system, which was programmed to measure the solder joint resistance after each drop until failure occurred. Failure was defined as a resistance exceeding 100 Ω for three consecutive measurements. This failure criterion follows JEDEC standards and is widely used in solder joint reliability studies [14], [17]. The number of drops required to induce failure in any solder joint was recorded, and the resulting data were fitted to a Weibull distribution to assess solder joint reliability.

An accelerometer was mounted directly on the drop table to measure the input acceleration during setup. During testing, the shock table was raised to the prescribed height using guide rods and then released. Upon release, the table impacted a felt cloth mounted on the seismic base, which was configured to generate the desired shock pulse.

C. Failure Analysis and IMC thickness measurements

A randomly selected subset of boards from each test condition was selected for microstructural analysis. Samples were first extracted from the boards using a precision saw equipped with a diamond sectioning blade. Sectioning was performed along the component using a TrinSaw 2x™ system (Allied), ensuring that the solder joints were not contacted in order to prevent microstructural damage from the cutting process, as indicated by the orange lines in Fig. 2. The extracted samples were mounted in epoxy prepared by mixing resin and hardener in a 6:1 ratio and placed in molds. After curing for 24 hours, the samples were removed for grinding and polishing using a MetPrep 4x™ system (Allied).

Grinding was conducted in six successive steps using 120, 240, 400, 600, 800, and 1200 grit papers, followed by polishing in four stages with 3 µm, 1 µm, 0.05 µm diamond suspensions, and silica. The prepared samples were

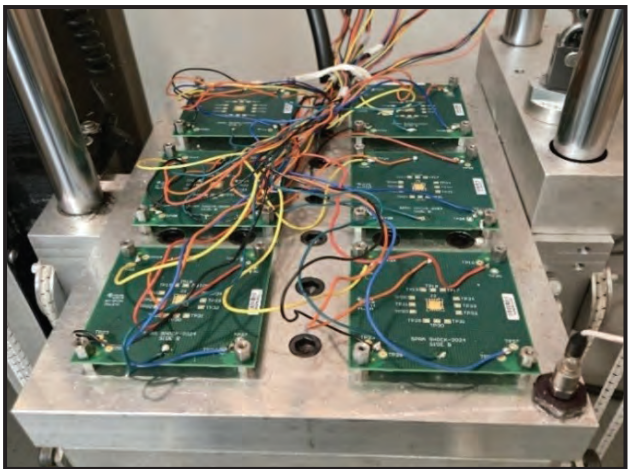


Fig. 5: Lansmont model 23 drop table, showing 6 boards mounted on top of the shock table.

examined using a ZEISS M2m optical microscope equipped with an Axiocam 503 color camera to capture and process microstructural images. These images were used to assess grain recrystallization, identify failure modes and mechanisms, and measure intermetallic compound (IMC) thickness.

IMC thickness measurements were performed using ZENCore2 software by calculating both the IMC area and the IMC length on the board side. The IMC thickness was then obtained by dividing the measured area by the corresponding length, as illustrated in Fig. 6. This procedure was repeated for seven solder joints, and the average IMC thickness was reported.

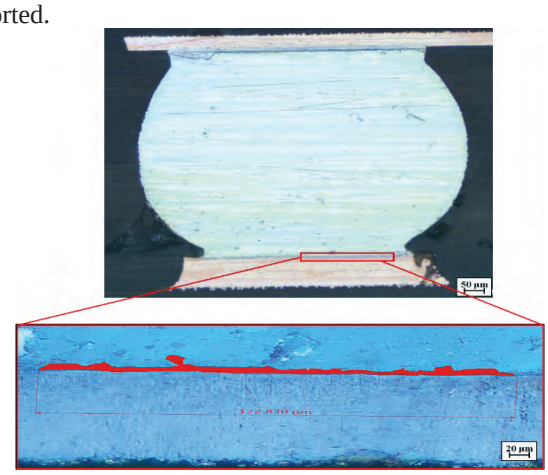


Fig. 6: IMC thickness calculations using ZENCore2 software.

RESULTS AND DISCUSSION

A. Weibull Analysis

All boards were tested until failure, and the failure data for each tested board were analyzed using a 2-parameter Weibull

distribution. The two-parameter cumulative Weibull distribution function is given by $F(t) = 1 - \exp[-(t/\eta)^{\beta}]$, where F(t) is the cumulative density function and η is the characteristic lifetime corresponding to the point where 63.2% of the assembles are predicted to fail. β is the shape parameter that characterizes the distribution of the lifetime data and the behavior of the failure rate. Characteristic life is used in this study because it is physically meaningful, and a standard reliability metric for failure data that follow a Weibull distribution in solder joint reliability studies [14], [15], [16], [18]. A total of 68 boards were subjected to drop shock tests. The characteristic life results from all mechanical drop shock tests are shown in Fig. 6. The results indicate that the characteristic life decreased as aging time increased. Fig. 7 shows the Weibull plots for the samples at each aging time, respectively.

The results demonstrate that aging time significantly reduces the characteristic life of solder joints. Prolonged aging leads to a consistent decline in characteristic life, primarily due to the thickening of the intermetallic compound (IMC) layer and the coarsening of IMC particles, while forming Ag_3Sn within the bulk solder. The Cu_6Sn_5 layer, in particular, transitions from a scallop-like morphology to a thicker, more uniform structure with extended aging duration [19].

The characteristic life decreased from 630 cycles in the unaged condition to 419 after 2 days of aging, further declining to 353 and 99 cycles after 10 and 60 days, respectively. The formed IMC for the samples is mainly Cu_6Sn_5 and Su_3Sn, which is hard and brittle [19].

In addition to affecting the characteristic life, aging also influenced the variability of the failure distribution. The Weibull shape parameter increased with increasing aging time, indicating enhanced stability and predictability of the results. The shape parameter increased from approximately 2.4 (unaged) to over 4 after 60 days of aging, as illustrated in Fig. 8. Aging leads to consistent microstructural changes, specifically, the growth and stabilization of IMC layers, reduction in ductility, and homogenization of failure modes [20]. The correlation plot shown in Fig. 9 highlight the inverse relationship between aging time and joint reliability. The regression model was used to predict the characteristic life as a function of aging, as shown in Equation (1):

$$\eta = AT^{b} \quad (1)$$

where η is the characteristic life (number of drops or cycles), A is a material constant, *T* is the aging time (days), and b is the aging exponent. For the test samples used in this study, A = 345.73 and b = -0.176.

B. Failure analysis

The failure analysis process involved cross-sectioning the failed samples and utilizing microscopy techniques to study the microstructural changes and identify the failure modes, providing insights into the primary causes of solder joint degradation.

The cross-sectional photographs in Fig. 10 show illustrative examples of the microstructural failure modes for the test samples, corresponding to various aging times. All failures occurred on the board side along the brittle interface. The nature and location of the failures were consistent with the aging changes, provided that there were no weak points, such as voids. The crack initiated at the interface between the copper pad and the IMC, then propagated along the IMC regardless of aging time. The location of each crack is highlighted with a rectangular red box to indicate the region of interest. The IMC is the most brittle region and highly susceptible to overstress during mechanical drop shock [21]. The likelihood of brittle failure increases with longer aging times, as the IMC becomes thicker, harder, and more brittle.

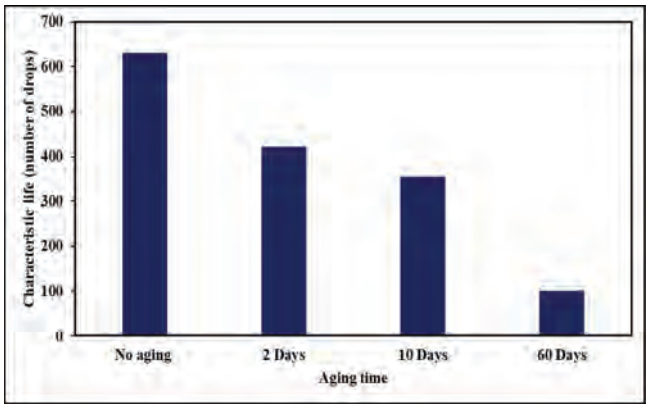


Fig. 7: Influence of aging time on drop shock characteristic life for ImSn finishes.

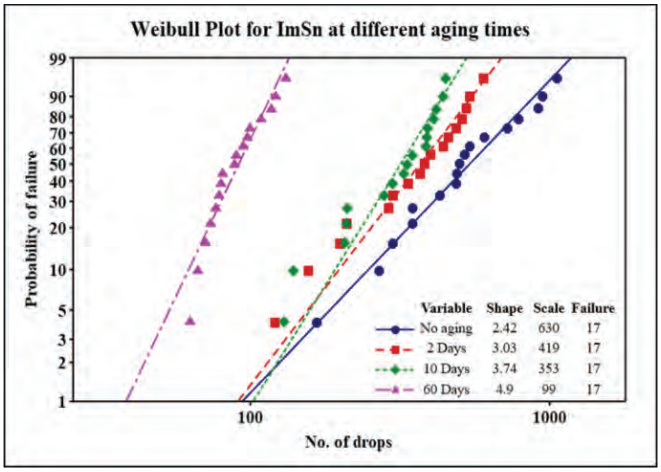


Fig. 8: Weibull reliability analysis for SAC305 solder joints with ImSn finish under different aging periods.

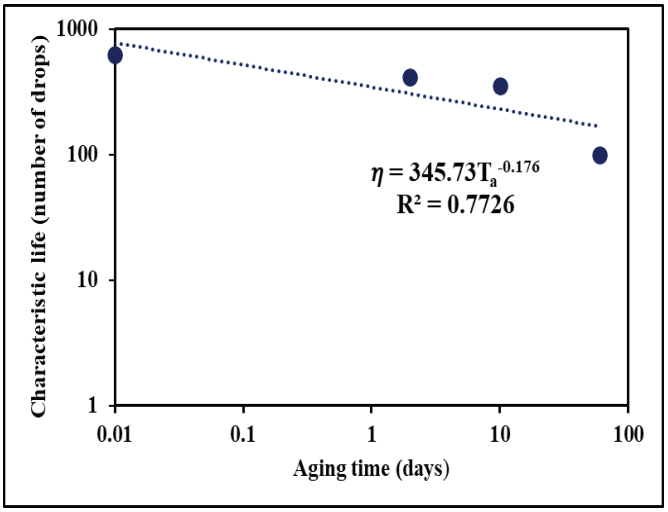


Fig. 9: Correlation between aging time and characteristic life.

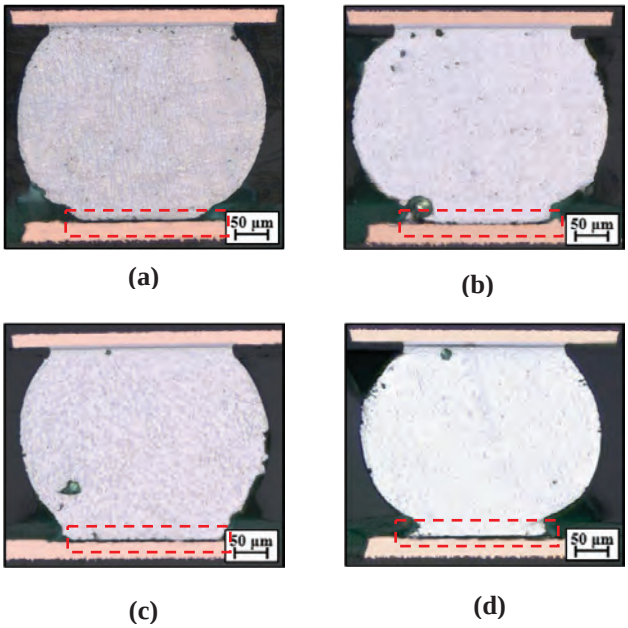


Fig. 10: Failure mode in SAC305 solder joints under different aging times. (a) no aging, (b) 2 days aging, (c) 10 days aging, (d) 60 days aging.

C. IMC thickness analysis

The thickness of the intermetallic compound (IMC) layer plays a critical role in determining the mechanical performance of solder joints [9]. During isothermal aging, the IMC layer continues to grow. Although a thin IMC layer is necessary to promote strong metallurgical bonding, excessive IMC growth can adversely affect solder joint reliability. Increased IMC thickness leads to the formation of a hard and brittle interfacial region, which promotes crack initiation and propagation under mechanical shock loading. As a result, the ability of the solder joint to absorb mechanical energy is reduced, leading to a shorter service life. IMC analysis clearly demonstrates a strong inverse correlation between IMC thickness and solder joint durability; for example, samples with thicker IMC layers exhibited a substantial reduction in the number of drops to failure [7].

To accelerate microstructural evolution within a practical testing timeframe, an aging temperature of 125 °C was selected. Although aging behavior is highly temperature dependent, both IMC growth and solder bulk softening follow Arrhenius-type behavior. Therefore, similar degradation mechanisms are expected to occur at lower or higher operating temperatures over extended timescales [19], [22], [23].

Microscopy images (Fig. 6) were obtained to characterize the IMC layer at various aging durations. The IMC thickness was determined by measuring the total IMC area and dividing it by the corresponding IMC length for each failed joint. For each aging condition, eight joints were analyzed, and the average IMC thickness was calculated along with the standard deviation. For the tested samples, the average IMC thicknesses at no aging, 2 days, 10 days, and 60 days of aging were 2.96 µm (standard deviation: 0.13), 3.63 µm (standard deviation: 0.09), 3.99 µm (standard deviation: 0.14), and 4.17 µm (standard deviation: 0.08), respectively. These results indicate a progressive increase in IMC thickness with aging time, as further illustrated in Fig. 11.

The relationship between average IMC thickness and characteristic life under different aging conditions is presented in Fig. 12. A regression model was employed to predict the characteristic life as a function of IMC thickness for both surface finishes, as expressed in Equation (2):

$$\eta = AW^{b} \tag{2}$$

where η is the characteristic life (number of drops or cycles), A is a material constant, W is the IMC thickness (µm), and b is the thickness exponent. For this study, A = 69708 and b = -4.177. It should be noted that these regression parameters are empirical and specific to the applied loading conditions (1500 G, 0.5 ms) and the test vehicle. They are influenced by several factors, including strain rate, board stiffness, pad design, and component geometry [16], [24]. Consequently, changes in drop severity, pulse duration, or board design will alter the stress distribution and failure mechanisms, necessitating recalibration of the model.

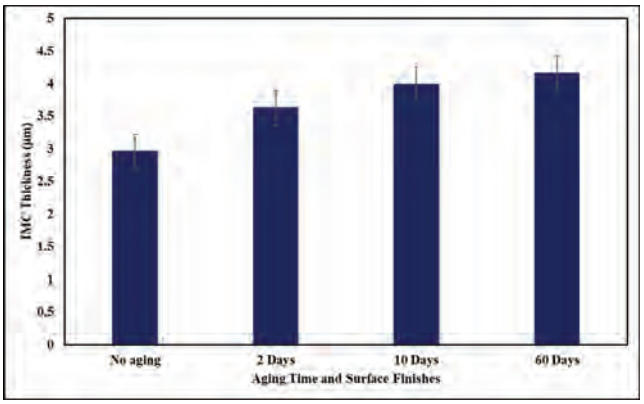


Fig. 11: Average intermetallic compound (IMC) thickness for SAC305 solder joints for different aging durations. The plot highlights the progressive increase in IMC thickness with aging.

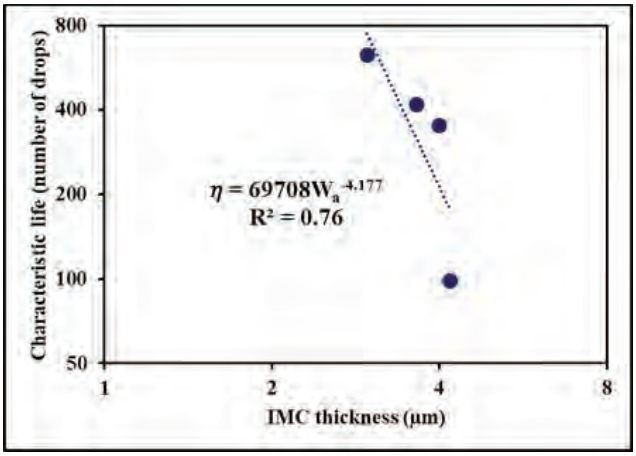


Fig.12: Correlation between IMC thickness and characteristic life for SAC305 with ImSn surface finish.

III. CONCLUSIONS

This study examined the effect of isothermal aging time on the drop shock reliability of SAC305 solder joints with ImSn surface-finished board pads. The results indicate that aging significantly affects solder joint microstructure,

mechanical behavior, and reliability under mechanical shock loading.

Microstructural characterization showed that prolonged aging increased both the thickness and coarsening of intermetallic compounds (IMCs), which in turn degraded joint reliability. Although the bulk solder experienced softening, the IMC layers became progressively harder, leading to interfacial embrittlement and accelerated failure during drop shock testing. The key findings of this study can be summarized as follows:

- Aging reduces drop shock reliability due to increased IMC thickness and coarsening, which promote embrittlement.
- Aging decreases the hardness of the bulk solder while increasing the hardness of the IMC layers, resulting in localized stress concentrations.

These findings establish a foundation for future integrated reliability models that account for aging conditions, microstructural evolution, material properties, surface finishes, operating environments, and packaging design parameters, thereby enhancing predictive accuracy and relevance to real-world operating conditions.

ACKNOWLEDGMENT

This work was supported by the Solder Performance and Reliability Assurance (SPRA) project funded through the United States Partnership for Assured Electronics (USPAE) by Cornerstone Initiate Request (CIR) CS-20-1302 for Lead-Free.

REFERENCES

[1] H. Y. Zahran, A. S. Mahmoud, and A. F. Abd El-Rehim, “Effect of Bi Content on the Microstructure and Mechanical Performance of Sn-1Ag-0.5Cu Solder Alloy,” *Crystals (Basel).*, vol. 11, no. 3, p. 314, Mar. 2021, doi: 10.3390/cryst11030314.

[2] P. P. Vyas *et al.*, “Drop Shock Test of PCB at Elevated Temperature,” in *2024 23rd IEEE Intersociety Conference on Thermal and Thermomechanical Phenomena in Electronic Systems (ITherm)*, 2024, pp. 1–6. doi: 10.1109/ITherm55375.2024.10708973.

[3] M. A. Maruf, G. Rakib Mazumder, S. Chakraborty, J. C. Suhling, and P. Lall, “Effects of Combined Isothermal Aging and Mechanical Cycling Exposures on the Mechanical Behavior of Lead-Free Solder Alloys,” in *2024 23rd IEEE Intersociety Conference on Thermal and Thermomechanical Phenomena in Electronic Systems (ITherm)*, 2024, pp. 1–8. doi: 10.1109/ITherm55375.2024.10709399.

[4] A. Alakayleh *et al.*, “Microhardness Analysis of Reflowed Solder Joints: Effect of Paste Alloy and Paste Volume,” in *2024 23rd IEEE Intersociety Conference on Thermal and Thermomechanical Phenomena in Electronic Systems (ITherm)*, 2024, pp. 1–8. doi: 10.1109/ITherm55375.2024.10709600.

[5] S. H. Kim, H. Tabuchi, C. Kakegawa, and H. Park, “IMC Growth Mechanisms of SAC305 Lead-Free Solder on Different Surface Finishes and Their Effects on Solder Joint Reliability of FCBGA Packages,” *Journal of Microelectronics and Electronic Packaging*, vol. 6, pp. 119–124, 2009, [Online]. Available: http://meridian.allenpress.com/jmep/article-pdf/6/2/119/2248239/1551-4897-6_2_119.pdf

[6] J. Xu, Y. Fu, X. Zhou, J. Zhang, and S. Xue, “Reliability of SnPbSb/Cu Solder Joint in the High-Temperature Application,” *Crystals (Basel).*, vol. 12, no. 12, Dec. 2022, doi: 10.3390/cryst12121724.

[7] S. Daradkeh *et al.*, “Aging Effect on Drop-Shock Reliability of SnAgCu305 Solder Alloy,” in *2024 23rd IEEE Intersociety Conference on Thermal and Thermomechanical Phenomena in Electronic Systems (ITherm)*, 2024, pp. 1–8. doi: 10.1109/ITherm55375.2024.10709567.

[8] A. Alakayleh, S. Hamasha, S. Daradkeh, S. Tahat, J. Evans, and A. Alahmer, “Microstructural Evolution of SAC-Based Solder Joints Exposed to Thermal Cycling: Effect of Paste Alloy, Paste Volume, and Surface Finish,” *IEEE Trans. Compon. Packaging Manuf. Technol.*, p. 1, 2025, doi: 10.1109/TCPMT.2025.3587693.

[9] A. Alakayleh, S. Hamasha, and A. Alahmer, “The impact of paste alloy, paste volume, and surface finish on solder joint,” *Microelectronics Reliability*, vol. 160, p. 115457, 2024, doi: https://doi.org/10.1016/j.microrel.2024.115457.

[10] Z. Huang, P. Kumar, I. Dutta, R. Sidhu, M. Renavikar, and R. Mahajan, “Effects of Microstructure and Loading on Fracture of Sn-3.8Ag-0.7Cu Joints on Cu Substrates with ENIG Surface Finish,” *J. Electron. Mater.*, vol. 43, no. 12, pp. 4485–4496, 2014, doi: 10.1007/s11664-014-3441-6.

[11] S.-M. Lee, J.-W. Yoon, and S.-B. Jung, “Board Level Drop Reliability of Epoxy-Containing Sn-58 mass% Bi Solder Joints with Various Surface Finishes,” *Mater. Trans.*, vol. 57, no. 3, pp. 466–471, 2016, doi: 10.2320/matertrans.M2015260.

[12] N. S. Safee, W. Y. Wan Yusoff, A. Ismail, N. Ismail, M. Abu Bakar, and A. Jalar, “Effect of Blast Wave on Intermetallics Formation, Hardness and Reduced Modulus Properties of Solder Joints,” *Solid State Phenomena*, vol. 307, pp. 31–36, Jul. 2020, doi: 10.4028/www.scientific.net/SSP.307.31.

[13] Q. Fei, W. Xiaoliang, and A. Tong, “Effects of aging time on interfacial fracture behaviors of Sn3.5Ag0.5Cu/Cu joints,” in *2013 14th International Conference on Electronic Packaging Technology*, 2013, pp. 857–860. doi: 10.1109/ICEPT.2013.6756598.

[14] P. P. Vyas, A. Alahmer, S. S. Alavi, M. E. A. Belhadi, and S. Hamasha, “Comparative Drop Shock Reliability Study of SAC-Based Alloys in BGA Assemblies,” *IEEE Trans. Compon. Packaging Manuf. Technol.*, vol. 14, no. 3, pp. 406–416, Mar. 2024, doi: 10.1109/TCPMT.2024.3365819.

[15] JEDEC Solid State Technology Association, “Board Level Drop Test Method of Components for Handheld Electronic Products,” Arlington, VA, USA, 2016.

[16] S. Daradkeh *et al.*, “The Effect of Board Design on the Drop Shock Performance of Lead-Free Solder Alloys.”

[17] R. Chen, M.-H. Wang, S. Lee, J. Ho, I. Hu, and S. Shih, “New / Old JEDEC board level drop reliability test standards evaluation: Measurement and simulation study,” in *2017 IEEE CPMT Symposium Japan (ICSJ)*, 2017, pp. 211–215. doi: 10.1109/ICSJ.2017.8240119.

[18] H. Ma and T.-K. Lee, “Effects of Board Design Variations on the Reliability of Lead-Free Solder Joints,” *IEEE Trans. Compon. Packaging Manuf. Technol.*, vol. 3, no. 1, pp. 71–78, 2013, doi: 10.1109/TCPMT.2012.2223214.

[19] T.-C. Chiu, R. Stierman, D. Edwards, and K. Ano, *Effect of thermal aging on board level drop reliability for Pb-free BGA packages*, vol. 2. 2004. doi: 10.1109/ECTC.2004.1320275.

[20] R. Al-Athamneh, M. Abueed, and D. Bani Hani, “Effect Of Aging on SAC 305 Solder Joints Reliability in Accelerated Fatigue Shear Test,” 2018. [Online]. Available: https://www.researchgate.net/publication/329735469

[21] Z. Liu, M. Fang, L. Shi, Y. Gu, Z. Chen, and W. Zhu, “Characteristics of Cracking Failure in Microbump Joints for 3D Chip-on-Chip Interconnections under Drop Impact,” *Micromachines (Basel).*, vol. 13, no. 2, Feb. 2022, doi: 10.3390/mi13020281.

[22] C. K. Shin, Y. J. Baik, and J. Y. Huh, “Effects of microstructural evolution and intermetallic layer growth on shear strength of ball-grid-array Sn-Cu solder joints,” *J. Electron. Mater.*, vol. 30, no. 10, pp. 1323–1331, 2001, doi: 10.1007/s11664-001-0119-7.

[23] D. R. Frear and P. T. Vianco, “Intermetallic growth and mechanical behavior of low and high melting temperature solder alloys,” *Metallurgical and Materials Transactions A*, vol. 25, no. 7, pp. 1509–1523, 1994, doi: 10.1007/BF02665483.

[24] W. Sun, W. H. Zhu, E. S. W. Poh, H. B. Tan, and R. Te Gan, “Study of five substrate pad finishes for the co-design of solder joint reliability under board-level drop and temperature cycling test conditions,” in *2008 International Conference on Electronic Packaging Technology & High Density Packaging*, 2008, pp. 1–8. doi: 10.1109/ICEPT.2008.4607074.

Part 1: Analysis of Electrode Ageing Based on Signatures of Electrical Arcs

Raul Carreira Rufato
Safran Tech
Blagnac, France
raul.carreira-rufato@safrangroup.com

Malyk Benmouffok
IRT Saint Exupéry
Toulouse, France
malyk.benmouffok@irt-saintexupery.com

Cyril Van de Steen
Safran Tech
Blagnac, France
cyril.van-de-steen@safrangroup.com

Patrick Schweitzer
Institut Jean Lamour-UMR 7198,
University of Lorraine
Nancy, France
patrick.schweitzer@univ-lorraine.fr

***Abstract*— The introduction of power supplies comprising continuous sources in both aeronautics (270 VDC) and domestic applications (solar panels, electric vehicles) requires electrical safety measures, particularly in view of series arc faults, which are difficult to detect. The development of detection strategies is often carried out in laboratories using electrical loads, cable types, and different circuit configurations. Nevertheless, the ageing of electrodes in high-voltage systems significantly impacts the reliability and lifespan of the equipment. This study presents an analysis of electrode ageing, focusing on the electrical signatures—specifically current and voltage—generated during arc faults in a DC network. Two experimental setup approaches were used to generate arc fault signatures: a moving electrode table and a connection terminal block on a vibrating table. Through the acquisition and processing of electrical signals, this work proposes to analyse the evolution of these signatures across multiple test cycles. The findings can show a correlation between changes in electrical signatures and the degradation of electrodes. This work highlights the potential for using electrical signature analysis as a diagnostic tool for assessing electrode ageing, offering insights for the predictive maintenance of high-voltage systems.**

Keywords*— *Electrode ageing, arc fault detection, electrical signatures, high-voltage systems, aeronautics.

I. INTRODUCTION

The growing demand for embedded electrical power in aircraft is imposing the aeronautical industry to modify and modernize existing system configurations. This increased requirement for embedded electricity directly impacts the necessary voltage levels, as raising the current would result in higher weight. Consequently, distribution networks are expected to evolve towards High Voltage Direct Current (HVDC) architectures, typically at voltages such as 540 VDC, 800 VDC, and even 1 kVDC.

In this context, the occurrence of electrical arcs—whether in series or parallel with the load—presents significant safety concerns for flight operations. Therefore, with the trend towards more electric aircraft, this issue is becoming increasingly critical, since the energy dissipated during arc events is directly related to the onboard power levels. Electrical arcs can appear in various places within an aircraft, such as inside contactor switching chambers, on terminal blocks due to vibration, or even during maintenance when disconnecting connectors. The intermittent manifestation of an electrical arc, if undetected, can lead to electrode degradation, potentially shortening the equipment's lifespan.

During the separation of electrodes—such as when contacts are opened—an electrical arc can form across the gap, posing a significant threat to the integrity and longevity of electrical components [7]. This phenomenon directly impacts the contact materials, inevitably accelerating their physical and electrical degradation [3,4]. At the microscopic scale, solid surfaces are far from smooth; they are covered with asperities resulting from manufacturing processes and material properties [2,3,5,6]. When two electrodes make contact, the interface comprises discrete points where these microscopic asperities interact mechanically, rather than forming a uniform surface. Consequently, the true area where physical contact occurs is only a small fraction of the nominal apparent area, and the effective electrical contact surface is even smaller due to the need for current transfer at these limited surfaces [2,4,5].

These so-called "conduction spots" are decisive for ensuring efficient current flow. Their number and size are influenced by numerous factors, such as the force applied during contact, the precise roughness of each electrode, the hardness of the constituent materials, and the cleanliness or contamination of the surfaces [2,4,5,6]. As the contacts begin to separate, both the quantity and quality of these conduction spots decrease, which leads to a substantial rise in local electrical resistance. This increased resistance is a critical factor in the initiation and propagation of electrical arcs [3–6], further accelerating localized heat generation and material erosion at the electrode tips. Repeated arc formation and interruption under these conditions enhance the degradation process, altering the contact's geometry and surface properties, thereby compromising their long-term reliability and potentially impacting the overall safety of aircraft electrical systems [1,3,4,7].

The objective of this study was to analyze the impact of electrode aging under intermittent electrical arcs, with a specific focus on whether such aging affects electrical observables, such as current and voltage. This analysis is vital for understanding potential impacts on detection algorithms based on electrical signatures, which are commonly used, as well as for the development of health monitoring systems that aim to proactively replace aging components. The study primarily concentrates on DC series arcs, which are considered among the most challenging to detect. Experimental tests were conducted to accurately represent distinct types of arc occurrence: (i) moving electrodes, and (ii)

a terminal block over a vibration table. Both setups used various current intensities and electrode materials to ensure comprehensive coverage of operational scenarios.

II. Setup and Database Generation

The database used in this study is the same as that described in the part 2 paper that contains all details [8]. This applies to both the raw and labelled data.

The scheme could be resumed as:

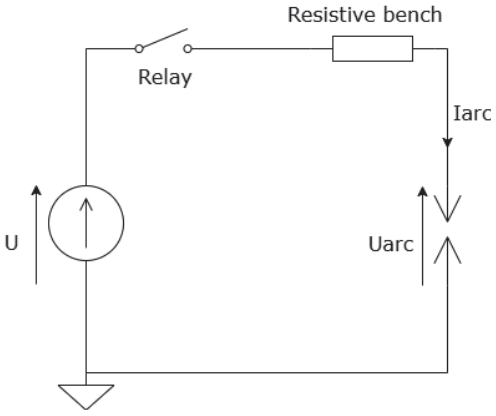


Fig. 1. Schematic representation of the test bench.

A schematic diagram of the electrical circuit used is shown in Figure 1. Further details regarding the experimental setup and electrical characteristics are provided in [8] of this work. Three types of tests were performed under 200 V DC with current levels of 10A and 20A.

The tests consist of generating an arc by opening the circuit while the current is already established. On the first 3 tests, the electrodes were modified.

On test 1, a pod and a terminal block were used. On test 2, a pod and a Cupper plate were used, and on test 3, a pod and a ferrous plate were used. Ferrous plate was used since the terminal block was mostly made of iron.

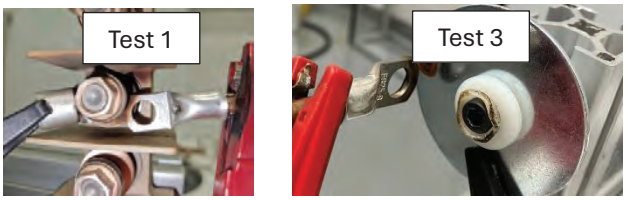


Fig. 2. Representation of different tests electrodes (test 1 & 3).

On last test (number 4), a vibrating pot was used to have terminal block loss connections

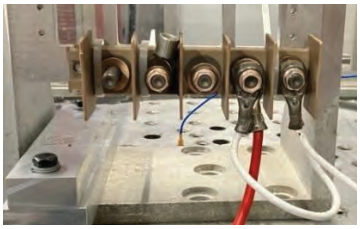


Fig. 3. Representation of terminal loss connection for test 4.

Each experiment, 5s of measured was acquired at 1MHz sampling. All electrodes were kept the same for all experiments made at each test and were not cleaned between each trial.

III. Methodology of the Numerical Analysis

A. *Arc data signatures*

After acquisition, current signals were segmented into 0.1 ms windows, a duration chosen to capture only the region around each arc fault ignition. Labelling of the arc windows was guided by arc the voltage (Uarc) measurements, which serve as definitive indicators of arc faults but are only available under controlled laboratory conditions [7]. For each window, if the arc voltage was found within the range [10V, Uarc], an arc event was considered present, and the window was stored. Only transient current regions were retained to capture the dynamic behaviour associated with arc ignition; windows representing steady-state arc conditions were excluded [9,10]. See an example of labelled window on Fig. 4, that shows arc current signals based on their temporal appearance order during the test campaigns.

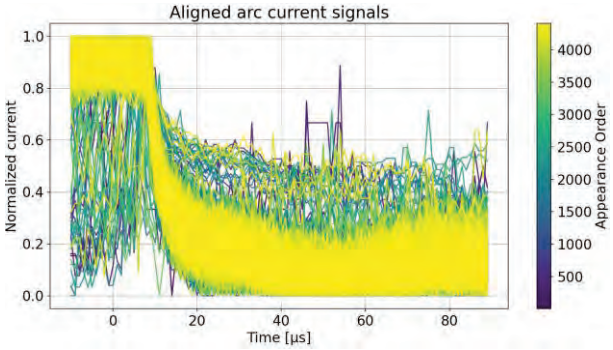


Fig. 4. Example of labelled current windows for Test 4. Signals have different colours depending on their appearance order.

It is important to highlight that the number of arcs generated may be greater than the number of times the electrodes were separated. This is because, during the tests, the arcs can extinguish and reappear until they become stable and well established. Thus, a single separation of electrodes can produce several arcs until this stabilization occurs. A summary of the quantity of labeled data for each type of test is presented in TABLE I.

TABLE I. NUMBER OF LABELLED WINDOWS PER TEST

Test	Number of labelled windows
1	167
2	144
3	75
4	4200

B. Features extraction

To quantitatively characterize the aging caused by the DC series arcs, some features were extracted from the current signals. These features have been selected based on their sensitivity to the physical phenomena associated with arc formation and their potential ability to capture both dynamic and statistical aspects of the signal. More details about the features can be found on [11]:

- **High-Frequency RMS (HR):** RMS value of the detrended current in the window after arc appearance.
- **Post-Transition Mean (PM):** Mean value of the current after the arc transition event.
- **Crest Factor (CF):** Maximum absolute value divided by the RMS of the current.
- **Current slope (CS):** Linear slope estimated over a moving window throughout the signal.
- **Mean Frequency (MF):** Mean frequency, amplitude-weighted, of the current's frequency spectrum.
- **Current Energy (EG):** Total energy of the current signal after arc appearance.
- **Current Entropy (ET):** A measure of the randomness or complexity in the current signal, calculated via Shannon entropy after arc appearance.
- **Transition index (TI):** The difference in number of samples between the moment when arc voltage becomes greater than 10V and the appearance of the equivalent current drop.

These features could provide a comprehensive description of the signal in the presence of a DC series arc. They were proposed to capture both the deterministic and stochastic variations.

C. Aging index calculation

Principal component analysis (PCA) was then applied to the feature matrix to extract a low-dimensional representation of the degradation process. PCA is a widely used multivariate analysis technique that identifies orthogonal directions maximizing variance in the data and has been employed for degradation analysis in condition monitoring applications [8,9]. By projecting data onto the direction of maximum variance, PCA enables the identification of a latent variable that captures the dominant evolution shared across the different features.

In this work, only the first principal component was retained to represent the aging variable, under the assumption that progressive degradation constitutes the primary source of correlated variability among the extracted features. This assumption is made because there is no variability in the type of data (no nominal regimes from load transients); there is no variation in the type of test (they are analyzed individually); and there is no variation in the circuit connected to the electric arc. The resulting aging variable was then linearly rescaled to the interval [0,1], in order to have a normalized aging index.

The mathematical description is the following: let $\mathbf{s}_n(t)$ denote the current amplitudes inside a time window for sample $n = 1, \dots, N$, with $t = 1, \dots, T$. Each window was individually normalized to map all values into the interval of $[0,1]$:

$$\tilde{\mathbf{s}}_n(t) = \frac{\mathbf{s}_n(t) - \min(\mathbf{s}_n)}{\max(\mathbf{s}_n) - \min(\mathbf{s}_n)}, \quad t = 1, \dots, T \qquad (1)$$

This ensures that the normalized current amplitudes inside a window $\tilde{\mathbf{s}}_n(t)$ are bound between 0 and 1, improving feature comparability. Therefore, from each normalized window $\tilde{\mathbf{s}}_n(t)$, the set of P features (P = 7) $x_{n,P}$ was calculated, forming the feature matrix

$$\mathbf{X} = \left[x_{n,p}\right] \in \mathbb{R}^{N \times P} \qquad (2)$$

PCA was then applied to $\mathbf{X}$ to extract a low-dimensional representation of the degradation process. PCA identifies orthonormal directions $\mathrm{P_{Ck}} \in \mathbb{R}^P$ that sequentially maximize the projected variance:

$$\mathrm{P_{C1}} = \arg\max_{\|\mathbf{w}\|=1} \mathrm{Var}(\mathbf{X}\mathbf{P_C}) \qquad (3)$$

where $\mathrm{P_{C1}}$ corresponds to the first principal component, representing the dominant shared variation among features. The aging variable is obtained by projecting each feature vector onto $\mathrm{P_{C1}}$:

$$z_n = \mathbf{x}_n^{\mathsf{T}} \mathrm{P_{C1}}, n = 1, \dots, N \qquad (4)$$

Finally, the aging variable is also normalized between 0 and 1:

$$Aging\ Index = \frac{z_n - \min(z)}{\max(z) - \min(z)}, n = 1, \dots, N \qquad (5)$$

Because all the current windows are temporally aligned, $Aging\ Index$ is directly comparable across different samples at the same degradation stage.

To enhance physical interpretability, the weights associated with the first principal component were evaluated. PCA weights quantify the contribution of each original feature to the aging direction, such that features with large absolute weights are identified as dominant contributors to the inferred degradation process. This analysis could provide insights into the underlying physical mechanisms captured by the proposed aging indicator.

This analysis can be obtained by using the PCA weights $\mathrm{P_{C1}} = [w_{1,1}, \dots, w_{1,P}]^{\mathsf{T}}$, where features with large absolute weights $|\, w_{1,p}|$ are the most important for the computation of this specific component.

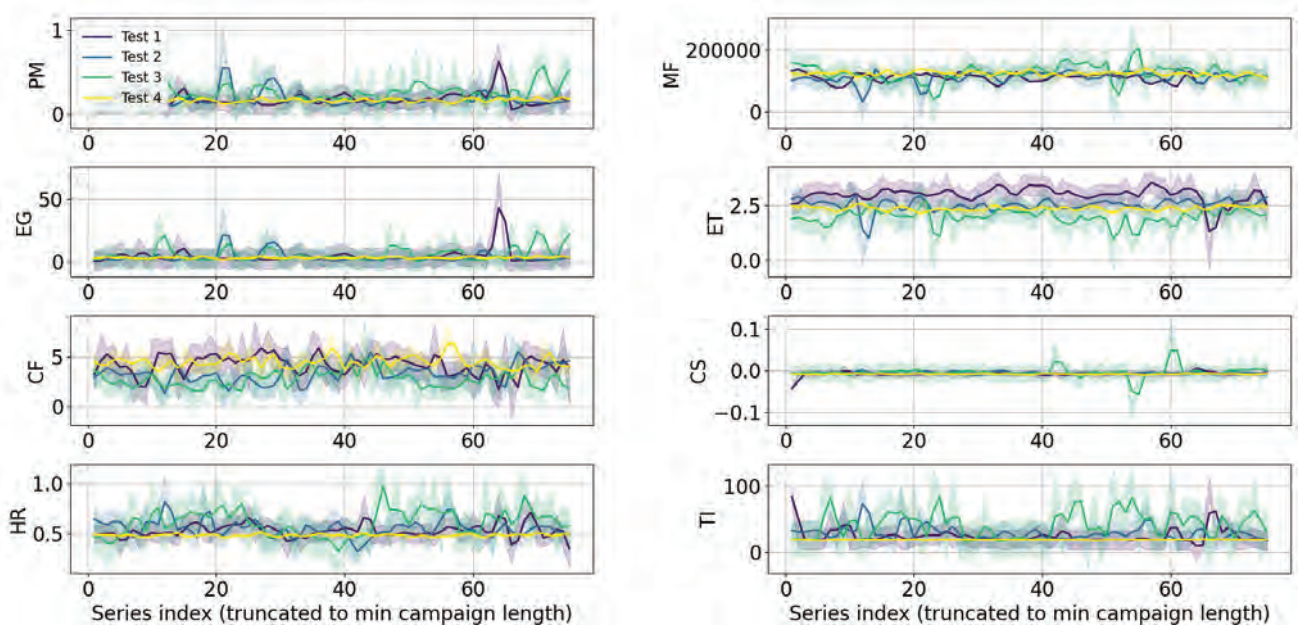


Fig. 5. Evolution of the calculated features for the different test numbers.

IV. RESULT ANALYSIS

After calculating the features for each window of each test, it was possible to generate a curve (Fig. 5) illustrating the variation of each variable, aligned according to the moment of the window's occurrence. In other words, points on the left side of the curve represent newer electrodes, while points on the right correspond to electrodes that are more degraded. For comparison between different tests, the values were plotted in an overlapping manner, limited by the lowest number of arcs available across all tests. In this case, Test 3 was the limiting factor, with a total of 75 windows. The mean curves were generated by applying a three-point moving average, and the variance across tests is also shown.

Firstly, it can be observed that some features are not test-dependent, meaning they do not show significant variation across different types of tests. This is the case for EG, MF, and CS. However, other features exhibit more pronounced differences, such as PM, CF, HR, ET, and TI, with ET showing a particularly notable difference.

Secondly, regarding aspects related to aging, limited information can be derived from the average value of the individual variables. There is, however, a slight increase in variance for the majority of the features. One reason for this lack of clear visualization is the limited number of tests considered, which restricts the ability to better observe these trends. Due to this constraint, analyzing the aging index becomes particularly useful, as it accounts for the total number of windows obtained from each test. The results obtained after computing this index can be seen in Fig. 6, Fig. 7, Fig. 8 and Fig. 9.

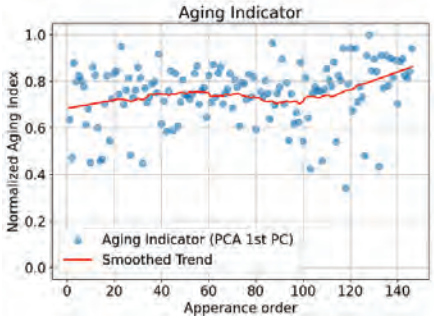


Fig. 6. Aging indicator calculated for all labelled windows from Test 1. A smothed trend is calculated based on their appearance order to evaluate the aging aspects.

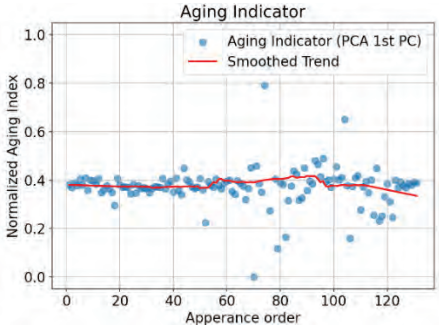


Fig. 7. Aging indicator calculated for all labelled windows from Test 2. A smothed trend is calculated based on their appearance order to evaluate the aging aspects.

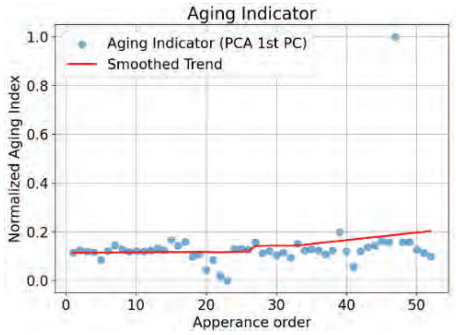


Fig. 8. Aging indicator calculated for all labelled windows from Test 3. A smothed trend is calculated based on their appearance order to evaluate the aging aspects.

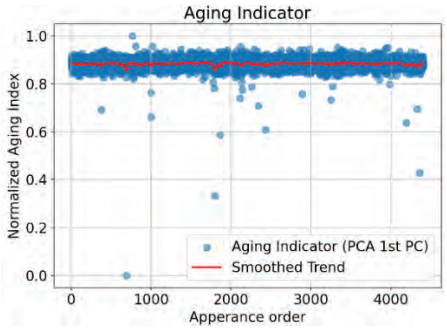


Fig. 9. Aging indicator calculated for all labelled windows from Test 4. A smothed trend is calculated based on their appearance order to evaluate the aging aspects.

Upon analyzing the curves obtained, it can be observed that Tests 1 and 3 show a trend for the aging indicator to increase with the test duration. In contrast, Test 2 demonstrates a decreasing trend. There is no issue with the trend being opposite, as the weighting of the features may differ among the different features calculated. Furthermore, for Test 4, the variation is negligible and hardly noticeable. This observation is consistent with the physical expectations for this type of test. This outcome is primarily due to the nature of Test 4—performed on terminal blocks over a vibrating table—which does not produce long-duration arcs compared to the other test types, thereby limiting electrode degradation. Another, although less probable, factor could be the selection of features that may not have been effective in extracting relevant aging indicators from the electrical current alone.

V. Conclusions and Perspectives

In this work, we propose an analysis of the aging of electrodes subjected to series DC electrical arcs across different test configurations. A systematic approach was used to derive an aging factor by calculating specific features from the measured electrical current during discharges.

Upon evaluating the results, it was observed that the test configuration involving terminal blocks on a vibrating table showed minimal signs of degradation—based solely on the calculated features—when compared to the other test setups. Furthermore, a higher Transition Index (TI) value was detected for Test 3 relative to the other campaigns. This outcome may be attributed to the particular type of arc initiation or the electrode material employed.

Although the obtained results are of interest, the analysis could be further refined by tailoring the selection of degradation features to the requirements of specific applications. A more comprehensive investigation into the degradation features is recommended for future work to enhance the representativeness of the analysis.

It is well known that contact resistance is among the variables most affected by electrode aging. However, this study focused exclusively on evaluating electrical current, as it is a measurement commonly collected in aircraft systems. Incorporating contact resistance would require measurements of arc voltage, which is challenging in series arc scenarios due to the difficulty in identifying the exact arc location. For this reason, the investigation was limited to current measurements.

References

[1] A Novel Approach for Arc-Flash Detection and Mitigation: At the Speed of Light and Sound (2013) J. Clerk Maxwell, A Treatise on Electricity and Magnetism, 3rd ed., vol. 2. Oxford: Clarendon, 1892, pp.68–73.

[2] Kim, M.; Lim, J.W.; Lee, D.G. Electrical contact resistance between anode and cathode bipolar plates with respect to surface conditions. Compos. Struct. 2018, 189, 79–86.

[3] P.G. Slade. Electrical Contacts: Principles and Applications. CRC Press Taylor & Francis Group edition, New York, 2014.

[4] R. Holm. Electric Contacts: Theory and Applications. Springer Verlag GmbH, fourth edition, 1967.

[5] L. Féchant. Le contact électrique : phénomènes physiques et matériaux. Collection SEE, Hermes édition, 1997.

[6] W. Rieder. Electrical Contacts: an introduction to their physics and applications. VDE Verlag, 2005.

[7] S. Vacquié, ‘Arcs électriques’, Eyrolles, 2000.

[8] R. C. Rufato, M. Benmouffok, C. Van de Steen and P. Schweitzer, "Part 2: Reflection and Methodology for Arc Database Signal Generation in Aircraft Systems," in Proceedings of the International Conference on Electrical Contacts (ICEC 2026), Trondheim, Norway, 2026.

[9] R. C. Rufato, T. Ditchi, C. V. de Steen, T. Lebey, and Y. Oussar, “DC serial arc fault recognition in aircraft using machine learning techniques,” International Journal of Electrical Power & Energy Systems, vol. 164, p. 110408, Mar. 2025, doi: 10.1016/j.ijepes.2024.110408.

[10] R. C. Rufato, T. Ditchi, C. Rond, C. Van de Steen, T. Lebey, and Y. Oussar, “Impact of the Sampling Frequency on the Detection of Series DC Arc Faults in an Aeronautical Environment Using Machine Learning Techniques,” in 2023 IEEE 68th Holm Conference on Electrical Contacts (HOLM), Oct. 2023, pp. 1–6. doi: 10.1109/HOLM56075.2023.10352186.

[11] R. C. Rufato. “Arc fault recognition in aircraft using machine learning techniques”. Phd Thesis, Sorbonne Université, 2025.

Part 2: Reflection and Methodology for Arc Database Signal Generation in Aircraft Systems

Malyk Benmouffok
IRT Saint Exupéry
Toulouse, France
malyk.benmouffok@irt-saintexupery.com

Raul Carreira Rufato
Safran Tech
Blagnac, France
raul.carreira-rufato@safrangroup.com

Cyril Van de Steen
Safran Tech
Blagnac, France
cyril.van-de-steen@safrangroup.com

Patrick Schweitzer
Institut Jean Lamour-UMR 7198,
University of Lorraine
Nancy, France
patrick.schweitzer@univ-lorraine.fr

***Abstract*— The use of artificial intelligence is spreading at an exponential pace nowadays. However, there are still fields where its application remains a subject of debate. Aircraft safety is among them. The implementation of new safety systems, particularly electrical ones, is a key area for improving security, especially in the detection of electrical arcs. The increase in onboard voltage and power will inevitably raise both the likelihood of these phenomena occurring and their potential danger. IA could help to improve the efficiency of those systems and the global aircraft safety. As with any subject related to the use of artificial intelligence, one of the major challenges is the representativeness of experiments and the generation of databases that truly reflect real-world conditions. In this work, we propose exploring the possibility of completing realistic aeronautical testing with the use of a vibration table to simulate connection loss on a power terminal block. We will then simplify the setup as much as possible, ultimately working only with electrodes made of selected materials. Finally, we will compare the results in terms of database relevance and present our conclusions.**

Keywords*— *Electrode ageing, arc fault detection, electrical signatures, high-voltage systems, aeronautics.

I. INTRODUCTION

Artificial intelligence (AI) is transforming many industries by enhancing performance across a wide range of applications. This transformation is largely driven by the ability of AI to model complex phenomena and to extract hidden patterns from large volumes of data. Because of these capabilities, the aeronautical sector has also shown growing interest in AI solutions, particularly as data availability and acquisition capabilities on aircraft continue to expand.

The increasing amount of data expected on future aircraft is a direct consequence of the growing electrification and connectivity of embedded devices. However, this evolution also introduces new challenges that were not encountered in conventional aircraft systems, such as the detection of series arc faults. These discharges, especially when in series with the load, are particularly difficult to detect. Distinguishing the electrical signatures of arc phenomena from nominal circuit behavior is challenging, as the induced variations are often subtle and easily masked by normal operating conditions.

As a result, the use of AI techniques for series arc fault detection has gained interest [4, 7, 8]. Such approaches have been reported in various fields, including photovoltaic systems, electric vehicles, residential electrical installations [1,2], and aeronautical applications [3,4]. Nevertheless, the uncritical application of these algorithms can be problematic when the characteristics and limitations of the underlying datasets are not fully understood.

One of the main challenges in designing datasets for training arc recognition algorithms is ensuring that they are representative of the electrical signatures encountered in real operational conditions. This issue is particularly critical for future generations of more-electric aircraft, for which many systems are still under development, making it difficult to accurately anticipate the actual behavior of series arc faults.

A common approach to build series arc fault datasets consists of separating two horizontally aligned electrodes [5, 6] at a constant speed while they are connected to an electrical circuit comprising a power supply, cabling, and a set of loads [10, 11]. However, in aircraft systems, series arc faults most frequently occur at terminal blocks (see Fig. 1). In these components, aircraft vibrations experienced during successive flights can gradually loosen screws connections, allowing contacts to move slightly and randomly apart, thereby generating repeated arc events.

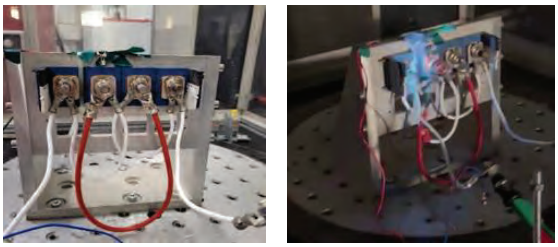


Fig. 1. Terminal losing connection block

In this paper, we address the problem of constructing a representative series arc fault dataset for DC aeronautical systems, with the objective of learning a decision function capable of recognizing such faults. Specifically, we investigate the representativeness of different experimental test setups. We compare whether controlled electrode separation produces electrical signatures similar to those generated by arcs occurring in terminal blocks with loosened connections mounted on a vibration table. Although the latter configuration can generate a larger number of arc events, it may be difficult to implement in

practice due to the cost and limited availability of the required equipment. This constraint partly explains why the electrode separation method is commonly used for dataset construction. However, important questions remain regarding how representative this testing approach is of real-world aeronautical arc fault conditions.

II. Setup and Database Generation

The dataset consists essentially of four types of series DC electrical arc tests, each generated by distinct methods and utilizing different materials.

TABLE 1 SUMMARY OF TEST CONFIGURATIONS

	Test 1	Test 2	Test 3	Test 4
Configuration	Pod - terminal	Pod – Cu plate	Pod – Fe plate	Terminal on Shaker
Anode	Pod	Pod	Pod	Pod
Cathode	Terminal	Copper plate	Iron plate	Terminal
Current Intensity	10A 20A	10A 20A	10A 20A	10A 20A
Voltage	200VDC	200VDC	200VDC	200VDC

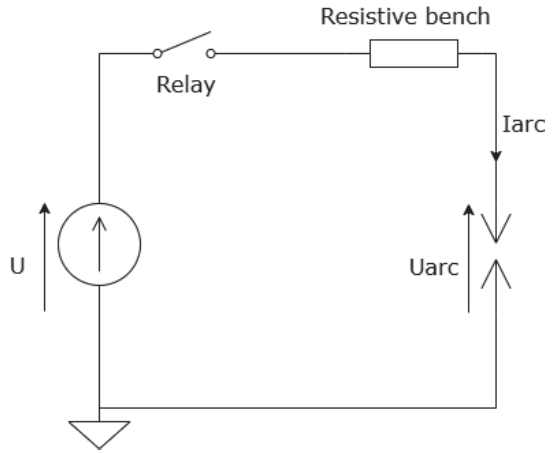


Fig. 2. Electric circuit scheme

An electrode actuation system enables the anode and cathode to be brought into contact and subsequently separated to open the circuit. The DC power supply is set to 200 VDC. A series resistor (10 Ω and 20 Ω) is used to limit the current to a range of 10–20 A. The electrode materials were modified whenever feasible, while maintaining application-oriented consistency. Arc voltage as well as supply voltage were measured. A relay was connected in series with the resistive load bank to ensure system safety when no tests were being performed. This relay is energized shortly before circuit opening and arc ignition. The DC voltage is applied to the system shortly before contact separation. The current is already established at the moment the electrodes separate. Upon contact opening, an arc is initiated and progressively elongates. This elongation is driven by a step-motor and a microcontroller.

Test 1 consists of establishing contact and then opening the circuit, using the terminal thread as the cathode and a cable lug as the anode. The materials are mainly steel.

Tests 2 and 3 are simplified versions of Test 1, in which the threaded terminal was replaced by a metallic washer (copper or steel).

Test 4 is a shaker test referred to as a “loose terminal” test. It simulates terminal loosening and the resulting spark generation.

A. Features extraction

To quantitatively characterize the aging caused by the DC series arcs, some features were extracted from the current signals. Those features are the same used in the Part 1 paper of this series [9]:

- **High-Frequency RMS:** RMS value of the detrended current in the window after arc appearance.
- **Post-Transition Mean:** Mean value of the current after the arc transition event.
- **Crest Factor:** Maximum absolute value divided by the RMS of the current.
- **Current slope:** Linear slope estimated over a moving window throughout the signal.
- **Mean Frequency:** Mean frequency, amplitude-weighted, of the current’s frequency spectrum.
- **Current Energy:** Total energy of the current signal after arc appearance.
- **Current Entropy:** A measure of the randomness or complexity in the current signal, calculated via Shannon entropy after arc appearance.

The only difference is that in this work we computed all the proposed features using current and arc voltage signals.

III. Result Analysis

One approach to achieving the main objective of this study was to align the waveforms with respect to the start of the labeling window. Subsequently, an average curve and its associated variance were calculated for each test, excluding outlier values. This straightforward calculation enables visualization of the waveforms and the trends exhibited by each curve. The results can be seen in Fig. 3.

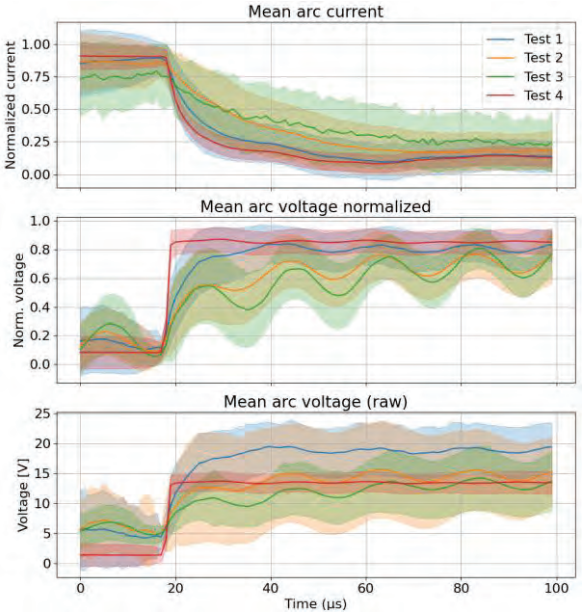


Fig. 3. Mean and variance arc current and voltage for the different test campaigns. An individual normalization was applied to each test campaign.

Fig. 3 presents the normalized values of current and voltage for the electrical arcs, as well as the unnormalized arc voltage. By examining only the electrical current, it is particularly noteworthy that Tests 1 and 4 exhibit strong similarities. Both tests utilized electrodes composed of the same materials (Cote Cosse), although the arc generation methods differed: Test 1 was performed by adjusting electrode spacing, whereas Test 4 used terminal blocks on a vibrating table. Raw voltage are also plotted to show that the arc voltage behavior is different from test to another. Test 1 has a higher voltage due to the ignition mechanism (shaker) which allows us to reach 20V faster than the opening step motor. We have observed a very short duration. For longer time test 2,3 and 4 have higher value of arc voltage than test one, the electrode gap increases with time.

The average values further highlight this similarity, which may be of interest for test cost reduction, as the equipment required for Test 4 is significantly more complex than that used for Test 1. However, it should also be noted that Test 4 produces up to 40 times more arcs than Test 1.

Another interesting observation is that the arc voltage in Test 4 is considerably less variable compared to the other test types. For absolute voltage values, it is expected that Test 1 displays a higher average voltage (after arc initiation), which can be attributed to the greater possible electrode spacing in this configuration.

To quantitatively assess the observed similarity in the electrical signals, we used the Euclidean distance to measure, in the feature space, the distance between the average signals calculated for each test and their respective variances. The resulting values were normalized between 0 (indicating low similarity) and 1 (indicating complete similarity). These similarity values are presented in the correlation matrices shown in Fig. 4, Fig. 5, Fig. 6 and Fig. 7.

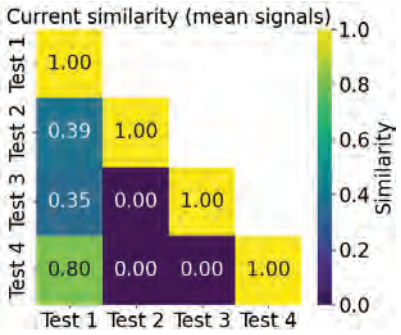


Fig. 4. Current distribution similarity between different tests campaigns using all calculated features and mean signals. Values lower than 0.00 are approximated to 0.

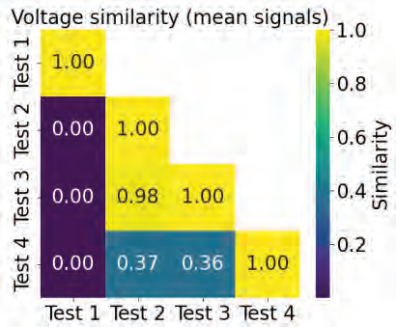


Fig. 5. Arc voltage distribution similarity between different tests campaigns using all calculated features and mean signals. Values lower than 0.00 are approximated to 0.

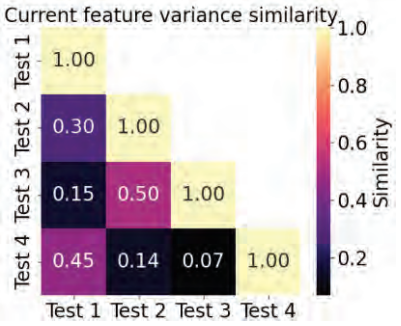


Fig. 6. Current distribution similarity between different tests campaigns using all calculated features and variance signals. Values lower than 0.00 are approximated to 0.

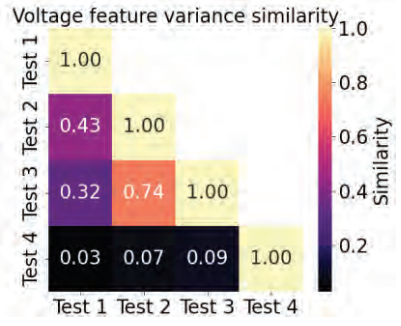


Fig. 7. Arc voltage distribution similarity between different tests campaigns using all calculated features and variance signals. Values lower than 0.00 are approximated to 0.

Upon examining Fig. 4, we can observe an 80% similarity between Tests 1 and 4, which was expected given the temporal signals. Notably, this similarity is also reflected in the feature space. In terms of variance, however, these two

tests show a weaker similarity, which can be attributed to the larger number of samples generated in Test 4—thus granting it greater statistical significance.

For the normalized voltage signals, this correlation is not as evident, except for a high similarity observed between Tests 2 and 3, which also demonstrate substantial similarity in terms of variance.

IV. Conclusions and perspectives

The objective of this article was to compare the electrical signatures of different series arc tests, generated using two distinct initiation methods: electrode spacing and terminal blocks with poor connections over a vibrating table. The primary motivation for this analysis is to address a major challenge in the development of arc fault detection algorithms based on artificial intelligence: the construction of representative test databases for model training. If this database is not sufficiently representative, the learned detection function will not achieve optimal performance. However, conducting fully representative tests—such as those involving terminal blocks on a vibrating table—can be both costly and complex.

This work therefore enabled a comparison between these complex test setups and more simplified tests, such as electrode gap spacing, to assess whether substitution is feasible. Based on the results and the features selected, we found that the correlation between the two types of tests remains high, although not perfect, which is a strong indicator for potential cost reduction in database creation for this application.

We observed that this correlation is more prominent in the current signatures than in those for arc voltage. Nevertheless, this is not necessarily a significant issue, as arc voltage is rarely used for detection purposes due to measurement difficulties in practical scenarios. In our study, arc voltage was used only as a labeling variable, effectively fulfilling its role—the underlying physics of electrical discharge ensures that arc voltage always exceeds a threshold during arc events.

Future research should focus on selecting features directly aligned with the chosen detection algorithm. In this work, detection analysis was not performed, as it would require "nominal" electrical signatures containing current transients under the same test conditions. A promising direction for future investigation would be to pre-select features relevant to detection and then apply the proposed methodology to measure the signal correlation within this subgroup of variables, thereby confirming their closeness and suitability for database construction.

References

[1] F. Ferracuti, R. Felicetti, L. Cavanini, P. Schweitzer and A. Monteriù, "Real-Time Series Arc Fault Detection and Appliances Classification in AC Networks Based on Competing Convolutional Kernels," in *IEEE Open Journal of the Industrial Electronics Society*, vol. 6, pp. 1050-1065, 2025, doi: 10.1109/OJIES.2025.3582482.

[2] P. Schweitzer, A. Maoukouf, E. Tisserand, Y. Berviller and S. Weber, "Multi-Criteria Analysis of Series Arc Faults in a Low-Voltage Electrical Network," *2024 IEEE 69th Holm Conference on Electrical Contacts (HOLM)*, Annapolis, MD, USA, 2024, pp. 1-5, doi: 10.1109/HOLM56222.2024.10768444.

[3] E. Calderon, P. Schweitzer, S. Weber, and G. P. du Perray, "Algorithm for locating series arc faults in an AC aircraft electrical system," in *15th International Conference on Developments in Power System Protection (DPSP 2020)*, 2020, doi: 10.1049/cp.2020.0032.

[4] Raul Carreira Rufato, Thierry Ditchi, Cyril Van de Steen, Thierry Lebey, Yacine Oussar, DC serial arc fault recognition in aircraft using machine learning techniques, International Journal of Electrical Power & Energy Systems, Volume 164, 2025, 110408, ISSN 0142-0615, https://doi.org/10.1016/j.ijepes.2024.110408.

[5] V. Psaras et al., "Review of DC Series Arc Fault Testing Methods and Capability Assessment of Test Platforms for More-Electric Aircraft," in IEEE Transactions on Transportation Electrification, vol. 8, no. 4, pp. 4654-4667, Dec. 2022, doi: 10.1109/TTE.2022.3189970.

[6] J. -R. Riba, M. Moreno-Eguilaz and J. A. Ortega, "Arc Fault Protections for Aeronautic Applications: A Review Identifying the Effects, Detection Methods, Current Progress, Limitations, Future Challenges, and Research Needs," in IEEE Transactions on Instrumentation and Measurement, vol. 71, pp. 1-14, 2022, Art no. 3504914, doi: 10.1109/TIM.2022.3141832.

[7] R. D. Telford, S. Galloway, B. Stephen and I. Elders, "Diagnosis of Series DC Arc Faults—A Machine Learning Approach," in *IEEE Transactions on Industrial Informatics*, vol. 13, no. 4, pp. 1598-1609, Aug. 2017, doi: 10.1109/TII.2016.2633335.

[8] Thakur, Kriti, et al. "Advancements in arc fault detection for electrical distribution systems: A comprehensive review from artificial intelligence perspective." *arXiv preprint arXiv:2311.16804* (2023).

[9] R. C. Rufato, M. Benmouffok, C. Van de Steen and P. Schweitzer, "Analysis of Electrode Ageing Based on Signatures of Electrical Arcs," in *Proceedings of the International Conference on Electrical Contacts (ICEC 2026)*, Trondheim, Norway, 2026.

[10] Underwriters Laboratories, "UL 1699B: Photovoltaic (PV) DC Arc-Fault Circuit Protection," Standard, Underwriters Laboratories, IL, USA, 2018.

[11] IEC 63027:2023, "Photovoltaic power systems – DC arc detection and interruption," International Electrotechnical Commission, Geneva, Switzerland, 2023.

Contact characteristics monitored by AI-Methods

1st Daniel Kupka
Electrical Products
Siemens AG
Amberg, Germany
daniel.kupka@siemens.com

2nd Armin Strahl
Electrical Products
Siemens AG
Regensburg, Germany
armin.strahl@siemens.com

3rd Thomas Zimmermann
Electrical Products
Siemens AG
Amberg, Germany
thomas.zimmermann@siemens.com

4th Arthur Zimmermann
Electrical Products
Siemens AG
Amberg, Germany
arthur.zimmermann@siemens.com

***Abstract*—During the investigation of the reliability of electrical contact systems throughout their lifetime a vast amount of data, like voltage and current signals, is created. In general, most of this data is not exploited for analytical purposes, even though it might contain valuable information about the reliability and condition of the contact system. The main impediment to using the complete data is that specific patterns which are related to the contact condition are not directly visible. Meanwhile, the broad availability of AI-methods offers the possibility to reveal such patterns in large datasets. The application of these methods is demonstrated using datasets of arcing contacts generated on a model switch installation. This installation, furthermore, allows us to compare the findings from the AI-driven analysis with the contact condition monitored directly by a camera system. It is shown that the application of AI driven analysis of the electrical signals can identify patterns that can be related to the condition of the contact system.**

***Index Terms*—contact material, contact tip, signal analysis, low voltage switchgear, low voltage, model switch, condition monitoring.**

I. Introduction

The characteristics of electrical contact systems change in the course of their life due to mechanical and thermal stresses caused by the electric arc. These changes may result from settling of components of the contact system such as springs or levers, but are predominantly caused by the erosion of the contact tips. As an example, consider a double contact system with two electrcical contacts that develop different levels of erosion. This will likely lead to asymmetry in the closing operation and, consequently, can change the bouncing behavior of the contact during the make operation, or concentrate the arc energy on the worn contact tip during a break operation. In general, these changes cannot be observed directly (i.e., visually) when switching electrical devices. Analyzing electrical signals – such as current, contact voltage and grid voltage – can provide indications of changes in the contact behavior, but does not specifically identify a particular contact state.

Due to the vast amount of data generated during switching experiments, indications of the contact state are mainly derived from the analysis of energy integrals, such as bouncing energy or breaking energy, thereby summarizing entire switching cycles into one or two quantities. This, however, implies a loss of information on the switching cycle. As an example, patterns in the contact voltage during bouncing may be relevant but are lost. Today, the widespread availablility of artificial intelligence (AI) methods – more precise, machine learing (ML) techniques – enables handling of the vast amount of data generated in switching investigations and assists in identifying patterns that may be related to the contact state.[1], [2], [3]

In this study we have investigated the relationship between the state of electrical contact tips and the corresponding electrical signals. Using a model switch installation enabled both, the visual inspection of the contacts and precise measuerement of electrical signals and mechanical signals, such as the force on the contacts and the contact position.

II. Experiments

The experiments described below were conducted on a model switch installation – a synthetic switching environment designed to provide high variability of contact systems and easy accessibility of switching data. A pneumatic cylinder serves as drive for the opening and closing operations providing the ability to adjust the contact movement speed. The contact force is controlled by a system of contact springs and the position of the movable contacts is precisely measured. The make and break angles with respect to the grid voltage can either be controlled or left random. Details of the installation are described in [4].

The installation allows the investigation of a wide variety of contact systems. For the present work the linear double-contact system of a commercial contactor was examined, featuring four silver-nickel contact tips ($\mathrm{AgNi\,80/20}$) for the electrical contact. All experiments have been conducted at a nominal voltage of $230\,\mathrm{V}$, with a power factor $\cos\varphi = 0.9$ and an overtravel of $1\,\mathrm{mm}$. The experiments were designed to accomplish two objectives: (i) demonstrate that changes of the contact system can be monitored by intentional variation of specific contact system properties and (ii) examine the changes occuring in a contact system over its lifetime. The intentional modification of contact system properties was achieved by: varying the opening and closing speed (i.e., the pressure input of the pneumatic cylinder), the break angle, and the nominal current. Multiple runs were conducted with each of these modifications. Table I summarizes the modifications of the contact system and the respective experimental runs.

While the electrical data are being recorded, a visual inspection of the contact tips is required to assess their condition. For this purpose, the model switch installation was equipped with a camera system to track the erosion of the contact tips.

TABLE I
CONTACT SYSTEM MODIFICATIONS
(ψ_{break}: BREAKING ANGLE, v: CLOSING SPEED, I: NOMINAL CURRENT)

Sequence	ψ_{break}	v	I	cycles	no. of specimens
1	30°/210°	$0.7\,\mathrm{m\,s^{-1}}$	120 A	10 000	2
2	30°/210°	$0.3\,\mathrm{m\,s^{-1}}$	120 A	10 000	5
3	30°/210°	$0.3\,\mathrm{m\,s^{-1}}$	80 A	10 000	4
4	random	$0.7\,\mathrm{m\,s^{-1}}$	120 A	10 000	4
5	random	$0.3\,\mathrm{m\,s^{-1}}$	120 A	10 000	3
6	random	$0.7\,\mathrm{m\,s^{-1}}$	80 A	50 000	3

An image of the fixed contacts was taken after each switching cycle.

III. AI-MODELS FOR DATA ANALYSIS

Artificial Intelligence is a powerful toolset, enabling, among other things, both signal analysis and image recognition. However, it is necessary to develop a suitable model to enable recognition of the contact state through analysis of the electrical and mechanical signals of the switching cycles. In addition, an image recognition model must be refined to allow monitoring of the contact tip condition.

A. Autoencoder for signal analysis

The model switch installation provides access to the electrcical current I, the grid voltage U, the contact voltage U_{c}, as well as the contact position x and the contact force F_{c}. Each of these signals is recorded as a function of the time during every switching cycle. To recognize patterns in these signals that may be relevant for the analysis of the contact condition, the data must be compressed into a format suitable for such an analysis. This can be achieved, e.g., by employing an autoencoder architecture, which is particularly useful because the patterns are unknown beforehand. Details of the conditional variational autoencoder used in this work are provided below.

The fundamental model is a convolutional autoencoder [5] that compresses the 1.536 normalized[1] data points of each input channel into 16 latent-space values. Since the make and break angles $\psi_{\mathrm{make}}, \psi_{\mathrm{break}}$ would dominate the analysis without providing additional information about the contact system they are bypassed to the decoder part in the model, as well as the phase shift resulting from the experimentally fixed power factor. Moreover, the grid voltage signal is not expected contribute any information regarding the contact condition and was therefore compressed seperately by a convolutional network and bypassed for reconstruction in the decoder. While some patterns indicating the contact condition may appear in a single switching cycle, many relevant patterns are likely to emerge only through the analysis of multiple cycles. Therefore, a Gated Recurrent Unit (GRU) was integrated into the model prior to the final compression step to retain information across 20 switching cycles. Lastly, to enhance the model's discriminative ability, the final compression into the latent-space was implemented using a variational layer. A schematic of the Conditional Variational Autoencoder [6], [7] is shown in Figure 1.

The test sequence data as given in Table I was split reserving one test run per sequence for testing the model. During training, when encoding the n-th switching cycle, the $(n+1)$-th switching cycle is used as reference for comparison with the decoded signal. This approach directs the model's attention to contact properties while mitigating the effect of controlled variables such as phase shift. As usual the training of the Conditional Variational Autoencoder is unsupervised.

B. Image recognition by U-net

Images of the contact tips are captured after each switching cycle. The contact tip condition may be assessed by determining its remaining area. However, the large number of switching cycles requires automation of this inspection process. This can be achieved by employing a U-net model [8] since such a model is capable of identifying the contact surface regardless of its geometry, meaning that no particular features are required for the process. The main challenge deploying this model is obtaining high-quality labeled training data. To address this, 1000 images were manually annotated to mark the contact surfaces subsequently used for model training. Figure 2 depicts the surface of a contact tip after $10\,000$ cycles of switching sequence 5 along with its annotation.

IV. RESULTS AND DISCUSSION

A. Signal analysis

The model takes signals from 20 switching cycles and outputs a 16-component latent vector, that can be represented as a point in the latent-space. Significant changes in the switching system's behavior should result in the model mapping the input signals to a different region of the latent-space.

Prior to assessing the performance of the CVAE in analyzing contact conditions, its overall capability to detect variations in switching behavior was examined. A current increase from $80\,\mathrm{A}$ to $100\,\mathrm{A}$ not only accelerates contact erosion but also introduces variations in making behavior (e.g., bouncing) and breaking behavior (e.g., arc duration). Switching cycles with identical currents are grouped within the same cluster in the latent-space representation. Figure 3 illustrates the projection of the latent-space on the plane defined by dimensions 1 and 3, where two distinct clusters are observed, each associated with a specific current value. Varying the opening/closing speed between $0.3\,\mathrm{m\,s^{-1}}$ and $0.7\,\mathrm{m\,s^{-1}}$ has a similar effect. Each speed

[1] the values of the input channels are mapped to the interval $[0, 1]$

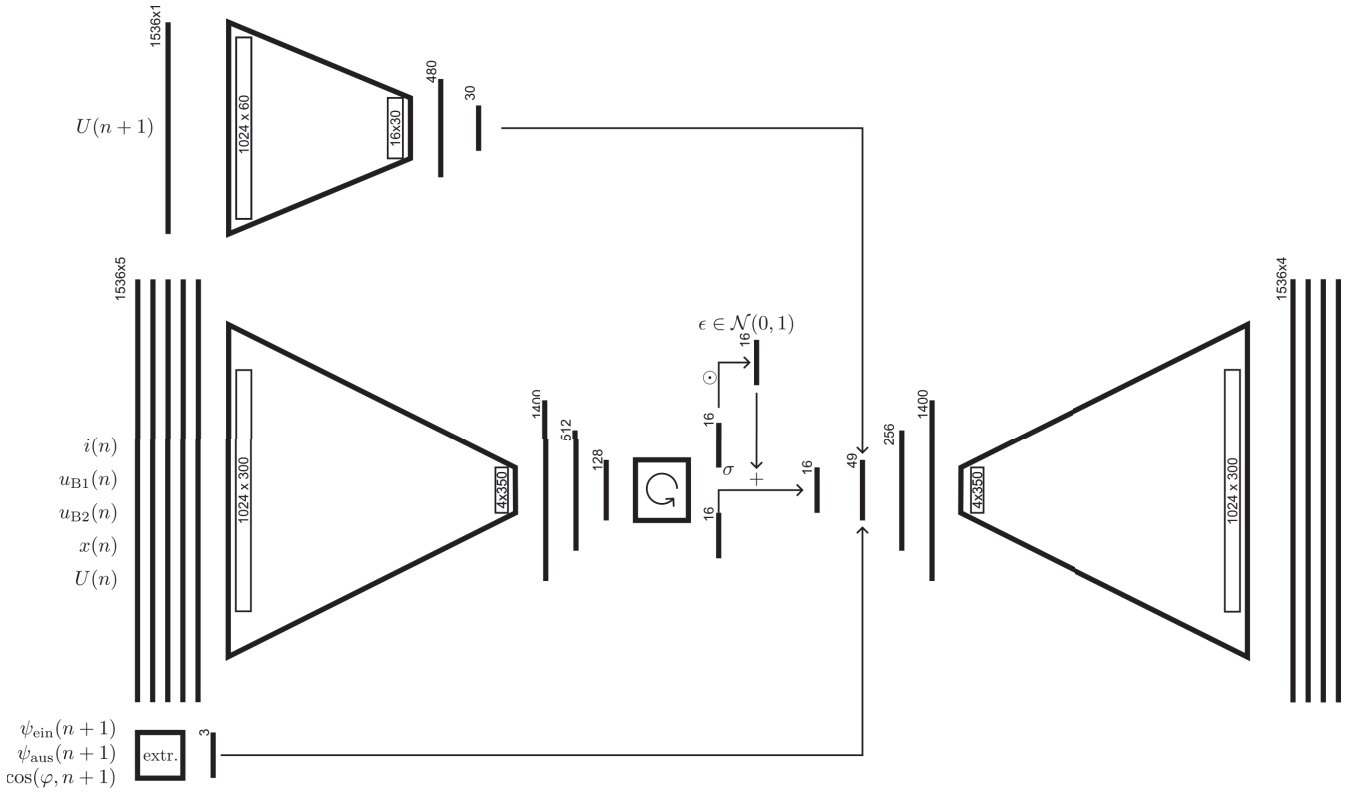


Fig. 1. Conditional Variational Autoencoder for signal analysis

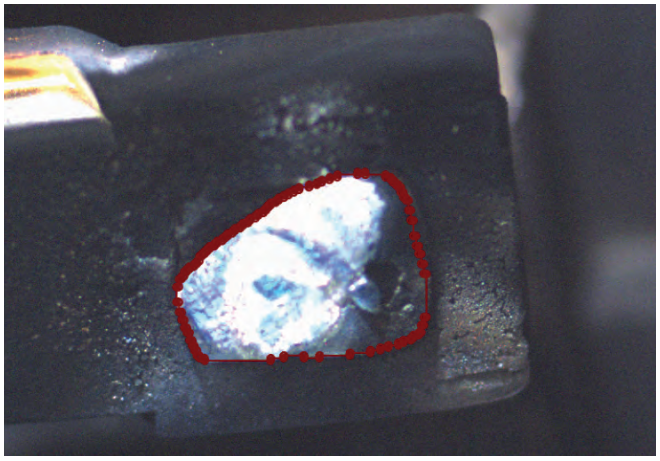


Fig. 2. Contact surface after 5000 switching cycles from sequence 4. Red marking is the manual labeling of the contact surface.

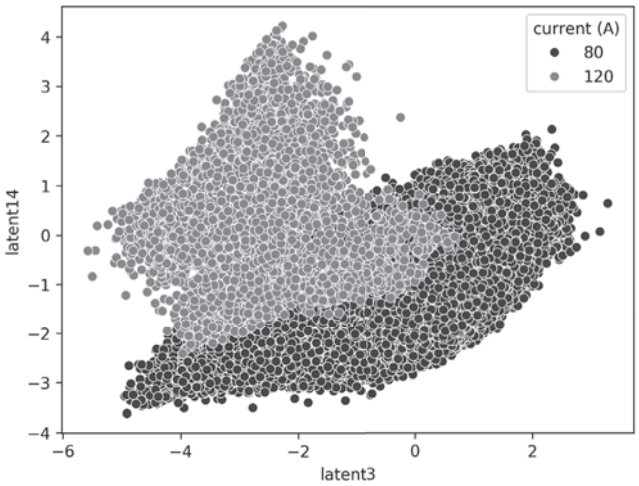


Fig. 3. Latent-space representation of 80 A and 120 A switching cycles (sequences 4 and 6).

value is mapped to clearly distinct clusters. Figure 4 depicts the projection of the latent-space spanned by the dimensions 9 and 12, showing two separated clusters corresponding to the respective speed. The mapping of fixed opening angles, in contrast, does not form clusters in the latent-space. This is because bypassing the opening angle, as described in section III-A, eliminates its influence. The mapping results obtained under intentionally controlled variations of contact system behavior confirm the model's capability to detect and analyze differences in contact behavior.

However, the primary objective of this work is to identify changes of the contact beahvior over its lifetime, for example those resulting from contact tip erosion. The clusters in the latent-space shown in Figures 3 and 4 correspond to contacts that undergo changes over their lifetime. These changes in

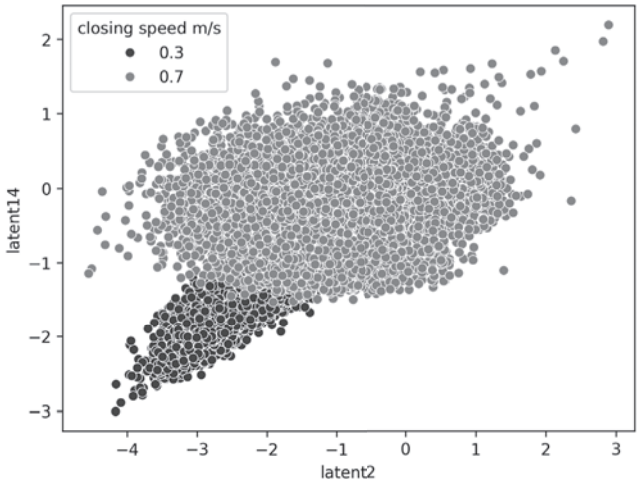


Fig. 4. Latent-space representation of $0.3\,\mathrm{m\,s^{-1}}$ and $0.7\,\mathrm{m\,s^{-1}}$ switching cycles (sequences 1 and 2).

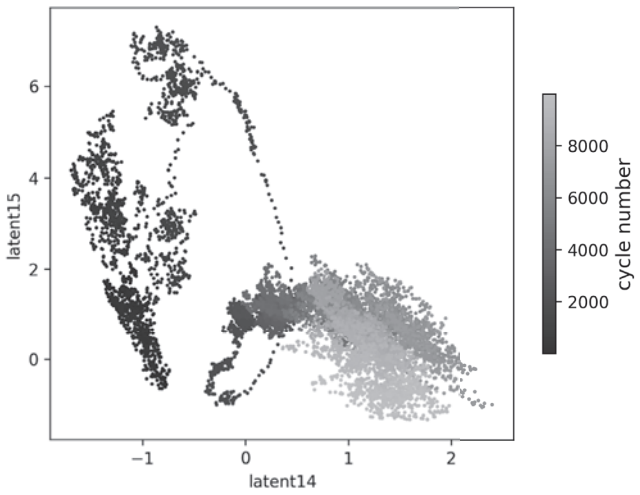


Fig. 5. Latent-space representation of a contact from sequence 4 considering the number of switching cycles

contact condition can be revealed incorporating the number of switching operations performed on the contact into the latent-space representation (see Figure 5). Nonetheless, detecting relevant changes in a latent space spanned by 16 dimensions remains challenging. Therefore, spectral analysis[9] was applied to reduce the dimensions of the latent-space to a single dimension, which may be interpreted as a modification regarding the original contact state D_e[2]. Figure 6 illustrates the spectral analysis of the latent-space representation provided in Figure 5. The value of D_e evolves with the number of cycles, showing abrupt transitions at distinct cycle counts. Hence, spectral analysis is effective in detecting variations in the contact system behavior.

[2] D_e is referred to as the embedding

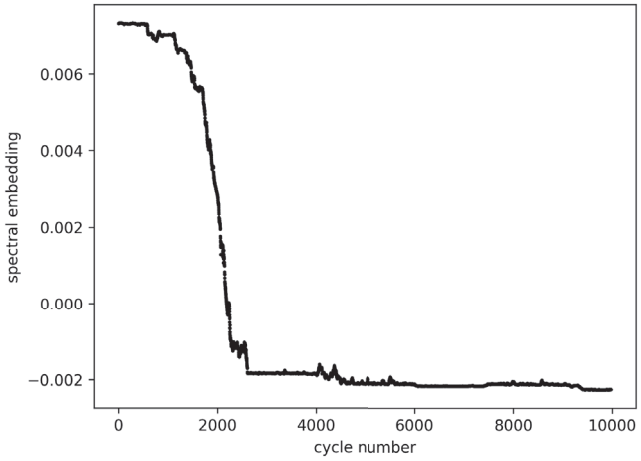


Fig. 6. Spectral analysis of the latent-space representation given in Figure 5

B. Contact surface detection

Interpreting the signal analysis provided by the CVAE model requires knowledge of the contact condition, which in this work is obtained through visual inspection. By processing a sequence of images captured after each switching cycle through the trained U-net model the erosion process can be effectively illustrated. Figure 7 depicts the contact tip area over the contact's lifetime. Depending on the contact condition, the detected area may vary significantly between successive images; however, the rolling mean over 20 values reveals a distinct trend of material loss during the first half of the contact's life. This trend is partially reversed in the second half of the contact's lifetime, as the apparent contact area increases. This is accompanied by a more pronounced scatter in the detected contact surface values.

The observed erosion properties result from the damage mechanism that is typical for the silver nickel contact material under these switching conditions. This material is susceptible thermo-mechanically induced fatigue cracks that commonly cause delamination of the contact tip from the contact carrier. In the early stage of erosion, material loss occurs predominantly at the contact edges, leading to a gradual reduction of the contact area. During this phase the contact tips undergo contraction. After the cracks have propagated sufficiently, portions of the contact tip break off and migrate between the moving and stationary contacts. The U-net model recognizes transferred material as belonging to the original contact surface. On the one hand, when considering the original contact surface, this is an incorrect classification. On the other hand, the transferred contact material may significantly affect the contact behavior. To provide a more detailed assessment of the contact condition, the transferred material must be distinguished from the original contact tip. In the future, this can be achieved, for example, by using a multi-class U-Net model (e.g., [10]). However, this requires separate labeling of the transferred material for the learning process. In any case, the combination of visual inspection and a U-Net model enables

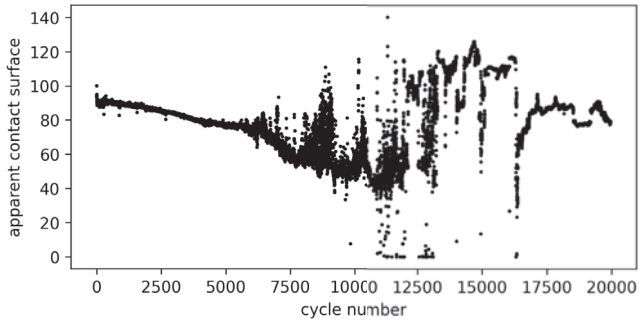


Fig. 7. Erosion process of one specimen of sequence 2 determined by visual inspection and analysis through the U-net.

monitoring of changes in the contact condition throughout the contact tip's lifetime.

C. Identifying the contact condition by analysis of the electrical signals

To demonstrate its relevance, the analysis of the switching patterns by the CVAE must be correlated with the contact condition and convetional assessment of the switching cycle characteristics. For one specimen of sequence 3 the make and break energy were calculated for each switching cycle and compared to the CVAE-based spectral analysis. Additionally, data from the contact erosion – represented by the apparent contact surface and the contact position in the model switch – were incorporated into the overview. Figure 8 illustrates this comparison. The analyzed contact system exhibits three pronounced changes after approximately 3000, 19 000, and 27 000 switching cycles. At each of these contact stages, the break-energy values change discontinuously, and the contact position shifts more or less abruptly. The embedding signal reflects the latter two discontinuities by showing abrupt changes at 19 000 cycles and a pronounced peak at 27 000 cycles, whereas the first discontinuity is not clearly visible in the embedding data. At 19 000 cycles, the scatter of the apparent contact area increases significantly, indicating the onset of material transfer between the movable and fixed contacts. The trend of an increasing apparent contact area between 19 000 and 27 000 cycles reverses toward the end of this interval for approximately 1000 cycles and is followed by the onset of pronounced scatter. This comprehensive analysis, including machine learning techniques, offers detailed indications of the condition of the contact system—particularly of the contact tips—beyond what can be obtained using conventional techniques alone.

V. Conclusion and Outlook

Artificial intelligence techniques facilitate the identification of contact conditions, enable analysis of damage onset, and inform contact development in terms of material choice, geometry, and manufacturing. By analyzing switching signals using a Conditional Variational Autoencoder (CVAE) variations in the contact properties can be detected wheras a U-net model

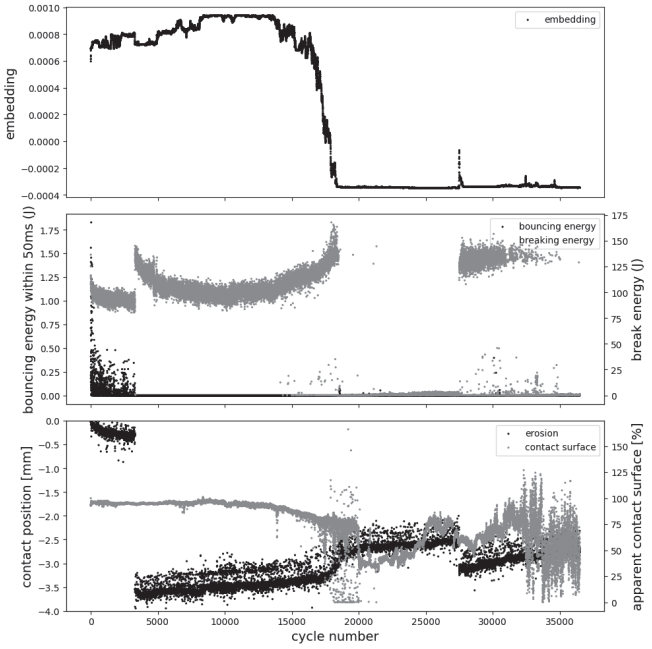


Fig. 8. Embedding for pattern recognition, make and break energies and contact tip erosion of a specimen of sequence 3.

was successfully adapted to measure the contact erosion. Comparison with make and break energies revealed further changes in contact properties that are not explained by energy-based measurements.

Future work will focus on improving the AI-models and the measurement system:

- The interpretability of the CVAE will be enhanced by determining meaningful combinations of the 16 latent-space components linked to switching characteristics.
- Multi-class classification will be implemented into the U-net model to identify material transferred between the contact surfaces
- The visual inspection capabilities of the model switch system will be extended to visualize both the fixed and movable contacts

References

[1] A. A. Neloy, M. R. Islam, S. S. Tamanna, M. A. Kabir, and Y. Cho. A comprehensive study of auto-encoders for anomaly detection. *Machine Learning with Applications*, 17:100548, 2024.

[2] T. Sattarov and C. Heinze. Explaining anomalies using denoising autoencoders for time-series data. Technical Report 2209.10658, 2022. arXiv preprint arXiv:2209.10658.

[3] S. Dhyani. Autoencoders for ecg anomaly detection: A survey. *Journal of Computer Engineering and Signal Processing*, 1(1):1–15, 2025.

[4] A. et al. Strahl. Gerätenahe kontaktmaterialprüfungen mithilfe von modellschaltern. In *Proceedings Albert-Keil-Kontaktseminar*, 2023.

[5] D. Bank, N. Koenigstein, and R. Giryes. Autoencoders: A comprehensive review. *arXiv preprint arXiv:2003.05991*, 2020.

[6] Diederik P. Kingma and Max Welling. Auto-encoding variational bayes. *arXiv preprint arXiv:1312.6114*, 2013.

[7] Z. Chen, R. Barbano, and B. Jin. Conditional variational autoencoder for learned image reconstruction. *arXiv preprint arXiv:2110.11681*, 2021.

[8] O. Ronneberger, P. Fischer, and T. Brox. U-net: Convolutional networks for biomedical image segmentation. *arXiv preprint arXiv:1505.04597*, 2015.

[9] Ulrike von Luxburg. *A Tutorial on Spectral Clustering*. PhD thesis, Universität Tübingen, 2007.

[10] M. Jafari, R. Li, Y. Xing, D. Auer, S. Francis, J. Garibaldi, and X. Chen. Fu-net: Multi-class image segmentation using feedback weighted u-net. In *International Conference on Image and Graphics*, pages 157–168. Springer, 2020.

Diagnostic of DC Arc Plasmas in Aeronautic Conditions: Application to Arc Fault Detection

A. Hellé
Institut Jean Lamour
CNRS, Université de Lorraine
Nancy, France
arthur.helle@univ-lorraine.fr

R. Hugon
Institut Jean Lamour
CNRS, Université de Lorraine
Nancy, France
robert.hugon@univ-lorraine.fr

F. Brochard
Institut Jean Lamour
CNRS, Université de Lorraine
Nancy, France
frederic.brochard@univ-lorraine.fr

G. Marcos
Institut Jean Lamour
CNRS, Université de Lorraine
Nancy, France
gregory.marcos@univ-lorraine.fr

***Abstract*—This study presents an experimental investigation of DC electric arcs generated by contact separation, focusing on the plasma dynamics and electrical signatures relevant to arc faults in aeronautical environments. Using a combination of electrical measurements and high-speed imaging, we analyze the behavior of arc plasmas under controlled conditions, with the goal of improving arc fault detection in DC power distribution systems**

Keywords—electric arc, fast camera, electrical signature

I. INTRODUCTION

Detecting electric arc faults remains a major challenge for the electrification of transportation systems, particularly in the aeronautics sector, and more broadly for the deployment of DC power distribution. While parallel faults can generally be detected using conventional overcurrent protection systems, series arc faults mimic the behavior of an active load within the system, making them much harder to identify. In DC systems, they are also more difficult to detect and more prone to causing fires than their AC counterparts [1]. Unlike AC systems, DC arcs do not naturally extinguish at zero current, making them more difficult to detect and extinguish, and more prone to causing fires. The initiation of a DC arc plasma within an electrical network can have severe consequences, as it involves significant energy release and a high risk of electrical fires. These hazards are even more critical than in AC systems, since a voltage of approximately 30 V is sufficient to sustain a continuous DC arc. The risk associated with DC arcs is therefore both real and increasing, as the deployment of DC systems continues to expand.

Aeronautics provides a particularly illustrative case of this challenge, as all electric aircraft (AEA) are expected to become increasingly widespread in the near future. At the same time, onboard power requirements continue to grow with the development of the more-electric aircraft (MEA), with operating voltages projected to approach 1000 V by the 2030s [2]. In the MEA concept, propulsion relies on a conventional jet engine, whereas all secondary systems are electrical. The extent of onboard cable networks is already substantial, with total lengths reaching several hundred kilometers and exceeding 500 km in large aircraft such as the Airbus A380. Pressure under aeronautical operating conditions is also a key parameter, as it may decrease to values as low as 0.1 bar depending on the location within the aircraft during flight. This reduction in pressure affects not only arc ignition, which generally becomes easier, but also the subsequent plasma behavior.

Under such conditions, a wide range of situations may result in the ignition of an arc plasma between two conductors, including cable severing, unintended contact between conductive components, or the transition from partial discharges to a fully developed arc following insulation degradation [3]. These scenarios may result in either series or parallel arc faults.

To address this issue, recent detection strategies increasingly rely on machine learning techniques to identify arc plasma formation within extensive cable networks. However, the effectiveness of these data-driven approaches strongly depends on the availability of large, high-quality, and well-characterized datasets, which remain difficult to obtain and validate. Improving the reliability of databases therefore requires integrating physical insight into arc behavior, which can also enable the development of hybrid detection strategies combining data-driven and physics-based approaches.

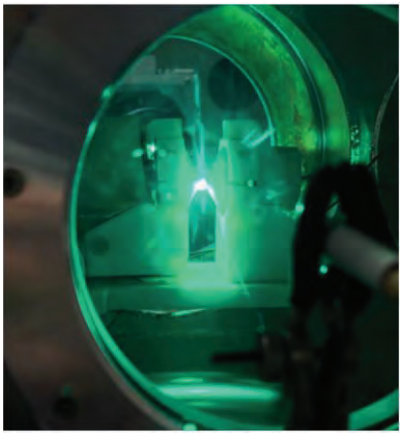


Fig. 1. Photograph of an arc ignited between two copper electrodes mounted on alumina supports at the center of the reactor. The arc is operated at a regulated current of 4 A under atmospheric pressure, with a final inter-electrode gap of 5 mm.

In this context, the present work proposes to investigate the electrical signature of arc discharges such as the one shown in Figure 1 using plasma diagnostic methods. This approach aims to extract characteristic descriptors of arc plasmas by analyzing their electrical behavior. Particular attention is paid to the pronounced noise appearing in electrical signals following arc ignition. By applying plasma diagnostic techniques under aeronautical fault conditions, this study seeks to improve the understanding of arc plasma dynamics and to establish meaningful correlations between plasma behavior and its electrical signatures.

II. Experimental setup

The experimental setup which is used for this work is presented in Figure 2. It depicts the reactor with the contacts used for the arc ignition, the power supply, plasma diagnostic devices and trigger system.

A. Power supply, reactor and contacts

Arc plasmas are generated inside a pressure-regulated reactor by separating electrical contacts, a process achieved through the controlled motion of the anode driven by a stepper motor. This system ensures accurate and repeatable displacement, allowing precise control of both the separation velocity and the final inter-electrode gap. The anode is powered by a DC supply (EA-PS 91500-3) capable of delivering voltages up to 1500 V and currents up to 30 A, and can be operated either in voltage-controlled or current-controlled mode depending on the experimental conditions. In the present study, the current-controlled mode is employed.

The electrical contacts are cylindrical electrodes with a diameter of 5 mm. After each experiment, the electrodes are polished to ensure surface reproducibility, and different materials, such as copper (Oxygen Free High Conductivity OFHC) and aluminum, can be employed. The present work focuses on the case of copper electrodes. The experiments are carried out in ambient air, with the reactor pressure controlled using a rotary vane pump and a micrometric valve to regulate the intake of external air. This capability is especially important for investigating electric arcs under high-altitude aeronautical conditions, where portions of the aircraft may be exposed to reduced or unpressurized environments (down to 0.1 bar).

B. Plasma diagnostics

The arc plasmas are characterized through a combination of electrical signal acquisition and high-speed imaging. Plasma imaging is performed using two Photron SA-Z fast cameras. In this work, the acquisition frame rate is set to 100 000 frames per second in order to preserve a sufficiently large recording window, while the spatial resolution is set to 20 µm.

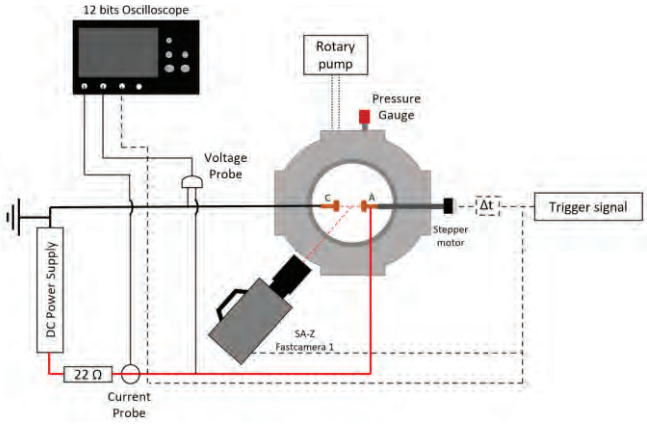


Fig. 2. Schematic of the experimental setup, including the power supply and diagnostic devices. A and C refer to the anode and cathode, respectively.

The two cameras are positioned in a stereoscopic configuration, allowing three-dimensional reconstruction of plasma-related phenomena. The minimum exposure time permitted by the cameras is used, corresponding to 159 ns. Nikon 200 mm lenses are also employed to ensure a sufficient spatial resolution of 20 µm per pixel. A camera records images with a 12-bit depth, corresponding to 4096 gray levels per pixel. An example frame from an arc recording is shown in Figure 3.

Simultaneous measurements of current and voltage are performed using dedicated probes connected to a digital oscilloscope (HDO6104B, Teledyne LeCroy). This oscilloscope provides a bandwidth of 1 GHz, a 12-bit vertical resolution, and a memory depth of up to 250 million points. Data are typically acquired on three channels, current, voltage, and trigger, with a temporal resolution better than 1 µs, resulting in datasets exceeding 10 million samples per acquisition. Voltage measurements are carried out using a Testec TT-SI8052 differential probe, featuring a 200 MHz bandwidth and a maximum rating of 1500 V. Current is measured with a Sefram CP6550 probe, which offers a 500 kHz bandwidth and a maximum current rating of 50 A.

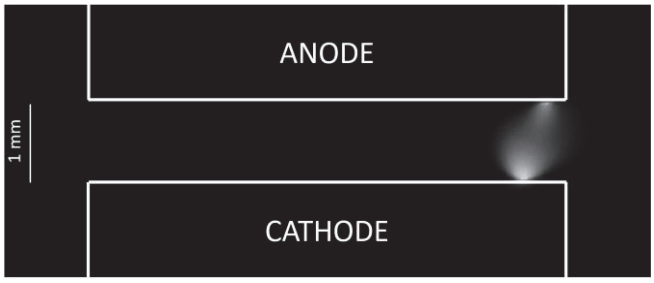


Fig. 3. High-speed camera image of a 4 A arc at atmospheric pressure between copper electrodes with a 1 mm gap. White rectangles outline the contours of the two electrodes. The image has been rotated 90° to the left for clarity.

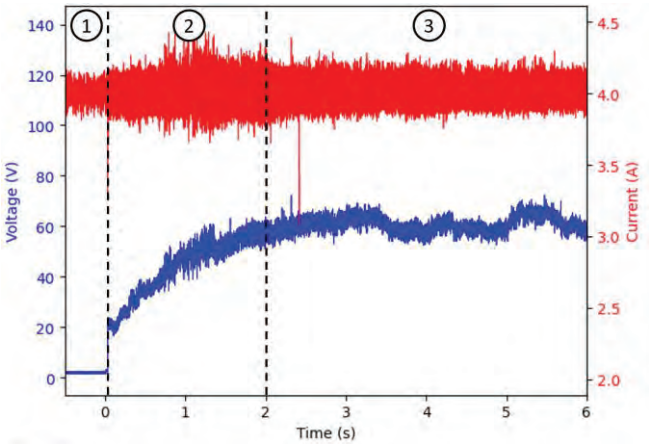


Fig. 4. Voltage and current signals recorded for a 4 A arc at atmospheric pressure between copper electrodes with a final gap of 10 mm. The three phases are separated by dashed lines, with the second one corresponding to the anode displacement.

C. Arc ignition

At the beginning of each experiment, the electrodes are in contact and a current flows through the circuit. At t = 0 µs, a TTL signal simultaneously triggers both high-speed cameras and the oscilloscope. After a delay of 50 µs, the stepper motor initiates the anode motion, leading to electrode separation. As the contacts start to move apart from each other, the effective contact area shrinks, which increases the local current density and produces intense Joule heating. This process leads to the formation of a molten bridge that eventually ruptures due to mechanical and thermal constraints. The vapor generated during the evaporation of the molten metal bridge rapidly occupies the inter-electrode gap [4, 5]. Owing to the low ionization potential of copper, combined with the elevated temperatures at the bridge attachment points, the conditions become favourable for the arc ignition [6].

Subsequently, the anode continues to move until the target inter-electrode gap is reached, resulting in the elongation of the arc column. This process corresponds to the third phase observed in Figure 4, during which the arc voltage increases as a consequence of the arc stretching. In this process, the anode is translated at a constant speed, set to 5 mm/s in the present study.

During the third phase shown in Figure 4, the contacts remain stationary, and the arc plasma evolves freely along their surfaces until the power supply is switched off.

III. Results

The electrical noise generated by arc plasmas consists of numerous frequency components spanning a wide spectral range. This broad bandwidth reflects the diversity of physical mechanisms underlying the observed electrical fluctuations. Investigating these mechanisms is particularly important, as they strongly depend on experimental parameters relevant to the aeronautical environment, such as current, pressure, and contact material. Consequently, the electrical signature of the arc also depends on these parameters.

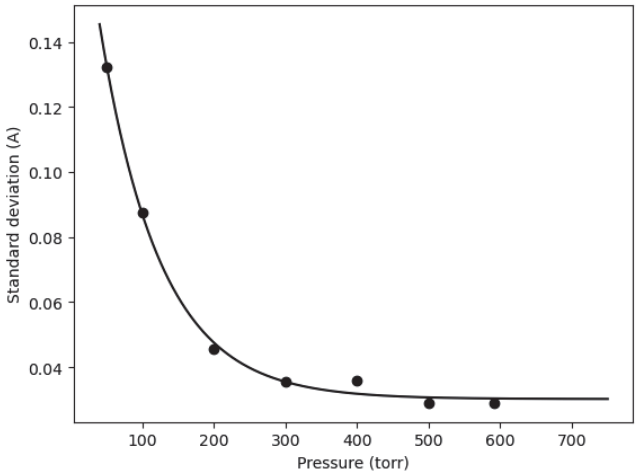


Fig. 5. Standard deviation of the current signal at different pressures during 6 A arc discharges with a 5 mm gap.

This effect can be clearly observed by examining the amplitude of the arc-induced noise as the pressure is reduced to levels representative of cruising altitudes. This behavior is illustrated in Figure 5 for a 4 A arc with an inter-electrode gap of 5 mm. This highlights the significantly altered arc behavior under reduced-pressure conditions.

The electrical noise generated by arc-related phenomena can originate from multiple sources. Arc dynamics are particularly complex in the present configuration, especially under reduced pressure conditions, which may partly account for the trend observed in Figure 5. In addition, recent studies have shown that contact erosion and the mechanisms involved can also contribute significantly to the electrical signatures of arcing faults [7, 8]. This work presents the extraction and identification of distinct signatures from a representative time interval shown in Figure 6.

A. Plasma dynamics

In a first approximation, the arc voltage U_{Arc} can be expressed as the sum of three components: the column voltage U_{column}, the cathodic fall voltage U_C and the anodic fall voltage U_A. By considering the electric field E(z) in the column, the arc voltage can therefore be expressed as:

$$U_{Arc} = U_A + U_C + \int_A^C E(z)dz$$

The electric field should ideally be measured between the two fall regions, delimited here by points A and C, which is difficult in practice. Since the sheaths are usually very small compared to the column length, the latter can be approximated as the entire arc length, which is easier to measure. Following the collapse of the molten bridge, arc ignition leads to the formation of anodic and cathodic sheaths, resulting in a net increase in the discharge voltage to approximately 20 V, as shown in Figure 4. This value is consistent with the commonly reported fall voltage of about

10 V per sheath in the literature [9]. Subsequent electrode separation stretches the arc column, leading to an increasing contribution of the column voltage U_{column} to the total arc voltage until the final gap is reached.

During the final stage of the experiment, the evolution of the arc voltage can no longer be attributed to artificial arc stretching induced by electrode separation. Nevertheless, the signal continues to be influenced by low-frequency perturbations associated with arc dynamics, as the motion of the arc column is governed by multiple interacting forces that continuously deform the plasma and drive its movement. The overall arc dynamics is further influenced by reduced pressure conditions, which enhance the mobility of the arc roots. Ongoing studies are exploring electrical fluctuations associated with rapid arc length variations through high-speed stereoscopic imaging. These studies have already yielded promising results that confirm the trends observed in this work. Therefore, arc dynamics could provide useful features for arc detection, particularly under low-pressure conditions.

B. Signature of the contacts erosion

Arc roots are the primary sites of energy exchange during a discharge, particularly at the cathodic root [10]. As a result, the electrode surface undergoes significant deformation and material ejection. This phenomenon is particularly critical in an aeronautical environment, as the ejected droplets consist of high-temperature molten metal and can therefore trigger secondary fires in the vicinity of the arc [11]. The ejected droplets were tracked using high-speed camera recordings and the AX R&D tracking software, which enables the detection and tracking of luminous objects in each camera recording. The three-dimensional trajectories of the droplets were then reconstructed by correlating the data obtained from the two cameras arranged in a stereoscopic configuration. An example of this reconstruction is shown in Figure 7 for a 4 A arc at atmospheric pressure with a 3 mm inter-electrode gap, over a time interval of 100 ms.

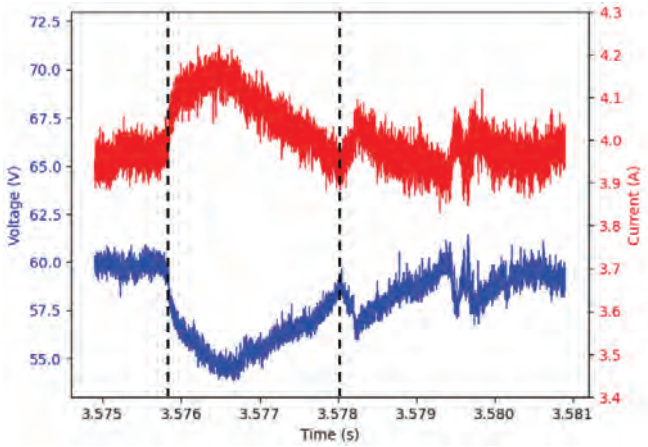


Fig. 6. Zoomed view of a 6 ms time interval of the current and voltage signals shown in Figure 4.

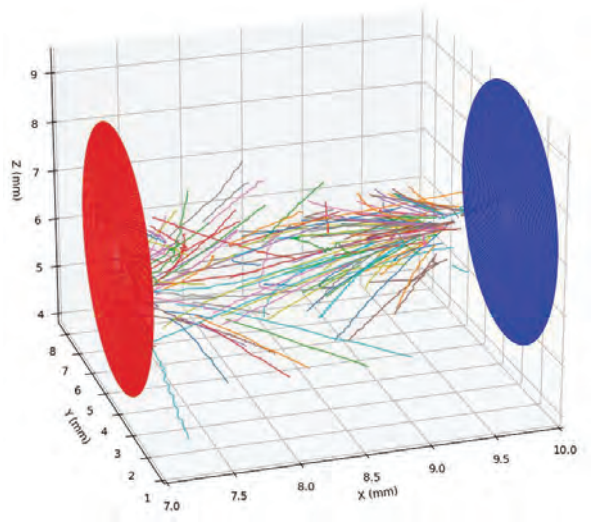


Fig. 7. Superposition of reconstructed droplet trajectories ejected from the electrodes, obtained using high-speed camera stereoscopy over a 100 ms time interval. The red and blue disks correspond to the anode and cathode surfaces, respectively.

The reconstructed droplet trajectories indicate that the ejected material mainly originates from the arc root region and its periphery, with ejection occurring preferentially from the cathode. The tracked droplets, with sizes ranging from 1 µm to 100 µm, are expelled in all directions with velocities on the order of several tens of meters per second. At atmospheric pressure, the velocity of these droplets decreases significantly while they traverse the inter-electrode gap due to drag forces. At reduced pressure, this deceleration is strongly diminished, which considerably increases the hazard associated with arc faults in an aeronautical environment.

Material ejection also contributes to the generation of electrical fluctuations, as it can both provide a significant influx of material into the plasma and alter the cathode geometry, thereby affecting electron emission. A zoomed view of a 6 ms time interval of the signals shown in Figure 4 is presented in Figure 6. The erosion of the contacts and the resulting material ejection give rise to higher-frequency perturbations than those described in Section III.A. Such phenomena result in voltage variations of a few volts and current variations of several tenths of an ampere. In the signals shown in Figure 6, the first perturbation, at time 3.576 s, can be correlated with the appearance of droplets in the gap. These droplets were tracked, and their trajectories are shown in Figure 8.

A pronounced decrease in arc voltage is observed at the moment when droplets are first detected in the tracking data. This suggests a correlation between droplet appearance in the plasma and electrical fluctuations, making it a promising avenue for feature extraction [7]. To better understand this relationship, the ejection mechanisms need to be investigated in greater detail. The ejection of liquid material occurs simultaneously with the formation of a jet emerging from the cathodic root. Several mechanisms may contribute to the release of material into the plasma. Among them, one that has long been overlooked but has recently attracted attention involves the formation and subsequent rupture of molten metal bubbles at the periphery of the arc root,

predominantly at the cathode. An example of a molten metal bubble formed at the cathode surface is shown in Figure 9.

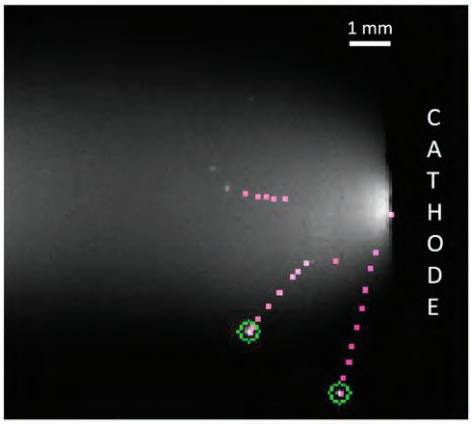


Fig. 8. Trajectory of the ejected droplets which led to the first electrical fluctuation observed in Figure 6.

Bubble formation may result from the supersaturation of gaseous species within the molten metal layer present at the cathode surface near the arc root. This process leads to the nucleation of a cavity that grows until the internal pressure exceeds the mechanical stability of the thin molten metal layer forming the bubble envelope. The bubble then ruptures, releasing a significant amount of material into the plasma, depending on its size prior to explosion. The expelled material originates both from the gas contained within the bubble and from the liquid metal forming its envelope. In addition, an upward Rayleigh jet generated during surface reformation after rupture further contributes to material ejection [12]. These material contributions introduce a significant amount of copper vapor into the plasma, increasing the density of neutral copper species. Since copper is more easily ionized than the surrounding gas species (Cu: 7.72 eV, H: 13,59 eV, O: 13,61 eV, N: 14,53 eV), this process can lead to an increase in the electron density within the plasma and, consequently, to an increase in plasma conductivity.

The resulting electrical fluctuation can be regarded as the signature of bubble formation and rupture, as it can be electrically distinguished from other arc-related phenomena. This observation led to the development of an initial bubble detection method reported in [8]. The method was subsequently tested, and its potential was confirmed using automated video detection based on shadowgraphy recordings. This imaging technique provides enhanced visualization of surface geometry, making it particularly well suited for bubble detection. Thus, this signature proved to be particularly promising for the detection of arc faults.

IV. Conclusion

This work contributes to the understanding of arc fault signatures in aeronautical environments by evaluating, on the same test sample, the electrical signatures of several mechanisms induced by the presence of an arc plasma, which could support the development of detection devices. The benefits of this approach are twofold. First, it provides a means to build a database of well-characterized arc signatures under various conditions, including pressure, contact material, gap, and current. Second, it helps to characterize the plasma formed under fault conditions and to assess the damage it can cause both to the contacts and to the surrounding environment.

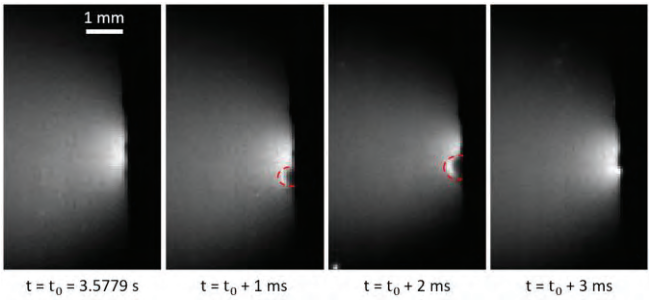


Fig. 9. High-speed camera images showing the formation and explosion of a bubble responsible for the second electrical fluctuation highlighted in Figure 6. The outline of the bubble envelope is shown with a dashed line to help visualization.

The various mechanisms leading to surface erosion, by altering the electrode surface and releasing material into the plasma, have been shown to play a significant role in generating electrical noise in the signals. The formation and explosion of bubbles provides a striking example of how plasma-related phenomena can be used for arc fault detection.

Our findings highlight the role of plasma dynamics, contact erosion, and material ejection in generating electrical noise, which can be leveraged for fault detection. Future work will focus on high-speed stereoscopic imaging to further elucidate the 3D dynamics of the arc column and roots, with the goal of developing robust, physics-based detection strategies.

References

[1] W. Xu, X. Wu, Y. Li, H. Wang, L. Lu and M. Ouyang, “A comprehensive review of DC arc faults and their mechanisms, detection, early warning strategies, and protection in battery systems”, Renewable and Sustainable Energy Reviews, vol. 186, p. 113674, 2023.

[2] G. Buticchi, P. Wheeler and D. Boroyevich, “The more-electric aircraft and beyond”, Proceedings of the IEEE, vol. 111, pp. 356-370, 2022.

[3] R. Boukadoum, R. Landfried, T. Leblanc, Ph. Teste and J. Andrea, “Role of the pressure in the DC electric arc characteristics. Application: case of the more electrical aircraft”, Proceedings of the 28th International Conference on Electric Contacts ICEC, p. 153, 2016.

[4] P. Slade, “Opening electrical contacts: The transition from the molten metal bridge to the electric arc”, IEICE Transactions on Electronics, vol 93, pp. 1380-1386, 2010.

[5] D. M. Sanders, L. Boxman, and P. J. Martin, “Handbook of Vacuum Arc Science and Technology”, William Andrew, 1995.

[6] M. Baeva and D. Uhrlandt, “Characterization and applications of direct current microarcs: a review”, Journal of Physics D: Applied Physics, vol. 58, p. 263001, 2025.

[7] A. Hellé, R. Hugon, F. Brochard, S. Chouchene, G. Marcos, J. Moritz, and P. Schweitzer, “Dynamics of the material ejection in a dipolar arc in continuous regime”, Journal of Physics D: Applied Physics, vol. 57, p. 425201, 2024.

[8] A. Hellé, R. Hugon, F. Brochard, and G. Marcos, “Metal bubbles formation induced by electric arc plasmas: detection and behavior”, Journal of Physics D: Applied Physics, vol. 58, p. 265205, 2025.

[9] I. I. Beilis, *The phenomenon of a cathode spot in an electrical arc: the current understanding of the mechanism of cathode heating and plasma generation*, Plasma, vol. 7, pp. 329–354, 2024.

[10] N. Vogel and B. Juttner, “Measurements of the current density in arc cathode spots from the zeeman splitting of emission lines”, Journal of Physics D: Applied Physics, vol. 24, p. 922, 1991.

[11] K. M. Armijo, P. G. Clem, D. Kotovsky, B. Demosthenous, A. Tanbakuchi, R. J. Martinez, A. B. Muna and C. B. LaFleur, “Electrical arc fault particle size characterization”, Sandia Report, 2019, doi:10.2172/1592574.

[12] A. G. Guézennec, J. C. Huber, F. Patisson, P. Sessiecq, J. P. Birat and D. Ablitzer, “Dust formation in electric arc furnace: birth of the particles”, Powder Technology, vol. 157, pp. 2–11, 2007.

Frequency Band Importance Estimation for Arc Faults via Multi-Branch Neural Networks

Abdelhak Maoukouf
University of Lorraine
Jean Lamour Institute, CNRS
Nancy, France
abdelhak.maoukouf@univ-lorraine.fr

Patrick Schweitzer
University of Lorraine
Jean Lamour Institute, CNRS
Nancy, France
patrick.schweitzer@univ-lorraine.fr

***Abstract*—Electrical arc faults generate high-frequency arc noise in load currents; however, this noise is often difficult to identify because it is buried within background disturbances and other non-arc-related spectral components. This paper proposes an attention-based, frequency-aware neural network for arc fault detection using current-only measurements, with the objective of isolating the frequency content most relevant to arc-related signatures.**

Arc data are generated in a controlled lab environment compliant with IEC 62606. One-cycle current segments sampled at 1 MHz are transformed into the frequency domain and decomposed into consecutive frequency bands, which are processed by a multi-input encoder equipped with an attention mechanism. This architecture enables direct interpretation of frequency-band relevance. Results show that the low-frequency band [0-10] kHz acts as a normality cue associated with no-arc operation, while arc-related information is localized within the [10-70] kHz range, with the highest concentration between [10-40] kHz.

Keywords: Arc faults, Neural networks, Explainable AI, Signal processing.

I. INTRODUCTION

An arc fault is a high-power electrical discharge between two conductors. Electrons jump across the air gap, ionizing the surrounding air and creating a conductive plasma channel. Electrical arc faults exhibit multiple coupled physical phenomena, including intense optical radiation in the ultraviolet and infrared ranges, often observed as arc flashes, audible noise of crackling, extreme localized heat reaching several thousands of kelvins, and broadband electromagnetic disturbances arising from rapid variations in current and voltage.

One observable consequence of these electromagnetic emissions is the presence of high-frequency arc noise in the current spectrum. Numerous studies have sought to identify the frequency bands that characterize the occurrence of arc faults. Guan et al. [1] analysed the power spectrum of current signals generated by arc faults occurring between two electrodes under various load conditions. They identified the frequency band from 3 to 50 kHz as a discriminative range for arc-fault detection. Müller et al. [2] observed a significant increase in spectral current amplitude over a broad frequency range spanning from 100 Hz to 1.5 kHz. They attributed this phenomenon to the broadband nature of arc faults and to temporal jitters associated with arc re-ignition. Zhou et al. [3] believe that arc-fault noise is concentrated around 100 kHz and 900 kHz. Based on this observation, they designed an arc-fault detection device employing a two-stage band-pass filtering scheme centred on these frequencies. Yang et al. [4] demonstrated that the frequency range from 1.5 to 30 MHz is highly discriminative for arc-fault detection, noting that frequencies below 1.5 MHz are strongly affected by grid-related noise. Similarly, Martel et al. [5] found that a portion of the arc energy is concentrated around 22 MHz ± 300 kHz. Ji et al. [6] developed an arc-diagnosis algorithm based on arc signal energy analysis and designed a band-pass filter covering 2.4–39 kHz to distinguish between normal and arc-fault operating conditions. Guo et al. [7] proposed a detection method combining Variational Mode Decomposition (VMD) and the Wigner–Ville Distribution (WVD). Their results showed that, compared with normal operation, arc faults lead to a noticeable increase in frequency-edge energy within the 5–20 kHz band. Wang et al. [8] proposed ArcNet, a convolutional neural network (CNN)–based model operating directly on raw current signals, selecting the 3–12 kHz band as the characteristic frequency range for arc-fault detection. In a later work, Wang et al. [9] developed an arc-fault detection model based on Mel-Frequency Cepstral Coefficients (MFCCs) and a fully connected neural network, concluding that the 1–10 kHz range captures most of the relevant spectral characteristics of arc currents. Ning et al. [10] proposed an interpretable and lightweight detection approach based on an attention-enhanced CNN. Their analysis identified the 5–10 kHz and 15–25 kHz bands as the most influential frequency ranges for arc-fault detection. Finally, Chu et al. [11] introduced a method combining time-domain imaging and Long Short-Term Memory (LSTM) networks. By decomposing and reconstructing intrinsic mode functions of arc-fault currents, they determined that the characteristic high-frequency components lie within the 10–200 kHz range.

Aside from arc-generated noise, several major noise sources influence the measured current spectrum. These include power source-related noise arising from harmonic distortion in the AC supply; load-related disturbances, particularly from non-linear loads, which introduce harmonic distortion and frequency-localized spectral peaks; experiment-related noise originating from sensors and cabling; and noise associated with data-acquisition system artifacts. When an arc occurs, the arc-generated noise is superimposed –and masked by– these pre-existing noise sources, making it challenging to isolate the arc components and localize its frequency band in the spectrum.

Spectral flatness (SF) is a measure that quantifies how noise-like a waveform's spectrum is. It is computed as the ratio of the geometric mean to the arithmetic mean of the power spectrum.

Given a signal x and its FFT sequence X. The Spectral Flatness can be calculated in a specific band B as follows:

$$SF_B(x) = \frac{\sqrt[N]{\prod_{k\in B} X[k]}}{\frac{1}{N}\sum_{k\in B} X[k]}$$

When SF zero, the waveform exhibits a harmonic spectral signature; conversely, when SF approaches one, the spectrum is noise-like. Figure 1 illustrates two current cycles measured from a vacuum cleaner, corresponding to normal operation (in blue) and arc-fault (in red). Figure 2 represents the spectral flatness for both scenarios, evaluated across successive 10 kHz bands spanning up to 500 kHz, with each band's central frequency represented along the x-axis.

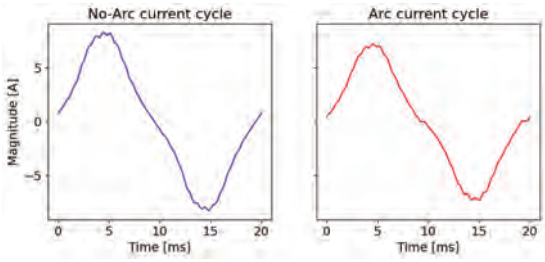


Figure 1: Two current cycles of a vacuum cleaner (No-arc & Arc).

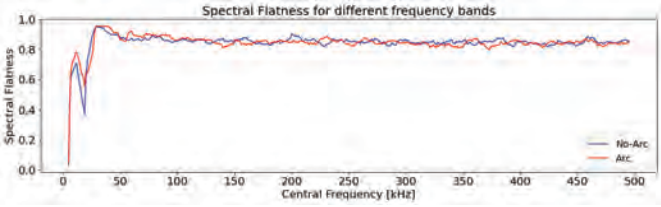


Figure 2: The corresponding spectral flatness..

Spectral flatness remains unchanged between arc and no-arc cases above 30kHz, indicating strong masking of the arc-noise by other noise sources, especially those originating from the vacuum cleaner itself. As a result, spectral flatness is unable to identify a specific arc-noise-related frequency band.

Neural Network interpretability offers a promising approach for frequency-band identification, potentially replacing conventional signal-processing methods in complex load scenarios. In this project, an encoder-based neural network is trained for arc-fault detection, and the attention mechanism is subsequently analysed to identify the relative importance of different frequency bands with regard to the arc-noise, The arc-fault data are generated using a test bench and then are pre-processed prior to model training.

II. Data Acquisition and Preparation

A. *Experimental Setup*

To generate arc-fault data, an open-contact arc generator compliant with IEC 62606 is employed, using copper and graphite electrodes. Figure 3 illustrates the experimental setup, in which the arc generator is connected in Branch 2 together with one or more loads. Branch 1, connected in parallel, contains zero, one or multiple masking loads; increasing the RMS current of these masking loads increases their masking effect on the arc noise. The system is supplied by a 220 V/50 Hz power source, and the current and voltage signals are acquired using sensors and an oscilloscope.

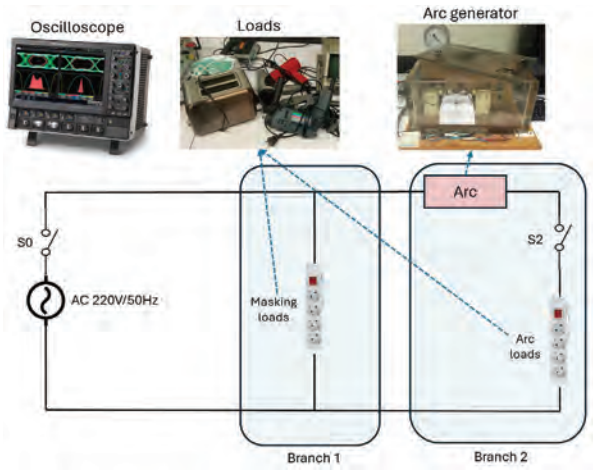


Figure 3: The experimental setup.

The loads used in the experiments are listed in Table 1. For the motor-based loads, it was specified whether they were loaded or running freely. When loaded, the motor draws higher current, resulting in slightly different electrical characteristics compared to the unloaded condition.

Table 1: Loads used in the experiments.

Resistive loads and lamps	**Switch-mode power supply**	**Motor load**
Resistance (3 values)	PC	Vacuum cleaner A (loaded)
Kettle	Screen	Vacuum cleaner B (loaded)
Filament lamps	Oscilloscope	Vacuum cleaner B (unloaded)
Halogen lamp (50%)	Function generator	Drill (unloaded / low power)
Halogen lamp (100%)	Electric scooter charger	Drill (unloaded / high-power)
HID lamp		Jigsaw (unloaded)
		Blender (loaded)

Combining different loads in the experimental setup enables the generation of current waveforms with diverse dynamics and complex shapes. The masking loads further challenge the model by masking arc-related noise and improve the representativeness of real-world conditions.

Figure 4 illustrates two current cycles obtained from the same configuration. Branch 2 (arc branch) includes an electric scooter charger and a vacuum cleaner, while Branch 1 (masking loads) consists of three filament lamps and on halogen lamp. The red cycle has an arc, the blue one has no arc, and the green curve is their pointwise difference. The two cycles appear nearly identical, making it hard to visually distinguish between the two cases. Figure 5 presents the corresponding frequency spectra.

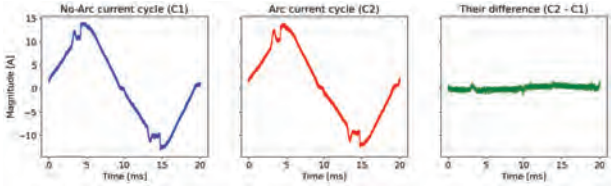


Figure 4: Arc vs No-arc cycles of a multi-load configuration.

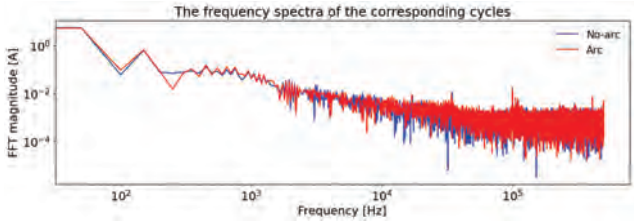


Figure 5: Frequency spectra of the current cycles above.

B. Measurements parameters

Data acquisition was conducted under three experimental scenarios, as summarized in Table 2. Each waveform has a duration of 1 s and was sampled at a rate of 1 MHz. For each acquisition, the first 0.4 s correspond to normal operation, while the remaining 0.6 s correspond to arc-fault conditions. For each acquisition, the current, arc voltage, and supply voltage waveforms are recorded. The current signal serves as the input to the model, while arc voltage is used for labelling.

Table 2: Different scenarios for data acquisition based on load configuration.

Scenario	Arc loads	Masking loads	N° waveforms	Duration (s)	Sampling rate (MHz)	No-arc/Arc ratio (%)
A	1	0	96	1	1	40/60
B	1	1	144	1	1	40/60
C	2-4	2-4	124	1	1	40/60

C. Segmentation & Labelling

Each waveform has a duration of 1 s, which, at a sampling rate of 1 MHz, results in a large vector of samples. To reduce computational and memory requirement, the signals are segmented into one-period windows. A single-period segment retains sufficient information to analyse the spectral content.

Each current segment is labelled using the corresponding arc voltage segment. A voltage threshold of 13 V is used: segments below this threshold are labelled “No-arc”, while those above are labelled “Arc”. Note that even if a segment exhibits a very brief arc, the entire segment still must be labelled as arc. Figure 6 illustrates the labelling procedure.

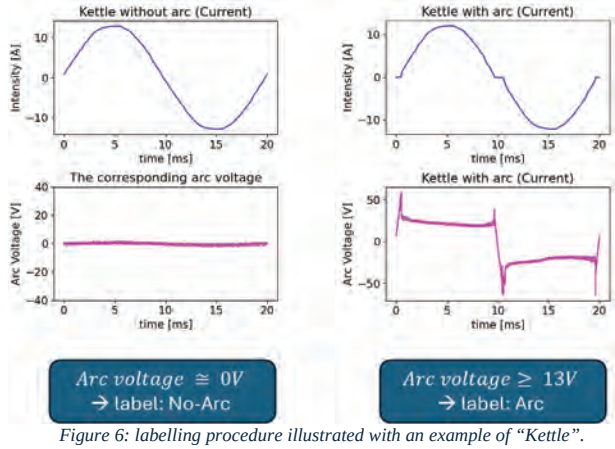


Figure 6: labelling procedure illustrated with an example of “Kettle”.

III. Preprocessing & Modelling

The core idea of this work is to decompose each input segment into multiple frequency bands and feed them into a multi-input neural network, where each input corresponds to a specific band. The model is trained to distinguish between arc and no-arc conditions, and its learned parameters are subsequently analysed to assess the relative importance of each frequency band for the detection task.

Each segment is transformed into the frequency domain using FFT. The resulting spectrum is then divided into N consecutive windows (Figure 7), each with a bandwidth of $\frac{F_S}{2N}$, where $\frac{F_S}{2}$ denotes the Nyquist frequency (500 kHz). In this work, $N = 50$, so the window bandwidth is 10 kHz.

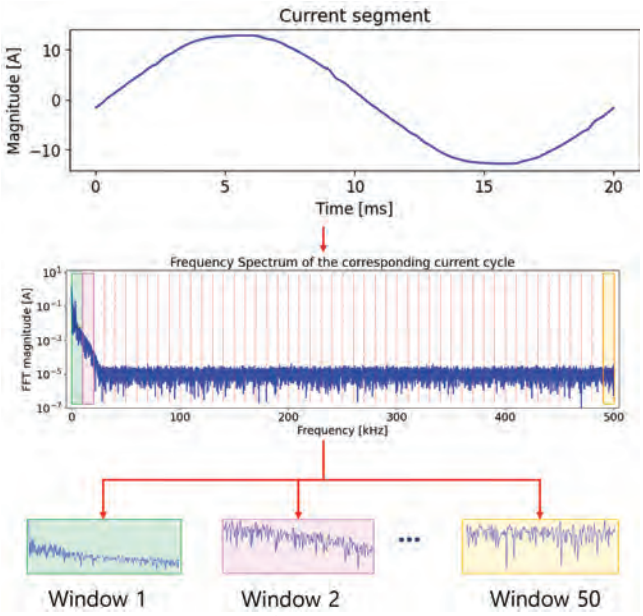


Figure 7: Steps of preprocessing the input data.

The neural network employs a shared encoder across all frequency windows. The **frequency-bin order** is provided alongside to the **spectral magnitude**, enabling the model to preserve the relative position of each band in the frequency domain. As lower-frequency bands exhibit higher spectral power, each window is standardized prior to encoding, while its **spectral power** is extracted a priori and retained as an additional feature.

The neural network model consists of three main blocks. The first block is a multi-input encoder: for each input k, it takes the standardized FFT window of the k^{th} frequency band denoted X_k , along with the corresponding frequency-bin indices denoted I_k, and outputs a 32-dimensional embedding vector e_k.This embedding is concatenated with the band’s spectral power P_k to form a 33-dimensional vector e'_k. The second block is a Multi-Layer Perceptron-based attention block, which assigns a scalar weight α_k to each frequency band, quantifying its relative importance. In the final block, a context vector $z = \sum_{k=1}^{N} \alpha_k . e'_k$ is computed and fed into a single-neuron classifier to predict the arc probability. Figure 8 illustrates the model architecture, including the preprocessing steps. It’s worth noting that the encoder block consists of 2 Fully Connected layers and 3 1D-Convolutional layers.

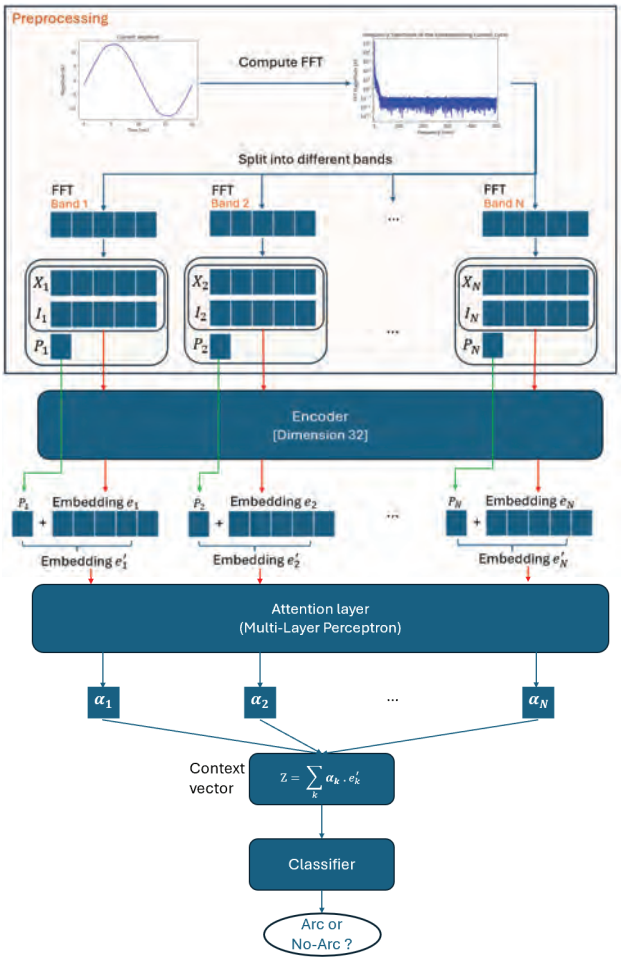


Figure 8: The model architecture (including preprocessing).

IV. Results

A. Training results

To ensure that the attention scores are meaningful for interpretation, the model should be trained to convergence. The training parameters are summarized in Table 3. The dataset was split into training, validation, and test subsets using stratified sampling, ensuring that each subset has the same proportion of load configurations. The model achieved a training accuracy of 99.66% and a validation accuracy of 97.40%. Figure 9 shows the training and validation accuracy curves.

Table 3: Training parameters

Parameter	Value
Number of data points	18,200
Train-validation-test split	80% - 10% - 10%
Epochs	25
Batch size	32
Optimizer	Nadam
Learning rate	0.001 with exponential decay

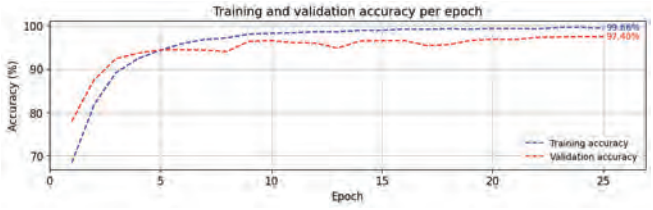


Figure 9: Training/validation accuracy curves

B. Analysis of Frequency-band Relevance for Arc Detection

Once trained, the model can be applied to any current segment x. After preprocessing and forward propagation through the network, the attention weights associated with each frequency band are obtained $\alpha_k(x)$, reflecting the relative attention assigned to each band in the final arc/no-arc decision. It's worth noting that the α scores sum up to 1. Figures 10 and 11 show a current cycle of an oscilloscope under arc along with its spectrum respectively, the corresponding attention scores were all zero except for the 2nd and 3rd band ([10-20] kHz and [20-30] kHz), with $\alpha_2 = 0.3$ and $\alpha_3 = 0.7$. The [10-30] kHz region is highlighted in the spectrum, illustrating the focus of the model when predicting an arc for this specific example.

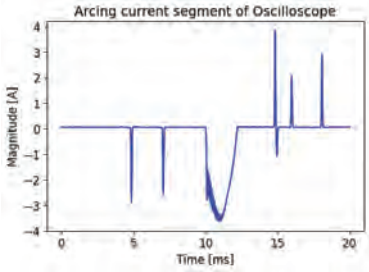


Figure 10: Arc current cycle of an oscilloscope.

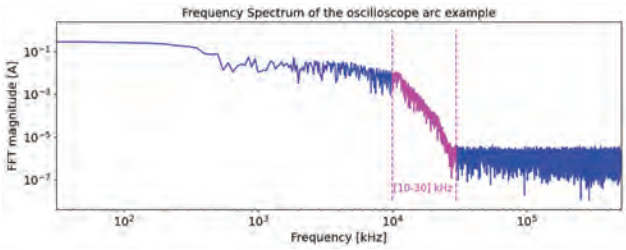


Figure 11: The corresponding spectrum, highlighting the frequencies [10-30] kHz.

However, attention weights alone are not sufficient to directly infer bands importance. Instead, a discrimination score is defined by combining the attention scores α_k, the classifier weights W, and the band embeddings e'_k, and aggregating this measure over the entire test set.

The contribution of the k^{th} band for a sample x is defined:

$$C_k(x) = \alpha_k(x).W^T.e'_k(x)$$

The final discrimination score of the k^{th} band is:

$$D_k = E_{x\sim test}[\alpha_k(x)] \, . E_{x\sim test}[C_k(x)]$$

Figure 12 illustrates the detection score D_k for each band. When evaluated over the entire dataset, the proposed score exhibits a structures and interpretable distribution across frequency bands. The first frequency band [0-10] kHz (in green) yields a large negative value, indicating that it contributes actively to the identification of normal operating conditions rather than arc occurrences. This band is dominated

by stable low-frequency components, whose amplitude and structure are primarily governed by the supply and load behaviour and remain relatively consistent in the absence of arcing. As a result, strong energy in this band serves as a reliable normality cur for the classifier, explaining why it is the only band with a negative contribution. In contrast, 2nd to 9th bands exhibit positive scores reflecting frequency regions where arc-related noise becomes more pronounced. The 3rd band [20-30] kHz (in red) provides the largest positive contribution, while the 2nd, 4th, 5th, 6th and 7th bands (orange) also contribute meaningfully, indicating that the arc noise is distributed across the [10-70] kHz band, with a high concentration in the [20-30] kHz band. Subsequent bands show smaller contribution, and higher-frequency bands have zero contribution, so they were omitted from the graph.

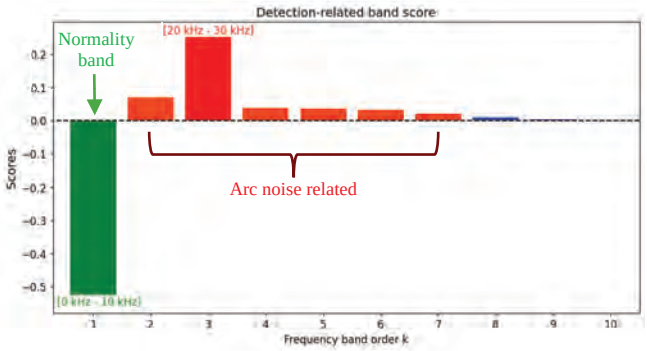


Figure 12: Detection score for each band.

C. Additional Analysis of Frequency-band Discriminability

The embeddings e'_k are 33-dimensional vectors that encode the information of the k^{th} frequency band. To analyse their discriminative structure, t-SNE, a nonlinear manifold learning technique, is used to project the high-dimensional embeddings into a three-dimensional space. The projection is performed on the test set, where red points correspond to arc samples and blue points to no-arc samples.

The resulting components (x, y, z) are abstract dimensions constructed to preserve local similarity between data points. Points that are close in this 3D space represent samples that are similar in the original feature space.

First, t-SNE is applied using embeddings from all 50 frequency bands $e'_1, e'_2, \dots, e'_{50}$, which corresponds to the entire [0-500] kHz band (Figure 13). The resulting projection shows a clear separation between arc and no-arc samples, except for a small number of points. Notably, a narrow line of arc samples appears between the two clusters, indicating residual overlap when all bands are included.

Next, t-SNE is applied using only the embeddings of the first seven frequency bands $e'_1, e'_2, \dots, e'_7$, which corresponds the band [0-70] kHz (Figure 14). In this case, the separation between arc and no-arc samples becomes more pronounced, and the intermediate overlap is significantly reduced. This improvement indicates that the low-frequency bands carry the most discriminative information for arc detection.

These results demonstrate that restricting the analysis to the [0-10] kHz range is sufficient to achieve strong separability between arc and no-arc conditions. Moreover, the [0-10] kHz band primarily serves as a normality cue, while the [10-70] kHz band contains the frequency components most strongly associated with the arc-noise.

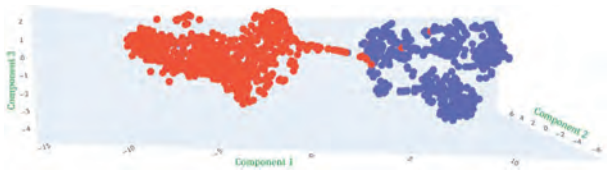


Figure 13: t-SNE visualization of band embeddings for arc and no-arc samples, using all the frequency bands ([0-500] kHz).

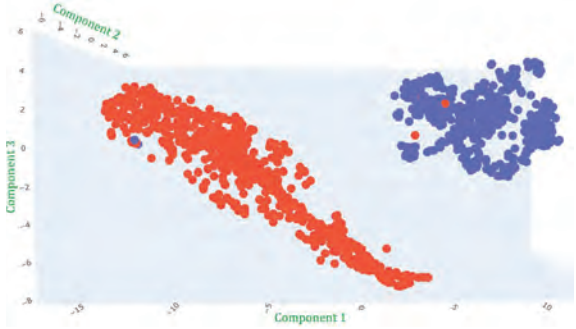


Figure 14: t-SNE visualization of band embeddings for arc and no-arc samples, using the first seven frequency bands ([0-70] kHz).

V. Conclusion

This work addresses arc fault detection using current-only measurements and an attention-based neural network trained on experimentally generated arc data. Arc faults were produced in a controlled laboratory setup compliant with IEC 62606, under multiple load and masking configurations designed to reproduce realistic operating conditions. One-cycle current segments were transformed into frequency bands and processed by a multi-input encoder with an attention mechanism, enabling both accurate arc detection and direct assessment of the contribution of each frequency band.

The analysis reveals a clear separation of roles across frequency ranges. The low-frequency band **[0-10] kHz** consistently contributes as a normality cue, being strongly associated to no-arc operation and actively counterbalancing arc-related evidence. In contrast, arc-noise information is localized within the **[10-70] kHz** range, with the highest concentration of discriminative content observed between **[10-40] kHz**. Higher-frequency bands beyond this range were found to provide negligible contribution.

These findings demonstrate that reliable arc fault detection can be achieved using a limited and well-defined frequency range, while also providing insight into how different spectral components support or inhibit the arc decision.

References

[1] H. Guan, B. Wang, Z. Zhao, S. Bimenyimana, and Q. Wang, "Arc Fault Current Signal's Power Spectrum Characteristics and Diagnosis Based on Welch Algorithm," *International Journal of Engineering Science and Computing (IJESC)*, vol. 6, no. 8, 2016.

[2] P. Müller, S. Tenbohlen, R. Maier and M. Anheuser, "Characteristics of Series and Parallel Low Current Arc Faults in the Time and Frequency Domain," *2010 Proceedings of the 56th IEEE Holm Conference on Electrical Contacts*, Charleston, SC, USA, 2010, pp. 1-7.

[3] Zhou et al., "Arc Fault Circuit Interrupter and Series Arc Fault Detection Method Using Plural High Frequency Bands," U.S. Patent 7,633,727 B2, Dec. 15, 2009.

[4] K. Yang, R. Zhang, J. Yang, C. Liu, S. Chen, and F. Zhang, "A novel arc fault detector for early detection of electrical fires," *Sensor*, vol. 16, no. 4, pp. 1–24, 2016.

[5] J-M. Martel, M. Anheuser and F. Berger, "A Study of Arcing Fault in the Low-Voltage Electrical Installation," *2010 Proceedings of the 56th*

IEEE Holm Conference on Electrical Contacts, Charleston, SC, USA, 2010, pp. 1-11.

[6] H-K. Ji, G. Wang, W.-H. Kim, and G.-S. Kil, "Optimal design of a band pass filter and an algorithm for series arc detection," *Energies*, vol. 11, no. 4, p. 992, 2018.

[7] F. Guo, H. Gao, Z. Wang, J. You, A. Tang and Y. Zhang, "Detection and Line Selection of Series Arc Fault in Multi-Load Circuit," *IEEE Transactions on Plasma Science*, vol. 47, no. 11, pp. 5089-5098, Nov. 2019.

[8] Y. Wang, L. Hou, K. C. Paul, Y. Ban, C. Chen, and T. Zhao, "ArcNet: Series AC arc fault detection based on raw current and convolutional neural network," *IEEE Trans. Ind. Informatics*, vol. 18, no. 1, pp. 77–86, Jan. 2022.

[9] Y. Wang, D. Sheng, H. Hu, K. Han, J. Zhou and L. Hou, "A Novel Series Arc Fault Detection Method Based on Mel-Frequency Cepstral Coefficients and Fully Connected Neural Network," *IEEE Access*, vol. 10, pp. 97983-97994, 2022.

[10] X. Ning, D. Sheng, T. Lan, W. He, J. Xiong, and Y. Wang, "Lightweight Low-Voltage AC Arc-Fault Detection Method Based on the Interpretability Method," *Electronics*, vol. 13, no. 13, Art. no. 2662, 2024.

[11] R. Chu, P. Schweitzer, and K. Yang, "Series Arc Fault Detection Method Based on Time Domain Imaging and Long Short-Term Memory Network for Residential Applications," *Algorithms*, vol. 18, no. 8, p. 497, 2025.

Image Processing–Based Quantification of Contact Microstructure for Erosion Assessment in High Voltage Gas Circuit Breakers

Milad Mohammadhosein
Electrical and Computer Engineering
University of Tehran
Tehran, Iran
Mohammadhosein@alumni.ut.ac.ir

Kaveh Niayesh
Department of Electric Energy
Norwegian University of Science and Technology
Trondheim, Norway
kaveh.niayesh@ntnu.no

Abstract— **The influence of contact surface morphology particularly micro-scale structural features such as the size, distribution, and contiguity of constituent phases—on erosion behavior in high-voltage gas circuit breakers is well recognized in the existing literature. Numerous studies have demonstrated that the spatial arrangement of copper and tungsten phases plays a decisive role in arc–contact interaction and, consequently, in erosion performance. However, despite this qualitative understanding, limited attention has been devoted to the development of objective and quantitative metrics that enable systematic comparison of contact microstructures with identical geometry and material composition. In this paper, a set of numerical indices derived from image processing of contact surface micrographs is proposed to characterize and compare the quality of contact microstructures. Experimental results show that contacts with the same dimensions and Cu/W mass ratio, but different microstructural characteristics, exhibit markedly different erosion behaviour under identical short-circuit current conditions. The proposed numerical descriptors successfully discriminate between such contacts and provide a quantitative basis for microstructural assessment, complementing conventional quality-control criteria used in high-voltage laboratories.**

Index Terms*-- *arc contacts, contact erosion, contact morphology, microstructural image of contact surface, image processing indices.

I. Introduction

Arcing contacts in high-voltage gas circuit breakers are typically manufactured from composite materials that combine a refractory phase with high thermal stability, such as tungsten, and a highly conductive phase, such as copper or silver. These materials are commonly produced using powder metallurgy processes, including powder blending, pressing, and liquid-phase sintering. During sintering at temperatures exceeding the melting point of the conductive phase, copper or silver melts and infiltrates the interconnected network of tungsten particles. Since the boiling temperature of copper or silver, which acts as the conductive phase of arcing contacts, is significantly lower than the melting point of tungsten, which provides the thermally resistant framework, the sintering process represents a practical and widely adopted method for manufacturing tungsten–copper arcing contacts. However, the production technology of such contacts is highly sensitive to processing parameters, and seemingly minor variations can lead to substantial differences in the resulting microstructure [1-3].

The influence of arcing contact design on erosion behavior has been extensively investigated in the literature, particularly with respect to macroscopic parameters. These include contact geometry and surface area, contact gap, and the weight fraction of refractory constituents, all of which have been shown to affect arc stability, energy dissipation, and material loss during current interruption [4-9]. In parallel, a substantial body of work has established that the microstructural characteristics of Cu–W contacts—such as size, spatial distribution, and connectivity—have a decisive influence on erosion resistance, arc root behavior, and thermo-mechanical performance [10]. These studies collectively indicate that contact microstructure is a key factor governing erosion behavior under short-circuit interruption conditions.

Despite this qualitative recognition, the assessment of contact microstructure in both research and industrial practice remains largely descriptive [11]. Microstructural evaluation is typically limited to visual inspection of metallographic images or to indirect indicators such as bulk composition and density [12]. Consequently, there is currently no widely accepted quantitative framework that allows objective comparison between contacts that share identical dimensions and material compositions but differ in micro-scale structural features [13, 14]. This lack of numerical descriptors limits the ability to correlate microstructure with erosion performance in a systematic and reproducible manner, and complicates quality control beyond conventional checks such as dimensional tolerances and Cu/W mass ratio verification.

In parallel, considerable efforts have been devoted to defining electrical endurance and lifetime indicators for circuit breakers based on thermal and electrical stress parameters, including peak short-circuit current, transferred charge, and arc energy [15-19]. While such indices are useful at a system level, their applicability implicitly assumes comparable contact material behavior. Experimental evidence increasingly suggests that this assumption may not hold when contacts exhibit different microstructural configurations, even when subjected to identical interruption stresses [11]. As discussed in [11], the spatial accommodation and distribution of microscale copper and tungsten domains play a critical role in determining contact performance. From the perspective of arc root formation, a connected network of tungsten regions is associated with improved erosion resistance. At the final points of contact prior to separation, the current preferentially flows through copper due to its higher electrical conductivity compared to tungsten, and arc roots therefore tend to initiate on copper-rich regions.

Under these conditions, if copper domains are uniformly distributed and spatially constrained by a continuous tungsten network, the expansion of arc roots is limited and more effective cooling can occur at the arc attachment points. Conversely, if copper regions are large or form a connected network on the contact surface, arc roots can readily spread over these copper-rich areas, leading to intensified thermal loading and significantly increased erosion. The ideal microstructural configuration thus consists of finely distributed copper domains embedded within a continuous tungsten framework. These findings, reported in [11], demonstrate that contacts with identical nominal composition but different microscale structures can exhibit markedly different erosion behavior.

The present paper focuses on the development of quantitative microstructural descriptors derived from image processing of contact surface micrographs. Short-circuit interruption experiments are performed on two sets of arcing contacts with identical geometry and identical Cu–W composition (80 wt.% W and 20 wt.% Cu), but with distinct microstructural characteristics in terms of phase size and spatial distribution. By correlating measured contact mass loss with numerical indices describing microstructural features, this study demonstrates that contacts with nominally identical specifications can exhibit markedly different erosion behavior. The results underline the necessity of incorporating quantitative microstructural assessment into erosion analysis and quality-control procedures for high-voltage gas circuit breakers.

II. Experimental Setup and Results

To isolate the influence of contact microstructure on erosion behavior, two sets of arcing contacts with identical geometry, dimensions, and Cu/W mass ratio have been subjected to controlled short-circuit interruption tests. All conventional acceptance criteria routinely verified in high-voltage laboratories—such as dimensional tolerances, density, and material composition—are satisfied for both contact sets and lie within the standard acceptable ranges. The only distinguishing factor between the two sets is the micro-scale arrangement of copper and tungsten phases, resulting from differences in their manufacturing routes. Notably, this microstructural characteristic is not part of the routine inspection or acceptance criteria in laboratory quality-control procedures. This controlled condition therefore ensures that any variation in erosion performance can be directly attributed to microstructural features rather than to macroscopic parameters that are normally assessed.
Following each interruption operation, the contacts are removed from the chamber for detailed post-test analysis. The mass loss of both moving and fixed contacts is measured, and the evolution of surface morphology is documented using digital microscopy at magnifications of 100× and 200×. These images form the basis for the image-processing procedure used later in the paper to extract quantitative microstructural descriptors.

The interruption stress is generated using the high-current branch of a synthetic test circuit designed for current interruption testing of power circuit breakers. The test circuit and the measuring devices has been illustrated in [11] in details.



(a) (b)

Fig 1. Eroded arcing contacts after interruption of the rated short circuit current: a) Moving Contact, b) Fixed Contact.

It is well known that the shape, dimensions, and weight percentage of tungsten and copper influence the mass loss imposed by current interruption. All macroscopic parameters have been kept identical in two sets of contacts. However, due to different manufacturing processes, the microstructural parameters of contacts like size and contiguity of copper and tungsten powders are different. Fig. 1 shows eroded moving and fixed contacts used in the experiments. To investigate the influence of morphological structure on contact erosion, a series of experiments was conducted under comparable electrical stresses, specifically with respect to current amplitude and arcing time, on two sets of contacts. In both test series, the fixed contacts were identical, while the moving contacts were supplied by two different manufacturers, resulting in distinct microstructural characteristics. Fig. 2 illustrates the microstructural differences between these two moving contacts at various magnifications.

Table I compares the erosion behavior of the two moving contacts, designated A and B. The experiments were carried out at five different current amplitudes with a half-cycle arcing duration. The fixed contacts, originating from the same manufacturer and subjected to identical test conditions, exhibited nearly identical mass loss in both test series. The deviation between the fixed-contact erosion values was negligible; therefore, their average mass loss is reported in Table I. This similarity confirms that the thermal and electrical stresses imposed on the two sets of contacts were effectively equivalent; therefore, only one representative set of fixed-contact data is presented.

In contrast, a substantial difference is observed in the mass loss of the moving contacts. Since the applied stresses can be considered comparable, this discrepancy can be directly correlated with differences in the microstructural characteristics of the moving contacts, underscoring the critical role of morphology in contact erosion performance.

TABLE I
THE MEASURED MASS LOSS OF CONTACTS (MILLI GRAM)

Current(kA) / *Contact*	*13*	*21*	*29*	*33.4*	*36.2*
Fixed Contact	29	246	359	501	593
Moving Contact A	25	132	257	409	488
Moving Contact B	50	323	712	1035	1186

III. Image Processing of the Contact Surface

This section presents the results obtained from digital image analysis of the contact surfaces. The objective of this procedure is to quantitatively characterize the microstructural features of the contacts and enable a reliable comparison between different samples based on the spatial distribution and connectivity of their material phases. Rather than relying solely on visual inspection, this approach translates microstructural observations into measurable numerical parameters that can be systematically analyzed and compared. For this purpose, the OpenCV library was employed within a Python environment, providing a robust and flexible framework for image segmentation and quantitative evaluation. The use of programmatic image processing allows repeatable, operator-independent analysis of the contact surfaces and facilitates the extraction of consistent metrics from multiple images. This computational approach forms the basis lfor correlating microstructural characteristics with the experimentally observed erosion behavior of the contacts. The main stages of the implemented image processing procedure are as follows:

- **Grayscale Image Conversion**

The original color images were converted into grayscale format to eliminate unnecessary color information and reduce computational complexity. Since the distinction between copper and tungsten regions in optical microscope images is primarily reflected in differences in light intensity rather than color hue, grayscale representation preserves the essential information required for segmentation. This step also minimizes the influence of illumination variations and color noise. It is important to emphasize that the accuracy of this stage is strongly dependent on image quality. The use of high-resolution images captured by a dedicated camera would further enhance the reliability of grayscale intensity differentiation between material phases.

- **Thresholding**

After grayscale conversion, thresholding was applied to transform the image into a binary representation. In this process, pixels with intensity values above a selected threshold are assigned to one class (e.g., tungsten), while those below the threshold are assigned to the other class (e.g., copper). This operation significantly enhances the contrast between the two material regions and simplifies the image into clearly distinguishable domains. Careful selection of the threshold value is essential to ensure accurate separation, as inappropriate thresholding may lead to misclassification of pixels, especially near material boundaries or in regions with non-uniform illumination.

- **Mask Formation**

Based on the binary image, masks were generated to isolate the regions corresponding to each material. These masks act as filters that selectively extract copper and tungsten domains from the original image. By applying complementary masks, each material phase can be analyzed independently while preserving its spatial location and shape within the contact surface. This step is crucial for enabling separate quantitative analysis of each material's distribution and connectivity.

- **Area Calculation**

Using the generated masks, the area associated with each material phase was computed in terms of pixel count. In addition to total area, further parameters such as the largest connected region and the average area of material domains were calculated. These quantities serve as numerical descriptors of the microstructural organization, including the connectivity and characteristic size of copper and tungsten regions. Such metrics provide a quantitative basis for comparing different contacts and correlating microstructural features with observed erosion performance.

Fig. 2 presents the material phase identification performed by the custom Python-based image processing script developed for this study. The image corresponds to 100× and 200× magnification micrograph of Contact A and Contact B. In the original micrographs, the copper phase appears in a reddish tone, whereas the tungsten phase is distinguishable by its grayish appearance. The script successfully identifies and delineates the distinct regions of copper and tungsten on the contact surface, demarcating them with green borders. Following this segmentation, the script proceeds to calculate the respective surface areas of the copper and tungsten phases. This quantitative analysis provides a direct measure of the phase distribution, which is critical for correlating material microstructure with erosion performance.

As can be inferred from the results presented in Table II, the largest connected copper and tungsten areas differ significantly between the two contacts. This index effectively reflects the degree of surface connectivity between copper and tungsten regions. In Contact A, which exhibits substantially higher erosion than Contact B (approximately 2.5 times greater under rated short-circuit conditions), the largest detected copper area is even larger than the largest tungsten area. This observation indicates that the interconnected network on the contact surface is primarily formed by copper, with tungsten zones embedded within this network. Considering that arc roots preferentially form on copper regions, this structural feature leads to severe erosion of the contact under short-circuit conditions.
In contrast, Contact B, which exhibits lower erosion, contains a significantly smaller largest copper domain. In this case, the interconnected network on the contact surface is predominantly formed by tungsten. This configuration limits the extent of copper regions where arc roots preferentially form and enhance heat dissipation at these locations, ultimately resulting in substantially lower contact erosion compared to Contact A. Another important observation is the average area of copper and tungsten domains on the two contacts. In Contact B, the average tungsten domain area is considerably larger. Additional image analysis of the contact surfaces at 200× magnification is summarized in Table II. The calculated parameters at this higher magnification are consistent with those obtained at 100×, thereby confirming the reliability of the observations. This agreement across different magnification levels reinforces the validity of the image processing approach and the associated interpretation of the contact microstructure.

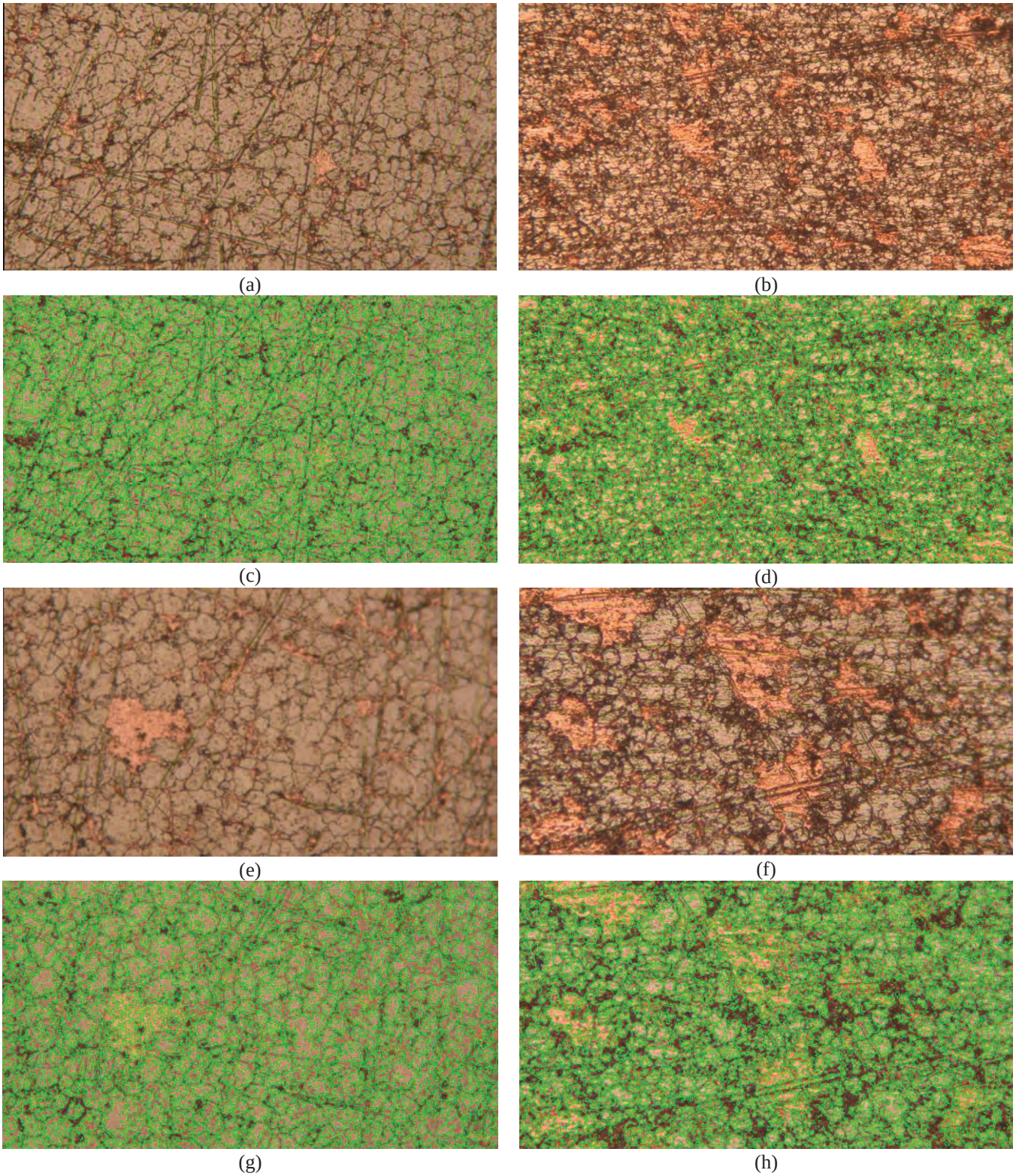


Fig. 2. Illustration of surface morphology of moving contact A (left) and moving contact B (right) with magnifications of: (a) and (b) 100X; (c) and (d)100X segmented; (e) and (f) 200X; (g) and (h) 200X segmented;

This type of image analysis can be introduced as an additional quality control criterion in the manufacturing laboratory of contacts or circuit breakers, alongside conventional parameters such as mass percentage and nominal contact area. By means of image processing and numerical quantification, the microscale structural characteristics of the contacts can also be incorporated into the evaluation process.

TABLE II
THE CALCULATED IMAGE INDICES OF CONTACTS A AND B COMPUTED IN TERMS OF PIXEL COUNT

Index(px) / Contact	Total Pixels	Copper Area	Tungsten Area	Largest Connected Copper Areas	Largest Connected Tungsten Areas	Average Copper Region Area	Average Tungsten Region Area
A(100x)	1.957.918	786.714(41.17%)	1.124.204 (%58.83)	97.369	1.093.687	269	2028
B(100x)	**1.907.968**	**834.697(%43.75)**	**1.073.271 (%56.25)**	**625.739**	**151.976**	**551**	**588**
A(200x)	1.969.407	450.553(22.88%)	1.518.854 (77.12%)	13.996	1.495.814	235	7994
B(200x)	**1.957.918**	**762.971(38.95%)**	**1.196.404 (%61.05)**	**551.345**	**496.050**	**461**	**1039**

IV. DISCUSSION

In this study, Energy Dispersive Spectroscopy (EDS) was used to analyze and identify particles deposited on nozzle surfaces following a short-circuit interruption. Two nozzles—denoted as Nozzle A (associated with Contact A) and Nozzle B (associated with Contact B)—were subjected to a single rated short-circuit interruption, then disassembled for surface examination. The EDS results revealed significant differences between the two nozzles. Nozzle B exhibited substantial deposition of contact material particles, primarily copper and tungsten, on its surface (Fig. 3). In contrast, only carbon and oxygen were detected in the eroded regions of Nozzle A, with no metallic transfer observed (Fig. 4).

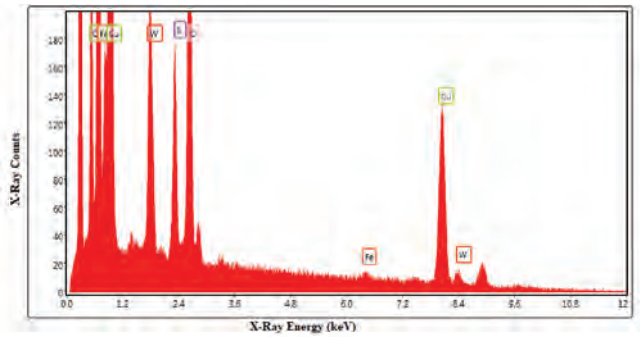
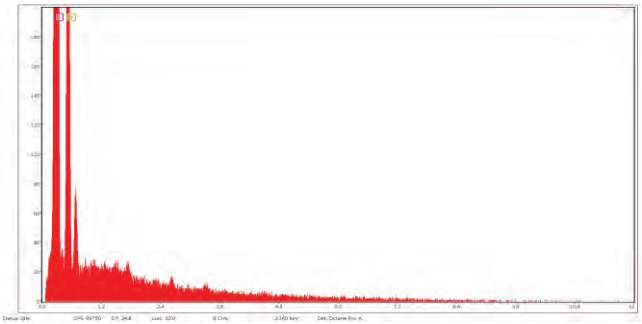


Fig. 3. EDS analysis result of selected burned areas of nozzle B

The metallic particles deposited on Nozzle B can degrade the dielectric performance of the interruption chamber, particularly under the transient recovery voltage stress that follows current zero. These findings indicate that the microstructure of the electrical contacts not only influences the thermal endurance of the chamber but also critically affects its dielectric withstand capability.


Fig. 4. EDS analysis result of selected burned areas of nozzle A

The results presented in this work demonstrate that quantitative image processing of contact surface microstructures provides insight that cannot be obtained through conventional quality control measures typically used in contact manufacturing laboratories. Although the two sets of contacts examined in this study would be considered comparable based on standard criteria—such as material composition, nominal dimensions, and mass-based assessments—their erosion behavior under identical electrical and thermal stresses was markedly different. This discrepancy was shown to be directly associated with differences in the spatial distribution and connectivity of copper and tungsten phases on the contact surface.

By applying systematic image processing techniques, it was possible to extract numerical descriptors of the microstructure, such as the largest domain area and average domain area of copper and tungsten regions. These parameters revealed fundamental differences in the morphological organization of the two contacts. In Contact B, the copper phase formed the dominant interconnected network, creating favourable conditions for arc root formation and sustained thermal loading of copper-rich regions, ultimately leading to severe erosion. In contrast, Contact A exhibited a tungsten-dominated interconnected network, effectively restricting the extent of copper regions exposed to arc attachment and improving heat dissipation at arc root locations. This structural distinction explains the significantly improved erosion performance of Contact B.

An important observation is that existing laboratory inspection and acceptance procedures are not capable of detecting such microstructural differences in a quantitative manner. Contacts that appear identical according to current measurement practices may, in fact, possess fundamentally different erosion characteristics due to their internal morphology. This highlights the need for introducing computable, reliable, and repeatable indices that describe the microstructural arrangement of contact materials rather than relying solely on bulk material properties or visual inspection.

The methodology presented in this paper can be regarded as an initial step toward the development of more advanced image-based characterization techniques for electrical contacts. By extending this approach to larger image datasets, higher-resolution imaging, and more sophisticated segmentation and feature extraction algorithms, it is possible to define robust numerical indices that truly represent the microstructural quality of contacts. Such indices could be incorporated into quality control procedures in

manufacturing laboratories, alongside conventional parameters such as mass percentage and nominal geometry.

With the rapid advancement of image processing and computational analysis tools, the integration of these techniques into contact evaluation practices is both feasible and promising. The findings of this study indicate that microstructural image analysis has the potential to bridge the gap between laboratory inspection criteria and actual erosion performance, providing manufacturers and researchers with a more reliable basis for assessing and optimizing contact materials.

V. Conclusion

This study demonstrated that image processing techniques can be used to quantitatively characterize the microstructure of tungsten–copper arc contacts and relate it directly to their erosion performance. Despite appearing similar under conventional laboratory inspection methods, two sets of contacts exhibited markedly different mass loss under identical electrical and thermal stresses. Image-based analysis revealed that this difference originates from the distinct spatial connectivity of copper and tungsten phases on the contact surface. The results highlight the limitation of current quality control practices, which do not account for microscale structural organization. The proposed methodology shows that computable image-derived indices can distinguish contacts with significantly different erosion behavior. This work serves as a foundation for developing more advanced image-based evaluation methods that can be integrated into manufacturing and testing laboratories to better assess and predict contact performance.

VI. References

[1] K. Kaliszuk et al., "Arc erosion tests and study of surface of Ag-WC contacts after arc switching operations," in Proceedings of the 50th IEEE Holm Conference on Electrical Contacts and the 22nd International Conference on Electrical Contacts Electrical Contacts, 2004., 2004: IEEE, pp. 75–82.

[2] P. G. Slade, Electrical contacts: principles and applications. CRC press, 2017.

[3] M. Kesim, H. Yu, Y. Sun, M. Aindow, and S. Alpay, "Corrosion, oxidation, erosion and performance of Ag/W-based circuit breaker contacts: A review," Corrosion Science, vol. 135, pp. 12–34, 2018.

[4] Y. Zhou, J. E. Humphries, J. W. Spencer, J. D. Yan, Z. Wang, and G. R. Jones, "Contact erosion induced by free-burning arcs in an experimental gas circuit breaker," IEEE Transactions on Power Delivery, vol. 40, no. 3, pp. 1353-1364, June 2025.

[5] Y. Zhou, J. E. Humphries, J. W. Spencer, J. D. Yan, Z. Wang, and G. R. Jones, "Contact erosion at high currents in high-voltage gas circuit breakers—Part I: Experimental research and material testing," IEEE Transactions on Power Delivery, vol. 40, no. 2, pp. 776-785, April 2025.

[6] Y. Zhou, J. Humphries, J. Spencer, and J. Yan, "Experimental study of arc erosion in gas-blasting and free-burning conditions in high-voltage circuit breakers," PLASMA PHYSICS AND TECHNOLOGY, vol. 10, no. 1, pp. 32–35, 2023.

[7] O. Homaee and A. Gholami, "Influence of the Shapes of Arcing Contacts on Prestrike Phenomenon in SF 6 Circuit Breakers," IEEE Transactions on Plasma Science, vol. 47, no. 8, pp. 4127–4135, 2019.

[8] W. Wilson, "High-current arc erosion of electric contact materials [includes discussion]," Transactions of the American Institute of Electrical Engineers. Part III: Power Apparatus and Systems, vol. 74, no. 3, pp. 657–664, 2008.

[9] M. Mohammadhosein, K. Niayesh, A. A. S. Akmal, and H. Mohseni, "Sensitivity of dynamic resistance of gas circuit breakers to the arc-induced contact erosion," in 2019 5th International Conference on Electric Power Equipment-Switching Technology (ICEPE-ST), 2019: IEEE, pp. 34–37.

[10] Y. Wang, L. Wen, and J. Xu, "An investigation into the mechanism of arc erosion of a WCu composite contact and its dependence on the temperature," Journal of Materials Engineering and Performance, vol. 32, no. 1, pp. 326–333, 2023.

[11] M. Mohammadhosein, K. Niayesh, A. A. S. Akmal, and H. Mohseni, "Impact of surface morphology on arcing induced erosion of CuW contacts in gas circuit breakers," in 2018 IEEE Holm conference on electrical contacts, 2018: IEEE, pp. 99–105.

[12] H. Jiang et al., "Current Service Times Prediction of Low‐Voltage DC Circuit Breakers Based on Morphological Features of Arc Plate," IEEJ Transactions on Electrical and Electronic Engineering, vol. 21, no. 1, pp. 67–76, 2026.

[13] W. Ren, Z. Zheng, C. Zhang, J. Liu, and X. Liu, "Characterization method for electric arc erosion based on the in-situ measurement of electrode surface morphology," Measurement, vol. 221, p. 113501, 2023.

[14] Z. Zheng, W. Ren, and C. Zhang, "Visualization and characterization of cumulative arc erosion behavior using 2-D microscopic images," IEEE Transactions on Components, Packaging and Manufacturing Technology, vol. 13, no. 1, pp. 34–44, 2023.

[15] M. Mohammadhosein, K. Niayesh, A. A. Shayegani-Akmal, and H. Mohseni, "Online assessment of contact erosion in high voltage gas circuit breakers based on different physical quantities," IEEE Transactions on Power Delivery, vol. 34, no. 2, pp. 580–587, 2018.

[16] N. Zhou, Y. Xu, S. Cho, and C. T. Wee, "A systematic review for switchgear asset management in power grids: condition monitoring, health assessment, and maintenance strategy," IEEE Transactions on Power Delivery, vol. 38, no. 5, pp. 3296–3311, 2023.

[17] A. A. Razi-Kazemi and K. Niayesh, "Condition monitoring of high voltage circuit breakers: past to future," IEEE Transactions on Power Delivery, vol. 36, no. 2, pp. 740–750, 2020.

[18] K. Hadda, A. Beloufa, M. Amirat, and A. Boutte, "Investigation on contact surfaces damage of copper contacts by an electric arc," Archive of Mechanical Engineering, pp. 251–271–251–271, 2024.

[19] P. Hedayatnia, M. H. Samimi, M. Mohammadhosein, and K. Niayesh, "Ai-enhanced reliability centered maintenance for high voltage gas circuit breakers," International Journal of *Electrical Power & Energy Systems*, vol. 170, p. 110919, 2025.

Electrical Performance Study of $AgSnO_2In_2O_3$ Materials with Different Preparation Processes Under High Current Surge Conditions

Yibo You
Technology Center
Fuda Alloy Materials Co., Ltd.
Zhejiang, China
yyb@fudar.com

Yangfang Chen
Technology Center
Fuda Alloy Materials Co., Ltd.
Zhejiang, China
cyf@china-fuda.com

Dai Wan
Technology Center
Fuda Alloy Materials Co., Ltd.
Zhejiang, China
wd@fudar.com

Xiaofang Yan
Technology Center
Fuda Alloy Materials Co., Ltd.
Zhejiang, China
sophyan@fudar.com

Qinghong Wei
Technology Center
Fuda Alloy Materials Co., Ltd.
Zhejiang, China
Weqhong@fudar.com

Zhenyang Song
Technology Center
Fuda Alloy Materials Co., Ltd.
Zhejiang, China
szy@fudar.com

***Abstract*—To optimize electrical contact materials performance under high current surges, this paper investigates the dynamic performance of $AgSnO_2In_2O_3$ materials prepared by four processes (atomization, internal oxidation, coated powder process and powder mixing) subjected to 250 V/200 A surge impact (1s on, 3s off, 20k cycles). Using FEI Apreo C SEM for arc erosion morphology and microstructure analysis, combined with high-speed camera (8000 FPS) observation, investigating the impact of the microstructure on electrical endurance and welding resistance performance and other dynamic behaviors, and research has shown that: ① Arc energy and time order: I.O. less than atomization less than coated powder process less than powder mixing. I.O. process showing the best overall electrical performance. ② Laboratory simulation of electrical endurance: I.O.greater than atomization greater than coated powder processgreater thanpowder mixing. I.O. process achieves electrical endurance of 24k cycles, 30% higher than that of powder mixing process. ③ Welding resistance performance: I.O. greater thanatomizationgreater than coated powder process greater thanpowder mixing. I.O. process forms SnO_2-In_2O_3 intergranular defects, inhibiting recrystallization, reducing arc erosion and formation of spatter-like morphology on contact surfaces. The study provides a process foundation and analytical method for developing high-performance electrical contact materials for smart grids, NEV and aerospace.**

Keywords—$AgSnO_2In_2O_3$ electrical contact material， high speed dynamic capture， high current surge conditions， welding resistance performance;， arc erosion morphology

I. INTRODUCTION

In power electronic devices, the performance of electrical contact materials is directly related to the reliability and safety of the system. Surge current, as a common transient overload phenomenon, poses a severe challenge to the electrical performance of electrical contact materials. $AgSnO_2In_2O_3$ materials, owing to their excellent arc erosion resistance and anti-welding properties, are gradually replacing traditional toxic materials and becoming an ideal choice for key components such as relays and switches [1–3]. However, different preparation processes have a significant impact on the microstructure of the material, which in turn determines the differences in their electrical behaviour under high surge current conditions. In addition, the stability of contact resistance, erosion resistance, and thermal stability of the material under surge current stress have become the core bottlenecks restricting their engineering applications [4-6].

Currently, research on $AgSnO_2In_2O_3$ materials, both domestically and internationally, mainly focuses on compositional optimization and fundamental property characterization [7-9]. Chinese investigators have reported that minor additions of rare-earth elements (e.g., La, Ce) markedly improve anti-welding performance; nevertheless, the dynamic response mechanisms under high surge current conditions remain insufficiently understood. Wang Haitao team achieved nanoscale dispersion of SnO_2 particles (particle size<50nm) by precisely controlling the ball milling time, reducing the contact resistance fluctuation rate of the material by 42% in simulated surge current (peak current 200A) testing; however, In_2O_3 agglomeration during high-temperature sintering restricts the material's applicability in high-frequency switching devices. In DZ6-60 automatic-switch trials, Gong observed that internally oxidized specimens exhibited a 58 % enhancement in anti-welding resistance relative to AgCdO, whereas the graded distribution of SnO_2 particles induced localized overheating under inrush-current stress.

This study targets high surge current duty and, by comparing the influence mechanisms of different preparation routes on the electrical lifetime of $AgSnO_2In_2O_3$ materials, aims to provide a theoretical basis for optimized material design and thus enhance reliability under harsh operating conditions.

II. EXPERIMENTS

A. Raw materials and instruments

Raw materials: silver plate (Ag, purity equal to or greater than 99.99%), tin ingot (Sn, purity 99.9% minimum), indium ingot (In, purity 99.9%minimum), tin oxide powder (SnO2, purity 99.9%minimum), indium oxide powder (In2O3, purity 99.9%minimum), other additives (purity 99.9%minimum).

Testing instruments: Field emission scanning electron microscope (SEM, model Apreo C, Thermo Fisher Scientific, USA), high-speed camera (8000FPS, NAC, Japan), analog electrical performance equipment (contact material electrical performance simulation experimental system, CES-3000, Harbin Institute of Technology), metallographic microscope

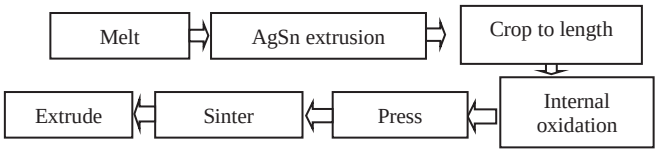
(SOPTOP, Ningbo Shunyu Instrument Co., Ltd.), Keyence metallographic microscope (VHX-5000, Keyence).

B. Material preparation

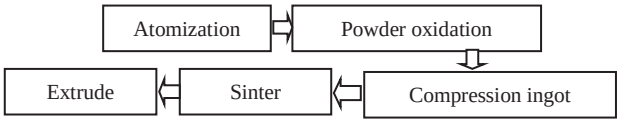
$AgSnO_2$ electrical-contact materials were fabricated by four routes: internal oxidation, atomization, and two powder-metallurgy variants (coated-powder and powder mixing). Ag, SnO_2 and the additives were weighed according to the ratios listed in Table 1 and processed into extruded wires. The wires were hot-drawn on a mains-frequency machine to φ 1.88 mm wire, which was then cold-headed into rivet-type $AgSnO_2$ contacts using a composite-contact heading machine. The detailed process flow is given in Fig.1.

TABLE I. CONTACT COMPOSITION PRODUCED BY DIFFERENT PROCESSES

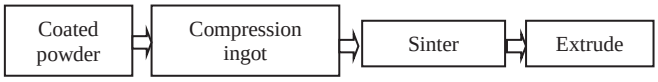
Name	Preparation process	Composition			
		Ag /%	***SnO_2 /%***	***In_2O_3 /%***	***Other /%***
$AgSnO_2T1$	internal oxidation	85	11	3	1
$AgSnO_2T2$	atomization				
$AgSnO_2T3$	coated powder process				
$AgSnO_2T4$	Powder mixing				



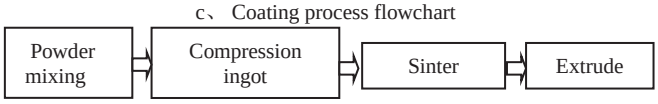
a、 Internal oxidation process preparation flowchart



b、 Atomization process preparation flowchart



c、 Coating process flowchart



d、 Powder mixing process flowchart

Fig 1: Process Flow Chart for Four Materials Preparation
a、 Internal oxidation , b、 Atomization , c、 Coated powder process, d、 Powder mixing

C. Testing and characterization

Four groups of $AgSnO_2$ rivets, each produced by a different process, were assembled by riveting and subjected to 20 000 make-break operations under capacitive load.Three sets of samples prepared by each process were used for testing. One set per material was evaluated; all other test parameters were identical. The detailed conditions are summarized in Table below.

Characterization ： Field-emission scanning electron microscopy (FE-SEM) was employed to observe the micro-morphology of the contact materials; chemical compositions were determined by energy-dispersive X-ray spectroscopy (EDS) at 20 kV and 8 mA. Arc-erosion dynamics were recorded and analysed with a high-speed camera. Microstructures were examined using an optical metallurgical microscope and a Keyence VHX-5000 digital microscope.

TABLE II. TEST CONDITIONS FOR DYNAMIC WELDING OF CONTACTS PREPARED BY DIFFERENT PROCESSES

Contact material	contact size	Test conditions	Parameter Settings
$AgSnO_2In_2O_3$	R4.0mm×0.79 mm ＋ 2.0mm×2.55 mmSR10 (Specification of Moving point) F4.0mm×0.79 mm ＋2.0mm ×2.55 mm (Static point specification)	***Test environment***	Temperature: 19-22 ℃ Humidity: 50-65%
		Time	20000
		Action frequency	1S on: 3S off
		Load nature	Capacitive capacity
		Steady state current/peak current	20A/200A
		Contact opening distance	0.5mm
		Static pressure	1.0N

III. RESULTS AND DISCUSSION

This study systematically compared the dynamic properties of $AgSnO_2$ In_2O_3 materials produced by four processes: internal oxidation, atomization, and powder metallurgy (coated powder and powder mixing) under 250V/20A (steady-state current) and 200A (surge current) impact conditions. Combined with arc erosion morphology analysis, electrical life test data comparison, and high-speed dynamic observation, the correlation mechanism between the microstructure and macroscopic electrical properties of the materials was revealed.

A. Welding force

Under different preparation processes, the scatter plot of the welding force after the electrical life test of $AgSnO_2In_2O_3$ contact material is shown in Fig 2, the microstructure structure is shown in Fig 3, and the results of the electrical life test are shown in Table 3. All three sets of samples prepared by each process showed identical electrical endurance.

TABLE III. ELECTRICAL LIFE TEST RESULTS OF ELECTRICAL CONTACT MATERIALS PRODUCED BY DIFFERENT PROCESSES

name	$AgSnO_2T1$	$AgSnO_2T2$	$AgSnO_2T3$	$AgSnO_2T4$
preparation process	Internal oxidation process	Atomization process	Coated powder process	Powder mixing process
Number of electrical life cycles (ten thousand times）	24	20	20	18.5
	24.1	20	19	18.4
	24	19	19	18.6

Figure 2 shows that $AgSnO_2$-T1 (internal-oxidation route) exhibits the longest electrical life, with welding forces concentrated between 0.05 N and 0.12 N and only minor scatter, indicating strong resistance to arc erosion and easy break-away. In contrast, $AgSnO_2$-T4 (blended-powder route) gives the shortest life; its welding forces span 0.03–0.18 N

with large fluctuations, revealing poor stability under the test conditions.

Microscopic analysis shows that the internally oxidized material exhibits the lowest welding force. Its coarse, fence-like grains (Fig. 3) effectively suppress local overheating and material transfer under the arc, thereby reducing arc-vapor generation and enhancing anti-welding performance. In contrast, the powder-metallurgy process—especially the powder mixing process—contain loosely distributed SnO_2 particles with weak inter-particle bonding; under prolonged arc bombardment they suffer enhanced material transfer, leading to a marked decline in anti-welding capability.

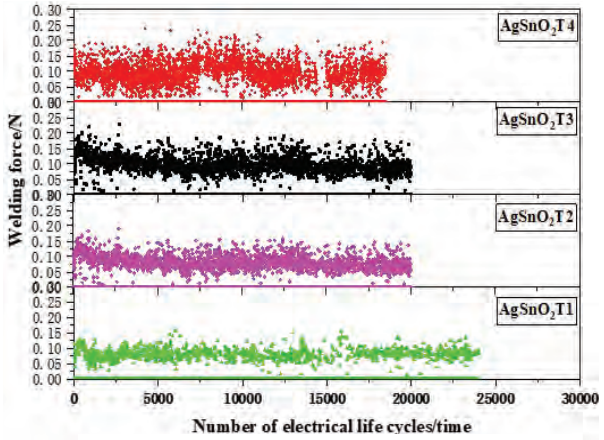


Fig 2 Scatter plot of material welding force under different preparation processes

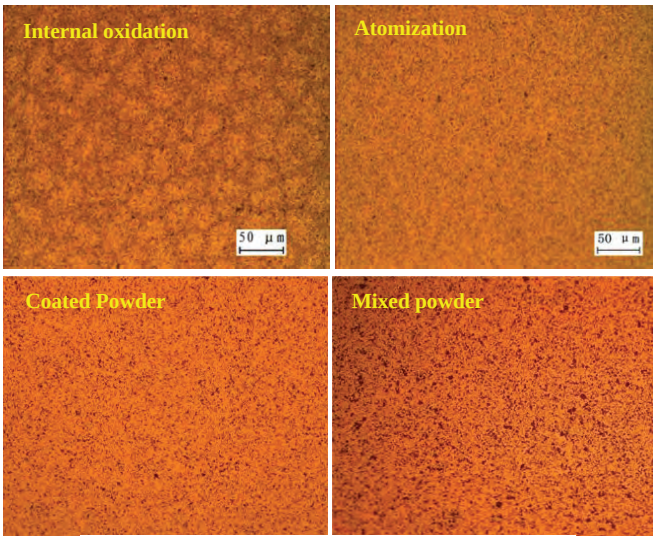


Fig 3 Material Metallography under Different Preparation Processes

B. *Arc energy and arc time*

Under different preparation processes, the normal distribution of arc energy and arc time in the electrical life test of $AgSnO_2In_2O_3$ electrical contact material is shown in Fig 4 and Fig 5, respectively. The maximum arc moment of the 5000th dynamic welding closure in the electrical life test is shown in Fig 6.

Figures 4 and 5 show that the "typical values" for the duration of arc discharge and energy release differ among the materials. The arc-ignition energy of $AgSnO_2$-T1 peaks at ≈ 0.03 mJ, whereas that of $AgSnO_2$-T4 is ≈0.28 mJ, indicating that T1 concentrates energy release in the low-energy region with small fluctuations and high stability. The internally oxidized material develops a dense, high-resistivity oxide layer that suppresses arc discharge and lowers arc energy; the same dense structure also minimizes direct contact between the arc and the substrate, shortening arc duration. In contrast, T4—prepared by mechanical mixing—shifts toward the medium-energy range and exhibits large scatter in both arc energy and arc time. Mechanical mixing introduces impurities and residual pores: impurities act as discharge centres that reduce breakdown voltage and raise arc energy, while enlarged inter-particle pores prolong the arc lifetime.

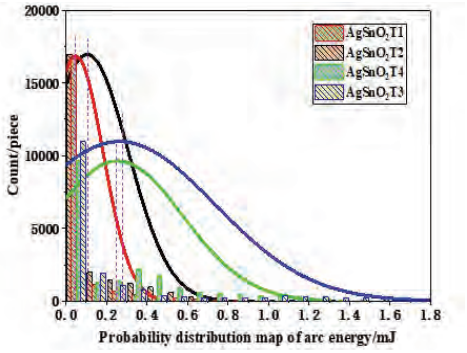


Fig 4 Normal distribution of arc energy

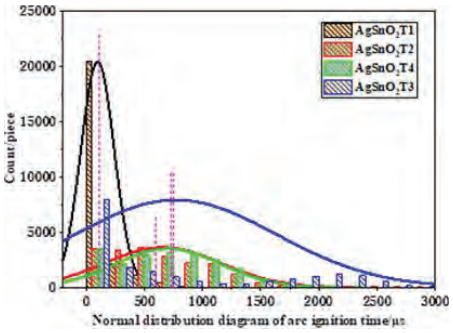


Fig 5 Normal distribution of arc ignition time

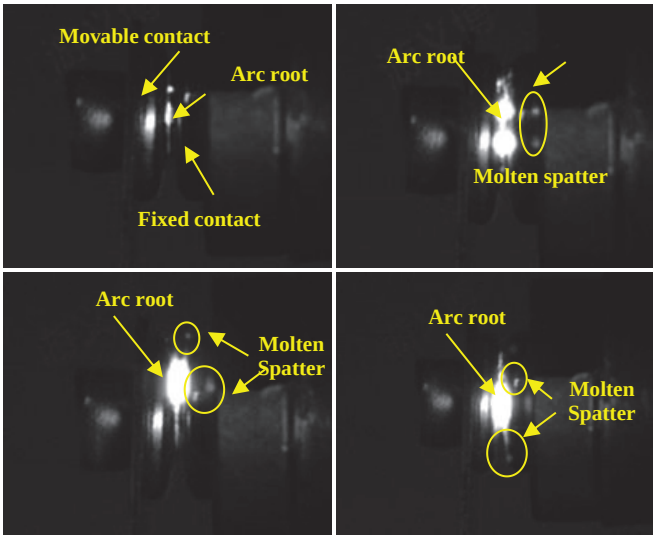


Figure 6: Maximum arcing moment after the 5000th contact closure captured by high-speed dynamic capture

Research shows[1-4] that arc energy equals arcing time multiplied by arc power: the higher the arc power, the greater the arc energy and the more pronounced the arcing behavior.

When the material exceeds its withstand limit, the contact surface melts and a welding force develops. According to Figs. 2, 4 and 5, $AgSnO_2$-T1 exhibits the lowest welding force and should therefore produce the smallest arc. To verify whether this theoretical prediction matches actual performance, we compared the maximum arc instant recorded at the 5 000-th dynamic-welding closure during the electrical-life test. The welding forces measured for $AgSnO_2$-T1, T2, T3 and T4 at this point were 0.08 N, 0.104 N, 0.140 N and 0.145 N, respectively.

As shown in Figure 6, the spatial distribution of arc roots varies significantly among the four materials. After 5 000 operations $AgSnO_2$-T1 ignites only a small, localized root at the instant of closure and produces virtually no spatter, demonstrating that it still suppresses arc expansion effectively in the mid-life region. $AgSnO_2$-T2 establishes two distinct roots—one in the upper and one in the lower contact zone; although their number is higher, each occupies a smaller area. In contrast, $AgSnO_2$-T3 and $AgSnO_2$-T4 both initiate a single, centrally located arc that rapidly expands outward, leaving a large footprint and ejecting pronounced spatter. For $AgSnO_2$-T4 the discharge is exceptionally intense: the resulting material loss (evidenced by a thickened erosion layer) increases contact resistance, which in turn intensifies the next arc, thereby establishing a positive-feedback loop of arcing → material loss → even stronger arcing that ultimately shortens electrical life. Consequently, the arc behaviour observed for all four compositions is consistent with theory.

C. Arc erosion morphology

Under different preparation processes, the arc erosion morphology of $AgSnO_2In_2O_3$ electrical contact material after electrical life test is shown in Fig 7, and the arc erosion profile is shown in Fig 8. From Fig 7 and Fig 8, it can be seen that there are differences in the erosion morphology of the contact surface under different processes. After the $AgSnO_2T1$ test, the contact surface was relatively flat, but due to multiple tests, the surface burn area was large, and there was slight silver accumulation at the edge of the profile. However, after the $AgSnO_2T3$ and $AgSnO_2T4$ tests, the contact surface was uneven and the profile was serrated.

Research suggests[5-8] that the internal oxidation process can improve the interfacial bonding between oxides and metal substrates, reduce material brittleness and local thermal stress concentration caused by grain boundary defects. This bonding effect can effectively suppress metal melting and splashing during the arc process, while enhancing the material's oxidation resistance and conductivity stability, thereby significantly extending the electrical life (manifested as 24000 high test cycles). However, $AgSnO_2T4$ only achieves component mixing through physical means, with the worst microstructure uniformity. Its SnO_2 and Ag are prone to agglomeration and segregation, resulting in high local current density and intensified material melting and splashing during the arc process. The final electrical life is only 18500 times, showing the weakest performance. In summary, different preparation processes can directly affect the stability of materials in arc environments through dimensions such as microstructure, composition distribution, and surface properties.

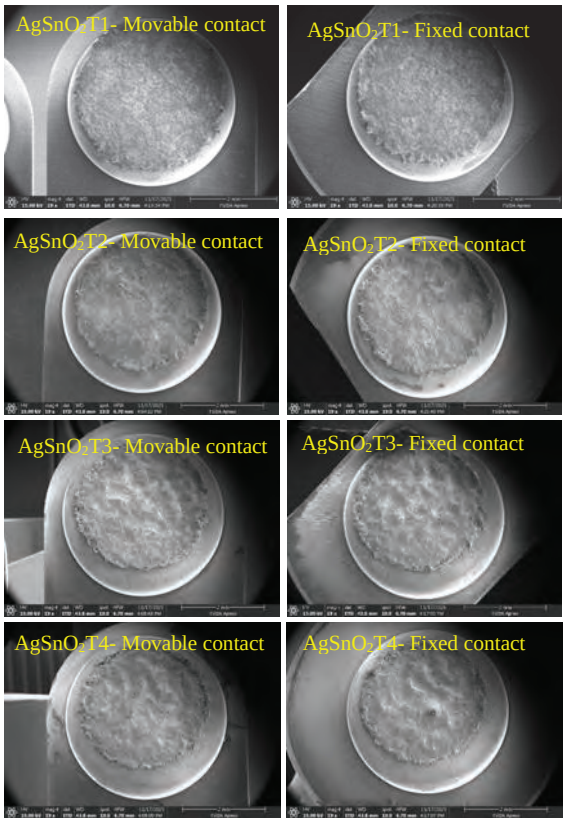


Fig 7 SEM morphology of arc erosion under different preparation processes

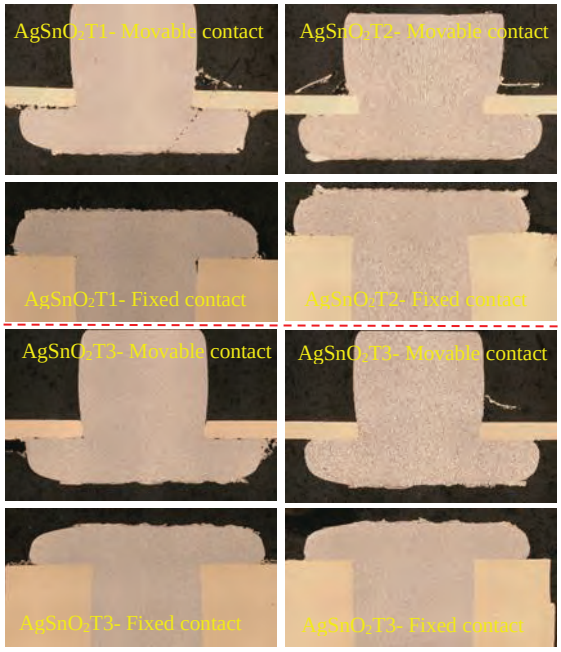


Fig 8 Arc erosion profile morphology under different preparation processes

IV. Conclusions and Prospects

This study systematically compared $AgSnO_2$–In_2O_3 contact materials produced by four processes—internal oxidation, atomization, and two powder-metallurgy variants (coated powder and powder mixing), and established the link between microstructure and macroscopic electrical performance.

(1) High-speed imaging of dynamic welding and arc-erosion patterns shows that microstructure, composition distribution and surface texture jointly determine arc stability. The internally oxidized grade exhibited the most stable behavior.

(2) Both arc energy and arc duration increased in the sequence: internal oxidation < atomization < coated powder < powder mixing. Contacts made by internal oxidation survived 24 000 operations—30 % longer than those from the powder mixing process. Longer arc duration consistently correlated with higher arc energy.

(3) Anti-welding tests revealed that the internally oxidized material contains a coarse, fence-like network of SnO_2 and In_2O_3 particles which generate dense dislocation-pinning sites. These sites hinder recrystallization, markedly reduce arc erosion and suppress spattering, thereby giving the contacts a significantly higher resistance to welding.

(4) The findings provide a clear processing guideline for high-reliability contacts and pave the way for their adoption in smart grids, electric vehicles and aerospace systems.

References

[1] Li Z, Wang ZB, Chen KN, et al. Comparative study of preparation processes and arc erosion characteristics of Ag-SnO_2 contacts[J]. Electrical Engineering Materials, 2021(04):3-9. DOI:10.16786/j.cnki.1671-8887.eem.2021.04.001.

[2] Zhang M, Zhao H, Li XF. Research progress on preparation technology of silver-based electrical contact materials[J]. Materials Reports, 2022, 36(12):121-128. DOI:10.11896/cjdb202112010.

[3] Zhou M, Wu H, Zheng L. Effect of rare earth oxides on the microstructure and electrical properties of Ag-SnO_2 contact materials[J]. Materials & Design, 2023, 218: 110567.DOI:10.1016/j.matdes.2022.110567.

[4] Zhou M, Wu H, Zheng L. Effect of rare earth oxides on the properties of Ag-SnO_2-In_2O_3 electrical contact materials[J]. Rare Metal Materials and Engineering, 2023, 52(3):1-8. DOI:10.11858/rare.2023.03.001.

[5] Chen J, Sun W, Wu D. Quantitative analysis of arc erosion morphology on Ag-SnO_2 contact materials[J]. Wear, 2022, 498-499: 204567.DOI:10.1016/j.wear.2022.204567.

[6] Li ZY, Wang XT, Yang F. Dynamic performance of electrical contact materials under high current density[J]. Proceedings of the CSEE, 2024, 44(8):1-10. DOI:10.13334/j.0258-8013.pcsee.230584.

[7] Zhang L, Wang Y, Chen X, et al. Microstructure and electrical properties of Ag-SnO_2-In_2O_3 contact materials prepared by internal oxidation[J]. Journal of Materials Science & Technology, 2022, 118: 1-10.DOI:10.1016/j.jmst.2022.05.033.

[8] Zhao Y, Zhou W, Li M. Research progress on surface modification technologies of electrical contact materials[J]. Surface Technology, 2023, 52(5):1-12. DOI:10.11964/j.issn.1001-3810.2023.05.001.

[9] Wang L, Zhang H, Liu F. Application status of electrical contact materials in new energy vehicles[J]. Automotive Engineering, 2024, 46(3):1-8. DOI:10.19537/j.1000-680X.2024.03.001.

Contact material testing - modern model switch methods

1st Armin Strahl
Electrical Products
Siemens AG
Regensburg, Germany
armin.strahl@siemens.com

2nd Daniel Kupka
Electrical Products
Siemens AG
Amberg, Germany
daniel.kupka@siemens.com

3th Andreas Kammerl
Electrical Products
Siemens AG
Regensburg, Germany
andreas.kammerl@siemens.com

4rd Marina Logvinova
Electrical Products
Siemens AG
Amberg, Germany
marina.logvinova@siemens.com

***Abstract*—This arcticle shows possibilities to measure the arc movement, especially with regard to the movement of the root point. The concepts for detecting optical radiation and the magnetic field were combined to one test setup and compared with existing concepts based on the same principle. The magnetic flux density generated by the arc is meausred with a sensor arc array. The paper shows also a first approach to determine the position derived by the sensor data. Furthermore, the current through the fired contact was measured separately from the arc runner. The provided test results are compared with qualitative statements of known literature.**

***Index Terms*—contact tip, model switch, contact material, contact material testing, low voltage switchgear, low voltage.**

I. Introduction

During electrical switching operations, contact bounce arcs and switching-off arcs unavoidably occur. In general, arcs appear — depending on the contact material — at voltages of approximately $\gtrsim 30\,\mathrm{V}$ and currents of $\gtrsim 1\,\mathrm{A}$. Depending on the specific application and design of the low-voltage switchgear, the make-and-break behavior must be analyzed as part of the development process. A contact bounce arc occurs when the contacts close as a result of a kinetic motion sequence of a contact mechanism, which can be modeled as a spring–mass–damper system. The switching arc, by contrast, is generated during the opening of the contacts. [1]

Prior to testing contact tips in a circuit breaker during development, it is often more efficient to evaluate the material characteristics of the contacts in a model switch. The model switch experiments are intended to quantitatively determine and compare the switching and contact erosion behavior of different contacts. Both contact erosion and switching behavior are largely governed by the arc. The arc causes significant thermal stress on the contact, the current path, and surrounding components. This thermal stress reduces the service life of the devices. The high arc temperature can also cause plastic outgassing, leading to sooting and reduced insulating properties, which may result in flashovers. The switching process is likewise directly negatively affected, since arc formation delays the disconnection, which can represent a hazard to both equipment and personnel, especially in protective devices. Therefore, a thorough analysis of the switching behavior of the contact tip is essential.

In arc and switching analyses, the exclusive evaluation of electrical measured quantities such as current i and arc voltage u_{arc} is often insufficient, as information on arc position (root and column), initial dwell time and movement tendencies cannot be obtained thereby. In most low-voltage switchgear contact systems, the arc is intentionally commutated from the contact tip to an arc runner to minimize contact erosion. Determining when the arc commutates from the contact tip to the arc runner — and possibly back — is challenging. A more detailed analysis shows that knowledge of the position enables additional insights and improves the understanding of the switching behavior. This enables a more effective verification of the performance of the magnetic arc manipulation. Furthermore, modifications to the contact coatings and their material composition, as well as to the arc runners, can be investigated in more detail. Likewise, a gradual degradation of the switching performance due to progressive wear of the contact piece or the arc runner can be observed. In essence, knowledge of the arc position and movement allows for an improved understanding of its behavior, properties, and influencing factors. This article addresses methods for determining the arc root movement in a model switch.

II. Methodology

A. State of the art

The energy input during the opening and closing of the contacts is defined according to equation (1).

$$\int_{t_1}^{t_2} i(t) \cdot u_{arc}(t)\,\mathrm{d}t \tag{1}$$

The formulation simplifies that the integral of measured current i and arc voltage u_{arc} acts on the contact tips. The distinction between bounce and switching energy is determined by the integration limits t_1 and t_2. On the one hand, the evaluation of the integral during the making phase of the switching operation provides the contact bounce energy.

On the other hand, arc runners are commonly used in switchgear like circuit breaker to reduce the arc energy. The commutation of the arc from the contact tips to the arc chute is not directly visible in the arc voltage u_{arc}. This behavior can be analyzed using a high-speed camera. However, a large

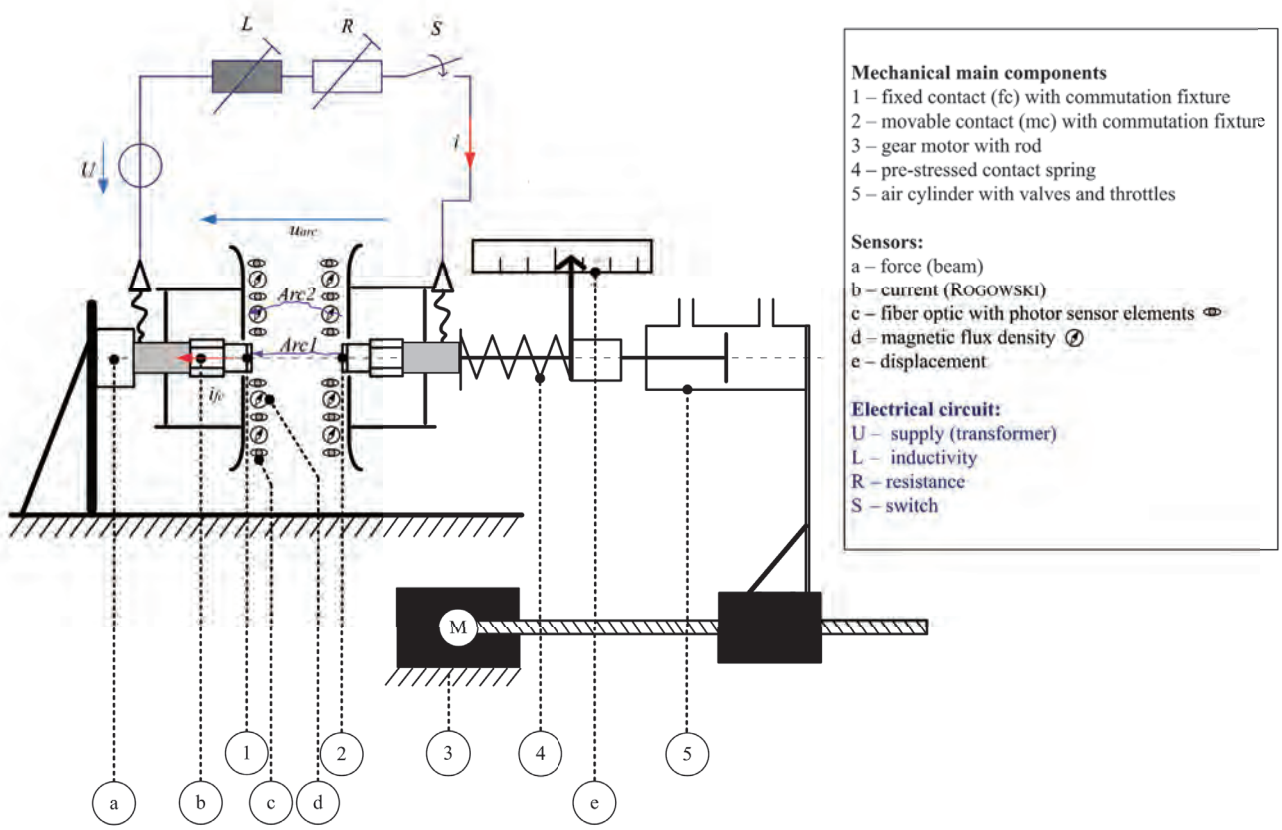


Fig. 1. Concept Sketch

volume of data and images is generated, which is subsequently analyzed and summarized. Therefore, the calculation of the bouncing or arcing energy, particularly with respect to the energy input into the contact tips, is challenging. To examine this more precisely, the following experimental setup was designed.

B. Test setup

As shown in **Figure 1**, the model switch is composed of a fixed and a movable contact piece (1) and (2) as well as a copper commutation fixture. A motor (3) automatically adjusts the movable contact to a defined overtravel. The contact force is set using a pre-stressed contact spring (4). With a known spring constant, the contact force can be calculated at contact engagement as well as during overtravel, and is additionally determined by the force sensor (a).

In addition to the test setup described in mechanically adjustable commutation fixtures are provided close to the contact tips. These can be continuously adjusted with respect to the mechanical opening angle as well as the height offset relative to the contact surface. Furthermore, the current at the fixed contact tip i_{fc} is measured by means of a ROGOWSKI coil (b). The energy input of the arc into the fixed contact tip is calculated in accordance with (2).

$$\int_{t_1}^{t_2} i_{fc}(t) \cdot u_{arc}(t)\,\mathrm{d}t \tag{2}$$

When the arc commutates from the contacts "Arc1" to the commutation fixture "Arc2", the current i_{fc} becomes zero and the integral no longer raises **(see Figure 1)**. Additionally, sensors (c) and (d) are added to the test setup and are explained later.

III. IMPLEMENTATION

A. Preliminary considerations

The influence of additional sensors on the switching process should be reduced to a minimum, to ensure that the respective contacts can be specifically examined. Similar to a switching device, a detailed investigation of the light arc and especially its interaction with the contacts is not possible using only the electrical quantities i, u_{arc}. **Table I** summarizes the essential characteristics and requirements.

A high measurement rate and a sufficiently large measurement range are necessary for accurate recording of the arc root. The spatial resolution should be as high as possible to track the position of the arc. Since subsequent temporal data synchronization of the various measurement systems is diffi-

TABLE I
SENSOR REQUIREMENTS

Feature	Requirement
Sensors	min. 16
Spatial resolution	$< 2\,\mathrm{mm}$
Light intensity	–
Resolution	min. 8 bit
Magnetic resolution	$< 50\,\mu\mathrm{T}$
Sampling rate	min. 10 kHz
Measurement range	min. $2\,\mathrm{mm} \times 50\,\mathrm{mm}$

cult, the switching pulse of the model switch is additionally used as a pulse to start all measured values.

B. Optical Sensor

An electric arc emits, among other things, radiation in the visible range, which can be used to record the movement. Due to the high light intensity, filtering is a challenge in addition to the actual optical measurement. The optical measuring device is based on capturing the light of the passing arc using optical fibers and then transmitting it to photosensors. This allows the position of the arc to be detected. It is also possible to calculate the speed of the arc by the time difference between the activation of two successive photosensors and the distance between the inputs of the associated photosensors. The optical fibers can be arranged on the fixed or moving contact side in two (or more) rows parallel to the contact and running surface, as shown in **Figure 1**. The optical fibers are located a short distance inside a tube made of optically absorbing material, ensuring that the photosensor only reacts when the arc is actually below the optical fiber and no lateral interference signals are recorded. The photosensor outputs a voltage signal that is proportional to the measured light intensity. This signal is amplified and then sent via a measurement card to the evaluation computer to be displayed. In parallel, the current i, the arc voltage u_B and the contact position x are also sent from the measuring card to the computer. The system's measurement rate depends on the measurement card and is 25 kHz in the presented case with a spatial resolution of up to 1.2 mm. A simplified block diagram of the sensor setup can be seen in **Figure 2**.

TABLE II
CONCEPT COMPARISON WITH [2]

Feature	[2]	Presented Arrangement
Sensors	1024	16 (expandable)
Spatial resolution	$\approx 2\,\mathrm{mm}$	$1.2\,\mathrm{mm}$
Light intensity resolution	8 bit	16 bit
Sampling rate	1 MHz	250 kHz
Measuring range	–	$15\,\mathrm{mm} \times 77.5\,\mathrm{mm}$
Data storage duration	500 ms	5000 ms

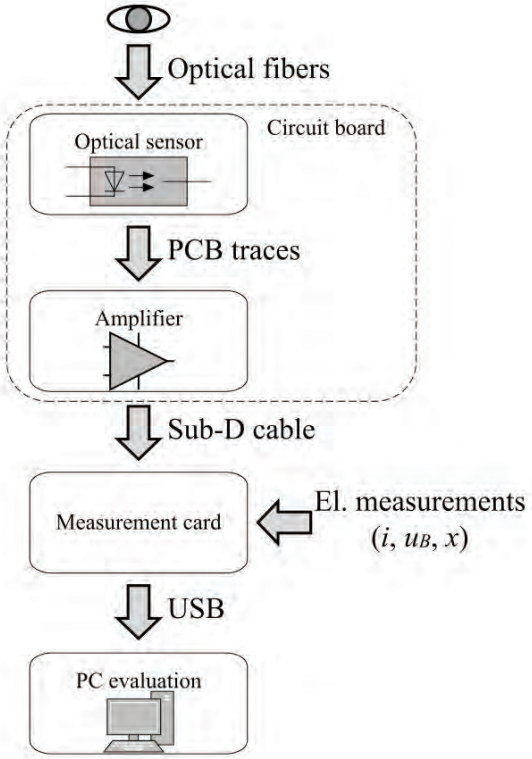


Fig. 2. Block Diagram Optical Sensor

[3] presents another concept for detecting arcs using an optical fiber-based imaging system. **Table II** compares the most important aspects of the two concepts. The work in [3] presents a concept with a higher number of sensors. The number of sensors used varies greatly depending on the application. In both concepts, the position of the optical fibers can be chosen from a multitude of locations, and the spatial resolution is similar in both concepts. The concept presented in this article offers improved resolution of the light intensity, but this leads to a reduction in the measurement rate. Despite this limitation, the measurement rate remains sufficient for the intended application.

C. Magnetic field sensor

An electric arc, like a current-carrying conductor, generates a magnetic field around it. A magnetic field sensor based on the $HALL$ effect can measure the vectorial magnetic field strength. For the presented application, 32 sensors arranged in a row are attached in the same way as the optical fibers, see **Figure 1** (d). Since switching operations are often performed under magnetic blowing, it is important to consider these interfering influences for a meaningful assessment (e;g. as an offset). Magnetic blowing is used to deliberately steer and influence the arc in one direction.

The magnetic field sensors make it possible to detect and observe the arc even behind an opaque housing. This

achieves increased practical relevance, as the findings can also be applied to switchgear. Thus, for example, additional information can be gained during product development and enable optimization. The signals originating from the sensor board are processed by an evaluation unit and then also sent to the evaluation PC.

The magnetic sensor strip can cover an area of $2.5\,\mathrm{mm} \times 77.5\,\mathrm{mm}$ and is capable of detecting the magnetic field strength with a measurement rate of up to $20\,\mathrm{kHz}$. A simplified block diagram of the sensor setup is shown in **Figure 3.**

Another concept for magnetic arc detection is presented in article [2]. **Table III** compares the most important parameters of the two concepts.

The central task is to reconstruct the spatial positions and the associated current intensities of the individual arc plasma channels from these measured magnetic fields and the total current. This is a classic inverse problem: the unknown cause (arc configuration) is to be deduced from the measured effect (magnetic fields). To initially reduce the complexity of the inverse problem and create a robust basis for initial calculations, specific simplifying assumptions are made in this phase accroding formula (3):

$$\vec{B} = \frac{\mu_0 I}{2\pi} \cdot \frac{1}{(x_s - x_{\mathrm{arc}})^2 + (y_s - y_{\mathrm{arc}})^2} \begin{pmatrix} -(y_s - y_{\mathrm{arc}}) \\ (x_s - x_{\mathrm{arc}}) \\ 0 \end{pmatrix} \tag{3}$$

Broken down, there are two equations for B_x formula (4) and B_y by formula (5):

$$B_x = -\frac{\mu_0 I}{2\pi} \cdot \frac{(y_s - y_{\mathrm{arc}})}{(x_s - x_{\mathrm{arc}})^2 + (y_s - y_{\mathrm{arc}})^2} \tag{4}$$

$$B_y = \frac{\mu_0 I}{2\pi} \cdot \frac{(x_s - x_{\mathrm{arc}})}{(x_s - x_{\mathrm{arc}})^2 + (y_s - y_{\mathrm{arc}})^2} \tag{5}$$

With two unknowns, x_{arc} and y_{arc}, the system of equations is uniquely solvable, and after rearranged to formula x_{arc} and y_{arc}

$$x_{\mathrm{arc}} = x_s - \frac{\mu_0 I\, B_y}{2\pi\,(B_x^2 + B_y^2)} \tag{6}$$

$$y_{\mathrm{arc}} = y_s + \frac{\mu_0 I\, B_x}{2\pi\,(B_x^2 + B_y^2)} \tag{7}$$

TABLE III
CONCEPT COMPARISON WITH [2]

Feature	Arrangement in [2]	Presented Arrangement
Sensors	6	32
Magnetic resolution	$160\,\mu\mathrm{T}$	$4\,\mu\mathrm{T}$
Measurement	2D	3D
Sampling rate	80 kHz	20 kHz
Measurement range	$42\,\mathrm{mm} \times 60\,\mathrm{mm}$	$2.5\,\mathrm{mm} \times 77.5\,\mathrm{mm}$

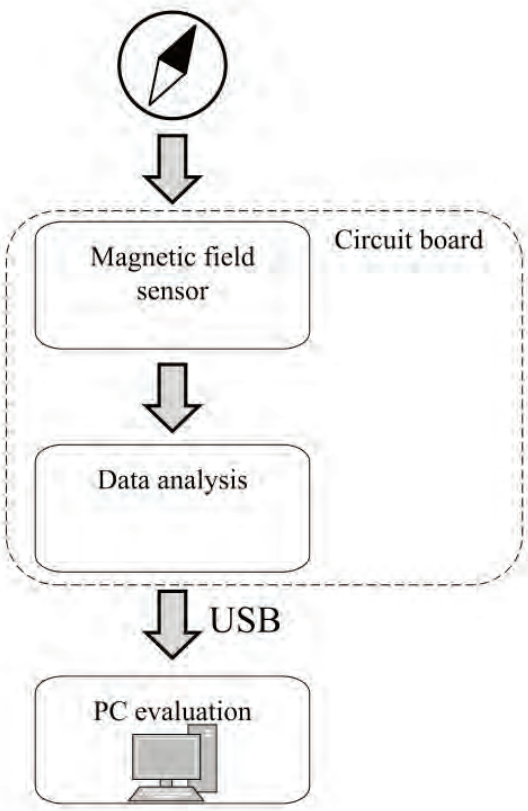


Fig. 3. Block Diagram Magnetic Sensor

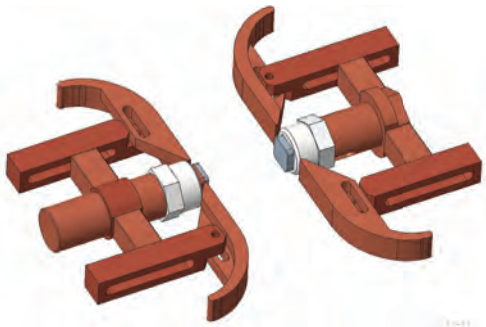


Fig. 4. Contact Arrangement

D. Contact arrangement

For clarity, **Figure 4** shows the CAD model of the contact arrangement.

The adjustability of the commutation device with regard to gap angle and height offset to the contact surface is evident here. The sensor device, which is not shown, is located above the commutation rails. Depending on the question at hand, the suitable positions can be chosen for the optical fibers.

IV. Designe of Expirement

A. Planning

The test parameters of the carried out tests are shown in **Table IV** below. According to literature [4, chapter site 302] the arc running behaviour of AgW is significantly worse than that of AgNi. This statement will be verified using the presented measurement technique. Five contact pairs will each be subjected to ten switching cycles at 230V.

TABLE IV
Test plan

Test parameters	Material AgW	Material AgNi
100 A, $\cos(\varphi) = 0.9$	5x	5x
500 A, $\cos(\varphi) = 0.9$	5x	5x

B. Test Execution

Figure 5 shows the switch-off process at 100 A. The zero point of the time axis is the initialization of the measuring system and the subsequent start of the movement. The contacts open at approximately 2165 ms or approximately 210°, which can be recognized by an increase in arc voltage (approximately 10 V). The optical fibers of the optical sensor array are arranged approximately symmetrically to the contacts. Sensors 4 and 5 are mounted directly above the contact piece, while sensors 1 to 3 and 6 to 8 are located above the guide rails; the sensor spacing is approximately 1.5 mm. The distance between the guide rail and the sensors is approximately 10 mm. In the illustration, thick dark markings indicate a high detection of the optical signal, suggesting that the arc is located at this point. In contrast, thin light markings show a low optical detection. Sensors 9 to 16 are located 3 mm away from the first sensors in the direction of the moving contact. Before the start of the test, the commutation device was cleaned in the direction of arc travel with extra fine grit sandpaper to remove soot and dirt from previous tests.

C. Evaluation

Using the signal from the optical sensors, an average arc position and thus an arc movement can be determined along a sensor row (e;g. sensor 1-8). From this, the first time derivative can be calculated: the speed of the arc. The signals from the magnetic sensors show a proportional, sinusoidal curve from the start of the current until the contact opens, depending on their orientation to the current path. A recursion of the magnetic signal for the temporal and spatial resolution of the arc is currently still being verified and will be presented at a later date. The signal of the current i_{FC} is also evaluated according to **formula 2**. The lower this energy, the faster the arc moves from the contact point to the guide rail. The investigation of commutation processes under different test conditions has already been discussed extensively in [5].

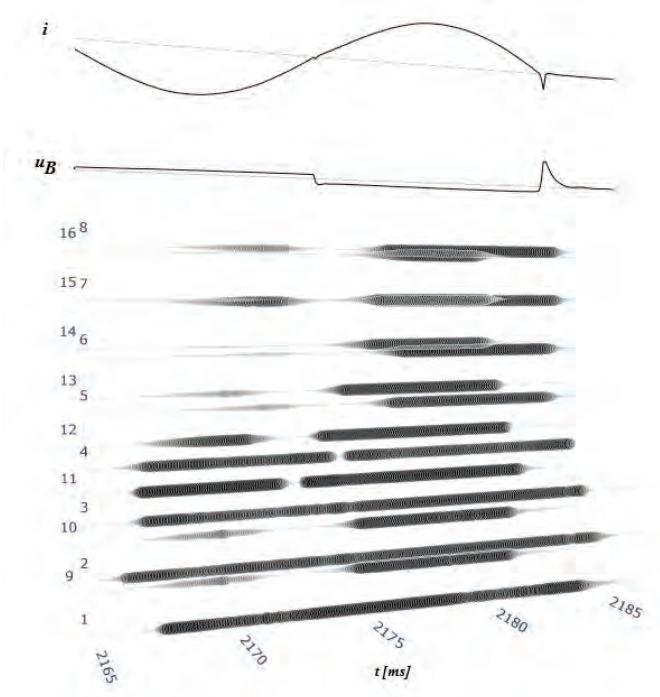


Fig. 5. 3D-Plot Optical Sensor

V. Discussion

For the optical sensors, measurements show an arc movement speed — from the contact area to the runner rail — of approximately $2\,\mathrm{mm/ms}$. The following **Table V** provides a comparison of the mean values. This quantitatively confirms the assertion made in [4, chapter site 302].

TABLE V
Arc speed at contact opening

Test parameters	Material AgW	Material AgNi
100 A, $\cos(\varphi) = 0.9$	$1.4\,\mathrm{m/s}$	$2.1\,\mathrm{m/s}$
500 A, $\cos(\varphi) = 0.9$	$1.3\,\mathrm{m/s}$	$1.9\,\mathrm{m/s}$

Within the framework of the presented measurements, the speed of movement of the arc foot point for the AgW material — depending on the test current — is approximately 30% slower than for AgNi. The movement of the arc on the commutation rails shows slightly more scatter and is identical in all tests, as the same material was used.

The evaluation according to Formula 2 showed a similar tendency in the tests, as can be seen in **Table VI**.

TABLE VI
Contact switching work

Test parameters	Material AgW	Material AgNi
100 A, $\cos(\varphi) = 0.9$	4.3 Ws	3.3 Ws
500 A, $\cos(\varphi) = 0.9$	21 Ws	15 Ws

However, the energies differ significantly due to the test current. Nevertheless, the experiments and evaluations demonstrate the potential of the measurement system to assess the arc's mobility and thus determine the local energy input.

VI. Further work

Due to the current state of work, the initial focus of further activities is on verifying the magnetic field sensor signals. If necessary, several magnetic field sensor PCBs can be integrated into the test setup.

Especially at test currents above 100 A, the signal from the optical sensor is more strongly influenced by scattered light from the arc. To improve this, optical attenuation of the individual sensor signals is conceivable (e;g. using partially absorbing material) to reduce this influence.

In addition to the presented arrangement, the sensors are currently also being integrated into test setups close to the devices [6]. This enables the investigation of contact arrangements of various switching devices and offers the opportunity to develop quantitative differences when examining series contacts or material batches. Furthermore, an application of the presented measurement technology to series or pre-series switching devices is also conceivable. The optical fibers can be attached to arc chambers with manageable integration effort (e;g. drilling or integrated channels).

VII. Summary

The presented method demonstrates several possibilities for quantitatively recording the arc's behavior on contacts. This was shown using the example of AgW and AgNi contacts and compared with qualitative observations from relevant literature. Due to the different measurement methods, there are various characteristic values for the mobility of the arc root. On the one hand, the chosen arrangement shows an approximately 30% slower speed of the arc root for AgW. On the other hand, an approximately 20% lower energy input can be observed for AgNi contacts via the current flow in the contact.

Thus, the suitability of contact materials for product requirements can be verified. Furthermore, for existing switching devices, detailed contact material changes or constructive changes at the contact point can be investigated.

References

[1] W. Rieder. *Plasma und Lichtbogen*. 1967.

[2] C. Reil, H.-P. Schmidt, M. Anheuser, and F. Berger. Study of arcing processes in circuit breakers by means of spatially resolved magnetic field recordings. In *30th International Conference on Electrical Contacts*, Switzerland, June 2021.

[3] J. W. McBride and K. J. Cross. Studies of high current arcs using an optical fiber array based imaging system. In *1st International Conference on Electric Power Equipment*, China, 2011.

[4] E. Vinaricky et al. *Elektrische Kontakte, Werkstoffe und Anwendungen*. Springer, 3 edition, 2016.

[5] Armin Strahl. *Empirisches Verfahren zur rechnergestützten Ermittlung des Backup-Schutzes in Niederspannungsnetzen*. PhD thesis, Technische Universität Ilmenau, 2025.

[6] Armin Strahl, Lisa Malterer, Sebastian Vogl, and Michael Anheuser. Gerätenahe Kontaktmaterialprüfungen mithilfe von Modellschaltern. In *27. Albert-Keil-Kontaktseminar*.

The current transfer to a copper cathode in low-voltage, low-current arcs of short lengths

Margarita Baeva
Leibniz Institute for Plasma Science and Technology
Greifswald, Germany
baeva@inp-greifswald.de

Jonas K. C. Ballentin
Institute of Electrical Power Engineering
University of Rostock
Rostock, Germany
jonas.ballentin@uni-rostock.de

Dirk Uhrlandt
Leibniz Institute for Plasma Science and Technology
Institute of Electrical Power Engineering
Greifswald, Rostock, Germany
uhrlandt@inp-greifswald.de

***Abstract*—Metal vapours play a significant role in atmospheric pressure plasmas since they change their properties. A unified non-equilibrium model is used to study the conditions of current transfer to the cathode in low-voltage, low-current arcs of short lengths generated in air between electrodes made of copper. A mixture of air and copper metal vapour is considered and electrical measurements are used to match results from modelling and experiments. In particular, a maximum of the electric potential in the region close to the cathode has been predicted, which influences the ratio of the electron and ion current densities on the cathode. The results indicate that the ratio of the ion current density to the total current density on the cathode amounts to 0.41-0.76.**

Keywords—current transfer, copper electrode, modelling

I. INTRODUCTION

The presence of metal vapour originating from the electrodes in arc plasma has been studied in many works related to e.g., arc plasma welding [1] and low-voltage switching [2]. Metal vapours play a significant role in atmospheric pressure plasmas since they greatly change the plasma properties. Metal atoms are more easily excited and ionized, since their ionization potential is lower than that of the surrounding gas. The radiative properties and electrical conductivity are therefore influenced by the presence of metal atoms and ions.

A presence of a potential hump close to the cathode made of volatile materials has been related to a need for field reversal that preserves the current continuity. Modelling works have been done in [3] to consider the building of a double sheath on cathodes due to the ionization of cold metal atoms released from the cathode surface. Ions produced between the cathode surface and maximum of the electric potential are driven to the cathode, while those produced beyond the maximum go toward the plasma bulk. The collisionless space-charge sheath in [3] is solved numerically assuming vaporization as the dominant mechanism for release of atoms from the cathode, a very rapid ionization of those atoms by electron impact, a transfer of the energy of electrons emitted from the cathode to the plasma electrons as well as a Maxwellian distribution of the plasma electrons with the electrostatic potential obtained from the Poisson equation. The electron temperature is considered as an input parameter. An overview of relevant works to the problem is provided in [3] as well. Some of them assume that the ionization of atoms released from the cathode occurs in the quasi-neutral plasma bulk [4,5]. Others doubt this assumption based on estimates of characteristic lengths [6]. The occurrence of a double sheath in a model with account for electron emission from a hot cathode was considered in [7].

In recent works [8,9], we carried out experimental and modelling studies of direct current (DC) electric arcs of short lengths, which are generated between copper electrodes in atmospheric pressure air during the contact separation. The modelling studies employed a unified non-equilibrium model, which resolved the entire inter-electrode region without separation of the sheaths and the quasi-neutral bulk, coupled the plasma and the electrodes, accounted for the plasma chemistry, release of atoms and electron emission from the cathode, and the increase of the gap length during contact opening. Since an initial gap length had to be set in the model, a mixture of air and copper atoms was considered according to the current general understanding of a breaking molten metal bridge and mixing the metal vapour with the surrounding air [2]. A brief description of the model is given in below for the sake of completeness. The experimental studies involved electrical measurements, high-speed imaging and optical emission spectroscopy that allowed us to relate the voltage to the discharge geometry. A proper match of experimental and modelling results was achieved in parametric studies concerning the discharge radius, the factor accounting for the enhancement of the electric field at the cathode surface, and the mole fraction of copper atoms in the plasma.

This work is concerned with the analysis of the current transfer on the copper cathode. In particular, the ratio of the ion and electron current components is analysed in relation with the self-consistently obtained plasma parameters. The paper is organized as follows. A general description of the model is given in section II. Results and discussed are presented in section III. Concluding remarks are formulated in section IV.

II. THE COMPUTATIONAL MODEL

A. Governing equations

The unified non-equilibrium model employed in this study is based on a fluid description of the plasma containing electrons and heavy species of air and copper (neutral and singly charged molecules and atoms). The electrons are assumed to have a Maxwellian velocity distribution characterized by a temperature T_e, while the heavy particles are in equilibrium with each other at a common temperature T. The electron temperature relates to the mean electron energy $\bar{\epsilon} = n_\epsilon/n_e$ through the expression $T_e = 2\bar{\epsilon}/3k_B$ with n_ϵ, n_e and k_B representing respectively the density of electron energy, the electron number density, and the

Boltzmann constant. Time-dependent conservation equations for n_e and n_ϵ are solved in terms of the classical drift-diffusion approximation

$$\frac{\partial n_e}{\partial t} + \nabla \cdot \boldsymbol{\Gamma_e} = S_e \quad (1)$$

$$\frac{\partial n_\varepsilon}{\partial t} + \nabla \cdot \boldsymbol{\Gamma_\varepsilon} + e\boldsymbol{E} \cdot \boldsymbol{\Gamma_e} = S_\varepsilon - Q_h - Q_{rad} \quad (2)$$

In (1) and (2), the following notations are used for the elementary charge (e), the electron particle flux ($\boldsymbol{\Gamma_e}$), the electron energy flux ($\boldsymbol{\Gamma_\varepsilon}$), the electric field ($\boldsymbol{E}$), the source terms for electrons (S_e) and electron energy (S_ε), the change of energy due to elastic collisions (Q_h) and radiation (Q_{rad}).

The electric potential V is obtained from the Poisson equation and the electrostatic field $\boldsymbol{E}$ from its gradient

$$\Delta \mathrm{V} = -\frac{e}{\varepsilon_0}(n_+ - n_e), \quad \boldsymbol{E} = -\nabla V \quad (3)$$

with the total number density of positive ions (n_+) and the dielectric constant (ε_0).

The conservation of heavy species of kind *k* is governed by the general diffusion equation written for the mass fraction Y_k

$$\rho \frac{\partial Y_k}{\partial t} + \nabla \cdot \boldsymbol{J_k} = S_k \quad (4)$$

which includes the mass density of the gas (ρ) that follows from the ideal gas law using the gas temperature (electron pressure is neglected), the corresponding mass flux ($\boldsymbol{J_k}$), and the source terms (S_k).

The heat transfer in the plasma and the electrodes is solved to obtain the temperature in the gas mixture and the electrodes.

$$A_s \rho C_p \frac{\partial T}{\partial t} + \nabla \cdot \boldsymbol{q} = A_s Q_h + A_s Q_{iJ} \quad (5)$$

$$A_s \rho_s C_{ps} \frac{\partial T}{\partial t} + \nabla \cdot \boldsymbol{q}_s = 0 \quad (6)$$

The notations in (5) and (6) incorporate the cross-section area of the discharge (A_s), the heat capacity at constant pressure (C_p), the conductive heat flux multiplied by the cross-section area ($\boldsymbol{q}$), the Joule heating of the ions (Q_{iJ}), and ρ_s, C_{ps}, $\boldsymbol{q}_s$ representing the corresponding quantities in the electrodes.

The electric current density in the plasma is defined as

$$\boldsymbol{j} = -e(\boldsymbol{\Gamma_e} - \textstyle\sum_k \boldsymbol{\Gamma_{i,k}}) \quad (7)$$

The particle and the mass fluxes of the ion of kind *k* are related by the particle mass $m_{i,k}$, i.e., $\boldsymbol{\Gamma_{i,k}} = \boldsymbol{J_{i,k}}/m_{i,k}$.

An external electrical circuit (Fig. 1) is used to set the desired electric current *I*. The discharge voltage is obtained from the potential at the anode (V_A).

$$V_A = U_0 - R_b I \quad \text{with } I = \textstyle\int_{A_s} \boldsymbol{n} \cdot \boldsymbol{j} dS \quad (8)$$

The plasma-chemical model involves the 11 species reaction scheme by Dunn and Kang [10] for air (e, N_2, O_2, NO, N, O, N_2^+, O_2^+, NO^+, N^+, and O^+) and atoms and singly charged ions of copper (Cu, Cu^+). Cross-sections for electron impact processes with copper species are adapted from [11]. Note that negative ions are not included in the reaction scheme of air. At gas temperatures of several thousand Kelvin, electrons are detaching from the negative ion. In addition, multiply charged Cu ions are neglected here, since the second ionization potential of Cu amounts to 20.29 eV, i.e., it is exceeding by far the ionization potential of the

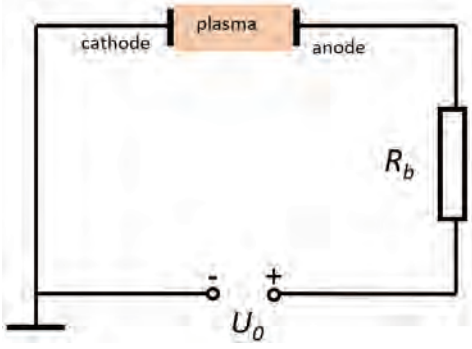


Fig. 1 Schematic representation of the discharge and the electrical circuit including a voltage source (U_0) and a ballast resistor (R_b).

gaseous background. The rate coefficients for electron impact ionization and 3-body recombination of the copper species are computed taking into account the large number of excited states of copper atoms employing the modified diffusion approach [12]. The latter considers the ionization and recombination as diffusion of bound electrons over the energy levels of the atom. The main concern here is the low ionization energy of the copper atoms in comparison to that of the air species.

The thermodynamic properties (e.g., enthalpy, heat capacity) of the species are implemented as functions of the gas temperature in the region from 300 K up to 20000 K [13]. The heat conductivity is computed from Stiel-Thodos correlation with the dynamic viscosity as the latter is calculated from the gas kinetic theory [14]. Note that the non-equilibrium model does not imply a definition of the electrical conductivity of the plasma. It follows self-consistently from the particle fluxes of electrons and ions building the total current density (see Eq. (7)). Data for the radiation losses [15] are considered in the energy balance of the electrons, since the excitation of atoms occurs mainly by electron impact. Material properties of the electrodes are used as reported in [16].

B. Boundary conditions

The boundary conditions to (1) and (2) are set on the electrodes in terms of fluxes.

$$\boldsymbol{n} \cdot \boldsymbol{\Gamma_e} = \tfrac{1}{4} n_e v_{th,e} - \gamma \textstyle\sum_k \boldsymbol{\Gamma_{i,k}} \cdot \boldsymbol{n} - \boldsymbol{\Gamma}_{TF} \cdot \boldsymbol{n} \quad (9)$$

$$\boldsymbol{n} \cdot \boldsymbol{\Gamma_\varepsilon} = \frac{1}{4} n_e v_{th,e} \cdot 2k_B T_e - \gamma \sum_i \epsilon_{s,i} \boldsymbol{\Gamma_{i,k}} \cdot \boldsymbol{n} - \epsilon_{TF} \Gamma_{TF} \cdot \boldsymbol{n} \quad (10)$$

The notations in (9) and (10) include the unit outward normal vector $\boldsymbol{n}$, the thermal velocity of electrons, $v_{th,e}$, the coefficient γ of secondary emission of electrons with energy, ϵ_s, for the ions of the air components, the particle flux of electrons released with energy ϵ_{TF} from the cathode due to thermo-field emission, $\boldsymbol{\Gamma}_{TF}$.

The electric potential is set to zero on the cathode and takes a value V_A that follows from (8).

For the heavy species, the flux boundary conditions are

$$\boldsymbol{n} \cdot \boldsymbol{\Gamma_k} = \tfrac{1}{4} n_k v_{th,k} + a\mu_k n_k \boldsymbol{E} \cdot \boldsymbol{n} \quad (11)$$

with number density n_k and the thermal velocity of heavy species of kind *k*, $v_{th,k}$, a parameter a with the value of one

if $\boldsymbol{E}\cdot\boldsymbol{n}>0$ and zero otherwise, and the ion mobilty μ_k expressed by the Einstein relation with the temperature T.

The boundary conditions to (5) and (6) that describe the heat transfer in the plasma region and the electrodes employ a temperature value of 300 K at the ends that are not in contact with the plasma and heat fluxes from the plasma to the cathode, q_c, and the anode, q_a that add up the heat conduction fluxes. These additional fluxes are written as [17]

$$q_c = \sum_k [j_{i,k}(E_{ion,k}-W) - j_{s,k}(E_{ion,k}-W)] - j_{TF}\left(W+\frac{1}{e}2k_BT_c\right)+\frac{1}{4}n_e v_{th,e}\cdot(2k_BT_e+eW) - \epsilon\sigma_{SB}{T_c}^4 - \mathcal{L}\Gamma_{vap}m_{Cu} \quad (12)$$

$$q_a = \sum_k j_{i,k}(E_{ion,k}-W)+\frac{1}{4}n_e v_{th,e}(2k_BT_e+eW) - \epsilon\sigma_{SB}T_a^4 - \mathcal{L}\Gamma_{vap}m_{Cu} \quad (13)$$

The terms $j_{i,k}$, $j_{s,k}$ and j_{TF} in (12) and (13) are related to the corresponding fluxes in (9), (10) and (11) and express the current densities of ions, secondary emitted electrons and electrons due to thermo-field emission, $E_{ion,k}$ is the ionization energy of the corresponding ion, W and ϵ are respectively the work function and the emissivity of the electrode material, $T_{c,a}$ is the temperature on the cathode (c) and the anode (a) end in contact with the plasma, and σ_{SB} is the Stefan-Boltzman constant. The last terms on the right hand side of (12) and (13) account for cooling due to evaporation of electrode material, $\mathcal{L}$ represents the latent heat of evaporation. Γ_{vap} is expressed by the Langmuir equation as a function of the surface temperature of the electrode and the equilibrium vapour pressure of the electrode material.

Lookup tables for the current density j_{TF} and the mean energy ϵ_{TF} as functions of the electric field strength and the temperature of the cathode surface are prepared prior to the simulation employing the Transferred Matrix Method [18].

C. Model setting

The computational model is one-dimensional and therefore estimates of the radial extent of the discharge are needed for realistic values of the electric current density. These estimates are obtained from high-speed imaging in the experiments. The radial extent of the discharge is modified during the contact separation.

Solution of the model equations along with the boundary conditions is sought on the computational platform COMSOL Multiphysics®, V6.4, with customized features needed to implement terms and boundary conditions required in the model. A time-dependent direct solver (MUMPS). A fully coupled approach based on the Newton method forms a single system of equations for all variables within a single iteration. The initial time step is 10^{-13} s and automated increase of the time step is enabled. The computational grid in the gap typically has 3000-6000 mesh elements as their size is exponentially decreasing toward the electrodes. The increase of the gap length during the contact opening is represented by the deformed mesh method. The discretization of the electrodes uses 200 mesh elements as their size linearly increases toward their ends that are not in contact with the plasma.

III. RESULTS AND DISCUSSION

The simulations are performed likely the experiments [8, 9]. The discharge is burning at DC of 2 A for 11 ms in a gap of 30 μm length before the contacts are separated within 51 ms and the gap length is increased up to 3 mm as it can be seen Fig. 2, where a series of gap lengths and moving times are shown along the measured and computed arc volage. It is worth noting that the simulation results are obtained in parametric studies with respect to the key parameters, i.e., the radial extent of the discharge, the value of the field enhancement factor, and the concentration of Cu metal vapour in the air/Cu mixture (results in more detail are presented in [9]). The results presented here correspond to the values of these parameters for which computed and measured arc voltages match.

As reported in [9], based on experimental data a temporal development of the discharge radius was adopted to account for the increase of the discharge radius with the increase of the gap length. This means that a cylindrical shape of the discharge is assumed preserved in the framework of the 1D model while the radius increases during the contact opening. The expansion in the middle of the discharge gap cannot be covered by the 1D model.

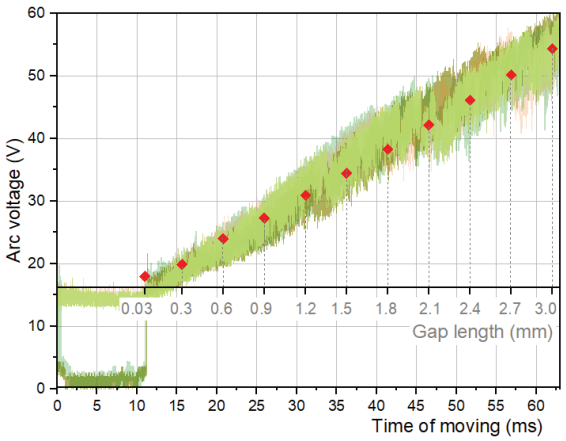


Fig. 2. Measured (lines) and computed (symbols) arc voltage during contact opening.

The simulation results are quite sensitive with respect to the field enhancement factor, which is another model parameter that can be adjusted in comparisons with the measured voltage. This factor multiplies the electric field obtained from the Poisson equation (3) in order to account for a surface roughness and/or a presence of protrusions that cannot be otherwise captured in the 1D model. The match of the arc voltage in Fig. 2 is achieved with a value of 140. It has been shown in [9] that the factor strongly influences the conditions on the cathode and in the space-charge region and in turn the cathode fall and the arc voltage. Higher factor values lead to a substantial decrease of the arc voltage.

The concentration of Cu metal vapour is hugely important to the plasma parameters and the computed arc voltage. The parametric study in [9] indicated that even a mole fraction of 0.002 is enough to see the Cu^+ ion being the dominant ion in the Air/Cu plasma. Higher concentrations of copper metal vapour significantly lower the arc voltage.

Fig. 3 shows the distribution of the electric potential in the discharge gap for the series of gap lengths corresponding to those in Fig. 2. The predicted spatial distribution of the electric potential indicates a large potential drop in the vicinity of the cathode and the occurrence of multiple reversals of the electric field, while a smaller voltage drop occurs in the vicinity of the anode. A well extended increase of the electric potential from the middle of the gap distance toward the anode is obtained

for all selected gap lengths except the initial one (30 μm). This increase relates to the increase of the electron and gas temperatures in the bulk plasma as reported in [9]. The formation of the potential hump in the vicinity of the anode reduces the electron flux to the anode and ensures the current continuity similarly to arcs at higher currents. However, the interest in this work is focused on the potential hump near the cathode, which affects the current transfer on the cathode.

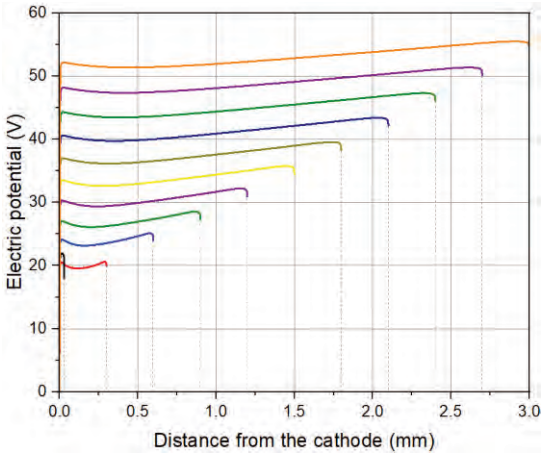


Fig. 3 Distribution of the electric potential in the discharge gap for gap lengths corresponding to the values in Fig. 2.

The current density on the cathode surface (j) is computed as the sum the current densities of electrons (j_e) and ions (j_{ion}), i.e., $j = j_e + j_{ion}$. The electron current density sums up the current densities due to thermo-field emission of electrons (j_{TF}), secondary electron emission caused by ion impact (j_{se}) and back diffusion of electrons to the cathode (j_{bd}), i.e., $j_e = j_{TF} + j_{se} - j_{bd}$. The ion current density to the cathode represents the sum of the corresponding terms in (12) assigned to the species of kind k. Components of the current density, the total value, and the ratio of the ion current density and the total current density are listed in Table I for the series of gap lengths considered in Figs. 2 and 3.

The results obtained show that $j_{TF} > j_e$. This is due to the opposite sign electron current density j_{bd}. The total current density j decreases with the increase of the gap length due to the constant current of 2 A and the increase of the discharge radius during the contact separation. The ratio of the ion and the total current density increases from 0.41 up to 0.76 indicating values that are well above the values in gases without metal vapour. Note that a value exceeding 0.5 has been reported in [3] for arcs burning in metal vapour in agreement with data extracted from experiment. The plasma in the air/Cu mixture in the present study is dominated by the Cu^+ ion although the concentration of metal vapour is low. This behaviour confirms the reports related to welding arcs [1] showing that even a small amount of metal vapour strongly affects the plasma properties since the ionization potential of the metal vapour is significantly lower than that of the background gas. In what follows, the peculiarity of the current transfer on the cathode, i.e., the large value and the increase of the ratio j_{ion}/j, is analysed. The ion current depends on the production of ions, the plasma parameters that influence this production and the ion mobility, and the voltage drop in the space-charge sheath of the cathode U_c.

TABLE I. CURRENT DENSITY ON THE CATHODE

Gap length (mm)	Components of current density (10^6 A/m^2)				Ratio j_{ion}/j
	j_{TF}	j_e	j_{ion}	j	
0.03	4.69	4.58	3.26	7.84	0.41
0.3	1.23	1.17	1.91	3.08	0.62
0.6	0.86	0.81	1.58	2.39	0.66
0.9	0.68	0.64	1.38	2.02	0.68
1.2	0.56	0.53	1.25	1.78	0.70
1.5	0.49	0.46	1.17	1.63	0.72
1.8	0.43	0.41	1.09	1.50	0.73
2.1	0.38	0.36	1.02	1.38	0.74
2.4	0.34	0.33	0.97	1.30	0.75
2.7	0.31	0.30	0.92	1.22	0.75
3.0	0.29	0.27	0.88	1.15	0.76

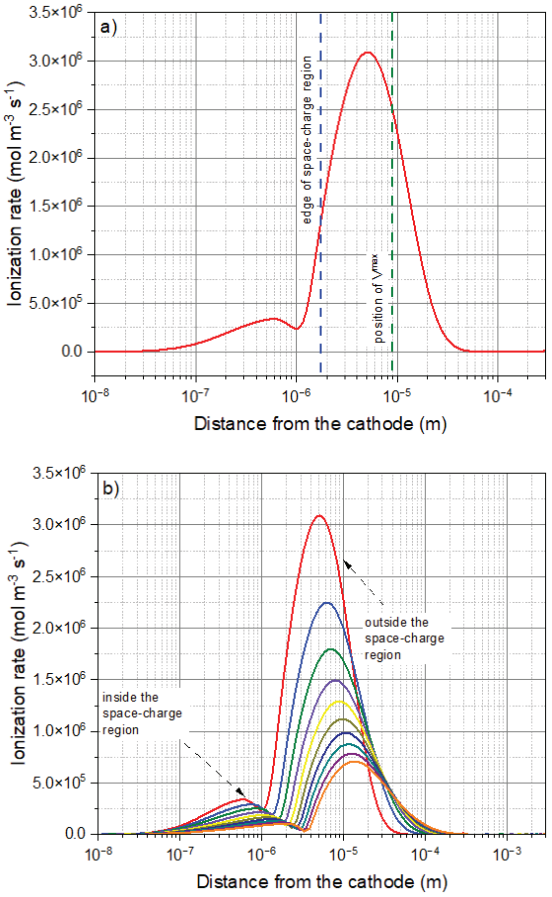


Fig. 4 Spatial distribution of the ionization rate in the discharge gap for a gap length of 0.3 mm (a) and series of gap lengths corresponding to values in Fig. 2.

The spatial distribution of the ionization rate in the discharge gap is shown in Fig. 4a for the gap length of 0.3 mm and for a number of arc lengths during the contact opening in Fig. 4b. In Fig. 4a, the position of the edge between the space-charge region and the quasineutral plasma is shown. In addition, the position of the maximum electric potential in the vicinity of the cathode (see also Fig. 3) is indicated. Fig. 5 shows the spatial distributions of the electron temperature T_e and the electric potential V obtained respectively from (2) and (3) for the gap length of 0.3 mm in order to underline the influence of the plasma parameters. The results in Fig. 4 show

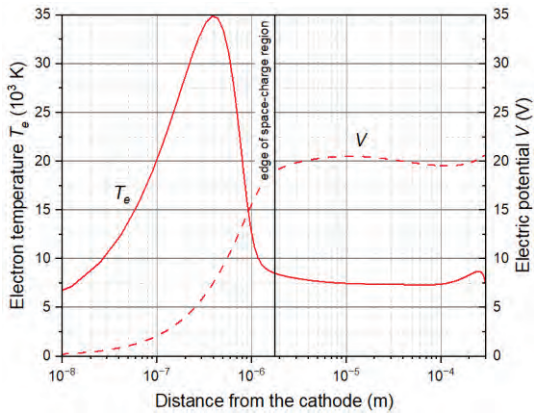


Fig. 5 Spatial distribution of the electron temperature and the electric potential in the discharge gap for a gap length of 0.3 mm.

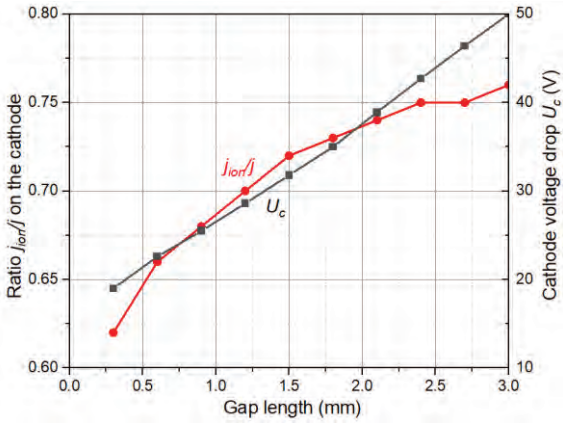


Fig. 6 The ratio j_{ion}/j and the cathode voltage drop U_c for a series of gap lengths.

that the ionization rate has two maxima. One of them is reached within the region of space-charge, while the second one is reached in the quasineutral part of the discharge though before the maximum of the electric potential is reached. Unified non-equilibrium modelling of DC arcs in argon (see e.g., [19]) predicted a single maximum of the ionization rate in the vicinity of the cathode. The electron temperature has a strong peak in the cathode space-charge region. It decreases due to the loss of electron energy due to the ionization process. Note that the first peak in the ionization rate occurs while the electron temperature is still increasing (distances up to $\sim 4 \times 10^{-7}$ m in Fig. 5). The ions produced in the region before the potential maximum is reached move toward the cathode. In contrast, the ions produced beyond the potential maximum move toward the quasineutral plasma. This behaviour is caused by the reversal of the electric field. This means that due to the potential hump in the vicinity of the cathode a part of the ion flux enters the bulk plasma. Note that the ratio of the two peak values of the ionization rate inside and outside the cathode space-charge region (Fig. 4b) and the positions of the maxima change with the increase of the gap length. This results from the decrease of the electric current density with increase of the discharge radius at constant current due to the contact opening. As a results, the spatial extent of the cathode space-charge region increases.

Fig. 6 shows for gap lengths from 0.3 mm up to 3 mm the values of the ratio j_{ion}/j on the cathode along with the voltage drop in the cathode space-charge region U_c. The latter is evaluated from the value of the electric potential V on the edge to the quasineutral plasma bulk (the cathode is grounded). It causes the acceleration of the ions in the region of space-charge of the cathode. The results show that the U_c increases with the increase of the discharge gap almost linearly. A similar behaviour is obtained for the mobility of the ion Cu^+, which is not shown in order to not overload the graph. The increase of the ratio j_{ion}/j on the cathode with the increase of the gap length can be attributed to the relative increase of the ion current with respect to the total current caused by the increase of the ion mobility and drift velocity that overrules the decrease of the ionization rate and in turn the ion number density in the space-region adjacent to the cathode, where ionization occurs as well.

IV. Concluding Remarks

In this work, analysis of the current transfer on the copper cathode is presented for a switching arc arrangement operated at DC of 2A at atmospheric pressure in a mixture air/Cu. The analysis is based on a unified non-equilibrium model that provides in a self-consistent manner the spatial distribution of the plasma properties needed for this analysis accounts for the increase of the gap length during the contact opening.

The main results can be summarized as follows. The presence of metal vapour in the plasma even in the considered mole fraction of 0.002 leads to the dominance of the singly charged copper ion. Ionization process occurs both in the space-charge region of the cathode and beyond the edge to the quasineutral plasma bulk. The ionization in the space-charge region occurs while the electron temperature is still increasing due to the low ionization potential of the copper atoms. The computed spatial distribution of the electric potential indicates a maximum in the vicinity of the cathode, which causes an ion flux toward the plasma bulk. The predicted ratio of the ion to total current density amounts to 0.41-0.76 as a result of the interplay of increasing cathode voltage drop and in turn increasing ion mobility and drift velocity that overrules the decrease of the ion number density.

With respect to the application of the model at higher current levels, the following remarks should be given. The unified non-equilibrium approach, which spatially resolves the regions of space charge as well as the quasineutral plasma bulk becomes computationally intense for high values of the current density. At such conditions, the gradients of the electrostatic potential, temperatures and number densities of the species are very steep so that extremely fine spatial and temporal resolution is required in order to ensure numerical stability and accuracy. While the use of the model is challenging but still doable in 1D, its application in multidimensional models becomes impractical.

Acknowledgment

The work is funded by the German Research Foundation (DFG) project number 524731006.

REFERENCES

[1] A. B. Murphy, "The effect of metal vapour in arc welding," J. Phys. D: Appl. Phys., vol. 43, pp. 434001, 2010, DOI:10.1088/0022-3727/43/43/434001

[2] P. G. Slade, Electrical contacts, CRC Press, Boca Raton, 1999.

[3] M. S. Benilov and L. G. Benilova, "The double sheath on cathodes of discharges burning in cathode vapour," J. Phys. D: Appl. Phys., vol. 43, pp. 345204, 2010, DOI:10.1088/0022-3727/43/34/345204

[4] I. Beilis, "Theoretical modeling of cathode spot phenomena," in Handbook of Vacuum Arc Science and Technology: Fundamentals and Applications, R. L. Boxman, D. M. Sanders and P. J. Martin, Eds. Park Ridge: Noyes Publications, 1995, pp. 208–256.

[5] K.-U. Riemann, "Theory of the cathode sheath in a vacuum arc," IEEE Trans. Plasma Sci., vol. 17, pp. 641–643, 1989, DOI:10.1109/27.41172

[6] M. S. Benilov, "Space-charge sheath with ions accelerated into the plasma," J. Phys. D: Appl. Phys., vol. 43, pp. 175203, 2010, DOI:10.1088/0022-3727/43/17/175203

[7] P. D. Prewett and J. E. Allen, "The double sheath associated with a hot cathode," Proc. R. Soc. Lond. A, vol. 348, pp. 435–446, 1976, http://doi.org/10.1098/rspa.1976.0048

[8] J. K. C. Ballentin, M. Baeva and D. Uhrlandt, "Experimental studies of microarcs between copper electrodes in atmospheric pressure air," Plasma Phys. Technol., vol. 12, pp. 95–98, 2025, DOI: 10.14311/ppt.2025.2.95

[9] M. Baeva, J. K. C. Ballentin and D. Uhrlandt, "Modelling studies of arcs of short lengths between copper," Plasma Phys. Technol., vol. 12, pp. 40–45, 2025, DOI: 10.14311/ppt.2025.1.40

[10] P. A. Gnoffo, R. N. Gupta and J. L. Shinn, "Conservation equations and physical models for hypersonic air flow in thermal and chemical nonequilibrium," Technical Paper **2867**, 1989 NASA:Washington DC

[11] A. Bogaerts, R. Gijbels and R. J. Carman, "Collisional-radiative model for the sputtered copper atoms and ions in a direct current argon glow discharge," Spectrochimica Acta Part B: Atomic Spectroscopy, vol. 53, 1679–1703, 1998, https://doi.org/10.1016/S0584-8547(98)00201-8

[12] L. M. Biberman, V. S. Vorob'ev and I.T. Yakubov, "Kinetics of impact-radiation ionization and recombination," Soviet Physics Uspekhi, vol. 15, pp. 375–394, 1973, DOI: 10.1070/PU1973v015n04ABEH004987

[13] M. J. Zehe, S. Gordon and B. J. McBride NASA/TP-2001-210959, 2001, Glenn Research Center, Cleveland, OH USA.

[14] R. R. Bird, W. E. Steward, E. N. Lightfoot, Transport phenomena, Wiley, Hoboken, 2002.

[15] A. Gleizes, Y. Cressault and P. Teulet, "Mixing rules for thermal plasma properties in mixtures of argon, air and metallic vapours." Plasma Sources Sci Technol, vol. 19, pp. 055013, 2010, DOI:10.1088/0963-0252/19/5/055013

[16] M. Baeva, V. F. Boretskij, D. Gonzalez, R. Methling, O. Murmantsev, D. Uhrlandt, A. Veklich, "Unified modelling of low-current short-length arcs between copper electrodes", J. Phys. D: Appl. Phys., vol. 4, pp. 025203, 2021, DOI:10.1088/1361-6463/abba5d

[17] M. Baeva and D. Uhrlandt, "Characterization and applications of direct current microarcs: a review", J. Phys. D: Appl. Phys., vol. 58, pp. 263001, 2025, DOI:10.1088/1361-6463/ade44d

[18] M. Baeva, "Application of the transfer matrix method to a unified evaluation of the cathodic electron emission," AIP Advances, vol. 8 pp. 0853222018, https://doi.org/10.1063/1.5041314

[19] M. Baeva, D. Loffhagen and D. Uhrlandt, "Unified non-equilibrium modelling of tungsten-inert gas microarcs in atmospheric pressure argon", Plasma Chem. Plasma Process., vol. 39, pp. 1359–1378, 2019, https://doi.org/10.1007/s11090-019-10020-x

Pathways to Sustainability in Connector Development: Influence of material and design changes

Dr. Isabell Buresch
Fellow
TE Connectivity
Wört, Germany
isabell.buresch@te.com

Jan van Cauwenberge
Design for Sustainability Lead
TE Connectivity
Oostkamp, Belgium
jan.van-cauwenberge@te.com

Johannes Weis
Sustainability Specialist
TE Connectivity
Bensheim, Germany
johannes.weis@te.com

Chiara Mondino
Sustainability Management
TE Connectivity
Bensheim, Germany
chiara.mondino@te.com

Dorothea Wilhelm
Master´s student
TE Connectivity
Bensheim, Germany
dorothea.wilhelm@te.com

Sustainability is increasingly influencing connector development alongside electrical performance, mechanical reliability and cost requirements. This paper examines how regulatory frameworks, international standards and engineering design choices jointly shape sustainable connector solutions. Key European regulations and relevant standards are mapped to practical design levers such as material selection, miniaturization, surface finish optimization, energy-efficient manufacturing, re-use of components and tools and product carbon footprint metrics. Furthermore, the sustainability drivers will be translated into concrete design requirements and levers relevant to the engineering of electromechanical connectors, with the aim of reducing the product's environmental impact.

Keywords – connectors, circularity, miniaturization, copper alloys, precious metals, product carbon footprint, recycling, durable coatings, end of life, resins, charging inlet, wear resistant, DPP, ROHS

I. Introduction

Connectors are key enablers of electrical and electronic systems and are produced in very high volumes across all industries. Despite their small size, the five most impacting factors that determine the sustainability profile of connectors are: (1) Material Selection & composition, (2) Size and Dimensions, (3) Manufacturing Decarbonization and Process Efficiency, (4) Design for Circularity, which are influenced, among other aspects, by regulatory compliance obligations. As a result, sustainability has become a central design driver in connector development, motivating approaches that reduce environmental impact, improve regulatory and functional robustness and strengthen long-term economic resilience.

II. Sustainability Drivers in Connector Development

Sustainability in product development increasingly extends beyond the reduction of isolated environmental impacts and requires a life cycle-oriented perspective on materials, performance and product longevity. In this context, sustainability objectives translate into concrete design requirements such as material efficiency, durability, information transparency and compatibility with regulatory and market expectations [1] [2]. To structure these requirements consistently across the product lifecycle, current sustainability frameworks adopt the concept of circularity [3]. At its core, the circular economy represents an economic system in which the traditional concept of product end of life is replaced by strategies aimed at reducing, reusing and recovering materials. These principles are applied across the entire value chain, encompassing manufacturing, distribution and consumption processes. The objective is to enable development that aligns the three dimensions of sustainability – economic prosperity, environmental quality and social equity – by decoupling value creation from resource depletion and waste generation [4]. These principles translate into concrete constraints for product development and thus provide the basis for the environmental, regulatory and market driven sustainability drivers shaping connector development, as discussed in the following chapter.

A. Environmental Resource-Related Drivers

Environmental drivers arise primarily from increasing resource scarcity, rising material costs and growing volumes of electronic waste. Connector production relies heavily on resource-intensive materials such as copper, precious metals and engineered polymers, whose extraction and processing contribute significantly to global environmental impacts. The availability and extraction of virgin copper will be increasingly constrained, while demand continues to rise; in contrast, high-quality recycled copper offers a substantially lower environmental footprint and reduces dependency on volatile primary resource markets [5]. In the broader electronics sector, circularity strategies – such as increasing recycled content, improving material recovery and reducing waste streams – are becoming essential to maintain economic resilience while lowering environmental burdens.

B. Regulatory Drivers

Regulatory frameworks in the European Union (EU) increasingly require connector manufacturers to demonstrate sustainability, transparency, and material efficiency across the product lifecycle. The Ecodesign for Sustainable Products Regulation (ESPR) introduces product requirements related to durability, reparability, recyclability

and recycled content, while the Digital Product Passport (DPP) mandates detailed, machine-readable information on material composition, environmental impacts and compliance to enable traceability and circularity in sectors including electronics as currently envisaged under draft implementing measures [6]. These measures sit within the broader framework of the current Circular Economy Action Plan (CEAP), which structures the EU's shift toward circular product design; however, the CEAP is being prepared for revision and will be further developed through the upcoming Circular Economy Act, expected in 2026.

In parallel, sector-specific regulations such as the End-of-Life Vehicles (ELV) Directive – which is currently in revision and will be updated with more ambitious targets – impose material restrictions (e.g. on lead containing metals) and require product designs that facilitate removal, reuse and high-quality recycling of components and materials at end-of-life [7]. Complementary frameworks such as Registration, Evaluation, Authorization and Restriction of Chemicals (REACH), Restriction of Hazardous Substances Directive (RoHS) and Corporate Sustainability Reporting Directive (CSRD) impose substance restrictions, documentation requirements and sustainability reporting obligations that directly influence material selection and engineering decisions. REACH regulates the use of substances of very high concern (SVHC), including toxic heavy metals such as lead, which are relevant for connector materials and finishes. RoHS restricts hazardous substances in electrical and electronic equipment, requiring manufacturers to avoid or minimize materials like lead, mercury or cadmium in connector components to ensure market access [8]. The CSRD expands non financial reporting obligations and obliges companies to disclose environmental impacts at product and material level, including carbon footprints, resource use and circularity related indicators [9]. Together, these regulations increase the need for transparent material data, traceable supply chains and lifecycle-oriented product design – requirements that strongly align with the circularity and sustainability considerations outlined in this paper.

Beyond regulatory requirements, international standards provide practical guidance for implementing these obligations in industry. The ISO 59000 family defines core circular economy principles and offers structured guidance for integrating circularity into product design, value chains and performance measurement [10]. In parallel, the European standards family EN 4555x focuses on material efficiency for energy related products, covering topics such as reparability, recyclability, recycled content and information provision. Together, these standards offer practical tools and consistent methodologies that enable manufacturers to meet regulatory obligations under ESPR, DPP and related EU legislation while ensuring comparability, traceability and technical robustness in sustainability reporting and product development [11].

C. Customer and Market Drivers

Customer and market expectations increasingly reinforce the regulatory push toward sustainable connector solutions. Car Makers and system integrators already request detailed information on recycled content, carbon footprint and compliance with circular-economy principles as part of their supplier evaluations. This growing level of expectation increasingly positions sustainability as a decisive criterion within supplier selection and design-related decision-making processes. Consequently, market demand is shifting toward components with lower environmental impact, greater transparency and improved circularity performance. As a result, connector manufacturers must demonstrate the ability to meet both regulatory requirements and customer sustainability criteria, making sustainability a competitive differentiator across global supply chains alongside cost and fulfilling the technical requirements [12].

III. Engineering Design Levers and their Impact

Within sustainability-oriented product development, four complementary approaches are commonly distinguished: 1. the increase in material efficiency demand, low carbon material usage and the use of high recycled content have the largest and most immediate sustainability impact, 2. the decarbonization of manufacturing processes, 3. the extension of product and component use through successive cycles and durable long-lasting materials and designs, and 4. the recovery of materials at the end of use. Together, these approaches aim to limit resource consumption and environmental impacts while maintaining economic value creation. Circular-economy principles provide a structured framework to organize these strategies coherently across the product lifecycle [4].

In the context of connectors, the largest and most immediate sustainability impact is typically achieved through the reduction of resource demand. This includes the selection of materials with lower product-related carbon footprint, reduced use of critical or precious materials, and the optimization of material efficiency per functional unit. In addition, engineering decisions influencing manufacturing efficiency – such as energy-efficient processes, reduced scrap rates, simplified process chains and the use of low-carbon energy sources – directly affect embedded emissions and resource consumption. Strategies addressing extended use phases and end-of-use recovery represent important components of sustainable connector development, but their realization typically involves higher system complexity and coordination across the value chain.

For this reason, the following section concentrates mostly on resource-efficiency-oriented engineering levers, which can be evaluated more directly at the component design level, before considering further sustainability strategies.

For the integration of sustainability into engineering practices we implemented a "House of Sustainability" (Fig. 1), it serves as our internal framework for systematically integrating sustainability principles into engineering workflows. The House of Sustainability is built up so that each box gives different technical solutions and a clear explanation of what, why and how this helps improving sustainability performance and by this environmental impact reduction of our products, verified with the material and process experts. It provides designers with structured guidance, reference metrics and best practice levers – ranging from material selection to circularity-oriented design

choices – to ensure that environmental considerations are embedded into every stage of product development. As a practical toolbox, it supports consistent decision making and helps translate high level sustainability goals into actionable engineering requirements.

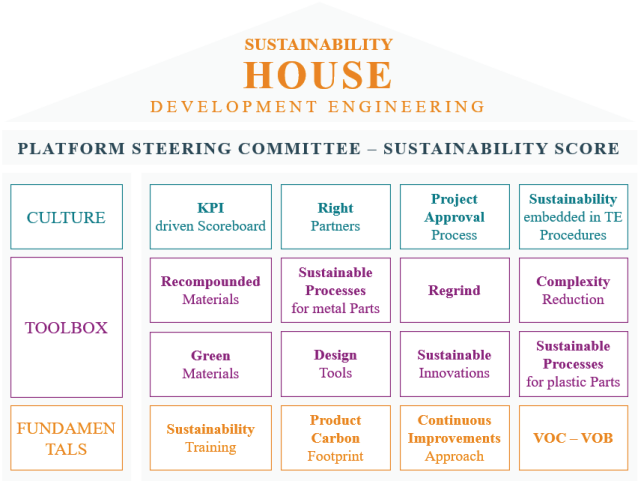


Fig. 1. The House of Sustainability - toolbox for engineers

A. *Material Selection and Composition*

The selection of materials is a key factor in determining sustainability performance, since the environmental impact of purchased materials accounts for a significant proportion of a products life cycle footprint and for the carbon emissions of a company – the emissions from scope 3 for purchased goods and services account for 79 % of the total emissions in Fiscal Year 2024. For metals the biggest lever to reduce scope 3 emissions is the increase in recycled content (Fig. 2). For resins, a transition to an optimized material is often more effective (e.g. Nylon to Poybutylenterephthalat (PBT)). Research and advisory insights stress supplier engagement, industry collaboration, investing in recycling plants and recycling concepts and ecosystem activation (shared tools, standards, co-investment) to reveal data, set targets, and abate material emissions. Procurement becomes a key lever for decarbonization by embedding carbon criteria into sourcing, while engineering must justify and critically evaluate design decisions.

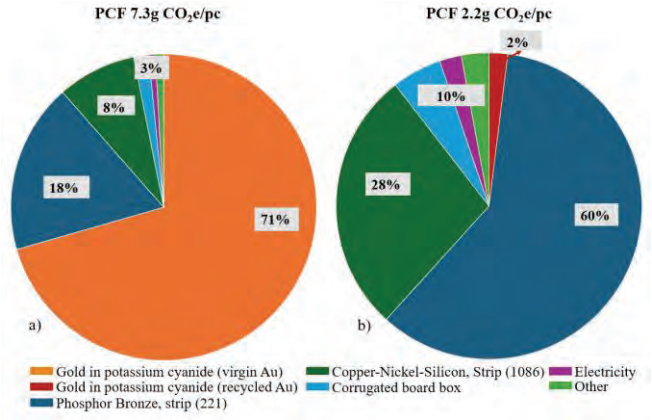


Fig. 2. Impact on product carbon footprint (PCF) by increasing recycled content of materials used: comparison between gold (Au)-coating plated with 100 % virgin Au (a) and Au-coating plated with ~ 90 % recycled Au (b) (same plating area and thickness, same terminal)

To increase the availability of recycled gold, sustainability and Circularity Design principles are crucial. To optimize the recyclability of precious metals out of connectors, modern recycling plants and processes can separate small cutted pieces plated with gold or silver if overlapping / run-out zones can be avoided during plating. This helps to increase the recycled Au content out of electronic scrap.

B. *Miniaturization*

Miniaturization is the reduction in size, weight, and volume of products, components, or systems while maintaining their functionality, performance, and reliability. It is a common design principle across industries such as electronics, medical devices, automotive, aerospace, and consumer products. Miniaturization can lead to increased complexity in manufacturing and require advanced materials that enable the technical requirements of a product. Miniaturization results in several positive effects across the product life cycle and application – from raw material extraction to production, distribution, use, and disposal – such as reduced material and energy consumption, reduced production and shipping costs, reduced waste and packaging, reduced weight and installation space, among others. With this miniaturization supports circularity and resource efficiency over life time.

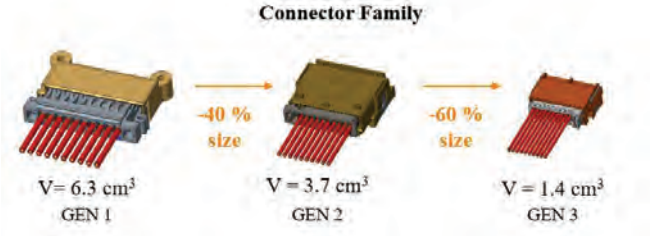


Fig. 3. Reduce material usage and foster miniaturisation without downgrade and material change within a miniaturised connector family over 3 generations.

Our product portfolio is supporting the trend for miniaturization by the introduction new generations within a terminal family to replace the first generation, since years. This goes in line with a size reduction of 40 % (Fig. 3). The step of miniaturization from second to third generation is resulting in an additional size reduction of 60 %. The effect on printed circuit board (PCB) footprint reduction for a 10 pin-count connector is up to 49 % going the first step from GEN 1 to GEN 2 and additional ~78 % for the second step to Gen 3 This results in a PCF reduction of approximately 55 % for the GEN 2 and additional ~35 % for the GEN 3 overall. The downscaling is limited to for example the wire diameter, which can be used in certain applications. Furthermore, miniaturized parts from a certain size downwards are more complex during handling and automatization.

C. *Manufacturing decarbonization and Process Efficiency*

Increasing manufacturing and process efficiency begins with optimal product design and improved material-use efficiency, reducing the amount of material needed to meet functional requirements and production needs.

Injection molding process optimizations which reduce resources and waste are for example direct gating and

regrind. Direct gating eliminates resin waste and sprues – the plastic material that connects the molding screw to the product – by designing the molding tool in such a way that the nozzle of the molding machine is touching directly the product. Sometimes, direct gating is not feasible, and sprues are often generated. In such cases, we typically reintroduce sprues into the molding cycle under closed-loop conditions after mechanically grinding them, so-called regrind. The UL-standard supports a 25 % regrind over closed loop without technical influence. In several cases, depending on the required performance and application, higher regrind-% can be feasible, secured by the needed life-cycle testing. For very small parts, the sprue-to-part ratio can be excessive, making complete reuse in the same product impractical. Our sprues are generally diverted from landfill through internal reuse or recycling pathways. One of such solution involves using 100 % of the sprue waste to manufacture a new product, as illustrated in (Fig. 4). This example shows a protection cover created out of 100 % recycled polybutylene terephthalate with 10 % glass fiber content (PBT-GF10), for a high voltage (HV) application. This process has to be treated appropriately, by not mixing other material types into the same source, also dedusting and drying are an important step to secure a stable molding process afterwards.

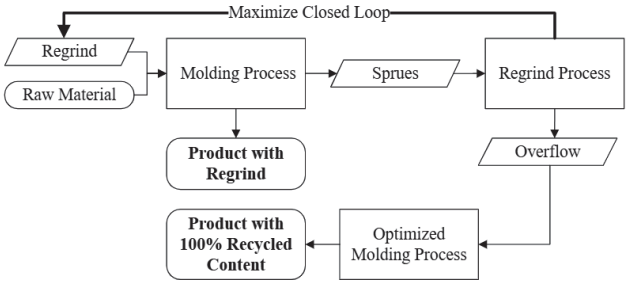


Fig. 4. Protection cover made of 100 % regrind waste of PBT-GF10 in this example

Process efficiency can also be increased by the optimization of plating processes or by switching from conventional galvanic plating to innovative selective plating processes. The newly developed E-Beam plating technology depositing an AgCu-coating [13] highly selective shows beside the technical advantage of a high ambient temperature stability and good friction behavior, also significant benefits on PCF reduction (Fig. 5). This sustainable surface technology – an AgCu-alloy – will be applied by physical dry deposition and based on that, doesn't need any water, excess chemicals and additional processes like wastewater treatment. As a high selective plating the energy consumption is reduced by around 35 % [14] and the usage of coating material is coming close to the minimum needed – the functionality by the coating, is given only where it is needed

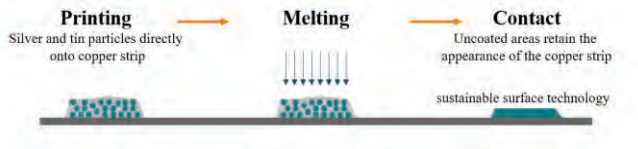


Fig. 5. Principle process steps of a sustainable surface technology

D. Design for Circulartiy

Design for Circularity (DfC) is a central enabler of the transition from linear to circular product systems. By designing products such that components and materials can return to the economy, DfC directly supports resource conservation and waste reduction. Since up to 80 % of a product's environmental impacts are determined during the design phase [15], design represents the most influential stage for reducing emissions, material consumption, and end-of-life losses. Achieving circularity therefore requires rethinking product and system architectures to ensure that circular economy principles are embedded throughout the entire lifecycle. However, this transition is still ongoing and demands stronger engagement from designers and design practitioners.

In the context of the Circular Economy Action Plan (CEAP), DfC encompasses design strategies such as material efficiency, increased recycled content, durability, reparability, reusability, upgradability, and end-of-life recoverability [1].

A key component within these strategies is Design for Disassembly (DfD), which focuses on enabling components to be separated, removed and recovered efficiently at end of life. DfD supports circularity by facilitating material sorting, reducing cross-contamination, enabling high-quality recycling streams and improving the feasibility of repairing or upgrading products [16]. The design of screwed connections for interconnecting battery cell modules especially when connecting different materials like Copper and Aluminum for use instead of welded connections show a big advantage in performance and usage [17]. Together, DfC and DfD shift product design from purely functional performance toward creating products that enable circular material flows, lower reliance on virgin resources, and align with emerging regulatory expectations under the CEAP.

Design for Longevity (DfL) further strengthens circularity by extending the useful lifetime of products and components, thereby reducing the frequency of replacement and the demand for new material cycles [17]: one example for DfL is an Ag-Graphit coating co-depositing Ag and Graphit, developed for the pin contacts at the charger inlet connectors with required 10.000 mating cycles plus. This coating can withstand up to 75.000 mating cycles [19] (Fig. 6). A better wear behavior allows a thinner coating thickness and reduces the precious metal usage. The use of the standard surface silver in this application will lead to a fast wear through even with coating thicknesses up to 40 µm, in line with a significant increase in resistance. Therefore, charger inlet pins or complete charger inlet connectors need to be changed, often several times, during the lifetime of an electrical vehicle to ensure a short and reliable charging time. The good performance of this Ag-Graphit coating significantly reduces the likelihood that the contacts or the inlet need to be exchandes under typical use conditions. An additional environmental effect is based on the fact, that the low and stable contact resistance of the connection with Ag-Graphit plated parts will not turn much electrical energy into heat during charging and therefore waste the energy. The

efficiency factor of is up to 30 % better than the one of a classical silver surface leading to shorter charging times.

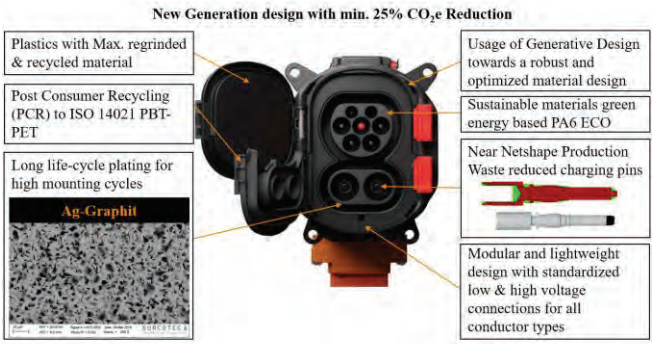


Fig. 6. New generation of a charging inlet with embedded sustainable features like cold forged lead-free pins plated with the high durable Ag-Graphit coating reducing precious metal content and PCR related plastic material usage

Beside the coating optimization, the pin production for this charging inlet was changed from machining to a near-net shape production method with a significant scrap reduction and materials efficiency increase to up to 40 %. Nearly all different materials and parts can be dismantled and separated.

Beyond coating optimization and near-net-shape manufacturing, material substitution represents another powerful lever within Design for Circularity. In this context, the transition from lead-containing to lead-free copper (Cu) alloys provide a particularly relevant example. Such substitutions reduce the presence of hazardous substances in recycling streams, improve material recovery quality and support regulatory compliance under RoHS and REACH. The following example illustrates how a lead-free copper connector design can further enhance circularity performance.

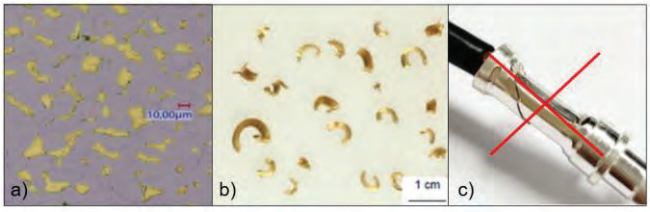


Fig. 7. Lead free copper alloys, not always new but challenging for manufacturing: CuZn40 with (a) homogeneous distribution of the ß-phase allowing good machinability forming short chips (b); cracking during crimping (c) can be eliminated with appropriate production steps.

Lead-free brass alloy with approx. 40 % Zinc (Zn) complies with the EN CW509L standard alloy with limited lead content < 0.1 % (RoHS conformity) is a traditional Cu-alloy. It might be a good replacement for the traditional used CuZn37Pb3 alloy if beside the alloy composition, the microstructure and the mechanical properties are relevant to ensure good machinability and acceptable cold formability for processes such as crimping, flanging, riveting, etc. The material produced with appropriate production steps can then easily be hot and cold formed, opening up new possibilities in component manufacturing (Fig. 7).

The newest Inlet (Fig. 6) is a great example of combined efforts of material experts, top designers and sustainability knowledge. Next to the metal-related improvements, also in plastic designs, several tools (ref. the House of Sustainability) were used. Plastic usage was minimized by the use of our AI-Generative Design-Software. The selection of resins was optimized with components designed for PBT-PET, PCR recycled material.

IV. Risks Trade-Offs and Conclusion

The preceding chapters show that sustainability requirements in connector development arise directly from the combination of high PCF materials, energy-intensive manufacturing processes, high production volumes and increasing regulatory obligations. The analysis of CEAP-related instruments, especially ESPR and the DPP, makes clear that connector manufacturers must provide structured data on material composition, recycled content and PCF at component level [1]. These requirements directly constrain engineering decisions on materials, coating solutions and manufacturing processes.

The evaluated design levers indicate that resource demand reduction has a high immediate impact within connector engineering. Material selection with lower PCF, reduced precious-metal usage and miniaturization per functional unit directly lower embedded emissions, provided that electrical and mechanical performance is maintained. Avoiding overdesign by simulation of form, fit and function upfront needing appropriate material datas became mandatory. Manufacturing-related levers – such as energy-efficient processes, reduced scrap rates and internal material loops – further contribute to measurable PCF reductions and can be implemented without fundamental product redesign. In contrast, circular end-of-life strategies remain limited at component level due to system dependencies and advanced recycling processes for complex connector compositions.

Reliability vs. circularity is a question often asked when it comes to recycled content. Metals can be recycled multiple times with minimal or no performance degradation; resins with >30 % recycled content can shift reliability and performance profiles. A full new validation with accelerated testing or decisions for “low performance / low-cost versions (e.g. for lower applications temperatures).” will be necessary. Certification timelines seen with new PFAS free resin compositions and the ROHS/ELV lead-free campaign require product re-testing and Car Maker qualification and early planning to avoid program delays or production stops are needed.

This paper concludes that sustainable connector development is primarily an engineering innovation and execution challenge, not a conceptual one. Regulatory frameworks under the CEAP define the required data and performance transparency, while standardized sustainability and circularity metrics enable translation into concrete design targets. Metrics such as recycled content and PCF allow sustainability tradeoffs to be assessed alongside traditional performance criteria and support alignment between engineering, procurement and the customer.

In the short to medium term, the greatest sustainability gains in connectors will be achieved through material efficiency, increase in recycled content, miniaturization, manufacturing and footprint optimization. Future developments should therefore focus on improving component level footprint data, integrating Digital Product Passport requirements into development processes and validating circularity metrics for small electromechanical components in order to move from compliance driven reporting to design driven sustainability.

The data burden: CSRD/EPD LCAs and tracking of CO_2 emissions to show the path for Science Based Targets initiative (SBTi) for example demand robust data governance across sites and suppliers, scalable processes and databases are the fundament for comparable product PCF values.

REFERENCES

[1] European Comission, “A new Circular Economy Action Plan”, 2020, [Online]. Available: https://eur-lex.europa.eu/legalcontent/EN/TXT/HTML/?uri=CELEX:52020DC0098.

[2] Ellen MacArthur Foundation, “Completing the picture: How the circular economy tackles climate change”, 2021, [Online]. Available: https://content.ellenmacarthurfoundation.org/m/3eac8667edd240cc/original/Completing-the-picture-How-the-circular-economy-tackles-climate-change.pdf

[3] ISO, “ISO 59004:2024 – Circular economy – Vocabulary, principles and guidance for implementation. Geneva: International Organization for Standardization”, 2024

[4] Kirchherr, J., Reike, D., & Hekkert, M.,”Conceptualizing the circular economy: An analysis of 114 definitions. Resources, Conservation and Recycling”, 2017, pp.221-232.

[5] International Copper Association, “Copper Environmental Profile”, [Online]. Available: https://sustainablecopper.org/wp-content/uploads/2018/07/ICA-EnvironmentalProfileHESD-201803-FINAL-LOWRES.pdf

[6] European Union, “REGULATION (EU) 2024/1781 OF THE EUROPEAN PARLIAMENT AND OF THE COUNCIL of 13 June 2024 establishing a framework for the setting of ecodesign requirements for sustainable products, amending Directive (EU) 2020/1828 and Regulation (EU) 2023/1542 and repealing Directive 2009/125/EC”, 2024, [Online]. Available: https://eur-lex.europa.eu/legal-content/EN/TXT/PDF/?uri=OJ:L_202401781

[7] European Union, “DIRECTIVE 2000/53/EC OF THE EUROPEAN PARLIAMENT AND OF THE COUNCIL of 18 September2000 on end-of life vehicles”, 2000, [Online]. Available: https://eur-lex.europa.eu/resource.html?uri=cellar:02fa83cf-bf28-4afc-8f9f-eb201bd61813.0005.02/DOC_1&format=PDF

[8] Bundesministerium für Umwelt, Klimaschutz, Naturschutz und nukleare Sicherheit, “REACH“, 2025, [Online]. Available: https://www.bundesumweltministerium.de/themen/chemikaliensicherheit/reach

[9] European Union, “DIRECTIVE (EU) 2022/2464 OF THE EUROPEAN PARLIAMENT AND OF THE COUNCIL of 14 December 2022 amending Regulation (EU) No 537/2014, Directive 2004/109/EC, Directive 2006/43/EC and Directive 2013/34/EU, as regards corporate sustainability reporting”, 2022, [Online]. Available: https://eur-lex.europa.eu/legal-content/EN/TXT/PDF/?uri=CELEX:32022L2464

[10] Heras-Saizarbitoria, I., Boiral, O. & Testa, F., “ISO 59000 Standards for the Circular Economy: a Call for Accuracy”, 2024, [Online]. Available: https://link.springer.com/article/10.1007/s43615-024-00370-w

[11] CEN/CENELEC, “Definitions related to material efficiency”, PD CLC/TR 45550:2020-23-34, 2020

[12] Cicerelli, F., Ravetti, C., “Sustainability, resilience and innovation in industrial electronics: a case study of internal, supply chain and external complexity”, J Econ Interact Coord 19, pp.343–372, 2024, [Online]. Available: https://doi.org/10.1007/s11403-023-00396-7

[13] S. Sachs, F. Greiner, et.al.: Green-Silver Oberflächentechnologie: Überlegene Eigenschaften und Nachhaltigkeit im Herstellungsprozess; Anwenderkongress Steckverbinder 2022, ElektronikPraxis.

[14] Chun-Wei Chen, “ Hybrid Framework for Evaluating and Selecting Sustainable Materials in Product Developmet,” 2025,

[15] European Commission, Directorate-General for Energy, and Directorate-General for Enterprise and Industry, “Ecodesign your future - How Ecodesign can help the environment by making products smarter,” 2012, doi: 10.2769/38512

[16] C. Favi, M. Marconi, M. Germani, M. Mandolini, A design for disassembly tool oriented to mechatronic product de-manufacturing and recycling, Adv. Eng. Informatics. 39 (2019) 62–79, https://doi.org/10.1016/j.aei.2018.11.008

[17] TE Connectivity White Paper BCON+: https://www.te.com/content/dam/te-com/documents/hybrid-and-electric-mobility-solutions/deu/battery-module-connector-whitepaper-05-2020-de.pdf

[18] Carlsson, S., Mallalieu, A., Almefelt, L. and Malmqvist, J. (2021). DESIGN FOR LONGEVITY - A FRAMEWORK TO SUPPORT THE DESIGNING OF A PRODUCT’S OPTIMAL LIFETIME. *Proceedings of the Design Society*, [online] 1, pp.1003–1012. doi:https://doi.org/10.1017/pds.2021.100.

[19] Whitepaper: TENDUR - Ultra anti abrasion high-voltage contact plating; TE Connectivity 2021; TENDUR Ultra Anti-Abrasion High-Voltage Contact Plating

TE expressly disclaims any implied warranty regarding the information contained herein, including, but not limited to, the implied warranties of merchantability or fitness for a particular purpose.

Sustainable Contact Materials: Comparison between different Contact Materials for MV Switchgears regarding their Resistance and CO2 Equivalent

1st Nils Wilm Rosebrock
elenia Institute for High Voltage Technology and Power Systems
Technical University Braunschweig
Braunschweig, Germany
n.rosebrock@tu-braunschweig.de

2nd David Cziumplik
elenia Institute for High Voltage Technology and Power Systems
Technical University Braunschweig
Braunschweig, Germany
david.cziumplik@tu-braunschweig.de

3rd Michael Kurrat
elenia Institute for High Voltage Technology and Power Systems
Technical University Braunschweig
Braunschweig, Germany
m.kurrat@tu-braunschweig.de

***Abstract*— The selection of contact materials has a significant impact on the efficiency and sustainability of medium-voltage switchgear. This study investigates the electrical resistance of selected contact materials for vacuum switchgear applications using three complementary approaches: finite element simulations, analytical calculations based on material-specific resistivity values, and experimental long-term measurements serving as a reference for model validation. In the experimental setup, a constant current is applied to the contact arrangement inside a vacuum chamber, and the electrical resistance is measured automatically from the measured voltage drop using high-precision instrumentation. This approach allows the assessment of long-term-effects, e.g. temperature related reduction of the resistance, that are not fully captured by numerical or analytical models. The combined evaluation enables a systematic comparison of simulated, calculated, and measured resistances, thereby highlighting both the predictive capabilities and the limitations of each method. In addition to the resistance-based analysis, literature-derived CO_2-equivalent values are incorporated using the Ashby methodology, providing an extended perspective on sustainability-oriented material selection.**

Keywords—VCB, contact materials, electric contact resistance, sustainability

I. Introduction

Medium-voltage switchgear plays a key role in modern electrical power systems, where increasing demands on energy efficiency, reliability and sustainability are driving the optimization of individual components. Within this context, electrical contact materials constitute a key design parameter, as they directly affect conduction losses, thermal behaviour, and the long-term performance of switching devices. Even small reductions in contact resistance can lead to measurable efficiency gains over the operational lifetime of a switchgear, while material choice increasingly needs to account for environmental and sustainability-related criteria [1].

From a sustainability perspective, the environmental impact of medium-voltage switchgear must be assessed over the entire life cycle, including raw material extraction, manufacturing, operation, and end-of-life treatment. A life-cycle assessment (LCA) has shown that the use phase represents a significant share of the overall environmental impact, primarily due to electrical losses occurring during long-term operation [2]. This finding highlights the importance of minimizing conduction losses at the component level and provides the motivation for the present study.

Despite their relevance, electrical contact resistances in vacuum switchgear are inherently difficult to predict with high accuracy. The effective resistance is influenced not only by the bulk properties of the contact materials, but also by complex phenomena at the contact interface, including microscopic contact spots, surface topology, mechanical contact force, and time-dependent effects such as ageing or material degradation. Consequently, purely analytical or numerical approaches often capture only selected aspects of the underlying mechanisms, while experimental investigations are required to assess realistic operating behaviour.

From a sustainability perspective, the environmental impact of medium-voltage switchgear must be assessed over the entire life cycle, including raw material extraction, manufacturing, operation, and end-of-life treatment. A life-cycle assessment conducted within the project framework has shown that the use phase represents a significant share of the overall environmental impact, primarily due to electrical losses occurring during long-term operation. This finding highlights the importance of minimizing conduction losses at the component level and provides the motivation for the present study.

II. Methodology

To investigate the electrical resistance of contact materials used in medium-voltage vacuum switchgear, three approaches were applied: finite element simulations, analytical calculations, and experimental long-term measurements. Each method addresses different physical aspects of the contact behaviour and is associated with specific advantages and limitations. Rather than aiming for a direct numerical equivalence, the approaches are used to assess the predictive capability and applicability of resistance evaluation methods across different material classes.

A. Finite Element Simulation

Finite element simulations were performed using COMSOL Multiphysics to analyze the electrical behavior of the contact arrangement under steady-state current conditions. The simulations are based on material-specific electrical resistivity values and realistic contact geometries. The geometric model is based on the experimental setup used for the long-term measurements. Therefore, the vacuum chamber, including its electrically conducting components, is explicitly modelled, as shown schematically in Fig. 1. This ensures geometric consistency between simulation and experiment and allows a realistic representation of current paths within the system.

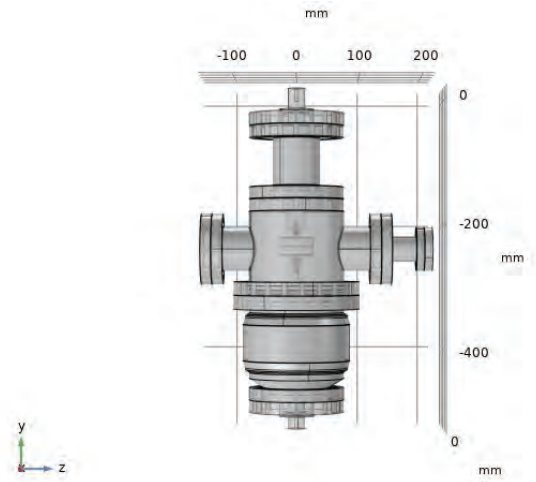


Fig. 1. 3D-model of the vacuum chamber.

The conducting parts of the chamber, including the contact bodies and current-carrying structural components, are assigned material-specific electrical properties. A constant current is applied under steady-state conditions to evaluate the resulting current density distribution, voltage drop, and resistive losses within the contact assembly.

In COMSOL Multiphysics, the electrical resistance is obtained from the solution of the stationary current conduction equation, with the constitutive relation

$$J = \sigma E = -\sigma \nabla V \tag{1}$$

where J is the current density, σ the electrical conductivity, E the electric field, and V the electric potential. The total resistance is then derived from the simulated voltage drop ΔV and the applied current I according

The simulations were performed for a set of commonly used copper- and silver-based contact materials, including copper–tungsten (WCu), copper–molybdenum (MoCu), tungsten carbide–silver (WCAg), and tungsten carbide–copper (WCCu) composites.

It is important to note that this approach captures the volume resistance of the contact bodies and conducting structures, while the microscopic contact resistance at the interface is not explicitly resolved [3]. Nevertheless, the resulting resistance values correctly represent the electrical losses associated with bulk conduction and provide a consistent basis for comparing different contact materials under identical boundary conditions. The simulation framework is applicable to all investigated materials and enables a systematic assessment of their influence on resistive losses.

B. Analytical Calculation of Contact resistance

In contrast to the macroscopic volume resistance considered in the finite element simulations, the contact resistance originates from the microscopic nature of real electrical contacts. Although the nominal contact area is defined by the macroscopic geometry (e.g. the contact diameter), the actual current transfer occurs through a large number of microscopic contact spots, commonly referred to as a-spots, first introduced by Holm [4]. These arise from surface roughness and elastic–plastic deformation under load.

According to Holm's contact theory, the contact resistance is primarily influenced by the material properties and mechanical loading conditions. Key parameters include the electrical resistivity ρ, material hardness H, applied contact force F, and surface condition, such as roughness and the presence of oxide layers.

For metallic contacts, the contact resistance can be approximated by

$$R_C = \frac{\rho}{2a} \tag{2}$$

where a is the effective radius of a single contact spot. The contact spot radius is related to the applied contact force and material hardness by

$$a = \sqrt{\frac{F}{\pi H}} \tag{3}$$

Here, F denotes the normal contact force and H the hardness of the softer contact material. These relations highlight that the contact resistance decreases with increasing contact force and electrical conductivity [4].

Due to the strong dependence on surface-related parameters the analytical calculation was restricted to pure copper contacts, for which reliable material data and reference values are available. While this method provides valuable physical insight into the origin and magnitude of contact resistance, its applicability to composite contact materials is limited. Consequently, the analytical approach is primarily used as a theoretical reference rather than a universal prediction tool.

C. Experimental long-term measurements

To experimentally determine the electrical resistance of the contact arrangement, a four-wire measurement principle is applied using a constant impressed current. In this configuration, the current is injected through the contact system via dedicated current leads. The resulting voltage drop is measured independently using separate sense leads positioned close to the contact region inside the vacuum chamber [5].

This separation of current and voltage paths minimizes the influence of lead resistances and contact resistances of the measurement wiring, which is essential for accurately resolving low resistance values in the micro-ohm range. A constant direct current is applied to the contact assembly inside the vacuum chamber, and the resistance is calculated according to Ohm's law [6].

Unlike the finite element simulations, this measurement approach inherently captures both the volume resistance of the contact bodies and the contact resistance at the interface, as the voltage probes are placed in close proximity to the contacting surfaces. Furthermore, the continuous measurement under constant current enables the observation of time-dependent resistance variations, thereby providing insight into potential long-term effects that are not fully represented in analytical or numerical models.

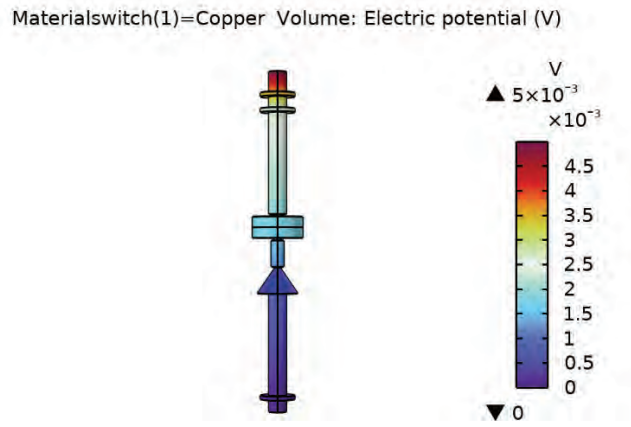


Fig. 2. Electrical potential in conducting paths of the vacuum chamber.

D. Experimental long-term measurements

In addition to the resistance-based analysis, a simplified sustainability assessment was performed based on literature-derived global warming potential (GWP) values of the investigated materials. The GWP is expressed in terms of CO_2-equivalent emissions and enables a comparative evaluation of the environmental impact of different material systems. The applied approach follows the general principles of the Ashby methodology and is intended as a relative comparison of material-related environmental impacts rather than a comprehensive life-cycle assessment.

III. Results and Comparison

Based on the complementary nature of the applied methods, the following section presents a comparative evaluation of simulated, analytically calculated, and experimentally measured resistance values.

A. Simulation Results

The steady-state current simulations were performed for all investigated contact materials using identical geometric and electrical boundary conditions. The resulting electrical resistances were derived from the simulated voltage drop across the conductive parts of the vacuum chamber.

Fig. 2 shows the electric potential within the modelled contact arrangement, confirming a homogeneous current flow in the bulk material. The calculated resistance values represent the volumetric resistance of the contacts and serve as a comparative baseline for the different materials.

TABLE I. Simulated Resistance Values for Different Materials

Material	Resistance in μΩ
Cu	50.009
WCu10	63.262
WCu20	58.903
MoCu50	52.213
MoCu20	58.285
WCAg20	59.587
WCAg40	57.724
WCCu30	60.049

Table I summarizes the simulated electrical resistance values obtained from the steady-state current analysis for the investigated contact materials. The results show material-dependent variations in resistance within a comparatively narrow range. The obtained resistances range from 50.009 μΩ for copper to 63.262 μΩ for WCu10 under identical geometric and electrical boundary conditions.

Pure copper exhibits the lowest resistance among the investigated materials, while copper-based composites and refractory metal-containing materials show moderately increased resistance values. The resistance values of the different material combinations reflect the influence of their effective electrical conductivity within the modelled contact geometry.

B. Analytical Results

To provide an analytical reference for the contact resistance, the contact resistance was estimated using the classical Holm theory for metallic contacts. As a representative example, a copper–copper contact was considered.

For the investigated configuration, a normal contact force of F = 1500 N was assumed, corresponding to the mechanical loading applied in the experimental setup [2]. The hardness of copper was taken as approximately H = 100 MPa, while the electrical resistivity was set to $\rho = 1.72\times10^{-8}$ Ωm [7].

Under these assumptions, the effective contact spot radius can be estimated from the applied force and material hardness, yielding a value in the order of $a \approx 2.18$ mm.

Using Holm's approximation for metallic contact resistance as in (2), the resulting contact resistance is calculated to be approximately $R_C = 3.95\times10^{-6}$ Ω.

This value represents an idealized lower bound for a clean copper contact under steady mechanical loading and does not account for surface films, oxidation, or surface roughness effects.

C. Experimental Results

The experimental investigation was carried out under high-vacuum conditions to determine the electrical resistance of the contact arrangement under realistic operating parameters. A constant DC current of 100 A was applied to the contacts inside the vacuum chamber, and the resulting voltage drop was measured close to the contact interface in order to minimize the influence of lead and cable resistances.

The vacuum chamber was operated at an internal pressure in the range of 10^{-5} mbar, ensuring stable vacuum conditions throughout the measurement. The movable contact was actuated by a motor-driven mechanism, applying a defined contact force of 1500 N in the closed state. All measurements were performed under steady-state conditions after thermal stabilization of the system [2].

The long-term measurement was conducted to investigate the temporal evolution of the electrical resistance under constant current loading. The resistance was continuously monitored over a measurement duration of 540 minutes using the four-wire measurement setup described previously.

At the beginning of the measurement, the resistance exhibits a comparatively high initial value of approximately 456 μΩ. During the early phase of the experiment, a

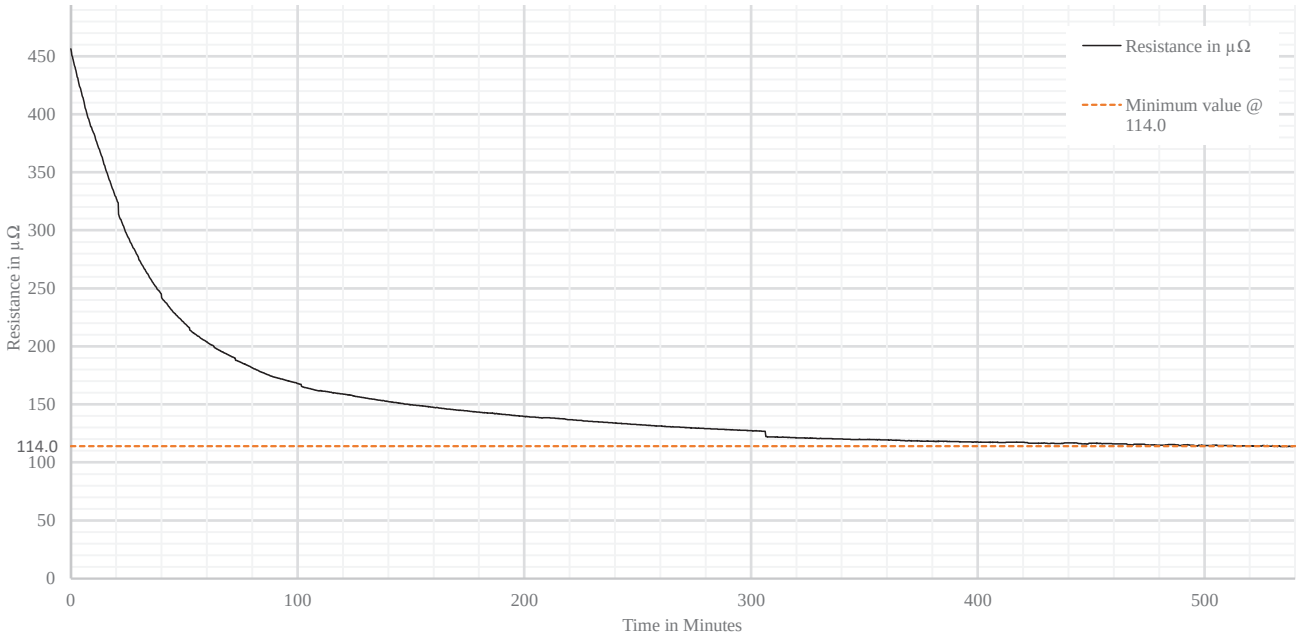


Fig. 3. Time-dependent evolution of the electrical resistance measured under constant current conditions.

pronounced decrease in resistance is observed. Within the first 20 minutes, the resistance is reduced by more than 25 %, indicating a rapid transient behavior. Following this initial phase, the resistance continues to decrease gradually with a significantly lower slope. After approximately 100 minutes, the resistance reaches a value of approximately 168 μΩ, and the rate of change further diminishes. Toward the end of the measurement, the resistance stabilizes at 114 μΩ, with only minor fluctuations.

Over the final phase of the experiment, the resistance variation remains within a narrow band, indicating a quasi-steady-state condition. No abrupt resistance jumps or instabilities were observed throughout the entire measurement duration. Fig. 3 summarizes the experimentally determined resistance values for the investigated contact materials. The measured resistance represents the combined contribution of bulk resistance and contact resistance under realistic operating conditions.

In addition to absolute resistance values, the experimental setup allows for the observation of resistance evolution over time under constant current loading. This long-term measurement captures effects that are not represented in analytical calculations or steady-state simulations, such as gradual changes at the contact interface.

D. Resistance–GWP Comparison

To complement the experimental and simulated results presented in the previous sections, the relationship between the electrical performance of the investigated contact materials and their environmental impact is analysed. The electrical resistance values correspond to the simulated results obtained in Section 3.3, while the global warming potential (GWP, expressed in CO_2-equivalents) of the constituent base materials was derived from the ecoinvent database [8] and calculated proportionally for the respective alloys.

Fig. 4 illustrates the relationship between the simulated electrical resistance and the calculated global warming potential (GWP) of the investigated materials. Pure copper exhibits both the lowest electrical resistance and a comparatively low GWP. WCu and MoCu composites show a moderate increase in electrical resistance while maintaining a relatively low environmental impact, representing a balanced trade-off between electrical performance and sustainability. In contrast, silver-containing materials (WCAg20 and WCAg40) exhibit significantly higher GWP values due to the high environmental burden associated with silver production, without providing a substantial advantage in electrical resistance.

The comparison highlights that materials with excellent electrical performance do not necessarily incur the highest environmental impact. Copper-based composites such as WCu and MoCu provide a favorable compromise, whereas silver-containing variants, despite high material costs and environmental burden, do not offer proportional functional benefits. These insights underscore the importance of integrating environmental considerations into the design and selection of electrical contact materials.

IV. Discussion and Outlook

The results presented in this study are based on three complementary approaches to evaluate the electrical resistance of contact materials for vacuum switchgear applications: analytical estimation, numerical simulation, and experimental measurement. Each method addresses different physical scales and assumptions, resulting in specific strengths and limitations. A comparative discussion is therefore essential to assess the validity, transferability, and predictive capability of the individual approaches.

A. Comparability of the three Approaches

While the analytical estimation based on Holm theory provides valuable physical insight into the formation of contact resistance, its applicability is inherently limited when compared to experimental measurements. The theory assumes idealized contact conditions, such as clean metallic surfaces, purely elastic–plastic deformation, and a well-defined effective contact spot radius. In practice, these assumptions are only partially fulfilled in vacuum switchgear applications.

One major limitation lies in the treatment of surface conditions. Holm theory does not explicitly account for surface roughness, residual oxide layers or contamination, all of which can significantly influence the real contact area and, consequently, the contact resistance. Furthermore, the analytical model assumes a static contact force and neglects time-dependent effects.

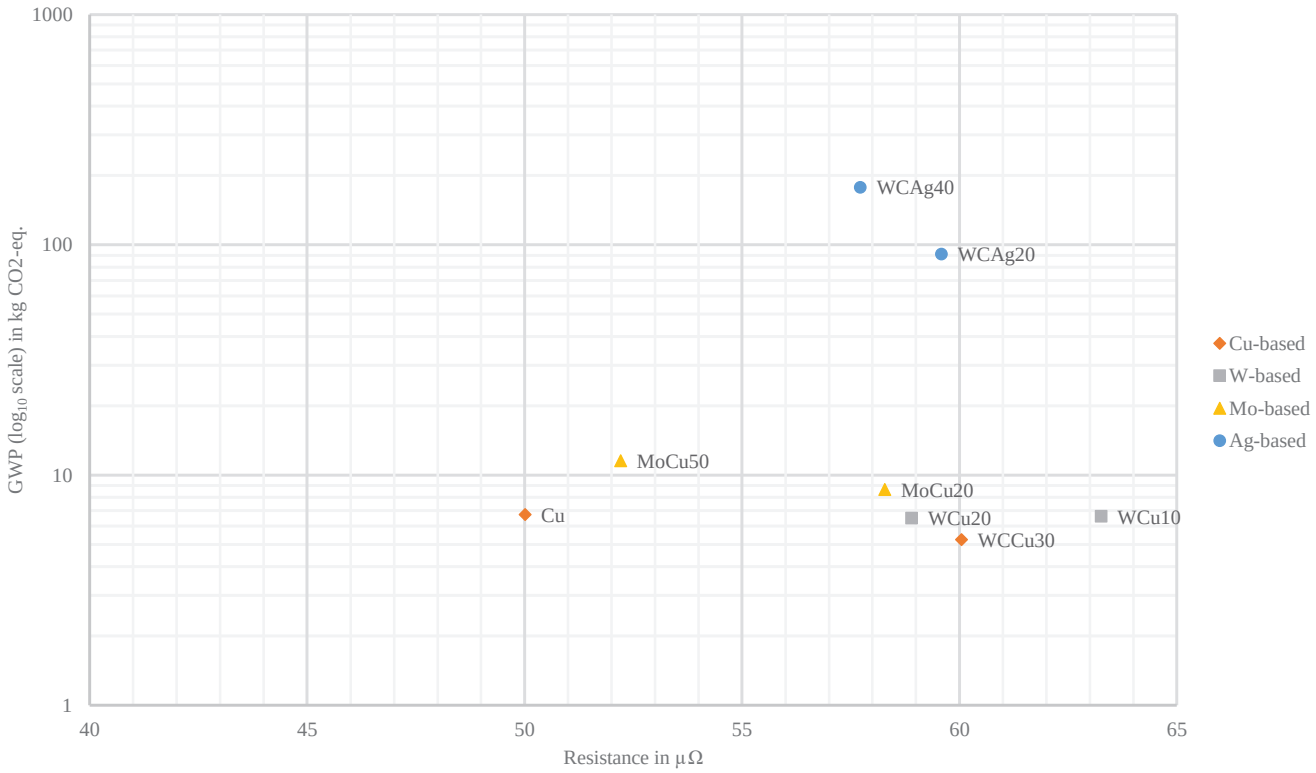


Fig. 4. Comparison of electrical resistance and global warming potential (GWP) of different copper-, tungsten-, molybdenum-, and carbide-based contact materials.

In contrast, the finite element simulations capture the geometrical current distribution within the conducting components and allow for a spatially resolved evaluation of the volume resistance and associated loss mechanisms. However, the simulation relies on a simplified representation of the contact geometry and does not explicitly resolve the microscopic contact resistance at the interface. Local effects such as real contact spot formation and material inhomogeneities are therefore only indirectly captured. While this simplification allows for efficient comparison between materials and loss mechanisms, it may lead to deviations from real operating conditions. As a result, both analytical and numerical approaches primarily describe conditions.

Experimental four-wire measurements, on the other hand, inherently include both volume resistance and contact resistance under realistic conditions. Moreover, the long-term measurements performed under constant current loading enable the observation of temporal effects that are not accessible through analytical or simulation-based methods. Consequently, the experimental results serve as a reference for contextualizing the analytical and numerical models, highlighting the complementary nature of the three approaches.

In addition to the methodological limitations discussed above, it should be emphasized that the evaluation of contact materials based on electrical resistance and sustainability metrics alone does not provide a complete assessment of their suitability for vacuum interrupter applications. In practice, contact materials must satisfy a range of additional functional requirements, including arc erosion resistance, dielectric recovery capability, and mechanical stability under repeated switching operations. The results presented in this study should therefore be interpreted as a comparative analysis within a preselected set of technically relevant material systems, rather than as a comprehensive material qualification.

B. *Outlook*

The methodologies presented in this work provide a solid foundation for a systematic and multi-criteria material selection process for medium-voltage vacuum switchgear contacts. In future studies, the combined evaluation of analytical models, finite element simulations, and experimental long-term measurements can be consistently extended to a broader range of candidate materials and contact geometries. This enables a more comprehensive assessment of electrical performance, durability, and sustainability already at an early design stage.

Future work could focus on refining the geometrical and physical representation of the contact interface, for example by incorporating experimentally derived contact resistances, and multi-scale simulation approaches. In combination with extended long-term experimental investigations, this may further improve the predictive capability of the models and strengthen their applicability for sustainable material selection in vacuum switching technology.

V. Acknowledgment

The authors acknowledge the use of the AI language model ChatGPT (OpenAI) for language editing support. The AI system was used only to improve clarity and readability of the authors' original text and did not generate scientific content or results.

The project GreEner Tech, on which this paper is based, was funded by the German Federal Ministry of Economic Affairs and Climate Action under the funding code 03EI6101D.

REFERENCES

[1] Slade, Paul G. The vacuum interrupter: theory, design, and application. CRC press, 2018.

[2] S. Rader et al., "GreEner Tech: Sustainable Technology for Medium-Voltage Switchgear Systems," ETG Kongress 2025; Voller Energie – heute und morgen., Kassel, Germany, 2025, pp. 684-691.

[3] Multiphysics, C. O. M. S. O. L. "Introduction to comsol multiphysics®." COMSOL Multiphysics, Burlington, MA, accessed Feb 9.2018 (1998): 32.

[4] R. Holm, Electric Contacts, Springer, Berlin, Heidelberg, 1967, https://doi.org/ 10.1007/978-3-662-06688-1*)*

[5] Popov, Valentin L. Contact mechanics and friction. Berlin: Springer Berlin Heidelberg, 2010.

[6] J. J. Shea and J. A. Bindas, "Measuring molded case circuit breaker resistance," in IEEE Transactions on Components, Hybrids, and Manufacturing Technology, vol. 16, no. 2, pp. 196-202, March 1993, doi: 10.1109/33.219405.

[7] Rau, G. Kontakte: Grundlagen; Werkstoffe, Gestaltung, Auswahl. 1965.

[8] https://ecoquery.ecoinvent.org/3.12/cutoff, last visited: 10:11.2025

Geometric Influence on Repulsion Forces in Butt Contacts

Sergey Perekopskiy
Global automotive
TE Connectivity Germany GmbH
Berlin, Germany
sergey.perekopskiy@te.com

***Abstract*—The advancement of fast-charging technologies in electric vehicles imposes stringent requirements on high-voltage switching devices, particularly under short-circuit conditions. Ensuring operational reliability at elevated voltages requires a deeper understanding of the mechanical and electromagnetic behavior of current-carrying contact systems. This study examines the influence of butt contact conductor's geometry on electrodynamic repulsion forces, which can lead to contact separation and compromise switching system destruction. A simulation-based approach was employed to analyze the distribution of forces within a representative butt contact configuration during high-current events. Experimental validation using a custom test setup enabled refinement of the model by incorporating real surface characteristics, resulting in improved correlation between simulated and measured forces. A comparative analysis between standard and geometrically optimized contact designs revealed a significant reduction in repulsion effects with the latter. These findings demonstrate the potential of butt contact conductor's design as a parameter for improving the stability and short-circuit performance of high-voltage switching systems. The study also highlights the relationship between current amplitude and repulsive force, offering valuable insights for future design strategies aimed at enhancing the reliability of electric powertrain components.**

Keywords—electric contacts, short-circuit current, magnetic field, repulsion, butt contacts, levitation, constriction

I. MOTIVATION

The next generation of battery architectures for electric vehicles require state-of-the-art Battery Disconnect Units (BDUs) capable of operating at system voltages of 800 V and higher. Increasing the battery voltage enables higher charging power at comparable losses, which directly translates into reduced charging times, what is the most important benefit for the end users. In addition, the BDU performs an important safety function by providing reliable galvanic isolation between the battery and the vehicle's electrical system. To ensure this function, the BDU includes various safety-related components, including fuses, sensors, busbars, and high-voltage switching devices.

High-voltage switching devices or contactors play an important role in providing normal operation and safety in emergency situations. They act as electrically controlled switches that connect the battery to the load during starting, pre-charging, and normal vehicle operation, and provide fast electrical and galvanic isolation in the event of malfunctions such as vehicle collisions, thermal overloads, current overloads, or short circuits. With the constant increase of battery voltage and improvement of battery cell resistance, short-circuit currents increase proportionally, placing increasingly demanding requirements on the design of high-voltage switching devices.

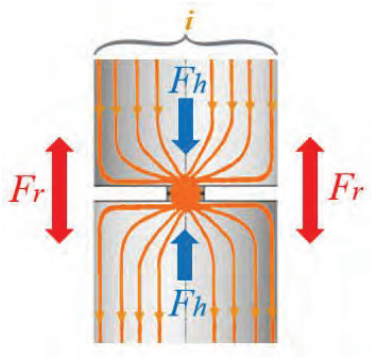


Fig. 1. Current passage and forces acting between conductors of typical contact system

By the current passage through the conducting terminals and the contact elements or short-circuit events, fast-rising current can cause the electrodynamic repulsive force *Fr* to exceed the mechanical contact holding force *Fh*, potentially leading to unintended contact separation. Repulsion force is caused by non-uniform current distribution, which occurs across the contact cross-section, resulting in magnetic flux concentration and generation of electrodynamic forces. These forces, often named repulsion forces, provoke contact separation and are caused by Lorentz forces. They arise from the interaction between the current and associated magnetic fields. As illustrated in Fig. 1, this interaction of current paths *i* on opposing contact surfaces produces a repulsive force component that increases rapidly with current magnitude. Dependent on the design of the conductive structure, these electrodynamic forces are highly unfavorable, because they can cause levitation of electric contacts which lead to high-energy arcing, contact erosion, mechanical breakdown, and, in extreme cases, destruction or explosion of the switching device. Therefore, today's high-voltage device designs are required to provide sufficient contact force and structural mechanical strength to withstand these electromagnetic loads.

Thus, modern technical requirements for high-voltage switching devices stipulate that they must withstand certain loads during short-circuit events without critical damage. According to various industry-based standards [1,2], these requirements translate into safe operation without smoke, fire, explosion, or emission of conductive particles inside the BDU, which results in operational reliability and safety of high-voltage battery systems in electric vehicles.

This paper presents a comparative analysis of a solid contact conductor and a geometrically optimized conductor with a hollow cylindrical shape. The study focuses on the effect of this geometric modification on current reduction and electrodynamic repulsive forces under short-circuit conditions. Numerical modeling and experimental testing are

used to identify and quantify the effect of conductor geometry on the value of repulsion force.

II. Contributors to the Repulsive Force

A. Model of Force Interaction

In the literature, recommendations for the calculation of electrodynamic forces are often limited to formulas for the simplest cases, which is clearly incomplete for reliable design of contact system. For example, in [4] the initial stages of contact separation in an automotive relay with bridge-type contacts were investigated, demonstrating that the balance of mass, momentum, and energy equations, without the influence of magnetic fields. Furthermore, the model of force interaction by the short-circuit current was briefly described in [3]. Fig. 2 shows a schematic representation of the forces acting in the switching device during a short-circuit current event, where P is the weight of the moving contact, F_s is the contact spring force, F_{lor} is Lorentz electrodynamic force caused by geometric arrangement (loop) of conductors, F_{con} are electrodynamic forces due to the current constriction, F_g are forces caused by gas pressure during arcing and evaporation of contact materials.

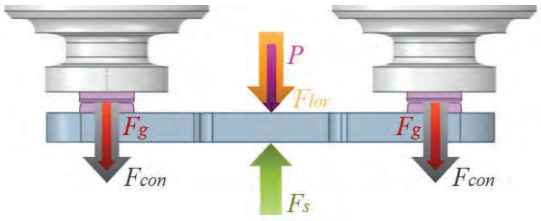


Fig. 2. Forces acting during short-circuit current event

B. Lorentz Electrodynamic Force

The subject of the direction of Lorentz electrodynamic forces by different arrangements of conductors is practically very important. To determine the direction of force on a current conductor in a magnetic field, there are a number of known rules. First of all, Fleming's rule should be mentioned, which defines the direction of the force acting on a conductor carrying current, or, in other words, the direction of the Lorentz force.

C. Arcing and Gas Pressure

The contact resistance provokes local heating in the contact area due to current constriction and thermoelectric effects, like the Peltier, Thomson, and Cooler phenomena [10]. During the initial phase of contact separation, the high temperature that arises leads to rapid evaporation of the material, plasma formation, and a sharp increase in pressure, which creates an additional thermodynamic repulsive force that accelerates contact separation and contributes significantly to contact erosion [11–14].

D. Electrodynamic Forces due to the Current Constriction

The electrodynamic forces resulting from the flow of short-circuit current are also referred as electrodynamic forces in areas of abrupt change in the cross-section of conductors and, in particular, in the contact parts. These forces can be called forces due to the constriction. In the analysis of contact systems, special calculation models are used, the most well-known of which is the Holm equation, based on an idealized description of the contact between two isotropic conductors [5]:

$$F_{rep} = \frac{\mu_0}{4\pi} \cdot i^2 \cdot \ln\frac{r_2}{r_1} \tag{1}$$

Where F_{rep} represents the electrodynamic repulsion force between the contacts, i is the current through the contacts, μ_0 is the permeability of free space, r_1 is the effective radius of the contact constriction and r_2 is the outer radius of the current path.

The magnitude of electrodynamic forces due to the constriction was also originally described by Dwight [6], where the final expression used to calculate the forces in a constricting cylinder is represented by equation (Fig. 3, left):

$$F_{rep} = 10^{-7} \cdot i^2 \cdot \ln\frac{D}{d} \tag{2}$$

Where i represents the current, D is defined as the outer diameter of the contact, and d is the diameter of the actual contact surface.

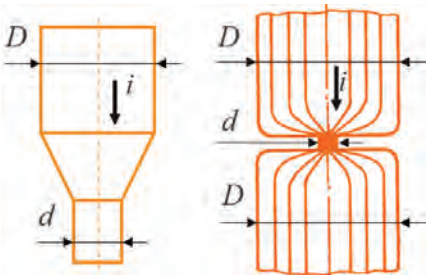


Fig. 3. Forces in a constricting cylinder (left) and constriction of current lines at the contact point (right)

The magnitude of electrodynamic forces due to the constriction is most frequently required to be calculated at the points of current crossing from one contact part to another, where usually a constriction of current lines at the contact point and then their expansion again takes place (Fig. 3, right). Therefore, the importance of the description of the contacting model becomes relevant. According to the [7] for low currents, a spherical contact model can be used, where the current spread out in a radial direction, and the equipotential and isothermal surfaces are spherical. For devices conducting high-current like in case of short-circuit current event, an elliptical contact model is more appropriate, where the contact area is represented as an infinitely thin disk through which the current enters a semi-infinite region, and the equipotential and isothermal surfaces of the contacting elements are cofocal ellipsoids.

More convenient is to use the empirical formula for electrodynamic force due to the current constriction as it was presented in [3]:

$$F_{con} = k \cdot i^2 \cdot 10^{-7} \tag{3}$$

The coefficient k introduced in the formula should be taken into account as an increase of electrodynamic forces of constriction due to additional repulsion of current lines of

both contacts and was determined by a least-squared fit to the experimental data. Past work in this area made by [8] on butt contacts in high vacuum has shown that this coefficient is assumed to be 4.45 to 5.0. The decision to use butt contacts for determination of coefficient *k* is not accidental, as it allows us to eliminate the influence of any other conducting parts in the circuit as it was provided by [9].

In analytical calculations related to the determination of the electrodynamic forces of contact repulsion for butt contacts, the main challenge is to identify the actual contact points between contacts. The quantity of contact zones can be various, resulting in the formation of several parallel current line densities. As a result, the electrodynamic repulsion force of contact is reduced. Despite a significant number of publications, there is still no consensus on the theoretical description of the physical processes involved in the interaction of electrical contacts during a short-circuit event, which creates difficulties in the systematic mathematical modelling of the dynamics of contact connections for the purpose of theoretically predicting their technical characteristics. Existing analytical formulas do not consider the hollow geometry of butt contacts. Currently, the design and modernization of these objects are mainly associated with costly experimental research or complex simulation models. One of the main difficulties in developing adequate mathematical models reflects the dynamics of electrodynamic interaction with acceptable accuracy. It is especially difficult to evaluate the effect of constriction on butt contacts by modification of geometry of conductors. For example, decrease of the repulsion force by butt contacts can be achieved in case of contacts with a cross-section other than full-filled, e.g. hollow. Then Equation 1 becomes non-applicable because of presence of forces which are resulting from the interaction between cylinder end sections with direct effect on the value of repulsion force. Additionally, it is expected that an interaction of electromagnetic forces of flat surfaces of the hollow cylinders can reduce the repulsion force.

III. Methodology

As described in the previous section, contributors to the repulsion force are influenced by the combined effect of various factors, which may lead to the levitation of electric contacts. To isolate and clearly understand factors of electrodynamic forces caused by the current constriction, a butt contact investigation was conducted. The butt contact is often used in testing or specific applications where the simplicity of the connection and the direct nature of the current flow are important. Butt contacts are essential in scenarios where it's necessary to study the fundamental aspects of electrical contact behavior, such as the relationship between contact force and the flow of current, without the influence of more complex mechanical factors of conducting loop. To investigate the influence of geometric parameters of conducting path on constriction factor, a series of steps on numerical simulation-based and experimental level were carried out. The aim of these investigations was to determine correction factors for literature references and to provide a clear understanding of the interaction between the applied contact force and the short-circuit current value for two different geometries of butt contacts – solid and hollow.

A. Simulation Model of Contact Systems

Because the contact interface is enclosed, the current constriction and the associated magnetic field cannot be observed directly. Therefore, a finite-element electromagnetic model was used as a supporting tool to compute the integral electrodynamic force from the volume distribution of current density (J) and magnetic flux density (B), i.e., $F = \iiint (J \times B)\, dV$.

Geometry and materials followed Fig. 4: two copper cylinders with welded $AgSnO_2$ (88/12) plates. The electrical current was applied through the cylinder ends, and the return path was represented by a remote reference boundary so that the calculated force captures the ‘blow-apart’ contribution of the butt interface rather than forces from a specific external busbar loop. Electrical conductivities for Cu and the contact plates were set according to standard material data. The contact interface was represented in two steps: (i) an idealized symmetric contact spot for the initial exploration; (ii) a measured contact-spot area (a-spot) implemented as a thin conducting disk/cylinder located on the contact axis for correlation to the experiment.

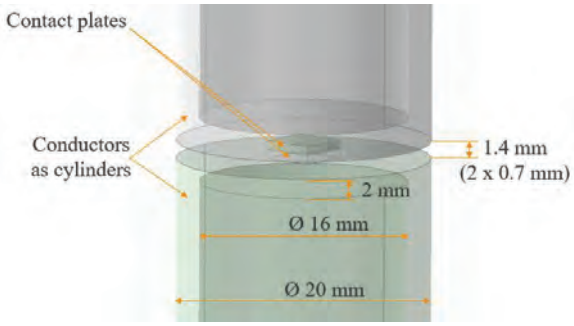


Fig. 4. Geometrical parameters of modeled contact systems

The model output used in this paper is limited to: (a) the spatial distribution of $|B|$ and $|J|$, as shown in Fig. 5, and (b) the resulting repulsion force. The model is not used to make claims about detailed current-stream redistribution inside the hollow cylinder wall. Frequency-dependent redistribution (skin and proximity effects at spectral components defined by the current rise time) is not explicitly quantified here and the geometry effect is demonstrated primarily by the measured levitation thresholds. To avoid over-interpretation, only the final force-current relationship derived from the model is retained in the paper.

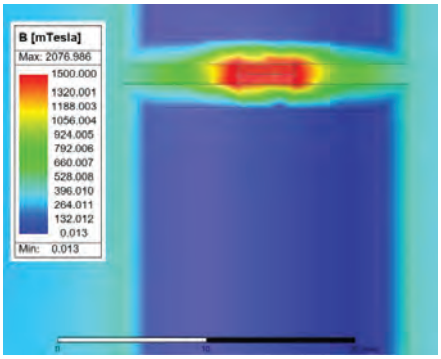


Fig. 5. Magnetic field distribution by current of 21.4 kA passing through modeled contact system

By the first iteration of the simulation, the relation between current and repulsion force was identified using the value of current stepwise with step of a 2.5 kA and up to 25 kA. Results of the described iteration steps are depicted in Fig. 6.

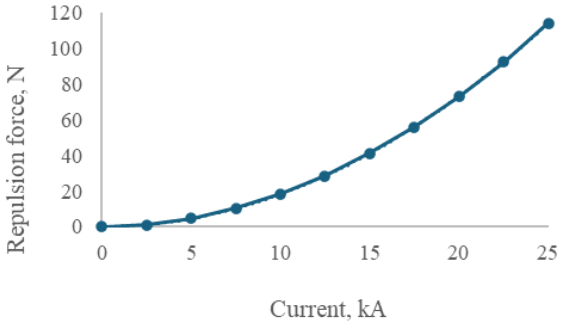


Fig. 6. Repulsion force in relation to the current value: calculation for hollow cylinders

B. Experimental Setup

On the next step, the calculated repulsion force was validated through a test on a specially designed setup. The setup for the measurement of repulsion force by defined contact force and short-circuit current value is presented in Fig. 7 and includes several key components to accurately assess the electrical and mechanical characteristics of the contact points. Here are the parts and elements used in the measurement setup:

- Copper cylinders: these are cylinders equipped with contact plates 4x4 mm made of $AgSnO_2$ 88/12 material by using the soldering process. $AgSnO_2$ 88/12 was assumed as the standard material for the study. Those contact plates are flat, parallel surfaces that press directly against each other. The bottom conducting cylinder was fixed and the top cylinder was movable. Both cylinders are integrated in specially designed plastic housings, which also provide additional guiding along the axis of the cylinders in case of lifting of contacts.
- Contact force mechanism: this system applies a controlled force to the contact surfaces to ensure they are pressed together with a known pressure. In the presented setup, the variation of the weight applied to the top cylinder was used for adjustment of the resulting contact forces.
- Measurement system for voltage and current: to measure electrical characteristics such as voltage drop and current flow through the contacts during the test the data acquisition system PICO device was used.
- Power supply: was represented by electric circuit, which provides the current required for the experiment.

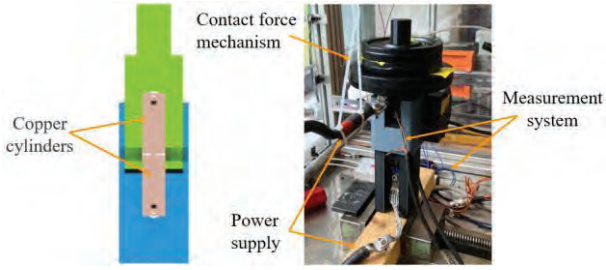


Fig. 7. Setup for the measurement of repulsion force by defined contact force and short-circuit current value

C. Test Procedure and Interpretation

At the first phase of every experiment, the contact force was set to a predetermined value using different weights. Compared to numerical simulations, the contact force in the experiment was only adjustable in discrete steps of 5–10 N, which resulted in a lower resolution of the experimentally determined repulsion force. After setting the contact force, a test current was applied, which was increased to a predetermined level. The current value was taken as the maximum load that could be consistently delivered by the power supply by 500 V and an upper limit of 21.4 kA. The maximum current level was chosen intentionally, since at lower current values, the effect of discrete steps in contact force adjustment becomes more noticeable, making it difficult to reliably identify the levitation threshold. Therefore, the key result of each test was evaluated qualitatively, pointing out whether separation of contacts occurred or not. During the test, the voltage drop between the cylinders and the corresponding current were measured. The duration of the current pulse was limited to 2 ms to avoid thermal overload and damage of the copper samples, while achieving the current value needed. Each test condition was repeated multiple times to ensure reproducibility

The most significant experimental parameter was the current value at which the contacts opened due to electrodynamic repulsion (i.e., the repulsive force exceeded the preset contact force). In addition, the onset of levitation was identified from the contact voltage: during stable contact the measured voltage remained at an elevated but comparatively constant level (≈ 1 V), while during levitation the voltage increased sharply and reached values > 12 V.

Because ≈ 1 V is above the classical melting voltage reported for clean Cu-Cu or Ag-Cu contacts (~ 0.43 V), its influence must be considered. In the present setup the contact plates are $AgSnO_2$ (88/12), and the measured voltage includes the dynamic constriction resistance of a non-ideal interface (oxide/film, real roughness) under a fast high-current pulse. Such conditions can raise the apparent ‘stable’ voltage above the clean-metal melting voltage. Nevertheless, a voltage level close to 1 V may still promote local melting and micro-welding before repulsion, which could bias the levitation threshold to higher currents (stronger holding by welded asperities) and/or increase the effective a-spot area.

Furthermore, the voltage is measured between the ends of the copper cylinders rather than directly at the microscopic contact interface. For the present geometry, a simple resistive estimate shows that the voltage drop along the two copper cylinders at 21.4 kA is on the order of 0.5 V. Consequently, the measured voltage represents an integral macroscopic

quantity and cannot be directly equated to the local melting or boiling voltage at the contact spot.

To analyse these effects and to interpret the results conservatively, the current pulse duration was limited to 2 ms, each condition was repeated, and post-test microscopy of the contact spot was performed. The experimentally measured a-spot area after a non-levitation pulse was then used as an input to the force calculation, which implicitly captures any enlargement of the conducting spot caused by transient melting/welding under the applied voltage. Therefore, the reported geometry comparison remains valid, while the absolute threshold currents should be understood as 'as-tested' values that may shift with different initial interface conditions or lower pre-arcing contact voltages.

IV. Results

A. Definition of Levitation Limit and Actual Spot Value

From the test series by the stepwise lowering of contact force the non-levitation threshold was defined as 129.4 N with a short-circuit current magnitude of 21.4 kA. A characteristic oscillogram of the test for hollow cylinders is shown in Fig. 8.

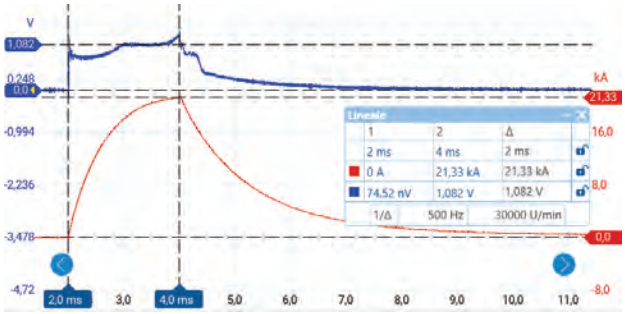


Fig. 8. Oscilloscope snapshot of the test by current of 21.4 kA for hollow cylinders

The red line represents the current value, and the blue line stays for the load voltage during the test. As it can be observed, the voltage increases in the last 200-300 µs of the current pulse, which demonstrates that the levitation threshold closely matches the applied contact force. The measurement showed that the applied contact force is high enough to withstand short-circuit current value of 21.4 kA without contact levitation.

The resulted contact surfaces after the short-circuit current test of 21.4 kA are presented in Fig. 9 (left). From the microscopic picture it could be clearly identified the melting area, which represents the actual a-spot for the applied contact force under adjusted short-circuit current level. The value of the contact spot size was measured using a microscope and has a value of 4.11 mm^2 as it is presented in Fig. 9 (right).

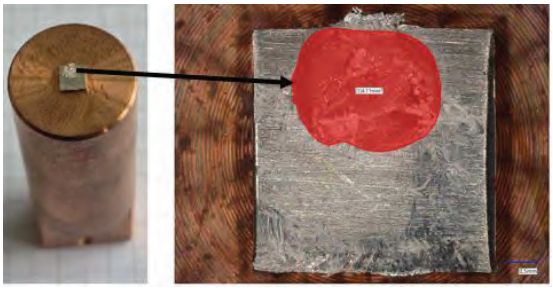


Fig. 9. Not levitated sample with generated a-spot after the test by current of 21.4 kA and contact force of 129.4 N (left) and microscopic measurement of the area of generated contact spot (right)

B. Influence of Actual a-Spot on Simulation Model

The measurement showed a significant difference in the levitation limit of 45.8 N between simulated (83.6 N) and tested (129.4 N) results. This discrepancy indicates that the actual a-spot for applied current level had a lower value than the one used in the simulation. It can be explained by less current constriction, which results in a lower repulsion force. Additionally, a higher contact area explains the lowering of the repulsion force, because distribution of the current by a bigger contact area decreases the density and value of the produced magnetic field and an interaction between generated magnetic fields is lower.

In an idealized system, we assumed to use an a-spot as cylinder which area is defined by the properties of the contact material, current value and contact force. Thus, the contact area measured after non-levitated condition in the model was substituted in the model between both electric contacts as a cylinder with a radius of 1.14 mm and a height 0,01 mm, placed symmetrically along the axis of cylinders. The small axial height was chosen to reflect an idealized contact interface during the short-circuit event.

The distribution of the magnetic field generated at the top and bottom contacts by the passing of short-circuit current and by the applying of an actual a-spot value is shown in Fig. 10. As expected, the distribution of these magnetic fields for both contacts corresponds to a certain extent to the distribution of currents, i.e., the highest repulsive force density occurs in areas with the highest current density.

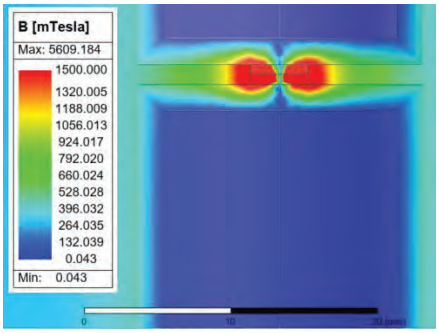


Fig. 10. Magnetic field distribution by current of 21.4 kA passing through modeled contact system with integrated contact spot

After substituting the experimentally defined a-spot area into the model, the second iteration of simulation showed precise agreement with the experimental results. The calculated repulsion force has a value of 133.2 N and was very close to the measured value of 129.4 N, demonstrating a strong correlation between simulation and experiment. This agreement validated both the applied simulation methodology and the importance of accurately representing the actual contacting area.

C. Influence of Conductor Shape on Repulsion Force

This section represents the main result of the study. For comparison reasons, the geometry of butt contacts was analyzed. The series of short-circuit current tests was repeated for solid (cross-sectional) and modified (hollow) shape of butt contacts.

Compared with a solid cylinder, a hollow cylinder forces the current to flow through a reduced effective cross-section and changes the proximity between opposing current streams near the butt interface. Therefore, the spatial overlap of current paths that produce repulsion is modified. In the present work, the geometry effect is quantified experimentally by the current level at which the repulsion force exceeds the applied contact force. Under identical outer dimensions and identical initial contact force, the hollow design reaches the levitation threshold at a lower current than the solid design, confirming that butt-contact conductor geometry is a first-order parameter for 'blow-apart' behavior.

The square factor *k* mentioned below, which depicting the dependence between repulsion force and current value for a hollow conductor obtained experimentally differs from the values used in classical formulas for calculation of repulsive force. This coefficient, which combines the repulsive force and the current value, is lower than the values for solid butt contacts and in case of current value of 21.4 kA and has a value of 2.8-2.9. Thus, the geometry of the conductor has a direct and measurable effect on electrodynamic repulsion, as shown in Table I. Hollow butt contacts demonstrate a reduction in electrodynamic repulsive force of approximately 26% compared to solid contacts under equal short-circuit current conditions. By the integration of the experimentally measured a-spot area into the numerical model, the simulated repulsion force corresponds closely to the value from the experiment, which confirms the validity of the proposed modeling methodology.

TABLE I. COMPARISON OF REPULSION FORCES FOR SOLID AND HOLLOW BUTT CONTACTS AT 21.4 KA

Geometry	**Method**	**Contact spot area, mm²**	**Repulsion force, N**	**Relative force reduction**
Solid	Experiment	-	176	Reference
Hollow	Simulation	16	83.6	-52.5%
Hollow	Experiment	4.11	129.4	-26.5%
Hollow	Simulation	4.11	133.2	-24.3%

V. CONCLUSION

The study confirms that geometric modification of butt contact geometry has an influence on electrodynamic repulsive forces during the short-circuit event. Hollow butt conductors decrease repulsion force by influencing the process of current constriction and magnetic field interaction, which is confirmed by simulation and experimental results.

Key findings of the study can be summarized as follows:

- constriction of carried currents is concentrated in the offered cross-section of the conductor,
- the hollow butt-contact geometry results in an experimentally observed reduction of the electrodynamic repulsion force by approximately 26% under identical boundary conditions,
- integration of the actual a-spot value in the simulation model increases the accuracy of the simulation results.

From the results, the relationship between current values and contact forces can be observed, which provides valuable insights for the development of future high-voltage devices. These insights could help in designing high-voltage devices that either eliminate levitation or reduce its impact.

Presented study has succeeded in minimizing the effects of electromagnetic repulsion due to short-circuit current by modification of the geometric parameter of the butt contact by extraction of the inner part of the solid cylinder. Offering a comprehensive framework for addressing short-circuit current challenges, this research sets the stage for further advancements in electric vehicle technology.

ACKNOWLEDGMENT

The author would like to express his deep gratitude to the teams of the laboratory, sample shop, and research and development departments at TE Connectivity site in Berlin, Germany for their invaluable assistance and guidance throughout this research. Additionally, the author would like to express special thanks to Dr. Matthias Kroeker and Roman Dietrich for their constant readiness to discuss theoretical aspects and explain practical results.

REFERENCES

[1] VW 80000 "Electrical and Electronic Components in Motor Vehicles up to 3,5 t, General Requirements, Test Conditions, and Tests", Issue 2021-07.

[2] Volvo Car Corporation "DESIGN PREREQUISITES, DC/DC, Booster Inverter, Contactor (S1)", Release Date 2021-09-21.

[3] P. Slade, *Electrical Contacts Principles and Applications*. Marcel Dekker, New York, 1999.

[4] C. M. Ewuntomah, J. Oberrath, "3D Simulation of Electric Arcing and Pressure increase in an Automotive HVDC Relay During a Short Circuit Situation," *2020 IEEE 66th Holm Conference on Electrical Contacts and Intensive Course (HLM)*, 2020, pp. 58-64.

[5] Holm R., E Holm E.: Electric Contacts: Theory and Applications. New York: Springer-Verlag, 4th ed., 2000.

[6] H. B. Dwight, *Electrical coils and conductors*. New-York-London, Mac Graw Hill Book, Co., 1945.

[7] A. F. Burkov and N. D. Kritskiy, "Raschet kontaktnykh sistem kontaktorov pri ikh rabote v spetsial'nykh rezhimakh," [*Calculation of Contact Systems of Contactors During Their Operation in Special Modes*], Dalpubvtuz, Vladivostok, Russia, 2007.

[8] P. G. Slade and E. D. Taylor, "The repulsion or blow-off force between closed contacts carrying current," in *Proc. 62nd IEEE Holm Conf. on Electrical Contacts*, Clearwater Beach, FL, USA, Oct. 2016, pp. 1–8.

[9] P. Barkan, A new formulation of the electromagnetic repulsion phenomenon in electric contacts at very high currents, in: *Proc. of the 11th ICEC Berlin, June 1982*, VDE-Verlag GmbH, pp. 185-188.

[10] G. N. Aleksandrov, V. V. Borisov et al., *Teoriya elektricheskikh apparatov [Theory of electrical devices]*. Eds. Moscow: Vysshaya Shkola, 1985.

[11] M. Bizjak, S. Kharin, and H. Nouri, "Influence of vapor pressure on the dynamics of repulsion by contact blow-off," *Proc. 21st Conference Electrical Contacts*, Sep. 9–12, 2002, pp. 268–275.

[12] A. Krätzschmar et al., "Gas dynamic processes as the main reason for contact levitations in switching of high operating overload currents", *24th Int. Conf. Electrical Contacts*, 2008, pp. 315-323.

[13] S. Lindmayer, J. Kramer, and R. Witzmann, "Experimental and Numerical Investigation of Contact Separation in High Voltage Relays," *IEEE Trans. on Components, Packaging and Manufacturing Technology*, vol. 9, no. 7, pp. 1421–1430, Jul. 2019.

[14] S. N. Kharin and M. Sarsengeldin, "Influence of Contact Materials on Phenomena in a Short Electrical Arc," *Key Engineering Materials*, 2012, vols. 510–511, pp. 321–329.

An integrated BEM-FEM simulation framework for the calculation of constriction resistances between rough surfaces

Robert Scherr
Central Laboratory
Weidmüller Group
Detmold Germany
robert.scherr@weidmueller.com

Thomas Wielsch
Central Laboratory
Weidmüller Group
Detmold Germany
thomas.wielsch@weidmueller.com

***Abstract*—The constriction resistance (CR) plays a key role in the design of electrical contact systems. Usually, attempts are made to minimize it in order to reduce the power loss-induced heating of electrical contacts. This can be achieved by increasing the normal force, which leads to a larger actual contact area between the two contact partners. In order to derive tangible design recommendations for contact systems, however, the relationship between normal force and constriction resistance has to be known.**

For this reason, an efficient simulation framework for the calculation of the constriction resistance from the contact between two rough surfaces depending on the normal force has been developed. At first, an open-source boundary element method (BEM) solver is used to calculate the elastoplastic contact between the two surfaces to determine the distribution of microcontacts. Based on this, the CR is calculated using a simplified finite element method (FEM) model for steady-state DC conduction.

As the FEM simulation was found to be the computational bottleneck, a novel area-preserving block aggregation algorithm was developed to downsample the determined contact areas and reduce simulation times. The correctness of the two simulation steps was verified using analytical solutions. Finally, CR predictions from the presented simulation framework were compared to experimentally measured values for a sphere-plane contact system.

***Keywords*—electrical contacts, contact mechanics, a-spots, numerical modeling, boundary element method, finite element method**

I. Motivation

The quality of electrical contact spots is crucial for the reliability of electrical engineering products. Therefore, it is important to generate an understanding of the physical phenomena at the interface in order to improve the design of electrical contact systems. A particularly important parameter to consider in this context is the contact resistance R, as it leads to a local heating of the contact spot based on ohmic losses and can therefore limit the performance of electrical contact systems.

In the case of an electromechanical contact between two rough surfaces, the contact resistance R results from the combination of the foreign layer resistance R_f and the constriction resistance R_c. The latter arises from the current flow through the interface being confined to the actual contact area, which is substantially smaller than the apparent one. Depending on the topography of the two surfaces, the actual contact area consists of numerous microcontacts, often referred to as a-spots [1].

In addition to the surface roughness and geometry of the two contact partners, the contact resistance also significantly depends on the normal force F. This relationship usually corresponds very well to the equation

$$R = KF^{-\gamma}, \tag{1}$$

which was empirically determined by Kesselring [2]. Here, K and γ represent material-, geometry- and surface-dependent parameters [3]. Since this correlation is crucial for the design of contact systems as used in connectors, for example, the aim of this work was to develop a simulation tool that can be used to predict the contact resistance based on the geometry, mechanical material properties and surface roughness of two contact partners as well as the normal force between them. The initial focus was placed on the numerical calculation of the constriction resistance. In a subsequent step, the influence of foreign layers will be implemented.

Early studies on calculating the constriction resistance of different contact geometries were conducted by Nakamura, who used the boundary element method (BEM) to do so [4], [5]. However the contact areas were specified as a given input in these works. Later, Leidner [6] developed a simulation software, in which the contact mechanics between coated surfaces was calculated using an approach based on Papkovich-Neuber potentials and various numerical solution methods such as the conjugate gradient method [7]. To determine the constriction resistance, the Laplace equation for the electric potential was then solved using the Gauss-Seidel method. Due to the limited computing power available at the time, calculations were typically performed with a lateral resolution of 128×128 data points.

Besides that, the finite element method (FEM) can also be utilized to calculate constriction resistances. McBride et al. [8] used an FE model developed in *ANSYS* to determine the real

contact area between rough surfaces. Subsequently, the Holm equation was employed to calculate the constriction resistance. In contrast, Zhang et al. [9] presented a combined electromechanical FE model developed using *COMSOL Multiphysics*, in which the FE method was used to calculate both the contact mechanics and electric potential distribution.

In this work, an efficient BEM-FEM simulation framework for calculating the constriction resistance between arbitrary rough surfaces is presented. In doing so, the performance advantages of the BEM for the contact mechanics calculations are exploited, while a commercial FEM software is employed for the steady-state current flow simulation due to its ease of use. We demonstrate how the coupling of the two simulation models can be implemented in a fully automated way and further present a novel method for downsampling the determined a-spots, while preserving the total contact area as precisely as possible.

II. Concept

A. Initialization

Fig. 1 shows an overview of the concept behind the developed simulation framework. In the upper half, a simplified flowchart visualizes the individual steps involved in calculating the constriction resistance, while exemplary images are depicted below. The framework was written in Python and uses common libraries such as *numpy*, *pandas* and *scipy*. At the beginning, the simulation parameters are initialized, with the material parameters – in particular, the Young's modulus E, Poisson's ratio ν and yield strength R_p – as well as the force values to be applied F_i being specified as part of the input.

Afterwards, the surfaces to be examined are defined. To do this, it is possible to either generate two surfaces with random roughness profiles or load real surfaces that have been previously scanned. For these, a resolution of 768×768 data points was typically used in this study. From the imported surfaces, the edge length L and grid spacing Δx can then be evaluated. As a next step, it is possible to apply a Gaussian low-pass filter with a defined cutoff wavelength λ to the surfaces in order to filter out any imaging artifacts and minor roughness features.

To increase the numerical stability, the simulation parameters are subsequently converted into a dimensionless unit system, in which E is used as the characteristic pressure-related quantity and L is taken as the characteristic length. For example, the unitless force F^* is calculated using $F^* = F/(EL^2)$. The final step in the preprocessing stage is setting up the simulation domain for the contact mechanics simulation using *numpy meshgrids*, in which the geometric discretization is determined by the distance between the measurement points of the imported surfaces Δx.

B. Contact mechanics

In order to solve the contact mechanics problem, the boundary element method (BEM) is used because it only requires the surface to be discretized. Also, the surface tractions are calculated directly at the interface rather than being derived from node displacements. The Python library *tamaas* [10] is used for this purpose, as it is based on highly optimized C++ code and thus offers a high level of performance. Additionally, its open-source nature provides flexibility in adapting the numerical methods.

The elastostatic deformation of the two contacting bodies can be described using the Navier-Cauchy equation [11]

$$0 = G\left(\Delta \boldsymbol{u} + \frac{1}{1-2\nu}\nabla(\nabla \cdot \boldsymbol{u})\right) + \rho \boldsymbol{g}, \tag{2}$$

with G being the shear modulus, $\boldsymbol{u}$ the displacement, ρ the density and $\boldsymbol{g}$ representing the gravitational acceleration. Within the framework of the BEM, a boundary integral equation (Somigliana identity [12]) can be derived for the displacement $\boldsymbol{u}$ at point $\boldsymbol{x}$ [13], [14]:

$$\boldsymbol{u}(\boldsymbol{x}) = \int_\Gamma \left[\boldsymbol{\mathcal{U}}(\boldsymbol{x},\boldsymbol{y})\boldsymbol{t}(\boldsymbol{y}) - \boldsymbol{\mathcal{T}}(\boldsymbol{x},\boldsymbol{y})\boldsymbol{u}(\boldsymbol{y})\right] \mathrm{d}\Gamma, \tag{3}$$

where $\Gamma = \partial\Omega$ stands for the boundary of the elastic body Ω, $\boldsymbol{t}$ for a surface traction vector and $\boldsymbol{y}$ denotes a point on the surface. In addition, the displacement and traction kernel functions $\boldsymbol{\mathcal{U}}$ and $\boldsymbol{\mathcal{T}}$, respectively, represent the half-space fundamental solution of elastostatics, such as the Boussinesq-Cerruti solution or the Westergaard solution. Numerically, the displacements at the surface are solved in the software according to the model by Rey et al. [15], in which an elastic energy functional is minimized using the conjugate gradient method [7].

During the subsequent evaluation, the deformation of the surfaces and the true contact area are determined, which is shown in white in Fig. 1 (bottom, second from left) as an example. The contact area is then saved as a 2D binary array in the form of a plain text file, which can be displayed graphically as a binary mask and is referred to as the contact mask in the following.

C. Stationary current flow

In the subsequent second simulation step, a FEM simulation of the DC current flow through the a-spots is performed to determine the constriction resistance (see Fig. 1, bottom right). For this purpose, the contact mask is read from the text file and mapped to a surface in the second simulation domain. The voltage drop across the contact surface is then determined by solving the Poisson equation

$$\nabla \cdot (\sigma \nabla V) = 0. \tag{4}$$

Here, σ stands for electrical conductivity and V for electric potential. Since this second simulation step has been found to be the numerical bottleneck, the contact mask can be coarsened in advance during the preprocessing. To do that, an algorithm that preserves the total contact area as precisely as possible has been developed.

For the DC conduction simulation, *COMSOL Multiphysics 6.1* is used, since this commercial software already offers efficient solvers and convenient methods for an optimized meshing of the geometry. This is done using the Java

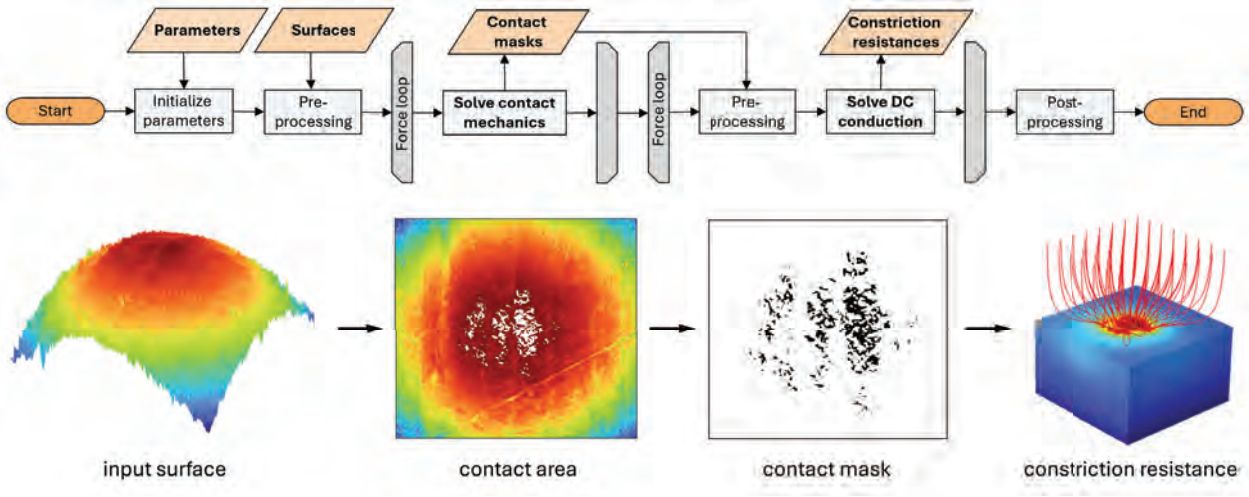


Fig. 1. Overview of the workflow of the developed simulation framework. Top: Simplified program flow chart. Bottom: Exemplary images showing the results of the contact mechanical and DC current flow simulation for a real surface. The red lines in the right-hand image represent the current density distribution.

API in order to automate the model setup, computation and evaluation. Based on the initially specified force values, the simulation workflow is repeated iteratively, using two separate force loops for the contact mechanical and current flow simulations, as this reduces the computational overhead and thus the simulation times. Finally, during the post-processing, all relevant results are plotted and saved.

III. BEM Simulation: Calculation of the Contact Area

To simplify the numerical problem, the equivalent sum surface method is used in the BEM simulation, i. e. the surface topographies of the two rough surfaces in contact are added together to create a sum surface, which is pressed against a smooth, rigid plane in order to calculate the true contact area [16]. This is based on a study by Greenwood and Tripp [17], who found that this simplified scenario is equivalent to the real contact situation if certain simplifying assumptions can be made, such as homogeneity, isotropy and linear elasticity of the material [10]. In doing so, the contact modulus E' has to be used instead of the Young's modulus, which is defined by

$$\frac{1}{E'} = \frac{1-\nu_1^2}{E_1} + \frac{1-\nu_2^2}{E_2} \tag{5}$$

using the two Young's moduli of the contact partners E_1 and E_2 as well as the corresponding Poisson's ratios ν_1 and ν_2.

The simulated contacts are assumed to be frictionless and without adhesion. In the following, pure Cu with the properties $E = 110$ GPa, $\nu = 0.3$ and $R_\mathrm{p} = 200$ MPa is used as the material of both contact partners. In addition, a hardness-limited pseudoplasticity model with a saturation pressure p_max can be applied, where $p_\mathrm{max} = 3R_\mathrm{p}$ is commonly specified [18]. In this context, Shi et al. [19] have shown that the equivalent sum surface model can still be reasonably applied when using such a perfectly plastic material model. After the contact computation, the true contact area A_c is calculated from the surface pressure field p_{ij} with the two indices i and j of the uniform grid with size $N \times N$ via

$$A_\mathrm{c} = \sum_{1 \le i,j \le N} \mathrm{sgn}(p_{ij}) \Delta x^2. \tag{6}$$

In order to verify the correctness of the employed boundary element method, numerical simulation results for a purely elastic Hertzian contact between a semi-sphere and a plane were compared to the corresponding analytical solution. The semi-sphere had a curvature radius of 50 µm, while the edge length of the simulation domain was set to 300 µm. The material was pure Cu and the applied normal force was specified as 30 N. With these values, the theoretical spherical contact area was calculated to be approximately 1390 µm².

Fig. 2 shows the comparison between the analytical solution and the numerically calculated values of the contact area for different discretizations. The results demonstrate that the simulated contact area approaches the analytical solution gradually as the grid becomes finer, until a relative numerical error of only approx. $2 \cdot 10^{-4}$ remains at a discretization of 5000×5000 grid points. This confirms that, in principle, the used BEM solver calculates elastic contacts correctly and the contact area is properly evaluated.

IV. FEM Simulation: Calculation of the Constriction Resistance

In the subsequent FEM simulation, the steady-state DC current flow through the previously determined actual contact area is calculated in order to determine the constriction resistance. To do this, the geometry shown in Fig. 3a is used. It consists of two cuboids stacked on top of each other with a total height of 250 µm, creating a horizontal internal boundary in the middle, onto which the contact mask is mapped to spatially modulate the local surface resistance ρ_s. In particular, the 2D binary array (which contains a 1 for each cell that is in contact and a

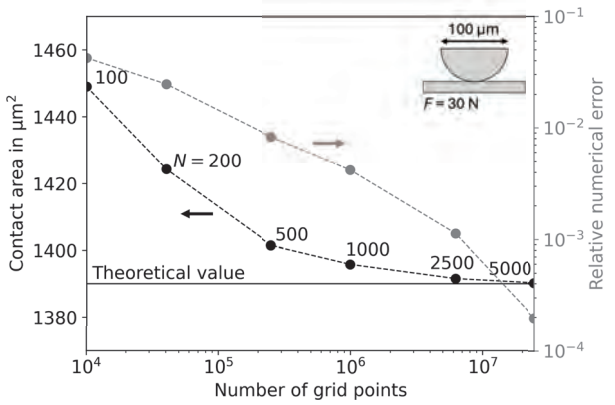


Fig. 2. Verification of the BEM simulation using an analytical solution for the contact area of an elastic Hertzian contact between a Cu sphere and a Cu plane at a normal force of 30 N.

0 otherwise) is read from the plain text file and used to create a 2D grid-based interpolation function $\mathcal{I}(x, y)$ for the local coordinate system (x, y). Based on this, ρ_s is defined as

$$\rho_s(x,y) = \begin{cases} \rho_1, & \text{if } \mathcal{I}\left(\frac{x}{\Delta x}, \frac{y}{\Delta x}\right) = 1 \\ \rho_0, & \text{if } \mathcal{I}\left(\frac{x}{\Delta x}, \frac{y}{\Delta x}\right) = 0\,, \end{cases} \tag{7}$$

where ρ_1 is set to 10^{-20} Ω·m² and ρ_0 to 10^{10} Ω·m². In order to resolve the surface resistance distribution with sufficient accuracy, the corresponding interface is meshed quadratically with an edge length of $L/(2N)$, while a tetrahedral mesh with the element size setting 'extra fine' is applied to the volume.

The lateral edge length is taken from the BEM simulation and therefore corresponds to the width of the scanned surfaces. To generate a stationary current flow, the lower horizontal boundary is grounded, while a constant current of $I_0 = 10$ A is applied to the upper one. The conductivity of the material σ is specified as 58 MS/m. Thus, the material-dependent bulk resistance has to be subtracted when evaluating the constriction resistance:

$$R_c = \frac{\Delta V}{I_0} - \frac{h}{\sigma L^2}, \tag{8}$$

with ΔV being the voltage drop across the entire domain. This setup was defined using *COMSOL* API commands and is stored as a template in the form of a Java source file, in which the necessary parameters (primarily L, N and Δx) are auto-adjusted by the developed Python framework. The source code is then automatically compiled and executed before the evaluated simulation result is returned and further processed.

To verify that the FEM setup also provides correct results – especially with regard to the definition of the current-carrying constriction in the middle plane – another verification simulation was performed. For this purpose, the geometry shown in Fig. 3b was used, which consists of an elongated cylinder with a diameter of $2a$ that contains a current-carrying circular area with a diameter of $2b$ in its center. In the case of an infinitely long cylinder, Rosenfeld and Timsit [20] derived an analytical solution for the constriction resistance:

$$R_\mathrm{c} = \frac{\rho}{2a}\left(1 - 1.41584\left(\frac{b}{a}\right) + 0.06322\left(\frac{b}{a}\right)^2 + 0.15261\left(\frac{b}{a}\right)^3 + 0.19998\left(\frac{b}{a}\right)^4\right), \tag{9}$$

which serves as a reference in the following. The analytical total resistance $R_\mathrm{tot}^\mathrm{ana}$ in dependence of the cylinder height was obtained from the sum of the constriction resistance according to (9) and the bulk resistance, which is calculated analogously to the second term of (8). Fig. 3b shows the comparison between $R_\mathrm{tot}^\mathrm{ana}$ and the numerically calculated total resistance $R_\mathrm{tot}^\mathrm{num}$ for different h.

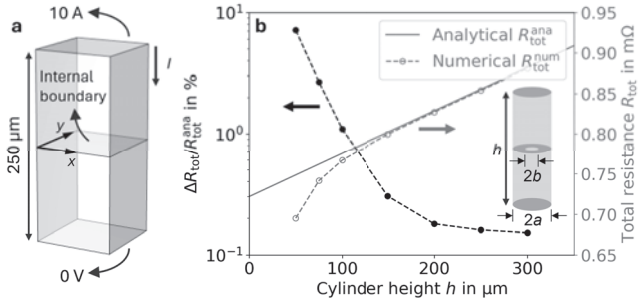


Fig. 3. (**a**) Geometry of the FEM simulation for the calculation of the constriction resistance by mapping the contact mask onto the internal boundary. (**b**) Verification of the FEM setup using the Rosenfeld-Timsit solution for a constricted cylinder [20], showing that a minimum height is necessary so that the numerical solution is not affected by the boundary conditions. The quantity ΔR_tot is calculated by $\Delta R_\mathrm{tot} = |R_\mathrm{tot}^\mathrm{num} - R_\mathrm{tot}^\mathrm{ana}|$.

As the cylinder height increases, the numerically calculated resistance value approaches the analytical solution, confirming that the developed method of mapping the contact mask to an inner boundary can indeed yield correct results. At the same time, however, it becomes apparent that if the height of the simulation domain is too low, the influence of the upper and lower boundary conditions on the current density distribution near the constriction plane lead to significant errors in the calculated constriction resistance. For this reason, the height of the FEM setup shown in Fig. 3a was set to 250 µm, which ensures a correct calculation of R_c.

V. Downsampling of the Contact Mask

In order to reduce the computation time of the FEM simulation step, an algorithm was implemented that coarsens the contact masks (i.e. the 2D binary arrays with a 1 for each cell that is in contact and a 0 otherwise) to a desired resolution. This is based on the block aggregation method, which is shown in Fig. 4a using an exemplary section with a black-colored contact area. In the illustrated case, a coarsening factor f of 2 was selected, which means that areas of 2×2 cells are merged into individual blocks. In the standard method, a fixed rule for the conversion is specified: The block is defined as contact area

if $f^2/2$ or more cells are contact cells. However, this leads to errors in the conversion of all areas that do not entirely consist of contact area or non-contact area, resulting in a potential accumulation of errors during the downsampling process.

Therefore, this method was modified as part of the presented work by means of two measures. Firstly, an alternating conversion to contact area or non-contact area, respectively, is performed consecutively for all areas that consist of exactly 50 % contact cells (ambiguous cases). Secondly, an error tracker ε was implemented, which stores the number of incorrectly lost or gained contact cells at each conversion process. Based on this, blocks at the edge of a-spots (in the von Neumann neighborhood) are randomly selected at the end of the downsampling procedure and converted to the other type in order to reduce the accumulated error. The number of blocks to be converted is given by $\lfloor \varepsilon / f^2 \rfloor$, while for the residual contact area error A_ε, we have $A_\varepsilon \leq (f^2 - 1)(\Delta x)^2 \propto f^2$.

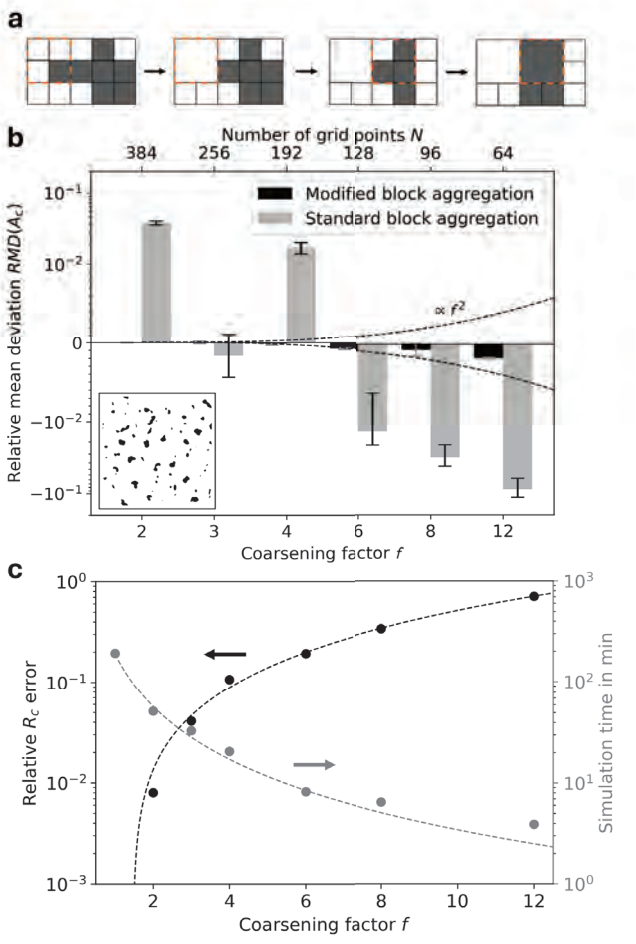


Fig. 4. (**a**) Schematic illustration of the block aggregation method for a coarsening factor f of 2. (**b**) Comparison of the contact area error between the standard and modified algorithm for different f. (**c**) Relative R_c error and simulation times in dependence of f.

Fig. 4b shows a comparison of the relative mean deviation of the contact area A_c between the coarsened contact mask and the reference for different f after using both the standard block aggregation method and the modified version. To generate the contact masks for each examined case, five different pure Cu surfaces with a width of $L = 100$ µm were elastoplastically deformed with a normal force of 1 N. The randomly generated 768×768 sum surfaces were based on a power spectral density (PSD) curve with the wave vectors $q_0 = 8\pi/L$, $q_1 = 16\pi/L$ and $q_2 = 64\pi/L$. The Hurst coefficient H was set to 1 and the RMS height was approximately 6 µm. Overall, it can be seen that the modified algorithm leads to significantly smaller errors, while consistently underestimating the contact area. This results from the contact area only covering a small fraction of the considered surfaces (see the inset of an exemplary contact mask in Fig. 4b), which favors the conversion to non-contact area for blocks at a-spot edges. With increasing f, the effect becomes stronger as the proportion of edge blocks increases. This phenomenon can also be observed when using the standard algorithm. For $f = 2$ and $f = 4$, however, the effect is superimposed by a strong overestimation of A_c due to the occurrence of a particularly high number of ambiguous cases with 50 % contact area, in which the blocks are always converted to contact area.

In order to assess which coarsening factors can reasonably be applied to the contact masks, the next step is to consider the f-dependent relative error of the evaluated contact resistance R_c in comparison to the uncoarsened reference, which is plotted in Fig. 4c for one exemplary sum surface. As expected, the error increases gradually with higher f. Since the maximum tolerated error was set to 1 % in this study, only a coarsening factor of 2 will be considered a viable option. At the same time, it can be observed that downsampling the contact mask saves a considerable amount of computation time. For example, with $f = 12$, the simulation time t is reduced from approximately 200 min to 4 min – but even with a f value of only 2, t already decreased to around 50 min, which is a reduction by a factor of 4. Here, it should be noted that only a single sample surface was examined and that a comprehensive evaluation with different real surfaces is necessary in order to make reliable statements.

VI. Experimental validation

After its development, the presented simulation framework was experimentally validated using the test setup shown in Fig. 5. It consisted of two pure Cu blocks that were pressed together in 1 N increments with a normal force between 3 N and 20 N, while the resistance was measured using the 4-point probe method. In order to create a defined sphere/plane contact geometry, a semi-sphere with a diameter of 6 mm was milled into the upper block, while a raised plateau was designed into the lower one. To minimize the influence of foreign layers on the measured values and to obtain a defined surface roughness, the contacting surfaces of the Cu blocks were deoxidized with a 10 % HCl solution and then ground with 320 grit sandpaper immediately before the experiments.

The prepared surfaces were then captured using the *Keyence VK-X1000* laser scanning microscope with a 20x objective

lens and a resolution of 768×768 grid points, so that the numerical comparison curves could be calculated. Before that, a Gaussian low-pass filter with a cutoff wavelength of $\lambda = 3\Delta x \approx 2.06$ µm was applied to the scanned surfaces. The true contact area was calculated elastically using the pure Cu parameters from Sec. III before the contact mask was coarsened with the coarsening factor $f = 2$. To generate the $R_c(F)$ curve, the input force array F_i was specified as ranging from 2 N to 20 N in steps of 2 N.

In order to ensure the comparability between the simulation results and the experimental measurements, the bulk resistance has to be taken into account. Using an additional DC current flow simulation, in which the experimental setup was precisely replicated, a value of 0.077 mΩ was calculated for that, which was added to the numerical curve. For statistical reasons, the experiment was repeated 15 times in total. Finally, Fig. 5 shows a comparison of the two determined $R(F)$ curves, which demonstrate a very good agreement. The only notable difference is the slightly flatter decline of the simulated curve, which is related to the smaller force exponent determined by fitting the data to (1). In addition to other experimental and numerical influencing factors, this can probably be attributed to the fact that a realistic plasticity model has not yet been implemented.

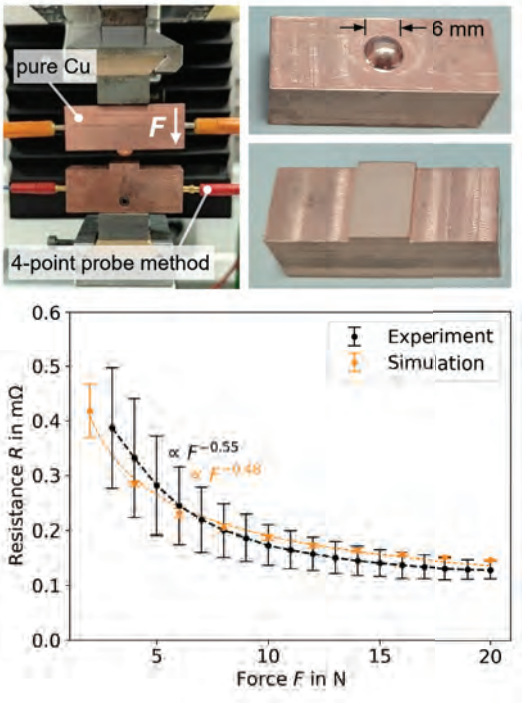


Fig. 5. Top: Depiction of the experimental setup for measuring the contact resistance of a pure Cu sphere/plane contact. Bottom: Comparison between the experimentally measured and numerically simulated $R(F)$ curves.

VII. Conclusion

As part of this work, an efficient BEM-FEM simulation framework for calculating constriction resistances was developed. Both simulation steps were successfully verified analytically. In addition, the first experimental validation tests yielded promising results. However, further validation is necessary to assess the applicability and limitations of the developed simulation tool. The next planned steps are the implementation of a realistic plasticity model and the consideration of coatings and oxide layers.

References

[1] R. Holm, *Electric Contacts. Theory and Application*. Heidelberg: Springer-Verlag Berlin, 1967.

[2] F. Kesselring, *Theoretische Grundlagen zur Berechnung der Schaltgeräte*. Berlin, Boston: De Gruyter, 1950.

[3] R. Scherr, M. Mainka, and T. Wielsch, "An analytical model for the total contact resistance of cross-contacted stranded conductors," in *2024 IEEE 69th Holm Conference on Electrical Contacts (HOLM)*. IEEE, Oct. 2024, pp. 1–8.

[4] M. Nakamura, "Constriction resistance of conducting spots by the boundary element method," *IEEE Trans. Compon. Hybrids Manuf. Technol.*, vol. 16, no. 3, pp. 339–343, May 1993.

[5] ——, "Computer simulation for the constriction resistance depending on the form of conducting spots," *IEEE Transactions on Components, Packaging, and Manufacturing Technology: Part A*, vol. 18, no. 2, pp. 382–384, Jun. 1995.

[6] M. Leidner, "Kontaktphysikalische Simulation von Schichtsystemen," Ph.D. dissertation, TU Darmstadt, 2009.

[7] I. A. Polonsky and L. M. Keer, "A numerical method for solving rough contact problems based on the multi-level multi-summation and conjugate gradient techniques," *Wear*, vol. 231, no. 2, pp. 206–219, Jul. 1999.

[8] J. McBride and H. Liu, "The relationship between contact resistance and roughness (sq) of a bi-layered surface using a finite element model," in *2020 IEEE 66th Holm Conference on Electrical Contacts and Intensive Course (HLM)*, 2020, pp. 176–181.

[9] C. Zhang and W. Ren, "Modeling of 3D surface morphologies for predicting the mechanical contact behaviors and associated electrical contact resistance," *Tribol. Lett.*, vol. 69, no. 1, Mar. 2021.

[10] L. Frérot, G. Anciaux, V. Rey, S. Pham-Ba, and J.-F. Molinari, "Tamaas: a library for elastic-plastic contact of periodic rough surfaces," *Journal of Open Source Software*, vol. 5, no. 51, p. 2121, 2020.

[11] L. D. Landau, L. P. Pitaevskii, E. M. Lifshitz, and A. M. Kosevich, *Theory of elasticity*, 3rd ed. Oxford, England: Butterworth-Heinemann, Jan. 1984.

[12] T. A. Cruse and W. Suwito, "On the somigliana stress identity in elasticity," *Comput. Mech.*, vol. 11, no. 1, pp. 1–10, 1993.

[13] F. Rizzo, "An integral equation approach to boundary value problems of classical elastostatics," *Quarterly of Applied Mathematics*, vol. 25, pp. 83–95, 1967.

[14] J. Chen, F. De Goes, and M. Desbrun, "Somigliana coordinates: an elasticity-derived approach for cage deformation," in *SIGGRAPH 2023*. New York, NY, USA: ACM, Jul. 2023, pp. 1–8.

[15] V. Rey, G. Anciaux, and J.-F. Molinari, "Normal adhesive contact on rough surfaces: efficient algorithm for FFT-based BEM resolution," *Comput. Mech.*, vol. 60, no. 1, pp. 69–81, Jul. 2017.

[16] P. Pawlus, R. Reizer, and W. Zelasko, "Prediction of parameters of equivalent sum rough surfaces," *Materials (Basel)*, vol. 13, no. 21, p. 4898, Oct. 2020.

[17] J. A. Greenwood and J. H. Tripp, "The Contact of Two Nominally Flat Rough Surface," *Proceedings of the Institution of Mechanical Engineers*, vol. 185, no. 1, p. 625–633, Jun. 1970.

[18] D. Tabor, *The hardness of metals*. Clarendon Press, 1951.

[19] X. Shi and Y. Zou, "A comparative study on equivalent modeling of rough surfaces contact," *Journal of Tribology*, vol. 140, no. 4, Mar. 2018.

[20] A. M. Rosenfeld and R. S. Timsit, "The potential distribution in a constricted cylinder: An exact solution," *Quarterly of Applied Mathematics*, vol. 39, no. 3, pp. 405–417, 1981.

Setup for electrical and mechanical characterization of copper junctions at the microscale

Jonas Diaz
Laboratory for Mechanics of Materials and Nanostructures
Empa
Thun, Switzerland
jonas.diaz@empa.ch

Toni Ivas
Laboratory for Advanced Materials Processing
Empa
Dübendorf, Switzerland
toni.ivas@empa.ch

Rafael Philipona
School of Biomedical and Precision Engineering
University of Bern
Bern, Switzerland
rafael.philipona@students.unibe.ch

Philipp Scheidegger
Laboratory for Transport at Nanoscale Interfaces
Empa
Dübendorf, Switzerland
philipp.scheidegger@empa.ch

Rolf Brönnimann
Laboratory for Transport at Nanoscale Interfaces
Empa
Dübendorf, Switzerland
rolf.broennimann@empa.ch

Jacim Jacimovic
Motion Services
ABB
Turgi, Switzerland
jacim.jacimovic@ch.abb.com

Johann Michler
Laboratory for Mechanics of Materials and Nanostructures
Empa
Thun, Switzerland
johann.michler@empa.ch

Lorenz Herrmann
Advanced Materials and Surfaces
Empa
Dübendorf, Switzerland
lorenz.hermann@empa.ch

Abstract— **The interplay between electrical and mechanical properties is an essential aspect of electrical contact phenomena. However, the complex correlation between them often makes it difficult to disentangle their effects at the microscale. In this work, we propose a simple nanoindentation setup complemented with custom-made copper tips to characterize copper-to-copper junctions under mechanical and electrical load. We do this by monitoring the evolution of their DC contact resistance. The accessible range of forces and currents in the setup translates into pressure and current density values comparable to those used in real-world applications such as busbar joints in electrical machines.**

Keywords—contact resistance, microscale, spreading resistance

I. Introduction

Improving our understanding of electric conduction between contacting surfaces is of both fundamental and technological interest. From a basic science perspective, the establishment of quantitative relationships linking material properties like composition and microstructure to functional performance remains challenging and is often approached phenomenologically. From a technologically perspective, the constant need for better performance and reliability in engineered electrical contacts, such as relays and switches, demands a finely tuned match between design, material selection and fundamental properties under relevant conditions.

A key aspect of electrical contact behaviour is the coupling between mechanical and electrical properties at the micro and nanoscale, since variables such as surface roughness, current-induced heating of contact spots and oxide layer formation greatly affect the overall performance of contact junctions and determine potential failure mechanisms [1,2]. Given the very precise control of mechanical loads and spatial displacements in modern nanoindentation instruments, it did not take long for the extension of this technique to also include electrical measurement capabilities [3,4,5]. In this so-called conductive nanoindentation, a rigid, sharp and conductive tip, often made from boron-doped diamond (BDD) or tungsten carbide (WC), penetrates the sample while the evolution of mechanical load, tip displacement as well as of current and/or voltage between tip and sample is monitored. This approach has been used to investigate topics such as fracture of oxide layers [6], performance of MEM switches [7], phase transformations in Si [1], nanoscale plasticity in GaAs [8] and film delamination [9]. These studies have focused mainly on thin films and semiconducting materials and devices. In this work we propose a further extension of the conductive nanoindentation setup to investigate the behaviour of bulk copper-to-copper junctions by fabricating custom-made copper tips and pressing them against samples of the same material to create a solid metallic junction. We chose copper as a test material given the possibility to machine it with relative ease and its prominence in electrical contact applications.

II. Experimental Methods

A. In-situ nanoindentation setup

A schematic view of the setup is shown in Fig. 1. The nanoindenter used was an Alemnis Standard Assembly (ASA) system, which employs a piezo actuator to carefully drive the indenter head (Z stage), together with the corresponding tip, towards the sample. A displacement and a load sensor precisely record the resulting tip displacement, h, and mechanical load, P, as the sample is pressed down. Resolution in the range of micronewtons and nanometres is typically accessible. Current and voltage leads were attached to the ASA system and connected to a Keithley 2400 DC source-meter. This instrument allows for precise voltage and current control and measurement, using both 2-point or 4-point configurations. The nanoindenter and the electrical leads can be fitted into a Scanning Electron Microscope

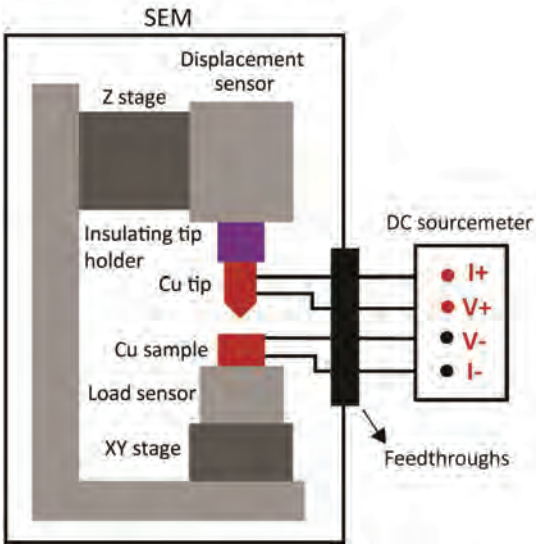


Fig. 1. Schematic of the in-situ measurement setup based on the Alemnis nanoindenter. A 4-point configuration for electrical sensing is shown.

(SEM), making it possible to observe the measurement process in-situ with high spatial resolution.

B. Cu tips

Specially designed copper tips were machined from Cu-ETP and fitted into the nanoindenter using a custom-made insulating tip holder made of commercial Macor. This machinable glass-ceramic material provides good mechanical stiffness (Young's modulus ≈ 65 MPa) and very good electrical insulation, which prevents the current from escaping through the instruments' frame. The tip design includes a hole where a screw is placed to mechanically fasten the electrical leads. After the conventional turning process to machine the Cu tips, these were further sharpened with a Xenon plasma focused ion beam (FIB) (see Fig. 2 (a)). The use of the plasma FIB with high currents allows for a relatively fast polishing of the tip and reduces the risk of ion contamination, which is more likely from the conventional Ga-sourced FIB. The result was a well-defined and very flat tip surface of roughly circular shape with a nominal area of approx. 29000 μm^2. Albeit smooth, the tip still shows the presence of vertical stripes or grooves that were formed during polishing with the FIB. This is a well-known effect, often referred to as "curtaining", and is caused by the presence of small irregularities on the top of the material's surface (where the ion beam initially hits the sample) that lead to spatial variations of the FIB milling rate. In this case, SEM images suggest that the depth of the grooves is typically in the sub-µm range. Although some rounding of the tip is inevitable, the estimated radius of curvature is well within the millimetre range. It is important to note that in contrast to traditional nanoindentation, where a sharp and rigid tip made of a hard material penetrates a softer sample, the use of a tip made from the same material as the sample means that the measured mechanical response will be that of the whole tip-sample system, i.e., the junction, rather than that of softer sample alone.

C. Bulk Cu samples

The samples studied in this work were cut from a commercial Cu-ETP busbar (typically used for industrial applications), sectioned into dimensions of approx. 10 mm x 25 mm x 10 mm and mechanically polished using conventional metallographic grinding methods. No ion beam milling was used after the mechanical polishing, so a native oxide layer in the nanometre range is expected to form on the surface. A typical smooth sample surface can be observed in Fig. 2 (b), where a regular loading measurement with the Cu tip is presented. The electrical leads were attached to the samples using a highly conductive silver paste.

III. Results and Discussion

A. Consecutive loadings on the same spot

Fig. 3 shows the mechanical response of the tip and sample junction during loading, while sourcing a constant current, *I*, of 500 mA (*I*-bias mode) in a 4-point configuration. This value of *I* corresponds to a nominal current density magnitude, *J*, on the order of $J \approx 10^7$ A/m^2, comparable to those found in certain industrial applications such as high-power transmission. In this case, a maximum force of 800 mN was applied in two consecutive steps at the same sample spot. The purpose of this was to examine the evolution of contact conditions with successive measurements. Considering the nominal tip area, this load magnitude corresponds to a pressure of ≈ 28 MPa, which is similar to those found in real bolted joints [10].

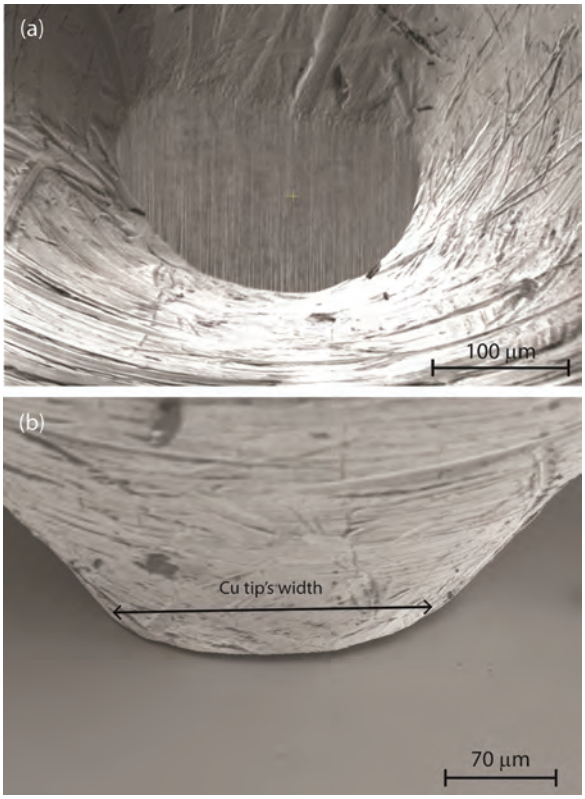


Fig. 2. SEM images of Cu tip and sample. (a) Tip after polishing with the Xenon plasma FIB. (b) Tip approach to the sample during a loading measurement.

The initial load-displacement, *P-h*, curve (Loading 1) shows a broad curvature at lower forces during loading, followed by a more linear dependence as the force increases to its maximum and eventually goes back to zero during unloading. This kind of broader feature at the beginning of the *P-h* curve is known to occur in mechanical

nanoindentation using flat tips, and it is caused by the misalignment between the flat surface of the tip and the surface of the sample. In those cases, the broadening is usually smaller since the dimensions of the tips are also smaller. In this case, given the relatively large radius of the tip, the same effect of misalignment is expected to be more pronounced.

The successive *P-h* curve (Loading 2) exhibits a much sharper curvature at low forces, with the linear (elastic) behaviour starting quickly and covering most of the load and unloading sections. This difference could be explained by improved contact conditions after the intial loading step, in particular, by the flattening of parts of the tip that were initially responsible for the broad feature observed during the initial loading (Loading 1). This flattening is consistent with the more prominent (yet still small) plastic contribution of the *P-h* curve in Loading 1 compared to Loading 2. In this regard, it is important to mention that given the dimensions of the tip and the maximum force used, it is expected that no overall plastic deformation take place when the whole tip area is the area of contact. The maximum pressure at the tip (≈28 MPa) is well below the typical yield strength of copper (≈100 MPa). This is consitent with the linear behaviour of the *P-h* curve in Loading 2, and the absence of any visual feature of large plastic deformation on the sample after such loading step. After Loading 1, small but discernible features (a few μm in size) of plastic deformation and residual material were observed on the sample, especially around the perimeter of the tip, suggesting that this was the initial area of contact.

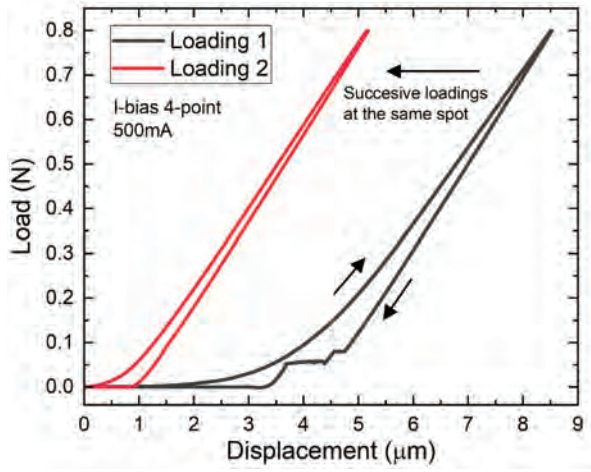


Fig. 3. Load-displacement curve for two consecutive loading measurements, sourcing 500 mA of current and measuring voltages in a 4-point configuration. The arrows indicate the loading (up) and unloading (down) directions.

The evolution of the corresponding measured resistance and mechanical load with time is presented in Fig. 4. The resistance includes a contribution from the bulk resistance of the tip and the sample. To estimate this contribution, we performed finite element simulations with COMSOL considering the tip and sample geometry as a single system made of copper. For a sourced current of 500 mA (same as in the experiment) and a nominal circular tip area with a radius of 100 μm, the simulations showed a voltage drop of around 70 μV for the bulk contribution. This is about 25 times smaller than the measured voltage (itself in the order of 2mV), suggesting that the bulk affects only weakly the overal voltage signal.

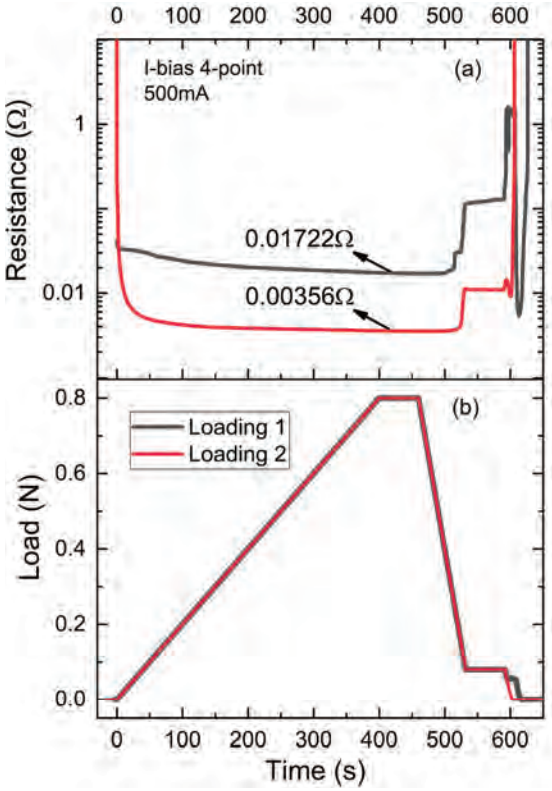


Fig. 4. (a) Resistance and (b) load vs time during the same measurement steps presented in Fig. 3.

Fig. 4 (b) shows in detail the applied load profile (for both Loading 1 and 2), which includes a linear loading section at 2 mN/s, followed by a holding section of 60 s at maximum force, then an unloading section to 80 mN at 10 mN/s with an additional 60 s holding section at that load, and a finally a fast retraction of the tip. These sections are also mirrored on the curve of the measured resistance, further supporting the assumption that the voltage signal is mostly driven by the contact resistance, R_c. The initial touching point is marked by a sharp jump in resistance from the open circuit configuration (no touch). A similar feature is observed when the tip finally detaches from the sample. Furthermore, the evolution of the contact conditions discussed previously is also manifested in the measured resistance. As can be seen in Fig. 4 (a) the Loading 2 step led to smoother resistance dependence with load (especially at lower loads) and to resistance values almost five times lower than with Loading 1. This sensitivity to resistance evolution opens the door to studies of mechanical cycling and its effects on electrical performance using the current setup.

B. Voltage-current (VI) curves and contact resistance load dependence

VI curves are important indicators of the junction's behaviour, most importantly, regarding their Ohmic character. In this section, we present results of VI curve measurements, with particular emphasis on the relatively low-load regime where the formation of contact spots is more precarious and the contact resistance tends to be more

unstable. Fig. 5 (a) shows the resulting VI curves, measured on ten steps of constant load during a single loading cycle from 4 mN up to 40 mN, and by sweeping the current up to 500 mA with both polarities. The Ohmic nature of the junctions is clear for all the load values explored, suggesting the formation of a solid metallic junction over the whole current range. It is plausible that the formation of such Ohmic contacts is further aided by the high maximum currents used during the VI sweeps of Fig. 5 (a). The local Joule heating can lead to softening and eventual melting of local asperities, increasing the effective area of contact and thus lowering the resistance across the junction [11]. This is consistent with the observation of strong adhesion during the retraction of the Cu tip, although a causality link between current magnitude and adhesion strength is not yet clear. To estimate the increase in temperature ΔT on the contact (from ambient temperature), the Kohlrausch relation [1] can be applied:

$$\Delta T = V_c^2 \sigma / 8\lambda \qquad (1)$$

Where V_c is the applied voltage across the contact, σ is the electrical conductivity and λ the thermal conductivity. Using the maximum voltage present in the VI curves (around 4.5 mV) ΔT is only in the order of 0.4°C, suggesting that thermal softening of the local asperities might not be a dominant effect in this case.

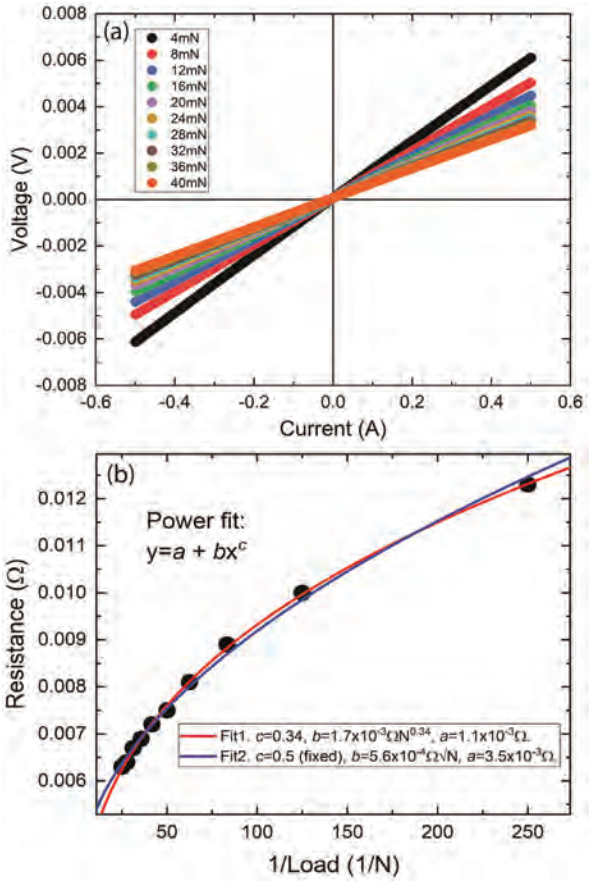


Fig. 5. (a) VI curves at different constant loads and (b) corresponding resistance vs inverse loads. In (b), *Fit1* corresponds to a fit of all parameters of the indicated power function, while *Fit2* corresponds to a fit with c=0.5 fixed, as predicted by (1).

It is interesting to explore the load dependence of the measured resistance, as calculated from the slopes of the VI curves in Fig. 5(a). In the standard Holm's theory, the magnitude of the contact resistance depends on the contact area, which in turn depends mainly on the plastic deformation of the surface asperities. Such deformation is naturally related to the hardness, H, of the material and an expression for R_c can be written in the following form [1]:

$$R_c = (\rho^2 \eta \pi H / 4P)^{1/2} \qquad (2)$$

Where, ρ is the electrical resistivity and η an empirical coefficient of order unity for clean surfaces. Fig. 5 (b) shows the contact resistance versus the inverse mechanical load, $1/P$, alongside two different associated data fits. The fits correspond to a power function of the form $y = a + bx^c$ and follow the functional dependence of (2) on the inverse load. In the first fit, *Fit1*, all independent variables are fitted, resulting in an exponent value of c =0.34 and an overall good agreement between the measured data and the fit model. The exponent found is not too distant from the value of c = 0.5 predicted by Holm's theory in the very simplified case of clean surfaces in contact, without additional factors such as contaminant elements or oxide layers. These factors can lead to load dependencies different to the one expressed in (2). In the second fit, *Fit2*, presented in Fig. 5 (b), the exponent c is kept fixed at the value c=0.5. A relatively good agreement with the data is also observed in this case, with a fit parameter $b \approx 5.6\text{x}10^{-4}$ $\Omega\sqrt{\text{N}}$ that compares rather well with the theoretical value of $\approx 5.8\text{x}10^{-4}$ $\Omega\sqrt{\text{N}}$ predicted by (2) (taking η=1, H_{Cu}=1.5 GPa and $\rho_{Cu}=1.7\text{x}10^{-8}$ Ωm). Overall, these results suggest that the experimentally observed load dependence of the measured resistance is consistent with the basic force scaling of the contact resistance in Holm's theory, supporting the picture that the electrical contact in the load range investigated is predominantly determined by plastically deformed microcontacts. Holm's theory thus provides a suitable physical basis for describing the observed contact behavior, even though exact quantitative agreement might require additional effects.

C. Discharge effects

To further showcase the capabilities of the setup, in this section we report the observation of discharge phenomena during a loading experiment with an initial voltage bias of 20 V. Fig. 6 (a) shows SEM images of the junction after a load profile similar to the one presented in Fig. 4(b) was applied. Fig. 6 (b) shows SEM images of the tip after it was removed from the setup for postmortem analysis. Residues of localized molten material are clearly visible and highlighted on both sample and tip. During the loading step, no electrical signal was measured up to ≈ 300 mN, that is, the junction behaved as an open circuit. This could have originated from insulating films or oxide layers that eventually suffered an electric breakdown and led to a sudden discharge and material transfer around the area highlighted in Fig. 6. After this, the contact resistance jumped down rapidly to around 2 Ω, with a total current of 100 mA passing through the junction (*I*-bias mode). This overall behaviour is consistent with the phenomenon of fritting, where current-conductive channels are formed after the voltage breakdown of an insulating film present on the metal surface [1,12]. Recent studies on Al-Sn point contacts with a similar geometry to the one presented here have highlighted the role of fritting in the complex set of mechanisms governing the evolution of contact resistance [13].

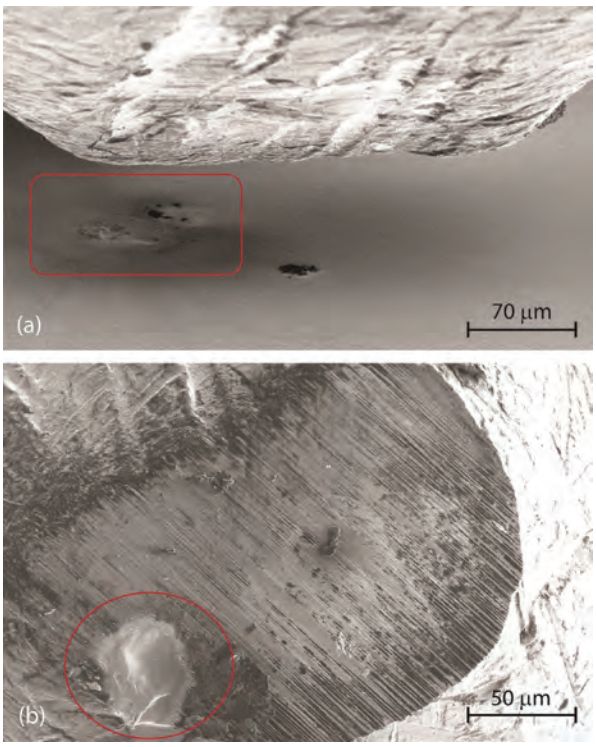


Fig. 6. SEM images of (a) the junction and (b) the Cu tip (postmortem) after a discharge event (highlighted in red).

Mechanically, a jump was also observed in the load and displacement signals. Upon increasing load as well as during the unloading section, the contact resistance remained rather close to 2 Ω albeit showing some irregular behaviour. The observation of this kind of fritting phenomena with our setup is encouraging and points to potential experiments where they can be investigated further by, for example, optimizing the tip design and dimensions to induce discharge under lower voltage and/or current values, as well as improving the cable shielding on the electrical leads, which can also pick up spurious voltages during rapid signal changes.

IV. Conclusions

In this work we have presented a modified conductive nanoindentation setup for the in-situ investigation of DC electrical contact resistance in copper-to-copper junctions under mechanical load. By incorporating a copper tip into the nanoindenter, the junctions could be formed and characterized continuously at the microscale thanks to the high resolution of the instrument. Additionally, since both tip and sample were prepared from bulk copper, the material characteristics of the junction resemble more closely those of real-world conditions. This avoids the potential material and microstructure differences faced in other approaches where micro-junctions are prepared by methods such as physical vapor deposition or sputtering. We successfully monitored the evolution of the contact resistance and could correlate it with changes in the mechanical contact conditions after successive loading steps, as well as characterize the Ohmic character of the junction over a large current interval. The load dependence of the contact resistance is consistent with Holm's theory, which further validates the proposed setup as a suitable tool for measurements of this property. The approach presented in this work offers a great deal of versatility for future investigations, thanks to the possibilities of changes in tip and sample design (using the FIB or other relevant methods), the wide range of option for mechanical loading profiles (for example, to explore fatigue cycles), as well as compatibility with other in-situ analytical tools that could provide fruitful insights into the behaviour and performance of electrical contacts.

Acknowledgment

The authors would like to thank Thomas Rytz and Peter Ramseier for their assistance preparing the bulk Cu samples, and Tijmen Vermeij for his help in polishing the Cu tips with the FIB.

This work has been supported by Innosuisse Innovation Contract 114.696 IP-ENG.

References

[1] Paul G. Slade, "Electrical Contacts: Principles and Applications", 2nd Edition, CRC Press, Boca Raton, 2014.

[2] Q. Huang et al, “Research progress on the characteristics of current-carrying tribology in electrical transmission”, Space Solar Power and Wireless Transmission, vol. 1, pp. 37-47, 2024.

[3] S. Ruffel, J.E. Bradby, J.S. Williams and O.J. Warren, “An in situ electrical measurement technique via a conducting diamond tip for nanoindentation in silicon”, J. Mater. Res., vol. 22, pp. 578-586, 2007.

[4] S. Comby-Dassonneville et al, "Development and Application of a Multifunctional Nanoindenter: Coupling to Electrical Measurements and Integration In-Situ in a Scanning Electron Microscope", 2019 IEEE Holm Conference on Electrical Contacts, pp. 1-8, 2019.

[5] J. George, S. Mannepalli and K. S. R. N. Mangalampalli, “Understanding Nanoscale Plasticity by Quantitative In Situ Conductive Nanoindentation”, Adv. Eng. Mater., vol. 23, 2001494, 2021.

[6] D. D. Stauffer et al., “Plastic response of the native oxide on Cr and Al thin films from in situ conductive nanoindentation”, J. Mater. Res., vol. 27, pp. 685-693, 2012.

[7] Adrien Broué et al., “Multi-physical characterization of micro-contact materials for MEMS switches”, 56th IEEE Holm Conference on Electrical Contacts, pp. 1-10, 2010.

[8] R. Nowak et al, “An electric current spike linked to nanoscale plasticity”, Nature Nanotech., vol. 4, pp. 287–291, 2009.

[9] H. H. Nguyen, P. J. Wie and J. F. Lin, “Electric contact resistance for monitoring nanoindentation-induced delamination”, Adv. Nat. Sci: Nanosci. Nanotechnol., vol. 2, 015007, 2011.

[10] M. B. Marshall, R. Lewis and R. S. Dwyer-Joyce, “Contact Pressure Distribution in Bolted Joints”, Strain, vol. 42, pp. 31-43, 2006.

[11] A. Fortini, M. I. Mendelev, S. Buldyrev and D. Srolovitz. “Asperity contacts at the nanoscale: Comparison of Ru and Au”, J. Appl. Phys., vol. 104, 074320, 2008.

[12] M. Braunovic, V. V. Konchits and N. K. Myshkin, "Electrical Contacts: Fundamentals, Applications and Technology", CRC Press, Boca Raton, 2006.

[13] M. Oberst, C. Hildmann and S. Schlegel, "Deterioration and Breakdown Mechanisms in force-fitted current-carrying Connections between Aluminum and Tin", 66th IEEE Holm Conference on Electrical Contacts, pp. 1-7, 2021.

Mass Transfer from a Molten Metal Bridge to Opening Electrical Contacts

Paul C. Slade
paulslade@verizon.net

Roland S. Timsit
Timron Advanced Connector Technologies
Toronto, ON, Canada M5M 1L6
rtimsit@timron-inc.com

Abstract— **The formation of a molten metal bridge on opening a current-carrying electrical contact is a well-known phenomenon. The continuing parting of the bridge as the contact surfaces separate eventually leads to bridge rupture and deposition of contact material on the cathode and anode surfaces. Bridge rupture is followed by arc formation in the metal vapor released by the ruptured bridge if the voltage across the separated contact is sufficiently large. The subsequent arc erosion of the electrodes often prevents a measurement of the amount of bridge material deposited on each of the separating surfaces after rupture. This paper describes the use of radioactive tracers to measure the amount of material deposited on the cathode and the anode of separating contacts about one hundred nanoseconds after bridge rupture. From observations on Ni, Au and Pt-Ir contacts, it was determined that there is a preferred transfer of bridge material to the cathode contact. It is proposed that this preferential mass transfer to the cathode stems from an electromigration mechanism within the molten bridge before rupture.**

Keywords—molten contact bridge; contact resistance; arcing ; electromigration

I. INTRODUCTION

When two electrical surfaces consisting of the same material are brought together with a force F the resistance R_C at the point of contact is given by [1,2]:

$$R_C = \frac{\rho}{2}\sqrt{\frac{\pi H}{F}} \quad (1)$$

where H and ρ are respectively the microhardness and the electrical resistivity of the contact material. When a current I passes through the contact spot, the contact voltage U_C is given by:

$$U_C = R_C I \quad (2)$$

In accordance with Eq.(1), the contact resistance increases if the contact force F is gradually decreased. If the current is maintained constant while F is decreased, the voltage drop U_C across the contact also increases. At some juncture while the contact force is being decreased but the mating surfaces are maintained in contact, U_C eventually reaches the melting voltage U_M of the contact material (e.g. for Ag, U_M = 0.38V and for Cu, U_M = 0.45V [3]). At this point, the region of contact melts, thus leading to rapid local mixing of materials from the contacting surfaces. If the contact surfaces are now separated slightly while electrical current flow is maintained, a column of liquid metal forms between the separated surfaces. The liquid column is sustained if the separation gap remains small. As the separation gap increases and the electrical current is maintained through the molten metal, the length of the molten column continues to increase the molten metal bridge [4]. During this stage it is reasonable to assume that the bridge contains equal volumes of metal from both contacts. As the surfaces continue to part the voltage across the bridge increases and so does the average temperature within the molten column. The temperature may not be uniform along the liquid bridge since the ends of the column are rooted to slightly cooler solid. Eventually the liquid bridge becomes unstable and ruptures.

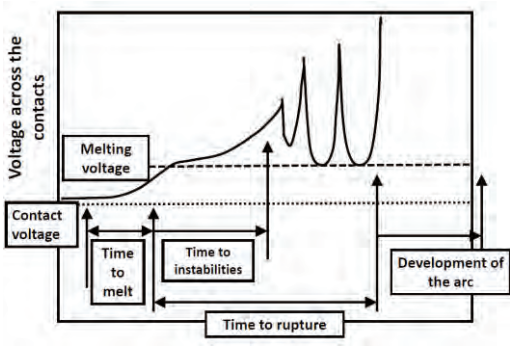


Fig. 1. Voltage waveform across contact surfaces as they separate.

The changes in the voltage drop across a separating contact are illustrated schematically in Fig. 1. As the surfaces begin to separate after the contact melting temperature U_M is reached, the voltage U_B across the liquid bridge increases beyond the melting temperature to the boiling temperature of the metal. During the temperature ascension, the liquid bridge becomes increasingly unstable as indicated by the rapid voltage fluctuations in Fig. 1, and eventually ruptures. It is worth pointing out that the voltage fluctuations probably lead to corresponding rapid temperature fluctuations within the evolving liquid metal bridge before rupture.

Figure 2 shows an example for an Ag contact opening a 1kA circuit. The molten metal bridge is clearly visible as the contact surfaces separate in (a) and (b), followed by rupture and (c) the subsequent expansion of the high-pressure metal vapor [5]. The voltage across the contacts at the time of rupture is close to the boiling voltage U_B of the contact material (e.g. for Ag, U_B = 0.75V, for Au, U_B = 0.9V, and for Cu, U_B = 0.8V [6]). Immediately after the molten bridge ruptures a region of very high-pressure metal vapor (~ 100 atmospheres) exists between the contacts [4] which transitions into an arc formed in the vapor of the contact material.

Measurements of metal transfer from the liquid metal bridge

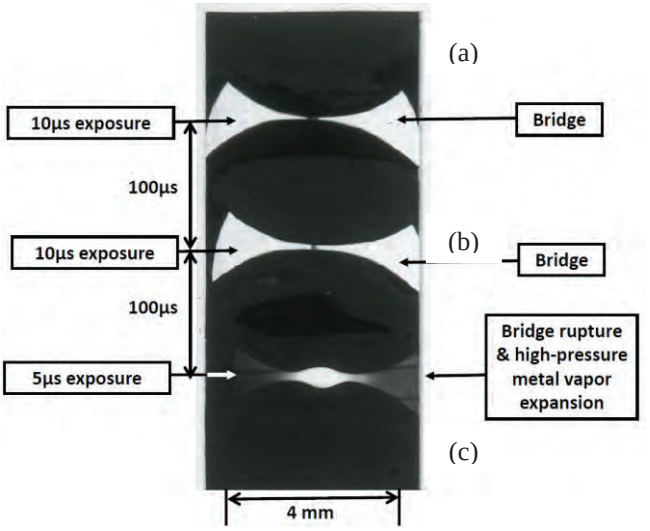


Fig. 2. Images of the molten metal bridge formed in an Ag-Ag contact passing 1kA, at increasingly longer time intervals (a)-(c) after separation.

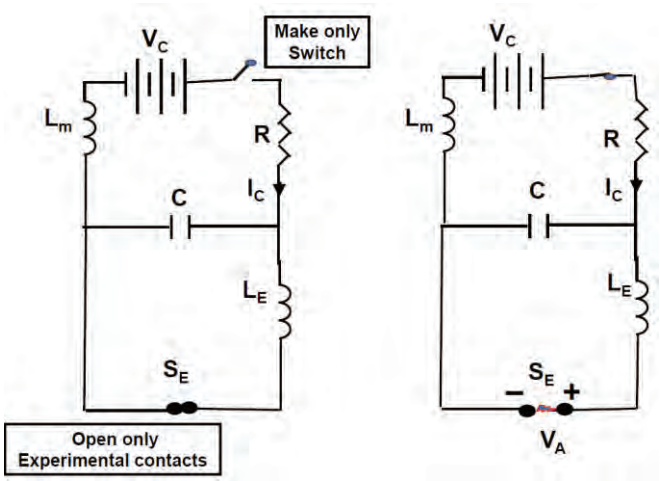


Fig. 3. Low voltage DC circuit used to determine the contact erosion as the experimental contacts open.

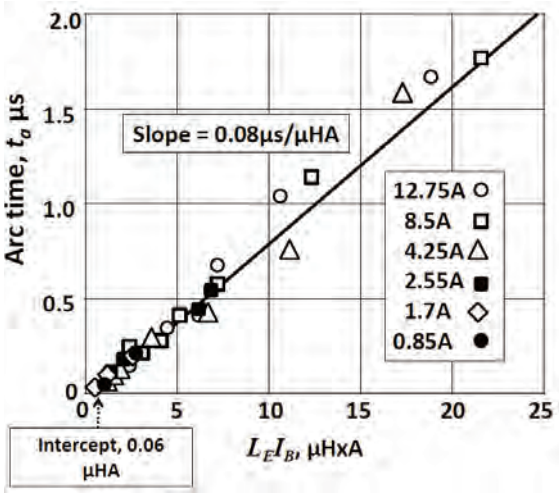


Fig. 4. Duration of the short arc function of L_E x I_B

to the separating electrodes are unavailable. It was initially thought that rupture of the molten metal bridge resulted in a net gain of contact material on the cathode from the accumulation of positive ions from the conducting liquid metal bridge [7]. This is certainly true for very low dc currents [8,9]. However, for currents greater than a few tens of milliamperes an electric arc always develops between the separating contacts, even at voltages only slightly larger than about 16 V [4]. Under these conditions, the measurement of material gain or loss on the separating surfaces due to metal transfer from the liquid bridge is difficult because it is obscured by mass transfer caused by arcing. This paper describes an experiment that allows the accurate measurement of material deposited on the cathode and anode of a separating contact after a time interval of only tens of nanoseconds after bridge rupture for currents ranging from 1A to 25A in Ni, Au, and Pt:Ir contacts, thus avoiding the obscuring effect of metal transfer from arcing. The high accuracy of the measurements allows the exploration of electromigration as a material transfer mechanism in a liquid metal bridge during contact opening, as proposed by Timsit [10].

II. EXPERIMENTAL

The examination of metal transfer from one contact to the other when opening a dc circuit was carried out using the low voltage dc circuit described by Slade [11] and shown in Fig.3. Here U_C (V_C in Fig. 3) is 6V, I_C varies from 1A to 25A, C has a capacitance of 4µF. The capacitor C across the experimental switch, S_E, absorbs the voltage surge that can result from the inductance in the main circuit when S_E interrupts the current. The contact opening speed was relatively slow. Riddlestone [12] calculated that the voltage U_A that forms as the contact opens depends only upon the local inductance L_E. In the circuit of Fig. 3, we have L_E = 0.09µH. The duration t_a of the voltage after rupture of the molten metal bridge is then calculated as [13]:

$$t_A = \left\{\frac{L_E}{R}\right\} log_e \left\{\frac{U_A - U_B}{U_A - U_C + U_0}\right\} = \left\{\frac{L_E I_B}{U_C - U_B}\right\} log_e \left\{\frac{U_A - U_B}{U_A - U_C + U_0}\right\} \quad (3)$$

or

$$t_A = K L_E I_B$$

where U_0 is the voltage at current zero and I_B is the circuit current at the time of the bridge rupture. Here U_0 equals zero. As examples for Ag and Cu, where U_A is respectively 12 V and 13 V, and U_B is 0.75 V and 0.8 V respectively for the two metals, the calculated value of K varies between 0.12 and 0.11 µs/µH-A. As indicated in Fig. 4, the measured value is K = 0.08 µs/µH-A for Ag and Cu contacts [11]. So, for the value of L_E of 0.045µH in Fig. 3, and for a current I_B of 8.5A, t_A = 0.05µs. This is a very short arcing time, thus causing an insignificant amount of metal deposition. An example of the variation of the voltage across the separating contact for the case of Au as a function of time I_B = 8.5 A is shown in Fig. 5.

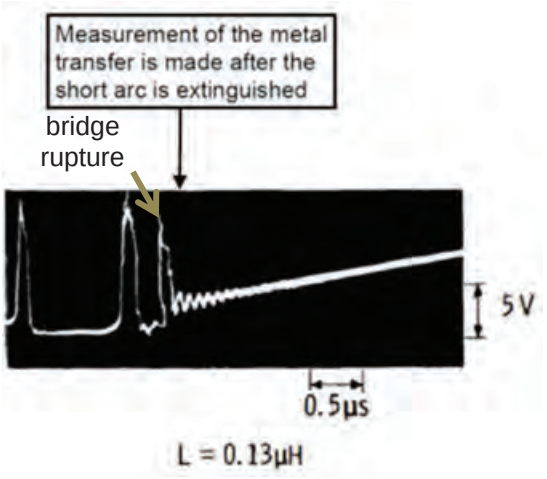


Fig. 5. Time after the molten metal bridge rupture and duration of the subsequent short arc during which the metal transfer to the cathode and the anode is measured (for the condition with L_E = 0.13 µH and I_B = 8.5A).

Once the molten metal bridge ruptures, the high-pressure metal vapor expands. The expansion of the metal vapor is limited by the speed of sound in air (340m/s) [5]. Metal deposition occurs by ionic conduction and direct deposition on the electrodes from the liquid bridge before rupture. Measurements of metal migration between the contacts are measured after the short arc is extinguished. For the currents in this experiment the average amount of material measured per operation is very small (e.g. measured as << $11x10^{-11}$ cm^3 for a current of 8.5A). In order to measure accurately such a small volume of material, Slade used a radioactive tracer method [14]. In this method one of the contacts is made radioactive and is operated against the inactive contact. By measuring the activity on the initially inactive contact, the volume of metal deposited onto it from the other contact can be determined. The advantages of this method are:

1. the number of operations required for an appreciable activity count is small (750 ops),
2. the method of assessing the volume is accurate,
3. by making the radioactive electrode the cathode in one experiment and the anode in another, the deposit on the cathode from the anode and the deposit on the anode from the cathode can be measured separately.

The contact metals used in these investigations are Ni , Au and Pt-Ir(10wt%). The current varied from 1 A to 25 A as indicated for each of the contacts in Table 1.

III. MEASUREMENTS OF METAL TRANSFER FROM THE MOLTEN METAL BRIDGE

Immediately before rupture of the molten metal bridge, the visible diameter is approximately equal to its visible length [7]. Utsumi [15] gives the ratio of diameter d_B cm to the current I_B at bridge rupture for Au bridges as

$$\frac{d_B}{I_B} = 5.25\ x\ 10^{-5}\ cm/A.$$

In the present work, measurements of material transfer after collapse of the liquid metal bridge pointed to the presence of a deposit onto the cathode from the anode and onto the anode from the cathode. As indicated in Fig. 5, the bridge lifetime was estimated as 50-70 ns before rupture, thus leading to an estimated total accumulation time on both the anode and the cathode of 38-53x10^{-6} s after 750 operations. The results of measurements of transferred volumes after 750 operations for all the contact materials used in this investigation, at various currents, are summarized in Table 1. There is significant accumulation of metal transfer to the anode in all cases, ranging from a volume of about 10^{-11} cm^3 at a current of 10 A, to about 25x10^{-11} cm^3 at 25 A in Ni-Ni contacts. Somewhat larger transfer volumes to the anode are measured in Au-Au contacts. Transfer to the anode is larger than to the cathode in Pt-Ir contacts at currents of up to 3 A. We now propose that these amounts of material transfer are explained in terms of electromigration of ions through the metal bridge before rupture.

Table 1
Volumes of Accumulated Contact Materials for Various Current Values

Metal	current (A)	Cathode Deposit (x10^{-11}cm^3)	Cathode deposit fraction	Anode Deposit (x10^{-11}cm^3)	Anode deposit fraction
Ni	10	5.78	0.83	1.16	0.17
	15	10.35	0.79	2.8	0.21
	20	17.4	0.75	5.8	0.25
	25	23.71	0.77	6.91	0.23
Au	10	3.64	0.65	1.94	0.35
	15	5.65	0.61	3.61	0.39
Pt-Ir	1	0.147	0.46	0.175	0.54
	2	0.197	0.34	0.391	0.66
	3	0.716	0.49	0.759	0.51
	4	1.742	0.70	0.759	0.30
	5	2.827	0.79	0.732	0.21

IV. DESCRIPTION OF ELECTROMIGRATION

In a liquid metal column, the conductor temperature overcomes local binding forces, and ions subsequently diffuse rapidly throughout the conductor. The motion of the diffusing ion population is influenced by two forces: (i) a direct electrostatic force F_i from the action of the external field E on the electric charge of the migrating ions, and (ii) a force F_e arising from the transfer of momentum from electrons flowing towards the ions and thus acting in the direction of electron motion. The effect of F_e on migrating ions is particularly pronounced if the electronic current density is large. It is for this condition of large electronic current density that measurable material transport is characterized as arising from "electromigration", and F_e is labeled as the "electron wind" force.

As illustrated schematically in Fig. 6, the forces F_e, and F_i

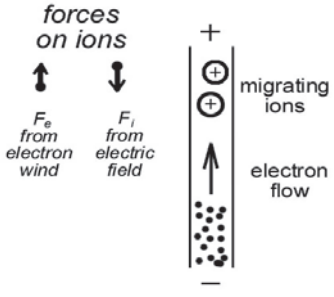


Fig. 6. Schematic description of the forces acting on migrating ions in a conductor, under the action of an electric field and the "electron wind".

act in opposite directions. The net force F_t on an activated ion in the electrical field is thus [16]

$$F_t = F_i - F_e = Z^* eE = Z^* e j_e \rho \qquad (4)$$

where Z**e* is an effective characteristic charge of the moving ion, *E* is the electric field, ρ is the conductor resistivity and j_e is the electron current density. As ions move in a solid or liquid metal, they are surrounded by a cloud of free electrons that act to reduce the effective ionic charge. The charge number Z* relates to the degree of Coulombic shielding provided by free electrons. If shielding is nearly complete, the ionic charge is essentially neutralized and the ions may be viewed as essentially neutral particles dragged along by the streaming electrons i.e. by the "electron wind", and are transported toward the anode. This situation corresponds to the case where $Z^* < 0$. In contrast, if the shielding provided by free electrons is incomplete, the ions maintain a net positive charge ($Z^* > 0$) and migrate towards the cathode under the action of the external electric field. The effective charge Z^*e is affected by temperature and properties of the conductor material presence of solutes in the host matrix[16]. Z* may also be positive or negative in liquid metals. The ionic flux due to electromigration under the action of a current *I* is given as [16]

$$J = \frac{nZ^*|e|D(T_B)\rho(T_B)j_e}{kT_B} \qquad (5)$$

where *n* is the ion density, *e* is the electronic charge, $D(T_B)$ is the self-diffusion coefficient of the metal at the boiling temperature T_B (*K*), $j_e = I/(\pi a^2)$ where *a* is the average radius of the liquid bridge, $\rho(T_B)$ is the resistivity of the liquid metal at the temperature T_B, and *k* is the Boltzmann constant. Equation (5) may also be expressed as a volume v_{ion} per second (i.e. m^3s^{-1}) across the cross-section πa^2 of the molten bridge column as a volume transfer-rate coefficient $u(T_B)$ at the boiling temperature as

$$v_{ion} = \frac{Z^*|e|D(T_B)\rho(T_B)I}{kT_B} = u(T_B)I. \qquad (6)$$

We now evaluate the volume flow rate v_{ion} in the liquid bridge of the separating Ni-Ni, Au-Au and Pt-Ir-Pt-Ir contacts listed in Table 1at the respective boiling temperatures. These evaluations use reported (or estimated) values of ρ and *D*, and a best-fit value of *Z**.

V. CALCULATED RATES OF METAL TRANFER DUE ELECTROMIGRATION

Ni-Ni CONTACTS

(a) Transfer to the Anode

The evaluation of $u(T_B)$ requires experimental values of the self-diffusion coefficient $D(T_B)$ and the resistivity $\rho(T_B)$ at the boiling temperature of Ni. The variation with temperature of the diffusion coefficient $D(T)$ for liquid Ni was derived from the measurements of Meyer *et al* [17] yielding

$$D(T) = 77\ x\ 10^{-9} e^{-\frac{Q}{RT}}\ m^2 s^{-1}$$

where the activation energy Q = 45,348 *J* mol^{-1}, *R* is the universal gas constant and *T* is the temperature. At the boiling temperature of Ni (2913^0C = 3186 K), the self-diffusion coefficient is evaluated as 1.39 x 10^{-8} m^2 s^{-1}. The reported electrical resistivity ρ of liquid Ni at the boiling temperature varies from 93 x 10^{-8} Ωm [18] to 111 x 10^{-8} Ωm [19]. The value of 100 x 10^{-8} Ωm was used in the present calculations. Substituting these values of $D(T_B)$ and $\rho(T_B)$ into Eq. (6) yields

$$v_{ion} = Z^* 5.06\ x\ 10^{-14} I\ m^3 s^{-1} \quad . \qquad (7)$$

At a current of 10 A and an estimated cumulative time of 45 x 10^{-6} s (i.e. 750 operations of 60 ns), the volume transfer to the anode due to electromigration becomes 2.28 x 10^{-11} Z^* cm^3. If the effective charge number $Z^*$is assumed as 1, this deposit volume is about twice the measured value of 1.16 x 10^{-11} cm^3 listed in Table 1. The agreement between the calculated and measured values of transferred volume to the anode improves at a current of 15 A. In this case, the calculated value becomes 3.42 x 10^{-11} cm^3as compared with the measured value of 2.8 x 10^{-11} cm^3 for Z^*=1. The calculated and measured values of transferred volume of Ni for all the currents listed in Table 1 are shown in Fig. 7. There is reasonable agreement between the measured and calculated volume accumulations in all cases.

(b) Transfer to the Cathode

Calculations of the volume accumulation of Ni on the cathode are based on the values of the self-diffusion coefficient $D(T_B)$ and the resistivity $\rho(T_B)$ evaluated in ***(a)***. Thus, the volume flow rate v_{ion} for cathode deposition is also given by Eq.(7). For a current of 10 A, reasonable agreement between the calculated and the measured volume transfers to the cathode requires Z^* = 3.5. In this case the resulting calculated value is 8.0x10^{-11} cm^3 , which compares well with the measured value of 5.78x10^{-11} cm^3. At a current of 15 A, the calculated value becomes 12.0 x 10^{-11} $cm^3$and also compares well with the measured value of 10.35 x 10^{-11} cm^3 for Z^*=3.5. The calculated and measured values of transferred volume of Ni for all the currents listed in Table 1 are shown in Fig. 8. There is reasonable agreement between the measured and calculated volume accumulations in all cases.

Au-Au CONTACTS

(c) Transfer to the Anode

Experimental values of self-diffusivity in liquid Au are available only up to 1800 K [20]. Self-diffusivity at the boiling temperature of 2856^0C (3129 K) was obtained from results of molecular-dynamics and Monte Carlo simulations using a many-body potential for liquid Au [21].

The variation with temperature of the self-diffusion coefficient $D(T)$ for liquid Au at the boiling temperature is given as

$$D(T) = 8.69\ x\ 10^{-8} e^{-\frac{Q}{RT}}\ m^2 s^{-1}$$

where the activation energy Q = 39,559 *J* mol^{-1}. At the boiling temperature, the self-diffusion coefficient $D(T_B)$ is evaluated as 1.90 x 10^{-8} m^2 s^{-1}. The reported electrical resistivity $\rho(T_B)$ of liquid Au at the boiling temperature was taken as 80 x 10^{-8} Ωm [22]. Substituting these values of $D(T_B)$ and $\rho(T_B)$ into Eq. (6) yields

$$v_{ion} = Z^* 5.638\ x\ 10^{-14} I\ m^3 s^{-1} \quad . \qquad (8)$$

At a current of 10 A and an estimated cumulative time of 45 x 10^{-6} s, the volume transfer to the anode due to electromigration becomes 2.54 x $10^{-11}$$cm^3$ for Z^* =1. This deposit volume agrees well the measured value of 1.94 x 10^{-11} cm^3 listed in Table 1. An

improved agreement between the calculated value of 3.81 x 10^{-11} cm^3 and the measured value of 3.61 x 10^{-11} cm^3 is achieved at a current of 15 A also using Z^* =1. The calculated and measured values of transferred volume of Au for all the currents listed in Table 1 are shown in Fig. 7.

(d) Transfer to the Cathode

The volume flow rate v_{ion} for cathode deposition of Au is also given by Eq.(8). For a current of 10 A, there is reasonable agreement between the calculated value of 3.81x10^{-11} cm^3 and the measured volume of 3.64x10^{-11} cm^3 for transfer to the cathode using Z^* = 1.5. At a current of 15 A, the calculated value becomes 5.71 x 10^{-11} cm^3 and also compares well with the measured value of 5.65 x 10^{-11} cm^3 for Z^*=1.5. The calculated and measured values of transferred volume of Au for all the currents listed in Table 1 are shown in Fig. 8.

Pt-Ir-Pt-Ir CONTACTS

(e) Transfer to the Anode

Experimental values of self-diffusivity and electrical resistivity in liquid Pt-Ir alloys are unavailable. Values of v_{ion} from Eq.(6) could thus only be estimated on the basis of diffusivity and resistivity information on pure Pt.

The variation with temperature of the diffusion coefficient $D(T)$ for liquid Pt up to the boiling temperature is given as [23]

$$D(T) = 0.22\ x\ 10^{-4} e^{-\frac{Q}{RT}}\ m^2 s^{-1}$$

where the activation energy Q = 278,845 $J\ mol^{-1}$. At the boiling temperature of 3825^0C (4098 K) the self-diffusion coefficient $D(T_B)$ is evaluated as 6.138 x 10^{-9} $m^2\ s^{-1}$. The reported electrical resistivity $\rho(T_B)$ of liquid Pt at the boiling temperature was estimated as 95 x 10^{-8} Ωm [24]. Substituting these values of $D(T_B)$ and $\rho(T_B)$ into Eq. (6) yields

$$v_{ion} = Z^* 1.651\ x\ 10^{-14} I\ m^3 s^{-1} \quad . \qquad (9)$$

At a current of 1 A and a cumulative time of 45 x 10^{-6} s, the volume transfer to the anode becomes 1.86 x $10^{-12}$$cm^3$ for Z^* = 2.5. This volume agrees well with the measured value of 1.75 x 10^{-12} cm^3 listed in Table 1. Reasonable agreement between

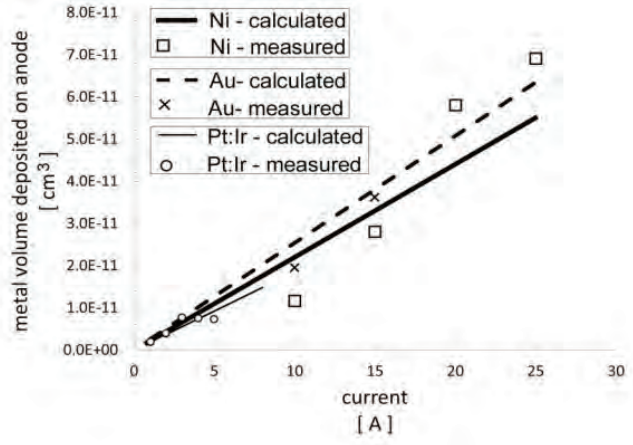


Fig. 7. Calculated and measured volumes of metal accumulated on the anode for the contact materials listed in Table 1.

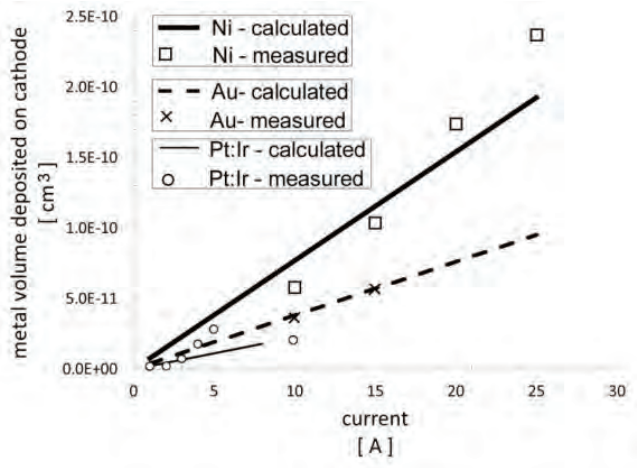


Fig. 8. Calculated and measured volumes of metal accumulated on the cathode for the contact materials listed in Table 1.

the calculated and measured values at currents ranging from 2 A to 5A was achieved using Z^* = 2.5 as shown graphically in Fig. 7.

(f) Transfer to the Cathode

The volume flow rate v_{ion} for cathode deposition is also given by Eq.(9). For a current of 1 A, reasonable agreement between the calculated value of 2.23x10^{-12} cm^3 and the measured volume of 1.47x10^{-12} cm^3 for transfer to the cathode using Z^* = 3. The calculated and measured values of transferred volume of Pt for all the currents listed in Table 1 are shown in Fig. 8. There is general agreement between the calculated and measured values.

VI. ADDITIONAL REMARKS

As already mentioned, the charge number Z^* relates to the degree of Coulombic shielding provided by free electrons to an ion moving in the liquid metal bridge. If shielding is nearly complete, the ionic charge is essentially neutralized and the ions behaves essentially as neutral particles dragged along by the streaming electrons i.e. by the "electron wind", towards the anode. This situation corresponds to the case where $Z^* < 0$. In the case of the liquid Ni bridge, Table 1 indicates that an average of 22% of transferred material is deposited on the anode for currents ranging from 10 A to 25 A. Thus 22% of moving ions in the liquid bridge are characterized with a negative effective charge number of Z^* = -1 and are pushed by the electron flow towards the anode. Correspondingly, 78% of the ions are characterized with a net positive effective charge number of Z^* = 3.5 and become strongly driven toward the cathode by the electric field within the liquid bridge.

Similarly from Table 1, an average of 37% of moving Au ions are characterized by a negative effective charge number of Z^* = -1 and are driven towards the anode, while 63% of the ions carry a net positive charge number of Z^* = 1.5 and are attracted to the cathode. It is worth noting that the net electrical charge on positively charged Au ions is appreciably smaller than on positively charged Ni ions for which Z^* = 3.5.

For Pt ions (assumed to be descriptive of a Pt-Ir mix), the fraction of negatively charged ions (Z^* = 2.5) pushed by the "electron wind" to the anode decreases from 54% at 1 A to 21% at 5 A. Correspondingly the fraction of ions carrying a net

positive charge number of $Z^* = 3.5$ and landing on the cathode increases from 46% to 79% as current is increased.

VII. POTENTIAL CONTRIBUTION FROM THE THOMSON EFFECT

In the Thomson Effect, an electric current I flowing across a temperature difference (T+ - T-) in a conductor liberates Thomson heat at a rate Q given as [1]

$$Q = \sigma_t (T^+ - T^-) I$$

where σ_t is the Thomson coefficient. In the liquid bridge of a monometallic junction, the temperature reaches a maximum in the middle of the bridge. Thus the generation of Thomson heat is possible with the effect of displacing the plane of highest temperature towards the cathode if σ_t is positive and towards the anode if σ_t is negative. The accumulation of material on either electrode during contact break stems from the ensuing asymmetry in the temperature profile along the liquid bridge just before breakup [1].

Holm [1] estimated the volume ΔV of a pip formed from the Thomson Effect as

$$\Delta V = \frac{0.325 \tau \rho^3 I^3}{{V_B}^2} \text{ where } \quad \tau = \frac{1}{L}\frac{d\sigma_t}{dT}$$

and ρ is the average resistivity of the metal in the liquid bridge, V_B is the boiling voltage of the contact material, T is the temperature in K, L is the Wiedemann-Franz constant (2.44 x 10-8 $V^2 K^{-2}$) and I is the current through the liquid bridge. The volume ΔV is independent of time. Because (i) the available experimental information indicates that σ_t is essentially zero in liquid metals [25,26] and (ii) the metal transfer volumes described in this paper are time dependent (for a given current), it is concluded that the Thomson Effect had a negligible effect on the reported metal transfer rates.

VIII. CONCLUSIONS

This paper has presented calculations of rates of metal volume transport through the liquid metal bridge formed between two separating electrodes, due to electromigration. These evaluations were made on the basis of measured values of self diffusion coefficients in liquid Ni, Au and Pt:Ir and using measured values of density and resistivity of the respective liquid metals. The absolute value of the effective ionic charge Z^*e was chosen to provide a best-fit to the experimental data, and consistent with published properties of electromigration in various liquid metals. The sign of the electrical charge Z^*e was assumed positive or negative for consistency with experimental observations of metal transfer respectively from the anode to the cathode and vice-versa during contact separation.

On the basis of the evaluations in this paper, we propose that material transfer in an opening contact, in the absence of arcing, occurs largely by electromigration in the liquid bridge. We conjecture that a similar effect occurs in all non-arcing contacts and that mechanical damage in such contacts may be mitigated through the appropriate choice of contact alloys where the effective ionic charge Z* is nearly zero.

REFERENCES

[1] R. Holm, **Electric Contacts, Theory and Applications**, (Springer-Verlag, Berlin, Heidelberg, New York, 2000).

[2] R.S. Timsit, in Electrical Contact Resistance: Fundamental Principles, Ch. 1, pp. 3-111, **Electric Contacts, Principles and Applications**, P.G. Slade Ed., , (CRC Press, Boca Raton, 2014).

[3] **Electrical Contacts : Principles and Applications** (CRC Press, Boca Raton, London, New York. 2014), Ch. 24, Table 24.1A, p. 1198.

[4] P.G. Slade, "Opening Contacts: the Transition from the Molten Metal Bridge to the Electric Arc", IEICE Trans. Electron. E93-C(6), pp. 1380–1386, 2010.

[5] P.G. Slade and M.D. Nahemow, "Initial Separation of Electrical Contacts Carrying High Currents", J. Appl. Phys. 42(9), pp. 3290–3297, 1971.

[6] P.G. Slade, in The Arc and Interruption, Ch. 9, p. 553 **Electrical Contacts : Principles and Applications** (CRC Press, Boca Raton), 2014.

[7] J.J. Lander and L.H. Germer, "The Bridge Erosion of Electrical Contacts : Part 1, J. Appl. Physics, **19**(10), pp. 910-928, 1948

[8] K. Hiltmann, A. Schumacher, K. Guttmann, E. Lemp, H. Sandmaier and W. Lang, "New Micromechanical Membrane Switches in Silicon Technology", IEEE Trans. Components Packaging Technology, **25** (3), pp. 397–401, 2002.

[9] J.W. McBride, L Jiang and C. Chianrabutra, "Fine Transfer in Electrical Switching Contacts Using Gold Coated Carbon-Nanotubes", Proc 26th Int. Conf. on Electric Contact Phenomena, pp. 353–358, 2012.

[10] R.S. Timsit, "Electromigration in a Liquid Bridge Before Contact Break", Proc. 56th IEEE Holm Conference on Electrical Contacts, pp. 564-569, 2010.

[11] P.G. Slade, "Current Interruption in Low Voltage Circuits", IEEE Trans. Parts Hybrids Packaging PHP-5 (1), pp. 56-61, 1969.

[12] J. Riddlestone, "The Variation with Current and Inductance of Metal Transfer Between Platinum Contacts", Proc. IEE–C, **102**(1), pp. 29–34, 1954.

[13] W. B. Ittner III, "Bridge and Short Arc Erosion of Copper, Silver, and Palladium Contacts on Break", J. App. Phys., **27** (4), pp. 382-388,1956.

[14] F.L. Llewellyn-Jones, M.R. Hopkins and C.R. Jones, "Measurement of Metal Transfer in Electrical Contacts by Radioactive Tracer Method", British J. App. Physics, **12** (9), pp. 485–489, 1961.

[15] T. Utsumi," Theoretical and Experimental Investigations of the Dynamic Molten Bridge", IEEE Trans. Parts Materials. Packaging. **PMP 5**(1), pp. 62–68, 1969.

[16] H.B. Huntington, **Electro- and Thermomigration in Metals in Diffusion**, (American Society for Metals, Metals Parks, OH), pp. 155 – 184, 1973.

[17] A. Meyer,S. Stüber, D. Holland-Moritz, O. Heinen and T. Unruh, "Determination of Self-Diffusion Coefficients by Quasielastic Neutron Scattering Measurements of Levitated Ni Droplets", Phys. Rev. B, **77**, pp. 092201-1-4, 2008.

[18] U. Seydel and W. Fucke,"Sub-Microsecond Pulse Heating Measurements of High Temperature Electrical Resistivity of the 3d – Transition Metals Fe, Co and Ni", Z. Naturforschung A, 1977.

[19] R.S. Hixson, M.A. Winkler and M.L. Hodgdon, "Sound speed and Thermoyhysical Properties of Liquid Iron and Nickel", Phys. Rev. B, **42**, pp. 6485-6491, 1990.

[20] N. Dubinin, "Self-Difusion in Liquid Copper, Silver, and Gold", Metals, **10** (12), p. 1651, 2020.

[21] A. Bogicevic, L.B. Hansen and B.I. Lundqvist, "Simulations of Atomic Structure, Dynamics, and Self-diffusion in Liquid Au", Phys. Rev. E, **55** (5), pp. 5535-5545, 1997.

[22] R.A. Matula, "Electrical Resistivity of Copper, Gold, Palladium and Silver", J. Phys. Chem. Ref. Data, **8** (4), pp. 1147-1298, 1979.

[23] F. Cattaneo , E. Germagnoli and F. Grasso, "Self-Diffusion in Platinum", Philos. Mag., **7**, pp. 1373-1383, 1962.

[24] B. Wilthan, C. Cagran, C. Brunne and, G. Pottlacher, "Thermophysical Properties of Solid and Liquid Platinum", **415** (1–2), pp. 47-54, 2004.

[25] N.E. Cusack, "The Electronic Properties of Liquid Metals", Rep. Prog. Phys., **26**, pp. 361-409, 1963.

[26] R.A. Howe and J E. Enderby, " The thermoelectric Power of Liquid Ag-Au", Philos. Mag., **16** (141), pp. 467-476, 1967.

Influence of contact geometry and interfacial force on contact behavior: Combined theoretical and simulation validation

Akshata Sangle & Stefan Goetz
Chair of Mechatronics & Electrical Drives
RPTU Kaiserslautern-Landau
Kaiserslautern, Germany

Florian Bruhn
Research & development
iwis smart connect GmbH
Rieden, Germany

***Abstract*—The behaviour and reliability of electrical contacts are determined not only by the intrinsic properties of the materials involved but also by the mechanical and geometrical conditions at the interface. Contact geometry and interfacial force directly influence the size of the real contact area, the level of constriction resistance, and the magnitude of local heating during current conduction. Understanding these factors is essential for predicting current carrying capacity and preventing premature failure in high-reliability applications. This study presents a closed-form and finite-element (FE) validated framework linking contact geometry and preload to electrical ampacity in CuSn6 sheet-metal contacts. Results demonstrate that larger radii and higher forces increase ampacity by reducing constriction resistance and distributing current uniformly. However, the benefit diminishes at higher values due to thermal bottlenecks and localized plastic deformation. A combined analytical–numerical approach is used to derive and validate a geometry–force dependent ampacity relationship, enabling the construction of a design-oriented operating map.**

***Index Terms*—Electrical contacts,Interfacial force,Constriction resistance,Coupled structural–electrical–thermal simulation**

I. Introduction

Electrical contacts enable current transfer across separable interfaces in connectors, terminals, and switching devices, and are often critical to system reliability in applications such as aerospace, electrified transport, and industrial control. Their performance is governed by coupled electrical, mechanical, thermal, and environmental effects rather than bulk material properties alone [1]–[3]. Even when conductors are highly conductive, degradation at a single interface can lead to increased resistance, localized heating, intermittency, or failure.

Conduction occurs through microscopic asperity junctions ("a-spots") see Figure 1, resulting in an effective contact area much smaller than the apparent geometry and causing current constriction and elevated resistance [1], [4], [5]. Since this resistance depends on local pressure and deformation, contact performance is strongly influenced by preload, compliance, and geometry, and is sensitive to service conditions such as vibration, thermal cycling, and oxidation [2], [3].

Field and experimental studies further show that interconnection failures are a major reliability concern, often linked to degradation mechanisms such as fretting, corrosion, and mechanical defects, which can produce intermittent and difficult-to-diagnose faults [6]–[10]. These challenges highlight the importance of designing contacts with controlled geometry and preload to stabilize real contact area, reduce constriction resistance, and limit Joule heating, thereby improving robustness and thermal margin [1]–[3].

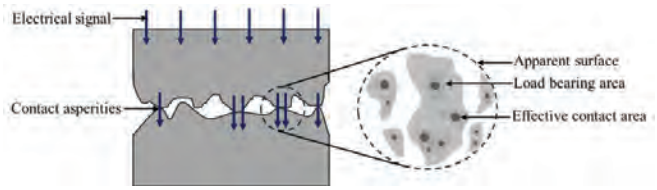


Fig. 1. Sketch illustrating asperities: current concentration through micro-contact asperities leads to locally high current density and an additional voltage drop across the interface.

A. Problem: Geometric and Mechanical Drivers of Contact Overheating and Failure

Power connectors often operate near thermal limits, where small increases in contact resistance can significantly raise temperature due to Joule heating ($P = I^2R$). Since current flows through discrete micro-contacts rather than the full apparent area, resistance is highly sensitive to the formation and evolution of real contact area under load [1], [2], [11].

Geometry plays a key role in this behavior. Tight radii and sharp features concentrate stress, reduce effective contact area, and increase constriction resistance, promoting localized hotspots. Edge effects can further intensify current crowding and nonuniform heating, particularly in thin or constrained geometries [1], [11], [12].

Mechanical loading also strongly influences performance. Low preload results in small contact area and high resistance, while higher preload improves conduction but may induce local plasticity. Although plastic deformation can initially reduce resistance, it may degrade long-term stability. Additionally, stress relaxation and creep—especially at elevated

temperatures—reduce preload over time, increasing resistance and reinforcing thermal buildup [2], [11], [16], [17].

Overall, overheating arises from coupled electro-thermo-mechanical effects. Geometry and preload together determine contact area, current distribution, and heat dissipation, governing the formation of thermal hotspots. This interaction can lead to feedback-driven temperature rise, highlighting the need to select stable geometry–preload combinations that avoid thermal bottlenecks and prevent failure [13], [14].

B. Objectives: Geometry-Force Interdependence and Its Impact on CuSn6 Ampacity

The performance of separable contacts is governed by a coupled relationship between geometry and preload, which determines real contact area, pressure distribution, and consequently constriction resistance, current crowding, and Joule heating. These interactions directly control the temperature rise and current-carrying capability, making geometry and force key design parameters.

Due to nonlinear effects such as asperity evolution, temperature-dependent resistivity, and possible elasto-plastic behavior, increasing area or preload alone yields diminishing returns and may introduce new thermal limitations. Building on established contact theory and multiphysics modeling approaches [1]–[3], [11], [14],the main contributions of this work are:

- A closed-form analytical relationship linking curvature radius and preload to ampacity
- A finite-element validation capturing 3D current density and temperature fiels
- A design-oriented interpretation defining practical operating ranges [18].

II. Materials and contact concept

This section defines the material system and modeling assumptions used to estimate steady-state current-carrying capability. To isolate the influence of geometry and preload, the contact interface is modeled as an idealized clean metal-to-metal junction. Effects such as surface roughness, oxide films, and degradation are neglected, which may underestimate resistance in practical systems.

A. Material: CuSn6 R560 with 0.6 mm thickness

TABLE I
CuSn6 R560 with 0.6 mm thickness: Key material properties used in the model

Property	Symbol	Value
Young's modulus	E	120 GPa
Poisson's ratio	ν	0.34
Electrical resistivity	ρ	$1.112 \times 10^{-7}\ \Omega \cdot \mathrm{m}$
Thermal conductivity	λ	$75\ \mathrm{W/(m \cdot K)}$
Strip thickness	h	0.6 mm
Maximum allowable temperature	$T_{\max}$	125 °C
Reference/ambient temperature	T_0	25 °C

CuSn6 is selected for its balanced combination of mechanical strength, spring properties, and electrical conductivity, enabling stable contact force and controlled resistance under load. Its good formability, wear, and corrosion resistance make it suitable for reliable connector applications. These properties support consistent contact behavior and long-term stability under mechanical and thermal cycling. The key material parameters used in both analytical and numerical models are summarized in Table I [19], [20].

B. Contact concept: concave radius on flat counterface (geometry definition)

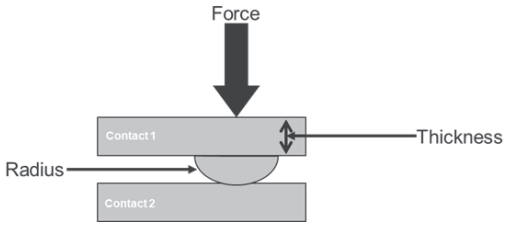


Fig. 2. Schematic of the contact concept: a concave radius R on Contact 1 pressed against a flat counter face (Contact 2) . The upper sheet thickness is T, and the concave feature.

Figure 2 shows the idealized contact geometry used in this study. A concave feature with radius R on Contact 1 is pressed against a flat Contact 2 under a normal force F. The upper sheet has thickness T, and the concave depth defines the extent of the curved profile. Under load, a localized contact spot forms at the interface, represented analytically as an equivalent circular area governed by Hertzian contact theory. Its size depends on F, R, and the effective elastic properties. This formulation enables a consistent parameterization of curvature, load, and thickness for both analytical and numerical evaluation.

III. Design of Experiments

This section defines the parameter space used to systematically evaluate the contact model under realistic geometric and loading variations. A discrete design of experiments (DoE) is adopted to quantify how curvature and preload influence the contact spot size, constriction resistance, and the resulting steady-state current limit.

A. Factors and levels

TABLE II
DoE factors and levels

Factor	Levels
Concave radius R (mm)	0.5, 1.0, 1.5, 2.0, 2.5, 3.0
Preload F (N)	1, 5, 10, 15, 20, 25, 30

Two independent factors are considered: the concave curvature radius R of Contact 1 and the applied normal preload F. The curvature radius is swept from a tight radius representative of the minimum expected forming radius up to a comparatively flat geometry, using uniform increments to enable trend analysis. The preload is evaluated at discrete levels to capture low-force sensitivity as well as higher-force behavior relevant to

assembly and retention loads. Table II summarizes the factors and their levels used in this study.

B. Response variables

TABLE III
RESPONSE VARIABLES EVALUATED FOR EACH (R, F) COMBINATION

Response	Abbreviation
Hertzian contact radius	a_H
Hertzian contact area	A_H
Constriction resistance	R_c
Maximum current	$I_{\max}$

For each combination of (R, F), a set of mechanical, electrical, and thermo-electrical response variables is computed to characterize the contact behavior and enable direct comparison between analytical predictions and simulation results. The primary mechanical outputs are the Hertzian contact radius a_H and the corresponding contact area A_H, which define the effective size of the current-carrying constriction. These outputs are then used to evaluate the Holm constriction resistance R_c, which links the mechanical contact state to electrical losses. In addition, local current density hotspot metrics are extracted to quantify electrical crowding near the contact spot, as peak current density is a key driver of localized heating and potential material degradation. Finally, the thermal response is summarized by the maximum contact temperature $T_{\max}$ under steady-state Joule heating, and the associated maximum admissible current $I_{\max}$ defined by the allowable temperature limit.

IV. THEORETICAL FRAMEWORK

This section outlines the analytical framework linking contact geometry and preload to electrical and thermal performance under steady-state conditions. Elastic Hertzian contact theory is used to estimate contact size, which is combined with Holm's constriction model to evaluate contact resistance. The resulting Joule heating is then coupled with a steady-state thermal balance to determine temperature rise and maximum allowable current. Together, these models provide a physics-based baseline for interpreting design trends and validating simulations.

A. Hertzian apparent contact radius/area (baseline for geometry-force effects)

The apparent contact area is first estimated using Hertzian contact theory. The concave feature on Contact 1 pressed against the flat counterface is approximated as a sphere-on-flat contact with effective radius R [21]. Under elastic deformation, the contact forms an equivalent circular area with radius a_H, as illustrated in Fig. 3. This radius directly links mechanical loading to electro-thermal behavior: increasing a_H reduces current constriction and resistance, thereby lowering temperature rise for a given current [1], [22].

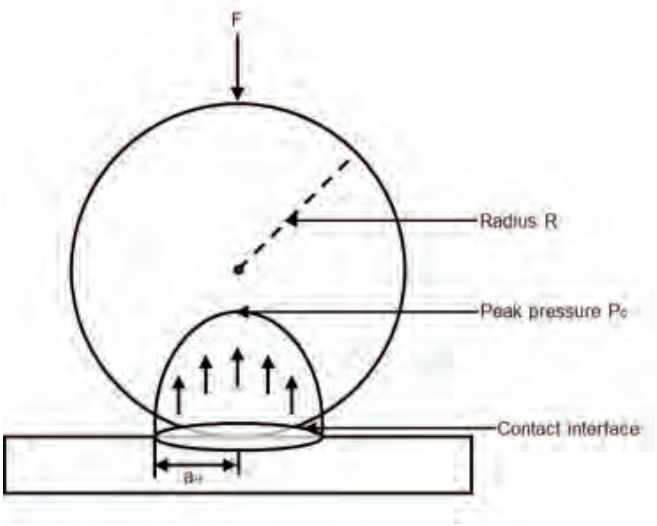


Fig. 3. Geometry schematic of a Hertzian contact spot for a curved surface of radius R loaded by a normal force F, forming an apparent contact radius a_H at the interface.

For two isotropic bodies in frictionless normal contact, with principal radii of curvature R_{x1}, R_{y1} and R_{x2}, R_{y2} at the contact point, the combined (effective) curvatures are [22]:

$$\frac{1}{R'_x} = \frac{1}{R_{x1}} + \frac{1}{R_{x2}}, \qquad \frac{1}{R'_y} = \frac{1}{R_{y1}} + \frac{1}{R_{y2}}. \tag{1}$$

For an axisymmetric curved feature (e.g., spherical/rounded) on a flat counterface, $R_{x1} = R_{y1} = R$ and $R_{x2} = R_{y2} = \infty$, so:

$$R'_x = R'_y = R. \tag{2}$$

For isotropic materials with Young's moduli E_1, E_2 and Poisson ratios ν_1, ν_2, the effective modulus is [22]:

$$\frac{1}{E^*} = \frac{1-\nu_1^2}{E_1} + \frac{1-\nu_2^2}{E_2}. \tag{3}$$

For identical materials on both sides ($E_1 = E_2 = E$, $\nu_1 = \nu_2 = \nu$):

$$E^* = \frac{E}{2(1-\nu^2)}. \tag{4}$$

Hertz theory yields a circular contact region of radius a_H (axisymmetric case) such that the normal load F relates to a_H via [22]:

$$F = \frac{4E^*}{3R}\, a_H^3. \tag{5}$$

Solving Eq. (5) for a_H gives the Hertz contact radius:

$$a_H = \left(\frac{3FR}{4E^*}\right)^{1/3}. \tag{6}$$

The apparent nominal contact area is the area of the circular Hertz patch:

$$A_H = \pi a_H^2. \tag{7}$$

Substituting Eq. (6) into Eq. (7) gives an explicit force-radius area expression:

$$A_H = \pi \left(\frac{3FR}{4E^*} \right)^{2/3}. \tag{8}$$

This shows the key Hertz scaling:

$$A_H \propto (FR)^{2/3}, \tag{9}$$

i.e., both higher preload and larger curvature radius increase the nominal footprint, but with diminishing returns due to the $2/3$ exponent.

Hertz theory provides the nominal contact patch for smooth elastic bodies, while real electrical conduction occurs through micro-contacts within this area due to roughness and material effects. Despite this, the apparent contact area A_H remains a useful baseline, as it captures how geometry (R) and preload (F) influence the macroscopic contact region, which in turn governs current spreading and hotspot formation [1], [2], [4], [23], [24].

Accordingly, Eqs. (6) and (7) describe the primary geometry–force relationship: increasing F or R enlarges a_H and A_H, reducing constriction effects in the electrical response.

Below are some assumptions made while using Hertz theory,

- Small strains, linear elasticity, frictionless normal contact.
- Smooth surfaces with locally quadratic geometry near the contact.
- Contact dimensions small compared to body dimensions (half-space approximation).

B. Holm constriction resistance (baseline $R_c(F, R)$)

Using the Hertzian contact size, the baseline electrical loss is described by Holm's constriction resistance, which links geometry and preload to an equivalent resistance across the interface. The contact is idealized as a clean metal-to-metal junction with a single circular spot, where resistance arises from current crowding and spreading in the bulk.

For a given material, a smaller contact radius a increases resistance due to stronger current constriction, while a larger a reduces resistance by allowing smoother current distribution. This behavior is captured by Holm's model, which represents the contact as a circular spot in a semi-infinite conductor. As illustrated in Fig. 1, current is forced through localized micro-contacts, leading to elevated current density and an additional voltage drop despite high bulk conductivity.

Under these assumptions for a single circular contact spot of effective radius a, Holm's expression for the constriction resistance is

$$R_c = \frac{\rho}{2a}, \tag{10}$$

where ρ is the electrical resistivity of the contact material. In the present framework, the effective radius is approximated by the Hertzian apparent contact radius, $a \approx a_H$. Substituting (6) into (10) yields an explicit relationship between constriction resistance, preload, and curvature radius:

$$R_c(F, R) \approx \frac{\rho}{2a_H} = \frac{\rho}{2} \left(\frac{4E^*}{3FR} \right)^{1/3}. \tag{11}$$

Equation (11) makes the governing trends transparent: R_c decreases with increasing preload and increasing curvature radius, following approximately a $F^{-1/3}$ and $R^{-1/3}$ dependence. This scaling is useful when interpreting DoE results, because it explains why small radii combined with low preload tend to produce the highest contact resistance and, consequently, the highest local Joule heating for a given current.

C. Maximum steady-state current model (closed form $I_{\max}(F, R)$)

The maximum admissible current is obtained by enforcing a steady-state temperature limit at the contact. The contact power loss is modeled as Joule heating concentrated at the constriction,

$$P_c = I^2 \, R_{c,\mathrm{eff}}(F, R), \tag{12}$$

and the associated temperature rise is approximated using the effective thermal resistance from the contact region to the surrounding bulk,

$$\Delta T = T_{\max} - T_0 \approx P_c \, R_{\theta,\mathrm{eff}}(F, R). \tag{13}$$

Requiring $T_{\max} \leq T_{\mathrm{allow}}$ gives the closed-form current limit

$$I_{\max}(F, R) = \sqrt{\frac{T_{\mathrm{allow}} - T_0}{R_{c,\mathrm{eff}}(F, R) \, R_{\theta,\mathrm{eff}}(F, R)}}. \tag{14}$$

Using Holm's constriction resistance with the Hertzian apparent contact radius ($a \approx a_H$),

$$R_{c,\mathrm{eff}}(F, R) = k_t \frac{\rho}{2a_H}, \tag{15}$$

and the two-body spreading resistance for identical materials,

$$R_{\theta,\mathrm{eff}}(F, R) = k_\theta \frac{1}{2a_H \lambda}, \tag{16}$$

the product in (14) simplifies and yields a compact expression:

$$I_{\max}(F, R) = 2a_H \sqrt{\frac{\lambda \, (T_{\mathrm{allow}} - T_0)}{k_t k_\theta \rho}}. \tag{17}$$

Finally, substituting the Hertzian radius

$$a_H = \left(\frac{3FR}{4E^*} \right)^{1/3} \tag{18}$$

gives the closed-form dependence on preload and curvature radius:

$$I_{\max}(F, R) = 2 \left(\frac{3FR}{4E^*} \right)^{1/3} \sqrt{\frac{\lambda \, (T_{\mathrm{allow}} - T_0)}{k_t k_\theta \rho}}. \tag{19}$$

Equation (19) Equation (19) represents the central result of this work, linking mechanical loading and geometry directly to ampacity. While based on classical models, this unified formulation enables direct prediction of design-relevant performance.

V. Numerical Methodology

The FE model is used to validate the analytical framework by resolving 3D current density and temperature fields under realistic boundary conditions. The FE model complements the analytical framework by resolving three-dimensional current density, Joule heating, and steady-state temperature under realistic boundary conditions. The simulations use the same geometric parameters (R, T, D) and preload levels F to ensure consistency with the analytical study. Post-processing provides key quantities including constriction resistance R_c, peak current density metrics ($J_{\max}$), maximum temperature $T_{\max}$, and the corresponding current limit $I_{\max}$ for each design point.

A. Structural contact model in ANSYS Workbench (contact patch extraction)

The structural analysis is used to extract the numerical contact patch under the prescribed preload, which then provides the geometric input for the electro–thermal evaluation. In ANSYS Workbench, the two sheet-metal parts are assembled as in Fig. 2: Contact 1 includes the concave radius R, while Contact 2 is a flat counter-face. The preload is applied as a normal force according to the DoE, and the remaining constraints are selected to suppress rigid-body motion without over-stiffening the contact region. Figure 4 summarizes the applied load and support conditions.

The interface is modeled with a standard surface-to-surface contact definition. To remain consistent with the Hertzian baseline, the material is treated as linear elastic and the analysis is solved in the small-deformation regime unless required otherwise by the geometry. The mesh is locally refined at the interface to resolve the contact pressure field and the contact boundary, while a coarser mesh is used elsewhere. Mesh convergence is verified by ensuring that the extracted contact area and peak pressure change only marginally with further refinement.

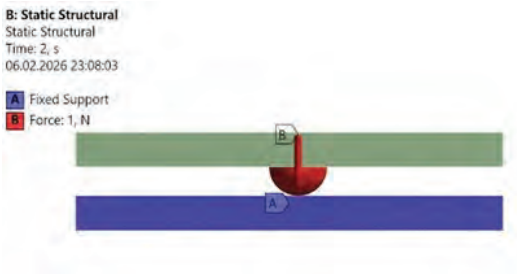


Fig. 4. ANSYS Static Structural setup used for contact patch extraction, showing the applied preload and fixed support boundary conditions.

After solving, the contact patch is extracted from the contact status and/or contact pressure fields. The contact area is taken as the region where pressure exceeds a small threshold to suppress numerical noise at the contact edge. An equivalent circular radius is then computed as

$$a_{\mathrm{num}} = \sqrt{\frac{A_{\mathrm{num}}}{\pi}}, \tag{20}$$

where A_{num} is the extracted contact area. The resulting a_{num} is compared against the Hertzian prediction a_H and is used as an input for estimating R_c and thermal spreading resistance. Peak and mean contact pressures are also recorded to check whether the elastic assumption remains reasonable over the applied force range.

B. ANSYS thermal-electric setup (boundary conditions, Joule heating, coupling)

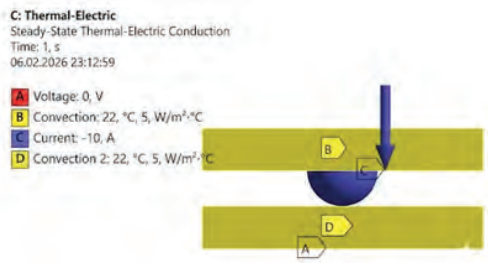


Fig. 5. ANSYS steady-state thermal–electric setup showing representative electrical boundary conditions (current/voltage) and thermal boundary conditions (convection) used for the coupled analysis.

The coupled electro–thermal model is used to compute the current-density field, the associated Joule heating, and the steady-state temperature distribution around the contact. A transport current (or equivalent voltage) is applied between terminals on Contact 1 and Contact 2, placed sufficiently far from the interface to avoid biasing the local constriction region; all other exterior faces are electrically insulated. The interface is treated as a clean metal-to-metal connection using the appropriate Workbench electrical contact formulation (e.g., bonded electrical contact or an equivalent conductance), consistent with the baseline assumption of no additional film resistance. Figure 5 summarizes the applied electrical and thermal boundary conditions.

Joule heating is activated so that heat generation follows the local electrical solution, and the thermal problem is solved in steady state with convection and/or fixed-temperature references on selected faces. Unless otherwise stated, constant ρ and λ are used to isolate geometry and preload effects, while the mesh is locally refined near the contact to resolve steep current-density and temperature gradients. Mesh sensitivity is checked on representative extreme cases (low-R/low-F and high-R/high-F).

C. Extraction of $R_c = \Delta V/I$ (Kelvin-style definition)

To obtain a simulation-based constriction resistance that is comparable across the DoE, R_c is evaluated using a four-terminal (Kelvin) approach. The transport current is applied through a pair of current terminals, while the voltage drop is measured between two separate probe locations placed on each part close to the interface but outside the strongest potential gradients. The constriction resistance is then computed as

$$R_c = \frac{\Delta V}{I}, \tag{21}$$

with $\Delta V = \bar{V}_1 - \bar{V}_2$ taken as the area-averaged potential difference between the probe faces. This definition minimizes sensitivity to terminal placement and supports a consistent comparison with the Holm baseline.

D. Ampacity evaluation procedure in simulation ($T_{\max} \rightarrow I_{\max}$)

For each (R, F) case, the coupled model is solved at prescribed current levels and the peak steady-state temperature $T_{\max}$ is extracted from the contact vicinity. The ampacity is defined as the maximum current that satisfies

$$T_{\max}(I; F, R) \leq T_{\text{allow}}. \tag{22}$$

I is stepped until the threshold is reached (or slightly exceeded), and $I_{\max}$ is obtained by interpolation between the two nearest current levels.

VI. Results and Discussion

This section presents the main outcomes of the study and connects the observed trends back to the underlying contact physics. Results are organized to first establish the analytical expectations for how geometry and preload influence contact size, constriction resistance, and heating. The numerical results are then used to confirm where the closed-form trends hold and to highlight where three-dimensional field effects, boundary conditions, or finite thickness become important. Finally, the

A. Analytical baselines

Implications for practical design of sheet-metal contacts are discussed in terms of robustness, sensitivity, and usable current margins.

Before analyzing simulation results, it is useful to establish baseline trends from the closed-form model. The analytical framework relates preload and curvature radius to the apparent contact radius a_H, which governs both the constriction resistance R_c and the effective thermal spreading resistance. It predicts that increasing either the applied force F or the radius R enlarges the contact area, thereby reducing R_c and permitting higher steady-state current. These analytical trends serve as a reference for interpreting numerical results and identifying deviations from ideal assumptions.

1) Hertzian apparent contact area $A_H(F, R)$: Figure 6 presents the analytical Hertzian contact area A_H across the DoE grid. Two main trends are observed. The contact area A_H increases with preload and curvature radius, consistent with Hertzian scaling. However, the sub-linear behavior leads to diminishing gains, indicating reduced sensitivity at higher loads.

The influence of radius becomes more pronounced at higher preload, leading to increased separation between curves. For instance, at $F = 30$ N, $R = 3.0$ mm produces the largest contact area (on the order of 3×10^{-2} mm^2), while $R = 0.5$ mm remains below 1×10^{-2} mm^2. Such differences are significant for electrical behavior, since $a_H = \sqrt{A_H/\pi}$ and thus variations in A_H directly affect constriction resistance and current density.

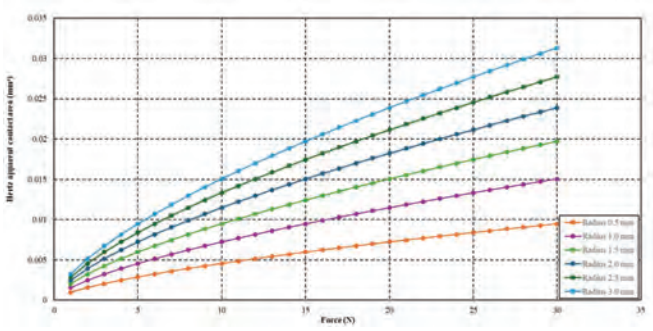


Fig. 6. Hertzian apparent contact area A_H as a function of preload F for different concave radii R (Hertz contact area).

These trends are consistent with Hertzian scaling, where $A_H \propto (FR)^{2/3}$. As a result, the rate of increase in contact area diminishes with higher preload, implying reduced gains in resistance and ampacity. Overall, Fig. 6 establishes the mechanical baseline for subsequent electro-thermal analysis.

2) Holm constriction resistance $R_c(F, R)$: Figure 7 shows the Holm-based constriction resistance R_c across the DoE grid, using the Hertzian contact radius as the effective spot size. For all radii, R_c decreases sharply with preload at low forces and more gradually at higher forces, reflecting the combined scaling $R_c \propto (FR)^{-1/3}$. This behavior highlights the strong sensitivity of constriction resistance to contact size in the small-area regime, followed by diminishing returns as the contact spot grows.

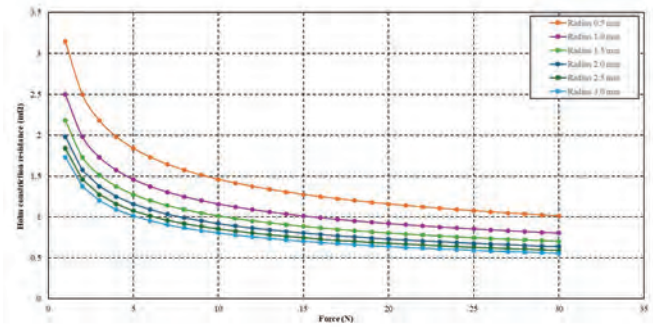


Fig. 7. Holm constriction resistance R_c as a function of preload F for different concave radii R (Holm_CR_01).

Curvature radius has a consistent effect over the full range: larger R yields lower R_c at a given preload due to improved current spreading, while smaller radii produce higher resistance, particularly at low forces. At higher preload, the curves converge, indicating reduced sensitivity as the contact area becomes sufficiently large.

These results represent an idealized baseline for a single-spot contact in a semi-infinite conductor. In thin sheet-metal geometries, finite thickness can increase resistance due to restricted current paths. This effect is commonly incorporated using a thickness factor $k_t \geq 1$, such that $R_{c,\text{eff}} = k_t R_c$.

While this shifts the resistance magnitude upward, it does not alter the underlying trends with preload and curvature.

3) Maximum steady-state current $I_{\max}(F, R)$ from the coupled analytical model: Figure 8 presents the maximum steady-state current $I_{\max}$ predicted by the coupled analytical model under a temperature constraint. Two clear trends emerge. First, $I_{\max}$ increases with curvature radius for all preload levels, as larger radii enlarge the contact area, reducing constriction resistance and improving thermal spreading. Second, at a fixed radius, increasing preload raises $I_{\max}$ by further expanding the contact spot and lowering Joule heating.

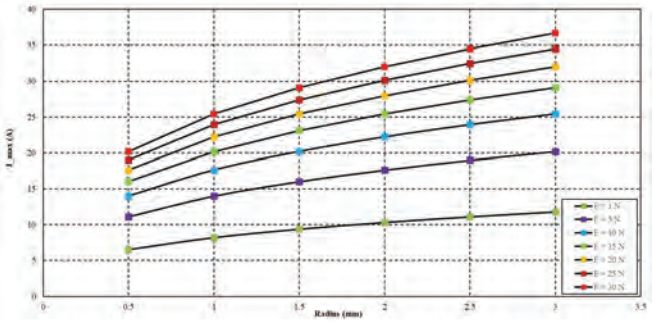


Fig. 8. Analytical prediction of maximum steady-state current $I_{\max}$ as a function of curvature radius R for different preload levels F (Imax_Radius).

The sensitivity to preload is strongest at small radii, where the contact is most restricted. As R increases, the curves remain distinct but exhibit diminishing gains, consistent with the sub-linear Hertzian scaling. Thus, increases in F or R yield progressively smaller improvements once the contact area becomes sufficiently large.

Overall, Fig. 8 summarizes the analytical baseline: minimum ampacity occurs at low preload and small radius, while maximum ampacity is achieved at high preload and large radius within the elastic regime. These trends provide a reference for subsequent numerical results, where additional physical effects may shift absolute values but generally preserve the same behavior.

B. ANSYS results

This subsection presents the numerical results from the ANSYS Workbench simulations and compares them with the previously established analytical baselines. The FE model captures contact deformation under preload and the coupled electro-thermal response, while inherently accounting for finite geometry, boundary conditions, and three-dimensional field effects. The results are evaluated in terms of consistency with analytical trends and relevant deviations for practical design.

1) Contact area evolution (structural): The structural contact simulations yield the numerical contact area A_{num} and equivalent radius $a_{\text{num}} = \sqrt{A_{\text{num}}/\pi}$ for each (R, F) point. Across the DoE, the results follow the same trends as the Hertzian model: the contact area increases with preload and curvature radius.

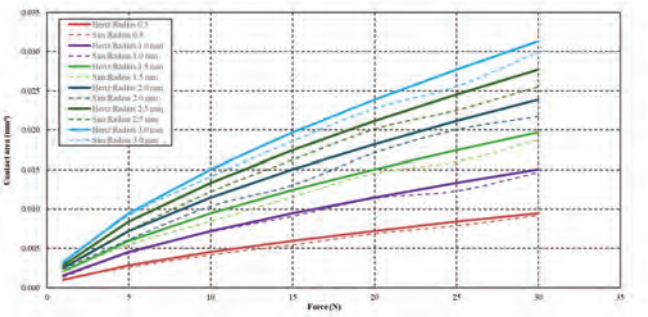


Fig. 9. Comparison of contact area from Hertz theory (A_H) and ANSYS structural simulation (A_{num}) as a function of preload F for different radii R.

Figure 9 compares numerical and analytical predictions, showing close agreement and confirming that Hertzian theory provides a reliable first-order approximation. Minor deviations, most noticeable at low preload, arise from modeling factors such as contact formulation, mesh resolution, and the criterion used to define the contact area.

2) Constriction resistance (thermal-electric): The coupled thermal-electric simulations provide numerical estimates of constriction resistance using $R_c = \Delta V/I$. Figure 10 compares these results with the Holm baseline. Both approaches show the same trend: R_c decreases rapidly with preload at low forces and more gradually at higher forces, reflecting reduced current crowding as the contact area grows.

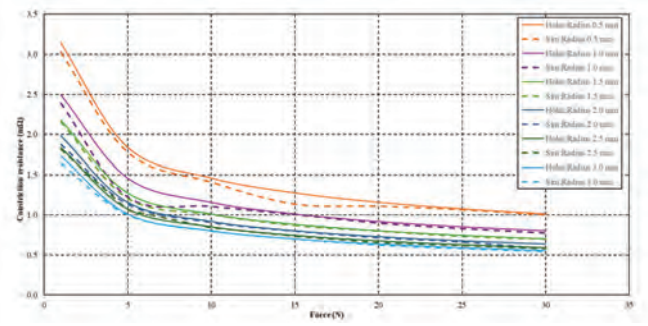


Fig. 10. Comparison of constriction resistance from the Holm baseline and ANSYS coupled thermal-electric simulation as a function of preload F for different radii R.

The effect of curvature radius is also consistent. Larger radii result in lower resistance at a given preload due to improved current spreading, while smaller radii remain more resistive, particularly at low forces. The differences between radii are most pronounced in the small-contact regime.

Overall, the simulations agree well with the Holm prediction, confirming that Hertzian contact size combined with Holm's model captures the dominant behavior. Remaining deviations arise from factors not included in the analytical model, such as finite geometry, three-dimensional current paths, and numerical aspects of contact and voltage extraction, with the largest discrepancies occurring at low preload.

3) Ampacity map ($T_{\max} \rightarrow I_{\max}$): analytical vs. simulation: Figure 11 compares the maximum steady-state current from the analytical model with FE simulation results. In both cases, $I_{\max}$ increases monotonically with curvature radius, as larger contact areas reduce constriction resistance and improve heat dissipation.

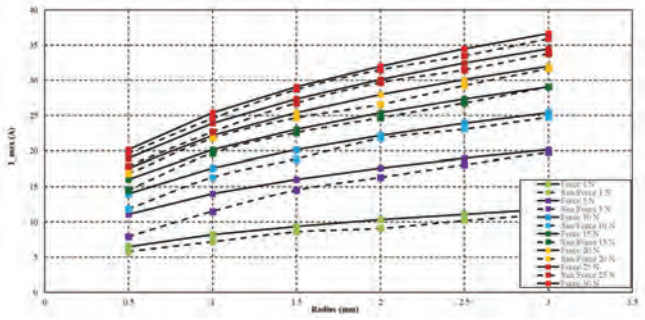


Fig. 11. Comparison of maximum steady-state current $I_{\max}$ from the coupled analytical model and ANSYS thermal-electric simulation as a function of radius R for different preload levels F.

A similar dependence is observed for preload: higher forces increase $I_{\max}$ by enlarging the contact patch and lowering Joule heating. The sensitivity to preload is strongest at small radii, while at larger radii the gains become less pronounced, consistent with sub-linear Hertzian scaling.

Overall, the analytical and numerical results are in close agreement, indicating that the closed-form model captures the dominant physics. Minor deviations arise from three-dimensional and finite-geometry effects in the FE model, such as thickness and current-path distribution. Despite this, the consistent trends confirm the analytical approach as a reliable tool for initial design, with simulations providing higher-fidelity validation.

C. Interpretation: diminishing returns, thermal bottlenecks, current crowding, and onset of local plasticity

The combined analytical and numerical results show that preload and geometry primarily influence performance through the effective contact area, which governs both electrical constriction and thermal spreading. The largest improvements occur at small contact sizes, where increases in F or R significantly enlarge the contact patch, reducing R_c and increasing $I_{\max}$. As the contact grows, gains diminish due to Hertzian scaling, leading to saturation at higher preload and radius.

Thermal limitations remain important even when electrical resistance is reduced. While I^2R_c defines heat generation, the ability to dissipate this heat depends on spreading resistance. At larger contact areas, the limiting factor shifts from localized constriction to global heat flow, where finite thickness and boundary conditions become more influential.

Current crowding persists as a critical factor. Simulations show peak current density concentrated near the contact perimeter, meaning local hotspots can govern temperature limits even when global resistance appears low. Thus, while analytical models capture overall trends, FE analysis is necessary to resolve these localized effects.

Finally, the assumption of purely elastic contact may break down at higher preload or smaller radii. Local plasticity can increase contact area beyond Hertzian predictions, reducing resistance further, but at the cost of potential permanent deformation and reduced reliability. This transition should therefore be treated as a design limit and verified using structural FE analysis.

D. Design Implications: Effective Ranges of Radius and Preload

The results provide clear guidance on effective design choices for radius and preload. The largest performance gains occur in the low-to-mid preload regime and for small radii, where increases in F or R significantly enlarge the contact area, reducing R_c and increasing $I_{\max}$. This highlights the importance of avoiding very tight radii (if feasible) and ensuring a minimum preload to move beyond the highly constricted regime.

At moderate-to-high preload and larger radii, improvements diminish due to sub-linear scaling. In this range, further increases in preload offer limited benefit and must be balanced against mechanical risks (e.g., plasticity, wear) and the system's ability to dissipate heat. The limiting factor increasingly shifts from contact resistance to overall thermal management.

From the trends observed across the DoE, a practical design strategy is therefore:

- **Prioritize geometry first:** moving from a very tight radius toward a moderate radius typically yields a strong improvement in both R_c and $I_{\max}$ without increasing mechanical load.
- **Set a minimum preload:** ensure preload is high enough that the contact is stable and not in the highly sensitive low-force regime where small variations in F cause large swings in A and R_c.
- **Avoid chasing the last increments:** beyond moderate preload and larger radii, gains diminish and the design becomes more sensitive to thermal boundary conditions, thickness limits, and potential local plasticity.
- **Use FE results for final sizing:** once a feasible (R, F) region is selected, the coupled simulation should be used to confirm hotspot temperature and current-density limits under realistic terminals and heat-loss conditions.

VII. Conclusions

This work combined an analytical contact framework with coupled ANSYS simulations to estimate the steady-state current carrying capability of a concave CuSn6 sheet-metal contact pressed against a flat counterface. The results consistently show that preload F and concave radius R influence ampacity primarily through their effect on the effective contact spot size. As the contact patch grows, Holm constriction resistance decreases and heat can spread more effectively, which delays the onset of the allowable temperature limit and increases the maximum admissible current.

Across the investigated range (R = 0.5-3.0 mm, F = 1-30 N), the Hertzian baseline captured the measured contact-area trends and provided a reliable predictor for the direction and magnitude of R_c changes. The coupled analytical model reproduced the main ampacity trends observed in the thermal-electric simulations: R_c decreases rapidly at low preload and then approaches a more gradual reduction at higher preload, while $I_{\max}$ increases with both R and F but exhibits diminishing returns. The simulation results further confirmed that local current crowding near the contact region remains the driver for hotspot formation even when global resistance becomes relatively small, highlighting the importance of assessing peak current density and peak temperature rather than relying on averaged quantities alone.

For CuSn6 concave contacts in thin sheet form, the results suggest prioritizing geometry choices that avoid extremely tight radii when packaging permits, since increasing R provides a direct benefit by enlarging the contact spot without increasing mechanical load. A minimum preload should be selected to move the design out of the low-force regime where contact area and constriction resistance are highly sensitive to small variations in F. Beyond moderate preload and larger radii, further increases provide smaller improvements in R_c and $I_{\max}$, and the limiting mechanism increasingly shifts toward thermal boundary conditions and heat rejection through the surrounding structure. For final sizing, coupled simulation (or targeted testing) is recommended to verify that the peak temperature remains below the allowable limit and that local current-density hotspots are acceptable for the intended duty cycle.

The present study intentionally focused on a clean, idealized metal-to-metal interface in order to isolate geometry and preload effects. In practical applications, surface films and oxidation can introduce an additional, often dominant, resistance contribution and may alter the temperature rise and ampacity significantly. Future work should therefore incorporate film resistance models and surface-state variation, as well as temperature-dependent material properties. In addition, the current study addressed steady-state behavior; extended validation under current cycling, mechanical vibration, and fretting is needed to capture the evolution of contact resistance with wear and surface damage. Finally, investigating the onset of local plasticity and the transition from elastic to elastic-plastic contact in thin sheets would improve confidence at higher assembly loads and provide a more complete design envelope.

ACKNOWLEDGMENT

The authors wish to express their gratitude to Andreas Görmer and Dominic Thurner from iwis mobility systems for their support.

This research is funded by Bayern Innovativ: 2-TPP-2105-0003.

iwis smart connect GmbH strives to provide accurate and reliable information in this article; however, no guarantees are made regarding its correctness, completeness, reliability, or currentness. The content is provided *as is,* and iwis reserves the right to modify or update the information at any time without prior notice.

iwis is a trademark owned or licensed by the iwis SE & Co. KG group of companies. All other product names, logos, and company names mentioned may be the trademarks of their respective owners.

REFERENCES

[1] R. Holm and E. Holm, *Electric Contacts: Theory and Application*, 4th ed. Springer-Verlag, 1967.

[2] P. G. Slade (Ed.), *Electrical Contacts: Principles and Applications*, 2nd ed. CRC Press, Boca Raton, FL, 2013, doi:10.1201/b15640.

[3] M. Braunovic, N. K. Myshkin, and V. V. Konchits, *Electrical Contacts: Fundamentals, Applications and Technology*. CRC Press, 2006, doi:10.1201/9780849391088.

[4] J. A. Greenwood and J. B. P. Williamson, "Contact of nominally flat surfaces," *Proc. Roy. Soc. A*, vol. 295, no. 1442, pp. 300-319, Dec. 1966, doi: 10.1098/rspa.1966.0242.

[5] Leidner, M., Myers, M., Schmidt, H., Sachs, S. & Stefan Thoss, - . Enhancing the contact interface by matching the surface pressure and current density distribution. *ICEC 2014; The 27th International Conference On Electrical Contacts*. pp. 1-6 (2014)

[6] M. Antler, "Electrical effects of fretting connector contact materials: A review," *Wear*, vol. 106, no. 13, pp. 5-33, Nov. 1985, doi:10.1016/0043-1648(85)90101-2.

[7] C. Maul, J. W. McBride, and J. Swingler, "Intermittency phenomena in electrical connectors," *IEEE Trans. Components and Packaging Technologies*, vol. 24, no. 3, pp. 370-377, Sep. 2001.

[8] J. Swingler and J. W. McBride, "Fretting corrosion and the reliability of multicontact connector terminals," *IEEE Trans. Components and Packaging Technologies*, vol. 25, no. 4, pp. 670-676, Dec. 2002, doi:10.1109/TCAPT.2002.808007.

[9] D. Galler and G. Slenski, "Causes of Aircraft Electrical Failures," in *Proc. National Aerospace and Electronics Conference (NAECON)*, Dayton, OH, USA, May 20-24, 1991.

[10] W. S. Ahmad, S. Perinpanayagam, I. Jennions, and S. Khan, "Study on intermittent faults and electrical continuity," *Procedia CIRP*, vol. 22, pp. 71-75, 2014, doi:10.1016/j.procir.2014.07.015.

[11] R. S. Timsit, "Electrical contact resistance: Properties of stationary interfaces," *IEEE Trans. Compon. Packag. Technol.*, vol. 22, no. 1, pp. 85-98, Mar. 1999, doi: 10.1109/6144.759357.

[12] P. Zhang, Y. Y. Lau, and R. S. Timsit, "On the spreading resistance of thin-film contacts," *IEEE Trans. Electron Devices*, vol. 59, no. 7, pp. 1936-1940, Jul. 2012, doi: 10.1109/TED.2012.2195317.

[13] E. Carvou, R. El Abdi, J. Razafiarivelo, N. Benjemaa, and E. M. Zindine, "Thermo-mechanical study of a power connector," *Measurement*, vol. 45, no. 5, pp. 889-896, Jun. 2012, doi: 10.1016/j.measurement.2012.02.007.

[14] Y.-H. Li, F. Shen, and L.-L. Ke, "Multi-physics electrical contact analysis considering the electrical resistance and Joule heating," *Int. J. Solids Struct.*, vol. 256, Art. no. 111975, Dec. 2022, doi: 10.1016/j.ijsolstr.2022.111975.

[15] Y. Zhou, J. Gao, T. Zhang, and J. Lei, "Thermal behavior of plated electrical connectors under high-power and high-frequency excitation," *Electronics*, vol. 14, no. 12, Art. no. 2353, 2025, doi: 10.3390/electronics14122353.

[16] J. Song, D. Hilmert, and F. Kiel, "Mechanisms of failure and state analysis of electrical connectors in automobiles," *Eng. Fail. Anal.*, vol. 173, no. 5, Art. no. 109427, May 2025, doi: 10.1016/j.engfailanal.2025.109427.

[17] L. Zhu, M. Liu, R. Feng, and X. Lin, "Research on the electrical contact performance degradation of aviation connectors under high-temperature conditions," in *Proc. 11th Frontier Academic Forum of Electrical Engineering (FAFEE 2024)*, *Lecture Notes in Electrical Engineering*, vol. 1293, pp. 615-622, Dec. 2024, doi: 10.1007/978-981-97-8832-3_62.

[18] IEC 60512-5-2:2002, *Connectors for Electronic Equipment Tests and Measurements Part 5-2: Current-Carrying Capacity Tests Test 5b: Current-Temperature Derating*. Geneva, Switzerland: International Electrotechnical Commission, 2002.

[19] Aurubis AG, "Material Datasheet CuSn6 (C519 • PNA 282)," document code EN_2024_06, 2024.

[20] KME, “C51900 - CuSn6 (Engineering Copper Solutions)” datasheet, document code “C51900 - CuSn6_2023,” 2023.
[21] Budynas, R. & Nisbett, J. Shigley’s Mechanical Engineering Design. (McGraw-Hill,2014)
[22] K. L. Johnson, *Contact Mechanics*. Cambridge, U.K.: Cambridge Univ. Press, 1985.
[23] F. P. Bowden and D. Tabor, *The Friction and Lubrication of Solids*. Oxford, U.K.: Clarendon Press, 1950.
[24] J. A. Greenwood, “Constriction resistance and the real area of contact,” *Brit. J. Appl. Phys.*, vol. 17, no. 12, pp. 1621-1632, Dec. 1966, doi: 10.1088/0508-3443/17/12/310.
[25] J. F. Archard, “Elastic deformation and the laws of friction,” *Proc. Roy. Soc. A*, vol. 243, no. 1233, pp. 190-205, Dec. 1957, doi: 10.1098/rspa.1957.0214.

Contacting of Copper-Clad Aluminum Hairpins for Electric Drives using Laser Welding

Felix Wirthmann
Institute for Factory Automation and Production Systems (FAPS)
Friedrich-Alexander-Universität Erlangen-Nürnberg (FAU)
Nuremberg, Germany
felix.wirthmann@faps.fau.de

Marcel Baader
Institute for Factory Automation and Production Systems (FAPS)
Friedrich-Alexander-Universität Erlangen-Nürnberg (FAU)
Nuremberg, Germany
marcel.baader@faps.fau.de

Tobias Zürrlein
Institute for Factory Automation and Production Systems (FAPS)
Friedrich-Alexander-Universität Erlangen-Nürnberg (FAU)
Nuremberg, Germany
tobias.zuerrlein@faps.fau.de

Fabian Giesbert
Institute for Factory Automation and Production Systems (FAPS)
Friedrich-Alexander-Universität Erlangen-Nürnberg (FAU)
Nuremberg, Germany
fabian.giesbert@fau.de

Thorsten Ihne
Institute for Factory Automation and Production Systems (FAPS)
Friedrich-Alexander-Universität Erlangen-Nürnberg (FAU)
Nuremberg, Germany
thorsten.ihne@faps.fau.de

Florian Risch
Institute for Factory Automation and Production Systems (FAPS)
Friedrich-Alexander-Universität Erlangen-Nürnberg (FAU)
Nuremberg, Germany
florian.risch@faps.fau.de

***Abstract*— The increasing demand for raw materials driven by industrial and societal electrification has intensified interest in alternative conductor materials for electric machines. Copper, while traditionally favored for its excellent electrical properties, poses economic and resource-based challenges due to rising prices and limited availability. Copper-clad aluminum (CCA) presents a promising alternative, combining the advantageous conductivity of copper with the low density and resource abundance of aluminum. This study investigates the applicability of CCA in hairpin winding technology for traction drives, focusing on the laser welding process as a viable contacting method. Key laser parameters - including power, feed rate, and beam path geometry - were varied systematically and evaluated with regard to weld seam morphology. Based on preliminary results, a full factorial design of experiments (DoE) was conducted for mechanical and electrical validation. The presented findings allow for a foundational understanding of CCA hairpin contacting and provide a basis for future optimization, such as detailed comparative studies with conventional copper and aluminum hairpins.**

Keywords—Copper-clad aluminum, Laser Welding, Contacting, Electric Drives, Hairpin

I. Introduction

The rapid global increase in electric vehicle sales has led to a surging demand for high-performance electric traction drives. In this context, hairpin winding technology has established itself as an industry standard because it enables high fill factors and high degrees of automation. However, this massive market expansion has intensified the pressure on raw material resources, particularly copper, leading to economic challenges due to rising prices and limited availability. To address these issues, Copper-clad aluminum (CCA) has emerged as an alternative for electric vehicle windings, as it combines the high electrical conductivity of copper with the low density and resource abundance of aluminum.

However, joining CCA conductors either with each other or with auxiliary components proves to be challenging, as copper and aluminum have different joining properties. Welding in particular is difficult, due to the different melting temperatures of copper and aluminum, which often results in the use of the significantly slower soldering process for joining copper with aluminum, and thus for joining CCA [1]. To establish a foundational understanding of reliable CCA contacting, this study systematically investigates the laser welding process for rectangular CCA hairpins in traction drives for electric vehicles.

The results, published in this publication, are based on a research project named "E|Form – Dreistufig automatisiertes Endformen von Flachleiterspulen im Blechpaket", FKZ 01MV23011C, funded by the German Federal Ministry for Economic Affairs and Climate Action (BMWK) and managed by the German Aerospace Center (DLR).

II. State of the Art

A. Conductor materials

Copper and aluminum are the most widely used conductor materials in electrical applications due to their excellent electrical conductivity. While copper offers superior conductivity, aluminum provides significant advantages in terms of its lower density and substantially greater global availability [2]. Due to these characteristics, aluminum has gained increasing attractiveness as an alternative, especially in large-scale or weight-sensitive conductor applications.

A promising alternative is copper-clad aluminum. It combines the low density and weight advantages of aluminum with the favorable electrical conductivity of copper. However, CCA is not a metallic alloy; rather, it consists of two distinct materials that remain physically separate. Fig. 1 shows a schematic cross-section of a round and a flat CCA conductor. The aluminum forms the core of the conductor, while the copper is applied as an outer cladding layer.

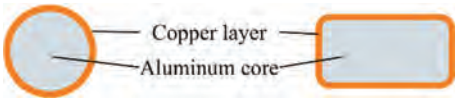


Fig. 1. Schematic illustration of round and flat CCA conductors

1) Characteristics of Copper-Clad Aluminum

Table I highlights the differences between copper, aluminum, and copper-clad aluminum, demonstrating their physical, electrical, and economic characteristics. Aluminum shows the highest natural abundance in the earth's crust (7.57 %) [2], contrasting with copper's much lower presence

(0.006 %) [3], which directly impacts the global market availability. Copper, on the other hand, possesses the highest thermal and electrical conductivity at room temperature of the three materials, while CCA shows slightly but not significantly higher values than aluminum. The mechanical strength follows a similar trend, with copper showing the highest tensile strength, followed by CCA and aluminum [4].

TABLE I. CHARACTERISTICS OF COPPER, ALUMINUM, AND CCA

Key figures	Copper	CCA (15%)	Aluminum
Content in the earth's crust	0,006%	-	7,57%
Density	8.96 g/cm³	3.63 g/cm³	2.70 g/cm³
Melting point	1083 °C	658 °C	658 °C
Thermal conductivity	385 W/mK	240 W/mK	235 W/mK
Electrical conductivity AC	> 58.5 m/(Ωmm²)	> 37.5 m/(Ωmm²)	> 35.8 m/(Ωmm²)
Tensile strength	> 217 MN/m²	> 130 MN/m²	> 90 MN/m²
Price (April 2020)	4.5 €/kg	3.6 €/kg - 25.0 €/kg	1.3 €/kg
Price (May 2025)	8,5 €/kg		2.5 €/kg

The density of aluminum is significantly lower than copper and CCA, offering advantages for weight-critical applications [4]. The density of CCA can be calculated from the ratio of copper to aluminum in the conductor, as shown in (1). The proportion of the material is indicated by p, while the formula symbol ρ is used for the corresponding density.

$$\rho_{CCA} = p_{Cu} * \rho_{Cu} + p_{Al} * \rho_{Al} \quad (1)$$

In addition, the weight savings of CCA conductors compared to copper conductors can also be calculated. For copper-clad aluminum with 15 % copper proportion, the weight savings amount to 40,7 % for each conductor, when compared to pure copper [4]. Moreover, the economic comparison between copper and aluminum illustrates a substantial price increase for the former between 2020 and 2025 [3], while aluminum remains more affordable [2]. The price for CCA varies significantly depending on the supplier and the copper proportion.

In summary, most of the properties of aluminum are improved by the copper coating in CCA conductors. However, the copper coating also leads to different thermal conductivities, which is likely to cause challenges in further processing and, in particular, contacting.

2) Fabrication of copper-clad aluminum conductors

CCA conductors are fabricated through a range of metal forming and bonding processes that aim to achieve a robust metallurgical interface. Among these, extrusion-based techniques represent the dominant industrial approaches, frequently combined with subsequent deformation steps such as rolling or drawing to refine dimensions and enhance bonding quality [5]. Hydrostatic extrusion, for example, enables the formation of a seamless, highly conductive copper sheath around an aluminum core by applying extremely high hydrostatic pressures through a fluid medium [5].

Sequential and combined forming processes are commonly employed to obtain the final conductor geometry [6]. A notable example is co-extrusion followed by multi-stage wire rolling, which can be used to produce rectangular CCA conductors for electric machine windings [5]. Other approaches incorporate casting combined with cold extrusion or employ electroplating of copper onto a prepared aluminum surface to mitigate oxidation and improve subsequent bonding during co-extrusion [5].

3) Fields of application for copper-clad aluminum

CCA is used across various technical disciplines and is applied particularly in electronics and electrical engineering, signal and communication technologies, as well as to some degree in automotive engineering [7]. In addition, CCA is sometimes used in stepper as well as universal motors. The latter can be found in household appliances such as vacuum cleaners, electric drills, or mixers [8]. Depending on the specific application, the copper area proportion relative to the conductor's cross-sectional area can vary substantially. The proportions can range from around 5 % for antennas up to 50 % for drives. Typical commercially available conductors have a copper proportion of 10 - 20 % (see Fig. 2) [1].

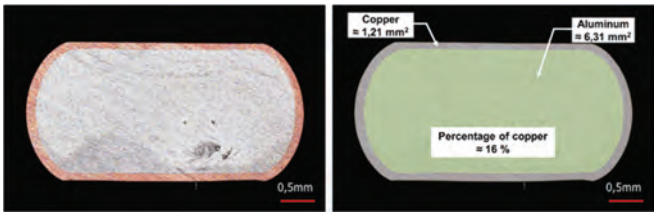


Fig. 2. Microsection of the CCA conductor cross-section used in this study

Furthermore, it is also essential to differentiate between low-frequency and high-frequency applications. In low-frequency applications, the advantage of CCA merely lies in the lower weight of the conductor. In high-frequency applications, however, current displacement occurs in the conductors due to the skin effect, which CCA takes advantage of [7]. Because of the current displacements, the electrical resistance of CCA is comparable to the electrical resistance of copper in these high-frequency applications [1].

Beyond leveraging the skin effect, as well as utilizing the lower weight of aluminum, CCA conductors also contribute to saving copper as a raw material by using aluminum in the core [4]. While global copper reserves are estimated at approximately 3.5 billion metric tons [3], aluminum reserves are projected to lie between 55 and 70 billion metric tons [2]. Due to the lower amount of copper used in the conductors, CCA also utilizes raw material cost savings [4].

However, despite these advantages, the fabrication of CCA conductors is significantly more complex and cost-intensive compared to the fabrication of pure copper or aluminum conductors. Ueda and Hung [1] note that CCA conductors cannot serve as a direct replacement of copper conductors, since it is necessary to adjust the cross-sectional areas of the conductors in an electric use-case due to the difference in electrical conductivity [4].

Furthermore, the joining of CCA conductors proves to be challenging. Welding in particular is difficult, due to the different melting temperatures of copper and aluminum, which often results in the use of soldering, a significantly slower process, for CCA [1].

B. Hairpin production

Many modern traction drives utilize rectangular flat wire conductors, as they enable a high copper fill factor within the stator slots. In addition, flat wire conductors allow for a significantly higher degree of automation in the stator winding production process. Therefore, flat wire technology, especially hairpin technology, has become widely established as the standard for traction drives in numerous sectors [9]. However, the use of hairpins also results in a large number of contacting spots in the stator.

The manufacturing process for stators with flat wire winding differs substantially from that of conventional round wire stators, as described in [9]. Fig. 3 shows the four major steps for the production of hairpin windings. First, the enameled flat wire is formed into the characteristic U-shape. The resulting hairpins are then assembled into a hairpin basket and inserted into the stator lamination stack. In a subsequent step, the open ends of the hairpins are separated, twisted, and electrically connected via a suitable contacting method to ensure a conductive joint [10].

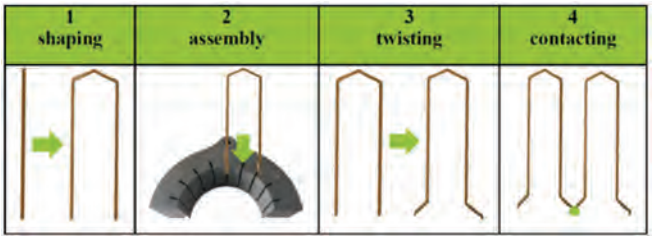


Fig. 3. Major steps in the hairpin winding production chain [10]

The most widely used process for contacting hairpins in traction drives is laser welding. This process creates an electrically and mechanically reliable connection by melting the joining partners using a focused laser beam, thereby forming a metallurgical bond. In order to create a melt pool, the laser radiation must be absorbed by the materials and converted into thermal energy. Therefore, laser welding is suitable only for materials exhibiting sufficient absorption at the specific laser wavelength.

III. Copper-clad aluminum hairpins for traction drives in electric vehicles

In recent years, there has been increased research regarding the application of CCA conductors for electric vehicles. However, most publications only consider round wire applications. Only [5] examines the utilization of CCA in flat wire conductors for hairpin windings. For stators of electric vehicles, CCA offers the opportunity to partly substitute pure copper in the windings with aluminum, which is less expensive and more widely available. The most apparent advantage of CCA in this context is the utilization of the skin and proximity effects of current-carrying conductors.

However, solely considering skin and proximity effects does not sufficiently explain the current distribution within conductors of an electrical motor. Reference [11] identified a range of influencing factors that affect the current displacement in hairpin windings of electric vehicles. Fig. 4 depicts the current density distribution for a copper winding.

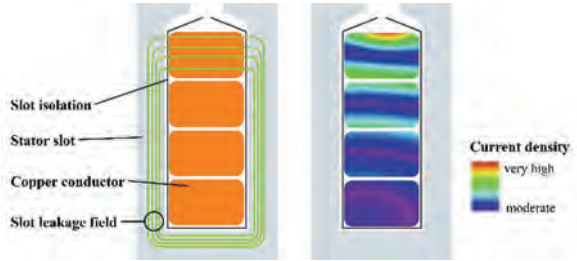


Fig. 4. Current density distribution in stator slots [11]

The current density is significantly greater in hairpins located on the inner side of the stator, close to the air gap, than in those situated on the outer side of the slot [11]. However, it can be assumed that CCA has advantages over pure copper and aluminum windings depending on the motor frequency during operation. Thus, further research is needed to identify the actual current displacement of CCA conductors in hairpin windings.

Nevertheless, the application of CCA poses specific manufacturing challenges. Reference [5] already addresses the manufacturing of rectangular CCA conductors. Further, the mechanical integrity of the copper-aluminum interface during the forming process has not yet been sufficiently validated. The forming contains the risk of copper delamination from the aluminum core during the bending operations of hairpins or of aluminum fracture during cold forming. But most importantly, the contacting process in the stator manufacturing must accommodate two dissimilar materials - copper and aluminum - posing complications in terms of joint quality and reliability. Therefore, the following experimental setup will examine the contacting of CCA flat conductors for hairpin windings, focusing on one of the most common contacting procedures for electric traction drives - laser welding.

IV. Experimental Setup and Methodology

The goal of this study is to determine whether it is possible to reliably join two CCA hairpins using laser welding. First preliminary tests are conducted. Based on these results, a design of experiments (DoE) for systematic electrical and mechanical validation is created. Important laser parameters include power, feed rate, beam path geometry, number of repetitions, as well as the power distribution in the beam shaping functionality BrightLineWeld.

A. Experimental Setup

The welding experiments are conducted using a TRUMPF TruDisk8001 laser system. This diode-pumped Yb:YAG solid-state disk laser operates at a wavelength of 1030 nm and provides a maximum power output of 8000 W. The optic is equipped with the TRUMPF BrightLineWeld function, which allows for the creation of a stable keyhole during welding.

Straight flat-wire segments with a length of 100 mm are used for the experiments in this study. The pins have a cross-sectional area of 4.00 mm x 2.00 mm. In preliminary tests, various beam path geometries are tested. Fig. 5 depicts the two beam path geometries with the best welding results in the initial tests. Thus, these two beam path geometries are used in the DoE.

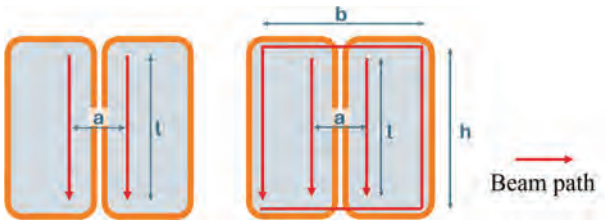


Fig. 5. Beam path geometries 1 (left) and 2 (right) used for the DoE

In addition, various combinations of power and feed rate were investigated. The preliminary tests show that the total energy required to melt the CCA hairpins is similar to the energy required for welding pure aluminum.

However, applying parameters used for pure aluminum results in weld spatter and poor mechanical strength of the joints. The latter is evident from the fact that the samples break at the joint at a bending angle of 30° using manual force. Also, none of the preliminary test samples show sufficient mechanical strength as well as good weld bead quality.

B. Design of Experiments (DoE)

Based on the results of the preliminary tests, the DoE is developed. Due to the high number of factors, a fractional factorial design is chosen to reduce the number of experiments, while still being able to investigate the weldability of CCA and identify viable parameter combinations. In the DoE, a total of twenty parameter combinations are tested. The laser power varies between 2000 W and 8000 W. At the same time, a higher feed rate is set for higher laser power, while the feed rate is reduced for lower laser power in order to systematically vary the specific energy input. Furthermore, the distance between the beam lines is adjusted to investigate whether the distance influences the formation of the weld pool and thus the quality of the joint. Uncontrolled noise factors were kept constant by conducting experiments in a controlled laboratory environment and using samples from a single production batch.

The samples are then visually inspected and manually tested for mechanical strength. The inspection culminated in four viable parameter combinations with promising results. These parameter combinations are samples number 12, 16, 17, and 18, which are also shown in Table II. All of these four samples showed good weld beads with completely melted edges as well as high mechanical strength under manual stress.

TABLE II. PROMISING PARAMETER SETS AFTER PRELIMINARY TESTS

Sample Number	PFO-Geometry used	BrightLine-Weld %Core	Power Melting [W]	Feed rate Melting [mm/s]	Distance between beam lines (a) [mm]	Beam line Length (l) [mm]	PFO-Repetitions Melting
12	4	0,80	8000	200	1,0	3,0	1 time per pin
16	4	0,30	6000	300 first line, 150 second line	1,0	3,0	1 time per pin
17	4	0,80	8000	300 first line, 150 second line	1,0	3,0	1 time per pin
18	4	1,00	2000	75	0,6	3,0	1 time per pin

V. VALIDATION AND RESULTS

For the validation of the four promising parameter sets, eight samples are fabricated for each combination. The eight samples are then measured first electrically using the four-wire method, subsequently mechanically using a peel test, and finally optically with the help of micrographs. For all test setups a Measurement System Analysis was conducted separately from the experiments described in this paper.

To perform the electrical and mechanical tests, all samples were bent into a T-geometry before the experimental investigations. It is also important to note that no stripping of the conductors is required for the measurement since the samples do not have an enamel layer.

A. Electrical Tests

For the electrical tests, a measurement setup based on the four-wire method is used to determine the electrical resistance in the contact zone. A defined current is applied to the sample, and the voltage drop through the joint is measured, allowing determination of resistance. Fig. 6 illustrates the test setup.

For each sample, the resistance was measured ten times at a room temperature of 20.8 °C to compensate for random errors, as well as to minimize external influences, and the mean value is calculated. Under the investigated conditions, parameter set 18 yields the lowest mean contact resistance of one sample (211.143 µΩ), whereas parameter set 16 shows the highest values (up to 270.049 µΩ). However, the measurement values for samples 1 and 5 of parameter set 18 are significantly lower than all the other resistance values.

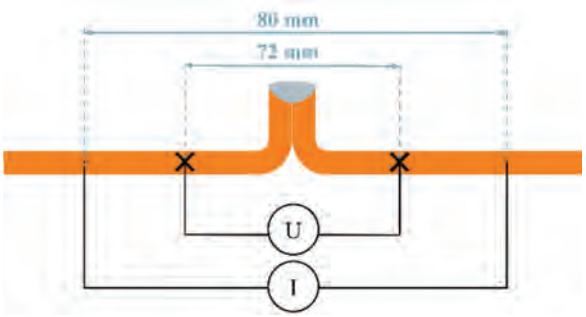


Fig. 6. Four-wire measurement setup for electrical resistance tests

The samples, which were welded with the laser parameter combination 12, offer the least median contact resistance. Still, three of the four parameter sets have very similar median values, and only parameter set 16 shows a slightly higher average contact resistance. Fig. 7 depicts the results of the four-wire measurement as a box plot.

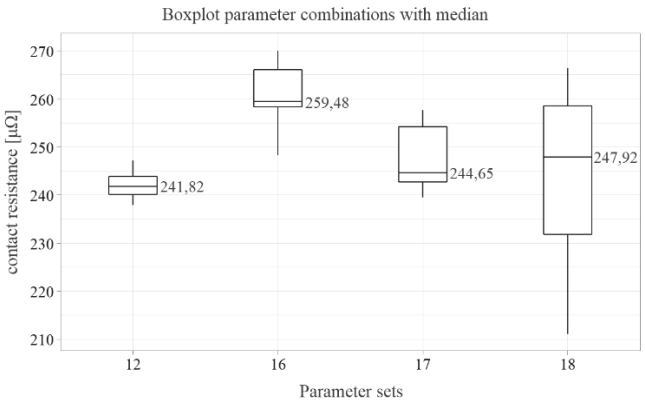


Fig. 7. Box plot of four-wire measurement with median

In order to evaluate the measured contact resistances, the values can be compared with the calculated conductor resistance using (2). Here, the conductor resistance R depends on the specific resistance of the conductor material ρ and the ratio of conductor length l to conductor cross-sectional area A.

$$R_{conductor} = \rho_{material} * \frac{l_{conductor}}{A_{conductor}} \qquad (2)$$

The distance between the measuring points in the four-wire measurement was set at 72 mm. Furthermore, a specific resistance of 0.0267 $\frac{\Omega * mm^2}{m}$ is assumed for CCA. This results in a calculated contact resistance of 240.3 µΩ for the samples. In comparison to the median values shown in Fig. 8, the calculated contact resistance is close to but slightly lower than the measured values. To rule out any deviations attributable to the laser welding process, a 72 mm long unprocessed CCA conductor with the same cross-sectional area is also measured using the four-wire measurement. This results in a resistance of 241.901 µΩ for the conductor, which is slightly higher than the calculated resistance as well, but also slightly lower than the measured values.

Overall, the electrical tests show that all parameter combinations result in good electrical conductivity of the samples, which also implies that at least an acceptable weld quality has been achieved throughout the laser welding process of the CCA hairpins. Based on this finding, not having brittle fractures in the joint is far more important than minor variations in electrical resistance.

B. *Mechanical Tests*

The goal of the mechanical tests is to determine the mechanical strength of the joint. This was done by performing peel tests on a ZwickRoell Z010 tensile testing machine. The experimental setup is depicted in Fig. 8 and is based on a modified peel test in accordance with DIN EN ISO 14270 [12].

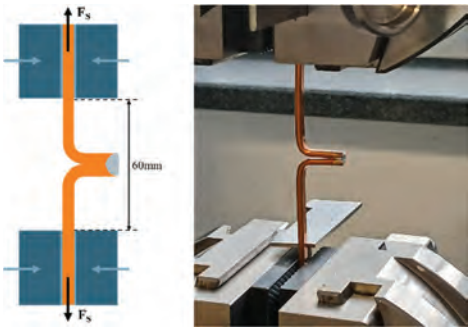


Fig. 8. Peel testing setup based on DIN EN ISO 14270 [12]

Each sample is clamped into the tensile testing setup, and the pre-force is set to 20 N before test execution. For each parameter set, eight samples are tested. Fig. 10 shows the force-displacement diagrams for the four investigated parameter sets.

The evaluation of the tests shows that all samples in parameter set 16 suffered brittle fractures. The maximum force measured is 33.85 N, while the mean value for all eight samples is 27.11 N.

Parameter set 17 results in five brittle fractures. However, three samples show good results for the peel force, with the maximum measured at 168.89 N. In the tests for parameter set 12, only three brittle fractures occurred. For this parameter set, the maximum peel force measured is 177.41 N.

Only parameter set 18 results in no brittle fractures. A plastic deformation begins between 25 N and 40 N for each sample. The maximum peel force is at 204.59 N for sample 2, while the mean value for the maximum peel force for all samples is 175.27 N. Furthermore, it can be observed in the investigations that these samples fracture below the contact point rather than at it. Fig. 9 also shows that after the aluminum core broke, the copper layer was pulled off the core. Residues of the aluminum core remained stuck to the pulled-off copper layer.



Fig. 9. Pulled-off copper layer on a sample of parameter set 18

The results indicate that no mechanically resilient joints can be achieved with parameter set 16. However, the investigation results of parameter set 18 are promising and show high peel forces. This also indicates a high mechanical stability of the joint for welds done with parameter combination 18.

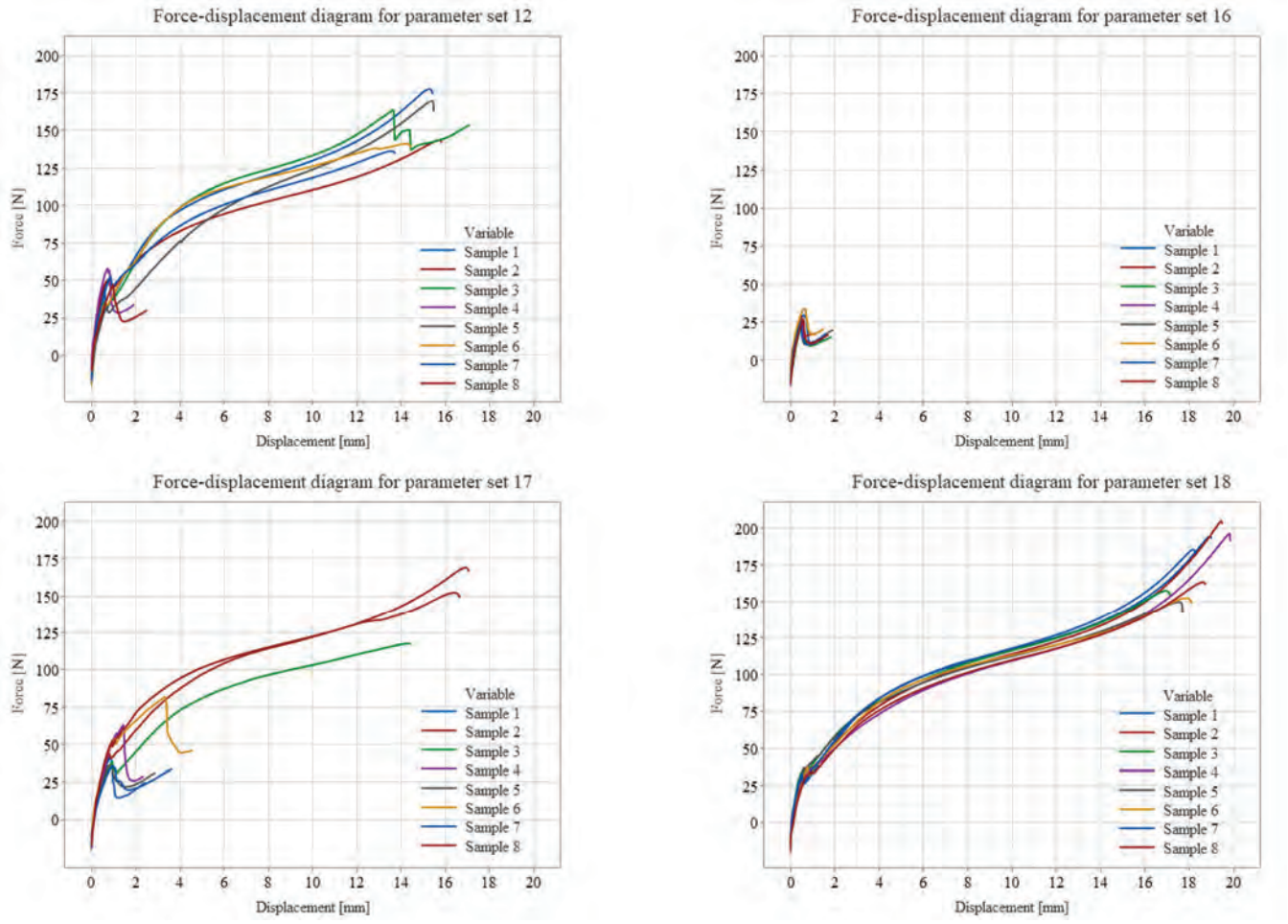


Fig. 10. Force-displacement diagrams for parameter sets 12,16,17 and 18

C. Microsections of samples

In the final investigation, the microstructure of the samples is analyzed. For this, polished microsections of the samples are prepared and examined under a microscope.

When examining the samples of parameter sets 12 and 17, a particularly large number of small pores can be detected alongside a few large ones. While parameter set 12 has more and larger small pores in comparison, the size of the large pores in set 17 is bigger. These larger pores may be the reason for the brittle fractures of these samples. The samples of parameter set 18 contain almost no pores, which accounts for the high mechanical strength of the joint. However, in comparison to the samples of 12 and 17, the depth of the keyhole in parameter set 18 is significantly lower. (Fig. 11)



Fig. 11. Microsections of samples welded with parameter set 12 (left), 17 (middle), and 18 (right) with light grey being the heat affected zone

None of the micrographs shows any melting of the outermost copper layer, even though the melting zone extends to the clad copper layer. This can be explained by the relatively low energy input for copper and the laser beam geometry used.

After completion of the validation, it can be concluded that parameter set 18 achieved very good results in terms of electrical conductivity and mechanical stability. The good electrical and mechanical properties can be attributed to a low number of pores in the weld pool. Even though the electrical resistance of these samples varies much more, not having brittle fractures in the joints is far more important.

Parameter set 16, on the other hand, exhibited the highest electrical resistances. In addition, the formation of a brittle joint was observed, as shown in the results of the peel tests.

In terms of welding parameters, this means that the best results for CCA were achieved with low power and low feed rates. In addition, a reduced distance between the lines has a positive effect on the formation of the melt pool in the joint zone.

VI. Summary and Outlook

The main goal of this study was to gain a fundamental understanding of how to reliably contact rectangular CCA hairpins for use in traction motors for electric vehicles using laser welding. The results confirm the technical feasibility of creating reliable metallurgical joints using this method. Optimal joint characteristics, including high mechanical stability and electrical conductivity comparable to unprocessed conductors, were achieved using a strategy of low laser powers and slow feed rates. While excessive energy input led to increased porosity and brittle joint behavior, the optimized parameters resulted in nearly pore-free welds where mechanical failure occurred primarily in the base material rather than the joint itself.

Future research should build upon these findings by focusing on optimizing the process parameters as well as a detailed analysis of micro segregation and the formation of intermetallic phases at the copper-aluminum interfaces, as these metallurgical interactions are critical for controlling joint ductility. Furthermore, evaluating the long-term stability of the connection under operational load cycles is essential; given the differing thermal expansion coefficients of copper and aluminum, the joint's integrity must be validated through thermal-mechanical fatigue testing.

Future studies will also evaluate the impact of insulation residues and the quality of the stripping process on the results, as enamel remnants are known to influence gas formation and porosity. Finally, comprehensive benchmarking against conventional pure copper and aluminum hairpins is necessary to fully assess the industrial potential of CCA as a resource-efficient alternative in high-performance electric motor production.

Acknowledgment

The corresponding author thanks Tobias Zürrlein, Matthias Beranek, and Andreas Morello for their revisions and consulting. Furthermore, the author thanks Simon Stauber, Thorsten Ihne, Prof. Dr. Florian Risch, and Prof. Dr. Jörg Franke for their review. Additionally, the authors thank Fabian Giesbert and Marcel Baader for their support during practical experiments.

References

[1] K. Ueda and C. Hung, "The high-frequency phenomenon of copper clad aluminum wires which are lower the alternating current resistance than copper solid wires, and the application of copper clad aluminum wires to the electrical equipment," *Electrical Engineering Japan*, vol. 216, no. 3, 2023, Art. no. e23435, doi: 10.1002/eej.23435.

[2] U.S. Department of the Interior, Ed., "Aluminum in June 2025," 2025. Accessed: Nov. 23, 2025. [Online]. Available: https://www.usgs.gov/centers/national-mineralsinformation-center/mineral-industry-surveys.

[3] U.S. Department of the Interior, Ed., "Copper in March 2025," 2025. Accessed: Nov. 23, 2025. [Online]. Available: https://www.usgs.gov/centers/national-mineralsinformation-center/mineral-industry-surveys.

[4] VDM Metals International GmbH, Ed., "Data sheet Cuponal," Frankfurt am Main, 2021. Accessed: Nov. 23, 2025. [Online]. Available: https://www.vdm-metals.com/de/cuponal.

[5] B. Finateri, B. Williams, N. Kar, and A. Edrisy, "Pilot scale production of copper clad aluminum e-motor windings through combined extrusion-rolling," 2025, doi: 10.21203/rs.3.rs-7402640/v1. unpublished.

[6] T. T. Sasaki, R. A. Morris, G. B. Thompson, Y. Syarif, and D. Fox, "Formation of ultra-fine copper grains in copper-clad aluminum wire," *Scripta Materialia*, vol. 63, no. 5, pp. 488–491, 2010, doi: 10.1016/j.scriptamat.2010.05.010.

[7] N. Ahmed, "Extrusion of copper clad aluminum wire," *Journal of Mechanical Working Technology*, no. 2, pp. 19–32, 1978.

[8] A. Bareggi, F. Casiraghi, and L. de Rai, "Copper-clad aluminum as an alternative to copper flexible conductors for electric power cables: opportunities and challenges," *9th International Conference on Insulated Power Cables*, 2015.

[9] A. Riedel *et al.*, "Challenges of the hairpin technology for production techniques," *21st International Conference on Electrical Machines and Systems (ICEMS)*, 2018. [Online]. Available: https://ieeexplore.ieee.org/document/8549105.

[10] T. Gläßel, J. Seefried, and J. Franke, "Challenges in the Manufacturing of Hairpin Windings and Application Opportunities of Infrared Lasers for the Contacting Process," *7th International Electric Drives Production Conference (E|DPC)*, 2017. [Online]. Available: http://ieeexplore.ieee.org/servlet/opac?punumber=8326424.

[11] M. Lindner, P. Moritz, and J. Jung, "Hairpin-Wicklungen für elektrische Fahrantriebe," *2. Freiberger Kolloquium Elektrische Antriebstechnik*, pp. 140–154, 2019.

[12] *Resistance welding - Destructive testing of welds - Specimen dimensions and procedure for mechanized peel testing resistance spot, seam and embossed projection welds*, DIN EN ISO 14270, Deutsches Intstitut für Normung e.V., Berlin, Nov. 2016.

Effect of Ag/TiO_2 Nanoparticles on the Electrical Performance and Durability of Silver Coatings for Electrical Contacts

Alsayed *Abdel Aal*
Precision Engineering Laboratory
Ostwestfalen-Lippe University of Applied Sciences and Arts
32657 Lemgo,
Germany
alsayed.ibrahim@th-owl.de

Michael Blauth
Precision Engineering Laboratory
Ostwestfalen-Lippe University of Applied Sciences and Arts
32657 Lemgo,
Germany
michael.blauth@th-owl.de

Jian Song
Precision Engineering Laboratory
Ostwestfalen-Lippe University of Applied Sciences and Arts
32657 Lemgo,
Germany
jian.song@th-owl.de

Abstract*—The growing use of electronic systems is increasing demand for durable electrical connectors that withstand harsh environments while maintaining low contact resistance. The silver's high electrical conductivity, resistance to oxidation, and stable low contact resistance under mechanical and thermal stresses make it well suited for electrical contact coatings. The electrodeposition of nanocomposite coatings incorporating metal oxide particles, such as Titanium dioxide (TiO_2) nanoparticles, can enhance the mechanical strength and tribological performance. This work investigates the effect of Ag-coated TiO_2 (Ag/TiO_2) nanoparticle incorporation into Ag coatings on their mechanical and electrical properties. The silver coatings with varying Ag/TiO2 nanoparticle concentrations were fabricated by electroplating and systematically characterized. The impact of embedded Ag/TiO_2 nanoparticles on the electrical contact resistance, hardness, and service lifetime was examined. The results indicate that nanoparticle incorporation enhances microhardness and prolongs the service lifetime, while only slightly increasing electrical contact resistance.

***Keywords*—Connectors, electrical resistance, silver coatings, nanocomposite, mechanical properties, friction, tribology**

I. Introduction

Reliable electrical contacts are essential for stable signal and power transmission in e.g. modern electronic, automotive and aerospace systems. Their performance is strongly affected by thermal and vibration-induced fretting, which leads to surface degradation, debris formation, and increases in electrical contact resistance (ECR) [1], [2]. Ensuring low ECR together with high wear resistance is therefore critical for long-term connector reliability. In industrial applications, such as automotive, aerospace, and power distribution systems, maintaining low ECR prevents energy loss, overheating, and potential system failures, ensuring efficient and safe operation [3], [4].

Silver coatings are widely used as a cost-effective alternative to gold because of their high electrical conductivity and favourable tribological behaviour [1], [2], [3]. Experimental and modelling studies show that oxide formation, particularly in the base material and barrier layer, debris accumulation, and localized deformation accelerate coating breakdown, resulting in rapidly rising ECR and reduced electrical performance [5], [6].

Electrodeposition offers a scalable method to produce protective coatings with controlled microstructures and to incorporate hard reinforcement phases [7]. Titanium dioxide nanoparticles are effective in strengthening various metal matrices, improving hardness and wear resistance, but their low electrical conductivity limits their application in silver contact coatings where insulating particles can increase ECR [8], [9], [10].

The core–shell particles offer a promising design strategy to achieve both mechanical reinforcement and electrical conductivity. The metallic shells improve dispersion, control interfacial chemistry, and mitigate the insulating effects of ceramic cores, as demonstrated in prior silver–ceramic systems [11]. Building on this concept, this study synthesizes the core–shell Ag/TiO_2 nanoparticles design and incorporates them into electrodeposited silver coatings. The resulting Ag–Ag/TiO_2 composite films are evaluated for their impacts on ECR, hardness, and tribological behaviour, offering guidance for designing durable, high-performance silver-based electrical contacts.

II. Experimental procedure

A. Synthesis of Nanoparticles

The Ag/TiO_2 nanoparticles were synthesized through electroplating utilizing a rotating plating apparatus. Detailed descriptions of the equipment configuration and experimental conditions have been previously documented in the literature [12], [13]. The Ti content and its spatial distribution were analysed by X-ray fluorescence (XRF, Helmut Fischer GmbH) using elemental mapping of the Ag–Ag/TiO_2 composite coatings. For SEM imaging of synthesized nanoparticles, the dried nanoparticles were gently placed onto carbon adhesive tape, ensuring adhesion without significantly altering their morphology.

B. Composite Coatings Preparation

Copper (Cu-DHP), a deoxidized grade characterized by high electrical conductivity, was utilised as the base material. The substrates were precisely fabricated into spherical and flat specimens with a contact radius of 4.5 mm, a width of 3.0 mm, and a thickness of 0.3 mm, as illustrated in Fig. 1.

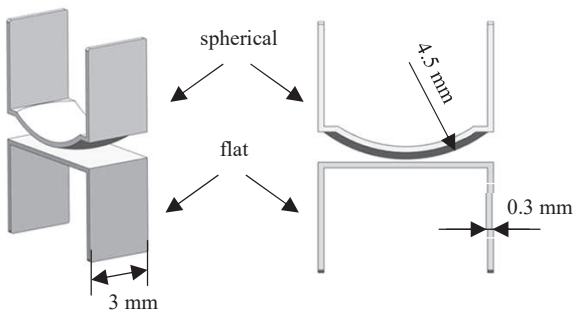


Fig. 1. Geometry and dimensions of the electrical contact specimens.

In order to suppress copper diffusion into the subsequently deposited silver layer, a nickel barrier layer (2 – 2.5 µm thick) was applied. The electrodeposition of Ni was performed from a Watts bath in Table 1.

TABLE I COMPOSITION AND PARAMETERS OF WATT'S ELECTROLYTE

Composition and Parameters	Value
Nickel sulphate	250 g/L
Nickel chloride	45 g/L
Boric acid	40 g/L
Temperature	50 °C
pH	4.5
Current density	1 A/dm^2

The copper substrates were pre-treated by electrolytic degreasing to remove oxides and passive layers. Degreasing was performed cathodically for 1 minute and anodically for 10 seconds at a current density of 10 A/dm². The substrates were then pickled in 10% H_2SO_4 for 30 s. During the nickel electroplating, the samples were mounted as cathodes on a rotating holder (100 rpm). The electrolyte was homogenized with a magnetic stirrer at 500 rpm. Silver electroplating was performed on the nickel-coated copper substrates to achieve a coating thickness of 3.0 ± 0.3 µm, utilizing an alkaline bright silver electrolyte under ambient laboratory conditions. In order to ensure uniform current distribution and homogeneous deposition, a silver wire anode was configured in a circular arrangement surrounding the specimens. The plating was conducted at a current density of 1 A/dm², with electrolyte agitation maintained by a magnetic stirrer operating at 750 rpm.

The co-deposition of silver with Ag/TiO_2 nanoparticles was accomplished by dispersing nanoparticle concentrations of 25, 50, and 100 mg/L into the bright silver electrolyte using ultrasonic treatment (Labsonic M, Sartorius Stedim Biotech GmbH). The resulting electrodeposited coatings are denoted as Ag (pure silver), Ag–NP25, Ag–NP50, and Ag–NP100, corresponding to nanoparticle loadings of 25, 50, and 100 mg/L, respectively.

C. Characterization Methods

The morphology of the synthesized Ag/TiO_2 nanoparticles was examined using scanning electron microscopy (SEM / Zeiss EVO 50). Line-scan energy-dispersive X-ray spectroscopy (EDX) was conducted to evaluate the spatial distribution and incorporation of Ag/TiO_2 nanoparticles within the deposited silver coatings. The surface roughness of the Ag and composite Ag–Ag/TiO_2 coatings was characterized using a confocal microscope (µsurf explorer; NanoFocus AG, Germany). Microhardness measurements (HV0.01) were performed to evaluate the influence of co-deposited nanoparticles on the hardness of silver coatings. The tests were carried out using a Vickers microhardness tester (ZwickRoell GmbH & Co. KG) under a load of 0.098 N.

Wear tests were conducted to assess the tribological performance of the silver and silver–nanoparticle coatings under fretting conditions. The experiments were performed on a wear and fretting test rig (Fig. 2) at a frequency of 2 Hz, an amplitude of 100 µm, and a normal load of 2 N. The ECR was continuously recorded using a constant current source (Keithley 6220) in combination with a nanovoltmeter (Keithley 2182A). The coefficient of friction (CoF) was determined from the friction force measured with a laser distance sensor. A ECR of 50 mΩ was defined as the termination criterion. Prior to the tribological tests, the silver and silver nanoparticle coatings were cleaned with isopropanol.

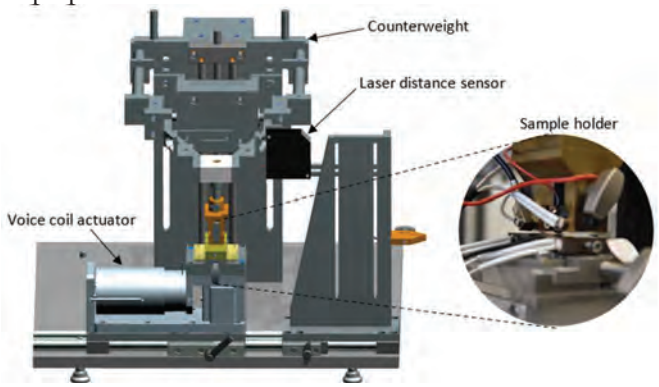


Fig. 2. Setup of wear and fretting test rig.

III. RESULTS AND DISCUSSION

A. Fabrication of Nanoparticles and Composite Coatings

The elemental characteristics of the synthesized Ag/TiO_2 nanoparticles were examined through EDX, as depicted in Fig. 3. The quantitative elemental analysis reveals a silver content of 79.01 wt.%, oxygen at 16.85 wt.%, titanium at 2.65 wt.% and carbon at 1.94 wt.%. These results indicate the coexistence of TiO_2 and Ag within the sample. The intended core–shell architecture has been previously demonstrated by our group [12].

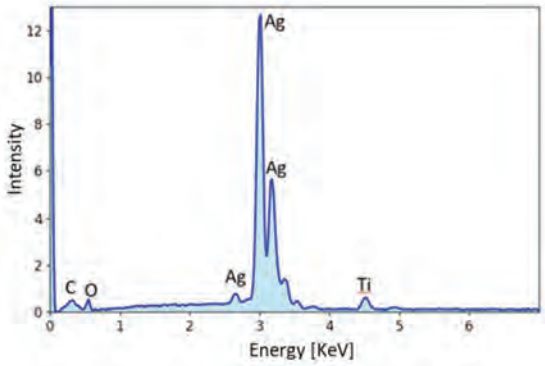


Fig. 3. EDX analysis of Ag/TiO_2 nanoparticles.

The structural features of the synthesized Ag/TiO_2 nanoparticles were characterized using SEM, as shown in Fig. 4. The image reveals a distinct dendritic morphology, indicating that the silver coating on the TiO_2 core forms a highly branched, tree-like structure. This pattern suggests anisotropic nucleation and growth of the silver shell, typical of electroplating processes [14]. It should be noted that these dendritic features correspond to agglomerates of nanoparticles rather than individual particles.

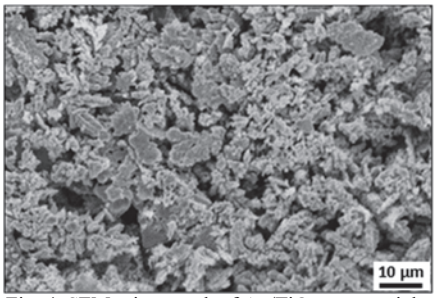


Fig. 4. SEM micrograph of Ag/TiO_2 nanoparticles.

Fig. 5 shows the particle size distribution for uncoated TiO_2 and Ag–coated TiO_2 nanoparticles. The particle size of uncoated TiO_2 is in range of 4–10 nm. On the other hand, the coated particles exhibit a narrower and more symmetric size distribution, with distinct maxima appearing in the ranges of 25–45 nm, 90–140 nm, and 200–300 nm. The pronounced primary peak indicates more uniform silver shell formation, resulting in smaller and more monodisperse Ag/TiO_2 nanoparticles.

The occurrence of larger particle sizes at the second and third distribution peaks (90–300 nm) could be indicative of either agglomeration of particles initially formed at the primary peak or an increase in particle dimensions due to thickening of the silver coating layer. Notably, in coated particle size distribution, no particles are detected within the 4–10 nm range, the expected size domain of uncoated TiO_2 cores, suggesting effective coverage of the TiO_2 particles by the silver phase.

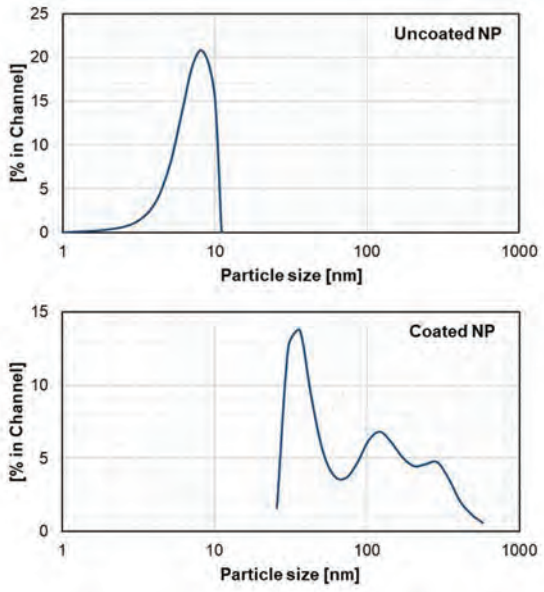


Fig.5. Particle size distribution of dispersed uncoated TiO_2 nanoparticles compared with Ag/TiO_2-coated nanoparticles.

EDX line-scan was utilized to assess the spatial distribution and incorporation of Ag/TiO_2 nanoparticles within the silver coatings. Fig. 6 illustrates the elemental distribution of titanium across the surface of the composite coating, as determined by EDX line-scan analysis. A spatial resolution of one measurement point per micrometer was employed to accurately capture localized compositional heterogeneities. The titanium content exhibited a positive correlation with increasing nanoparticle concentration in the plating bath, reaching approximately 0.3–1.5 wt.% for Ag-NP25, 0.4–1.7 wt.% for Ag-NP50, and 0.3–1.9 wt.% for Ag-NP100. This trend reflects the improved co-deposition efficiency at higher nanoparticle concentrations.

To complement the EDX line-scan analysis, XRF elemental mapping was performed to evaluate the spatial distribution of Ti within the $Ag–Ag/TiO_2$ composite coatings (Figure 7). For the Ag–NP25 coating, Ti is distributed within a narrow concentration range (0.01–0.03 wt.%) and appears relatively uniform across the analysed area, with only limited localized enrichments. This behaviour indicates to a homogeneous incorporation of nanoparticles at low concentration.

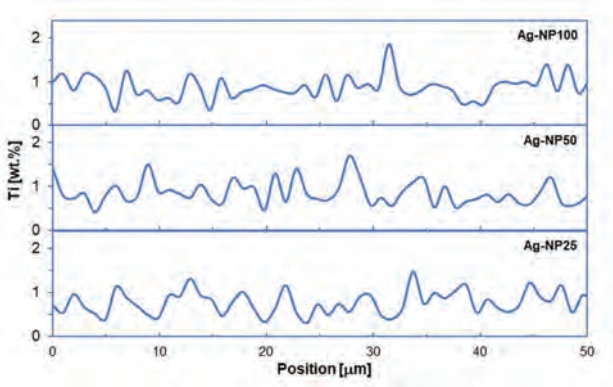


Fig. 6. EDX line-scan analysis of Ti-content in composite coatings.

With increasing nanoparticle content (Ag–NP50), the Ti distribution shifts toward higher values (0.03–0.06 wt.%) and exhibits greater spatial variation. While a generally uniform distribution is still observed, regions with elevated Ti content (0.10 wt.%) become more frequent, suggesting increased particle incorporation accompanied by the onset of localized clustering. At the highest concentration (Ag–NP100), the Ti distribution becomes more heterogeneous. The dominant Ti-content range increases further (0.05–0.08 wt.%), and distinct Ti-rich regions are observed across the surface. This behavior indicates enhanced nanoparticle incorporation together with more pronounced agglomeration at elevated particle concentrations.

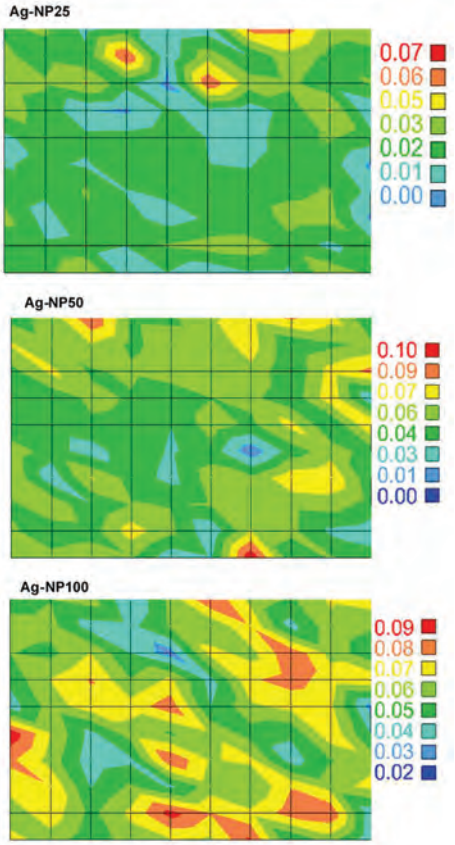


Fig 7. XRF elemental mapping of Ti distribution in composite coatings over a 10 µm×10 µm area: the colour scale representing Ti content (wt.%).

These findings demonstrate that the XRF elemental mapping corroborates the EDX line-scan analysis, confirming that higher nanoparticle concentrations in the electrolyte result in increased Ti incorporation while simultaneously decreasing spatial uniformity. The differences in absolute Ti values

between both techniques can be attributed to their distinct sampling characteristics: EDX provides localized, near-surface measurements, whereas XRF represents an average over a larger area and depth.

B. Electrical and Mechanical Properties

Although the bulk resistivity of the contacting materials contributes to the total resistance, the ECR arising between two mating bodies, here, a flat and a spherical surface, is primarily dictated by the characteristics of the interfacial region. The surface topography and mechanical attributes of the applied coatings play a decisive role in determining the real contact area [15]. Consequently, incorporation of Ag/TiO_2 nanoparticles can modify the coating structure, altering surface roughness and mechanical behavior, which in turn influences ECR by affecting both the number and effectiveness of conductive micro-contacts at the interface.

To examine such correlation, the initial ECR of the flat–sphere configuration was measured for all coatings, pure silver (Ag) and the nanoparticle-reinforced composites coatings (Ag–NP25, Ag–NP50, Ag–NP100), prior to the onset of fretting testing. As shown in Fig. 8, embedding Ag/TiO_2 nanoparticles into the silver coating results in a distinct increase in the initial ECR, with average values of 0.442, 0.526, 0.680, and 0.860 mΩ for Ag, Ag–NP25, Ag–NP50, and Ag–NP100, respectively.

These trends are further supported by XRF elemental mapping (Fig. 7), which shows increasing Ti incorporation and greater spatial heterogeneity at higher nanoparticle concentrations. The local variations in nanoparticle distribution correspond to surface microstructural inhomogeneities that can influence the number and stability of conductive micro-contacts, providing a spatial basis for the observed ECR behavior.

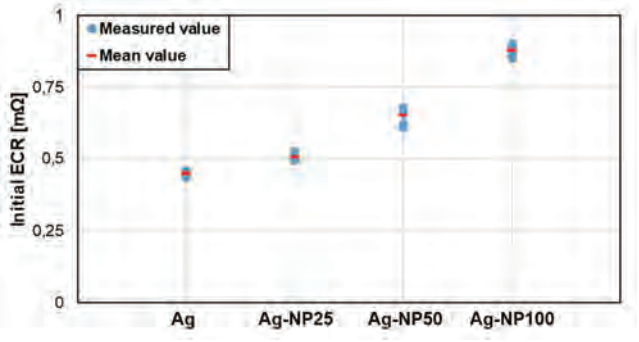


Fig.8. Measured initial contact resistance values and corresponding mean values (n = 5) of silver and silver–nanoparticles coatings.

Additional clarification regarding the increase in initial ECR is provided through an examination of the surface roughness of the Ag and Ag–Ag/TiO_2 composite coatings using confocal microscopy, as presented in Fig. 9. The quantitative measurements indicate that the average roughness (Ra) increases from 0.032 µm for the pure Ag coating to 0.075 µm, 0.131 µm, and 0.218 µm for the Ag–NP25, Ag–NP50, and Ag–NP100 coatings, respectively. The nanoparticle incorporation progressively increases surface roughness, reflecting the embedding of nanoparticles within the silver matrix and the formation of a more heterogeneous surface microstructure. The observed roughening is consistent with the rise in ECR shown in Fig. 8, as higher surface roughness generates larger and more irregular asperities that reduce the formation of effective contact spots.

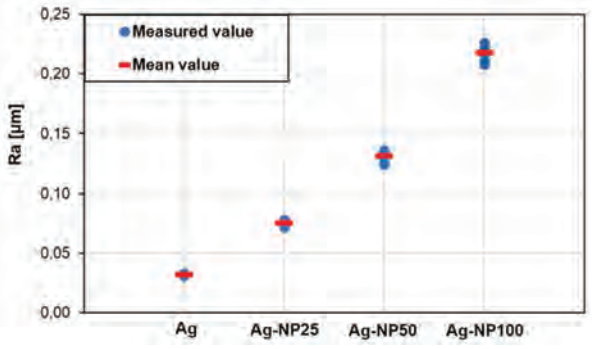


Fig. 9. Measured surface roughness values and corresponding mean values (n = 5) of silver and silver–nanoparticle coatings.

In addition, the mechanical performance of the coatings was evaluated via Vickers microhardness measurements (HV0.01, Fig. 10). The pure silver coating exhibits the lowest hardness (average 93 HV0.01). With increasing concentrations of Ag/TiO_2 nanoparticles, the microhardness systematically rises, reaching a maximum for the Ag–NP50 coating. A slight decrease in hardness is observed for Ag–NP100, which corresponds to the higher nanoparticle concentration and the increased likelihood of particle agglomeration, as indicated by the XRF elemental mapping (Fig. 7). These observations demonstrate that moderate incorporation of co-deposited Ag/TiO_2 nanoparticles enhances the microhardness of the silver coating, consistent with previous studies on nanoparticle-reinforced coatings [16,17], while excessive nanoparticle loading can reduce the effectiveness of this reinforcement due to local heterogeneities.

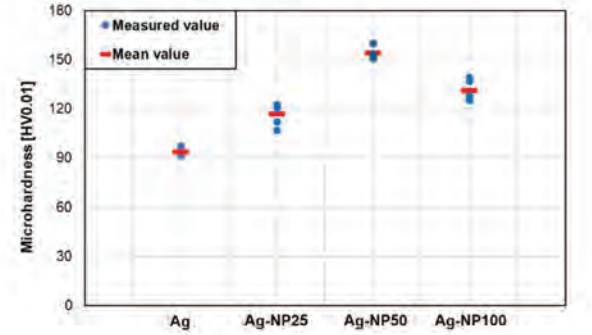


Fig. 10. Measured microhardness values and corresponding mean values (n = 5) of silver and silver–nanoparticle coatings.

A clear interdependence between initial ECR, surface roughness, and microhardness is evident in the examined silver and silver–nanoparticle composite coatings.

Up to the Ag–NP50 coating, ECR increases with nanoparticle concentration, paralleling the increase in average microhardness and average surface roughness. The higher microhardness reduces plastic deformation of asperities under load, thereby decreasing the average real contact area. On the other hand, the increased roughness generates more irregular asperities that further limit effective conductive spots. Both effects contribute to the observed rise in ECR.

For the Ag–NP100 coating, although the average microhardness slightly decreases, ECR reaches its highest value due to the substantial increase in average surface roughness and higher content of non-conductive TiO_2 nanoparticles. At this stage, surface topography dominates the average real contact area, superseding the contribution from mechanical strengthening.

These results quantitatively demonstrate that the combined effects of average roughness, average microhardness, and nanoparticle incorporation govern the contact behavior and explain the observed ECR trends across the coatings.

C. Tribological Performance under Fretting Conditions

The fretting wear represents a significant degradation mechanism in electrical contact systems. Fig. 11 presents the average service lifetime of silver coatings under fretting tests: 12,560, 15,229, 27,767, and 19,910 cycles for Ag, Ag–NP25, Ag–NP50, and Ag–NP100, respectively. The data show that moderate incorporation of Ag/TiO_2 nanoparticles (NP25 and NP50) enhances coating durability. In particular, the Ag–NP50 coating exhibits the longest average lifetime, correlated with the highest microhardness (Fig. 10) and controlled surface roughness (Fig. 9). For Ag–NP100, the average lifetime decreases despite higher roughness, which is associated with a slight reduction in microhardness.

This quantitative comparison demonstrates that service lifetime is primarily influenced by the combined effects of microhardness, surface roughness, and nanoparticle incorporation, highlighting the optimal nanoparticle concentration for improved coating performance.

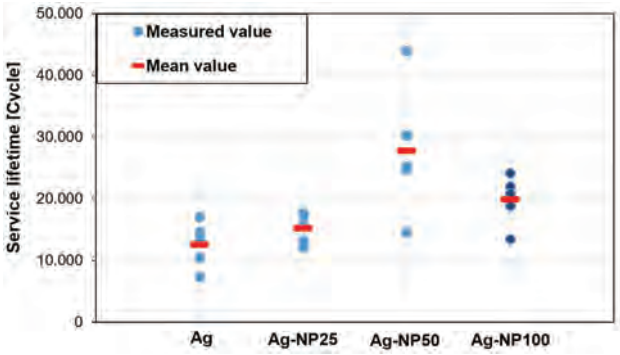


Fig. 11. Measured service lifetime spread values and corresponding mean values (n = 5) of silver and silver–nanoparticles coatings.

The frictional response of the Ag and nanocomposite coatings (Ag–NP25, Ag–NP50, Ag–NP100) was assessed over successive sliding cycles. Fig. 12 illustrates the corresponding evolution of the CoF for silver and composite coatings. All coatings exhibit a characteristic running-in period during the initial cycles, evidenced by a pronounced decrease in CoF as the surfaces conform and stable contact conditions are established in the early stages of wear [18]. Following this adaptation phase, the CoF reaches a relatively stable plateau in same the range for all samples, indicating that steady-state friction is largely unaffected by nanoparticle concentration.

The insignificant influence of Ag/TiO_2 nanoparticle incorporation on the CoF can be attributed to the predominance of silver–silver contact at the sliding interface. The embedded nanoparticles, enveloped by a ductile silver shell, do not substantially modify the interfacial shear response, which remains governed by the intrinsic mechanical properties of the silver matrix. These findings indicate that while nanoparticle incorporation can improve wear resistance, its influence on frictional behaviour under the present testing conditions remains limited

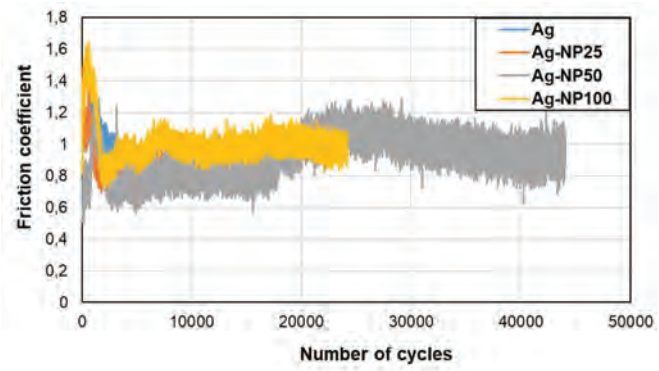


Fig.12. Evolution of the coefficient of friction (CoF) for silver and silver–nanoparticle composite coatings over successive fretting cycles.

IV. Conclusion

This research reports on the integration of Ag/TiO_2 nanoparticles into silver coatings to enhance tribological performance for electrical contact applications. The nanoscale Ag/TiO_2 particles were incorporated into silver coatings via electrodeposition under controlled plating conditions, enabling co-deposition of nanoparticles within the metallic matrix. The increasing of Ag/TiO_2 nanoparticle concentrations (25–100 mg/L) in the plating baths produces a corresponding rise in particle incorporation in silver layer, as confirmed by EDX compositional analyses and XRF mapping. The initial contact resistance increases with both surface roughness and microhardness, reflecting the influence of nanoparticle dispersion. However, beyond a critical hardness level, surface topography becomes the dominant factor. The microhardness improves substantially with Ag/TiO_2 addition, while excessive loading causes a slight decline due to particle clustering. The fretting-wear tests show a marked improvement in electrical service lifetime at 50 mg/L, more than doubling that of pure silver coatings. The frictional behaviour exhibits insignificant changes with nanoparticle incorporation, consistent with the dominance of the silver matrix in controlling interfacial shear. These findings highlight the importance of optimizing nanoparticle concentration and dispersion to achieve balanced mechanical and electrical performance in silver coatings for durable electrical contacts. Further investigations are necessary to optimize the dispersion of nanoparticles within the silver matrix and to minimize variability in the coating service lifetime.

ACKNOWLEDGMENT

This study was conducted within the framework of the research project *HighPerfSilver*, which focuses on the development of high-performance silver-based coatings for electrical contact applications. The project is financed by the Federal Ministry for Economic Affairs and Energy (BMWE).



REFERENCES

[1] K. H. Ziegler, "Electrical contact phenomena in automotive connectors under vibration," *Wear*, vol. 251, pp. 1334–1341, 2001. DOI: 10.1016/S0043-1648(01)00777-2.

[2] J. Kassman and S. Jacobson, "Surface degradation of silver-plated contacts subjected to fretting corrosion," *Wear*, vol. 160, pp. 153–161, 1993. DOI: 10.1016/0043-1648(93)90219-6.

[3] J. Laporte, O. Perrinet, and S. Fouvry, "Prediction of the electrical contact resistance endurance of silver-plated coatings subject to fretting wear, using a friction energy density approach," *Wear*, vol. 330–331, pp. 170–181, 2015, doi: 10.1016/j.wear.2014.12.006.

[4] J. Cheng, L. Zhao, X. Zhou, T. Ren, S. Jin, T. Xie, P. Liu, Z. Peng, and Q. Wang, "Research on the characteristic of the electrical contact resistance of strap contacts used in high voltage bushings," Energies, vol. 16, p. 4702, 2023, doi: 10.3390/en16124702.

[5] P. G. Slade, Electrical Contacts: Principles and Applications, Boca Raton, FL: CRC Press, 2013.

[6] J. Ding, D. F. Drees, S. B. Lee, and J. O. Peters, "Multiscale modeling of fretting wear in silver electrical contacts," *Wear*, vol. 319, pp. 121–131, 2014. DOI: 10.1016/j.wear.2014.07.015.

[7] M. Paunović and M. Schlesinger, *Fundamentals of Electrochemical Deposition*, 2nd ed., Hoboken, NJ: Wiley, 2006.

[8] A. Vlasa, S. Varvara, A. Pop, C. Bulea, and L. M. Muresan, "Electrodeposited Zn–TiO_2 nanocomposite coatings and their corrosion behavior," *Journal of Applied Electrochemistry*, vol. 40, no. 8, pp. 1519–1527, Aug. 2010, doi: 10.1007/s10800-010-0130-x.

[9] A. A. Kasach, D. S. Kharytonau, A. V. Paspelau, J. Ryl, D. S. Sergievich, I. M. Zharskii, and I. I. Kurilo, "Effect of TiO_2 concentration on microstructure and properties of composite Cu–Sn–TiO_2 coatings obtained by electrodeposition," *Materials*, vol. 14, no. 20, p. 6179, 2021, doi: 10.3390/ma14206179.

[10] A. Spanou and E. A. Pavlatou, "Ni–TiO_2 composite electrodeposits: effect of TiO_2 concentration on hardness and wear," *Electrochim. Acta*, vol. 56, pp. 3884–3891, 2011. DOI: 10.1016/j.electacta.2011.02.001.

[11] F. Caruso, "Nanoengineering of particle surfaces," *Adv. Mater.*, vol. 13, no. 1, pp. 11–22, 2001.

[12] H. Yuan, R. Probst, and J. Song, "Influence of core/shell nanoparticles on the fretting behavior of electrical contacts," in *Proc. IEEE 67th Holm Conf. Electr. Contacts (HLM)*, Tampa, FL, USA, 2022, pp. 1–8. DOI: 10.1109/HLM54538.2022.9969773.

[13] Z. Qiao, L. Zhang, Z. Wei, and H. Yang, "Rotatable electroplating experimental device for loading spherical micrometer particles," Chinese Patent CN104894626A, Sept. 9, 2015.

[14] Z. Q. Cheng, Z. W. Li, J. H. Xu *et al*., "Morphology-controlled fabrication of large-scale dendritic silver nanostructures for catalysis and SERS applications," *Nanoscale Research Letters*, vol. 14, no. 89, 2019, doi: 10.1186/s11671-019-2923-0.

[15] R. Holm, *Electric Contacts: Theory and Application*, Berlin: Springer-Verlag, 1967.

[16] B. Riemer, M. Schlesiger, and J. Böttcher, "Effect of co-deposited particles on hardness and wear resistance of electrodeposited coatings," *Wear*, vols. 332–333, pp. 1120–1127, 2015. DOI: 10.1016/j.wear.2015.02.044.

[17] H. Hu, M. Gao, and L. Wang, "Electrodeposition and characterization of Ni–TiO_2 nanocomposite coatings," *Surf. Coat. Technol.*, vol. 201, pp. 3721–3727, 2006. DOI: 10.1016/j.surfcoat.2006.08.073.

[18] J. F. Archard, "Contact and rubbing of flat surfaces," *J. Appl. Phys.*, vol. 24, pp. 981–988, 1953.

Advanced Silver Coatings for Connector Applications in E-Mobility

Sönke Sachs
TE Connectivity
Bensheim, Germany
ssachs@te.com

Isabell Buresch
TE Connectivity
Wört, Germany
isabell.buresch@te.com

***Abstract*— High-current connections in vehicles should maintain low contact resistance over their lifespan and be thermally stable. Depending on the application, factors such as vibrations, elevated temperatures, or a high number of mating cycles must not lead to unacceptable aging of the connection. Silver, as the metal with the highest electrical conductivity, is predestined for use as a coating material. Known negative functional properties of pure silver surfaces in connector applications, such as cold welding, a comparatively high coefficient of friction, and limited wear resistance, can be eliminated or at least mitigated through various measures. The aim of this work is to develop advanced silver coatings that enhance the performance and durability of connector applications in e-mobility. This has been achieved through systematic evaluation and testing of coating compositions on model system and connector level representative of modern electric vehicle environments.**

Keywords—silver, electric vehicles, hard silver, dispersion coating

I. INTRODUCTION

The electrification of automotive drivetrains imposes several critical performance requirements that significantly exceed those of conventional automotive applications. Modern electric vehicle (EV) connectors must demonstrate low contact resistances to maintain the capability to conduct high currents reliably throughout their operational lifetime. The pursuit of material efficiency and carbon footprint reduction has led to optimized connector designs that maximize material utilization, resulting in operational peak temperatures ranging from 150°C to 180°C—substantially higher than traditional automotive connector applications.

Contemporary EV applications demand robust performance under high-current transient conditions, including vehicle acceleration phases, regenerative braking operations, and rapid DC charging scenarios. In addition, these systems must withstand significant mechanical stresses, as EV connectors are typically larger and heavier than conventional counterparts, subjecting them to substantial vibration loads throughout the vehicle's lifetime.

Short charging times are crucial to increase the acceptance of electric vehicles. The aim is, for example, to achieve a range of 300 km with a charging time of only five minutes. This is only possible if higher power levels and thus higher currents are transmitted during charging from the charging inlet connector to the battery. In order to achieve these goals, the various high-current connections must have stable and low contact resistances over their service life combined with excellent wear behavior as requirements regarding several ten thousand mating cycles must be fulfilled.

The topic of 'charging time' is one of the most discussed topics in connection with the purchase of an electric vehicle; fast charging or high-current charging is therefore the point that needs to be realized from a technical perspective. High-power charging (HPC) requires DC charging capacities with currents > 500 A. Such high currents cause significant heat generation in the charging connection due to power loss caused by the inherent resistances present in the system. In particular, the resistance directly in the contact zone and thus the condition of the contact surface in use are significant influencing factors. The performance and condition of the surface of the contacts in the inlet and the charging gun determine whether HPC charging can be guaranteed over the service life. Wear due to the high number of mating cycles over the service life, combined with other environmental exposure factors such as humidity, sand, and salt, lead to wear of the contact coating in the inlet and the charging gun resulting in an increase in contact resistance which must be prevented.

A. Contact Coating Technologies in Automotive Applications

Within automotive connector applications, three primary contact coating materials dominate: tin, hard gold, and silver [1]. Each material presents distinct advantages and limitations when evaluated against the stringent requirements of EV applications. Among these options, silver demonstrates superior performance characteristics that align most closely with EV system demands.

The exceptional suitability of silver for EV applications stems from several fundamental properties. The lowest electrical resistivity of all metals (1.59×10^{-8} Ω·m at 20°C), combined with moderate contact hardness enable very low contact resistances [1]. Silver coatings demonstrate excellent temperature stability, maintaining performance integrity up to 140°C in standard configurations and extending to 160°C when applied over nickel barrier layers. Additionally, silver exhibits superior corrosion resistance under typical automotive environmental conditions while maintaining

relatively modest costs compared to gold or palladium-based contact coatings [2], [3].

Despite these advantages, conventional silver contact coatings present several significant limitations that challenge their application in demanding EV environments. Silver exhibits a tendency to tarnish in sulfur-containing atmospheres, requiring the implementation of specialized passivation treatments to prevent tarnishing. The material demonstrates relatively high friction coefficients (μ = 0.8-1.2), which can result in elevated insertion and withdrawal forces in connector applications [3].

Extended mating cycle applications reveal additional challenges, with conventional silver coatings experiencing significant frictional wear when subjected to more than 50 insertion/withdrawal cycles. Perhaps most critically, silver demonstrates a tendency towards cold welding, particularly under conditions of high contact pressure and elevated temperature scenarios commonly encountered in high-current EV applications.

B. *Advanced Silver Coating Development Strategies*

To address these fundamental limitations of silver while preserving its inherent advantages, researchers and manufacturers have developed several innovative approaches to enhance silver contact coating performance. These strategies can be categorized into four primary modification techniques, each targeting specific performance improvements for EV applications [4], [5], see Figure 1.

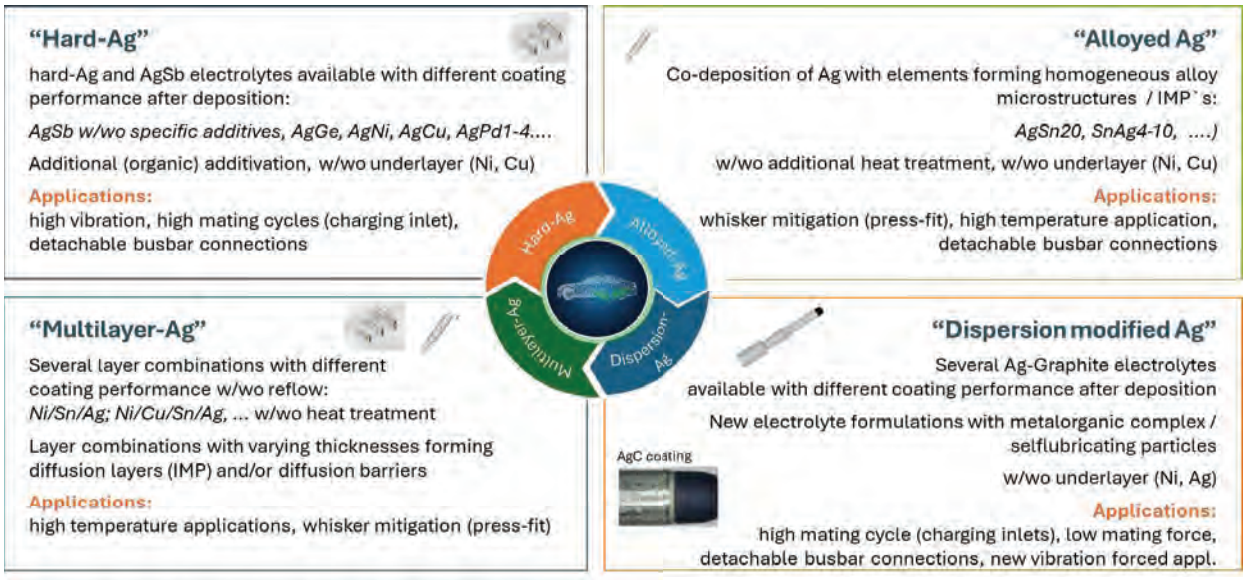


Figure 1: Overview of advanced Silver Coating Approaches

This paper presents a comprehensive investigation of advanced silver coatings specifically developed for electric mobility applications. The research focuses on four primary coating technologies: hard silver antimony (AgSb) coatings and hard silver metal alloy coatings, designed for enhanced mechanical durability, dispersion-modified silver systems incorporating carbon-based [6], [7] and metalorganic additives, and advanced composite silver matrices optimized for EV connector requirements [8], [9].

II. Experimental

A hierarchical testing approach was implemented, progressing from model systems to single components and complete connector assemblies. Model system testing utilized cap and flat sample geometries (Figure 2) fabricated on CuNiSi base material substrates. This approach enabled systematic characterization of fundamental contact properties before evaluating complex connector geometries.

A. *Model system testing*

Contact resistance measurements were performed using a contact resistance probe capable of reciprocating motion analysis. The apparatus enabled independent control of contact normal force and measurement of friction forces and contact during sliding contact conditions [10]. Contact resistance as a function of normal force was characterized to determine baseline resistance values and evaluate surface layer effects. Testing protocols included measurement of coefficient of friction (COF) and contact resistance over predetermined cycle counts to assess wear behavior and electrical stability.



Figure 2: Flat and cap samples with carrier strips. The base material is CuNiSi, the formed cap has a radius of 4 mm.

Two material conditions were evaluated: as-deposited (initial condition) and thermally aged samples. Thermal aging was conducted according to automotive industry standards.

Contact property measurements were supplemented with analytical techniques including microhardness testing and scanning electron microscopy (SEM), and focused ion beam (FIB) cross section analysis. These methods provided correlation between microstructural properties and macroscopic contact performance.

B. Single Component Testing

Single component evaluation utilized 8 mm diameter round pin/socket combinations in a dedicated mating cycle test system. The apparatus measured insertion and retraction forces simultaneously with contact resistance during mating operations. Test configuration employed standardized tulip-type socket contacts with 10 µm silver coating over copper base material for all evaluations. Pin contact coatings were varied to isolate the effects of different coating types. This approach ensured consistent socket interface conditions while enabling systematic evaluation of pin coating performance. The mating cycle apparatus provided continuous monitoring of electrical and mechanical parameters throughout the test duration, enabling real-time assessment of coating performance degradation mechanisms.

C. Test platings

The following plating were tested on model system level (a) and on component level (b):

Silver type	Plating material	Tests
Hard silver	AgSb, type 1	(a)
Hard silver	AgSb, type 2	(a), (b)
Hard silver	Ag metal type 2 alloyed	(a), (b)
Dispersion modified Ag	AgC, silver graphite	(a), (b)
Dispersion modified Ag	AgMO, metal organic modified silver	(a), (b)

III. Results and Discussion

In order to test the advanced silver materials, first model system tests were performed to characterize the basic contact properties. Test results of 5 different contact finishes are presented: two AgSb variants, another hard silver metal alloy, silver graphite (AgC), and metal organic modified silver (AgMO).

A. "Hard Ag" contact coatings – model system testing

Different hard silver variants were tested, two types of AgSb coatings and a hard silver metal alloy type 2 coating.

1) AgSb contact finishes

Many different variants of hard silver alloy coatings are on the market. In this investigation different electroplating baths were tested, indicated by type 1 and type 2. The AgSb contact finishes have approximately 2 wt-% of Sb co-deposited. This added Sb increases the hardness of the silver coating to 130-170 HV in the as-plated state compared to typical hardness values of pure silver coatings in the range of 70-100 HV.

Contact resistances data is shown in Figure 3 for the two types of AgSb contact finishes in the as plated condition and after dry heat exposure (150 °C, 1000 h). The two types differ in the composition of the respective electrolytic baths and in the process parameters employed for electroplating. In the initial condition, contact resistances are similar, showing values well below 1 mΩ for contact normal forces above 1 N. However, after dry heat exposure, the type two plating shows significantly higher contact resistances, especially at low contact normal forces.

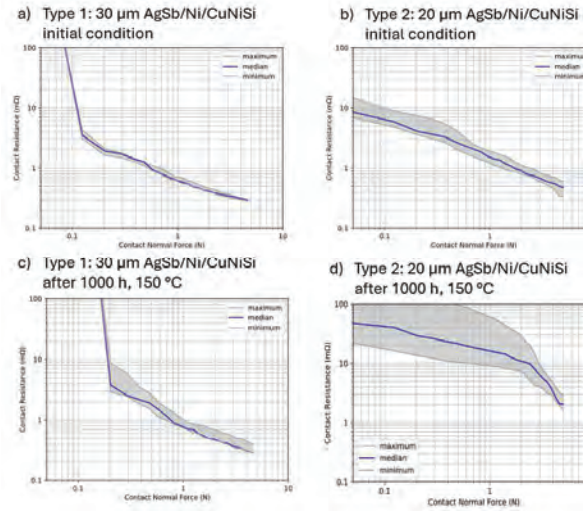


Figure 3: Contact resistances of two types of AgSb contact finishes in the a), b) initial/as-plated state and c), d) after dry heat exposure. The blue lines indicate the average values for a given contact normal force. The grey area indicates the variance of the individual measurements.

Focused ion beam (FIB) cross sections are depicted in Figure 4 for the type 1 AgSb coating. In the initial state, a fine grain structure of the contact material with grain sizes well below 1 µm is visible. The dry heat exposure changes the structure of the material, resulting in grain sizes larger than 1 µm. This structural change results also in a reduction of the hardness of the material to about 120 HV.

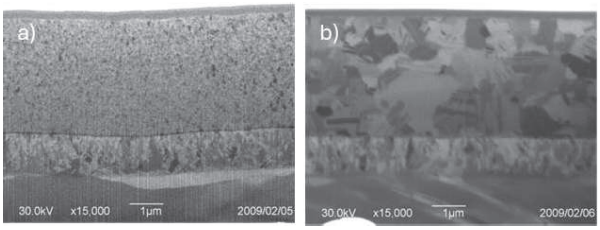


Figure 4: FIB cross sections of the type 1 5 µm AgSb/1 µm Ni coating: a) before and b) after dry heat exposures, 150 °C, 1000 h

The structure of both the type 1 and 2 coatings is shown in Figure 4. Both variants show a similar fine grain structure of the material, no apparent differences are visible. The contact resistance and COF data of the reciprocating motion

tests is also documented in Figure 5. While the COF is very similar for both types in the range of 0.8-1.4, the contact resistance data shows higher values for the type 2 contact material. It is not possible to derive these differences in functional performance from the composition of the AgSb contact coatings or from the microstructure. More in-depth investigations are needed, like x-ray diffraction measurements [11], to narrow down the macroscopic behavior to differences in the coating morphology.

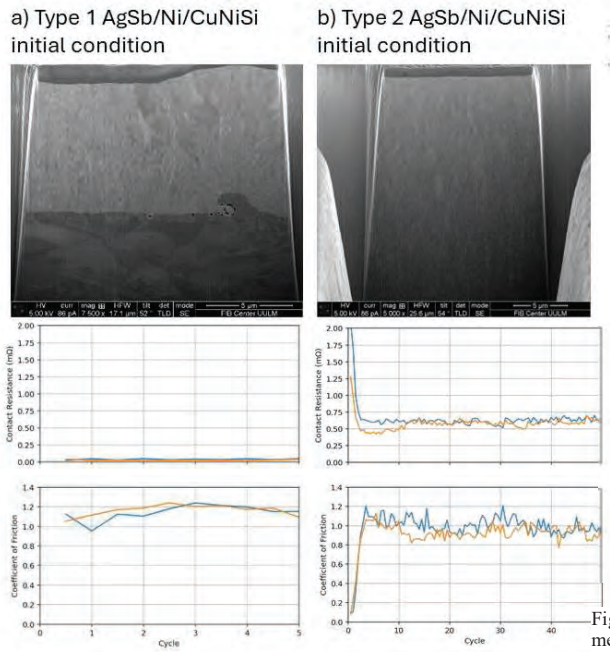


Figure 5: FIB cross sections of a) type 1 and b) type 2 AgSb coatings and COF and resistance data for 50 cycles with a contact normal force of 2 N and a displacement of 1 mm.

In the case of the type 2 AgSb finish, an additional change of the composition can be assumed: segregation of Sb to the surface of the contact finish at elevated temperature which results in higher contact resistances.

2) Hard silver metal alloy type 2 contact finish

In addition to the AgSb coating, another "hard silver", a silver metal type 2 alloy with a second metal co-deposited with the silver was tested. This coating has higher as plated hardnesses than AgSb in the range of 220-240 HV.

Contact resistance data in the initial state and after dry heat exposure is depicted in Figure 6. The contact resistances are significantly higher than the resistances of the AgSb coatings, typically in the range > 1 mΩ for contact normal forces > 1 N. This is due to the high hardness of the material and due to a higher resistivity of the hard silver metal type 2 alloy. After dry heat exposure, the contact resistance decreases slightly. The layer structure looks somewhat coarser than that of the AgSb contact finishes. Also, the structure does not significantly change after thermal exposure at 150 °C, 1000 h, the alloying element suppresses grain growth effectively. However, in the backscattered contrast, a change is more clearly visible: at the interface to the nickel underlayer, a coarser grain structure forms, and small spots are visible in the top portion of the contact finish thickness. These indicate that alloying element and organic additives which are codeposited during the electroplating process segregate and can act as an embedded lubricant.

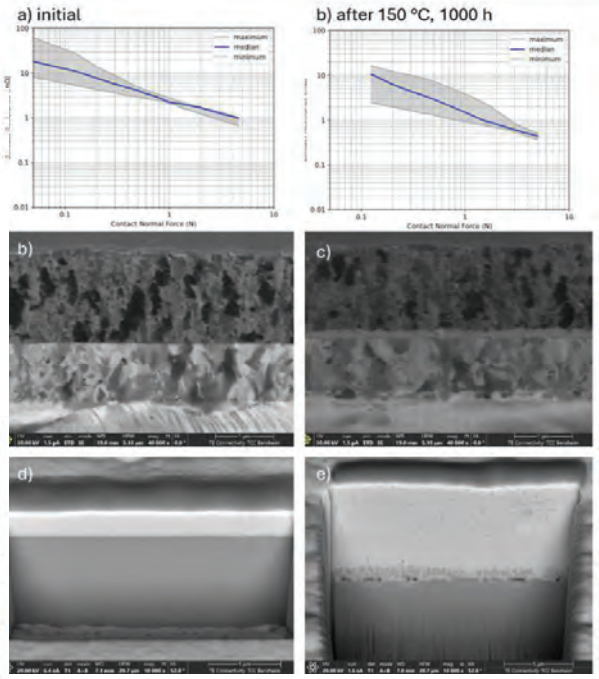


Figure 6: Contact resistance data and FIB cross sections of a 3 µm hard silver metal type 2 alloy/2 µm Ni contact finish a) before and b) after dry heat exposure, b), c) with ion beam contrast d), e) and with backscattered electrons contrast.

B. Dispersion modified silver: AgC and AgMO – model system testing

Another approach to improve the properties of silver contact finishes is to embed particles into the silver matrix during the electroplating process. Such particles can improve the friction and wear if they have lubricating properties, like graphite or sulfur compounds. On the other hand, the silver matrix keeps its advantageous properties, like high electrical conductivity, enabling low contact resistances. Though, the concentration of the embedded particles needs to be below a certain threshold, to keep the silver matrix un-effected.

Two examples of such dispersion modified silvers are depicted in Figure 7: a silver matrix with embedded graphite particles (AgC) and a silver matrix, modified with embedded organic compounds (AgMO). The contact resistances show very low values, well below 1 mΩ for contact normal forces above 0.5 N. This is due to an unaffected silver matrix which maintains good electrical conductivity of the composite material and is a significant advantage for high power contacts. Also the COF shows low values in the range 0.1-0.3, much lower than for pure silver contact finishes which have COF in the range of 0.8-1.2 [1].

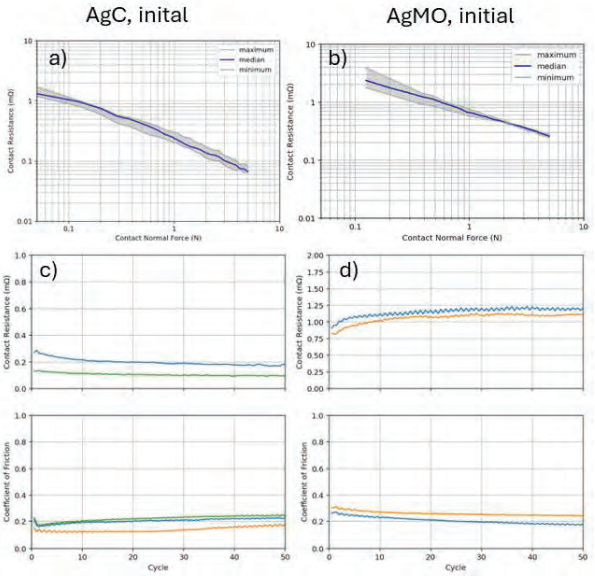


Figure 7: a), b) Contact resistance and c), d) COF data of an AgC and an AgMO dispersion contact finish. COF data was recorded with a contact normal force of 2 N and 50 reciprocating motion cycles with a displacement of 1 mm, showing c) 2 measurement and d) 3 measurements, respectively.

The FIB cross sections of these contact materials look significantly different, (Figure 8). While the graphite particles are clearly visible in the AgC coating, the AgMO coating shows a fine grain, homogenous structure, with much smaller particles embedded than in the case of AgC. The embedding of such lubricious particles in the silver matrix has a significant advantage over lubricants which are applied just to the surface: During wear cycles, new lubricant material is exposed if part of the contact material is worn out. In this way, a constant lubrication of the contact interface is possible during the wear over the whole coating thickness.

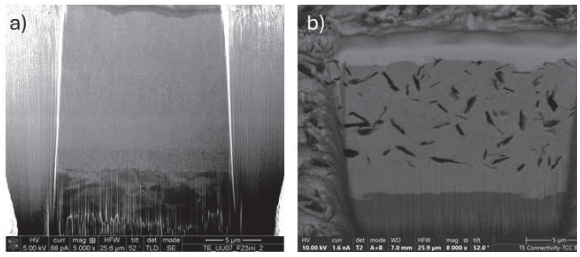


Figure 8: FIB cross sections of a) AgMO and b) AgC contact finishes.

C. *Component level testing*

The investigation of functional properties of contact finishes should serve as the foundation for subsequent tests at product or component level. Such tests validate whether fundamental laboratory results can be successfully translated to actual product geometries and mechanical configurations. In this study, mating cycle tests were conducted using charger inlet contacts. Figure 9 presents the results of these tests for a 10 µm AgC contact finish applied to a 9 mm socket contact lamella. The SEM image in this figure reveals the surface morphology of the AgC coating on the socket lamella, clearly showing graphite particles embedded within the silver matrix, some of which protrude from the surface. The figure inset illustrates progressive wear after 10,000, 22,000, and 75,000 cycles. The contact area on the lamellas exhibits a characteristic black, smooth appearance, indicative of smeared graphite within the contact zone that provides lubrication at the interface with the pin counterpart. While the worn area progressively increases with the number of mating cycles, no wear-through to the base material is observed even after 75,000 cycles. Furthermore, the electrical resistance of the connection remains stable throughout this extensive cycling regime, demonstrating the durability and reliability of the coating system.

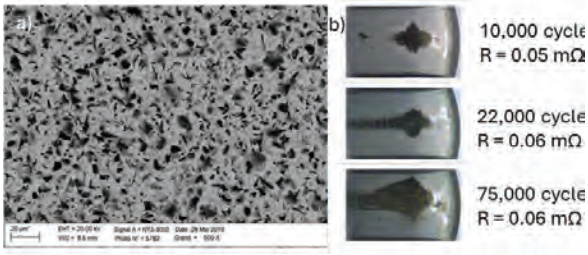


Figure 9: a) 20 µm AgC contact surface SEM image and b) wear characteristics on a 9 mm socket contact surface showing a thin graphite film in the contact areas after mating cycles tests.

More examples for wear after 10,000 mating cycles are shown in Figure 10 for 8 mm pin contacts with various contact finishes connected to a pure silver coated test socket.

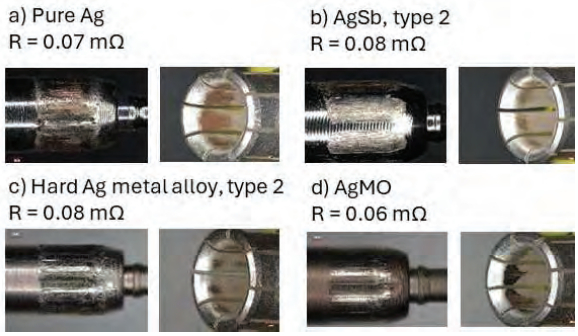


Figure 10: Wear on 8 mm pin parts with advanced silver contact coatings after 10,000 mating cycles. The resistance values are measured after the 10,000 mating cycles and include a bulk resistance contribution.

For the 8 µm Ag/Ni pin coating (Fig. 10 a), both socket and pin surfaces exhibit clearly visible wear-through to the copper base material after 10,000 cycles, indicating insufficient wear protection.

In contrast, the 10 µm type 2 AgSb/Ni contact finish (Fig. 10 b) shows no wear-through, although both pin and socket contact surfaces display rough morphology characteristic of adhesive wear with material transfer between the mating surfaces. Importantly, the silver coating remains intact with no exposure of the underlying base material.

The 10 µm hard silver metal alloy type 2/Ni contact finish (Fig. 10 c) demonstrates comparatively smoother worn surfaces than AgSb, suggesting reduced adhesive wear and minimized material transfer. However, the worn areas on the socket counterpart are larger than those observed with AgSb, though still without wear-through to the base material. This

difference can be attributed to the greater hardness difference between the hard silver metal alloy type 2 pin contact finish and the pure Ag socket finish compared to the hardness pairing in the AgSb configuration.

The 11 µm AgMO/Ni coating (Fig. 10 d) exhibits a shiny appearance after mating cycle testing, indicative of predominantly burnishing wear rather than abrasive or adhesive mechanisms. The embedded compounds within the silver matrix evidently provide effective lubrication that substantially reduces wear during mating cycles.

IV. Conclusions and Outlook

Increasing requirements for connector surfaces in vehicles, particularly in the field of electromobility, such as transmissions of high currents and enhanced wear resistance, can be very well met with newly developed advanced silver variants. Especially hard silver alloy coatings and dispersion coatings with solid state lubricants embedded into a silver matrix show significant performance improvements compared to pure silver contact finishes. To evaluate these coatings for use in automotive applications, detailed investigations of the coating properties are necessary.

The investigations show that hard silver variants with different alloying elements and even with the same alloying elements, have different contact properties. Hard silver variants with what appears at first glance to be the same chemical composition, e.g. AgSb2 can differ in their properties, like shown for the contact resistance after dry heat exposure. Differences in morphology can only be determined with a detailed chemical and microstructural characterization of each coating. Furthermore, an appropriate specification for the respective applications is needed.

Compared to hard silver alloys, silver dispersion coatings are a very interesting alternative. In the tests a favorable combination of low contact resistances with low friction coefficients and little wear could be determined.

The selection of appropriate contact materials depends significantly on the specific application requirements and operating conditions. For applications involving relative motion during mating cycles, dispersion coatings appear to be well suited due to their ability to accommodate sliding contact dynamics. In contrast, applications characterized by high loads concentrated on small contact surface areas, such as those subjected to vibration, hard silver alloys that can withstand mechanical stress without excessive wear are well suited.

Furthermore, a hybrid approach utilizing a combination of hard contact material on one side and soft contact material on the other side could offer advantages in terms of increased durability while simultaneously ensuring low contact resistances. This asymmetric material pairing allows the hard surface to provide mechanical stability while the softer counterpart maintains favourable electrical properties and conformability at the contact interface.

Acknowledgements

The authors would like to thank Bohnni Shikha Biswas, Drashti Jayeshbhai Vaghani, Markus Antoni, Martin Hottes, Felix Greiner, and Frank Ostendorf for valuable contributions and discussions.

Disclaimer

TE expressly disclaims any implied warranty regarding the information contained herein, including, but not limited to, the implied warranties of merchantability or fitness for a particular purpose.

References

[1] H. Endres, *Compendium of Electrical Connectors*. Vogel Verlag, 2021.

[2] M. Braunovic, N. K. Myshkin, and V. V. Konchits, *Electrical contacts: fundamentals, applications and technology*. CRC press, 2006.

[3] M. Myers, "The Performance Implications of Silver as a Contact Finish in Traditionally Gold Finished Contact Applications," in *Proceedings of the 55th IEEE Holm Conference on Electrical Contacts*, 2009, pp. 310–318.

[4] I. Buresch, H. Schmidt, and S. Sachs, "Steckverbinderoberflächen für hohe Temperaturen," presented at the Albert-Keil-Kontaktseminar, Karlsruhe, 2019.

[5] I. Buresch, H. Schmidt, and S. Sachs, "Special connector requirements call for specific contact coatings: new silver alloys show characteristics never seen before," in *Proceedings ICEC 2020*, 2021.

[6] R. Wagner, "Silber-Graphit-Dispersionsschichten als Kontaktoberfläche in Steckverbindern: Herausforderungen und Chancen bei Anwendungen in der Serienproduktion," in *Elektrische und optische Verbindungstechnik 2023, 9. Symposium Connectors*, Lemgo, 2023.

[7] T. Israel, M. Oberst, C. Hildmann, and S. Schlegel, "Self-lubricating coatings for high-current connectors," p. 7, 2022.

[8] Y. Yoon, J. Chen, M. Lipschutz, P. Gumbley, M. Rodriguez, and K. Griffin, "A Durable Electroplated Silver Contact Finish for Reusable Connectors," presented at the IEEE Holm Conference on Electrical Contacts, 2021.

[9] J. Chen *et al.*, "A High Durability, Reliable, Cyanide-Free Silver Finish," in *Proceedings ICEC 2022*, Sapporo, 2022, p. 5.

[10] S. Sachs, H. Schmidt, A. Bäumer, S. Thoss, A. Jeblick, and M. Schecker, "Systematische und effiziente Charakterisierung der Kontaktphysik von Steckverbindern mit einer neu entwickelten Messapparatur," in *Elektrische und optische Verbindungstechnik 2013*, Lemgo, Germany, 2013.

[11] S. Sachs, I. Buresch, and F. Ostendorf, "Hard silver surfaces: Is the variety of layers with different properties helpful?," presented at the Albert-Keil Kontakt Kontaktseminar, Karlsruhe, 2023.

Tribological and electrical properties of electrodeposited tin-zinc coatings.

Aurore Brézard Oudot
Université Paris-Saclay, CentraleSupélec, CNRS, Laboratoire de Génie Electrique et Electronique de Paris, 91192, Gif-sur-Yvette, France, Sorbonne Université, CNRS, Laboratoire de Génie Electrique de Paris, 75252, Paris, France.

Sophie Noël
Université Paris-Saclay, CentraleSupélec, CNRS, Laboratoire de Génie Electrique et Electronique de Paris, 91192, Gif-sur-Yvette, France, Sorbonne Université, CNRS, Laboratoire de Génie Electrique de Paris, 75252, Paris, France.

Julien Acquadro
Université Paris-Saclay, CentraleSupélec, CNRS, Laboratoire de Génie Electrique et Electronique de Paris, 91192, Gif-sur-Yvette, France, Sorbonne Université, CNRS, Laboratoire de Génie Electrique de Paris, 75252, Paris, France.

Thierry Leblanc
Université Paris-Saclay, CentraleSupélec, CNRS, Laboratoire de Génie Electrique et Electronique de Paris, 91192, Gif-sur-Yvette, France, Sorbonne Université, CNRS, Laboratoire de Génie Electrique de Paris, 75252, Paris, France.

Philippe Testé
Université Paris-Saclay, CentraleSupélec, CNRS, Laboratoire de Génie Electrique et Electronique de Paris, 91192, Gif-sur-Yvette, France, Sorbonne Université, CNRS, Laboratoire de Génie Electrique de Paris, 75252, Paris, France.

Frédéric Houzé
Université Paris-Saclay, CentraleSupélec, CNRS, Laboratoire de Génie Electrique et Electronique de Paris, 91192, Gif-sur-Yvette, France, Sorbonne Université, CNRS, Laboratoire de Génie Electrique de Paris, 75252, Paris, France.

***Abstract* — Several studies have shown that tin-zinc coatings can offer corrosion protection in harsh environments. Therefore, much interest has been shown in the field of electrodeposition process to understand the relationship between the deposition process and the corrosion properties. Sn-Zn coatings were also reported to have interesting electrical and frictional properties for particular applications. The aim of this study is to present first results on the general electrical and tribological properties of tin-zinc coatings. Large amplitude friction tests were performed with a hard NiP coated ball on electroplated Sn-Zn plane contacts. The electrical and tribological results and various analyses of the composition and topography of the wear tracks are analyzed. The role of the transfer of material and of the third body on electrical behavior is highlighted.**

Keywords—tin-zinc, friction, wear, electrical contact, intermittencies.

I. Introduction

Tin-zinc coatings have been known for a long time (Marino in 1915 in [1]). Different works have been going on since tin-zinc coatings have been shown to be excellent candidates for the protection of various types of substrates, the tin-zinc layer acting as a sacrificial layer to protect metallic substrate [1,2]. Many investigations have been devoted to the development and improvement of the deposition process [1-7] which is often an electrodeposition one. The main applications in literature are the replacement of cadmium [2] and the anti-corrosion protection of electrical devices [3-5]. Some work reports on the corrosion properties of Sn-Zn solder as a replacement for SnPb, often with a low concentration of Zn [8]. The best corrosion properties for electrodeposited Sn-Zn are reported to be obtained with around 20 wt.% of Zn [1, 4, 7]. Papers usually refer to Sn-Zn as an homogeneous anti-corrosion coating with good conduction and friction properties [10], but to our knowledge no work specifically reports on the tribological properties of such coatings, while much work has been done on the friction and wear properties of electrodeposited tin coatings [9-11] for electrical contacts, either in dry or lubricated conditions.

This paper describes first results on the electrical and tribological properties of a tin-zinc coating, in a general way, by means of a friction test coupled to electrical measurements.

II. Experimental

A commercial linear friction device was used to investigate the properties of a tin-zinc coating.

A. Samples

The tin-zinc coating tribological properties were investigated in a hemisphere on plane configuration. Both parts of the contact were aluminum slabs 1 mm thick with a 10 µm high phosphorus NiP coating. The dimensions of the plane samples were 20 mm × 30 mm planes while hemisphere shape with a radius of curvature of 1.4 mm was obtained by stamping. The plane samples were coated with an electrodeposited layer of tin-zinc in the framework of a large project (CadSTAR). The targeted layer thickness is between 7 and 10 µm and the targeted composition was around 20 wt% of Zn. Many other properties of these platings were investigated but not reported here.

B. Experimental tests and characterization techniques

A reciprocating linear tribometer fitted with specific electrical measurement was used. Fig. 1 shows a diagram of the set up.

1) Tribological device for the friction tests

The friction tests involved a sine displacement (2 mm peak to peak, frequency of 0.08 Hz) at different normal load *Fn*: 0.5 N, 1 N and 2.5 N. The maximum speed was 0.5 mm/s. The friction force was recorded with an acquisition rate of 80 Hz by the tribometer internal software.

2) Electrical measurement

A sourcemeter Keithley 2450, (1) in Fig. 1, delivered a 20 mA DC current intensity during friction while the voltage drop Uc in the contact was measured with a QED Gnostic64 acquisition system (3), after amplification with a Stanford Research SR560 low noise preamplifier (2). The Gnostic64 device also monitored the displacement. The four-wire method was used as described in Fig. 1. Before friction tests, a value of the contact resistance Rc_0 was measured in static. The acquisition rate was also 80 Hz for the electrical signals.

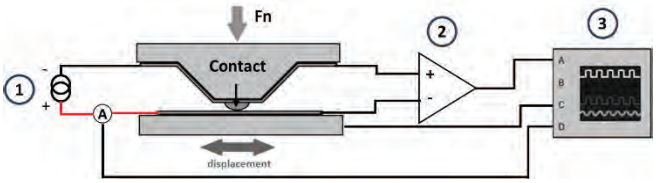


Fig. 1. Schematic diagram of the four wire contact resistance measurement.

3) Characterization

a) Observation

After the friction tests, the wear tacks were observed with a ThermoFisher Phenom XL G2 SEM fitted with an Energy Dispersive X-Ray (EDX) device.

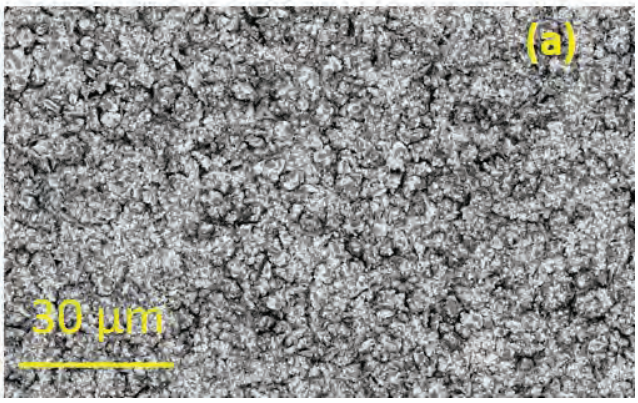
b) Composition

The compositions in various locations of the wear tracks were obtained with the SEM EDX.

c) Topography 3D profiler

The topography of the samples and the wear tracks were measured with a Bruker Contour GT-X 3D optical profiler.

III. Results



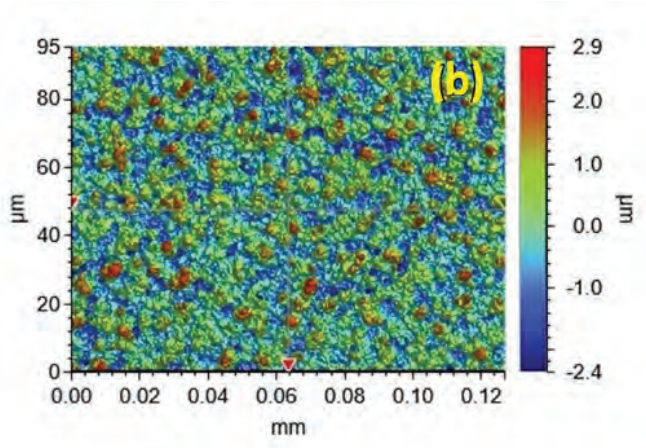


Fig. 2. a) SEM image of the surface (BSD mode, 10 kV) showing the topography of the surface and b) profilometric image showing the roughness.

Fig. 2 a shows the surface of the Sn-Zn deposits in back scattered mode: some large nodules (about 5µm in diameter) can be observed, but the surface is rather homogeneous. The average composition of the coatings of the study is 77% Sn 23% Zn. This composition has been reported [7] to give the best anti-corrosion properties. The roughness, shown in Fig. 2 b, is characterized by a arithmetic mean height *Sa* value of 0.8 µm with maximum height *Sz* values as high as 7 µm.

A. *Influence of normal force on the friction and wear properties.*

These first tests to evaluate the effect of the normal load were performed without voltage limit. Mean values of μ, of the friction coefficient, and of *Rc*, the contact resistance, are plotted versus the number of friction cycles. The normal load is applied by a dead weight.

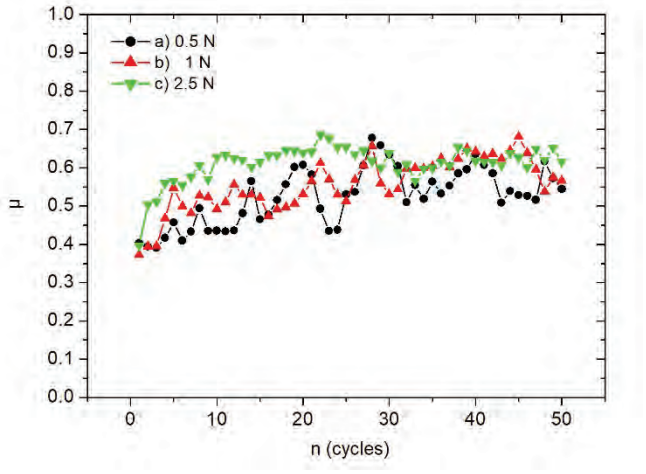


Fig. 3. Mean values per cycle of the friction coefficient μ for 2.5 N, 1 N and 0.5 N for 50 friction cycles.

Fig. 3 shows the evolution of μ for the three different normal loads during 50 cycles. For each case at least three runs were made and gave repeatable results. The friction coefficient varies very little for the 3 normal loads. The μ values are

between 0.4 and 0.65. Fig. 4 depicts the contact resistance (*Rc*) evolution. *Rc* depends on *Fn* and is higher (between 100 mΩ and 500 mΩ) for the smallest load 0.5 N. The graph also shows the value of 6.5 Ω (dotted line) corresponding to a voltage contact drop of 0.130 V under 20 mA. 0.130 V corresponds to the melting voltage of tin [12]; it can serve as a reference.

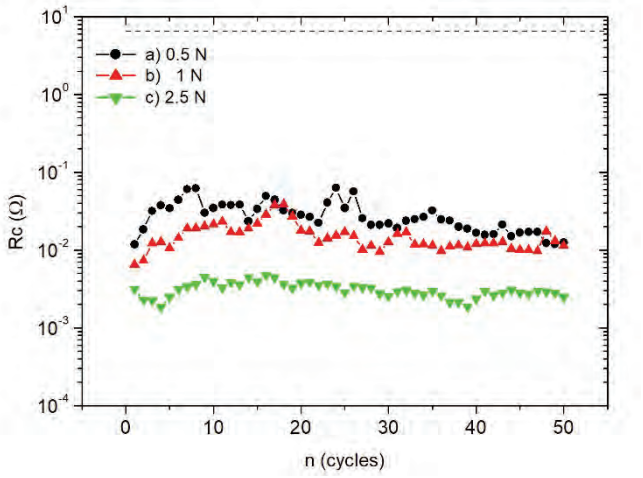


Fig. 4. Mean contact resistance *Rc* values for 2.5 N, 1 N and 0.5 N. The dotted line represents the value of 6.5 Ω corresponding to a voltage drop of 0.130 V (the tin voltage value for melting) under 20 mA.

The tin-zinc coating shows interesting electrical and tribological properties for the different normal load values investigated. The values of the mean Hertz pressure can be evaluated at 860 MPa, 635 MPa and 500 MPa for the loads 2.5 N, 1 N and 0.5 N respectively, taking into consideration the thick hard NiP layer (10 µm, *E*= 170 GPa, *Hv*= 5 GPa). Such values of pressure could correspond to various types of applications.

Longer tests were then performed to evaluate the durability of the coating. The runs were performed for more friction cycles. Fig. 5 shows the evolution of μ with the number of cycles, while Fig. 6 shows that of *Rc*. Very large differences can be observed for the three normal loads.

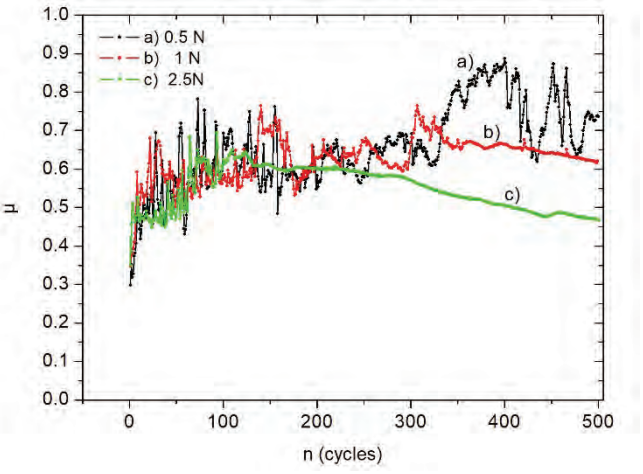


Fig. 5. Mean values per cycle of the friction coefficient μ for 2.5 N, 1 N and 0.5 N for 500 friction cycles.

The 50 first cycles of Fig. 5 show the same behavior as in Fig. 3. After this, differences of behaviour for the 3 loads are observed: for the highest load there is an increase in μ followed by a steady decrease.

For the lowest load, μ increases steadily for a higher number of cycles before increasing with large fluctuations.

The 1 N load has an intermediate behavior.

The associated evolution of *Rc* with the number of cycles in Fig. 6 shows three different regimes: at high load *Rc* is low (few mΩ), increases then up to a value of 20 mΩ and remains constant till the end of the run.

At low load, the *Rc* values are higher, decrease to about 10 mΩ, then start increasing with large fluctuations. It can be noted that the threshold value of 6.5 Ω is reached after 300 cycles.

For the medium load, an almost constant value of *Rc* is recorded followed by large fluctuations and then a very slow increase in values.

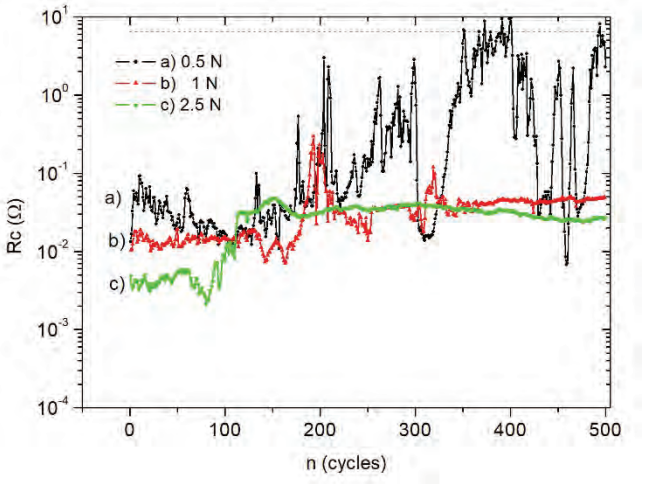


Fig. 6. Mean value contact resistance *Rc* for 2.5 N, 1 N and 0.5 N. The dotted line represents the value of 6.5 Ω corresponding to a voltage drop of 0.130 V.

B. Discussion

Contact resistance values were measured in static, before each run. The mean values of Rc_0 in static for each normal load are plotted in Fig. 7. Two trends can be observed. First, the Rc_0 values are lower for higher loads, which is expected since the load and the real area of contact are linked. Secondly there is more dispersion in the values for low load.

A Hertz calculation of the radius of contact *a* for 0.5 N, taking the values of the Young modulus (170 GPa) and the Poisson ratio (0.3) of NiP gives a value of about 20 µm for *a*. Taking a value of 10^{-6} Ω.m for the resistivity of the Sn-Zn layer gives a value of the contact resistance of Rc_0= 25 m Ω . This corresponds to the experimental values of Fig.7. The surface morphology of the coatings shown in Fig. 2 a) and b) shows that the distribution of nodules can vary from a location to

another, their different levels of plastic deformation could explain the scattering of the values.

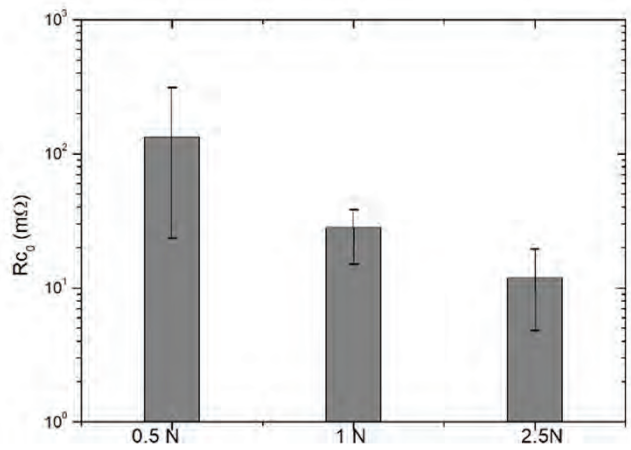


Fig. 7. Mean values of Rc_0 for 2.5 N, 1 N and 0.5 N coresponding to all the runs; the maximum and minimum values are also shown.

SEM images of the wear tracks for the 50-cycle runs are shown in the next figures.

Fig. 8 shows the wear track for the 2.5 N run. Several typical zones are observed. Zone (a) is composed of Sn, Zn and O, zone (b) is composed of Ni only, zone (c) is composed of Sn, Zn. The wear track on the hemisphere (not shown here; no wear tracks on the hemispheres will be presented in the remainder of this document) is composed of Ni at the centre; this centre is surrounded by Sn-Zn transferred from the plane to the ball. The Sn-Zn layer has been deformed and pushed out of the wear track during friction. The depth of the wear track on the plane is 4.2 µm. Note that the thickness of the layer is around 8 µm.

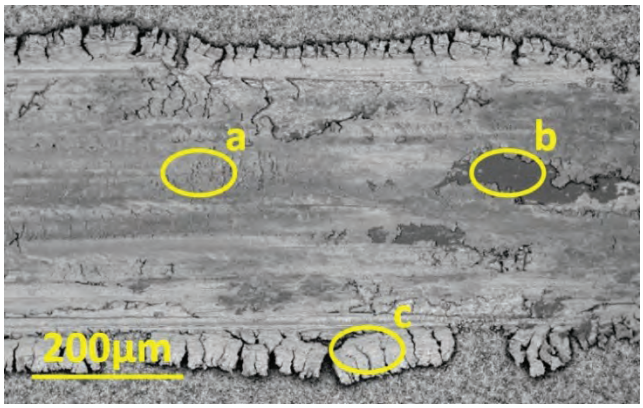


Fig. 8. SEM (EBDS mode) image of the wear track on the plane for the 50 cycles friction test at 2.5 N (image at 15 kV).

Fig. 9 corresponds to the wear track at 1 N after 50 cycles. Zones (a) and (b) are composed of Sn, Zn and O, zone (c) is composed of Sn-Zn. The wear scar on the hemisphere is composed of Sn-Zn without any Ni indicating the presence of a thick film transfer from the plane to the ball. The depth of the wear track on the plan is 1.5 µm.

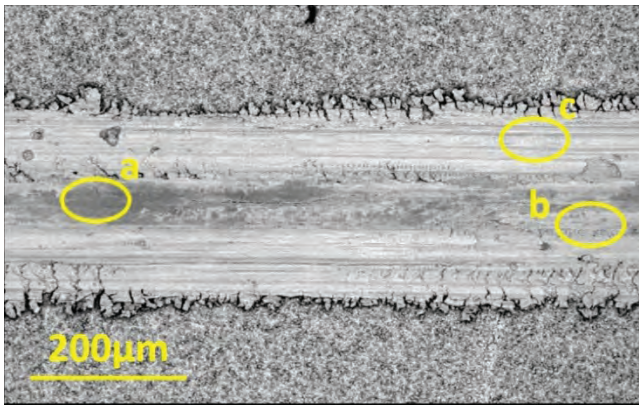


Fig. 9. SEM (EBDS mode) image of the wear track on the plane for the 50 cycles friction test at 1 N (image at 15 kV).

The wear tack of the 50-cycle run for 0.5 N is shown in Fig. 10. Zones (a) and (c) are composed of Sn, Zn and O, zone (b) is composed of either Sn or Zn according to the location of the spot and corresponds to the as deposited surface. The wear scar on the hemisphere is composed of Sn-Zn without any Ni indicating a thick film transfer from the plane to the ball. The wear track depth is 4.1 µm.

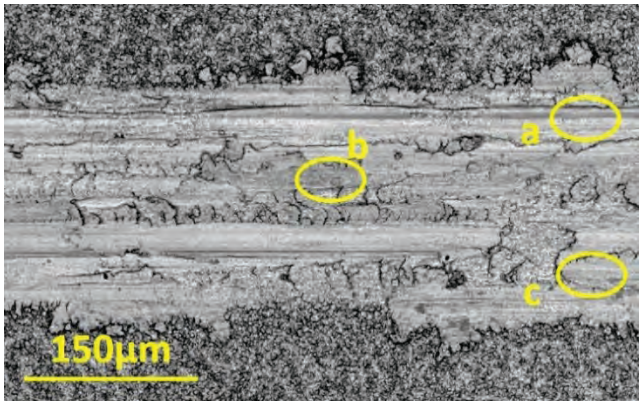


Fig. 10. SEM (EBSD mode) image of the wear track on the plane for the 50 cycles friction test at 0.5 N (image at 10 kV).

The wear mechanisms involved in the friction of a hard hemisphere on the Sn-Zn coating at different loads are different. From the analysis of the 500-cycle runs (not shown here) it can be observed that transfer of material from the plane to the ball occurs for the three values of normal force but with various kinetics:

- for high normal force, the third body at the interface between the plane and the ball is destroyed (ejection of particles) and the contact resistance remains low (20 mΩ after 500 cycles).

- for low normal force, the third body remains longer in the interface, the adhering particles are work-hardened and oxydized and the contact resistance fluctuates and becomes higher than 1 Ω.

- for 1 N an intermediate behaviour is observed; the wear track is less deep so less third body builds up in the interface.

C. *Influence of the electrical measurement conditions for low normal load*

In order to investigate the occurrence of high values of *Rc* at 0.5 N during the longer 500 cycles runs (6500 s), as observed in Fig. 6, the voltage drop in the contact *Uc* versus time was studied. In [13] the authors show that the measurement and plot of *Uc* is more relevant to what happens. Fig. 11 shows the evolution of *Uc* with time for the 3 values of the load.

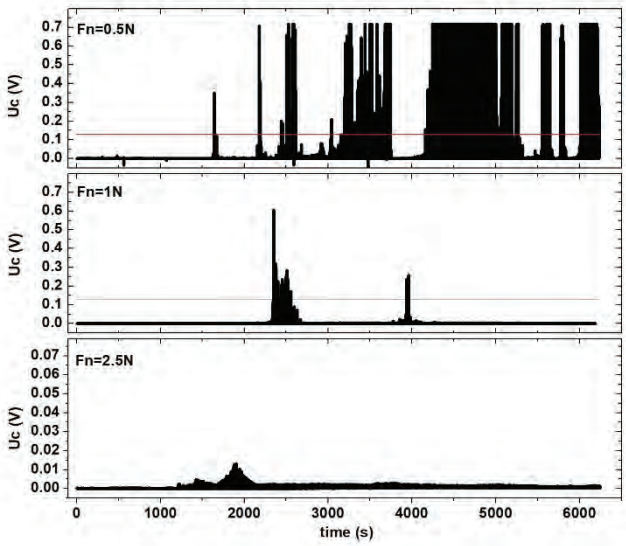


Fig. 11. Values of the voltage drop in the contact *Uc* versus time for 2.5 N, 1 N and 0.5 N. The value of 0.130 V is also plotted.

At 0.5 N and 1 N, the instantaneous values of *Uc* show increases (intermittencies) well above the reference value of 0.130V after 1500 s (120 cycles) and 2500 s (200 cycles) respectively. This was not observed in Fig. 6 showing the average values of *Rc* since the intermittencies are short. Note that for 2.5 N a maximum voltage drop about 10 mV is recorded. This is due to the large transfer of Sn-Zn on the hemisphere as discussed above for the 50 cycles run.

D. *Influence of a voltage limit on the sourcemeter at low normal load (0.5 N).*

For the next runs, a voltage limit at 0.130 V was set and the current was measured with a Tektronix AC/DC current measurement system including a TCP312A probe and a TCPA3000 amplifier. The signal is then monitored through another channel of the QED Gnostic 64. The measurement range was 1 A/V with the lowest measurable current of 1 mA.

An example of friction test at 0.5 N for 500 cycles is shown in Fig. 12. This run presents many early increases of the voltage drop in the contact. The current is seen to vary when the voltage limit of the sourcemeter is reached. This avoids a damage of the surface induced by the experimental conditions.

From the *Uc(t)* curves, any chosen single cycle can be extracted; for example, cycle 275 is shown in Fig. 13.

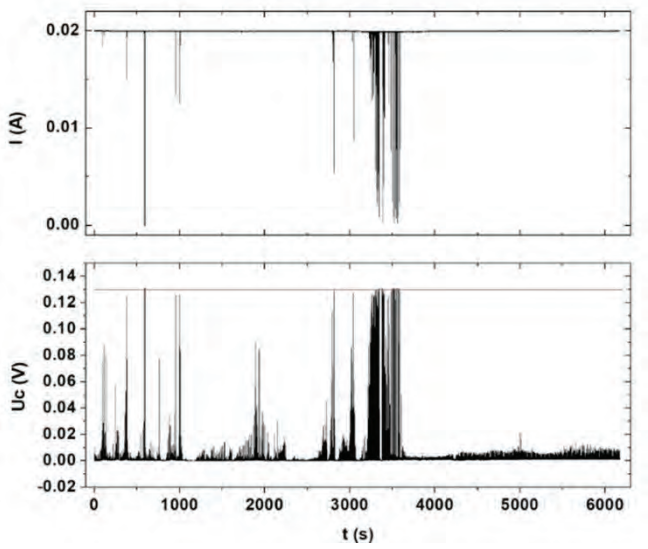


Fig. 12. *Uc(t)* and *I(t)* for a 500 cyles (6500 s) friction test at 0.5 N. The value of 0.130 V is also plotted

Fig. 13 shows that at this stage many intermittencies are recorded within the cycle. The effect of measuring the current is depicted in Fig. 14 which compares a plot of the resistance calculated as the ratio of the measured voltage over the measured current, and a plot of the resistance calculated as the ratio of the measured voltage over the programmed value of the current. In this case the values of the resistance are over-estimated.

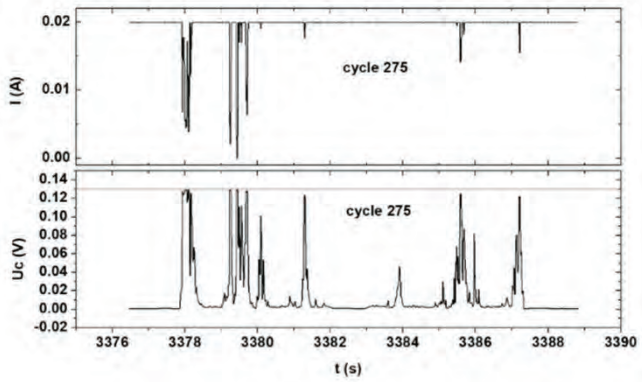


Fig. 13. Detail of *Uc(t)* and *I(t)* for cycle 275 from Fig.12.

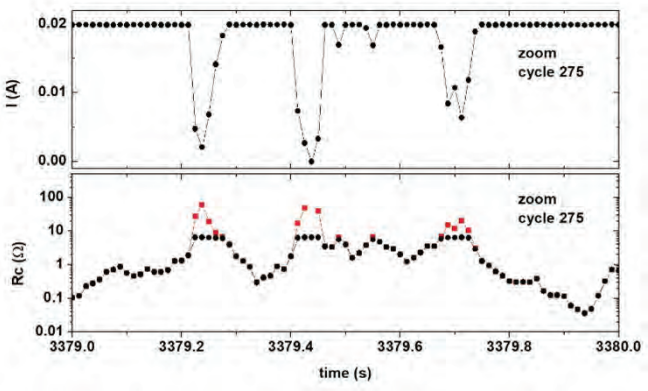


Fig. 14. Plot of the current *I(t)* and contact resistance *Rc(t)* taking into account the measured values of the current (black curve with dots) or the programmed value 20 mA (red curve with squares); zoom extracted from Fig.13.

This shows that care must be taken when comparing measurements from the literature for which experimental conditions are not precisely depicted. Runs with no voltage limit give correct values of the resistance *Rc*, but when a voltage limit is imposed it is necessary to measure the current.

IV. CONCLUSION

This work was performed in order to gain some general knowledge of the electrical and tribological behaviour of tin-zinc coatings. The properties of tin-zinc coatings in a friction context were investigated in a hemisphere on plane asymmetrical configuration. The Sn-Zn coatings about 8 µm thick, with a 23 wt.% Zn composition were electroplated on aluminium slabs coated with 10 µm high phosphorous chemical nickel, while the hemispheres stamped in the same slabs were not coated. Several normal forces were applied to the contact (0.5 N, 1 N and 2.5 N). It is shown that for 50 friction cycles the friction coefficients do not vary much and that the contact resistance, under 20 mA, remains between a few mΩ to a few tens of mΩ.

The wear mechanisms in these cases involve transfer of Sn-Zn onto the NiP hemisphere with different kinetics according to the normal load. For longer runs (durability testing) of 500 cycles, very different behaviours are recorded:

For the 0.5 N normal load and the 1 N one, large voltages drop values are recorded. These voltage increases are correlated to the formation of a transferred pad of oxidized tin-zinc (third body) which is not eliminated from the contact interface at low loads.

At 2.5 N the pad of oxidized Sn-Zn is evacuated from the interface as particles, and conduction occurs through metallic contacts.

Electrical measurements without a voltage limit and with a voltage limit are compared and it is shown that in the latter case the real value of the current must be recorded.

ACKNOWLEDGMENT

The authors wish to thank the DGA-RAPID program (régime d'appui pour l'innovation durable) for funding the CadSTAR project in the framework of which samples were fabricated.

REFERENCES

[1] S. Dubent, M.L.A.D. Mertens, M. Saurat, « Electrodeposition, characterization and corrosion behaviour of tin–20 wt.% zinc coatings electroplated from a non-cyanide alkaline bath », Materials Chemistry and Physics 120 (2010), pp. 371–380. *(references)*

[2] S. Dubent, M. De Petris-Wery, M. Saurat, H.F. Ayedi, « Composition control of tin–zinc electrodeposits through means of experimental strategies », Materials Chemistry and Physics 104 (2007), pp. 146–152.

[3] O.A. Ashiru, J. Shirokoff, « Electrodeposition and characterization of tin-zinc alloy coatings », Applied Surface Science 103 (1996) pp. 159-169.

[4] S. Taguchi, F. R. Bento, L. H. Mascaro, « Nucleation and Growth of Tin-Zinc Electrodeposits on a Polycrystalline Platinum Electrode in Tartaric Acid », J. Braz. Chem. Soc., vol. 19, No. 4, (2008), pp. 727-733.

[5] Y. Salhi, S. Cherrouf, M. Cherkaoui, K. Abdelouahdi, « Electrodeposition of nanostructured Sn–Zn coatings », Applied Surface Science 367, (2016), pp. 64–69.

[6] E. Guaus, J. Torrent-Burgués, « Tin-zinc electrodeposition from sulphate–tartrate baths », Journal of Electroanalytical Chemistry, Volume 575, Issue 2, 1 February 2005, Pages 301-309.

[7] E. Budman, D. Stevens, « Tin-zinc plating », Anti-corrosion methods and materials, vol45, N°5, (1998), pp.327-332.

[8] J.-C. Liu, Z.-H. Wang, J.-Y. Xie, J.-S. Ma, G. Zhang, K. Suganuma, « Understanding corrosion mechanism of Sn–Zn alloys in NaCl solution via corrosion products characterization », Materials and Corrosion, 67, No. 5, (2016), pp. 522-530.

[9] T. Hammam, « The impact of sliding motion and current load on the deterioration of tin-coated connectors », Proc. 45th IEEE Holm Conference on Electrical Contacts, Pittsburgh, USA, 1999, pp. 203-212.

[10] S. Noël, N. Lécaudé, D. Alamarguy, L. Tristani., « Lubrication mechanisms of hot-dipped tin separable electrical contacts », Proc. 47th IEEE Holm Conference on Electrical Contacts, Montréal, Canada, 2001, pp. 197-202.

[11] M. Mainka, T. Wielsch, « Accelerated lifetime testing of the tribo-electrical properties of a lubricated tin contact system », Proc. 69th IEEE Holm Conference on Electrical Contacts, Annapolis, USA, 2024, pp. 188-195.

[12] *Electrical Contacts*, P. Slade editor, CRC Press, Taylor and Francis, 2014, p. 1198.

[13] C. Maul, J. W. McBride, J. Swingler, « Intermittency Phenomena in Electrical Connectors », IEEE Trans. Comp. and Pack. Technol, vol. 24, No. 3, (2001), pp. 370-377.

Silver reduction through high-performance composite technologies and non-precious metal sub-layers

Timo Mützel
Doduco Contacts and Refining GmbH
Pforzheim, Germany
timo.muetzel@doduco.com

Havva Cinaroglu
Doduco Contacts and Refining GmbH
Pforzheim, Germany
havva.cinaroglu@doduco.com

***Abstract*—Solutions for saving silver by reducing the silver based functional layer and replenishing height by substructures with copper-based materials are known from auxiliary switches and relays, working under resistive load or even dry switching only. State-of-the-art technologies like cold bonding are used to manufacture these contacts but are not reliable enough for inductive and motor load applications. Under such load conditions the contacts will be delaminated in the bonding zone and subsequently lead to early failure of the device.**

The paper will present composite technologies for power applications such as power relays and contactors. Composites of Ag/SnO_2 and Ag/Ni contact materials in combination with sub-layers of Cu, CuSn6 or CuNi9Sn2 were manufactured by alternative technologies and successfully tested in switching devices under heavy duty load conditions.

Based on such technologies, precious metal surplus can be eliminated from power switching devices and substantial cost savings be achieved.

Keywords—bonding methods, precious metal saving, power applications, non-noble underlayers

I. Introduction

Silver is widely regarded as one of the most strategically significant functional materials in contemporary industry. The metal's combination of high electrical conductivity, excellent thermal conductivity, good solderability, and pronounced catalytic and antimicrobial properties renders it indispensable in numerous key technologies. In the disciplines of electronics, energy technology and photovoltaics, silver is not only a performance factor but also a technological enabler. Owing to its conductivity, the material exhibits low contact resistance and high current-carrying capacity. In the domain of photovoltaics, silver, in the form of pastes, functions as a contact material for solar cells and represents one of the most significant consumers in this sector. Furthermore, demand for electromobility is increasing.

Over the past three decades, the price of silver has evolved through several distinct phases, influenced by macroeconomic factors and shifts in industrial demand.



Fig. 1. Silver price development in dollars and ounces, (02.02.2026) [1]

The 30-year chart (Fig. 1) demonstrates a transition from a prolonged period of stable low prices to a volatile yet structurally elevated price range, influenced by macroeconomic factors and shifts in industrial demand. The growing significance of silver as a key industrial raw material, especially in the domains of electronics, energy technology, and photovoltaics, has fundamentally changed the market dynamics and is likely to remain a key driver of price developments in the future.

In many electrical contact applications, the high price of silver is putting increasing economic pressure on the metal. However, since silver has the highest electrical conductivity of any metal and offers excellent arc and switching properties, it is difficult to find a technical substitute. Nevertheless, two established strategies exist for reducing silver consumption, both of which have clear technical consequences.

One option is to increase the non-silver content of the contact material by using higher proportions of additives such as nickel or tin oxide. While this reduces material costs, it alters the functional properties of the contact. Typically, increasing the non-silver content leads to lower electrical conductivity and changes in arc behavior, which can potentially increase arc erosion. The processing properties, such as formability, solderability and weldability, also change because the microstructure and thermal properties of the material are no longer dominated by silver.

Secondly, silver consumption can be reduced by decreasing the thickness of the silver-containing contact

material. Multilayer coatings are increasingly being used for this purpose, with silver serving only as a functional top layer and more cost-effective metals, such as copper or copper alloys, acting as substrates underneath. This approach enables a significant reduction in silver content without significantly altering surface properties. However, adhesion strength, thermal stability and contact mechanics are subject to greater demands, as thinner silver layers can be worn away more quickly by mechanical abrasion or arcing.

There are various joining technologies available for fabricating multilayer contact materials, and each technology produces different thermal, mechanical and metallurgical properties. The choice of process influences the bond strength between the contact and carrier materials, as well as the electrical performance, thermal stability and cost-effectiveness of the entire contact component.

One common method is cold roll-cladding (Fig. 2), whereby the contact and carrier materials are joined together by cold deformation under high mechanical pressure in a single rolling pass. This process involves local plastic deformation and the breaking up of surface oxides, resulting in metallic contact. In most cases, subsequent annealing is performed to improve the quality and strength of the bond.

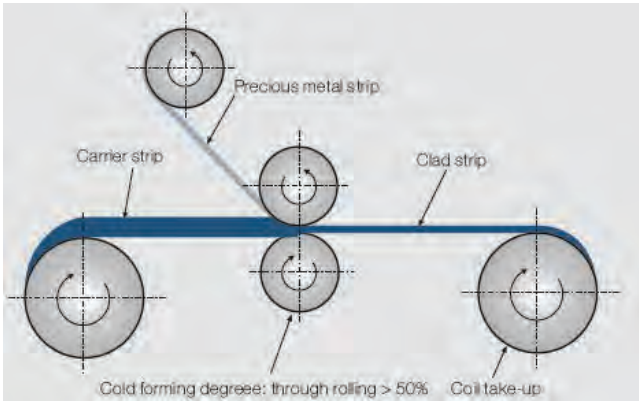


Fig. 2. Cold roll-cladding [2]

In hot cladding (Fig. 3), the bond is further strengthened by the elevated temperature. The materials to be clad are assembled into a cladding package in the form of blocks or plates. This package is then heated to around 800°C, at which point the materials are 'welded' together under high pressure. This combination of pressure and heat improves the metallurgical bond, increasing its strength. However, microstructural transformations, grain growth and diffusion processes may also occur simultaneously.

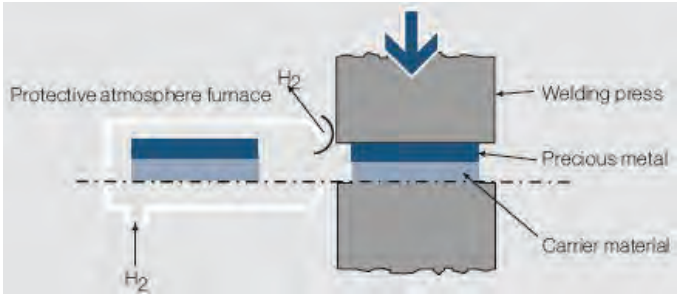


Fig. 3. Hot-cladding of materials [2]

In the case of welding or brazing contact and carrier materials (Fig. 4), both strips are usually fed into an induction brazing machine with an intermediate thin foil of brazing alloy. This process called toplay brazing creates a metallurgical bond through localized melting. While they enable high strengths and reproducible layered composites, precise process control is required to avoid defects such as pores or undesirable alloying zones.

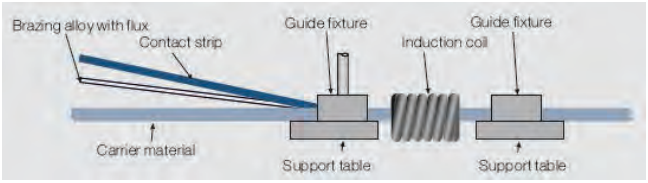


Fig. 4. Welding or brazing of contact strip and carrier material (toplay brazing) [2]

II. Contactor Application

It is evident that the bonding area between the silver containing material and the cost-effective substrates underneath exerts a significant influence on the electrical conduction and, more specifically, on the heat dissipation within the contact system. This phenomenon is commonly referred to as the "butterfly effect"[3]. The arc is the cause of the melting of the contact surface. Subsequent to this process, the phenomenon of 'shrinking stress' occurs during the subsequent phase of resolidification. In the event of inadequate bonding between the contact tip and the copper underlayer, the consequence may be delamination and elevation of the edges. It is an inevitable consequence of the elevated edges that there will be an increase in the erosion of the contact material. This, in turn, will result in a short-term failure [3, 4, 5].

In the field of motor load application (AC-3 / AC-4 rating), contactors are typically equipped with Ag/SnO_2 contacts, which are characterized by their ability to withstand anti-welding and erosion requirements. Accordingly, the tests were carried out using an Ag/SnO_2 88/12 powder metallurgical material, which had been extruded and which also contains the additives Bi_2O_3 and CuO.

In order to assess the hypothesis that a copper underlayer not only saves material but also adequately meets thermomechanical requirements, comparative electrical endurance tests simulating a heavy-duty load, under the test conditions shown in Table I were conducted.

TABLE I. Contactor Test Parameters

Parameter	***Value***
Voltage *U*	400 V
Current *I*	228 A
Power factor *cosφ*	1
Switching frequency	250 1/h
Number of operations *n*	30,000
Drive voltage	230 V (AC)

The tests were carried out with Ag/SnO_2 contact plates without a copper underlayer and with an Ag/SnO_2 contact tip with an integrated copper underlayer. The copper underlayer was applied to the Ag/SnO_2 strip by toplay brazing. Figure 5 illustrates the layer structure of the tested contacts. The incorporation of an additional copper layer enabled a reduction in the thickness of the Ag/SnO_2 contact material by approximately 35%. Both variants of contacts were then induction brazed to contactor carriers.

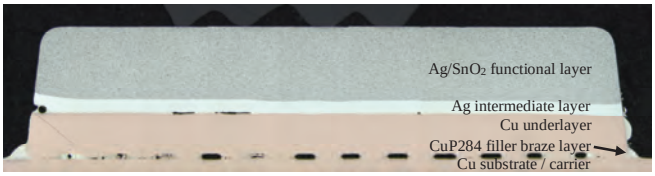


Fig. 5. Ag/SnO_2//Ag//Cu//CuP284 before test, brazed onto contactor carrier (cross section)

In order to evaluate the material erosion of both variants, the contacts were weighed prior to and during the lifetime test, and the material loss was calculated. Furthermore, following 30,000 switching cycles, the contacts were disassembled and a metallographic section was prepared to ascertain the development of delamination effects, i.e. the peeling of the contact material. Prior to the commencement of switching tests, ultrasonic tests were conducted to assure that the brazing area between the contact carrier and the contact tip was free of defects. The objective of this study was to eliminate the possibility that an insufficient brazing area of contact tip to carrier could distort the switching results or promote the delamination effect.

As shown in Figure 6, the material erosion at the moving contact for both variants is presented alongside its standard deviation. A comparison of the two curves reveals that no significant differences in the material erosion of the two analyzed variants can be discerned.

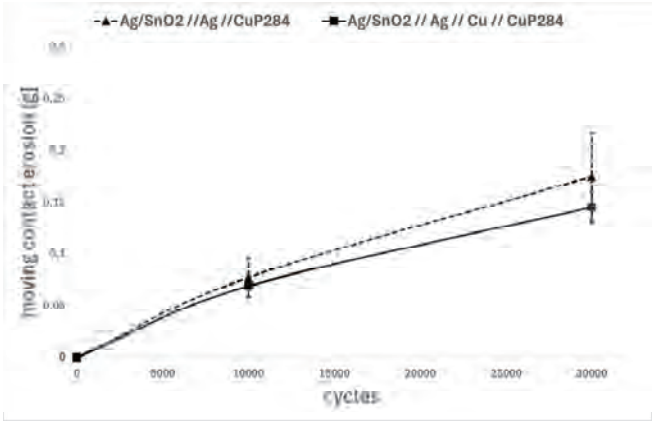


Fig. 6. Contact erosion over number of operations

The thermal energy introduced at the base of the arc root creates an extremely steep temperature gradient in the contact, extending over several thousand Kelvin within just a few millimeters. The resulting high thermal stress on the contact tip leads to significant thermomechanical stress in the material. These stresses can cause vertical thermo-mechanical cracks, which can be particularly critical if there are defects or structural weaknesses in the bonding zones between two different materials. Under such conditions, there is also a risk of delamination between the two joined materials.

The cross sections after the test (Fig. 7 and Fig. 8) show the severe impact of arcing on the contact surface, caused by decomposition and heat-induced stresses within the Ag/SnO_2 layer after 30,000 operations. Starting crack formation within the Ag/SnO_2 layer can be observed in both sections, but the bonding of silver to copper is free of any cracks or delamination.

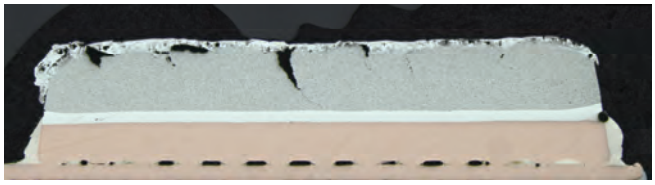


Fig. 7. Ag/SnO_2//Ag//Cu//CuP284 after test (cross section)



Fig. 8. Ag/SnO_2//Ag//Cu//CuP284 after test (longitudinal section)

In addition to investigating the contact material Ag/SnO_2 with a copper underlayer applied by toplay brazing in contactor applications, the material Ag/Ni30 with a hot-cladded copper underlayer was also analyzed with regard to its performance. The Ag/Ni30 contact material was first produced by powder mixing, extrusion, and subsequent rolling.

In order to evaluate the influence of the copper underlayer on the electrical lifetime, contactors were set up in which the massive Ag/Ni30-tips and hot-cladded Ag/Ni30//Cu-tips were installed.

Both variants were then subjected to an AC-1 resistive load test under the conditions shown in Table II. The electrical lifetime tests were performed with grounded neutral to avoid synchronism effects.

TABLE II. AC-1 CONTACTOR TEST PARAMETERS

Parameter	***Value***
Voltage *U*	400 V
Current *I*	324 A
Power factor *cosφ*	1
Switching frequency	250 1/h
Number of operations *n*	10,000
Drive voltage	24 V (DC)

A direct comparison allows for an assessment of the extent to which the hot-rolled copper underlayer influences the thermomechanical behavior, material wear, and overall lifetime of the contact system.

The analysis of the micrographs of both investigated variants clearly demonstrates the potential for crack formation in the Ag/Ni30 contact material (Fig. 9 and Fig. 10). Such cracking is of critical importance because, as has been previously described in [6], it can lead to discontinuous and locally increased material loss. This behavior is of particular relevance under conditions of high thermal and mechanical loads during switching operations.

However, a crucial difference becomes apparent in the micrograph of the Ag/Ni30 variant with a hot-cladded copper underlayer (Fig. 10). The bond between the Ag/Ni contact material and the copper underlayer is so robust that crack propagation along the bonding zone is effectively prevented. Instead, it is found to run within the Ag/Ni contact material itself. This suggests that the metallurgical bond between the two layers does not act as a weak point.

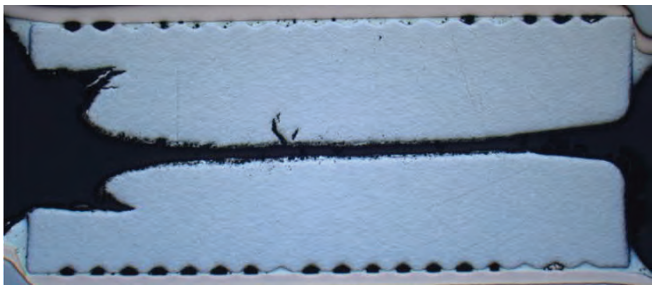


Fig. 9. Massive Ag/Ni30 after test

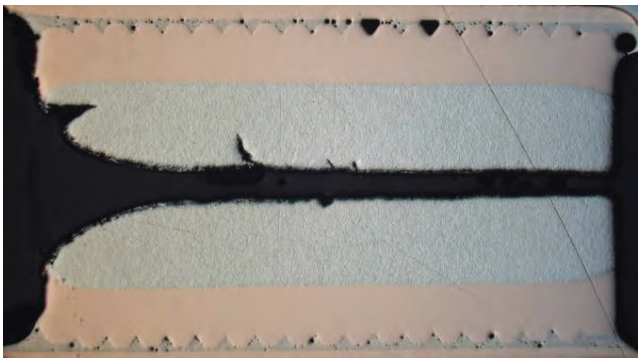


Fig. 10. Hot-cladded bi-layer Ag/Ni30//Cu after test

This observation is of great importance because it demonstrates that the copper underlayer does not generate any additional tendency for delamination. Instead, the bonding zone remains stable while cracking is limited to the contact material itself.

III. Power Relay Application

The investigations described in [7] clearly demonstrate the challenges involved in producing bimetallic rivets, as well as the influence of joint quality on relay switching behavior. In particular, a clear correlation was established between the presence of a high-quality metallurgical bond between the two materials and the occurrence of contact material peeling during lifetime testing. Inadequate bonding has been shown to result in the detachment of the contact layer, which can lead to accelerated wear and premature functional failure. Based on these findings, this work systematically investigated the influence of two joining techniques — diffusion welding and cold roll-cladding — on the lifetime of contacts. For this purpose, the Ag/SnO_2 contact with an integrated CuNi9Sn2 underlayer shown in Figure 11 was produced. This was done using both methods. Both profiles were resistance welded onto a copper carrier and mounted into power relays.



Fig. 11. Ag/SnO_2//Ag//CuNi9Sn2 profile before test

Subsequently, a lifetime test in acc. to IEC 61810-1 [8] was performed according to the conditions defined in Table III. A direct comparison of the two joining techniques allows for an assessment of the influence of the manufacturing method on the structural integrity of the bonded zone and its subsequent effect on the peeling behavior, material erosion, and the service life of the contact system.

TABLE III. Relay Test Parameters

Parameter	***Value***
Voltage *U*	250 V
Current *I*	30 A
Switching frequency	360 1/h
Number of operations *n*	75,000

First signs of a starting delamination of the contact were already observed after 20,000 operations on the cold roll-cladded material. The test was stopped and cross sections were made for evaluation (Fig. 12). A crack at lower area of the intermediate fine silver layer between Ag/SnO_2 and CuNi9Sn2 layer is already visible, and the functional layer starts peeling.



Fig. 12. Ag/SnO_2//Ag//CuNi9Sn2 profile (cold bonded) after test

Following a total of 75,000 operations, the entire Ag/SnO_2 contact material layer is detached from the cold roll-cladded multilayer structure by the peeling effect

(Fig. 13) within the contact overlap area. This results in a failure of the relay due to contact tack welding caused by the absence of the functional Ag/SnO_2 layer.

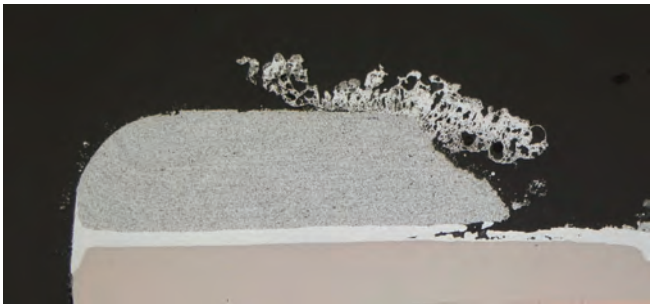


Fig. 13. Ag/SnO_2//Ag//CuNi9Sn2 profile (cold roll-cladded) after test

The high deformation of the cold bonding process most probably caused micro-cracks within the silver layer, which continue into a kind of low cycle fatigue during the electrical endurance test. The electric arc induces thermo-mechanical stress by the heat cycling and the stress is released by crack propagation and followed by peeling of the functional Ag/SnO_2 layer. With only poor connection to the CuNi9Sn2 underlayer the heat induced into the Ag/SnO_2 cannot be transferred any longer by heat conduction and the material loss increases exponentially, leading to an early failure of the relay.



Fig. 14. Ag/SnO_2//Ag//CuNi9Sn2 profile (diffusion welded) after test

Figure 14 shows the multilayer structure Ag/SnO_2//CuNi9Sn2, which was produced by diffusion welding and subsequently subjected to the electrical lifetime test. In contradistinction to the layered composite produced by cold rolling, neither cracking nor delamination is evident in the interface between the functional layer and the sublayer. This finding indicates a significantly higher metallurgical integrity of the diffusion-welded composite. However, it is notable that the weld to the contact carrier represents the structural weak point: Under the high thermal stress of switching operation, this connection begins to detach and one welding rail is bending upwards from the contact carrier, while the multilayer composite itself remains stable.

IV. Summary and Conclusion

Silver-containing contact materials are experiencing significant economic pressures due to the substantial increase in the price of silver. This has led to a growing focus on identifying methods to reduce silver consumption without compromising switching performance. A promising strategy is multilayer construction, in which silver is used only as a thin functional layer, while more cost-effective metals such as copper form the load-bearing base layer. However, the quality of the joining technology is crucial for the success of this approach, as only a stable metallurgical bond can reliably withstand the mechanical and thermal stresses of switching operation.

Investigations have shown that, with suitable joining processes such as hot cladding, toplay brazing, and diffusion welding the thickness of the silver-containing layer can be significantly reduced without causing delamination or increased material loss. In Ag/SnO_2 and Ag/Ni contacts, the bonding zones remained stable despite high thermal stress; cracks occurred exclusively within the contact material itself. Lifetime tests confirmed that correctly manufactured multilayer contacts exhibit comparable erosion resistance to solid contacts, while enabling significant silver savings. Further tests with Ag/SnO_2 contacts and a CuNi9Sn2 sublayer demonstrated that bond quality is crucial. While diffusion welding produced stable bonds, cold roll cladding resulted in microcracks that can lead to failure of the functional layer under cyclic thermal stress.

Therefore, these results clearly demonstrate that, provided the bonding technology employed ensures a flawless and resilient bond zone, multilayer systems represent a technically robust and economically attractive solution for reducing silver consumption even in power switching applications.

References

[1] https://www.gold.de/kurse/silberpreis/ (02.02.2026)

[2] Manufacturing of Semi-Finished Materials - Electrical Contacts (30.01.2026)

[3] Bolmerg, E, “Lifetime of Riveted and Welded Contacts in Powersupply Relay”, 19th International Conference on Electrical Contacts (ICEC), Nuremberg, Germany, 1998

[4] Späth, D. et al., “The Influence of the Bonding Area of Welded Contact Tips on Contact Erosion”, 52nd IEEE Holm Conference on Electrical Contacts, 2006, pp. 181-187.

[5] Mützel, T.; Bender, M.; Heringhaus, F.; Ma, D., “Thermo-mechanical Stress in Electrical Contacts due to Arcing Events”, 28th International Conference on Electrical Contacts (ICEC), Edinburgh, Scotland, 2016

[6] Karlson, B.; Herbst, R.; Kupka, D.; Krätzschmar, A., „Thermo-mechanische Schädigung von AgNi Kontaktauflagen (Versuch vs. Simulation“, 28. Albert-Keil-Kontaktseminar, Karlsruhe, Germany, 2025

[7] Chen, Z.K.; Witter, G.J., “A Correlation of Silver Tin Indium Oxide-Copper Composite Rivet Interface Bond Quality and Switching Endurance Life in DC Relays”, 26th International Conference on Electrical Contacts, Beijing, China, 2012

[8] IEC 61810-1:2015, Electromechanical elementary relays - Part 1: General and safety requirements

Simulation of the Electric Arc Motion between Bus-Bar Electrodes

Camille Gouze
Université de Toulouse, Toulouse INP, CNRS, LAPLACE
IRT Saint Exupery
Toulouse, France
camille.gouze@laplace.univ-tlse.fr

Yann Cressault
Université de Toulouse, Toulouse INP, CNRS, LAPLACE
Toulouse, France
yann.cressault@laplace-univ-tlse.fr

Flavien Valensi
Université de Toulouse, Toulouse INP, CNRS, LAPLACE
Toulouse, France
flavien.valensi@laplace.univ-tlse.fr

Malyk Benmouffok
IRT Saint Exupery
Toulouse, France
malyk.benmouffok@irt-saintexupery.com

Michael Darques
IRT Saint Exupery
Toulouse, France
michael.darques@irt-saintexupery.com

Cyril Van de Steen
Safran Group
Toulouse, France
cyril.van-de-steen@safrangroup.com

***Abstract* — The increase in voltage levels in aeronautical onboard electrical networks improves power distribution performance but increases the risk of electrical failures. Among these, electrical fault arcs constitute a critical threat to system dependability and overall system integrity. Their severity depends on voltage and current levels, the characteristics of the power supply, and environmental constraints specific to the aeronautical context. Parallel arcs, in particular, exhibit specific dynamics that may lead to damage to cables and their surrounding environment. This work aims to initiate a numerical modeling of parallel electrical arcs by reproducing reference results obtained from a simplified busbar geometry, in order to better characterize their mechanisms of motion and interaction.**

Keywords—Arc discharge, Bus-bar, Arc displacement, MHD, Ansys Fluent.

I. INTRODUCTION

More electrical aircraft is now a reality. The constant increase in voltage levels in aircraft onboard electrical networks constitutes a major lever for improving overall system performance, reducing weight and maintenance costs, and supporting the transition toward more energy-efficient architectures [1], [2]. However, this evolution takes place within a context of strong technological and environmental constraints, which makes the control of electrical failure phenomena particularly critical.

Among these phenomena, electrical fault arcing represents a major challenge for the protection of onboard equipment. When not properly detected and/or controlled, an arc can compromise system dependability and jeopardize the overall integrity of the aircraft [3]. With the continuous increase in requirements related to safety, redundancy, and power density, the management of electrical arcs is becoming an increasingly significant challenge for the aeronautical industry. Arc severity is closely linked to voltage and current levels, as well as to the nature of the power supply (AC or DC), that is, to the amount of power involved. Increasing voltage levels significantly exacerbate these risks by subjecting insulating materials to higher electrical stresses, further aggravated by the specific conditions of the aeronautical environment, such as low pressure and the presence of moisture [4], [5].

Depending on their location within the circuit, arc faults may occur in series (which occurs in serial with a load) or parallel (which short-circuit the load) configurations, each leading to distinct electrical signatures and dynamic behaviors [6].

In an aeronautical context, arc formation can cause localized damage that may propagate along cable harnesses. Such degradation can lead to the shutdown of onboard systems, the loss of critical functions, or even the initiation of a fire. A detailed understanding of the mechanisms governing arc initiation, motion, and propagation is therefore essential to improve detection and protection strategies [7], [8].

Within this framework, a numerical investigation of electrical arcs in a parallel configuration is essential in order to characterize their behavior and evolution along conductors, and to identify the physical parameters governing their dynamics. Moreover, such an approach makes it possible to reduce the number of full-scale experimental tests, which are complex to implement and highly costly. Despite the critical importance of these issues for aircraft safety and the design of onboard electrical networks, few numerical models are specifically suited to the conditions inherent to aeronautical environments, which limits the ability to reliably predict the actual behavior of arcs.

The present work is part of this effort and constitutes a first step toward modeling the mechanisms governing electrical arc motion and interaction. The objective is to establish a model that is benchmarked against the results reported in [9], obtained using a deliberately simplified geometry consisting of two parallel conductive bars (busbars). So, the geometry used in this work is the one used in [9]. This type of configuration is directly inspired by low-voltage circuit breaker devices, in which control of arc motion—under the combined effects of electromagnetic forces and pressure gradients—is a key issue for rapid and controlled arc extinction. These topics have been the subject of extensive research over several decades in the field of low-voltage circuit breakers, both experimentally and numerically [10], [11]. The current phase of methodological validation on an elementary constant-current geometry will subsequently enable the modeling approach to be extended to more complex configurations. Actually, even if a lot of work had been done regarding arc modelling, only sparsely investigate arc fault in aeronautical configuration. This work will try to complete and improve the arc behavior in this kind of application.

II. Implementation of the Model

A. Configuration

The geometry considered in this study is that presented in Lisnyak's thesis and shown in Fig. 1. It consists of two copper electrodes with a cross-section of 3.0 mm × 8.0 mm and a length of 20 mm. The inter-electrode gap ranges from 5 to 8 mm. The surrounding gas is air at atmospheric pressure; the gas transport coefficients and thermodynamic properties are computed by the Scipra team of the LAPLACE laboratory, see appendices for the data. In this study, the assumptions are that the arc is a laminar fluid and in local thermodynamic equilibrium (LTE). Furthermore, only the arc column is modeled; electrode interactions and metal vapors are not considered. The computational mesh is composed of approximately 650,000 hexahedral cells, with cell sizes ranging from 0.1 mm near the electrodes to 0.3 mm at the boundaries of the computational domain.

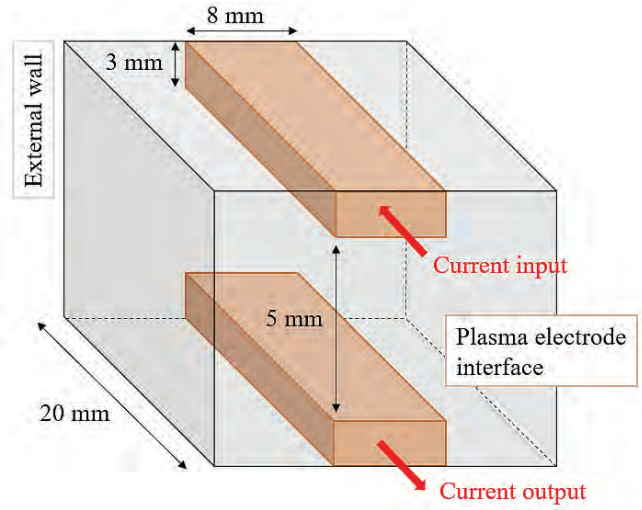


Fig. 1. Model geometry.

B. Model equations

The model applies the magnetohydrodynamics (MHD) approach. The governing equations are given as follows, combining the fluid and electromagnetic formulations. The fluid Navier–Stokes equations are augmented with source terms in the momentum conservation equation (Lorentz forces) and in the energy conservation equation (Joule heating, radiation, and electron enthalpy flux):

$$\frac{\partial \rho}{\partial t} + \vec{\nabla} \cdot (\rho \vec{v}) = 0 \quad (1)$$

$$\frac{\partial \rho \vec{v}}{\partial t} + \vec{\nabla} \cdot (\rho \vec{v}.\vec{v}) = -\vec{\nabla} P - \vec{\nabla} \cdot \vec{\tau} + \vec{j} \times \vec{B} \quad (2)$$

$$\frac{\partial \rho h}{\partial t} + \vec{\nabla} \cdot (\rho \vec{v} h) = -\vec{\nabla} \cdot \vec{Q} + \frac{\partial P}{\partial t} + \vec{v} \cdot \vec{\nabla} P + \vec{j} \cdot \vec{E} - Q_{rad} + \frac{5}{2}\frac{k_b}{e}(\vec{J} \cdot \vec{\nabla} T) \quad (3)$$

In the equations below, ρ denotes the density, $\vec{v}$ the gas velocity vector, t the time, P the pressure, $\vec{\tau}$ the viscous stress tensor, $\vec{j}$ the current density vector, $\vec{B}$ the magnetic field vector, h the enthalpy, $\vec{Q}$ the conductive heat flux, $\vec{E}$ the electric field, k_b the Boltzmann constant and e the elementary charge. The radiative loss term Q_{rad} is computed using the net emission coefficient (NEC) method [12], with a radius R_p = 5 mm [9], [11]. The electromagnetic formulation relies on the electric scalar potential and on the computation of the magnetic field using the vector potential method:

$$\vec{E} = \vec{\nabla} \varphi \quad (4)$$

$$\vec{B} = \vec{\nabla} \times \vec{A} \Rightarrow \Delta \vec{A} = \mu_0 \vec{j} \quad (5)$$

Here, φ denotes the electric potential, and, $\vec{A}$ represents the magnetic vector potential.

C. Boundaries conditions

At the domain boundaries, a pressure outlet boundary condition is applied at atmospheric pressure ("pressure outlet"). A fixed temperature of 300 K is imposed at the inlet and outlet faces of the current path. The imposed current is direct current and is set to 200 A at the cathode by applying a current density $J = I / S$, where S is the electrode surface area. The anode is grounded. All boundary conditions are summarized in Table I. The arc is initialized as a cylindrical channel with a radius of 0.7 mm and an initial temperature of 18,000 K. This temperature corresponds to an established hot and conductive arc plasma channel. This value is based on the initial temperature taken in [11].

TABLE I. Boundary Conditions of the Model.

	Type	Energy	Electric potential	Magnetic field
Plasma/electrode interface	Wall	$\left(\kappa\frac{\partial T}{\partial n}\right)_p = \left(\kappa\frac{\partial T}{\partial n}\right)_e$	$\left(\sigma\frac{\partial V}{\partial n}\right)_p = \left(\sigma\frac{\partial V}{\partial n}\right)_e$	$\left(\frac{\partial A_{r,z}}{\partial n}\right)_p = \left(\frac{\partial A_{r,z}}{\partial n}\right)_e$
Current input	Wall	300K	$J = I/S$	Zero flux
Current output	Wall	300K	0V	Zero flux
External walls	Pressure outlet P_{atm}	300K	Zero flux	Zero flux

The model is set up on a customised commercial platform. All numerical schemes are first order, with the exception of pressure, which is discretized using a second-order scheme. The pressure–velocity coupling algorithm is PISO. A transient simulation is performed with a time step of $\Delta t = 10^{-5}\ s$ and 500 sub-iterations per time step.

D. Arc displacement

The most significant feature of this type of arc is its motion. Indeed, due to Lorentz forces generated by the magnetic field of the electrodes, as well as pressure forces, the arc moves along the electrodes. However, accurately modeling this physics requires studying the arc attachment to the electrodes. Modeling the electrode–plasma interface is extremely challenging, as this region cannot be assumed to be in local thermodynamic equilibrium (LTE) due to perturbations caused by the presence of the wall. Quasi-neutrality, as well as thermal and chemical equilibria, are disrupted over a characteristic length on the order of 0.1 mm. A detailed analysis of this region is nevertheless necessary in certain applications to evaluate wall heat fluxes and quantify electrode erosion.

For the study of arc root dynamics alone, however, it is sufficient to use models that neglect these non-equilibrium effects. Several methods exist for this purpose:

1. Automatic coupling
2. Constant effective electrical conductivity σ_{eff}

3. Lindmayer model

We will now describe these methods. The first consists of allowing Fluent to handle the interface, which provides a boundary condition called “Coupled” (method (1)). In this case, the interface is managed automatically by the software. The resulting formulation is:

$$\sigma_{electrode}\left(\frac{\partial V}{\partial n}\right)_{electrode} = \sigma_{plasma}\left(\frac{\partial V}{\partial n}\right)_{plasma} \quad (6)$$

The second method involves imposing a constant electrical conductivity at the electrode surface (method (2)). A very steep conductivity gradient exists between the electrode, with $\sigma_{electrode} = 5.9 \times 10^7\ S/m$ and the plasma. Indeed, the electrical conductivity values are very low (below 10 S/m) for temperatures under 6000 K. As a result, current continuity between the cathode and the plasma column under LTE conditions is not ensured. To restore this continuity in the region of steep temperature gradients, the electrical conductivity has been deliberately increased. Consequently, it is assumed that, in the region near the electrodes, the plasma’s minimum electrical conductivity is limited to a value equivalent to that at 10,000 K, approximately 3000 S/m.

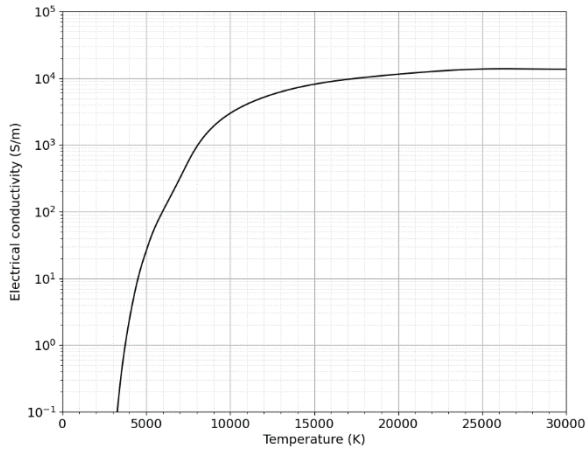


Fig. 2. Electrical conductivity as a function of temperature for air at atmospheric pressure.

The final method (method (3)) is based on the model proposed by Lindmayer [13], originally developed for the analysis of electrical arcs in low-voltage circuit breakers. This model aims to reproduce the voltage increase induced by the presence of separators by introducing an additional resistivity localized in the arc channels. Its principle consists of imposing a specific voltage drop, ΔU, at the boundaries of the cathode region for a given current density, J. Current conservation in this region then allows the definition of a nonlinear effective conductivity, applied to a layer of cells adjacent to the electrodes, with thickness Δx, representing the extent of the non-LTE region. The schematic in Fig. 3 illustrates methods (2) and (3).

The electrical conductivity is derived from the following equation:

$$J = \sigma_{eff}\frac{\Delta U}{\Delta x} \Rightarrow \sigma_{eff} = J\frac{\Delta x}{\Delta U} \quad (7)$$

The relationship between ΔU and J is shown in Fig. 4, taken from the study by Mutzke [14] on low-voltage circuit breakers.

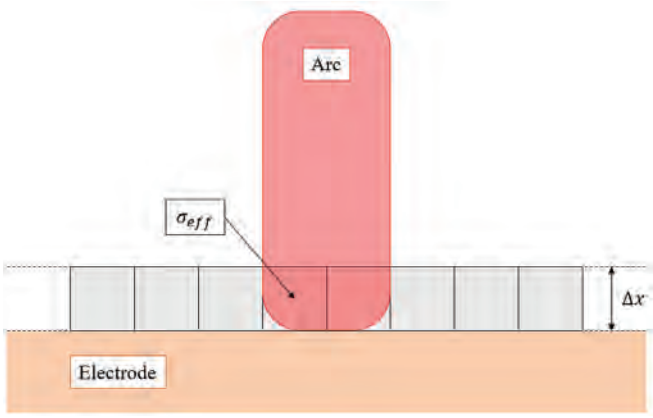


Fig. 3. Diagram of methods (2) and (3).

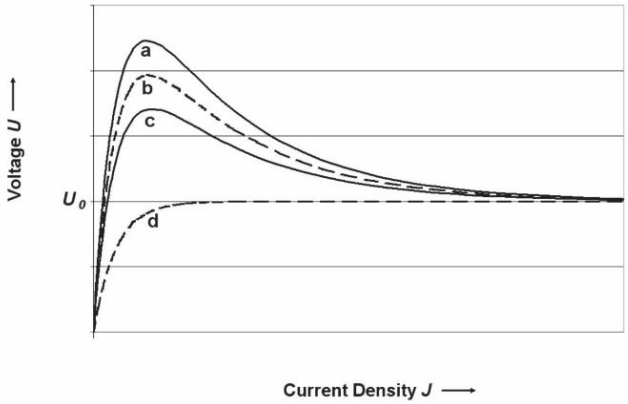


Fig. 4. Voltage-current curves proposed by Mutzke [14], (a) ignition voltage = 22.3 V ; (b) 19.7 V ; (c) 17.1 V and (d) 0 V.

III. Results

Figure 5 shows the arc temperature fields for different time steps: 0.01 ms, 0.2 ms, and 0.4 ms. The first time step corresponds to arc initialization. Subsequently, the arc moves under the action of Lorentz and pressure forces, particularly at the arc root regions. Methods 1 and 3 appear to produce similar results for the temperature field. A hot channel around 18,000 K is observed, with higher temperatures near the electrodes (approximately 23,000 K). A protrusion of hot gas upstream of the arc (right-hand side) is also visible. This characteristic morphology, known as the “nose,” has been documented in experimental work by Zeller [15] and in theoretical studies by Wu [16]. Furthermore, the motion of the arc root at the anode (Fig. 6) shows very similar results between these two methods, with comparable propagation velocities, summarized in Table II. The magnitude of these velocities is consistent with the literature [10]. It is noted that the arc root moves faster at the cathode (the electrode where current is applied). This is due to the electron enthalpy flux (the last term in Equation (3)). Electrons leaving the cathode collide with the surrounding gas, heating the plasma near the electrode; the enlarged heated zone thus facilitates the arc’s motion.

The results for method 2, which imposes a constant electrical conductivity at the electrode surfaces, are, however,

markedly different from the other methods. A broader, nearly isothermal hot channel at approximately 17,000 K is observed, with a slight increase on the anode side. Imposing a constant electrical conductivity at the electrode surface profoundly alters the relationship between the electric current distribution and the plasma thermal state, since conductivity is in reality a strongly nonlinear function of temperature. This assumption artificially homogenizes the current density within the plasma column, significantly reducing the electric field gradients and Joule dissipation that are normally concentrated near the electrodes. The result is a more uniform volumetric heating and the formation of an expanded, quasi-isothermal thermal channel around 17,000 K. Although numerically stable, this approach produces an excessively diffused representation of the arc and fails to accurately reproduce its thermal and dynamic structure.

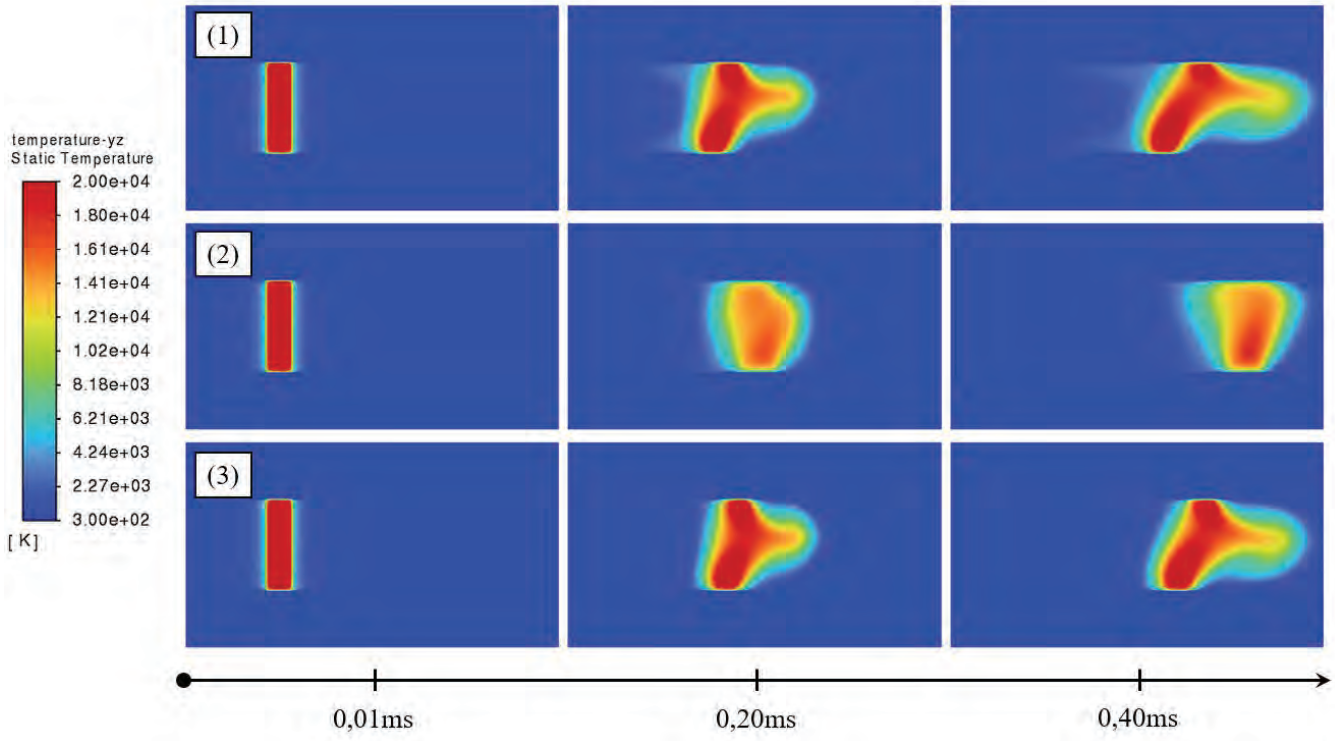


Fig. 5. Temperature ranges for the three methods (1) Coupled (2) $\sigma_{eff} = 3000\ S/m$ and (3) Lindmayer.

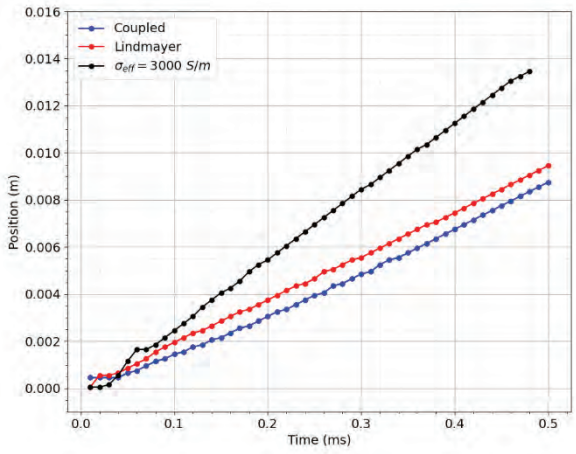


Fig. 6. Movement of the arc root at the anode for the three methods.

TABLE II. Arc root propagation velocities (m/s) at the anode and cathode for the three methods (1) Coupled (2) $\sigma_{\text{eff}} = 3000$ S/m and (3) Lindmayer.

	Anode	Cathode
(1)	17.5	22.7
(2)	28.0	27.9
(3)	18.9	22.7

IV. Conclusion

This work established and validated a numerical approach for modeling a parallel electrical arc between busbars, based on MHD coupling in ANSYS Fluent. The primary objective was to reproduce reference results from the literature on a simplified geometry, both in terms of the arc's thermal structure and its motion along the electrodes. The comparison of the three arc–electrode attachment modeling strategies clearly highlights the decisive influence of boundary conditions on arc physics. The "Coupled" and Lindmayer approaches yield consistent results that closely match experimental observations reported in the literature, in terms of both arc temperature and structure, as well as arc foot propagation velocities. In contrast, imposing a constant effective electrical conductivity near the electrodes significantly alters the current distribution and Joule heating, resulting in an excessively diffused and unrealistic representation of the arc. These results confirm that even a simplified consideration of non-local thermodynamic equilibrium effects in the attachment regions is essential to accurately reproduce arc motion dynamics. Within this framework, the Lindmayer model appears to offer a relevant compromise between physical fidelity and computational cost for the study of arc displacement.

This study constitutes a crucial methodological step before extending the model to more complex geometries and conditions representative of aeronautical electrical networks, including the application of alternating current and pressures closer to those encountered in aircraft. One of the objectives of this work is also to provide the reader with a clearer understanding of the impact of the phenomena considered. This study does not aim to favor or draw conclusions in support of any particular method; rather, it presents a comparative analysis based on observation. The reader is thus left free to evaluate the results and draw their own conclusions.

V. APPENDICES

In this appendix, you will find the baseline data for air at a pressure of 1 bar, calculated by the Scipra team. For further details on their calculation method, please contact the authors.

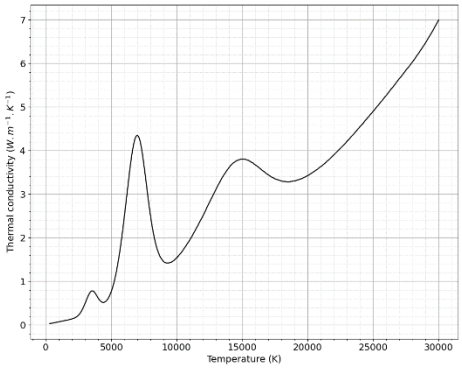


Fig. 7. Thermal conductivity for pure air at a pressure of 1 bar.

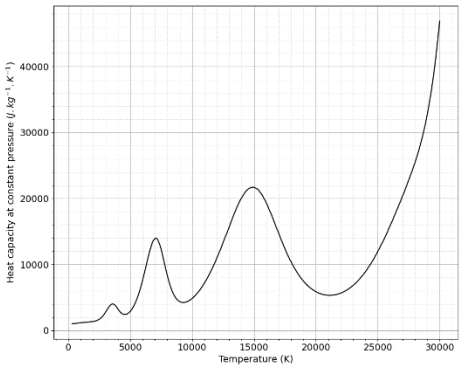


Fig. 8. Heat capacity at constant pressure for pure air at a pressure of 1 bar.

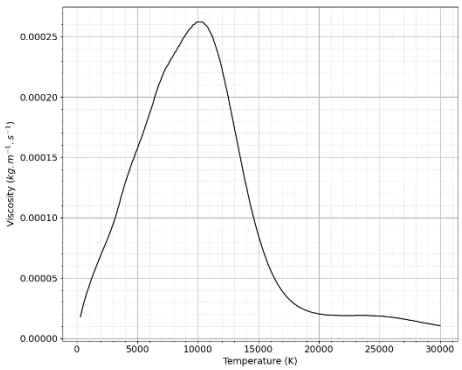


Fig. 9. Viscosity for pure air at a pressure of 1 bar.

REFERENCES

[1] A. AbdElhafez and A. Forsyth, "A Review of More-Electric Aircraft," *Int. Conf. Aerosp. Sci. Aviat. Technol.*, vol. 13, no. AEROSPACE SCIENCES, pp. 1–13, May 2009, doi: 10.21608/asat.2009.23726.

[2] B. C. Brusso, "History of Aircraft Wiring Arc-Fault Protection [History]," *IEEE Ind. Appl. Mag.*, vol. 23, no. 3, pp. 6–11, May 2017, doi: 10.1109/MIAS.2017.2659022.

[3] Gouvernement du Canada, "Vol Swissair 111." Accessed: May 26, 2025. [Online]. Available: https://www.tsb.gc.ca/fra/medias-media/fiches-facts/A98H0003/sum_a98h0003.html

[4] F. R. Frontzek, D. Konig, M. D. Judd, and H. J. Reher, "Fault arc propagation on cables for space applications in vacuum, oxygen-enriched air and air," *IEEE Trans. Dielectr. Electr. Insul.*, vol. 2, no. 2, pp. 190–197, Apr. 1995, doi: 10.1109/94.388239.

[5] A. Hammoud, M. Staven, J. Suthar, and J. Laghari, "Effects of thermal and electrical stressing on the breakdown behavior of space wiring," in *Proceedings of 1995 Conference on Electrical Insulation and Dielectric Phenomena*, Virginia Beach, VA, USA: IEEE, 1995, pp. 266–269. doi: 10.1109/CEIDP.1995.483714.

[6] NASA Technical Standard, "Flammability, offgassing, and compatibility requirements and test procedures," 2008.

[7] R. C. Rufato, T. Ditchi, C. V. De Steen, T. Lebey, and Y. Oussar, "DC serial arc fault recognition in aircraft using machine learning techniques," *Int. J. Electr. Power Energy Syst.*, vol. 164, p. 110408, Mar. 2025, doi: 10.1016/j.ijepes.2024.110408.

[8] J.-R. Riba, M. Moreno-Eguilaz, and J. A. Ortega, "Arc Fault Protections for Aeronautic Applications: A Review Identifying the Effects, Detection Methods, Current Progress, Limitations, Future Challenges, and Research Needs," *IEEE Trans. Instrum. Meas.*, vol. 71, pp. 1–14, 2022, doi: 10.1109/TIM.2022.3141832.

[9] M. Lisnyak, "Theoretical, numerical and experimental study of DC and AC electric arcs," phdthesis, Université Orléans, 2018. Accessed: Mar. 06, 2024. [Online]. Available: https://theses.hal.science/tel-01808258

[10] B. Swierczynski, J. J. Gonzalez, P. Teulet, P. Freton, and A. Gleizes, "Advances in low-voltage circuit breaker modelling," *J. Phys. Appl. Phys.*, vol. 37, no. 4, pp. 595–609, Feb. 2004, doi: 10.1088/0022-3727/37/4/011.

[11] A. Gatri, P. Freton, and J.-J. Gonzalez, "Limitation de courant dans une chambre de coupure à basse tension," *J. Int. Technol. Innov. Phys. Energ. Environ.*, vol. 9, no. 1, 2025, doi: 10.52497/jitipee.v9i1.%20369.

[12] A. Truilhé, C. Gouze, Y. Cressault, and F. Valensi, "Étude théorique de la modélisation du rayonnement d'un plasma thermique : application à l'arc libre," *J. Int. Technol. Innov. Phys. Energ. Environ.*, vol. 9, no. 1, Jan. 2025, doi: 10.52497/jitipee.v9i1.383.

[13] M. Lindmayer, E. Marzahn, A. Mutzke, T. Ruther, and M. Springstubbe, "The process of arc-splitting between metal plates in low voltage arc chutes," in *Proceedings of the 50th IEEE Holm Conference on Electrical Contacts and the 22nd International Conference on*

Electrical Contacts Electrical Contacts, 2004., Sep. 2004, pp. 28–34. doi: 10.1109/HOLM.2004.1353090.

[14] A. Mutzke, T. Ruther, M. Kurrat, M. Lindmayer, and E.-D. Wilkening, "Modeling the Arc Splitting Process in Low-Voltage Arc Chutes," in *Electrical Contacts - 2007 Proceedings of the 53rd IEEE Holm Conference on Electrical Contacts*, Sep. 2007, pp. 175–182. doi: 10.1109/HOLM.2007.4318213.

[15] P. Zeller and W. Rieder, "Arc structure, arc motion and gas pressure between laterally enclosed arc runners," in *Electrical Contacts - 1998. Proceedings of the Forty-Fourth IEEE Holm Conference on Electrical Contacts (Cat. No.98CB36238)*, Oct. 1998, pp. 69–74. doi: 10.1109/HOLM.1998.722429.

[16] Y. Wu, M. Rong, Z. Sun, X. Wang, F. Yang, and X. Li, "Numerical analysis of arc plasma behaviour during contact opening process in low-voltage switching device," *J. Phys. Appl. Phys.*, vol. 40, no. 3, pp. 795–802, Feb. 2007, doi: 10.1088/0022-3727/40/3/016.

Big-Data-Driven Screening and Optimization Design of Gassing Materials (PAs) for DC Circuit Breakers

Qian Wang
Xi'an University of Technology
Xi'an, China
qianwang@xaut.edu.cn

Yuxuan Liu
Xi'an University of Technology
Xi'an, China
1132045156@qq.com

Weidong Cao
Xi'an Jiaotong University
Xi'an, China
wdcao@stu.xjtu.edu.cn

Xinzhan Chen
Xi'an University of Technology
Xi'an, China
971324163@qq.com

Yi Shang
Xi'an University of Technology
Xi'an, China
1730190487@qq.com

Xu Zhong
Xi'an University of Technology
Xi'an, China
3433615644@qq.com

***Abstract*—Driven by the "dual carbon" goals, the new energy industry has developed rapidly. Low-voltage DC circuit breakers, as the core protection equipment of DC power systems, their arc quenching performance directly affects the safety and stable operation of the power grid. Since DC current has no natural zero-crossing point and brings great challenges to arc extinction, the selection and optimization of high-performance gassing materials have become a critical technical issue. To break through the performance bottlenecks of existing polyamide (PA)-based gassing materials and the inefficiency of traditional trial-and-error R&D mode, this paper proposes a big-data-driven intelligent screening and optimization design methodology for PA-based energetic gassing materials for low-voltage DC circuit breakers. This work first constructed a standardized filler database with approximately 44 million data entries of C/H/O/N system compounds from authoritative public databases, which provides a high-quality data foundation for material performance prediction. Then, a dual-track machine learning prediction strategy was established: a graph neural network (GNN)-based model was built for melting temperature (T_m) prediction, and a transfer learning prediction framework based on Directed Message Passing Neural Network (D-MPNN) was constructed for thermal decomposition temperature (T_n) prediction. At the current research stage, the pre-training of the T_n prediction model has been completed, with an accuracy (ACC) over 0.995 and an average F1-score of 0.990 in the pre-training phase. Meanwhile, a complete ReaxFF reactive force field molecular dynamics (ReaxFF-MD) simulation scheme for pyrolysis mechanism analysis was established, and a full closed-loop R&D framework spanning database construction, machine learning performance prediction, microscopic mechanism simulation, and experimental verification was constructed. The methodology proposed in this study provides a new paradigm for the rational design of high-performance PA-based gassing materials for DC circuit breakers, and the pre-trained model lays a solid core foundation for the subsequent high-throughput screening and performance optimization of new gassing materials.**

Keywords—Machine Learning, Energetic Gassing Materials; Low-Voltage DC Circuit Breakers, Arc-Quenching Performance, ReaxFF

I. INTRODUCTION

With the in-depth advancement of the "dual carbon" goals, DC (Direct Current, the core power supply system studied in this paper) application scenarios such as new energy distributed generation and electric vehicle charging facilities have been rapidly popularized, and the DC distribution system has become a core component of the new power system[1].

Low-Voltage Hybrid DC Circuit Breakers (LVDCCBs, the core protection equipment studied in this paper, for which all methods are developed for its gassing material R&D), as the key equipment for fault current interruption and system protection, its arc quenching performance directly determines the power supply reliability and equipment service life. Unlike AC (Alternating Current, the conventional power supply system corresponding to DC), DC has no natural zero-crossing point, and the fault arc is characterized by concentrated energy, difficult arc quenching, and long arcing time. The technical bottleneck of arc quenching has become a key constraint to the large-scale application of low-voltage DC systems[4].

Gas-blast arc quenching is the mainstream arc quenching technical solution for low-voltage DC circuit breakers. Its core principle is to use the rapid pyrolysis of gassing materials under the high temperature of the arc to generate a large amount of high-pressure gas. On the one hand, the air pressure difference in the chamber drives the arc to quickly enter the arc chute to realize arc cutting and cooling. On the other hand, the high thermal conductivity gases such as hydrogen generated by pyrolysis can enhance the convective heat dissipation of the arc, accelerate the dissipation of arc energy, and finally realize the reliable interruption of the fault current[5].

Polyamide (PA, commonly known as Nylon, the core matrix of gassing materials studied in this paper, whose amide bonds can form a dense hydrogen bond network) materials are rich in amide groups in the main chain, which can form a dense intermolecular hydrogen bond network, endowing the materials with excellent structural stability, heat resistance and film-forming properties, and are the mainstream matrix materials for gassing materials in DC circuit breakers[6].

Among them, Polyamide 66 (PA66, the most widely used gassing material for circuit breakers in current engineering, used as the performance benchmark in this paper) has become the most widely used gassing material in current engineering applications due to its balanced heat resistance,

This work was supported by the National Natural Science Foundation of China (52277163) and Shaanxi Provincial Department of Education key laboratory project (22JS025)..

flame retardancy and gas production characteristics[10]. However, in the practical application of low-voltage DC conditions, traditional PA66 still has three core bottlenecks:

1. Insufficient working condition adaptability: The transient temperature of low-voltage DC arc is relatively low, so the gas production rate and gas yield of PA66 are easily restricted by temperature; meanwhile, conductive by-products such as tar and coke generated during high-temperature pyrolysis will adhere to the surface of the arc extinguishing chamber, which significantly reduces the insulation recovery performance and increases the risk of secondary arcing[12].

2. Insufficient analysis of microscopic gas production mechanism: Most existing studies use macroscopic characterization methods such as Gas Chromatography-Mass Spectrometry (GC-MS, the mainstream experimental method for characterizing final pyrolysis products in existing studies) and Thermogravimetric-Infrared Spectrometry (TG-IR, a conventional test method for material thermal properties), which can only capture the final products of pyrolysis, and cannot track the dynamic process of chemical bond breaking, free radical reaction and product generation under arc high temperature in real time. It is difficult to fully reveal the internal correlation between material structure, pyrolysis behavior and arc quenching performance[15].

3. Lagging material R&D mode: The development of traditional new gassing materials relies on "trial-and-error" synthesis and experimental verification, which has a long R&D cycle and high cost. A forward design method based on materials informatics has not yet been formed, which restricts the R&D efficiency of high-performance adaptive materials[18].

The essence of the above problems is that the design of gassing materials lacks a full-link correlation model from molecular structure to macroscopic arc quenching performance, which leads to material screening relying on engineering experience, microscopic mechanism analysis relying on offline characterization, and it is difficult to realize the precise forward regulation of material properties.

In recent years, the rapid development of Materials Informatics (an interdisciplinary subject integrating materials science, machine learning and data science, for rapid prediction and forward design of functional materials) and machine learning technology has provided a new paradigm for the efficient R&D of functional polymer materials[19].

In the field of material thermophysical property prediction, Hong et al. constructed a hybrid model integrating Graph Neural Network (GNN, a machine learning model specially processing molecular graph structure data) and residual network, which can realize second-level high-precision prediction of material melting point only through molecular chemical composition[19]. In the field of thermal decomposition temperature prediction of energetic materials, Liu et al. developed the EM-thermo framework, which adopted Directed Message Passing Neural Network (D-MPNN, a graph neural network model for molecular property prediction, used to build the core prediction model of thermal decomposition temperature in this paper) combined with Transfer Learning (the strategy of large-sample pre-training and small-sample fine-tuning used in this paper, to solve the core pain point of poor model generalization on small sample datasets), and achieved high-precision classification and regression prediction of thermal decomposition temperature on a dataset of more than 5000 CHNO compounds. By introducing RDKit molecular descriptors and Minimum Bond Dissociation Energy (BDE_min, the core structural parameter determining the onset temperature of material thermal decomposition) as auxiliary features, the generalization ability of the model in small sample scenarios was significantly improved[20], which provides a methodological basis for thermal performance prediction of gassing materials.

At the same time, ReaxFF Reactive Force Field Molecular Dynamics (ReaxFF-MD, a simulation method that can simulate the chemical bond breaking and reaction process of materials at high temperature at atomic scale, used to reveal the microscopic pyrolysis mechanism of gassing materials in this paper) technology provides an effective means for atomic-scale analysis of the microscopic mechanism of material pyrolysis, and has been widely used in the fields of polymer high-temperature pyrolysis and energetic material decomposition[21].

Through ReaxFF-MD simulation, the chemical bond breaking path, small molecule product generation law and carbon residue formation mechanism of materials under arc high temperature can be tracked in real time, which provides a microscopic basis for the mechanism explanation of arc quenching behavior of gassing materials[23], and forms complementary support of "macro performance prediction - microscopic mechanism analysis" with the machine learning prediction model.

Based on the above analysis, this paper proposes an intelligent screening and optimization method for PAs-based energetic gas-generating materials that integrates materials informatics, machine learning, and ReaxFF molecular dynamics simulations. The core innovations of this study are reflected in three aspects: at the methodological level, a closed-loop research framework was established, spanning database construction, machine learning prediction, molecular dynamics simulation, and experimental validation; at the technical level, a dual-track machine learning strategy was adopted to efficiently predict pyrolysis and melting temperatures, while ReaxFF simulations were used to elucidate the pyrolysis mechanism; at the application level, intelligent material design methods were applied for the first time to the screening and optimization of PA-based energy-releasing gas-generating materials.

II. Methodology

This section details the full intelligent screening and optimization methodology for PA-based gassing materials established in this paper. The complete closed-loop technical route of the whole research framework is shown in Fig. 1, which consists of five core stages: standardized filler database construction, dual-track machine learning performance prediction, process-adaptive advanced filtering, pyrolysis mechanism analysis via ReaxFF molecular dynamics simulation, and final experimental performance verification. The details of each stage are elaborated in the following subsections.

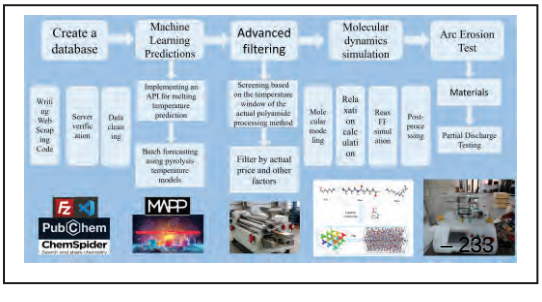


Fig. 1. Full closed-loop technical route of the intelligent screening and optimization methodology for PA-based gassing materials established in this paper

A. Construction of Standardized Filler Database

The database is the cornerstone of data-driven material design. To address the specific performance requirements of PA-based energetic gassing materials, a dedicated standardized filler database was established, following a systematic technical workflow consisting of multi-source data collection, screening and cleaning, feature extraction, and standardized storage.

First, a targeted crawler script was developed in Python to acquire basic data of compounds exclusively composed of four elements (C, H, O, N) from authoritative public databases including PubChem, NIST, and ChemSpider. The core characteristics, advantages and applicable scenarios of the three data sources used for database construction are compared in Table 1, which fully demonstrates the multi-source complementarity of the database constructed in this paper. The integrity of the collected data was remotely validated through the FTP protocol, resulting in a multi-source raw dataset. Subsequently, three rounds of rigorous core screening were implemented using in-house custom code: (1) deduplication to eliminate redundant records; (2) type screening to retain only neutral compounds; and (3) secondary element verification to ensure all remaining compounds strictly meet the element composition requirements of energetic gassing materials (i.e., containing only C, H, O, and N).

TABLE I. COMPARISON OF THREE DATABASE TYPES

Characteristics	Database Website		
	ChemSpider	***NIST***	***PubChem***
Data volume	Over 128 million compounds, covering 278 data sources	Approximately 100,000 compounds, focusing on thermodynamic and spectral data	Over 150 million compounds, with a focus on bioactivity and safety
Advantages	Structure Retrieval, Multi-Source Integration, API Extensibility	High-precision experimental data, standard reference values	Bioactive Data, Free Download
Applicable Scenarios	Daily compound lookup, synthetic route design, software integration	Theoretical calculation verification, thermodynamic simulation	Drug development, high-throughput screening

In the environment configuration and information extraction phase, a virtual environment was configured via Conda, and SDF files were parsed offline using the RDKit open-source chemoinformatics toolkit[25]. Key parameters including CID and molecular formula were extracted and imported into a MySQL database, forming a structured, extensible dedicated filler dataset that provides a solid data foundation for subsequent machine learning prediction tasks.

B. Machine Learning Prediction and Screening

Separate prediction models were developed and deployed for melting temperature (T_m) and pyrolysis temperature (T_n) to ensure prediction accuracy tailored to each property. For feature engineering, molecular graphs and 208 topological descriptors were generated using the RDKit open-source chemoinformatics toolkit, and the minimum bond dissociation energy (BDE_{min})—a critical indicator of thermal stability—was calculated as an auxiliary feature to enhance model interpretability and prediction performance.

For T_m prediction, the state-of-the-art graph neural network (GNN) model proposed by Hong et al. was utilized, which was pre-trained and fine-tuned on experimental data of approximately 9,400 inorganic compounds, achieving a test set root-mean-square error (RMSE) of 160 K. For T_n prediction, a directed message passing neural network (D-MPNN)-based transfer learning framework was constructed to address the scarcity of labeled T_n data: first, large-scale unsupervised/semi-supervised pre-training was conducted on a curated CHNO dataset, followed by supervised fine-tuning with about 10,000 high-quality T_n-labeled data points. To predict the pyrolysis temperature T_n, we developed a transfer learning framework based on a directed message-passing neural network (D-MPNN) that is optimized for large datasets, in order to address the challenge of insufficient labeled T_n data. The complete framework and workflow of the D-MPNN model are shown in Figure 2.

The screening process was implemented in two sequential stages: (1) Preliminary Screening: Strict property constraints were applied to ensure compatibility with PA processing and thermal stability requirements. T_m must fit the processing window of common PA grades (PA6: 235–260 °C, PA66: 270–295 °C, PA46: 300–320 °C). $T_m < T_n$ to avoid premature melting during pyrolysis. $T_n \geqslant 500$ K to ensure sufficient thermal stability under arc impact, (2) Fine Screening: Combined with local interpretable model-agnostic explanations (LIME) for interpretability-driven selection, molecules containing positive functional groups (e.g., nitro groups, azide groups) that promote gas generation were prioritized. Engineering feasibility factors, including raw material cost and synthetic accessibility, were also comprehensively evaluated, ultimately narrowing down to 5–8 candidate target compounds.

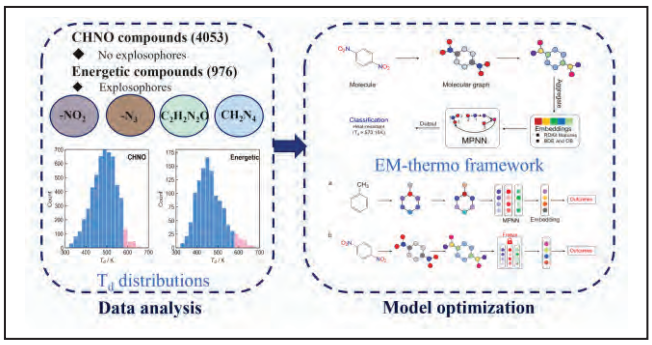


Fig. 2. The D-MPNN Framework

C. ReaxFF Molecular Dynamics Simulation for Pyrolysis Mechanism Analysis

ReaxFF molecular dynamics (ReaxFF-MD) simulations were performed on the candidate materials using the ReaxFF force field parameter set optimized for CHON systems, to

track the sequence of chemical bond scission, free radical evolution, and the formation of small gas molecules including H_2, CO, and CO_2 [26]. Visualization and analysis were conducted via VMD and OVITO to correlate the microscopic product characteristics with the arc quenching performance (i.e., gas yield and gas production rate). The simulation results establish a bidirectional validation mechanism with the machine learning (ML) predictions: the priority of a candidate material will be downgraded if its simulated H_2 yield is insufficient or carbonaceous residue is excessive; meanwhile, the microscopic mechanism revealed by the simulations can guide the optimization of feature engineering.

D. Closed-Loop Experimental Verification Framework (Follow-Up Research Plan)

This section describes the complete closed-loop experimental verification framework designed for the intelligent screening methodology established in this paper, which is the downstream validation link of the full research paradigm. The relevant experimental work (including PD measurements and arc interruption tests) has not been carried out in the current research stage. The detailed framework is designed as follows:

1. Sample preparation: Polyamide (PAs) composite film samples blended with the high-priority candidate compounds screened by the method in this paper will be prepared.

2. Performance characterization: Arc ablation tests and partial discharge (PD) measurements in compliance with IEC 60270 will be carried out on a simulated arc quenching chamber test platform. The core goal of PD measurements is to characterize the insulation degradation and recovery performance of the materials after arc ablation, which is the key intermediate indicator to evaluate the final DC arc interruption performance of the materials.

3. Closed-loop iterative optimization: The experimentally measured data (including actual melting temperature T_m, thermal decomposition temperature T_n, hydrogen yield, gas production rate and PDIV) will be compared with the machine learning predicted values and ReaxFF-MD simulation results to identify the sources of deviation. The deviation data will be fed back to the database and prediction model for iterative optimization, to establish a complete quantitative correlation spanning from molecular structure to pyrolysis product characteristics and ultimately to macroscopic arc quenching performance.

III. Preliminary Results

A. Statistics of Standardized Filler Database

Multi-source data acquisition from PubChem, NIST, and ChemSpider was completed via Python web crawler technology. After triple screening and feature extraction, the data were finally imported into MySQL to form a structured dataset. The current database covers core fields including molecular formula, exact molecular weight, melting point, elemental composition, and topological descriptors, with a cumulative data volume of approximately 40 million entries. The final structured dataset covers core fields including molecular formula, exact molecular weight, topological descriptors and other basic properties of compounds, and typical examples of the standardized dataset are shown in Table 2.

TABLE II. Dataset examples include compounds and their basic properties

Molecular Formula	**Properties of Compounds**			
	Molecular Weight (g/mol)	***Topological Polar Surface Area ($Å^2$)***	***Molecular Volume ($Å^3$)***	***Fraction CSP3***
$C_9H_{17}NO_4$	203.1158	66.43	48.08	0.778
$C_7H_8O_4$	156.0423	77.76	36.87	0.286
C_3H_9NO	75.0684	46.25	20.74	1

B. Machine Learning Prediction Performance

We have used the established graph neural network (GNN) model to perform batch melting point predictions for compounds in a standardized database; typical examples of the prediction results are shown in Table 3. Figure 3 illustrates the pre-training results of the pyrolysis temperature prediction model. The model underwent training and validation. Model performance was evaluated using 5-fold cross-validation. For T_n prediction, the model achieved an accuracy (ACC) of over 0.995 and an average F1 score of 0.990 during the pre-training phase, demonstrating a significant improvement over the original Expectation-Maximization (EM) model, which lays a solid foundation for subsequent transfer learning tasks.

TABLE III. Example of a dataset after predicting melting temperatures

Molecular Formula	**Properties of Compounds**		
	Melting temperature (K)	***Standard error of melting temperature (K)***	***Melting temperature (°C)***
$C_9H_{17}NO_4$	337.93057	11.50105	64.78057
$C_7H_8O_4$	229.43161	46.75300	-43.71838
C_3H_9NO	375.70657	10.86507	102.55657

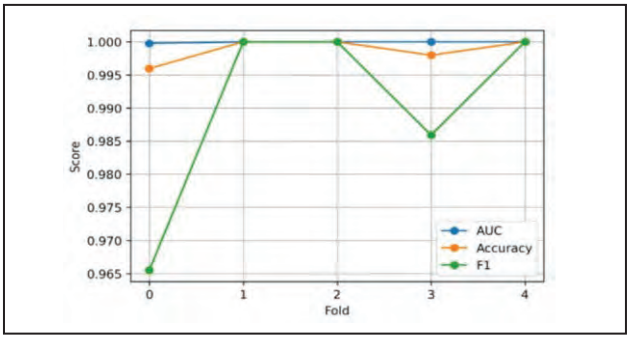


Fig. 3. Pyrolysis Temperature Prediction Model Parameters

IV. Discussion

A. Theoretical Value and Methodological Innovation

Before elaborating the innovation of this study, we first clarify the core mechanism that the interruption performance of low-voltage DC circuit breakers based on gas-blast arc quenching is determined by two core dimensions of PAs gassing materials, which run through the whole process of arc extinction and post-interruption insulation recovery, and this mechanism has been fully verified in our team's published research [14]:

1. Pyrolysis gas production characteristics: The type and content of high thermal conductivity arc-quenching gases (H_2, CO, etc.), total gas yield and gas production rate directly determine the arc cooling rate and arc extinction efficiency;

2. Pyrolysis carbon residue characteristics: The yield of tar and coke, structural stability of carbon rings and distribution of conductive residues directly determine the PDIV and anti-re-ignition ability of the system after interruption, which is the core guarantee for the success of breaking operation.

Meanwhile, the intrinsic correlation between PD characteristics and DC arc interruption performance is fully verified: PDIV obtained from PD test is the most direct quantitative indicator to characterize the insulation degradation degree of materials after arc ablation, and is the core intermediate parameter to evaluate the final interruption performance of materials.

Based on the above core mechanism, this study makes three fundamental contributions at the theoretical and methodological levels:

1) A design paradigm that bridges the full chain from molecular structure to pyrolysis behavior and further to gas production performance is proposed. Conventional research and development (R&D) of gas-generating materials follows a linear workflow of synthesis, testing, and analysis, where material screening relies on empirical trial-and-error, and the elucidation of microscopic mechanisms depends on ex-situ characterization. In this study, a quantitative correlation between molecular structure and thermal properties is established via machine learning, and a micro-macro correlation between pyrolysis behavior and gas production performance is constructed through ReaxFF molecular dynamics (ReaxFF-MD) simulations, achieving for the first time end-to-end prediction and optimization from molecular structure to macroscopic performance.

2) A dual-track prediction strategy integrating established baseline models and optimized models is constructed, with ReaxFF simulations introduced to validate the underlying microscopic mechanisms. For melting temperature prediction, a mature graph neural network (GNN)-based melting point prediction model was adopted; for thermal decomposition temperature prediction, an optimized prediction model was developed based on the Directed Message Passing Neural Network (D-MPNN) framework. ReaxFF simulations were performed to reveal the pyrolysis pathways and product distribution of the target compounds at the atomic scale, and to correlate the microscopic reaction mechanism with the macroscopic arc quenching performance (e.g., H_2 yield, gas composition), which significantly improves the interpretability of the proposed method.

3) A closed-loop R&D framework with collaborative validation between data-driven machine learning and physics-based simulation is established. Machine learning enables high-efficiency screening, while ReaxFF simulations provide validation of the microscopic mechanisms, forming a bidirectional feedback mechanism between the two: simulation results can be used to verify the rationality of the screening outcomes, and the microscopic mechanisms revealed by the simulations can guide the optimization of the machine learning model. This framework breaks through the inherent limitations of single-method approaches, and combines both high screening efficiency and excellent mechanistic interpretability.

B. Limitations and Future Directions

The current study has three main limitations, with corresponding targeted future research directions proposed as follows:

1) The current database is mainly constructed based on publicly available data, and the limited number of experimentally measured T_n values may impair the generalization ability of the model. In the future, the experimentally measured dataset will be systematically supplemented to enhance the model's generalization performance.

2) The three-dimensional (3D) molecular conformation has not been taken into account in the adopted Directed Message Passing Neural Network (D-MPNN) model. A three-dimensional graph neural network (3D-GNN) will be introduced in subsequent work to further optimize the prediction performance of the model.

3) There are inherent discrepancies between the ReaxFF molecular dynamics (ReaxFF-MD) simulation conditions and the actual arc operating conditions. More systematic arc ablation tests will be carried out to narrow the gap between simulation and real working conditions, and further optimize the overall model system.

V. Conclusion

This paper focuses on the engineering demand of high-performance PA-based gassing materials for low-voltage DC circuit breakers, and proposes a complete intelligent screening and optimization design methodology integrating materials informatics, machine learning and ReaxFF molecular dynamics simulation. The core research results and contributions are summarized as follows:

1. A standardized filler database of C/H/O/N system compounds with approximately 44 million entries was constructed through multi-source data collection, rigorous screening and standardized processing. The database covers the core molecular structure and basic property parameters of candidate compounds for gassing materials, which solves the problems of scattered data and non-standard format in traditional R&D, and provides a solid data foundation for the data-driven design of gassing materials.

2. A dual-track machine learning prediction strategy for the key thermal properties of gassing materials was established. For melting temperature T_m, a mature GNN-based prediction model was adopted to realize batch prediction of material processing performance; for thermal

decomposition temperature T_n, a high-precision transfer learning prediction framework based on D-MPNN was constructed, which solves the industry pain point of low prediction accuracy under small sample conditions of energetic modified PA materials. At the current stage, the pre-training of the T_n prediction model has been completed, with an accuracy (ACC) over 0.995 and an average F1-score of 0.990, which lays a core foundation for the subsequent performance prediction and screening of candidate materials.

3. A complete ReaxFF-MD simulation scheme for the pyrolysis process of PA-based gassing materials was established, which can track the chemical bond breaking, free radical evolution and product generation law of materials under high temperature in real time. This scheme forms a complementary support of "macro performance prediction - microscopic mechanism analysis" with the machine learning model, and provides a theoretical basis for the subsequent analysis of the pyrolysis mechanism and arc quenching performance of candidate materials.

4. A full closed-loop R&D paradigm for gassing materials spanning "database construction - dual-track machine learning prediction - process-adaptive screening - microscopic mechanism simulation - experimental performance verification" was constructed. This framework breaks through the efficiency bottleneck of the traditional trial-and-error R&D mode, and provides a new systematic paradigm for the rational design of high-performance PA-based gassing materials for low-voltage DC circuit breakers.

The methodology proposed in this study is not only suitable for the screening and optimization of PA-based energetic gassing materials, but also can be extended to the design and development of other functional polymer materials. In the follow-up research, we will complete the transfer fine-tuning of the pre-trained T_n prediction model, carry out high-throughput screening of candidate materials, conduct pyrolysis mechanism analysis via ReaxFF-MD simulation, and complete the experimental verification of the material performance in turn, to form a complete R&D closed loop..

REFERENCES

[1] S. Chen, Z.-N. Wei, W. Gu, “Transformation and reform of energy system under carbon neutrality target: multi-energy flow collaboration technology,” Electric Power Automation Equipment, vol. 41, no. 9, pp. 3–12, Sep. 2021.

[2] H. Li, D. Liu, D.-Y. Yao, “Research and judgment on development of China's power system towards carbon peaking and carbon neutrality goals,” Proceedings of the CSEE, vol. 41, no. 18, pp. 6245–6259, Sep. 2021.

[3] Z. Ma, Y.-Y. Sun, Z.-G. Zhao, “Key technologies of low-voltage DC power supply and utilization,” Distribution & Utilization, vol. 39, no. 8, pp. 2–5, Aug. 2022.

[4] D.-G. Chen, “Function and selection of gas-generating materials in low-voltage arc quenching systems,” Low Voltage Apparatus, no. 8, pp. 1–5, Apr. 2012.

[5] X.-W. Li, D.-G. Chen, Q. Wang, “Simulation and experimental research on electric arc in low-voltage circuit breakers,” Low Voltage Apparatus, no. 24, pp. 1–7, Dec. 2010.

[6] J. Liang, Y. Xu, Z. Wei, “Mechanical properties, crystallization and melting behaviors of carbon fiber-reinforced PA6 composites,” Journal of Thermal Analysis and Calorimetry, vol. 115, no. 1, pp. 209–218, Jan. 2014.

[7] F. Jiang, Y.-Q. Shi, S. Chen, “Research status of glass fiber modified nylon composites,” Plastics, vol. 52, no. 3, pp. 100–104, May 2023.

[8] S.-J. Huang, S.-M. Jiang, X.-L. Liang, “Effect of glass fiber content on properties of glass fiber reinforced nylon 66 composites,” Industrial Technology Innovation, vol. 7, no. 6, pp. 6–9, Dec. 2020.

[9] C.-Y. Li, H.-L. Yuan, “Study on PA66 modified by GF/MAH-g-SEBS,” Engineering Plastics Application, vol. 40, no. 5, pp. 24–27, May 2012.

[10] P. André, “The influence of graphite on the composition and thermodynamic properties of plasma formed in ablated vapour of PMMA, PA6-6, PETP, POM and PE used in circuit-breakers,” Journal of Physics D: Applied Physics, vol. 30, no. 3, p. 475, Feb. 1997.

[11] J. J. Shea, “Gassing arc chamber wall material effect on post current-zero recovery voltage breakdown,” in Proceedings of the 48th IEEE Holm Conference on Electrical Contacts, 2002, pp. 70–79.

[12] W. Cao, C. Luo, Q. Wang, “Evaluation and analysis of gassing material performance used in low-voltage circuit breakers,” IEEE Transactions on Power Delivery, vol. 40, no. 2, pp. 728–738, Apr. 2025.

[13] X. Zhou, X.-P. Su, J. Li, “Experimental study on influence of different gas-generating materials on arc motion characteristics,” Low Voltage Apparatus, no. 15, pp. 1–4, Aug. 2009.

[14] Q. Wang, Y. Liu, W. Zhao, “Arc-induced ablation behavior of gassing materials based on molecular dynamics,” Journal of Applied Polymer Science, vol. 142, no. 3, p. e56234, Mar. 2025.

[15] L. S. Tran, R. De Bruycker, H. H. Carstensen, “Pyrolysis and combustion chemistry of tetrahydropyran: experimental and modeling study,” Combustion and Flame, vol. 162, no. 11, pp. 4283–4303, Nov. 2015.

[16] Y. Duan, Y. Ning, N. Gao, “Effect of hydrothermal process on the pyrolysis of oily sludge: characterization and analysis of pyrolysis products,” Fuel, vol. 338, p. 127347, May 2023.

[17] Coralli I, Fabbri D, Facchin A, et al. Analytical pyrolysis of polyethyleneimines[J]. Journal of Analytical and Applied Pyrolysis, 2023, 169: 105838.

[18] Q. Wang, W.-M. Zhao, W.-D. Cao, “Pyrolysis and kinetic analysis of gas-generating materials based on ReaxFF,” Transactions of China Electrotechnical Society, vol. 40, no. 10, pp. 3082–3096, May 2025.

[19] Q. J. Hong, S. V. Ushakov, A. van de Walle, “Melting temperature prediction using a graph neural network model: from ancient minerals to new materials,” Proceedings of the National Academy of Sciences of the United States of America, vol. 119, no. 36, p. e2209630119, Sep. 2022.

[20] H. Liu, P. Chen, C. Zhang, “Interpretable and physicochemical-intuitive deep learning approach for the design of thermal resistance of energetic compounds,” The Journal of Physical Chemistry A, vol. 128, no. 42, pp. 9045–9054, Oct. 2024.

[21] Y. Wang, H. Liu, C. Zhang, “Investigating the decomposition mechanism of DNAN/DNB cocrystal explosive under high temperature using ReaxFF/lg molecular dynamics simulations,” Journal of Molecular Modeling, vol. 31, no. 2, p. 51, Feb. 2025.

[22] H. Ren, G. Luo, X. Xiao, “Investigation of the thermal decomposition reactions of HMX using online photoionization mass spectrometry,” Proceedings of the Combustion Institute, in press, 2025.

[23] H. Zheng, Y. Wang, T. Yang, “Investigation on cold flow properties of natural ester insulating oils based on molecular dynamics,” IEEE Transactions on Dielectrics and Electrical Insulation, vol. 31, no. 3, pp. 1323–1330, Jun. 2024.

[24] Y. Wang, H. Xu, B. I. Ayubi, “Insulation failure mechanism of polyimide under high-frequency electrical stress: a synergistic analysis of aging experiments and molecular dynamics simulations,” IEEE Transactions on Dielectrics and Electrical Insulation, vol. 32, no. 1, pp. 246–253, Feb. 2025.

[25] G. Landrum, “RDKit: open-source cheminformatics software,” RDKit Official Website, 2024. [Online]. Available: https://www.rdkit.org

[26] B.-F. Chen, Z.-L. He, Y.-N. Dai, “Study on ablation characteristics of arc contacts during switching operation of SF6 circuit breakers,” High Voltage Apparatus, vol. 60, no. 12, pp. 57–65, Dec. 2024.

[27] C. Ashraf, A. C. T. van Duin, “Extension of the ReaxFF combustion force field toward syngas combustion and initial oxidation kinetics,” The Journal of Physical Chemistry A, vol. 121, no. 5, pp. 1051–1068, Feb. 2017.

Investigation of dynamic microarcs in air complementing a unified nonequilibrium model

Jonas Karl Christian Ballentin
Institute of Electrical Power Engineering
University of Rostock
Rostock, Germany
jonas.ballentin@uni-rostock.de

Margarita Baeva
Leibniz Institute for Plasma Science and Technology
Greifswald, Germany
baeva@inp-greifswald.de

Dirk Uhrlandt
Leibniz Institute for Plasma Science and Technology
Institute of Electrical Power Engineering
Greifswald, Rostock, Germany
uhrlandt@inp-greifswald.de

***Abstract*—Low-voltage and low-current DC arcs with small arc length occur among others in mechanical switching devices and in micro-welding applications. Understanding their properties and behaviour is important for the device operation. In this work, a microarc in air between copper electrodes is investigated by means of electrical measurements, high-speed imaging and spectroscopic diagnostics. The focus is on the dynamic behaviour of the microarcs, which manifests itself in fluctuations in intensity and the dynamics of the electrode attachment and the plasma column. It is quantified trough the arc voltage and densities of excited copper atoms. High-speed imaging reveals pronounced fluctuations in arc luminosity, with episodes of enhanced radiative output coinciding with voltage drops of several volts. Side-on spectroscopic measurements further demonstrate that the observed emission dynamics is governed by temporal variations in the copper population within the plasma. The population of excited states exhibit fluctuations exceeding an order of magnitude, both in the immediate vicinity of the anode and throughout the plasma column. The excited state densities are compared to the predictions of a collisional-radiative model.**

***Index Terms*—microarc, electrode spots, plasma spectroscopy**

I. Introduction

Switching and interrupting low-voltage direct current (LVDC) is becoming increasingly important due to the growing adoption of DC technologies such as batteries and photovoltaic systems. When mechanical switches in the LVDC range rely on contact separation, microarcs form that lead to contact erosion. In switching applications, copper is often used as contact material because of its good electrical properties and low cost, however, it has a low melting point. The microarcs are generally undesirable because they generate heat, impair switching performance, and pose safety risks. However, microarcs are deliberately employed in industrial micro-welding applications to achieve precise and controlled material bonding [1].

Inhomogeneous surface morphology causes locally enhanced current density and Joule heating during the contact opening that results is melting and evaporation of electrode material. The metal vapour significantly changes the plasma properties, as the ionization potential of the metal atom is well below than that of the surrounding gas. The microarc is generally classified as falling within the transition region between thermal arcs and glow discharges. It is typically characterized by dimensions ranging from the sub-mm scale to a few mm, and currents spanning several hundred mA to a few A. While the electron emission mechanisms are the same as in thermal arcs, the small scale makes deviations from local thermodynamic equilibrium (LTE) particularly significant. Consequently, a detailed investigation of microarcs is required. A general overview and classification of microarcs can be found in [2]. To gain a deeper understanding, experimental investigations on microarcs should be carried out across various dimensions, electrode materials, and surrounding gases [3]–[5]. Corresponding modelling studies have been carried out during the last decade [6], [7].

This work aims at a further characterization of a microarc between copper electrodes in atmospheric pressure air by employing electrical measurements, high-speed imaging, and spatially resolved spectroscopic diagnostics. In earlier studies [8], it was found that the microarcs exhibit pronounced dynamical behaviour, making an accurate characterization of their plasma properties far from trivial. This applies even to the arc geometry itself, as the arcs electrode attachment spots undergo rapid variations in shape and intensity. The present work focuses therefore on analysing the underlying arc dynamics in order to establish a more robust basis for interpreting diagnostic measurements and for developing reliable, physics-based models of microarc behaviour. The results support the development of a unified non-equilibrium plasma model that resolves the entire discharge and is designed to predict key plasma parameters such as electric potential, temperatures, and spatially resolved number densities of heavy particles and electrons [7].

II. Experimental Setup

The microarc is ignited by the separation of two copper electrodes, each $4\,\mathrm{mm}$ in diameter, in atmospheric pressure air. The setup consist of a fixed electrode with a flat surface and a moveable electrode with a slightly curved surface, driven by a stepper motor with a velocity of roughly $60\,\mathrm{mm/s}$. A direct current of $2\,\mathrm{A}$ is used. A signal generator produces a constant voltage pulse that is amplified to the target current by

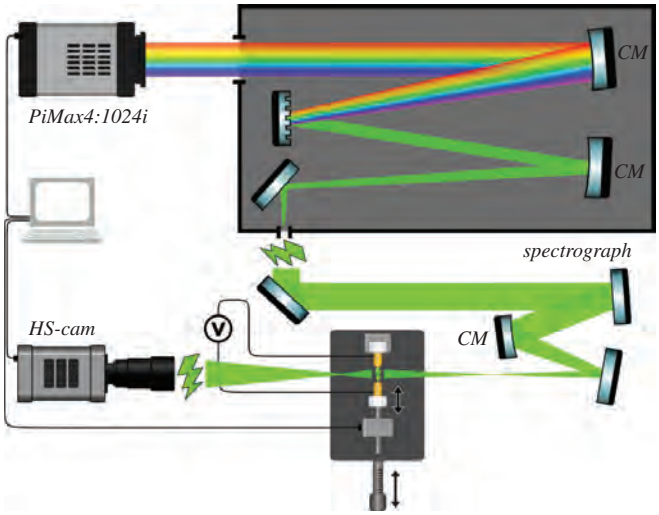


Fig. 1: Schematic of the experimental setup. The copper electrodes with their opening mechanism, are installed on a linear translation stage. A curved mirror (*CM*) projects the arc onto the narrow entrance slit of the spectrograph.

a power amplifier (FM1295, FM Elektronik Berlin) operating in current mode. Approximately 11 ms after the current begins to flow, the electrodes begin to separate, and a discharge gap of 3 mm is reached after an additional 50 ms of operation.
The arc is optically imaged onto the entrance slit of a spectrograph. The slit ensures that only a thin axial slice of the arc is analysed. A linear translation stage, on which the electrode assembly is mounted, allows precise adjustment of the axial position at which the spectrum is recorded. An Acton SpectraPro-500i spectrograph equipped with an optical grating with 1200 lines/mm disperses the emitted light, and an intensified CCD camera (PI-Max4:1024i) captures single-frame images with gate widths of approximately 0.1 ms.
The side-on arrangement provides two-dimensional data with a spatial sampling interval of 6 μm along the radial direction and a spectral sampling interval of 0.02 nm. Since the measurements yield line-of-sight integrated intensities over the arc cross section rather than spatially resolved emission, a geometrical reconstruction is performed. For this purpose, the selected emission lines are fitted with Voigt profiles for every side-on position y and subsequently integrated to obtain the emission intensity $I(y)$. The resulting intensity profiles are well approximated by Gaussian functions on the y coordinate. These profiles are subjected to an Abel inversion to retrieve the radial dependence of the emission coefficient $\varepsilon(r)$. The emission coefficient of a transition $k \to i$ is directly related to the population density n_k of the upper level trough the relation

$$n_k = \varepsilon_{ki} \frac{4\pi\lambda_{ki}}{hc} \frac{1}{A_{ki}} \tag{1}$$

The width of the entrance slit of the spectrograph is optimized to minimize the instrumental broadening of emission lines. This is done prior to the data acquisition using a low-pressure Hg(Ar) discharge lamp, whose intrinsic line widths are negligible compared to the instrumental broadening.
In addition to the side-on spectroscopy, electrical measurement and high-speed imaging with a Photron Fast-Cam NOVA R3 are performed to further characterize the arc at the moment when the spectra are recorded. The chip of the camera detects light in the full visible wavelength range. The voltage probes are directly connected to the electrodes. A full scheme of the experimental setup is depicted in Fig. 1.

III. Collisional-Radiative Model

A previously developed unified non-equilibrium plasma model [7], [9] is employed to obtain the properties of an air–copper mixture under microarc conditions. The deformed mesh method is used to simulate the contact opening. The model is based on a one-dimensional fluid formulation that solves the continuity equations for particles, the energy continuity equations for electrons and heavy particles, the Poisson equation for the electric potential, and the heat transport in the electrodes, with the discharge current prescribed by an external circuit. For electrons in the plasma, the classical drift-diffusion approximation is applied. The fluid model is extended to a collisional–radiative model to determine level-resolved excited-state populations. Species equations are solved for selected individual levels or level groups, using plasma parameters obtained from the fluid solution. The considered states and their excitation energies and statistical weights read as follows: $4s^2\ ^2D_{5/2}$ (1.39 eV, 6), $4s^2\ ^2D_{3/2}$ (1.64 eV, 4), $4^2P_{1/2}$ (3.79 eV, 2), $4^2P_{3/2}$ (3.82 eV, 4), Cu($^4P^o$,$^4D^o$,$^4F^o$) (5.20 eV, 60, in the following called "group A"), $5^2S_{1/2}$ (5.35 eV, 2), Cu($5^2P_{1/2}$, $5^2P_{3/2}$, $4^2D_{3/2}$, $4^2D_{5/2}$) (6.17 eV, 16, in the following called "group B").
The extended model includes electron-impact excitation and ionization as well as spontaneous emission, using published cross-sections and transition probabilities from [10], [11].

IV. Results and Discussion

A typical arc voltage record during the electrode separation is shown in Fig. 2. Before $t = 0$, when current flows but the electrode separation has not yet started, a voltage of approximately 15 V is already measured. This occurs because the electrodes are not pressed against each other by springs. Poor electrical contact caused by tiny protrusions and possibly copper oxide on the electrode surface can lead to local material evaporation by Joule heating, resulting in plasma formation. This voltage corresponds to the voltage drop across the electrode sheaths, with the cathode sheath being the main contribution [7]. At $t = 0$ ms, the electrode separation starts and the arc voltage increases roughly linearly with the gap length; this voltage rise is associated with the plasma column. In Fig. 2, the voltage from the modelling during the contact opening is shown for two different copper concentrations of 0.2 % and 0.5 %. A higher copper content leads to a lower mean electric field across the arc. Note, that the contact opening in the model starts with a non-zero gap

[7], so that the closed switching state of the experiment can be omitted.

The power supply operating in current mode introduces high-frequency ripple into the arc, causing significant arc voltage fluctuations. Besides these, distinct sudden voltage drops of approximately $5,\mathrm{V}$ occur, indicating changes of the arc plasma properties. An example of such an event was observed between $t = 33.9\,\mathrm{ms}$ and $34.0\,\mathrm{ms}$. Fig. 3 shows a detailed view of this example and other similar voltage drops. In addition to the voltage, the near-electrode arc radiation intensity obtained from high-speed images (without spectral filters) in a region extending up to $0.25\,\mathrm{mm}$ in front of each electrode is shown. The voltage drops are accompanied by increased radiation on both electrode sides, which mainly originates from copper, as confirmed by spectroscopic measurements. Previous studies with spectral filters have shown that these voltage drops result from a sudden increased release of copper vapour into the plasma, leading to enhanced CuI emission, while a decrease in OI emission intensity at $777\,\mathrm{nm}$ is observed [8]. However, this effect is stronger pronounced in the anode region, where the radiation is in general stronger fluctuating. Fig. 4 shows the corresponding high-speed photographs, just before and after the voltage drop. The high-speed imaging reveals strong fluctuations in both the brightness and the position of the electrode spots. While the anode spot appears relatively stable in position for the microarcs with a length of a few millimetre, the cathode spot not only moves rapidly but also occasionally splits, allowing two cathode spots to coexist for several tens of microseconds. Bright regions up to one millimetre in front of the anode can occur, indicating a metal vapour emission. Fig. 5 shows a record capturing the coexistence of two attachment spots of the plasma on the cathode. The spots originate from a single spot that splits and after that both move apart. After

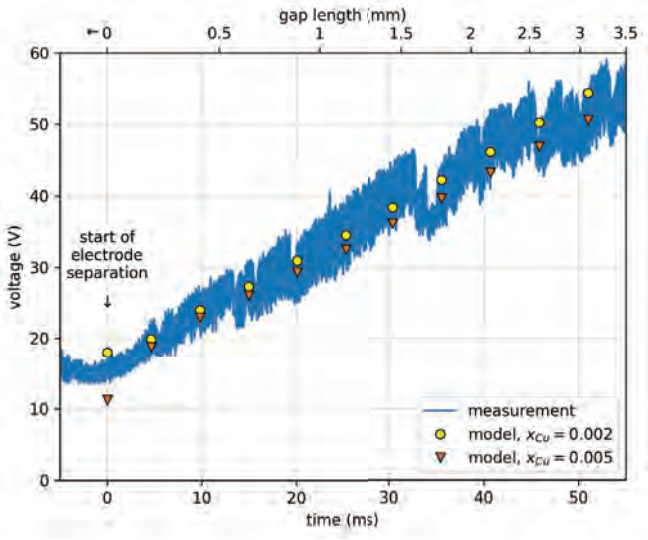


Fig. 2: Arc voltage during the opening process. At $t = 50\,\mathrm{ms}$, the discharge gap length amounts to $3\,\mathrm{mm}$.

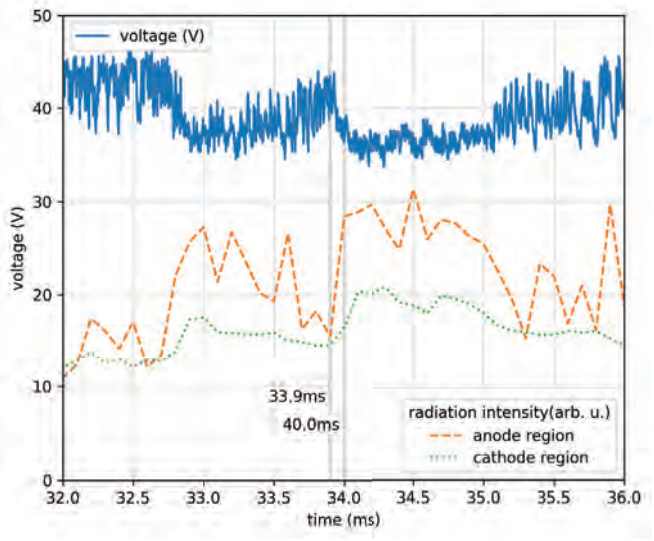


Fig. 3: Extract of the arc voltage from Fig. 2 for a gap length of about $0.25\,\mathrm{mm}$ along with the radiation intensity taken in the vicinity of the electrodes.

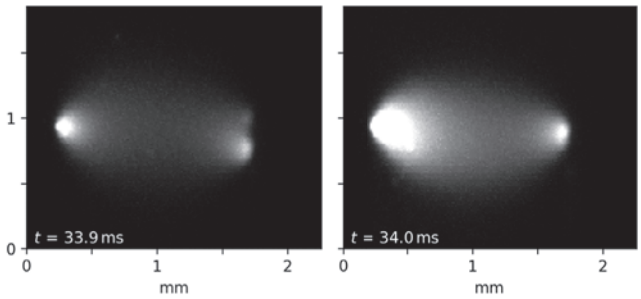


Fig. 4: Images of the arc to the instants of $33.9\,\mathrm{ms}$ and $34.0\,\mathrm{ms}$ indicated in Fig. 3. The (fixed) anode is on the left-hand side, and the (moving) cathode on the right. Acquisition time is $5\,\mu\mathrm{s}$.

approximately $30\,\mu\mathrm{s}$, the emission from one spot lowers and the spot vanishes. The observations showed that the increase of the gap length relates to the longer co-existence of multiple spots and longer distance between them. Side-on spectroscopy must be performed with care in the cathode region, as cylindrical symmetry cannot be assumed in the presence of multiple spots.

In the following, the dynamic behaviour of the microarc is investigated spectroscopically in order to quantify it and directly relate the observations to the population of excited states considering selected transitions.

The arc spectra clearly indicate that the discharge is metal-vapor dominated, as CuI lines constitute the major contribution to the emission, note that Cu II lines remain barely visible. Furthermore, the metal content in the plasma exhibits pronounced temporal fluctuations. Fig. 6 presents

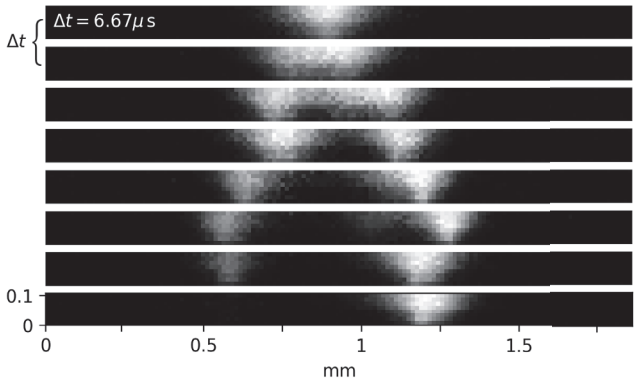


Fig. 5: High speed images of multiple cathode spots, captured in the vicinity of the cathode surface. The frame interval is $6.67\,\mu$s while the acquisition time is $3.8\,\mu$s. The arc length amounts to 4 mm during the recording.

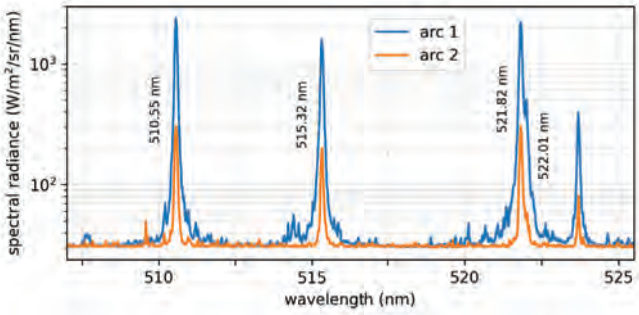
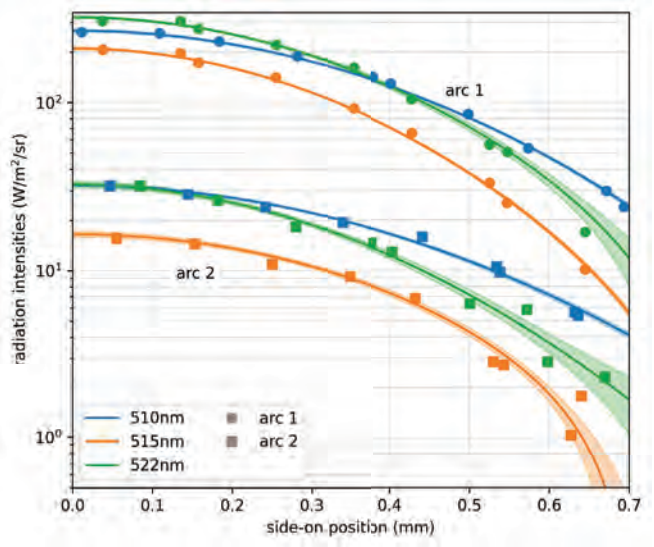


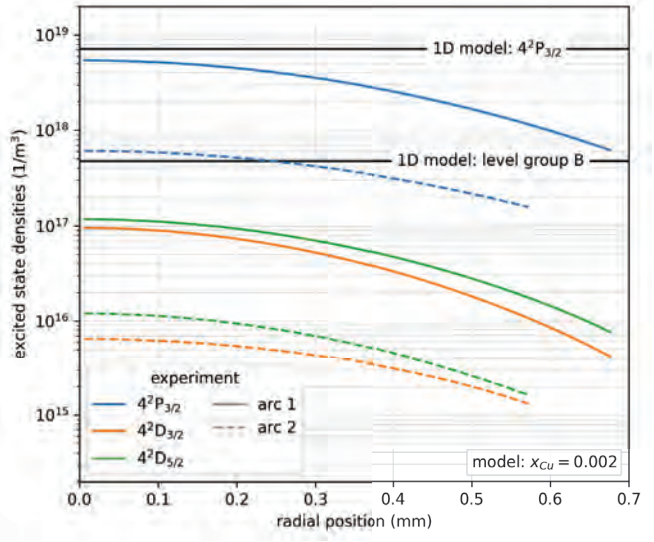
Fig. 6: Side-on spectra of two arcs taken under identical conditions in the centre of the arc ($y = 0$). The spectra are recorded 0.35 mm in front of the anode of a 3 mm arc. The four indicated lines originate from CuI.

the spectra of two arcs for selected copper emission lines, recorded at an axial observation position 0.35 mm in front of the anode. The selected spectral lines have wavelengths of 510.5 nm, 515.3 nm, and 521.8 nm. The integrated line intensity of the latter one has to be obtained subtracting correctly the adjacent 522.0 nm line. Both spectra were recorded under identical operating conditions: a discharge current of 2 A and an arc length of 3 mm. The displayed spectra correspond to the arc center (at side-on position $y = 0$). The results show significant differences in intensity, indicating strong fluctuations of the CuI content in the plasma. This relates to the intensity fluctuations from high speed imaging. At the time of observation, the brighter arc (arc 1) is characterized by a voltage of approximately 50 V, whereas arc 2 operated at about 52 V.

The integrated line intensities across the side-on coordinate for both of these arcs are shown in Fig. 7a. The radial profiles are well described by Gaussian fits. Figure 7b presents the populations of the corresponding excited states according to



(a)



(b)

Fig. 7: Radial profiles from three CuI emission lines for two measurements under identical conditions, 0.35 mm in front of the anode, the arc length is 3 mm. a) Side-on profiles of radiation intensities of three emission lines for two arcs. The experimental data is fitted with a Gaussian profile. b) Radial profile of exited state densities, reconstructed from the fitting curves in (a). The compared modelled values assume a copper concentration of $0.5\,\%$.

(1), obtained after Abel inversion. For the sake of comparison, the results are juxtaposed with those predicted by the model, where the copper mole fraction $x_{\mathrm{Cu}} = 0.005$ is assumed in the plasma. Since the model is one-dimensional, a constant value along the radius is considered. In case of the $4^2P_{3/2}$ level, the prediction of the excited state density corresponds to the center value obtained in the measurements of arc 1. The number

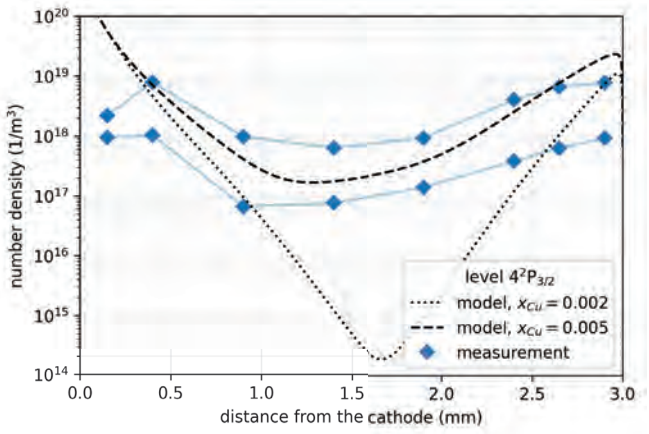
density of the lumped level 4^2D in the model represents the total number density of 4 single levels, among others the $4^2D_{3/2}$ and $4^2D_{5/2}$. Therefore, it is consistent that the model prediction is by a factor 4 larger than the corresponding values from measurements of arc 1. However, the measurements for arc 2 indicate number densities which are lower by more than one order of magnitude in comparison to the model results. Note that since the model is one-dimensional, certain limitations such as variable but still radius of arcs as well as a stable temporal development make a a quantitative agreement with experimental findings difficult. A comparison of the overall qualitative behaviour should be seen as preferable.

To capture the dynamics along the entire arc, spectra were recorded at eight axial positions, with 20 arcs measured at each position. Since the arc can vary greatly depending on the contain of metal vapour, the dynamic is not considered as a statistical error but rather as a parameter range within which the arc.

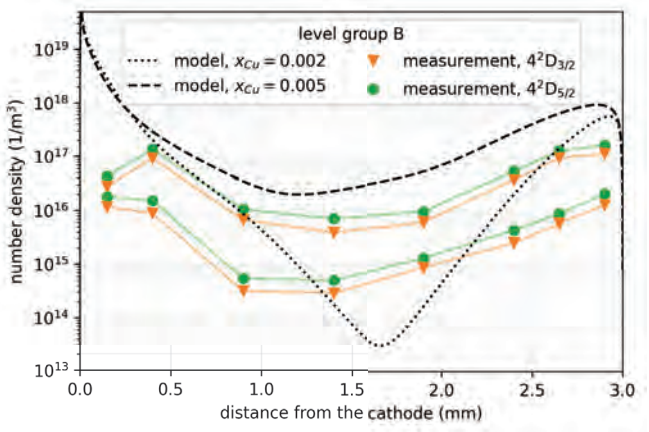
Fig. 8 depicts the axial distribution of the population of excited-states in the arc centre. Instead of using an Abel inversion, the number densities of excited states were estimated by dividing the radiation intensity for the central side-on position by the estimated arc diameter, a simplification justified by the small optical thickness of the arc. A number of data points around the central side-on position is used and averaged to improve the accuracy of the radiation intensity. The arc diameter here is estimated from the width of the Gauss fit of the intensity profiles. The figure shows the minimum and maximum density values from the 20 measured arcs for each axial position. The model predictions of the number densities for the $4^2P_{3/2}$ level and the lumped level 4^2D for two given mole fractions 0.002 and 0.005 of copper are shown along with the measured values.

As it was already indicated by the examples in Fig. 7, the experimental results for the minimum and maximum of the number densities differ by about one order of magnitude for almost all axial positions. This demonstrates the high dynamic of the copper vapour generation at the arc roots. The comparison for the level $4^2P_{3/2}$ in Fig. 8a shows, that the predicted number densities in case of the given mole fraction 0.005 are in the range of the experimental results with the exception of the regions near the electrodes. This can be caused by the limitation of the 1D description of spatial distribution of the arc attachment on the electrodes. The axial variation is very similar. This also holds for the axial distribution of the lumped level 4^2D in comparison with the experimental results for the $4^2D_{3/2}$ and $4^2D_{5/2}$ levels. As mentioned in the discussion of Fig. 7, the computed values for the lumped level should be larger than the sum of both measured densities, and a sufficient qualitative agreement is obtained for a given mole fraction 0.005.

The model underestimates the number densities for a mole fraction of 0.002 and axial positions in the middle of the arc column, i.e. far from the electrodes, as it can be seen in Fig.



(a)



(b)

Fig. 8: Fluctuations in excited level populations of the microarc. Shown are the minimum and maximum values measured across 20 captured arcs for each position, alongside the predictions of the 1D model. a) State $4^2P_{3/2}$, b) Group B, including states $5^2P_{1/2}$, $5^2P_{3/2}$, $4^2D_{3/2}$ and $4^2D_{5/2}$.

8a, b. In contrast, the number densities are overestimated near the electrodes. This behaviour could relate to an enhanced migration of copper ions to the electrodes caused by reversals of the electric field. The ions return as neutral atoms into the plasma where they can be excited. The 1D description implies a constant current density for the arc attachment on the electrodes, while the real structure is inhomogeneous.

V. Conclusion

This work presents the dynamics of microarcs with a DC current of 2 A and a length of 3 mm generated between copper electrodes in atmospheric pressure air. The studies are carried out by means of electrical measurements, high-speed imaging and emission spectroscopy.

The microarcs exhibit pronounced dynamic behaviour, which can be seen in the high-speed imaging as a flickering of the electrode attachment points, and fluctuations in the arc column. While the intensity flickering is more pronounced on the anode

side, the arc attachment on the cathode can appear as several spots, which can be observed for a few tens of microseconds and are more than half a millimetre apart in arcs of a few millimetres in length. An analysis of the total arc voltage revealed that radiation bursts can be interpreted as sudden increase of the copper content and are accompanied by a drop in arc voltage of several volts.

The side-on spectroscopy technique is used to record radial and axial profiles of CuI spectral lines and to derive the population of the upper states for the corresponding transitions. The spectra of recorded arcs show that the fluctuations observed in high-speed imaging are mainly due to emission from excited copper states. Twenty arc spectra are recorded for eight different axial positions up to $0.1\,\mathrm{mm}$ in front of the electrode surfaces. The results show that the experimentally obtained number density of excited copper states in the anode region and in the plasma column varies in about one order of magnitude, while the variation is less pronounced near the cathode. The results are compared with the predictions of an 1D collisional–radiative model for different copper densities, where a density of $0.5\,\%$ is found to provide the best agreement with the experimental data.

ACKNOWLEDGMENT

The work is funded by the German Research Foundation (DFG) project number 52473006.

REFERENCES

[1] M. Park, Y. Hirata, and T. Urabe, "Development of controlled micro-discharge at the atmospheric pressure," *Welding in the World*, vol. 58, no. 1, pp. 47–54, 2014.

[2] M. Baeva and D. Uhrlandt, "Characterization and applications of direct current microarcs: a review," *Journal of Physics D: Applied Physics*, 2025.

[3] E. Siewert, M. Baeva, and D. Uhrlandt, "The electric field and voltage of dc tungsten-inert gas arcs and their role in the bidirectional plasma-electrode interaction," *Journal of Physics D: Applied Physics*, vol. 52, no. 32, p. 324006, 2019.

[4] J. Sekikawa and T. Kubono, "Voltage-current characteristics of breaking arc at constant opening speed in the air," *IEEE Transactions on Components and Packaging Technologies*, vol. 27, no. 1, pp. 167–171, 2004.

[5] M. Becerra, J. Nilsson, S. Franke, C. Breitkopf, and P. André, "Spectral and electric diagnostics of low-current arc plasmas in co2 with n2 and h2o admixtures," *Journal of Physics D: Applied Physics*, vol. 57, no. 1, p. 015202, 2023.

[6] S. I. Eliseev, A. A. Kudryavtsev, H. Liu, Z. Ning, D. Yu, and A. S. Chirtsov, "Transition from glow microdischarge to arc discharge with thermionic cathode in argon at atmospheric pressure," *IEEE Transactions on Plasma Science*, vol. 44, no. 11, pp. 2536–2544, 2016.

[7] M. Baeva, J. Ballentin, and D. Uhrlandt, "Modelling studies of arcs of short length between copper electrodes," *Plasma Physics and Technology*, vol. 12, no. 1, pp. 40–45, 2025.

[8] J. K. C. Ballentin, M. Baeva, and D. Uhrlandt, "Experimental studies of microarcs between copper electrodes in air," *Plasma Physics and Technology*, vol. 12, no. 2, pp. 95–98, 2025.

[9] M. Baeva and D. Uhrlandt, "Modelling of microarcs in copper metal vapour dominated air," *J. Phys. D: Appl. Phys.*, vol. 58, no. 9, p. 095204, 2024.

[10] A. Bogaerts, R. Gijbels, and R. J. Carman, "Collisional–radiative model for the sputtered copper atoms and ions in a direct current argon glow discharge," *Spec. Acta Part B: At. Spec.*, vol. 53, no. 12, pp. 1679–1703, 1998.

[11] I. Babich, V. Boretskij, A. Veklich, and R. Semenyshyn, "Spectroscopic data and stark broadening of Cu I and Ag I spectral lines: Selection and analysis," *Adv. Space Res.*, vol. 54, no. 7, pp. 1254–1263, 2014.

Comparison of numerical solving for electric arc modelling*

Cyril Van de Steen
Safran Tech (Safran)
Toulouse, France
cyril.van-de-steen@safrangroup.com

Camille Gouze
Université de Toulouse, Toulouse INP, CNRS, LAPLACE
IRT-Saint Exupéry
Toulouse, France,
camille.gouze@laplace.univ-tlse.fr

Malyk Benmouffok
IRT-Saint Exupéry
Toulouse, France
malyk.benmouffok@irt-saintexupery.com

Yann Cressault
Université de Toulouse, Toulouse INP, CNRS, LAPLACE
Toulouse, France
yann.cressault@laplace-univ-tlse.fr

***Abstract*— New strategies are now available to simulate an electric arc. We investigate a commercial solution provided by Ansys and a more in-house approach using UDFs in Fluent. The ability to model an arc correctly is increasingly important. Electrification and all associated failure modes must be taken into account in the design process. Knowing the benefits and disadvantages of different modelling strategies is crucial to optimise computation time during product development.**

Keywords—Modelling, Stationary arc, comparison methods

I. Introduction

With the advent of More Electric Aircraft (MEA) and Fully Electric Aircraft (FEA), both onboard electrical power and voltage levels are sharply increasing. Moving to direct-current (DC) distribution and operating in reduced-pressure environments (100–1000 mbar) make electrical arc formation a critical risk for the safety and reliability of aeronautical systems. Numerical simulation of stationary arcs is the first step to study the coupled thermal radiative, hydrodynamic and electromagnetic phenomena, thanks to a magnetohydrodynamic (MHD) modelling. This modelling allow us to guide, in the future, the design of arc-protection measures. However, such simulations remain computationally expensive and delicate to set up, especially under conditions representative of aeronautics. This work reproduces the well-known free-burning argon arc of Hsu et al. [1], an experimentally validated atmospheric-pressure arc, to compare two numerical strategies:

- Strategy 1: A MHD model using only fluent for the hydrodynamic part and the electromagnetic part is implemented within a homemade User Define Functions (UDF) using the same fluent solver.
- Strategy 2: A strong coupling between ANSYS Fluent (fluid dynamics) and ANSYS Electronics Desktop/Maxwell (electromagnetics) via System Coupling, with iterative exchange of electrical conductivity, Lorentz forces and Joule heating [2,3].

The same geometry is used for both solvers , but the mesh is different, in fact in the same Strategy 1 only the fluent mesh is taken into account for the whole MHD simulation meanwhile in the strategy 2, there is a mapping technic between two mesh the Ansys EM one which is based on the Finite Element Method (FEM) and Fluent based on the Volume Finite Method (FVM).. The study evaluates and contrasts their accuracy, computational cost, scalability and ease of use, with the goal of identifying the optimal approach for simulating electric arcs in aeronautical applications. Ansys 2025.R2 was used for this comparison.

II. Theoritical Background

A. Magnetohydrodynamic model under LTE

Under the Local Thermodynamic Equilibrium (LTE) assumption, the arc plasma is described by:

• Mass continuity:

$$\partial\rho/\partial t + \nabla\cdot(\rho\,\mathbf{V}) = 0 \qquad (1)$$

• Momentum (Navier–Stokes with Lorentz force):

$$\partial\rho\mathbf{V}/\partial t + \nabla\,\rho\mathbf{V}\otimes\mathbf{V} = -\nabla p - \nabla\hat{\pi} + \mathbf{J}\times\mathbf{B} \qquad (2)$$

• Energy conservation (including conduction, radiation and Joule heating):

$$\rho\,Cp(\partial T/\partial t + \mathbf{V}\cdot\nabla T) = \nabla\cdot(\kappa\nabla T) + \mathbf{J}\cdot\mathbf{E} - q_rad \qquad (3)$$

The fluid mass density ρ evolves according to the mass-continuity equation, which involves the time variable t and the velocity field **V**. The momentum balance uses the Navier–Stokes formulation, where p denotes the static pressure and $\hat{\pi}$ the viscous tensor, and where the Lorentz force arises from the cross-product between the electric current density **J** and the magnetic flux density **B**.

Energy conservation is expressed in terms of the temperature T, the specific heat at constant pressure Cp, the thermal conductivity κ, and the radiative heat-loss term q_rad, with additional contributions from Joule heating through the scalar product **J**·**E**, where E is the electric field.

Maxwell's equations in quasi-static form provide the electric field $\mathbf{E} = -\nabla\varphi$ and the current density $\mathbf{J} = \sigma\mathbf{E}$. The magnetic flux density B is obtained from $\nabla\times B = \mu_0 J$ and $\nabla\cdot\mathbf{B} = 0$.

B. Radiation modelling

Thermal radiation losses are treated via the Net Emission Coefficient (NEC) method [4], where the radiative power term is written

$$q_rad = 4\,\pi\,Rp\,\varepsilon_net(T) \qquad (4)$$

Rp is an effective plasma radius, ε_net(T) is the tabulated net emission coefficient under LTE hypothesis.

C. Plasma properties

All thermodynamic and transport properties—density ρ (T,p), specific heat Cp (T,p), electrical conductivity σ (T,p), viscosity μ (T,p), thermal conductivity κ (T,p) and NEC tables—were provided by the Scipra team at the LAPLACE laboratory. We can not certified that the properties used in this paper are rigorously the same as in other paper we cited.

D. Model presentation

A brief presentation is given in this paper; for more details, see Hsu [1] or Baudoin's thesis [5]. Geometry, dimensions and boundary conditions are well explained there.
For this paper, the symmetry axis is Y. The upper face of the anode is at y = 0 and the lower face of the cathode is at y = 10 mm.

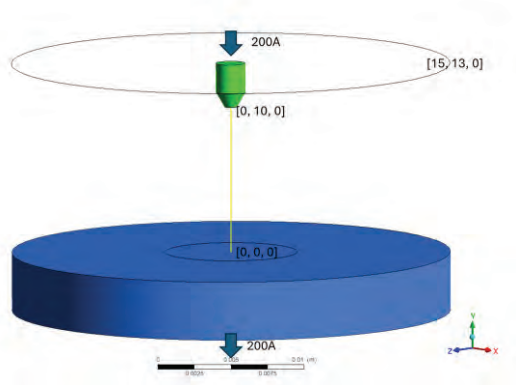


Fig. 1 Schematic representation of the geometry

III. Different Strategy for Modelling

A. Strategy 1 : Fluent with UDF

Fluent natively solves continuity, momentum and energy using the internal SIMPLE solver with the laminar model. Une proposition: A group of UDFs, here called *UDF A* was developed to solve the electromagnetic equations written previously, in order to provide the force and energy source term in the hydrodynamic equations and also electronic enthalpy, radiation (with the NEC approximation) and plasma properties. All of these UDFs run at each Fluent iteration.

Fluent residuals were fixed at 1×10^{-4} for continuity, 1×10^{-5} for the velocity components and 3×10^{-6} for the energy equation.

B. Strategy 2: SyC: Fluent + AEDT

Fluent solves the continuity, momentum and energy equations with fixed σ(T,p), and supplies T and σ to Ansys Electronics Desktop (AEDT). AEDT solves $\nabla\cdot(\sigma\nabla\varphi) = 0$ and $\nabla\times\mathbf{B} = \mu\mathbf{J}$ and returns $\mathbf{J}\times\mathbf{B}$ and $\mathbf{J}\cdot\mathbf{E}$ to Fluent. The convergence criteria were set to 1% on exchanged data fields, 1% for the AEDT solver, and the Fluent criteria were kept the same as for Strategy 1. AEDT runs for three iterations before exchanging data, and Fluent runs for 50 iterations. The UDF (UDF B) in Fluent contains only the plasma properties (radiative, thermodynamics and transport properties)

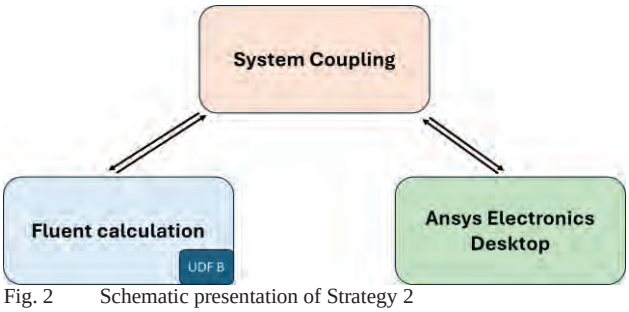


Fig. 2 Schematic presentation of Strategy 2

C. Comparison metrics

For both strategies, we quantify:
- Accuracy versus Hsu's temperature and field profiles [1].
- CPU time on 3–24 cores.
- Scalability.
- Setup complexity and robustness

D. Limits and remarks

The Fluent parameters in both strategies are set in the same way and were optimised to fit Strategy 1. This means that, with other optimisations (other Fluent schemes for example), the CPU-time results could differ. The Fluent mesh was identical for the Fluent models, and the AEDT mesh was set to maximise the correlation between the Fluent and AEDT meshes. The mesh partition in Fluent was imposed as a cylindrical RY coordinate. This allows us to split the geometry into different cylindrical regions to distribute more efficiently the parameter fields during the calculations.

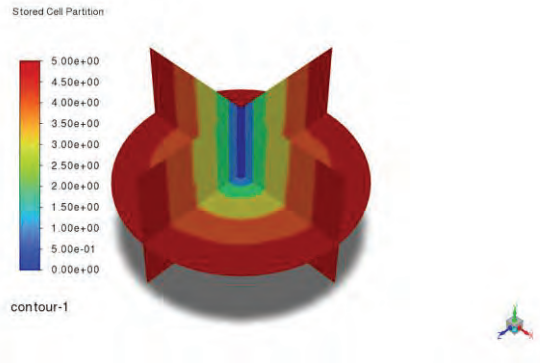


Fig. 2 Example of mesh distribution for 6 processors distribution

IV. Results

A. Arc voltage and current distribution

TABLE I. Summary of Simulated Arc Voltage

Arc voltage value (V)		
Number of processors	Strategy 1	Strategy 2
3	13.66	11.92
6	13.67	12.17
12	13.7	12.17
24	13.89	12.09

The values of arc voltage in the table (see Table 1) are close to other values found in the literature. Hsu [1] found 13.3 V and Baudoin 11.2 V [5]. This supports the ability of both models to compute the arc-column voltage for other applications (such as circuit breakers, for example). The

variation of column voltage depending on the number of processors involved, one can say that they are relatively independent of it in our work.

For the remainder of the analysis (before subsection F), all simulation results for Strategy 1 and Strategy 2 were obtained using three processors.

Our current distributions differ between the two strategies but remain close in magnitude. Both are below some currents reported in the literature. However, Hsu [1] and Baudoin [5] performed 2D axisymmetric simulations, not 3D simulations as in the presented work. This may explain the difference in values between the two types of simulation (for voltage value but also for all the paper distribution value).

In stationary MHD configurations with cylindrical symmetry, axisymmetric 2D simulations enforce exact rotational invariance by solving the equations in the meridional plane and analytically treating the singular terms at r = 0. This produces smooth and strictly symmetric electromagnetic and thermal fields along the axis. In contrast, 3D simulations discretise the domain in Cartesian space, where the axis is not a true boundary and small mesh-induced asymmetries or non-axisymmetric numerical modes may appear. These slight deviations can affect the balance of Lorentz forces, heat diffusion and Joule heating, leading to a temperature profile along the axis that is less smooth and differs subtly from the perfectly symmetric 2D solution.

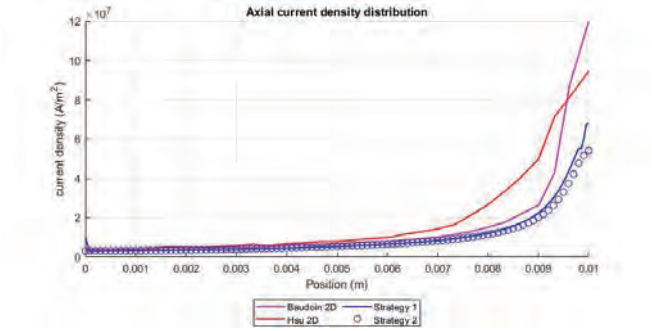


Fig. 3 Axial current distribution for different simulations

B. *Comparison of Temperature on axial distribution for three Processors between both strategies*

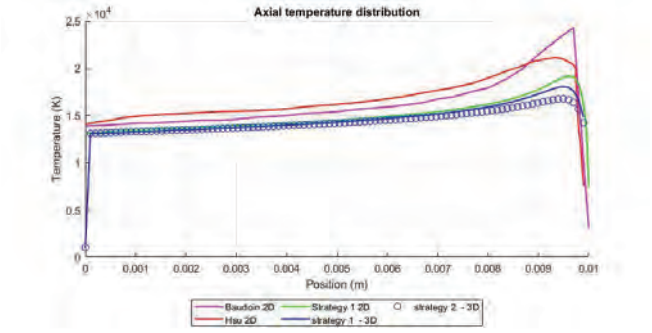


Fig. 4 Axial temperature distribution for different simulations

Variations can be observed between literature results and our calculations. For the temperature distribution, we added a 2D axisymmetric simulation using Strategy 1 (not possible using Strategy 2) to compare with three results. We observe that the 2D axisymmetric simulation provides a higher temperature distribution than the 3D ones. Some differences can also be noted between the two 3D simulations: Strategy 1 provides higher values than Strategy 2. However, the difference between the two methods is not large (<10%), as visible in part F (Processor dependence). One can also observe that the temperature value between 9 and 10mm have also significant variation between Hsu and Baudoin calculations.

C. *Comparison of Pressure on axial distribution for 3 Processors between both strategies*

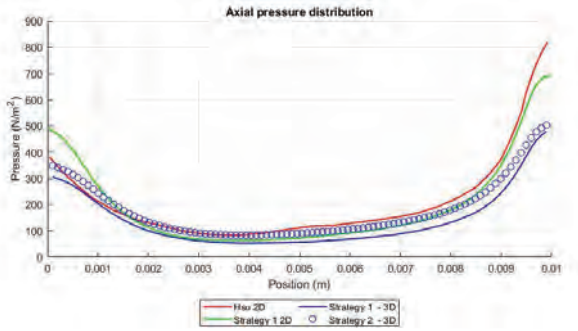


Fig. 5 Axial pressure distribution for different simulations

As for the temperature, the 2D axisymmetric simulations provide higher value, mostly near walls than the 3D modelling. However, when we are at 1 mm from walls (1 to 9mm) all methods provide relatively close values.

D. *Comparison of velocity on axial distribution for 6 Processors between both strategies*

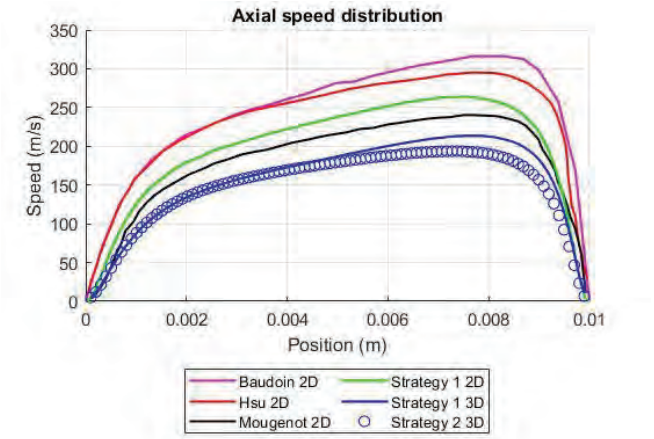


Fig. 6 Axial speed distribution for different simulations

For this last comparison, we also include results found in Mougenot's PhD thesis [6]. Mougenot also propose also a 2D axisymmetric simulation using the Saturne Code.

Again, all 2D modelling provide higher value (but are more disperse than previously) and 3D modelling are close to each other. The highest value of velocity goes from 200 to 320m/s, who is quite different. However, it is complicate to measure experimentally this value to ensure one or another method.

E. *Time calculation*

This section illustrates wall-clock time depending on the strategy, the computer and the number of processors used. Wall-clock time is the actual time between launching the calculation and completion.

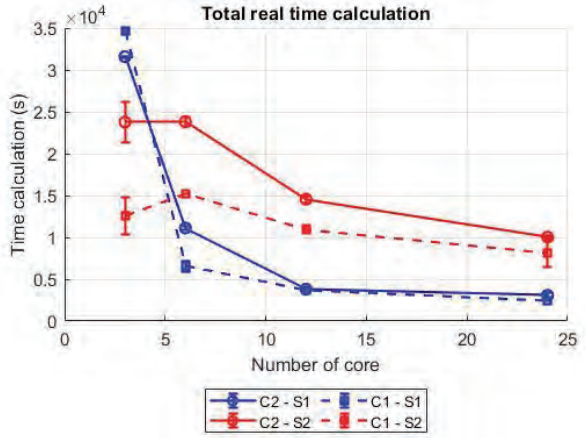


Fig. 7 Wall Clock time calculation

Calculations were made on two different computers: (C1) a physical workstation (32 processors, Intel® Xeon® w5-2465X) and (C2) a virtual machine (32 processors, Intel Xeon (Sapphire Rapids)). Random-access memory (RAM) was high enough not to affect these calculations (500 and 250 GB).

At low parallelisation, Strategy 2 provides faster results. However, once parallelisation increases, Strategy 1 becomes the faster approach.

Looking in details, for the fluid part exclusively, Strategy 1 is always the fastest. And as expected, since in Strategy 1, only Fluent is running, whereas in Strategy 2 Fluent must restart at each System Coupling iteration.

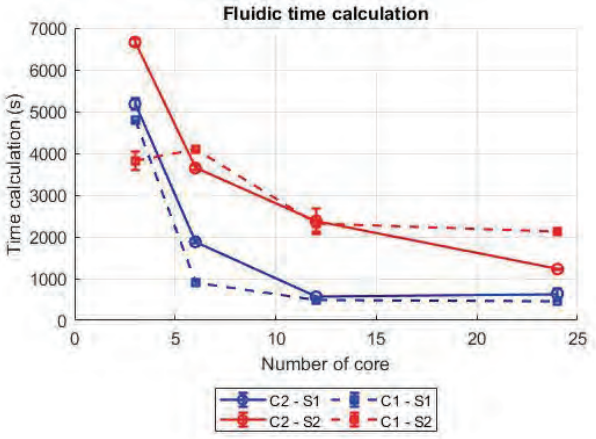


Fig. 8 Fluid time calculation

It can be noted that, for both strategies, parallelisation provides good reductions in computation time.

For the electromagnetic part, parallelisation is less beneficial for Strategy 2. Here again, the solver must reload the case at each System Coupling iteration.

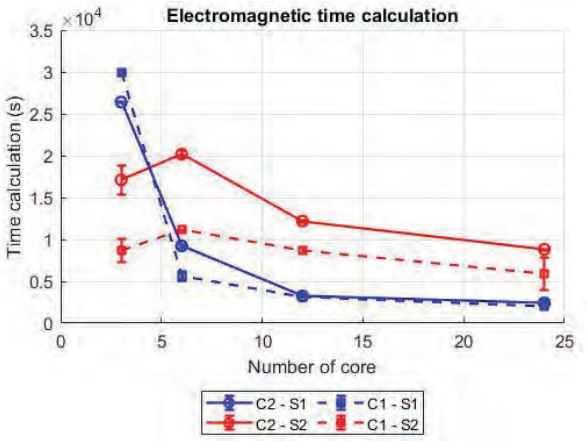


Fig. 9 Electromagnetic time calculation

F. *Processor dependence*

We also examine the accuracy of each strategy depending on the level of parallelization. It is important to note that only residuals in fluent were observed for the Fluent convergence (and that a value of $1x10^{-6}$ for the energy is recommended, unlike the $3x10^{-6}$ used in our work).

For Strategy 2, parallelization has no impact on 12 processors and below, however at 24 processors an impact can be seen, as presented on Fig. 12. A maximum of 7% in the temperature can be observed near the needle wall where temperature was imposed as 3000K.

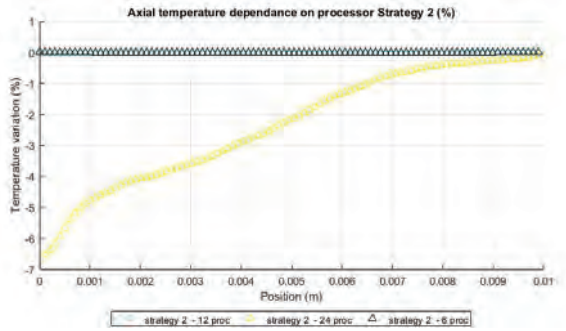


Fig. 10 Temperature dependence on number of processors used for Strategy 2

The impact of parallelization is even more important using Strategy 1 only. In this configuration, the dependence is visible even from 6 processors. With this strategy, a variation of 18% could be observed near the needle wall.

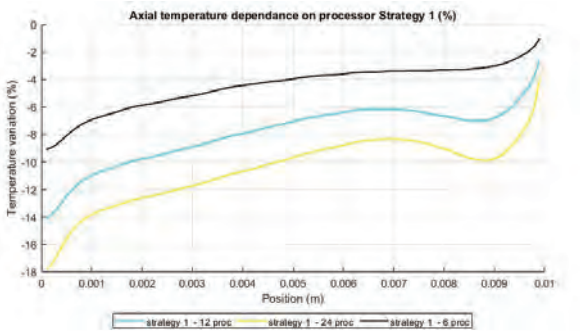


Fig. 11 Temperature dependence on number of processors used for Strategy 1

A more accurate comparison strategy would have been to decrease residual of energy to $1x10^{-6}$ and to examine the balance between heat transfer rate (HTR), the electromagnetic temperature source (EMS) and the NEC losses radiative (NLR) ensuring a small imbalance at the end. This last check is only possible automatically in stationary solutions.

G. Complexity

Strategy 1 is more complex at the beginning. The user must write and test all the required UDFs. However, once the UDFs are written and mastered, this method is easier to use (and to verify calculations) than Strategy 2.
Strategy 2 to use a commercial software for Electromagnetics calculations. This mean that you can have internal tools to verify your calculations and adapted software for adding specific boundary conditions.
Nevertheless, for simplicity's sake Strategy 2 is the easier way to start. Each software solves the adapted equations and then the data are coupled using the System Coupling software. The only warning is to carefully verify the good correlation between the FEM (AEDT) and FVM (Fluent) meshes.

TABLE II. SUMMARY OF STEPS VARIATION IN BOTH STRATEGIES

	Strategy 1	Strategy 2
Meshing	1 Step (fluent)	2 Steps (Fluent + AEDT)
Meshing correlation verification	0 Step	1 Step
EM UDF	3 Steps (creation, verification and attribution)	0 Step
Boundary Condition	2 Steps in fluent (Fluid and UDF BC)	2 Steps (Fluent and AEDT)
Coupling	1 Step (in fluent)	3 Steps (Fluent, AEDT and SyC)

V. CONCULSION

Both numerical strategies evaluated in this work successfully reproduce the main physical characteristics of the free-burning argon arc benchmark. Strategy 1, fully implemented in Fluent with UDFs, and Strategy 2, coupling Fluent with AEDT, yield comparable trends for voltage, temperature, pressure and velocity distributions, with differences generally within 10%. As expected, 2D axisymmetric results from the literature show higher peak values than the present 3D simulations.

Although the present study focuses solely on modelling the arc column, it is important to note that state-of-the-art simulations require, at minimum, accounting for plasma–electrode interactions. This first step nonetheless enables a clean comparison between the two approaches, as including such interactions would have introduced additional complexity without offering clearer insight into their relative behaviour

From a performance standpoint, Strategy 2 is faster at low core count, while Strategy 1 becomes more efficient as parallelisation increases. However, both strategies show sensitivity to processor number, particularly near boundary regions. In terms of usability, Strategy 1 requires more initial development but offers greater control once implemented, whereas Strategy 2 is easier to set up but depends on careful mesh correlation between solvers.

Overall, both modelling approaches are suitable for stationary arc simulations in aeronautical contexts. The optimal choice depends on user expertise, available software and desired balance between flexibility, robustness and computational efficiency.

ACKNOWLEDGMENT

The authors would like to express their sincere gratitude to Fatiha Ouchar for the valuable discussions and constructive collaboration throughout this work. Their insights and support have greatly contributed to the quality and advancement of this study.

REFERENCES

[1] K. C. Hsu, K. Etemadi, P. E. Pfender, "Study of the free-burning high-intensity argon arc," J. Appl. Phys., vol. 54, no. 3, p. 1293-1301, 1983.

[2] F. Ouchar, C. Van de Steen, P. Rivière, T. Lebey, A. Soufiani, "Influence of Radiation Modelling on the Simulation of Wall-Stabilized Electrical Arc," Proc. IEEE 69th Holm Conf. Electr. Contacts, 2024.

[3] W. Shang et al., "Validations of Electric Arc Simulation," Proc. IEEE 70th Holm Conf. Electr. Contacts, 2025.

[4] J. Lowke, "*Predictions of arc temperature profiles using approximate emission coefficients for radiation losses.*" Journal of Quantitative Spectroscopy and Radiative Transfer, 111_122, 1974

[5] F. Baudoin, PhD thesis "Contribution à la modélisation d'un arc électrique dans les appareils de coupure basse tension", Université Blaise Pascal (Clermont-Ferrand 2) ; 2004

[6] J. Mougenot, PhD thesis "Modélisation de l'interaction entre un arc électrique et matériau : application au soudage TIG », Université Toulouse 3, 2013.

Advanced Contact Materials for Hot switching MEMS Relay Applications

Martin Köhne
Department of Advanced Technologies and Micro Systems
Robert Bosch GmbH
Renningen, Germany
martin.koehne@de.bosch.com

***Abstract*—Hot-switching in MEMS relays - where contacts engage and disengage under continuous electrical load - induces local surface temperatures above 3000 °C, causing material transfer and rapid wear. While materials such as ruthenium achieve lifetimes near 10^8 cycles at ~3.5 V, performance drops sharply at higher voltages, motivating the search for contact materials with higher melting points. This work evaluates refractory metals, borides, carbides, and nitrides based on their bulk and thin-film properties (100–300 nm). Tungsten and molybdenum offer the highest thermal conductivities, while borides (ZrB_2, HfB_2, TaB_2) combine high hardness with moderate thermal transport. Carbides (HfC, ZrC, TaC) provide extreme hardness and melting points above 3500 °C, whereas nitrides (TiN, ZrN, HfN) exhibit vacuum decomposition near similar temperatures. Thin-film properties deviate substantially from bulk due to deposition-induced microstructure, affecting hardness, conductivity, and resistivity. Overall, no single material class is universally optimal, but each presents advantages for targeted MEMS contact applications.**

Keywords—MEMS relays, hot switching, contact materials, refractory metals, borides, carbides, nitrides, thin films, contact resistance, material selection

I. INTRODUCTION

Microelectromechanical systems (MEMS) relays present compelling advantages for power switching applications, including superior galvanic isolation, lower power consumption compared to complementary metal-oxide-semiconductor (CMOS) devices, and zero leakage current [1].

Cold switching MEMS relays have demonstrated exceptional performance, achieving lifetimes exceeding 10^8 cycles with minimal contact degradation [1][2]. However, hot switching operation - wherein contacts engage and disengage under electrical load -creates fundamentally different degradation mechanisms rooted in localized thermal phenomena [1].

During hot switching, contact asperities experience rapid temperature rise driven by two mechanisms: Joule heating and arcing processes. Basu et al. show that for ruthenium contacts, under controlled hot-switching conditions, local surface peak temperatures can already reach the boiling point of ruthenium (4150 °C) at a switching voltage of 3.5 V [1]. These thermal transients induce material transfer through melting, evaporation, and field emission; adhesion enhancement through local softening; and mechanical wear from contact bounce and micro-slip [1][3].

The fundamental challenge in hot switching material selection arises from conflicting property requirements. Materials with high thermal conductivity frequently exhibit lower hardness and mechanical strength. Conversely, hard materials typically possess lower thermal conductivity. Materials with exceptional electrical conductivity often soften at elevated temperatures, while materials stable at high temperatures may exhibit elevated electrical resistivity. These incompatibilities necessitate systematic material screening and careful trade-off analysis [1].

This investigation evaluates four principal material classes:

1) Refractory metals (W, Mo, Ta)
2) Borides (ZrB_2, HfB_2, TaB_2)
3) Carbides (HfC, ZrC, TaC)
4) Nitrides (TiN, ZrN, HfN)

Each class is analysed across critical properties: melting point, melting behaviour, boiling point, electrical conductivity, thermal conductivity, and hardness. Thin-film effects are evaluated systematically for the 100-300 nm thickness range typical of MEMS contact deposits.

An inert atmosphere as the operational environment, influences significantly material selection by eliminating oxygen-driven oxidation and preserving metallic contact behaviour [4]. In addition, their compatibility to a commonly used inert nitrogen atmosphere is evaluated.

II. HOT SWITCHING THERMAL AND ELECTRICAL DEMANDS

A. Contact Temperature and Joule Heating

Local contact temperature rise during hot switching is caused by the sudden discharge of capacitively or inductively stored energy within an extremely short time of closing or opening contacts. The current is concentrated at a few to some tens of contact asperities with individual spot areas of 0.008-0.03 μm² (50-100 nm radius) within the contact area of 10-100 μm² [5][6]. When the contacts are separated by only a few tens of nanometers, electrons are emitted from the cathode via Fowler–Nordheim field emission.

This field-emitted electron current causes intense impact heating on the opposite contact (anode), which leads to local evaporation of anode material. The evaporated anode material then re-deposits on the cathode, producing a net material transfer from anode to cathode [7]. This generates local temperatures that may reach extreme values exceeding the boiling point of e.g. ruthenium due to the very high current density and

The IPCEI ME/CT project is supported by the Federal Ministry for Economic Affairs and Energy on the basis of a decision by the German Parliament, by the Ministry for Economic Affairs, Labor and Tourism of Baden-Württemberg based on a decision of the State Parliament of Baden-Württemberg, the Free State of Saxony on the basis of the budget adopted by the Saxon State Parliament, the Bavarian State Ministry for Economic Affairs, Regional Development and Energy and financed by the European Union - NextGenerationEU.

constriction resistance at these nanoscale contact spots [1][2].

B. Material Property Requirements for Hot switching

Hot-switching crater formation and material loss are strongly linked to local temperatures at the microcontact reaching the material's melting or boiling point, so a higher melting point increases the voltage or current required to reach those temperatures [1][8].

However, a high melting point alone is not sufficient; adequate hardness, thermal conductivity, and suitable chemical behavior are also required [9][10].

Requirements derived from ruthenium:

Ruthenium is the state-of-the-art contact material for hot switching MEMS [1][2]. Properties of alternative thin film materials should be close or superior to ruthenium's as depicted in Table I.

TABLE I.

Property	***Ru***
Melting Point (°C)	2334
Melting behaviour	Congruent
Boiling Point (°C)	4150
Bulk Thermal Conductivity (W/m·K)	117 [11]
Thin-Film Therm. Conductivity 100 nm (W/m·K)	40-75 [12]
Bulk Electrical Resistivity (μΩ·cm)	7.6 [11]
Thin-Film Electrical resistivity 100 nm (μΩ·cm)	8.0 [13]
Bulk Hardness (GPa)	2-5 [11]
Thin-Film Hardness 100 nm (GPa)	15.3 [14]

1) Higher reliability of the MEMS relay could be reached when the melting and boiling point are significantly higher than for ruthenium [1].

2) High thermal conductivity at least close to 40-75 W/m·K (Ru thin film 100 nm) to conduct Joule heat away from the contact point.

3) Electrical resistivity < 7.6 μΩ·cm (100 nm thick Ru film). Reduces Joule heating per unit current.

4) Hardness > 15.3 GPa (Ru film with 300 nm). Resists plastic deformation and prevents cold-welding.

Additional requirements:

5) Stable in inert atmosphere (ideally nitrogen) without phase decomposition.

6) Compatible with MEMS fabrication process. Excludes most transition metals (Ti, V, Cr, Mn, Fe, Co, Ni, Cu) as they cause rapid contamination through interstitial diffusion and deep-level trap formation with dramatically increasing rates from Ti→Cu [15].

III. THIN-FILM EFFECTS: MECHANISMS AND QUANTITATIVE ASSESSMENT

A. Boundary Scattering and Matthiessen's Rule

All thin-film materials exhibit property degradation from bulk values when thickness decreases below twice the electron mean free path (typically 50-100 nm for metals and compounds). Boundary scattering - electrons colliding with film surfaces and grain boundaries - reduces momentum relaxation length [16][17].

For electrical conductivity *r*, Matthiessen's rule predicts: $\rho_{total} = \rho_{phonon} + \rho_{boundary} + \rho_{defect}$, where boundary and defect contributions emerge in thin films [18].

Experimental validation demonstrates electrical resistivity increases of 40% at 100 nm thickness, 20% at 200 nm, and 10% at 300 nm for typical metals, as compared to their bulk values [16].

Thermal conductivity reduction follows similar physics. Phonon-boundary scattering at surfaces typically dominates, yielding net thermal conductivity reduction of 30–50% at 100 nm [16].

B. Grain Size and Hall-Petch Strengthening

Thin films deposited at room temperature exhibit grain sizes of 10-50 nm [19], substantially smaller than bulk polycrystalline materials (1-100 μm). Smaller grain size increases grain boundary area per unit volume, enhancing electron and phonon scattering.

In nanocrystalline materials (d < 100 nm), reduced grain size decreases dislocation density through energetic constraints and dislocation starvation, which can limit work hardening and may cause Hall-Petch breakdown, which partially offsets the hardness increase normally achieved through boundary strengthening.

Net result for the evaluated material class: slight to strong hardness increase (10-600%) compared to substantial electrical resistivity increases (40-150%), with respect to the bulk material.

IV. MATERIAL CLASS

A. Refractory Metals

The refractory metals - tungsten, molybdenum, and tantalum - exhibit exceptional thermal stability and hardness, see Table II. Tungsten possesses the highest melting point (3422 °C) and the highest thermal conductivity (173 W/m·K) among refractory metals [11], while molybdenum offers high thermal conductivity (138 W/m·K) with lower density [20][11]. All three materials react with nitrogen under arcing [21].

TABLE II.

Property	***W***	***Mo***	***Ta***
Melting Point (°C)	3422	2620	3017
Melting behaviour [43]	Con-gruent	Con-gruent	Con-gruent
Boiling Point (°C) [22]	5930	4885	5698
Bulk Thermal Conductivity (W/m·K)	173 [11]	138 [11]	57.5 [11]
Thin-Film Therm. Conductivity 100 nm (W/m·K)	60-80 [12]	42-44 [23]	14.6 (WFL) [24]
Bulk Electrical Resistivity (μΩ·cm)	5.5 [11]	5.0 [11]	12.8 [11]
Thin-Film Electrical resistivity 100 nm (μΩ·cm)	14-23 [25]	14-37 [25]	50-175 [26]
Bulk Hardness (GPa)	6 [11]	4 [11]	3.5 [11]
Thin-Film Hardness 100 nm (GPa)	18–21 [27]	22–33 [28]	10–11 [29]

WFL: Wiedemann-Franz-Law

Advantages: Exceptional melting and boiling points, no decomposition; superior hardness; established MEMS fabrication compatibility; negligible nitrogen atmosphere reactivity.

Limitations: Electrical resistivity of molybdenum and tantalum as thin film particularly problematic for low-resistance contacts.

B. Borides

Table III presents the borides ZrB_2, HfB_2, and TaB_2 which combine exceptional hardness and melting points with metallic electrical conductivity, unusual for ceramics [30][31]. The metal-boride bonding exhibits mixed covalent-metallic character.

TABLE III.

Property	***ZrB_2***	***HfB_2***	***TaB_2***
Melting Point (°C)	3131 [32]	3258 [32]	3011 [32]
Melting behaviour (1 bar Ar) Reaction with N_2 < $T_{melting}$ [58]	Con-gruent	Con-gruent	Con-gruent
Bulk Thermal Conductivity (W/m·K)	53-56.4 [33]	72-105 [33]	38 [34]
Thin-Film Thermal Conductivity 100 nm (W/m·K)	N/A	N/A	N/A
Bulk Electrical resistivity (μΩ·cm)	8-16 [33]	2.5-12.5 [33]	14 [31]
Thin-Film Electrical Resistivity 100 nm (μΩ·cm)	208-250 [35]	230-320 [36]	120-150 [36]
Bulk Hardness (GPa)	22.5 [31]	29 [31]	25-26 [36]
Thin-Film Hardness 100 nm (GPa)	25-45 [36]	13-60 [36]	27-43 [37]

N/A: Not available

Advantages: Exceptional thin film hardness (up to 60 GPa) among all contact material classes; high melting points; no decomposition at 4000°C [38]; brittle fracture mode prevents cold-welding adhesion.

Limitations: Electrical resistivity of thin films two orders of magnitude higher than for refractory metals; reaction with nitrogen starts already before melting [39].

C. Carbides

Transition metal carbides HfC, ZrC, and TaC exhibit mixed covalent-metallic bonding [40] with exceptional hardness and melting points, see Table IV. Carbides will react under arcing with nitrogen [41][42].

TABLE IV.

Property	***HfC***	***ZrC***	***TaC***
Melting Point (°C)	3923 [30]	3540 [30]	3768 [43]
Melting behavior (1 bar N_2) [18]	Con-gruent	Con-gruent	Con-gruent
Boiling Point (°C)	4960 dec. [44]	4700-5200 [44][45]	4850 [44]
Bulk Thermal Conductivity (W/m·K)	21–27 [46]	18-44 [46]	22-28 [46]
Thin-Film Therm. Conductivity 100 nm (W/m·K)	N/A	N/A	N/A
Bulk Electrical Resistivity (μΩ·cm)	37 [30]	43 [30]	15–42 [47]
Thin-Film Electrical Resistivity 100 nm (μΩ·cm)	N/A	770-1100 [48]	N/A
Bulk Hardness (GPa)	26.1 [30]	25.9 [30]	9-19 [49]
Thin-Film Hardness 100 nm (GPa)	10-35 [49]	20-27 [48]	9-21 [49]

Advantages: Thin films possess exceptional hardness close to borides; extremely high melting points (> 3500 °C); low electrical resistivity as bulk.

Limitations: Thermal conductivity substantially lower than refractory metals; higher electrical resistivity for ZrC thin film; missing data for thin film properties; adhesion challenges to silicon substrates for TaC [50].

D. Nitrides

Transition metal nitrides (TiN, ZrN, HfN) are extensively used in semiconductor processing as diffusion barriers and metal gates. This enables straightforward integration with established fabrication protocols [51][52]. Table V presents the properties of TiN, ZrN, and HfN.

TABLE V.

Property	***TiN***	***ZrN***	***HfN***
Melting Point (°C)	2945 [53]	2980 [11]	3387 [31]
Melting behaviour (1 bar N_2) Decomposition in vacuum [42]	Con-gruent	Con-gruent	Con-gruent
Bulk Thermal Conductivity (W/m·K)	19.2 [31]	20.5 [31]	21.7 [31]
Thin-Film Therm. Conductivity 100 nm (W/m·K)	63 [52]	47 [54]	N/A
Bulk Electrical Resistivity (μΩ·cm)	12-16 [55]	7-21 [31]	33 [31]
Thin-Film Electrical Resistivity 100 nm (μΩ·cm)	45-120 [56]	11-20 [57]	20-27 [58]
Bulk Hardness (GPa)	18-21 [31]	15.8 [31]	16.3 [31]
Thin-Film Hardness 100 nm (GPa)	Up to 30 [59]	23-26 [60]	26-36 [61]

Advantages: Excellent MEMS fabrication process compatibility; outstanding thin-film property retention compared to carbides/borides; thin film possess lower electrical resistivity than borides/carbides; excellent adhesion to silicon substrates.

Limitations: Melting temperature decreases significantly with lower pressure [62]. Above the melting temperature nitrides are prone to releasing nitrogen due to a wide substoichiometric stability range [63] [64][65]. TiN is at least one order of magnitude more volatile than ZrN or HfN [66]; thermal conductivity lower and electrical resistivity higher than refractory metals.

V. Material Recommendation

The recommendation considers the four principal material classes:

1) Refractory metals (W, Mo, Ta)
2) Borides (ZrB_2, HfB_2, TaB_2)
3) Carbides (HfC, ZrC, TaC)
4) Nitrides (TiN, ZrN, HfN)

The criteria for this recommendation are focused on the thin film properties. These are a high melting and boiling point, a high thermal conductivity, and a low electrical resistivity. Thin films of tungsten are most appropriate

according to the above criteria and are therefore recommended.

Tungsten (W): Attractive combination of high melting and very high boiling point (5930 °C). Properties degrade for thin films but still low electrical resistivity (14-23 μΩ·cm) and competitive thermal conductivity (60-80 W/m·K) compared to ruthenium.

Of all the other analysed materials borides possess as bulk an attractive combination of good thermal conductivity and low electrical resistivity in combination with exceptional hardness. For thin films only very limited data are available or even missing (e.g. thermal conductivity). Optimization of their thin film properties is an attractive research opportunity.

VI. Conclusions

This systematic material assessment evaluates four distinct material classes suitable for hot switching MEMS relay contacts operating in inert nitrogen atmosphere. Hot switching creates extreme local thermal conditions (surface temperatures > 3000 °C) and high current density (> 10^4 A/cm²) simultaneously, demanding materials that simultaneously achieve properties, which are conventionally incompatible [1].

A. Key Findings

1) Partially or fully missing data for thin films of carbides, borides, and nitrides show the need for further research.

2) Thin-film properties are very different from bulk properties. Known data show always an increase in hardness. But thermal conductivity and electrical resistivity can increase or decrease depending on material.

3) No single material as thin film surpasses ruthenium in all metrics [1]:

- Refractory metals provide superior melting and boiling point and electrical resistivity, but thermal conductivity is lower. Nitrogen atmosphere is not recommended due to reaction with nitrogen under arcing [21].
- Borides provide exceptional hardness. Argon as atmosphere is a must because borides react with nitrogen. They offer unique erosion resistance not achievable with metal contacts [30][31]. But electrical resistivity for thin films is orders of magnitudes too high for a good ohmic contact.
- Carbides offer exceptional hardness, but their electrical resistivity as thin film is only known for ZrC which is about 2 order of magnitude higher than for ruthenium.
- Nitrides provide balanced properties with superior thin-film behaviour but are prone to releasing nitrogen already below melting point due to a wide substoichiometric stability range [64][65].

The material with the most promising property profile to improve the lifetime of MEMS relays is the refractory metal tungsten, due to its combination of a high melting point and one of the highest boiling points of all materials (shared only with rhenium) [11][22].

Acknowledgment

I gratefully acknowledge my colleagues Simon Frommherz, Thomas Gerrer, Jens Hofmann, Mordechai Kornbluth, Daniel Pantel, and Christoph Schelling for their careful reading of the manuscript and for their constructive comments and suggestions, which have substantially improved the clarity and quality of this work.

References

[1] Basu, A., Hennessy, R. P., Adams, G. G., & McGruer, N. E. (2014). Hot switching damage mechanisms in MEMS contacts—Evidence and understanding. Journal of Micromechanics and Microengineering, 24(10), 105004. https://doi.org/10.1088/0960-1317/24/10/105004

[2] Coutu, R. A., Kladitis, P. E., Leedy, K. D., & Crane, R. L. (2004). Selecting metal alloy electric contact materials for MEMS switches. Journal of Micromechanics and Microengineering, 14(8), 1157–1164. https://doi.org/10.1088/0960-1317/14/8/307

[3] Toler, B. F., Coutu, R. A., & McBride, J. W. (2013). A review of micro-contact physics for microelectromechanical systems (MEMS) metal contact switches. Journal of Micromechanics and Microengineering, 23(10), 103001. https://iopscience.iop.org/article/10.1088/0960-1317/23/10/103001

[4] Weber, A. C. (2008). MEMS relays for make-break power switching applications:{111} silicon etched planar electrical contacts (Doctoral dissertation, Massachusetts Institute of Technology).

[5] Liu, H., Leray, D., Pons, P., & Colin, S. (2013, September). An asperity-based finite element model for electrical contact of microswitches. In 2013 IEEE 59th Holm Conference on Electrical Contacts (Holm 2013) (pp. 1-10). IEEE.

[6] Timpe, S. J., & Komvopoulos, K. (2005). An experimental study of sidewall adhesion in microelectromechanical systems. Journal of microelectromechanical systems, 14(6), 1356-1363.

[7] Vincent, M., Rowe, S. W., Poulain, C., Mariolle, D., Chiesi, L., Houzé, F., & Delamare, J. (2010). Field emission and material transfer in microswitches electrical contacts. Applied Physics Letters, 97(26).

[8] Chianrabutra, C. (2014). Investigation into the switching characteristics of gold coated carbon nanotubes under low current conditions (Doctoral dissertation, University of Southampton).

[9] Jiang, L., Wang, L., Huang, X., Huang, Z., & Huang, M. (2024). Implementation of highly reliable contacts for RF MEMS switches. Micromachines, 15(1), 155.

[10] Czaplewski, D. A., Nordquist, C. D., Dyck, C. W., Patrizi, G. A., Kraus, G. M., & Cowan, W. D. (2012). Lifetime limitations of ohmic, contacting RF MEMS switches with Au, Pt and Ir contact materials due to accumulation of ‘friction polymer’on the contacts. Journal of Micromechanics and Microengineering, 22(10), 105005.

[11] Warlimont, H., & Martienssen, W. (Eds.). (2018). Springer handbook of materials data. Springer.

[12] Islam, M. R., Karna, P., Bhatt, N., Thakur, S., Heinrich, H., Hirt, D. M., ... & Hopkins, P. E. (2025). Unveiling Phonon Contributions to Thermal Transport and the Failure of the Wiedemann-Franz Law in Ruthenium and Tungsten Thin Films. arXiv preprint arXiv:2505.07613.

[13] Milosevic, E., Kerdsongpanya, S., & Gall, D. (2018, November). The resistivity size effect in epitaxial Ru (0001) and Co (0001) layers. In 2018 IEEE Nanotechnology Symposium (ANTS) (pp. 1-5). IEEE.

[14] Lee, H., Coutu, R. A., Mall, S., & Leedy, K. D. (2006). Characterization of metal and metal alloy films as contact materials in MEMS switches. Journal of Micromechanics and Microengineering, 16(3), 557

[15] Weber, E. R. (1984). Diffusion, complexing and precipitation of transition metals in silicon. MRS Online Proceedings Library (OPL), 36,

[16] Islam, M. R., Karna, P., Tomko, J. A., Hoglund, E. R., Hirt, D. M., Hoque, M. S. B., ... & Hopkins, P. E. (2024). Evaluating size effects on the thermal conductivity and electron-phonon scattering rates of copper thin films for experimental validation of Matthiessen's rule. Nature Communications, 15(1), 9167.

[17] Zheng, P., & Gall, D. (2017). The anisotropic size effect of the electrical resistivity of metal thin films: Tungsten. Journal of Applied Physics, 122(13).

[18] Matula, R. A. (1979). Electrical resistivity of copper, gold, palladium, and silver. Journal of Physical and Chemical Reference Data, 8(4), 1147-1298.

[19] Dulmaa, A., Cougnon, F. G., Dedoncker, R., & Depla, D. (2021). On the grain size-thickness correlation for thin films. Acta Materialia, 212, 116896.

[20] Broué, A., Dhennin, J., Charvet, P. L., Pons, P., Jemaa, N. B., Coccetti, F., & Plana, R. (2010, October). Multi-physical characterization of micro-contact materials for MEMS switches. In 56th IEEE Holm Conference on Electrical Contacts (pp. 10-pages).

[21] Shen, L., & Wang, N. (2011). Effect of Nitrogen Pressure on the Structure of Cr‐N, Ta‐N, Mo‐N, and W‐N Nanocrystals Synthesized by Arc Discharge. Journal of Nanomaterials, 2011(1), 781935.

[22] Zhang, Y., Evans, J. R., & Yang, S. (2011). Corrected values for boiling points and enthalpies of vaporization of elements in handbooks. Journal of Chemical & Engineering Data, 56(2), 328-337.

[23] Miao, T., Ma, W., Zhang, X., Kubo, K., Kohno, M., Takata, Y., ... & Takahashi, K. (2014). Study on the cross plane thermal transport of polycrystalline molybdenum nanofilms by applying picosecond laser transient thermoreflectance method. Journal of Nanomaterials, 2014(1), 578758.

[24] Rossnagel, S. M. (2002). Characteristics of ultrathin Ta and TaN films. Journal of Vacuum Science & Technology B: Microelectronics and Nanometer Structures Processing, Measurement, and Phenomena, 20(6), 2328-2336.

[25] Rane, G. K., Menzel, S., Gemming, T., & Eckert, J. (2014). Microstructure, electrical resistivity and stresses in sputter deposited W and Mo films and the influence of the interface on bilayer properties. Thin Solid Films, 571, 1-8.

[26] Tabassum, T. (2017). Correlating Thermal Properties Of Sputtered Tantalum And Tantalum Nitride Thin Films Of Varying N_2 Content With Mechanical, Electrical And Structural Properties.

[27] Sun, H. L., Song, Z. X., Guo, D. G., Ma, F., & Xu, K. W. (2010). Microstructure and mechanical properties of nanocrystalline tungsten thin films. Journal of Materials Science & Technology, 26(1), 87-92.

[28] Makeswaran, N., Orozco, C., Battu, A. K., Deemer, E., & Ramana, C. V. (2022). Structural, optical and mechanical properties of nanocrystalline molybdenum thin films deposited under variable substrate temperature. Materials, 15(3), 754.

[29] Abadias, G., Colin, J. J., Tingaud, D., Djemia, P., Belliard, L., & Tromas, C. (2019). Elastic properties of α-and β-tantalum thin films. Thin Solid Films, 688, 137403.

[30] Das, S., Sozal, M.S.I., Li, W., John, D. (2024). Ultra-High-Temperature Ceramic Coatings ZrC, ZrB_2, HfC, and HfB_2. In: Pakseresht, A., Amirtharaj Mosas, K.K. (eds) Ceramic Coatings for High-Temperature Environments. Engineering Materials. Springer, Cham.

[31] Pierson, H. O. (1996). Handbook of refractory carbides and nitrides: properties, characteristics, processing and applications. William Andrew.

[32] Thorpe, F., Converse, E. S., Rivera, J., Rosenberg, W., & McCormack, S. J. (2026). Melting point of group IV and V transition metal diborides. Journal of the American Ceramic Society, 109(1), e70299.

[33] Niraula, Alin Babu, "Transport Properties of Binary and Doped Diborides" (2021). MSU Graduate Theses. 3672.

[34] Matkovich VI, Samsonov GV, Hagenmuller P, Lundstrom T, editors. Boron and Refractory Borides. New York: Spring-Verlag Berlin Heidelberg; 1977. p. 23.

[35] Magnuson, M., Hultman, L., & Högberg, H. (2022). Review of transition-metal diboride thin films. Vacuum, 196, 110567.

[36] Zhang, Z., Liang, H., Chen, H., Ding, L., Song, M., & Wang, J. (2021). Physical properties of high-temperature sintered TaB_2 under high pressure. Ceramics International, 47(7), 9061-9067.

[37] Šroba, V., Fiantok, T., Truchlý, M., Roch, T., Zahoran, M., Grančič, B., ... & Mikula, M. (2020). Structure evolution and mechanical properties of hard tantalum diboride films. Journal of Vacuum Science & Technology A, 38(3).

[38] Failla, S., Galizia, P., Fu, S., Grasso, S., & Sciti, D. (2020). Formation of high entropy metal diborides using arc-melting and combinatorial approach to study quinary and quaternary solid solutions. Journal of the European Ceramic Society, 40(3), 588-593.

[39] Simonenko, E. P., Simonenko, N. P., Kolesnikov, A. F., Chaplygin, A. V., Lysenkov, A. S., Nagornov, I. A., ... & Kuznetsov, N. T. (2022). Investigation of the Effect of Supersonic Flow of Dissociated Nitrogen on ZrB_2–HfB_2–SiC Ceramics Doped with 10 vol.% Carbon Nanotubes. Materials, 15(23), 8507.

[40] Li, H., Zhang, L., Zeng, Q., Guan, K., Li, K., Ren, H., ... & Cheng, L. (2011). Structural, elastic and electronic properties of transition metal carbides TMC (TM= Ti, Zr, Hf and Ta) from first-principles calculations. Solid State Communications, 151(8), 602-606.

[41] Sanches, D. M., Zillinger, J. M., Haghighat, A., & Hamilton, S. R. (2024). UZrCN Formation via Arc Melting–A Novel Synthesis Study (No. INL/CON-24-78745-Rev000). Idaho National Laboratory (INL), Idaho Falls, ID (United States).

[42] Aisyah, I. S., Wyszomirska, M., Calka, A., & Wexler, D. (2017). Nitrogenation of hafnium carbide powders in AC and DC plasma by Electrical Discharge Assisted Mechanical Milling. Journal of Alloys and Compounds, 715, 192-198.

[43] Mukasyan, A. S., & Rogachev, A. S. (2025). Combustion synthesis of ultra‐high temperature ceramics. International Journal of Applied Ceramic Technology, 22(6), e70044.

[44] Calculated according: Storms, E. K. (2013). The refractory (Vol. 2). Elsevier.

[45] A. K. Kuriakose and J. L. Margrave 1964 J. Electrochem. Soc. 111 827 DOI 10.1149/1.2426263

[46] Binner, J., Porter, M., Baker, B., Zou, J., Venkatachalam, V., Diaz, V. R., ... & Murthy, T. S. R. C. (2020). Selection, processing, properties and applications of ultra-high temperature ceramic matrix composites, UHTCMCs–a review. International Materials Reviews, 65(7), 389-444.

[47] Nino, A., Hirabara, T., Sugiyama, S., & Taimatsu, H. (2015). Preparation and characterization of tantalum carbide (TaC) ceramics. International Journal of Refractory Metals and Hard Materials, 52, 203-208.

[48] Craciun, D., Socol, G., Lambers, E., McCumiskey, E. J., Taylor, C. R., Martin, C., ... & Craciun, V. (2015). Optical and mechanical properties of nanocrystalline ZrC thin films grown by pulsed laser deposition. Applied Surface Science, 352, 28-32.

[49] Lasfargues, H., Glechner, T., Koller, C. M., Paneta, V., Primetzhofer, D., Kolozsvari, S., ... & Mayrhofer, P. H. (2017). Non-reactively sputtered ultra-high temperature Hf-C and Ta-C coatings. Surface and Coatings Technology, 309, 436-444.

[50] Schmid, B. (2024). Development of transition metal carbide-based superlattices (Doctoral dissertation, Technische Universität Wien).

[51] Merie, V., Pustan, M., Negrea, G., & Bîrleanu, C. (2015). Research on titanium nitride thin films deposited by reactive magnetron sputtering for MEMS applications. Applied Surface Science, 358, 525-532.

[52] Saha, B., Koh, Y. R., Feser, J. P., Sadasivam, S., Fisher, T. S., Shakouri, A., & Sands, T. D. (2017). Phonon wave effects in the thermal transport of epitaxial TiN/(Al, Sc) N metal/semiconductor superlattices. Journal of Applied Physics, 121(1).

[53] Ushakov, S. V., Navrotsky, A., Hong, Q. J., & van de Walle, A. (2019). Carbides and nitrides of zirconium and hafnium. Materials, 12(17), 2728.

[54] Rawat, V., Koh, Y. K., Cahill, D. G., & Sands, T. D. (2009). Thermal conductivity of (Zr, W) N/ScN metal/semiconductor multilayers and superlattices. Journal of Applied Physics, 105(2).

[55] Chawla, J. S., Zhang, X. Y., & Gall, D. (2013). Effective electron mean free path in TiN (001). Journal of Applied Physics, 113(6).

[56] Patsalas, P., Kalfagiannis, N., & Kassavetis, S. (2015). Optical properties and plasmonic performance of titanium nitride. Materials, 8(6), 3128-3154.

[57] Horita, S., Kobayashi, M., Akahori, H., & Hata, T. (1994). Material properties of ZrN film on silicon prepared by low-energy ion-assisted deposition. Surface and Coatings Technology, 66(1-3), 318-322.

[58] Yuan, L., Fang, G., Li, C., Wang, M., Liu, N., Ai, L., ... & Zhao, X. (2007). Influence of N_2 flow ratio on the properties of hafnium nitride thin films prepared by DC magnetron sputtering. Applied surface science, 253(20), 8538-8542.

[59] Aissani, L., Alhussein, A., Zia, A. W., Mamba, G., & Rtimi, S. (2022). Magnetron sputtering of transition metal nitride thin films for environmental remediation. Coatings, 12(11), 1746.

[60] Ul-Hamid, A. (2020). The effect of deposition conditions on the properties of Zr-carbide, Zr-nitride and Zr-carbonitride coatings–a review. Materials Advances, 1(5), 988-1011.

[61] Tillmann, W., Dias, N. F. L., Stangier, D., Tolan, M., & Paulus, M. (2019). Structure and mechanical properties of hafnium nitride films deposited by direct current, mid-frequency, and high-power impulse magnetron sputtering. Thin Solid Films, 669, 65-71.

[62] Aristova, N. M., Onufriev, S. V. E., & Savvatimskiy, A. I. (2024). Thermodynamic properties of zirconium nitride in the condensed state. Uspekhi Fizicheskikh Nauk, 194(10), 1082-1094.

[63] Seki, I., & Yamaura, S. I. (2017). Reduction of titanium dioxide to metallic titanium by nitridization and thermal decomposition. Materials transactions, 58(3), 361-366.

[64] Harrison, R. W., & Lee, W. E. Processing and properties of ZrC, ZrN and ZrCN ceramics: a review, Adv. Appl. Ceram. 115 (2016) 294–307.

[65] Pang, M., Peng, Y., Zhou, P., & Du, Y. (2018). Thermodynamic modeling of the Hf-N system. Journal of Mining and Metallurgy, Section B: Metallurgy, 54(1), 111-118

[66] Hoch, M., Dingledy, D. P., & Johnston, H. L. (1955). The Vaporization of TiN and ZrN. Journal of the American Chemical Society, 77(2), 304-306.

Characterisation of Pt/PEDOT/Si Layered Structures for MEMS Contacts

Nasser Aldhahri[a], Yoshishige Tsuchiya[a], Liam Boodhoo[a], Tomoyuki Kurioka[b], Punvinai Vinaisuratern[b], Joji Higuchi[b], Tso-Fu Mark Chang[b], Masato Sone[b], Thomas Bull[c], Yan Yang[d], and John W. McBride[c,d]

[a]School of Electronics and Computer Science, University of Southampton, Southampton, U.K.
[b]Institute of Integrated Research, Institute of Science Tokyo, Yokohama, Japan
[c]School of Engineering, University of Southampton, Southampton, U.K.
[d]TaiCaan Technologies, Southampton, U.K.

***Abstract*—Micro-electromechanical systems (MEMS) switches can be operated as electrical switches, enabling circuit opening and closing. However, MEMS contacts face reliability challenges, particularly under hot switching conditions where electrical loads pass directly through the contact. Failures often arise from mechanical wear, adhesion, or high contact resistance. Introducing a soft underlayer can improve contact reliability as demonstrated in previous work where Au coated CNT (Au/CNT) contacts demonstrated significantly longer lifetimes under hot switching compared to pure Au contacts [1]. Building on this approach, we investigate whether a conductive polymer Poly(3,4-ethylenedioxythiophene) (PEDOT) can serve as the soft underlayer. The Pt/PEDOT/Si layered structure was fabricated via electrodeposition and the electrical and mechanical properties of the contact were tested using an In-situ Contact Evaluation (ICE) system. Steady and reproducible molten metal bridge behaviour under hot switching has been identified from the voltage change across the contact in cyclic testing. Multiple step-like structures in the opening indicate transition to softening, and then to melting. Surface morphology observation of the contact region after the hot switching test suggests material removal after repeated switching cycles. Peculiar morphology observed around the indented region might be relevant to the fact that the underlayer is a polymer material.**

***Keywords*—MEMS switches, microscale contact, hot switching, material testing**

I. Introduction

Micro and Nano-Electromechanical System (MEMS/NEMS) fabrication technology has opened the door to switching devices which combine the advantages of mechanical switching, with the miniaturization associated with micro-fabrication technology. The advantages of MEMS switching are: high galvanic isolation when "off", leading to "zero" stand-by power with ultralow signal leakage, low resistance when "on", leading to low power loss with reduced Joule heating, and high compatibility with Si-based micro and nanofabrication technologies, leading to saving overall costs. Reliability challenges posed by electrical contact fatigue have remained for the more demanding, hot-switching condition where current flows as the contact opens and closes, resulting in deformation and wear, leading to increased contact resistance or adhesion and failure. A number of material combinations have been proposed for the MEMS switching solution [2–4], but to date there have been few commercially available devices.

For the hot-switching condition, a key factor is the switched voltage and current. In this study, a DC voltage of 4 V is used with a current range 10-20 mA. Under these conditions a molten metal bridge (MMB) will form on most switching cycles. The MMB and the associated transfer of material between two switching surfaces has been described in a number of publications [5, 6]; the key observation is that the MMB process leads to thin film surface wearing through to the substrate material, causing an increase in contact resistance and device failure after a relatively low number of hot switching cycles.

In [7, 8] an automated MEMS testing platform was introduced, to allow for the development and analysis of switching surfaces. The automated In-situ Contact Evaluation (ICE) apparatus is used to study contact performance for a low contact force (< 5 mN) switching application. The system uses a metrology frame to combine the controlled switching of surfaces up to a switching frequency of 2.5 kHz with the ability to measure the surface changes in-situ. After a defined number of switching cycles, the surfaces are separated within the metrology frame and the surface measured, then replaced to the same physical location to a precision of 50 nm.

The ICE system has been used in studies of contact wear for MEMS switching contacts [1, 8], where a gold coated ball (1 mm radius) makes contact with a gold coated carbon-nanotube structure, referred to as Au/CNT. The Au/CNT surface has two main physical attributes, firstly it allows for a contact resistance below 1 Ω, for a range of contact force below 2 mN; secondly the Au/CNT is very soft compared to the Au coated ball surface, which increases the area available for wear, increasing the number of cycles to failure. In [1], an investigation was conducted into surface wear over one million switching cycles using supply voltages of 4 and 8 V DC and hot-switching current levels ranging from 20 to 50 mA. In [8] the ICE system was used to investigate near cold-switching (zero current) with 4 billion cycles demonstrated.

Building on this approach, we investigate whether a conductive polymer (CP) Poly(3,4-ethylenedioxythiophene) (PEDOT) can serve as the soft underlayer, replacing the CNT

structure. Conducting polymers (CPs) are unique materials: mechanically soft or flexible as a polymer while conductive electrically. Recently, direct electrodeposition of CPs onto silicon has been demonstrated towards the development of CP/Si heterogeneous integration technology [9]. In addition, limited evidence exists for the use of PEDOT as a contact sublayer, which makes this investigation novel. PEDOT was also chosen because suitable samples were available through collaboration with the Institute of Science Tokyo (IST). The fabrication process can be explained in (II-B). Other soft conductive materials will be considered in future work.

Initial investigation of the PEDOT coated with a thin layer of platinum have been reported, in a surface referred to as Pt/PEDOT [10]. Hot-switching tests were conducted at a contact force of 1 mN and a switching frequency of 250 Hz using a 4 V DC supply. Under these conditions, a contact resistance of approximately 120 Ω was observed with a circuit current of about 15 mA, and molten metal bridge formation was identified during switching.

In this work we extend the previous study [10], in the evaluation of the Pt/PEDOT surface over 1 Million hot switching cycles at a nominal DC current of 20 mA, for direct comparison with benchmark studies of Au/CNT reported in [1].

II. Methodology

A. ICE system

The ICE system is a specialised apparatus designed to evaluate MEMS contacts under realistic operating conditions, see Fig. 1. It simulates MEMS switch cycling using a controlled piezo actuator and is capable of performing millions of switching cycles under precisely regulated force levels. Originally developed by TaiCaan [11], the system is designed to operate in both cold-switching and hot-switching modes. Hot switching involves applying an electrical current through the contact during actuation, enabling the study of electrical and mechanical interaction effects.

Furthermore, the ICE system is equipped with a confocal white light sensor that provides high-resolution 3D visualisation of the contact surface. This capability allows detailed assessment of wear, surface roughness, and deformation throughout the testing process.

B. Contact Materials

The contact evaluation procedure involves two primary contacts: the upper contact, mounted on the piezoelectric actuator, and the bottom contact, which serves as the main test surface. Fig. 2 depicts the two electrical contacts.

The upper contact is a stainless-steel sphere with a radius of $1\ \mathrm{mm}$. It is coated with a $10\ \mathrm{nm}$ chromium adhesion layer, followed by a $500\ \mathrm{nm}$ gold layer that forms the contact interface. The upper contact is mechanically mounted on the piezoelectric actuator, which provides high-precision vertical displacement. This enables accurate, repeatable, and controlled engagement with the bottom contact during each switching cycle.

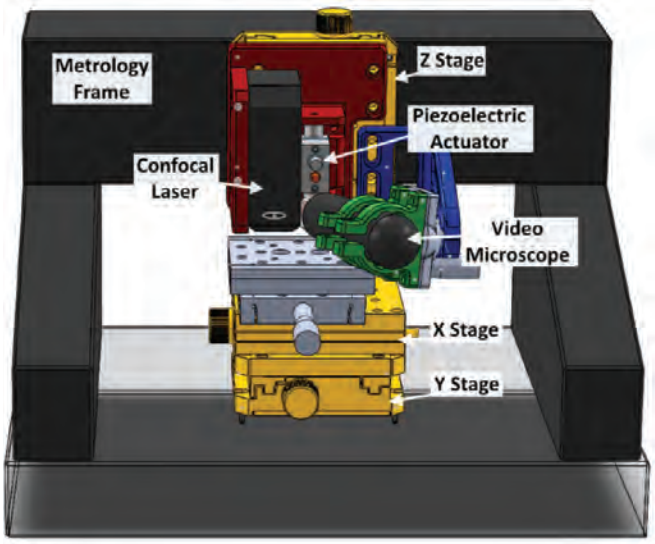


Fig. 1. A 3D representation of the ICE system, including an integrated actuator and sensor.

The bottom contact, representing the sample under test, consists of a Pt/PEDOT multilayer structure deposited on a silicon substrate. PEDOT, a conductive polymer known as poly(3,4-ethylenedioxythiophene), possesses desirable mechanical properties, particularly its elastic response, which can improve contact durability. Previous studies have shown that incorporating a soft underlayer can significantly increase the number of switching cycles [1]. For this reason, PEDOT was selected as the compliant underlayer in the contact structure. The PEDOT film was deposited via an electrodeposition method, as detailed in [10]. The PEDOT samples were fabricated at IST by electrodeposition on p-doped Si substrates $(2\ \mathrm{cm} \times 1\ \mathrm{cm})$. The substrates were first immersed in 5 wt.% HF and rinsed with deionised water. Electrodeposition was then carried out in a monomer-containing electrolyte. The amount of deposited polymer was controlled by the total charge passed. This process produced PEDOT-coated Si substrates for testing. The PEDOT layer had an estimated thickness of approximately $4\ \mu\mathrm{m}$. A platinum film with a thickness of $200\ \mathrm{nm}$ was then deposited onto the PEDOT, forming the final contact surface.

C. Contact Resistance Measurement

We employed two approaches to determine the contact resistance: a four-wire measurement and a measurement using a data acquisition (DAQ) device.

1) 4-wire Measurement:

The four-wire measurement technique is widely used for precise low-resistance measurements, making it suitable for evaluating contact resistance in MEMS switch contacts. Unlike the conventional two-wire method, the four-wire configuration eliminates the influence of lead, probe, and wiring resistance, thereby providing significantly improved accuracy. In this method, two wires supply a constant current through the

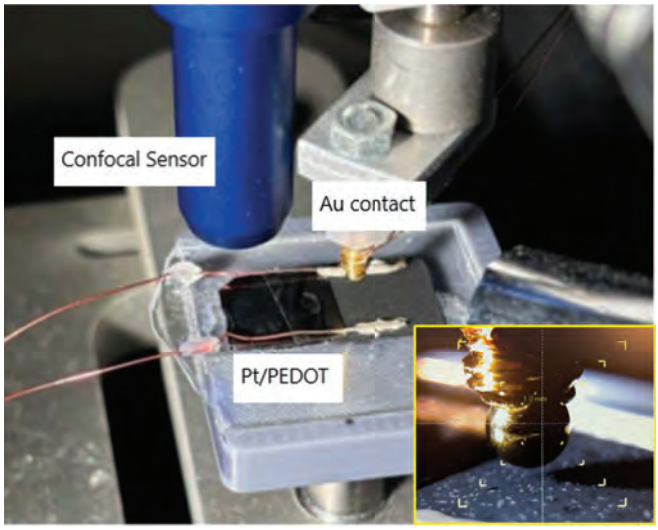


Fig. 2. Gold-coated sphere mounted on the actuator and the lower Pt/PEDOT contact, with a confocal sensor used for measuring the contact surface (bottom right). Close-up view of the gold-coated sphere and Pt/PEDOT contact interface, showing micro-scale white features that correspond to non-conductive materials.

contact, while the other two wires function as voltage-sensing leads that measure only the voltage drop across the contact. Because the sensing voltmeter has an extremely high input impedance, the current flowing through the sense wires is negligible, ensuring that the measured voltage reflects the true contact resistance. In this experiment, two wires were mounted on the gold spherical contact, while two additional wires were connected to the Pt/PEDOT bottom contact, as shown in Fig. 2. The contact resistance was measured using a Keithley 580 Micro-Ohmmeter, a precision instrument designed specifically for accurate low-resistance characterisation.

2) DAQ-Based Contact Resistance Measurement:
A data acquisition (DAQ) device was employed to measure the contact resistance as part of the experimental setup. The DAQ system provided a convenient method for simultaneously recording the voltage drops and current levels within the circuit, enabling an alternative estimation of the contact resistance, see Fig. 3.

In this configuration, a known series resistor ($R_a = 210\ \Omega$) was incorporated into the circuit. The DAQ measured the voltage drop across this resistor (V_a), from which the circuit current was calculated using Ohm's law. The DAQ also recorded the voltage drop across the contact (V_c). Using the measured values of V_a, V_c, and the known resistor R_a, the contact resistance was calculated as $R_c = V_c/(V_a/R_a)$.

This DAQ-based approach enabled continuous monitoring of the electrical behaviour of the contact under varying operating conditions. Although less precise than the four-wire ohmmeter measurement, it provided a practical means of tracking relative changes in contact resistance throughout the experiment.

D. Measurement of Contact Resistance responding to Displacement (Static Testing)

The contact resistance varies with the contact area, such that an increase in contact area leads to a reduction in contact resistance. The contact displacement refers to the movement of the upper contact toward the bottom contact. The contact resistance varies with the indentation depth of the spherical upper contact into the target contact. As the displacement increases, the contact resistance decreases because the upper contact is pressed further toward the lower contact. This behaviour occurs because the effective contact area enlarges with increasing normal force, thereby reducing the overall resistance at the contact [12].

The ICE system provides precise control over the vertical displacement of the top contact. By integrating the ICE apparatus with the four-wire measurement configuration, it is possible to simultaneously record both the contact resistance and the corresponding contact displacement. The gold spherical contact (Au ball) is mounted on a piezoelectric actuator, which is positioned on a computer-controlled Z-stage. The Z-axis motion is controlled using the TaiCaan XYris software. The piezoelectric actuator is capable of delivering high-precision displacement adjustments ranging from 0 to 20 μm.

E. Measurement of Contact Resistance responding to Contact Force (Dynamic Testing)

A force sensor is integrated into the ICE system, enabling direct measurement of the impact and retraction forces during both closing and opening cycles. In the dynamic testing, the closing impact force was recorded. The force signal is monitored through an oscilloscope connected to the ICE system, where a sensitivity of 1 V corresponds to 1 mN of force.

The piezoelectric actuator is driven by a function generator, which controls the rate of closing and opening through an adjustable waveform. A square-wave signal at 0.1 Hz was used in this study, as it provides a clear and well-defined force profile, simplifying the measurement of both contact force and contact resistance.

The Au-Pt/PEDOT contact was evaluated under varying contact forces. The applied force was adjusted by increasing the average position of the piezo controller while monitoring the corresponding force displayed on the oscilloscope. Both the contact resistance and the contact force were measured simultaneously using the ICE system. The contact resistance was characterised using both the four-wire measurement technique and the DAQ-based method. Fig. 3 illustrates the contact switching setup and its electrical connections, including the function generator and the DAQ device used for resistance measurements. This configuration allowed a detailed evaluation of the Au-Pt/PEDOT contact response under different applied forces.

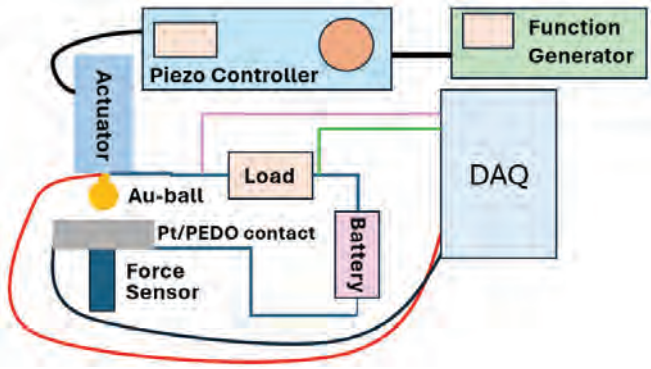


Fig. 3. Contact switching testing setup using a function generator and a DAQ device for resistance measurements.

F. One Million Cycles Switching Test

A one-million-cycle switching test was conducted to evaluate the contact performance under hot switching conditions using the ICE system.

The switching operation was driven by a sine-wave signal at 250 Hz for a total of one million cycles, as this has been shown to best reflect cycling in a MEMS cantilever device. The test duration was approximately 66.5 minutes. During the test, the contact resistance was measured using a DAQ device. Contact resistance measurements were taken every 5 minutes, corresponding to approximately 75,000 switching cycles between the measurements. The signal shape and frequency were temporarily modified only for the purpose of contact resistance measurement; once the measurement was completed, the signal was returned to the original running conditions.

A 4 V DC battery was connected to the circuit with a 210 Ω load resistor in series with the contact. An impact force of 1 mN was applied and controlled using a piezo controller, and the force level was monitored using an oscilloscope to ensure it remained constant throughout the test.

G. Site Measurement

The tested sites were visualised using a confocal sensor, which enabled observation of contact surface structure after testing and measurements of the depth of deformation at the contact site.

III. Results and Discussion

A. Contact Resistance Response to Contact Displacement

Two static tests were conducted at the same contact site to observe the variation of contact resistance as the upper contact was incrementally displaced toward the Pt/PEDOT contact. The tests were performed using the ICE system in combination with the four-wire measurement technique, which allows precise measurement of the Au-Pt/PEDOT contact resistance at each incremental displacement level, ensuring a clear correlation between displacement and electrical contact resistance.

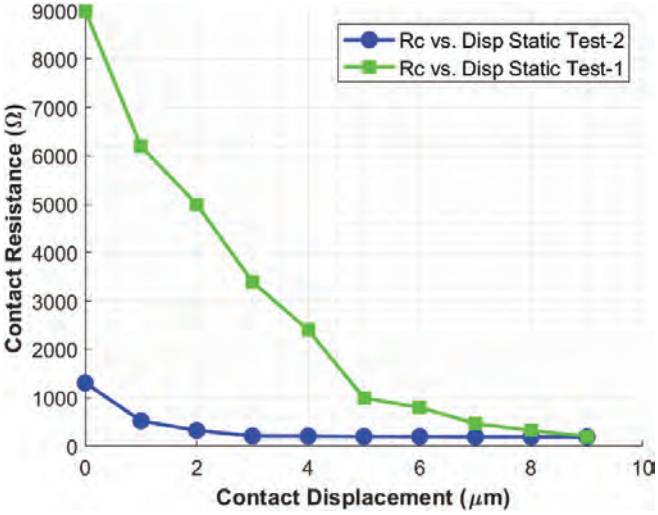


Fig. 4. Contact resistance as a function of contact displacement for two static tests conducted at the same contact site. Square markers (green) represent the first measurement, while circle markers (blue) correspond to the second measurement, showing a lower initial contact resistance during the second test.

Fig. 4 shows the measured contact resistance as the displacement was increased in steps of 1 μm. The result of the first test shows a clear decrease in resistance during the initial stages of displacement, which can be attributed to the increase in effective contact area. After several displacement increments, the resistance stabilises and exhibits minimal variation, reaching approximately 195 Ω.

The second test exhibits a lower initial contact resistance compared to the first test, particularly at the early displacement stages. The higher resistance observed during the first static test is attributed to the presence of non-conductive micro-asperities at the contact interface, as shown in Fig. 2. The second test result suggests that the contact was established between more conductive regions with a larger effective contact area and fewer non-conductive asperities.

B. Contact Resistance vs. Contact Force Under Dynamic Switching

Dynamic switching tests were conducted four times to evaluate the contact resistance of the Pt/PEDOT contact as a function of applied force: two measurements were performed using a four-wire ohmmeter and two using a DAQ-based measurement approach. As expected, the contact resistance decreases with increasing applied force due to the enlargement of the effective contact area. Beyond a certain force level, further increases in force result in minimal change in resistance, indicating that the contact interface has reached a mechanically stable electrical condition.

The same dynamic force-dependent measurements were then repeated to measure contact resistance using DAQ. The results from both measurement techniques are shown in Fig. 5. While both methods exhibit the same overall behaviour of decreasing contact resistance with increasing

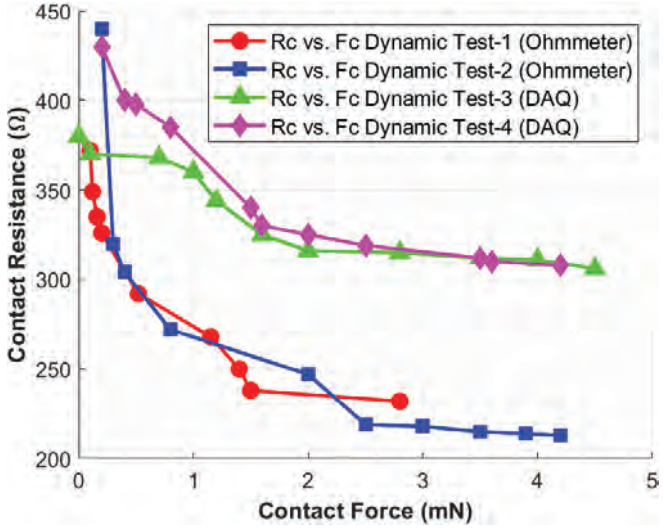


Fig. 5. Contact resistance as a function of applied contact force measured at the same contact site using four dynamic tests. Two measurements were performed using a four-wire ohmmeter, and two using a DAQ-based method.

force, the DAQ-device measurements consistently report higher resistance values than those obtained using the four-wire ohmmeter. This discrepancy is primarily attributed to the measurement configuration: the DAQ-based method effectively operates as a two-wire measurement, making it more susceptible to additional series resistance introduced by connecting wires and leads. Nevertheless, the DAQ-based measurements remain suitable for capturing relative changes in contact resistance.

C. Contact Resistance During one million cycles in hot switching

The one-million-cycle hot switching test was conducted using the ICE system to evaluate the endurance of the Au-Pt/PEDOT contact under dynamic switching conditions.

Fig. 6 shows the contact resistance as a function of the number of switching cycles under hot switching conditions at an applied contact force of 1 mN. The measured contact resistance showed no significant variation over the course of the one million switching cycles, with an average value of approximately 320 Ω. A slight decrease in contact resistance was observed after the first measurement interval, which is likely associated with the hot switching process promoting the removal or thinning of the contaminant layer formed by the Pt frictional polymer at the contact surface. From Fig. 5, the DAQ method measurement shows a contact resistance in the range of 360–370 Ω at a contact force of 1 mN. In Fig. 6, the initial contact resistance measured at the same physical location on the contact surface is approximately 370 Ω, which decreases to around 320 Ω after one million hot-switching cycles.

Based on the applied voltage and total circuit resistance, the average current flowing through the contact was estimated to be approximately 7.5 mA. No abrupt changes in resistance

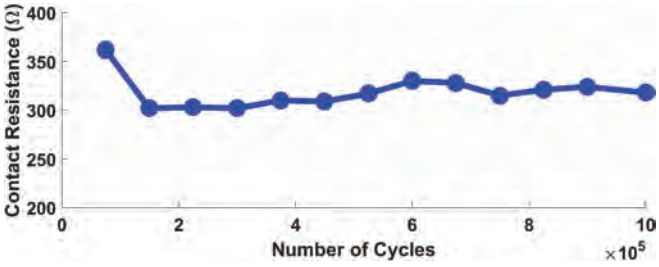


Fig. 6. Contact resistance as a function of switching cycles measured during a one-million-cycle hot switching test at 1 mN contact force and 250 Hz, showing stable resistance behaviour with an average value of approximately 320 Ω.

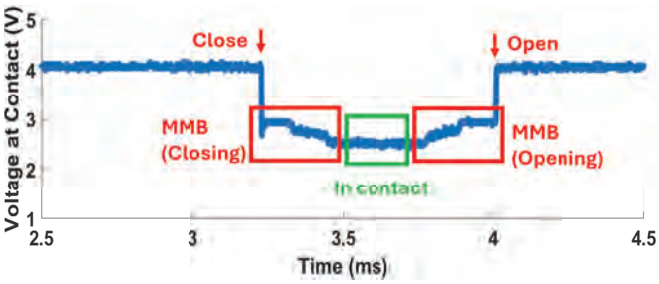


Fig. 7. Transient voltage signals recorded between 0.9 million and 1 million hot switching cycles at 1 mN contact force and 250 Hz, showing a voltage of approximately 2.5 V across the contact and evidence of molten metal bridge formation during opening and closing.

were observed, indicating consistent electrical behaviour throughout the one million cycle hot switching test.

D. Transient Voltage During Hot Switching

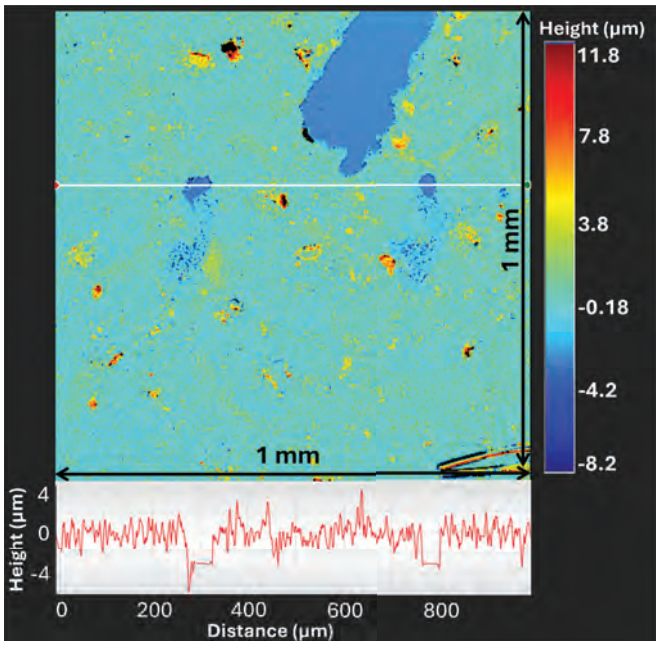
Transient voltage signals were recorded during the cycling interval between 0.9 million and 1 million switching cycles. The switching was performed under hot switching conditions using a 4 V DC battery, resulting in an approximate current of 7.5 mA. Fig. 7 shows a transient voltage signal for a single closing and opening event recorded during this interval, with the voltage drop across the contact measured at closure approximately 2.5 V. The recorded transient voltage waveforms indicate the formation of a molten metal bridge (MMB) during both the opening and closing phases of the switching cycle. Specifically, the MMB formation is observed as a voltage interaction between approximately 3 V and 2.5 V, corresponding to a voltage difference of about 0.5 V, remaining for a duration of approximately 0.5 ms during the moments of contact closing and opening. The formation of the MMB is attributed to the contact between the Au upper contact and the Pt/PEDOT bottom contact, where the softening voltage of Au is lower than that of Pt, leading to targeted melting of the gold at the contact interface. A molten metal bridge is a temporary molten metallic connection formed between the contacting electrodes due to local heating during hot switching.

E. Site Measurement Results

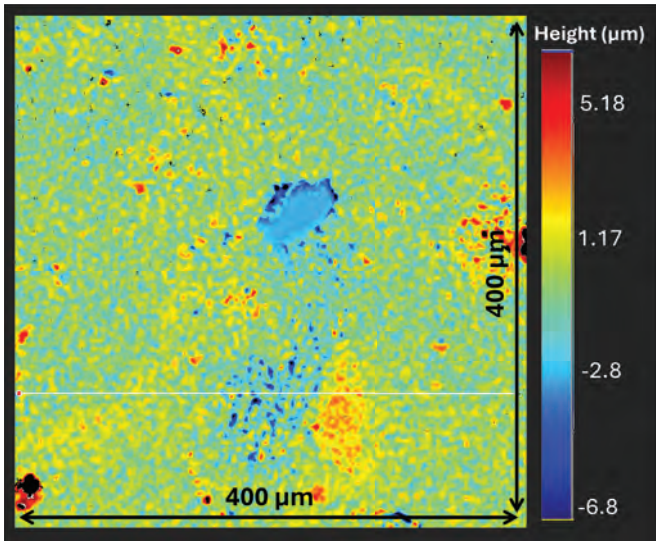
The contact site was examined using a confocal sensor to visualise the surface morphology and to measure the

depth of deformation resulting from repeated switching. This non-contact optical technique enabled accurate characterisation of the contact surface features following the switching test.

Fig. 8a shows two tested contact sites following one million hot-switching cycles. Site A, shown on the right-hand side of the figure, corresponds to a previously conducted test [10], while Site B, shown on the left-hand side, represents the contact site evaluated in this work. Fig. 8b presents the magnified image of Site B. Confocal sensor measurements indicate that both sites exhibit a wear region where the Pt/PEDOT surface is removed, exposing the base Si surface, where the depth is approximately 3 μm after one million hot-switching cycles. This deformation reflects the mechanical impact of repeated hot switching on the Pt/PEDOT contact, highlighting the combined effects of electrical loading and impact contact force during the switching process.



(a)



(b)

Fig. 8. (a) Surface profile of the Pt/PEDOT contact showing two contact sites after hot switching cycles: Site A corresponds to a previously tested contact location [10], while Site B represents the contact site evaluated in this work. (b) Measurement results for Site B (current test), showing a deformation depth of approximately 3 μm.

In this study, a sensor was used to measure the contact surface and generate its topography for feature analysis. the contact surface showed a deformation of approximately 4 μm , which is not considered suitable for MEMS contact applications. Therefore, the Pt/PEDOT structure requires further improvement. This may include depositing an Au layer to reduce the contact resistance and increasing the metal layer thickness to improve the overall contact surface condition.

F. Comparison of Pt/PEDOT and Au/MWCNT Contacts

A comparison with Au/MWCNT revealed several differences in the behaviour of Pt/PEDOT contacts. ICE testing showed that the contact resistance of Au/MWCNT was below 1 Ω, which was lower than that of Pt/PEDOT. Surface topography also showed that Au/MWCNT had lower roughness than Pt/PEDOT, where the higher roughness of Pt/PEDOT was attributed to the electrodeposition process. In terms of deformation, Au/MWCNT exhibited a contact deformation of approximately 8 μm after 10 million cycles, whereas Pt/PEDOT showed about 4 μm after 1 million cycles. Both Au/MWCNT and Pt/PEDOT exhibited molten metal bridge formation during hot switching. However, Au showed softer behaviour, likely because its softening and melting voltages are lower than those of Pt. Overall, Au/MWCNT showed better reliability than Pt/PEDOT as a contact material for MEMS switches.

IV. Conclusion

We fabricated the Pt/PEDOT/Si layered structure via electrodeposition and investigated the electrical and mechanical properties of the contact using an In-situ Contact Evaluation (ICE) system. In cyclic testing, steady molten metal bridge behaviour under hot switching was confirmed, where characteristic step-like structures at switching indicate transition to softening and melting. Surface morphology of the contact region observed after the hot switching test suggested removal of materials after repeated switching cycles. The relatively high contact resistance could be caused by a rough and thin Pt surface affected by the surface roughness of the polymer underneath. The wear performance of over 1 million hot switching cycles suggests that further developments to the formulation could improve the overall performance. The results from two different testing sites on their morphology and electrical characteristics were found to be consistent. Peculiar morphology observed around the indented region could be specific to polymer underlayers.

We are investigating the effect of PEDOT thickness on contact resistance. The results may indicate an influence on

contact resistance due to the conductivity of the Pt layer on PEDOT. Nevertheless, the contact resistance may still remain relatively high, which is not desirable for MEMS contact applications. Therefore, a more effective approach to reducing contact resistance may be to modify the contact material structure. One possible approach is to deposit an Au layer on Pt/PEDOT to reduce the contact resistance, since Au has higher electrical conductivity than Pt.

Simulation of the mechanical behaviour of the Pt/PEDOT structure under applied load might be considered in future work. Such an analysis may provide insight into the effects of varying contact force and contact area on the mechanical and electrical characteristics of the MEMS contact.

REFERENCES

[1] J. McBride and T. Bull, "The in-situ wear of a hot and cold switched au on au coated mwcnt electrical contact for a mems switch application," in *2019 IEEE Holm Conference on Electrical Contacts*. IEEE, 2019, pp. 149–155.

[2] B. F. Toler, R. A. Coutu, and J. W. McBride, "A review of micro-contact physics for microelectromechanical systems (mems) metal contact switches," *Journal of Micromechanics and Microengineering*, vol. 23, no. 10, p. 103001, 2013.

[3] R. A. Coutu Jr, P. E. Kladitis, K. D. Leedy, and R. L. Crane, "Selecting metal alloy electric contact materials for mems switches," *Journal of Micromechanics and Microengineering*, vol. 14, no. 8, p. 1157, 2004.

[4] A. Basu, G. Adams, and N. McGruer, "A review of micro-contact physics, materials, and failure mechanisms in direct-contact rf mems switches," *Journal of Micromechanics and Microengineering*, vol. 26, no. 10, p. 104004, 2016.

[5] F. L. Jones, "Physics of electric contacts," 1947.

[6] J. McBride, "The wear processes of gold coated multi-walled carbon nanotube surfaces used as electrical contacts for micro-electro-mechanical switching," *Nanoscience and Nanotechnology Letters*, vol. 2, no. 4, pp. 357–361, 2010.

[7] J. McBride and T. G. Bull, "An automated in-situ contact evaluation (ice) system for mems/nems electrical contact material evaluation," *Metrology Letters*, 2022.

[8] T. G. Bull, J. W. McBride, and L. Jiang, "The influence of circuit parameters on molten bridge surface degradation in a au/mwcnt mems switch contact," in *2018 IEEE Holm Conference on Electrical Contacts*. IEEE, 2018, pp. 359–365.

[9] T. Kurioka, P. Vinaisuratern, J. Higuchi, K. Okamoto, T. M. Chang, N. Aldhahri, J. W. McBride, Y. Tsuchiya, and M. Sone, "Electrodeposition of conducting polymers on silicon towards integrated autonomous sensor systems," in *Proceedings of the 51st International Micro and Nano Engineering Conference (MNE 2025)*, Southampton, UK, September 2025.

[10] Y. Tsuchiya, T. Kurioka, P. Vinaisuratern, J. Higuchi, T. M. Chang, M. Sone, N. Aldhahri, L. Boodhoo, T. Bull, Y. Yang, and J. W. McBride, "Mechanical and electrical contact testing for Pt/PEDOT/Si layered structures," in *Proceedings of the 51st International Micro and Nano Engineering Conference (MNE 2025)*, Southampton, UK, September 2025.

[11] TaiCaan Technologies. Ice system. TaiCaan Technologies. [Online]. Available: https://taicaan.com/ice-system/

[12] P. G. Slade, *Electrical contacts: principles and applications*. CRC press, 2017.

Mating Cycle Component-Level Testing for E-Mobility: Mating Force, Micro-Ohm Contact Resistance, and Wear

Felix GREINER
TE Connectivity
Bensheim, Germany
felix.greiner@te.com

Sönke SACHS
TE Connectivity
Bensheim, Germany
ssachs@te.com

Frank OSTENDORF
TE Connectivity
Bensheim, Germany
frank.ostendorf@te.com

***Abstract*— The terminal mating force accounts for approximately 70%-80% of the total connector mating force and is closely related to the contact resistance. To address this critical factor, specialized equipment called a "mating cycle machine" was developed for this research, with particular focus on metal terminals that serve as an intermediate testing level between basic cap-and-flat model evaluations and complete connector assemblies with housings.**

During testing, both mating forces and contact resistances are simultaneously monitored and recorded throughout the entire process. The mating cycle machine enables detailed analysis of individual mating events, revealing how mechanical components interact and progressively develop enhanced mechanical and electrical functionality as penetration advances.

By examining data collected across thousands of mating cycles, researchers can establish correlations between wear patterns and various factors including surface finish characteristics, materials, and lubricant properties.

This study outlines the testing methodologies employed and presents comprehensive test findings.

Keywords*— *component level testing, mating, High-Power Charging (HPC) terminals

I. Introduction

The rapid advancement of electric mobility has intensified the need for precise and repeatable methods to characterize the mechanical and electrical performance of metal terminals. As charging technologies progress toward High-Power Charging (HPC) and emerging Flash-Charging concepts capable of replenishing significant energy within only a few minutes, connector terminals must support extremely high current densities while maintaining stable contact interfaces. To enable this development, rigorous component-level testing, in which terminals are evaluated without the surrounding connector housing, has become essential for isolating fundamental contact behaviors.

This paper presents the design and application of a dedicated mating cycle machine developed specifically for such component-level investigations. The machine provides automated insertion and extraction motions with tightly controlled boundary conditions while measuring mating forces and contact resistance with high temporal and mechanical precision. Two representative terminal types are examined. The first is a flat power terminal typically mated only once during vehicle assembly, with occasional remating during service. The second is the 8 mm round HPC terminal defined by IEC 62196-1 [1], which must withstand 10,000 mating cycles, incorporating a substantial safety margin to reflect real-world user conditions.

By applying uniform test protocols to both terminal types, the mating cycle machine enables systematic evaluation of degradation mechanisms and offers key insights supporting the design of next-generation connectors capable of meeting the demanding reliability, thermal stability, and durability requirements of high-power and ultra-fast EV charging.

A. Component Level Testing

Fig. 1 illustrates six testing levels with increasing abstraction, ranging from operational tests down to model test. Component level testing is positioned between aggregate and specimen testing, enabling isolated evaluation of individual terminals. This level balances physical realism and experimental control, supporting systematic analysis of mechanical and electrical behavior independent of system-level influences like sealings or alignment of plastic housing features.

CATE-GORY	MEASUREMENT AND TESTING TECHNOLOGY		SYSTEM, ASSEMBLY, MODEL
I	Operational tests and operation-like tests: • Original system structure • Load simplified	OPERATIONAL TEST	
II		TEST BENCH TRIAL	
III		AGGREGATE TEST	
IV		COMPONENT TEST	
V	Model structure and simple load	SPECIMEN TEST	
VI		MODEL TEST	

Fig. 1. Categories of tribological measurement and testing techniques, [2].

B. Mating cycle test requirements and implementation

Table 1 summarizes the normative test requirements for both terminal types at the component-level and contrasts them with their realization in the mating cycle machine.

IEC 62196-1 does not specify all test parameters in detail. For instance, the mating speed for normal operation testing – defined as the primary use case of the mating cycle machine – is not specified in the standard ([1] §23). At the same time, IEC 62196-1 defines a mating speed in a different context, namely for tests related to braking capacity ([1] §22). As this

test scenario does not correspond to the intended use case of the mating cycle machine, the coexistence of these provisions may lead to ambiguity.

TABLE I. MATING CYCLE TEST REQUIREMENTS AND IMPLEMENTATION

Mating cycle test requirements for a) Automotive flat power terminal silver-plated specified generally according to [3], [4], e.g. MCON 12 Contact system [5]. b) 8 mm round High Power Charging terminals silver-plated acc. to IEC 62196-1:2022 [1].	**Implementation in the mating cycle machine**
a) [5] max. 20 N insertion and withdrawal force of the terminal b) [1] §16.16: max. 100 N insertion and withdrawal force of the whole connector with at least two terminals	max. ± 200 N
a) [3], [4] TG 11: 50 mm/min insertion and withdrawal speed b) [1] §23: not specified for normal operation	max. ± 100 mm/s a) 50 mm/min = 0.83 mm/s b) typ. ± 20 mm/s and 24 strokes per min
a) [3], [4] TG 11: For silver-plated terminals 50 cycles without current load b) [1] §23.3: 10 000 cycles without current load	electric x-stage with several Mio. cycles lifetime
Not specified for mating test but generally relevant for judging on functionality of the terminal: a) [3], [4] TG 12: For silver-plated terminals, 50 K temperature rise is the basis for definition of the rated current b) [1] §24.1: max. 50 K temperature rise of the terminal when rated current applied, see Fig. 10, depending on the wiring mostly in two digits µΩ range.	µΩ resistance 4 wire online measurement with ≤ 1.5 A at ≤ 2 V or dry circuit conditions (≤ 100 mA at ≤ 20 mV) and thermal simulation
b) [1] §23.3: after each 1 000 cycles exposed to salt and sand and allowed to dry completely before resuming the cycling test	manual (adjacent lab)
a) [3], [4]: after test: min. 20% silver remaining b) [1] §23.3: after the test: no wear impairing the further use	a) typ. SEM / EDX (adjacent lab) b) microscopic inspection (adjacent lab)

II. EXPERIMENTAL

A. Layout of the mating cycle machine

Fig. 2 presents a schematic overview of the mating cycle machine, comprising a manual y–z alignment stage, force sensor, terminal pair, electrically driven x-stage, and contact resistance measurement.

Fig. 3 shows the laboratory apparatus, which modularly integrates four identical test stations in parallel. The same figure presents a detailed photograph of one test station, illustrating the real-world implementation of the components depicted schematically in Figure 2.

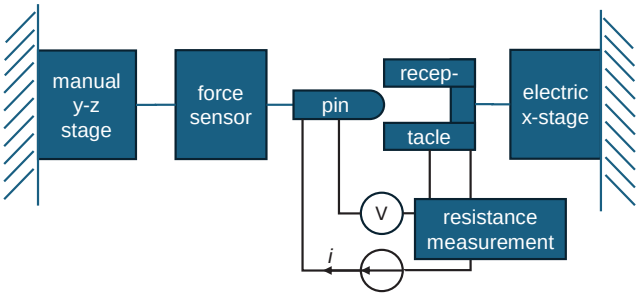


Fig. 2. Layout of one mating cycle machine test station.

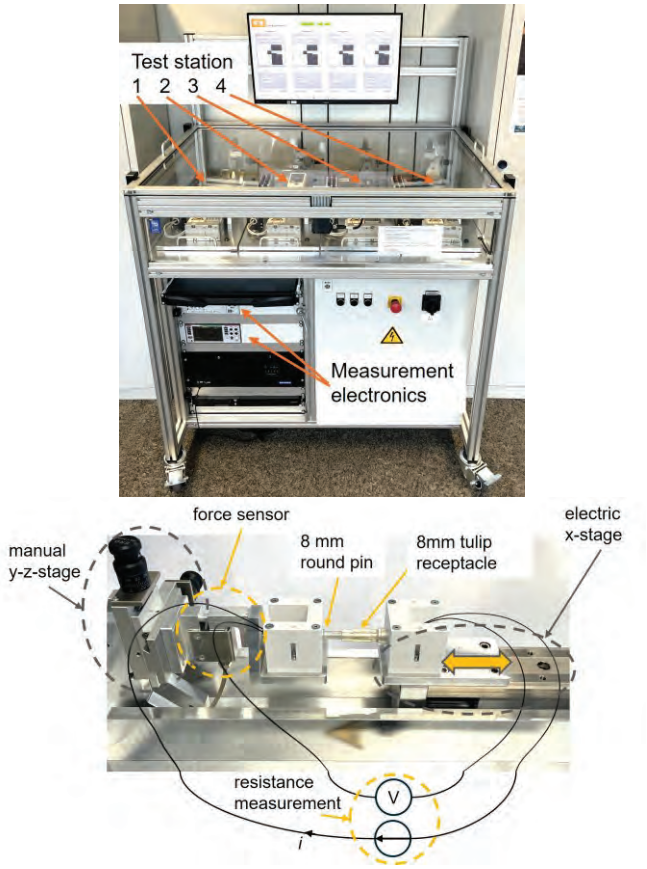


Fig. 3. Overview on the mating cycle machine (top), test station with details (bottom).

B. Calibration studies – resistance measurement

Calibration studies were conducted to ensure measurement accuracy and data reliability, which is particularly critical for the custom-built mating cycle machine with its modular configuration options. Fig. 4 illustrates the implementation of the reference shunt and reference force sensor used for system verification.

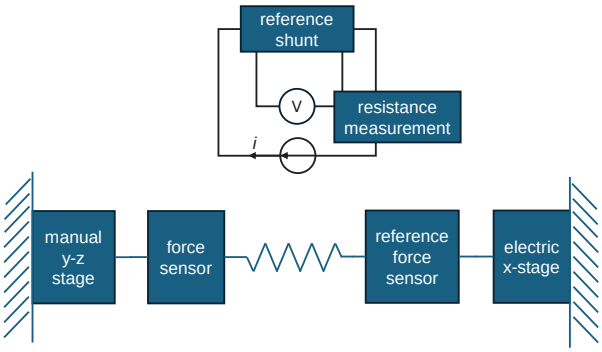


Fig. 4. Concept of reference shunt and reference force sensor implementation for calibration studies.

As a first step, the resistance measurement was investigated across all 4 test stations. For accelerated testing, achieving a high sampling rate is essential. A rate of 15 Hz was achieved for both evaluated variants: (a) test current fulfilling the dry-circuit conditions ≤ 100 mA at ≤ 20 mV without thermoelectric voltage offset compensation and (b) energized measurement mode of ≤ 1.5 A at ≤ 2 V. Other configurations, including offset-compensated measurements, were available by the equipment but not considered here due to their lower sampling rates.

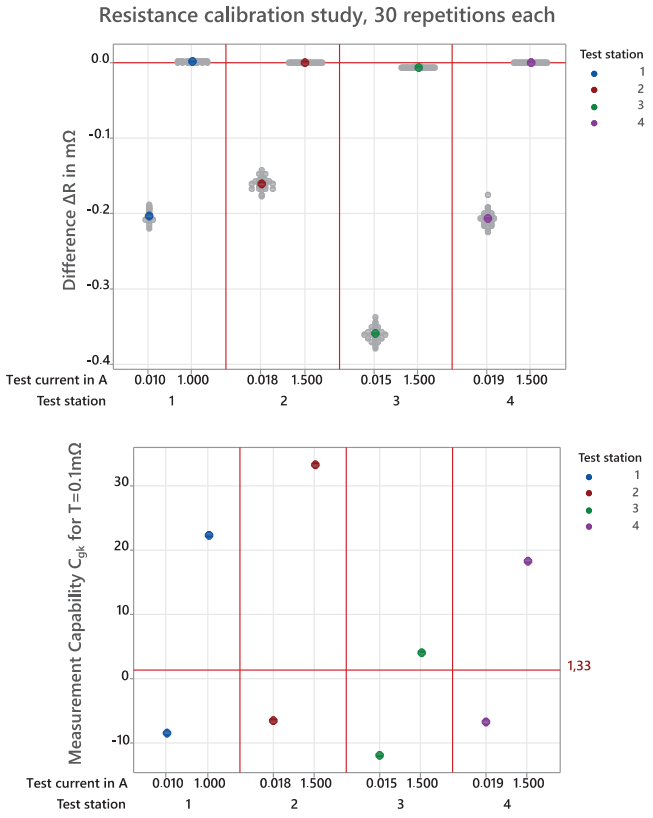


Fig. 5. Resistance calibration study: readings and capability results.

Fig. 5 summarizes the resistance calibration results obtained with a R_{shunt} = 1.00006 mΩ reference shunt. The difference ΔR to the measured resistance R_{measured} is defined by

$$\Delta R = R_{\text{measured}} - R_{\text{shunt}} \tag{1}$$

The top graph difference ΔR in mΩ over test stations and applied test currents reveals pronounced measurement errors under (a) dry-circuit conditions. This behavior is also illustrated in the bottom graph of Fig. 5, which depicts the measurement capability C_{gk}

$$C_{\text{gk}} = \frac{0.1\,T\ - |\bar{x} - x_{\text{m}}|}{3\,s} \tag{2}$$

In this expression, T denotes the tolerance range, x_{m} is the resistance of the reference shunt resistor, s represents the standard deviation of the measured resistance values, and $\bar{x}$ is the mean of the measured resistance values [6]. For a typical high power terminal tolerance specification of T = 0.1 mΩ tested under dry-circuit conditions, the capability study shows $C_{\text{gk}} < 1.33$, indicating that only qualitative trends can be detected.

In contrast, the (b) energized measurement mode (≤ 1.5 A at ≤ 2 V) shows $C_{\text{gk}} > 1.33$, demonstrating that the mating cycle machine is well suited for accurate absolute resistance evaluation under these conditions.

The inadequate performance under dry-circuit conditions is primarily caused by the internal wiring between the central resistance measurement units and the test stations, which exhibits 1-2 Ω resistance while a 1 mΩ resistor is under test. Due to the ≤ 20 mV voltage limit, the thermoelectric voltage offset due to the Seebeck effect at uncontrolled room temperature become significant and cannot be compensated at high sampling rates. Additionally, temperature-dependent wiring resistances directly enter the measurement equation, causing a substantial increase in uncertainty and rendering dry-circuit conditions unsuitable for power terminals testing at 1 mΩ and below.

C. Calibration studies – force measurement

The reference force sensor was implemented as shown in Fig. 4. For the force calibration study, a spring has been mounted instead of the terminal pair, so the electric x-stage facilitated to repeatedly apply different force levels. In Fig. 6, the output of the mating cycle machine force sensor F_{measured} is plotted against the reference force sensor $F_{\text{reference}}$. A secondary y-axis at an enlarged scale depicts the force difference ΔF defined by

$$\Delta F = F_{\text{measured}} - F_{\text{reference}} \tag{3}$$

This characterization has been conducted on all test stations, while only test station 2 results are shown here as an example.

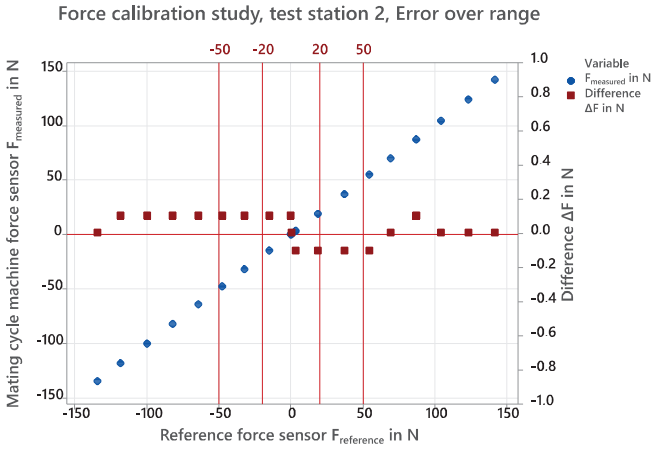


Fig. 6. Force calibration study: characterization results.

In Fig. 7, the same values scaling is applied in the subsequent comparison across four force levels and four test stations, revealing superior performance of test station 2. In Fig. 8, for a typical power-contact force tolerance of T = 20 N, the calculated measurement capability fulfils $C_{\text{gk}} > 1.33$ for all test stations, confirming reliable force characterization with the mating cycle machine.

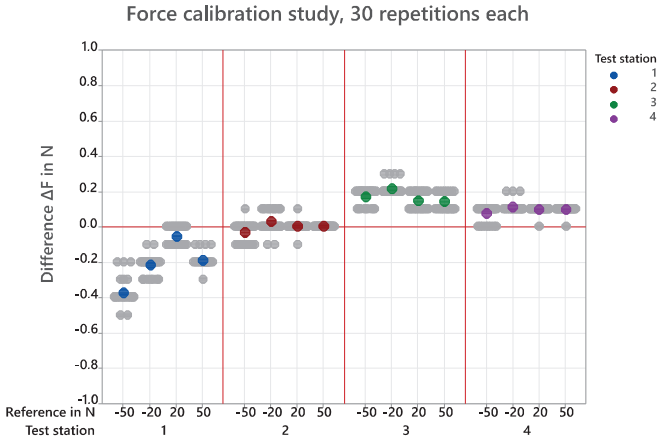


Fig. 7. Force calibration study: repeated testing readings.

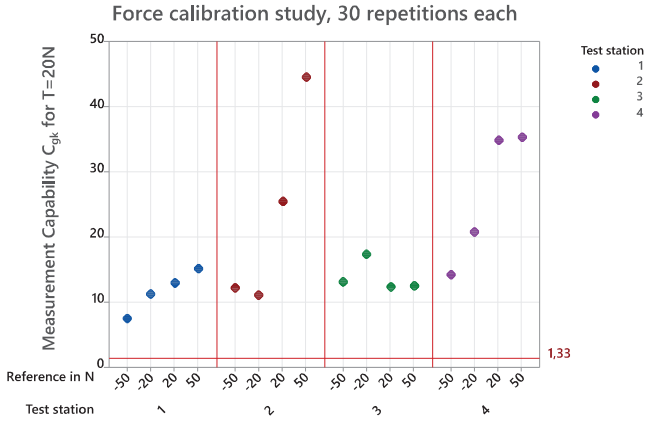


Fig. 8. Force calibration study: repeated testing capability results.

III. Results

A. *Flat power terminal testing*

For automotive flat power terminals, the first mating cycle is critical, as it defines the maximum mating force relevant to car assembly factory ergonomics requirements. Understanding the contribution of individual terminal spring elements to this initial force is therefore essential. At the same time, identifying how these elements influence terminal resistance enables targeted optimization. Fig. 9 correlates mating force and contact resistance with the specific receptacle-terminal elements, providing a comprehensive and previously unavailable insight. Alongside the engagement of successive contact rows, a superposed decrease in bulk resistance over the mating position becomes apparent. This combined analysis supports the tailored design of terminals that achieve low mating forces, low electrical resistance, and high vibration resilience simultaneously.

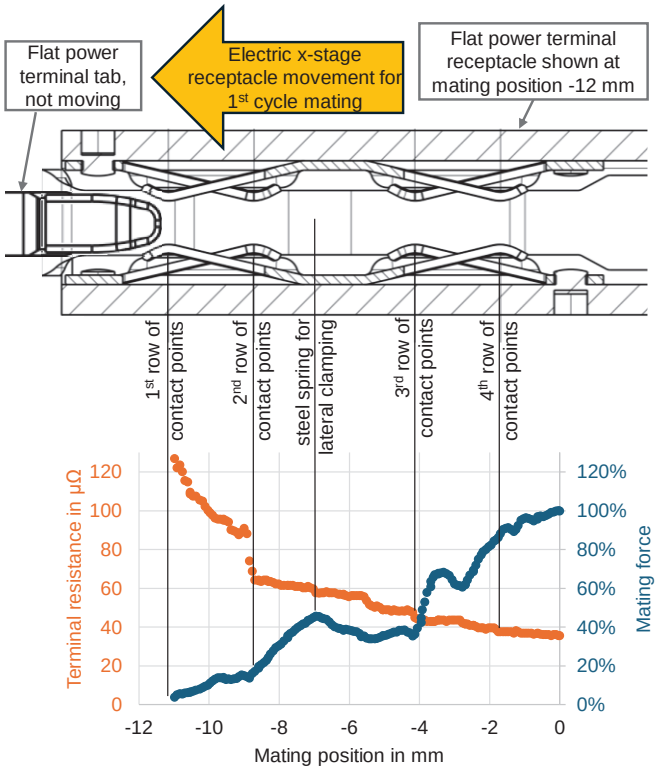


Fig. 9. Silver plated flat power terminal 1st cycle testing results, pre-serial conditions.

B. *8 mm round HPC terminal testing*

For the 8 mm round contact system, durability over several thousand mating cycles is the primary focus. While the mating cycle machine records force and resistance continuously over the entire stroke, direct evaluation of this high-resolution dataset is possible but impractical for assessment of the resistance in the completely plugged charging situation.

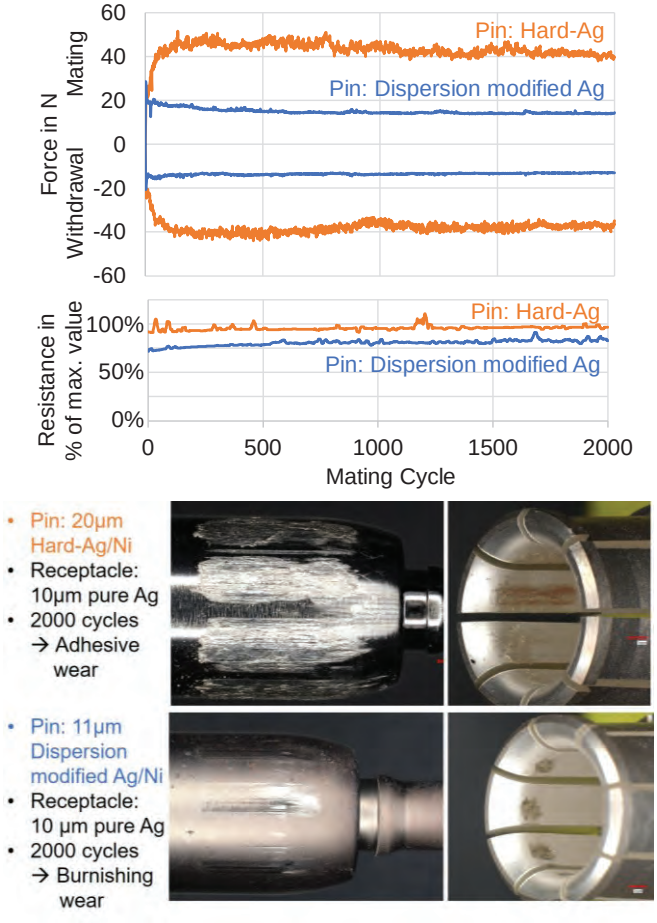


Fig. 10. 8 mm round HPC 2 000 cycles terminal testing results

Therefore, Fig. 10 presents the maximum mating and withdrawal forces plotted over the number of mating cycles for 2 000 cycles maximum, enabling clear trend analysis. As an example, two significantly different pin plating variants are shown to present the spectrum of the mating cycle machine. The pin with the Hard-Ag plating under test shows a significant increase in mating force reaching the maximum allowed force after some tens of cycles. The pin with dispersion modified Ag plating under test shows less than half of this mating force value and a very stable behavior.

In addition, the contact resistance at the plugged position is shown. Again, the performance of the Dispersion modified Ag excels the one of Hard-Ag. In this measurement series, the resistance includes the complete bulk resistances of receptacle and pin. For relative comparison, the current entry and the voltage drop need to be executed identically from test to test. For the plot, the resistance value is scaled to % of the final resistance of the Hard-Ag plated pin.

Complementary microscopic images illustrate typical wear mechanisms on both pin and receptacle, supporting the

interpretation of the mechanical and electrical evolution observed during cycling.

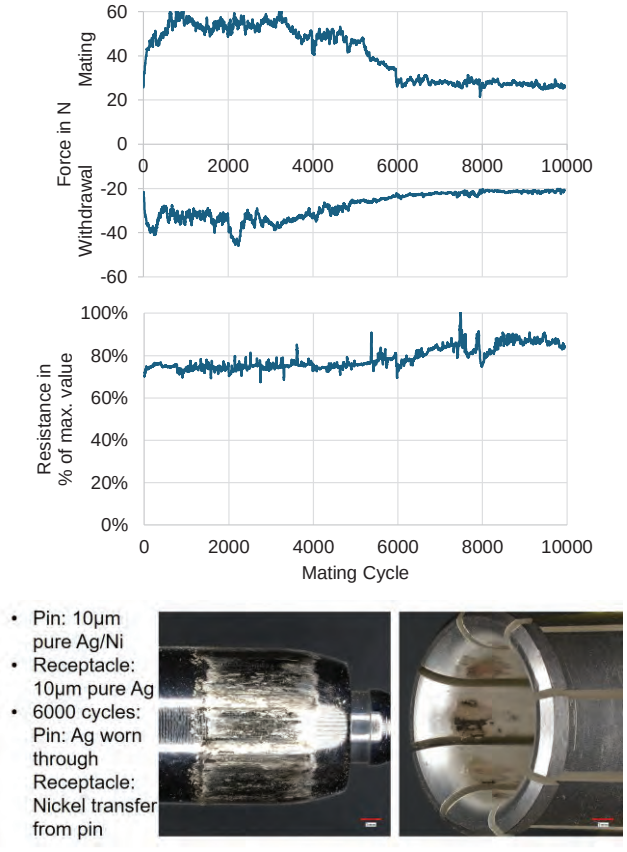


Fig. 11. 8 mm round HPC 5x2 000=10 000 cycles terminal testing results.

Similarly, Fig. 11 presents the results of 10 000 mating cycles, conducted in five sections, with optical inspections performed after every 2 000 cycles. Images taken after 2 000 and 4 000 cycles show the pin to be intact, whereas the receptacle already exhibits exposed copper. After 6 000 cycles, partial wear-through of the silver plating on the pin down to the nickel layer is observed, while the receptacle shows black nickel transferred from the pin. Correspondingly, the force curve reveals a reduction in force between 4 000 and 6 000 cycles, which aligns well with the observed wear behavior.

After 8 000 cycles, partial wear-through of the pin's nickel plating becomes evident, progressing further up to 10 000 cycles. Although the contact resistance scaled to the maximum value of this test exhibits only minor changes over most of the cycling, an increase is observed once copper is exposed on both mating surfaces.

C. Electrical performance evaluation

While mating-force requirements are well defined (Table I) – case-specific for flat power terminals and < 50 N for 8 mm round HPC terminals – the evaluation of contact resistance is less straightforward. Low resistance values in the mating cycle machine alone are insufficient, as freshly cleaned copper surfaces from accelerated testing in the mating cycle machine may appear advantageous without representing oxidation taking place in the car and without ensuring thermal robustness. The 50 K temperature-rise criterion in physical testing is therefore the most relevant performance metric to judge on the electrical performance of the terminal.

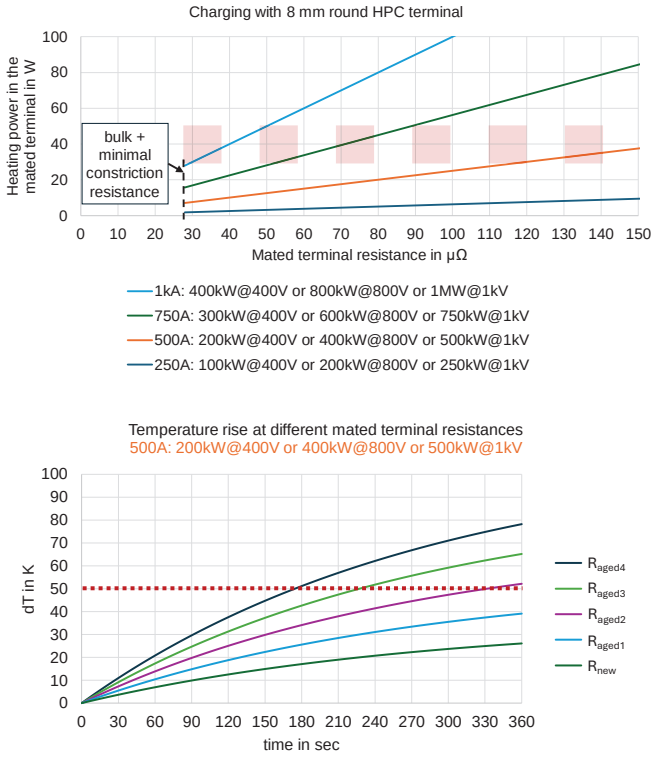


Fig. 12. Fundamental thermal calculations on 8 mm round HPC terminal connected to 95 mm² copper or 200 mm² aluminum conductors (inside car, no cooling) and actively cooled charging gun: Heating power of mated terminal over mated terminal resistance for four load cases (top); For load case 500A: temperature rise over time for different terminal conditions (bottom).

To put the terminal resistance into general context, Fig. 12 illustrates the impact of increasing contact resistance on an 8 mm round HPC terminal based on fundamental thermal simulations [7]. Therefore, this is a rough estimation of what may happen during high power charging, not exactly representing the test conditions acc. to [1]. For 95 mm² copper and 200 mm² aluminum conductors in the car (no cooling in the car) and an actively cooled charging gun, the terminal heating power rises rapidly above 30-50 W (top graph), necessitating current derating. While charging at 250 A remains thermally uncritical, the widely used 500 A charging scenario in European vehicles generally requires current derating after several minutes, depending on the thermal behavior of both terminals – the vehicle-side pin and the charging-gun receptacle. In the bottom graph, the temperature rise dT over time is given for an exemplary new pair of terminals with the resistance R_{new} as well as multiple resistances after hypothetical terminal aging steps R_{aged1} to R_{aged4}. Starting from a lab environment of $T = 25°C$, d$T = 50°C$ corresponds to a terminal temperature of $T = 75°C$.

The megawatt-level flash charging poses a significant challenge to the 8 mm round terminal size, making minimal contact resistance essential for sustained high-power operation as well as cooling at the charging gun and in the car.

IV. Conclusions

The mating cycle machine has demonstrated high versatility in revealing detailed terminal behavior and wear mechanisms at component level facilitating the benchmarking of terminal products as well as plating variants. The calibration studies have identified measurement capabilities, therefore limitations are known and can be handled to prevent from wrong conclusions to component behavior. Testing individual terminals instead of complete connectors with housings significantly simplifies experimentation while increasing analytical depth.

For flat power automotive terminals, the machine provided in-depth insights into first-mating behavior and force–resistance interactions. For the 8 mm round HPC automotive terminal, during testing up to 10 000 cycles, plating quality and environmental exposure were shown to have a strong influence; customer-unacceptable surface grease must therefore be functionally integrated into the plating [8], [9].

The accelerated testing of 8 mm round HPC terminals at 24 strokes per minute suppresses any effect of oxidation that may apply in car applications. To better simulate and analyze “real world” conditions, an accelerated oxidation step could make sense like heating of the terminals. Further, testing with salt and sand exposure and “allow to dry completely” without a measure of “dry” brings the risk of unknown lubrication of thin films of water.

Future improvements include simplified alignment, easier clearance adjustment, automated time-lapse wear imaging, and assessment of temperature logging as well as defined heating and cooling of the terminals.

Acknowledgment

The authors would like to thank Michael Ludwig for his valuable support with the thermal simulations. Special thanks are extended to Vaibhavi Deogharkar and Drashti Jayeshbhai Vaghani for their excellent contributions to the development, setup, and operation of the mating cycle machine. The authors also thank Jan Hartmann for his patience and valuable support during the data analysis phase.

Disclaimer and Trademark

TE expressly disclaims any implied warranty regarding the information contained herein, including, but not limited to, the implied warranties of merchantability or fitness for a particular purpose. TE Connectivity, TE, TE connectivity (logo) and MCON are trademarks owned or licensed by the TE Connectivity plc family of companies.

References

[1] *IEC 62196-1:2022-05 Plugs, socket-outlets, vehicle connectors and vehicle inlets - conductive charging of electric vehicles*, May 2022. https://webstore.iec.ch/en/publication/59922

[2] H. Czichos and H. Sturm, ‘Tribologische Mess- und Prüftechnik’, in *Tribologie-Handbuch: Tribometrie, Tribomaterialien, Tribotechnik*, H. Czichos and K.-H. Habig, Eds, Wiesbaden: Springer Fachmedien, 2020, pp. 245–310. doi: 10.1007/978-3-658-29484-7_9.

[3] Zentralverband Elektrotechnik und Elektronikindustrie e.V., Ed., ‘ZVEI Technical Guideline TLF0214 Validation-of-Low-Voltage-Automotive-Connectors’. Jun. 2024. https://www.zvei.org/en/press-media/publications/technical-guideline-tlf-0214-validation-of-low-voltage-automotive-connectors

[4] *Tentative Standard DIN/TS 70214:2025-11 Road vehicles - Validation of automotive low-voltage connectors*, Nov. 2025. https://www.dinmedia.de/de/vornorm/din-ts-70214/391951202

[5] TE Connectivity, Ed., ‘MCON 12 Contact System: Product Specification 108-94518’. https://www.te.com/commerce/DocumentDelivery/DDEController?Action=srchrtrv&DocNm=108-94518&DocType=Specification%20Or%20Standard

[6] Verband der Automobilindustrie e. V., Ed., ‘VDA_05 Measurement and Inspection Processes’. Jul. 2021. https://webshop.vda.de/QMC/de/volume-05-measurement-and-inspprocesses_072021

[7] M. Ludwig, M. Leidner, H. Schmidt, and F. Ostendorf, ‘Thermal Equivalent Circuits: An Approach to Rate High-Power Connectors for Electric Mobility Applications’, in *30th International Conference on Electrical Contacts*, Online Switzerland, 2021.

[8] S. Sachs and I. Buresch, ‘Advanced Silver Coatings for Connector Applications in E-Mobility’, in *submitted to 33rd International Conference on Electrical Contacts, unpublished*, Trondheim Norway, 2026.

[9] T. Israel, M. Oberst, C. Hildmann, and S. Schlegel, ‘Self-lubricating coatings for high-current connectors’, in *31st International Conference on Electrical Contacts*, Sapporo Japan, 2022.

Innovative Stamped Terminals plated with reel-to-reel Silver Graphite for Automotive Connectors

Porte Maxime
Product Engineering
APTIV Services Deutschland GmbH
Neumarkt in der Oberpfalz, Germany
Maxime.porte@aptiv.com

Rene Lehmann
Product Engineering
APTIV Services Deutschland GmbH
Neumarkt in der Oberpfalz, Germany
Rene.lehmann@aptiv.com

Abstract — With the increasing demands of autonomous driving systems, predictable automotive terminal performance and high lifetime reliability have become more critical than ever. This paper presents an innovative reel-to-reel silver-graphite electroplating technology for automotive stamped terminals, addressing long-standing limitations of conventional gold- and silver-plated solutions — particularly in the context of rising precious-metal prices. Traditional silver coatings exhibit known vulnerabilities including atmospheric sulphuration, unstable friction coefficients, and degradation caused by cold-welding effects, prompting the search for more robust and cost-effective alternatives.

In this work, silver-graphite reel-to-reel post-plated terminals were produced and subjected to a comprehensive series of evaluations, including mating-cycle performance, contact resistance after thermal ageing, coefficient-of-friction measurements, and detailed plating and cross-sectional analyses. Preliminary results demonstrate that silver-graphite plating offers lower and more stable friction, superior resistance to sulphuration and cold welding, and consistent electrical resistance over lifetime-relevant conditions.

Furthermore, the impact of stamping on the performance and integrity of the silver-graphite layer was investigated. Metallurgical analyses of the silver and graphite composition were conducted to define material-concentration specifications and the associated quality-control requirements necessary for serial manufacturing processes.

Keywords— connectors, plating, silver-graphite, AgC, silver, automotive, precious metal reduction

I. Introduction

With the recent strong price increase of precious metals, the engineers need to find alternatives to gold plating for the automotive terminals. Gold plating on copper alloys requires a barrier layer, mostly based on Nickel to avoid copper diffusion into the functional gold layer. Moreover Nickel is improving adhesion and robustness of the gold plating of the terminal systems [1]. Indeed for these applications (Safety, Airbag control units ECU, ABS) low signals/currents below 40mA need to be transmitted through the terminals of the connectors and for such cases standard tin plating could lead to a risk of malfunction due to surface oxidation and a consequential contact resistance increase. Pure silver material (over nickel) is at that stage not a suitable candidate because of its susceptivity to sulfide compounds present in the atmosphere leading to contact resistance increases. Moreover the usage of anti-tarnish is also subject to complains and it is almost impossible to control in production neither at the material manufacturer nor at terminal supplier. Its effects are still subjected to investigations [2],[3].

Several studies have reported investigations of terminals coated using post-plating processes, such as barrel plating, highlighting the effects of these methods on coating uniformity, adhesion, and long-term electrical performance. These investigations often focus on how the post-plating approach influences critical characteristics such as contact resistance, wear resistance, susceptibility to sulphuration, and overall mechanical reliability under repeated mating cycles [4],[5].

In this paper, we investigate the use of silver-graphite (AgC) material in a reel-to-reel plating process for automotive terminals. The plated terminals, which are subsequently welded to cables, form part of a connector together with other electrical components (e.g., ferrite elements) (Figure 1). Integrated into an automotive wiring harness, the connector must reliably transmit signals to a specific ignition device.



Fig. 1. *Example of connectors for critical safety applications.*

Gold plating on terminals offers low insertion force which benefits a mechanical stability of the connector design and reduce significantly mechanical wear and fretting corrosion susceptibility.

In the first part of this paper we will present the product, requirements and the silver graphite plating parameters for reel-to-reel. Spheric and flat coupons will be realized first to proceed to the material characterization, then the terminals will be plated and evaluated through a comprehensive testing [6],[7]. The coefficient of friction (CoF), contact resistance, optical and electronic microscopy will be performed. Finally a discussion on the results will be provided and the next steps to this study will be proposed.

II. Presentation and Requirements

A. Plating presentation

The Table 1 and 2 gather the AgC electrolyte and some key plating parameters for which the coupons and terminals have been plated for this study.

Parameter	Value
Silver content	25 – 35 g/l
Graphite content	80 – 120 g/l
Cyanide	90 – 150 g/l
Temperature	18 – 25 °C
Plating speed	1 µm in 0.25 min at 6 ASD
Plating Technology	R2R

Table 1. AgC electrolyte parameters

Solid dispersion	1 – 2 wt% graphite particles in silver matrix
Plating thickness	~ 4 – 6 µm
Density	9.8 g/cm³
Hardness	70–80 HV 0.025 after storage
Appearance/color	semibright, white/grey

Table 2. silver graphite plating parameters

On top of the nickel layer deposited on the copper alloy substrate, a thin silver strike (<1 µm) is applied. This strike layer serves to ensure optimal adhesion of the subsequent silver graphite (AgC) layer, which has a thickness of 6 µm maximum. The silver strike is critical because it promotes strong metallurgical bonding between the nickel underlayer and the AgC coating, preventing delamination during mechanical stress or repeated mating cycles. It is also important to note that no passivation treatment is applied after plating, allowing the AgC surface to retain its electrical conductivity and low-friction properties. Figure 2 illustrates the complete layer structure, showing the copper alloy substrate, nickel underlayer, silver strike, and the silver graphite topcoat. This layered arrangement is commonly used in automotive terminals to provide a balance of mechanical durability, corrosion resistance, and stable electrical performance under the demanding conditions of connector applications.

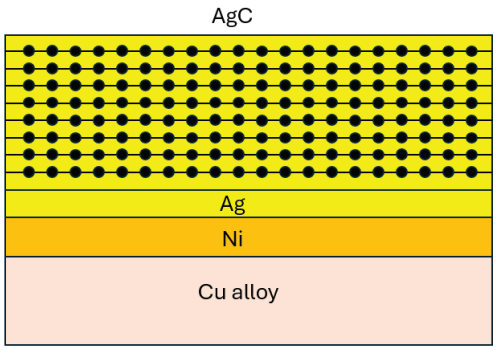


Fig. 2. *Plating layer construction above the base metal.*

Figure 3 describes the reel to reel process applied to plate the male and female parts. The EP degreasing and surface activation are the first necessary steps before plating the nickel layer. Then a strike of silver is applied before AgC deposition for final layer adhesion purposes. Finally an ultrasonic cleaning is made.

The AgC plating line should be isolated due to contamination risk by graphite particles into other processes and due to dispersion condition an individual cell setup is required.



Fig. 3. *R2R Plating line setup*

B. Sphere / Flat coupons

Some sphere-flat coupons have been produced to perform some testing independently of any design and to set the initial specifications for the AgC material performance. The band of metal is 0,25mm thick and the radius of the sphere is 1,6mm. Samples with gold and silver graphite have been created (Figure 4).

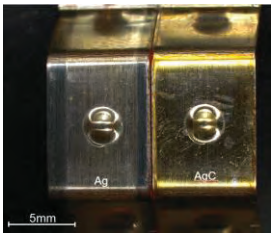


Fig. 4. *Photograph of the sphere coupons plated with gold and AgC.*

C. Terminal for Safety Restraint System

The reel-to-reel stamped and formed terminals have a round shape and 3 contact springs in order to have a stable mechanical behaviour and balance once the cylindrical pin (1mm diameter) is inserted. The contact type is crossed cylinder on cylinder. Some exemplary pictures of the terminals, contact springs and gap size are shown in the Figure 5.

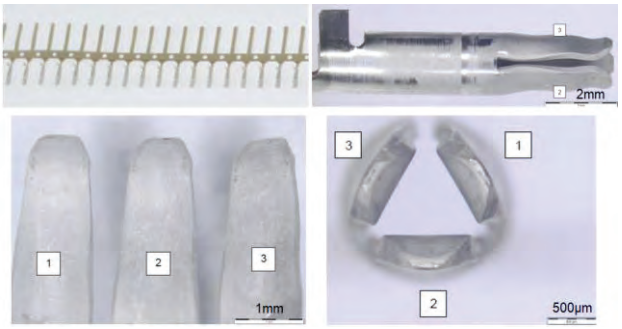


Fig. 5. *Photograph of the stamped terminals.*

The male pins are also plated with silver graphite and gold for the test references. Figure 6 gather some photographs of the plated pin terminals and the plated surfaces.

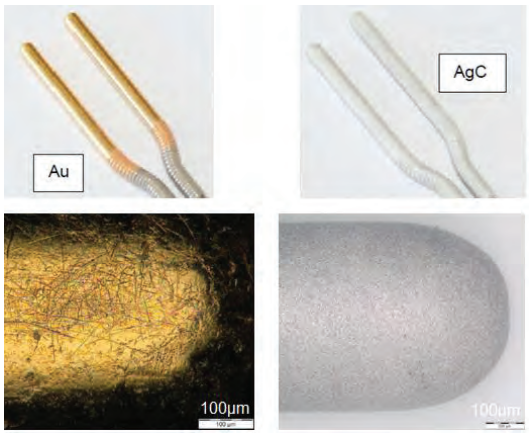


Fig. 6. *Photograph of the male pins plated with gold and silver-graphite.*

III. METHODOLOGY

A. *Contact normal force and insertion force*

The contact normal forces were examined using a measuring device specially adapted to the 1mm terminal system. Figure 7 is a description of the test device and force measurement principle.

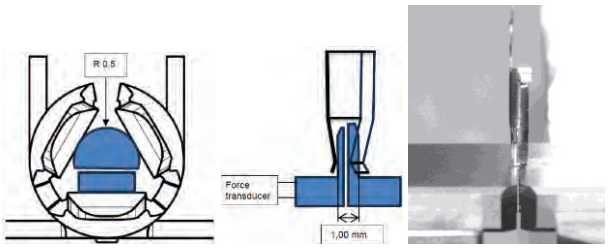


Fig. 7. *Principe of the test apparatus to measure the contact normal force.*

In order to evaluate the range of contact normal force to apply in the sample characterization, the terminals have been subjected to an thermal ageing at 125°C for up to 1000 hours in order to evaluate the drop in contact normal force due to mechanical and thermal relaxation of the design and the material. The results collected in Figure 8, show an initial force of 2.5N, a minimum of 1.5N is reached after 1000h hours. The remaining contact normal force after the temperature stress are still in appropriate range for having a reliable electrical contact between the surfaces.

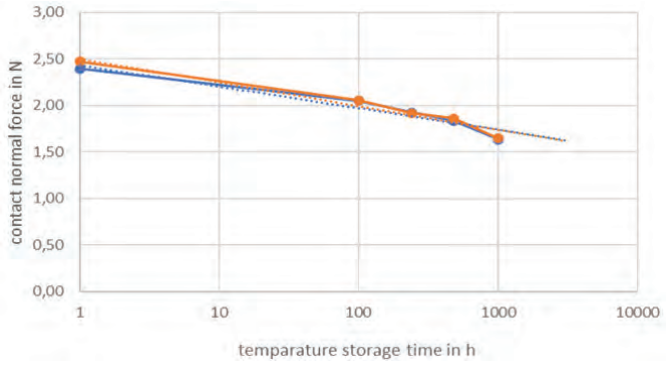


Fig. 8. *Contact normal force versus ageing time at 125°C.*

Figure 9 gathers some optical pictures of the mating areas after 1000 hours ageing and male terminal extraction. The AgC surface isn't looking much different than the initial samples, no specific tarnishment of the female or male parts can be noticed. In addition, the extractions of each male terminal didn't lead to any significant cold weld surface degradation.

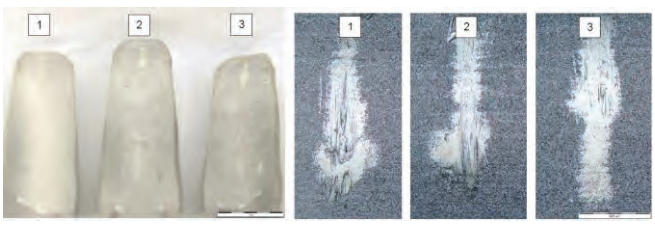


Fig. 9. *Photograph of the female after* 1000 hours ageing and male terminal extraction. 1, 2 and 3 are the male/female contacting areas.

The measurement of the force during the mating cycles of the plated terminals will be one of the most important criteria in this paper. Figure 10 show the device enables to align perfectly the male and female terminal. The forces will be recorded over a contact overlapping of 3mm.

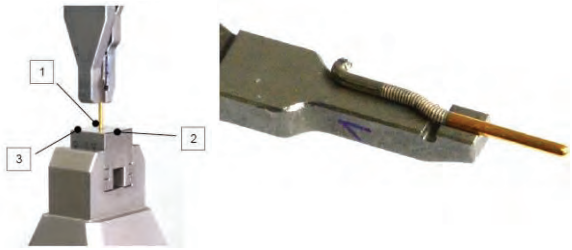


Fig. 10. *Photograph of the clamping device for terminal mating.*

B. *Coefficient of friction on coupons*

A constant normal force of 1 N and 2.5 N will be applied to sphere-on-flat coupons in order to represent the minimum and maximum contact forces of the terminal evaluated in the terminal characterization. These loads correspond to contact pressures in the range of 670–800 MPa. The coupons will be mounted in a test apparatus capable of measuring both the coefficient of friction and the variation in electrical contact resistance.

In our case (sphere on flat), the contact pressure is calculated as the following :

$$P = 3 \times Fn / 2a$$

Fn is the normal force, a the contact surface

Calculated separately,

First a1 (Fn= 1N) = 32µm

and a2 (Fn= 2.5N) = 38µm

Finally Pmin = 670 Mpa

and Pmax = 800 MPa

For each sample, 100 sliding cycles of 3 mm have be performed (one cycle corresponds to a forward and backward motion of twice 3 mm), which is representative of connector mating cycles in the automotive industry. Figure 11 shows the test device used to measure the coefficient of friction and the contact resistance. The contact resistance has been measured using a four-wire test method, in which two leads supply the current through the contact interface while two separate leads measure the voltage drop across it.

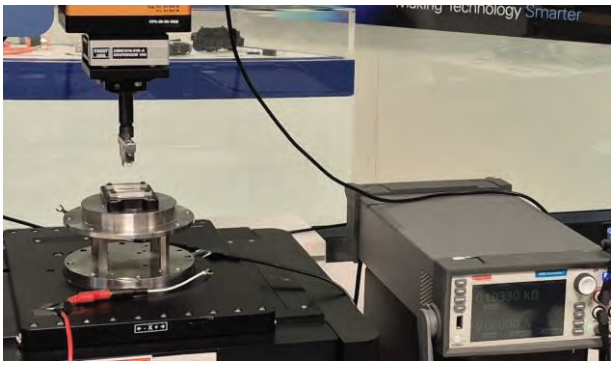


Fig. 11. *Test device to measure the coefficient of friction and the electrical contact resistance.*

IV. Test Results

A. Investigations of AgC plated coupons

A cross section of the AgC plating deposit was first characterized by scanning electron microscopy at an accelerating voltage of 8 kV. A 1.7 µm-thick nickel layer with a columnar grain structure is clearly observed. On top of this layer, a thin silver interlayer (estimated to be < 0.3 µm) aims to act as an adhesion layer for the silver graphite (AgC) top coating, which is 5–6 µm thick. The different light-grey regions within the AgC layer correspond to variations in silver grain size. The dark features are graphite particles, which are homogeneously distributed throughout the silver matrix at the silver grain boundaries. These graphite regions appear thin and elongated, extending between adjacent silver grains (Fig. 12). The size of a majority of this graphite particle appears to be around 0,5µm.

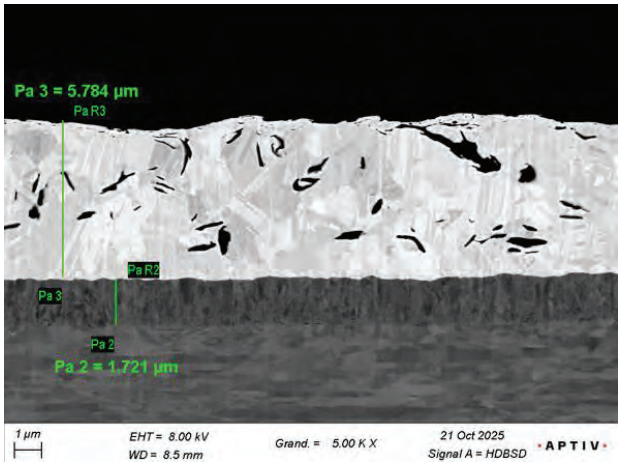


Fig. 12. *SEM picture of a AgC deposits.*

Figure 13 and 14 show the coefficient of friction (CoF) results for the two plating combinations under the two test loads (1N and 2.5N). For both contact forces, the same behaviour has been observed: the AgC samples exhibit stable friction with a CoF below 0.2, whereas the gold-plated samples show less stable behavior, with CoF values ranging between 0.3 and 0.6. In all cases, a few initial cycles are required to remove surface asperities and condition the contact. This running-in process is evident from the sharp drop in CoF observed during the first 0 to 5 cycles.

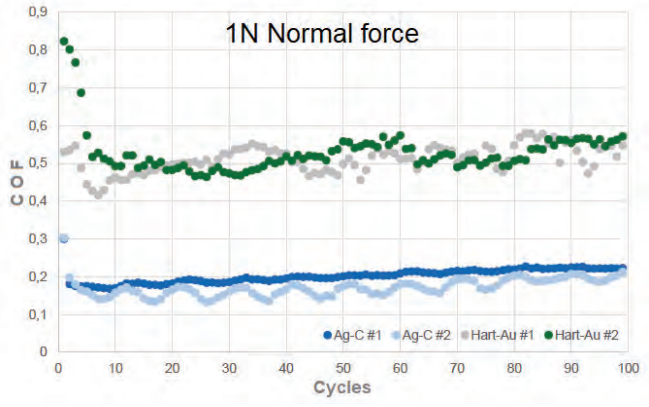


Fig. 13. *Coefficient of friction of the AgC and Au deposits under 1N contact normal force.*

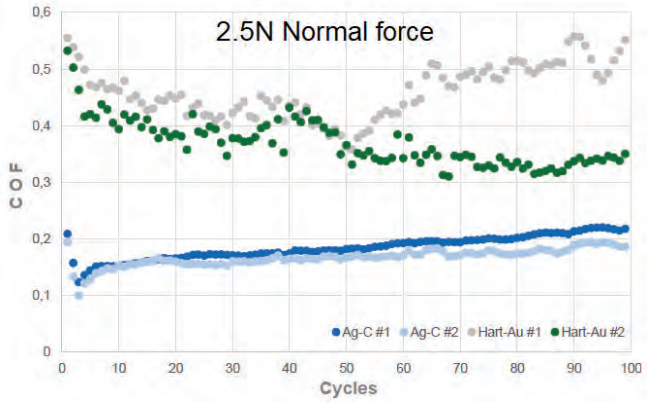


Fig. 14. *Coefficient of friction of the AgC and Au deposits under 2.5N contact normal force.*

Figure 15 shows the electrical contact resistance measured during each mating cycle for the two plating systems under the two test loads (1N and 2.5N). The initial contact resistance is slightly above 1 mΩ in all cases. Although small increases are observed, the AgC samples maintain low and stable contact resistance throughout the test. In contrast, the gold-plated samples exhibit several resistance increases, reaching values up to 3 mΩ. While these increases remain within acceptable limits, they highlight the superior electrical stability of the AgC coatings. The contact resistance increases within the automotive specifications [8] are to low to calculate a time to failure like it has been done in some recent reliability studies on connector applications ([9], [10]). Because no electrical abnormality was observed in any of the experiments, it is also not possible to assess any potential risk of signal interference caused by graphite particles at that stage.

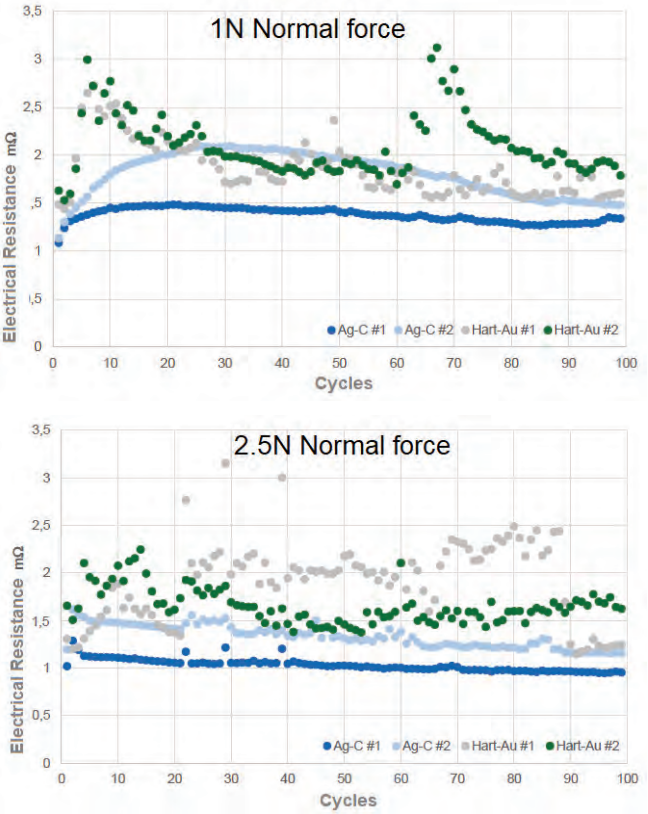


Fig. 15. *Electrical resistance for AgC and Au coupons under 1N (top) and 2.5N (bottom) contact normal force.*

At first, the wear tracks have been examined using optical microscopy (Fig.16). For the AgC coatings, the wear tracks are uniform and show very little debris. In contrast, the gold-plated (Au) samples exhibit greater variability in track width from sample to sample, and debris is visible along the edges of the tracks. At a normal load of 2.5 N, the light-yellow nickel underlayer is exposed in the centre of the wear track, indicating that the gold layer has been worn through. The width of the wear tracks for gold plated coupons are 0,25mm (1N) and 0,35mm (2,5N). For the AgC coupons the width are 0,15mm (1N) and 0,20mm (2.5N).

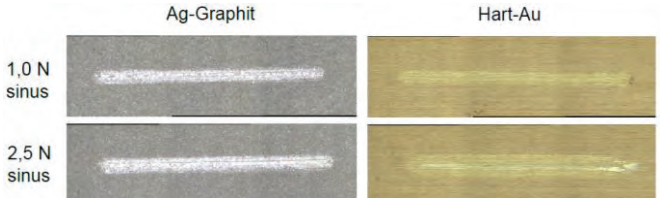


Fig. 16. *Optical picture of the wear tracks after 100 mating cycles.*

Scanning electron microscopy (SEM) images confirm the observations made by optical microscopy. Gold wear debris, highlighted in red in Figure 17, is clearly visible. For the AgC surfaces, the images further show that after 100 mating cycles the wear track has become smoother, indicating that the initial surface roughness has been progressively reduced. This roughness does not appear to increase friction; instead, it likely contributes to surface lubrication during mechanical contact.

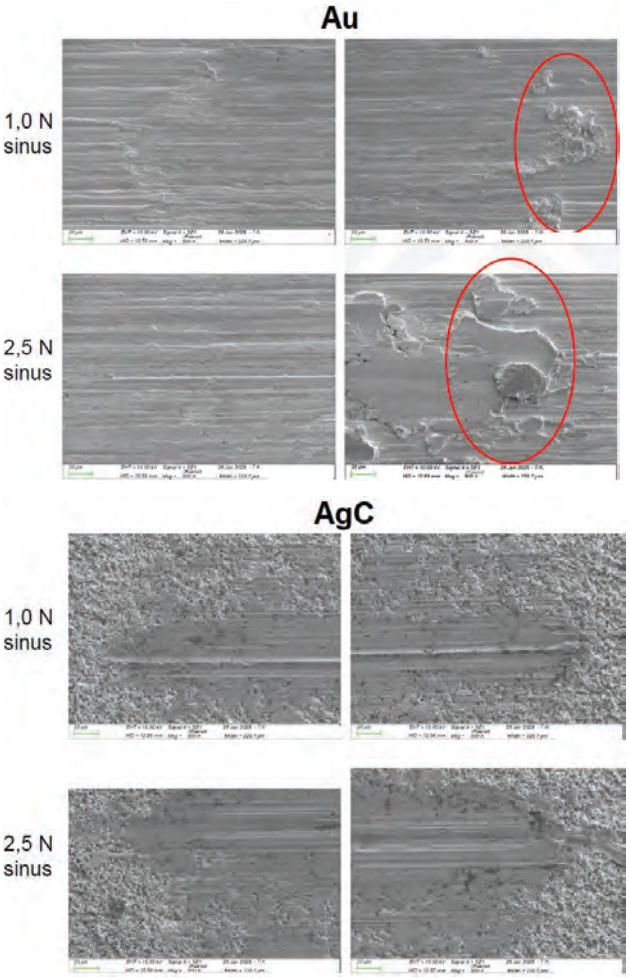


Fig. 17. *SEM pictures of the wear tracks after 100 mating cycles.*

Analysis of the spheres (Figure 18 and 19), which serve as the test counterparts, shows significantly less material degradation when sliding against AgC coatings than against Au plating. At a load of 2.5N, the wear on the gold-plated samples is relatively severe, as evidenced by the exposure of the nickel underlayer in the center of the radial wear scar. It is also important to note that the sphere experiences much higher wear and debris accumulation than the flat contact during these tests.

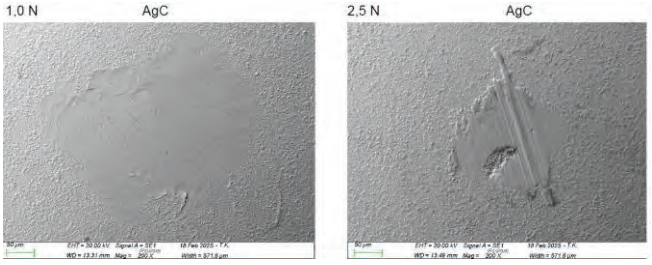


Fig. 18. *SEM pictures of the AgC plated spheres after 100 mating cycles.*

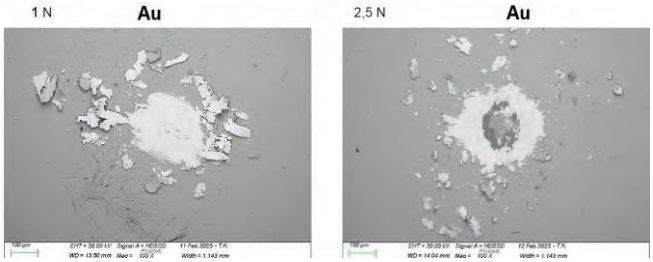


Fig. 19. *SEM pictures of the gold plated spheres after 100 mating cycles.*

B. Investigations on plated terminals

The AgC plated stamped terminals have been tested in mating/unmated 20 times according the specification DIN EN 60512-1-1 and the needed mating application. The test has been carried out with state of the art Au plated reference pins and as well with AgC plated pins. In fact we want to check the two different scenarios, first when the plating of the pins of the device hasn't been changed to AgC then the benefit of having the device pins also plated with AgC. The mating force curves have been collected in Figure 20 and 21. Both diagram show similar force behaviour with a smooth force peak at 2N.

Some slight variations in mating force has been observed when the terminal engages with AgC pins. These results indicate that while plating the male part with AgC is possible, it is not strictly necessary to improve the overall mechanical behaviour of the system.

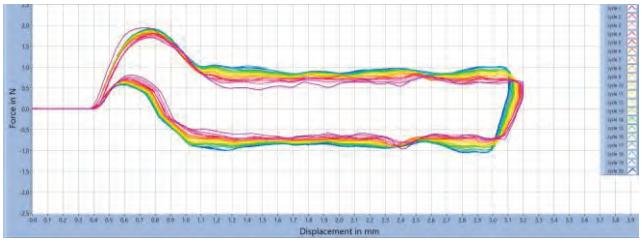


Fig. 20. *Mating cycle curves of the AgC plated female terminal with gold plated pins.*

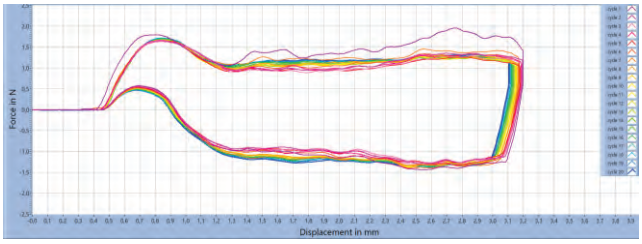


Fig. 21. *Mating cycle curves of the AgC plated female terminal with AgC plated pins*

The contact spring and wear tracks were examined using optical microscopy (Fig.22 and 23). The material wear doesn't reach the nickel underlayer. The wear traces on the AgC pins are relatively smaller, which could lead to higher local contact pressures and potentially more debris generation. Nevertheless, both tested samples exhibit good performance and do not show any significant cold welding effect, which is commonly observed with silver-plated terminals [11].

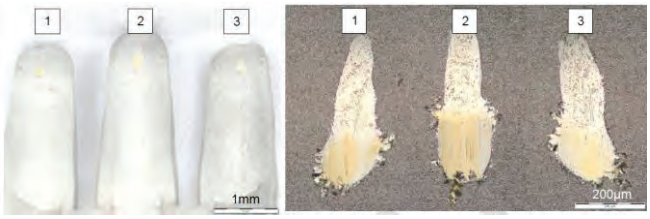


Fig. 22. Photograph of the contact points of the AgC plated female terminal with gold plated pin.

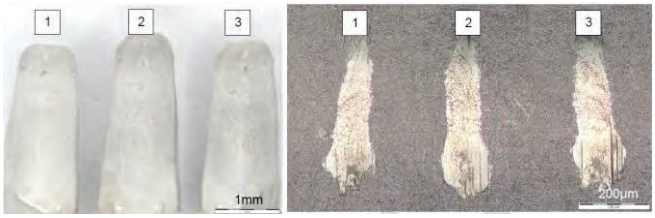


Fig. 23. Photograph of the contact points of the AgC plated female terminal with AgC plated pin.

V. CONCLUSIONS

The study confirms that silver graphite plating is a promising candidate to replace gold in sensitive connector applications. We could notice that the samples and results obtained don't show any tarnish behaviour usually common with fine silver plated terminals. Further investigations are pending, but so far we assume that passivation can be completely dispensed, which also has the advantage that additional organic compounds cannot influence the electrical resistance.

We also observed that the coefficient of friction of AgC plated terminals stay low and stable even if the irregularities of the contact surface need to be removed during the first mating cycles (drop of CoF).

We investigate the possibility to have not paired surfaces as the possibility to combine gold and AgC (e.g. device pins remain silver plated). As main result, applying AgC at least on the female terminal (harness side) is crucial, as it is more susceptible to debris and electrical degradation. Low COF contributes to lower insertion forces and improved terminal durability, even under high-current or high-voltage requirements. The future work will include comprehensive product validation with vibration testing and extended thermal ageing sequences.

REFERENCES

[1] M. Myers, "The Performance Implications of Silver as a Contact Finish in Traditionally Gold Finished Contact Applications." Interconnection and Process Technology Tyco Electronics Harrisburg, USA . ICEC 2009.

[2] E. Philipp, A, Vogt, E. Flegel, "Neue Methode zur Bestimmung und Charakterisierung der ODT-Be-legung und deren Wirkung auf versilberte, Elektrische Kontaktoberflächen", 7. Symposium Connectors conference, VDE/VDI, Lemgo, 2019.

[3] M. Porte, "The silver anti-tarnish affecting the electrical stability of automotive terminals," ICEC Switzerland, 2021, pp. 355.

[4] S. Sachs, I. Buresch, H. Schmidt, M. Oberst, F. Ostendorf, „Silber ist nicht gleich Silber, Eigenschaften und Charakteristika von High-Performance-Silberoberflächen für verschiedene Applikationen.", Symposium Connectors conference, VDE/VDI, Lemgo, 2023.

[5] R. Wagner, C. Dandl, A. Stadler, "Silber-Graphit - Dispersionsschichten als Kontaktoberfläche in Steckverbindern", 7. Symposium Connectors conference, VDE/VDI, Lemgo, 2019.

[6] A. Fares Karam, A. Franchini, A. Torrealba, D. Comte, A. Brézard-Oudot, S. Noel, D. Anderson, J. Toran, " Compatibility of Gold, Palladium and hard Silver based plating systems for connector applications", 30th International Conference on Electrical Contacts (ICEC 2020), 2021.

[7] M. Blauth, S. Tülling, J. Song "Untersuchung zum Einfluss der Betriebtemperatur un der Applikationsmenge von Schmierstoffen bei Reibversuchen an Silberkontakten", Symposium Connectors conference, VDE/VDI, Lemgo, 2025.

[8] ZVEI, Technischer Leitfaden Ausfallraten für Bordnetz-Komponenten im Automobil, 2021.

[9] M. Porte, "Novel method for determining a failure rate of electrical terminals by vibration testing of designs with contact forces extremely reduced", VDE/VDI, Lemgo, 2025.

[10] P., Shukla A., Song J.. Prediction of failure in time (FIT) of electrical connectors with short term tests, Microelectronics Reliability, 2022.

[11] R. Wagner, C. Dandl, A. Gruber, R. Hogger, M. Eicher, "Investigations on cold welding and galling of various connector platings", 30th International Conference on Electrical Contacts (ICEC 2020), 2021.

Investigation of contact dynamic welding mechanisms of silver tin-oxide based on the evolution of eroded surface morphology

Chao Zhang
School of Electrical Engineering and Automation & School of Instrumentation Science and Engineering, Harbin Institute of Technology
Harbin, China
zhangchao100@hit.edu.cn

Guoliang Chen
School of Electrical Engineering and Automation, Harbin Institute of Technology
Harbin, China
mrglc0929@163.com

Yubin He
School of Electrical Engineering and Automation, Harbin Institute of Technology
Harbin, China
22b906012@stu.hit.edu.cn

Wanbin Ren
School of Electrical Engineering and Automation, Harbin Institute of Technology
Harbin, China
renwanbin@hit.edu.cn

***Abstract*—Contact welding failure events seriously limit the reliability of low current switching devices. Up to now, the relationship between the measured welding force and the real welding trace are not fully understood. In this work, a novel test rig, which can in-situ measure the surface morphology and the visual images during arc erosion cycling is described. Then, a series of electrical endurance experiments were conducted under a resistive load with a voltage of AC 220 V and a current of 16 A. The variation trends of arc energy and welding force with the number of operations were obtained. Meanwhile, the evolution processes of both 2D visual images of electrical erosion and 3D electrical erosion morphologies were characterized. Furthermore, the degradation trend of surface roughness and elemental distribution were derived. Finally, the mechanism governing the dynamic welding of silver tin-oxide contact materials was proposed.**

Keywords—arc erosion, contact welding, welding force, surface morphology, electrode material

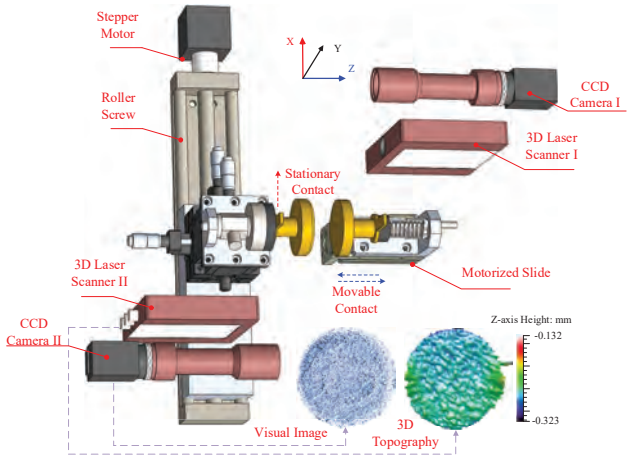
I. INTRODUCTION

Electromagnetic relays remain indispensable in critical sectors such as industrial control, automotive electronics, and data computing due to their irreplaceable advantages over solid-state devices [1-2]. In recent years, with the rapid advancement of the 5G communications, advanced manufacturing, aerospace, and data computing, stringent requirements have been imposed on the switching capacity, electrical endurance, and contact performance of electromagnetic relays [3-4]. The contact system is the core component responsible for making and breaking load circuits, and the electrical endurance of a relay is intrinsically linked to contact performance. The most critical degradation issue regarding contact performance is the increase in welding force [5-6]. This phenomenon causes significant delays in switching actions and signal transmission hysteresis. The occurrence of welding is directly related to arc erosion on the contact surface and is closely associated with factors such as the actuation mechanism, electrical load, environmental conditions, and contact materials. The phenomenon of electrical erosion during electrical endurance experiments is dynamically correlated with contact welding behavior. To address contact welding failures caused by the degradation of physical properties, previous studies have focused on morphological evolution. Wu *et al.* compared contact surface morphologies over 40,000 operations and observed that the diameter and depth of electrical erosion gradually increased with the number of operations [7]. Späth *et al.* observed that frequent electrical erosion and thermal stress cycles caused the surface metal at the edges to deform and lift under AC4 load conditions. This led to a continuous reduction in the bonding area and bonding rate with the underlying Cu base [8]. Furthermore, Xu *et al.* found that the probability of contact welding failure increased significantly due to the peak instantaneous current when the welding moment occurred at a phase angle of 90° [9]. However, existing research on cumulative electrical erosion primarily relies on offline measurement methods. These approaches make it difficult to reconstruct the complete evolutionary process from the initial state to welding failure.

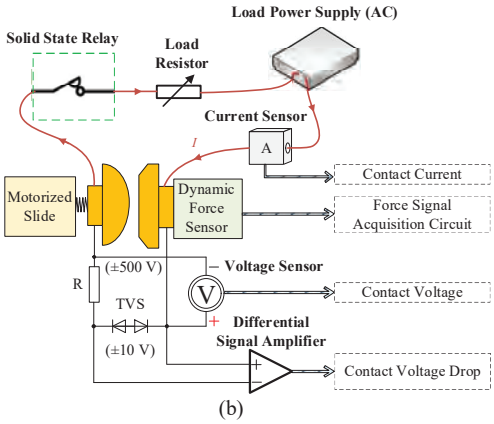
Consequently, a comprehensive law governing the accumulation of electrical erosion has not yet been established. To address this limitation, this paper designs an electrical erosion simulation and in-situ observation system. This system is capable of simulating contact arcing behavior while simultaneously providing in-situ observation capabilities for electrical parameters, welding force, visual images, and 3D topographies. And experiments were conducted on Ag/SnO_2 contact materials to analyze electrical performance and welding characteristics. Finally, the correlation between electrical performance degradation, the evolution of electrical erosion features, and the variation in welding force during electrical endurance testing is determined.

II. EXPERIMENTAL DETAILS

The test apparatus used in these experiments is described in detail in [10], and a brief summary is provided here. Fig. 1(a) illustrates the schematic of the contact electrical erosion simulation mechanical structure, which is designed to simulate the make-and-break actions of contacts and control the transition between the arc discharge position and the observation position. The movable contact was driven by a motorized slide located beneath it. A helical spring was installed behind the movable contact to provide the elastic restoring force and rebound behavior. By tuning the spring stiffness, the actuation behavior of the movable contact was made generally comparable to that of a practical relay. Specifically, when the stationary contact moves along the positive X-axis to align with the CCD Camera I and the 3D Laser Scanner I, the movable contact is simultaneously positioned at the center of the field of view of the corresponding observation instruments, which allows for the in-situ observation of the morphological details of electrical erosion. The system features a Z-axis measurement range of ±10 mm with a resolution of 1 μm and a repeatability of 0.4 μm, while the field of view in the XY plane is 80 mm × 50 mm with a resolution of 40 μm. As shown in Fig. 1(b), the measurement unit primarily comprises acquisition circuits for electrical signals (contact voltage and current) and mechanical signals (stationary contact force). A dynamic force sensor installed behind the stationary contact could measure the static contact force during closure and the welding force during breaking. Ag/SnO_2 contact materials were selected as specimens. The welding failure was defined as an event where the welding force exceeds the breaking force of 0.3 N, which corresponds to force provided by the movable spring of the actual electromagnetic relay. The experiment continued until the preset 40,000 operations were completed. In the present study, the AC phase angle during switching was not intentionally controlled, and the making/breaking process occurred at random phase angles to better simulate practical operating conditions. Detailed experimental conditions are listed in Table 1. The contact is composed of an $AgSnO_2$ functional contact region supported by a Cu-based base material.



(a)



(b)

Fig. 1. Schematic diagram of the experimental apparatus designed for electrical erosion simulation and in-situ measurement. (a) The mechanical structure. (b) The measurement unit for acquiring electrical and mechanical signals.

TABLE I. EXPERIMENTAL CONDITIONS

Parameters	Value
Load voltage	220 V (AC)
Load current	16 A (AC)
Operation cycle	1 s ON/1 s OFF
Static contact force	2 N
Electrical erosion observation interval	Every 500 operations
Total Number of Operations	40000

III. RESULTS AND DISCUSSION

A. Trends in arc energy and welding force

A total of five repeated tests were carried out under identical experimental conditions. Similar overall degradation behavior and surface morphology evolution trends were observed among the tested samples. The results shown in this paper correspond to one representative test run. Fig. 2 illustrates the variation of arc energy as a function of the number of operations. And the average arc energy was calculated to be 795.93 mJ. Fig. 3 presents the welding force results obtained from the experimental system, which shows an overall upward trend in the average welding force. The standard deviation of the welding force distribution was calculated every 2,000 operations to characterize the fluctuation of the welding force across different experimental stages as shown by the blue data points in Fig. 3. At the 37,915th operation, the welding force reached a maximum value of 0.36 N and exceeds the failure threshold of 0.3 N. After this initial welding failure, the force exceeded the limit again after an interval of only 620 operations. During the first 5,000 operations, the distribution of welding force values was relatively concentrated with the standard deviation gradually decreasing to 0.011 N. Subsequently, the welding force for certain data points increased to approximately twice the average value of that stage. It is defined as "strong welding" when the welding force is greater than 0.15 N. Although the occurrence probability of strong welding was only 0.67%, the standard deviation of the distribution increased significantly and reaches a local peak of 0.016 N around 12,000 operations. In the final stage of the electrical endurance test, the probability of strong welding rose sharply to 8.04%, and the corresponding standard deviation also reached a maximum of 0.022 N just prior to the welding failure. Since non-opening failure is mainly associated with unusually high welding force events, the 95th

percentile (P95) was additionally introduced as a failure-oriented statistical indicator. The obtained P95 welding force was 0.14 N.

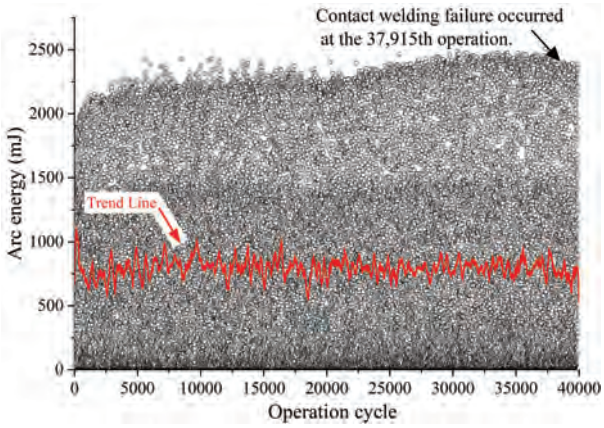


Fig. 2. Variation of arc energy as a function of the operation cylce.

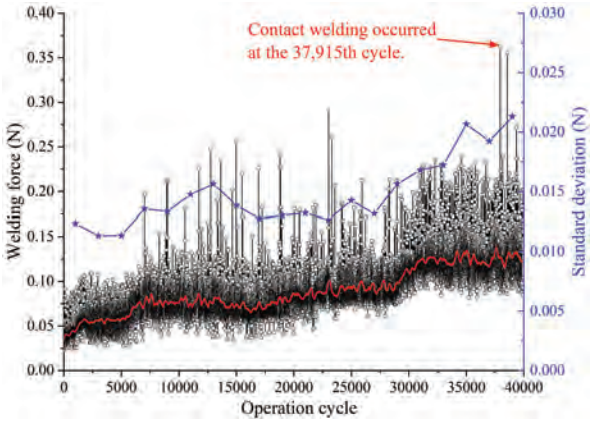
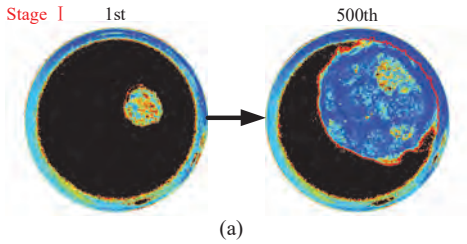


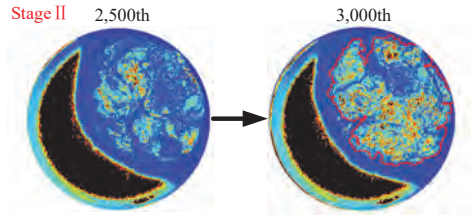
Fig. 3. Evolution of the welding force and its distribution standard deviation versus the operation cycle.

B. Migration and expansion of the erosion area

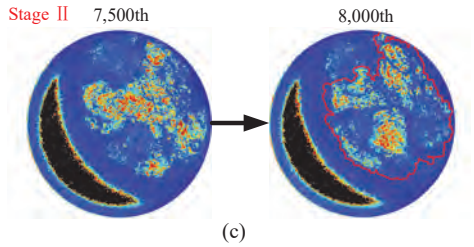
Fig. 4 illustrates the evolution of the visual images of contact electrical erosion. During the experiment, these images were recorded at intervals of 500 operations with the eroded areas outlined in red. Based on the migration features of the eroded areas, the electrical endurance test could be divided into three distinct stages. In Stage I (0–500 operations), the initial erosion area was located at the upper-right of the contact geometric center. Subsequently, the accumulated erosion area expanded outward in an approximately circular manner and reached the upper-right edge of the contact. During Stage II (500–20,000 operations), although the erosion area partially reached the contact edge, the overall erosion pattern tended to migrate in the opposite direction. By the 17,500th operation, the accumulated erosion covered the entire contact surface. Finally, in Stage III (20,000–40,000 operations), the migration features of the erosion area became even more pronounced.



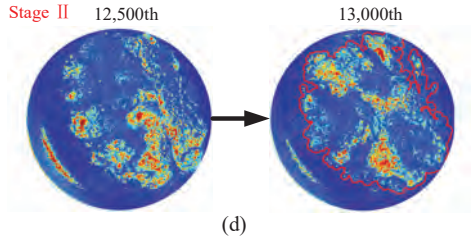
(a)



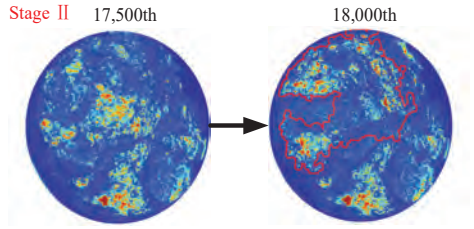
(b)



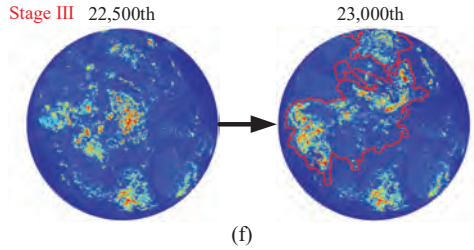
(c)



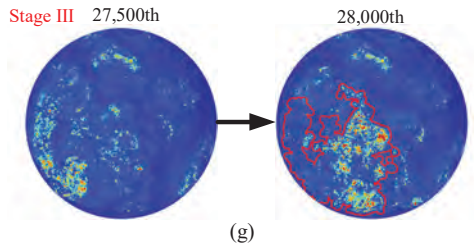
(d)



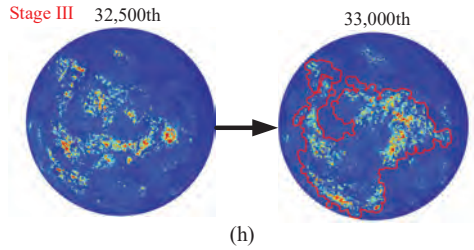
(e)



(f)



(g)



(h)

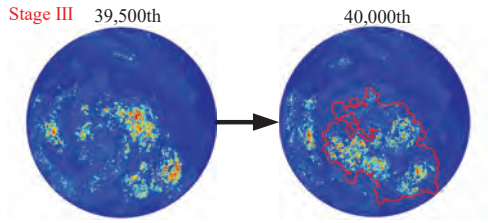


Fig. 4. Evolution of the electrical erosion area during the electrical endurance test (Load condition: 220 V / 16 A AC). Erosion morphology (a) from 1 to 500 operations. (b) from 2500 to 3000 operations. (c) from 7500 to 8000 operations. (d) from 12500 to 13000 operations. (e) from 17500 to 18000 operations. (f) from 22500 to 23000 operations. (g) from 27500 to 28000 operations. (h) from 32500 to 33000 operations. (i) from 39500 to 10000 operations.

C. Morphological evolution of surface topography

Fig. 5 illustrates the morphological evolution of electrical erosion on both the movable and stationary contacts. Initially, the surface height distribution of the stationary contact exhibited uniformity. At 5,000 operations (corresponding to Stage II), an overall increase in height was observed in the erosion area of the stationary contact. Simultaneously, a distinct sharp protrusion appeared at the edge of the erosion area on the movable contact. As the number of operations increased, the height difference between this protrusion and the reference plane of the movable contact grew to 0.36 mm. Subsequently, as the erosion area gradually expanded to cover the entire contact surface, the protrusion migrated toward the contact edge and eventually vanished. After 20,000 operations (Stage III), a surface depression was evident at position A on the edge of the movable contact, while the stationary contact exhibited a corresponding interlocking surface morphology at position A'. After 40,000 operations, contact material at the edge of the movable contact gradually peeled off and transferred to the center. Consequently, the height of the center increased relative to the blue reference plane, forming an approximate circular protrusion B with a diameter of about 1.2 mm.

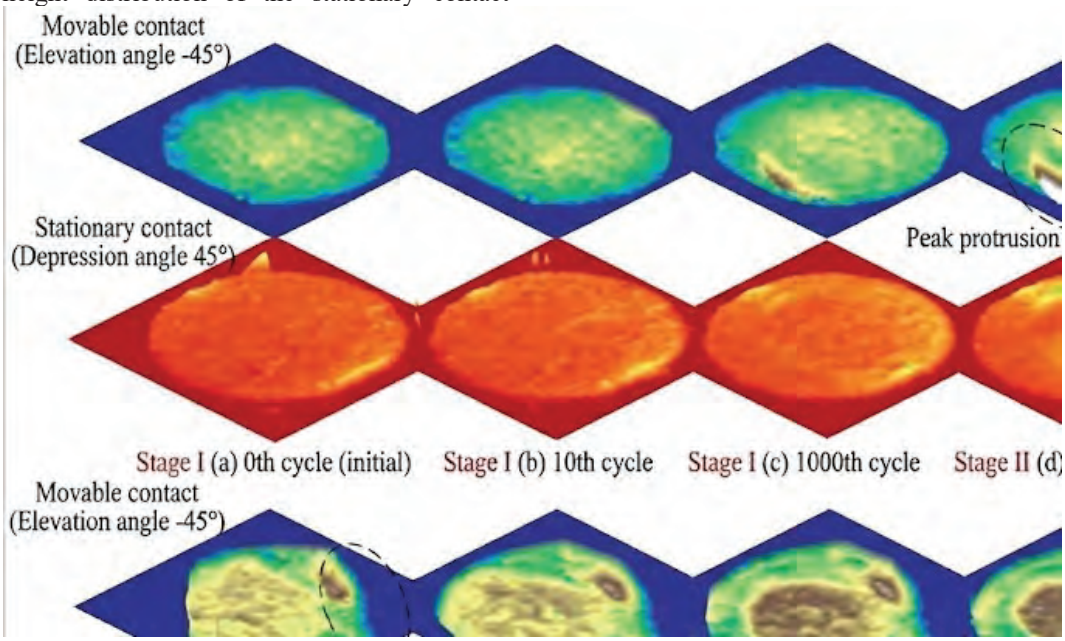


Fig. 5. Evolution of 3D morphology for contact electrical erosion.

As shown in Fig. 6, the initial contact surface was flat with no significant height difference at the contact interface. The data in Fig. 6 were obtained from reconstructed contact interfaces based on the measured surface topographies after different operation cycles. By virtually closing the contact pair according to the measured force–displacement relationship, the overlapped regions were identified as contact spots. These data were used to quantitatively characterize the real contact state after different degrees of arc erosion and to reveal the influence of surface degradation on the contact condition. Therefore, as the force increased to 2 N, the number of contact spots rapidly increased and exceeded 10. However, the number of contact spots dropped to only 1–2 and showed no significant change with increasing static force after 1,000 and 5,000 operations. This corresponds to the previously mentioned experimental phenomenon where contact is limited by sharp protrusions. Subsequently, the disappearance of surface protrusions caused the contact spots to migrate and redistribute at the contact center, restoring the number of contact spots to the initial level.

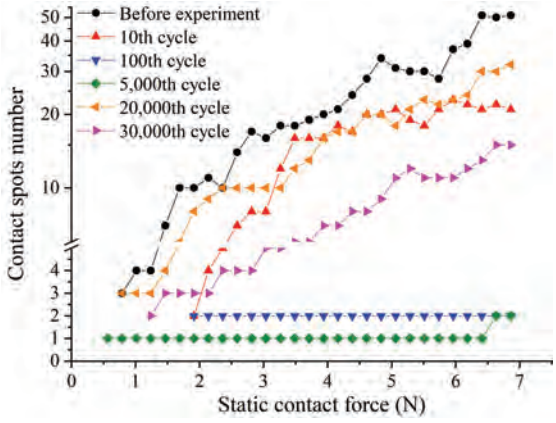


Fig. 6. Evolution of contact spots number with the static contact force.

In the initial stage of the experiment, material accumulation in the erosion area resulted in peak-to-peak contact between the contact pair, which led to poor electrical contact state. These surface peaks disappeared with further accumulation of electrical erosion, and the number of

asperities capable of serving as contact spots increased. However, mass loss at the contact edge caused a reduction in height in the final stage of the electrical endurance test, and led to a continuous shrinkage of the effective contact area. Since this morphological evolution of electrical erosion is irreversible, the corresponding electrical contact characteristics gradually deteriorated until contact welding failure occurred. Fig. 7 presents the distribution results and evolution trends of the surface roughness parameters, S_a and S_z, for each contact spot. Both S_a and S_z exhibited an increasing trend, and reached maximum values of 0.06 mm and 0.19 mm at 10,000 operations, respectively. This is attributed to the gradual wear of the sharp protrusions at the contact edge, which causes the contact spots to shift toward the geometric center and distribute along the transitional slope between the two regions. On one hand, this maintained S_a and S_z at high levels; on the other hand, significant differences in the height of individual contact spots resulted in increased standard deviations for S_a and S_z, rising to 0.03 mm and 0.08 mm, respectively.

Consequently, the contact spots contracted, split, and disconnected sequentially during contact breaking. In this process, the contact voltage drop increased and exceeded the melting voltage of the material. As the electrical erosion energy concentrated on the remaining contact spots, the material melted and resulted in liquid bridge welding during breaking. This could explain the intermittent occurrence of strong welding observed after 10,000 operations in Fig. 3.

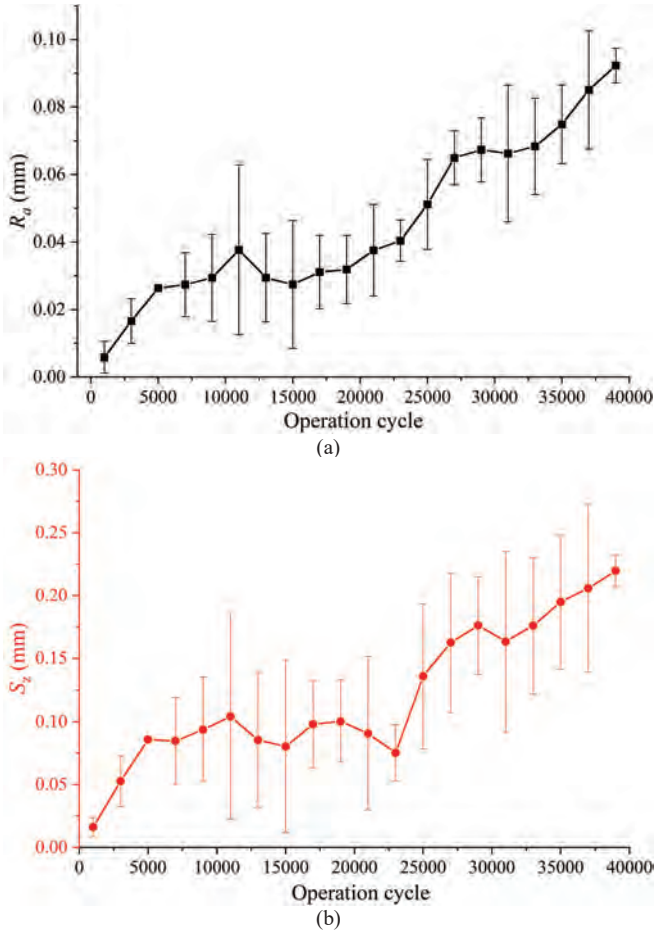


Fig. 7. Evolution trends of the roughness parameters. (a) Arithmetic mean height S_a. (b) Maximum height of the surface S_z.

D. Variation of elemental composition

The tests were interrupted at different degradation stages, and the contact interfaces were then characterized using a scanning electron microscope (SEM, Sigma 300, ZEISS, Germany) equipped with energy-dispersive spectroscopy (EDS) to obtain the surface morphology and elemental distribution information. It should be noted that the EDS analysis provides elemental distribution information only and does not directly identify the chemical state of the detected elements. Fig. 8 and Fig. 9 display the surface microstructures and elemental distributions of the contacts after 1,000, 5,000, 10,000, 20,000, 30,000, and 40,000 operations. The results from Region 1 represent the initial state of the contact material. After 1,000 operations, the Ag content in the eroded area (Region 2) decreased sharply to 65.4%, while the Sn content increased to 15.6%. This indicates that the arc caused the molten Ag to splash outward, which left behind SnO_2 and Sn particles decomposed from it on the surface. This phenomenon correlates with the trend observed in Fig. 3, where the average welding force increased continuously due to the segregation of Sn on the surface. The locations of the contact spots after 5,000 and 10,000 operations are marked as Region 3 and Region 4 in Fig. 8(c) and Fig. 8(d), respectively. During this stage, the contact spots were confined to the sharp protrusions at the contact edges. The Cu content increased to 27.7%, which suggested that the arc caused the copper from the contact substrate to melt and splash onto the surface. The formation of copper oxide increased the contact resistance and the heat generation power during welding, which further led to a step-like increase in the average welding force. Subsequently, the electrical endurance test involved a recurring cycle of erosion concentration at the contact edge to edge mass loss to migration of the erosion area. Consequently, the elemental contents of Sn and Cu on the contact surface fluctuated continuously, which could explain the variations in the average welding force shown in Fig. 3. However, the welding force remained high due to the consistently high proportion of Cu at the contact edge where the contact area was located.

As shown in Fig. 8(e), significant mass loss occurred at the contact edge, and the contact spots shifted to the protrusion at the contact center in the final stage of the electrical endurance test. The measurement results in Fig. 9 indicate that the in content at the contact center reached a minimum of 1.5%, which suggested significant decomposition of the In_2O_3 additive. Due to the lack of the wetting effect provided by the additive, the molten Ag formed spherical protrusions on the surface upon cooling as shown in Fig. 8(f). Between 10,000 and 25,000 operations, the roughness parameters gradually stabilized. As the erosion area migrated, the contact spots were primarily distributed along the contact edge, and the surface morphology showed no significant changes. In the final stage of the electrical endurance test, the contact spots migrated to the circular protrusion at the contact center. As observed in Fig. 8(f), this region was formed by the deposition and stacking of erosion spatters and contained numerous microscopic surface protrusions. Consequently, the corresponding S_a and S_z values exhibited a step-like increasing trend once again. The standard deviation of the roughness parameters decreased, which indicated that the various contact spots shared a similarly rough surface morphology. This increased the probability of liquid bridge welding during contact breaking,

which accounts for the experimental result shown in Fig. 4 where the phenomenon of strong welding intensified during the final stage of the electrical endurance test.

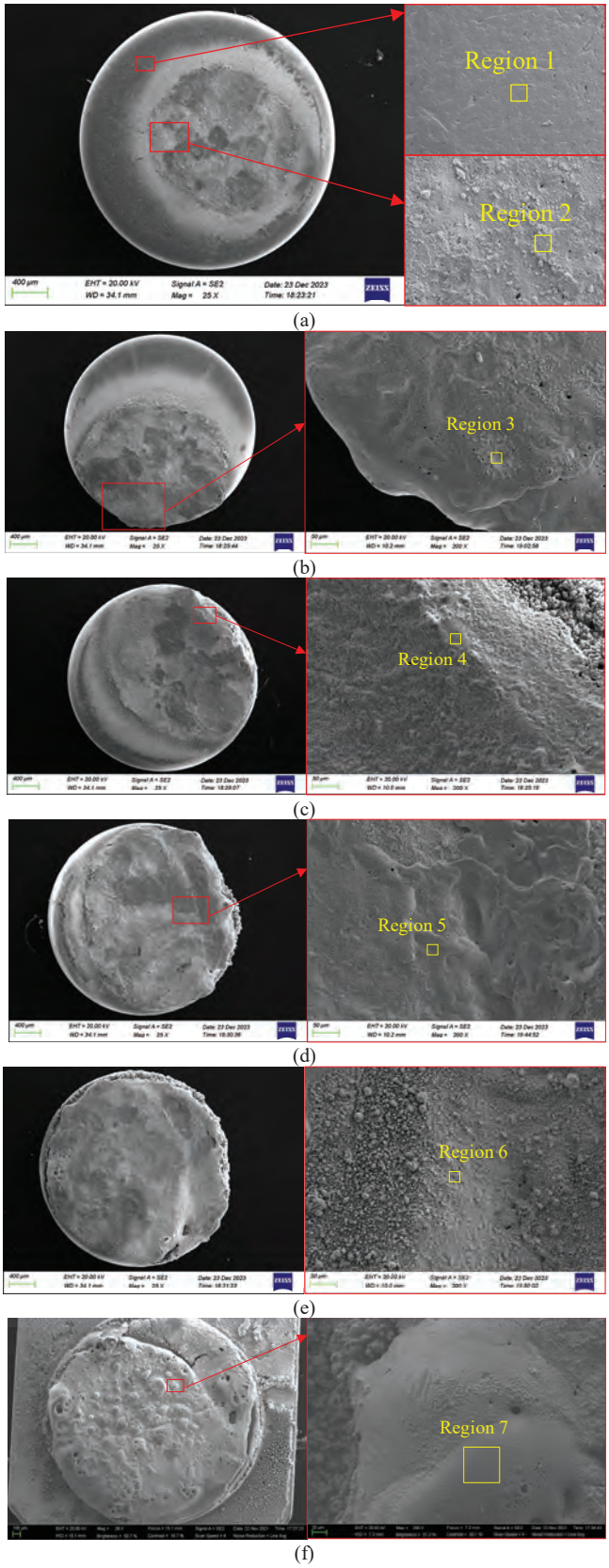


Fig. 8. Evolution of the contact surface morphology at different stages of the electrical endurance test. (a) 1,000 cycles. (b) 5,000 cycles. (c) 10,000 cycles. (d) 20,000 cycles. (e) 30,000 cycles. (f) 40,000 cycles.

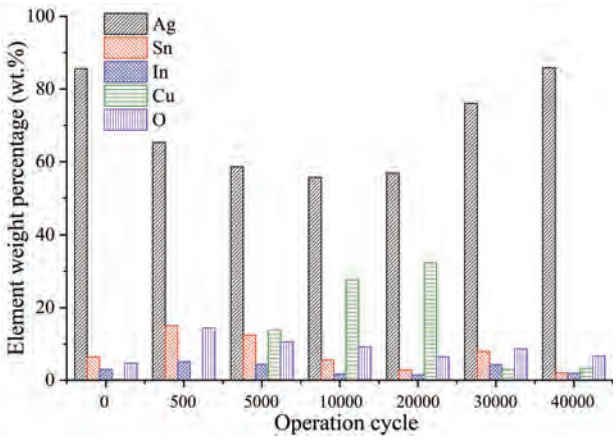


Fig. 9. Evolution of the elemental weight percentage within the contact spots as a function of the number of operations.

E. Mechanism of contact welding failure

The most direct manifestation of accumulated electrical erosion is the alteration in the elemental distribution of the contact material. Under high-temperature conditions, the segregation of Sn within the erosion zone first occurs driven by the difference in melting points between Ag and SnO_2. This leads to a deterioration in the material anti-welding capability and a gradual increase in the average welding force. Subsequently, electrical erosion concentrates at the contact edge, which causes mass loss in the functional layer and exposing the Cu substrate. The appearance of Cu in the heavily degraded regions is consistent with local exposure of the underlying Cu-based substrate after severe arc erosion and material redistribution of the $AgSnO_2$ contact layer. The segregation of Cu has a dual effect: on one hand, it intensifies contact heating; on the other hand, it increases the tensile strength of the welded interface. The combined action of these two processes results in a step-like increase in the average welding force. In the final stage of the electrical endurance test, accumulated arc erosion causes the decomposition and depletion of indium oxide (In_2O_3), which leads to the formation of Ag-segregated regions. When the welding interface formed during contact closure is located within this region, the material exhibits poor anti-welding capability and causes both the welding area and the corresponding average welding force to increase sharply once again.

Due to the cumulative effects of arc erosion, the 3D topographies of both the movable and stationary contacts undergo significant changes, which further complicates the electrical contact characteristics. Experimental results indicate that sharp protrusions initially appear at the erosion edge, which limits the distribution of contact spots. During contact breaking, these spots disconnect rapidly. Consequently, the phenomenon of strong welding is virtually non-existent in the initial stage. Subsequently, these sharp protrusions are worn down and eliminated by concentrated arc erosion. The contact mode transitions to a "slope contact" configuration, and the S_z value of each spot increases significantly, which triggers intermittent strong welding phenomena during breaking. In the final stage, a circular protrusion forms at the contact center. The surface of this protrusion is composed of accumulated molten metal, characterized by extreme roughness and a distinct internal porous structure, which causes a sharp increase in the contact spot parameter S_a. Since the welding force is far

more sensitive to variations in S_a than in S_z, the strong welding phenomenon intensifies during the final stage, which ultimately leads to contact welding failure.

IV. Conclusion

In this study, multimodal information including electrical parameters, mechanical force signals, visual images, 3D topographies, and elemental compositions was comprehensively integrated to elucidate the contact welding failure mechanism of electromagnetic relays during electrical endurance tests. The endurance experiments of Ag/SnO_2 contact materials were conducted under a resistive load with the voltage and current of AC 220 V and 16 A, respectively. The concentrated distribution of erosion areas and the increased surface roughness of contact spots were identified as the primary characteristics of contact welding failure. Both the average value and the fluctuation of the welding force serve as key metrics to characterize welding behavior during electrical endurance tests. Specifically, the average welding force correlates directly with the contact material anti-welding capability, while the fluctuation of the welding force reflects the intermittent nature of strong welding phenomena. The concentration of electrical erosion led to mass loss at the contact edge and triggered the segregation of Sn, Cu, and Ag elements. Consequently, the anti-welding capability of the material deteriorated sequentially, which resulted in a step-like increase in the average welding force. In future work, more systematic investigations will be conducted by varying key parameters, such as current level and contact material, to further clarify their effects on surface erosion evolution and welding behavior.

Acknowledgment

The authors express their gratitude for the kind support provided by National Natural Science Foundation of China (Grant Number 52377140 and U2441286).

References

[1] L. Morin, N. B. Jemaa, D. Jeannot, *et al.*, “Make arc erosion and welding in the automotive area,” *IEEE Trans. Compon. Packag. Technol.*, vol. 23, no. 2, pp. 240–246, 2000.

[2] Y. Zhang, J. Q. Wang, and H. L. Kang, “Study on conductive properties of rare earth elements doped $AgSnO_2$ contact materials,” *Sci. Adv. Mater.*, vol. 12, no. 12, pp. 1769–1775, 2020.

[3] T. Mohandoss and F. Robert, “Investigation of relay electrical contact failure using SEM and surface composition extraction with EDS and XED,” *Iranian J. Sci. Technol., Trans. Electr. Eng.*, vol. 47, no. 3, pp. 803–812, 2023.

[4] X. Q. He, H. D. Fu, J. H. Fang, *et al.*, “Effect of loading current on the arc erosion behavior of in-situ composite fiber-reinforced Ag-Cu-Ni-Ce alloy,” *Vacuum*, vol. 206, p. 111502, 2022.

[5] J. D. Huo, Y. F. Wang, and Y. Cao, “3D computational study of arc splitting during power interruption: The influence of metal vapor enhanced radiation on arc dynamics,” *J. Phys. D, Appl. Phys.*, vol. 54, no. 8, p. 085502, 2020.

[6] J. Swingler and A. Sumption, “Arc erosion of $AgSnO_2$ electrical contacts at different stages of a break operation,” *Rare Metals*, vol. 29, no. 3, pp. 248–254, 2010.

[7] H. Y. Li, X. H. Wang, Z. D. Hu, *et al.*, “Investigation of arc erosion mechanism for tin dioxide-reinforced silver-based electrical contact material under direct current,” *J. Electron. Mater.*, vol. 49, no. 8, pp. 4730–4740, 2020.

[8] D. Späth, V. Behrens, M. Finkbeiner, *et al.*, “The influence of the bonding area of welded contact tips on contact erosion,” in *Proc. 52nd IEEE Holm Conf. Electr. Contacts*, Montreal, QC, Canada, 2006, p. 284084.

[9] A. Ksiazkiewicz and J. Janiszewski, “Welding tendency for selected contact materials under different switching conditions,” *Eksploat. Niezawodn. – Maint. Rel.*, vol. 21, no. 2, pp. 237–245, 2019.

[10] Z. Zheng, W. B. Ren, and C. Zhang, “In situ interface characterization of arcing electrode materials and evolution in electrical endurance experiments,” *IEEE Trans. Instrum. Meas.*, vol. 73, Art. no. 5002309, 2024.

Experimental Verification on Forming Carbon Films onto the Friction Surface of Contact Wires when using Metalized Carbon Contact Strips

Kento Mitani
Frictional Materials,
Materials Technology Division
Railway Technical Research Institute
Tokyo, Japan
mitani.kento.97@rtri.or.jp

Yoshitaka Kubota
Frictional Materials,
Materials Technology Division
Railway Technical Research Institute
Tokyo, Japan
kubota.yoshitaka.77@rtri.or.jp

Fumiko Morimoto
Frictional Materials,
Materials Technology Division
Railway Technical Research Institute
Tokyo, Japan
morimoto.fumiko.27@rtri.or.jp

***Abstract*— When using carbon-based pantograph contact strips, it is reported that carbon films form on the friction surface of the contact wire. Previous study revealed that these films were transferred from contact strips and contain graphite-like sp2-bonded structures. In this study, we conducted friction experiments using metallized carbon contact strips against copper contact wires with a rotating disk-type friction test apparatus. The results showed that the film formed through two distinct processes, and that the wear of the contact strips decreased once the film was established. In the first process, carbon transfers from contact strips onto contact wires during sliding under conditions where electric arcs occur. In the second process, the transferred carbon is flattened and compacted into a film under conditions without electric arcs. In addition, nano-scratch testing revealed that the adhesion strength between the film and the contact wire was low, suggesting that the film is easily worn away if sliding continues without replenishment of carbon by arcs. While electric arcs are generally thought to accelerate contact strip wear, our results indicate that moderate electric arcs promote the formation of carbon films and consequently reduce wear when carbon contact strips are used.**

Keywords—carbon film, sliding contact, railway, carbon, copper

I. Introduction

In electric railways, vehicles collect current from a contact wire through pantograph contact strips. Carbon-based materials are widely used for pantograph contact strips because of their favorable friction characteristics. Copper and carbon sliding contacts are also found in slip rings and other applications, and many studies [1], [2] are being conducted to reduce the wear of these contact materials. These previous studies [1], [2] have inferred that in sliding contacts between copper and carbon, lubricating carbon films are formed on the copper friction surface thereby reducing wear. In railway contact wire and contact strip systems, it has been inferred that similar carbon films are formed on the surface of contact wires by sliding carbon contact strips. We reported that carbon films with a thickness of about 1 μm were formed on the contact wire taken from actual lines where metallized carbon contact strips were used [3]. However, because the friction phenomenon is complex and many parameters influence each other, the conditions for film formation have not yet been elucidated.

In this study, we conducted friction experiments using a rotating disk-type friction test apparatus to form films on the surface of contact wires. We investigated the conditions where films are formed by changing speed, current value, and contact force. The properties of the films were evaluated using Raman spectroscopy and nano-scratch tests, and the results were compared with those of contact wires taken from the field.

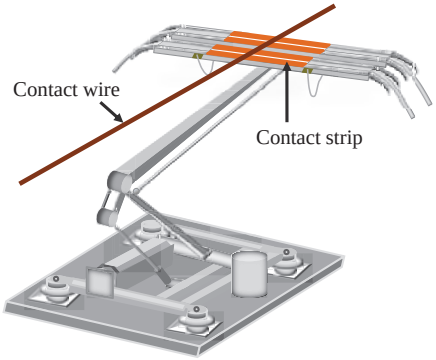


Fig. 1. Pantograph contact strip and contact wire

II. Experimental Procedure

A. Material

Carbon contact strips PC78A (TOYO TANSO Co., Ltd.) were used as contact strip specimens. PC78A are metallized carbon contact strips impregnated with copper and used on conventional railway lines in Japan. The chemical composition and physical properties of PC78A are shown in Table I. The carbon substrate of PC78A is non-graphitic carbon sintered at 1000-1500°C. The dimensions of the contact strip specimen were 60 mm wide × 25 mm long × 10 mm thick. Sn-added copper alloy contact wires, GT-Sn-110 (Mitsubishi Materials Corporation), were used. The contact wires (12.34 mm in diameter) were ground before use in the experiment so that the width of friction surface was approximately 5 mm.

Table I. Chemical Composition and Physical Properties of PC78A

Chemical composition (mass%)	C	52
	Cu	48
Physical properties	Density (10^3kg/m^3)	3.0
	Shore Hardness (HSD)	90
	Electric resistivity (μΩm)	1.8
	Flexural strength (MPa)	120
	Charpy impact value (kJ/m^2)	4.2

B. *Friction Experiments*

Friction experiments were conducted using a rotating disk-type friction test apparatus as shown in Fig. 2. This apparatus has a rotating disk with a diameter of 2 m, on which contact wires are fixed. During the experiments, a contact strip specimen was pressed against the contact wire, and an electric current was passed through them. To simulate the stagger of overhead contact wires in actual railway lines, the contact strip was moved left and right perpendicular to the sliding direction, at a speed of 5 mm/s with a stroke of 45 mm. The friction force and the pressing force were measured using load cells. Electric arcs sometimes occurred due to contact loss between the contact strip and the contact wire. Electric arc occurrence was defined as the condition in which the electric potential difference between the contact strip and the contact wire exceeded 10 V, as shown in Fig. 3. The ratio of the electric arc occurrence time to the total friction time was calculated as the occurrence ratio of electric arc.

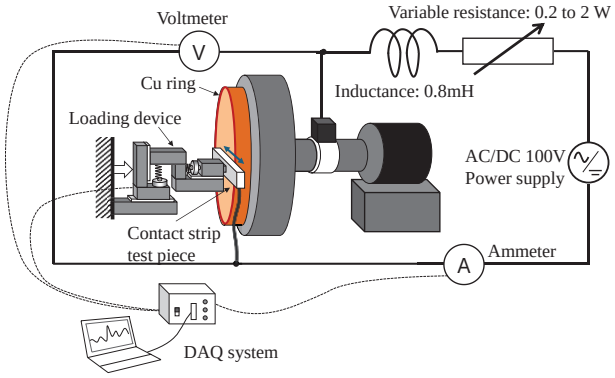


Fig. 2. Schematic image of friction test apparatus

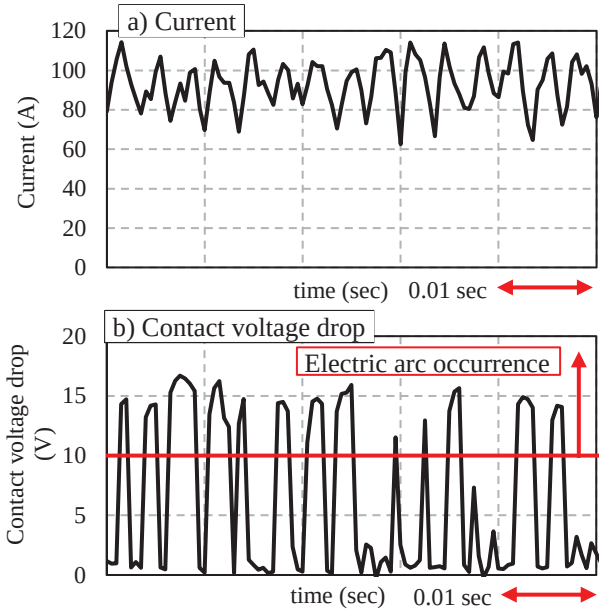


Fig. 3. Current and voltage waveforms during arc occurrence

C. *Experimental Conditions*

The experimental conditions are shown in Table II. The experiments were divided into two groups. First, the sliding speed, current, and sliding distance were varied to explore the conditions for carbon film formation under conditions 1-1 to 1-9. From these experiments, the conditions for forming carbon films were roughly identified. Second, experiments were conducted to form carbon films similar to those observed in actual railway lines, based on the conditions identified in conditions 1-1 to 1-9. A DC current flowed from the contact wire to the contact strip. The term “surface grinding” in Table II indicates whether the friction surface of the contact wire was ground before the experiment. When surface grinding was applied, the experiment started with a contact wire surface that had no prior friction history.

TABLE II. EXPERIMENTAL CONDITIONS

Condition number	Speed (km/h)	Current (A)	Sliding Distance (km)	Load (N)	Surface grinding
1-1	50	100	50	50	-
1-2	50	300	50	50	-
1-3	50	100	50	50	done
1-4	50	500	50	50	-
1-5	100	100	800	50	done
1-6	150	100	800	50	-
1-7	150	100	800	50	-
1-8	100	100	800	50	-
1-9	50	100	400	50	-
2-1	250	100	1000	50	-
2-2	100	100	800	50	-
2-3	150	100	636.5	20	done
2-4	50	100	300	50	-

D. *Raman Spectroscopy and Nano-scratch Tests for Carbon Films*

Carbon films formed in the experiments and those observed on contact wires taken from the field were observed using a scanning electron microscope (SEM) (S-3400N, Hitachi High-Tech Corporation), and elemental analysis was conducted using energy-dispersive X-ray spectroscopy (EDX) (XFlash Detector 4010, Bruker). To analyze the structure of the carbon films, Raman spectroscopy was performed using a Laser Raman spectrophotometer (NRS-7100, JASCO Corporation). The measurement conditions are shown in Table III. To evaluate the adhesion strength of the carbon films, we conducted nano-scratch test using nanoindenter (iMicro, KLA Corporation). The test conditions are shown in Table IV. First, a conical indenter (tip curvature radius: 1 μm) was brought into contact with the measurement surface and moved over a distance of 50 μm. Subsequently, the indenter was moved over a distance of 200 μm while the load was linearly increased.

TABLE III. CONDITION OF RAMAN SPECTROSCOPY

Wavelength of laser (nm)	532
Power of laser (mW)	2.8
Range of observed wave numbers (cm^{-1})	100-1450
Measurement time and number of iterations	5 sec × 1 time
Spot diameter of laser beam (μm)	4

TABLE IV. CONDITION OF NANO-SCRATCH TEST

Maximum load (mN)	10
Scratch distance (μm)	200
Scratch speed (μm/s)	20
Measurement number	5

III. RESULTS AND DISCUSSION

A. *Friction Experiments*

The friction surface of the contact wire after the experiments is shown in Fig. 4 and Fig. 5. The measurement results are shown in Fig. 6 and Fig. 7. The maximum height Ry, which is an index of surface roughness, is specified in JIS B 0601-1994 and is roughly equivalent to Rz in ISO 4287.

In conditions 1-1 to 1-5, where no electric arcs occurred, the friction surface of the contact wire remained a reddish-brown copper color. In conditions 1-6 and 1-7, where the speed was increased to 150 km/h and electric arcs occurred, the friction surface of the contact wire turned black. In condition 1-8, where the speed was reduced to 100 km/h and electric arcs did not occur, the friction surface of the contact wire became smooth and shiny. After condition 1-9, where the speed was decreased to 50 km/h, almost the entire friction surface became smooth and shiny. Fig. 6 b) shows that the wear rate of the contact wire was low in condition 1-7 to 1-9. Fig. 6 c) sows that the surface roughness was reduced in conditions 1-8 and 1-9 compared with conditions 1-5 to 1-7.

From the experiments under conditions 1-1 to 1-9, it was inferred that films could be formed by sliding under conditions where electric arcs occur, followed by sliding under conditions where electric arcs do not occur. After the carbon film was removed, the experiment was conducted under condition 2-1, where the speed was increased to 250 km/h. As a result, electric arcs occurred and part of the friction surface of the contact wire turned black. The occurrence rate of electric arcs in condition 2-1 was approximately 3%, as shown in Fig. 7 a). Subsequently, the experiment was conducted under condition 2-2, where the speed was reduced to 100 km/h. Although electric arcs did not occur, the black area disappeared, and films were not formed. In order to increase the occurrence of electric arcs, the experiment was carried out under condition 2-3, where the pressing load was set to 20 N and the speed was set to 150 km/h. Electric arcs occurred at approximately 20%, and almost the entire friction surface of the contact wire turned black. After that, in order to suppress electric arcs, the pressing load was again increased to 50 N and the speed was decreased to 50 km/h under condition 2-4. As a result, a smooth black film was formed on the friction surface of the contact wire, which was similar in appearance to that of the contact wire taken from the field, as shown in Fig. 8.

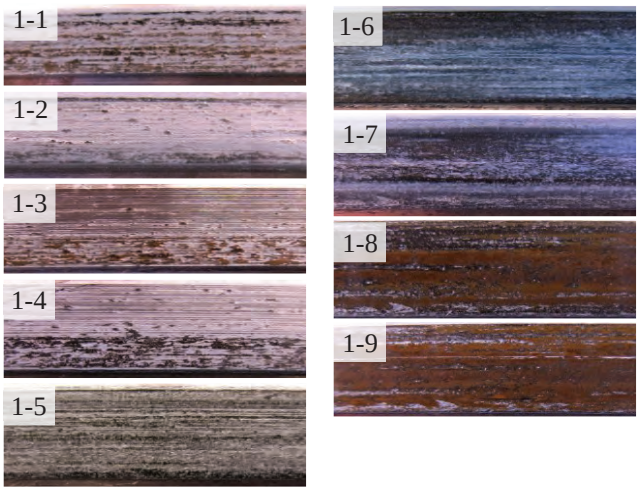


Fig. 4. Frictional surface of contact wire under condition 1-1 to 1-9

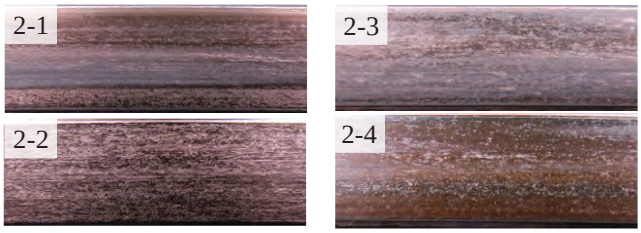


Fig. 5. Frictional surface of the contact wire under condition 2-1 to 2-4

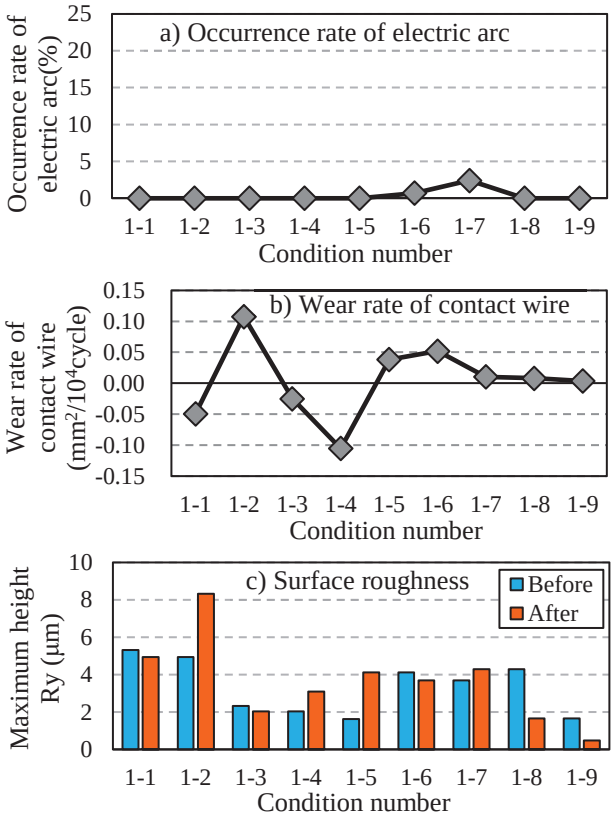


Fig. 6. Measurement results of electric arc, wear of contact wire, and surface roughness in conditions 1-1 to 1-9

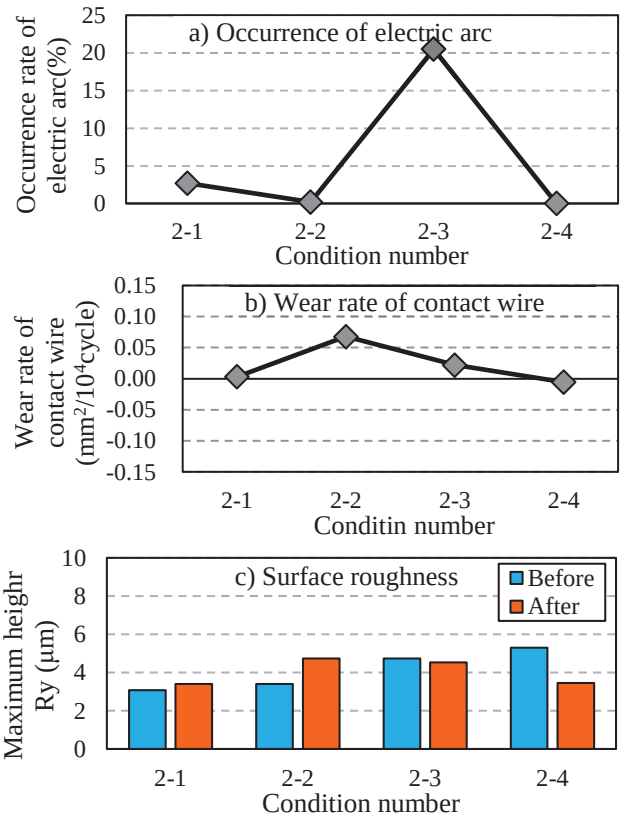


Fig. 7. Measurement results of electric arc, wear of contact wire, and surface roughness in conditions 2-1 to 2-4

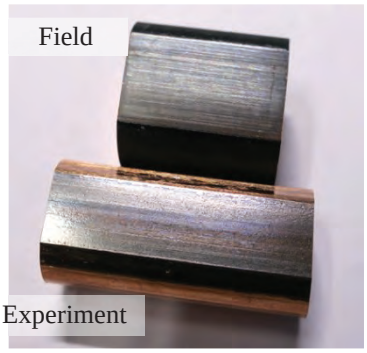


Fig. 8. Appearance of the friction surfaces of the field contact wire and the contact wire after the experiment under condition 2-4

B. Raman Spectroscopy and Nano-scratch Tests for Carbon Films

Fig. 9 shows SEM images of the friction surfaces of the contact wires. The friction surface of the contact wire taken from the field was generally smooth, although abrasion marks were observed. In contrast, the friction surface of the contact wire after the experiment exhibited several surface depressions and lower smoothness compared with that of the contact wire taken from the field. Table V shows the results of EDX analysis of the friction surfaces of the contact wires. Cu, C, and O were detected in both contact wires.

Fig. 10 shows the full width at half maximum (FWHM) of the G-band (1580 cm^{-1}) calculated from the results of Raman spectroscopy. The FWHM of the G-band of the contact strip decreased after the friction test. The FWHM of the G-band of the contact wire was close to that of the contact strip after the friction test. This indicates that the carbon films contain graphite-like sp^2-bonded structures. Fig. 11 shows the ratio of the D-band (1360 cm-1) peak intensity, I_D, to the G-band peak intensity, I_G. As observed for FWHM of G-band, I_D/I_G ratio of the contact strip decreased after the friction test. Although the I_D/I_G ratio of the contact wire was higher than that of the contact strip, this difference is likely attributable to material transfer from the contact strip to the contact wire during friction.

Fig. 12 shows the results of the scratch tests. As mentioned in Section II.D, the indenter load was increased linearly between scratch distances of 50 μm and 250 μm. For the contact wire taken from the field, the indenter depth displacement varied approximately linearly with increasing scratch distance. The contact wire after the experiment showed greater fluctuations in depth displacement than the contact wire taken from the field.

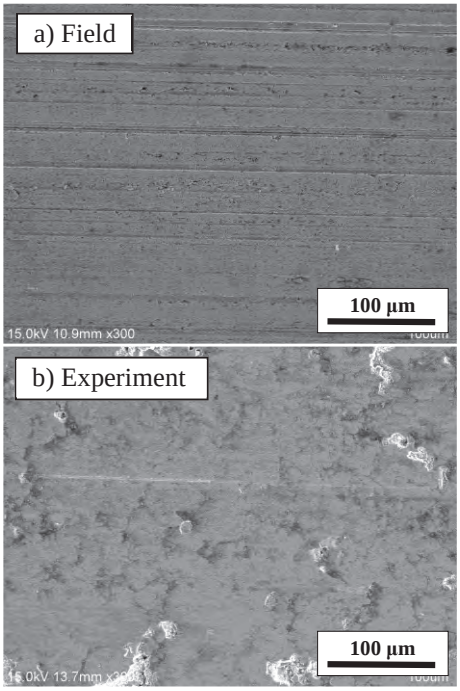


Fig. 9. SEM images of the friction surfaces of the field contact wire and the contact wire after the experiment under condition 2-4

TABLE V. ELEMENTAL ANALYSIS RESULTS OF THE FRICTION SURFACES OF THE FIELD CONTACT WIRE AND THE CONTACT WIRE AFTER THE EXPERIMENT UNDER CONDITION 2-4

	Semi-quantitative value (%)	
	Field	Experiment
Cu	79.6	75.5
C	12.7	20.8
O	7.7	3.6

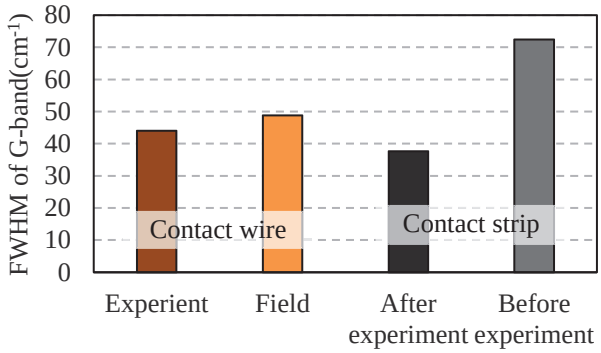


Fig. 10. Comparison of FWHM of G-band of the carbon-film on the friction surfaces of the contact strip before experiment, the contact strip after experiment, the field contact wire, and the contact wire after the experiment under condition 2-4

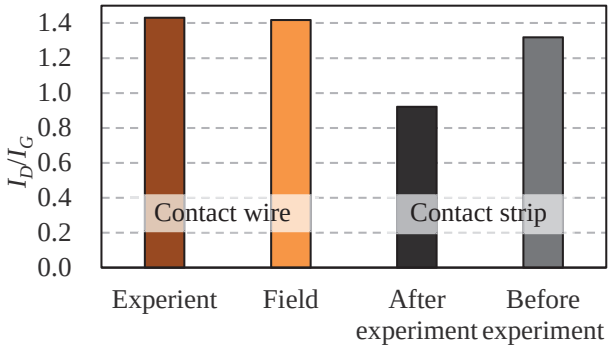


Fig. 11. Comparison of I_D/I_G, peak intensity ratio of D-band ot G-band, of the carbon-film on the friction surfaces of the contact strip before experiment, the contact strip after experiment, the field contact wire, and the contact wire after the experiment under condition 2-4

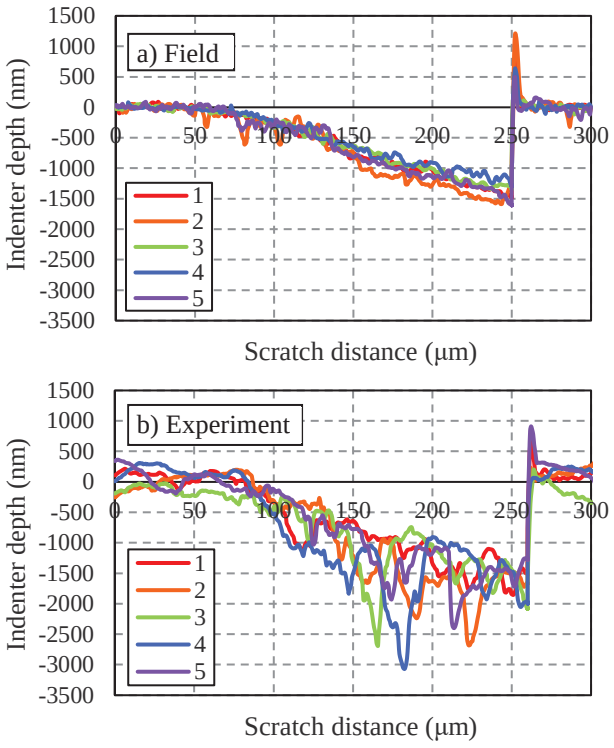


Fig. 12. Results of nano-scratch tests on the friction surfaces of the field contact wire and the contact wire after the experiment under condition 2-4

C. Discussions

From the elemental analysis and Raman spectroscopy, it was inferred that the film was formed as a result of carbon transfer from the contact strip. In conditions 1-1 to 1-5, when electric arcs did not occur, carbon transfer to the contact wire did not occur, even when the contact strip was worn. This suggests that the transfer is not simply caused by the wear of the contact strip, but that the electric arcs is one of the factors that promotes carbon transfer. Previous research [4] has shown that the electric arcs in the metallized carbon contact strip used in this study causes copper to dissolve from the friction surface, making it carbon-rich, and enhances the graphite-like sp^2-bonded structure of the carbon matrix. These factors may have promoted the carbon transfer to the friction surface of the contact wire, resulting in subsequent film formation. The transferred carbon may be compressed by repeated contact and friction, thereby forming a carbon film. In conditions 1-7 and 2-3, when electric arcs continued to occur, the compression of the transferred carbon may be hindered by electric arcs and contact strip bounce, thus preventing film formation. The reason why the friction surface became smooth after the film formation may be that the surface asperities were filled by the transferred carbon. The reason why the wear rate of the contact strip and the contact wire decreased when the film was formed is thought to be that the film prevented direct contact between the contact wire and the contact strip, thereby reducing the likelihood of adhesive wear.

As shown in Fig. 12, the indentation depth in this test was approximately 1.5 μm, which was comparable to the thickness of the carbon film on the friction surface of the contact wire in the field observed in a previous study [3]. Compared with the contact wire taken from the field, the contact wire after the experiment showed larger variations at each measurement point and also showed larger depth fluctuations within the scratch. This is thought to be due to the lower density of the carbon film formed in the experiment than taken from the field. The large depth fluctuations within the scratch observed in the contact wire after the experiment are thought to have occurred when the indenter penetrated into the surface depressions. It has been reported that when a hard coating delaminates from the substrate, a sudden and large drop in indenter depth was observed during the scratch [5]. However, such behavior was not observed for any of the contact wires. Therefore, it is considered that the carbon film was destroyed immediately after scratching began. This suggests that the carbon film may be easily removed by friction. Therefore, in order to maintain the carbon film, it is necessary to maintain a balance between the supply of carbon from the contact strip and the removal of the film due to friction.

IV. Conclusion

To investigate the conditions for forming carbon films when sliding metallized carbon contact strips against copper contact wires, we conducted friction experiments to form carbon films on the surface of contact wires using a rotating disk-type friction test apparatus. The following results were obtained:

- Carbon films were formed by sliding under conditions where electric arcs occur, followed by

sliding under conditions where electric arcs do not occur.

- From the results of Raman spectroscopy, the FWHM of the G-band of the carbon film formed in the experiment was close to that of the friction surface of the contact strip after the experiment. Therefore, it is considered that the carbon film was formed as a result of carbon transfer from the contact strip.
- Nano-scratch tests revealed that the adhesion strength between the film and the contact wire was low, suggesting that the film is easily removed by wear if sliding continues without a sufficient supply of carbon associated with electric arcs.

REFERENCES

[1] D.L. Dixon, "Development with carbons for current collection," Railway Engineering Journal, Vol. 2, No. 5, pp. 46-59, 1973.

[2] Q. Huang et al., "Research progress on the characteristics of current-carrying tribology in electrical transmission," Space Solar Power and Wireless Transmission, Vol. 1, Issue 1, pp. 37-47, 2024.

[3] Y. Kubota, "Raman spectroscopic analysis of carbon film on frictional surface of contact wire," 30th International Conference on Electrical Contacts, 2020.

[4] Y. Kubota and F. Morimoto, "Temperature rise and wear of metallized carbon contact strips under electric current of up to 1000A," 32nd ICEC and 69th IEEE Holm Conference on Electrical Contacts, 2024.

[5] B.D. Beake, V.M. Vishnyakov, and A.J. Harris, "Relationship between mechanical properties of thin nitride-based films and their behaviour in nano-scratch test," Tribology International, Vol. 44, Issue 4, pp. 468-475, 2011.

Influence of current waveform on km/s range electric sliding contact in the context of electromagnetic launchers

Vincent ANDRAUD
French-German Institute of Saint Louis (ISL)
Saint Louis, France
Vincent.andraud@isl.eu

Paul GAPENNE
French-German Institute of Saint Louis (ISL)
Saint Louis, France

Quentin HASSLER
French-German Institute of Saint Louis (ISL)
Saint Louis, France

Philippe BAUMANN
French-German Institute of Saint Louis (ISL)
Saint Louis, France

David BLUNTZER
French-German Institute of Saint Louis (ISL)
Saint Louis, France

Markus SCHNEIDER
French-German Institute of Saint Louis (ISL)
Saint Louis, France

***Abstract*— In the context of electromagnetic launchers, the projectile motion is driven by the Laplace force coming from the MA-range current injected in the rails. To reach velocities of a few km/s, a good electric contact must be ensured between the rails and the armature that is pushing the projectile inside the rails: indeed, any loss of contact could provoke the formation of a resistive plasma. This plasma can significantly reduce the current in the system, thus degrading the propelling force. Moreover, this plasma might also damage the rails, provoking their premature erosion. When it comes to the km/s range metal/metal sliding contact, the rails are also subject to the gouging phenomenon that can cause the formation of some craters inside the rails. To study and limit these effects, the Saint-Louis Institute (ISL) has conducted experiments of electromagnetic launches on different rail dimensions and armatures powered with a 10 MJ capacitive power supply. This presentation will give an insight into the complex phenomenology happening during the sliding contact for these launchers and will discuss the influence of the different experimental parameters, mainly the current waveform.**

Keywords—component, formatting, style, styling, insert (*key words****)***

I. Introduction

Railguns are electromagnetic launchers that have experimentally demonstrated muzzle velocities in the range of 2000 to 3000 m/s in this past, thus exceeding the capability of conventional guns using chemical propellants. From a military standpoint, this breakthrough technology offers substantial operational benefits. These include an extended range of over 200 km, faster target engagement, enhanced lethality, and improved ship survivability by eliminating the need for onboard propelling charges.

In Europe, the French-German Research Institute of Saint-Louis (ISL) has played a central role in the railgun development and maturation since the late 1990s [1]. The second part of this paper describes the railgun principle and addresses. The third part describes the 60 mm launcher NGL-60 and its associated 10 MJ power supply. Then, the fourth part gives insight into the complex phenomenology happening during a high energy railgun launch, focusing on the influence of the sliding contact on the launch efficiency. From this description, the fifth part relates the different experimental research strategies that have been carried on to optimize this sliding contact and thus optimizing the launch efficiency.

This research was supported by the French and German Ministries of Defence.

II. Experimental Launcher Principle

Based on developments from the early 20th century, the operating principle of the electromagnetic railgun relies on the Laplace rails experiment: the railgun itself consists of two fixed parallel rails mechanically connected by a metallic part called the armature. When the current provided by an external electric generator flows through the circuit, the armature is propelled by the Lorentz force resulting from the interaction between the MA range current and the Tesla range self-generated magnetic field. As a result, the typical complete launch package consisting of the armature, sabot and projectile is propelled towards the gun muzzle and exits it with a velocity in the range of few km/s.

For a Railgun application, the propelling Lorentz force F varies as the square of current intensity I and implies the inductance per unit of length of the rails L' according to the following equation.

$$F = \frac{1}{2} L' I^2 \qquad (1)$$

For square caliber railguns, the value of L' is supposed to be constant during the launch and has a value depending on the rails dimension between 0.4 and 0.5 µH/m. Using equation (1) as an initial estimation model, it can be seen that most railguns designed for military operations require gigawatts of electric power and mega-amperes of current. Indeed, the current pulse is delivered within a few ms which makes this specific application different from conventional electric machines, one of the main challenges being the achievement of an efficient sliding contact between the rails and the armature at speeds exceeding 2000 m/s, while handling current densities of approximately 100 kA/cm². Indeed, the quality of the sliding contact has a direct impact on the minimization of electrical losses – any contact degradation through the loss of solid contact between the armature and the rails to a plasma contact lowering the delivered current pulse thus reducing the propelling force according to (1).
The quality of this sliding contact has also a direct impact

on the rails degradation or destruction: high velocity sliding contact between two metals is subject to the occurrence of erosion – mainly due to arcing - or gouging – formation of teardrop-shaped craters in the rails [2]. If not addressed, these phenomena critically decrease the barrel lifetime which is of primary matter for military application. Indeed, to be developed at an industrial scale, Railgun barrels need to achieve a similar lifespan to conventional guns (e.g. up to several thousand shots for a 40 mm gun).

This article aims at illustrating the sliding contact phenomenology with the description of the experiments carried on with the ISL NGL-60 Railgun.

III. Experimental facility description

A. *The NGL-60 Railgun*

After several decades of experiments with smaller calibers guns, the 60 mm caliber railgun called NGL-60 (New Generation Launcher) has been built in 2017. This new dimension of caliber increases the available launch package volume to insert relevant embedded electronics components. Indeed, integrating electronic devices like magnetometers, accelerometers, and gyrometers into the projectile would allow for precise measurement of the time-varying magnetic field and the acceleration experienced by the projectile during the interior ballistic phase of a shot. Additionally, this setup could facilitate the measurement of the projectile's rotational motion, including roll, pitch, and yaw, throughout this phase. The resulting railgun, designated as the NGL-60, features a distinctive open-barrel design, as illustrated in Fig. 1. Additional information is provided in [3].

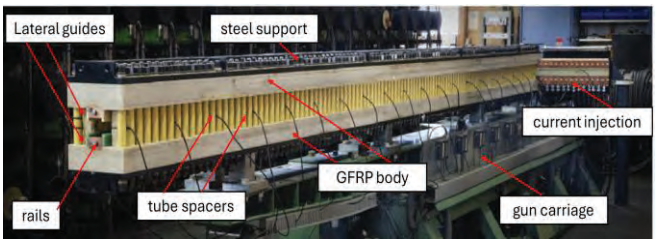


Fig. 1. Mechanical design of the Railgun NGL-60 with a 60 mm caliber.

As the designed launch package is heavier than the ones designed for smaller caliber, it requires more current than previously to reach muzzle speed exceeding 2 km/s. As a result, stronger magnetic forces act on the barrel during launch, and the mechanical structure has been engineered to endure the resulting pressures, which can reach hundreds of MPa in magnitude.

On the most recent version, flat rails have been replaced with convex rails and the launch package geometry has been accordingly adapted. This modification aimed at getting rid of the lateral guides that are likely to be damaged at high velocity and high magnetic pressure [4]. The armature is made of copper and has a classical C-shape geometry. It has a mass of 740 g whereas the rails are made of copper.

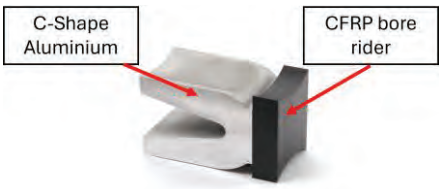


Fig. 2. C-shape aluminium armature with bore rider in carbone fiber reinforced plastic (CFRP)

B. *The 10 MJ PEGASUS Capacitive Power Supply and associated experimental diagnostics*

To propel a kg range projectile at a speed exceeding 2 km/s, the ISL 10 MJ PEGASUS capacitor bank is used. It consists of 13 parallel capacitor banks with an equivalent capacitance between 12 and 14 mF [5], the total number of capacitors being 193. Each capacitor is equipped with solid state switches, a gate unit, a pulse forming inductor and a ballast resistor, constituting a pulse forming unit. The bank can be charged to a maximum voltage of 10 kV and can deliver a current of up to 2 MA. Coaxial cables connect the current injection of the NGL-60 gun barrel to the power supply.

Electrical metrology is achieved using current probes to measure the total current flowing through the rails, along with voltage probes positioned at both ends of the rails—at the muzzle and breech. The projectile's position and velocity are tracked using B-dots strategically placed along the barrel. These sensors detect rapid changes in magnetic fields caused by the passage of the current-carrying armature. Velocity is further measured using lasers and photodiodes; two lasers and two photodiodes are installed at the rail exit to capture the exact moment the armature passes. Similarly, velocity determination is supported by capturing two distinct X-ray images of the armature. Additionally, fast cameras and X-ray imaging are employed to visualize the projectile’s trajectory as it exits the muzzle, aiding in the analysis of its ballistic behaviour outside the barrel. After each shot, endoscopy imaging of the rails is processed to check the rails condition and detect any degradation, damage or fracture.

IV. Interior Ballistic sliding contact phenomenology

The phenomenology of the sliding contact during the launch can be studied with the different diagnostics. Depending on the current slope and the projectile speed, four phases can be differentiated: the projectile initial acceleration, the maximum current plateau, the current downslope and the projectile muzzle exit. These different phases can be distinguished with the electric current and voltage waveforms during a launch represented in Fig. 3. The initial capacitive energy is 6.7 MJ: the capacitor banks are charged at 9 kV and discharged sequentially in the railgun through the crowbar circuit and the coaxial cables. The projectile consists of the sole aluminium armature with a bore rider for a total mass of 740 g. The different triggering instants of the 13 parallel capacitor during the first 2 ms banks are marked on the current waveform by the presence of inflexion points.

The muzzle voltage is measured between the rails at the barrel muzzle and is the image of the sliding contact quality: a value below 100 V is the sign of a good solid contact whereas a value over a few hundreds of volts is due to the formation of a plasma contact. The velocity and the position of the armature are interpolated from the B-dots measurements. The projectile exits the 6-meter barrel at 3.8 ms with a velocity of 2350 m/s.

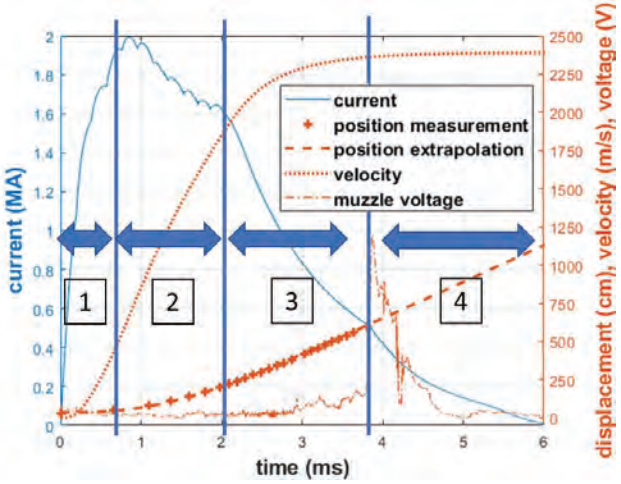
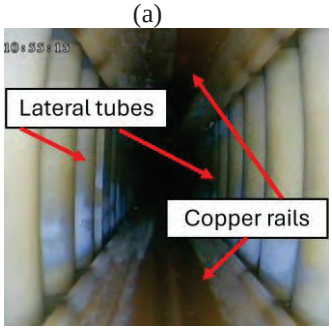


Fig. 3. Electric and ballistic measurement curves for a 6.7 MJ initial capacitive energy and succession of different phases: (1) projectile initial acceleration (2) maximum current plateau (3) current downslope (4) projectile exit.

A. Initial contact and acceleration phase

The initial contact and acceleration phase is marked by the rising current in the circuit : the first capacitor banks are discharged thus feeding the circuits inductor and the rails with magnetic energy. The projectile is initially inserted at distance of 35 cm from the breech end of the rails with an initial mechanical loading of several hundreds of kN to ensure a good initial solid electric contact with the rails. During this phase, the Laplace propelling force exerted by the current on the projectile has to overcome the initial static friction. After few cm, a thin deposit of aluminium is visible on Fig. 4(a) due to the establishment of the electric contact between the armature and the copper rails. The action integral in the projectile is not yet enough to provoke its contact surface melting: thus, no ejection of melted particles can be seen in Fig. 4(b).

(a)



(b)

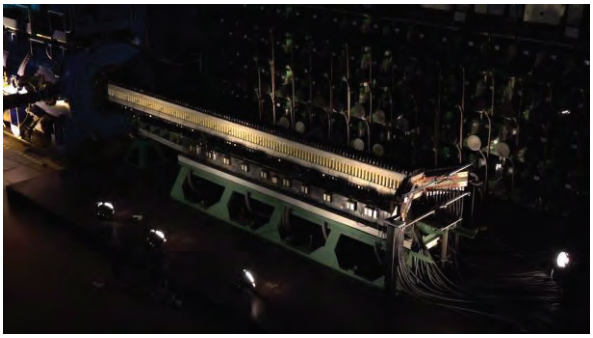
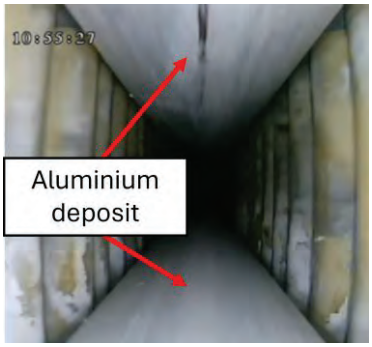


Fig. 4. Image of the rails after the passage of the armature (a) and of the barrel during a launch (b) in the first meter of the armature displacement between the rails.

B. Plateau of maximum current

Within the first ms, the current reaches its peak value while the armature moves at a relatively slow speed (below 2 km/s). This combination promotes the deposition of aluminium on the rails. A higher current intensifies the Joule effect in the armature, and the slower movement allows the armature to remain longer on a specific section of the rails. As a result, the aluminium deposition on the rails is both uniform and dense, as illustrated in Fig. 5(a) The melting of the armature and the rails surfaces is also marked by the very bright ejection of melted copper and aluminium particles as can be observed in Fig. 5(b). This phase is also characterized by the continuous activation of the remaining capacitor banks that remains the total current at a relatively high level despite the longer rails portion traversed during the launch increases the rails electrical resistance.

(a)



(b)

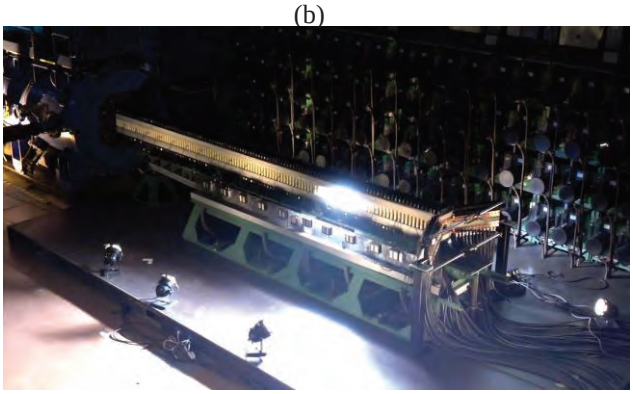


Fig. 5. Image of the rails after the passage of the armature (a) and of the barrel during a launch (b)

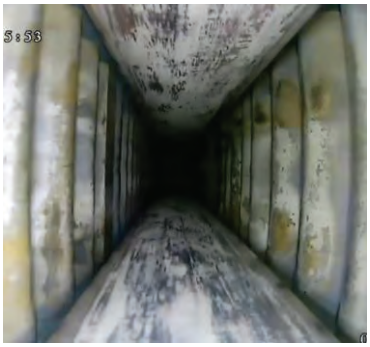
between two and three meters of the armature displacement between the rails.

C. *Downslope current*

After 2 ms, all the capacitor banks have been activated and the current in the rails is only maintained by the stored magnetic energy in the circuit inductors and in the rails inductance. In general, the current in the rails is decreasing faster than in the previous phase as the projectile is reaching a velocity of 2 km/s due to the additional rails portion conducting current and thus adding electric resistance. Thus, the propelling force is decreasing whereas the high speed is likely to provoke the armature enhanced torques producing yaw, pitch and roll. This can result in the formation of rails gouging that is reported in [2] and that will be discussed in the next section.

Additionally, as the projectile is faster than the previous phase, the deposition of aluminium on the rails becomes less homogenic and less dense as it can inferred from Fig. 6(a). Additionally, oxidation of the aluminium layer can be inferred from the visible black traces. This oxidation is likely to be due to the local formation of a plasma coming from the punctual melting of an a-spot and provokes the glowing aspect of Fig. 6(b).

(a)



(b)

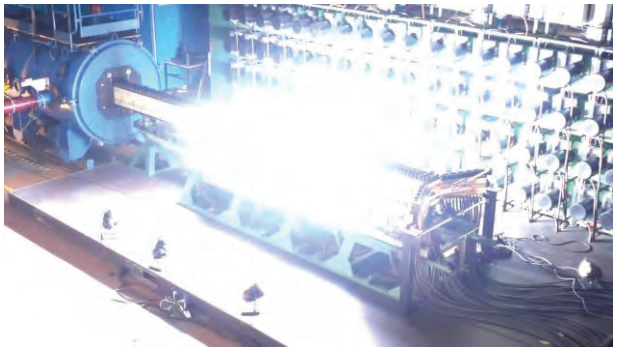


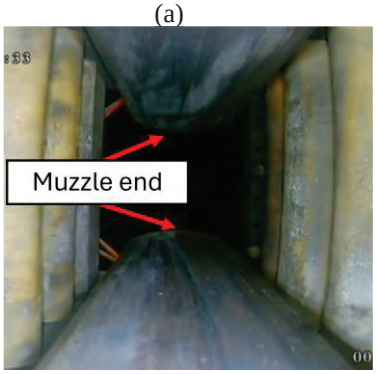
Fig. 6. Image of the rails after the passage of the armature (a) and of the barrel during a launch (b) between three and four meters of the armature displacement between the rails.

D. *Muzzle exit phenomenology*

When the armature reaches the muzzle exit, a current of more than 500 kA is remaining in the circuit and rails equivalent inductance. Thus, the opening of the solid contact produced by the armature leaving the rails tends to form electric arcs between each armature tail winglet and each rails termination. These electric arcs are responsible for the surge of voltage reaching more than 1.5 kV due to the spatial arcs extensions.

Fig. 7(b) shows evidence of these electric arc formation at the muzzle exit. At 6 m, the rails deposit layer is dusky as pictured in Fig. 7(a) showing coming from these electric arcs formation.

(a)



(b)



Fig. 7. Image of the rails after the passage of the armature (a) and of the barrel during a launch (b) at the muzzle exit.

V. Effect of the Current Waveform

A. *Formation of gouging*

As mentioned in the previous section, the gouging phenomenon is characterized by the formation of teardrop shaped craters in the rails. Fig. 8 shows the formation (Fig. 8.a) of a gouging after a launch and the enlargement of this gouging area after a second shot (Fig. 8.b).

(a) (b)

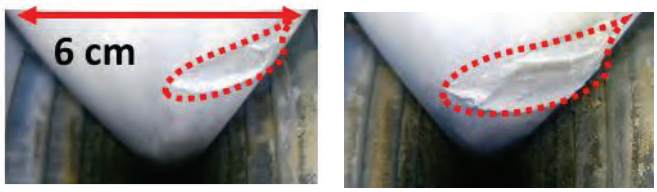


Fig. 8. Images of formation (a) and enlargement (b) of a gouging in the rails during two consecutive launches.

The formation of the gouging is likely to provoke the armature's destruction during the launch: Fig. 9 depicts the solid contact quality through X-ray images obtained in the

barrel. In Fig. 9(a), both winglets of the armature are in contact with the rails during the sliding contact thus enabling the current to flow through the projectile. In Fig. 9(b). The gouging has provoked a partial breaking of the armature's upper winglet thus the current flow inside the armature is severely degraded. In that case, the rail has to be replaced to ensure the canon functioning. For these two successive shots, the associated current and muzzle voltage waveforms are given in Fig. 10. It can be observed that the current waveform is not very affected by the gouging occurrence. However, from the gouging location, the muzzle voltage increases due to the partial loss of solid contact and the formation of a plasma. Even though the projectile is broken, the current flowing in the rails is not degraded by the formation of a plasma contact.

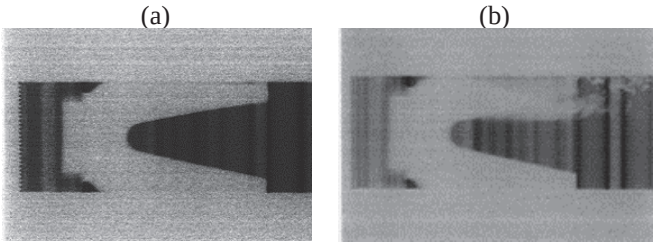


Fig. 9. X-ray imaging of the armature inside the rails without loss of contact (a) and with loss of contact (b) due to the formation of gouging in the rails.

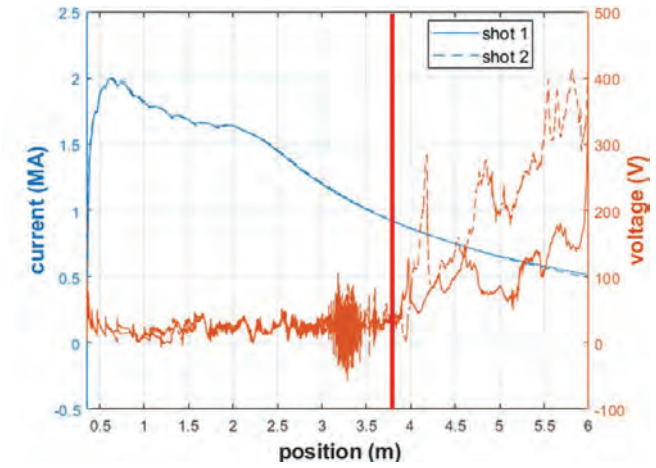


Fig. 10. Spatial current and muzzle voltage waveforms for experiments before and after gouging occurrence.

The mechanism for the formation of gouging is currently a research topic. However, several references [2],[6] estimated that the main factors are the irregularities of the rails surface, a parallelism defect of the rails or the presence of debris on the rail surface. It is worth noticing that this phenomenon does not only appear for the sole Railguns operation but is also intervening in any application with metal sliding contacts and mainly in the rocket sled experiments literature [7]. For Railgun applications, the role of the current, provoking the contact melting, is difficult to decouple from the effect of the speed. Some tests conducted at ISL focused on the decorrelation of these effects.

B. Effect of the speed

Several references have established the predominance of a threshold velocity, mainly depending on the hardness of the metals in contact and mainly on the yield stress of the harder material [8, 9]. For copper/aluminium contact, a threshold value of 1300 m/s can be found without the associated acceleration profile [8]. Additionally, it is experimentally observed that the gouging phenomenon is likely to occur when the acceleration is reduced (sled coast phase) [10]. For railgun launch, during the current downslope phase, the armature is subject to a reverse body-force that reduces the magnetic compressive force as described in [11]. Thus, the contact quality worsens as it can be inferred from the muzzle voltage increase in Fig. 10.

The influence of the current decrease has been experimentally tested with a 2 meters gun: four capacitors' banks are discharged initially in the rails to reach a maximum current of 2 MA (phase 1). Then the current in the rails decreases until the armature reaches the muzzle exit with no further activation of capacitor bank (phase 2). At the muzzle exit, 500 kA electric arcs are formed (phase 3). These different phases are depicted through the electric and ballistic waveforms in Fig. 11.

In that experiment, the current downslope during the phase 2 is similar to the current downslope during phase 3 of the experiments with the 6 meters barrel described in the previous section and depicted in the Figure 4. It is worth noticing that this experiment, despite showing a similar current downslope than the one for 6-meters barrels, did not lead to the formation of gouging on the rails whereas the armature's velocity does not exceed 1.1 km/s. This observation would tend to prove that the downslope current is not the only factor responsible for the formation of gouging and that the effect of a high velocity of the projectile cannot be neglected.

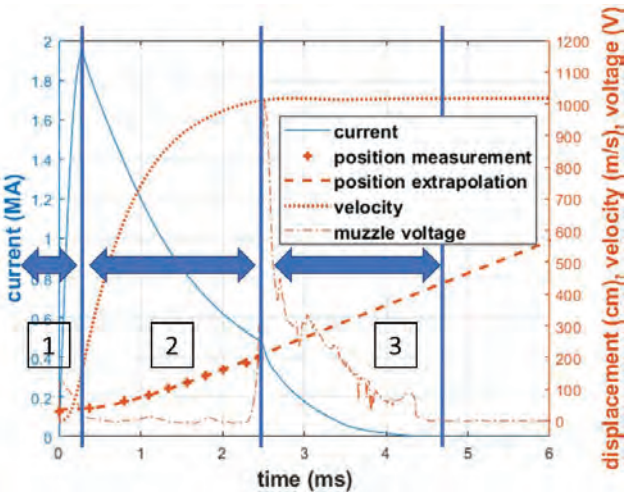


Fig. 11. Electric and ballistic measurement curves for a 2 MJ initial capacitive energy on a two meter railgun.

C. Effect of the current downslope

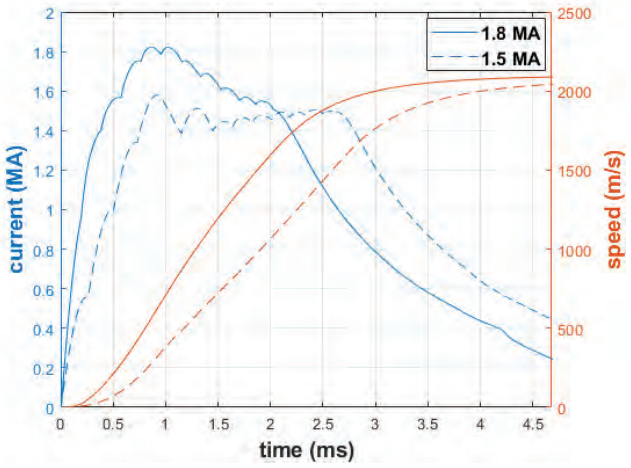
To check the effect of the current downslope at high speeds, the adopted strategy was to prioritize the pulse duration over the pulse intensity with the same initial energy. This strategy aimed at verifying whether a delayed apparition of the current downslope in the current waveform would lead to the distancing of the gouging apparition in the rails. To this aim, two current waveforms at 6 MJ have been tested: one with short term triggering and a 1.8 MA peak current (plain line) and one with long term triggering and a 1.6 MA peak current (dashed line) as shown in Figs. 12(a) and 12(b). It can be

seen in the time current profiles that in the case of the enlarged pulse, the current downslope appears at 2.7 ms whereas it appears at 1.9 ms for the shorter pulse.

However, if the current pulses over the barrel length are considered, the current downslope appears when the projectile is at 1.8 meters in the rails for the short pulse whereas it appears at 2 meters for the enlarged pulse. This is due to the fact that the projectile is faster for the short pulse since the current peak is higher than for the enlarged pulse: thus, the current downslope phase occurs sooner but at a similar distance than it appears for the enlarged pulse. The vertical lines in Fig. 12(b) shows the distance in the rails where the gouging occurred: it can be noted that the first gougings appeared at a comparable position for the two experiments for similar experimental conditions (a current of 800 – 900 kA and a 1.9 – 2 km/s speed). This leading to the equal importance of the current and the speed in the formation of gouging.

However, due to the limited 10 MJ capacitor bank and the value of the electrical parameters of the circuit (equivalent capacitance, inductance and resistance), it is not possible to feed the railgun with a constant current until the projectile exits the rails and thus conclude on the role of the current downslope in the formation of gouging. Such a current profile could be available in the near future with the development of dedicated inductive pulse power sources [12].

(a)



(b)

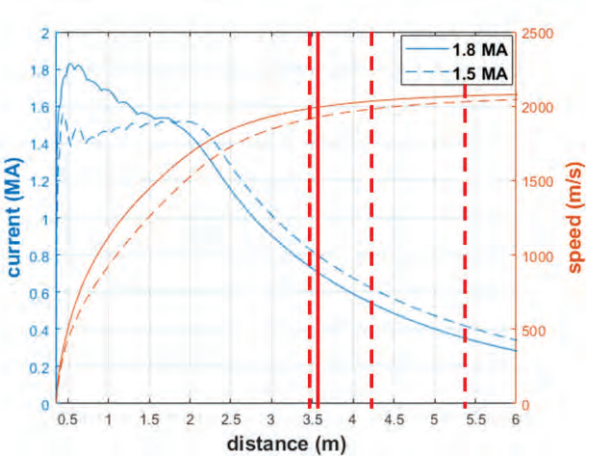


Fig. 12. Comparison of current and velocity temporal (a) and spatial (b) profiles for two experiments with shorter and enlarged pulses.

CONCLUSION

During a railgun launch, the sliding contact experiences different phases depending on the current slope and the relative speed between the armature and the rails. Their combined influences in the deposit of aluminium on the rails, on the quality of the electric contact and on the mechanical degradation of the rails is experimentally studied. It turns out that the most critical phase for the rails survivability is the downslope current phase when the armature reaches a velocity close to 2 km/s. After demonstrating that the sole downslope current is not sufficient to provoke gouging, attempts to postpone the occurrence of the downslope current phase during the pulse have shown the predominant importance of a 2 km/s range speed to provoke gouging. Further experiments will focus on the pulse elongation to study the relation between speed and current downslope at higher velocity levels.

REFERENCES

[1] P. Lehmann, and H. Peter, "ISL Studies on Electromagnetic Railguns", European Forum on Ballistics of Projectiles, Saint-Louis, France, April 11-14, 2000

[2] Cinnamon, J. D. (2009). *Hypervelocity gouging impacts*. American Institute of Aeronautics and Astronautics.

[3] S. Hundertmark, G. Vincent, F. Schubert, and J. Urban, "The NGL-60 Railgun", IEEE Transactions on Plasma Science, vol. 47, no. 7, July 2019

[4] Andraud, V., Gapenne, P., Hassler, Q., Scharf, H., & Schneider, M. (2025). Study and implementation of a new rail geometry for a 10 MJ large caliber electromagnetic launcher. *AIP Advances*, *15*(4).

[5] P. Lehmann, H. Peter, and J. Wey, "First Experimental Results with the ISL 10 MJ DES Railgun PEGASUS", IEEE Transactions on Magnetics, vol. 37, no. 1, January 2001

[6] Cinnamon, J. D., & Palazotto, A. N. (2022). Analysis and simulation of hypervelocity gouging impacts for a high-speed sled test. In *Handbook of Scholarly Publications from the Air Force Institute of Technology (AFIT), Volume 1, 2000-2020* (pp. 445-461). CRC Press.M. Young, The Technical Writer's Handbook. Mill Valley, CA: University Science, 1989.

[7] Laird, D. J., & Palazotto, A. N. (2004). Gouge development during hypervelocity sliding impact. *International Journal of Impact Engineering*, *30*(2), 205-223.D. P. Kingma and M. Welling, "Auto-encoding variational Bayes," 2013, arXiv:1312.6114. [Online]. Available: https://arxiv.org/abs/1312.6114

[8] Stefani, F., & Parker, J. V. (2002). Experiments to measure gouging threshold velocity for various metals against copper. *IEEE Transactions on Magnetics*, *35*(1), 312-316.

[9] Barber, J. P., & Bauer, D. P. (1982). Contact phenomena at hypervelocities. *Wear*, *78*(1-2), 163-169.

[10] Krupovage, D. J. (1984, September). Rail gouging on the holloman high speed test track. In *35th Meeting of the Aeroballistic Range Association*.

[11] Satapathy, S., & Vanicek, H. (2006). Down-slope contact transition in railguns. *IEEE Transactions on Magnetics*, *43*(1), 402-407.

[12] O. Liebfried and V. Brommer, "Demonstration of a 1 MJ XRAM Generator Supplying a Medium Caliber Railgun", IEEE Access, vol. 8, December 2020

Enhancing the Interruption Capability of Low Voltage DC Hybrid Circuit Breakers

Caizhi Gao
State Key Laboratory of Electrical Insulation and Power Equipment
Xi'an Jiaotong University
Xi'an, P.R.China
gaocaizhi@stu.xjtu.edu.cn

Zhaozi Zhang
State Key Laboratory of Electrical Insulation and Power Equipment
Xi'an Jiaotong University
Xi'an, P.R.China

Silei Chen
School of Electrical Engineering
Xi'an University of Technology
Xi'an, P.R.China

Xingwen Li
State Key Laboratory of Electrical Insulation and Power Equipment
Xi'an Jiaotong University
Xi'an, P.R.China
xwli@xjtu.edu.cn

Yinfang Huang
Shanghai Liangxin Electrical Co., Ltd.
Shanghai, P.R.China

***Abstract*—Natural commutation hybrid circuit breakers combine low loss, high performance, and simple structure and control, making them well-suited for protection in low voltage DC systems. This paper focuses on enhancing the interruption capability of such breakers. A prototype comprising a molded case circuit breaker and an electronic printed circuit board module is developed. First, two natural commutation strategies, turning on the insulated gate bipolar transistor at the instant of arc ignition versus during the arc current-limiting stage, are experimentally compared. As the current level increases, the latter demonstrates superior interruption capability. Another factor limiting the interruption capability is device failure due to latch-up, which necessitates optimizing the driver parameters or selecting an appropriate snubber circuit. Finally, an improved hybrid circuit breaker topology is introduced, which increases the switching voltage and accelerates the current-clearing process through the coordinated action of its mechanical and electronic components. This paper provides a reference for the design of high-performance low voltage DC hybrid circuit breakers.**

Keywords—hybrid circuit breaker, low voltage DC interruption, device failure, switching voltage

I. INTRODUCTION

With the rapid development of low voltage (LV) direct current (DC) systems such as photovoltaic installations, data centers, and electric vehicle charging piles, the demand for high-performance circuit breakers for system protection is becoming increasingly urgent. The primary reason is that once a fault occurs in a DC system, there is no natural current zero-crossing and the fault current rises rapidly, making interruption extremely challenging [1].

Currently, the most widely used type of circuit breaker is mechanical circuit breaker (MCB), which offers advantages such as low on-state loss, strong current-carrying capability, and low cost. It relies on stretching, splitting, and cooling arc to interrupt fault current, leading to challenges such as severe contact erosion, long interruption time (tens of ms). Existing technologies mainly focus on improving performance by enhancing the arc-extinguishing chamber structure, employing multi contacts in series, or adding gas-producing materials [2], [3], [4]. With the advancement of semiconductor technology, solid-state circuit breakers (SSCBs), which use power semiconductor devices to perform the main interruption task, have attracted significant attention. They offer arc-less operation and μs-level interruption time, but suffer from relatively high on-state losses and are generally designed for low-power applications. To increase the power rating, efficient thermal management systems must be integrated within limited volumes, as exemplified by a 1,000V/5kA SSCB prototype [5], which employs a novel insulating liquid cooling solution at a higher cost.

The hybrid circuit breaker (HCB) typically employs a parallel configuration of mechanical switch and power electronic device, integrating the advantages of both MCB and SSCB while maintaining relatively low development costs [6], [7]. Under normal operating conditions, the mechanical branch provides a low-resistance current path. During current interruption, the current is commutated to the electronic branch, which possesses a stronger breaking capability. In LV DC applications, circuit breakers are often required to be installed in distribution cabinets, imposing stringent demands on compact size and low cost. Therefore, unlike methods such as adding load commutation switches or coupling negative voltage devices to force current commutation, natural commutation is commonly adopted [8]. This method relies on the arc voltage generated upon mechanical contacts separation to drive the current commutation. Askan and Schasfoort developed a LV DC HCB prototype using a relay and an insulated gate bipolar transistor (IGBT) module, achieving a breaking capacity of 760 V/15 kA [9]. Their current commutation strategy involves turning on the IGBT, separating the contacts, and completing commutation (almost simultaneously) immediately upon fault detection. This requires both a high-speed mechanical switch and an IGBT module with a high current-carrying capability. In contrast, Feng et al. adopted a different coordination sequence: the electronic branch is engaged only during the final stage of the moulded case circuit breaker (MCCB) interruption process [10]. Using only four discrete IGBTs conducting briefly for 100 μs, they enhanced the MCCB's breaking capability to 750 V/10 kA. Existing studies on HCBs mainly focus on the analysis and design under a single specific mechanical-electrical coordination strategy. Nevertheless, the potential to enhance interruption capability is rarely explored. This paper compares the impact of two strategies on interruption performance, presenting results from both parameter optimization and topological improvement.

This work was supported by the National Natural Science Foundation of China (52277163) and the Shaanxi Provincial Science and Technology Plan Project (2022TD-59).

The remaining sections of this paper are organized as follows: Section II introduces the basic topology and test platform. Section III experimentally tests the feasibility of the two interruption strategies and provides a comparative analysis of their advantages and disadvantages. Section IV analyses the device failure mechanism and proposes improvement measures. Section V introduces an improved HCB with higher interruption capability. Section VI presents the conclusions.

II. HCB Prototype and Test Platform

The topology of the natural commutation DC HCB has been presented in previous papers [8]. It consists of three branches: the mechanical switch branch, the power electronic switch branch, and the protection branch. In this paper, the mechanical switch branch uses only a commercial 63A frame MCCB (single-pole, rated value I_n=40A). Both its fixed and mobile contacts feature silver tin oxide ($AgSnO_2$) tips (~5×5×1.2mm³) brazed onto copper substrates. It relies on its thermal-magnetic trip mechanism to detect faults and open contacts to generate an arc. The power electronic switch branch incorporates a TO-247 packaged IGBT, model IXYX110N120C4 (V_{CES} = 1,200V, I_{C110} = 110A). The protection branch employs a metal oxide varistor (MOV), model 431K40D, and a resistor-capacitor-diode (RCD) snubber circuit connected in parallel (to be discussed later). The power electronic switch branch and the protection branch are integrated on a printed circuit board (PCB), which is connected in parallel with the MCCB via wiring.

To test the performance of the HCB prototype, a resistor-inductor-capacitor (RLC) series circuit is established to simulate DC interruption, as shown in Fig. 1. The parameters are selected as follows: R = 0.17 Ω, L = 2.03 mH, C = 90 mF. Switches K_{S1} and K_{S2} are pre-closed to activate the capacitor charging circuit, and the initial voltage on the energy storage capacitor C is set to achieve different output current magnitudes and rates. At the beginning of the experiment, switch S is closed, allowing current to flow through the prototype under test. A prospective peak current level of approximately 600~1,000A is considered to ensure reliable tripping of the MCCB. The duration near the peak current can exceed 10ms. Therefore, this circuit effectively emulates the behaviour of a DC output.

III. Experimental Waveforms of the Two Strategies

This section compares two strategies that differ primarily in their commutation mechanisms, with the electronic part being activated at different time instants: at the moment of arc ignition (Type I) and during the current-decay stage of the arcing period (Type II). The following analysis elaborates on this distinction with reference to the experimental waveforms.

Fig. 2(a) shows the current and voltage waveforms of a successful interruption using the Type I strategy. Before the experiment, the initial voltage across capacitor C is set to 200 V, and the expected peak current is 684 A (occurring at 15.9 ms, with $di/dt \approx 43$ A/ms). From time 0, current flows through the mechanical contacts and gradually increases. When the current reaches 5~10 times the rated value of the MCCB, the trip unit detects the fault and opens the contacts. The contacts open at ~15.5 ms, generating an arc voltage of ~24 V. At this moment, the IGBT is turned on, and the arc extinguishes promptly. After a 300 µs delay, the IGBT is

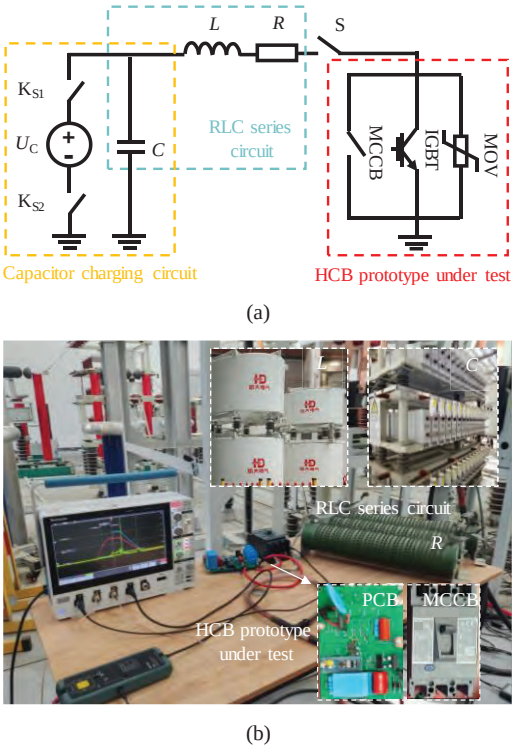
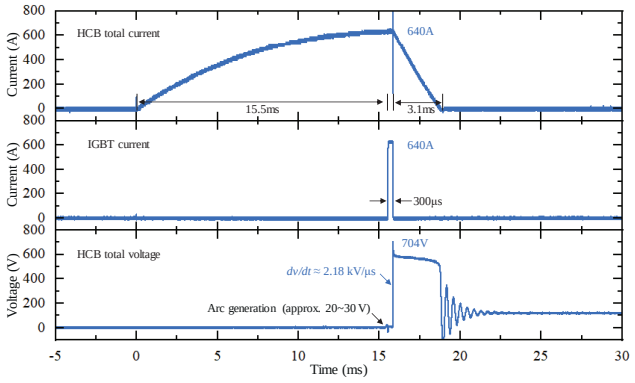


Fig. 1. HCB test platform. (a) Topology. (b) Experimental setup.

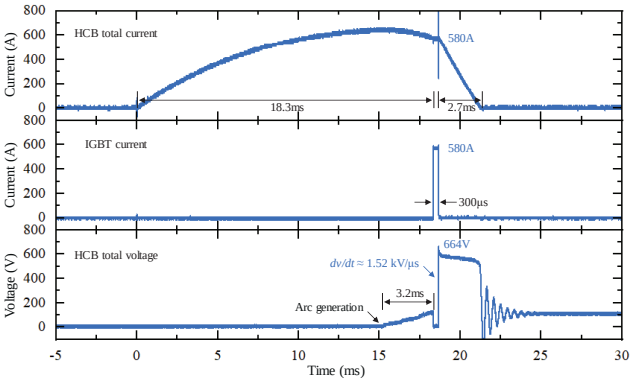
turned off. Due to the parasitic inductance of the circuit, overvoltage is generated when the IGBT interrupts the high current, with an overvoltage rise rate (dV_{CE}/dt) of ~2.18 kV/µs. Under the effect of the overvoltage, the MOV conducts and clamps the overvoltage, with a peak value of 704 V. The current then gradually decays to 0 over the next 3.1 ms. The total current clearing time is 18.9 ms.

Fig. 2(b) shows the current and voltage waveforms of a successful interruption using the Type II strategy under the same experimental conditions. A distinct difference from Type I is that the IGBT is not activated immediately upon arc ignition. Instead, it begins to conduct only after the arc has burned for ~3.2 ms. This duration depends on the time required for arc energy harvesting and gate driver IC initialization [8]. By this time, due to the current-limiting effect of the arc, the current has already started to decay, and the current that the IGBT and MOV need to handle is only 576 A. The dV_{CE}/dt during turn-off is ~1.52 kV/µs, with a peak value of 664 V, both lower than those of Type I. The time for the MOV to clear the current is 2.7 ms, shorter than that of Type I. Consequently, the PCB endures lower interruption stress. However, the total interruption time is slightly extended to 21.3 ms.

Comparing the Type I and Type II interruption strategies, both rely on the thermal-magnetic trip unit of the MCCB for fault detection, offering a simple structure and low cost. The advantages of Type I further include nearly arc-free operation and faster interruption time, while its drawback is the higher interruption stress imposed on the electronic part. Since a certain contacts separation distance must be achieved to prevent restrike, the IGBT conduction time cannot be set too short, which further increases the interruption stress on the IGBT (the IGBT is forced to conduct the short-circuit current for a relatively long period, typically resulting in extremely high temperature rise) [11]. This adverse effect

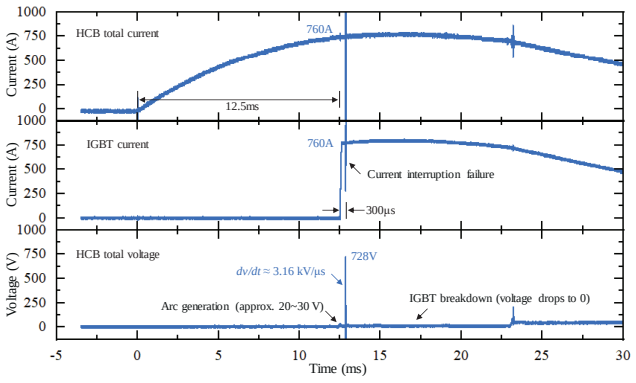


(a)

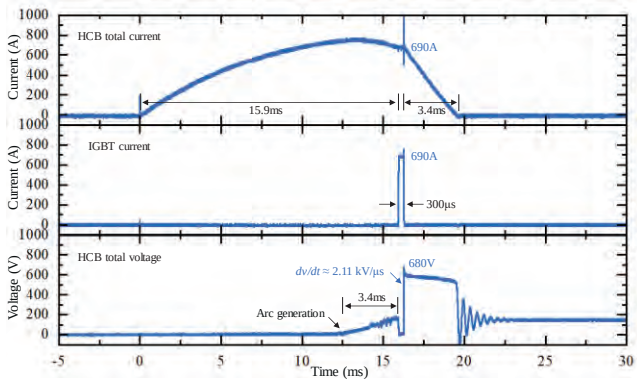


(b)

Fig. 2. Interruption waveforms of the HCB under different current commutation strategies with capacitor *C* pre-charged to 200V. (a) Type I strategy. (b) Type II strategy.



(a)



(b)

Fig. 3. Interruption waveforms of the HCB under different current commutation strategies with capacitor *C* pre-charged to 250V. (a) Type I strategy. (b) Type II strategy.

becomes more pronounced at higher current levels. Type II fully utilizes the MCCB's high current-carrying capability, using the arc to limit the current to a lower level. This represents an engineering lifespan trade-off: it deliberately sacrifices a portion of the mechanical contacts' electrical lifespan to ensure the safe commutation and reliability of the electronic part (especially the IGBT) under high fault currents. Since the commutation process occurs during the arcing period, repeated interruption operations inevitably lead to the degradation of the contact surface microstructure and a significant increase in contact resistance. It is necessary to properly assess the degree of contact degradation and replace the MCCB in a timely manner [10]. Before the IGBT turn-off signal is given, the MCCB has sufficient time (over 3ms) to reach its maximum contact gap of 10mm, reducing the probability of overvoltage breakdown across the contact gap.

When the pre-charged voltage of capacitor *C* reaches 250 V, the expected peak current is 856 A ($di/dt \approx 53.8$ A/ms). The experimental waveforms of the two interruption strategies under this condition are shown in Fig. 3. With the Type I strategy, an arc is generated at ~12.5 ms, and the current commutes to the IGBT branch. However, after conducting for 300μs, the IGBT fails to turn off normally; the short-circuit current continues to flow entirely through the IGBT until the device is destroyed. The recorded dV_{CE}/dt reaches ~3.16 kV/μs, with an overvoltage peak of 728 V (well below the device's V_{CES}), suggesting device failure likely caused by latch-up during high-current turn-off [12]. Under the same experimental conditions, using the Type II strategy, the MCCB arc burns for ~3.4 ms to limit the current to 690 A. The IGBT successfully conducts and then turns off, with an dV_{CE}/dt of ~2.11 kV/μs and a peak value of 680 V. The experimental comparison in Fig. 3 further demonstrates that the Type II strategy can operate effectively under more demanding scenarios, such as at higher short-circuit current levels. In the laboratory, the prototype successfully completes no fewer than 5 short-circuit interruptions under such conditions. Furthermore, rated-current interruption tests conducted at a frequency of 2 operations per minute indicate that the electrical lifespan of the HCB utilizing the Type II strategy exceeds 1,000 operations.

IV. Interruption Capability Enhancement

A. *Higher-Current Experimental Testing*

In LV DC HCB, constrained by size and cost, a small number of discrete IGBTs are required to interrupt pulsed high currents (several times the rated current). As shown in Fig. 4, when using the Type II interruption strategy with capacitor *C* pre-charged to 270 V (the expected peak current is 925 A, with a *di/dt* of 58.2 A/ms), the IGBT is turned on ~3.5 ms after arc ignition. Due to current-limiting by the arc, the arc current is already in the decay stage, at ~750 A. After 300 μs, the IGBT receives the turn-off signal, producing a turn-off overvoltage with a rate of ~2.98 kV/μs and a peak value of 704 V, and the IGBT fails to turn off. Combining the results from Fig. 2 and Fig. 3, it indicates that under the present design, the interruption capability of a single IGBT is

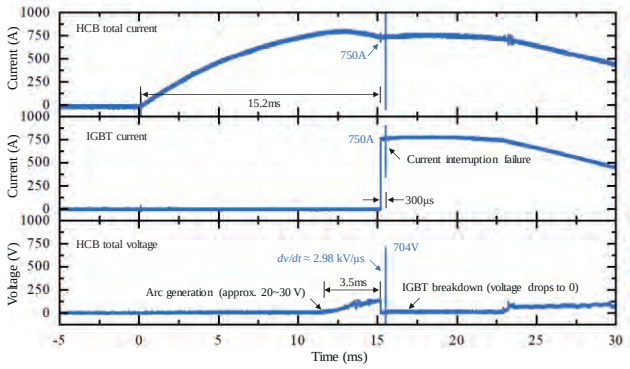


Fig. 4. Interruption waveforms of the HCB under Type II strategy with capacitor *C* pre-charged to 270 V.

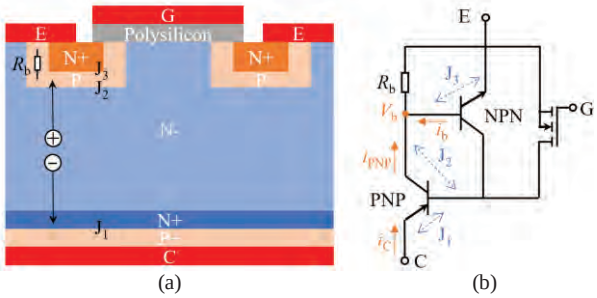


Fig. 5. IGBT structure and equivalent circuit diagram. (a) IGBT structure. (b) IGBT equivalent circuit.

~690 A (6.3 times the rated current). The same MOV is used in the experiments, so the clamped voltage peaks are similar and well below the IGBT's V_{CES}, while the dV_{CE}/dt values differ significantly. The dV_{CE}/dt at IGBT failure approaches or exceeds 3 kV/μs. High dV_{CE}/dt is likely the main cause of device failure.

The phenomenon of IGBT failure during high-current turn-off within the HCB is repeatedly observed. This failure directly relates to both the IGBT conduction duration and the arcing time (in the Type II strategy). The arcing time dictates the current magnitude at commutation, while the current continues to rise during the IGBT conduction phase. Currently, the 300μs conduction time is an empirical selection to ensure sufficient dielectric recovery of the MCCB contact gap, thereby preventing arc re-ignition. The arcing time (3.2~3.6ms) primarily accounts for the time needed to reach the maximum contact gap, and it is physically restricted by the efficiency of arc energy harvesting and component initialization. Optimizing this timing sequence to balance device safety, contact lifespan, and dielectric recovery remains a valuable subject for future research.

B. Latch-up Failure Mechanism

Fig. 5 shows the structure and equivalent circuit of the IGBT. When the gate drive voltage drops to zero, the electron channel connecting the N+ and N- regions disappears, causing the current to decrease and the device to turn off. This rapid turn-off induces an overvoltage between the collector and emitter. Subsequently, the depletion region of the J_2 junction expands into the N- region, prompting the electron-hole pairs accumulated there during conduction to move toward both sides. The motion of holes through the P region encounters the transverse resistance R_b, generating a voltage drop across it. If this voltage drop reaches the turn-on threshold of the parasitic NPN transistor, the gate loses its control capability, allowing the PNP transistor to remain conductive. This condition leads to latch-up.

Let V_b denote the base voltage of the parasitic NPN transistor. The following relationship holds:

$$V_b = (i_b + i_{PNP})R_b = (i_b + \alpha_{PNP} i_C)R_b \tag{1}$$

Where, i_b is the base current of the parasitic NPN transistor, i_{PNP} and i_C are the collector and emitter currents of the parasitic PNP transistor, respectively, as shown in Fig. 5(b).

The parameter α_{PNP} represents the common-base current gain of PNP transistor. Its value depends on the structural dimensions and doping concentration, typically ranging from 0.9 to 0.99. Consequently, (2) is approximately valid:

$$V_b = (i_b + i_C)R_b = i_b R_b + i_C R_b \tag{2}$$

From (2), it can be observed that the hole motion introduces a superimposed term $i_b R_b$. This component facilitates latch-up onset. Furthermore, a larger collector current also contributes to the latch-up effect due to the presence of the $i_C R_b$ term.

Assuming the hole charge passing through the P region is Q_P, we have:

$$i_b = \frac{dQ_P}{dt} = \frac{dQ_P}{dV_{J2}} \cdot \frac{dV_{J2}}{dt} = C_{J2} \frac{dV_{J2}}{dt} \tag{3}$$

Where, C_{J2} and V_{J2} are the equivalent capacitance and junction voltage of J_2, respectively. Since J_1 and J_3 are under forward bias, their junction voltages are negligible; thus, V_{J2} approximately equals the collector-emitter voltage V_{CE} of the IGBT. Consequently, (3) can be rewritten as:

$$i_b = C_{J2} \frac{dV_{CE}}{dt} \tag{4}$$

From (4), it is clear that the term $i_b R_b$ stems from the turn-off transient and depends on both C_{J2} and dV_{CE}/dt.

For a specific IGBT model, the value of R_b and C_{J2} is intrinsically determined by its internal structure and fabrication process. However, it can be stated that an excessively high turn-off speed leads to an elevated dV_{CE}/dt, which in turn raises the base voltage of the internal parasitic NPN transistor and increases the risk of parasitic junction turn-on. This ultimately results in uncontrolled instantaneous turn-off and device latch-up.

C. Improvement Methods and Verification

Based on the analysis in Section IV. B, eqs. (1) to (4), when an IGBT turns off at a given current level, reducing the dV_{CE}/dt can effectively reduce the risk of device latch-up. This allows the IGBT to sustain higher currents (~750 A), thereby improving the interruption capability of the HCB.

Therefore, two methods are considered:

1) Adopting an MOV-RCD snubber structure: Relying solely on an MOV for clamping is insufficient to effectively limit dV_{CE}/dt. an RCD snubber circuit is added in parallel

within the protection branch. To maintain a compact volume, the largest possible capacitance is chosen to ensure effective dV_{CE}/dt suppression. In this design, a snubber capacitor of 1μF is selected through experiments.

2) Increasing the gate turn-off resistance $R_{G(off)}$: Selecting a larger $R_{G(off)}$ value limits the discharge current of the gate charge in the driver circuit, thereby extending the fall time of the gate voltage. This deliberate slowing of the turn-off transient achieves a reduction in dV_{CE}/dt and improves device reliability. In this work, $R_{G(off)}$ is increased from 10 Ω to 30 Ω.

Following the same condition, Fig. 6 presents the interruption waveforms obtained using the two methods described above. In both cases, the HCB successfully interrupts the current, with the electronic branch handling ~750 A. A key difference compared to Fig. 4 is the significantly reduced turn-off transient dV_{CE}/dt, which decreases to 1.56 kV/μs and 1.05 kV/μs, respectively. This lowers the risk of device latch-up, allowing the IGBT to turn off smoothly and commutate the current to the protection branch. The energy is then dissipated by the MOV, completing current clearance. The overall fault-clearing time in both cases remains ~19.4 ms.

V. Improved HCB Based on Type II Strategy

This section briefly introduces our recent research work. Apart from the difference of Type I and Type II in current-handling capability, the Type II strategy offers a unique advantage: it can increase the switching voltage and accelerate the current-clearing process of the electronic part, which necessitates modifications to the existing structure.

In the improved HCB, the mechanical main branch consists of one MCCB configured in a multi-pole series connection. The electronic PCB module is connected in parallel across the pole closest to the negative power supply (denoted as interruption unit B, while the other series-connected poles are denoted as unit A), as show in Fig. 7. The IGBT is still triggered to conduct during the arc-current decay stage, which belongs to the Type II strategy. The core design concept is to utilize the arc at unit A and the electronic part working together to generate a higher switching voltage, the arc voltage across unit A plus the MOV clamping voltage, thereby accelerating the current-clearing process.

Fig. 8 shows the short-circuit interruption process using a two-pole design as an example. Stage I: During normal operation and the initial stage of the rising short-circuit current, the current flows successively through the two metal contacts. Stage II: The contacts of units A and B open to generate arcs, which limit the short-circuit current. Stage III: The IGBT conducts, and the arc voltage of unit B drives the current to commutate to the branch where unit A and the IGBT are located; the arc in unit B extinguishes. Stage IV: The IGBT is turned off, and the overvoltage exceeds the MOV varistor voltage. The short-circuit current flows through the branch containing unit A and the MOV, and gradually decreases under the combined effect of the MOV clamping voltage and the arc voltage of unit A. Stage V: The arc in unit A extinguishes, ending the interruption process, with unit A providing electrical isolation.

Fig. 9 shows the experimental comparison between the improved HCB and the existing technology, still using the

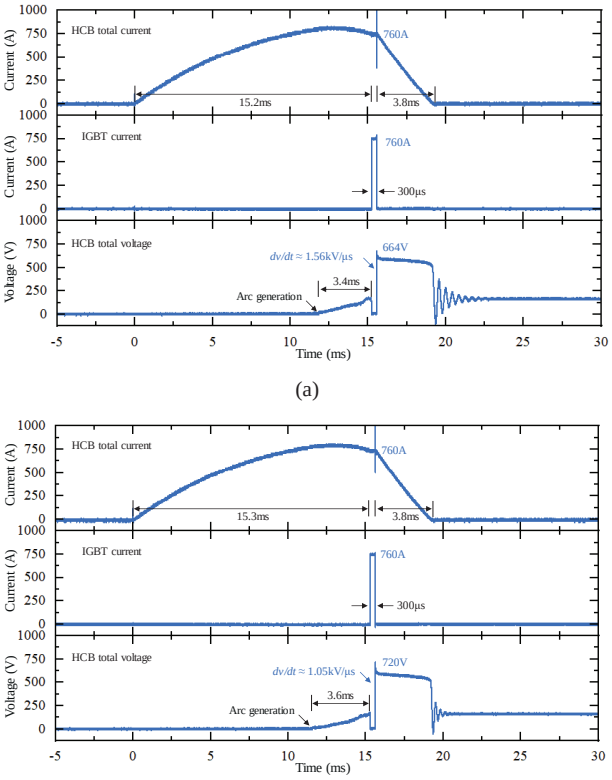


Fig. 6. Interruption waveforms of the HCB under Type II strategy with capacitor *C* pre-charged to 270V. (a) Adopting an MOV-RCD snubber structure. (b) Increasing the gate turn-off resistance.

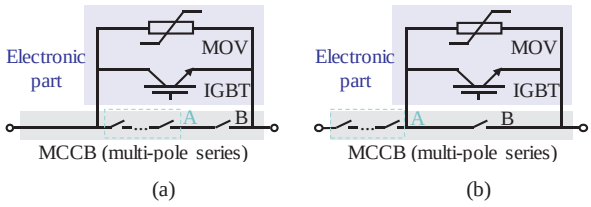


Fig. 7. Topologies of the conventional and improved HCBs. (a) Conventional HCB. (b) Improved HCB.

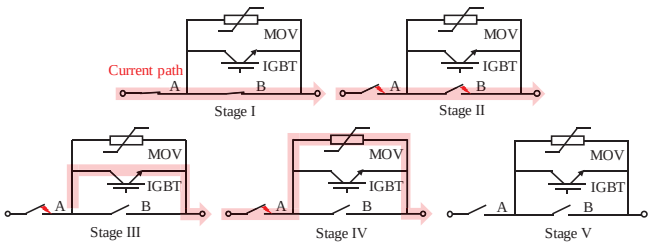
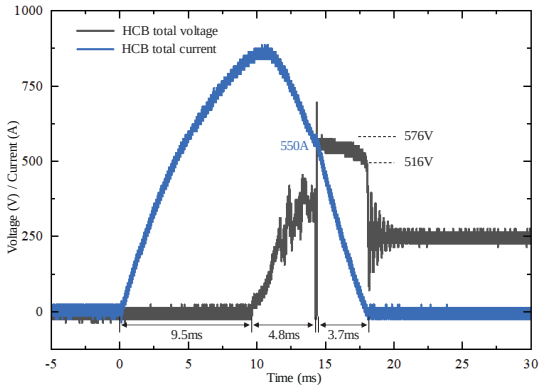
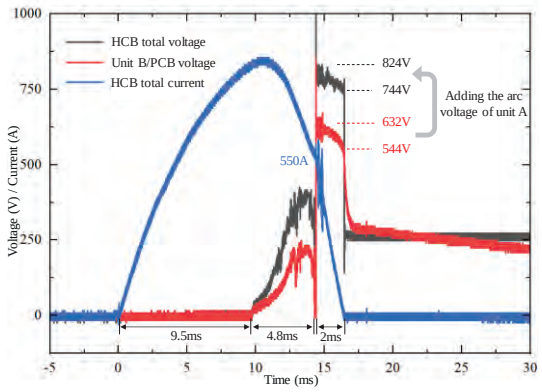


Fig. 8. Operating sequence of the improved HCB (two-pole series) under short-circuit fault.

two-pole design as an example. Capacitor *C* is pre-charged to 350 V, resulting in an expected peak current of 1,200 A and a rise rate of 75.5 A/ms. At ~9.5 ms, the contacts open. Due to the higher rise rate of the series arc voltage across the two poles, the current-limiting effect is stronger. After arcing for 4.8 ms, the current drops to 550 A, at which point the electronic PCB module is triggered to enter the interruption



(a)



(b)

Fig. 9. Interruption waveforms of the conventional and improved HCBs (two-pole series) with capacitor *C* pre-charged to 350 V. (a) Conventional HCB. (b) Improved HCB.

process. The test waveform of the original HCB structure is similar to that described earlier: under the clamping voltage (516 V~576 V) of the MOV, the current decays to 0 in 3.7 ms, completing the interruption. In the improved HCB, after the electronic part is activated, the arc in unit A has not yet extinguished (arc voltage ~200 V). Once the MOV conducts, the clamping voltage ranges from 544 V~632 V. Therefore, the HCB total voltage increases to 744 V~824 V, and the current-clearing time is reduced to 2 ms, representing a 46% reduction.

The improved HCB can flexibly adjust the distribution of the total voltage between the arc of unit A and the MOV, thereby maximizing the effect of increased switching voltage. This improved HCB holds potential for higher voltage level applications. Further details will be introduced in an upcoming paper [13].

VI. Conclusion

1) For an HCB prototype based on identical MCCB and electronic PCB modules, the interruption capability varies with the current commutation strategies, defined by the instant of IGBT triggering: Type I (at arc ignition) and Type II (during the current-decay stage of the arcing period). The Type II strategy proves more reliable for interruption under higher short-circuit current and steeper current rise rates. This is primarily because Type II strategy fully utilizes the MCCB's current-limiting and high current-carrying capabilities, thereby subjecting the PCB to lower interruption stress, at the expense of a reduced mechanical lifespan.

2) As the current level increases, the interruption stress on the electronic part rises, which is reflected in a higher dV_{CE}/dt during IGBT turn-off. When dV_{CE}/dt approaches 3 kV/μs, the device is prone to dynamic latch-up failure. Two effective methods to improve reliability are adopting an MOV-RCD snubber structure or appropriately increasing the gate turn-off resistance $R_{G(off)}$. The interruptible IGBT current level increases from 6.3 to 6.9 times its rated value.

3) The improved HCB possesses stronger interruption capability. The high switching voltage generated by mechanical-electronic coordination (arc voltage of unit A plus MOV clamping voltage) accelerates the current-clearing process, reducing the time by 46%.

References

[1] M. Dali, F. Charaabi and J. Belhadj, "Short-circuit fault analysis and protection of stand-alone AC and DC microgrids," 2022 IEEE International Conference on Electrical Sciences and Technologies in Maghreb (CISTEM), Tunis, Tunisia, 2022, pp. 1-6.

[2] J. Lin, J. Wu, S. Xia, R. Chen and M. Ma, "Multiobjective optimization of key parameters for the chamber of low-voltage DC circuit breakers based on MHD," in IEEE Transactions on Plasma Science, vol. 53, no. 1, pp. 88-98, Jan. 2025.

[3] J. J. Shea, "Low voltage power distribution level DC circuit breaking," 2017 4th International Conference on Electric Power Equipment - Switching Technology (ICEPE-ST), Xi'an, China, 2017, pp. 187-194.

[4] X. Zhou, "Technology innovation and evolution in circuit protection," 2023 IEEE 68th Holm Conference on Electrical Contacts (HOLM), Seattle, WA, USA, 2023, pp. 1-13.

[5] R. Rodrigues, Y. Zhang, U. Raheja, P. Cairoli, L. Raciti and A. Antoniazzi, "Robust 5 kA, 1 kV solid-state DC circuit breaker for next generation marine power systems," 2021 IEEE Electric Ship Technologies Symposium (ESTS), Arlington, VA, USA, 2021, pp. 1-7.

[6] A. R. F. Bento, F. Bento and A. J. M. Cardoso, "A review on hybrid circuit breakers for DC applications," in IEEE Open Journal of the Industrial Electronics Society, vol. 4, pp. 432-450, 2023.

[7] L. Claaßen, F. Anspach, E. -D. Wilkening and M. Kurrat, "Investigation of a Mechanical Switch within a Hybrid Circuit Breaker for Protection in DC Grids," 2020 IEEE 66th Holm Conference on Electrical Contacts and Intensive Course (HLM), San Antonio, TX, USA, 2020, pp. 123-130.

[8] C. Gao, Z. Zhang, Y. Liu, S. Chen, Q. Wang and X. Li, "Natural commutation characteristics of self-triggered low-voltage DC hybrid circuit breakers," in IEEE Transactions on Components, Packaging and Manufacturing Technology, vol. 15, no. 11, pp. 2399-2407, Nov. 2025.

[9] K. Askan and P. Schasfoort, "Variable voltage IGBT gate driver for low voltage hybrid circuit breaker," 2021 IEEE Fourth International Conference on DC Microgrids (ICDCM), Arlington, VA, USA, 2021, pp. 1-7.

[10] Y. Feng, X. Zhou, S. Krstic, Y. Zhou and Z. J. Shen, "Molded case electronically assisted circuit breaker for dc power distribution systems," in IEEE Transactions on Power Electronics, vol. 36, no. 6, pp. 6586-6595, June 2021.

[11] K. Askan, M. Bartonek and K. Weichselbaum, "Power module for low voltage DC hybrid circuit breaker," 2019 IEEE Third International Conference on DC Microgrids (ICDCM), Matsue, Japan, 2019, pp. 1-8.

[12] J. Wang, G. Liang, X. Zhang and L. Qi, "A refinement multilevel turn-off method for dynamic latch-up and tail current suppression in DC breaker ultra-high current switch applications," in IEEE Transactions on Industrial Electronics, vol. 71, no. 3, pp. 2177-2187, March 2024.

[13] C. Gao, Z. Zhang, Q. Wang, S. Chen, Y. Huang, and X. Li, "Research on the breaking characteristics of series arc asynchronous coordination for self-triggered low-voltage hybrid DC circuit breakers," Proceedings of the CSEE, pp. 1-12, Early Access. [Online]. Available: https://doi.org/10.13334/j.0258-8013.pcsee.251260.

Post-arc erosion of metal surfaces

Pierre Corfdir
ABB Switzerland Ltd
Segelhofstrasse 1K, 5405 Baden-Dättwil, Switzerland
pierre.corfdir@ch.abb.com
ORCID: 0000-0003-0084-1187

Luca Sulmoni
ABB Switzerland Ltd
Segelhofstrasse 1K, 5405 Baden-Dättwil, Switzerland
luca.sulmoni@ch.abb.com
ORCID: 0000-0002-5341-7032

Christoph Kenel
ABB Switzerland Ltd
Segelhofstrasse 1K, 5405 Baden-Dättwil, Switzerland
christoph.kenel@ch.abb.com
ORCID: 0000-0003-0800-2986

Patrick Sütterlin
ABB Switzerland Ltd
Segelhofstrasse 1K, 5405 Baden-Dättwil, Switzerland
ralf-patrick.suetterlin@ch.abb.com

Arcing in low-voltage electromechanical switchgear leads to a significant wear of the electrical contacts, arc runners and splitter plates. This wear has been attributed to the vaporization of the pool of molten metal that forms at the arc roots, as well as to the ejection of droplets from the molten pool. In this work, we show using laser shadowgraphy that erosion takes place not only during arcing, but also in the few ms after arc extinction during the cooling of the electrode. We observe during the cooling phase of the molten pool the growth of mm-size protrusions that develop into spheres and in some cases, detach from the electrode. We attribute this post-arc erosion to the Marangoni effect and Plateau-Rayleigh instabilities. The probability for this post-arc erosion process increases with increasing energy input into the electrode, and we show that the mass lost by post-arc erosion can be much larger than the one lost during arcing.

Keywords—electric arc, erosion, laser shadowgraphy, arc root, molten pool, Marangoni effect

I. Introduction

Current interruption in electromechanical switchgear relies on the formation of an arc between a pair of electrical contacts, and in the quick extinction of this arc by a combination of arc motion and elongation, cooling by outgassing wall materials and arc splitting by metal plates [1]. In low-voltage short-circuit breakers, the motion and elongation of the arc are obtained using so-called arc runners in copper and steel, while arc splitting is typically achieved with splitter plates in steel. Energy dissipation at the arc roots leads to the development of pools of molten metal at the surface of the electrical contacts, the arc runners and the splitter plates [2]. Erosion of the electrodes occurs via metal vaporization, as well as via emission of molten metal droplets and splashing of the molten pool [3].

Liquid metal droplets ejected from the arc roots during arcing are detrimental to the performance of the breaker. They can block the actuation mechanism [4], and accumulate on isolating walls thus decreasing the surface resistance [5]. Accumulation of copper or steel at the surface of electrical contacts results in an increased contact resistance [6]. The presence of metal droplets flying in the arcing chamber also contributes to restrikes after current interruption [7].

In this work, we present laser shadowgraphy tests carried out during arcing on electrodes in copper for currents up to 3 kA. We show that large droplets of molten metal can be detached from the electrodes even 15 ms after the interruption of the current. This post-arc formation of metals droplets with a diameter on the order of a mm arises from Marangoni flow during the cooling of the molten pool. We describe how the probability for the formation of these macroscopic droplets evolves with varying the current and the arcing time.

II. Experimental Details

A. Test object and arcing tests

The test object consists of two electrodes with a ring and a cylindrical geometry that are separated by a distance of 55 mm. The two electrodes are in Cu-ETP. The cylindrical electrode has a diameter of 10 mm. As shown in Fig. 1, the electrode exhibits a 6 mm tip with a diameter of 5 mm. The two electrodes are connected with a copper wire with a diameter of 0.127 mm. In the presence of a current, the wire heats up and explodes, initiating an electric arc.

The current source used in our arcing tests consists of a 3-level Buck converter. This source is used to provide a

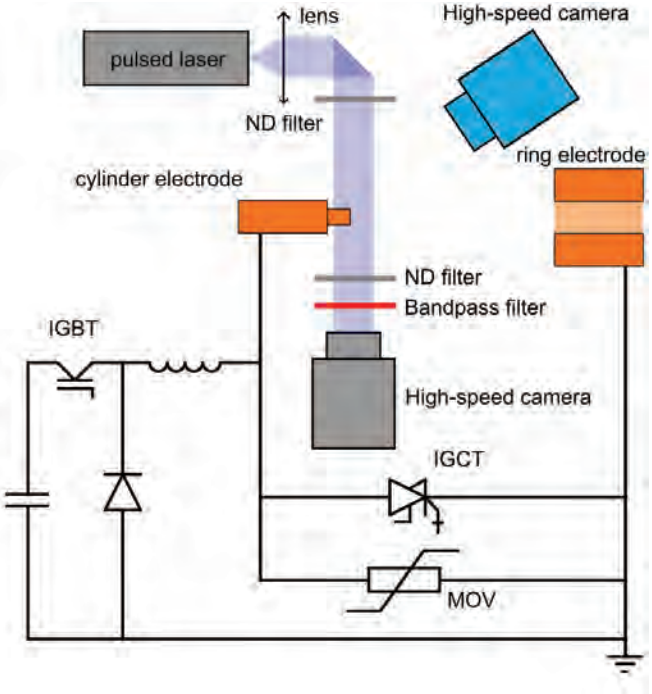


Fig. 1. Schematic representation of the experimental set-up. The current source consists of a Buck converter (only 1 level of the converter is shown). An IGCT and an MOV are mounted in parallel with the test object. A high-speed camera (blue) is used to monitor the electrode tip after cooling. Laser shadowgraphs are obtained illuminating the tip of the cylinder electrode with a pulsed laser beam and imaging it with a high-speed camera (shown in grey). For the laser shadowgraphy, neutral density (ND) filters and a bandpass filter centered at the laser wavelength are placed in the optical path.

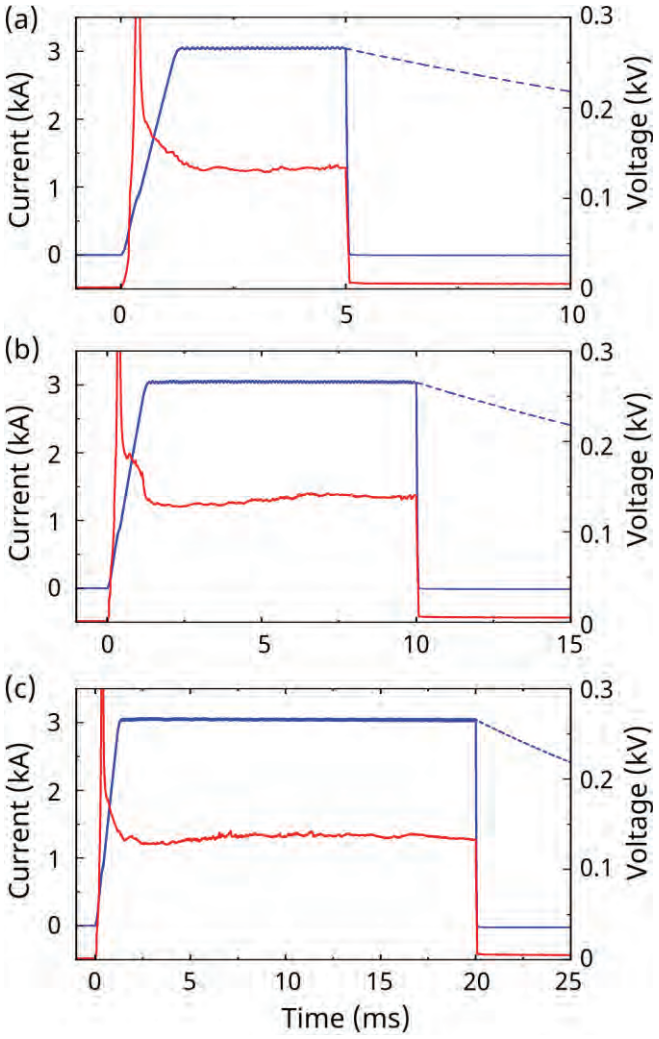


Fig. 2. Current (blue, left y-scale) and voltage (red, right y-scale) measured during a test at 3 kA on a copper anode. The dashed and solid blue lines are the current delivered by the current source and the arc current, respectively. The arcing time is (a) 5 ms, (b) 10 ms and (c) 20 ms.

constant current up to 3 kA. As shown in Fig. 1, an integrated gate-commutated thyristor (IGCT) and a metal oxide varistor (MOV) are mounted in parallel to the test object. At the beginning of the test, the IGCT is blocking. After a predefined delay (5, 10 or 20 ms), a trigger signal is applied to switch the IGCT into its on-state, leading to rapid arc extinction.

B. High-speed imaging and laser shadowgraphy

Laser shadowgraphy has been reported by different teams to visualize the molten pool development, the growth and burst of bubbles in the molten pool [8] as well as the generation and propagation of molten droplets during arcing [9,10]. We use here the system detailed in [8], also described in Fig. 1. A pulsed laser with a wavelength and a repetition rate of 785 nm and 10 MHz, respectively, is used to illuminate the tip of the cylindrical electrode. Videos of the tip during and after arcing are recorded with a high-speed camera (exposure time 0.285 µs per frame, 44000 frames per s). The intensity of the laser is adjusted using neutral density filters. A bandpass filter centred at the wavelength of the laser is mounted on the objective lens of the camera to attenuate the light emission from the arc.

Videos of the electrodes during the cooling phase after arcing are taken with a camera with an exposure time of 9.9 ms at 100 frames per s. The CMOS detector of the camera is sensitive between 400 and 1050 nm.

Electrodes were imaged after testing using a Zeiss Smartzoom 5 digital microscope. All images are recorded as HDR to compensate for the large brightness variation due to the reflectivity of copper. Image stacking is used to generate overviews with all areas of interest in focus.

III. Results and Discussion

Figure 2 displays typical oscillograms measured during tests at 3 kA. At time zero, the IGBTs of the Buck converter are turned on, initiating the discharge of the capacitor bank. The current rises nearly linearly, until the setpoint value is reached near 1.3 ms, and it remains nearly constant for longer times. A large spike in the voltage is seen near 0.4 ms, which we attribute to the explosion of the ignition wire placed between the two electrodes, and to the initiation of the arc [11]. Starting from 1.7 ms, the arc voltage only shows small fluctuations, suggesting that the arc configuration (length, radius) as well as the composition and the pressure of the plasma are stable. After a given time [5, 10 and 20 ms in Figs. 2(a), 2(b) and 2(c), respectively], the IGCT mounted in parallel to the test object is triggered. The arc current decreases to 0 in less than 40 µs. The current in the IGCT then slowly decreases.

Figure 3 shows images taken after arcing at 3 kA during 20 ms on two copper cathodes. In most cases, the surface of the electrode exhibits a shape comparable to that in Figs. 3(a,c) with smooth protrusions and craters. Comparable images were reported in [12] for steel surfaces after arcing. In some cases, however, we could observe the formation of spheres at the surface of the tip. As shown in Figs. 3(b,d), these spheres are located near the edge of the cylindrical tip. In particular, the distribution of the spheres along the edge [Fig. 3(d)] suggests that their formation is not exclusively driven by gravity.

Figure 4 displays high-speed camera images of a copper cathode after 20 ms of arcing at 3 kA. The images in Figs. 4(a-d) are taken 20, 80, 140 and 220 ms after the arc extinction. The image in Fig. 4(a) is taken with an external illumination. Spheres comparable to that seen in Figs. 3(b,d) are visible at the surface of the electrode. Interestingly, the sphere at the bottom of Fig. 4(a) is also visible without external illumination in Figs. 4(b-d). With increasing time, the shape of the sphere exhibits small variations, indicating that the sphere is still liquid. As a matter of fact, the position of the solidification front can be guessed in Fig. 4(b) from the transition from a rough to a smooth surface when going from the base to the tip of the sphere. With increasing time, the solidification front progresses towards the tip of the sphere. At the same time, the intensity of the signal decreases, which we associate with a decrease in the surface temperature and in the black-body emission from the sphere.

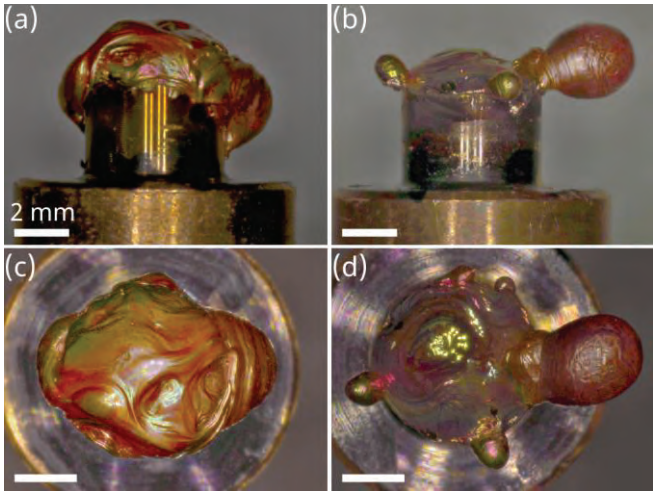


Fig. 3. (a,b) Side views of two copper cathodes after arcing for 10 ms at 3 kA. (c,d) Top-views of the electrodes shown in (a). The scale bars correspond to 2 mm in all panels.

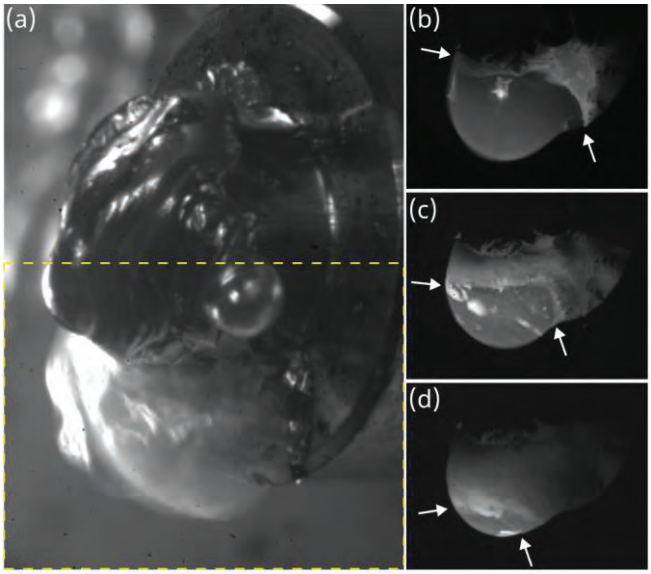


Fig. 4. Bird's eye view images of a copper cathode after 20 ms of arcing at 3 kA. (a) Image taken 20 ms after the arc extinction. An external light source illuminates the surface of the electrode. The yellow dashed line shows the area corresponding to the images in (b-d). (b-d) Magnified views of the molten sphere visible at the bottom of (a) and taken (b) 80 ms, (c) 140 ms and (d) 220 ms after the arc extinction and without external illumination. The arrows in (b-d) show the position of the solidification front.

To gain insight into the process leading to the different surface morphologies seen in Fig. 3, we have performed laser shadowgraphy. Figure 5 displays laser shadowgraphs obtained during arcing and after arc extinction for the same test as in Fig. 2(a) (i.e., after 5 ms of arcing). Laser shadowgraphs taken during and after the test in Fig. 2(c) are shown in Fig. 6 (i.e., after 20 ms of arcing). Figures 5(a) and 6(a) show shadowgraphs taken before the test. The illumination by the laser is not homogeneous due to the presence of interference rings. The shadow of the 5 mm diameter tip of the cylindrical electrode is seen to the right of the figure. The shadow of the copper wire used to initiate the arc is also visible.

Shadowgraphs recorded during arcing are shown in Figs. 5(b-d) and 6(b,c). Our observations are similar to that made in [8] for currents between 0.5 and 1 kA. With increasing time, the molten pool develops and after a few ms of arcing it fully covers the surface of the electrode tip. As noted in [8], black body emission from the molten pool leads to a brighter contrast for this region as compared to the electrode stem [Figs. 5(d) and 6(b,c)]. Even after 20 ms of arcing at 3 kA, the surface of the molten pool remains smooth, as expected from the low degree of bubbling reported previously for copper anodes [8]. This low bubbling arises from the fact that the thermal conductivity of copper is high and that the anode arc root is diffuse.

As shown in Figs. 5(d,e) and 6(c,d), the shape of the electrode 0.1 ms after the arc extinction does not change drastically from that measured before the interruption of the arc. However, the shape of the molten pool exhibits significant changes during the cooling phase after arcing. As shown in

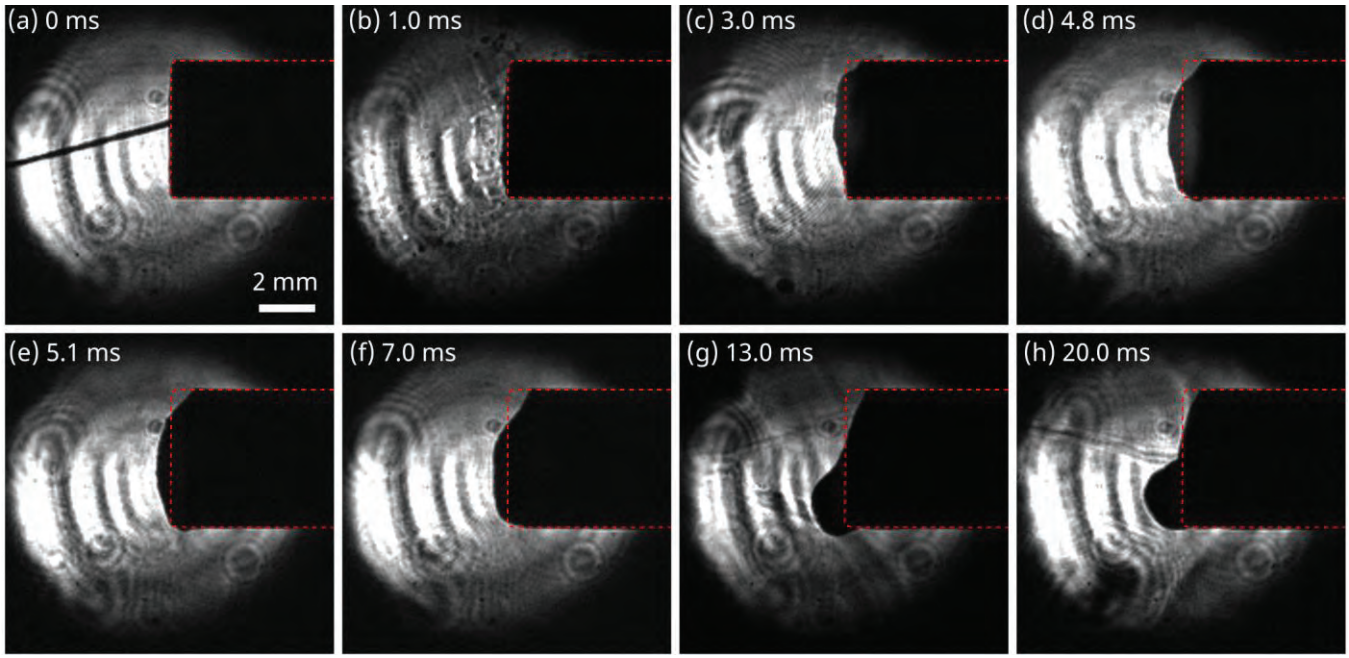


Fig. 5. Shadowgraph taken (a-d) during and (e-h) after arcing at 3 kA on a copper anode [same test as in Fig. 2(a)]. The arcing time is 5 ms. The recording time is indicted directly in each panel. The 2 mm scale bar in (a) applies to all panels. The red dashed line shows the outline of the electrode before the test. In all panels, gravity points downwards.

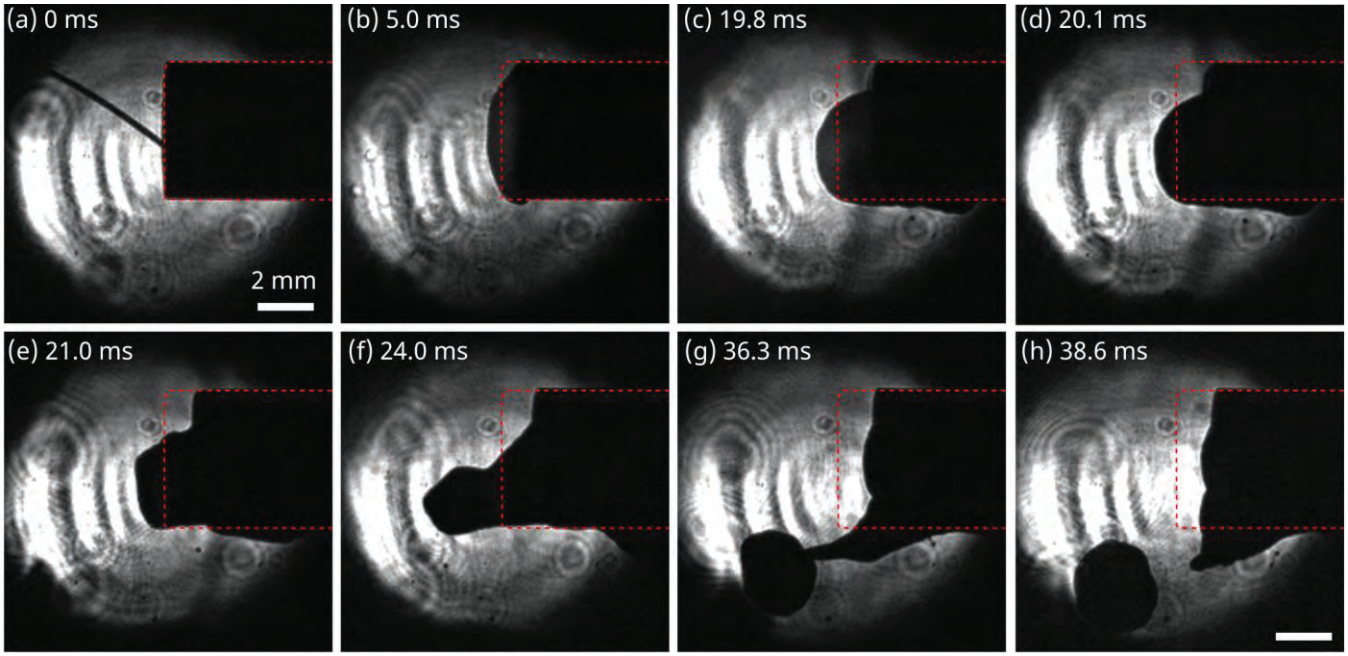


Fig. 6. Shadowgraph taken (a-c) during and (d-h) after arcing at 3 kA on a copper anode [same test as in Fig. 2(c)]. The arcing time is 20 ms. The recording time is indicted directly in each panel. The 2 mm scale bar in (a) applies to all panels. The red dashed line shows the outline of the electrode before the test. In all panels, gravity points downwards.

Figs. 5(e-h), the shape of the molten pool evolves from a hemisphere that covers the full tip of the electrode to a hemisphere with a diameter of 2.5 mm located on the lower half of the tip. Interestingly, from 13 to 20 ms (i.e. from 8 to 15 ms after the arc extinction), the hemisphere moves upwards, confirming that the flow of the liquid metal after arcing is not solely driven by the gravity. This behavior resembles the one reported in [8] after arcing at currents between 0.5 and 1 kA.

The changes in the surface morphology in Figs. 6(d-h) are more drastic. A protrusion slowly develops along the symmetry axis of the electrode tip [Figs. 6(e,f)]. After 24 ms, this protrusion exhibits a length and a thickness of 4 and 2 mm, respectively [Fig. 6(f)]. For times longer than 29 ms, the tip of the protrusion evolves towards a sphere, and the neck between this sphere and the stem of the electrode becomes thinner. The sphere and the stem eventually separate near 36.5 ms, i.e., 16.5 ms after the extinction of the arc. We refer to this mass loss by post-arc emission of droplets as post-arc erosion.

Pyrometry measurements performed on electrode surfaces after arcing have shown that cooling the surface down to the melting point can take longer than 15 ms [13], and that the larger the energy input to the electrode, the slower the surface cooling [14]. The slow solidification of the molten pool visible in Fig. 4 as well as the motion of the molten metal after arcing in Figs. 5 and 6 are consistent with this idea.

The Marangoni effect has been shown to play an important role in the shape changes of the molten pool during arc welding [15] or pantograph arcing processes [16]. Similarly, we expect that the temperature gradient from the stem of the electrode to the tip of the molten pool after arcing leads to surface tension gradients and to some mass flow of molten metal by the Marangoni effect. This mass flow can result in the development of protrusions as seen in Fig. 6(f). Plateau-Rayleigh instabilities lead to balling [Figs. 3(b,d) and 6(g)] and eventually to post-arc erosion by the emission of a droplet as seen in Fig. 6(h). Therefore, the post-arc erosion results from a competition between (i) the solidification of the molten via evacuation of heat by thermal conduction through the stem of the electrode, and (ii) Marangoni flow in the molten pool and Plateau-Rayleigh instability leading to balling and droplet emission.

Figure 7 shows the evolution of the mass lost by copper electrodes (anodes and cathodes) after arcing at 3 kA for 5, 10 and 20 ms (21 shots in total). For arcing times of 10 and 20 ms, the values measured for the mass loss exhibit a large scattering. In particular, the data points seem to group in two families of shots with low and high mass losses. For an arcing time of 20 ms, these two regimes correspond to a mass loss below 32 mg and above 140 mg, respectively. To estimate how much the post-arc erosion contributes to the total mass loss, we have measured the section area A of the droplet in the shadowgraph in Fig. 6(h). We define the effective radius of the droplet as $R = \sqrt{A/\pi}$ and we assume that the volume of

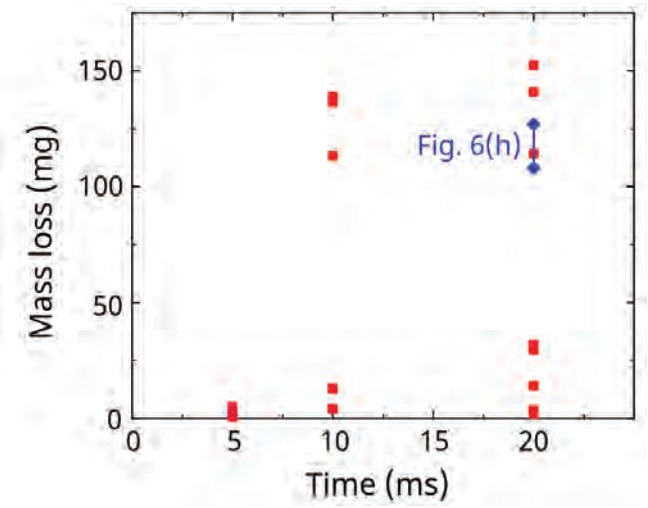


Fig. 7. Mass loss for copper electrodes during arcing at 3 kA as a function of the arcing time (squares). The figure compiles data obtained on anodes as well as cathodes. The diamonds and the blue line show the mass loss by post-arc erosion as estimated from Fig. 6(h) using the density of copper between the melting and boiling temperature.

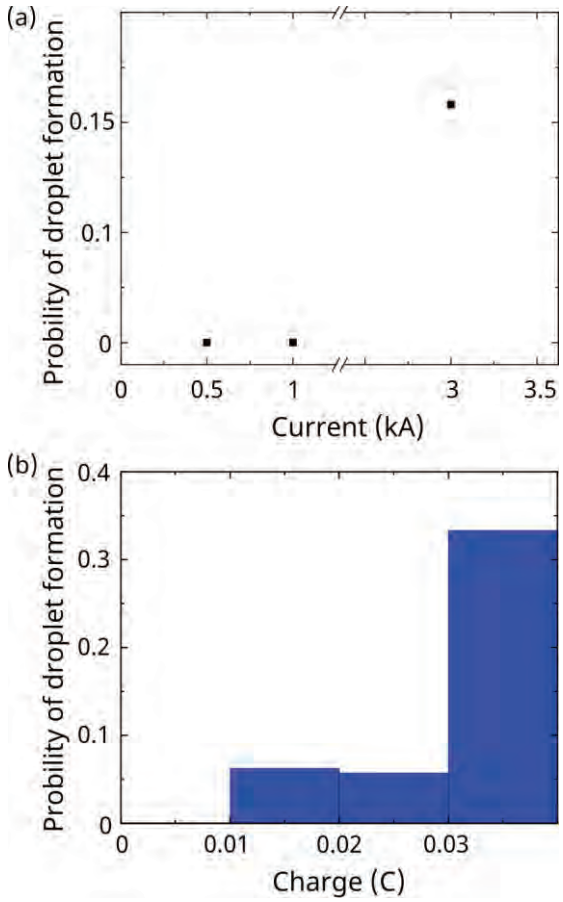


Fig. 8. Probability of post-arc erosion by emission of droplet as a function of (a) the current and (b) the charge transported through the copper electrode during arcing. Panels (a) and (b) compile data obtained on copper anodes and cathodes, at currents of 0.5, 1 and 3 kA and arcing times of 5, 10 and 20 ms.

the droplet is given by $4\pi R^3/3$, Using the results from [17], the density of liquid copper at the melting and at the boiling point is 7990 and 6807 kg/m^3. Therefore, the mass of the droplet in Fig. 6(h) is between 108 and 127 mg.

From these results, we conclude that post-arc erosion by droplet emission is what distinguishes between the arcing events with a low and a high mass loss in Fig. 7. As a matter of fact, the total mass lost during the test in Fig. 6 is 114.5 mg. Therefore, only a small fraction of the total mass has been removed during arcing, and most of it has been lost due to the slow formation and eventual detachment of a droplet, which completes approximately 16 ms after arc extinction.

We now discuss how the post-arc erosion process varies with varying the polarity, the current density the charge transported through the electrode and the material.

While the post-arc erosion process visible in Fig. 6 has been measured on a copper anode, some of the high mass loss events in Fig. 7 were observed on copper cathodes. At this stage, we do not have enough statistics to conclude on whether the post-arc erosion process is more likely on the anode or the cathode.

Figure 8(a) shows the evolution of the probability of post-arc erosion with increasing the current. Post-arc erosion is observed starting from 3 kA. We note that the arc root is more diffuse on the anode side, i.e., the current density is significantly lower for the anode than for the cathode. As we have observed the post-arc erosion process for currents starting from 3 kA for both the anode and the cathode, we conclude that this process does not depend directly on the current density at the arc root during the arcing phase.

Figure 8(b) displays the probability of emission of a large droplet during the post-arc phase as a function of the charge Q transported through the electrode during the arcing event. The figure compiles results obtained on copper anodes and cathodes, for currents of 0.5, 0.75, 1 and 3 kA and arcing times of 5, 10 and 30 ms. We note that $Q \geq 0.01$ C for all tests at 3 kA. With $Q < 0.01$ C, we have not observed any droplets forming during the post-arc phase. For $0.01 \leq Q < 0.03$ C, some post-arc erosion is seen, but the probability for a droplet to form during the post-arc phase remains below 0.07. In contrast, for $Q \geq 0.03$ C, the probability of post-arc erosion by droplets formation is above 0.3. The charge Q increases with increasing the current and the arcing time. As discussed in [14], the cooling rate of the molten pool decreases with increasing the arcing time. Therefore, with increasing Q, there is an increase in the time available for a large droplet to form and to detach before the molten pool solidifies. In other words, the probability of post-arc erosion by droplet formation increases with increasing Q.

We have not only observed post-arc erosion on copper, but also on steel electrodes. As for copper, the higher the charge Q transported through the electrode during arcing, the higher the probability of the emission of a large droplet during the post-arc phase. Interestingly, for $0.01 \leq Q < 0.03$ C, the probability for a large droplet to form increases from 0.06 to 0.10 when going from copper to steel (not shown). We attribute this finding to the low thermal conductivity of steel, which leads to a reduced cooling rate of the molten pool and to an increase in the time available for the formation of a large droplet.

Measurements of the mass lost during arcing events have been commonly used to deduce erosion rates during arcing [18] and compare the arc resistance of contact materials [19]. The results presented here show that great care must be taken when using such measurements, since erosion can occur during and after arcing, via processes that can be very different. The measured mass loss and erosion rate have also been used to deduce fall voltages at cathode and anode arc roots [20,21]. We highlight the fact that applying the methods in [20,21] to the test with post-arc erosion in Fig. 6 would lead to an overestimate of the erosion rate during arcing and, therefore, to an overestimate of the cathode and anode fall voltages (see Fig. 9 in [20]).

IV. CONCLUSIONS

To conclude, using laser shadowgraphy experiments, we have shown that the erosion of copper surfaces during switching events in electromechanical switchgear can occur during and after arcing. The post-arc erosion process is the result of the emission of mm-size droplets that form by Marangoni flow and Plateau-Rayleigh instabilities. This post-arc erosion is not specific to copper. We could observe it on steel surfaces and we expect that it also takes place when arcing on other surfaces. Obviously, as a result of their large diameter, these droplets can have dramatic consequences for the reliability of the switchgear. As a matter of fact, we have observed that the mass lost by post-arc erosion can exceed that lost during arcing, and that the probability of droplet emission

during the post-arc phase increases with increasing energy input to the electrode during the arcing phase. Finally, we have shown that post-arc erosion can lead to overestimated anode and cathode fall voltages, which can lead to inaccuracies in the arc root models that are used to model contact erosion [20,21] as well as the arc motion in electromechanical switchgear [22].

ACKNOWLEDGMENT

We acknowledge Gabriel Lantz for carefully reading our manuscript.

REFERENCES

[1] M. Lindmayer, E. Marzahn, A. Mutzke, T. Ruther and M. Springstubbe, "The process of arc-splitting between metal plates in low voltage arc chutes," Proceedings of the 50th IEEE Holm Conference on Electrical Contacts and the 22nd International Conference on Electrical Contacts Electrical Contacts, 2004., Seattle, WA, USA, 2004, pp. 28-34.

[2] P. G. Slade, "The Consequences of Arcing," in Electrical Contacts: Principles and Applications, 1st ed., CRC Press, 2014, pp. 487-533.

[3] G. A. Mesyats and I. V. Uimanov, "Hydrodynamics of the Molten Metal During the Crater Formation on the Cathode Surface in a Vacuum Arc," IEEE Transactions on Plasma Science, vol. 43, no. 8, pp. 2241-2246, 2015.

[4] C. Rümpler, R. Chechare, and A. Zacharias, "Arc modeling in industrial applications," Plasma Phys. Technol., vol. 6, pp. 200-207, 2019.

[5] X. Li, X. Liu, F. Zeng, X. Gou and Q. Zhang, "Ejection of Electrode Molten Droplet and Its Effect on the Degradation of Insulator in Gas Spark Switches," IEEE Transactions on Plasma Science, vol. 43, no. 4, pp. 1049-1053, 2015.

[6] M. Xue, Y. Heichal, S. Chandra, and J. Mostaghimi, "Modeling the impact of a molten metal droplet on a solid surface using variable interfacial thermal contact resistance," J. Mater. Sci., vol. 42, pp. 9-18, 2007.

[7] W. Yan et al., "The Effect of Contact Material on Particles Behavior in High-Current Vacuum Arcs," 2018 28th International Symposium on Discharges and Electrical Insulation in Vacuum (ISDEIV), Greifswald, Germany, pp. 19-22, 2018.

[8] P. Corfdir, L. Sulmoni, C. Kenel, and P. Sütterlin, "In-situ monitoring of electrode wear during arcing" 2025 IEEE 70th Holm Conference on Electrical Contacts (HOLM), 2025, pp. XXX (in press).

[9] Y. Wu, Y. Cui, M. Rong, A. B. Murphy, F. Yang, H. Sun, C. Niu, S. Fan, "Visualization and mechanisms of splashing erosion of electrodes in a DC air arc," J. Phys. D. Appl. Phys., vol. 50, p. 47LT01, 2017.

[10] X. Le, H. Xu, L. Chen, S. Shen, X. Huang, and S. Jia, "The Experimental study on the dynamic behavior of cathode molten pool particles during high-current vacuum interruption," 2025 31st International Symposium on Discharges and Electrical Insulation in Vacuum (ISDEIV), Chengdu, China, pp. 173-176, 2025.

[11] P. Corfdir et al., "Stark shift measurement as a temperature diagnostic of Cu-dominated thermal plasmas", J. Phys. D: Appl. Phys., vol.52, p. 275203, 2019.

[12] C. Kenel, P. Corfdir, L. Sulmoni, and P. Sütterlin, "Influence of Ni and Zn coatings on microstructure of steel splitter plates" 2025 IEEE 70th Holm Conference on Electrical Contacts (HOLM), 2025, pp. XXX (in press).

[13] J. J. Shea, and X. Zhou, "Contact material and arc current effect on post-current zero contact surface temperature," IEEE Transactions on Components and Packaging Technologies, vol. 29, pp. 286-293, 2006.

[14] P. Corfdir, J. Kalilainen, P. Sütterlin and M. Abplanalp, "Monitoring the post-arc molten pool cooldown with two-color pyrometry," 23rd International Conference on Gas Discharges and their Applications (GD2023), 2023, pp. 176-179.

[15] S. Wang, R. Nates, T. Pasang, and M. Ramezani, "Modelling of gas tungsten arc welding pool under Marangoni convection," Universal journal of mechanical engineering, vol. 3, pp. 185-201, 2015.

[16] P. Xu, Z. Yang, W. Wei, G. Gao, G. Wu; "Modeling and simulation of arc and contact wire molten pool behavior during pantograph lowering process," AIP Advances vol. 8, p. 115008 (2018).

[17] J. A. Cahill, and D. Kirshenbaum, "The density of liquid copper from its melting point (1356 K) to 2500 K and an estimate of its critical point," J. Phys. Chem., vol. 66, pp. 1080-1082, 1962.

[18] J. Shea, ""Erosion and Resistance Characteristics of AgW and AgC Contacts," IEEE Transactions on Components and Packaging Technologies, vol. 22, pp. 331-336 (1999).

[19] D. Kołacz, et al. "The Influence of Mechanical Alloying and Plastic Consolidation on the Resistance to Arc Erosion of the Ag–Re Composite Contact Material," Materials, vol. 14, pp. 3297, 2021.

[20] R. Hemmi, Y. Yokomizu, and T. Matsumura, "Anode-fall Voltages of Air Arcs Between Electrodes of Copper,Silver and Tungsten at Currents up to 1500A," IEEJ Transactions on Power and Energy, vol. 24, pp. 143-149, 2004.

[21] J. Tepper, M. Seeger, T. Votteler, V. Behrens, and T. Honig, "Investigation on erosion of Cu/W contacts in high-voltage circuit breakers," IEEE Transactions on Components and Packaging in High-Voltage Circuit Breakers, vol. 29, pp.658-665, 2006.

[22] P. Arrighetti, P. Corfdir, and T. Ilic, "System level and multiphysics approaches to simulate low voltage circuit breaker interruption", 2023 IEEE 68th Holm Conference on Electrical Contacts (HOLM), 2023, pp. 1-5.

Experimental characterization of DC fault arcs and comparative analysis with AC fault arcs

1st Frederik Mingers
Chair for High Voltage Technology
RWTH Aachen University
Aachen, Germany
f.mingers@iaew.rwth-aachen.de

2nd Verena West
Chair for High Voltage Technology
RWTH Aachen University
Aachen, Germany
v.west@iaew.rwth-aachen.de

3rd Willem Leterme
Chair for High Voltage Technology
RWTH Aachen University
Aachen, Germany
w.leterme@iaew.rwth-aachen.de

***Abstract*—With increasing decentralization of electricity generation, storage, and consumption, low- and medium-voltage DC systems gain increased attention. Ensuring safety of such systems requires a clear understanding of DC fault arcs, which until now remain less well characterized than AC fault arcs. By conducting fault arc experiments in a hermetically sealed, air-filled vessel using both DC and AC waveforms we characterized arcing energy, erosion, ablation, pressure build-up, and arc commutation behavior. We find comparable evaporation rates and pressure build-up between DC and AC fault arcs at similar energy levels, but DC fault arcs exhibit a higher likelihood of commutation into surrounding structures due to the absence of current zero crossings. These findings highlight the need for improved protective measures in future DC switchgear to ensure safety and reliability.**

***Keywords*—fault arcs, DC grids, AC grids, evaporation, pressure build-up, switchgear safety**

I. Introduction

Low- and medium-voltage DC systems can reduce conversion steps and associated losses by connecting DC loads directly to DC generation and storage, with application areas such as electromobility, DC microgrids, and decentralized technologies including batteries and electrolyzers [1]. A key technology for the operation of DC grids is switchgear, enabling switching operations, diagnostics, and protection of electrical systems and equipment. Potentially triggered by pollution, external objects or human error, fault arc events in these switchgear present a major safety risks for humans and for the system itself.

In fault arc events, the arc can reach core temperatures of several thousand Kelvin and dissipate large amounts of energy, leading to pressure build-up and pressure release in the switchgear installation space [2], [3]. The release of pressure, and worst-case molten switchgear components, may lead to severe damages and increases in downtime. Therefore, research on DC fault arcs is essential to assess their effects on the system and to develop protection measures.

Compared to AC fault arcs, the physical behavior and system effects of DC fault arcs remain less well researched. Current literature focuses mainly on DC fault arc detection and interruption of faults utilizing DC circuit breakers [4], [5].

This research project is funded by the German Federal Ministry of Education and Research (BMBF) through the Project HYPOWER under grant No. 03HY128A. The authors would like to thank the BMBF for providing the opportunity to conduct this research project.

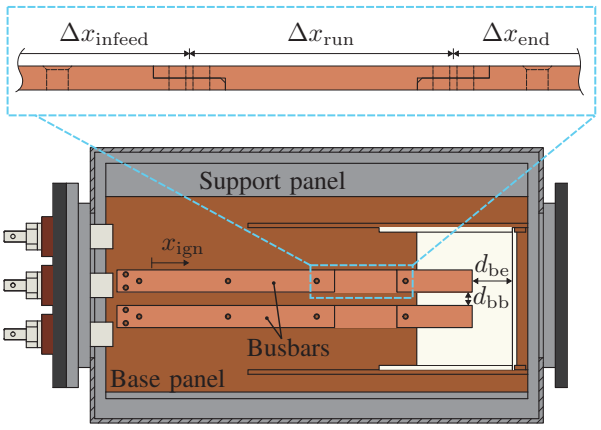


Fig. 1: Cross-section of the hermetically sealed vessel and segments of the split busbars [6]. The components are colored according to the material used.

To address this gap, we experimentally characterize DC fault arcs and compare them to AC fault arcs in a controlled, hermetically-sealed vessel, emulating typical switchgear design. The evaluation is focused on arcing energy, evaporation processes, pressure build-up, arc movement, and commutation behavior. The work in this paper provides quantitative and qualitative insights into how current waveform influences arc behavior with implications for protective design in DC switchgear.

II. Methodology

A. Test setup

To investigate the effects of DC and AC fault arcs, the test setup published in [6] is used. We use an air-filled steel vessel that emulates encapsulated, hermetically sealed switchgear compartments, with internal dimensions of $1\,\mathrm{m} \times 0.6\,\mathrm{m} \times 0.6\,\mathrm{m}$ ($0.36\,\mathrm{m}^3$). Two parallel copper busbars with rectangular cross-section are arranged horizontally inside the vessel to allow systematic investigation of single phase-to-ground faults. The busbar ends are surrounded on four sides by replaceable polymer panels (Polyamide 6.6 (PA 6.6)), and the busbars are split into three segments ($\Delta x_{\mathrm{infeed}}$, Δx_{run},

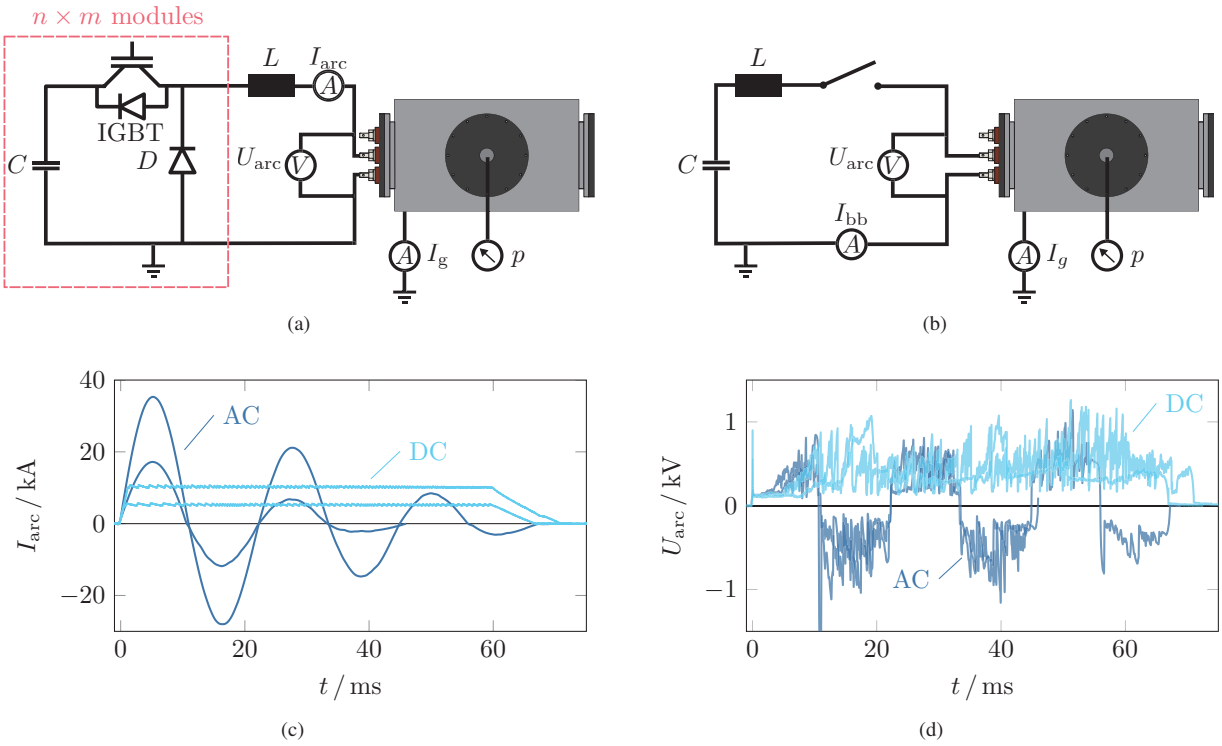


Fig. 2: Simplified circuit diagram of the electric DC (a) and AC (b) circuit [7], [8] and comparison of DC and AC arc current (c) and voltage (d) characteristics. The measurements have been filtered to reduce noise. The circuits are parameterized for $I_{\mathrm{arc,t}} = [5, 10]\,\mathrm{kA}$ and $\hat{I}_{\mathrm{arc}} = [18, 36]\,\mathrm{kA}$, respectively.

Δx_{end}) to resolve erosion processes spatially (Fig. 1). The distance between the busbars, and between the busbar ends and the polymer panel on the right side are kept constant at $d_{\mathrm{bb}} = 30\,\mathrm{mm}$ and $d_{\mathrm{be}} = 75\,\mathrm{mm}$, respectively. Electrical connections enter through two bushings on the left, and the vessel is instrumented to measure arc current, arc voltage, and pressure build-up. Before each test, a copper wire ($A_{\mathrm{wire}} = 0.1\,\mathrm{mm}^2$; $R = 0.6\,\Omega\,\mathrm{m}^{-1}$) is attached to the busbars to ignite the arc.

B. Electric DC and AC circuits

To compare DC and AC fault arcs, the test setup is supplied with currents by two different electric circuits. In the following, the DC and AC circuits and their measurement systems are introduced.

1) Electric DC circuit: The DC circuit corresponds to the setup in [7] and follows the power-electronic buck converter (PEBC) architecture, with capacitors serving as a DC source and insulated-gate bipolar transistors (IGBTs) with freewheeling diodes switching between two states (Figure 2a). The source is modularized with $n = 2$ series modules and $m = 60$ parallel modules to control fault current and system voltage; the total capacitance is $C = 60\,\mathrm{mF}$, the inductance is $L = 0.5\,\mathrm{mH}$, and the maximum source voltage is $U = 8\,\mathrm{kV}$.

Two-point control keeps the arc current within a defined band around a target current $I_{\mathrm{arc,t}}$, and arc current I_{arc} is measured via a coaxial shunt ($R_{\mathrm{s}} = 294.4\,\mu\Omega$) placed upstream of the vessel. Vessel-to-ground current I_{g} is measured by a Rogowski coil (CWT150B) to capture commutation into the vessel, and arc voltage U_{arc} is measured with a 1000:1 divider (Northstar PVM-5). Vessel pressure p is recorded using a piezoelectric sensor (Kistler 601CAA, sensitivity of $-36.89\,\mathrm{pC\,bar}^{-1}$) mounted concentrically in a polyoxymethylene insert on the front flange, shielded by a copper sheet to mitigate radiative coupling [9].

2) Electric AC circuit: The AC circuit corresponds to the setup in [8] (Figure 2b) and is a damped LC resonance circuit powered by a capacitor bank ($C = 17\,\mathrm{mF}$) and an inductance ($L = 0.63\,\mathrm{mH}$), with a resonance frequency of $f = 45.12\,\mathrm{Hz}$ and a maximum source voltage of $U = 8\,\mathrm{kV}$.

Currents are measured separately busbar-to-ground I_{bb} and vessel-to-ground I_{g} using Rogowski coils (CWT150B), with arc current I_{arc} equal to the sum of the two. An active differential probe (TESTEC SI 9010, divider ratio of 1:1000) measures arc voltage between the high voltage busbar and ground potential, and vessel pressure is recorded as in the DC setup.

C. Experimental setup and evaluation method

Between DC and AC experiments, we hold boundary conditions constant: busbar gap ($d_{\mathrm{bb}} = 30\,\mathrm{mm}$, ignition position $x_{\mathrm{ign}} = 80\,\mathrm{mm}$, filling pressure $p_{\mathrm{fill}} = 100\,\mathrm{kPa}$, and distance from busbar end to the right polymer panel $d_{\mathrm{be}} = 75\,\mathrm{mm}$. DC experiments target $I_{\mathrm{arc,t}} = [5, 10]\,\mathrm{kA}$, while AC experiments investigate peak currents $\hat{I}_{\mathrm{arc}} = [18, 36]\,\mathrm{kA}$, with nominal test durations of approximately 66 ms to 70 ms. The selected

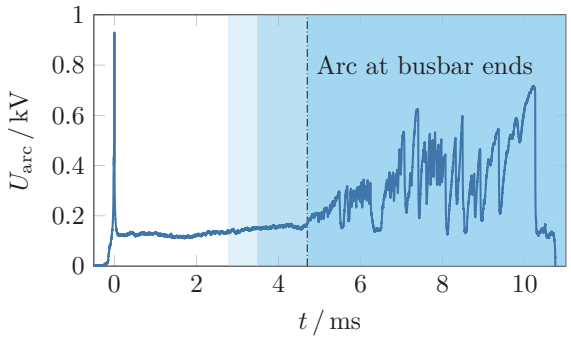


Fig. 3: Exemplary arcing voltage over time. The shaded backgrounds indicate the arc movement on the different busbar segments and the dash-dotted line indicates the point in time where the arc reaches the busbar ends [6].

current levels were chosen to enable evaluation based on comparable arc energy levels rather than identical peak current values. To account for stochastic effects, each test is repeated five times. As the capacitor voltages decay during the tests, the current may reach zero before the target time; we therefore evaluate energy-specific ablation, energy-specific pressure rise, and charge-transfer-specific erosion to normalize across waveforms.

Mean arc velocity $[\bar{v}_{\mathrm{arc}}] = \mathrm{m\,s^{-1}}$, ablation rates $[m_{\mathrm{rate,PA\,6.6}}] = \mathrm{\mu g\,J^{-1}}$, and erosion rates $[m_{\mathrm{rate,Cu}}] = \mathrm{mg\,C^{-1}}$ follow the evaluation procedure established in [6]. The arc power P_{arc} and arc energy E_{arc} are calculated from the measured current and voltage

$$P_{\mathrm{arc}} = U_{\mathrm{arc}}(t)\left(I_{\mathrm{g}}(t) + I_{\mathrm{bb}}(t)\right), \tag{1}$$

$$E_{\mathrm{arc}} = \int_{t_0}^{t_{\mathrm{end}}} P_{\mathrm{arc}}(t)\,\mathrm{d}t. \tag{2}$$

Whereas $I_{\mathrm{bb}} = I_{\mathrm{arc}} - I_{\mathrm{g}}$ is valid for the DC investigations as I_{bb} is not measured directly.

Ablation rates are determined by measuring the weight difference before and after each test for each polymer panel and dividing it by the arc energy according to (2). Since the main ablation processes take place while the arc is in front of the polymer panels, t_0 is set to the moment in time where the arc reaches the busbar's end.

Erosion rates are determined by measuring the weight difference before and after each test for each busbar segment of each busbar and dividing it by the charge transfer through the busbar's surface. The charge transfer through the vessel after arc commutation is not included for estimation of the erosion rate of the lower busbar. Therefore, the point in time at which the arc roots cross the busbar segments are determined.

Since the setup is hermetically sealed, estimating the points in time, where the arc crosses the busbars' segments is impossible. To estimate the average arc velocity, the time where the arc reaches the busbars end is determined by analyzing the temporal progression of U_{arc} (Fig. 3). The arc accelerates along the busbars after ignition, as indicated by a voltage peak at $t = 0\,\mathrm{ms}$. Since the arc column accelerates

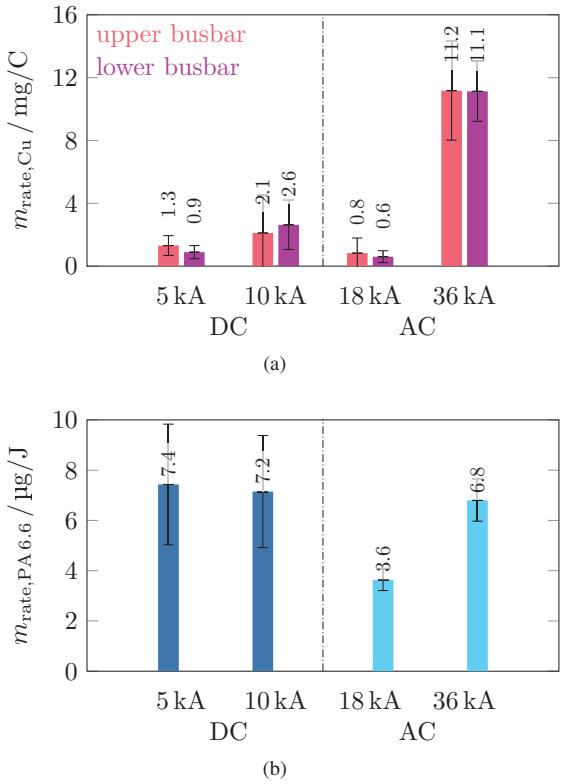


Fig. 4: Comparison of mean copper erosion (a) and polymer ablation rates (b) for DC and AC fault arc experiments. The error bars indicate the experiments standard deviation.

slightly faster than the arc roots, the arcing voltage increases continuously. At $t = 4.7\,\mathrm{ms}$, the arc roots reach the busbar ends, and Lorentz forces cause the arc to expand further, resulting in a steeper voltage rise. Based on this point in time, the average arc velocity is estimated, and segment-wise arc durations are derived, assuming instantaneous acceleration to the average velocity.

III. Results

We present results on electrode erosion and polymer ablation (Section III-A), pressure build-up (Section III-B), and arc movement and commutation (Section III-C). To reduce measurement uncertainty, we focus on the erosion rates for the busbars' end segments and the ablation rates for the polymer panel on the right side. The comparable highest ablation rates and masses can be identified for this panel due to the highest radiative penetration from the arc. The highest erosion rates and masses are measured on the end segments due to the comparable long arc duration on the end segments. The eroded masses on the remaining segments are negligibly small [6].

A. Evaporation processes

As this study focuses on the difference between DC and AC, only the busbar section and the polymer panel with the highest mass loss, and thus the lowest measurement uncertainty, are considered. The highest mass loss is repeatedly measured at

the end section Δx_{end} and the polymer panel on the right side of the busbars.

1) Electrode erosion $m_{\mathrm{rate,Cu}}$: Across all experiments, erosion rates of the upper and lower busbars at Δx_{end} are comparable (Fig. 4a). In AC tests, this symmetry is expected because the anode and cathode alternate with each current zero-crossing, while DC tests maintain fixed polarity; in the literature, anode erosion is often lower than cathode erosion [10], but our measurement may not resolve that difference due to small mass changes at 5 kA to 10 kA, in combination with scale resolution limits.

At similar current levels, DC erosion rates are higher than AC erosion rates. For DC, approximately $0.9\,\mathrm{mg\,C^{-1}}$ to $1.3\,\mathrm{mg\,C^{-1}}$ at 5 kA and $2.1\,\mathrm{mg\,C^{-1}}$ to $2.6\,\mathrm{mg\,C^{-1}}$ at 10 kA. For AC, approximately $0.6\,\mathrm{mg\,C^{-1}}$ to $0.8\,\mathrm{mg\,C^{-1}}$ at 18 kA and $11.1\,\mathrm{mg\,C^{-1}}$ to $11.2\,\mathrm{mg\,C^{-1}}$ at 36 kA. Further experimental investigations are needed to identify the reason for the higher DC erosion rates. Possible reasons include the constant polarity and the higher likelihood of splattering in DC tests.

At higher power levels, the expansion of evaporated copper in deeper material layers ejects molten copper at the surface. This ejection likely increases the apparent erosion rate due to the release of droplets. Accordingly, a higher erosion rate is observed at $\hat{I}_{\mathrm{arc}} = 36\,\mathrm{kA}$. This occurs despite a lower overall charge transfer compared to the DC tests (Fig. 6b). Therefore, higher erosion rates are observed than those reported in the literature [11], [12], [13].

2) Polymer ablation $m_{\mathrm{rate,PA\,6.6}}$: DC ablation rates are similar to AC ablation rates observed at higher peak currents, with DC mean ablation rates of $7.2\,\mathrm{\mu g\,J^{-1}}$ to $7.4\,\mathrm{\mu g\,J^{-1}}$ at 5 kA to 10 kA and AC mean ablation rates of $3.6\,\mathrm{\mu g\,J^{-1}}$ to $6.8\,\mathrm{\mu g\,J^{-1}}$ at 18 kA to 36 kA (Fig. 4b).

DC tests show greater variability in ablation rates, likely because of the absence of current zero-crossings. Due to the lack of zero crossings and re-ignitions in DC compared to AC, arc elongation in front of the polymer panels is less stable and constant. However, according to our experiments the ablation rates are comparable between experiments at both target currents.

B. Pressure build-up

For both DC and AC arcs, pressure build-up Δp correlates linearly with arcing energy E_{arc}, with high coefficients of determination ($R^2 = 0.99$ for DC $R^2 = 0.988$ for AC) and a slightly higher slope for AC (Fig. 5). Because only two current levels were tested per waveform, more experiments at varied arcing energies are needed to strengthen confidence in the linear approximation.

Differences in eroded and ablated mass between DC and AC have only minor influence on pressure build-up at similar energy levels particularly for the high erosion rate at $\hat{I}_{\mathrm{arc}} = 36\,\mathrm{kA}$ (Fig. 4), the negligible difference in pressure build-up between DC and AC at similar arcing energy strengthens the assumption that parts of the apparent erosion rates are based on liquid copper splattering as liquid copper droplets do not affect the arc nor the pressure build-up.

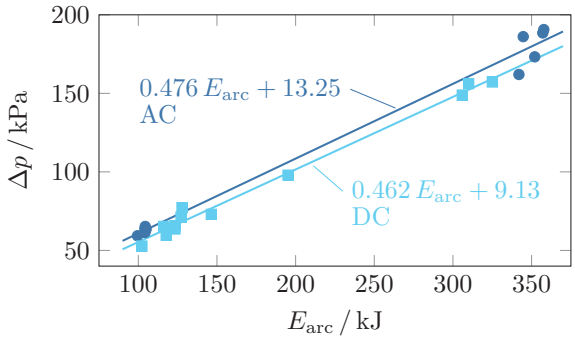


Fig. 5: Correlation between pressure build-up and arc energy for considered DC and AC fault arc experiments. The coefficients of determination are $R^2 = 0.99$ and $R^2 = 0.988$, respectively.

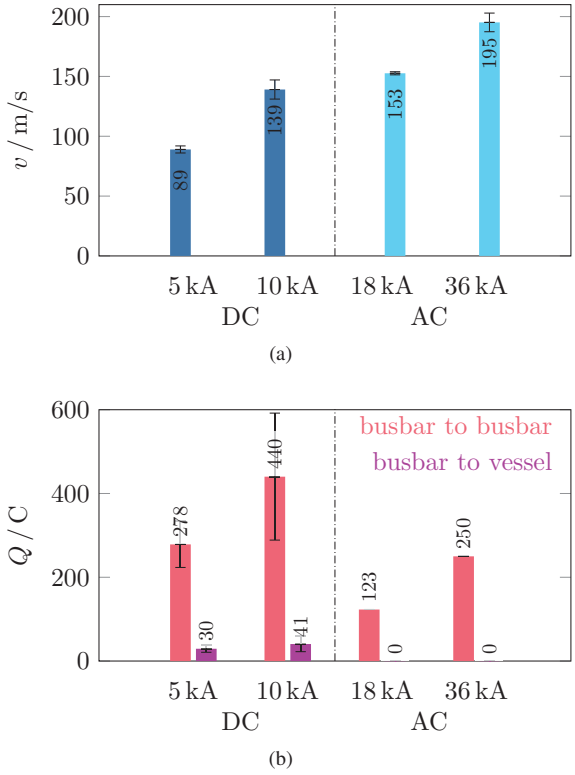


Fig. 6: Comparison of mean arc velocity $\bar{v}$ along the busbars (a) and mean charge transfer $\bar{Q}$ between both busbars and between busbar and vessel (b) for DC and AC fault arc experiments. The error bars indicate the experiments standard deviation.

C. Arc velocity and commutation behavior

The current zero-crossings constrain arc elongation and reduce the probability of commutation to the vessel or other grounded structures. In our experiments, commutation to the vessel occurred only in DC tests, with approximately 10 % of

total charge measured at the vessel's ground connection, while no commutation was recorded in AC tests (Fig. 6b).

Mean arc velocities along the busbars were lower for DC ($89\,\mathrm{m\,s^{-1}}$ to $139\,\mathrm{m\,s^{-1}}$) than for AC ($153\,\mathrm{m\,s^{-1}}$ to $195\,\mathrm{m\,s^{-1}}$), yet DC arcs widened more due to constant current flow, increasing commutation risk. Because commutation can lead to burn-through of the vessel, this DC-specific risk must be accounted for in the design of future DC switchgear. The lower velocities in the DC tests are due to the lower mean current during the acceleration along the busbars, resulting in lower electromagnetic forces.

IV. Conclusion

The most significant finding is that while both DC and AC fault arcs exhibit comparable orders of magnitude for erosion and ablation, the absence of current zero-crossings in DC systems significantly increases arc elongation and the likelihood of commutation to surrounding structures. These insights were obtained through systematic experiments that measured arcing energy, pressure build-up, and material erosion in a hermetically sealed vessel. Additionally, by normalizing evaporation and pressure to energy or charge transfer, we quantify differences and similarities between DC and AC fault arcs under controlled conditions. Our results indicate that pressure build-up correlates linearly with arcing energy for both waveforms. Overall, our results highlight critical safety implications for future DC switchgear design with respect to arc commutation.

Future work will focus on expanding parameter variations to further explore waveform-dependent behavior and its impact on protective measures in switchgear. By calibrating and validating magnetohydrodynamic fault arc models using the insights gained from this research, we aim to contribute to the development of eco-friendly DC switchgear solutions.

Acknowledgment

We thank the institute's workshop for producing test specimens and Felix Wisniowski and Aron Kischporski for assistance with experiments.

References

[1] A. W. Adegboyega, S. Sepasi, H. O. R. Howlader, B. Griswold, M. Matsuura, and L. R. Roose, "DC Microgrid Deployments and Challenges: A Comprehensive Review of Academic and Corporate Implementations," *Energies*, vol. 18, no. 5, p. 1064, 2025. DOI: 10.3390/en18051064.

[2] A. Gleizes, J. J. Gonzalez, and P. Freton, "Thermal plasma modelling," *Journal of Physics D: Applied Physics*, vol. 38, no. 9, R153–R183, 2005. DOI: 10.1088/0022-3727/38/9/R01.

[3] X. Zhang, G. Pietsch, and E. Gockenbach, "Investigation of the Thermal Transfer Coefficient by the Energy Balance of Fault Arcs in Electrical Installations," *IEEE Transactions on Power Delivery*, vol. 21, no. 1, pp. 425–431, 2006. DOI: 10.1109/TPWRD.2005.852274.

[4] S. Lu, B. T. Phung, and D. Zhang, "A comprehensive review on DC arc faults and their diagnosis methods in photovoltaic systems," *Renewable and Sustainable Energy Reviews*, vol. 89, pp. 88–98, 2018. DOI: 10.1016/j.rser.2018.03.010.

[5] R. P. P. Smeets and N. A. Belda, "High–voltage direct current fault current interruption: A technology review," *High Voltage*, vol. 6, no. 2, pp. 171–192, 2021. DOI: 10.1049/hve2.12063.

[6] F. Mingers, S. Kimpeler, and W. Leterme, "Experimental characterization of evaporation processes of copper and polyamide 6.6 caused by fault arcs," *Physica Scripta*, vol. 100, no. 7, pp. 1–18, 2025. DOI: 10.1088/1402-4896/ade2ab.

[7] N. Langenberg, "Flexible test method for MVDC circuit breakers utilizing a modular power electronic buck converter," Dissertation, RWTH Aachen University, Aachen, 2023. DOI: 10.18154/RWTH-2023-05375.

[8] F. Mingers, T. Ballweber, S. Kimpeler, and A. Moser, "Validation Approach for a Spatially and Temporally Resolved Fault Arc Model," *Plasma Physics and Technology*, vol. 10, no. 2, pp. 64–68, 2023. DOI: 10.14311/ppt.2023.2.64.

[9] T. Ballweber, "Untersuchungen zur Druckentwicklung in leistungsstarken Niederspannungs-Schaltanlagen im Störlichtbogenfall," Dissertation, RWTH Aachen University, 2023. DOI: 10.18154/RWTH-2024-00217.

[10] R. J. Munz, R. N. Szente, and M. G. Drouet, "Arc behaviour and plasma chemistry in electrode erosion," *Pure and Applied Chemistry*, vol. 64, no. 5, pp. 657–663, 1992. DOI: 10.1351/pac199264050657.

[11] R. N. Szente, R. J. Munz, and M. G. Drouet, "Electrode erosion in plasma torches," *Plasma Chemistry and Plasma Processing*, vol. 12, no. 3, pp. 327–343, 1992. DOI: 10.1007/BF01447029.

[12] S. Coulombe and J.-L. Meunier, "Theoretical prediction of non-thermionic arc cathode erosion rate including both vaporization and melting of the surface," *Plasma Sources Science and Technology*, vol. 9, no. 3, pp. 239–247, 2000. DOI: 10.1088/0963-0252/9/3/301.

[13] A. M. Essiptchouk, A. Marotta, and L. I. Sharakhovsky, "The influence of the arc current on the cold electrode erosion," *Physics of Plasmas*, vol. 10, no. 9, pp. 3770–3773, 2003. DOI: 10.1063/1.1599856.

Break arc behaviors of Ag, $AgSnO_2$, AgNi, and AgZnO in inductive DC loads up to 20V/20A under magnetic field application

Makoto Hasegawa
Dept.of Opto-Electronic System Engineering
Chitose Inst. of Science & Technology
Chitose, Hokkaido, Japan
hasegawa@photon.chitose.ac.jp

Reo Oikawa
Dept.of Opto-Electronic System Engineering
Chitose Inst. of Science & Technology
Chitose, Hokkaido, Japan

Haruto Oiwa
Dept.of Opto-Electronic System Engineering
Chitose Inst. of Science & Technology
Chitose, Hokkaido, Japan

Yuna Onishi
Dept.of Opto-Electronic System Engineering
Chitose Inst. of Science & Technology
Chitose, Hokkaido, Japan

***Abstract*—The authors' research group has studied break arc behaviors in inductive DC load conditions up to 20V and 20A. Those load conditions have been selected because systematic research results seem not to be available, although satisfactory DC switching performances are often required in those conditions. In the authors' previous studies, when $AgSnO_2$ contact pairs were operated to break an inductive DC load circuit under external magnetic field application up to about 150mT, some strange arc behaviors were repeatedly observed. Specifically, arc shortening due to magnetic field application was confirmed, not only in the cases with magnetic arc blowing, but also in the cases at slower opening speeds and/or smaller current levels where magnetic blowing was not observed. In those cases without magnetic blowing even with the applied external magnetic field, break arc was likely to finally extinguish after moving in the direction opposite to the Lorentz force direction, while showing certain arc shortening tendencies. Such arc movements were confirmed not to be caused by gravity. In this paper, similar experiments and observations were conducted in DC inductive load conditions up to 20V/20A with/without external magnetic field application of about 150mT with Ag, AgNi, and AgZnO contact pairs in addition to $AgSnO_2$ contact pairs, and break arc duration characteristics were compared among those contact materials.**

Keywords—break arc, magnetic blowing, arc movements, DC breaking, arc shortening

I. INTRODUCTION

Shortening schemes for break arc discharges are crucial to realize better performances and reliabilities of mechanical relays. This is especially true in DC interruptions, since there are no current zero points in those DC applications. Well-known schemes for arc shortening purposes include increases in contact opening speeds [1-6] and magnetic blowing with application of external magnetic fields [7-8]. Although a lot of research works were done and published up to now with respect to those arc shortening schemes, further investigations are still required to realize sufficient understandings of DC breaking phenomena.

While the magnetic blowing phenomena have been mainly studied with larger load levels, investigations in lighter load levels may become important in view of possible new automotive applications, for example, with power supply voltages up to DC50V and load current levels less than 100A.

The authors' research group has been interested in DC break arc phenomena in such lighter load conditions, and conducted several experiments to understand influences of contact opening speeds as well as effectiveness of the external magnetic field applications on break arc shortening in those load conditions with $AgSnO_2$ contact pairs [9-12]. As a result, when $AgSnO_2$ contacts were operated to break an inductive DC load circuit up to 20V/20A under the applied external magnetic field up to about 150mT, slight shortening of break arc durations was observed in operating conditions with smaller load current levels and/or at slower opening speeds, even when magnetic arc blowing did not occur [13-19]. Furthermore, in such cases, break arc was likely to finally extinguish after moving in the direction opposite to the expected Lorentz force direction. Such phenomena were observed repeatedly. However, any explanations for such arc movements have not yet been found.

In view of such backgrounds, in this paper, for obtaining further understandings of DC arc shortening phenomena with applied external magnetic field, break operations of Ag, $AgSnO_2$, AgNi, and AgZnO contact pairs were conducted in a DC inductive load circuit with 14V-6A, 14V-8A, 20V-9A and 20V-16A at different contact opening speeds from 1 to 200mm/s and with/without external magnetic field application of about 150mT in air. Break arc durations were measured from arc voltage waveforms. Based on the obtained results, DC break arc characteristics of those contact materials, as well as comparisons among the materials, were tried to be studied.

II. EXPERIMENTAL CONDITIONS AND PROCEDURES

A. Setup of the experimental system

The same experimental setting as in the authors' previous studies was again used in this study, as shown in Fig.1. The similar descriptions as can be found in the authors' previous reports [20] are shown below.

The switching mechanism includes a motorized stage driven by an AC servo motor. The motorized stage is placed onto a stable metal platform. On the same stable metal platform, one electrode of a contact pair is also fixed as a

stationary electrode via a certain attachment jig. Another electrode is mounted onto the motorized stage to be served as a movable electrode. Switching operations of the contact pair are realized via movements of the motorized stage by controlling the AC servo motor through instructions from a PC program.

Upon opening of the mating electrodes, the movable electrode is moved from its closed position by 2mm at a selected speed level (in the range of 1 to 200mm/s). After the opening movement and a certain period of waiting time, the movable electrode is moved back to its closed position at the predetermined closing speed of 5mm/s. After another waiting, the next opening movement is initiated. These speed values are the defined target values, except for acceleration and deceleration time periods.

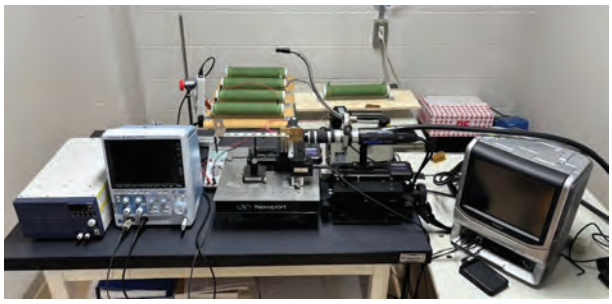


Fig. 1. The experimental system in this study.



Fig. 2. Movable (left) and stationary (right) electrodes in this study.

TABLE I. CONTACT MATERIALS AND EXPERIMENTAL CONDITIONS IN THIS STUDY

Contact material	(a) Ag (b) Ag(88.3%)-SnO_2(11.7%) (internal oxidation with no additives) (c) Ag(90.0%)-Ni(10.0%) (d) Ag(91.0%)-ZnO(9.0%)
Load circuit	DC inductive (L = 5 mH)
Load conditions	14V-6A, 14V-8A, 20V-9A, and 20V-16A
Ambient environment	laboratory air (no control)
Contact opening speed	1, 3, 5, 8, 10, 30, 50, 100, 150, 200 mm/s
External magnetic field	0 mT and about 150 mT

Fig.2 shows a pair of electrodes employed in this study, which was similar to those used in the authors' previous investigations. Both movable (left in Fig.2) and stationary (right in Fig.2) electrodes were of solid rivet-type with a head thickness of about 1mm and a head diameter of about 3mm. The head of the movable electrode (left in Fig.2) was attached onto a spring metal plate (18mm x 6mm, thickness of 0.2mm) made of phosphor bronze, while the head of the stationary electrode (right in Fig.2) was attached onto a metal plate (18mm x 6mm, thickness of 0.6mm) made of oxygen-free copper.

Table I summarizes the experimental conditions employed in this study, which were almost the same as in the authors' previous studies.

Load current values were adjusted by means of combination of several 1Ω-resistors as well as a 0.5Ω-resistor in the load circuit. Specifically, the 14V-8A circuit included one 1Ω-resistor and one 0.5Ω-resistor, while the 20V-16A circuit included one 1Ω-resistor. The remaining 14V-6A and 20V-8A circuits included two 1Ω-resistors. It should be noted that the load circuit also included some resistance components due to terminals as well as wirings.

The inductive load circuit in this study further included an inductive component of about 5mH. It was not intended to realize any specific applications, but rather, it was intended to mitigate influences of unregulated inductive components in the circuit (e.g., stray inductance components due to wirings) by employing such an intentional inductive component. No specific control for the load current flow was employed during switching operations and thus both break and make arc discharges were actually occurred. Among them, only break arc discharges were investigated in this study.

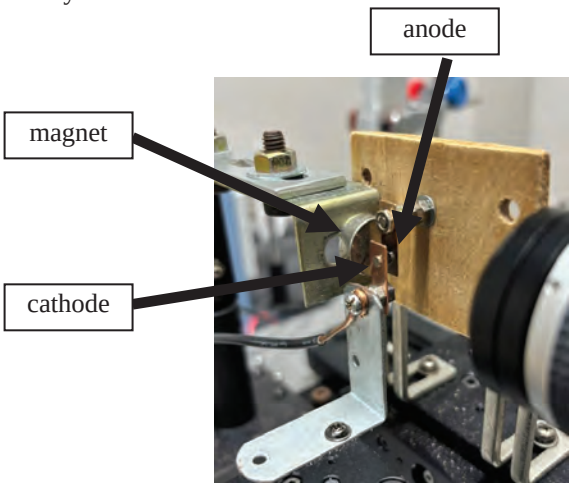


Fig. 3. A piece of magnet placed close to the contact gap, as well as a stationary cathode (left) and a movable anode (right) in this study.

For application of external magnetic field, one piece of neodymium magnet (with 0.5cm in height and 1.5cm in diameter) was placed close to the contact gap position and in the horizontal direction, as shown in Fig.3. In this study, the magnet was normally placed so that its N-pole surface was facing the contact gap, leading to the magnetic field in the direction from left to right in the photo of Fig.3. The load current flowed in the direction from right to left in Fig.3, resulting in the expected Lorentz force being applied in the upward direction.

The resultant magnetic flux density at the contact gap was measured with a Tesla Meter to be about 150mT. It should be noted that it was not possible to confirm whether

or not the magnetic flux density was uniform at around the contact gap, because only one piece of magnet was employed, instead of two pieces facing each other, in this study. In addition, the afore-mentioned values were not exact values, but rather approximate values, because the measured value was very sensitive to the positional deviation of a probe head.

Before the test, the surfaces of both electrodes of a test contact pair were polished with #1000 sandpaper and then wiped with methyl alcohol. Thereafter, the contact pair was mounted onto the switching mechanism with the movable electrode as an anode and the stationary electrode as a cathode. The movable electrode was placed in the downward direction, while the stationary electrode was placed in the upward direction, resulting in the staggered mating placement, as shown in Fig.3.

At the closed position, the movable anode electrode was slightly pushed backward by the mating stationary cathode electrode, thereby resulting in slight bending of the spring plate (an electrode assembly arm for the movable anode electrode) due to its elasticity. This may cause some wiping between the electrode surfaces as is usual in commercial relays. In addition, recovery period from the bending situation seems to at least partly include acceleration period of the movable electrode from its rest position in the opening process.

B. Experimental procedures

Measurements of break arc durations were conducted as follows.

In each of the test conditions, voltage waveforms (in addition, current waveforms) across the separating contacts upon contact opening were recorded with a digital storage-scope. The total of 10 waveforms were analyzed to determine respective arc durations in each condition. The total break arc duration was determined as a time period from the voltage rising point to the point corresponding to an abrupt change in the voltage waveform induced by current termination and inductance components in the load circuit.

It should be noted that under application of external magnetic field, re-ignition phenomenon was sometimes observed. However, for the purpose of simplification, such a re-ignition period was not taken into account in the arc duration analysis in this paper.

Observations of break arc movements were also possible with a high-speed camera with conditions of 4000fps, exposure time 1/8000 sec, and 320 x 240 pixels. A lens of the high-speed camera was also placed closed to the contact gap, at the opposite to the magnet, as can be seen in Fig.3. Unfortunately, in this study, arc movement observations could not be performed simultaneously with arc voltage/current waveform acquisitions.

III. EXPERIMENTAL RESULTS AND DISCUSSIONS

Figs.4-7 respectively show the relationships between the average total break arc durations and the contact opening speeds with/without the applied external magnetic field for each of the tested operating conditions. In each of these figures, black triangular plots indicate the obtained results without any applied external magnetic field (i.e., B=0mT), while white square plots indicate the results with the applied magnetic field of about 150mT. In these figures, each plot indicates the average value calculated from the 10 measured data. Variations among the data in the respective conditions were not so large, and thus, only the average values are being plotted for the purpose of simplification.

A. Influences of contact opening speeds on break arc durations when no external magnetic field was applied

In the characteristics in the 14V-6A condition as shown in Fig.4, without the applied external magnetic field, the average break arc durations of $AgSnO_2$, AgNi and AgZnO contact pairs are likely to gradually become shorter with faster contact opening speeds. However, such shortening effects seem not to follow the inversely-proportional relationship with the contact opening speed values. Moreover, the shortening tendencies become less significant in the faster opening speed range for $AgSnO_2$ and AgNi contact pairs.

For some reasons, Ag contact pair shows almost no shortening tendencies in the break arc durations in 1 to 5 mm/s opening speed ranges, while the shortening tendencies are recognizable in the faster opening speed range. The similar tendencies for Ag contact pair was also reported in the authors' previous work [9, 13].

In the 14V-8A condition as shown in Fig.5, the similar tendencies as in the 14V-6A condition can be found.

In the cases of the 20V-9A condition as shown in Fig.6 and the 20V-16A condition as shown in Fig.7, the arc shortening effects with faster contact opening speeds can be found more clearly over the whole opening speed range from 1 to 200mm/s with each of those contact materials, including Ag contact pair. It should be noted that such shortening tendencies with increased contact opening speed become less significant at faster opening speed levels.

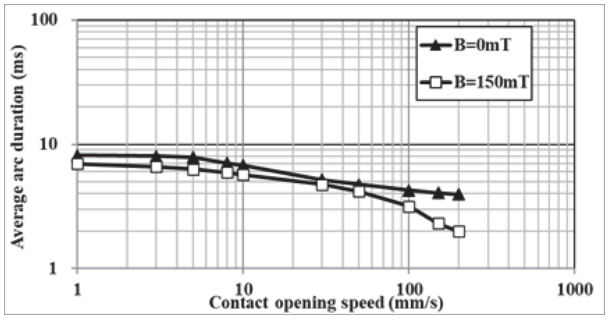
With respect to less significant shortening tendencies of break arc durations with faster contact opening speeds, the authors' previous work pointed out possible trade-off effect between a faster decrease in arc plasma density and a possible increase in a di/dt value with larger contact opening speeds. The former factor will lead to faster extinction of break arcs, while the latter factor will induce a larger voltage between the opening contact gap, preventing extinction of a break arc [9-10].

B. Influences of external magnetic field application on break arc durations

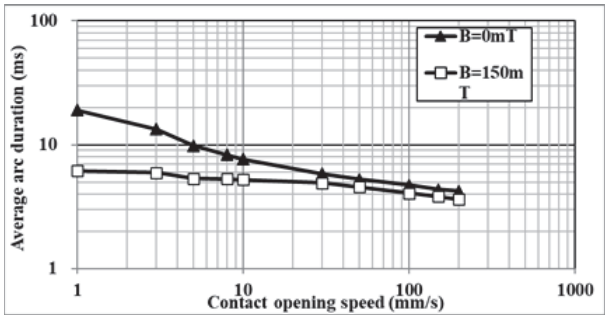
As shown in Fig.4, with the applied external magnetic field of about 150mT in the 14V-6A condition, Ag contact pair and AgNi contact pair show clear reductions in the average break arc durations with in the faster contact opening speed range due to magnetic blowing effect. AgNi contact pair also exhibited certain arc shortening tendencies with slower contact opening values, although no arc blowing was observed in such cases.

In contrast, $AgSnO_2$ contact pair and AgZnO contact pair fail to show such clear shortening with magnetic blowing with faster opening speed levels, while some arc shortening effects were recognizable with slower opening speed levels.

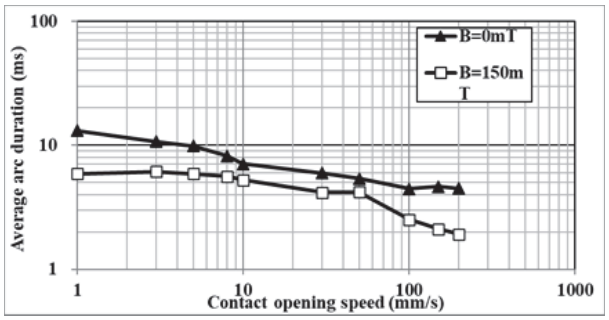
In the 14V-8A condition as shown in Fig.5, the similar tendencies as in the 14V-6A condition can be found, except that $AgSnO_2$ and AgZnO contact pairs show clear arc shortening tendencies with magnetic arc blowing.



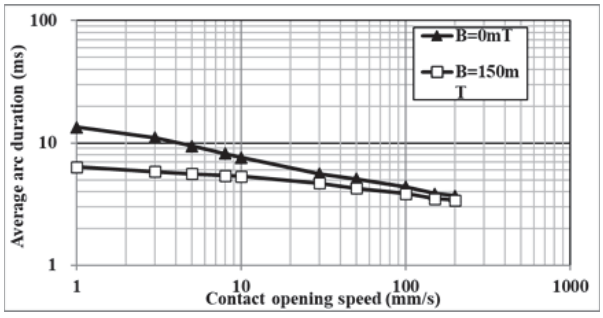
(a) Ag



(b) $AgSnO_2$

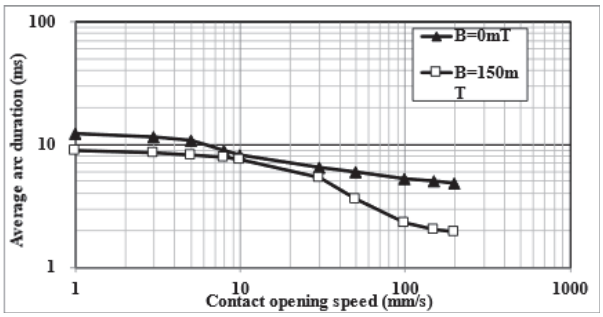


(c) AgNi

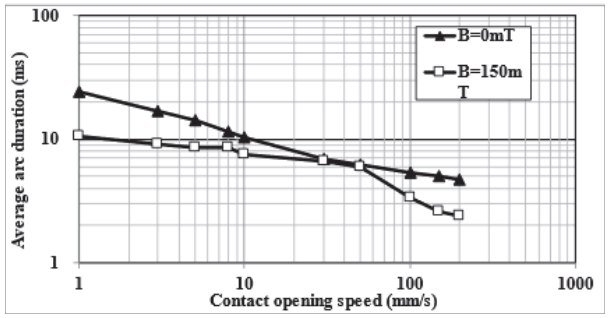


(d) AgZnO

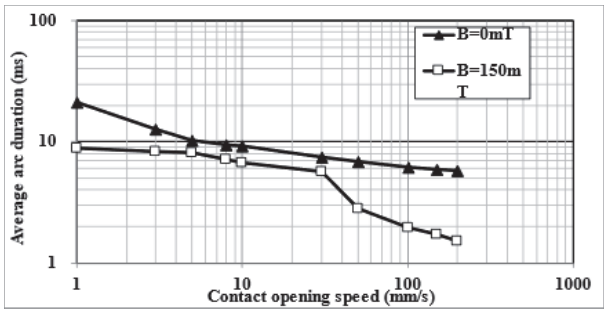
Fig. 4. Break arc duration characteristics in the 14V-6A load condition of the respective contact pairs.



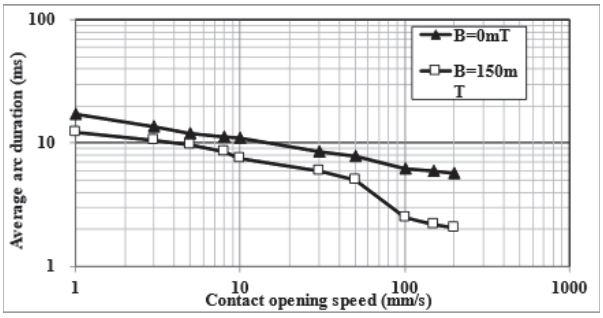
(a) Ag



(b) $AgSnO_2$



(c) AgNi

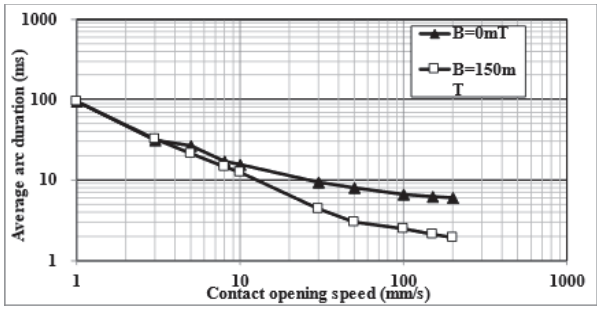


(d) AgZnO

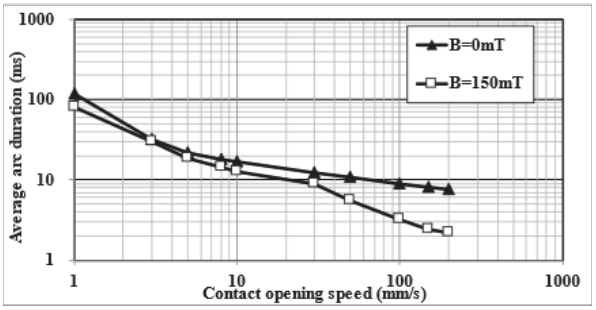
Fig. 5. Break arc duration characteristics in the 14V-8 A load condition of the respective contact pairs.

With higher voltage level of 20V in the 20V-9A condition and the 20V-16A condition as shown in Fig.6 and Fig.7, arc shortening tendencies due to magnetic arc blowing at faster opening speed levels can be clearly recognized.

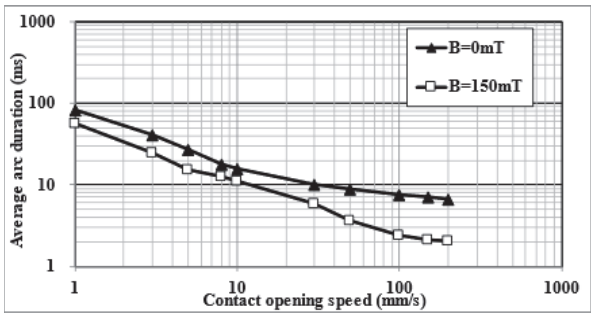
Arc shortening effects at slower contact opening speeds are also recognizable for each contact material under each condition, although more clearly in some cases than others.



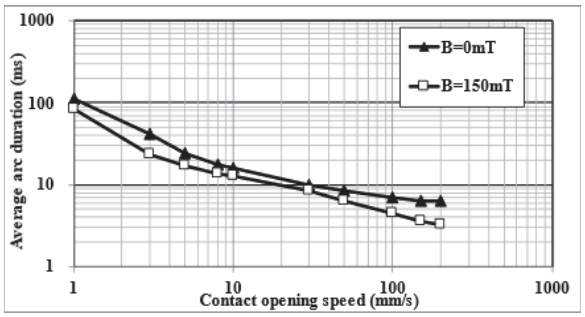
(a) Ag



(b) $AgSnO_2$

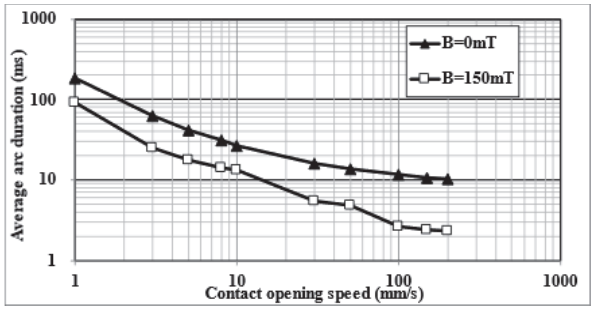


(c) AgNi

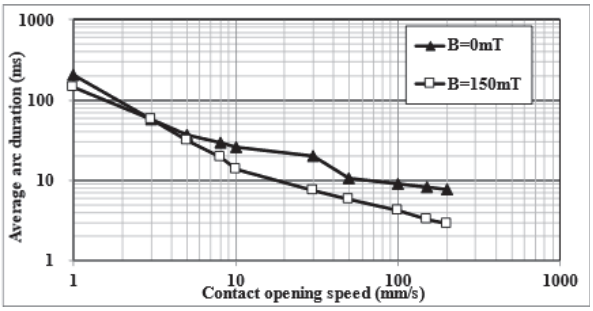


(d) AgZnO

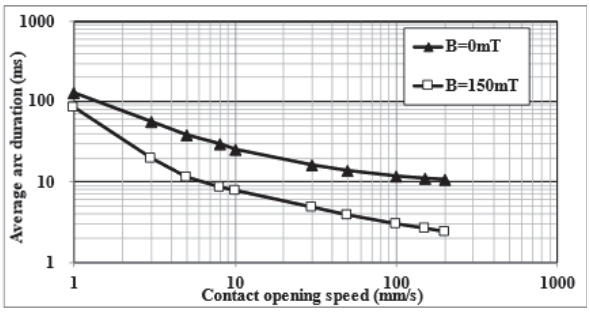
Fig. 6. Break arc duration characteristics in the 20V-9A load condition of the respective contact pairs.



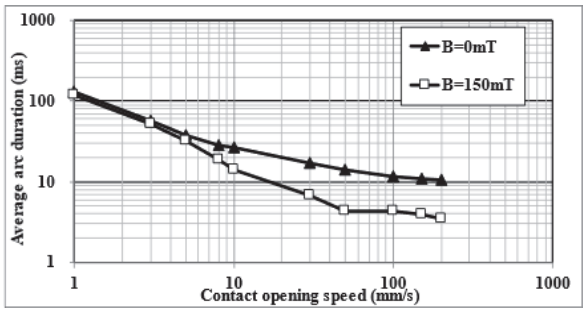
(a) Ag



(b) $AgSnO_2$



(c) AgNi



(d) AgZnO

Fig. 7. Break arc duration characteristics in the 20V-16A load condition of the respective contact pairs.

C. Comparisons among the contact materials

The four contact materials tested in this study seem to exhibit the similar break arc duration tendencies with each other. However, there are certain differences, for example, on whether or not clear arc shortening effects are recognizable with no magnetic arc blowing.

Certain peculiar arc movements were also observed when magnetic arc blowing did not occur, as reported in the authors' previous work. Any differences in such arc behaviors among the different contact materials under different test conditions will be related to break arc characteristics.

IV. SUMMARY

For the purpose of obtaining further understandings of DC arc shortening phenomena with/without applied external magnetic field, break operations of Ag, $AgSnO_2$, AgNi, and AgZnO contact pairs were conducted in a DC inductive load circuit with 14V-6A, 14V-8A, 20V-9A and 20V-16A at different contact opening speeds from 1 to 200mm/s and with/without external magnetic field application of about 150mT in air. Measurements of break arc durations as well as arc movement observations were conducted.

Shortening tendencies with increased contact opening speed levels were confirmed for each of the four contact materials. Break arcs were also shortened due to the external magnetic field application, not only with faster contact opening speed levels and/or larger load current levels, apparently caused by magnetic arc blown-out phenomena, but also in the cases with slower opening speed levels and smaller load current levels where magnetic arc blowing was not observed. The peculiar arc movements in the direction opposite to the expected Lorentz force in the cases without magnetic blowing were repeatedly observed as in the authors' previous reports, which can be considered to have certain influences on arc shortening effects without magnetic blowing. However, any reasonable explanations for these phenomena are still unknown.

The similar arc shortening tendencies are recognizable for the four contact materials in this study. Meanwhile, there are certain differences observed in break arc characteristics depending on the contact materials and the operating conditions. Further investigations, especially analysis of break arc movements, are necessary to realize further understandings.

For the purpose of realizing clear view for high-speed observation of arc movement, only a single magnet piece was employed in this study. This inevitably induced non-uniform magnetic field distribution, which in turn possibly resulted in undesirable influences on arc behaviors. Investigations are required in this regard.

Further data acquisitions and investigations will be done with different load conditions, including resistive load conditions as well as different external magnetic field levels, in order to realize further understandings on shortening effects of DC break arc durations obtainable from external magnetic field application.

ACKNOWLEDGMENT

The authors thank Tanaka Kikinzoku Kogyo Co., Ltd. for supplying contact samples used in this study.

REFERENCES

[1] J.W.McBride and S.M.Sharkh, "The influence of contact opening velocity on arc characteristics", Proc. of 16th Intl. Conf. on Electrical Contacts, pp.395-400, September 1992.

[2] N. BenJemaa, L. Doublet, L. Morin, and D. Jeannot, "Break arc study for the new electrical level of 42 V in automotive applications", Proc. 47th IEEE Holm Conf. on Electrical Contacts, pp.50-55, September 2001.

[3] N. BenJemaa, "Contacts conduction and switching in DC levels", Proc. 48th IEEE Holm Conf. on Electrical Contacts, pp.1-15, October 2002.

[4] Liang Huimin, Ma Guangcheng, Cai Ling, Xie Yong and Xie Guoqiang, "Research on the relationship between contact breakaway initial speed and arc duration", Proc. 49th IEEE Holm Conf. on Electrical Contacts., pp.204-210, September 2003.

[5] L. Doublet, N. BenJemaa, F. Hauner and D. Jeannot, "Electrical arc phenomena and its interaction on contact material at 42 volts DC for automotive applications", Proc. 50th IEEE Holm Conf. on Electrical Contacts, pp.8-14, Sepember 2004.

[6] G. Witter and Z. K. Chen, "A comparison for the effects of opening speed, contact gap and material type on electrical erosion for relays interrupting inductive automotive loads", Proc. of 23rd Intl. Conf. on Electrical Contacts, pp.17-21, June 2006.

[7] A. Vassa, E. Carvou, S. Rivoirard, L. Doublet, C. Bourda, D. Jeannot, P. Ramoni, N. BenJemaa, and D. Givord, "Magnetic blowing of break arcs up to 360VDC", Proc. of 56th IEEE Holm Conf. on Electrical Contacts, pp.96-100, October 2010.

[8] A. Vassa, E. Carvou, S. Rivoirard, L. Doublet, C. Bourda, N. BenJemaa, and D. Givord, "DC-arc blowing under pulsed magnetic field", Proc. of 26th Intl. Conf. on Electrical Contacts, pp.23-29, May 2012.

[9] M. Hasegawa, H. Sonobe and Y. Ohmae, "Influences of contact opening speeds in the range of 0.5 to 200mm/s on break arc behaviors of Ag and $AgSnO_2$ contacts in DC14V inductive load circuits of 1 to 5A", Proc. of 60th IEEE Holm Conf. on Electrical Contacts, pp.14-18, October 2014.

[10] M. Hasegawa, H. Sonobe and N. Ohkawa, "Influences of contact opening speeds in the range of 0.5 to 200mm/s on break arc behaviors of $AgSnO_2$ contacts in DC conditions", Proc. of 61st IEEE Holm Conf. on Electrical Contacts, pp.166-170, October 2015.

[11] M. Hasegawa and S. Tokumitsu, "Break arc duration characteristics of $AgSnO_2$ contacts under magnetic field application with contact opening speeds in the range up to 200mm/s in DC load conditions", Proc. of 62nd IEEE Holm Conf. on Electrical Contacts, pp.119-124, October 2016.

[12] M. Hasegawa and S. Tokumitsu, "Influences of contact opening speeds up to 200mm/s and external magnetic field application on break arc duration characteristics of $AgSnO_2$ contacts in DC14V load conditions up to around 10A", IEEE Trans. on Components, Packaging and Manufacturing Technology, vol.8, no.3, pp.375-382, March 2018.

[13] S. Tokumitsu and M. Hasegawa, "Effective shortening of break arc durations of Ag and several Ag-based contacts in DC load conditions with increased contact opening speeds and external magnetic field", Proc. of 64th IEEE Holm Conf. on Electrical Contacts (together with 29th Intl. Conf. on Electrical Contacts), pp.87-94, October 2018.

[14] S. Tokumitsu and M. Hasegawa, "Arc movement investigations of break arcs of $AgSnO_2$ contacts under applied external magnetic field in inductive DC load conditions", Proc. of 65th IEEE Holm Conf. on Electrical Contacts, pp.95-100, September 2019.

[15] S. Tokumitsu and M. Hasegawa, "Relationships between break arc behaviors of $AgSnO_2$ contacts and Lorentz force to be applied by an external magnetic force in a DC inductive load circuit up to 20V-17A", IEICE Trans. on Electronics, vol.E102-C, no.9, pp.641-645, September 2019.

[16] M. Hasegawa and S. Tokumitsu, "Observations of peculiar break arc movements of $AgSnO_2$ contacts under applied external magnetic field in inductive DC load conditions up to 20V-17A", Proc. of 66th IEEE Holm Conf. on Electrical Contacts, pp.79-84, October 2021.

[17] M. Hasegawa and S. Kosugi, "Observation of break arc movements of $AgSnO_2$ contacts under external magnetic field in light-level inductive DC load conditions," Proc. of 68th IEEE Holm Conf. on Electrical Contacts, pp.147-152, October 2023.

[18] R. Oikawa, Y. Asari and M. Hasegawa, "Break arc duration characteristics and arc behavior observations of $AgSnO_2$ contacts in an inductive load circuit up to DC20V", Proc. of 69th IEEE Holm Conf. on Electrical Contacts (together with 32nd Intl. Conf. on Electrical Contacts), pp.121-126, October 2024.

[19] R. Oikawa and M. Hasegawa, "Influences of external magnertic field application on break arc characteristics of $AgSnO_2$ contact pairs in a DC inductive load circuit up to DC20V", IEICE Technical Report, EMD2024-37, February 2025 (written in Japanese).

[20] R. Oikawa and M. Hasegawa, "Observations of break arc behaviors of $AgSnO_2$ contacts in an inductive load circuit up to DC20V under external magnetic field application of different levels", Proc. of 70th IEEE Holm Conf. on Electrical Contacts, pp.245-250, October 2025.

Determination of post-arc conductance by hybrid switching of low voltage DC currents

Diego Gonzalez
Leibniz – INP

Greifswald, Germany
diego.gonzalez@inp-greifswald.de

Luz Gonzalez
Ludwig-Jahn Gymnasium

Greifswald, Germany
lucy.ochsenknecht@gmail.com

***Abstract*— Zero voltage hybrid switching exhibiting arcing (e.g. by using the arc for current commutation) relies on the dielectric recovery behaviour of the contact gap (by hybrid switching ~ some 100 µm). To investigate this factor, which is critical to avoid arc-reignition and to permit successful current interruption an experimental model switch setup was used. It consists of a high-performance linear motor for contact separation and a semiconductor to electronically interrupt the current. The arc extinction occurs after some µs arcing-time. High-speed imaging and spatially and time resolved spectroscopy revealed primary a high metal vapor content in the plasma indicating a similar vacuum-arc characteristic. Combining the current source with a high resistive voltage source it was possible to characterize the timely behaviour of the post-arc conductance. Results for currents up to 400 A and arcing times between 100 µs and 500 µs were used to estimate the post-arc conductivity and gas temperature decay.**

Keywords—arc, arcing, conductance, hybrid switching, high-speed imaging, spectroscopy, plasma

I. INTRODUCTION

In order to achieve a safe and controlled supply of electric energy, different connecting/disconnecting devices are required, which are integrated and fulfil specific tasks at different places in modern electric grids. There, circuit breakers accomplish the critical task to ensure power interruption, either under normal conditions, but more importantly during fault conditions, providing safe and consistent disconnection.

The actual changes of the energy sector call for the development of switching devices for DC grids of higher voltages (250 V or higher) and up to several kV for upcoming medium voltage (MV) DC grids. Moreover, modern grids incorporate different types of customers, which may act as providers as well (prosumers). The increased system complexity exhibits multi-directional power flows, which also have a fluctuating character also. Furthermore, there is a growing demand for "smart" devices with higher levels of data processing, communication features and integrability in super ordinate systems.

The simple function of switching devices conceals nonetheless a more complex interaction of involved physical, technical and safety factors. In particular, the type of signal AC or DC, the characteristics of the power source (power grid, generator, solar-power cell, battery, capacitor, etc.), the network and the required voltage and current levels are decisive. While for devices operating at low voltages under 24 V in DC, current interruption may not pose major difficulties, several challenges arise with increasing source i.e. grid voltage. In either case, most of the power switching devices of actual grids are arc-based, by which the interruption of the current involves the ignition and subsequent extinction of an electric arc through natural (in AC) or forced (in DC) current zero (CZ).

To support the structural changes of modern power grids, and specifically for developing direct current (DC) power grids, circuit breakers (CB) are needed that can react and operate in less than one millisecond (sub-millisecond range). Standard DC air circuit breakers or sealed (encapsulated) electro-mechanical circuit breakers typically have operation times ranging from several milliseconds up to tenths of a millisecond, making them too slow for these applications. As a result, current developments in switching devices for DC grids involve using hybrid-switching solutions, which combine traditional electromechanical contacts and power electronic-based switching devices, so- called hybrid circuit breakers (HCB). Hybrid-switching devices, which have been in use for nearly four decades, were previously employed only in limited cases due to their higher costs and complexity. However, advances in power semiconductor technology and greater demand for high-power DC switching have recently renewed interest in hybrid-switching technology.

For DC applications, owing to the requirements to force the current to zero, the development of CB considers two main streams to handle current interruption: Zero voltage and zero current concepts. Several variations of the mentioned concepts have been developed over the last few decades (e.g. [1-17]). In particular, the zero-voltage concept [1] has found the broadest interest recently and should be feasible for low to medium voltage hybrid switchgear. In these devices, the semiconductor components provide fast and reliable switching (power supply and interruption), while the metal contacts ensure low power losses during regular operation and provide effective electrical isolation when disconnected. Furthermore, HCBs are easily integrated into power systems and can control power flows in multiple directions, making them suitable for both DC and alternating current (AC) grids.

Results of different researchers [1-17] indicate three key factors defining a successful current interruption using HCB: 1st a contact opening as swift as possible that permit to reach a large-enough contact gap. 2nd, a quick current commutation (by-passing) to the semiconductor in order to reduce arcing. 3rd well dimensioned semiconductor size and time regimes to permit feasible manufacturing and costs while permitting optimal recovery performance. Since an amount of arcing is either desired [3] or technically difficult to avoid, the dielectric behaviour in the post-arc phase is decisive. The optimal selection of size and active time of the

semiconductor is therefore limited by the conditions governing an arc re-ignition after CZ.

This paper presents results of the temperature decay of post-arc plasmas after hybrid-switching at dynamic (opening) gaps obtained using optical emission spectroscopy, high-speed imaging and the recorded electrical signals. The results permit the estimation of the dielectric recovery behaviour of the gap, which can be used to improve the characteristics and operation times for the required power semiconductors.

II. Experimental Setup and Methodology

A. Model hybrid switch

The setup permits to emulate the switching behaviour of low voltage (LV) air contactors, with realizable gaps in µm-scale (some hundredths of µm, opening speeds ~ 1 … 2 m/s, see Fig. 3 in [18]). The arc is ignited by contact opening under load using a linear motor (LinMot P01-23). To emulate hybrid-switching the current will be by-passed after a pre-defined (variable) arcing time to a Silicon Controlled rectifier (SCR) (IXYS MCO150-16o1) connected in parallel to the main contact (Figure 1). The SCR branch was connected as near a possible to the contacts path to reduce inductive loops and improve commutation. Nevertheless, a parasitic inductivity of around 100 nH was estimated. DC currents between 80 … 400 A were delivered by a RLC-circuit. Contact rivets of standard material Ag/SnO2 92/8 with 5 mm contact surface diameter and 1 mm contact-head height were used. Arcing times of ~ 100 µs and up to 1.5 ms were used.

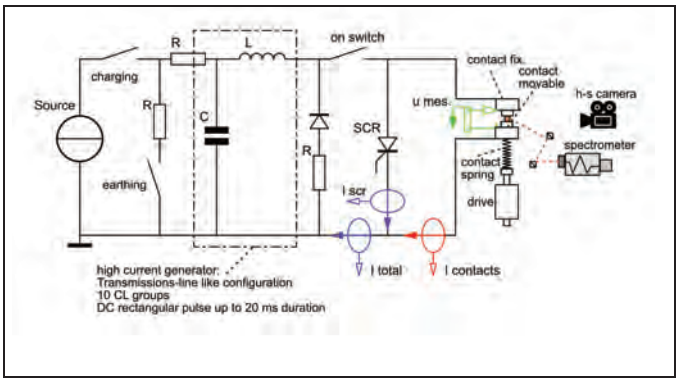


Fig. 1. Schematics of the experimental setup

B. Measurement devices and techniques

Optical emission spectroscopy (OES) was applied for plasma characterization. Overview spectra were obtained with a compact spectrometer (Avantes AvaSpec-ULS2048) using a quartz glass fibre (600 µm diameter) and a quartz 2.5x magnifying collimation lens with 15 mm focal length, which collected around the whole contact region (diameter 10 mm). Spatially solved spectroscopy was realised using 1/2 m spectrometer (Roper Acton SP500i, SP2500i) equipped with different gratings (150, 600 and 1200 l/mm) and ICCD detectors PI-MAX2, PI-MAX4). The gap region between the electrodes was projected on the spectrometer slit using a mirror system. Slit widths of 30 to 50 µm were used. Exposure times between 100 and 500 µs were required. The opening characteristic of the contact was determined combining a framing camera (Specialized Imaging) and a high-speed camera (Photron Nova S12). Video imaging was carried out using a high-speed camera (Photron Nova S6, S16), partially equipped with metal interference filters (atomic line emission of Ag). The spectral intensity was calibrated using a tungsten-strip lamp. Line calibration was performed using a UVP standard mercury Pen-Ray lamp.

The total current (i_total) was detected with a Yokogawa clamp-on probe (Yokogawa 701931). The by-passed current to the SCR (i_SCR) was detected with a Hioki 3275 clamp-on probe (equivalent to Yokogawa 701931). Space limitations by short wiring prevented the direct measurement of the current through the contacts (i_contacts). This current was therefore determined subtracting i_SCR from i_total (after calibration of both clamp-on probes). The voltage at the contacts was measured using an active-differential voltage probe (Yokogawa PBDH0150). Probe signals were recorded using a digital oscilloscope (Yokogawa DLM3034).

III. Results

A. Characteristics of current, gap opening and arc-voltage

Figure 2 in [18] presents examples of typical voltage and current traces from our experiments. In Figure 2 in this paper, we reproduce a close-up of a hybrid-switching operation of 150 A [19], highlighting the arcing interval. The stages presented in Figure 2 are as follows: (I) current conduction by closed contacts, characterized by a low contact voltage. (II) Initiation of the switching process, characterized by a slight voltage increase as the contact force reduces i.e. contact-resistance increase due to contact displacement. (III) The reduction of the effective contact area leads to a higher current density and building the so-called molten contact-bridge. (IV) The increased current density and elongation lead to the explosion of the molten contact-bridge, which is now optically detected and characterized by a sudden voltage increase. The arc develops by further ionizing the remaining metal vapour of the molten-bridge explosion. The voltage remains at around 12 to 13 V and in our experiments has shown to be characteristic for the used electrode material (Ag/SnO2) and independent of the amplitude of the current (provided the arcing time remains short i.e. the gap remains in the sub-millimetre range). (V) By firing the semiconductor (SCR), the current commutation begins and the voltage drops until reaching the residual voltage-drop at the semiconductor's junction (~ 1 … 2 V), which is too low to further support arcing[1]. At this point, the current commutation is finalized. The next stage (VI) is determined by the used method to finally interrupt the current (turn-off of the semiconductor). This final stage is not considered in this paper.

B. Optical and spectral characteristics of hybrid switching

Former tests indicated the difficulties in observing the arc of small gap-lengths (~ 100 µm) and shorter arcing times (~ 100 µs) by hybrid-switching [18,19]. In addition, the much larger diameter of the contact piece (5 mm) compared to the expected gap length poses difficulties for adequate depth focus at the expected arcing region. High-speed images of a switching operation are shown in Figure 3.

Experiments using OES indicated that detection exposure times of the order 100 µs or longer were required. These are comparable with the maximum expected times for feasible hybrid-switching in real applications and are therefore

[1] This depends on the used semiconductor's technology as well as on the number of semiconductors connected in series when required.

unsuitable for the determination of the intensity decay after arcing using the available OES. Besides, the same reasons prevented the use of optical absorption spectroscopy (OAS) to determine plasma temperature decay as in [20].

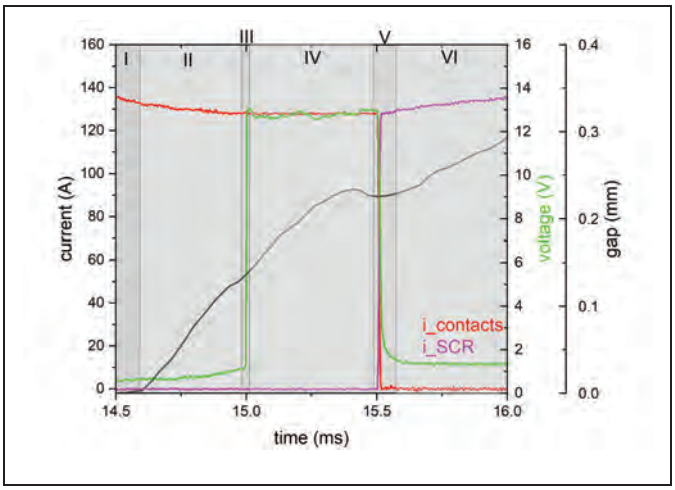


Fig. 2. Close-up of the arcing interval (Figure 2 in {18] showing the defined stages for a hybrid-switching operation in our experiments. The red and magenta lines idicate the currents, the green line the voltage and the black line the gap course, repectively.

Consequently, the measurements of arcing spectra permit only to narrow down the plasma conditions before CZ. Figure 5 in [19] shows the characteristic spectrum during the high current arcing phase exemplarily. The detected line intensities were intense enough and well defined. The lines correspond to atomic and ionic species of Ag and some of Sn (Table I in [19]). For spectra classification, we used the atomic spectroscopy database of NIST [21].

C. Gap conductance behaviour during arcing and post-arc

Owing to the difficulties in applying OES to determine the post-arc characteristics and dielectric recovery of the gap, we modified the experimental setup according to [22] using an additional voltage source to enable the determination of the conductance of the gap (Figure 4).

The DC voltage source allows to superimpose a measurement current (i_residual) of up to 10 mA, which was detected by a 100 Ω shunt. The circuits were decoupled using soft recovery diodes (IR 60EPF10). An additional differential voltage probe (Yokogawa PBDH0150) was used to cover the resulting higher voltage range (up to 1 kV DC) at the contacts. The i_residual is limited by the 100 kΩ resistor so that an eventual re-ignition is avoided. Tests with different currents between 150 and 500 A were carried out.

IV. DISCUSSION

A. Voltage characteristics of hybrid switching arcing for AgSnO2 contacts

Comparable voltages during arcing by static and opening Ag and AgSnOx contacts were found in [23], reporting values under 15 V for static gaps of 50 µm. This value corresponds well with our measurements for gaps of up to 300 µm and currents up to 400 A. Further values reported in [23] for opening contacts (DC currents under 150 A) indicate increasing arcing voltages up to 20 to 25 V by gap lengths around 500 µm in air. Similar low voltage values are reported e.g. by [24], for vacuum arcs by different electrode materials. Values of voltage during arcing by hybrid-switching in [20,25] for copper electrodes and static gaps are of the order of 18 to 20 V (gap = 1 mm) and of 30 to 34 V (gap = 1.6 mm). Currents between 70 A and up to 200 A were considered there. Results in [20,25] are nevertheless not directly comparable with our measurements: In [24], the arc was initiated by breakdown applying a voltage surge. In [25] the arc was first initiated by contact separation until stabilisation using a low-current, prior the injection of the main current. Therefore, for both cases, the metal vapour content in the plasma is expected to be of less importance.

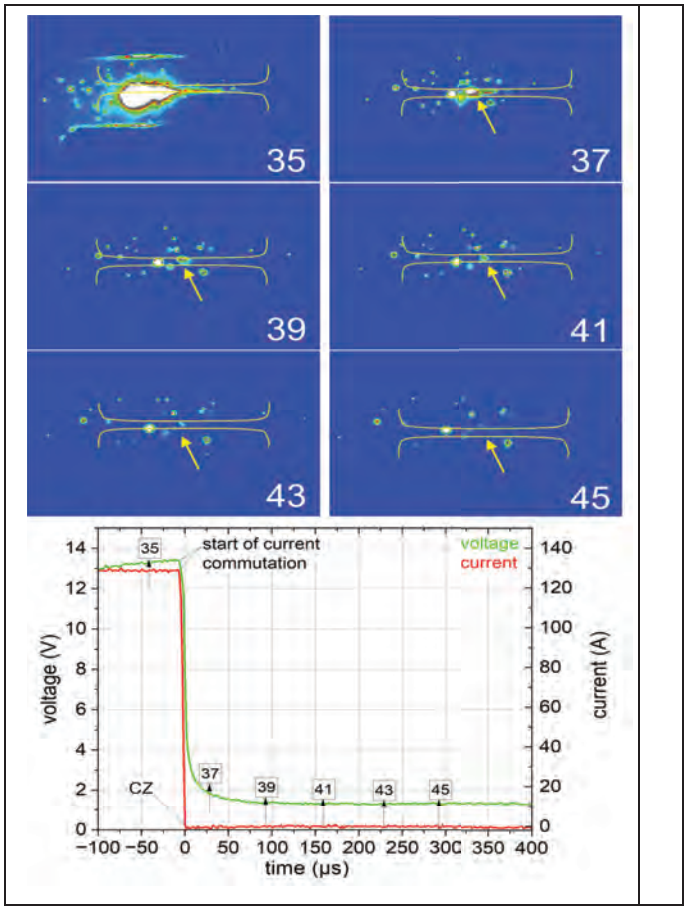


Fig. 3. Composition of high-speed images and current and voltage traces of a hybrid-switching operation at arcing's end (stage V of e.g. Figure 4 by CZ). Exposure time 5 µs/image. The contours of the electrodes are highlited by the yellow lines. The arows point to the region of the former arc.

The obtained results permit us to conclude that hybrid-switching arcing occurs predominantly in the metal vapor of the molten bridge. An important contribution of the surrounding air to the plasma is due to the expected higher pressure in this region not important. The lower voltage value is a further indication of this behaviour since ionization voltages of the involved metals (mainly Ag) are around half that of nitrogen or oxygen as main air components. Furthermore, the pre-mature arc extinction and gap length limitations avoid the formation of a columnar air arc, as reported in [20,25].

B. Plasma temperature and arc characteristics

As mentioned in part IV-B, the results of OES may just be used to estimate the plasma conditions before current commutation. The recorded voltage values and also the acquired spectra (Table 2 in [18]) showing predominantly

silver and tin species, which correspond to the electrode materials (Ag/SnO2), confirm the assumption that the arcing process occurs predominantly in metal vapor from molten-bridge explosion. The high-speed images indicate that the arcing process resembles a spark. A defined geometry cannot be assumed. The relatively long exposure time of the camera images (5 µs) in Figure 3 permits, to observe several metal droplets in the contact region, hot enough to emit detectable radiation and lasting hundredths of µs after arc extinction.

Considering the rather undefined arc geometry, it is not advisable to perform Abel-inversion [26] to obtain the volumetric radiation intensity of the observed lines (i.e. to determine emission coefficients and plasma temperature). Also, after consideration of the energy levels of the selected lines (Ag, Sn) [21], it was concluded that to use the Boltzmann-plot or the 2 lines method [26] was not advisable to determine the plasma temperature since the upper values do not differ sufficiently.

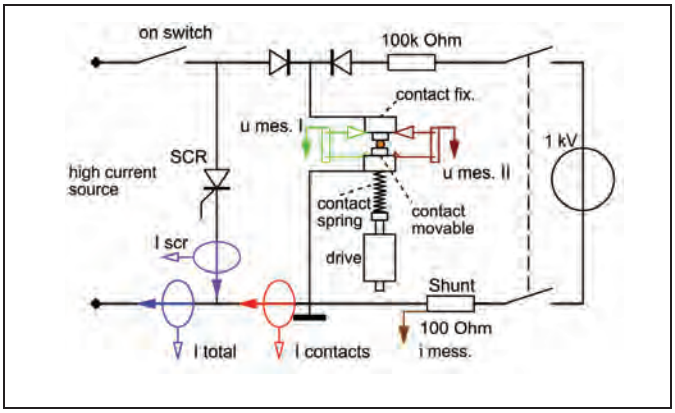


Fig. 4. Schematics of the modified setup (Figure 2) including an additional voltage source for the determination of post-arc conductance (after [22]).

To estimate the plasma temperature, a spectra simulation was used. For that, the Laser Induced Breakdown Spectroscopy – LIBS simulation tool of NIST [27] was applied. The tool permits narrowing down the expected plasma temperature and species density during the high current interval. The calculation method assumes plasma in local thermal equilibrium (LTE). It allows, in addition, to charge experimental obtained spectra to facilitate the comparison and species determination. The fitting criteria to determine plasma composition, electron temperature and particle densities was as follows: 1st. The shape of the simulated spectra shall give the same distribution and dominant species (higher intensities) as in the measurement. 2nd. The peak values of observed species shall correspond (value and proportion among them) to the absolute calibrated spectra (except for actual continuum level). After narrowing down the expected temperature (Te) and density of a pure Ag-Plasma using the observed atomic and ionic lines, the plasma composition was adjusted until intensities and observed lines of the simulation corresponded to the spectra (spectral region: 510 to 560 nm). The results are exemplarily presented in Figure 5.

The best fit was obtained for plasma compositions having 88 to 91 % Ag and 9 to 12 % Sn. The fitting results as well as detected spectra indicate that Oxygen, although bound as an electrode Material, do not appears to play an important role during the arcing process. Same conclusion can be stated for other possible elements coming from the surrounding air (N, H, C) or from impurities over the electrodes (from e.g. manipulation) like Na or S. Contrary to previous approximations in [18,19], the best fit was obtained with a Te = 1.17 eV which by consideration of LTE [26] indicates a mean temperature of about 12 800 K and a ne = 1e16 cm-3. This temperature indicates the initial plasma conditions before the start of the commutation and subsequent post-arc plasma.

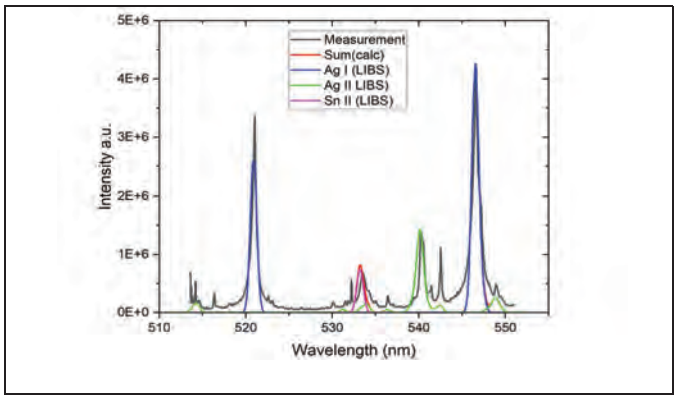


Fig. 5. Comparison of measured spectrum and with LIBS-tool calculated spectrum for a Ag/Sn plasma

C. *Post-arc conductance and dielectric recovery*

To estimate the dielectric recovery behaviour of the gap we followed the works of [22] to measure conductance. Figure 8 in [19] shows an example of the measured courses of currents (i_contacts, i_residual, i_SCR) and voltage used for the determination of the gap resistance (Figure 9 in [19]).

In order to determine the decay of the post-arc conductivity and gas temperature, we combined the values of voltage, current (i_contacts + i_residual) and the images of the high-speed camera. The used method considers the arcing plasma and post-arc gas to perform like a linear cylindrical resistor. To determine its geometry (and therefore to extract the conductivity) we used the determined gap-length over time and the value of full width to half maximum (FWHM [26]) of light intensity in the gap region obtained from the high-speed images (e.g. in Figure 3) as equivalent mean diameter. The results of obtained conductivity decay from several measurements with hybrid switched currents between 150 A and 400 A and 500 µs arcing time are presented in Figure 9.

To estimate the temperature of the post-arc gas, we used computed values of conductivity for a pure Ag-plasma (1 bar pressure) as a function of temperature [28]. As shown in Figure 6, the estimated conductivity during arcing corresponds to a mean Ag-plasma temperature of ~ 12 000 K (150 A to 400 A) and fits well with the estimated mean temperature value from spectroscopy of 12 800 K (Section V-B). Moreover, Figure 6 indicates that the plasma gas temperature decays from ~ 12 000 K to ~ 3000 K in about 9 µs, which corresponds to the experimentally observed order of the commutation time. This temperature value increases later slightly (lower than 100 K in figure 6), which is probably a consequence of the artificially injected current (i_residual = 2mA), increasing the collision rate. Then, the temperature decays further down to ~ 2000 K during the next 450 µs. Although no available values for temperature decay for small gap arcs in pure Ag-plasma were available in the consulted literature, it is possible to assume that the continued diffusion of the post-arc gas and the continuously increasing gap length lead to similar conditions for thermal

or dielectric re-ignition as in air-arcs. According to [29], the border between these is of around 3000 K (air, 1 bar). This limit is reached in our experiments already at the end of the commutation time. Therefore, from this point, an eventual reignition may be assumed as of a dielectric nature and governed by Paschen's law. Using experimental results of [30] for dielectric recovery by N2 arcs (400 A) between Cu-electrodes and assuming similar behaviour for low pressure arcs and hybrid switching short arcs, we estimate for a gap around ~ 300 µm after 500 µs a Paschen p·d-value of ~ 0.3 bar mm, which would correspond to Figure 6a in [30] by a recovery voltage around 500 V during the first 100 µs after CZ.

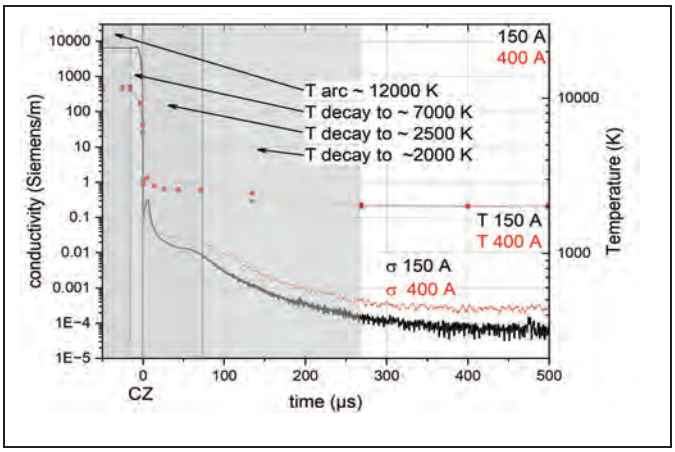


Fig. 6. Determined conductivity and estimated gas temperature by arcing and during post-arc after hybrid-switching. Axis left and continued lines: conductivity. Axis right, continued lines with bullet point: Temperature.

The last result permits us to explain the arc-reigniting behaviour observed during our experiments when using voltages for the i_residual source higher than ~ 400 V. In such cases, the resulting higher measurement current (i_residual) led to a shift of the dielectric recovery border by ionizing the post-arc gas. This behaviour is shown in Figure 7. Notice that for higher source-voltage, the post-arc gas temperature increases several times, leading to "re-strikes" (voltage drops), which under real conditions would mean an arc re-ignition i.e. failed interruption.

The results of the experiments increasing the voltage of the measurement current source were used to estimate the required gap to full recovery as a function of an equivalent recovery voltage. Figure 8 indicates the important role of the superimposed voltage after current commutation on the capability of the gap to dielectrically recover. As expected, higher superimposed voltages require a larger gap to avoid arc re-ignition. This is coupled to the defined arcing time, since during arcing, the gap increases further. The tendency appears to vary linearly with the applied voltage i.e. the magnitude of the supplied i_residual is minimal. Considering that the opening characteristic is different for each circuit breaker type, the results of Figure 8 cannot be directly extended to real applications. Nevertheless, they indicate the required order of magnitude.

V. Conclusions

The recovery behaviour of hybrid-switching gaps was studied using a model switch and applying different diagnostics.

Hybrid-switching times of up to several 100 µs and currents of up to 400 A were considered. The used drive for contact opening permitted to reach gaps of the order of some 100 µm.

Spectroscopy analysis of the high-current period indicates arcing in almost pure Ag-vapour. A mean plasma temperature value of ~ 12 800 K was estimated using a spectra-simulation tool.

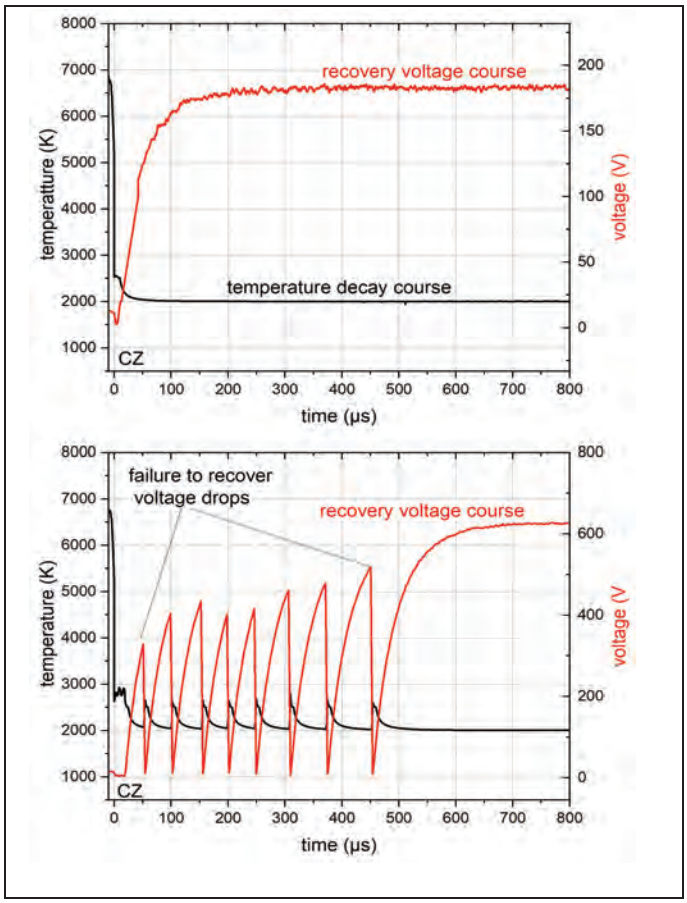


Fig. 7. Comparison of voltage recovery behaviour for hybrid switching gaps depending on the voltage of the measurement current (i_residual). Top: 300 A arc, 200 V for i_residual driving voltage. Bottom: 300 A arc, 650 V for i_residual driving voltage.

The estimation of the gas temperature decay during post-arc was realized indirectly through the determination of the conductance using an additional voltage source, which superimposes a low current through the gap after current commutation. The results indicate that at least for hybrid-switching with opening contacts and distances under ~ 500 µm, the used superimposed measurement current shall be rather low (<4 mA) to avoid further post-arc gas ionization and a re-igniting behaviour.

The results indicate that the plasma temperature decays very quickly, going from ~ 12 000 K to ~ 3 000 K already within the ~ 10 µs of current commutation (determined by the circuit). After that, the temperature decay is rather slow, taking several hundredths of µs for it to sink down to ~ 2000 K.

ACKNOWLEDGMENT

D. Gonzalez thanks the former "German Ministry for Economic Affairs and Climate Action- BMWK" for funding the Project "AutoHybridS" No. 03EI6006D and all the

colleagues of the participant companies. Ms. L. Gonzalez thanks the Leibniz Institute for Plasm Science and Technology for allowing her to carry out an internship during 2024.

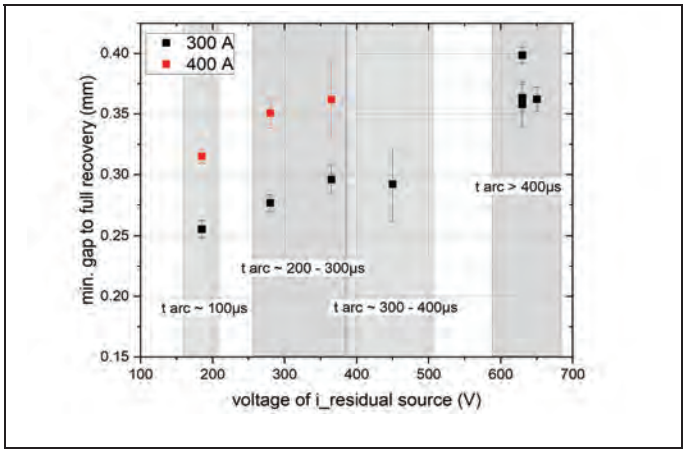


Fig. 8. Minimum estimated gap to full recovery depending on the used voltage for the i_residual (see fig. 6) for hybrid switching arcs of 300 A and 400 A

Supported by:
Federal Ministry for Economic Affairs and Climate Action
on the basis of a decision by the German Bundestag

Supported by:
Federal Ministry for Economic Affairs and Energy
on the basis of a decision by the German Bundestag

REFERENCES

[1] H. Koepf, P. Stegmueller, A. Labs, and S. Holbe, "Hybrid switching concepts – Advantages and disadvantages", in Proc. 27th Albert-Keil-Kontaktseminar, pp. 13-21, September 2023.

[2] I.C. Kizilyali, Z.J. Shen, D. W. Cunningham (Editors), Direct Current Fault Protection, ISBN 978-3-031-26572-3, Springer 2023.

[3] D. Bösche, Investigation on the residual arc conductance in the mechanical part of hybrid circuit breakers before and after current commutation, dissertation TU Brunswick, 2022.

[4] A. R. Figuereido Bento, F. Bento, A. J. Marques Cardoso, "A review on hybrid circuit breakers for DC applications", IEEE open jour. Ind. Electr. Soc. vol. 4, pp. 432-450, DOI: 10.1109/OJIES.2023.3320900.

[5] W. Hauer, M. Bartonek, H. Stammberger, "New switching Technology for DC grids", in Proceedings of Int. Conf. on Elec. Contacts – ICEC 2020/21 Sankt Galler/on-line, pp. 149-156, 2021

[6] Z. Jiang, C. Guo, C. Ye, Y. Ding, X. Tang, and Y. Fang, "Design and implementation of an auto-oriented bidirectional ZCS hybrid circuit breaker", pp. 152421-152429, vol. 9, 2021, IEEE Access, DOI: 10.1109/ACCESS.2021.3126313

[7] S. J. Kjelling Berg, Solid state circuit breakers in medium voltage direct current systems. MSc. Thesis, Norwegian University of Science and Technology- NTNU, June 2018.

[8] J-M. Meyer, A. Rufer, "A DC hybrid circuit breaker with ultra-fast contact opening and integrated Gate-Commutated Thyristors (IGCTs), IEEE Trans. on Power Delivery, Vol. 21, No. 2, pp. 646-651, April 2006.

[9] X. Zhou, "Technology innovation and evolution in circuit protection", in Proc. of the IEEE Holm 2023, pp. 38-51, Oct. 2023, Seattle, Washington, USA.

[10] Y. Wu, Y. Xiao, Y. Wu, M. Rong, F. Yang, "Hybrid MVDC circuit breaker based on enhanced arc voltage of vacuum interrupter", IEEE Trans. Ind. Electronics, Vol. 69, No. 5, pp. 4776-4785, May 2022.

[11] Y. Wu, Y. Wu, M. Rong, F. Yang, "Development of a novel HVDC circuit breaker combining liquid metal load commutation switch and two-stage commutation coil", IEEE Trans. Ind. Electronics, Vol. 66, No. 8, pp. 6055-6064, August 2016.

[12] C.N. Muhammed Ajmal, I. Venkata Raghavendra, S. Naik, and H. S. Krishnamoorthy, "A modified hybrid DC circuit breaker with reduced arc for low voltage DC grids", IEEE Access, Vol. 9, 2021, pp. 132267-132277, DOI: 10.1109/ACCESS.2021.3115456

[13] X. Song, C. Peng, A. Q. Huang, "A medium-voltage hybrid DC circuit breaker, Part I: Solid-state main breaker based on 15 kV SiC emitter turn-off Thyristor". IEEE Journal of Emerging and Selected Topics in Power Electronics, Vol. 5, No. 1, pp. 278-288, March 2017.

[14] X. Song, C. Peng, A. Q. Huang, "A medium-voltage hybrid DC circuit breaker, Part II: Ultrafast mechanical switch". IEEE Journal of Emerging and Selected Topics in Power Electronics, Vol. 5, No. 1, pp. 289-296, March 2017.

[15] L. Novello, F. Baldo, A. Ferro, A. Maistrello and E. Gaio, "Development and testing of a 10 kA hybrid mechanical-static DC circuit breaker", IEEE Trans. Appl. Superconductivity, Vol. 21, No. 6, pp. 3621-3627, Dec. 2011.

[16] L. Liu, J. Zhuang, C. Wang, Z. Jiang, J. Wu and B. Chen, "A hybrid DC vacuum circuit breaker for medium voltage: Principle and first measurements", IEEE Trans. Power Delivery, Vol. 30, No. 5, pp. 2096-2101, Oct. 2015.

[17] R. Lazzari, L. Piegari, "Design and Implementation of LVDC Hybrid Circuit Breaker", IEEE Trans. Power Electronics, Vol. No. 8, pp. 7369-7380, Aug. 2019, DOI: 10.1109/TPEL.2018.2878655

[18] D. Gonzalez, R. Methling, S. Gortschakow, H. Koepf, P. Steegmueller, and S. Holbe, "Investigation of the Plasma of a DC hybrid-switch model at beginning of contact separation", in proc. of 67th IEEE Holm, pp. 206-211, Oct. 2022, Tampa, Fl, USA.

[19] D. Gonzalez, R. Methling, S. Gortschakow, H. Koepf, P. Steegmueller, and S. Holbe, "Characterization of arc plasma during hybrid-switching using a DC-Hybrid model switch", in proc. of 68th IEEE Holm, pp. 246-251, Oct. 2023, Seattle, WA, USA.

[20] R. Methling, et al., "optical investigation of a spark gap for DC protection around current zero", in Plas. Phys. and Technology, vol. 10, nr. 3, pp. 154-158, 2023. DOI: 10.14311/ppt.2023.3.154

[21] A. Kramida, Y. Ralchenko, J. Reader, and NIST ASD Team, "NIST atomic spectra database," version 5.9. URL: physics.nist.gov/asd.

[22] D. Bösche, P. Vieth, F. Anspach, E. Peters, E-D. Wilkening, and M. Kurrat, "Test Setup Design for Measuring the Conductance in the Mechanical Part of Hybrid-Circuit-Breakers Before and After Current Commutation", IEEE Access, Vol. 9, pp. 155262-165270, 2021. DOI: 10.1109/ACCESS.2021.3135138

[23] T. Klonowski, R. Andlauer, T. Leblanc, F. Faure, R. Meyer, and Ph. Teste, "Experimental study of the consequences of molten bridge phenomena on power contacs", in Proceedings of the 23rd Int. Conf. on Elec. Contacts - ICEC 2006, pp. 510-515, June 2006, Sendai, JP.

[24] K. Tsuruta, M. Nakajima, and T. Yanagidaira, "Experimetal characterization of vacuum arc instabilities for different electrode metals", IEEE Trans. Plasma Sci., Vol. 31, no. 5, pp. 953-957, Oct. 2003.

[25] D. Bösche, "Investigation on the residual arc conductance in the mechanical part of hybrid-circuit-breakers before and aftere current commutation", Dissertation TU Brunswick, 2024.

[26] W. Lochte-Holtgreven, "Plasma diagnostics", Nort-Holland Pub. Co., 1968.

[27] A. Kramida, K. Olsen, and Yu. Ralchenko, "NIST LIBS Database", https://physics.nist.gov/PhysRefData/ASD/LIBS/libs-form.html

[28] E-T-A Eletrotechische Apparate GmbH, Dehn SE, Technische Universität Ilmenau, Leibniz Insitute for Plasma Science and Technology (INP), and PTB Braunschweig, „Verbundvorhaben AutoHybridS – Autonom gesteruerter hybridschalter mit effizienter wiederverfestigungsdetektion". Abschlussbericht BMWK Förderkennzeichnen- 03EI6006 A – E, 2019-2023, pp. 82, 2024. https://www.tib.eu/de/suchen/id/TIBKAT:1925509745/Verbundvorhaben-AutoHybridS-Autonom-gesteuerter?cHash=2322cefc788feb0c66d1a33aa6672ae5

[29] W. Rieder, „Plasma und Lichtbogen", Friedr. Vieweg & Sohn, Brauschweig, Germay, 1967, pp. 125-126.

[30] G. A. , Farral, and J. D. Cobine, "Recovery strengh measurements in arcs from atmospheric pressure to vacuum", IEEE Trans. on Power Apparatus and Systems, Vol. Pas. S6, No. 8, pp. 927-932, 1967.

LPBF-based, additively manufactured contact ring segments for closed-form coil stators

Alexander Vogel
Institute for Factory Automation and Production Systems
Friedrich-Alexander-University Erlangen-Nuremberg
Nuremberg, Germany
alexander.vogel@faps.fau.de

Felix Wirthmann
Institute for Factory Automation and Production Systems
Friedrich-Alexander-University Erlangen-Nuremberg
Nuremberg, Germany
felix.wirthmann@faps.fau.de

Muhammed Kilic
Institute for Factory Automation and Production Systems
Friedrich-Alexander-University Erlangen-Nuremberg
Nuremberg, Germany
muhammed.kilic@fau.de

Thorsten Ihne
Institute for Factory Automation and Production Systems
Friedrich-Alexander-University Erlangen-Nuremberg
Nuremberg, Germany
thorsten.ihne@faps.fau.de

Jörg Franke
Institute for Factory Automation and Production Systems
Friedrich-Alexander-University Erlangen-Nuremberg
Nuremberg, Germany
joerg.franke@faps.fau.de

Florian Risch
Institute for Factory Automation and Production Systems
Friedrich-Alexander-University Erlangen-Nuremberg
Nuremberg, Germany
florian.risch@faps.fau.de

***Abstract*—The stator is the most expensive motor component and thus a prime target for automation, yet steps like insulation assembly and contacting remain largely manual due to the challenge of flexible, and mostly limp wire ends, which can be handled with great effort or by expensive machines or robots at high volumes. In compact, highly power-dense drives that do not use hairpin technology, the coil contacting process must be redesigned to overcome manual operations. A promising approach is to replace manual handling with a contact ring combined with laser-assisted contacting to reduce complexity. The goal is a low-resistance, electrically conductive joint with high mechanical stability. Building on an existing concept, this work introduces an additively manufactured contact ring and precise laser welding.**

Keywords— stator production, stator manufacturing, electric drives production, contact elements, contact ring, busbar

I. INTRODUCTION

To meet climate goals, electric drives must be cost-competitive across road, rail, air, and marine uses. Stator designs often raise copper fill factor by replacing round windings with rectangular or flat wires. Hairpin technology, or also closed-form coil windings achieve those targets and offers several advantages, but also challenges during assembly. The process for manufacturing flat wire stators with open and closed form coils differs primarily in the shaping and assembly of the winding, as already demonstrated in [1] and [2] before. While Hairpin stators are mostly contacted directly by using laser welding, shown in [3], wound stators or stators, based on closed-form coil technology, need additional geometries and actions for sufficient phase-contacting. With this scientific contribution, the Institute for Factory Automation and Production Systems (FAPS) from Friedrich-Alexander-Universität Erlangen Nürnberg (FAU) addresses an alternative contact ring design, as well as an alternative procedure for its manufacturing.

II. STATE OF THE ART OF TRACTION DRIVES

A. Stator topologies

Hairpin technology has largely replaced wound stators in traction drives, as it offers particular advantages from a manufacturing perspective. It combines a high degree of automation with relatively low unit costs and high output, which is especially desirable in the automotive manufacturing sector. While this technology appears ideal for automotive applications, it cannot be considered a viable alternative for other applications or industries. The main factor here is the voltage class of the drive. For example, significantly higher operating voltages are required in railway technology, which means that the insulation system used in hairpins is overwhelmed. In order to meet these requirements, the railway industry relies on closed molded coils, which, however, involve significantly higher technical effort in terms of contacting and cannot be easily used with automated processes such as laser welding, without changing the geometry of the contact spots.

B. Common stator contacting

Modern traction motors have 100–250 connection points, making reliable contacting critical, as a single fault can cause failure of the motor. Connections must ensure high conductivity, low resistance, defect-free surfaces, and sufficient mechanical and fatigue strength to withstand thermal, electromagnetic, and vibrational stresses. While conventional mechanical contacting methods lack the quality, stability, and automation needed for mass production, joining processes like laser welding require precise, short-duration, and high-energy input to minimize heat impact.

For laser welding, the stator is first clamped on a rotary fixture in the welding cell. The wire ends of the stator are melted due to the energy input by the laser beam. This leads to a metallurgical bond in the contacting zone, while shielding gas, typically pure argon, prevents oxidation at the joint. [4, 5]

III. CONTACT RINGS AS INNOVATIONS

A. Topology of a contact ring

The electrification of the mobility sector and the rising demand for electric drive systems necessitate ongoing innovation in electric motor manufacturing, particularly with the integration of contact rings. These circular components are essential for connecting and organizing stators and offer opportunities to optimize manufacturing processes. Contact rings not only connect the wire ends of stator coils but also serve multiple functions due to their intricate, stator-specific designs.

The results, published in this publication, are based on a research project named "E|Form – Dreistufig automatisiertes Endformen von Flachleiterspulen im Blechpaket", FKZ 01MV23011C, funded by the German Federal Ministry for Economic Affairs and Climate Action (BMWK) and managed by the German Aerospace Center (DLR).

B. *Functionality of a contact ring*

Contact rings are components in electric motor manufacturing that are usually designed in a circular shape and matched to the respective stator. They consist of copper rails and various support components. The copper rails are responsible for conductively connecting the associated form coils of the stator. Each of these copper rails consists of a connecting element and at least two contact elements, as shown in Fig. 1 [6].

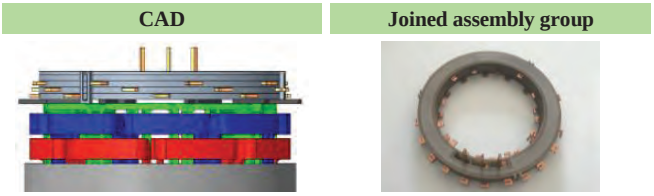


Fig. 1. Welding-ready contact ring

C. *The contact ring as a product*

In hairpin traction motors, prefabricated contact rings act as ring-shaped busbars linking the stator winding to inverter phases, consolidating winding ends for standardized, automation-ready stator wiring. Their large, flat contact areas reduce resistance and improve reliability, especially with a three-sided encasing connector that enlarges the interface and outperforms soldered or pressed joints, enabling robust, precise electrical connections. High currents cause significant heating at contacts and in conductors, requiring a careful material selection and a cooling concept to prevent hot spots. Space at the winding head is tight, contact rings must align with wires precisely while staying insulated from the lamination and other phases, which is mainly done by insulating components that add additional complexity for manufacturing and assembling.

Fig. 2 shows, on the one hand, an exploded view of a contact ring and, on the other hand, a fully welded flat wire stator. The copper conductor elements are shown in orange, and the PEEK-printed support elements are shown in gray.

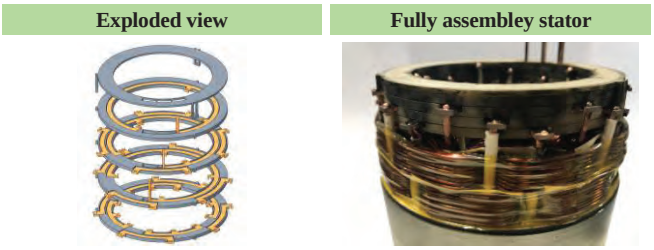


Fig. 2. Exploded and assembled a contact ring

D. *Production of a contact ring*

Contact rings significantly enhance the automation of traction motor manufacturing. Their motor-specific geometries and defined contact points eliminate the need for manual coil handling, making them suitable for robot-assisted processing. This improves efficiency, quality, and reduces human error. Predefined contact points also streamline the joining process, saving time and lowering labor costs. Their design allows for pre-assembly and reliable automatic attachment to the winding head of the stator's connection side, facilitating integration into automated assembly lines. Besides the advantages, contact rings add material, pre-manufacturing requirements, assembly steps, and costs to the final product. More contact points also raise failure risk and inspection needs. Thermal expansion demands careful design and specific materials.

This makes it all the more important to conduct an in-depth investigation into the suitability of alternative processes, such as additive-manufactured contact elements, to make the manufacture and use of contact rings more attractive and to make the challenges described above manageable.

IV. Overview of Different Contact Element Topologies

A. *U-shaped contact structure*

The geometry and connection technology are based on the use of a U-shaped contact structure to connect the copper rails to the molded coil ends. The contact width of the U-shape is deliberately wider than the ends of the molded coils to enable smooth attachment of a contact ring. In addition, the contact surfaces shown in Fig. 3 have been precisely dimensioned to ensure complete contact with all three surfaces of the coil ends while maintaining the required conductor cross-sectional area, thereby ensuring maximum conductivity.

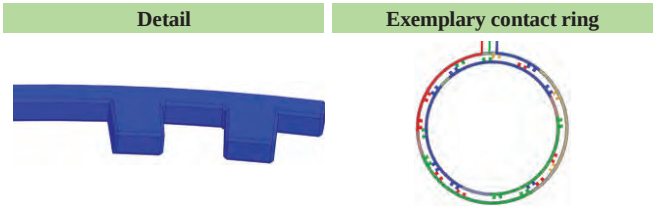


Fig. 3. Detailed view of the U-shaped connection geometry

B. *THT-based structure*

Another geometric approach is based on a proven approach to power semiconductor integration that focuses on the use of through-hole technology, or THT for short. This approach aims to optimize contact integration and system performance by pursuing a comprehensive design strategy that takes electrical, mechanical, and structural aspects into account. As shown in Fig. 4, the contact elements are equipped with rectangular through holes. This allows the ends of the wires to be threaded directly and welded from above. Furthermore, this contour enables automated detection by camera optics, both for position finding during assembly and during welding.

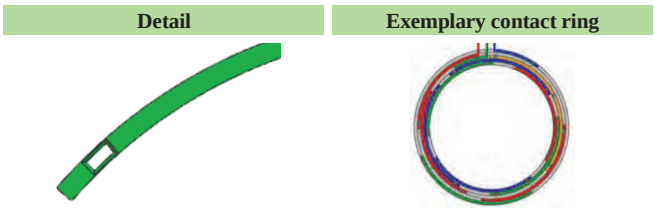


Fig. 4. Detailed view of the THT-based connection geometry

The contact ring design uses an architecture with all copper rails being located on a single level, enabling one-step assembly. High-performance epoxy resin strengthens the contact ring-stator bond, and a wide-geometry fastening scheme allows direct mounting of molded coils.

C. *V-shaped contact structure*

This design places particular emphasis on optimizing the contact geometry in order to further improve the electrical connection technology. A key design feature, shown in Fig. 5, is the V-shaped geometric configuration of the contact points,

which are positioned below the copper rails. The engineered design of the contact points minimizes the connection gap between the mold coil end and the contact geometry and creates an open, flattened chamfer. This geometry results in a significantly increased capillary filling pressure, which in turn improves the quality of the brazing connection and ensures reliable current flow.

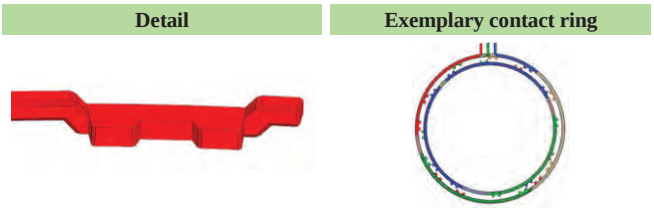


Fig. 5. Detailed view of the V-shaped connection geometry

In addition to the optimized contact geometry, it also relies on proven materials and design principles. The individual layers of the contact ring are mounted on the molded coil ends using T-joint connection technology and brazing to create a material bond. To ensure mechanical stability, the stator serves as the supporting structure for the contact ring. In addition, structural integrity is increased by bandaging.

D. Directly linked by wire

This variant represents an innovative approach to optimizing winding connection technology in electrical machines. The focus here is on a tab contact geometry with specific features. The geometric characteristics include rectangular, curved conductor rails positioned below the stator. One of these tab connections is shown in Fig. 6.

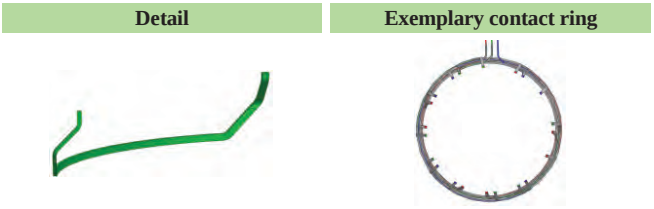


Fig. 6. Detailed view of the directly linked connection geometry

Manufacturing this solution requires consideration of critical conditions, such as limiting the maximum copper wire bend to 60 degrees to avoid plastic deformation that could impair conductivity. This geometry enables the use of a parallel welded joint, while the long tabs ensure a maintained cross-section for safe current transmission. A flexible sleeve insulation is applied over the individual coil group, star-connector, and phase-connector to insulate and protect them from external environmental influences.

V. MANUFACTURING OF CONTACT RING SEGMENTS

A. Support elements

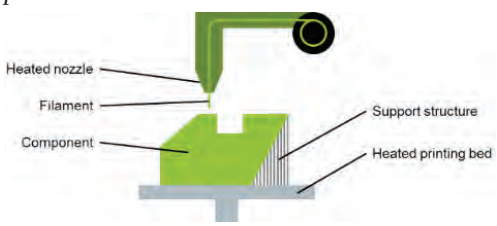


Fig. 7. FDM, based on [7]

A contact ring usually consists of conductive, insulating, and supporting components. The former are responsible for connecting coil groups of a phase. The insulators, on the other hand, are designed to provide mechanical stability and protection against environmental influences in addition to their insulating effect. Their geometry has a significant influence on the appearance and, thus, on the accessibility of the connection points. Most support elements consist of electrically isolating plastic material. For small quantities, most injection molding processes are too expensive, and fused deposition modeling, or FDM for short, is commonly used. It is an additive manufacturing process in which a component is built up from several layers of melted plastic. This process uses mainly thermoplastics such as ABS, PC, or PET. Fig. 7 shows a schematic representation of FDM. The material is fed in filament or rod form from a reservoir to the nozzle of the printer. There, the filament is melted and applied to the usually heated print bed through a hot end and the nozzle according to the specified CAD model. The nozzle heats the filament to just above the melting temperature. This causes the material to solidify quickly on the print bed, allowing further layers to be applied to the solidified plastic. [7, 8]

B. Massive contact elements

As already shown in [6], spark erosion can meet the process requirements for producing the copper rails. Based on electrical discharge machining (EDM), this technology uses a moving wire to create a kerf without touching the workpiece. Material is removed by generating an electrical charge between the wire and the conductive component. When the dielectric strength is exceeded, sparks form, generating heat that melts the workpiece material, which then vaporizes or splashes out of the kerf. [9]

Even though EDM has already proven to be a good option for manufacturing contact elements, its subtractive approach is still relatively inefficient, as a flat semi-finished product must always be used for the typically curved or round contours, leaving a large amount of waste material behind. This is where the present work comes in, demonstrating an alternative, additive manufacturing method that does not result in a significant amount of waste from the incoming semi-finished product.

C. Additive-manufactured contact elements

1) Laser Powder Bed Fusion (LPBF)

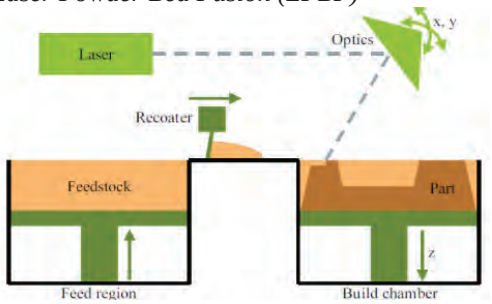


Fig. 8. LPBF, based on [10]

LPBF fully melts metal powder with a laser, fusing particles in a melt pool. It delivers near-theoretical density, tensile strengths comparable or superior to conventional methods, a finer, more homogeneous microstructure than other techniques with fewer pores, and higher powder utilization. However, support structures may be required. [11]

Layer thicknesses between 10 µm and 50 µm at a printing speed of 50 mm/s to 250 mm/s are possible with most common LPBF systems. The basic design of the systems is

shown in Fig. 8 above. The decisive factors for component quality are the laser power, scanning speed, track width spacing, layer thickness, focus position relative to the component, and the scanning strategy. [11, 12]

2) Selective electron beam melting (EBM)

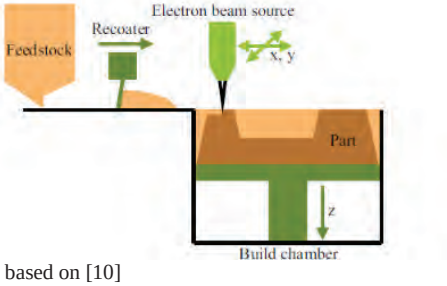


Fig. 9. EBM, based on [10]

Unlike the LPBF described above, energy is not introduced using a laser, but rather a directed electron beam. The metal powder is supplied as shown in Fig. 9 below. In high vacuum, electrons emitted from a cathode are accelerated and focused by electromagnetic coils. Their kinetic energy melts the powder upon impact. The high energy density enables coarser powders, thicker layers, and higher build rates, but demands strong thermal insulation. [11]

3) Technology comparison

Based on a previously conducted and significantly more comprehensive analytical review of all methods available on the market in [13], this application-oriented study focused solely on the two relevant methods, LPBF and EBM. [13] show that many additive manufacturing technologies are capable of producing copper parts with an electrical conductivity close to 100% International Annealed Copper Standard (IACS), which is defined as the conductivity of pure copper at 58,0 MS/m [14]. Nevertheless, LPBF and EBM were rated as most suitable thanks to the resulting material properties and the fact that no additional substrate is required, which enables the contact ring to fulfill all electrical and mechanical requirements. Ultimately, the LPBF process was chosen because its process control is much more robust and easier to manage than that of EBM. Furthermore, unlike EBM, no vacuum is required is a significant advantage of this technology, combined with a lower machine investment. In addition, the technology can be applied to a wider range of products, thus ensuring the transferability of the findings.

VI. Experimental Setup

A. Geometries of the investigated contact elements

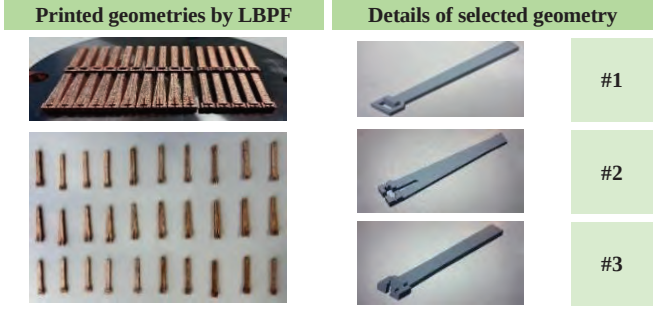


Fig. 10. Investigated THT-based contact elements

In publication [15], a large number of advantageous contact geometries have been identified already. The variant described as THT technology in particular promises a high degree of automation when considering the joining process of contact elements and wire ends, since the geometry also allows for positioning of the winding ends for downstream contacting. The variant shown in [6], with C-shaped contacts, has only been able to automate this step at great expense. Three THT-variants, shown in Fig. 10, were examined further for suitability.

B. Additively LPBF-manufacturing

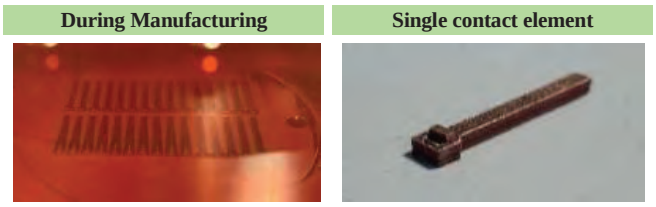


Fig. 11. Additively manufactured contact elements

An Aconity Mini system was used to produce the test specimens, as demonstrated in Fig. 11. This system is equipped with a TruDisk 1020 disk laser, which focuses green laser light with a wavelength of 515 nm and a power of up to 1 kW onto a focal diameter of approximately 220 µm. A resistive high-temperature preheater heats the metal build plate to 800 °C and is controlled by thermocouples placed below. To prevent oxidation, the process chamber is flushed with nitrogen, maintaining an oxygen content of less than 100 ppm. The used printing paramters are shown below in TABLE I.

TABLE I. Parameter set for printing of contact elements

Parameter	Value	Unit
Laser power	800	W
Scanning speed	300	mm/s
Focus diameter	220	µm
Rotation between layers	90	°
Hatch-distance	100	µm
Layer thickness	30	µm

C. Wire-stripping

Reliable copper wire welds require removing the wire insulation. While lasers can strip insulation during welding, the high energy and vaporization pressures often cause severe spatter, risking damage to parts, tools, and surroundings. Therefore, insulation is typically stripped in a separate upstream step before laser welding. Due to process fluctuations during thermal stripping and the environmental impact of chemicals, mechanical brush stripping, shown in Fig. 12, was used, where two brushing rolls remove the enamel of the wire.

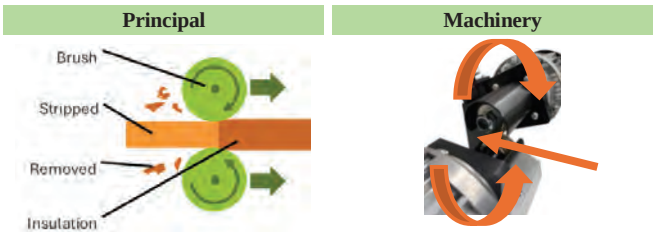


Fig. 12. Mechanical stripping by BTM-V2

D. Laser-welding

For the experiments, a TruDisk 8001 laser was used. A wire cut to length was inserted into the contact element and positioned and fixed below the laser optic. Fig. 13 demonstrates the described arrangement, as well as a fully

welded assembly group of a wire and a contact element. To perform the tests, several welding parameter sets were examined, and finally, a laser power of 7.5 kW, a feed rate of 1000 mm/s, and a BrightLine-Weld percentage of 50 % were used, which means that half of the 7.5 kW was applied to the direct welding zone, while the other half was applied to the surroundings to create a stable keyhole.

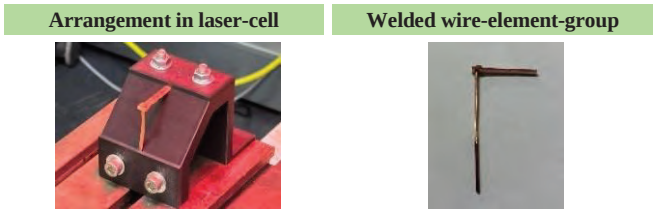


Fig. 13. Welding arrangement and fully contacted wire-element-group

VII. Results and Result Discussion

A. Benchmarking geometry

To be able to compare and evaluate the technical quality of the investigated LPBF-joins later, a brief, validated, and comparable topology is required. Therefore, in a further investigation [6], a contact ring was fully developed and assembled. Fig. 14 shows the mentions topology in detail, as well as assembled with the test-stator.



Fig. 14. Developed use-case in full assembly [6]

B. Investigation of the specimen after welding

1) Electrical testing

The electrical measurement was conducted using a Keithley 6221/2181A four-wire measurement setup to determine the resistance of the joint, as demonstrated in Fig. 15. It was operated in delta mode to ensure high-precision, low-noise DC-resistance determination. This test setup eliminates the electrical conductor resistance of the cables and devices used in the measurement setup. Although their resistance is very low, with expected measurement values close to zero, even these expected conductor resistances make a difference. Due to the high precision requirements, the measurement was performed under optimized and constant environmental conditions with regard to temperature and humidity.

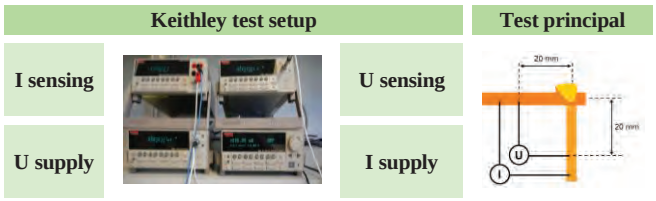


Fig. 15. Illustration of Keithley four-wire-measurment test setup

The results of the four-wire measurement for all three investigated geometries are summarized in TABLE II. Fig. 16 compares those values with the values obtained in the preliminary tests for the setup from [6]. In order to enable comparison, the samples from [6] were brought to the same length as wire-element-groups 1, 2, and 3, and measured with the same test setup again.

The value of 189.012 µΩ determined during the resistance measurements of geometry two must be interpreted as a product error, as it deviates significantly from all other values in its measurement series. Therefore, a new measurement series without this test specimen was generated within the measurement series for geometry two, the values of which are marked with an asterisk.

TABLE II. Resistance Values for the Specimen

Geometry	Min	Median	Mean	Max	Unit
1	127,746	141,322	141,406	157,664	µΩ
2	109,346	126,633	130,259	189,012	
2*	109,346	126,398	124,918	135,423	
3	122,808	135,606	141,439	178,687	
HOLM	113,564	131,370	130,221	143,008	

Depending on the selected connection geometry, it should be noted that the resistance values are minimally above (geometry one and three) or even below (geometry two) the comparative geometry, based on solid copper elements. This is mainly due to air pockets, unclean stripping beforehand, or a minimal gap between the contact element and the wire during welding. In any case, welding the wires with additively manufactured contact elements delivers resistance values that are very similar to those of a comparable geometry with solid copper contact elements, which proves the technology as stable and competitive.

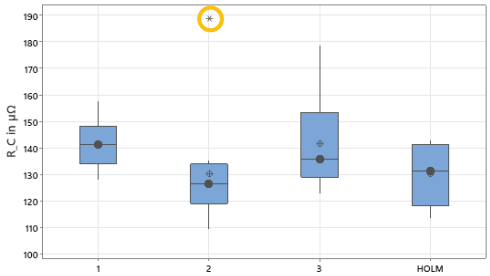


Fig. 16. Boxplot of the detected resistances

2) Mechanical testing

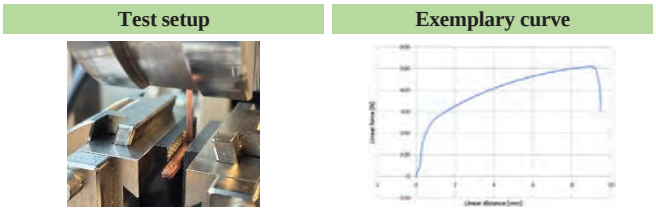


Fig. 17. Test setup and exemplary recorded force-displacement-curve

In order to evaluate not only the electrical conductivity but also the mechanical strength of the welded joint, a tensile test is required. First, the sample is clamped into the testing machine using a suitable clamping device. The machine pulls the wire linearly apart at a constant speed in accordance with the standard. The force and the displacement are recorded continuously. The sample first deforms elastically, then plastically. Once the tensile strength is reached, the measured stress drops, and the sample is finally pulled apart completely. Fig. 17 demonstrates des test-setup as well as an exemplary force-displacement curve.

The welding defect described above is also evident in the mechanical tests, as shown in TABLE III. This value within the geometry two measurement series deviates significantly from the recorded values in the series and was therefore not considered further, and the series, marked with an asterisk, was re-evaluated.

TABLE III. TENSILE FORCES FOR THE SPECIMEN

Geometry	Min	Median	Mean	Max	Unit
1	352,939	467,955	464,788	528,291	N
2	158,127	437,608	421,714	537,029	
2*	365,954	438,919	451,002	537,029	
3	382,891	489,379	480,255	554,141	
HOLM	134,285	262,397	274,050	404,276	

The recorded data are shown in Fig. 18. as a boxplot. Compared to the reference geometry from [6], all bent geometries exhibit higher mechanical stiffness. However, the reference geometry was welded more than a year ago and has been stored under atmospheric conditions since then.

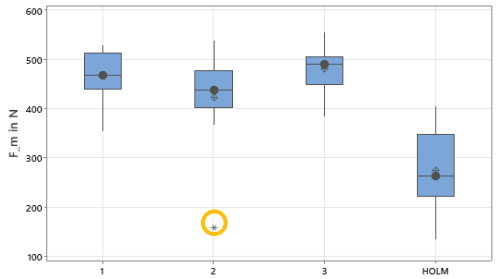


Fig. 18. Boxplot of recorded tensile force during linear pull-test

3) *Optical testing*

To complete the analysis, polished sections of all test specimens and reference samples were also prepared. These revealed no structural abnormalities that could not be explained by the pressure or additive manufacturing of the test specimens using LPBF. Fig. 19 compares the best-case and the worst-case of all three geometries, based on their resistance values, demonstrated in TABLE II before.

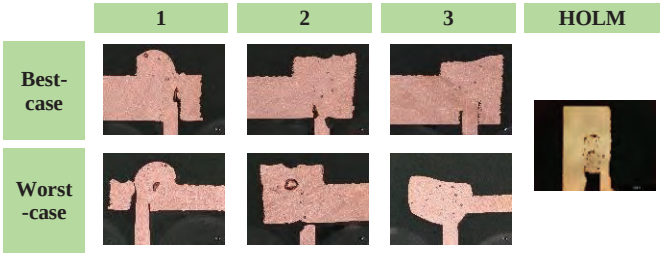


Fig. 19. Optical comparison of the welding zones

While visual analysis cannot provide clear information about electrical resistance, it does reveal some pores and cavities, which are reflected in the mechanical strength. The more inclusions there are in the weld zone, the lower the quality of the joint. Nevertheless, it is not really possible to deduce the electrical quality from the micrographs.

VIII. SUMMARY AND CONCLUSION

Additive-manufactured contact elements, for example, using LPBF, enable large flat contact surfaces and precise fits, combined with a technology of the future. In combination with laser welding, reproducible metallurgical bonds with low contact resistance and high mechanical reliability are created, which can be automated more easily than classic crimp connections. Compared to manual soldering, welding, or pressing, assembly costs, tolerance chains, and sources of error can be reduced, with comparable or potentially superior electrical and mechanical properties. This makes the combination of additively printed contacts and laser welding a powerful alternative for contacting applications for the production of electric drives in small series.

IX. ACKNOWLEDGMENT

The corresponding author thanks Felix Wirthmann, Muhammed Kilic, and Thorsten Ihne for their revisions and consulting. Furthermore, the author thanks Prof. Dr. Jörg Franke and Prof. Dr. Florian Risch for their reviews. Additionally, the author thanks Daniel Hößelbarth, Yusuf Ertem, and Lorenz Gradel for their support during practical investigations.

REFERENCES

[1] A. Riedel *et al.*, "Challenges of the Hairpin Technology for Production Techniques," in *2018 21st International Conference on Electrical Machines and Systems (ICEMS)*, Jeju, Korea (South), Oct. 2018 - Oct. 2018, pp. 2471–2476.

[2] A. Vogel, F. Wirthmann, N. Steinfelder, M. Baader, J. Franke, and F. Risch, "Process analysis of multi-stage forming of closed-form coils for automated stator assembly of large, rail-bound traction drives," in *2025 International Conference on Electrical Drives and Power Electronics (EDPE)*, Dubrovnik, Croatia, 2025, pp. 1–8.

[3] M. Baader, A. Mayr, T. Raffin, J. Selzam, A. Kuhl, and J. Franke, "Potentials of Optical Coherence Tomography for Process Monitoring in Laser Welding of Hairpin Windings," in *2021 11th International Electric Drives Production Conference (EDPC)*, Erlangen, Germany, 2021, pp. 1–10.

[4] K. Feldmann, V. Schöppner, and G. Spur, *Handbuch Fügen, Handhaben, Montieren*, 2nd ed. München: Hanser, 2014.

[5] T. Gläßel, *Prozessketten zum Laserstrahlschweißen von flachleiterbasierten Formspulenwicklungen für automobile Traktionsantriebe*. FAU Studien aus dem Maschinenbau Band 354. Erlangen: FAU University Press, 2020.

[6] A. Vogel, M. Baader, F. Wirthmann, A. Kuehl, J. Franke, and F. Kassel, "Design, Construction, and Laser Welding of a Contact Ring for Automated and Reliable Coil Connection for Wound Power-Dense Flat Wired Stators," in *2024 IEEE 69th Holm Conference on Electrical Contacts (HOLM)*, Annapolis, MD, USA, 2024, pp. 1–10.

[7] C. Klahn and M. Meboldt, *Entwicklung und Konstruktion für die Additive Fertigung: Grundlagen und Methoden für den Einsatz in industriellen Endkundenprodukten*, 1st ed. Würzburg: Vogel Business Media, 2018.

[8] R. Lachmayer, K. Rettschlag, and S. Kaierle, *Konstruktion für die Additive Fertigung 2020*. Berlin: Springer Vieweg, 2021.

[9] F. Klocke and W. König, *Fertigungsverfahren 3: Abtragen, Generieren und Lasermaterialbearbeitung*, 4th ed. Berlin: Springer Verlag, 2007.

[10] *DIN EN ISO 17296-2:2016-12, Additive Fertigung_- Grundlagen_- Teil_2: Überblick über Prozesskategorien und Ausgangswerkstoffe (ISO_17296-2:2015); Deutsche Fassung EN_ISO_17296-2:2016*, Berlin.

[11] R. Aliyev, *Planung von additiven Fertigungsprozessen*. Berlin: Springer Vieweg, 2025.

[12] F. Brenne, *Selektives Laserschmelzen metallischer Materialien*. Dissertation. Kassel: kassel university press, 2018.

[13] S. Stauber, F. Wirthmann, M. Baader, J. Franke, and F. Risch, "Evaluation of Additive Manufacturing Technologies for Copper Conductors in Electric Drives," in *2025 International Conference on Electrical Drives and Power Electronics (EDPE)*, Dubrovnik, Croatia, 2025, pp. 1–8.

[14] *DIN EN 13601:2021-07, Kupfer und Kupferlegierungen_- Stangen und Drähte aus Kupfer für die allgemeine Anwendung in der Elektrotechnik; Deutsche Fassung EN_13601:2021*, DIN - Deutsches Institut für Normung e. V., Berlin.

[15] C. Putz, T. Grundmann, and J. H. Schleifenbaum, "Investigation of Design Potentials for Welding PBF-LB/M Manufactured Pure Copper Busbars to Conventional Copper Conductors," *Berg Huettenmaenn Monatsh*, vol. 170, no. 3, pp. 148–157, 2025, doi: 10.1007/s00501-025-01561-0.

Separable connection of prismatic batteries

Tag Hammam
Materials Development
Swerim AB
Kista, Sweden
tag.hammam@swerim.se

Peter Andersson
Materials Development
Swerim AB
Kista, Sweden
peter.andersson@swerim.se

Lars Gunnarsson
Scania CV AB
Södertälje, Sweden
lars.gunnarsson@scania.com

Therese Källgren
Traton AB
Södertälje, Sweden
therese.kallgren@scania.com

***Abstract*—This study reviews how to temporarily connect prismatic batteries equipped with flat aluminum terminals. The maximum contact force that can be applied is 200 N, which is challenging because this is exceptionally low in relation to the electric current, which can reach 300 A, while the contact voltage drop should be low and stable throughout many power-cycles. A screen test was performed consisting of an uncoated aluminum contact block, rhodium-plated aluminum contact blocks and a contact block with many rhodium-plated test probes as well as an electroless nickel-plated contact block. A gold-plated brass block was also included and experiments with lubrication and contact paste were performed. Furthermore, experiments using a metallic foam sheet placed in between the battery terminal and the aluminum contact block were conducted. In conclusion, the metallic foam sheet met the specified requirements without grinding the contact block or contact paste, which is advantageous in the present application. The gold-plated contact block required contact paste to achieve low and stable contact resistance, while the uncoated aluminum block required grinding. Finally, a 5-degree back-and-forth rotation of the contact block just after the contact force was applied resulted in a significant reduction in the contact voltage drop.**

Keywords*— *Battery terminal, aluminum, gold, rhodium, electroless nickel, metallic foam sheet, contact paste

I. Introduction

There are two main types of batteries for electric vehicles: prismatic cells and cylindrical cells. A prismatic cell is a cell whose chemistry is enclosed in a rectangular can, and it is much larger than a cylindrical cell. Prismatic batteries are interconnected by joining busbars to the battery terminals. Screw terminals are used in some cases [1], but laser welding is generally preferred for high-volume production [2]. Prismatic batteries intended for laser welding typically have flat aluminum terminal plates, see Fig. 1. The battery cells need to be tested and evaluated before they are permanently joined together both for research and development as well as for production, and therefore, a temporary electric connection is needed.

C. Bolsinger et al. have investigated the electrical contact resistance of clamped battery cell connectors for cylindrical 18650 battery cells [3]. The applied force was 400 N while the current was 2 A. For a prismatic battery with an approximately 0.6 mm thick aluminum can, the maximum force that can be applied vertically before total collapse has been measured to be 2000 N [4]. With two battery terminals sharing the load and with a safety factor of five, the maximum acceptable contact force that can be applied to a battery terminal is 200 N, while the continuous current can be as high as 325 A [5].

Thus, it is a challenge to achieve a reliable, separable electrical connection for a prismatic battery with flat battery terminals because the maximum allowable contact force is exceptionally low relative to the electrical current.

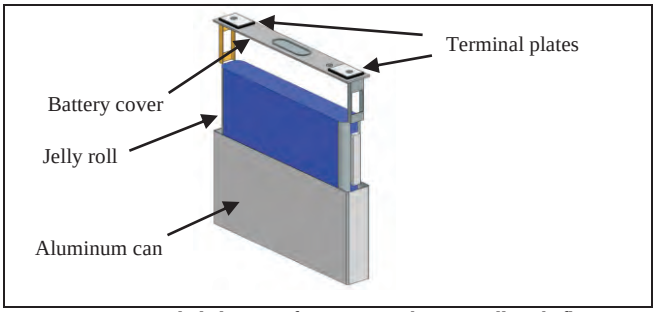


Figure 1. Exploded view of a prismatic battery cell with flat terminal plates.

A. Introduction to aluminum contacts

Aluminum instantly forms a thin oxide layer when exposed to air, which protects it from further corrosion. The growth rate of the oxide layer is extremely rapid initially, but a limiting thickness will be reached after a short time [6]. However, the thickness of the oxide layer increases due to environmental factors, such as temperature and humidity [7]. The oxide layer is electrically insulating and needs to be removed or ruptured to achieve good electrical contact [8].

A well-established recommendation is that uncoated aluminum contacts should be abraded and cleaned before assembly and a suitable contact aid (e.g. lubricant or contact pate), should be applied [9, 10]. A rough abrasion will increase the number of metal-metal contacts at much lower loads than a smooth surface thereby reducing the contact resistance [11].

To reduce the risk of thermal-induced fretting due to a mismatch in the Coefficient of Thermal Expansion (CTE) between the flat aluminum contact terminal on the battery and the connecting contact, the connecting contact should preferably be made of aluminum.

Rhodium-coated contacts are used when good electrical contact with aluminum is required, e.g. Rh-coated molybdenum discs are used to electrically connect high-power thyristor dies that have a top coating of aluminum [12].

René von Kaenel et al. [13] have demonstrated that a metallic foam sheet placed in between two contact members can significantly reduce the contact voltage drop at equal contact force. The metallic foam is flexible which results in many contact points even at a low surface pressure. This, in combination with an efficient penetration of oxide layers by the foam, results in reduced contact resistance.

For battery applications, test probes generally consist of gold-plated brass probes with a micro-structured contact area with uniform height and width. The probe design has evolved from test probes intended for completely different applications and requirements than batteries, such as test probes for printed circuit boards. However, a new probe design intended for prismatic battery cells has been presented [14]. The main test probe consists of 30 separate spring-loaded flat-headed probes, see Fig. 2. The probes are mainly made of copper and brass, and the probe heads are silver-plated. Moreover, the clamping force is in the range of 240 N to 300 N, while the current rating is 400 A and typically contact resistance is 0.2 mΩ or below [15].



Figure 2. A test probe intended for prismatic battery cells. The main test probe consists of 30 separate spring-loaded test probes. The contact force is 240 N to 300 N, while the current rating is 400 A [15].

B. Requirements for the electrical connection of prismatic batteries

Battery testing is performed over a wide range of electric current, number of cycles and maximum temperature depending on the purpose of the test. However, some typical requirements for a 150 Ah prismatic battery are as follows:

- Material of battery contact: Aluminum 3003-H14
- Maximum permitted contact force: 200 N
- Maximum current: 300 A DC, i.e. 2C / 30 minutes
- Size of the contact area: 22 mm x 32 mm
- Maximum temperature of the battery: 70 °C
- Contact aid should preferably not be applied since laser welding without cleaning should be possible.
- The contact block should preferably not need to be abraded before testing.

Moreover, a battery test can last from everything from a few cycles up to several thousand current cycles. The contact voltage drop should initially be maximum 20 mV and at the end of the test maximum 30 mV [16].

The purpose of this study is to screen different concepts for temporarily connecting prismatic batteries equipped with flat aluminum terminals, with the aim of proposing one or more suitable contact concepts for further extensive testing. This study is limited to the high current connection, while connection to the battery terminal for e.g. measuring the voltage drop is not included.

II. Experiments

A. Experimental set-up

A specially designed test bench was used to evaluate different contact concepts, see Fig. 3. The upper part of the prismatic battery cell, i.e. the cover plate complete with contact terminals and current collectors, was placed and locked in an anvil that was placed in the lower part of the test bench. The contact block, i.e. the connecting contact of the flat aluminum contact terminal, was mounted on a holder, and the contact force was applied using weights.

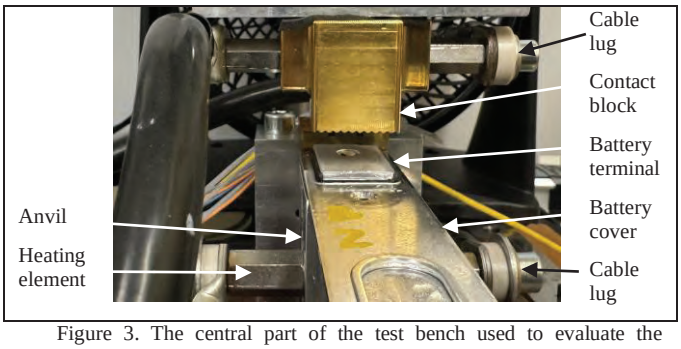


Figure 3. The central part of the test bench used to evaluate the different contact concepts. The electric current was applied to both sides of the lower fixture and the contact block. A resistive heating element was placed between each cable lug and fixture, and the contact force was applied using weights.

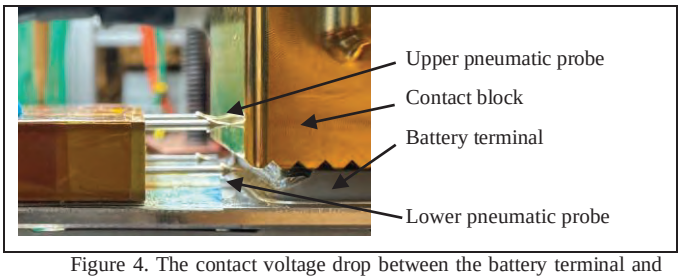


Figure 4. The contact voltage drop between the battery terminal and the contact block was measured with pneumatic probes. The distance between the upper and lower probe was 5.0 mm. The plastic insulation at the short ends of the battery terminal was removed to be able to measure the voltage drop.

The contact voltage drop (U_C) was measured with two pneumatic probes pairs on each short side of the contact terminal, see Fig. 4. The distance between the measuring probes for each pair of probes was 5 mm. Each contact block had two holes, 1 mm in diameter, for thermocouples. The distance from the contact surface to the holes was 5 mm and the depth was to the center line of the contact block. The electric current was applied to both sides of the upper and lower fixture. A resistive heating element was placed between each cable lug and fixture, see Fig. 3.

B. Test samples

The concepts that were tested and evaluated are presented below together with motivation.

1. Uncoated contact blocks made of aluminum EN-AW-6082 (42 % IACS). *Motivation: aluminum eliminates the risk of thermal-induced fretting due to CTE mismatch, and an uncoated aluminum block is the easiest to manufacture.*

2. Electroless nickel-plated (EN, medium phosphorus) aluminum contact blocks made of EN-AW-6082. *Motivation: electroless nickel is used in some contact applications [17]. Electroless-nickel plating is a relatively low-cost process and is therefore interesting to evaluate.*

3. Rhodium-coated contact block. The rhodium coating consisted of three layers plated on the aluminum block (EN-AW-6082). The first layer was a medium phosphorus electroless nickel coating, and samples with three different thicknesses of the electroless nickel (medium phosphorus) were produced: 9 µm, 20 µm and 25 µm. The second layer was a bond layer consisting of 0.07 - 0.09 µm gold, and the top coating was 0.4 – 0.5 µm rhodium.

Motivation: Rh-coated contacts are used to create good electrical contact with aluminum in some demanding applications [12]. Different thicknesses of the electroless nickel coating will reveal the impact of the thickness of the EN coating.

4. Contact block with rhodium-plated test probes. A contact block was prepared with 44 rhodium-plated spring-loaded test probes with flat probe heads. The diameter of the probe head was 2.5 mm, and the current rating was 6 A DC. However, the probes were subjected to a slight overcurrent since the current was 300/44 = 6.8 A DC in this test.

Motivation: a large number of spring-loaded probes will ensure that the contact force is distributed equally over the entire contact area. Moreover, Rh-coated contacts are used to create good electrical contact with aluminum in some demanding applications [12].

5. Gold-plated contact block made of brass with micro-pyramid structured surface. The size of the pyramid's top area was 0.5 mm x 0.5 mm, and the pitch was 2.5 mm.

Motivation: a gold-plated contact block with a micro-pyramid structured contact area is commercially available.

6. Uncoated aluminum contact block with a 1.6 mm thick metallic foam sheet.

Motivation: the metallic foam sheet is intended to be used for aluminum contacts.

In addition, two different types of contact aids were evaluated: Perfluoropolyether, PFPE, (type Fomblin Z 25), and a contact paste (Noalox), consisting of polybutene, suspended zinc particles, and silicon dioxide.

In all experiments, the battery terminals were abraded with grinding paper (grit 180) and cleaned with ethanol before the test, see Fig. 5.

The experiments were performed in two parts: the first part aimed to measure the initial stationary contact voltage drop at a clamping force of 200 N and 300 A DC, and the second part was to perform power cycling at 300 A DC of selected concepts.

III. Results

A. Stationary contact voltage drop at 300 A DC

For the first part of the experiment, 300 A DC was applied, and the contact voltage drop was measured for one minute. The test matrix and the result of the first part are presented in Table I, and photographs of the contact blocks after the tests are presented in Figs. 6 to 16.

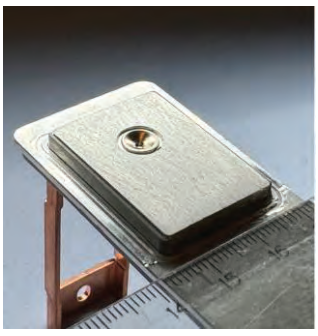


Figure 5. The battery terminals were abraded and cleaned with ethanol before the test.

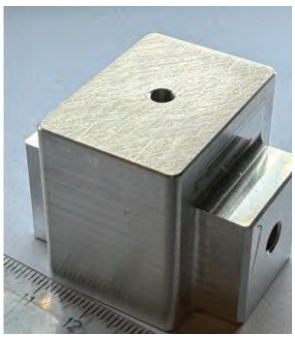


Figure. 6. Test #1. The uncoated aluminum contact block after testing

TABLE I. Stationary Contact voltage drop at 300 A DC

Test	*Test sample*	*Comments*	*Average U_C (mV)*
1	Abraded Al contact block		21
2	Abraded Al contact block	Fomblin Z25	5
3	Abraded Al contact block	Noalox	4
4	EN-plated contact block	EN 7 µm	9
5	Rhodium-coated contact block	EN 9 µm	27
6	Rhodium-coated contact block	EN 20 µm	48
7	Rhodium-coated contact block	EN 25 µm	12
8	Contact block with Rh-plated test probes*		76
9	Au-plated contact block with micro-pyramid structured surface		15
10	Au-plated contact block with micro-pyramid structured surface	Fomblin Z25	14
11	Au-plated contact block with micro-pyramid structured surface	Noalox	7
12	Uncoated Al-contact block with a metallic foam sheet		15

*The voltage drop between the aluminum block and the probe head was measured to be below 1 mV.

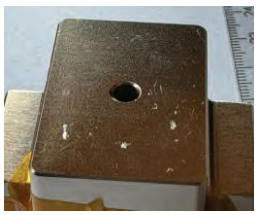


Figure 7. Test #4. The electroless nickel-plated contact block after measurements. Some spots with melted Al on top of the electroless nickel-plating are visible.

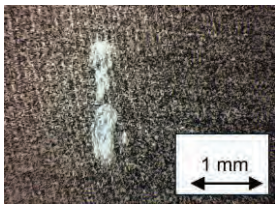


Figure 8. Test #4. Close-up of one of the areas where aluminum is visible on the surface of the EN-plated contact block.

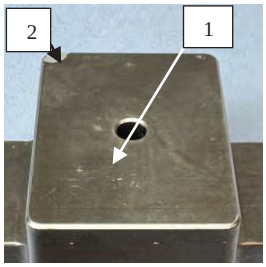


Figure. 9. Test #5. Rh-coated contact block. EN 9 µm. Arrow 1 points at some spots with melted aluminum on top of the rhodium. A tape test revealed poor adhesion of the coating to the substrate; the coating partly detached from the substrate, (arrow 2).

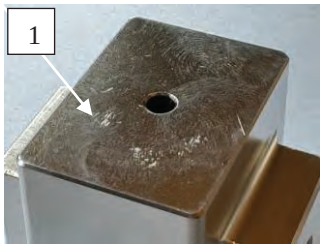


Figure. 10. Test #7. Rhodium-coated contact block. EN 25 µm. Some spots with melted aluminum on top of the rhodium plating are visible (arrow 1).



Figure 11. Test #8. The contact block with 44 spring-loaded Rh-coated contact probes. Diameter of the probe heads: 2.5 mm.

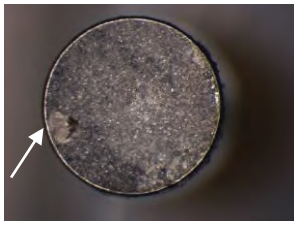


Figure 12. One of the Rh-coated contact probes after testing. The arrow points to an area where the coating has detached.

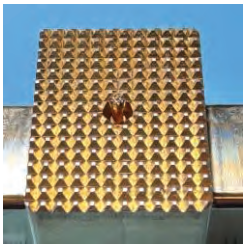


Figure. 13. Test #9. The gold-plated contact block with a micro-pyramid structured contact area.

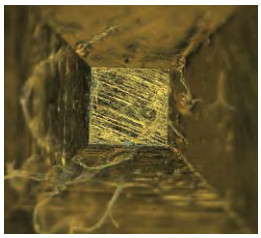


Figure. 14. Close-up of the gold-plated contact block. Size of the pyramid's top area: 0.5 mm x 0.5 mm, pitch 2.5 mm. The Au layer is very thin.

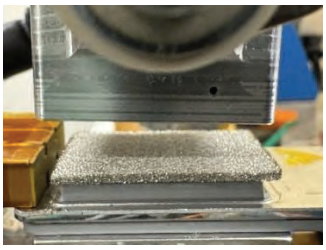


Figure. 15. Test #12. The battery terminal with the metallic foam sheet.

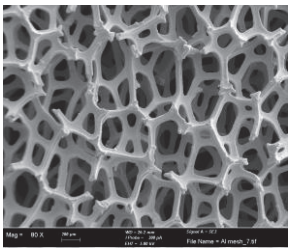


Figure 16. Close-up of the metallic foam sheet. SEM-EDS analysis revealed that the metallic foam consisted of a Ni-core with an intermediate layer of Cu and a top coating of Sn.

B. Power cycling at 300 A DC

Power cycling was performed to simulate the conditions during battery testing. However, a slight over temperature of 10 °C was chosen. Power cycling was performed by applying 300 A DC until the temperature of the contact block reached 80 °C, which took 30 to 40 minutes. Thereafter, the test sample was cooled down to ~30 °C. Each test consisted of 30 power cycles, and the current was reversed for each new power cycle. Additionally, the battery terminals were always abraded and cleaned with ethanol before power cycling.

Experiments were performed to investigate the effect of a small rotation of ~5 degrees back-and-forth of the contact block. The 5-degree rotation resulted in a maximum back-and-forth slip of 1.5 mm, which occurred at the short edge of the contact terminal. The test samples were an abraded Al contact block, a Au-plated contact block with a micro-pyramid structured surface and contact paste, and finally, an uncoated abraded Al contact block, with a metallic foam sheet. The results are presented in Table II. The rotation of the contact block reduced the contact voltage drop by ~50 %, and therefore a 5-degree back-and-forth rotation of the contact block after the contact force had been applied was introduced for all power cycling experiments.

TABLE II. THE IMPACT OF ROTATION, POWER CYCLING AT 300 A DC

Test	*Test sample*	*Average U_C (mV) before rotation*	*Average U_C (mV) after rotation*
13	Abraded aluminum contact block	13.5	6.5
14	Au-plated contact block with a micro-pyramid structured surface and contact paste (Noalox)	30	10
15	Uncoated abraded Al-contact block, with a metallic foam sheet	17	9.5

Based on the results of the steady-state contact voltage drop measurements, neither the coated Al-contact blocks nor the contact block with Rh-plated probes were included in the power cycling test. In addition, experiments were also performed with Al-contact blocks that were not abraded.

The test matrix and the results of the power cycling test are presented in Table III. Strictly speaking, it is the absolute maximum voltage drop that is shown since the current was reversed for each new cycle. The maximum contact voltage drop for each power cycle is presented in Figs. 17 to 19.

TABLE III. POWER CYCLING AT 300 A DC

Test	*Test sample*	*Comments*	*Maximum UC (mV)*
16	Aluminum contact block	Noalox	8.6
17	Abraded aluminum contact block		7.3
18	Abraded aluminum contact block	Noalox	6.6
19	Au-plated contact block with a micro-pyramid structured surface		14
20	Au-plated contact block with a micro-pyramid structured surface	Fomblin Z25	5.2
21	Au-plated contact block with a micro-pyramid structured surface	Noalox	7.3
22	Uncoated aluminum contact block with a metallic foam sheet		15.4
23	Uncoated abraded Al contact block with a metallic foam sheet		14.7

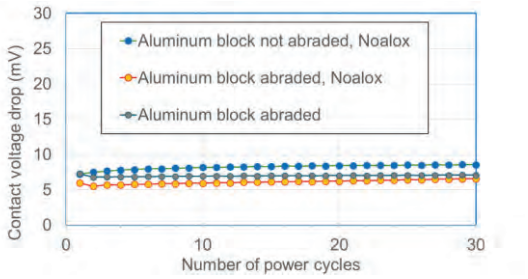


Figure 17. Test #16 to test #18. The maximum U_C for each power cycle versus the number of power cycles.

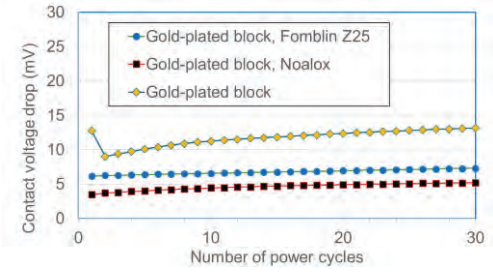


Figure 18. Test #19 to test #21. The maximum U_C for each power cycle versus the number of power cycles. Note the increase in voltage drop for the Au-plated contact block without lubrication.

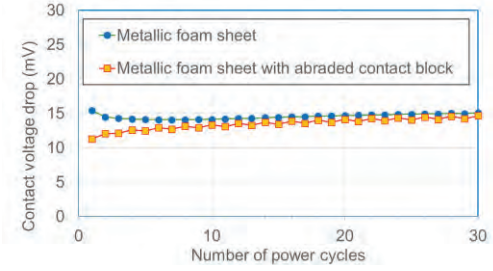


Figure 19. Test #22 and test #23. The maximum U_C for each power cycle versus the number of power cycles.

C. Analysis of the contacts after power cycling

The unlubricated Al-contact block and the battery cell terminal were intact after the test, see Fig. 20. The Au-plated brass block with a micro-pyramid structured surface made imprints in the battery terminal for all cases tested (unlubricated, Fomblin Z25 and Noalox), see Fig. 21. However, the thin gold layer on top of the micro-pyramids was intact after the power cycling, see Fig. 22. Tests #22 and #23 with a metallic foam sheet between the Al-block and the contact terminal, showed that the Al-block and the contact terminal were visually intact after the test, see Fig. 23.



Figure 20. Test #17. The Al-contact block (to the left) and the battery cell terminal (to the right), after power cycling without lubrication, both contacts were intact after the power cycling test.



Figure 21. Test #20 The contact terminal after power cycling with a gold-plated contact block and Fomblin Z25. Imprints from the gold-plated contact block surface are visible.

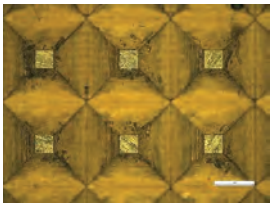


Figure 22. Close-up of the micro-pyramid structured surface of the gold-plated contact block with a after power cycling.

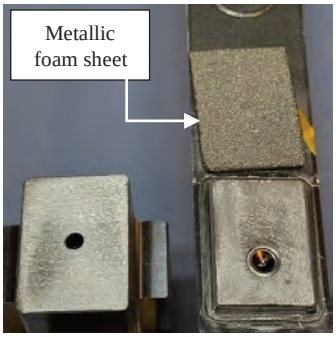


Figure 23. Test #23, the uncoated abraded aluminum contact block, with a metallic foam sheet. The aluminum contact block (to the left) and the battery cell terminal (to the right), after power cycling, all contacts were visually intact after the power cycling test.

IV. Discussion

All coated Al contact blocks, i.e. electroless Ni-plated blocks and Rh-coated blocks, showed melted aluminum spots on top of the coating. This was probably due to the low contact force resulting in a too-small contact area in relation to the current, which resulted in local high temperatures, i.e. hot spots. For the Rh-coated contact blocks the area of melted aluminum was a function of the thickness of the underlaying Electroless nickel. The resistivity for EN, medium phosphorus is 40 – 70 x 10^{-8} Ωm [18] compared to 7 x10^{-8} Ωm for electrolytic nickel coating [19], and thus, electroless nickel has relatively high resistivity and increased thickness results in more heat and more melted aluminum. Moreover, a tape test revealed poor adhesion of the rhodium coating to the substrate.

The Rh-plated probes also suffered from detachment of the coating. The concept of using spring-loaded Rh-plated contact probes to distribute the real contact area over a larger area resulted in the highest voltage drop of 76 mV, well above the limit of 30 mV. The voltage drop between the Al block and the probe head was measured at below 1 mV, and thus, almost the entire volt drop of 76 mV occurred at the contact interface. Probably, the high voltage drop was caused by insufficient mechanical penetration of the aluminum oxide layer, which in turn was due to flat probe heads. Flat probe heads in combination with low surface pressure results in restricted plastic deformation of the surface asperities and thus limit mechanical break-up of the aluminum oxide layer. This concept has similarities to the test probe in Fig.2 which consists of 30 separate spring-loaded test probes. According to the data specification, the expected contact resistance is 0.2 mΩ or below, which at 300 A DC results in a contact voltage drop of 60 mV. This value is quite close to the measured voltage drop for the contact block with rhodium-coated probes. However, the 60 mV is more than the present threshold limit of 30 mV at the end of the test.

A small rotation of approximately 5 degrees back-and-forth from the contact block just after the contact force had been applied, resulted in a ~50% reduction in the contact voltage drop, which is significant. This rotation has the same effect as the insertion stroke when mating a plug-in connector. The insertion stroke cleans the contact interface between the surface asperities in contact and increases the oxide-free metal-to-metal contact area, which in turn reduces the contact resistance. Moreover, the contact block can be designed to be forced to rotate while the force is applied as described in patent US5456621A [20].

With a 5 degrees rotation back-and-forth, the abraded Al-block without contact paste achieved a remarkably low contact voltage drop of 7.3 mV, which was the same value as for the gold-plated contact block with Noalox. An Al-block without any grinding but with contact paste (Noalox) resulted in a slightly higher contact voltage drop of 8.6 mV. All these values are well below the limit of 30 mV at the end of the test. However, without a 5 degrees rotation back-and-forth the abraded Al-contact block achieved an initial contact voltage drop of 21 mV which was just above the threshold limit of 20 mV.

The Au-plated brass block with micro-pyramid structured contact area made imprints in the battery terminal for all cases tested (unlubricated, Fomblin Z25 and Noalox). The local surface pressure in the imprints was estimated to have been 10 – 15 MPa. This indicates that the temperature had probably been relatively high in the contact area. The Fomblin Z25 lubricant used for the gold-plated contact block resulted in a reduced voltage drop but less than for Noalox. The amount of lubricant Z25 that needs to be applied is very small and significantly less than for Noalox. However, Fomblin Z25 is a Perfluoropolyether (PFPE) lubricant, and the European Chemicals Agency (ECHA) has proposed regulating poly- and perfluoroalkyl substances (PFAS) as

one large group of chemicals in the EU based on their structural characteristics [21].

The Au-plated contact block without any lubrication resulted in the largest increase in contact voltage drop during power cycling compared to all other tests, see Figs 14 to 16. The increase was probably caused by thermal-induced fretting. However, the increase of the contact voltage drop was restricted when a lubricant or contact paste was used. Thus, a lubricant or contact paste is needed to reduce the risk of fretting due to a mismatch in thermal expansion between the gold-plated brass block and the battery terminal of aluminum.

The metallic foam sheet achieved higher contact resistance than both the uncoated Al-block in direct contact with the battery terminal and the Au-plated contact block. The voltage drop was reduced somewhat when the Al-block was abraded, from 15.4 mV to 14.6 mV. Part of the voltage drop is probably caused by the resistance of the 1.6 mm thick metallic foam. However, the measured voltage drop was in all cases below the threshold requirement of an initial max of 20 mV and a max of 30 mV at the end of the test.

It is worth noting that the recommended contact pressure for the metal foam sheet is 7 N/mm^2 [22], which with the current size of the contact terminal (22 mm x 32 mm) results in a contact force of almost 5000 N. This is ~25 times higher than the contact force that can be applied to the battery terminal. Furthermore, the metal foam is designed to be compressed from 1.6 mm to 0.2 mm at full load.

The metallic foam sheet was the only concept that met the specified requirements without grinding the contact block or contact paste in the present screen test. Thus, further experiments with many more contacts to obtain a statistical basis, as well as tests with many more power cycles could be considered to verify the concept.

V. Conclusions

Prismatic batteries for electric vehicles are in general interconnected by laser welding busbars to the battery cell terminals made of aluminum. The battery cells need to be tested and evaluated before they are welded together both for research and development as well as for production, and therefore, a reliable, separable electrical connection of the batteries is needed. However, the maximum permitted contact force of 200 N is exceptionally low in relation to the current, which can be as high as 300 A DC, making it a challenge to achieve a reliable contact. Based on the experiments performed in this study the following conclusions have been reached:

- The metallic foam sheet met the specified requirements without grinding the contact block or contact paste, which is advantageous in the present application.
- The gold-plated brass contact block required contact paste to achieve low and stable contact resistance, while the uncoated aluminum block required grinding.
- A 5-degree back-and-forth rotation of the contact block just after the contact force was applied resulted in a significant reduction in the contact voltage drop.

Acknowledgment

The authors gratefully acknowledge Scania CV AB for supporting this work.

References

[1] Available: https://www.benergytech.com/

[2] H. Saariluoma, H, A. Piiroinen, A. Unt, J. Hakanen, T. Rautava, and A. Salminen, “Overview of Optical Digital Measuring Challenges and Technologies in Laser Welded Components” in EV Battery Module Design and Manufacturing, volume 6, no.3, 2020.

[3] C. Bolsinger, M. Zorn, K. P. Birke, “Electrical contact resistance measurements of clamped battery cell connectors for cylindrical 18650 battery cells”, Journal of Energy Storage, volume 12, pp. 29-36, 2017.

[4] D. Cioni, et al., “Testing and modelling of aluminium cans for prismatic lithium-ion cells under crash loading” International Journal of Impact Engineering, volume 192, 2024.

[5] Available: https://eveurope.eu/en/product/catl-26s-nmc-lithium-battery-module-2/

[6] J. Evertsson, et al. “The thickness of native oxides on aluminum alloys and single crystals”, Applied Surface Science, volume 349, pp. 826-832, 2015.

[7] H. P. Godard, “Oxide Film Growth over Five Years on Some Aluminum Sheet Alloys in Air of Varying Humidity at Room Temperature”, Journal of The Electrochemical Society, volume 114, no. 4, 1967.

[8] R. Timsit, "Some Fundamental Properties of Aluminum-Aluminum Electrical Contacts," in IEEE T-CPMT, vol. 3, no. 1, pp. 71-79, March 1980.

[9] M. Braunovic “Further studies of different contact aid compounds for aluminum-to-copper connections” Proceedings of the Forty-Fifth IEEE Holm Conference on Electrical Contacts, 1999.

[10] P. G. Slade, "Bus Bar Bolted Connections: Reliability and Testing," Holm Conference on Electrical Contacts, pp. 209-216, 2021.

[11] M. Braunovic, “Effect of Connection Design on the Contact Resistance of High Power Overlapping Bolted Joints” IEEE Transactions on Components and Packaging Technology, vol., 25, No. 4, December 2002.

[12] W. Wang, X. Zhang, X. Xie, K. Huang and Y. Tan. "Research on thermal characteristics of IGCT based on structure function." Journal of Physics: Conference Series, IOP Publishing, vol. 1907, no. 1, 2021.

[13] R. von Kaenel, J. Antille, M. Pillet, and M. Lindeboom, “Non-Linear Behavior of a Metallic Foam for the Reduction of Energy Losses at Electrical Contacts in the Aluminum Industry”. In Light Metals, Springer International Publishing, pp. 717—722, 2014.

[14] Available:https://www.ptr-hartmann.com /fileadmin/media/ downloads/Presse/eng/PTR-HARTMANN-Press-Release HSK5455.pdf

[15] Available: https://ptr.ptr-hartmann.com/en/testing-technology/test-probes/high-current-test-probes/hsk-5455

[16] R. D. Malucci and F. R. Ruffino, "Rating power connectors using voltage drop," Proceedings of the Fifty-First IEEE Holm Conference on Electrical Contacts, 2005., Chicago, IL, USA, 2005, pp. 176-17

[17] K. P. Thurlow, “Electroless nickel plating on aluminium connectors”, Transactions of the Institute of Metal Finishing, volume 67, pp. 82–86, 1989.

[18] Available: https://www.macdermidenthone.com/news/electroless-nickel-coatings-electric-vehicle-applications

[19] Available: https://langhe-industry.com/electroless-vs-electrolytic-nickel-plating/

[20] G. Y. Gan and O. Kans. “Self-wiping/self cleaning electrical contact”, U.S. Patent 5 456 621 A, Oct.10, 1995.

[21] A. R. Bock and B. E. Laird, "PFAS regulations: Past and present and their impact on fluoropolymers." in Perfluoroalkyl Substances: Synthesis, Applications, Challenges and Regulations, The Royal Society of Chemistry, pp. 1 – 21, 2022.

[22] Available : https://www.ecocontact.eu

Evaluation of current-carrying capacity of silver-based oxide contact pairs

Chang Sun
School of Electrical Engineering and Automation
Harbin Institute of Technology
Harbin, China
24b306007@stu.hit.edu.cn

Chao Zhang
School of Electrical Engineering and Automation
Harbin Institute of Technology
Harbin, China
zhangchao100@hit.edu.cn

Yinnan Zhang
School of Electrical Engineering and Automation
Harbin Institute of Technology
Harbin, China
23b906032@stu.hit.edu.cn

Wanbin Ren
School of Electrical Engineering and Automation
Harbin Institute of Technology
Harbin, China
renwanbin@hit.edu.cn

Yinghua Fu
Chixi Technology Co.
Nanchang, China
yhfu1018@163.com

***Abstract*—The current-carrying capacity of silver-based oxide electrical contact materials is a key factor governing the reliability of low-current switching devices. In this work, the melting characteristics of $AgSnO_2In_2O_3$ material are experimentally investigated under fixed mechanical load force, employing a stepwise DC current loading mode. The R-U characteristic curves under various load forces are measured, and the associated static welding behavior is quantified through welding force and trace analysis. The current for the first occurrence of welding was determined experimentally. Furthermore, the melting temperature of the material is inferred by correlating experimentally observed melted area with simulated temperature distribution results.**

Keywords—contact resistance, melting voltage, welding trace, welding force.

I. Introduction

Silver-based oxide electrical contact materials are widely used in different kinds of low-current switching devices, such as electromechanical relays, contactors, micro-switch and so on [1,2]. As known, when the applied current causes the local current density at the contact spot of contact pairs to exceed the limit, excessive Joule heating may occur, leading to local overheating, melting, and even welding [3]. Once the opening force is insufficient to overcome the generated welding force, the electrical circuit may remain unintentionally closed during the breaking operation, which can cause system failure. So, current-carrying capacity of the electrical contact material, that is, the safe current level below which welding does not occur under static contact conditions, is particularly important for the reliability design of electrical apparatus. However, to our best understanding, a practical method for relating them to static welding risk in silver-based oxide contacts such as $AgSnO_2$, AgNi, and AgC under a given contact configuration is still lacking.

Interests in softening and melting phenomena of stationary electrical contact is increasing since Ragnar Holm's academic monograph in the 1940s [4]. The resistance-voltage (R-U) characteristics of gold at load force of 2 and 10 gram is initially presented, in which the resistance exhibits a departure from the ideal trend with voltage drop, reflecting changes in the contact surface state. Meanwhile, the voltage-temperature relation was derived on the assumption of equilibrium between ohmic heating in the electrical constriction and thermal dissipation by conduction within the contacting materials. The relation was widely used to evaluate the potential drop required across a contact to cause melting of the electrical interface. Further, Timsit [5] found the melting voltage for Fe/Fe and Ni/Ni couples are smaller than the values predicted by the conventional voltage-temperature relation, and suggested that heat entrapment occurs at the melting temperature.

In addition, much efforts have been devoted in stationary contact welding characteristics. Książkiewicz *et al.* [6] statistically analyzed the number of welding occurrences and the change in separation force, using welding probability and welding strength to characterize the welding tendency and load-bearing limit of contact materials. Kübler-Riedinger *et al.* [7] inversely derived static melting conditions and equivalent contact radius, treating microscopic melting traces as criteria for the critical state. Some studies directly introduced "threshold welding current" as an evaluation metric [8,9]; Zhang *et al.* [10] proposed the welding current based on theoretical modeling and experimental verification to assess welding risk and current-carrying limits of materials in low-current switching.

In this study, $AgSnO_2In_2O_3$ is used as a representative material. Through experiments, the R-U characteristic curves under given load forces are measured along with the associated welding traces and welding forces, to illustrate in detail the softening and melting phenomena occurring during current loading. Furthermore, the influence of load force on the R-U characteristics is investigated. In addition, the melting temperature of the material is determined through FEM mechanical-electrical-thermal coupled simulation. From these, a method that to evaluate the current-carrying capacity of contact materials is proposed.

II. Experimental Details

The experimental setup in which the resistance-contact voltage curve measured is illustrated in Fig. 1. The resistance measurements are realized by the crossed rod contacts. The upper rod served as the stationary contact, and the lower rod served as the moving contact. The rods were approximately 35 mm in length and 2.38 mm in diameter. The samples were degreased using alcohol and distilled water in an ultrasonic cleaner, dried. Two brass fixtures were fitted around the metal rods and connected to lead wires. The normal contact force between two rods is assessed using a digital force transducer with a measurement range of 60 N with a resolution of 10 μN. The vertical actuation of the moving rod is realized by an electric motor mounted. The entire mechanical structure was mounted on a vibration isolation

platform. The four-wire method is configured to measure the electrical contact resistance. The contact current is provided by a programmable DC current source (PDC0220N, Actionpower electric, China) and measured by a Hall current sensor with a measurement range of 300 A. The contact voltage is measured using a Nano-Voltmeter (2182, Keithley, USA) with a resolution of 1 nV. The thermocouple (STTT-V, Sailing Technology, China) is glued in 7 mm from the contact point to monitor the temperature in real time during the experiment. All above signals are acquired by the commercial data acquisition card (PCI-1716L, Advantech, China) at sampling period of 4 μs. The instrument is interfaced to a personal computer using serial port RS232. The data acquisition and logging process are controlled through a PC with the help of LabVIEW software specifically programmed for this purpose. The $AgSnO_2In_2O_3$ contact rods used in this study consist of 85.5 wt% Ag, 10 wt% SnO_2 and 4.5 wt% In_2O_3, with an electrical conductivity of 2.7–3.1 μΩ·cm and a hardness of approximately 125 HV in the as-rolled state.

An experimental run proceeded as follows: with the two rods brought into contact under the given load force, the current source turned on and a direct current of 20 A was applied. Once a thermal equilibrium had been attained, the current was increased in a controlled manner from 20 A to 250 A at a ramp rate of 5 A/s. After 250 A was reached, the current was then rapidly reduced at a rate of 10 A/s, completing the loading-unloading cycle. Throughout this cycle, the electrical contact resistance (ECR), contact voltage drop, contact force, and temperature were simultaneously recorded. When the current returned to 20 A, the current source was switched off and the contacts were actuated to separate via a motor-driven mechanism. Real-time recording of the contact separation force was conducted during this process. The welding trace on the rod surface was examined to quantify the melted area. The details of the experimental conditions used are detailed in Table I.

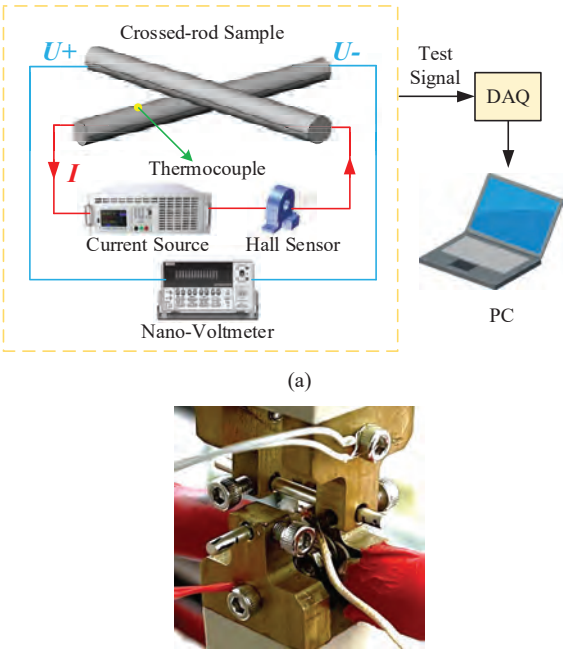


Fig. 1. Schematic diagram of (a) experimental circuit and (b) practical realization.

TABLE I. DETAILED EXPERIMENTAL CONDITIONS

Environment	Ambient temperature
Load current	20A-250A
Current loading velocity	5A/s
Current unloading velocity	10A/s
Mechanical load force	0.01N, 0.02N, 0.05N, 0.1N, 0.2N, 0.3N, 0.4N, 0.5N, 1N

III. RESULTS AND DISCUSSION

A. Typical R-U Characteristics

Fig. 2 shows the typical variations in resistance and temperature as a function of contact voltage drop during a current loading-unloading cycle under a load force of 0.02 N. At point a, the resistance corresponding to the initial current of 20 A is 1.01 mΩ. As the current gradually increases to 143.8 A, the voltage drop reaches 188.1 mV, while the resistance increases to its maximum value of 1.286 mΩ at point b. This is usually attributed to the increase in electrical resistivity with temperature. From point b to c, the ECR exhibits a distinct downward trend, decreasing to 1.012 mΩ at 224.1 A. Holm [4] attributed this to excessive interfacial temperature, which causes material softening and consequently an increase in the contact area. As the current further increases to 250 A, the ECR rises again from point c to point d, reaching 1.198 mΩ at a contact voltage drop of 303.3 mV. Holm believed that after the softening drop, the interfacial resistivity continues to increase with temperature, although the melting temperature has not yet been reached. When the current is subsequently reduced, the ECR immediately decreases from point d to e, forming an unloading curve that lies consistently below the loading curve. The R-U characteristic curve correlates well with the findings of other researchers [4, 7,11,12].

The measured temperature results obtained by thermocouples are also included in Fig. 2. As the current continues to increase, the temperature rises monotonically from 24 °C to a maximum of 180 °C and does not decrease during the b-c stage where the ECR drops. This continuous temperature rise indirectly reflects the evolution of the interfacial a-spot temperature, which will be further examined through FEM simulations in the following sections.

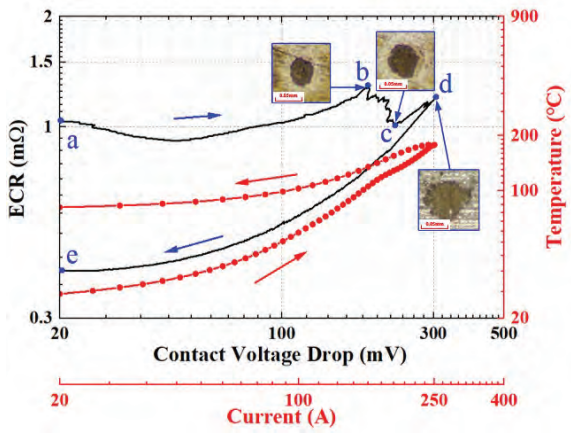


Fig. 2. Variations in ECR and temperature as a function of contact voltage drop and current during a current loading-unloading cycle under a load force of 0.02 N.

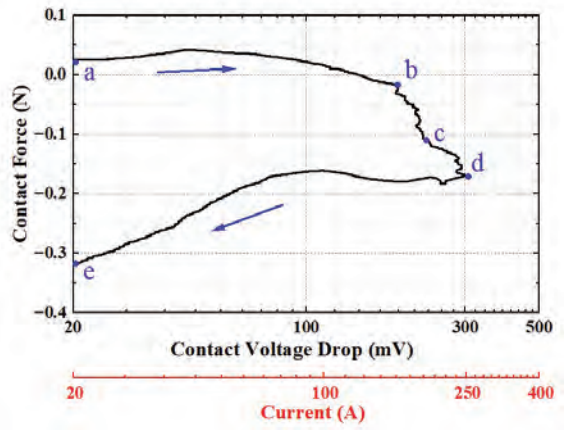


Fig. 3. Variations in contact force as a function of contact voltage drop and current during a current loading-unloading cycle under a load force of 0.02 N.

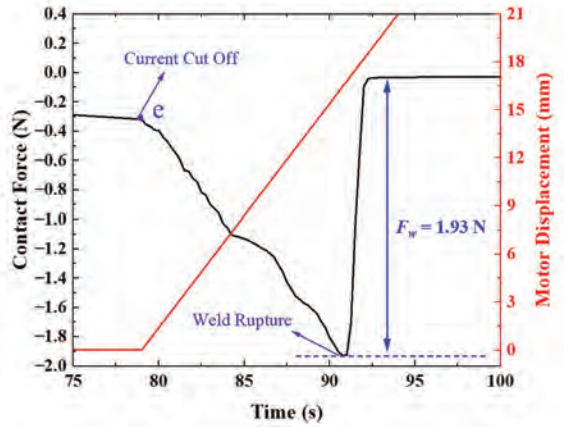


Fig. 4. Typical waveforms of the contact force and motor displacement during breaking process.

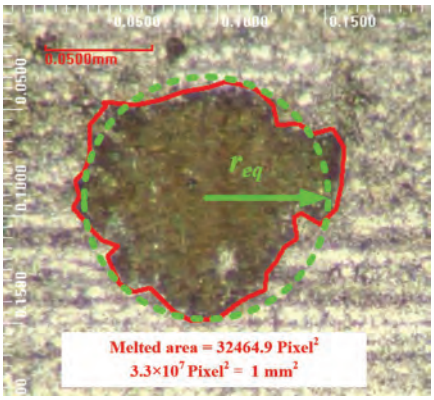


Fig. 5. Photograph of the contact surface obtained from the CCD camera (mechanical load force is 0.02 N).

Fig. 3 shows the variations in contact force as a function of contact voltage drop and current during a current loading-unloading cycle under a load force of 0.02 N. At point a, the contact force corresponding to the initial current of 20 A is 0.02 N. As the current gradually increases, the contact force first increases slightly, which may be attributed to thermal expansion of the contact system, and then exhibits a distinct downward trend. By point b, the force has crossed zero. This is likely associated with softening and local melting, which gradually consume the effective contact overtravel and continuously release the initial compressive preload. From point b to d, the contact force continues to increase in the negative direction. During unloading, the contact force further increases from point d to e. As the temperature decreases, the thermal expansion gradually recovers, while the interfacial softening and melting developed during loading remain largely irreversible.

Fig. 4 illustrates the measured contact force and motor displacement during the contact breaking process. As shown, after the current is cut off at point e (corresponds to point e in Fig. 2), a sharp drop is observed when the welded junction ruptures, and the separation force at this point corresponds to the welding force, measured as 1.93 N.

Fig. 5 shows the contact surface morphology after the experiment in Fig. 2 for the $AgSnO_2In_2O_3$ material. The melted area A_w is identified as the circular region enclosed by the red contour and quantified by image analysis using the scale bar in the micrograph for spatial calibration, yielding $A_w = 9.84\times10^{-3}$ mm^2. Assuming a circular molten region enclosed by the green dotted line, A_w is converted into an equivalent radius r_{eq}. The equivalent radius can be expressed as:

$$r_{eq} = \sqrt{\frac{A_w}{\pi}}. \quad (1)$$

The corresponding welding trace in Fig. 5 yields an equivalent radius r_{eq} of 0.056 mm.

To clarify the evolution of softening and melting phenomenon, three independent current-cycling experiments were carried out, each producing a representative state corresponding to points b, c, and d in Fig. 2. Prior to identifying point b, tests conducted at currents slightly below 144 A show no observable welding traces or measurable welding force, confirming that point b marks the minimum current for the onset of melting. At the maximum experimental current of 144 A, the experiment corresponding to point b yields a small melted area of 0.0015 mm^2 and a welding force of 0.16 N were obtained, indicating that the interface had not merely undergone softening but had also begun to exhibit non-negligible melting. In this paper, this current I_{fw} is defined as the current at which welding is first observed experimentally. In another experiment with an upper current limit of 224 A, the melted area increased to 0.0026 mm^2, and the corresponding welding force reached 0.58 N, indicating that local heating caused more pronounced interfacial melting. As plotted, the b-c stage in Fig. 2 is no longer the purely softening process described by Holm, but rather a stage in which softening and melting coexist. At point d in Fig. 2, the melted area reaches 0.0098 mm^2 and the welding force increases to 1.93 N. It is therefore reasonable to expect that further increases in current would lead to continued growth in both the melted area and the welding force.

B. Effect of Load Force on the R-U Characteristics

Fig. 6 presents the variations in ECR of $AgSnO_2In_2O_3$ material as a function of contact voltage drop and current under a current loading–unloading cycle at load forces of 0.02 N, 0.2 N, 0.5 N and 1 N. As expected, the initial ECR of 0.81 mΩ at 0.02 N decreases to 0.67 mΩ at 0.2 N, and further to 0.477 mΩ and 0.444 mΩ at 0.5 N and 1 N, respectively. Also, R-U curves show an overall decreasing trend as the load force increases.

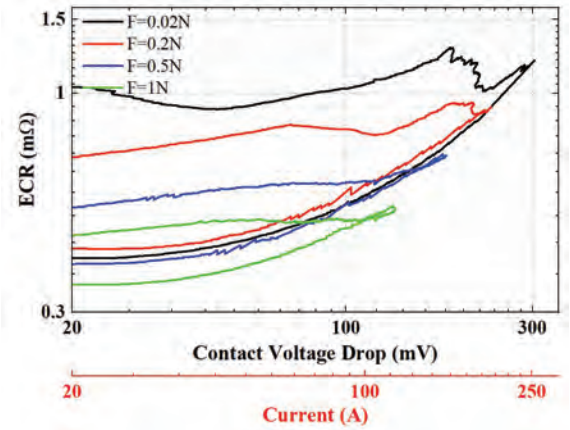


Fig. 6. Variations in ECR as a function of contact voltage drop and current during a current loading-unloading cycle under load forces of 0.02 N, 0.2 N, 0.5 N and 1 N.

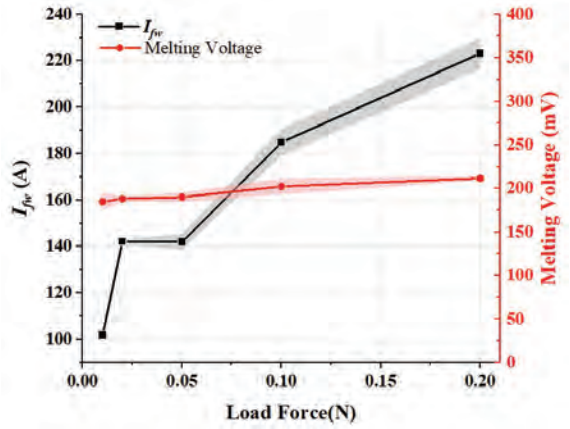


Fig. 7. Variations in I_{fw} and melting voltage as a function of load force.

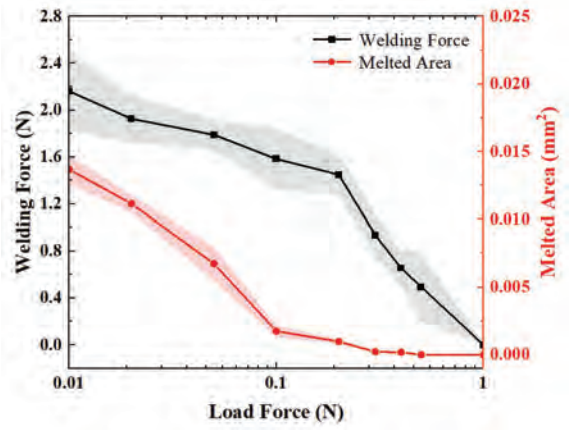


Fig. 8. Variations in welding force and melted area as a function of load force.

Fig. 7 shows the variations of I_{fw} and melting voltage as a function of load force. As illustrated, I_{fw} rises with increasing load force. Under higher force, a larger initial contact area reduces the attainable voltage drop and temperature rise at the same current, so a higher current is required to trigger this transition. At 0.5 N and 1 N, no clear onset is observed within the current of 250 A, suggesting that I_{fw} is higher. In contrast, the melting voltage remains relatively stable across different load forces, with an average value of approximately 195 mV. This indicates that the voltage at the onset of melting is an intrinsic property of the material and does not depend on the applied load condition.

Fig. 8 presents the variations of welding force and melted area as a function of load force. As the load force increases from 0.01 N to 1 N, the welding force shows a significant decrease with increasing load force consistent with the trend of I_{fw} in Fig. 7. This indicates that under lower forces, the smaller real contact area causes higher current density at asperities, which promotes melting and results in larger weld nuggets and higher welding forces. Welding traces show a similar decreasing tendency with the welding force. As the load force increases, the effective contact area is enlarged, thereby reducing the current density and thus restricting the extent of molten pool. It is worth noted that although the melted area changes with load force, the melting temperature remains essentially unchanged, indicating that load force primarily affects current distribution rather than the intrinsic melting condition.

C. Estimation of the Contact Spot Temperature

To determine the contact spot temperature, this study employs the commercial software COMSOL Multiphysics 6.3 and establishes a mechanical-electrical-thermal coupled model of the crossed rod configuration via the finite element method for simulation analysis. The contact pair material is $AgSnO_2$. In the simulation, the electrical conductivity, thermal conductivity, heat capacity, and density were treated as temperature dependent. In particular, the electrical conductivity of the contact material was expressed as

$$\sigma(T) = \frac{1}{\rho[1+\alpha(T-293.15)]} \tag{2}$$

where resistivity ρ = 2.7 μΩ·cm and temperature coefficient of resistance α = 0.0027 K^{-1}. By contrast, the Young's modulus ($E_1 = E_2$ = 83 GPa), Poisson's ratio ($v_1 = v_2$ = 0.34) and hardness (H = 125 HV) were treated as constants in the present model. The fixture material is a copper alloy, having a resistivity of 2.3 μΩ·cm and a temperature coefficient of resistance of 0.0026 K^{-1}.

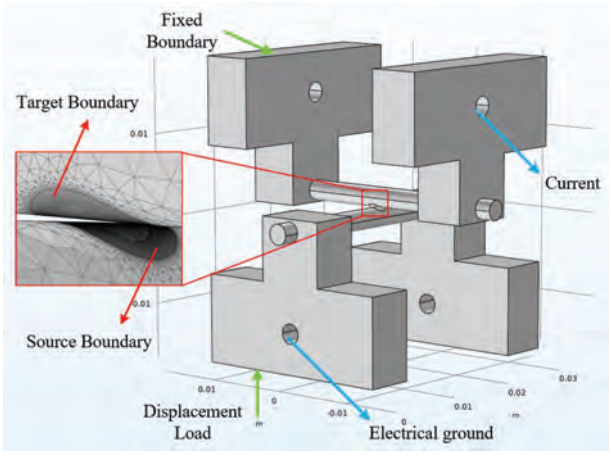
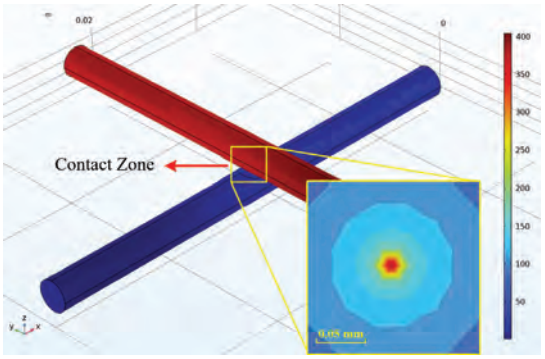
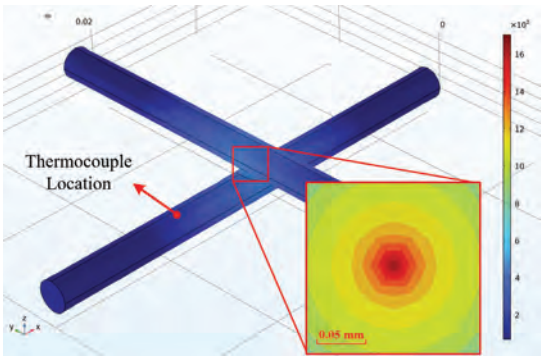


Fig. 9. Illustration of simulation model.



(a)



(b)

Fig. 10. Simulation results under a 250 A current load of the crossed-rod samples. (a) Contour map of electrical potential distribution. (b) Contour map of temperature distribution.

TABLE II. DEVIATION IN CONTACT RESISTANCE RESULTS

Resistivity ρ (μΩ·cm)	Temperature Coefficient of Resistance α (K^{-1})	Deviation of Minimum Contact Resistance Value (%)	Deviation of Maximum Contact Resistance Value (%)
2.7	0.0021	2.52	4.81
2.7	0.0024	1.43	7.30
2.7	0.0027	7.74	3.12

TABLE III. DEVIATION IN TEMPERATURE RESULTS

Convective Heat Transfer Coefficient h ($W \cdot m^{-2} \cdot K^{-1}$)	Deviation of Minimum Contact Resistance Value (%)	Deviation of Maximum Contact Resistance Value (%)	Deviation of Temperature at the Thermocouple Location (%)
2	1.42	9.76	0.62
5	12.13	8.91	74.35

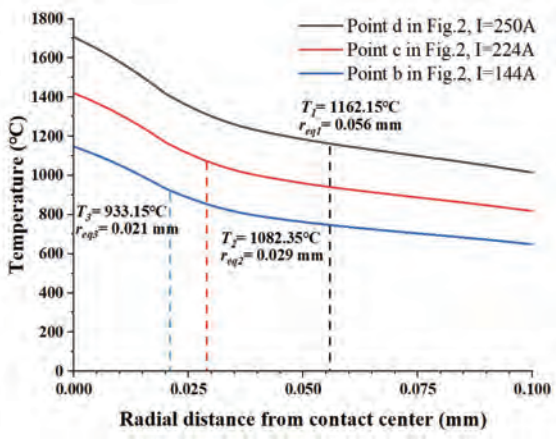
As shown in Fig. 9, the model consists of samples and fixtures. The lateral surfaces of two rods are defined as the contact pair. The entire geometry is meshed with 3D conventional tetrahedral elements. The contact surfaces are assigned an average roughness height of 0.12 μm and an average roughness slope of 1.05. In Solid Mechanics interface, the upper lateral surface of the stationary rod is fixed, and a prescribed displacement is applied to the lower lateral surface of the moving rod. For the electrical setup, a current increasing at a constant rate of 5 A/s is applied to one fixture, while the opposite fixture is grounded. In Heat Transfer in Solids interface, all outer surfaces are defined as heat dissipation surfaces with a convective heat transfer coefficient of 2 $W/(m^2 \cdot K)$. The multiphysics coupling is implemented using the Electromagnetic Heating module.

The simulation calculated the variations in ECR and voltage throughout this process and extracted the temperature at the experimental thermocouple location as well as at the center of the contact spot. Fig. 10 presents the contour map of the electrical potential distribution and the corresponding temperature distribution. In both figures, the zoomed-in view of results in the contact zone illustrates the distribution within approximately a 0.1 mm radial region around the contact center, enabling a detailed inspection of the highly localized gradients. Both the electric potential and the temperature are strongly concentrated at the contact center, where their values are markedly higher than those on the surrounding surface.

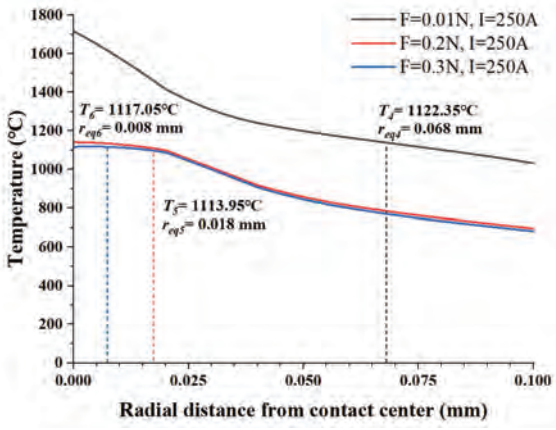
The simulation results for ECR are calculated as the ratio of the extracted contact voltage drop to the load current. The deviations between these simulation results and the experimental results, as calculated using (3), are presented in Table II.

$$Dev = \frac{|R_s - R_e|}{R_e} \times 100\% \tag{3}$$

where the Dev denotes the deviation between simulation result and experimental result, and R_s and R_e represent the simulation result and the experimental result, respectively.



(a)



(b)

Fig. 11. The simulated contact surface temperature profiles as a function of radial distance from contact center (a) of point b, c and d in Fig. 2 under load force of 0.02 N and (b) under load forces of 0.01 N, 0.2 N and 0.3 N.

A stepwise calibration strategy was adopted. The temperature coefficient of resistance α was first adjusted to reproduce the high-current behavior of the ECR curve, represented by the maximum contact resistance under a current of 250 A. As summarized in Table II, α = 0.0027 provides the most consistent match for the electrical response at high current. The convective heat transfer coefficient h was then calibrated by comparing the simulated temperature at the thermocouple location with the experimental measurement. As shown in Table III, h = 2 achieves the best thermal agreement, whereas a larger h leads to a larger deviation and affects the electrical metrics due to electro-thermal coupling. Consequently, the final parameter set used in this work is α = 0.0027, and h = 2.

Fig. 11 shows the simulated contact surface temperature profiles under different load currents and forces. The contact surface temperature is extracted along the centerline of the circular contact area, where the peak temperature corresponds to the contact center. The equivalent radius r_{eq} represents the location of the molten pool boundary on the contact surface. The distance along this centerline is treated as the radial distance from the contact center. By projecting r_{eq} onto this temperature profile, the temperature at the molten-pool boundary is obtained.

In Fig. 11(a), under a load force of 0.02 N, the equivalent radius r_{eq1} at point b (defined in Fig. 2) is 0.021 mm, and the corresponding molten-pool boundary temperature is 933.15 ℃. At point c, the equivalent radius r_{eq2} increases to 0.029 mm, while the boundary temperature becomes 1082.35 ℃. At point d, the equivalent radius r_{eq3} increases to 0.056 mm and the boundary temperature rises to 1162.15 ℃. The extracted boundary temperatures at point b to point d show a wide spread. This is mainly because the contact interface undergoes pronounced softening, local plastic deformation and contact area expansion from points b, c and d during loading, which changes both the peak temperature and the radial temperature gradient. Consequently, points b and c represent stages with lower current input and earlier softening/melting, where a fully developed molten pool is not ensured. In contrast, using the same reference stage (point d) for different load forces in Fig. 11(a) yields more consistent boundary temperatures.

As shown in Fig. 11(b), under a load force of 0.01 N, the equivalent radius r_{eq4} is 0.068 mm and the corresponding molten pool boundary temperature is 1122.35 ℃. When the load force increases to 0.2 N, r_{eq5} decreases to 0.018 mm, with a boundary temperature of 1113.95 ℃. At 0.3 N, the equivalent radius r_{eq6} further decreases to 0.008 mm, and the boundary temperature is 1117.05 ℃. Despite the differences in temperature distribution, the temperatures corresponding to the molten pool boundary exhibit only minor variations under different load forces. To obtain a representative melting temperature, the boundary temperature at point d (1162.15 ℃) in Fig. 11(a) is also included in the analysis. These four boundary temperatures yield an average value of approximately 1129 ℃ (with a standard deviation of 20 ℃), which is taken as the effective melting temperature of $AgSnO_2In_2O_3$.

This indicates that the temperature at the molten pool boundary remains nearly constant, regardless of the applied load force. This result shows that the melting temperature is an intrinsic material property and should not depend on external conditions such as load force or current level. Variations in load force primarily influence the heat generation and temperature gradient, while the melting temperature itself remains unchanged. Therefore, the proposed method, which determines the melting temperature by coupling experimentally measured molten spot size with numerically simulated temperature distribution, provides a reliable and physically consistent approach for evaluating the melting behavior of contact materials.

IV. Conclusion

This study systematically investigates the R-U characteristics and welding behavior of silver-based contact materials ($AgSnO_2In_2O_3$) under DC conditions, combining experiment and numerical simulation. The experiments demonstrate that softening and melting coexist during current increase, leading to a revised interpretation of the R-U curve. Accordingly, the current at which welding was first observed is identified by integrating evidence from the R-U characteristics, welding traces, and welding force, from which the melting voltage is inferred to be approximately 195 mV. The effects of load current and force were quantified, showing that higher current or lower load force produces greater current density, enlarged melted area, and higher welding force, whereas increasing load force shifts I_{fw} to a higher current level. Furthermore, an evaluation method is developed that links the equivalent melted area radius with simulated temperature fields to assess the current-carrying capacity of contact materials. Applying this approach, the melting temperature of $AgSnO_2In_2O_3$ is determined to be approximately 1129 °C.

Acknowledgment

The authors express their gratitude for the kind support provided by National Natural Science Foundation of China (Grant Number U2441286, 52377140).

References

[1] E. Walczuk, P. Borkowski, S. Księżarek, W. Missol, Z. Rdzawski and K. Durst, “Evaluation of Basic Electrical Parameters of Silver-Based Contact Materials of Different Chemical Composition and Manufacturing Technology,” in Proc. 56th IEEE Holm Conf. Electr. Contacts, Charleston, SC, USA, Oct. 2010, pp. 134–141.

[2] T. Muetzel and C. Hubrich, “Effect of Additives on the Switching Performance of Ag/SnO2 under AC-3 Conditions,” in Proc. 65th IEEE Holm Conf. Electr. Contacts, Milwaukee, WI, USA, Sept. 2019, pp. 128–134.

[3] Y. Mo, T. Zhang, G. Wang, C. Peng, and Z. Xv, “Simulation Study on Influence of Environmental Temperature on Current-Carrying Capacity of Automotive Electrical Connector,” SAE Int. J. Passeng. Cars – Mech. Syst., vol. 14, pp. 215–221, Dec. 2021.

[4] R. Holm, Electric Contacts: Theory and Applications, Springer-Verlag Berlin Heidelberg, 1967.

[5] R. S. Timsit, "The 'melting' voltage in electrical contacts," IEEE Trans. Compon., Hybrids, Manuf. Technol., vol. 14, pp. 285–292, Aug. 1990.

[6] A. Ksiazkiewicz, and J. Janiszewski, “Welding tendency for selected contact materials under different switching conditions”, Maint. Reliab., vol. 21, pp. 237–245, Mar. 2019.

[7] M. Kubler-Riedinger, J.-M. Bauchire, D. Hong, G. Déplaude, and P. Joyeux, “Electrical and Morphological Investigations of Electrical Contacts used in Low-Voltage Circuit-Breakers,” in Proc. 66th IEEE Holm Conf. Electr. Contacts and Intensive Course, San Antonio, TX, USA, Oct. 2020, pp. 115–122.

[8] S. N. Kharin, “An axisymmetric model of the heat and mass transfer in electrical contacts during short arc,” in Proc. 68th IEEE Holm Conf. Electr. Contacts, Seattle, WA, USA, Oct. 2023, pp. 1–5.

[9] P. G. Slade, “A Model to Determine the Current Level to Weld Closed Contacts,” IEEE Trans. Compon., Packag., Manuf. Technol., vol. 13, pp. 1202–1208, Aug. 2023.

[10] X. Zhang, and W. Ren, “Modeling and Experimental Verification of Material Welding Characteristics for Low Current Switching Devices,” Materials, vol. 13, p. 3666, Aug. 2020.

[11] N. Pandey, I. Jain, S. Reddy, and N. P. Gulhane, “Electro-thermal analysis of contact resistance,” AIP Conf. Proc., vol. 1966, p. 020017, 2018.

[12] P. Kacor, P. Bernat, T. Mlcak and L. Hrabovsky. “Realization of a Test Tool for Diagnosis of Contact Resistance and Measurement of Selected Types of Conductive Materials,” Sensors, vol. 23, p. 5867, June 2023.

The Role of Mechanical Stress in Electrical Contact elements during Short-Circuits

1st Toni Israel
R&D Contact Technology
Stäubli Electrical Connectors AG
Allschwil, Switzerland
t.israel@staubli.com

2nd Tom Kufner
R&D Contact Technology
Stäubli Electrical Connectors AG
Allschwil, Switzerland

3rd Philipp Strehler
R&D Numerical Simulation
Stäubli Electrical Connectors AG
Allschwil, Switzerland

4th Julian Angel Czajor
R&D Contact Technology
Stäubli Electrical Connectors AG
Allschwil, Switzerland

5th Michelle Pomsel
Dresden University of Technology
Chair of Components of Intelligent Energy Networks
Dresden, Germany

6th Christian Hildmann
Dresden University of Technology
Chair of Components of Intelligent Energy Networks
Dresden, Germany

7th Stephan Schlegel
Dresden University of Technology
Chair of Components of Intelligent Energy Networks
Dresden, Germany

***Abstract*— In high-current applications, such as gas-insulated switchgear and high-power charging devices, electrical contact elements for high power connectors face significant mechanical and electrical stress, especially during short-circuits. This study investigates physical mechanisms affecting these contact elements during DC short-circuits. The focus is the mechanical stress induced by deflection and its impact on connector performance. The influence of non-uniform contact resistance on current and temperature distribution during short-circuits is studied. Asymmetrical insertion, caused by electromagnetic forces or lateral forces, leads to variable deflection around the connector circumference and differential mechanical loads on individual contact louvers. Louvers with higher deflection exert higher contact force, resulting in lower contact resistance, leading to a higher current load and higher power loss during short circuits. Combined with increased mechanical stress due to deflection, these louvers experience a higher reduction in contact force under short-circuits. Finite element analysis quantifies mechanical stress within contact elements at different deflections. Experiments involving DC short-circuits lasting 0.3 s, 1 s and 4 s across three deflection levels highlight the relationship between mechanical stress and contact force reduction due to relaxation. By correlating experimental data with previous studies, this research enhances understanding of the short-circuit behavior of electrical contact elements in high-power applications.**

***Keywords*— connector, contact element, DC short-circuit**

I. Introduction

A. High Power Connectors with Contact elements

In AC and DC networks, a multitude of short circuit types, each with different characteristics and durations, can occur. Often, the short circuit current is 10…20 times higher than the rated current. High power connectors, for example used in gas insulated switchgear (GIS) or gas-insulated transmission lines (GIL), must safely carry this short circuit current. In contrast to other equipment, the contacts in connectors do have a significantly smaller cross section in comparison to the conductors. The contact elements have a smaller cross section than the surrounding conductors. This and the additional contact resistance results in higher power losses in the contacts when the connector is loaded with current. Thus, short-circuit tests on electrical equipment are an important subject of investigations and simulations. [1][2][3][4][5]

The specimen in this paper are two-component contact element for high demanding power contact solutions. The contact element strip consists of an adjustable number of periodic units (PU), with each PU consisting of two opposing individual louvers (Fig. 1). It can be used for connectors with a diameter from 40 mm to 300 mm (TABLE I.).

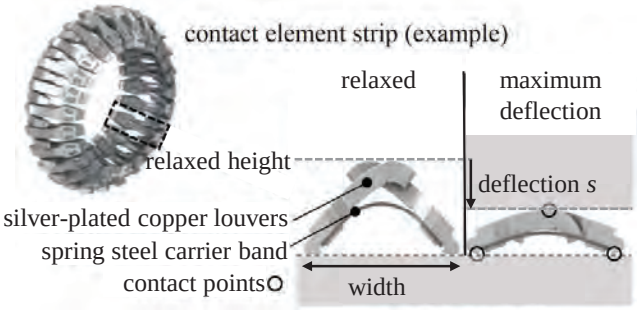


Fig. 1. Contact element strip ML-CUX (round) and lateral view (flat)

TABLE I. Technical Data of MULTILAM ML-CUX

Technical parameter	data for one periodic unit (PU)
Spacing / Periodic Unit	approx. 5 mm
Relaxed height	approx. 8.8 mm
Width	18,7 mm to 21 mm (depending on deflection)
Max. tolerance compensation	approx. 2.5 mm
Contact element resistance or transition resistance R_{PU}	105 µΩ
Max. rated current	120 A
Short circuit current I_{sc}	1600 A (4 s) to 2200 A (1 s)
Peak current	5600 A
Contact force (med. deflection)	14 N (typ.)
Max. continous operating temp.	105 °C

The higher the deflection, the higher the contact force, and the lower the contact resistance. The contact element resistance R_{PU} consists of the contact resistance of the lower and upper contact points, as well as material resistance of the louvers. Usually, only the sum is measurable and is referred to

as contact element resistance or transition resistance (Fig. 2). Medium deflection (s_{med} = 100 %) is considered the reference in this paper. The minimum deflection (s_{min} = 40 %) results in a lower contact force, and thus a higher contact element resistance. On the other end of the operating range, the contact force at maximum deflection (s_{max} = 156 %) is increased and the contact element resistance is the lowest (Fig. 2). The medium deflection provides the optimal balance of mechanical and electrical performance for most applications. The minimum deflection is configured to ensure sufficient contact force for safe contact behavior. The maximum deflection is a limit to keep plastic deformation of the contact element low.

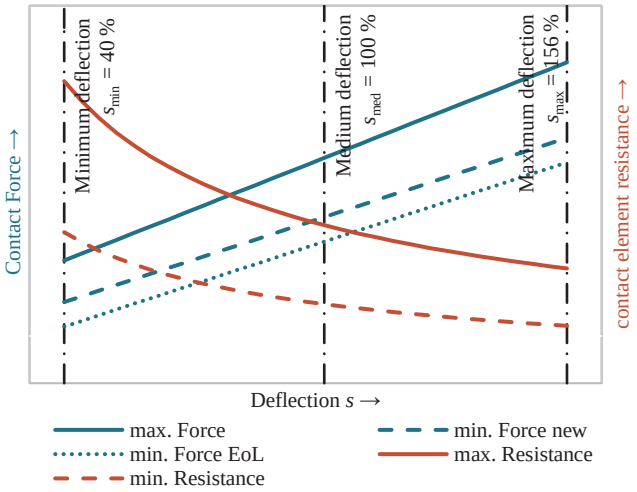


Fig. 2. Schematic force-deflection diagram and related contact element resistance in new condition and at End of Life (EoL)

B. *Short Circuit Load*

In a real-world application, both AC and DC short circuit I_{SC} might stress the contact element. In past investigations both AC and DC short circuits have been applied to the contact element [6]. It was found that the stress level of AC and DC short circuits is comparable at the same amperage and duration, with AC short circuit leading to slightly lower temperatures at the end of the short circuit due to the softening effects of the contact points during the peak currents, which reduce the contact resistance [1]. Since the thermal-mechanical impact of the short circuit on the contact element is the focus of this paper, tests in this investigation are done with DC circuit currents.

II. Considerations on the Stresses in Contact Elements during Asymmetric Deflection

For all design and test purposes of plug-in connectors, a center plugging is assumed. The geometry for contact element installation, plugs and sockets is designed in a way that minimizes off-center shifts. However, due to several mechanisms acting in unfavorable short circuit conditions, some amount of asymmetric stress on the contact element might happen:

- Electromagnetic forces on attached conductors
- Proximity effect (in AC applications)
- Contact elements used as tolerance compensation between connected devices and conductors
- Other lateral forces, such as the gravitational force on long conductors

Note that this asymmetry should be avoided in the respective application and is not covered by short circuit type testing according to standards. The electromagnetic effects are not a focus in this paper, as these have already been presented in previous publications [7], [8].

A. *Impact of Non-Uniform Plugging on Current Density*

Generally, the use of a contact element leads to a more homogeneous distribution of current between individual louvers compared to the conductor due to the higher electrical resistance of the contact elements in comparison to the bulk conductor material.

Off-center plugging leads to asymmetrical deflection of the contact elements within a plug-in connection. Asymmetrical deflection of the contact elements results in uneven contact element resistance distribution (Fig. 2). This influences the current density distribution in the contact elements (Fig. 3), as shown in [7] and [8] for a flat conductor arrangement of busbars connected by a fork connector (Fig. 3). The contact resistance was adjusted in this calculation so that the total contact element resistance R_{PU} matches the values at medium, minimum, and maximum deflection (see II.B). Evenly deflected contact elements result in an even distribution of contact element resistance between the contact elements of a plug-in connection and thus a symmetric distribution of current density between side a and side b (Fig. 3, left). If the contact elements are deflected asymmetrically, the current density distribution is no longer comparable for both contact elements (Fig. 3, right). On side a of the fork, the contact elements will be deflected more than on side b. This results in a higher mechanical stress in the louver, a higher contact force and a lower contact element resistance on the side a of the fork connector. On the other side b, the contact element resistance will be higher. The current density and the total current per louver are higher on the side with lower contact element resistance than on the side with higher contact element resistance. This local increase in current density can also increase thermal stress. To avoid overloading in the event of a short circuit, the short circuit withstand current of the contact elements is tested at different deflections (chapter IV).

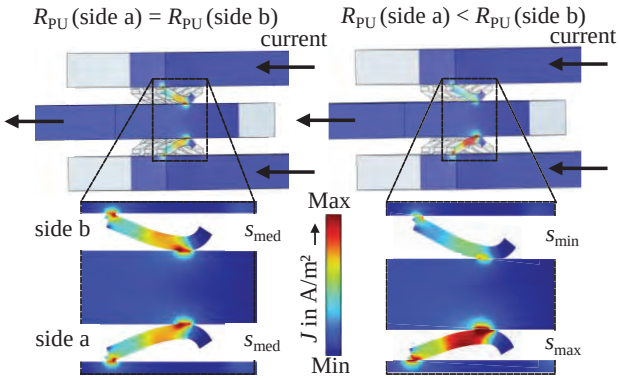


Fig. 3. Calculated current density distribution in a fork connector with symmetrically deflected contact elements (left), where the contact element resistance is symmetric R_{PU} (side a) = R_{PU} (side b) and unsymmetrically deflected contact elements (right), where the contact resistance is unsymmetric R_{PU} (side a) < R_{PU} (side b) for DC-load with I_{SC}, t = 4 s

B. *Implications for the Performance of Contact elements*

Off-center plugging leads to a higher contact force and lower contact element resistance on the side which

experiences a higher deflection (Fig. 2). This uneven resistance distribution leads to inhomogeneous current distribution and current load of individual louvers (chapter II.A). To account for different deflections, it is assumed that the voltage drop across all louvers must be the same during the short circuit, since they are connected in parallel.

$$dU = R_{\mathrm{PU_i}} \cdot I_{\mathrm{PU_i}} = \text{constant} \qquad (1)$$

A louver with maximum deflection will have a higher contact force per contact point, thus resulting in a lower contact element resistance (Fig. 2). Based on the force-gap diagrams of multiple contact elements of the shown type, the average contact element resistance at maximum deflection (s_{max}) is:

$$R_{\mathrm{PU}}(s_{\mathrm{max}}) = 0.8 \cdot R_{\mathrm{PU}}(s_{\mathrm{med}}) \qquad (2)$$

Likewise, the average contact element resistance at minimum deflection (s_{min}) is higher and typically:

$$R_{PU}(s_{\mathrm{min}}) = 1.8 \cdot R_{PU}(s_{\mathrm{med}}) \qquad (3)$$

III. SIMULATION OF MECHANICAL STRESS IN THE CONTACT ELEMENT

A. Model Setup

To gain insight into the mechanical stresses during deflection, a Finite Element (FE) simulation is made in ANSYS Mechanical. The geometry of half a periodic unit of the contact element, as shown in Fig. 4, is deflected between two plates to the mentioned deflections. The frictional contact behavior between the contact element and the conductors is defined with a specific value for the coefficient of friction (CoF) between lubricated silver surfaces. As the deflection is path-controlled, the CoF has no influence on the presented results. Additionally, displacement boundary conditions are applied so that the half-periodic unit in the model behaves like an infinitely long contact element. The materials are Cu-ETP for the louvers and high strength stainless steel for the carrier band. A bilinear elastic-plastic material model is used for both, with time and temperature effects being neglected.

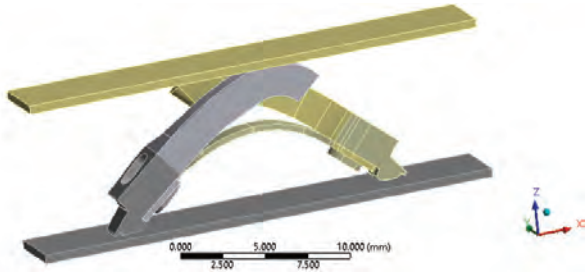


Fig. 4. Geometry for the Finite Element Simulation

B. Results

The Equivalent Stress (also called von Mises Stress) is given according to Equation (4) where σ_1, σ_1 and σ_3 are the principal stresses in the direction of the three spatial axes. The equivalent Stress allows a representation of the three-dimensional stress state as a positive scalar [9].

$$\sigma_{eq} = \sqrt{\frac{1}{2}[\,(\sigma_1 - \sigma_2)^2 + (\sigma_2 - \sigma_3)^2 + (\sigma_3 - \sigma_1)^2]} \qquad (4)$$

The distribution of the equivalent stresses at the corresponding deflection is shown in Fig. 5 (minimum deflection), Fig. 6 (medium deflection) and Fig. 7 (maximum deflection). The results show that the highest mechanical stresses occur in the carrier band between the junctions to the louvers, i.e., in the colored area visible in Fig. 5. Following evaluations are therefore focusing on this specific volume of interest.

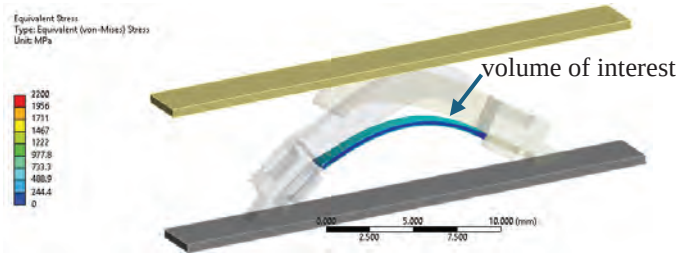


Fig. 5. Calculated equivalent stress in N/mm² at minimum deflection

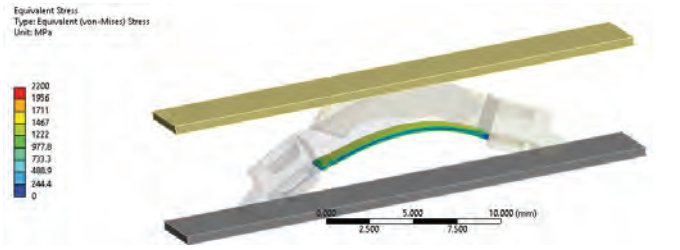


Fig. 6. Calculated equivalent stress in N/mm² at medium deflection

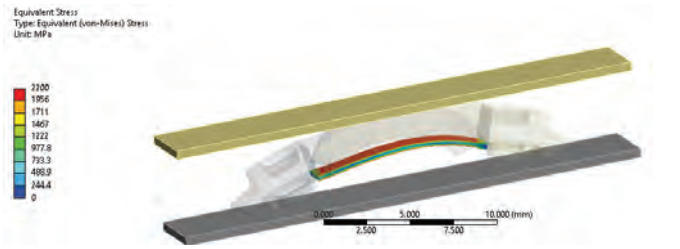


Fig. 7. Calculated equivalent stress in N/mm² at maximum deflection

To compare the stress states at the three different deflections, an average stress $\overline{\sigma}$ in the volume of interest is calculated according to Equation (5) where σ_i is the calculated equivalent stress in the finite element *i* and V_i is the volume of this element.

$$\overline{\sigma} = \frac{1}{V} \sum_i (\sigma_i \cdot V_i) \qquad (5)$$

TABLE II. shows an overview of the calculated average stresses $\overline{\sigma}$ for minimum, medium and maximum deflection. The higher the deflection, the higher the mechanical stress in the steel carrier band.

TABLE II. CALCULATED AVERAGE MECHANICAL STRESSES IN THE VOLUME OF INTEREST

	Calculated average mechanical stresses $\overline{\sigma}$		
	min. deflection	***medium deflection***	***max. deflection***
Carrier band	303 N/mm²	741 N/mm²	1115 N/mm²

IV. SHORT CIRCUIT TEST SETUP

A. Test stand

A short circuit test stand in Staubli's laboratory in Allschwil, Switzerland is used for the investigation. A DC short circuit generator (ACORE RG 2089 15kA/12V, three-phase IGBT bridge) supplies up to 15 kA current, which is fed

to the test samples. The samples are deflected with an apparatus in a material test machine (chapter IV.B) and the temperatures are measured with thermocouples and an infrared (IR) camera.

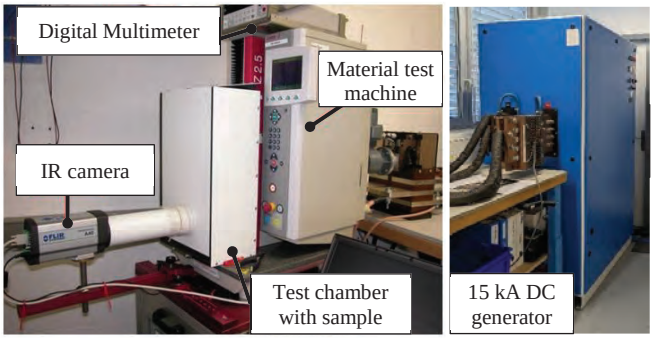


Fig. 8. DC short circuit test stand (left) with 15 kA DC generator (right)

TABLE III. TEST PROCEDURE

Step	Description	Measurement	Parameters
1	Before short circuit	contact element resistance and contact force in the operating range (Fig. 2)	R_{PU}, F_C for s_{min}, s_{med} and s_{max}
2	Adjust sample to test deflection		
3	Applying short circuit	Contact voltage and temperature	U_C, ϑ during short circuit
4	End of short circuit	Contact element resistance	R_{PU} at end of short circuit
5	Full separation of busbar from contact element (un-plugging)		
6	After short circuit	contact element resistance and contact force in the operating range (Fig. 2), inspection of contact points	R_{PU}, F_C for s_{min}, s_{med} and s_{max}

B. *Measurements*

Flat contact element strips are tested, because this allows a direct measurement of temperature, forces and contact voltage at a given deflection, which would not be possible in a concentric plug-in connector. All louvers are deflected by a specially developed apparatus in a material test machine (Zwick/Roell Z5, see Fig. 8 and Fig. 9). Only the middle three periodic units (PU) are stressed with short circuit current. This minimizes boundary effects, such as lower contact force on the louvers on either side of the contact element section. These boundary effects are taken into consideration when designing real-world round and flat applications.

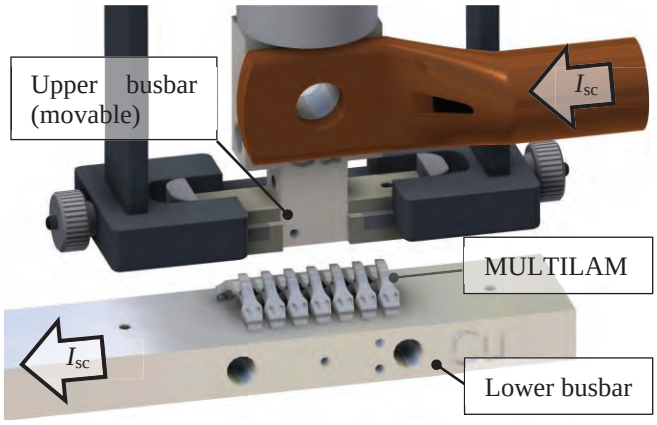


Fig. 9. Arrangement for application of mechanical deflection and short circuit current

Before and after the test, the contact elements are deflected from the minimum deflection up to the maximum deflection (TABLE III.). During this process, the contact force (Zwick) and contact voltage (DMM Keysight 34401A) is measured continuously and the contact element resistance R_{PU} is calculated. During the short circuit, the temperature distribution is measured with an IR camera FLIR Thermo Vision A40 as well as the contact voltage with the DMM. A total of 41 current-time pairs are tested (TABLE IV.), each with one to six contact element samples.

TABLE IV. TESTED SHORT CIRCUIT CURRENTS

SC duration t_{sc}	Tested short circuit current in kA for 1 periodic unit (PU)		
	min. deflection	*med. deflection*	*max. deflection*
0.3 s	1.2…1.8	2.5…3.1	2.6…2.8
1 s	1.0…1.4	2.2	1.7…2.3
4 s	0.9…1.3	1.6	1.1…1.5

V. SHORT CIRCUIT TEST RESULTS

Typical degradation effects of contact elements during short circuits have been examined in previous publications and include [1][6]:

1. Reduction of contact force and height
2. Welding of contact points
3. Increase of contact resistance
4. Blistering of the coating

The behavior of the contact elements during and after the short circuit depends on the deflection, which will be discussed in the following chapter. For each deflection and short circuit duration, the short circuit amperage was increased until a current threshold was reached, which caused a certain degradation (e.g. welding or excessive loss of contact force).

A. *Thermal Behavior*

The maximum temperature affects the damage mechanisms. Depending on the type of contact element, a maximum temperature of (250…350) °C is usually acceptable [11]. The higher the short circuit current is at a defined deflection, the higher the thermal load. The longer the short circuit lasts, the higher the maximum temperature. Depending on the current and the duration of the short circuit, maximum temperatures in the range (150…424 °C) have been measured. Both dependencies are shown exemplary for the maximum deflection s_{max} in Fig. 10. The scatter for a short circuit duration of 0.3 s is high, partly because the contact element is not heated up homogenously in this short period of time.

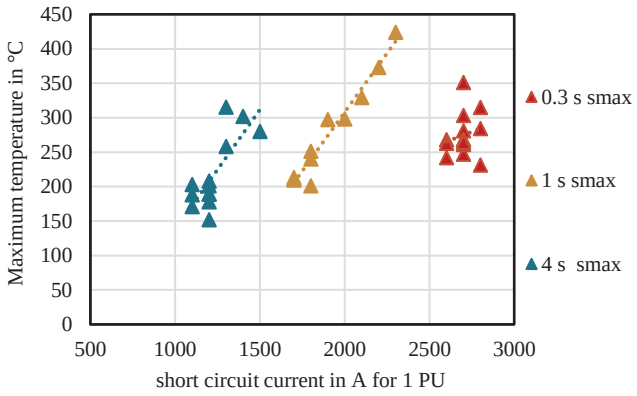


Fig. 10. Maximum temperature during the short circuit depending on short circuit duration and short circuit current for maximum deflection (s_{max})

With a given short circuit duration, the deflection affects the heating because a lower deflection results in a lower contact force and thus, a higher contact element resistance. This generates more heat, leading to similar maximum temperatures being reached at lower currents for the minimum deflection compared to medium and maximum deflection (Fig. 11). The difference in maximum temperatures for medium and maximum deflection is small, likely because the difference in resistance is low.

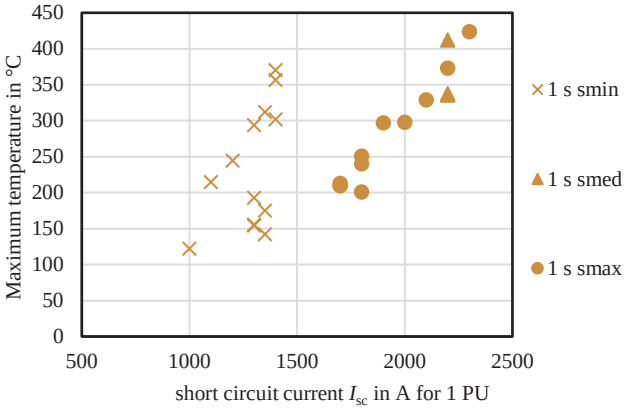


Fig. 11. Maximum temperature during the short circuit depending on deflection (s_{min}, s_{med}, s_{max}) and short circuit current

B. *Mechanical Behavior*

The contact force can decrease due to the short circuit and its thermal impact. For comparison, the contact forces at medium deflection are shown in Fig. 12, which were measured after the short circuit (TABLE III.). The actual short circuit was applied at the minimum, medium, or maximum deflection. After a short circuit is applied at minimum or medium deflection, the contact forces are comparatively high. The steel band is not significantly damaged by the short circuit. In a short circuit with a maximal deflected contact element, a considerable reduction in contact force is measurable. The higher the short circuit current, the lower the contact force after the short circuit. This can be explained by the higher mechanical stress at maximum deflection (chapter III), as the force reduction and plastic deformation in the steel band depends on temperature and mechanical stress. For the maximum deflection, the loss in contact force is the limiting factor.

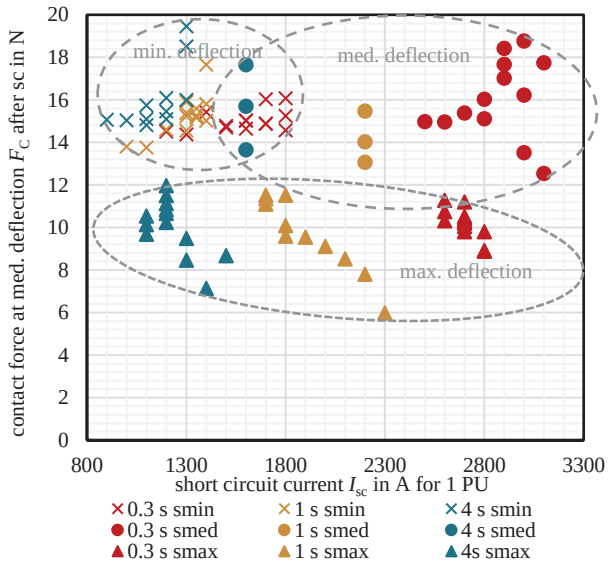


Fig. 12. Contact force at medium deflection depending on the short circuit duration and deflection (s_{min}, s_{med}, s_{max}) for 1 periodic unit (PU)

C. *Eletrical Behavior*

The contact and thus contact element resistance is directly dependent on the contact force. Particularly at low deflection, the contact element resistance responds sensitively to changes in the contact force (Fig. 2). Therefore, the following will examine the change in resistance at minimal deflection (Fig. 13).

$$dR = \frac{R_{PU,after\,sc} - R_{PU,before\,sc}}{R_{PU,before\,sc}} \cdot 100\,\% \qquad (6)$$

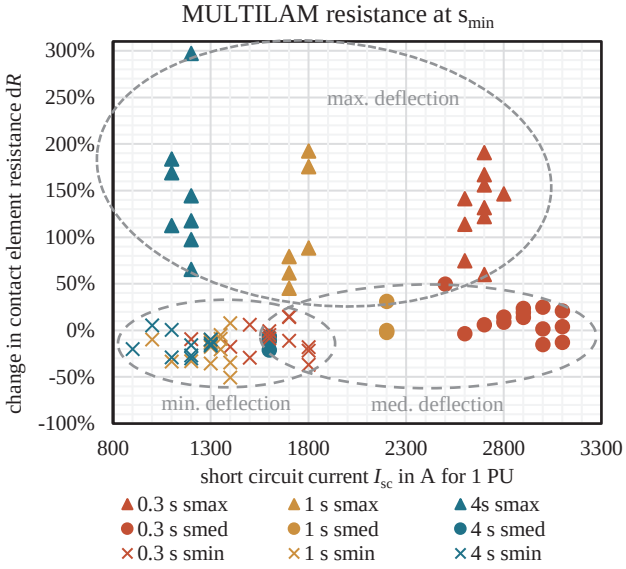


Fig. 13. Change in contact element resistance depending on the short circuit duration and deflection (s_{min}, s_{med}, s_{max}). Resistance was measured after separation and reconnecting at minimum deflection.

When the short circuit was applied to the contact element having a low or medium deflection, the change in contact element resistance after the short circuit and subsequent reconnecting is comparatively small. At relatively low current levels, the contact resistance tends to decrease due to softening processes in the coating, as detailly explained in [1][10][11][12], which explains the partial decrease in contact resistance. After a short circuit applied at maximum deflection, the contact force reduces significantly (Fig. 12). As a result, after re-connecting, the contact element resistance is comparably high, especially at the depicted minimal deflection.

The voltage drop over the contact element at the end of the short circuit dU_{max} correlates to the contact temperature, as shown by the Kohlrausch equation [1][2][10]. Since the voltages measured across the contact element includes the louver material resistance, this is a qualitative parameter. A clear correlation between the voltage drop and the deflection can be seen in (Fig. 14). The slope in the data sets corresponds to the heat generation in the contacts. The higher slope is attributed to higher contact voltages and temperatures. This shows that at minimum deflection, the contact element resistance is high, and more heat is generated at the same short circuit current level.

Slight welding was observed at minimal deflected contact elements above 1300 A for short circuit durations of 1 s and 4 s, as well as above 1700 A for a short circuit duration of 0.3 s. The cause is the high contact element resistance and the

exceeding of the welding voltage in the contacts. For the minimum deflection, the welding of contact points is the limiting factor.

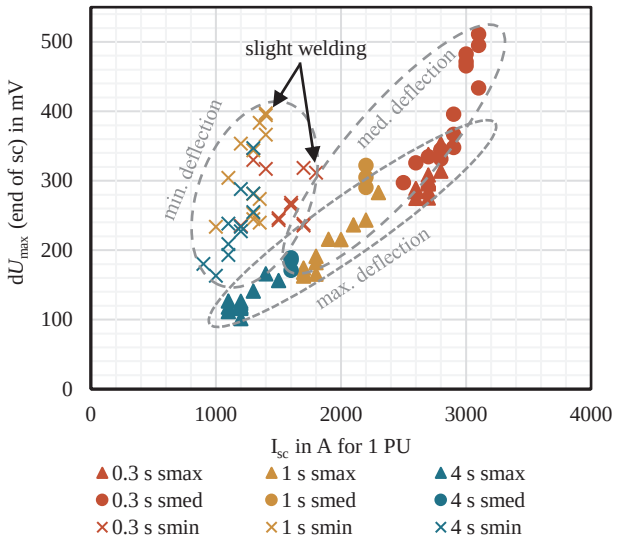


Fig. 14. Voltage drop across the CONTACT ELEMENT depending on deflection and short circuit duration

The results can be summarized as follows: With medium deflection, the highest short circuit currents are permissible for all short circuit durations. The damage is minimal. With minimum deflection, more heat is generated in the contacts due to the higher contact element resistance, and consequently, only lower short circuit currents can be permitted to prevent welding. With maximum deflection, the contact element resistance is low and less heat is generated in the contacts, but the higher mechanical stress in the steel carrier band causes a higher force reduction. Consequently, at maximum deflection, lower short circuit currents are achieved compared to medium deflection.

VI. Summary

The paper investigates the behavior of electrical contact elements, during DC short circuits in high-current applications such as gas-insulated switchgear and high-power charging systems. The study focuses on the mechanical stress induced by deflection and its impact on connector performance during and after short circuit load. Further, it analyzes how asymmetric deflection results in uneven contact element resistance distribution, affecting current density and temperature during short circuits.

DC short-circuit tests were conducted lasting 0.3 s, 1 s, and 4 s across three deflection levels (minimum, medium, and maximum) of the contact elements. These tests revealed that medium deflection allows for the highest possible short circuit currents with minimal damage. At low deflection, higher contact resistance generates more heat in the contacts, limiting short circuit currents to prevent welding. At maximum deflection, lower contact resistance leads to reduced heat generation in the contacts, but increased mechanical stress causes higher reduction in contact force, limiting short circuit currents compared to medium deflection.

Measures, such as guides or limiting the operating range in the design of high-current connectors, can be utilized to prevent asymmetrical deflection. The results indicate that the mechanical and thermal impacts of short circuits must be considered when designing contact systems, highlighting the importance of symmetrical deflection to ensure uniform mechanical stress, current density and temperature distribution.

References

[1] A. Zanetti and J.-C. Mauroux, “Current Carrying Capacity of an Earthing Switch for a Generator Circuit Breaker,” presented at the IEEE Holm Conference on Electrical Contacts, Albuquerque, 2018, p. 6.

[2] E. Walczuk, “Volt-Current Characteristics and Resistance of High Current Closing Contact During The Welding,” presented at the 8th International Conference on Electrical Contact Phenomena, Tokyo, 1976, p. 6.

[3] Xiangyu Guan, Naiqiu Shu, Bing Kang, and Minghan Zou, “Multiphysics Analysis of Plug-In Connector Under Steady and Short Circuit Conditions,” IEEE Transactions on Components, Packaging and Manufacturing Technology, vol. 5, no. 3, Art. no. 3, Mar. 2015, doi: 10.1109/TCPMT.2015.2396197.

[4] B. Novak, “Electrodynamic Forces in Circular Contact Systems,” presented at the 28th International Conference on Electric Contacts, Edinburgh, June 2016.

[5] B. Novák and L. Szabo, “Temperature rise of canted spring contacts during fault current,” in 2017 IEEE Holm Conference on Electrical Contacts, Sept. 2017, pp. 279–285. doi: 10.1109/HOLM.2017.8088100

[6] T. Israel, S. Schlegel, S. Großmann, T. Kufner, and G. Freudiger, “Recommendations for Testing the Short Circuit Behaviour of Power Plug-In Connectors.,” in International Conference on Electrical Contacts, Rohrschach, CH, 2021.

[7] M. Pomsel, T. Israel, C. Hildmann, S. Schlegel, and T. Kufner, “Electromagnetic modelling of current density distribution in power plug-in connectors,” in Proceedings of the 31th International Conference on Electric Contacts, Sapporo, Japan, June 2022.

[8] M. Pomsel, C. Hildmann, S. Schlegel, T. Kufner, and T. Israel, “Electric-Thermal Stresses of Three-Phase Loaded Plug-in Connectors Considering an Uneven Contact Resistance Distribution,” in 2024 IEEE 69th Holm Conference on Electrical Contacts (HOLM), Annapolis, MD, USA: IEEE, Oct. 2024, pp. 1–8. doi: 10.1109/HOLM56222.2024.10768386.

[9] “Ansys Mechanical User’s Guide,” pp. 2227-2228. ANSYS, Inc., Canonsburg, , July 2025.

[10] T. Israel, S. Schlegel, S. Großmann, T. Kufner, and G. Freudiger, “Zum elektrisch-thermisch-mechanischen Verhalten von silberbeschichteten Hochstrom-Steckverbindern – Das I²t-Kriterium bei der Kurzschlussprüfung von Steckverbindern Teil II,” in Elektrische und optische Verbindungstechnik 2019, Lemgo, 2019.

[11] T. Israel, S. Schlegel, S. Großmann, T. Kufner, and G. Freudiger, “The Influence of Peak Current and ECR on the Transmission Performance of High Power Connectors during Faults,” in 29th IEEE International Conference on Electrical Contacts, Albuquerque, 2018.

[12] C. Hildmann, T. Israel, S. Schlegel, and S. Großmann, “Recent Findings in the Long-term and Short Circuit Behavior of Power Connections and their Relevance for Testing,” in 2018 IEEE Holm Conference on Electrical Contacts, Oct. 2018, pp. 270–277. doi: 10.1109/HOLM.2018.8611751.

Author index

Last name	First name	Page
Aal	Alsayed Abdel	203
Acquadro	Julien	215
Alakayleh	Abdallah	96
Aldhahri	Nasser	255
Andersson	Peter	328
Andraud	Vincent	287
Baader	Marcel	197
Baeva	Margarita	146, 238
Ballentin	Jonas Karl Christian	146, 238
Baumann	Philippe	287
Benmouffok	Malyk	102, 107, 226, 244
Bjerrehorn	Erik	44
Blauth	Michael	203
Bluntzer	David	287
Boodhoo	Liam	255
Bösche	Dirk	13
Brauner	Thomas	55
Brochard	Frédéric	117
Brönnimann	Rolf	27, 176
Bruhn	Florian	187
Bull	Thomas	255
Buresch	Isabell	152
Buresch	Isabell	209
Cao	Weidong	19, 83, 232
Chang	Tso-Fu Mark	255
Chen	Yangfang	135
Chen	Xinzgan	232
Chen	Guoliang	274
Chen	Silei	293
Cinaroglu	Havva	221
Corfdir	Pierre	299
Cressault	Yann	226, 244
Crockett	Rowena	33
Czajor	Julian Angel	341
Cziumplik	David	13
Daradkeh	Saddam	96
Darques	Michael	226
Diaz	Jonas	27, 176
Dorraki	Naghme	55
Fairbrother	Andrew	33
Flowers	George	96
Flügel	Karen	13
Franke	Jörg	322
Fu	Yinghua	334
Gainey	Elizabeth	96
Gao	Caizhi	293
Gapenne	Paul	287
Gentsch	Dietmar	49
Giesbert	Fabian	197
Goetz	Stefan	187
Gonzalez	Diego	316
Gonzalez	Luz	316
Gortschacow	Sergey	55, 60
Gött	Gregor	60
Gouze	Camille	226, 244
Graskowski	Frank	55
Greiner	Felix	262
Gunnarsson	Lars	328
Hamasha	Sa’d	96
Hammam	Tag	328
Han	Ning	66
Hasegawa	Makoto	310
Hassler	Quentin	287

Last name	First name	Page
Hauch	Philipp	72
He	Yubin	274
Hellé	Arthur	117
Herrle	Thomas	90
Herrmann	Lorenz	27, 33, 176
Higuchi	Joji	255
Hildmann	Christian	341
Hilmert	Dirk	77
Hinz	Marius	13
Houzé	Frédéric	215
Huang	Yinfang	293
Hugon	Robert	117
Ihne	Thorsten	197, 322
Israel	Toni	341
Ivas	Toni	27, 176
Jacimovic	Jacim	27, 176
Källgren	Therese	328
Kammerl	Andreas	6.3
Kenel	Christoph	49, 299
Kiel	Frederik	77
Kilic	Muhammed	322
Köhne	Martin	249
Kubota	Yoshitaka	281
Kufner	Tom	341
Kupka	Daniel	111
Kupka	Daniel	6.3
Kurioka	Tomoyuki	255
Kurrat	Michael	13, 158
Laufer	Andreas	13
Lawall	Andreas	55
Leblanc	Thierry	215
Lehmann	Rene	268
Leterme	Willem	305
Li	Peng	66
Li	Xingwen	293
Liao	Yuchen	38
Liu	Yuxuan	83, 232
Logvinova	Marina	140
Magnusson	Niklas	44
Maoukouf	Abdelhak	123
Marcos	Grégory	117
McBride	John W.	255
McKeown	Siobhan	49
Methling	Ralf	60
Michler	Johann	176
Mingers	Frederik	305
Mitani	Kento	281
Moen	Olve	44
Mohammadhosein	Milad	129
Morimoto	Fumiko	281
Mukin	Roman	49
Mützel	Timo	221
Niayesh	Kaveh	129
Niggel	Vincent	33
Noël	Sophie	215
Oikawa	Reo	310
Oiwa	Haruto	310
Onishi	Yuna	310
Ostendorf	Frank	262
Oudot	Aurore Brézard	215
Perekopskiy	Sergey	164
Philipona	Rafael	176
Pomsel	Michelle	341
Porte	Maxime	268
Probst	Roman	77
Rault	Julien	49
Ren	Wanbin	38, 274, 334

Last name	First name	Page
Risch	Florian	197, 322
Rosebrock	Nils Wilm	158
Rufato	Raul Carreira	102, 107
Rumpelt	Patrick	72
Sachs	Sönke	209
Sachs	Soenke	262
Sangle	Akshata	187
Scheidegger	Philipp	27, 176
Scherr	Robert	170
Schlegel	Stephan	341
Schneider	Markus	287
Schweitzer	Patrick	102, 107, 123
Shang	Yi	83, 232
Slade	Paul G.	181
Sone	Masato	255
Song	Jian	77
Song	Zhenyang	135
Song	Jian	203
Strahl	Armin	111, 140
Strehler	Philipp	341
Suhling	Jeffrey	96
Sulmoni	Luca	299
Sun	Chang	334
Sütterlin	Patrick	299
Tahat	Sufyan	96
Tarman	Waad	96
Testé	Philippe	215
Thinn	Kristian Solheim	44
Thönnessen	Marco	72
Timsit	Roland S.	181
Tsuchiya	Yoshishige	255
Uhrlandt	Dirk	60, 146, 238
Valensi	Flavien	226
Van de Steen	Cyril	102, 107, 226, 244
Vinaisuratern	Punvinai	255
Vogel	Alexander	322
Volm	Dieter	90
Wan	Dai	135
Wang	Guanyu	19
Wang	Qian	19
Wang	Yong	66
Wang	Xiaojun	66
Wang	Qian	83, 232
Wei	Qinghong	135
West	Verena	305
Weuffel	Michael	72
Wielsch	Thomas	170
Wirthmann	Felix	197, 322
Yan	Xiaofang	135
Yang	Yan	255
Yao	Xiaofei	66
You	Yibo	135
Yu	Ming	66
Zhang	Boya	19
Zhang	Xingwen Li	19
Zhang	Yinnan	38
Zhang	Chao	38, 274, 334
Zhang	Zhaozi	293
Zhang	Yinnan	334
Zhao	Wanmeng	83
Zhong	Xu	83, 232
Zimmermann	Thomas	111
Zimmermann	Arthur	111
Zürrlein	Tobias	197

PROCEEDINGS OF THE 33RD INTERNATIONAL CONFERENCE ON ELECTRICAL CONTACTS

This publication contains papers from the the 33rd International Conference on Electrical Contacts (ICEC). Trondheim, Norway, 21–25 June, 2026.

The 56 contributions have authors from 15 countries and show the broad scope of the field, covering applications ranging from milliamp to kiloamp circuits, arcing and non-arcing contacts, stationary and sliding contacts, as well as both AC and DC applications.

The ICEC has become recognized as the principal worldwide meeting place for electrical contact scientists and engineers. It is a forum for the presentation and discussion of research on contact phenomena, developments in technologies and advancement in manufacture of a whole range of connective devices.

SINTEF Academic Press